# Université Blaise Pascal, Clermont-Ferrand, Ecole Doctorale des Sciences Fondamentales N° d'ordre : 433

Régis Doucelance

**Université Blaise Pascal, Clermont-Ferrand,**
**Ecole Doctorale des Sciences Fondamentales**

**N° d'ordre : 433**

**MEMOIRE PRESENTE EN VUE DE L'OBTENTION DE**
**L'HABILITATION A DIRIGER DES RECHERCHES**

par

**REGIS DOUCELANCE**

Maître de Conférences de l'Université Blaise Pascal
Laboratoire Magmas et Volcans, UMR UBP – CNRS – IRD

# SOURCE ET EVOLUTION DES EDIFICES VOLCANIQUES
# APPORT DES SYSTEMATIQUES ISOTOPIQUES RADIOGENIQUES

Soutenance le 19 janvier 2016, à Clermont-Ferrand

Devant le jury composé de :

| | | |
|---|---|---|
| Delphine Bosch | Directeur de recherche CNRS | Rapporteur |
| Pierre Cartigny | Directeur de recherche CNRS | Rapporteur |
| Catherine Chauvel | Directeur de recherche CNRS | Rapporteur |
| Hervé Martin | Professeur UBP | Examinateur |
| Pierre Schiano | Professeur UBP | Responsable tutélaire |
| Ivan Vlastélic | Chargé de recherche CNRS | Examinateur |

**SOMMAIRE**

Avant-propos et remerciements
Curriculum vitae

**Partie I – Synthèse des travaux de recherche**

1. NATURE ET TAILLE DES HETEROGENEITES MANTELLIQUES ..... 3
   - *L'archipel des Açores* ..... 8
   - *L'archipel du Cap Vert* ..... 9

2. LE RECYCLAGE DES MATERIELS DE SURFACE DANS LE MANTEAU VIA LA SUBDUCTION ..... 13
   - *Le volcan Merapi (Arc de la sonde, Indonésie)* ..... 13
   - *Le volcanisme de la Martinique (Arc des Petites Antilles)* ..... 14
   - *Les sanukitoïdes du Limpopo (Afrique du Sud)* ..... 15
   - *Le conglomérat basal du Groupe du Moodies (Afrique du Sud)* ..... 16

3. L'ORIGINE DES MAGMAS PARENTS DES CARBONATITES ..... 18

4. CONSTRUCTION / DESTRUCTION DES EDIFICES VOLCANIQUES ..... 21
   - *Le volcan Socompa (Zone Volcanique Centrale –CVZ- de l'arc andin, Chili)* ..... 21
   - *Le Mont Amarelo (Ile de Fogo, archipel du Cap Vert)* ..... 23

5. DEVELOPPEMENTS ANALYTIQUES ..... 27
   - *La mesure de haute précision des rapports isotopiques de plomb par TIMS* ..... 27
   - *La correction de l'effet de ''queue de pic'' (ou tailing)* ..... 27
   - *La correction du fractionnement de masse instrumental du Re par dopage W* ..... 29

6. PROJETS EN COURS ..... 31
   - *Détermination expérimentale des coefficients de partage des éléments U-Th-Pb lors du recyclage par subduction de croûte océanique carbonatée* ..... 31
   - *Reconstitution de l'histoire magmatique du Socompa à partir des produits d'avalanche de débris* ... 31
   - *Evolution magmatique et instabilité des volcans boucliers océaniques* ..... 33

7. PERSPECTIVES ..... 34
   - *Apport de la systématique Re/Os quant à la nature (et à l'évolution ?) de la source des carbonatites* ..... 34
   - *Dynamique interne des avalanches de débris* ..... 36
   - *Apport de la systématique La/Ce quant à l'origine du pôle mantellique EM1* ..... 37

8. REFERENCES BIBLIOGRAPHIQUES ..... 38

Liste de toutes les publications ..... 47

Liste des travaux présentés

*- Nature et taille des hétérogénéités mantelliques*

*Moreira, Doucelance, Kurz, Dupré et Allègre (1999) Helium and lead isotope geochemistry in the Azores Archipelago. Earth and Planetary Science Letters 169, 189-205* ..... 51

*Doucelance, Escrig, Moreira, Gariépy et Kurz (2003) Pb-Sr-He isotope and trace element geochemistry of the Cape Verde Archipelago. Geochimica et Cosmochimica Acta 67, 3717-3733* ..... 69

*Escrig, Doucelance, Moreira et Allègre (2005) Os isotope systematics in Fogo basalts: evidence for lower continental crust residing in the oceanic lithosphere beneath the Cape Verde Islands. Chemical Geology 219, 93-113* ..... 87

*Millet, Doucelance, Schiano, David et Bosq (2008) Mantle plume heterogeneity versus shallow-level interactions: A case study, the São Nicolau Island, Cape Verde archipelago. Journal of Volcanology and Geothermal Research 176, 265-276* ..... 109

*Millet, Doucelance, Baker et Schiano (2009) Reconsidering the origins of isotopic variations in Ocean Island Basalts ; Insights from fine-scale study of São Jorge Island, Azores archipelago. Chemical Geology 265, 289-302* ..... 121

*Mourão, Mata, Doucelance, Madeira, Millet et Moreira (2012) Geochemical temporal evolution of Brava Island magmatism: constraints on the variability of Cape Verde mantle sources and on carbonatite-silicate magmas link. Chemical Geology 334, 44-61* ..... 135

*- Le recyclage des matériels de surface dans le manteau via la subduction*

*Debaille, Doucelance, Weis et Schiano (2006) Multi-stage mixing in subduction zones : Application to Merapi volcano (Java island, Sunda arc). Geochimica et Cosmochimica Acta 70, 723-741* ..... 153

*Laurent, Martin, Doucelance, Moyen et Paquette (2011) Geochemistry and petrogenesis of high-K "sanukitoids" from the Bulai pluton, Central Limpopo Belt, South Africa: Implications for geodynamic changes at the Archaean-Proterozoic boundary. Lithos 123, 73-91* ..... 173

*Sanchez-Garrido, Stevens, Armstrong, Moyen, Martin et Doucelance (2011) Diversity in Earth's early felsic crust: Paleoarchean peraluminous granites of the Barberton Greenstone Belt. Geology 39, 963-966* ..... 193

*Laurent, Doucelance, Martin et Moyen (2013a) Differentiation of the late-Archaean sanukitoid series and some implications for crustal growth: insights from geochemical modelling on the Bulai pluton, Central Limpopo Belt, South Africa. Precambrian Research 227, 186-203* ..... 197

*Laurent, Paquette, Martin, Doucelance et Moyen (2013b) LA-ICP-MS dating of zircons from Meso- and Neoarchaean granitoids of the Pietersburg block (South Africa): crustal evolution at the northern margin of the Kaapvaal craton. Precambrian Research 230, 209-226* ..... 215

*Laurent, Rapopo, Stevens, Moyen, Martin, Doucelance et Bosq (2014a) Contrasting petrogenesis of Mg-K and Fe-K granitoids and implications for post-collisional magmatism: case study from the late-Archaean Matok pluton (Pietersburg block, South Africa), Lithos 196-197, 131-149* ..... 233

*Laurent, Martin, Moyen et Doucelance (2014b) The diversity and evolution of late-Archean granitoids: evidence for the onset of "modern-style" plate tectonics between 3.0 and 2.5 Ga. Lithos 205, 208-235* ..... 253

*Bellot, Boyet, Doucelance, Pin, Chauvel et Auclair (2015) Ce isotope systematics of island arc lavas from the Lesser Antilles. Geochimica et Cosmochimica Acta 168, 261-279* ..... 281

*- L'origine des magmas parents des carbonatites*

*Mourão, Mata, Doucelance, Madeira, Brum da Silveira, Silva et Moreira (2010) Quaternary extrusive calciocarbonatite volcanism on Brava Island (Cape Verde): A nephelinite-carbonatite immiscibility product. Journal of African Earth Science 56, 59-74* ..... 301

*Mata, Moreira, Doucelance Ader et Silva (2010) Noble gases and carbon isotopic signatures of Cape Verde oceanic carbonatites: implications for carbon provenance. Earth and Planetary Science Letters 291, 70-83* .....317

*Doucelance, Hammouda, Moreira et Martins (2010) Geochemical constraints on depth of origin of oceanic carbonatites: the Cape Verde case. Geochimica et Cosmochimica Acta 74, 7261-7282* .....331

*Mourão, Mata, Doucelance, Madeira, Millet et Moreira (2012) Geochemical temporal evolution of Brava Island magmatism: constraints on the variability of Cape Verde mantle sources and on carbonatite-silicate magmas link. Chemical Geology 334* .....135

*Doucelance, Bellot, Boyet, Hammouda et Bosq (2014a) What do cerium isotopes tell us about the deep source of oceanic cabonatites. Earth and Planetary Science Letters 407, 175-186*.....353

*- Construction / destruction des édifices volcaniques*

*Doucelance, Kelfoun, Labazuy et Bosq (2014) Geochemical insights into the internal dynamics of debris avalanches. A case study: the Socompa avalanche, Chile. Geochemistry, Geophysics, Geosystems 15, 2282-2300* .....365

*- Développements analytiques*

*Doucelance et Manhès (2001) Reevaluation of precise lead isotope measurements by thermal ionization mass spectrometry : comparison with determinations by plasma source mass spectrometry. Chemical Geology 176, 361-377* .....385

*Deschamps, Doucelance, Ghaleb et Michelot (2003) Further investigations on optimized tall correction and high-precision measurement of Uranium isotopic ratios using Multi-Collector ICP-MS. Chemical Geology 201, 141-160*...403

*Poirier et Doucelance (2009) Effective Correction of Mass Bias for Rhenium Measurements by MC-ICP-MS. Geostandards and Geoanalytical Research 33, 195-204*.....423

*Bellot, Boyet, Doucelance, Pin, Chauvel et Auclair (2015) Ce isotope systematics of island arc lavas from the Lesser Antilles. Geochimica et Cosmochimica Acta 168, 261-279*.....281

Ce mémoire présente mes activités de recherche depuis 1996, année pendant laquelle j'ai débuté ma thèse de doctorat à l'Institut de Physique du Globe de Paris. Celles-ci sont regroupées en 5 grands thèmes : 1) nature et taille des hétérogénéités mantelliques; 2) recyclage des matériels de surface dans le manteau via la subduction; 3) origine des magmas parents des carbonatites; 4) construction / destruction des édifices volcaniques; et 5) développements analytiques. Les différentes études liées à chacun de ces thèmes sont résumées brièvement, et seuls les 'grands' résultats sont exposés. Pour plus de détail, les papiers publiés sont regroupés à la fin du mémoire.

L'ordre dans lequel ces thèmes de recherche apparaissent n'a pas de réalité chronologique stricte, le sujet de ma thèse s'inscrivant, par exemple, dans les thèmes ''nature et taille des hétérogénéités mantelliques'' et ''développements analytiques''. Pour autant, certains des thèmes/études présentés ici sont très complémentaires les uns des autres. Ainsi c'est la connaissance des composants présents dans la source des basaltes du Cap Vert, et notamment la conclusion que le pôle appauvri correspond à la lithosphère capverdienne, qui permet de proposer le modèle génétique développé pour les carbonatites océaniques du Cap Vert et des Canaries. De même, c'est encore la connaissance de l'histoire géochimique à long terme de l'archipel du Cap Vert qui permet de discuter les variations observées de part et d'autre de la date d'effondrement du Mont Amarelo (Fogo) et de savoir si elles traduisent réellement l'effet (ou l'annonce) de cet effondrement.
Certaines de mes publications ne sont pas discutées dans ce mémoire. Vouloir tout lié aurait été par trop artificiel, et ces études sont donc uniquement citées dans la liste des publications.

Le style parfois un peu personnel de la rédaction est également à nuancer. Plusieurs des résultats présentés dans ce mémoire résultent en effet de discussions, projets en commun et/ou encadrements d'étudiants au niveau master et thèse. Par conséquent, l'utilisation du 'je' traduit plutôt le caractère leader dans telle ou telle étude qu'un travail purement personnel, qui, à mon avis, n'aurait pas abouti. C'est une évidence, mais c'est la confrontation des idées qui permet d'avancer.

Je tiens donc à remercier l'ensemble des collègues et des étudiants (non seulement les étudiants que j'ai encadrés, mais aussi les étudiants rencontrés au cours des enseignements), passés et actuels, qui, quelque part, ont contribué à ce travail ; ils se reconnaitront, à coup sur. J'aurais une pensée plus particulière pour Eric Humler, Claude Allègre, Gérard Manhès et Clément Gariépy, responsable de stage de DEA, directeurs de thèse et superviseur de post-doctorat, qui, chacun avec son style (et ce sont des styles extrêmement différents !), ont fait que j'ai eu envie de devenir enseignant-chercheur.

Enfin, je tiens à remercier l'ensemble des membres du jury, D. Bosch, P. Cartigny et C. Chauvel, rapporteurs, H. Martin et I. Vlastélic, examinateurs, et P. Schiano, responsable tutélaire, pour avoir accepté d'évaluer ce travail.

*Expérience*

*2003-* Maître de conférences, Université Blaise Pascal.

*2002-2003* Attaché Temporaire d'Enseignement et de Recherche (ATER), Université Blaise Pascal.

*2000-2002* Assistant de recherche (post-doctorat), Geotop (Centre de recherche en Géochimie isotopique et en Géochronologie), Université du Québec à Montréal (UQAM).

*1998-1999* Attaché Temporaire d'Enseignement et de Recherche (ATER), Université Denis Diderot.

*1996-1999* Thèse de l'Université au Laboratoire de Géochimie et Cosmochimie (Institut de Physique du Globe de Paris).

*1994-1996* Volontaire à l'aide technique au Bureau de Recherches Géologiques et Minières (BRGM) de Guyane.

*Formation*

*1996-1999* Doctorat de Géochimie fondamentale et appliquée.

Mention Très Honorable avec Félicitations.

Sujet: Mesure des compositions isotopiques de plomb par spectrométrie de masse à thermo-ionisation: Méthode du ''double spike''; Géochimie des panaches mantelliques: Approches locale et globale (Direction Claude Jean Allègre et Gérard Manhès).

*1993-1994* DEA de Géochimie fondamentale et appliquée; Université Denis Diderot.

Sujet: Etude des relations entre hétérogénéités isotopiques et hétérogénéités sismiques dans le manteau (encadrement Eric Humler).

*Bourses, primes*

*2012-2015* Prime d'Excellence Scientifique.

*2004-2008* Prime d'Encadrement Doctoral et de Recherche.

*2001-2002* Bourse post-doctorale Lavoisier, Ministère des Affaires Etrangères.

*2000-2001* Bourse d'excellence de la Fondation de l'Université du Québec à Montréal, post-doctorat.

*Responsabilités administratives*

*2012-* Membre titulaire de la commission préparatoire au recrutement des enseignants-chercheurs, section 35/36.

*2011-* Membre de la commission informatique du LMV, représentant l'équipe de géochimie.

*2003-2007* Vice-président rang B de la commission de spécialistes (CSE) section 35/36 de l'université Blaise Pascal de Clermont-Ferrand.

*Responsabilités pédagogiques*

*2012-* Responsable du Master 1 des Sciences de la Terre, Université Blaise Pascal.

*2010-2001* Représentant de l'équipe de Géochimie pour le Jury de Master 2 ''Magmas et Volcans'', Universités Clermont-Ferrand II - Blaise Pascal, Saint Etienne - Jean Monnet, et Réunion.

*2005-2006* Président de jury de baccalauréat, section S, Clermont-Ferrand.

*2004* Président de jury de baccalauréat, section ES, Moulins.

Responsable du groupe ad hoc Parcours ''géochimie'' pour le passage au LMD (Licence/Master/Doctorat)

*Responsabilités scientifiques*

*2014* Responsable du projet Carbone primordial vs. carbone recyclé dans la source des carbonatites: apport de la systématique La/Ce, Programme INSU-CNRS SYStème TERre, processus et couplages (SYSTER 2014); financement: 4250€.

Membre du projet Apport de la systématique La-Ce sur le recyclage de matériel en zone de subduction: étude des arcs intra-océaniques Izu-Bonin et Mariannes (Porteur Maud Boyet), Programme INSU-CNRS SYStème TERre, processus et couplages (SYSTER 2014); financement: 4250€.

*2013* Responsable du projet Systématique $^{138}$La-$^{138}$Ce appliquée aux carbonatites océaniques: nouvelles contraintes sur l'origine du carbone de carbonatites, Programme INSU-CNRS SYStème TERre, processus et couplages (SYSTER 2013); financement: 3400€.

Membre du projet La subduction d'un plateau océanique : effet sur la magmatogenèse (Porteur Hervé Martin), programme INSU-Actions de recherche LMV; financement: 2500€.

*2012* Jury de recrutement d'un ingénieur de recherche en spectrométrie de masse (concours IRG Ingénieur en conception et développement en expérimentation, CEREGE, Université Aix-Marseille).

*2011* Evaluation de projet SNSF blanc (Swiss National Science Foundation, Div. Mathematics, Physical and Engineering Sciences).

*2009* Evaluation de projet FCT blanc (Portuguese Foundation for Science and Technology, Earth and Space Sciences area).

Responsable du projet Utilisation des isotopes de l'Os comme traceurs du recyclage dans les carbonatites, Action incitative INSU-CNRS Sciences de la Terre; financement: 9000€.

*2008* Evaluation de projet ANR blanc Sciences de l'univers et géo-environnement.

*2007* Evaluation de projet INSU-CNRS Structure, Evolution et Dynamique de l'Intérieur de la Terre 2007 (SEDIT 2007).

Responsable du volet n°2 - Analyses géochimiques de l'avalanche et couplage avec sa dynamique du projet Processus de déstabilisation, de fragmentation des reliefs et modalités de mise en place des avalanches de débris (Porteur Karim Kelfoun), programme INSU-CNRS Reliefs de la Terre 2007 (RELIEFS 2007); financement: 2x10000€.

Membre du projet Les magmas juvénile potassiques archéens : marqueurs de l'évolution du manteau terrestre lors de la formation de la croûte continentale primitive (Porteur Hervé Martin), programme INSU-CNRS Structure, Evolution et Dynamique de l'Intérieur de la Terre 2007 (SEDIT 2007); financement: 5000€.

*2005-2006* Responsable du projet Géochimie des panaches océaniques et hétérogénéité du manteau terrestre; Archipels du Cap Vert et des Açores, programme INSU-CNRS Dynamique et Evolution de la Terre Interne 2005-2006 (DyETI 2005-2006); financement: 4500€.

*2004* Evaluation de projet INSU-CNRS Dynamique et Evolution de la Terre Interne 2004 (DyETI 2004).

Responsable technique et représentant du groupe Géodynamique chimique pour le projet ISOGEME (ISOtope GEochemistry MEssages) d'acquisition d'un spectromètre de masse à thermo-ionisation de dernière génération au laboratoire Magmas et Volcans, financements INSU-CNRS, région Auvergne et fonds FEDER: 700000€.

Responsable du projet Géochimie des panaches océaniques et hétérogénéite du manteau terrestre; Archipels du Cap Vert, des Açores et alignement de la Cameroon Line, programme INSU-CNRS Dynamique et Evolution de la Terre Interne 2004 (DyETI 2004); financement: 5000€.

Responsable du projet Géochimie des panaches océaniques et hétérogénéite du manteau terrestre; Archipels du Cap Vert, des Açores et alignement de la Cameroon Line; Apport des isotopes du plomb mesurés par la technique du Double Spike, programme BQR, Université Blaise Pascal, Clermont-Ferrand; financement: 4000€.

*2003* Responsable du projet Géochimie des panaches mantelliques; Archipel du Cap Vert, programme INSU-CNRS Dynamique et Evolution de la Terre Interne 2003 (DyETI 2003); financement: 6000€.

Membre du projet U, Th et K dans le noyau ? Etudes expérimentale et théorique: conséquences sur le flux de chaleur actuel et passé du noyau terrestre, programme INSU-CNRS Dynamique et Evolution de la Terre Interne 2003 (DyETI 2003), Responsable Valérie Malavergne.

*Encadrements scientifiques (Encadrement/co-encadrement de 7 doctorants et 11 masters)*

*Thèse*

Mélodie-Neige Cornu (2014- ), Evolution magmatique et instabilité des volcans boucliers océaniques (co-direction Raphaël Paris et Patrick Bachelery).

Nina Bellot (2012–2016), Développement du système isotopique La-Ce : application aux laves d'arc (co-direction Maud Boyet).

Oscar Laurent (2009–2012), Les changements géodynamiques à la transition Archéen-Protérozoïque (co-direction Hervé Martin).

Cyntia Mourão, doctorante au centre de géologie de Lisbonne (direction João Mata); Initiation à la géochimie isotopique Sr-Nd-Pb et application au volcanisme de l'île de Brava, archipel du Cap Vert (2008–2013).

Cynthia Sanchez-Garrido (2006–2011), Les magmas potassiques juvéniles archéens: marqueurs de l'évolution du manteau terrestre lors de la formation de la croûte continentale primitive; co-tutelle UBP – Université de Stellenbosch, Afrique du Sud (co-direction Hervé Martin, Jean-François Moyen et Gary Stevens).

Marc-Alban Millet (2004–2007), Géochimie des panaches océaniques et échelle d'hétérogénéités du manteau terrestre. Archipels du Cap Vert et des Açores (co-direction Pierre Schiano).

Vinciane Debaille (2002–2005), Etude isotopique (Sr, Nd, Pb) des variations spatiales et temporelles des basaltes océaniques (co-direction Pierre Schiano).

*Master 2*

Mélodie-Neige Cornu (2013-2014), Evolution magmatique et instabilité d'un volcan bouclier océanique: Fogo, Cap Vert (co-direction Raphaël Paris et Patrick Bachelery).

Oscar Laurent (2008-2009), Les changements géodynamiques à la transition Archéen-Protérozoïque: exemple de la pétrogenèse du pluton de Bulai, Ceinture du Limpopo, Afrique du Sud (co-direction Hervé Martin).

Cynthia Sanchez-Garrido (2005-2006), Les mécanismes magmatiques de genèse de la croûte continentale primitive. Exemple des terrain méso-Archéen de la région de Barberton, Afrique du sud (co-direction Hervé Martin).

Nicolas Vinet (2004-2005), Interaction entre basalte et encaissant pendant le magmatisme intra-plaque continental: contraintes isotopiques et élémentaires (co-direction Pierre Schiano).

Marc-Alban Millet (2003-2004), Utilisation des rapports d'éléments traces en tant que traceurs de source: exemple de l'archipel du Cap Vert.

*Master 1*

Antoine Delvoye (2014), Étude géochimique du dépôt de l'avalanche secondaire du volcan Socompa, Chili (co-direction Karim Kelfoun).

Morgan Chevreuil (2014), Datation Sm/Nd et caractérisation de la source des carbonatites de Spitskop, Afrique du Sud (co-direction Maud Boyet).

Mélodie-Neige Cornu (2013), Datation Sm/Nd et U/Pb et caractérisation de la source des carbonatites de Phalaborwa (co-direction Valérie Bosse).

Guillaume Jacques (2007), Compositions isotopiques de Sr et de Nd des basaltes de l'île de Sal, archipel du Cap Vert.

Pierre Bonnand (2006), Protocole d'analyse des éléments majeurs et quelques traces des chondrites ordinaires (co-direction André Poirier).

Marc Ulrich (2005), Is mantle convection chaotic? - analyse fractale de la segmentation des rides médio-océaniques (co-direction Kenneth Koga).

*Enseignements*

Géochimie isotopique, Géochronologie, Géodynamique chimique, Informatique, Modélisation numérique, Cartographie structurale, Cartographie numérique, SIG.

Partie I

# SYNTHESE DES TRAVAUX DE RECHERCHE

Mes travaux de recherche s'inscrivent dans deux grandes thématiques. D'une part, la géodynamique chimique, avec pour principaux sujets d'étude (1) la nature et la taille des hétérogénéités du manteau terrestre, (2) le recyclage des matériels de surface dans la manteau via la subduction, et (3) l'origine des magmas parents des carbonatites ; et d'autre part, la construction/destruction des édifices volcaniques.
Mes outils de prédilection sont les compositions isotopiques associées aux couples radioactif/radiogénique Rb/Sr, Sm/Nd, La/Ce, U-Th/Pb-He et Re/Os, ainsi que les concentrations en éléments traces.

Certains des résultats présentés ici ont été obtenus au cours des stages de recherche et/ou des thèses que j'ai encadrés ou co-encadrés au sein du LMV. Le nom des étudiants est souligné dans les listes de références associées à chaque sujet/thématique.

## 1. NATURE ET TAILLE DES HETEROGENEITES MANTELLIQUES

Parmi les questions essentielles qui demeurent quant à la structure et l'évolution chimique du manteau terrestre, une grande majorité est liée aux panaches mantelliques.

En tout premier lieu, que peut-on dire de l'origine en profondeur des panaches ? La trace laissée en surface par certains points chauds semble indiquer que leur source est relativement fixe vis-à-vis des mouvements de la croûte océanique [Duncan, 1980; Morgan, 1983; Molnar et Stock, 1987]. Elle ne semble donc pas sujette à la convection mantellique, au moins sur l'échelle de temps des plus vieux points chauds encore actifs, et on peut ainsi envisager deux réservoirs pour l'origine en profondeur des panaches mantelliques. Il s'agit respectivement de l'interface manteau supérieur-manteau inférieur, dans le cas où la discontinuité des vitesses sismiques à 670 km de profondeur traduit bien des variations de compositions chimiques, et de l'interface noyau-manteau [Loper, 1991; Davies et Richards, 1992]. L'état actuel des connaissances ne permet pas de statuer définitivement sur l'une ou l'autre de ces solutions, et il convient également de s'interroger sur l'unicité ou non de la source des points chauds. Tous les panaches proviennent-ils de la base du manteau supérieur, de 2900 km de profondeur, ou existe t-il plutôt deux classes de panaches mantelliques ayant pour origines respectives ces deux interfaces [Courtillot *et al.*, 2003] ?

Une question tout aussi fondamentale concerne la nature des panaches mantelliques. L'étude des basaltes d'îles océaniques -OIB- constitue un outil privilégié quant à l'appréhension de l'hétérogénéité du manteau terrestre, hétérogénéité liée, d'une part, à l'extraction de la croûte continentale, et, d'autre part, au recyclage de matériel de surface. Historiquement, Gast et collaborateurs [1964], puis Tatsumoto [1966], ont démontré les premiers l'existence de signatures isotopiques distinctes suivant, d'une part, la nature des basaltes océaniques (basalte de ride médio-océanique -MORB- ou OIB), et d'autre part, le lieu d'échantillonnage (variations isotopiques au sein d'une île, variations d'une île à l'autre). Depuis, l'analyse systématique des rapports isotopiques de strontium, néodyme et/ou plomb dans les basaltes océaniques a confirmé ces résultats et précisé la gamme de variations des signatures isotopiques au niveau des îles. La diversité des compositions a alors amené à la définition d'un certain nombre de pôles de mélange (ou compositions isotopiques extrêmes), dénommés par les acronymes DMM (rapports $^{206}Pb/^{204}Pb$ et $^{87}Sr/^{86}Sr$ faibles – au sens non radiogéniques) , EM1 (faible $^{206}Pb/^{204}Pb$, fort $^{87}Sr/^{86}Sr$), EM2 ($^{206}Pb/^{204}Pb$ intermédiaire, fort $^{87}Sr/^{86}Sr$) et HIMU (fort $^{206}Pb/^{204}Pb$, faible $^{87}Sr/^{86}Sr$) [Zindler et Hart, 1986a], qui permettent de décrire l'intégralité des mesures effectuées [Zindler *et al.*, 1982; Allègre et Turcotte, 1985; White, 1985; Zindler et Hart, 1986a; Allègre *et al.*, 1986/87; Hart *et al.*, 1992] (*Figure 1*). Toutefois, si l'on

excepte DMM, qui correspond au manteau supérieur appauvri (par l'extraction de la croûte continentale), la nature des différents pôles reste débattue. Ces derniers existent-ils en tant que réservoirs individualisés, s'agit-il de composants distincts, ou bien du mélange en proportions variables de composants purs qui ne sont jamais échantillonnés par les panaches mantelliques ? Ainsi, EM2 est généralement associé au recyclage de matériel continental (sédiments terrigènes) au sein du manteau [Zindler et Hart, 1986a; Hart, 1988; Weaver, 1991; Chauvel *et al.*, 1992], EM1, par contre, pourrait résulter de recyclage sédimentaire, d'origine terrigène et pélagique [Chauvel *et al.*, 1992] ou correspondre à la lithosphère continentale [McKenzie et O'Nions, 1983], tandis que HIMU est identifié à la croûte océanique [Hofmann et White, 1982; Weaver, 1991; Chauvel *et al.*, 1992]. Enfin, EM1 et HIMU ont également été liés au métasomatisme intra-mantellique [Vollmer, 1983; Hart, 1988; Hawkesworth *et al.*, 1990], bien que les volumes produits par ce processus, que l'on peut tenter de quantifier à partir des xénolites mantelliques présentant des évidences de celui-ci, semblent faibles au regard des volumes des sources des OIB [Hofmann, 1997].

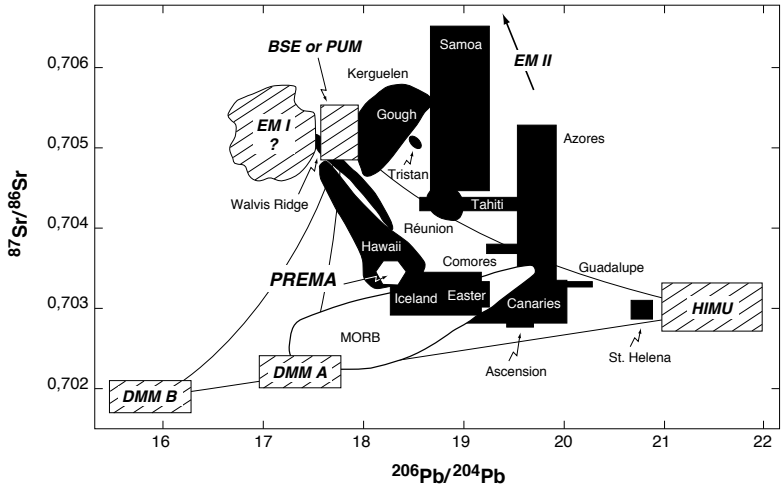


*Figure 1 - Définition des pôles mantelliques (ou compositions isotopiques extrêmes) DMM, EM I, EM II et HIMU, permettant d'expliquer, par mélange, l'ensemble des compositions mesurées dans les MORB et les OIB. D'après Zindler et Hart [1986a].*

Les gaz rares apportent également des contraintes fortes sur la nature de la source des OIB. La mesure systématique des rapports isotopiques de l'hélium, notamment, a permis de mettre en évidence un certain caractère dichotomique pour le manteau terrestre. L'ensemble des basaltes de ride médio-océanique affiche un rapport $^4He/^3He$ constant, de l'ordre de 90000 [Allègre *et al.*, 1995], représentatif du manteau supérieur dégazé, alors que les points chauds montrent de grandes variations. Plus précisément, certains basaltes d'îles présentent des rapports $^4He/^3He$ bien inférieurs à 90000 (19000 en Islande [Hilton *et al.*, 1999; Macpherson *et al.*, 2005], 20500 dans le cas du mont sous-marin Loihi [Kurz *et al.*, 1983; Valbracht *et al.*, 1997], ou encore 26000 pour Fernandina, dans l'archipel des Galapagos [Kurz et Geist, 1999; Kurz *et al.*, 2009]), quand d'autres, au contraire, affichent une valeur largement supérieure (*Figure 2*). La présence dans la source des panaches de matériel riche en uranium et thorium, tels la croûte océanique et/ou les sédiments, est généralement invoquée pour expliquer les signatures très radiogéniques des OIB. En effet, ces matériaux, réinjectés dans le manteau au niveau des zones de subduction, montrent un rapport (U+Th)/He élevé qui débouchera sur une signature très radiogénique après un certain temps de stockage, soit à l'interface manteau supérieur-manteau inférieur, soit à la base du manteau [Kurz *et al.*, 1982; Vance *et al.*, 1989; Staudacher *et al.*, 1989; Graham *et al.*, 1992; Hanyu et Kaneoka, 1997; Moreira et Kurz, 2001], à condition bien évidemment que les gaz rares (l'hélium notamment) ne soient pas recyclés dans le manteau, ou de manière négligeable. Cette dernière hypothèse a longtemps été avancée, le

dégazage lors de la subduction étant suffisamment efficace pour former une véritable barrière [Staudacher et Allègre, 1988; Allègre *et al.*, 1996], d'autant plus que l'hélium n'est pas retenu dans l'atmosphère par le champ de gravité terrestre. Des données récentes de pétrologie expérimentale suggèrent, toutefois, un recyclage possible d'hélium dans le manteau, via sa dissolution dans l'amphibole ou d'autres minéraux hydratés [Jackson *et al.*, 2013; 2015]. Les valeurs inférieures à 90000, que l'on qualifie généralement (et parfois abusivement) de primitives, sont quant à elles attribuées, par opposition, à l'existence d'un réservoir relativement peu dégazé. Ce dernier pourrait être le manteau inférieur [Kurz *et al.*, 1982], suggérant ainsi que la manteau terrestre est globalement stratifié, au moins jusqu'à aujourd'hui, puisqu'il permet de maintenir deux grands réservoirs pour ce qui est des concentrations d'hélium.

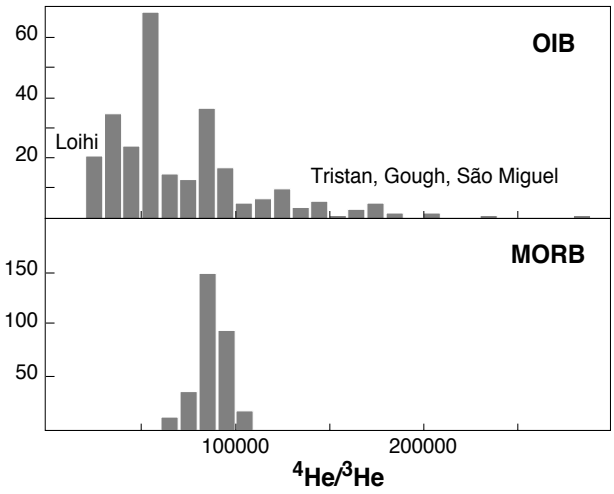


*Figure 2 - Histogrammes des valeurs du rapport isotopique $^4He/^3He$ mesurées dans les OIB et les MORB. D'après Moreira et Allègre [1998].*

Pour autant, maintenir des réservoir isolés, i.e., manteau supérieur et manteau inférieur, sur une grande échelle de temps n'est pas facilement conciliable avec les différents modèles de convection mantellique [van Keken *et al.*, 2007]. Une alternative à la notion de réservoirs individualisés, homogènes et bien mélangés (convectifs), propose ainsi que les compositions isotopiques mesurées dans les OIB et les MORB, rapports isotopiques d'hélium compris, traduisent plutôt l'échantillonnage-moyennage, via la fusion partielle, d'un manteau hétérogène. Ce dernier serait constitué de manteau appauvri dans lequel seraient distribuées, de manière aléatoire, des matériaux enrichis, de petite taille (1-100 km), d'origine crustale, et recyclés via la subduction [Anderson, 1998; Hellfrich et Wood, 2001; Meibom et Anderson, 2004]. Ce modèle, connu notamment sous l'acronyme SUMA (*Sampling Upon Melting and Averaging*) oppose donc la notion de réservoirs homogènes auxquels on peut associer des signatures géochimiques à celle de processus (ici la fusion partielle) générant, par moyennage local d'un grand réservoir hétérogène, ces mêmes signatures. Autrement dit, les réservoirs géochimiques sont remplacés par des distributions statistiques d'hétérogénéités. A noter également que ce modèle s'affranchit de l'existence des panaches mantelliques.

Un réservoir manteau inférieur, peu ou pas dégazé, l'effet de ''moyennage'' d'un manteau hétérogène ou encore une version hydride de ces deux visions du manteau (voir Courtillot *et al.* [2003]) ne sont pas les seules explications possibles aux rapports $^3He/^4He$ élevés mesurés dans les basaltes d'Islande, d'Hawaii, des Galapagos, mais aussi des Samoa ou encore de la Réunion [Füri et al., 2011; Jackson et al., 2014 ; et références incluses]. Bouhifd *et al.* [2013] ont montré récemment que des concentrations non négligeables d'hélium pouvaient être stockées dans le noyau à la suite de la différenciation noyau-manteau. Ces derniers ont mesuré le coefficient de partage de l'hélium entre métal et silicate, dans les conditions de formation du noyau (cellule à enclume diamant), et ils ont obtenu des valeurs comprises entre $4.7\times10^{-3}$ et $1.7\times10^{-2}$. Par conséquent, les rapports $^3He/^4He$ élevés de certains points chauds pourraient aussi témoi-

gner de l'interaction entre le manteau et le noyau. Bouhifd *et al.* [2013] estiment la contribution du noyau dans la source profonde des panaches à fort rapport $^{3}He/^{4}He$ entre 0.8 et 3%. Ces résultats sont à rapprocher des rapports $^{186}Os/^{188}Os$ élevés (par rapport à la valeur mesurée dans les MORBs) qui ont été mises en évidence dans des picrites d'Hawaii. Ceux-ci corrèlent avec leurs rapports $^{187}Os/^{188}Os$ et ont été expliqués de nouveau par une contribution du noyau à la source du panache mantellique d'Hawaii, de l'ordre de 0.5-1% [Brandon *et al.*, 1998; Brandon et Walker, 2005]. A noter, cependant, que l'incorporation, dans la source des panaches mantelliques, de sulfures métasomatiques liés à la fusion partielle de péridotite et/ou pyroxénite peut également expliquer la signature isotopique $^{186}Os$-$^{187}Os$ des basaltes océaniques [Luguet *et al.*, 2008].

De la même manière, l'origine de la signature radiogénique d'hélium des OIB ne fait pas consensus. Certains auteurs ne la lient pas au recyclage de matériaux de surface, mais lui attribuent une origine superficielle [Condomines *et al.*, 1983; Zindler et Hart, 1986b; Hilton *et al.*, 1995]. Le dégazage intense de la chambre magmatique d'un volcan, suivi d'une production radioactive d'$^{4}He$ dans un magma riche en uranium, permettrait également d'obtenir des rapports $^{4}He/^{3}He$ élevés. Alternativement, une interaction avec de la croûte océanique et/ou des sédiments lors de la mise en place des magmas tendrait aussi à augmenter le rapport $^{4}He/^{3}He$. A noter qu'une telle interaction, avec la lithosphère sous-continentale, riche en uranium, a déjà été proposée pour expliquer les compositions isotopiques de strontium, néodyme et plomb mesurées sur les basaltes des îles Canaries [Hoernle *et al.*, 1995].

Parallèlement à la définition des pôles DMM, HIMU, EM1 et EM2, un certain nombre d'auteurs ont proposé l'existence d'un composant supplémentaire, commun à l'ensemble des panaches mantelliques (la plus grande majorité du moins), et qui n'occuperait donc pas une position extrême dans les différents diagrammes isotopiques (Sr-Nd-Pb). Il s'agit respectivement du pôle FOZO (*FO*cus *ZO*ne) de Hart et collaborateurs [1992] (*Figure 3*), du pôle PHEM (*P*rimitive *HE*lium *M*antle) de Farley *et al.* [1992] et du pôle C (''*C*ommon component'') de White [1995] et Hanan et Graham [1996] (défini sur la base des échantillons de MORB uniquement pour Hanan et Graham). Bien que toutes ces propositions soient conceptuellement équivalentes, elles présentent néanmoins des compositions isotopiques différentes et correspondent, en termes de source, à des entités également différentes suivant les auteurs considérés. Hart *et al.* [1992] et Farley *et al.* [1992] proposent, sur la base des rapports isotopiques $^{3}He/^{4}He$ notamment, que le composant commun corresponde au manteau inférieur. Hanan et Graham [1996], par contre, bien que notant la possibilité d'une telle origine, rejettent cette hypothèse sur la base du rapport Ce/Pb, et préfèrent une source moins profonde. Le composant

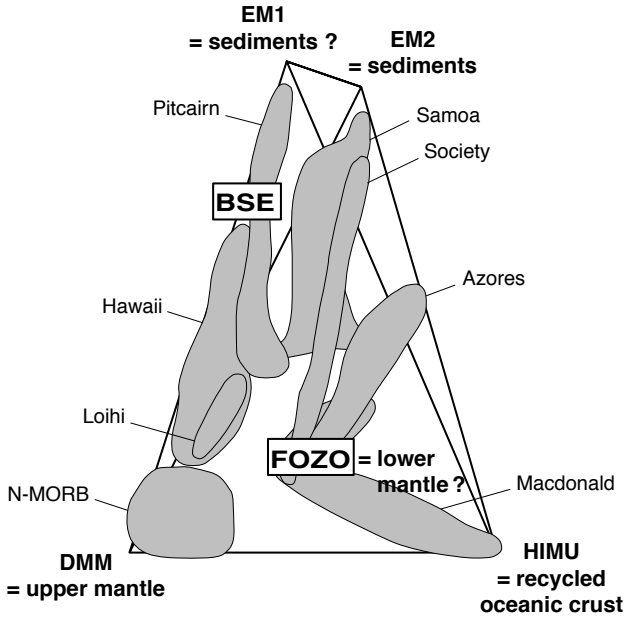


*Figure 3 - Définition du pôle FOZO, point de convergence des trends définis par chaque archipel dans le tétraèdre DMM-EM1-EM2-HIMU (modifié d'après Hauri et al. [1994]).*

commun correspondrait plutôt à la zone de transition située au-dessus de la discontinuité sismique à 670 km de profondeur. Stracke *et al.* [2005], plus récemment, associent FOZO au recyclage de croûte océanique, l'identifiant à une sorte de pôle ''young HIMU'' [Thirlwall, 1997] et proposent que ce dernier soit commun, et à la source des MORBS et à celle des OIB. Par ailleurs, ils transfèrent le rôle de pôle de mélange jusqu'à maintenant attribué au pôle HIMU à FOZO, HIMU étant considéré comme un composant rare du manteau, restreint aux basaltes des îles Sainte-Hélène, dans l'Atlantique Central, et Mangaia, Rurutu (pour les vieilles formations), Rimatara, Raivavae et Tubaii, de l'archipel des Australes-Cook, dans l'océan Pacifique. Dixon *et al.* [2002], quant à eux, proposent que le pôle FOZO représente le manteau primitif (ou légèrement appauvri), métasomatisé par des liquides de type HIMU, permettant ainsi de réconcilier les différentes caractéristiques isotopiques de FOZO: une composition isotopique de Pb relativement radiogénique pour un rapport $^{3}He/^{4}He$ élevé notamment. Par la même, ils lient, eux aussi, les pôles FOZO et HIMU, tout comme Castillo [2013] qui lie l'origine du pôle HIMU au recyclage de carbonates Archéens, alors que les carbonates Protérozoïques expliqueraient pour leur part le pôle FOZO. Enfin, Jackson *et al.* [2007] ont proposé que FOZO soit hétérogène, à grande échelle: le composant commun identifié dans les basaltes de Samoa (hémisphère sud), à fort rapport $^{3}He/^{4}He$, présente d'après ces auteurs une composition isotopique (Sr-Nd-Pb) significativement différente de celle du composant impliqué dans les basaltes d'Hawaii, d'Islande et des Galapagos (hémisphère nord).

Les variations isotopiques enregistrées à l'échelle locale, échelle de l'île ou de l'archipel, forment également des alignements dans les diagrammes isotopiques classiques (Sr-Nd-Pb). L'interprétation de ces différents alignements est de nouveau faite en termes de mélanges entre les différents pôles DMM, HIMU, EM1 et EM2. Néanmoins, la signification réelle de ces mélanges n'est pas définitivement acquise, et trois grandes hypothèses sont généralement proposées. Certains auteurs [Weaver, 1991; Chauvel *et al.*, 1992] associent les alignements observés à l'hétérogénéité isotopique des sources des panaches mantelliques. Les basaltes échantillonnés reflètent les différentes proportions de mélange entre les composants mantelliques présents au sein de la source et/ou les variations du taux de fusion partielle. Hart *et al.* [1992], par contre, proposent que la source des panaches soit, d'un point de vue isotopique, homogène. Chaque panache mantellique possède une signature isotopique de type FOZO, et les mélanges observés à l'échelle d'une île résultent de l'entraînement de matériel de type EM et/ou HIMU lors de la remontée des panaches. Enfin, la troisième explication repose sur des phénomènes d'interaction et de contamination avec l'asthénosphère et/ou la lithosphère océanique [Class et Goldstein, 1997; Claude-Ivanaj *et al.*, 1998]. Cette proposition est supportée par les mesures de composition

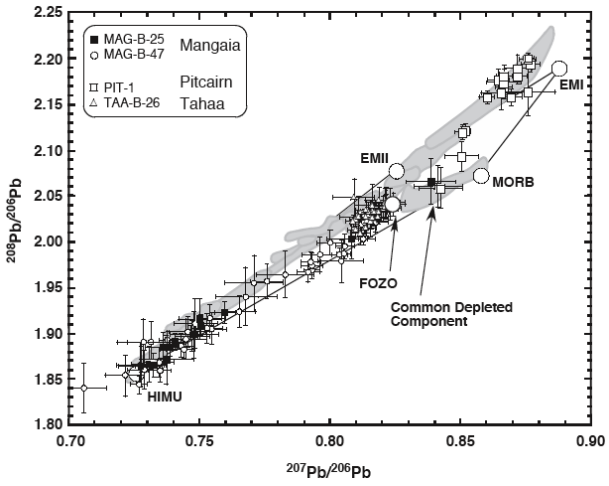


*Figure 4 - Compositions isotopiques de Pb d'inclusions d'olivines provenant d'échantillons représentatifs des pôles mantelliques EMI (Pitcairn), EMII (Tahaa) et HIMU (Mangaia). Les trends dessinés par les basaltes de chaque localité convergent vers une composition similaire à celle des MORB du Pacifique, ce qui suggère que les liquides piégés dans les olivines ont interagi avec la lithosphère océanique (modifié d'après Saal et al. [2005]).*

isotopique de plomb réalisées à l'échelle du minéral (*Figure 4*): les variations isotopiques y sont très importantes, dépassant les variations caractérisant un archipel, et convergent vers un composant appauvri ressemblant au pôle DMM [Saal *et al.*, 2005]. Cette observation remet en question l'idée que le composant commun représente le manteau inférieur, et, de façon plus générale, nous amène à nous interroger sur l'association entre pôles isotopiques et domaines du manteau.

Ma contribution à cette grande thématique ''Nature et taille des hétérogénéités mantelliques'' vise en premier lieu l'échelle régionale. Elle s'appuie sur l'étude des archipels des Açores et du Cap Vert, et plus particulièrement sur la caractérisation des basaltes échantillonnés sur leurs îles.

*L'archipel des Açores*

L'archipel des Açores est composé de neuf îles, Corvo, Faial, Flores, Graciosa, Pico, Santa Maria, São Jorge, São Miguel et Terceira, représentant la partie émergée d'un vaste plateau sous-marin. Ce dernier est situé au niveau de la jonction triple entre les plaques eurasienne, africaine et américaine. Il est, de plus, recoupé par la dorsale nord-Atlantique, si bien que sept îles se trouvent à l'Est de la dorsale (elles forment les groupes oriental - São Miguel et Santa Maria - et central – Terceira, Graciosa, Jorge Pico et Faial), et deux à l'Ouest (le groupe occidental - Corvo et Flores).

La présence d'un panache mantellique, à l'aplomb de l'archipel des Açores et profondément enraciné dans la manteau, est débattue. D'un coté, la tomographie sismique permet d'imager une colonne de type ''panache'' sous les îles, jusqu'à 400 km de profondeur environ [Montelli *et al.*, 2004; Yang *et al.*, 2006], et une diminution de l'épaisseur de la zone de transition à l'aplomb de ces dernières est également observée [Courtier *et al.*, 2007]. De l'autre, un flux de flottabilité (trop ?) faible, ainsi qu'une absence d'anomalie de vitesse des ondes S au niveau de la zone de transition, suggèrent plutôt que l'anomalie thermique à l'aplomb de l'archipel est restreinte au manteau supérieur [Courtillot *et al.*, 2003; Ritsema et Allen, 2003].

L'analyse géochimique des principales formations volcaniques à l'affleurement a permis de mettre en évidence l'existence d'hétérogénéités à grande échelle (échelle de l'archipel). Les compositions isotopiques de Pb définissent ainsi trois groupes d'échantillons: 1) les basaltes de l'île de São Miguel présentent les rapports isotopiques les plus radiogéniques de l'archipel. Ils se positionnent à gauche de la droite de référence de l'Atlantique Nord (NHRL, cf. Hart [1984]); 2) ceux de Santa Maria, Graciosa, Faial, Corvo et Flores, au contraire, présentent les compositions les moins radiogéniques. Ils se positionnent également à gauche de la NHRL; 3) les échantillons des îles Terceira et São Jorge, enfin, se distinguent clairement de deux premiers groupes en étant à droite de la NHRL. Ce découpage est également exprimé par les rapports isotopiques de Sr, de Nd et d'He. Les basaltes de des différentes îles montrent par exemple des signatures d'He contrastées, ''primitives'' (rapports $^{4}He/^{3}He$ faibles, <90000) pour les laves de Terceira, radiogéniques (rapports $^{4}He/^{3}He$ supérieurs à la valeur des MORB) pour celles de São Miguel, alors que les échantillons de Faial et Pico montrent des valeurs intermédiaires, de part et d'autre de celles des MORB, de faiblement ''primitives'' à radiogéniques. Ces variations ont amené à la définition de 4 pôles de mélange (ou compositions isotopiques extrêmes, *Figure 5*), dont l'origine est fortement débattue (composants ou mélange de composants, voir Millet *et al.* [2009]). Le premier de ces pôles présente les caractéristiques classiques de HIMU, à l'exception de rapports isotopiques d'hélium faibles (impliquant, en plus de la croûte océanique recyclée, du manteau profond ou l'apport par diffusion d'$^{3}He$); il explique les

compositions des échantillons de Terceira. Le second est spécifique à l'île de São Miguel; il traduit le recyclage par subduction, soit de sédiments [Turner *et al.*, 1997], soit de basaltes enrichis de type OIB [Beier *et al.*, 2007; Elliott *et al.*, 2007; Moreira *et al.*, 2012], ou l'incorporation de lithosphère sous-continentale, délaminée dans le manteau supérieur lors de l'ouverture de l'océan Atlantique [Widom *et al.*, 1997; Moreira *et al.*, 1999]. Le troisième concerne les échantillons de Faial et Pico; il est lié au recyclage de lithosphère également, soit océanique (métasomatisée et d'âge Archéen, voir Turner *et al.* [1997] et Schaeffer *et al.* [2002]), soit continentale [Millet *et al.*, 2009]. Le dernier, enfin, affiche une composition similaire à celle des basaltes de la ride médio-Atlantique, aux latitudes de l'archipel des Açores. L'existence à l'échelle de l'île de co-variations entre traceurs de source (les rapports isotopiques de Sr-Nd-Pb-He) et traceurs de processus (majeurs, traces et rapports de traces), par ailleurs, indique que les mélanges entre les composants discutés ci-dessus correspondent à des mélanges de liquides syn- et/ou post-différenciation. Ceci suggère, soit une ''plomberie'' relativement complexe entre le matériel plume localisé à la base de la lithosphère et son expression en surface, permettant le mélange des produits de fusion des différents matériaux portés par le panache, soit un effet de fusion, amenant à la dilution des composants les plus fusibles par les moins avec l'augmentation du taux de fusion partielle, ou encore l'interaction entre la source mantellique des échantillons, de composition relativement homogène, et des matériaux localisés superficiellement dans la lithosphère océanique [Millet *et al.*, 2009].

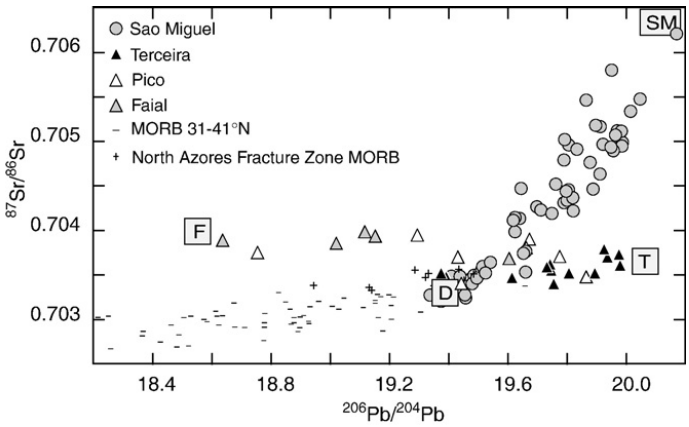


*Figure 5 - Variations des compositions isotopiques de Pb et Sr à l'échelle de l'archipel des Açores et définition des pôles de mélange São Miguel (SM), Terceira (T), Faial-Pico (F) et MORB (D) [Millet et al., 2009].*

*L'archipel du Cap Vert*

L'archipel du Cap Vert est situé au large du continent africain, à environ 500 km des côtes sénégalaises, entre les latitudes 15 et 17°N. Il est constitué de dix îles principales: au Sud, les îles sous le vent, respectivement Brava, Fogo, Santiago et Maio, et, au Nord, les îles au vent, Santo Antão, São Vicente, Santa Luzia et São Nicolau, qui s'étendent à l'Est avec les îles de Sal et Boa Vista. Les directions selon lesquelles ces deux ensembles s'alignent sont reliées, d'une part, à une structure profonde marquant cette partie de l'océan Atlantique depuis le Mésozoïque [Klerkx et De Paepe, 1971] et, d'autre part, à une zone de fractures transversales [Le Pichon et Fox, 1971]. L'archipel repose sur un vaste plateau océanique, dont l'altitude moyenne au dessus du plancher océanique avoisine les 2000 mètres. Bien que très proche du continent africain, sa position vis-à-vis du talus continental ne permet pas d'envisager la présence de croûte continentale sous les îles [Klerkx *et al.*, 1974].

Contrairement au point chaud des Açores, la présence d'un panache mantellique à l'aplomb des îles du Cap Vert est aujourd'hui peu débattue (si ce n'est pas du tout). L'existence d'anomalies gravimétriques et de flux de chaleur à l'aplomb de l'archipel [Dash *et al.*, 1976; Courtney et White, 1986] sont effectivement interprétées comme la réponse lithosphérique à la présence d'un panache mantellique, dont

l'ancrage profond, à la base du manteau, semble attesté par la tomographie sismique [Montelli *et al.*, 2006; Zhao, 2007; Forte *et al.*, 2010]. De manière similaire, en revanche, les principales formations volcaniques à l'affleurement, essentiellement des séries sous-saturées en silice (néphélinites, picro-basaltes, basanites et téphrites), montrent de fortes hétérogénéités de composition (échelle de l'archipel). Les basaltes des îles sous le vent, Fogo et Santiago, se positionnent à gauche de la NHRL dans les diagrammes isotopiques Pb-Pb, affichent des rapports isotopiques de Sr modérément radiogéniques et présentent une composition isotopique d'He constante, égale à la valeur moyenne des MORB. Les échantillons provenant des îles au vent, São Vicente, São Nicolau et Sal, par contre, sont situées du côté droit de la NHRL, présentent des compositions de Sr non radiogéniques et affichent des valeurs du rapports $^{4}He/^{3}He$ faibles (<90000). Cette dichotomie est non seulement marquée par les isotopes, mais aussi par les teneurs en éléments majeurs et traces. Les formations des îles sous le vent sont globalement plus alcalines que celles des îles au vent, par exemple; de même, les abondances en éléments traces des échantillons prélevés sur les îles sous le vent sont caractéristiques du pôle EM I, alors que les abondances des basaltes des îles au vent sont typiques du pôle HIMU [Doucelance *et al.*, 2003; Millet *et al.*, 2008; Mourão *et al.*, 2008; 2012]. Ces signatures géochimiques traduisent la présence (et le mélange) de plusieurs composants dans la source des basaltes du Cap Vert: (1) de la croûte océanique recyclée, d'âge environ 1.5-2.0 Ga; (2) de la lithosphère sous-continentale; (3) du manteau profond, riche en $^{3}He$; et (4) du matériel de composition isotopique identique à celle du manteau supérieur source des MORB. L'existence de co-variations entre traceurs de source (les rapports isotopiques de Sr-Nd-Pb-He) et traceurs de processus (majeurs, traces et rapports de traces) indique, comme pour les Açores, que les mélanges entre les différents composants décrits ci-dessus correspondent à des mélanges de liquides syn- et/ou post-différenciation (*Figure 6*). Les basaltes échantillonnés sur une même île montrent également des variations de composition chimique et isotopique. Celles-ci sont non seulement corrélées à l'âge des échantillons, le caractère EM1 des basaltes de Fogo est par exemple plus marqué dans les échantillons historiques que dans les coulées anciennes [Escrig *et al.*, 2005], mais elles dessinent aussi de bonnes co-variations entre traceurs de processus et rapports isotopiques, ainsi qu'observé à plus grande échelle spatiale [Millet *et al.*, 2008].

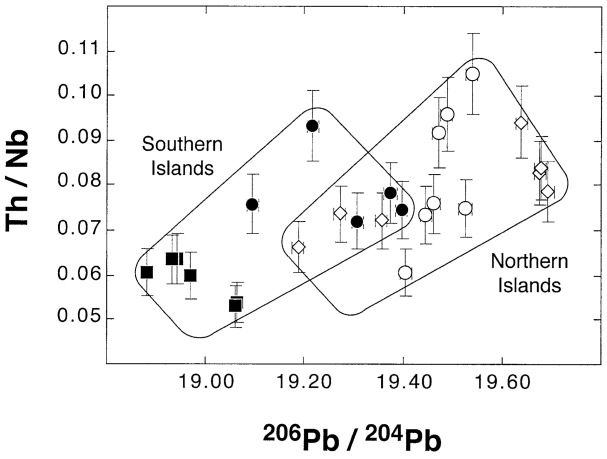


*Figure 6 - L'évolution couplée des rapports Th/Nd et $^{206}Pb/^{204}Pb$ mesurés dans les échantillons basaltiques de l'archipel du Cap Vert témoigne de mélanges syn- et/ou post-différenciation [Doucelance et al., 2003].*

La correspondance entre les compositions des îles et leurs positions géographiques au sein de l'archipel suggère que l'hétérogénéité chimique et isotopique globale du Cap Vert obéit à un contrôle structural. L'évolution temporelle des compositions et la co-variation des différents outils géochimiques suggèrent, quant à elles, que les variations de compositions enregistrés par les basaltes du Cap Vert résultent de l'interaction entre le panache du Cap Vert et la lithosphère océanique capverdienne. Cette dernière, hé-

térogène, a vraisemblablement incorporé des fragments de croûte inférieure, délaminés avec la lithosphère sous-continentale au cours de l'ouverture de l'océan Atlantique [Escrig *et al.*, 2005].

Les mesures présentées ci-dessus confirment donc la similitude de variabilité des compositions isotopiques entre échelle globale et échelle régionale: les échantillons du Cap Vert et des Açores présentent en effet des compositions typiques des 4 grands pôles mantelliques, dont la nature, toujours très discutée, peut éventuellement varier d'un archipel à l'autre. Le résultat le plus important de ces études concerne cependant le rôle de la lithosphère océanique. C'est cette dernière qui, assimilée par les magmas produits par fusion partielle du matériel lié aux panaches, crée vraisemblablement la grande majorité des variations isotopiques mesurées dans les échantillons. L'assimilation de matériel lithosphérique semble par ailleurs indépendante de l'âge de la lithosphère. Elle est tout aussi importante au niveau de l'archipel des Açores, qui recoupe la dorsale médio-Atlantique (d'âge zéro), ou du Cap Vert, à l'aplomb d'une des plus vieilles lithosphères océaniques (d'âge Jurassique). Les études menées sur ces deux archipels soulignent donc le rôle également thermique des panaches océaniques, qui permet l'assimilation et/ou la fusion partielle/assimilation de la lithosphère océanique.

Pour autant, la source des panaches du Cap Vert et des Açores n'est pas constituée d'un unique composant. Deux sont nécessaires pour expliquer les compositions isotopiques de Sr-Nd-Pb-He: d'une part, de la croûte océanique recyclée, vieille et altérée (d'âge globalement Protérozoïque), et d'autre part, du manteau profond, riche en $^{3}$He. La composition isotopique constante du mélange de ces deux composants implique des proportions également constantes, et par conséquent pose la question du rôle homogénéisateur respectif du brassage mécanique au sein des panaches mantelliques et de la fusion partielle à la base de la lithosphère océanique.

A plus grande échelle, l'identification de processus superficiels lithosphériques dans des localités jouant un rôle clef dans la définition de la topologie mantellique permet de discuter l'existence et la nature d'un composant primitif (ou sub-primitif), commun à tous les basaltes de point chaud, de type FOZO (*Figure 7*). Plusieurs des trends représentés dans le tétraèdre de Hart et collaborateurs [1992], dont le point de convergence définit la composition de FOZO, se résument à un ou deux points uniquement, une fois les interactions superficielles corrigées. FOZO pourrait donc correspondre, dans certains cas, à la lithosphère océanique enrichie (au sens large du terme) plutôt qu'au manteau inférieur, ce qui pose la question du caractère ubiquiste de ce dernier.

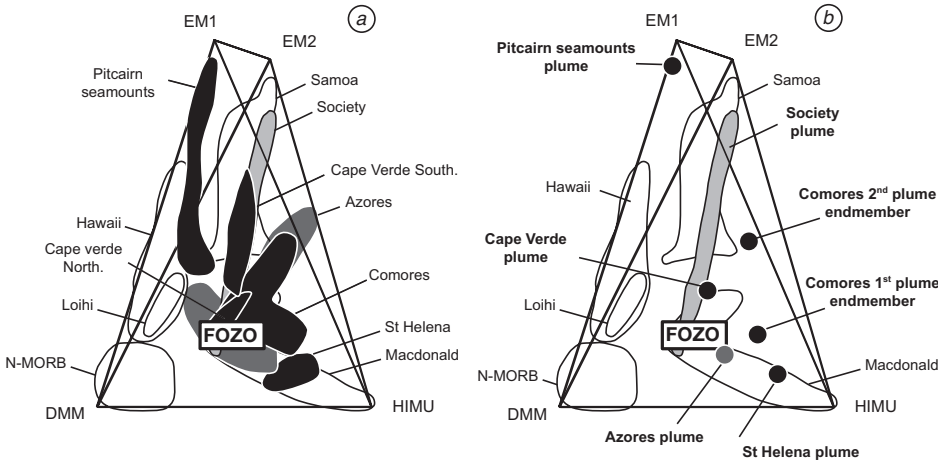


*Figure 7 - Champs des MORB et des OIB dans le tétraèdre des pôles mantelliques [Hart et al., 1992]: (a) données mesurées; (b) données corrigées des interactions lithosphériques. Si certains archipels, comme les îles de la société, conservent une variabilité isotopique importante, d'autres, comme les Açores, le Cap Vert, les Comores, les monts sous-marins de Pitcairn, ou encore Ste Hélène, voient leurs champs restreints à un ou deux points, détruisant la convergence des compositions vers FOZO. D'après Millet [thèse, 2007].*

Ce 1er thème couvre une partie de mes travaux de thèse (IPGP), de post-doctorat (Geotop, Montréal), et de mon activité de recherche et d'encadrement au sein du laboratoire Magmas et Volcans (LMV). Les différents résultats ont donné lieu aux publications suivantes (appelées en bleu dans le texte):

*- Moreira, **Doucelance** et al. (1999) Helium and lead isotope geochemistry in the Azores Archipelago. Earth and Planetary Science Letters 169.*
*- **Doucelance** et al. (2003) Pb-Sr-He isotope and trace element geochemistry of the Cape Verde Archipelago. Geochimica et Cosmochimica Acta 67.*
*- Escrig, **Doucelance** et al. (2005) Os isotope systematics in Fogo basalts: evidence for lower continental crust residing in the oceanic lithosphere beneath the Cape Verde Islands. Chemical Geology 219.*
*- Millet, **Doucelance** et al. (2008) Mantle plume heterogeneity versus shallow-level interactions: A case study, the São Nicolau Island, Cape Verde archipelago. Journal of Volcanology and Geothermal Research 176.*
*- Millet, **Doucelance** et al. (2009) Reconsidering the origins of isotopic variations in Ocean Island Basalts ; Insights from fine-scale study of São Jorge Island, Azores archipelago. Chemical Geology 265.*
*- Mourão, Mata, **Doucelance** et al. (2012) Geochemical temporal evolution of Brava Island magmatism: constraints on the variability of Cape Verde mantle sources and on carbonatite-silicate magmas link. Chemical Geology 334.*

*Thèse*
*- Marc-Alban Millet (2004-2007): Géochimie des panaches océaniques et échelle d'hétérogénéités du manteau terrestre. Archipels du Cap Vert et des Açores (co-encadrement Pierre Schiano).*
*- Cyntia Mourão (2008-2013), doctorante au centre de géologie de Lisbonne (direction João Mata): Initiation à la géochimie isotopique Sr-Nd-Pb et application au volcanisme de l'île de Brava, archipel du Cap Vert.*

*Master*
*- Marc-Alban Millet (2004): Utilisation des rapports d'éléments traces en tant que traceurs de source: exemple de l'archipel du Cap Vert.*
*- Nicolas Vinet (2005): Interaction entre basalte et encaissant pendant le magmatisme intra-plaque continental: contraintes isotopiques et élémentaires (co-encadrement Pierre Schiano).*
*- Guillaume Jacques (2007): Compositions isotopiques de Sr et de Nd des basaltes de l'île de Sal, archipel du Cap Vert.*

L'étude des basaltes d'îles océaniques, et plus particulièrement des archipels des Açores et du Cap Vert, montre le rôle important du recyclage de matériel de surface, notamment de la lithosphère océanique et de sa pile sédimentaire, dans la géochimie du manteau. Une part importante de mes travaux de recherche au sein du LMV traite également de la subduction au sens large. Plus particulièrement, quatre études distinctes, via le co-encadrement de quatre étudiants en thèse, permettent :

- de quantifier le rôle respectif des processus de fusion partielle et de déshydratation affectant les matériaux recyclés par subduction dans la genèse des basaltes d'arc;
- de tester le recyclage de sédiments marins, notamment des carbonates, via le développement de la systématique La/Ce;
- de discuter l'évolution des modalités de la subduction entre l'Archéen et l'actuel;
- d'apporter quelques contraintes temporelles sur le début de la subduction.

*Le volcan Merapi (Arc de la sonde, Indonésie)*

L'étude des produits éruptifs du volcan Merapi porte sur la contradiction apparente entre, d'une part, la complexité des processus (fusion partielle, déshydratation, métasomatisme, mélange) et des composants (coin de manteau, sédiments et croûte océanique recyclée) mis en jeu lors de la subduction et, d'autre part, la simplicité du message des systèmes isotopiques radiogéniques (Sr-Nd-Pb). Ces derniers montrent en effet, à l'échelle d'un édifice volcanique, de simples variations binaires caractéristiques d'un mélange à deux composants. Il s'agit toutefois de mélanges pseudo-binaires, autrement dit de la succession de mélanges dont seule la trace du dernier est enregistrée dans les compositions isotopiques des échantillons de surface (*Figure 8*). Par ailleurs, les résultats de la modélisation montrent que la signature des laves d'arc est surtout contrôlée par les compositions isotopiques des composants mis en jeu, plutôt que par l'intensité des processus de fusion partielle et de déshydratation affectant les matériels subduits [Debaille *et al.*, 2006]. Les coefficients de mobilité que l'on peut tout de même déterminer pour les éléments Sr, Nd et Pb, notamment lors de la déshydratation des sédiments, sont relativement élevés (≥50%), en désaccord avec les déterminations expérimentales qui suggèrent des valeurs très inférieures [Aizawa *et al.*, 1999, Johnson et Plank, 1999]. Les coefficients de partage, par contre, montrent des valeurs plus cohérentes avec les données de la pétrologie expérimentale [Hermann et Rubatto, 2009].

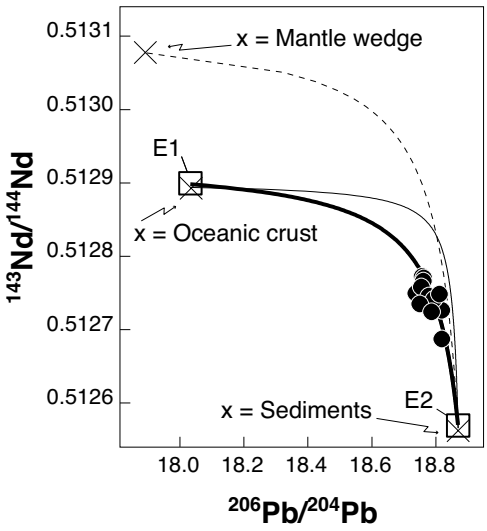


*Figure 8 - Les compositions des pôles E1 et E2 résultent du métasomatisme du coin de manteau, d'une part, par les fluides et liquides issus de la fusion partielle et déshydratation de la croûte océanique recyclée, et,* d'autre part, par les fluides et liquides issus de la fusion partielle et déshydratation des sédiments recyclés. *Le mélange entre E1 et E2 reproduit les compositions mesurées dans les laves, contrairement aux mélanges entre coin de manteau et sédiments ou coin de manteau et croûte océanique.* D'après *Debaille et al. [2006].*

*Le volcanisme de la Martinique (Arc des Petites Antilles)*

Les basaltes, andésites et dacites représentatifs des grandes formations volcaniques de la Martinique définissent également des mélanges binaires dans les diagrammes isotopiques classiques Sr-Nd-Pb (Labanieh *et al.* [2010] et références incluses). Les rapports isotopiques de Ce mesurées dans ces mêmes échantillons traduisent le recyclage de sédiments, dont la composition actuelle est accessible par le biais de forages au large de l'arc des Petites Antilles, dans le coin de manteau [Bellot *et al.*, 2015]. Les gammes de variations observées dans le diagramme εNd vs. εCe (où εNd et εCe représentent les déviations relatives - en $10^4$ - des rapports isotopiques $^{143}Nd/^{144}Nd$ et $^{138}Ce/^{142}Ce$ par rapport à la référence chondritique) nécessitent de prendre en compte, d'une part, l'intégralité de la variabilité isotopique mesurée dans les sédiments échantillonnés au large de la Martinique, et d'autre part, l'ensemble des fractionnements chimiques opérant entre les fluides et liquides issus de la déshydratation/fusion partielle des sédiments au moment de leur recyclage et ces mêmes sédiments [Johnson et Plank, 1999; Hermann et Rubatto, 2009]. Ce dernier point est en accord avec les résultats de Labanieh *et al.* [2012], notamment la co-variation des rapports La/Sm et $^{143}Nd/^{144}Nd$ dans la source des laves de la Martinique, et les nombreuses études qui concluent à la nécessité que les sédiments recyclés fondent partiellement afin de pouvoir transférer une part importante de leur Be et Th aux arcs (Elliott *et al.* [1997] et références incluses).

Les modèles qui permettent de reproduire les compositions isotopiques mesurées, ainsi que les anomalies de Ce, impliquent toutefois une contribution massique des fluides/liquides produits par déshydratation/fusion partielle très élevée pour les conditions de pression et température à l'aplomb du sud de l'arc des Petites Antilles (~4.5 GPa, 800°C ; Syracuse *et al.* [2010]). Cette forte contribution, jusqu'à 25% en masse pour les échantillons les plus radiogéniques en Ce (06MT37, voir *Figure 9a*), résulte du caractère très peu mobile et/ou compatible du Ce et du Nd lors de la déshydratation / fusion partielle des sédiments dans ces conditions P et T [Johnson et Plank, 1999; Hermann et Rubatto, 2009]. Seules les expériences de fusion de sédiments à plus hautes T (>1000°C) produisent des liquides enrichies en REE par rapport aux sédiments initiaux [Hermann et Rubatto, 2009], permettant ainsi une contribution d'autant moins forte du pôle ''sédiments'' (quelques

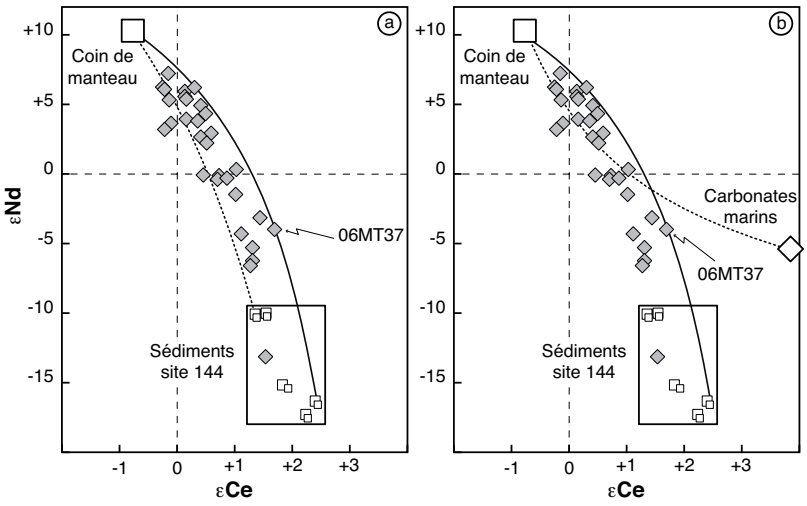


*Figure 9 - Compositions isotopiques de Ce et de Nd des basaltes/andésites de la Martinique. A) Les compositions de Ce les plus radiogéniques nécessitent de combiner les sédiments également les plus radiogéniques avec le fractionnement Ce/Nd le plus fort lors de la fusion/déshydratation de ces derniers. Les échantillons les moins radiogéniques, au contraire, associent les sédiments les moins radiogéniques et le fractionnement Ce/Nd le plus faible. B) La participation, jusqu'à 5% en masse, de fluides issus de la déshydratation de carbonates marins recyclés ne permet pas de réduire les très fortes proportions du pôle ''sédiments'' dans la source de basaltes/andésites de Martinique. Modifié d'après Bellot et al. [2015].*

%), en accord avec la modélisation géochimique des laves du Merapi qui concluait sur un comportement moyennement mobile et incompatible du Nd.

Une alternative possible à une telle contribution massique est d'invoquer la présence de sédiments carbonatés dans la source des basaltes et andésites de la Martinique, en plus des sédiments majoritairement terrigènes échantillonnés au large de l'arc des Petites Antilles. Des carbonates, en équilibre avec l'eau de mer au moment de leur formation, développent en effet des compositions isotopiques de Ce beaucoup plus radiogéniques que les sédiments terrigènes avec le temps. Le cérium est un élément de la famille des Terres Rares dont la valence (3+ ou 4+) est contrôlée par les conditions d'oxydo-réduction. Ainsi, le $Ce^{4+}$, produit par oxydation du $Ce^{3+}$ dans les couches superficielles des océans, est rapidement soustrait de ces dernières car peu soluble [Elderfield, 1988] et les sédiments marins en équilibre avec cette eau de mer présentent donc des fractionnements La/Ce élevés (anomalie négative de Ce). Un mélange à trois composants - coin de manteau, liquides issus des sédiments terrigènes et des carbonates marins (je reviendrai sur le recyclage des carbonates marins dans la section suivante) - permet de reproduire les compositions isotopiques de Ce et Nd des échantillons les plus radiogéniques pour le Ce (en considérant un appauvrissement similaire en REE dans les liquides issus de la fusion partielle des sédiments et des carbonates, voir *Figure 9b*). La proportion massique de liquides issus des sédiments terrigènes reste cependant élevée pour des proportions ''raisonnables'' des liquides liés aux carbonates. Un tel scenario est à rapprocher des conclusions de DuFrane *et al.* [2009], qui proposent une contribution à hauteur de 5% de fluides issus de la croûte océanique altérée et recyclée par subduction dans le coin de manteau enrichi par les sédiments. La croûte océanique altérée pourrait contenir notamment des carbonates secondaires.

*Les sanukitoïdes du Limpopo (Afrique du Sud)*

Les sanukitoïdes sont des diorites et des granodiorites magnésiennes, dont la géochimie est intermédiaire entre celle des suites BADR (Basalte-Andésite-Dacite-Rhyolite) modernes (*i.e.* série de différenciation calco-alcaline, fortes teneurs en K, Sr, Rb, Ba et en éléments de transition) et celle des TTG (Tonalite-Trondhjémite-Granodiorite) archéennes (*i.e.* faibles teneurs en Nb, Ta, Zr, Y ainsi qu'en terres rares lourdes, résultant en des spectres de terres rares très fractionnés) [Stern, 1989; Stern et Hanson 1991; Martin *et al.*, 2005; 2009]. Ils se sont mis en place autour de ~2.8-2.5 Ga dans tous les cratons archéens. Le caractère transitionnel de ces magmas, chronologique et compositionnel en fait des outils de choix pour étudier les changements géodynamiques globaux qui ont opéré à la transition Archéen–Protérozoïque, et plus particulièrement le passage de la ''subduction archéenne'' à la subduction moderne.

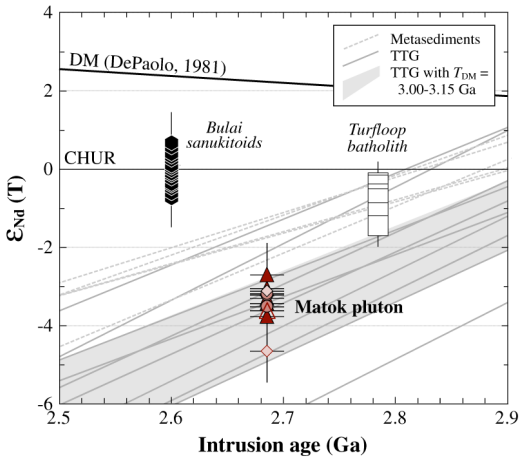


*Figure 10 : Rapport isotopique de Nd initial (exprimé en notation ε) en fonction de l'âge. Les sanukitoïdes s.s. montrent des signatures juvéniles alors que celles des sanukitoïdes marginaux et des granites comtemporains sont intermédiaires entre juvéniles et recyclées, en accord avec les modèles pétrogénétiques basés sur les éléments majeurs et en traces. D'après Laurent et al. [2014a].*

Les granodiorites du pluton de Bulai (intrusif dans la zone centrale de la ceinture du Limpopo, ~2600 Ma)

présentent des caractéristiques géochimiques hybrides témoignant de l'interaction entre une péridotite mantellique et un liquide de composition TTG [Laurent *et al.*, 2011; 2013a]. Il s'agit de sanukitoïdes au sens strict (*s.s.*). Les échantillons, également tardi-archéens, des plutons de Matok, Mashashane, Matlala et Molesti montrent des caractéristiques géochimiques communes avec les sanukitoïdes *s.s.* et aussi des différences, d'où leur dénomination de sanukitoïdes marginaux. Ils résultent de l'interaction entre des liquides de type sanukitoïde et des liquides provenant de la fusion de croûte pré-existante: TTG et/ou métasédiments [Laurent *et al.*, 2014a]. Enfin, certains granites contemporains des sanukitoïdes, comme ceux du batholite de Turfloop, témoignent de la fusion de croute pré-existante uniquement: TTG, métasédiments et/ou amphibolites [Laurent *et al.*, 2014b].

En Afrique du Sud, on passe donc de TTG essentiellement juvéniles (fusion de plancher océanique lors de la subduction) à des granitoïdes tardi- et post-archéens dont la pétrogenèse est dominée par les mécanismes de recyclage, notamment par introduction de matériel continental dans le manteau via la subduction (*Figure 10*). Cette évolution traduit l'impact du refroidissement du manteau terrestre sur les processus magmatiques opérant au niveau des zones de subduction [Laurent *et al.*, 2014b].

*Le conglomérat basal du Groupe du Moodies (Afrique du Sud)*

Les témoins de la croûte continentale primitive sont principalement composés de granitoïdes sodiques de type TTG (tonalite-trondhjémite-granodiorite) [Jahn *et al.*, 1981; Condie, 1993; Martin, 1994). Ces derniers se sont formés par fusion partielle de métabasaltes hydratés [Barker et Arth, 1976; Tarney *et al.*, 1979; Condie, 1981; Martin, 1986; Rapp *et al.*, 1991; Nair and Chacko, 2008]. Les granites au sens strict, par contre, sont généralement postérieurs aux TTG et apparaissent tardivement dans les cratons anciens, bien que l'existence de zircons hadéens présentant des inclusions minérales compatibles avec la cristallisation à partir d'un magma granitique péralumineux suggère que les roches granitiques faisaient aussi partie de la croûte primitive. Le conglomérat basal du groupe du Moodies, dans la région de Barberton (Afrique du Sud), comporte une grande variété de granites et de rhyolites péralumineux qui présentent de fortes teneurs en $K_2O$ pour de faibles en CaO. Ces roches se sont mises en place en même temps que les magmas TTG de la région de Barberton, pendant trois cycles magmatiques distincts [Sanchez-Garrido *et al.*, 2011]. Leurs principales caractéristiques, riches en K et pauvres en Ca, sont d'origine magmatique, comme l'atteste la présence majoritaire de feldspaths alcalins (plutôt que de plagioclases) en inclusions dans les zircons étudiés pour datation.

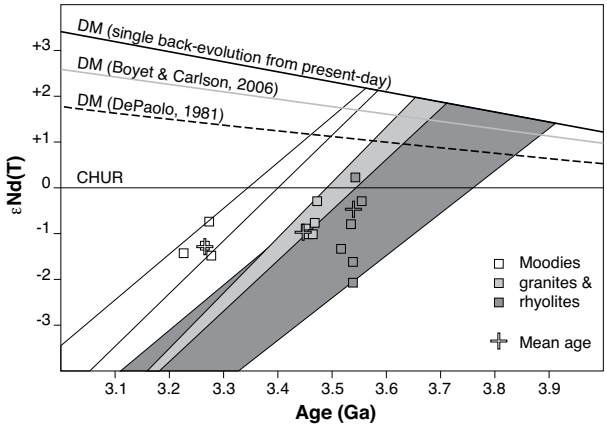


*Figure 11 : les âges modèles Sm-Nd des granites et rhyolites du Groupe de Moodies suggère que le protolithe de leur source date de 3.8-3.9 milliards d'années. D'après Sanchez-Garrido [thèse, 2012].*

Les granites et rhyolites du conglomérat basal du groupe de Moodies résultent vraisemblablement de la fusion partielle d'une source de type métagrauwacke à des pressions supérieures à celle de la stabilité du plagioclase. Ceci implique donc que des granites peralumineux riche en K et pauvre en Ca ont été générés durant le Paléo et Méso-Archéen, aux côtés des TTG sodiques, par la fusion partielle de sédiments à haute

pression. Cela suggère par la même que la Terre Primitive était capable de recycler du matériel relativement jeune et ce, dès 3.8-3.9 milliards d'années (*Figure 11*).

Cette 2ème thématique a donné lieu aux publications suivantes :

*- Debaille, **Doucelance** et al. (2006) Multi-stage mixing in subduction zones : Application to Merapi volcano (Java island, Sunda arc). Geochimica et Cosmochimica Acta 70.*
*- Laurent, Martin, **Doucelance** et al. (2011) Geochemistry and petrogenesis of high-K "sanukitoids" from the Bulai pluton, Central Limpopo Belt, South Africa: Implications for geodynamic changes at the Archaean-Proterozoic boundary. Lithos 123.*
*- Sanchez-Garrido, Stevens, Armstrong, Moyen, Martin, **Doucelance** (2011) Diversity in Earth's early felsic crust: Paleoarchean peraluminous granites of the Barberton Greenstone Belt. Geology 39.*
*- Laurent, **Doucelance** et al. (2013a) Differentiation of the late-Archaean sanukitoid series and some implications for crustal growth: insights from geochemical modelling on the Bulai pluton, Central Limpopo Belt, South Africa. Precambrian Research 227.*
*- Laurent, Paquette, Martin, **Doucelance**, Moyen (2013b) LA-ICP-MS dating of zircons from Meso- and Neoarchaean granitoids of the Pietersburg block (South Africa): crustal evolution at the northern margin of the Kaapvaal craton. Precambrian Research 230.*
*- Laurent, Rapopo, Stevens, Moyen, Martin, **Doucelance**, Bosq (2014a) Contrasting petrogenesis of Mg-K and Fe-K granitoids and implications for post-collisional magmatism: case study from the late-Archaean Matok pluton (Pietersburg block, South Africa), Lithos 196-197.*
*- Laurent, Martin, Moyen, **Doucelance** (2014b) The diversity and evolution of late-Archean granitoids: evidence for the onset of "modern-style" plate tectonics between 3.0 and 2.5 Ga. Lithos 205.*
*- Bellot, Boyet, **Doucelance** et al. (2015) Ce isotope systematics of island arc lavas from the Lesser Antilles. Geochimica et Cosmochimica Acta 168.*

*Thèse*
*- Vinciane Debaille (2002-2005): Etude isotopique (Sr, Nd, Pb) des variations spatiales et temporelles des basaltes océaniques (co-encadrement Pierre Schiano).*
*- Cynthia Sanchez-Garrido (2006-2012): Les magmas potassiques juvéniles archéens: marqueurs de l'évolution du manteau terrestre lors de la formation de la croûte continentale primitive (co-encadrement Hervé Martin, Jean-François Moyen et Gary Stevens).*
*- Oscar Laurent (2009-2012): Les changements géodynamiques à la transition Archéen-Protérozoïque (co-encadrement Hervé Martin).*
*- Nina Bellot (2012-2015) : Développement du système isotopique La-Ce : application aux laves d'arc (co-encadrement Maud Boyet).*

*Master*
*- Cynthia Sanchez-Garrido (2006): Les mécanismes magmatiques de genèse de la croûte continentale primitive. Exemples des terrain méso-archéens de la région de Barberton, Afrique du sud (co-encadrement Hervé Martin).*
*- Oscar Laurent (2009): Les changements géodynamiques à la transition Archéen-Protérozoïque : exemple de la pétrogenèse du pluton de Bulai, Ceinture du Limpopo, Afrique du Sud (co-encadrement Hervé Martin).*

Les carbonatites sont des roches magmatiques relativement rares, constituées pour majeure partie de carbonates de calcium (calcite), de magnésium (dolomite) ou de fer et de magnésium (sidéro-magnésite), et accompagnées de minéraux accessoires (silicates et/ou phosphates). Elles proviennent du manteau. C'est ce que suggèrent leurs compositions isotopiques qui correspondent généralement avec celles des OIB [Nelson *et al.*, 1988; Hoernle *et al.*, 2002]. C'est aussi ce que montrent les xénocristaux en provenance du manteau, généralement des spinelles chromifères [Bailey, 1989 ; Mourtada *et al.*, 1997], contenus dans certaines carbonatites extrusives.

L'origine mantellique des carbonatites s'appuie également sur les résultats de l'expérimentation en pétrologie. Différents auteurs ont démontré qu'il était possible d'obtenir des liquides carbonatés par fusion d'un mélange péridotite + $CO_2$ [Wyllie et Huang, 1976; Eggler, 1978; Wallace et Green, 1988]. La formation de ces liquides est conditionnée à la pression (*Figure 12*): pour des pressions inférieures à environ 2.5 GPa, les liquides sont silicatés (avec du $CO_2$ dissous). Au-dessus de cette valeur seuil, les liquides sont carbonatés et la température de fusion est abaissée d'environ 200°C. Ce changement de comportement s'explique par la réaction des silicates avec le $CO_2$ qui conduit à la formation de carbonates dont le point de fusion est relativement bas. Cette réaction a été étudiée expérimentalement : forstérite + diopside + $CO_2$ = dolomite + enstatite [Wyllie *et al.*, 1983].

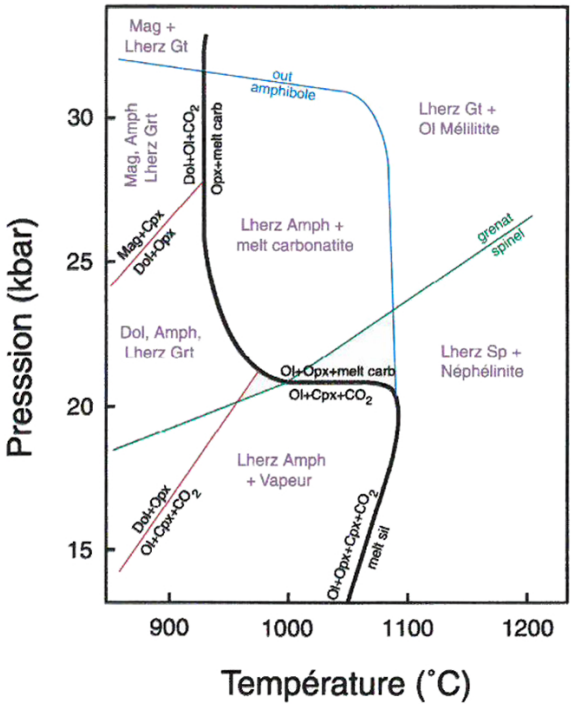


*Figure 12 : Réactions de carbonation et fusion partielle dans le système péridotite + $CO_2$. D'après Wallace et Green [1998].*

Toutes les indications semblent donc converger vers une origine mantellique des carbonatites. Il existe toutefois un paradoxe. Les données de la pétrologie expérimentale prédisent que les liquides carbonatés formés dans le manteau sont magnésiens (= dolomitiques). Or, la majorité des carbonatites observées à la surface de la Terre sont calciques [Woolley and Kempe, 1989; Woolley and Kjarsgaard, 2008]. Pour expliquer cette différence, certains auteurs ont suggéré que les carbonatites, magnésiennes à leur source, soient enrichies en calcium par réaction avec leur environnement mantellique pendant leur remontée [Dalton et Wood, 1993; Hammouda et al., 2014]. Ceci suggère que les liquides séjournent suffisamment au contact de leur encaissant, une hypothèse peu supportée par les propriétés physiques et les modèles de migration de liquides carbonatés [Hunter et McKenzie, 1989; Treimann, 1989; Hammouda et Laporte, 2000]. Une autre approche consiste à considérer que la source des carbonatites, bien que située dans le manteau, soit constituée de croûte océanique recyclée. Les expériences de fusion prenant comme composition source un mélange de basalte et de sédiments carbonatés ont montré qu'on pouvait fabriquer des liquides carbonatitiques, calciques, dans les conditions du gradient de la subduction [Hammouda, 2003; Kiseeva et al., 2012]. Ce mécanisme parvient

donc à expliquer la composition chimique en éléments majeurs de la majorité des carbonatites analysées. Par contre, il suppose le recyclage par subduction de croûte océanique carbonatée et également que toutes les régions sources contiennent ces matériaux. Le recyclage par subduction de sédiments carbonatés pose la question de la survie de ces derniers aux profondeurs des fosses océaniques, qui excèdent la profondeur de compensation des carbonates (CCD). La dissolution des carbonates dans les sédiments est limitée aux niveaux supérieurs, bioturbés, de ceux-ci [Archer, 1996]. Dès lors que ces derniers sont constitués de sédiments non carbonatés, la dissolution cesse, autrement dit l'enfouissement des carbonates marins leur permet de ''passer'' la CCD. A titre d'exemple, les carbonates forés au large de l'arc de la Sonde (sites ODP 765 et DSDP 261, voir Plank [2014]) proviennent d'une profondeur d'eau supérieure à 5600-5700 m ; ils sont dans ce cas précis enfouis sous un niveau argileux d'une cinquantaine de mètre d'épaisseur.

Si l'hypothèse de croûte recyclée a déjà été proposée, que ce soit sur la base des isotopes radiogéniques [Hoernle *et al.*, 2002] ou des isotopes stables [Ray *et al.*, 1999], les ambiguïtés demeurent toutefois. Ainsi, la similarité entre les rapports isotopiques du carbone entre certaines carbonatites et les sédiments marins pourrait s'expliquer par toute une série de phénomènes (altération basse température, haute température, dégazage, fusion), sans qu'on puisse en isoler un, faute de connaissance sur le fractionnement des isotopes stables à haute pression et haute température. De la même façon, la typologie des isotopes radiogéniques fait références à des pôles qui ne signifient pas nécessairement une nature de roche source.

La majorité des carbonatites affleure en domaine continental. Les rares échantillons que l'on trouve à l'affleurement en domaine océanique proviennent de l'archipel du Cap Vert et de l'île de Fuerteventura, aux Canaries. C'est sur ces échantillons que portent principalement mes travaux. La mesure des rapports isotopiques d'hélium et de carbone des échantillons du Cap Vert et des Canaries suggère une source profonde, en accord au 1er ordre avec leurs compositions isotopiques Sr-Nd-Pb typiques des OIB. Celle-ci pourrait être située au niveau de la couche D'', enrichie en gaz rares et en carbone primordial [Mata *et al.*, 2010]. Ce modèle, dans lequel le carbone n'est pas recyclé, ne permet pas de reproduire, par contre, les compositions isotopiques de Sr, Nd et Pb des échantillons (*Figure 13*), ni leurs spectres en éléments traces. La comparaison avec la géochimie des basaltes échantillonnés sur les mêmes îles que les carbonatites permet de proposer un nouveau modèle dans lequel les carbonatites ont une origine plus superficielle. Elles résultent de la fusion partielle de

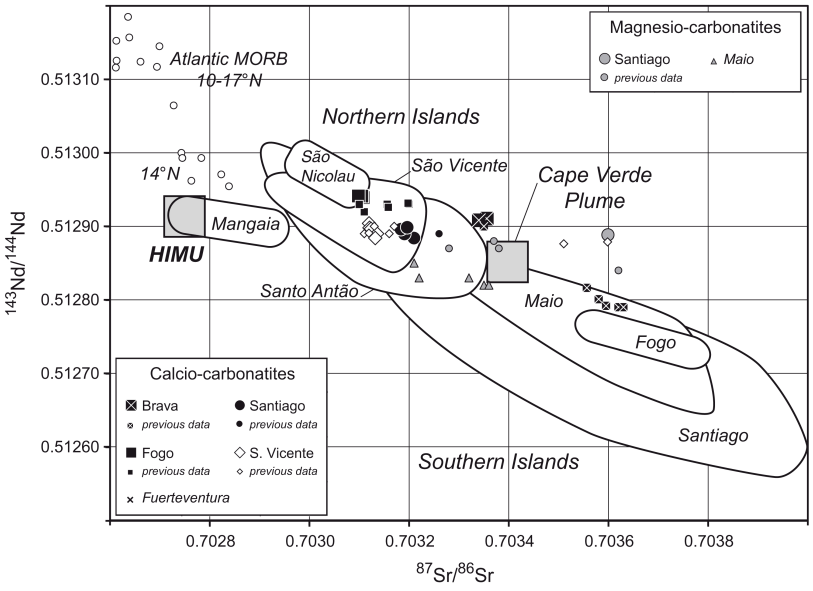


*Figure 13 : Les carbonatites de l'archipel du Cap Vert présentent des compositions isotopiques significativement différentes, bien que proches, de celles des silicates échantillonnés sur les mêmes îles, en faveur de sources distinctes. D'après Doucelance et al. [2010].*

la lithosphère océanique, préalablement métasomatisée par des liquides carbonatitiques liés au recyclage de carbone crustal par subduction [Doucelance *et al.*, 2010]. Le rôle des points chauds du Cap Vert et des Canaries est alors essentiellement thermique, comme discuté pour une partie des variations isotopiques des échantillons silicatés : il permet la fusion partielle de la lithosphère océanique. La participation dans une moindre mesure du matériel plume à l'origine des basaltes du Cap Vert et des Canaries est cependant requise pour expliquer les compositions isotopiques des gaz rares mesurées. Ce modèle suggère également des rapports isotopiques de carbone ($\delta$13C) non mantelliques contrairement à ce qui est observé. Cette dernière remarque pose la question du fractionnement des isotopes stables à haute pression et haute température. L'analyse des compositions isotopiques de Ce, un traceur potentiel des carbonates marins comme nous l'avons vu dans la section précédente, des échantillons de carbonatites du Cap Vert et des Canaries est en accord avec le modèle de recyclage [Doucelance *et al.*, 2014a]. Les carbonatites échantillonnées sur l'île de Brava (Cap Vert) font exception au modèle. La similitude des compositions isotopiques de Sr-Nd-Pb-Ce entre les formations volcaniques silicatées et les carbonatites suggèrent, dans le cas de Brava, une source commune et une séparation des liquides silicatés et carbonatitiques par immiscibilité [Mourão *et al.*, 2010; 2012].

Ce 3ème thème de recherche a donné lieu aux publications suivantes:

- *Mourão, Mata, **Doucelance** et al. (2010) Quaternary extrusive calciocarbonatite volcanism on Brava Island (Cape Verde): A nephelinite-carbonatite immiscibility product. Journal of African Earth Science 56.*
- *Mata, Moreira, **Doucelance** et al. (2010) Noble gases and carbon isotopic signatures of Cape Verde oceanic carbonatites: implications for carbon provenance. Earth and Planetary Science Letters 291.*
- ***Doucelance** et al. (2010) Geochemical constraints on depth of origin of oceanic carbonatites: the Cape Verde case. Geochimica et Cosmochimica Acta 74.*
- *Mourão, Mata, **Doucelance** et al. (2012) Geochemical temporal evolution of Brava Island magmatism: constraints on the variability of Cape Verde mantle sources and on carbonatite-silicate magmas link. Chemical Geology 334.*
- ***Doucelance** et al. (2014a) What do cerium isotopes tell us about the deep source of oceanic cabonatites. Earth and Planetary Science Letters 407.*

*Thèse*

- *Cyntia Mourão (2008-2013), doctorante au centre de géologie de Lisbonne (direction João Mata): Initiation à la géochimie isotopique Sr-Nd-Pb et application au volcanisme de l'île de Brava, archipel du Cap Vert.*

*Master*

- *Mélodie-Neige Cornu (2013) Datation Sm/Nd et U/Pb et caractérisation de la source des carbonatites de Phalaborwa (co-encadrement Valérie Bosse).*
- *Morgan Chevreuil (2014): Datation Sm/Nd et caractérisation de la source des carbonatites de Spitskop, Afrique du Sud (co-encadrement Maud Boyet).*

Parallèlement à cette grande thématique ‘‘Géodynamique chimique’’, je me suis intéressé à la construction/destruction des édifices volcaniques et plus particulièrement à l’apport des systématiques isotopiques vis-à-vis de cette problématique. Deux types de cibles, en relation avec mes travaux précédents, ont été étudiées dans ce but : d’une part le Socompa, au Chili, un stratovolcan en contexte de subduction, et d’autre part, le Mont Amarelo, sur l’île de Fogo dans l’archipel du Cap Vert, un volcan bouclier en contexte intraplaque océanique. Ces deux édifices volcaniques ont été affectés par une déstabilisation massive de leurs flancs (avalanche de débris).

*Le volcan Socompa (Zone Volcanique Centrale -CVZ- de l’arc andin, Chili)*

Les volcans sont des édifices instables, nés de l’accumulation souvent rapide, à l’échelle des temps géologiques, de matériaux aux propriétés mécaniques et physiques hétérogènes (coulées de laves, couches de cendres, scories et blocs plus ou moins cohérents et indurés). Leurs pentes atteignent parfois des valeurs proches de la limite de stabilité naturelle, autour de 30-35°, et souvent leurs roches subissent une double altération: une altération exogène ou météorique progressant depuis la surface et une altération endogène liée aux circulations de fluides hydrothermaux au cœur même du volcan. Ces mêmes roches subissent également les pressions du système magmatique, avec notamment de nouvelles intrusions de magmas, sous la forme de filons (dykes) ou de crypto-dômes. Par ailleurs, les volcans peuvent être situés dans une zone sismiquement active.

Les avalanches de débris proviennent de l’effondrement d’un flanc de volcan. Les volumes de roches impliquées vont de quelques millions de m³ à plusieurs dizaines voire centaines de km³, et les vitesses d’écoulement peuvent atteindre 100 m/s. Les avalanches de débris sont caractérisées par une très grande fluidité et s’écoulent sur des distances de plusieurs dizaines de kilomètres (e.g. Voight *et al.* [1981] et Siebert [1984]). Leur étude est donc essentielle à la gestion des risques volcaniques. Un des défis actuels de la volcanologie moderne est la compréhension des mécanismes qui conduisent à une telle fluidité. L’intensité et les modalités du broyage des roches impliquées dans ces avalanches, à savoir la dynamique interne des avalanches, sont des paramètres importants pouvant nous renseigner sur cet aspect.

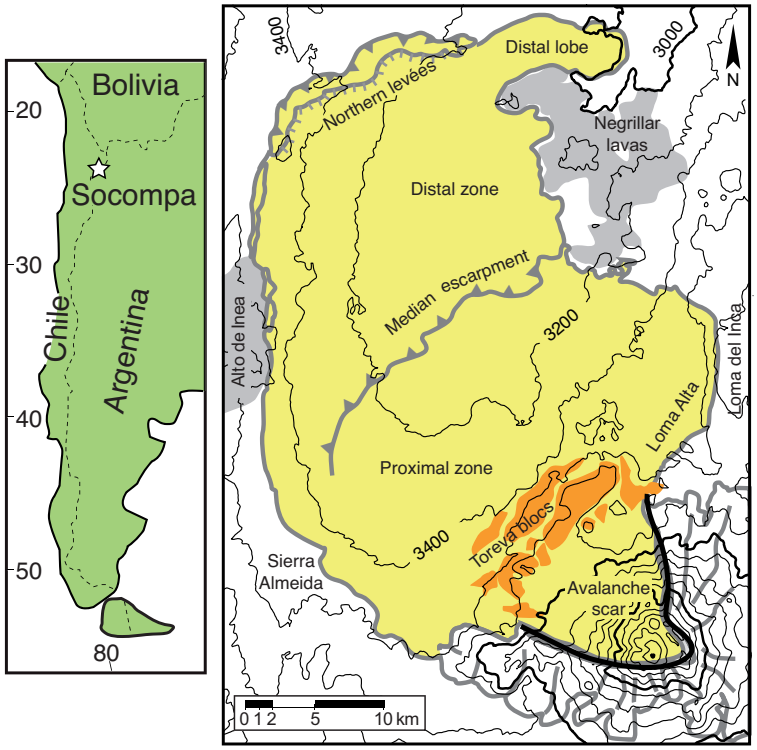


*Figure 14 : Localisation des dépôts de l’avalanche du Socompa, dans le désert de l’Atacama au Chili. D’après Kelfoun et al. [2008].*

L’avalanche du volcan Socompa (*Figure 14*) s’est formée par la déstabilisation de 36 km³ de son flanc nord

il y a environ 7200 ans. Les dépôts de l'avalanche de débris s'étendent sur 500 km$^2$ et s'étalent sur une distance de 40 km pour une épaisseur de quelques dizaines de mètres. Certaines études antérieures (terrain, imagerie, modélisation numérique) suggèrent un déplacement en masse de l'avalanche. Cette dernière se serait étalée sur une couche basale concentrant l'essentiel du cisaillement, ce qui implique que la stratigraphie initiale de l'édifice devrait être globalement conservée dans l'avalanche [Kelfoun et Druitt, 2005; Kelfoun *et al.*, 2008]. Autrement dit, il doit y avoir peu de mélanges au sein de l'avalanche (sauf à la base) et la matrice, la phase constituée des particules les plus fines, qui résulte du broyage des roches de l'édifice et qui ennoie généralement des blocs plus volumineux, doit être de la même composition que ces derniers. D'autres auteurs, cependant, ont avancé que la matrice de l'avalanche est majoritairement constituée des roches du soubassement du volcan (roches sédimentaires et ignimbrites) [Wadge *et al.*, 1995; van Wyk de Vries *et al.*, 2001]. Celles-ci, friables, auraient été broyées à la base et seraient remontées vers la surface en englobant les roches de l'édifice présentes dans le corps de l'écoulement. Cette deuxième hypothèse est validée notamment par la présence de ponces dans de nombreux échantillons de matrice. La situation géographique du Socompa, en plein désert de l'Atacama, une des régions les plus arides sur Terre, garantie la qualité de préservation des dépôts de l'avalanche depuis leur mise en place et permet ainsi d'utiliser les concentrations en éléments en traces et les rapports isotopiques pour discuter les deux grands modèles présenter ci-dessus et ainsi contraindre la dynamique interne de l'avalanche.

La stratégie développée a consisté à analyser les compositions chimique (concentrations en éléments majeurs et traces) et isotopique (Sr-Nd) des dépôts de l'avalanche, des produits du Socompa encore en place dans l'édifice, au niveau de la cicatrice, et des roches des formations à la base de l'avalanche, afin de déterminer si la matrice cendreuse est issue du broyage de roches voisines, de roches du substratum ou d'un mélange complexe de plusieurs roches initialement distantes. Le recours aux traceurs isotopiques est justifié par le faible contraste chimique entre les différents composants mis en jeu (roches de l'édifice, majoritairement des dacites, et ignimbrites basales).

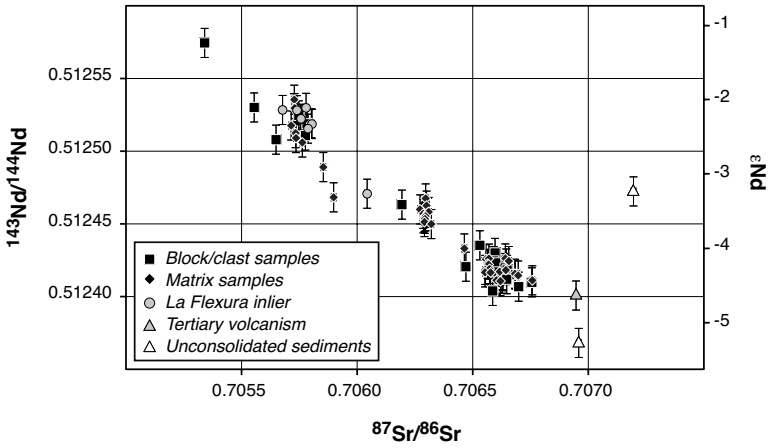


*Figure 15 : Diagramme $^{143}Nd/^{144}Nd$ vs. $^{87}Sr/^{86}Sr$. Les échantillons du dépôt de l'avalanche définissent un mélange binaire. Les roches du substratum (La Flexura inlier) se positionnent dessus. Leur grande homogénéité par rapport aux échantillons de matrice, ainsi que leur position intermédiaire sur la courbe de mélange, suggèrent que la matrice de l'avalanche résulte principalement du broyage des formations de l'édifice. D'après Doucelance et al. [2014b].*

Les différents échantillons de l'avalanche définissent une courbe de mélange unique dans le diagramme $^{143}Nd/^{144}Nd$ vs. $^{87}Sr/^{86}Sr$. Les roches du substratum se positionnent dessus, mais ne définissent pas un des deux pôles de mélange. Par ailleurs, seuls quelques échantillons de matrice affichent des compositions similaires à celles des roches du substratum (*Figure 15*). Il est donc peu probable que la matrice de l'avalanche corresponde au broyage et à l'incorporation de ce dernier ; l'essentiel de la matrice est plus vraisemblablement com-

posée des roches broyées (et éventuellement mélangées) de l'édifice. Les résultats isotopiques permettent également de mettre en évidence l'augmentation de l'hétérogénéité des dépôts de l'avalanche, c'est à dire une matrice de plus en plus différente des blocs qu'elle contient ou qui sont transportés à sa surface, avec la distance au Socompa (*Figure 16*). Cette dernière observation traduit la plus grande efficacité des mélanges au sein des dépôts durant leur mise en place [Doucelance *et al.*, 2014b].

Cette approche est à ma connaissance totalement originale, et il s'agit des premiers résultats qui traitent directement de la dynamique interne des avalanches de débris.

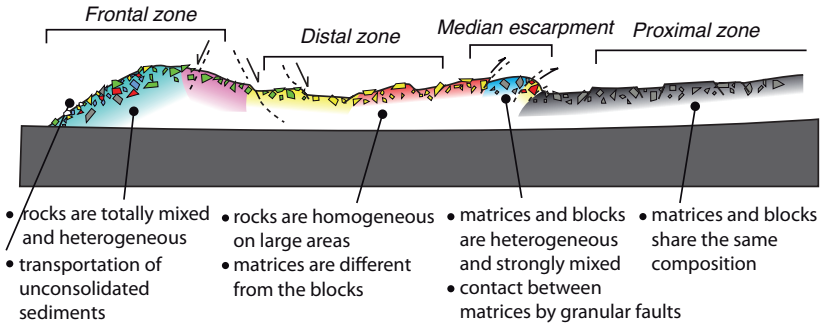


*Figure 16 : la mesure des compositions isotopiques de Sr et Nd, entre blocs et matrices au contact pour chaque secteur clé de l'avalanche du Socompa permet de reconstituer la dynamique interne de cette dernière, en fonction de la distance au volcan Socompa. D'après Doucelance et al. [2014b].*

L'échantillonnage des différentes formations des stratovolcans de la CVZ (et de l'arc andin de manière plus générale) est généralement rendu difficile par la faible accessibilité et surtout l'altitude des édifices volcaniques (le Socompa, notamment, culmine à plus de 6000 mètres). L'utilisation des produits ''non modifiés'' des dépôts d'avalanche de débris, i.e. les différents blocs transportés à la surface de l'avalanche, est un moyen de s'affranchir de cette difficulté. L'échantillonnage des formations du flanc de volcan qui s'est effondré permet alors de reconstituer, via l'analyse géochimique, une partie de l'histoire magmatique du volcan. La contre partie de cette approche de l'échantillonnage, toutefois, est la perte de chronologie relative entre les différentes formations (le simple principe de superposition n'est plus possible). L'étude de la source du Socompa est actuellement en cours ; je reviendrai sur ce point dans la section Projets en cours.

*Le Mont Amarelo (Ile de Fogo, archipel du Cap Vert)*

Malgré un volcanisme beaucoup moins explosif et des pentes beaucoup moins fortes, les volcans boucliers des îles océaniques nées de l'activité de points chauds, telles que les îles du Cap Vert, des Canaries ou d'Hawaï, connaissent des déstabilisations massives de leurs flancs. Ces phénomènes sont de faible récurrence et n'ont encore jamais été observés. L'instabilité des volcans boucliers océaniques se traduit non seulement par des cicatrices de grande ampleur (plusieurs $km^3$) ou des discontinuités structurales marquées, mais également par des dépôts d'avalanches de débris sous-marins très étendus (ex. Canaries, Hawaï). Faute d'observations, les facteurs de déclenchement de ces déstabilisations majeures, leurs mécanismes de rupture, et les éventuels précurseurs ne sont pas bien connus. En conséquence, l'évaluation de cet aléa et des tsunamis qu'il peut occasionner demeure extrêmement imprécise, voire hasardeuse, du fait des incertitudes sur les mécanismes de déstabilisation.

Plusieurs études ont déjà souligné les variations de composition des laves avant et après l'effondrement d'un flanc de volcan [Presley *et al.*, 1997; Hildenbrand *et al.*, 2004; Manconi *et al.*, 2009; Boudon *et al.*, 2013]. La question qui se pose alors est celle d'un éventuel contrôle en profondeur, via la productivité du

panache mantellique et les transferts lithosphériques des magmas, de la croissance du volcan et de son instabilité. Par ailleurs, la décharge lithostatique rapide liée à l'effondrement pourrait également avoir des conséquences sur les réservoirs magmatiques [Manconi *et al.*, 2009; Pinel et Albino, 2013].

L'île de Fogo est l'une des îles volcaniques les plus actives au monde. De forme quasi circulaire, elle présente un diamètre de 25 km. Son point culminant, le Pico de Fogo, est à 2 829 m au-dessus du niveau de la mer, soit à environ 7 000 m au-dessus du plancher océanique. Le Mont Amarelo, dont le Pico de Fogo occupe désormais la place, a connu un effondrement majeur de son flanc est il y a environ 100000 ans (entre 123000 et 86000 ans, cf. Foeken *et al.* [2009] et Paris *et al.* [2011]). Cet effondrement lui a donné sa morphologie en fer à cheval, ouvert vers l'est, et a également laissé un escarpement de plus de 1 000 m de hauteur, nommée la Bordeira, ainsi que 150 km$^3$ environ de dépôts d'avalanche de débris en mer [Masson *et al.*, 2008]. Des dépôts du tsunami générés par ce glissement ont été retrouvés sur l'île de Santiago, à Tarrafal, à environ 35 km à l'est de l'île de Fogo [Paris *et al.*, 2011]. Les produits éruptifs pré-effondrement (> 90 ka) affleurent essentiellement dans les parois de la Bordeira, et sont fossilisés par des phases post-effondrement à la base et sur les rebords de cette dernière. Hildner *et al.* [2012] ont mis en évidence des variations temporelles des conditions de pression avant et après effondrement, basées sur les clinopyroxènes (géothermobaromètre de Putirka *et al.* [2003]) que l'on retrouve en très forte abondance dans les échantillons des laves de Fogo (*Figure 17*).

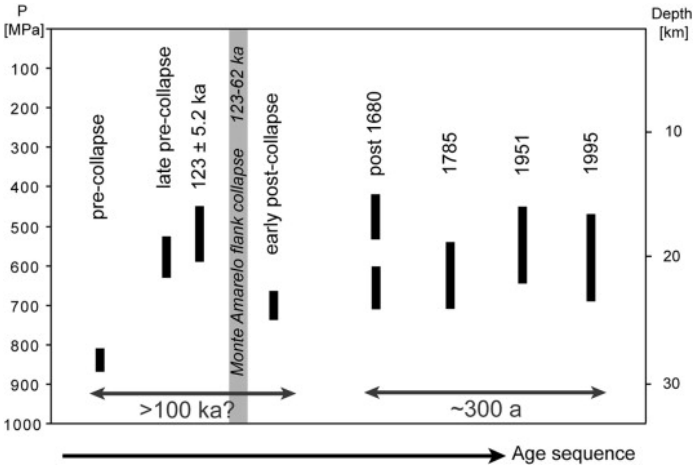


*Figure 17 : Variation des conditions de pression en fonction de la chronologie relative des laves de Fogo. D'après Hildner et al. [2012].*

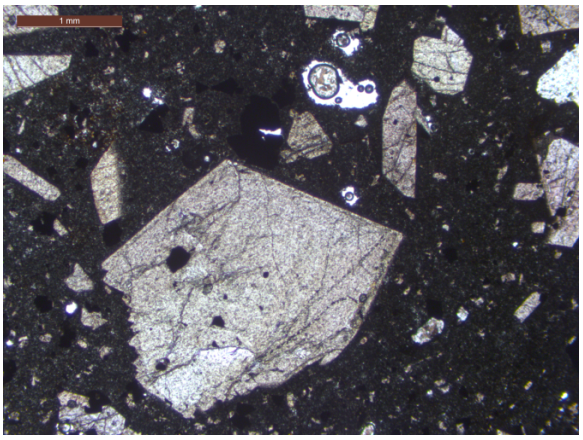


*Figure 18 : Fragment de cristal de pyroxène classiquement observé dans les laves de Fogo (LPnA ; taille : 2x2 mm environ). D'après Cornu [Master, 2014].*

L'étude du Mont Amarelo vise à comprendre les liens éventuels entre les variations de source des magmas, les rythmes de croissance d'un édifice volcanique et son instabilité. Elle a débuté via le stage de master de Mélodie-Neige Cornu et compose maintenant le sujet principal de sa thèse. Les premières analyses démontrent clairement l'origine cumulative de la majorité des clinopyroxènes présents dans les laves, ce qui pourrait amener à réviser les conclusions de Hildner *et al.* [2012], qui reposent par ailleurs sur un échantillonnage limité. Une grande majorité des cristaux sont en effet présents sous forme de fragments présentant à la fois des bordures typiques des cristaux automorphes et une limite fracturée (*Figure 18*). Ce type de morphologie est symptomatique de cristaux arrachés à un « mush » cristallin lors de mouvements convectifs au sein d'une chambre magmatique, ou lors de la remontée des magmas [Welsch *et al.*, 2013].

D'autres montrent des formes avec des traces de dissolution marquant un déséquilibre thermique ou compositionnel important à un moment de la croissance du cristal.

Pour autant, les produits éruptifs pré- et post-effondrement de l'île de Fogo semblent définir deux populations distinctes pour ce qui est de leurs compositions chimiques et isotopiques : les échantillons post-effondrement affichent par exemple des teneurs en silice, fer et titane plus élevées que ceux correspondant à l'activité pré-effondrement (*Figure 19a*). Ces distinctions correspondent également à des évolutions temporelles contrastées, de part et d'autre de la date supposée de l'effondrement du Mont Amarelo (*Figures 19b,c*). Alors que la teneur en silice des échantillons pré-effondrement semble croitre régulièrement, celle des laves post-effondrement définit un palier horizontal. De même, le rapport isotopique $^{206}Pb/^{204}Pb$ des produits pré-effondrement augmente graduellement avec le temps, alors que les laves

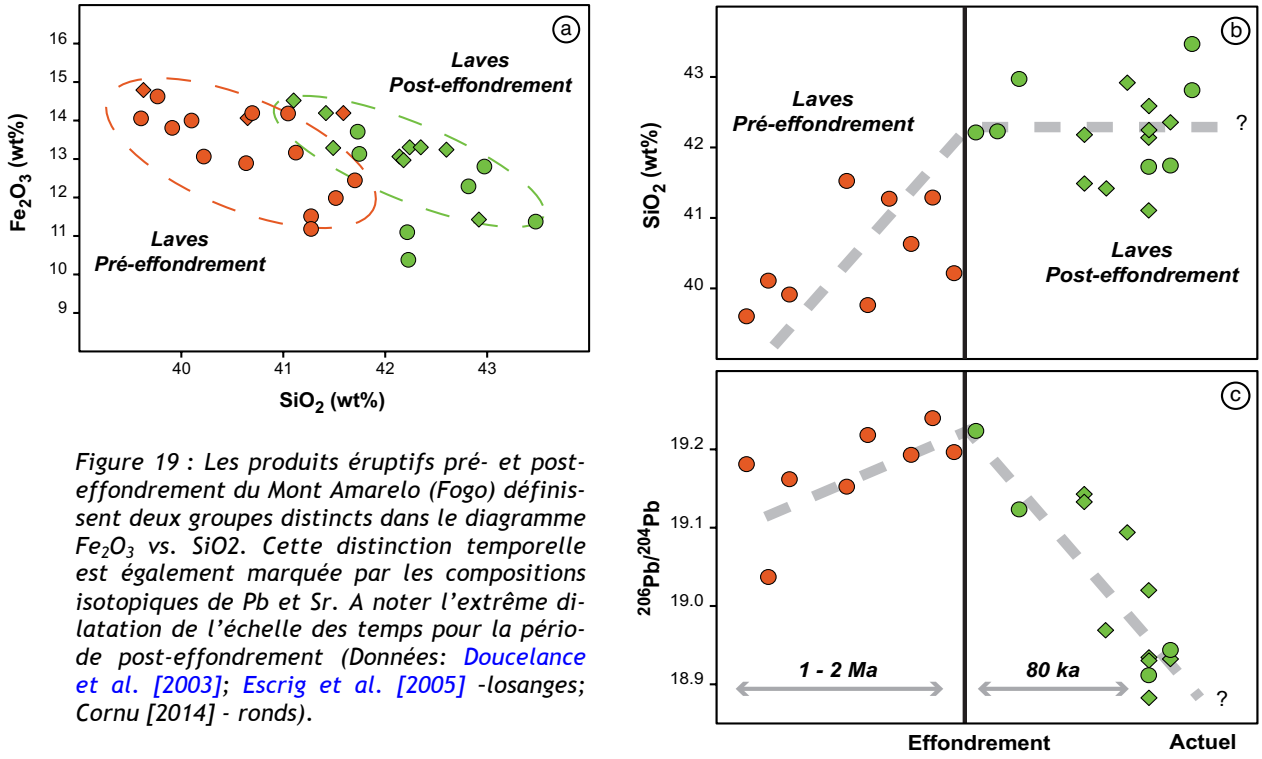


*Figure 19 : Les produits éruptifs pré- et post-effondrement du Mont Amarelo (Fogo) définissent deux groupes distincts dans le diagramme $Fe_2O_3$ vs. SiO2. Cette distinction temporelle est également marquée par les compositions isotopiques de Pb et Sr. A noter l'extrême dilatation de l'échelle des temps pour la période post-effondrement (Données: Doucelance et al. [2003]; Escrig et al. [2005] -losanges; Cornu [2014] - ronds).*

post-collapse voient leur composition isotopique de Pb diminuer de manière abrupte, en moins de 100000 ans (c'est l'inverse pour le strontium). Ces observations suggèrent donc qu'il existe un lien plus ou moins étroit entre magmatisme et effondrement. Plus précisément, la décharge lithostatique rapide liée à l'effondrement pourrait avoir entrainé (?) l'augmentation du taux d'assimilation de la lithosphère capverdienne, de composition EM1 [Doucelance *et al.*, 2003; Escrig *et al.*, 2005] par les liquides issus du panache, et ainsi la migration des compositions isotopiques de Sr et Pb vers des valeurs respectivement plus et moins radiogéniques.

Comme indiqué ci-dessus, cette étude est en cours. Mélodie-Neige Cornu se concentre maintenant sur la datation absolue des produits éruptifs pré- et post-effondrement (méthode K-Ar) qui permettra un calage chronologique fiable des tendances identifiées ici, ainsi qu'une estimation des rythmes d'accumulation de produits volcaniques le long des parois de la ''caldera'' du Fogo.

Ce 4ème thème de recherche a donné lieu aux publications suivantes:

- ***Doucelance** et al. (2014) Geochemical insights into the internal dynamics of debris avalanches. A case study: the Socompa avalanche, Chile. Geochemistry, Geophysics, Geosystems 15.*

*Thèse*

*- Mélodie-Neige Cornu (en cours), Evolution magmatique et instabilité des volcans boucliers océaniques (co-encadrement Raphaël Paris et Patrick Bachelery).*

*Master*

*- Mélodie-Neige Cornu (2014) Evolution magmatique et instabilité d'un volcan bouclier océanique : Fogo, Cap Vert (co-encadrement Raphaël Paris et Patrick Bachelery).*

*- Antoine Delvoye (2014) Étude géochimique du dépôt de l'avalanche secondaire du volcan Socompa, Chili (co-encadrement Karim Kelfoun).*

La qualité des données isotopiques occupe une place importante de mon activité de recherche depuis mon doctorat. Je terminerai donc cette partie ''Synthèse'' par un certain nombre de travaux concernant le développement, la mise au point et/ou l'amélioration des mesures isotopiques, notamment les aspects spectrométriques (TIMS et MC-ICP-MS).

*La mesure de haute précision des rapports isotopiques de plomb par TIMS*

L'intérêt de la mesure des rapports isotopiques de Pb, que ce soit en géologie endogène ou exogène, n'est plus à démontrer. La qualité des mesures, par contre, alimente encore régulièrement le débat scientifique. Sur un spectromètre de masse à source solide (TIMS), la justesse et la précision des analyses isotopiques de Pb sont avant tout liées à la détermination de l'effet de discrimination de masse (ou fractionnement de masse instrumental). Or, ce dernier ne suit pas les lois ''classiques'' (et semi-empiriques) de fractionnement dépendant de la masse (*Figure 20*), qui sont par exemple utilisées pour la correction en interne des rapports isotopiques de Sr et Nd, dès lors que la température de mesure est élevée (> 1050-1100°C) [Doucelance et Manhès, 2001]. Par conséquent, les analyses réalisées sur TIMS, généralement à des températures comprises entre 1200 et 1400°C afin de s'affranchir des interférences organiques, sont limitées en précision au niveau de quelques $10^{-4}$ relatif.

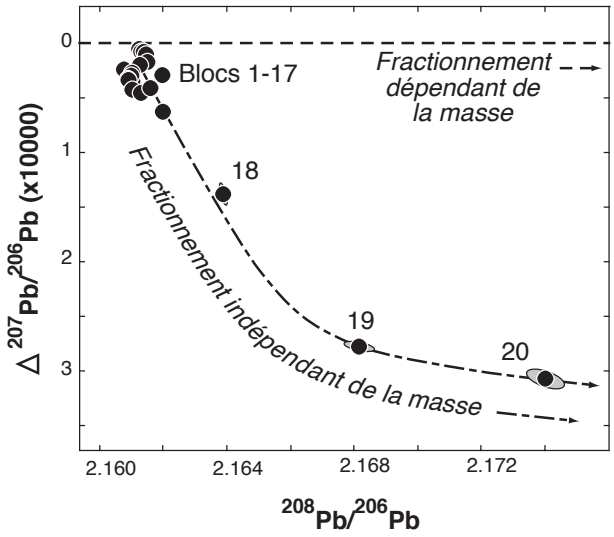


*Figure 20 : Evolution des rapports isotopiques $^{207}Pb/^{206}Pb$ et $^{208}Pb/^{206}Pb$ au cours d'une même acquisition (la température du filament augmente à chaque bloc de mesure), où $\Delta^{207}Pb/^{206}Pb$ représente la différence entre la valeur mesurée du rapport $^{207}Pb/^{206}Pb$ et la valeur théorique de ce dernier s'il obéissait à un fractionnement dépendant de la masse, pour une même valeur du rapport $^{208}Pb/^{206}Pb$. A haute température, le biais affiché par le rapport $^{207}Pb/^{206}Pb$ (valeur proche de 0.9 dans les échantillons naturels) peut atteindre plus de 300 ppm. Modifié d'après Doucelance et Manhès [2001].*

Le fractionnement anormal (non dépendant de la masse) affecte plus particulièrement le $^{207}Pb$, l'isotope de masse impaire. Il a également été mis en évidence pour les masses 67 du Zn et 111 et 113 du Cd [Manhès et Göpel, 2003]; il pourrait avoir comme origine une plus grande volatilité des isotopes de masse impaire par rapport aux pairs [Amelin *et al.*, 2006] ou résulter d'un changement d'état d'oxydation au sein du dépôt [Manhès et Göpel, 2007]. Un tel fractionnement n'est pas observé, par contre, sur les instrumentations ICP-MS multi-collecteurs [Doucelance et Manhès, 2001], sur lesquelles sont désormais réalisées, dans leur grande majorité, les analyses isotopiques de Pb.

*La correction de l'effet de ''queue de pic'' (ou tailing)*

Le système isotopique Lanthane - Cérium est basé sur la radioactivité β- du $^{138}La$ qui donne naissance au $^{138}Ce$ ($T_{1/2}$ = 292.5 Gans). Les éléments impliqués sont deux lanthanides adjacents, ce qui assure une très bonne cohérence géochimique, égale voire supérieure à celle du système Sm-Nd. Autrement dit, le rap-

port $^{138}Ce/^{142}Ce$ mesuré dans une roche est le reflet du rapport La/Ce intégré dans le temps de son réservoir source. Par ailleurs, le Ce présente la particularité de pouvoir exister dans la nature sous forme +3 ou +4, suivant les conditions d'oxydo-réduction (Ce et Eu sont les deux seules lanthanides à posséder une telle caractéristique). Le système isotopique La/Ce est donc un outil de premier ordre pour étudier les effets éventuels à long terme des composants issus d'environnements affectant potentiellement l'état de valence du Ce, notamment le recyclage par subduction plus ou moins profonde de matériaux ayant résidé à la surface du globe.

Une des grandes difficultés de la mesure précise des rapports isotopiques de Ce réside dans la correction de l'effet dit de queue de pic. Ce terme désigne l'interférence d'un ion majeur (le $^{140}Ce$, ~88.45% du Ce total) sur un ion mineur de plus basse masse (le $^{138}Ce$, ~0.25%, soit 1/350è du $^{140}Ce$), qui se produit suite à la perte d'une partie de l'énergie cinétique d'une petite fraction des ions de l'isotope majeur quand ils entrent en collision avec les molécules de gaz résiduels dans le tube du spectromètre de masse. Une telle interférence est bien connue des spécialistes des déséquilibres isotopiques U-Th, qui sont confrontés à des dynamiques bien supérieures à celle du Ce ($^{234}U/^{238}U$ ~1/18200 pour un échantillon à l'équilibre séculaire). Pour y remédier, on mesure classiquement le ''petit'' isotope sur un compteur d'ions, lui-même placé derrière un filtre en énergie, alors que le ''grand'' isotope est mesuré sur une cage de Faraday. Un tel dispositif permet de réduire significativement l'effet de queue de pic et d'éviter toute correction, toutefois la précision des analyses est alors limitée par la reproductibilité du gain entre le compteur d'ions et la cage de Faraday, au niveau du 1/1000è. Pour le Ce, une telle approche n'est pas possible. La précision recherchée est en effet de l'ordre de quelques dizaines de ppm, ce qui impose de travailler sur cages de Faraday uniquement, et donc d'effectuer la correction de tailing [Bellot *et al.*, 2015]. Cette dernière repose sur la mesure des masses 135.5 et 137.5, qui, couplées à un modèle exponentiel du tailing, permettent de déterminer la contribution du $^{140}Ce$ sur les isotopes $^{136}Ce$ et $^{138}Ce$ (*Figure 21*).

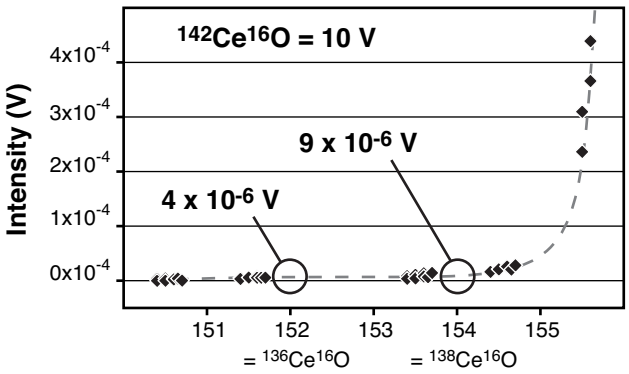


*Figure 21 : Forme du pic majeur de Ce ($^{140}Ce$ = ~80 V) du coté des basses masses, et interférences sur les masses mineures $^{136}Ce$ et $^{138}Ce$. A noter que les masses de Ce sont mesurées sous forme oxyde. Modifié d'après Bellot et al. [2015].*

Hormis les isotopes du Ce, une telle correction de tailing a été uniquement mise en place, à ma connaissance, pour les analyses effectuées sur la première génération du MC-ICP-MS Micromass Isoprobe™, qui soufrait d'une sensibilité en abondance relativement élevée, de l'ordre de 25 ppm [Thirlwall, 2001]. Les analyses isotopiques de Pb et U que j'ai réalisées sur ce type d'instrument au Geotop (Montréal) ne reposent pas, par contre, sur la mesure des masses intermédiaires pour ce qui est de la correction de tailing. Des solutions pures des isotopes $^{204}Pb$, $^{208}Pb$, $^{233}U$ et $^{238}U$ ont été mesurées à chaque début de session analytique afin de déterminer la forme réelle des pics des masses [Deschamps *et al.*, 2003; Doucelance *et al.*, 2003]. Il s'agissait donc d'une correction externe (offline) de l'effet de queue de pic. Le fait de mesurer le rapport $^{234}U/^{238}U$ en utilisant uniquement des cages de Faraday était initialement motivé par l'absence de compteurs d'ions opérationnels sur le MC-ICP-MS du Geotop. Pour autant, la qualité des mesures a été

améliorée d'un facteur environ 10 (~1‰ contre ~1%) vis-à-vis des précisions analytiques classiquement obtenues à l'époque de ce développement (*Figure 22*).

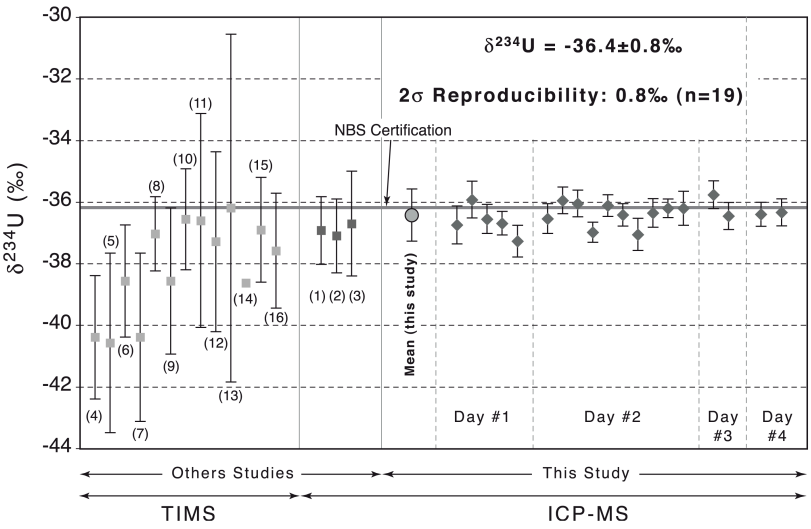


*Figure 22 : Gain de précision obtenu lors du développement de l'analyse des rapports isotopiques d'uranium par spectrométrie de masse à source plasma, multi-collecteur (ICP-MS). D'après Deschamps et al. [2003].*

*La correction du fractionnement de masse instrumental du Re par dopage au W*

Le dernier point que je souhaiterais souligner dans ce chapitre analytique concerne la mesure des rapports isotopiques de rhénium par spectrométrie de masse à source plasma (et dopage au tungstène). Le développement de ce type d'analyses est consécutif au choix de l'équipe de géochimie du LMV d'exclure toute trace de Re du spectromètre de masse à source solide Finnigan Triton, afin de pouvoir réaliser des analyses isotopiques de Re (pour la systématique Re/Os) sans risque de contamination par effet de mémoire. En effet, bien que la mesure des rapports isotopiques de Sr-Nd-Pb-U-Th, classiquement effectuée avec des filaments de Re, puissent être aussi réalisée avec des filaments de W (ou éventuellement de Ta), le côté cassant de ce dernier, une fois ''dégazé'', et surtout le moindre niveau de signal pour une quantité d'éléments déposés, ont rapidement montré les limites d'un tel choix. Par ailleurs, la mesure de très haute précision des rapports isotopiques $^{142}Nd/^{144}Nd$ (thématiques principalement associées à Maud Boyet au LMV), dont les résultats reposent sur de très faibles variations, nécessite d'employer une procédure identique à celle utilisée dans les autres laboratoires de géochimie isotopique, et l'usage du W était donc un frein. Les résultats principaux du développement de l'analyse du Re par MC-ICP-MS concernent principalement l'effet de matrice, qui rend la technique de standard ''bracketing'' inadaptée, et la différence de fractionnement instrumental entre Re et W (*Figure 23*), qui nécessite d'établir une relation empirique entre les facteurs de fractionnement [Poirier et Doucelance, 2009]. Ce dernier résultat est à rapprocher des conclusions de Thirlwall [2002] concernant le biais analytique observé pour les analyses isotopiques de Pb corrigées du fractionnement de masse par dopage au Tl vis-à-vis de celles obtenues avec la technique dite du double spike.

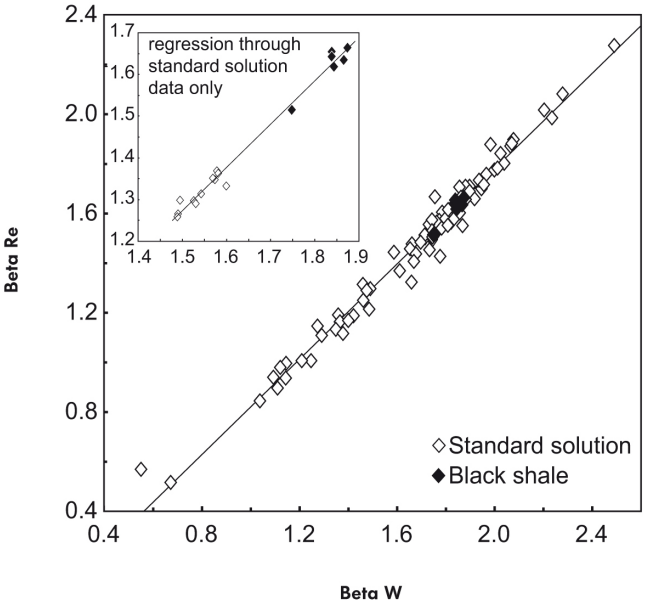


*Figure 23 : Relation empirique entre fractionnements instrumentaux du Re et du W (Beta Re ≠ Beta W). D'après Poirier et Doucelance [2009].*

Ce 5ème thème, analytique, a donné lieu aux publications suivantes :

- ***Doucelance**, Manhès (2001) Reevaluation of precise lead isotope measurements by thermal ionization mass spectrometry : comparison with determinations by plasma source mass spectrometry. Chemical Geology 176.*
- *Deschamps, **Doucelance** et al. (2003) Further investigations on optimized tall correction and high-precision measurement of Uranium isotopic ratios using Multi-Collector ICP-MS. Chemical Geology 201.*
- *Poirier, **Doucelance** (2009) Effective Correction of Mass Bias for Rhenium Measurements by MC-ICP-MS. Geostandards and Geoanalytical Research 33.*
- *Bellot, Boyet, **Doucelance** et al. (2015) Development of the Ce isotope systematics and its application to island arc lavas from Lesser Antilles. Geochimica et Cosmochimica Acta 168.*

*Thèse*

*- Nina Bellot (2012-2015) : Développement du système isotopique La-Ce : application aux laves d'arc (co-encadrement Maud Boyet).*

*Master*

*- Pierre Bonnand (2006), Protocole d'analyse des éléments majeurs et quelques traces des chondrites ordinaires (co-encadrement André Poirier).*

## 6. PROJETS EN COURS

Trois études, actuellement en cours, s'inscrivent dans la continuité directe de certaines des thématiques de recherche présentées dans les paragraphes précédents, à savoir la source des carbonatites océaniques, la subduction et la construction/destruction des édifices volcaniques.

*Détermination expérimentale des coefficients de partage des éléments U-Th-Pb lors du recyclage par subduction de croûte océanique carbonatée*

Les carbonatites présentent un intérêt particulier vis-à-vis de la systématique U/Pb car elles montrent souvent une signature isotopique de type HIMU. Cette observation a d'ailleurs amené à proposer que leurs régions sources aient été affectées par le recyclage de croûte océanique. Toutefois, un tel recyclage ne peut expliquer à lui seul l'origine du carbone des carbonatites. Il a donc été également proposé de combiner ce type de source avec le recyclage de carbonates, marins ou secondaires (Nelson *et al.* [1988]; Hoernle *et al.* [2002]; Doucelance *et al.* [2010]; [2014], voir aussi section 3).

La modélisation d'une source de type HIMU pour les carbonatites passe par la compréhension du comportement de éléments U, Th et Pb, à savoir les valeurs de leurs coefficients de partage entre les minéraux de la plaque subductée (grenat calcique + pyroxène sodique +/- amphibole et autre phases hydratées) ou du manteau (grenat magnésien + pyroxène ferro-magnésien) et les liquides ou fluides provenant de la plaque, qu'il soient silicatés, carbonatés ou aquo-carbonés. Les deux seules études disponibles dans la littérature concernent le partage entre clinopyroxène et liquide carbonaté (Jones *et al.* [1995] et Dasgupta *et al.* [2009]), et leurs résultats sont contradictoires. Dasgupta *et al.* [2009] proposent que le Pb soit moins incompatible que l'U et le Th, alors que Jones *et al.* [1995] observent la relation inverse. La différence de résultat est essentiellement liée au Pb qui montre un ordre de grandeur d'écart pour son coefficient de partage entre les deux études, alors que les valeurs pour U et Th sont comparables et ne diffèrent que d'un facteur 2. Si on compare les protocoles expérimentaux de ces deux études, les différences concernent assez peu la pression et la température, mais surtout la composition du liquide qui est sodi-dolomitique pour Dasgupta *et al.* [2009] et sodi-calcique pour Jones *et al.* [1995]. Une autre différence, peut-être critique, est la nature du matériau utilisé pour contenir les échantillons à haute pression et haute température ($Au_{80}Pd_{20}$ vs. MgO).

Cette étude est menée en collaboration avec Tahar Hammouda, de l'équipe de magmatologie physique du LMV. Nous avons mélangé un échantillon de MORB typique avec des carbonates dopés en U, Th, Pb, à hauteur de 500 ppm par élément. Les expériences HP-HT seront réalisées dans la presse multienclumes du LMV et les analyses seront effectuées avec le système d'ICP-MS couplé à l'ablation laser, également disponible au LMV. Les phases analysées seront les grenats et les clinopyroxènes (et amphiboles dans le cas où nous ajouterons de l'eau), et le liquide carbonaté.

*Reconstitution de l'histoire magmatique du Socompa à partir des produits d'avalanche de débris*

Comme évoqué dans la section 4, l'échantillonnage des différentes formations des stratovolcans de l'arc andin est généralement rendu difficile par la faible accessibilité et surtout l'altitude des édifices volcaniques. Dans le cas du volcan Socompa, un moyen de s'affranchir de cette difficulté consiste à utiliser les différents blocs transportés à la surface de l'avalanche de débris qui l'a affecté il y a quelques 7000 ans.

La contre partie d'une telle approche de l'échantillonnage est la perte de chronologie relative entre les différentes formations, bien que dans le cas précis du Socompa deux ensembles d'échantillons puissent être tout de même distingués sur la base de leur âge. En effet, la cicatrice de l'avalanche du Socompa a été partiellement comblée par de nouvelles laves et produits pyroclastiques, qui se sont eux-mêmes effondrés depuis, résultant en une seconde avalanche de débris, de moindre ampleur et dénommée avalanche secondaire. Les blocs échantillonnés sur l'avalanche secondaire sont par conséquent plus jeunes que ceux prélevés dans les dépôts de l'avalanche principale.

Les échantillons analysés présentent les caractéristiques chimiques des adakites, plus précisément des adakites riches en silice telles que définies par Martin et collaborateurs [2005], mais des compositions isotopiques de Sr et Nd, respectivement plus et moins radiogéniques que les valeurs mantelliques classiquement observées pour ce type d'échantillons ($^{87}Sr/^{86}Sr < 0.7045$ et $\varepsilon Nd > 0$; cf. Defant et Drummond [1990] et Castillo [2012]). La confrontation des analyses des concentrations en éléments majeurs et en traces, à l'échelle roche totale et minérale (plagioclases et amphiboles) et des compositions isotopiques de Sr et Nd montre que les échantillons du Socompa résultent de deux mélanges distincts, entre, d'une part, des matériaux dérivant du manteau, et, d'autre part, de la croûte continentale andine (*Figure 24*). Le passage d'un mélange à l'autre ne peut être attribué (ou simplement relié) à l'avalanche de débris principale du Socompa (contrairement aux évolutions géochimiques mises en évidence dans le cas de l'effondrement du Mont Amarelo au Cap Vert, cf. section 4), les échantillons de l'avalanche principale se distribuant sur les deux courbes de mélange. Le fait que les échantillons les plus récents (avalanche secondaire) appartiennent tous à la même courbe de mélange, par contre, suggère que les deux mélanges témoignent d'une évolution temporelle des processus magmatiques et/ou des sources. L'hypothèse privilégiée à ce stade de l'étude pour les produits les plus anciens du Socompa est l'assimilation en proportions variables de la croûte andine (gneiss paléozoïques et ignimbritiques d'âge miocène/pliocène) par des liquides résultant de la fusion partielle de la croûte océanique recyclée et ayant interagi avec le coin de manteau (hybridation). Les échantillons les plus récents, quant à eux, pourraient résulter de l'interaction directe entre les liquides issus de la fusion partielle de la croûte océanique recyclée et la croûte andine, les premiers liquides hybridés ayant ''ouvert des chemins'' permettant dès lors la remontée sans interaction avec le coin de manteau des liquides issus de la croûte recyclée. Un tel scénario implique que les relations observées entre concentrations et rapports isotopiques dans les différents diagrammes géochimiques (notamment la figure 24) correspondent à des mélan-

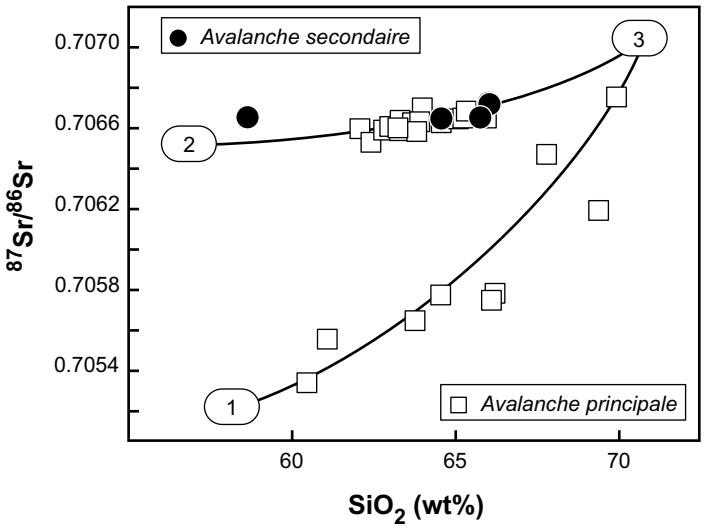


*Figure 24 : Variations des rapports isotopiques $^{87}Sr/^{86}Sr$ et des teneurs en $SiO_2$ dans les blocs provenant des avalanches principale et secondaire du Socompa. Les échantillons se distribuent sur deux courbes de mélange impliquant 3 pôles. Ces derniers correspondent à l'interaction, en proportions variables, du produit de fusion de la croûte océanique recyclée, du coin de manteau et de la croûte continentale andine.*

ges pseudo-binaires impliquant 3 à 4 composants (à rapprocher des résultats discutés dans la section 2 concernant le Merapi).

*Evolution magmatique et instabilité des volcans boucliers océaniques*

Cette troisième étude, qui compose le corps de la thèse de Mélodie Neige-Cornu (co-encadrement Raphaël Paris et Patrick Bachelery), est la moins avancée des travaux en cours. Les premiers résultats obtenus sur les échantillons provenant de l'île de Fogo (Cap Vert) montrent des variations de compositions avant et après l'effondrement du Mont Amarelo (section 4). Toutefois, leur interprétation est limitée par la connaissance uniquement relative de la chronologie des échantillons (*Figure 19*). Par conséquent, les laves de Fogo sont actuellement en phase de datation (K-Ar, en collaboration avec Hervé Guillou, LSCE). La connaissance de la chronologie absolue permettra d'affiner les premières observations, notamment de préciser la part des variations temporelles qui sont clairement à mettre en relation avec l'effondrement du Mont Amarelo de celles observées à plus grande échelle spatiale, au niveau de l'Archipel du Cap Vert, et qui montrent, par exemple, que les compositions isotopiques des basaltes de la branche sud de l'archipel ont une signature EM1, contrairement aux produits volcaniques de la branche nord, et que celle-ci tend à augmenter avec le temps [Doucelance et al., 2003; Escrig *et al.*, 2005; Millet *et al.*, 2008]. Elle permettra également d'estimer les rythmes d'accumulation des produits volcaniques (la productivité) le long des parois de la caldera de Fogo (la Bordeira, voir section 4), et de vérifier si l'effondrement du Mont Amarelo est corrélé à ces derniers, comme cela a été mis en évidence à Tenerife, La Gomera, La Palma ou El Hierro (archipel des Canaries), où les déstabilisations massives interviennent au pic de productivité des rift-zones volcaniques (*Figure 25*; voir aussi Carracedo *et al.* [ 2011]).

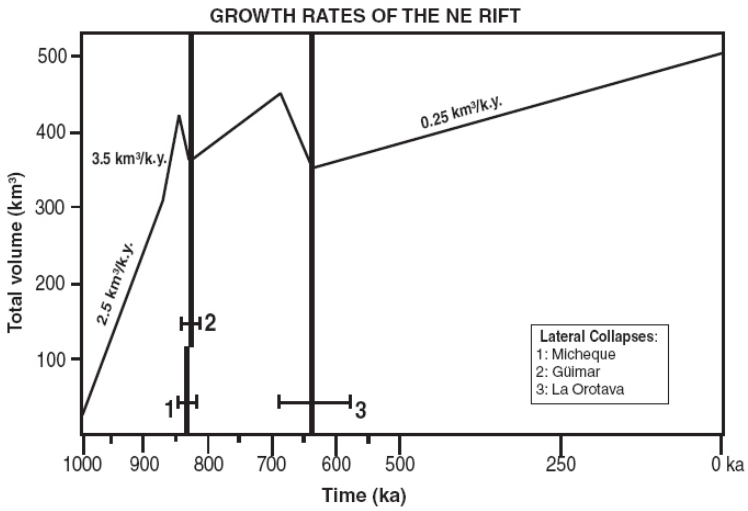


*Figure 25 : Rythmes de construction et déstabilisations massives des flancs de la rift-zone nord-est de Tenerife, archipel des Canaries : les déstabilisations massives correspondent au pic de productivité. D'après Carracedo et al. [2011].*

Dans cette logique, il a également été décidé de mener l'étude de l'effondrement de Güimar (daté d'il y a environ 830000 ans: Ancochea *et al.* [1990]; Carracedo *et al.* [2011]), sur la partie nord-est de l'île de Tenerife (Canaries), parallèlement à celle de l'effondrement du Mont Amarelo. La problématique demeure identique: l'effondrement est-il d'origine magmatique, et/ou influence-il l'activité magmatique. La stratégie est la même que celle développé pour Fogo, à savoir l'analyse des compositions chimiques et isotopiques, ainsi que la chronologie absolue, des produits avant et après effondrement, ces derniers étant principalement des basanites/téphrites, plus communes du volcanisme intra-océanique que les séries atypiques, sous-saturées en silice, présentes sur Fogo, et plus généralement sur les îles de la branche sud de l'archipel du Cap Vert.

## 7. PERSPECTIVES

A moyen terme, je compte poursuivre mes travaux de recherche dans les thèmes développés dans les sections 1 à 5, avec toutefois un travail plus conséquent vis-à-vis des axes Sources des carbonatites et Construction/destruction des édifices volcaniques.

*Apport de la systématique Re/Os quant à la nature (et à l'évolution ?) de la source des carbonatites*

L'osmium possède 7 isotopes, de masses 184, 186, 187, 188, 189, 190 et 192. Leurs abondances naturelles sont respectivement de 0.02, 1.59, 1.96, 13.24, 16.15, 26.26 et 40.78%. Le rhénium, quant à lui, possède 2 isotopes, $^{185}$Re et $^{187}$Re, dans les proportions 37.40 et 62.60%. Ils sont reliés par la désintégration radioactive du $^{187}$Re en $^{187}$Os (désintégration $\beta^-$, demi-vie de 41.2 Ga). Ces deux éléments sont par ailleurs chalco-sidérophiles, alors que les autres systèmes radiogéniques de longue période (Rb-Sr, Sm-Nd, Lu-Hf, U-Th-Pb) sont composés d'éléments lithophiles (à l'exception du Pb, chalcophile). De plus, l'Os, contrairement aux autres traceurs isotopiques utilisés en géochimie, est fortement compatible avec le résidu mantellique des magmas lors de la fusion partielle, alors que le Re est modérément incompatible. Par conséquent, les composants extraits du manteau (croûte océanique et matériaux de la croûte continentale, i.e. une des hypothèses à tester quant à la source des carbonatites) possèdent des rapports Re/Os très élevés par rapport au manteau supérieur, qui se traduiront très rapidement par des rapports très radiogéniques. Réinjectés dans le manteau lors des processus géodynamiques et recyclés dans la source des carbonatites, ils vont pouvoir être identifié par leurs compositions isotopiques radiogéniques en Os (ainsi les pôles mantelliques EM1 et HIMU, généralement interprétés comme des marqueurs du recyclage des croûtes continentale et océanique présentent des rapports isotopiques $^{187}$Os/$^{188}$Os compris entre 0.15 et 0.16, cf. Shirey et Walker [1998]). De même, l'eau de mer, et donc les carbonates marins, présentent un rapport encore plus radiogénique avec une valeur actuelle de 1.06 [Levasseur *et al.*, 1998]. Au contraire, la lithosphère sous-continentale va figer la composition isotopique de l'osmium, du fait de l'absence de Re, affichant ainsi des compositions sous-chondritiques ($^{187}$Os/$^{188}$Os < 0.1246, valeur affichée par le manteau supérieur; Snow et Reisberg [1995]). Par conséquent, dans l'hypothèse d'une contribution du recyclage de croûte océanique + carbonates à la source des carbonatites [Hoernle *et al.*, 2002; Doucelance *et al.*, 2010; 2014], le rapport $^{187}$Os/$^{188}$Os des carbonatites devrait être supérieur à la valeur du manteau supérieur (> 0.1246). A l'inverse, si les liquides carbonatés sont produits par fusion d'un mélange péridotite + $CO_2$, ces derniers afficheront des rapports $^{187}$Os/$^{188}$Os roches de 0.1246. Enfin, en cas de participation majoritaire de la lithosphère sous-continentale, des rapports isotopiques d'osmium < 0.1246 devraient être mesurés dans les carbonatites. Les caractéristiques du système Re-Os en font donc un outil particulièrement adapté à l'identification des composants (matériel recyclé, lithosphère sous-continentale et/ou manteau) présents dans la source des carbonatites.

L'osmium est très peu concentré dans les produits de fusion, du fait de son comportement compatible. Par conséquent, l'analyse des carbonatites nécessite un développement analytique important, avec la mise au point de la mesure des rapports $^{187}$Re/$^{188}$Os et $^{187}$Os/$^{188}$Os d'échantillons extrêmement pauvres (quelques ppt d'Os). Ceci dépasse largement le cadre de la compréhension de la source des carbonatites et explique aussi pourquoi une telle systématique n'a jamais été entreprise. Une alternative possible consiste à travailler sur des quantités importantes de matériel. Toutefois, cela implique aussi une attaque efficace des échantillons non actuels (> 1 Ma). Une troisième possibilité consiste à travailler sur des pha-

ses séparées qui concentrent l'Os. Dans ce cas, il faut vérifier, de manière indépendante, l'équilibre isotopique entre les phases séparées et les roches totales.

Quelle que soit l'approche, une connaissance précise de l'âge des échantillons (et non des formations) est nécessaire afin d'effectuer les corrections de décroissance radioactive du fait de la grande sensibilité du couple Re-Os (forts rapports $^{187}Re/^{188}Os$) à cet effet.

Enfin, il faut garantir la mise en solution totale des échantillons, et notamment des phases réfractaires, qui est, à l'heure actuelle, un des freins à la reproductibilité des analyses isotopiques d'osmium. Ceci est lié à l'homogénéité/hétérogénéité des échantillons et aux différentes techniques de mises en solution [Meisel *et al.*, 2003]. En choisissant de travailler sur des phases minérales séparées, il est possible de s'affranchir du problème lié à l'homogénéité/hétérogénéité des échantillons. Sinon, il est nécessaire de coupler les différents protocoles de mise en solution: digestion acide à basse température (<150 °C; Birck *et al.* [1997]), dissolution via les ''tubes Carius'' qui permet d'atteindre des températures significativement plus hautes (<250 °C; Shirey et Walker [1995]), ou encore système à micro-ondes.

A l'heure actuelle, peu de mesures de composition isotopique d'Os ont été publiées pour les carbonatites (6 au total). Deux échantillons de Fuerteventura (îles Canaries) ont été analysés par Widom *et al.* [1999]. Les compositions mesurées sont fortement radiogéniques ($^{187}Os/^{188}Os$ = 0.6138 et 0.4554) mais ne sont pas corrigées de la décroissance radioactive. Deux échantillons de Fogo (îles du Cap Vert) ont été analysés par Escrig *et al.* [2005]. Les compositions initiales montrent des valeurs également radiogéniques, de 0.1695 et 0.1716, supérieures à celles des différents réservoirs mantelliques (croûte océanique recyclée - HIMU, sédiments pélagiques et terrigènes recyclés – EM1/2, lithosphère sous-continentale - SCLM, manteau profond/inférieur - LM), mais inférieures à celles des carbonates marins (*Figure 26*). Ceci implique que les carbonatites du Cap Vert ne peuvent être expliquées par le mélange de matériel provenant du manteau supérieur et d'un autre (ou plusieurs) réservoir mantellique. Cela suggère, par contre, que leur source profonde contient une faible proportion de sédiments carbonatés. Au contraire des échantillons du Cap Vert, les deux mesures de Graham *et al.* [2004] effectuées sur les magnétites de deux carbonatites de Mt Weld (2.025 Ga, Australie) montrent des rapports initiaux (0.1037 et 0.1144) sous-chondritiques à mantelliques (le rapport $^{187}Os/^{188}Os$ du manteau à 2.025 Ga est proche de 0.115, cf. Shirey et Walker [1998]), en faveur d'une origine lithos-

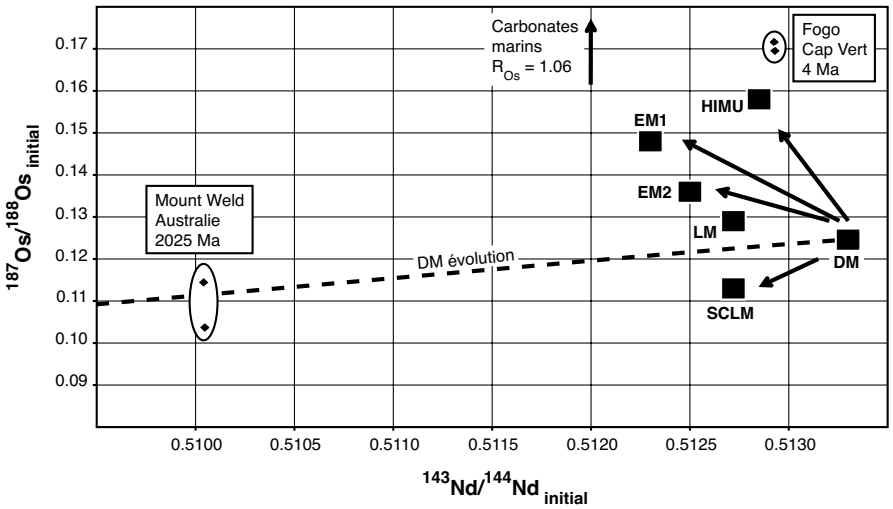


*Figure 26 : $^{187}Os/^{188}Os$ initial vs. $^{143}Nd/^{144}Nd$ initial. Les carbonatites australiennes présentent des signatures isotopiques similaires à celles du manteau supérieur appauvri ; les échantillons du Cap Vert, au contraire, montrent des compositions d'Os très radiogéniques, supérieures à celles des différents réservoirs mantelliques (HIMU, EMI/II, SCLM et LM), en accord avec l'incorporation de carbonates marins dans leur source. Données : Graham et al. [2004]; Escrig et al. [2005].*

phérique ou mantellique, montrant que le débat reste ouvert et qu'il faut peut-être envisager différentes sources pour les carbonatites.

La compilation des rapports isotopiques $^{87}Sr/^{86}Sr$ mesurés dans les carbonatites mondiales, comparée à l'évolution enregistrée pour ce même rapport par le manteau et l'océan (*Figure 27*), montre que les carbonatites plus vielles que 1.5 Ga suivent majoritairement une évolution mantellique, alors que les carbonatites plus récentes montrent des compositions plus radiogéniques, comprises entre les valeurs mantelliques et océaniques. Cette observation générale traduit-elle l'évolution temporelle de la source des carbonatites ? A savoir, entre 3.0 et 1.5 Ga, les carbonatites sont essentiellement générées par fusion de péridotites en présence de $CO_2$, alors que plus récemment, quand le recyclage de carbonates est opérationnel (les conditions de la subduction le permette – le gradient de la subduction est plus favorable - ou il y a enfin suffisamment de carbonates à recycler ?), la source des carbonatites est à relier préférentiellement au recyclage de matériel de surface via les panaches mantelliques (fusion d'éclogites carbonatées).

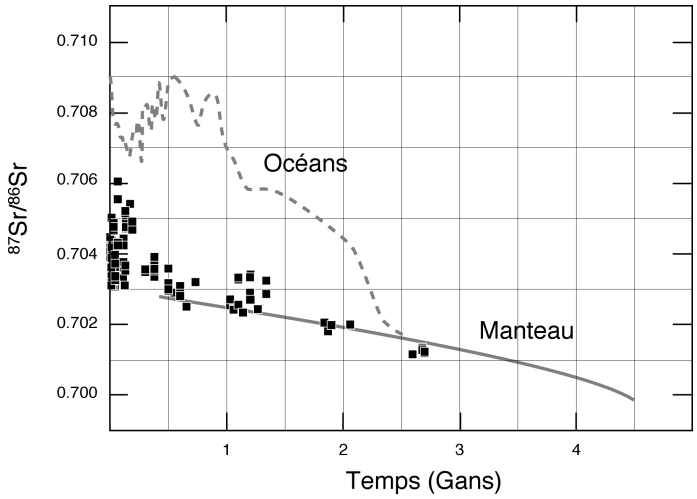


*Figure 27 : Compilation des compositions isotopiques de strontium mesurées dans les carbonatites calciques et magnésiennes mondiales (carrés noirs) en comparaison avec l'évolution du manteau et des océans.*

*Dynamique interne des avalanches de débris*

La complexité de l'édifice qui s'est déstabilisé, dans le cas du Socompa (voir sections 4 et 6), limite l'étude des mélanges à l'échelle des affleurements et ne permet pas réellement de répondre aux questions de dynamique à grande échelle. Quelle est la distance maximale de dispersion des blocs broyés dans l'avalanche ? Ou se situaient les blocs qui ont été broyés, autrement dit à quel endroit se forme la matrice ? Par ailleurs, les dépôts de l'avalanche étant particulièrement bien préservés, l'étude est concentrée sur la partie la plus superficielle de ces derniers, limitant les conclusions en ce qui concerne la dynamique 3D. Par conséquent, il est souhaitable d'étudier d'autres avalanches de débris. Je pense plus particulièrement à deux cibles : d'une part, l'avalanche du volcan Llullaillaco, situé environ 50 km au sud-ouest du Socompa (sur la frontière Argentine - Chili), et, d'autre part, les dépôts d'avalanche du Pichu Pichu, environ 30 km à l'est d'Arequipa, au Pérou. La première cible n'a pour but que de tester le caractère général ou, au contraire, local des résultats obtenus sur la dynamique de l'avalanche du Socompa. Les deux volcans sont en effet situés dans le même contexte général: activité quaternaire, aridité extrême du climat qui garantie la fraicheur des affleurements et la conservation des structures, et géologique identique (voir par exemple Richards et Villeneuve [2001]). Leurs avalanches ont par ailleurs toutes les deux parcouru de grandes distances horizontales, de plusieurs dizaines de km (40 pour le Socompa, 25 pour le Llullaillaco), et les dépôts couvrent des surfaces également du même ordre de grandeur (500 $km^2$ pour le Socompa, 165

pour le Llullaillaco). Les dépôts d'avalanche du volcan Pichu Pichu ne sont pas aussi bien préservés que ceux des avalanches du Socompa ou du Llullaillaco. Plusieurs affleurements, toutefois, sont très complémentaires à ces derniers car ils montrent, d'une part le contact avec le substratum (*Figure 28A*), et d'autre part des évidences de déplacements verticaux de matrice formée à la base (*Figure 28B*). Leur étude, et plus particulièrement celle des affleurements montrant le contact avec le substratum, permettra d'évaluer les interactions entre ce dernier et l'avalanche.


*Figure 28 : Affleurements de la base des dépôts de l'avalanche du Pichu Pichu. A) Le contact avec le substratum est avéré par la présence de pseudotachylites. B) La comparaison des compositions chimiques et isotopiques des filons et de la matrice environnante renseignera sur le comportement mécanique de l'avalanche au moment de l'injection des filons et sur l'homogénéité / hétérogénéité des particules les plus fines à la base des dépôts. Photos Karim Kelfoun.*

Ces deux projets à court et moyen termes, sur les thématiques Sources des carbonatites et Construction/destruction des édifices volcaniques, pourront aussi composer le corps de deux thèses.

*Apport de la systématique La/Ce quant à l'origine du pôle mantellique EM1*

Parallèlement, je souhaiterais également ''rebondir'' sur le développement de l'analyse isotopique du Ce, peut-être sous la forme d'un projet de master, avec notamment la question de l'origine du pôle mantellique EM1. Comme rappelé dans la section 1, deux grandes hypothèses, qui ne sont pas mutuellement exclusives, sont classiquement discutés pour l'origine de cet end-member géochimique. Il pourrait résulter du recyclage, via la subduction, de sédiments d'origine terrigène et pélagique [Chauvel *et al.*, 1992], ou correspondre à la lithosphère continentale [McKenzie et O'Nions, 1983]. Le rapport La/Ce élevé des sédiments pélagiques, couplé à l'âge moyen qui est généralement attribué au pôle EM1 (1-2 Gans), suggèrent que les basaltes d'îles océaniques de type EM1 associés au recyclage sédimentaire devraient afficher une composition isotopique de Ce radiogénique, ou tout du moins plus radiogénique, que celle des OIB de composition EM1 pour lesquels c'est l'hypothèse de la lithosphère sous-continentale qui est retenue. Dans ce cadre, la comparaison des archipels de Tristan da Cunha et du Cap Vert, par exemple, où les basaltes affichent des compositions de type EM1 dont l'origine est respectivement liée aux deux hypothèses discutées ci-dessus, constitue un projet intéressant vis-à-vis de cette problématique. En outre, ce travail pourrait être intégré, à plus long terme, aux thématiques de l'axe transverse <<Terre Primitive>> du LMV, et notamment au projet de Maud Boyet d'établir la corrélation terrestre pour les couples La/Ce et Sm/Nd (le ''Mantle array'') et ainsi tester l'hypothèse Terre chondritique pour les terres rares.

Aizawa, Y., Tatsumi, Y., Yamada, H., Element transport by dehydration of subducted sediments: implications for arc and ocean island magmatism, *Island Arc* 8, 38-46, 1999.

Allègre, C.J., Turcotte, D.L., Geodynamical mixing in the mesosphere boundary layer and the origin of oceanic islands, *Geophys. Res. Lett.* 12, 207-210, 1985.

Allègre, C.J., Hamelin, B., Provost, A., Dupré, B., Topology in isotopic multispace and origin of mantle chemical heterogeneities, *Earth Planet. Sci. Lett.* 81, 319-337, 1986/87.

Allègre, C.J., Moreira, M., Staudacher, T., $^{4}He/^{3}He$ dispersion and mantle convection, *Geophys. Res. Lett.* 22 , 2325-2328, 1995.

Allègre, C.J., Hofmann, A.W., O'Nions, R.K., The Argon constraints on mantle structure. *Geophys. Res. Lett.* 23, 3555-3557, 1996.

Amelin, Y., Davis, D.W., Davis, W.J., Mass parity-related changes in isotope fractionation of Pb analyzed by thermal ionization mass spectrometry, *GAC-MAC ann. Meeting abstr.* 31, 5, 2006.

Ancochea, E., Fuster, J.M., Ibarolla, E., Cendrero, A., Coello, J., Hernan, F., Cantagrel, J.M., Jamond, C., Volcanic evolution of the island of Tenerife (Canary Islands) in light of new K-Ar data, *J. Volcanol. Geotherm. Res.* 44, 231-249, 1990.

Anderson, D.L., A model to explain the various paradoxes associated with mantle noble gas geochemistry, *Proc. Natl. Acad. Sci. U.S.A.* 95, 9087-9092, 1998.

Archer, E.D., An atlas of the distribution of calcium carbonate in sediments of the deep sea, *Global Biogeochem. Cycles* 10, 159-174, 1996.

Bailey, D.K., Carbonate-rich melts from the mantle in the volcanoes of south–east Zambia, *Nature* 338, 415–418, 1989.

Barker, F., Arth, J.G. Generation of trondhjemitic-tonalitic liquids and Archean bimodal trondhjemite-basalt suites. *Geology* 4, 596-600, 1976.

Beier, C., Stracke, A., Haase, K.M., The peculiar geochemical signatures of São Miguel (Azores) lavas: metasomatised or recycled mantle sources? *Earth Planet. Sci. Lett.* 259, 186–199, 2007.

Birck, J.-L., Roy-Barman, M., Capmas, F., Re-Os *isotopic* measurements at the femtomole level in natural samples, *Geost. Newsletter* 20, 19-27, 1997.

Boudon, G., Villemant, B., Friant, A.L., Paterne, M., Cortijo, E., Role of large flank-collapse events on magma evolution of volcanoes. Insights from the Lesser Antilles Arc, *J. Volcanol. Geotherm. Res. 263*, 224-237, 2013.

Bouhifd, M.A., Jephcoat, A.P., Heber, V.S., Kelley, S.P., Helium in Earth's early core. *Nature Geosci.* 6, 982-986, 2013.

Brandon, A.D, Walker, R.J., The debate over core–mantle interaction, *Earth Planet. Sci. Lett.* 232, 211-225, 2005.

Brandon, A.D, Walker, R.J., Morgan, J.W., Norman, M.D., Prichard, H.M., Coupled 186Os and 187Os évidence for core-mantle interaction, *Science* 280, 1570-1573, 1998.

Carracedo, J.C., Guillou, H., Nomade, S., Rodríguez Badiola, E., Pérez Torrado, F.J., Rodríguez Gonzáles, A., Paris, R., Troll, V.R., Wiesmaier, S., Delcamp, A., Fernández Turiel, J.L., Evolution of ocean-island rifts: The northeast rift zone of Tenerife, Canary Islands, *Geol. Soc. Am. Bull.* 123, 562-584, 2011.

Castillo, P., Adakite petrogenesis, *Lithos* 134-135, 304-316, 2012.

Castillo, P., The Pb Paradox is a Consequence of $CaCO_3$ Recycling?, *Am. Geophys. Union*, Fall Meeting, abstract #DI21A-2251, 2013.

Chauvel, C., Hofmann, A.W., Vidal, P., HIMU-EM: the French Polynesian connection, *Earth Planet. Sci. Lett.* 110, 99-119, 1992.

Class, C., Goldstein, S.L., Plume-lithosphere interactions in the ocean basins: constraints from the source mineralogy, *Earth Planet. Sci. Lett.* 150, 245-260, 1997.

Claude-Ivanaj, C., Bourdon, B., Allègre, C.J., Ra-Th-Sr isotope systematics in Grande Comore Island: a case study of plume-lithosphere interaction, *Earth Planet. Sci. Lett.* 164, 99-117, 1998.

Condie, K.C., Archean greenstone belts, 434 pp., Elsevier, Amsterdam, 1981.

Condie, K.C., Chemical composition and evolution of the upper continental crust: Contrasting results from surface samples and shales, *Chem. Geol.* 104, 1-37, 1993.

Condomines, M., Grönvold, K., Hooker, P.J., Muehlenbachs, K., O'Nions, R.K., Oskarsson, N., Oxburgh, E.R., Helium, oxygen, strontium and neodymium isotopic relationships in Icelandic volcanic, *Earth Planet. Sci. Lett.* 66, 125-136, 1983.

Courtier, A.M., Jackson, M.G., Lawrence, J.F., Wang, Z., Lee, C.-T.A., Halama, R., Warren, J.M., Workman, R., Xu, W., Hirschmann, M.M., Larson, A.M., Hart, S.R., Lithgow-Bertelloni, C., Stixrude, L., Chen, W.-P., Correlation of seismic and petrologic thermometers suggests deep thermal anomalies beneath hotspots, *Earth Planet. Sci. Lett.* 264,

308-316, 2007.

Courtillot, V., Davaille, A., Besse, J., Stock, J., Three distinct types of hotspots in the Earth's mantle, *Earth Planet. Sci. Lett.* 205, 295-308, 2003.

Courtney, R.C., White, R.S., Anomalous heat flow and geoid across the Cape Verde Rise: evidence for dynamic support from a thermal plume in the mantle, *Geophys. J. R. Astr. Soc.* 87, 815–867, 1986.

Dalton, J.A., Wood, B.J., The compositions of primary carbonate melts and their evolution through wallrock reaction in the mantle, *Earth Planet. Sci. Lett.* 119, 511–525, 1993.

Dasgupta, R., Hirschmann, M.M., McDonough, W.F., Spiegelman, M., Withers, A.C., Trace element partitioning between garnet lherzolite and carbonatite at 6.6 and 8.6 GPa with applications to the geochemistry of the mantle and of mantle-derived melts, *Chem. Geol.* 262, 55-77, 2009.

Dash, B.P., Ball, M.M., King, G.A., Butler, L.W., Rona, P.A., Geophysical investigation of the Cape Verde archipelago, *J. Geophys. Res.* 81, 5249–5259, 1976.

Davies, G.F., Richards, M.A., Mantle convection, *J. Geol.* 100, 151-206, 1992.

Defant, M.J., Drummond, M.S., Derivation of some modern arc magmas by melting of young subducted lithosphere, *Nature* 347, 662-665, 1990.

Dixon, J.E., Leist, L., Langmuir, C., Schilling, J.-G., Recycled dehydrated lithosphère observed in plume-influenced mid-ocean-ridge basalt. *Nature* 420, 385-389, 2002.

DuFrane, S.A., Turner, S., Dosseto, A., vAn Soest, M., Reappraisal of fluid and sediment contributions to Lesser Antilles magmas, *Chem. Geol.* 265, 272-278, 2009.

Duncan, R.A., Hotspots in the southern ocean - an absolute frame of reference for motion of the Gondwana continents, *Tectonophysics* 74, 29-42, 1980.

Eggler, D.H., The effect of carbon dioxide upon partial melting of peridotite in the system sodium oxide –calcium oxide – aluminum oxide – magnesium oxide –silicon dioxide – carbon dioxide to 35 kb, with an analysis of melting in a peridotite – water – carbon dioxide system, *Am. J. Sci.* 278, 305–343, 1978.

Elderfield, H., The oceanic chemistry of the rare-earth elements, *Philos. Trans. R. Soc. Lond.* A325, 105–126, 1988.

Elliott, T., Plank, T., Zindler, A., White, W., Bourdon, B., Element transport from slab to volcanic front at the Mariana arc, *J. Geophys. Res.* 102, 14991–15019, 1997.

Elliott, T., Blichert-Toft, J., Heumann, A., Koetsier, G., Forjaz, V., The origin of enriched mantle beneath São Miguel, Azores, *Geochim. Cosmochim. Acta* 71, 219–240, 2007.

Farley, K.A., Natland, J.H., Craig, H., Binary mixing of enriched and undegassed (primitive?) mantle components (He, Sr, Nd, Pb) in Samoan lavas, *Earth Planet. Sci. Lett.* 111, 183-199, 1992.

Foeken, J.P.T., Day, S., Stuart, F.M., Cosmogenic $^{3}$He exposure dating of the Quaternary basalts from Fogo, Cape Verdes: Implications for rift zone and magmatic reorganisation, *Quat. Geochronol.* 4, 37-49, 2009.

Forte, A.M., Quéré, S., Moucha, R., Simmons, N.A., Grand, S.P., Mitrovica, J.X., Rowley, D.B., Joint seismic-geodynamic-mineral physical modelling of African geodynamics: a reconciliation of deep-mantle convection with surface geophysical constraints, *Earth Planet. Sci. Lett.* 295, 329–341, 2010.

Füri, E., Hilton, D.R., Murton, B.J., Hémond, C., Dyment, J., Day, J.M.D., Helium isotope variations between Réunion Island and the Central Indian Ridge (17°–21°S): New evidence for ridge–hot spot interaction, *J. Geophys. Res.* 116, doi: 10.1029/ 2010JB007609, 2011.

Gast, P.W., Tilton, G.R., Hedge, C., Isotopic composition of lead and strontium from Ascension and Gough islands, *Science* 145, 1181-1185, 1964.

Graham, D.W., Humphris, S.E., Jenkins, W.J., Kurz, M.D., Helium isotope geochemistry of some volcanic rocks from Saint Helena, *Earth Planet. Sci. Lett.* 110, 121-131, 1992.

Graham, S., Lambert, D., Shee, S., The petrogenesis of carbonatite, melnoite and kimberlite from the Eastern Goldfields Province, Yilgarn Craton, *Lithos* 76, 519-533, 2004.

Hammouda, T., High-pressure melting of carbonated eclogite and experimental constraints on carbon recycling and storage in the mantle, *Earth Planet. Sci. Lett.* 214, 357–368, 2003.

Hammouda, T., Laporte, D., Ultrafast mantle impregnation by carbonatite melts, *Geology* 28, 283–285, 2000.

Hammouda, T., Chantel, J., Manthilake, G., Guignard, J., Crichton, W., Hot mantle geotherms stabilize calcic carbonatite magmas up to the surface, *Geology* 42, 911–914, 2014.

Hanan, B.B., Graham, D.W., Lead and Helium evidence from oceanic basalts for a common deep source of mantle plumes, *Science* 272, 991-995, 1996.

Hanyu, T., Kaneoka, I., The uniform and low $^{3}$He/$^{4}$He ratios of HIMU basalts as evidence for their origin as recycled materials, *Nature* 390, 273-276, 1997.

Hart, S.R., A large-scale isotope anomaly in the Southern Hemisphere mantle, *Nature* 309, 753-757, 1984.

Hart, S.R., Heterogeneous mantle domains: signatures, genesis and mixing chronologie, *Earth Planet. Sci. Lett.* 90, 273-296, 1988.

Hart, S.R., Hauri, E.H., Oschmann, L.A., Whitehead, J.A., Mantle plumes and entrainment: isotopic evidence, *Science* 256, 517-520, 1992.

Hauri, E.H., Whitehead, J.A., Hart, S.R., Fluid dynamic and geochemical aspects of entrainment in mantle plumes, *J. Geophys. Res.* 99, 24275-24300, 1994.

Hawkesworth, C.J., Kempton, P.D., Rogers, N.W., Ellam, R.M., Van Calsteren, P.W., Continental mantle lithosphere, and shallow level enrichment processes in the Earth's mantle, *Earth Planet. Sci. Lett.* 96, 256-268, 1990.

Hellfrich, G.R. , Wood, B.J., The Earth's mantle, *Nature* 412, 501-507, 2001.

Hermann, J., Rubatto, D., Accessory phase control on the trace element signature of sediment melts in subduction zones, *Chem. Geol.* 265, 512-526, 2009.

Hildenbrand, A., Gillot, P.Y., Le Roy, I., Volcano-tectonic and geochemical evolution of an oceanic intra-plate volcano: Tahiti-Nui (French Polynesia), *Earth Planet. Sci. Lett.* 217, 349-365, 2004.

Hildner, H., Klugle, A., Hansteen, T., Barometry of lavas from 1951 eruption of Fogo, Cape Verde Islands: Implications for historic and prehistoric magma plumbing system, *J. Volcanol. Geotherm. Res.* 217-218, 73-90, 2012.

Hilton, D.R., Grönvold, K., Macpherson, C.G., Castillo, P.R., Extreme 3He/4He ratios in northwest Iceland: constraining the common component in mantle plumes, *Earth Planet. Sci. Lett.* 173, 53-60, 1999.

Hilton, D.R., Barling, J., Wheller, O.E., Effect of shallow-level contamination on the helium isotope systematics of ocean-island lavas, *Nature* 373, 330-333, 1995.

Hoernle, K., Zhang, Y.-S., Graham, D., Seismic and geochemical evidence for large scale mantle upwelling beneath the eastern Atlantic and western and central Europe, *Nature* 374, 34-39, 1995.

Hoernle, K., Tilton, G., LeBas, M.J., Duggen, S., Garbe-Schönberg, D., Geochemistry of oceanic carbonatites compared with continental carbonatites: mantle recycling of oceanic crustal carbonate, *Contrib. Mineral. Petrol.* 142, 520–542, 2002.

Hofmann, A.W., Mantle geochemistry: the message from oceanic volcanism. *Nature* 385, 219-229, 1997.

Hofmann, A.W., White, W.M., Mantle plumes from ancient oceanic crust, *Earth Planet. Sci. Lett.* 57, 421-436, 1982.

Hunter, R.S., McKenzie, D., The equilibrium geometry of carbonate melts in rocks of mantle composition, *Earth Planet. Sci. Lett.* 92, 347–356, 1989.

Jackson, C.R.M., Parman, S.W., Kelley, S.P., Cooper, R.F., Noble gas transport into the mantle facilitated by high solubility in amphibole. *Nature Geosci.* 6, 562-565, 2013.

Jackson, C.R.M., Parman, S.W., Kelley, S.P., Cooper, R.F., Light noble gas dissolution into ring structure-bearing materials and lattice influences on noble gas recycling, *Geochim. Cosmochim. Acta* 159, 1-15, 2015.

Jackson, M.G., Kurz, M.D., Hart, S.R., Workman, R.K., New Samoan lavas from Ofu Island reveal a hemispherically heterogeneous high $^{3}He/^{4}He$ mantle, *Earth Planet. Sci. Lett.* 264, 360–374, 2007.

Jackson, M.G., Hart, S.R., Konter, J.G., Kurz, M.D., Blusztajn, J., Farley, K., Helium and lead isotopes reveal the geochemical geometry of the Samoan plume, *Nature* 514, 355-358, 2014.

Jahn, B.M., Glikson, A.Y., Peucat, J.J., Hickman, A.H., REE geochemistry and isotopic data of Archean silicic volcanics and granitoids from the Pilbara Block, western Australia: Implications for the early crustal evolution, *Geochim. Cosmochim. Acta* 45, 1633–1652, 1981.

Johnson, M.C., Plank, T., Dehydration and melting experiments constrain the fate of subducted sediments, *Geochem. Geophys. Geosyst.* **1**, doi: 10.1029/1999 GC000014, 1999.

Jones, J.H., Walker, D., Pickett, D.A., Murrell, M.T., Beattie, P., Experimental investigations of the partitioning of Nb, Mo, Ba, Ce, Pb, Ra, Th, Pa, and U between immiscible carbonate and silicate liquids, *Geochim. Cosmochim. Acta* 59, 1307-1320, 1995.

Kelfoun, K., Druitt, T.H., Numerical modeling of the emplacement of Socompa rock avalanche, Chile, *J. Geophys. Res.* 110, doi: 10.1029/2005JB003758, 2005.

Kelfoun, K., Druitt, T., van Wyk de Vries, B., Guilbaud, M.-N., Topographic reflection of the Socompa debris avalanche, Chile, *Bull. Volcanol.* 70, 1169–1187, 2008.

Kiseeva, E.S., Yaxley, G.M., Hermann, J., Litasov, K.D., Rosenthal, A., Kamenetsky, V.S., An experimental study of carbonated eclogite at 3.5–5.5 GPa – implications for silicate and carbonate metasomatism in the cratonic mantle, *J. Petrol.* 53, 727–759, 2012.

Klerkx, J., De Paepe, P., Cape Verde Islands: evidence for a Mesozoic oceanic ridge, *Nature Phys. Sci.* 233, 117-118, 1971.

Klerkx, J., Deutsch, S., De Paepe, P., Rubidium, strontium content and strontium isotopic composition of strongly alkalic basaltic rocks from the Cape Verde Islands, *Contrib. Mineral. Petrol.* 45, 107-118, 1974.

Kurz, M.D., Geist, D., Dynamics of the Galapagos hotspot from helium isotope geochemistry, *Geochim. Cosmochim. Acta* 63, 4139-4156, 1999.

Kurz, M.D., Jenkins, W.J., Hart, S.R., Helium isotopic systematics of oceanic islands and mantle heterogeneity, *Nature* 297, 43-47, 1982.

Kurz, M.D., Jenkins, W.J., Hart, S.R., Clague, D., Helium isotopic variations in volcanic rocks from Loihi Seamount and the island of Hawaii, *Earth Planet. Sci. Lett.* 66, 388-406, 1983.

Kurz, M.D., Curtice, J., Fornari, D., Geist, D., Moreira, M., Primitive neon from the center of the Galápagos hotspot, *Earth Planet. sci. Lett.* 286, 23-34, 2009.

Labanieh, S., Chauvel, C., Germa, A., Quidelleur, X., Lewin, E., Isotopic hyperbolas constrain sources and processes under the Lesser Antilles arc. *Earth. Planet. Sci. Lett.* 298, 35-46, 2010.

Labanieh, S., Chauvel, C., Germa, A., Quidelleur, X., Martinique: a Clear Case for Sediment Melting and Slab Dehydration as a Function of Distance to theTrench, *J. Petrol.* 53, 2441-2464, 2012.

Le Pichon, X., Fox, P.J., Marginal offsets, fractures zones and the early opening of the North Atlantic, *J. Geophys. Res.* 76, 6294-6308, 1971.

Levasseur, S., Birck, J.-L., Allègre, C.J., Direct measurement of femtomoles of osmium and the 187Os/186Os ratio in seawater, *Science* 282, 272-274, 1998.

Loper, D., Mantle plumes, *Tectonophysics* 187, 373-384, 1991.

Luguet, A., Pearson, D.G., Nowell, G.M., Dreher, S.T., Coggon, J.A., Spetsius, Z.V., Parman, S.W., Enriched Pt-Re-Os Isotope Systematics in Plume Lavas Explained by Metasomatic Sulfides, *Science* 319, 453-456, 2008.

Macpherson, C.G., Hilton, D.R., Day, J.M.D., Lowry, D., Grönvold, K., High-$^{3}He/^{4}He$, depleted mantle and low-$\partial^{18}O$, recycled oceanic lithosphere in the source of central Iceland magmatism, *Earth Planet. sci. Lett.* 233, 411-427, 2005.

Manconi, A., Longpré, M.A., Walter, T.R., Troll, V.R., Hansteen, T., The effects of flank collapses on volcano plumbing systems, *Geology* 37,1099-1102, 2009.

Manhès, G. Göpel, C., Heavy stable isotope measurements with thermal ionization mass spectrometry: non mass-dependent fractionation effects between even and uneven isotopes, *Geophys. Res. Abstr.* 5, 10936, 2003.

Manhès, G. Göpel, C., Mass-independant fractionationation during TIMS measurements: Evidence of nuclear shift effect?, *Geochim. Cosmochim. Acta* 71, A618, 2007.

Martin, H., Effect of steeper Archean geothermal gradient on geochemistry of subduction zone magmas, *Geology* 14, 753-756, 1986.

Martin, H., The Archean grey gneisses and the genesis of the continental crust, in: Condie, K.C. (Ed.), The Archean Crustal Evolution, Developments in Precambrian Geology. Elsevier, Amsterdam, pp. 205-259, 1994.

Martin, H., Smithies, R., Rapp, R.P., Moyen, J.-F., Champion, D., An overview of adakite, tonalite–trondhjemite–granodiorite (TTG), and sanukitoid: relationships and some implications for crustal evolution, *Lithos* 79, 1–24, 2005.

Martin, H., Moyen, J.-F., Rapp, R.P., The sanukitoid series: magmatism at the Archaean-Proterozoic transition, Earth and Environmental Science, *Trans. Royal Soc. Edinburgh* 100, 15–33, 2009.

Masson, D.G., Le Bas, T.P., Grevemeyer, I., Weinrebe, W., Flank collapse and large-scale landsliding in the Cape Verde Islands, off West Africa, *Geochem. Geophys. Geosyst.* 9, doi: 10.1029/2008GC001983, 2008.

Meibom, A., Anderson, D.L., The statistical upper mantle assemblage, *Earth Planet. Sci. Lett.* 217, 123-139, 2004.

Meisel, T., Reisberg, L., Moser, J., Carignan, J., Melcher, F., Brügmann, G, Re-Os systematics of UB-N, a serpentinized peridotite reference material, *Chem. Geol.* 201, 161-179, 2003.

McKenzie, D., O'Nions, R.K., Mantle reservoirs and ocean island basalts, *Nature* 301, 229-231, 1983.

Molnar, P., Stock, J., Relative motions of hotspots in the Pacific, Atlantic and Indian oceans since late Cretaceous time, *Nature* 327, 587-591, 1987.

Montelli, R., Nolet, G., Dahlen, F.A., Masters, G., Engdahl, E.R., Hung, S.H., Finite-frequency tomography reveals a variety of plumes in the mantle, *Science* 303, 338-343, 2004.

Montelli, R., Nolet, G., Dahlen, F.A., Masters, G., A catalogue of deep mantle plumes: new results from finite-frequency tomography, *Geochem. Geophys. Geosyst.* 7, doi: 10.1029/2006GC001248, 2006.

Moreira, M., Allègre, C.J., Helium-neon systematics and the structure of the mantle, *Chem. Geol.* 147, 53-59, 1998.

Moreira, M., Kurz, M.D., Subducted oceanic lithosphere and the origin of the «High μ» basalt helium isotopic signature, *Earth Planet. Sci. Lett.* 189, 49-57, 2001.

Moreira, M., Kanzari, A., Madureira, P., Helium and neon isotopes in São Miguel island basalts, Azores Archipelago: New constraints on the "low $^{3}He$" hotspot origin, *Chem. Geol.* 322-323, 91-98, 2012.

Morgan, W.J., Hotspot tracks and the early rifting of the Atlantic, *Tectonophysics* 94, 123-139, 1983.

Mourtada, S., LeBas, M.J., Pin, C., Petrogenesis of Mg-carbonatites from Tamazert in the Moroccan High Atlas, *C. R. Acad. Sci. Paris* 325, 559–564, 1997.

Nair, R., Chacko, T., Role of oceanic plateaus in the initiation of subduction and origin of the continental crust, *Geology* 36, 583-586, 2008.

Nelson, D.R., Chivas, A.R., Chappell, B.W., McCulloch, M.T., Geochemical and isotopic systematics in carbonatites and implications for the evolution of ocean-island sources, *Geochim. Cosmochim. Acta* 52, 1–17, 1988.

Paris, R., Giachetti, T., Chevalier, J., Guillou, H., Frank, N., Tsunami deposits in Santiago Island (Cape Verde archipelago) as possible evidence of a massive flank failure of Fogo volcano, *Sediment. Geol.* 239, 129-145, 2011.

Pinel, V., Albino, F., Consequences of volcano sector collapse on magmatic storage zones: Insights from numerical modeling, *J. Volcanol. Geotherm. Res.* 252, 29-37, 2013.

Putirka, K., Mikaelian, H., Ryerson, F., Shaw, H., New clinopyroxene-liquid thermobarometers for mafic, evolved, and volatile-bearing lava compositions, with applications to lavas from Tibet and the Snake River Plain, Idaho, *Am. Mineral.* 88, 1542-1554, 2003.

Plank, T., The chemical composition of subducting sediments, *Treatise on Geochemistry (second edition)* ***4***, 607-629, 2014.

Presley, T.K., Sinton, J.M., Pringle, M., Postshield volcanism and catastrophic mass wasting of the Waianae Volcano, Oahu, Hawaii, *Bull. Volcanol.* 58, 597-616, 1997.

Rapp, R. P., Watson, E.B., Miller, C.F., Partial melting of amphibolite/eclogite and the origin of Archean trondhjemites and tonalites, *Precamb. Res.* 51, 1-25, 1991.

Ray, J.S., Ramesh, R., Pande, K., Carbon isotopes in Kerguelen plume-derived carbonatites: evidence for recycled inorganic carbon, *Earth Planet. Sci. Lett.* 170, 205-214, 1999.

Richards, J.P., Villeneuve, M., The Llullaillaco volcano, northwest Argentina: construction by Pleistocene volcanism and destruction by sector collapse, *J. Volcanol. Geotherm. Res.* 105, 77-105, 2001.

Ritsema, J., Allen, R.M., The elusive mantle plume, *Earth Planet. Sci. Lett.* 207, 1-12, 2003.

Saal, A.E., Hart, S.R., Shimizu, N., Hauri, E.H., Layne, G.D., Eiler, J.M., Pb isotopic variability in melt inclusions from the EMI-EMII-HIMU mantle end-members and the role of the oceanic lithosphere, *Earth Planet. Sci. Lett.* 240, 605-620, 2005.

Schaefer, B.F., Turner, S., Parkinson, I., Rogers, N., Hawkesworth, C., Evidence for recycled Archaean oceanic mantle lithosphere in the Azores plume, *Nature* 420, 304–307, 2002.

Shirey, S.B., Walker, R.J., Carius Tube Digestion for Low-Blank Rhenium-Osmium Analysis, *Anal. Chem.* 67, 2136-2141, 1995.

Shirey, S.B., Walker, R.J., The Re-Os isotope system in cosmochemistry and high-temperature geochemistry, *Annual Rev. Earth Planet. Sci.* 26, 423-500, 1998.

Siebert, L., Large volcanic debris avalanches: Characteristics of source areas, deposits, and associated eruptions, *J. Volcanol. Geotherm. Res.* 22, 163–197, 1984.

Snow, J.E., Reisberg, L., Os isotopic systematics of the MORB mantle: results from altered abyssal peridotites, *Earth Planet. Sci. Lett.* 133, 411-421, 1995.

Staudacher, T., Allègre, C.J., Recycling of oceanic crust and sediments: the noble gas subduction barrier, *Earth Planet. Sci. Lett.* 89, 173-183, 1988.

Staudacher, T., Sarda, P., Richardson, S.H., Allègre, C.J., Sagna, I., Dmitriev, L.V., Noble gases in basalt glasses from a Mid-Atlantic ridge topographic high at 14°N: geodynamic consequences, *Earth. Planet. Sci. Lett.* 96, 119-133, 1989.

Stern, R.A., PhD thesis, State University of New York at Stony Brook, 1989.

Stern, R.A., Hanson, G.N., Archaean high-Mg granodiorites: a derivative of light rare earth enriched monzodiorites of mantle origin, J. Petrol. 32, 201–238, 1991

Stracke, A., Hofmann, A.W., Hart, S.R., FOZO, HIMU, and the rest of the mantle zoo, *Geochem. Geophys. Geosyst.* 6, doi: 10.1029/2004GC000824, 2005.

Syracuse, E.M., van Keken, P.E., Abers, G.A., The global range of subduction zone thermal models, *Phys. Earth Planet. Int.* 183, 73-90, 2010.

Tarney, J., Weaver, B.L., Drury, S.A., Geochemistry of Archaean trondhjemitic and tonalitic gneisses from Scotland and E. Greenland, F. Barker, Editor, Trondhjemites, Dacites and Related Rocks, Elsevier, Amsterdam, pp. 275–299, 1979.

Tatsumoto, M., Genetic relations of oceanic basalts as indicated by lead isotopes, *Science* 153, 1094-1101, 1966.

Thirlwall, M.F., Pb isotopic and elemental evidence for OIB dérivation from young HIMU mantle, *Chem. Geol.* 139, 51-74, 1997.

Thirlwall, M.F., Inapropriate tail corrections can cause large inaccuracy in isotope ratio determination by MC-ICP-MS, *J. Anal. At. Spectrom.* 16, 1121-1125, 2001.

Thirlwall, M.F., Multicollector ICP-MS analysis of Pb isotopes using a 207Pb-204Pb double spike demonstrates up to 400 ppm/amu systematic errors in Tl-normalization, *Chem. Geol.* 184, 255-279, 2002.

Treiman, A.H., Carbonatite magma: properties and processes. In Carbonatites Genesis and Evolution (ed. K. Bell). Unwin Hyman, London, pp. 89–104, 1989.

Turner, S., Hawkesworth, C., Rogers, N., King, P., U–Th isotope disequilibria and ocean island basalt generation in the Azores, *Chem. Geol*. 139, 145-164, 1997.

Valbracht, P.J., Staudacher, T., Malahoff, A., Allègre, C.J., Noble gas systematics of deep rift zone glasses from Loihi Seamont, Hawaii, *Earth Planet. Sci. Lett*. 150, 399-411, 1997.

Vance, D., Stone, J.O.H., O'Nions, R.K., He, Sr and Nd isotopes in xenoliths from Hawaii and other oceanic islands, *Earth Planet. Sci. Lett*. 96, 147-160, 1989.

van Keken, P.E., Ballentine, C.J., Hauri, E.H., Holland, H.D., Turekian, K.K., Convective mixing in the Earth's mantle, in Treatise on Geochemistry, edited by R.W. Carlson, pp. 1–21, Pergamon, Oxford, U.K., 2007.

van Wyk de Vries, B., Self, S., Francis, P.W., Keszthelyi, L., A gravitational spreading origin for the Socompa debris avalanche, *J. Volcanol. Geotherm. Res.* 105, 225–247, 2001.

Voight, B., Glicken, H., Janda, R.J., Douglass, M., Catastrophic rockslide avalanche of may 18, in The 1980 Eruptions of Mount St. Helens, Washington, edited by P. Lipman and D.R. Mullineaux, *U.S. Geol. Surv. Prof. Pap.* 1250, 347–377, 1981.

Vollmer, R., Earth degassing, mantle metasomatism and isotopic evolution of the mantle, *Geology* 11, 452-454, 1983.

Wadge, G., Francis, P.W., Ramirez, C.F., The Socompa collapse and avalanche event, *J. Volcanol. Geotherm. Res.* 66, 309–336, 1995.

Wallace, M.E., Green, D.H., An experimental determination of primary carbonatite magma composition, *Nature* 335, 343–346 1988.

Weaver, B.L., The origin of ocean island basalt end-member compositions: trace element and isotopic constraints, *Earth Planet. Sci. Lett*. 104, 381-397, 1991.

Welsch, B., Faure, F., Famin, V., Baronnet, A., Bachèlery, P., Dendritic Crystallization: A Single Process for all the Textures of Olivine in Basalts, *J. Petrol*. 54, 539-574, 2013.

Widom, E., Carlson, R.W., Gill, J.B., Schmincke, H.-U., Th–Sr–Nd–Pb isotope and trace element evidence for the origin of the Sao Miguel, Azores, enriched mantle source, *Chem. Geol*. 140, 49–68, 1997.

Widom, E., Hoernle, K.A., Shirey, S.B., Schmincke, H.-U., Os Isotope Systematics in the Canary Islands and Madeira: Lithospheric Contamination and Mantle Plume Signatures, *J. Petrol*. 40, 279-296, 1999.

White, W.M., Sources of oceanic basalts : radiogenic isotopic evidence, *Geology* 13, 115-118, 1985.

White, W.M., The fifth plume component, in D.L. Anderson, S.R. Hart and A.W. Hofmann, convenors, Plume 2, Terra Nostra 3, 157-160, Alfred Wegener-Stiftung, Bonn, 1995.

Woolley, A.R., Kempe, D.R.C., Carbonatites: nomenclature, average chemical compositions, and element distribution. In: Bell, K. (Ed.), Carbonatites, Genesis and Evolution. Unwin Hyman, London, pp.1–14, 1989.

Woolley, A.R., Kjarsgaard, B.A., Carbonatite Occurrences of the World: Map and Database, Geological Survey of Canada, Open File. 1 CD-ROM +1 map, 2008.

Wyllie, P.J., Huang, W.-L., Otto, J., Byrnes, A.P., Carbonation of peridotites and decarbonation of siliceous dolomites represented in the system CaO–MgO–SiO2–CO2 to 30 kbar, *Tectonophysics* 100, 359–388, 1983.

Wyllie, P.J., Huang, W.L., Carbonation and melting reactions in the system CaO–MgO–SiO2–CO2 at mantle pressures with geophysical and petrological applications, *Contrib. Mineral. Petrol*. 54, 79–107, 1976.

Yang, T., Shen, Y., van der Lee, S., Solomon, S.C., Hung, S.-H., Upper mantle structure beneath the Azores hotspot from finite frequency seismic tomography, *Earth Planet. Sci. Lett*. 250,11–26, 2006.

Zhao, D., Seismic images under 60 hotspots: search for mantle plumes, *Gondwana Res.* 12, 335–355, 2007.

Zindler, A., Hart, S.R., Chemical Geodynamics, *Ann. Rev. Earth. Planet. Sci.* 14, 493-571, 1986a.

Zindler, A., Hart, S.R., Helium: problematic primordial signals, *Earth. Planet. Sci. Lett*. 79, 1-8, 1986b.

Zindler, A., Jagoutz, E., Goldstein, S., Nd, Sr and Pb isotopic systematics in a three-component mantle: a new perspective, *Nature* 298, 519-523, 1982.

Partie II

PUBLICATIONS

*Publications avec comités de lecture*

*(* désigne les publications présentées dans le mémoire)*

27*- Bellot, Boyet, **Doucelance**, Pin, Chauvel, Auclair (2015) Ce isotope systematics of island arc lavas from the Lesser Antilles. *Geochim. Cosmochim. Acta*, 168, 261-279.

26*- **Doucelance**, Bellot, Boyet, Hammouda, Bosq (2014) What coupled cerium and neodymium isotopes tell us about the deep source of oceanic carbonatites. *Earth Planet. Sci. Lett*. 407, 175-186.

25*- Laurent, Martin, Moyen, **Doucelance** (2014) The diversity and evolution of late-Archean granitoids: evidence for the onset of "modern-style" plate tectonics between 3.0 and 2.5 Ga. *Lithos* 205, 208-235.

24 - Cartier, Hammouda, **Doucelance**, Boyet, Devidal, Moine (2014) Experimental study of trace elements partitioning between enstatite and melt in Enstatite-Chondrites at low oxygen fugacity and 5 GPa. *Geochim. Cosmochim. Acta* 130, 167-187.

23*- **Doucelance**, Kelfoun, Labazuy, Bosq (2014) Geochemical insights into the internal dynamics of debris avalanches. A case study: the Socompa avalanche, Chile. *Geochem. Geophys. Geosys.* 15(6), 2282-2300.

22*- Laurent, Rapopo, Stevens, Moyen, Martin, **Doucelance,** Bosq (2014) Contrasting petrogenesis of Mg-K and Fe-K granitoids and implications for post-collisional magmatism: case study from the late-Archaean Matok pluton (Pietersburg block, South Africa), *Lithos* 196-197, 131-149.

21*- Laurent, Paquette, Martin, **Doucelance**, Moyen (2013) LA-ICP-MS dating of zircons from Meso- and Neoarchaean granitoids of the Pietersburg block (South Africa): crustal evolution at the northern margin of the Kaapvaal craton. *Precambrian Res.* 230, 209-226.

20*- Laurent, **Doucelance**, Martin, Moyen (2013) Differentiation of the late-Archaean sanukitoid series and some implications for crustal growth: insights from geochemical modelling on the Bulai pluton, Central Limpopo Belt, South Africa. *Precambrian Res.* 227, 186-203.

19*- Mourão, Mata, **Doucelance**, Madeira, Millet, Moreira (2012) Geochemical temporal evolution of Brava Island magmatism: constraints on the variability of Cape Verde mantle sources and on carbonatite-silicate magmas link. *Chem. Geol.* 334, 44-61.

18*- Sanchez-Garrido, Stevens, Armstrong, Moyen, Martin, **Doucelance** (2011) Diversity in Earth's early felsic crust: Paleoarchean peraluminous granites of the Barberton Greenstone Belt. *Geology* 39(10), 963-966.

17*- Laurent, Martin, **Doucelance**, Moyen, Paquette (2011) Geochemistry and petrogenesis of high-K "sanukitoids" from the Bulai pluton, Central Limpopo Belt, South Africa: Implications for geodynamic changes at the Archaean-Proterozoic boundary. *Lithos* 123, 73-91.

16*- **Doucelance**, Hammouda, Moreira, Martins (2010) Geochemical constraints on depth of origin of oceanic carbonatites: the Cape Verde case. *Geochim. Cosmochim. Acta* 74(24), 7261-7282.

15*- Mata, Moreira, **Doucelance**, Ader, Silva (2010) Noble gases and carbon isotopic signatures of Cape Verde oceanic carbonatites: implications for carbon provenance. *Earth Planet. Sci. Lett*. 291(1-4), 70-83.

14*- Mourão, Mata, **Doucelance**, Madeira, Brum da Silveira, Silva, Moreira (2010) Quaternary extrusive calciocarbonatite volcanism on Brava Island (Cape Verde): A nephelinite-carbonatite immiscibility pro-

duct. *J. African Earth Sci.* 56, 59-74.

13*- Poirier, **Doucelance** (2009) Effective Correction of Mass Bias for Rhenium Measurements by MC-ICP-MS. *Geost. Geoanal. Res.* 33(2), 195-204.

12*- Millet, **Doucelance**, Baker, Schiano (2009) Reconsidering the origins of isotopic variations in Ocean Island Basalts ; Insights from fine-scale study of São Jorge Island, Azores archipelago. *Chem. Geol.* 265(3-4), 289-302.

11*- Millet, **Doucelance**, Schiano, David, Bosq (2008) Mantle plume heterogeneity versus shallow-level interactions: A case study, the São Nicolau Island, Cape Verde archipelago. *J. Volcanol. Geotherm. Res.* 176(2), 265-276.

10 - Laubier, Schiano, **Doucelance**, Ottolini, Laporte (2007) Olivine-hosted melt inclusions and melting processes beneath the FAMOUS zone (Mid-Atlantic Ridge). *Chem. Geol.* 240(1-2), 129-150.

9*- Debaille, **Doucelance**, Weis, Schiano (2006) Multi-stage mixing in subduction zones : Application to Merapi volcano (Java island, Sunda arc). *Geochim. Cosmochim. Acta* 70(3), 723-741.

8 **-** Debaille, Blichert-Toft, Agranier, **Doucelance** (2006) Schiano & Albarede, Geochemical component relationships in MORB from the Mid-Atlantic Ridge, 22-35°N. *Earth Planet. Sci. Lett.* 241(3-4), 844-862.

7*- Escrig, **Doucelance**, Moreira, Allègre (2005) Os isotope systematics in Fogo basalts: evidence for lower continental crust residing in the oceanic lithosphere beneath the Cape Verde Islands. *Chem. Geol.* 219(1-4), 93-113.

6 - Deschamps, Hillaire-Marcel, Michelot, **Doucelance**, Ghaleb, Buschaert (2004) $^{234}U/^{238}U$ Disequilibrium along stylolitic discontinuities in deep Mesozoic limestone formations of the Eastern Paris basin: evidence for discrete uranium mobility. *Hydrology Earth Syst. Sci.* 8(1), 35-46.

5 - Poirier, **Doucelance**, Gariépy (2004) Radiogenic isotope investigation of the St-Robert H5 fall. *Meteoritics Planet. Sci.* 39(12), 1983-1993.

4*- Deschamps, **Doucelance**, Ghaleb, Michelot (2003) Further investigations on optimized tall correction and high-precision measurement of Uranium isotopic ratios using Multi-Collector ICP-MS. *Chem. Geol.* 201(1-2), 141-160.

3*- **Doucelance**, Escrig, Moreira, Gariépy, Kurz (2003) Pb-Sr-He isotope and trace element geochemistry of the Cape Verde Archipelago. *Geochim. Cosmochim. Acta* 67(19), 3717-3733.

2*- **Doucelance**, Manhès (2001) Reevaluation of precise lead isotope measurements by thermal ionization mass spectrometry : comparison with determinations by plasma source mass spectrometry. *Chem. Geol.* 176(1-4), 361-377.

1*- Moreira, **Doucelance**, Kurz, Dupré, Allègre (1999) Helium and lead isotope geochemistry in the Azores Archipelago. *Earth Planet. Sci. Lett.* 169(1-2), 189-205.

*Autres publications*

11 - Laurent, Martin, Moyen, **Doucelance**, Paquette (2010) Origin and significance of high-K series at the Archaean-Proterozoic boundary. Geological Survey of Western Australia, 86-89.

10 - Sanchez-Garrido, Stevens, Moyen, Martin, **Doucelance**, Harris, Armstrong (2010) Paleo-Archean rhyolites and the source of potassium in the proto-continental crust. Geological Survey of Western Australia, 127-130.

9 - Mourão, Mata, Madeira, Silva, Brum da Silveira, Moreira, **Doucelance** (2008) Peculiaridades da Ilha Brava no contexto da Geologia do Arquipélago de Cabo Verde. Memórias e Notícias 3 (Nova Série), 217-222.

8 - Nagel, Degay, **Doucelance**, Pallier, Hocquard, Urien, Joseph, Richard (1996) Inventaire Minier du département de la Guyane. Bilan des travaux et résultats. Rapport BRGM R38633.

7 - Nagel, Degay, **Doucelance** (1995) Inventaire Minier du département de la Guyane: le prospect aurifère de Langa Tabiki. Rapport BRGM R38415 SGN/GUY 95.

6 - Nagel, Degay, **Doucelance**, Maurizot (1995) Inventaire Minier du département de la Guyane: le prospect aurifère de Cazal. Rapport BRGM R38416 SGN/GUY 95.

5 - Nagel, Degay, **Doucelance**, Maurizot (1995) Inventaire Minier du département de la Guyane: le prospect aurifère de Mataroni. Rapport BRGM R38417 SGN/GUY 95.

4 - Nagel, Degay, **Doucelance**, Maurizot (1995) Inventaire Minier du département de la Guyane: le prospect aurifère de Montagne Française. Rapport BRGM R38418 SGN/GUY 95.

3 - Nagel, Degay, **Doucelance**, Maurizot, Pallier (1995) Inventaire Minier du département de la Guyane: le prospect aurifère de Maripa. Rapport BRGM R38419 SGN/GUY 95.

2 - Nagel, Degay, **Doucelance** (1995) Inventaire Minier du département de la Guyane: avancement des travaux au 28 février 1995. Rapport BRGM GUY R38317.

1 - Nagel, Degay, **Doucelance** (1994) Inventaire Minier du département de la Guyane: avancement des travaux au 10 octobre 1994. Rapport BRGM GUY R38125.

- 41 résumés dans des conférences internationales.
- 17 résumés dans des colloques (workshops) internationaux et nationaux.

ELSEVIER

Earth and Planetary Science Letters 169 (1999) 189–205

EPSL

# Helium and lead isotope geochemistry of the Azores Archipelago

Manuel Moreira [a,b,*], Régis Doucelance [a], Mark D. Kurz [b], Bernard Dupré [a,c], Claude Jean Allègre [a]

[a] *Laboratoire de Géochimie et Cosmochimie, URA CNRS 1758, Institut de Physique du Globe de Paris, Université Denis Diderot Paris 7, 4 Place Jussieu, 75252, Paris Cedex 05, France*

[b] *Department of Marine Chemistry and Geochemistry, Woods Hole Oceanographic Institution, 360 Woods Hole Road, MS25, Woods Hole, MA 02543, USA*

[c] *Laboratoire de Geochimie, OMP, UMR-CNRS 5563, 38 rue des 36 ponts, 31400, Toulouse, France*

Received 21 April 1998; revised version received 10 March 1999; accepted 11 March 1999

**Abstract**

New helium and lead isotopic data for basalts from the Azores archipelago (North Atlantic) show that the Azores have $^4He/^3He$ ratios both higher and lower than MORB values. Good covariations of helium and lead isotopes are observed at the scale of the archipelago, and suggest the coexistence of two mantle components in the Azores which are identified by data from São Miguel and Terceira. The eastern part of São Miguel island displays radiogenic helium ($^4He/^3He > 140{,}000$, $R/R_a < 5.1$) and lead (20.00, 15.75 and 40.33 for $^{206}Pb/^{204}Pb$, $^{207}Pb/^{204}Pb$ and $^{208}Pb/^{204}Pb$). The $^{207}Pb/^{204}Pb$ and $^{208}Pb/^{204}Pb$ ratios for São Miguel are unusually radiogenic for oceanic basalts. Terceira basalts contain relatively unradiogenic/primitive $^4He/^3He$ ratios, with a minimum value of 64,000 ($R/R_a = 11.3$), and relatively high lead isotopic ratios ($^{206}Pb/^{204}Pb = 20.02$, $^{207}Pb/^{204}Pb = 15.64$ and $^{208}Pb/^{204}Pb = 39.35$). We propose that the Terceira source has a composition produced by a mixing between recycled oceanic crust (high $^{206}Pb/^{204}Pb$) and entrained lower mantle (high $^3He$) material. The São Miguel island isotopic signature may be due to sampling of local (km-size) heterogeneity located at relatively shallow depth. The preferred origin of this heterogeneity is the Jurassic delamination of subcontinental lithosphere, which occurred during rifting and opening of the North Atlantic. The primitive helium ratios were also observed on the Mid Atlantic ridge at 38.5ºN, reflecting plume–ridge interaction, whereas radiogenic ratios (>100,000) were observed at latitude higher than 40ºN and may reflect the influence of the São Miguel component at the ridge.


*Keywords:* helium; lead; isotope ratios; Azores; magmas; mixing

## 1. Introduction

Helium isotopic ratios measured on Oceanic Island Basalts (OIB) display very large variations compared to Mid Oceanic Ridge Basalts (MORB). The relatively homogeneous MORB source reservoir has a $^4He/^3He$ mean value of 88,000 ± 5000 ($R/R_a = 8$) [1] whereas the $^4He/^3He$ isotopic ratios observed in OIB range from 25,000 ($R/R_a = 30$) for Loihi seamount samples [2] to values higher than 150,000 ($R/R_a = 4.8$) for the Gough–Tristan da

* Corresponding author. Fax: +1 508 457 2193; E-mail: mmoreira@whoi.edu

0012-821X/99/$ – see front matter 
PII: S0012-821X(99)00071-0

Cunha–St Helena island group [3–5]. A two-layered mantle best explains these results, where the upper mantle represents the MORB source, which is highly degassed and well mixed by convection [1], whereas the primordial signal observed in Loihi seamount basalts is attributed to the presence of a less degassed reservoir, which is probably located in the lower mantle [2,6].

The significance of the radiogenic helium signatures observed in the Gough–Tristan da Cunha–St Helena island group remains controversial. These signatures have been attributed to the injection, through subduction, of oceanic crust and sediments into the upper mantle, which will present high (U + Th)/$^3$He ratios and be stored for some time at the 670 km boundary layer, prior to eruption [3,5,7]. An alternate view attributing the high $^4$He/$^3$He ratios to shallow, magma chamber contamination processes (unrelated to the mantle), originally discussed by Condomines et al. [8] and Zindler and Hart [9,10], was more recently defended by Hilton et al. [11]. Based on results from Heard island (Indian Ocean), where both primitive and radiogenic helium isotopic ratios have been measured, Hilton and co-workers propose that most the hotspots are in fact 'low $^4$He/$^3$He' hotspots, and the observed radiogenic helium signature may reflect shallow depth contamination, either by interaction of the plume with oceanic crust or radiogenic $^4$He production in a degassed magma chamber.

Lead isotopes also display different histograms for MORB and OIB. Ocean island samples usually present more radiogenic signatures and, again, exhibit more variability, than lavas from spreading centers [10,12,13]. Differences in lead isotopic compositions between oceanic islands are still debated. They could reflect plume source heterogeneities [14,15], material entrainment during plume ascent [16,17] or interaction between plumes and lithospheric mantle [18]. Due to the different decay constants, lead isotopes are less sensitive to in situ production, and cannot be related to magma chamber outgassing.

This study focusses on the Azores archipelago, which is considered to belong to the 'high $^4$He/$^3$He' hotspot category [19–21], and presents new helium and lead isotopic results for six islands from the Azores archipelago: Faial, Graciosa, Pico, São Miguel, Santa Maria and Terceira. Good covariations between helium and lead isotopes are observed at the scale of the archipelago, and suggest the coexistence of two components in the Azores; the two end members are best identified by data from São Miguel and Terceira islands. The Eastern part of São Miguel island displays radiogenic helium ($^4$He/$^3$He > 140,000) and lead (20.00, 15.75 and 40.33 for $^{206}$Pb/$^{204}$Pb, $^{207}$Pb/$^{204}$Pb and $^{208}$Pb/$^{204}$Pb) signatures, whereas Terceira basalts present primitive $^4$He/$^3$He ratios, with a minimum value around 64,000 ($R/R_a$ = 11.3), similar $^{206}$Pb/$^{204}$Pb ratio (20.02), but significantly lower $^{207}$Pb/$^{204}$Pb (15.64) and $^{208}$Pb/$^{204}$Pb (39.35). All other island results are interpreted in terms of binary mixing between the local MORB mantle source and these two plume components.

## 2. Geographical situation and sample locations

The Azores archipelago is composed of nine islands (Corvo, Faial, Flores, Graciosa, Pico, Santa Maria, São Jorge, São Miguel and Terceira), which represent the emerged part of a large oceanic platform (Fig. 1). Located at the triple junction between the Eurasian, African and American plates, the plateau is crossed over by the Mid-Atlantic ridge; seven islands (Faial, Graciosa, Pico, Santa Maria, São Jorge, São Miguel and Terceira) stand at the East of the ridge, two (Corvo and Flores) are located to the west, on the American plate.

The oldest rocks are observed on Santa Maria (8 Myr) and São Miguel (4 Myr for the Eastern part) islands [22–25]. Other volcanics, including the central part of São Miguel, were erupted during the Pleistocene and Holocene. Historic lavas have been found in most areas of the archipelago (including São Miguel island), and the most recent volcanism occurred on Faial in 1957/58 (Capelinhos site). The lava compositions range from basalts to trachy-andesites and some peridotitic nodules have been observed on Pico, Faial and Terceira islands [26,27].

Samples from the islands of Santa Maria, São Miguel, Terceira, Pico, Graciosa and Faial, were analyzed. Sample locations are given on Fig. 2 and in Appendix A.

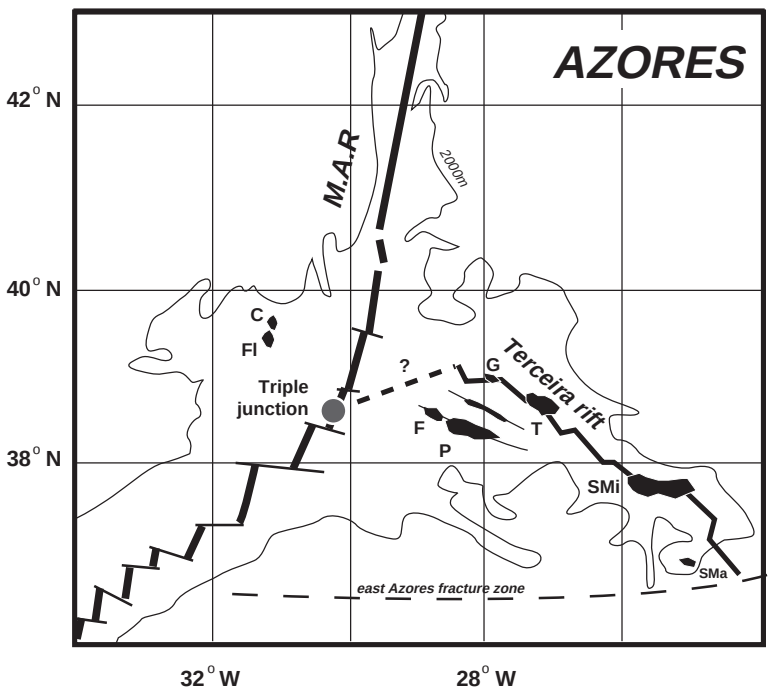


Fig. 1. Location map of the Azores archipelago (modified after Turner et al. [34]). Triple junction has been proposed to be located at 38.5ºN [41,57], rather than in the straight continuity of the Terceira rift. Abbreviations for the island names: Santa Maria (*SMa*), São Miguel (*SMi*), Terceira (*T*), Graciosa (*G*), Pico (*P*), Faial (*F*), Flores (*Fl*) and Corvo (*C*).

## 3. Analytical procedure

Helium analyses were performed on millimeter sized olivine and pyroxene phenocrysts separated from fresh lavas. Samples from the Eastern side of São Miguel island were ankaramites with large olivine and pyroxene crystals, up to 2 cm in size; most of the other lavas were alkali-basalts. Measurements were preferentially done by crushing, in order to avoid possible in-situ radioactive decay or production of $^{3}$He cosmogenic and to obtain the inherited helium trapped in inclusions [3,28]. The powder of the crushed olivines and pyroxenes from sample ACO95-68 (ankaramite from São Miguel) were also melted in vacuo to release the gases located in the matrix, which allows an evaluation of the contribution from radiogenic and cosmogenic helium.

Most of the helium measurements were performed in Paris using a glass mass spectrometer and extraction line. Due to diffusion, prior measurements with two purifications using hot titanium getters and trapping on a cold head in our KOVAR glass ARESIBO II mass spectrometer yielded significant $^{4}$He blanks for very low helium concentration samples such as phenocrysts (olivines, pyroxenes) from oceanic basalts [29,30]. Thus, we developed a shorter crushing procedure which now yields a $^{4}$He blank of $5 \times 10^{-10}$ $\pm 0.5$ cm$^{3}$ STP, a significant improvement to previous blank values of $1.5 \pm 0.5 \times 10^{-8}$ cm$^{3}$ STP. A charcoal trap was installed close to the crusher which retains all active gases, except He and Ne, during 30 minutes of cryo-pumping at liquid nitrogen temperature. $^{3}$He is analysed on an electron multiplier and $^{4}$He, depending of the absolute amount of gas, on a Faraday cup, or on the electron multiplier. Using only 30 minutes of purification in a very small volume, the helium introduced into the extraction line by diffusion is very small, leading to low blanks. This procedure makes possible the measurement on this mass spectrometer of very low level samples using 1 or 2 g of olivine or pyroxene.

This new procedure was tested by repeated analysis of a oceanite sample from Réunion island (Indian

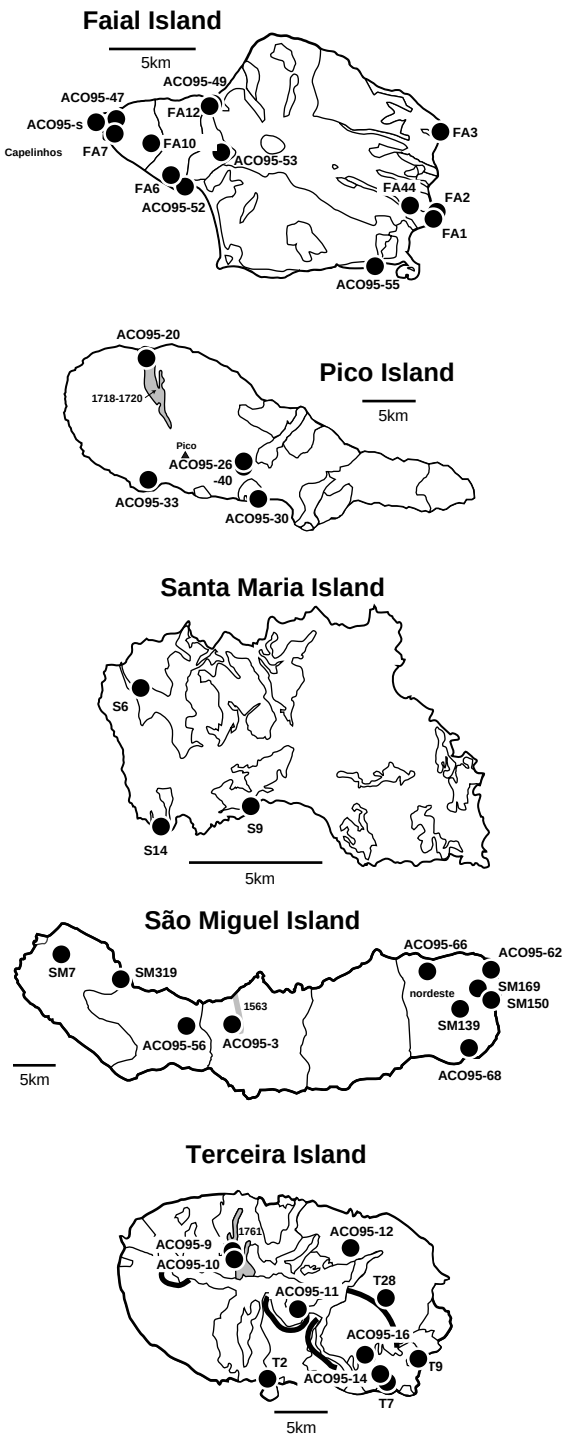


Fig. 2. Faial, Pico, Santa Maria, São Miguel and Terceira island sampling maps, modified after Forjaz et al. [67].

ocean), whose olivines are known to have a very homogeneous $^4He/^3He$ isotopic ratio of 56,000 ± 1000 ($R/R_a = 12.9 \pm 0.2$) [31,32]. Using different amounts of olivines (0.5, 0.8 and 1.3 g, respectively), we obtained reproducible $^4He/^3He$ results of 55,296 ± 3254, 55,918 ± 4152 and 55,591 ± 2740.

Some helium analyses were also performed in the Woods Hole Oceanographic Institution where the blank is typically 3 to $5 \times 10^{-11}$ cm$^3$ STP [33]; these data are italicized in Table 1. There is a good agreement between the data obtained in the two laboratories. Sample ACO95-3, which was collected at the 1563 lava flow from Queimado peak eruption, have given $^4He/^3He$ ratios of 149,600 and 133,830 similar to the ratio of 133,800 of one sample from the same lava flow analyzed by M.D. Kurz (sample #SM88-45, unpublished results) indicating good inter-laboratory agreement.

Lead chemical separation was performed on ~0.5 g of powdered samples using the procedure of Manhès et al. [34], in a clean room under controlled atmosphere. This permits one to maintain the total Pb blank below 0.35 ng. Lead isotopic ratios were measured on a Thomson THN 206 mass spectrometer and calibrated against SRM981 NBS [35] standard measurements, with a statistical mass discrimination factor of 1 ± 0.3‰ per amu. The total precision, tested by duplicate analysis, is better than 0.05% ($2\sigma$) per mass unit difference in the isotopic ratio.

## 4. Results

Results are given in Tables 1 and 2. Helium concentrations obtained by crushing range from

Footnote to Table 1: $R/R_a$ is the $^3He/^4He$ ratio normalized to the AIR value of $1.384 \times 10^{-6}$. $\sigma$ is the uncertainty. Uncertainty in the helium concentrations is approximately 5%. The last column gives the percentage of $^4He$ blank contribution (which was $^4He \approx 5 \times 10^{-10}$ cm$^3$ STP in Paris and 3 to $5 \times 10^{-11}$ at WHOI). Data in italics were analyzed in the Woods Hole Oceanographic Institution isotope facilities. Measurements were conducted on olivine (Ol.) and clinopyroxene (CPX). Re-crush means that samples were crushed a second time, sequentially, in an attempt to insure complete extraction, and also to resolve any contributions from radiogenic helium. The experiments conducted by melting of powder remaining after crushing are abbreviated mp.

Table 1
Helium concentration (in $10^{-8}$ $cm^3$ STP/g) and isotopic ratios (corrected for blank) for Azores samples

| Sample | Mineral | Weight (g) | $^4He$ ($\times 10^{-8}$) | $R/R_a$ | $^4He/^3He$ | Blank (%) |
|---|---|---|---|---|---|---|
| **Faial** | | | | | | |
| ACO95-sand | Ol. | 1.04 | 4.9 | 7.5 ± 0.5 | 95960 ± 6630 | 1 |
| | Ol. | 1.33 | 6.8 | 8.0 ± 0.2 | 90890 ± 1930 | 14 |
| ACO95-47 | Ol. | 1.79 | 0.53 | 8.3 ± 1.2 | 87160 ± 12090 | 4 |
| ACO95-49 | Ol. | 1.58 | 43 | 8.7 ± 0.1 | 86320 ± 1210 | 3 |
| ACO95-52 | Ol. | 1.08 | 4.5 | 7.2 ± 0.4 | 99940 ± 5940 | 1 |
| *ACO95-53* | *Ol.* | *0.38* | *1.2* | *8.4 ± 0.1* | *85970 ± 700* | *1* |
| ACO95-55 | Ol. | 1.01 | 0.54 | 5.6 ± 1.7 | 129720 ± 40520 | 11 |
| FA10 | Ol. | 1.13 | 2.0 | 7.8 ± 0.5 | 92280 ± 5780 | 3 |
| *FA12* | *Ol.* | *0.19* | *1.2* | *8.0 ± 0.1* | *89601 ± 2378* | *2* |
| **Pico** | | | | | | |
| *ACO95-20* | *Ol.* | *0.35* | *1.7* | *10.0 ± 0.1* | *72545 ± 415* | *2* |
| ACO95-20 | CPX | 1.84 | 3.6 | 10.0 ± 0.2 | 72110 ± 1730 | 1 |
| ACO95-26 | Ol. | 1.32 | 1.4 | 10.0 ± 0.3 | 72550 ± 2480 | 2 |
| ACO95-30 | Ol. | 0.96 | 36 | 8.8 ± 0.1 | 81820 ± 870 | 0.2 |
| ACO95-30 b | Ol. | 1.01 | 13 | 10.3 ± 0.1 | 70150 ± 890 | 1 |
| ACO95-30 b | CPX | 1.08 | 7.6 | 9.7 ± .0.1 | 74320 ± 1070 | 1 |
| ACO95-33 | Ol. | 1.17 | 3.2 | 8.9 ± 0.5 | 80910 ± 4620 | 1 |
| ACO95-40 | Ol. | 0.97 | 1.0 | 7.5 ± 0.9 | 95960 ± 10830 | 3 |
| **Santa Maria** | | | | | | |
| *S6* | *Ol.* | *0.17* | *0.19* | *7.7 ± 0.3* | *94376 ± 3242* | *17* |
| **São Miguel** | | | | | | |
| ACO95-3 | Ol. | 1.19 | 1.4 | 4.8 ± 0.6 | 149600 ± 17650 | 2 |
| | Ol. | 1.46 | 1.8 | 5.4 ± 0.5 | 133830 ± 13490 | 3 |
| ACO95-56 | Ol. | 1.02 | 0.50 | 4.5 ± 1.2 | 162070 ± 43520 | 29 |
| ACO95-62 | Ol. | 1.97 | 0.23 | 6.1 ± 1.9 | 118450 ± 36900 | 12 |
| ACO95-62 | CPX | 1.07 | 0.60 | 3.0 ± 1.1 | 240850 ± 88310 | 9 |
| ACO95-66 | Ol. | 1.42 | 0.33 | 5.9 ± 2.0 | 121640 ± 41160 | 16 |
| *ACO95-68* | *Ol.* | *0.33* | *0.20* | *4.1 ± 0.1* | *174317 ± 5047* | *7* |
| | | *Re-crush* | *0.06* | *3.8 ± 0.4* | *189644 ± 20408* | *25* |
| | *mp* | *0.31* | *0.37* | *4.4 ± 0.1* | *163180 ± 4310* | *4* |
| ACO95-68 | CPX | 1.61 | 3.3 | 2.6 ± 0.1 | 276840 ± 11670 | 1 |
| | CPX | 2.82 | 3.4 | 4.0 ± 0.3 | 180550 ± 11910 | 1 |
| ACO95-68 (melt) | CPX | 3.02 | 3.3 | 4.4 ± 0.7 | 163470 ± 24600 | |
| *ACO95-68* | CPX | 0.32 | 2.4 | 4.06 ± 0.03 | 178200 ± 1360 | 1 |
| | | *Re-crush* | *0.02* | *4.3 ± 0.8* | *170000 ± 30520* | *82* |
| | *mp* | *0.18* | *0.48* | *1.6 ± 0.1* | *461980 ± 18610* | *6* |
| **Terceira** | | | | | | |
| T2 | Ol. | 1.08 | 0.41 | 10.4 ± 1.6 | 69530 ± 10570 | 11 |
| | Ol. | 1.88 | 0.59 | 11.3 ± 0.8 | 63780 ± 4620 | 8 |
| T7 | Ol. | 1.02 | 1.5 | 11.0 ± 0.4 | 65510 ± 2140 | 3 |
| *T9* | *Ol.* | *0.34* | *1.4* | *9.3 ± 0.1* | *77550 ± 430* | *1* |
| T28 | Ol. | 1.74 | 0.23 | 7.0 ± 1.8 | 103070 ± 26910 | 9 |
| *T28* | *Ol.* | *0.30* | *0.13* | *8.5 ± 0.2* | *85165 ± 2350* | *13* |
| *ACO95-9* | *Ol.* | *0.10* | *1.6* | *9.5 ± 0.1* | *75858 ± 709* | *3* |
| *ACO95-10* | *Ol.* | *0.20* | *0.93* | *9.4 ± 0.1* | *76965 ± 680* | *3* |
| ACO95-11 | Ol. | 1.60 | 2.2 | 9.4 ± 0.5 | 77200 ± 3710 | 2 |
| *ACO95-12 ±* | *Ol.* | *0.27* | *0.14* | *9.7 ± 0.3* | *74604 ± 2326* | *13* |
| ACO95-14 | Ol. | 0.99 | 1.2 | 8.0 ± 0.8 | 90420 ± 8520 | 5 |
| *ACO95-16* | *Ol.* | *0.14* | *0.50* | *10.3 ± 0.2* | *70437 ± 1415* | *7* |
| **Graciosa** | | | | | | |
| *G1* | *Ol.* | *0.19* | *0.26* | *8.1 ± 0.2* | *89600 ± 2380* | *10* |

Table 2
Lead isotopic compositions determined for some Azores samples

| Sample | $^{206}Pb/^{204}Pb$ | $^{207}Pb/^{204}Pb$ | $^{208}Pb/^{204}Pb$ |
|---|---|---|---|
| **Faial** | | | |
| FA1 | 19.332 | 15.555 | 38.796 |
| | 19.318 | 15.541 | 38.746 |
| FA2 | 19.607 | 15.574 | 38.943 |
| FA3 | 19.137 | 15.601 | 38.814 |
| | 19.130 | 15.605 | 38.816 |
| FA6 | 19.471 | 15.619 | 39.123 |
| FA7 | 19.607 | 15.642 | 39.314 |
| FA10 | 19.707 | 15.635 | 39.296 |
| FA12 [a] | 19.20 | 15.60 | 38.89 |
| FA44 [a] | 19.60 | 15.59 | 39.10 |
| **Graciosa** | | | |
| G1 | 19.80 | 15.60 | 39.18 |
| **Pico** | | | |
| P1 [a] | 19.96 | 15.61 | 39.37 |
| **Santa Maria** | | | |
| S6 [a] | 19.14 | 15.56 | 39.07 |
| S9 [a] | 19.01 | 15.56 | 39.01 |
| S14 [a] | 19.28 | 15.58 | 39.30 |
| **São Miguel** | | | |
| *West* | | | |
| SM7 [a] | 19.47 | 15.59 | 39.32 |
| SM319 [a] | 19.48 | 15.62 | 39.37 |
| *Nordeste* | | | |
| SM139 [a] | 20.00 | 15.78 | 40.33 |
| SM150 [a] | 19.96 | 15.75 | 40.19 |
| SM169 [a] | 19.96 | 15.74 | 40.31 |

[a] Previously published by Dupré (PhD thesis).

$1.7 \times 10^{-9}$ $cm^3$ STP/g for olivines from sample S6 (Santa Maria) to $4.3 \times 10^{-7}$ $cm^3$ STP/g for olivines analysed in a xenolith from Faial island (ACO95-49). Helium isotopic ratio vary between 63,780 ($R/R_a = 11.3$) and 276,840 ($R/R_a = 2.6$) in T2 (Terceira) and ACO95-68 (São Miguel) samples respectively.

Helium concentrations obtained for melting after crushing of sample ACO95-68 were $3.7 \times 10^{-9}$ $cm^3$ STP/g for the olivines, with a $^4He/^3He$ ratio of 163,180 ± 4310 ($R/R_a = 4.4 \pm 0.1$) which is similar to the crushed ratio (4.1 ± 0.1), and $4.8 \times 10^{-9}$ $cm^3$ STP/g for the pyroxenes with a helium ratio of 461,980 ± 18,610 ($R/R_a = 1.6 \pm 0.1$). This ratio is much more radiogenic than the crushed ratio (4.06 ± 0.03). The agreement between $^4He/^3He$ ratios obtained by crushing in this sample, despite the presence of radiogenic $^4He$ in the clinopyroxene strongly suggest, that the crushing data reflects the magmatic helium. This point is illustrated in Fig. 3c, where good agreement in $^4He/^3He$ ratios is obtained for several different extractions and over a wide variation in $^4He$ concentrations.

Three distinctive island groups have been distinguished on the basis of helium isotopic results (Fig. 3):

(1) São Miguel island, for which 4 samples have been analysed, has the most radiogenic $^4He/^3He$ ratios. One sample (ACO95-3) was from a historical lava flow (Queimado peak eruption, 1563) whereas the 3 others are Pliocene ankaramites [23]. They all display very radiogenic $^4He/^3He$ ratios, from 121,640 ± 41,160 to 276,840 ± 11,670, with a weighted mean value of 140,660 for the historical sample ACO95-3 (crushed samples). These data agree with previous measurements from São Miguel by Kurz (fig. 8.10 of [36]).

(2) Faial, Graciosa and Santa Maria islands all exhibit a MORB-like helium signature, with $^4He/^3He$ ratios ranging from 85,970 ± 1210 to 94,380 ± 3240 (Faial ACO95-55 sample displays an higher but uncertain value of 129,720 ± 40,520).

(3) Pico and Terceira islands have a more dispersed helium signature and range from typical MORB ratios to relatively primitive values, such as 63,780 ± 4620 for Terceira T2 basalt and 70,150 ± 890 for Pico ACO95-30 sample.

Lead isotopic results (Table 2) for the Azores islands are all relatively radiogenic in composition compared to local MORB. However, the respective positions of the five islands in Pb–Pb space suggests a similar grouping of Azores islands (Fig. 4), with good helium and lead covariations at the scale of the archipelago:

(1) Eastern São Miguel samples have relatively high $^{206}Pb/^{204}Pb$ ratios, around 20, and very radiogenic $^{207}Pb/^{204}Pb$ and $^{208}Pb/^{204}Pb$ values, up to 15.78 and 40.33 respectively, which are clearly different from those measured on other islands.

(2) Faial and Santa Maria basalts represent the least radiogenic compositions of the archipelago, with a mean value of 19.50 for $^{206}Pb/^{204}Pb$, 15.60 for $^{207}Pb/^{204}Pb$ and 39.00 for $^{208}Pb/^{204}Pb$.

(3) Pico and Terceira samples exhibit lead isotope ratios ranging from Faial–Santa Maria values (19.50,

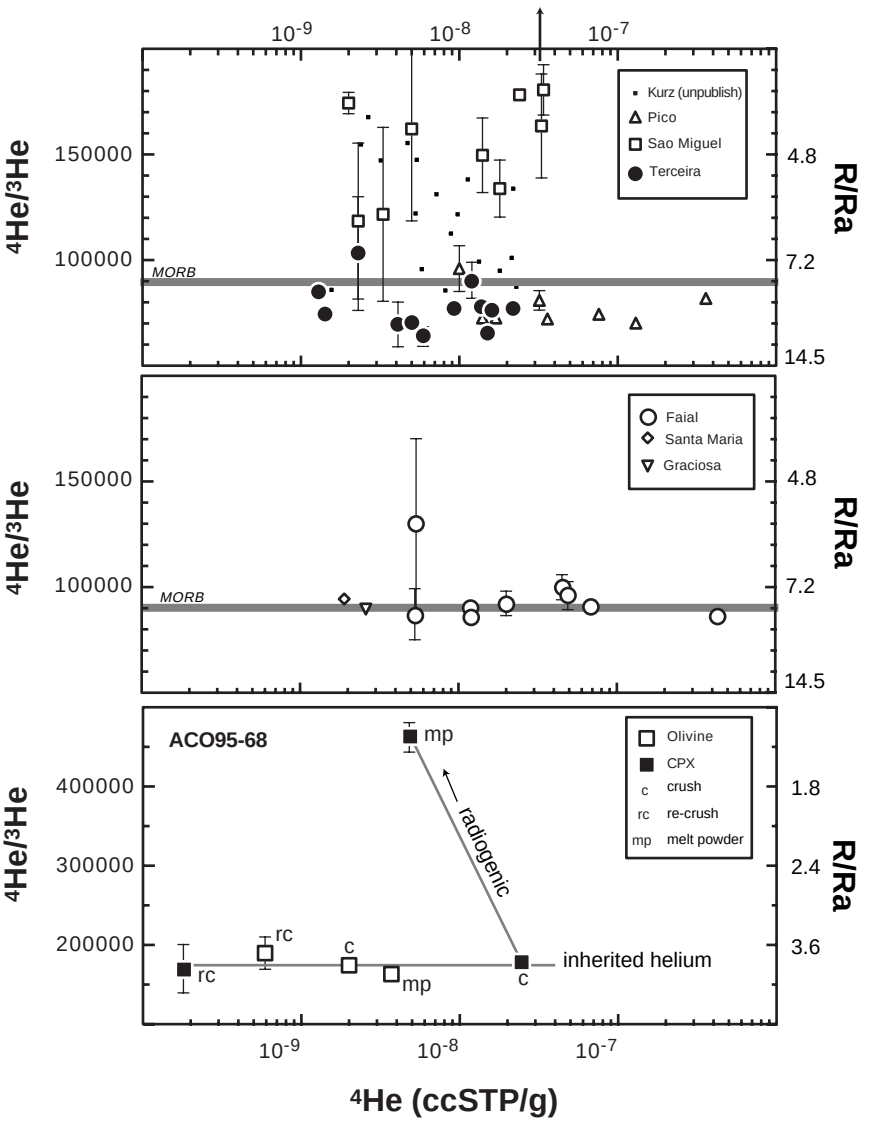


Fig. 3. $^4He/^3He$ ratios vs. $^4He$ concentrations (in $cm^3$ STP/g) for Azores samples. Grey lines correspond to the MORB $^4He/^3He$ mean value of ~90,000 [1,68]. Top figure represents the Pico, Terceira and São Miguel islands. Some São Miguel data from Kurz (unpublished) were added. Middle figure shows Faial, Santa Maria and Graciosa basalts. One can see the isotopic ratios are exactly the same as the mean MORB ratio. Bottom figure represents two experiments on the ankaramite ACO95-68 from the Nordeste area on São Miguel. Step crushing and powder melting extractions were performed on olivines and clinopyroxene to constrain the post eruption radioactive production of $^4He$. The results show that the $^4He/^3He$ ratios are always the same during crushing (olivine and CPX), but different for CPX melting due to the higher U content of CPX. This implies the $^4He/^3He$ ratios obtained by crushing are representative of the magmatic values, and have not been altered by post-eruptive radiogenic helium (see text).

15.60 and 39.00) to radiogenic compositions similar to São Miguel basalts for $^{206}Pb/^{204}Pb$ (20.02), lower for $^{207}Pb/^{204}Pb$ (15.64) and $^{208}Pb/^{204}Pb$ (39.35) [37,38]. Moreover, similarly to helium, Pico–Terceira and Faial–Santa Maria associated fields are not totally distinctive.

These three groups were also proposed by Turner et al. [38] based on trace element-isotope systematics

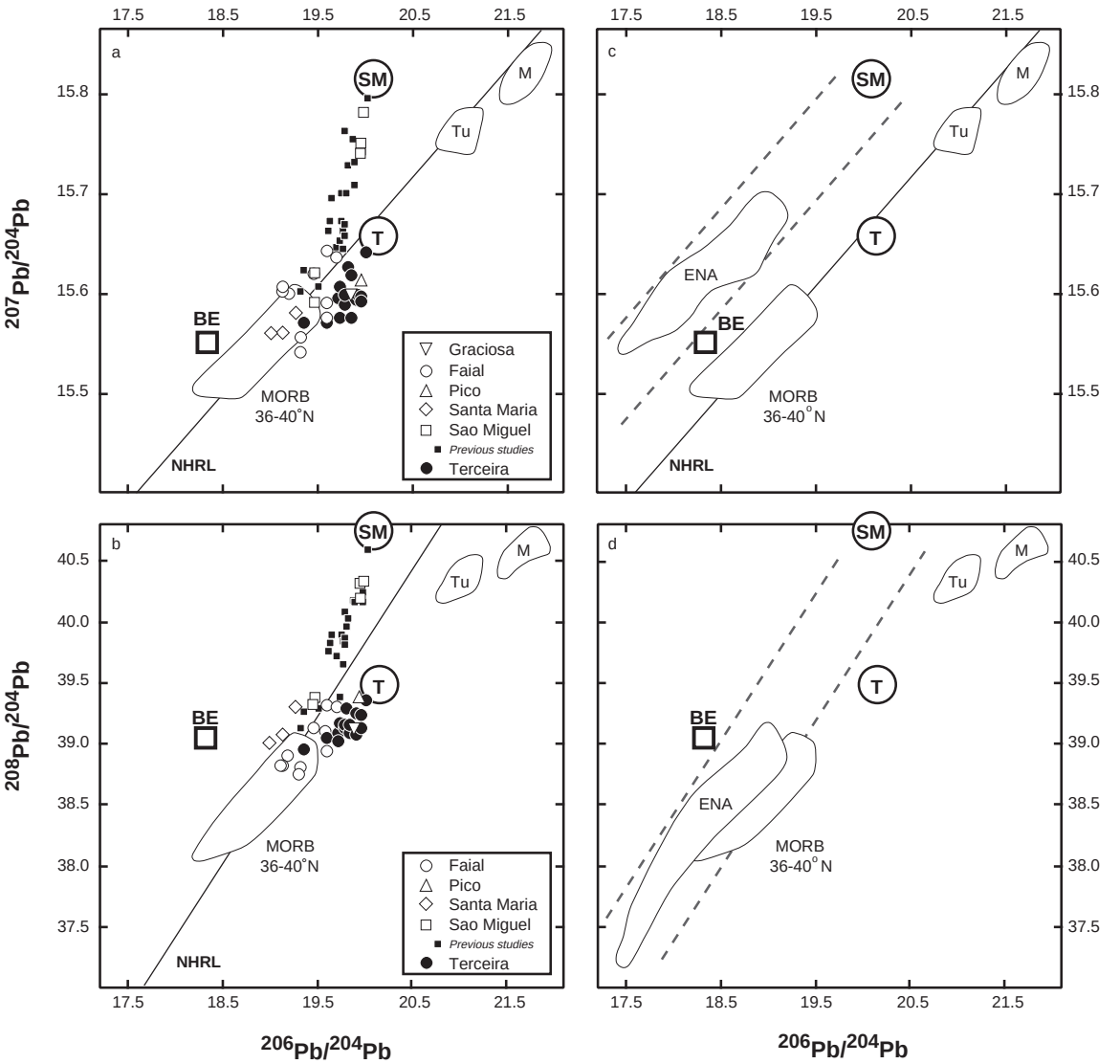


Fig. 4. Lead isotopic diagrams, showing end-member positions of São Miguel and Terceira [37] islands. (a) $^{206}Pb/^{204}Pb$ vs. $^{207}Pb/^{204}Pb$. (b) $^{206}Pb/^{204}Pb$ vs. $^{208}Pb/^{204}Pb$. Also reported are previous São Miguel [38,48] results, the Northern Hemisphere Reference Line (*NHRL*, as defined in [69]), Bulk Earth average value (*BE*) [58], and representative fields for local MORB [70–73], Tubuaii and Mangaia islands [74–76]. SM and T points are postulated to be representative of the Azores plume compositions. (c) $^{206}Pb/^{204}Pb$ vs. $^{207}Pb/^{204}Pb$. (d) $^{206}Pb/^{204}Pb$ vs. $^{208}Pb/^{204}Pb$. *ENA* fields (East North America tholeiitic samples [59]) can be interpreted as reflecting binary mixing between a end-member with low lead isotopic ratios and São Miguel end-member *SM*.

where for example, the Th/Nb is higher for São Miguel island [38].

Fig. 5 shows the $^{4}He/^{3}He$ ratio against the $^{206}Pb/^{204}Pb$ ratios for the different Azores archipelago islands. The three groups can be easily distinguished on this figure.

## 5. Discussion

### *5.1. The Eastern São Miguel radiogenic helium signature*

Since São Miguel island is one of the oldest islands in the archipelago (up to 4 Myr [23,25]), high

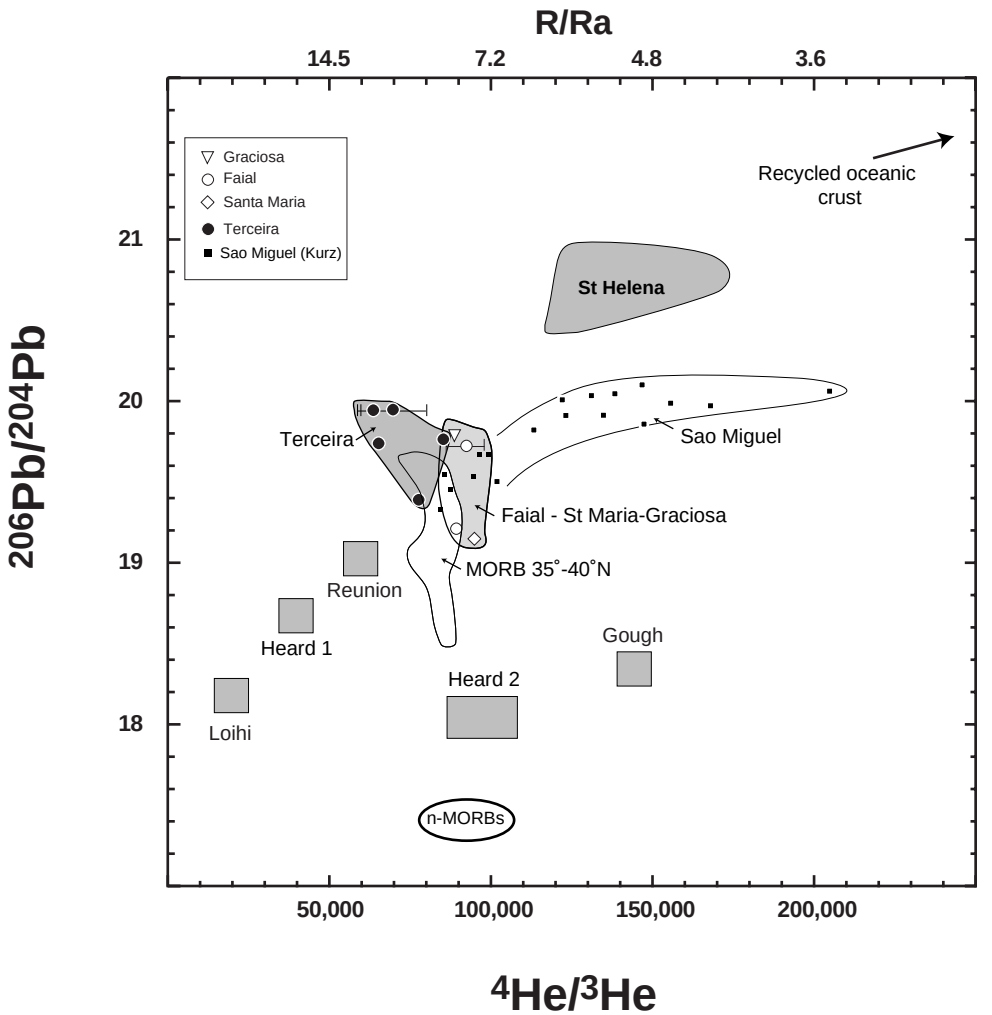


Fig. 5. $^{4}He/^{3}He$ ratios versus $^{206}Pb/^{204}Pb$ ratios for Azores Archipelago basalts and some other islands. Some São Miguel data from Kurz (unpublished) were added. Other data are from the literature.

$^{4}He/^{3}He$ ratios measured in some samples could be explained by post-eruptive decay of Th and U, particularly for samples with low helium and high U and Th contents. Sample crushing procedures are performed to liberate the inherited gases contained in fluid and melt inclusions, but $^{4}He$ production could occur in the matrix with subsequent diffusion into the inclusions, or partial release by crushing. However, both the low concentration Pliocene ankaramites (2.3 to $6.0 \times 10^{-9}$ $cm^3$ STP/g for ACO95-62, 66 and 68) and historical lava ACO95-3 (434 yr), whose olivines contain around $1.6 \times 10^{-8}$ $cm^3$ STP/g $^{4}He$, display radiogenic helium isotope ratios, which strongly suggests that the unique radiogenic signature of São Miguel cannot totally result from such a decay process. Only old samples could have been modified, starting from a minimum ACO95-3 olivines like radiogenic value (140,000, we will consider, in the following, as the Nordeste São Miguel helium signature) to reach ratios as high as 276,840 (ACO95-68 CPX) as illustrated by the melting experiment (Fig. 3).

The melt of the ACO95-68-CPX powder has given a $^{4}He/^{3}He$ ratio of 461,980 ± 18,610, much

more radiogenic than the crushed value of 178,200. This can easily be explained by post-eruptive $^4$He production since this sample has an age between 2 and 4 Ma [23]. Using a U concentration of 0.012 ppm and a Th/U ratio of 2.9 for CPX [39] we can obtain a U/He age of 1.2 Ma for sample ACO95-68. This age is in good agreement with the K/Ar age [23] considering the uncertainty on the U content and the Th/U ratio. However, for olivines, crushing and melting have given the same helium isotopic ratios (Fig. 3), indicating that $^4$He production from U and Th decay is negligible for olivines. This shows that the radiogenic helium isotopic ratios observed in the samples from the Nordeste area do not represent post-eruptive decay of Th and U.

Zindler and Hart [9,10] and Hilton et al. [11] have proposed that high $^4$He/$^3$He ratios measured in some OIB could reflect shallow depth contamination at high levels in the crust. The presence of ankaramite samples with low pressure pyroxenes (high total Al and low $Al^{VI}$) on São Miguel island is consistent with the existence of shallow magma chambers beneath the Azores archipelago [23]. Plume source contamination is modeled by a two-component mixing and the expression of the mass ratio between plume ($M_i$) and contaminant (oceanic crust) material ($M_c$) is then given by:

$$\frac{M_c}{M_i}\left\{\frac{\left(\frac{^4He}{^3He}\right)_{SM}-\left(\frac{^4He}{^3He}\right)_i}{\left(\frac{^4He}{^3He}\right)_c-\left(\frac{^4He}{^3He}\right)_{SM}}\right\}\times\frac{[^3He]_i}{[^3He]_c}$$

where $(^4He/^3He)_{SM}$, $(^4He/^3He)_i$ and $(^4He/^3He)_c$ refers to the São Miguel island, São Miguel plume and contaminant representative helium values, $[^3He]_i$ and $[^3He]_c$ to the plume and contaminant concentrations (cm$^3$ STP/g).

We used results obtained by Staudacher and Allègre [40] on 22 My old oceanic crust (which corresponds to the approximate age of the nearby Azores crust [41]) as a contaminant material ($[^3He]_c = 5\times10^{-14}$ cm$^3$ STP/g and $(^4He/^3He)_c = 2\times10^7$), the value of 140,000 for São Miguel island composition, and Terceira-like $^4$He/$^3$He ratio (60,000) for São Miguel 'plume'. The $^3$He concentration in the plume material is thought to be intermediate between lower ($2.5\times10^{-9}$ cm$^3$ STP/g) [42] and upper mantle ($1.1\times10^{-10}$ cm$^3$ STP/g) [43,44] values because the helium ratio we took is very different from the lower mantle ratio of 20,000. Let us take $5\times10^{-10}$ cm$^3$ STP/g for the $^3$He content for the Terceira plume. The $M_c/M_i$ result (4000%) suggests that important magma chamber outgassing, at least 99.9%, is required to be consistent with a plume contamination scenario.

In the previous calculations, we do not consider the possibility of radiogenic decay in a degassed magma chamber. Using $^3$He concentration estimated above ($5\times10^{-10}$ cm$^3$ STP/g) in the following $^4$He radioactive production equation ($t$ in Ma, U in ppm and He in cm$^3$ STP/g):

$$\left[\frac{^4He}{^3He}\right]_t=\left[\frac{^4He}{^3He}\right]_0+2.8\times10^{-8}\left\{4.35+\frac{Th}{U}\right\}\frac{[U]}{[^3He]}\times t$$

we can determine the time interval $t$ necessary to increase the initial helium ratio $(^4He/^3He)_0$ from 60,000 (Terceira less primitive value) to the present-day value $(^4He/^3He)_t$ of 140,000. Assuming a Th/U ratio of 2.75 [38] and a U concentration of 0.040 ppm (we postulate Terceira plume uranium to be intermediate between lower mantle material [6] and recycled altered oceanic crust [15] based on lead isotope systematics, cf. Section 5.2), we need to invoke very large outgassing (at least 99.999%) to obtain magma chamber interval time consistent with classical estimates of magma residence time (between 10 and 10,000 yr [45,46]).

Similar calculations can be done with lead isotopes. However, using a Terceira-like isotopic composition ($^{207}$Pb/$^{204}$Pb = 15.64) for the São Miguel plume and the most radiogenic value ($^{207}$Pb/$^{204}$Pb = 15.64) measured in old oceanic crust (14–37 My) near the Azores archipelago [47] as a contaminant does not allow to obtain $^{207}$Pb/$^{204}$Pb ratios that are as high as those determined on São Miguel samples ($^{207}$Pb/$^{204}$Pb = 15.78). Contamination by recent Atlantic sediments is also unlikely, given the high $^{208}$Pb/$^{204}$Pb ratios [48].

There is no evidence for such an extensive outgassing in the São Miguel olivine samples, which show similar He content to olivines from other islands, in particular from Terceira. Kurz et al. [20] have observed a variation of the $^4$He/$^3$He ratio with

the longitude on São Miguel island (with a decrease westward), similar to the $^{87}Sr/^{86}Sr$ and $^{206}Pb/^{204}Pb$ variations [20,48,49]. Because these variations and correlations are difficult to explain by shallow depth contamination, we propose a deeper origin for the high $^{4}He/^{3}He$ ratios measured in São Miguel basalts. A source effect also appears to be consistent with the helium–lead covariations observed at the scale of the archipelago. Kurz et al. [3], Vance et al. [4], Graham et al. [5], Hanan and Graham [16] and Hanyu and Kaneoka [7] have postulated that the radiogenic helium measured in Gough, Tristan, St Helena and some Pacific islands can be explained by recycling into the mantle of oceanic crust or sediments, and reinjection of this material in plume sources. Subducted plates should have high $(U + Th)/^{3}He$ ratios because helium is outgassed to the atmosphere during ridge magmatism and during subduction. After storage for some time in the mantle, this will give high $^{4}He/^{3}He$ ratios by U and Th α-decay. Lead and strontium isotope signatures are consistent with such a scenario [38,49], especially the high $^{207}Pb/^{204}Pb$ ratios which imply old U/Pb fractionation. Recycling of subducted altered oceanic crust and sediments allows to increase the U/Pb ratio [15,50], and then give very radiogenic $^{207}Pb/^{204}Pb$ ratios with time.

### 5.2. The Terceira helium signature

Kurz et al. [19] first proposed the presence of a "high $^{4}He/^{3}He$" plume beneath the Azores archipelago, based on helium isotopes measurements in MORB glasses near the Azores platform. However, it turns out that the Azores hotspot is also characterized by 'low $^{4}He/^{3}He$', since primitive values ($^{4}He/^{3}He \approx 65{,}000$) have been measured in this study in some Terceira and Pico samples. Production of cosmogenic helium [28] in Terceira or Pico samples remains very unlikely, as all the analysed basalts are relatively young (some are historical, see Table 1 and Appendix A) and were sampled at low altitude, generally in freshly exposed surfaces. Moreover, we have analyzed these samples by crushing which primarily releases the inherited helium trapped in inclusions; only a small fraction of the cosmogenic helium is released by crushing and should be negligible for these samples. Therefore, the primitive helium has to originate within the source of the plume. It may come from the lower mantle, source of primitive helium for most of oceanic islands (Hawaii, Iceland, Galapagos or Réunion islands). The $[^{3}He]_{LM}/[^{3}He]_{UM}$ concentration ratio between the lower and upper mantle should be roughly 10 [6,51] so even a small amount of entrained lower mantle could transfer a primitive helium isotopic signal. A helium signature similar to Terceira was found on nearby Atlantic MORB glasses (Fig. 6, [52]) thereby confirming the plume–ridge interaction already observed for REE, Sr, Nd and Th/U systematics [53–56]. The somewhat different helium observations by Kurz et al. [19], could simply be due to the different sampling scale of this study. For example, most of the MORB samples from 39ºN are very degassed, and may have been dredged off the ridge axis since the ridge is not well defined in this area. In fact, the helium signature recorded by MORB glasses displays very localized primitive values (around 38.5ºN; Moreira and Allègre [52]) which seems to correspond to the location of the triple junction [41,57] (Fig. 6).

Most primitive helium ratios measured on Terceira samples could be explained by mixing between primitive mantle having high $^{3}He$ ($^{4}He/^{3}He = 20{,}000$) and two other discrete mantle sources: MORB mantle ($^{4}He/^{3}He = 90{,}000$) and a low $^{3}He$ plume best represented by data from São Miguel ($^{4}He/^{3}He = 140{,}000$). Helium alone cannot resolve between the two hypotheses. However, lead isotopic ratios (Fig. 4a,b) show that the Terceira signature cannot result from binary mixing between the São Miguel plume and lower mantle material. The present-day composition of the lower mantle certainly corresponds to a binary mixing between Bulk Earth material and about 17% of depleted mantle [58], and then is few different from Bulk Earth composition. The Terceira signature probably reflects mixing of 'high $\mu$' material, lower mantle material and entrained depleted asthenospheric material, whereas the observed trend for Terceira island may represent shallow interaction between this specific material and the local MORB mantle source.

### 5.3. Terceira–São Miguel: same hotspot?

Since we excluded a shallow contamination origin for explaining the He data in São Miguel island, the

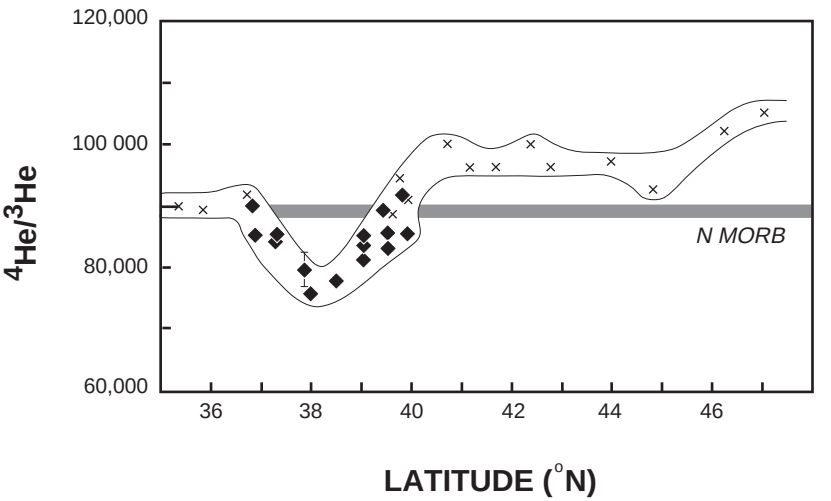


Fig. 6. $^{4}He/^{3}He$ ratios measured in MORB as a function of the latitude along mid Atlantic ridge between 35 and 40ºN, modified after Kurz et al. [19] (crosses) and Moreira and Allègre [52] (diamonds). Note that the minimum of the $^{4}He/^{3}He$ ratio is close to 38.5ºN, which is the supposed triple junction between African, American and European plates [41,57].

Azores archipelago helium signature, with coexistence of both radiogenic and primitive ratios, seems to be paradoxical. Identification of recycled terrigenous sediments in the source of São Miguel basalts does not give information about the depth of this specific material and there are two models for the generation of the Azores islands.

The first one proposes the Azores plume deep source may be isotopically heterogeneous, containing a mixture of recycled subducted terrigenous sediments, altered oceanic crust and lower mantle material. A low degree of melting has permitted to exhibit the sedimentary signature (radiogenic) of the source (the fertile part of the mixture, i.e. sediments melt preferentially) in São Miguel basalts (Nordeste), whereas other islands result from higher extent of melting and reflect mixing of recycled oceanic crust, lower mantle and upper mantle materials. The origin of this heterogeneous source may result of the entrainment by a plume coming from the lower mantle of material stored at the 670 km discontinuity or higher or reflects the heterogeneity of the source itself.

The second model proposes the Azores plume deep source is isotopically homogeneous, with a Terceira like signature (mixing of lower mantle material and 'himu' material). São Miguel island basalts sample a very localized upper mantle heterogeneity, melted by the rising of the Terceira plume or blob. This heterogeneity could correspond to subducted oceanic crust and sediments stored under the north america continent during the pre-Grenville subduction [59], recycled into the upper mantle by delamination occurring during the opening of the North Atlantic ocean (Fig. 4c,d and Fig. 7). Again, intermediate helium and lead compositions reflect interaction with the local MORB mantle source (Faial, Graciosa, Pico . . . ). Such a model can be validated by the fact that East North American basalts (ENA), that correspond to the nearest subcontinental material from the Azores, show linear trend in Pb–Pb diagrams (Fig. 4b) which could reflect mixing between a source with low $^{206}Pb/^{204}Pb$ $^{207}Pb/^{204}Pb$ and $^{208}Pb/^{204}Pb$ ratios, which could be subcontinental mantle [60,61], and a component with São Miguel-like signature which could be a mixing of sediments and recycled oceanic crust. We propose this component was stored below the North America before injection in the North Atlantic mantle by delamination during the opening of the North Atlantic. This model is similar to the proposal of Widom et al. [48], involving shallow interaction of the plume source with delaminated subcontinental lithosphere enriched by metasomatism. Radiogenic helium ratios measured in some continental xenoliths or continental basalts that sample the subcon-

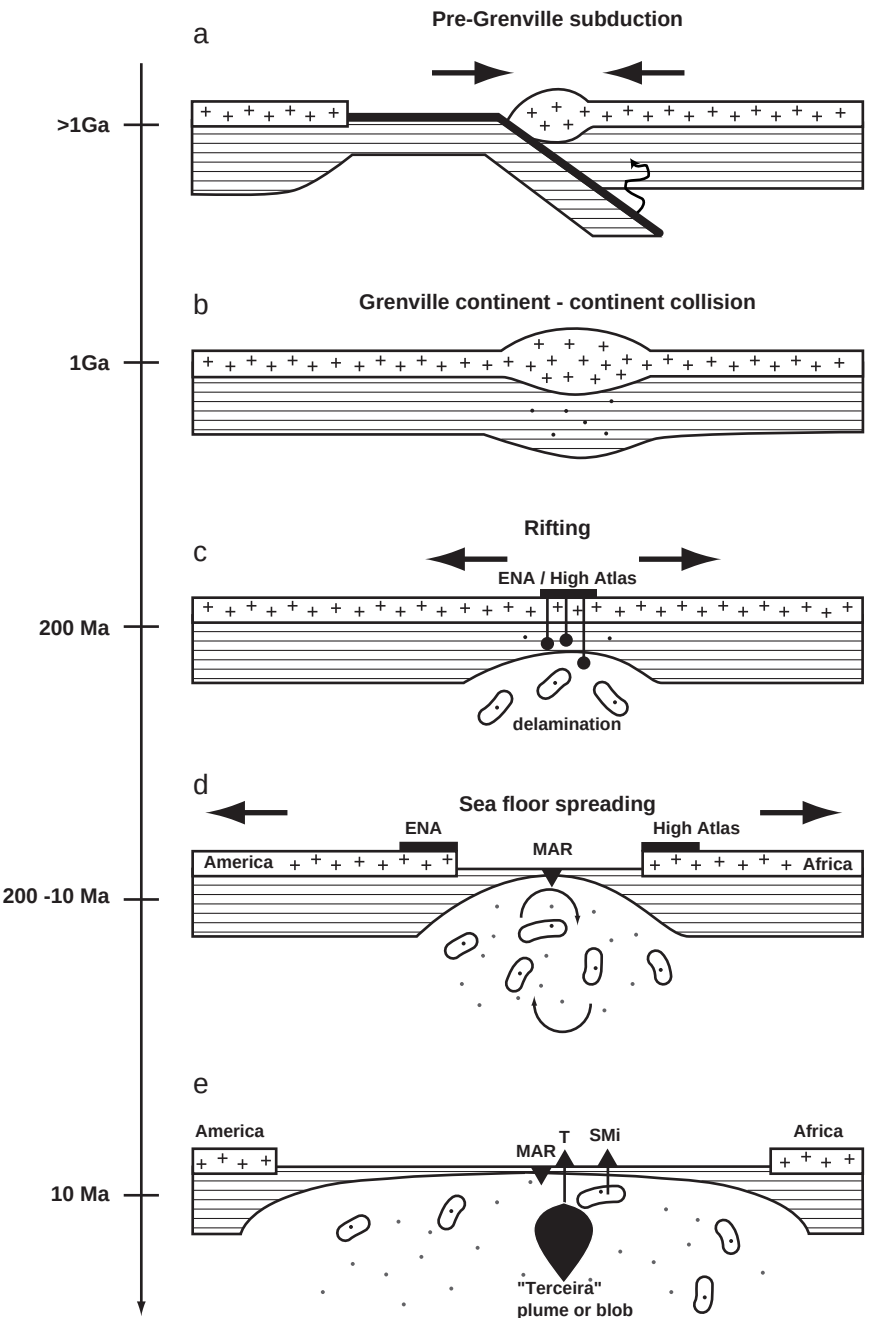


Fig. 7. Schematic evolution of the North Atlantic to explain the Azores isotopic data (model 2). (a) Pre-Grenville subduction [59] brings some oceanic crust and sediments into the subcontinental lithospheric mantle. (b) End of the subduction with the Grenville collision. (c) and (d) Opening of the Atlantic ocean is accompanied by some delamination, which provides regional enrichment of the Azores mantle. (e) São Miguel volcanism samples some localized km-size heterogeneity corresponding to old recycled material.

tinental lithosphere can account for such a model [62,63].

In both model 1 and model 2, we postulate a regional enrichment of the asthenosphere beneath the Azores. The observed radiogenic helium signature is not restricted to São Miguel island. Kurz et al. [19] have measured $^4He/^3He$ ratios higher than 100,000 in North Atlantic MORB glasses (for latitudes comprised between 40ºN and 50ºN; Fig. 6), which are consistent with contamination of the local MORB mantle source by delaminated subcontinental lithosphere (occurring during the opening of the Atlantic ocean). Such a hypothesis has been already proposed to explain specific Pb and Sr radiogenic signatures of the Oceanographer transform zone basalts [64] at 35ºN, and could also be proposed to explain similar isotopic anomalies identified on the Mid Atlantic Ridge at 14ºN [43,65], 43ºN and 46ºN [56]. Recent discovery of very old zircons in the Mid Atlantic Ridge are also consistent with such a model [66].

## 6. Conclusions

The Azores archipelago corresponds to the second hotspot where three distinctive helium isotopic signatures have been observed: MORB values found at Santa Maria, Graciosa and Faial islands, primitive values for some Terceira and Pico basalts, and radiogenic values in Eastern São Miguel. The only other oceanic island where $^4He/^3He$ ratios both higher and lower than MORB are found is Heard Island [11]. The helium data are correlated with lead isotopic compositions observed on the same islands and are interpreted in terms of source variations. The existence of such a multiple isotopic signature can be explained by two scenarios. The first model proposes that the heterogeneous Azores plume source has evolved from São Miguel to Terceira composition, by various degrees of melting of heterogeneous mantle. The second hypothesis is that the Azores plume is homogeneous with a Terceira like composition. The origin of the São Miguel signature would then correspond to sampling of very local km-size heterogeneities, resulting from the delamination of enriched subcontinental lithosphere, which occurred during the Jurassic opening of the North Atlantic.

## Acknowledgements

M.M. would like to thank Pascale Louvat very much for his help during the mission in Azores and patience during rock sampling, and the team of the Earth Sciences department from Universidade dos Açores, in particular Pr. Victor Forjaz and J.C. Nunes for discussions and help during the Azores trip. B. Bourdon, J. Kunz and Th. Staudacher are thanked for discussion and improvement of the manuscript. D. Graham, I. Kaneoka and R. Poreda helped to improve the quality of the manuscript by their review comments. Josh Curtis is thanked for his help during analyses in the Woods Hole Oceanographic Institution. This is IPGP contribution 1574 and WHOI contribution 9893. ***[CL]***

## Appendix A. Sample locations

Sample locations are also given on Fig. 2. Some location are in [37].

**Faial**

| | |
|---|---|
| ACO95-sand | Olivine rich sand from the Capelinho place. Results from projection of submarine eruption during the 1957 eruption. |
| ACO95-47 | Collected on the chimney in the rim that separates the historical eruption of the Capelinho (1957/58) from the Complexe do Capelo (<800 yr). |
| ACO95-49 | Xenolith taken on the beach of the Baia da Ribeira das Cabras. Unknown age. |
| ACO95-52 | Sand with olivines and augites taken in the beach of Varadouro. |
| ACO95-53 | Collected on the road leading to the caldera near the CabeodosTrinta Pic. |
| ACO95-55 | Porto de Feiteira. |

**Pico**

| | |
|---|---|
| ACO95-20 | Olivine and pyroxene rich basalts from the 1718-20 flow (Fase de Sta Luzia), collected near the airport. |
| ACO95-26 | Basalt collected on the road between São Roque do Pico and Lajes. Bottom of the Pic de Felipe (complexe da Madalena). |
| ACO95-30 | Xenolith collected in the Misterio de Silveira (phase de Sta Luzia, 1718-20). |
| ACO95-33 | Collected near Caelano (Ponta da Faca) (complexe da Madalena). |
| ACO95-40 | Same location as 26. |

**São Miguel**

| | |
|---|---|
| ACO95-3 | 1563 Queimado Pic lava flow. |
| ACO95-56 | Collected on the road between Ribeira Grande and Ponta Delgada near the Dr Ferreira Pic. |

*Nordeste*

ACO95-62 Ankaramite collected near the Guihermo ou dos Moinhos river. South of Lomba da Fazenda.
ACO95-66 Ankaramite collected near the Mulher river. South of Santana.
ACO95-68 Ankaramite collected near Faial da Terra.

**Terceira**

ACO95-9 1761 lava flow at the bottom of the Pico do Fogo.
ACO95-10 Collected near the road between Biscoitos and Angra Do Heroismo (near the Pico do Fogo).
ACO95-11 Collected in the Guiherme Moniz Caldeira (north).
ACO95-12 Collected near Faieis in a river (Rib. das Pedras).
ACO95-14 Collected near the road between São Sebastiao and Feteira (near Boavista).
ACO95-16 Collected near the road near Rossio de Sant Ana.

## References


[1] C.J. Allègre, M. Moreira, T. Staudacher, $^{4}He/^{3}He$ dispersion and mantle convection, Geophys. Res. Lett. 22 (17) (1995) 2325–2328.
[2] M.D. Kurz, W.J. Jenkins, S.R. Hart, D. Clague, Helium isotopic variations in volcanic rocks from Loihi Seamount and the island of Hawaii, Earth Planet. Sci. Lett. 66 (1983) 388–406.
[3] M.D. Kurz, W.J. Jenkins, S.R. Hart, Helium isotopic systematics of oceanic islands and mantle heterogeneity, Nature 297 (1982) 43–47.
[4] D. Vance, J.O.H. Stone, R.K. O'Nions, He, Sr and Nd isotopes in xenoliths from Hawaii and other oceanic islands, Earth Planet. Sci. Lett. 96 (1989) 147–160.
[5] D.W. Graham, S.E. Humphris, W.J. Jenkins, M.D. Kurz, Helium isotope geochemistry of some volcanic rocks from Saint Helena, Earth Planet. Sci. Lett. 110 (1993) 121–131.
[6] C.J. Allègre, T. Staudacher, P. Sarda, Rare gas systematics: formation of the atmosphere, evolution and structure of the earth's mantle, Earth Planet. Sci. Lett. 81 (1986) 127–150.
[7] T. Hanyu, I. Kaneoka, The uniform and low $^{3}He/^{4}He$ ratios of HIMU basalts as evidence for their origin as recycled materials, Nature 390 (1997) 273–276.
[8] M. Condomines, K. Grönvold, P.J. Hooker, K. Muehlenbachs, R.K. O'Nions, N. Oskarsson, E.R. Oxburgh, Helium, oxygen, strontium and neodymium isotopic relationships in Icelandic volcanic, Earth Planet. Sci. Lett. 66 (1983) 125–136.
[9] A. Zindler, S. Hart, Helium: problematic primordial signals, Earth Planet. Sci. Lett. 79 (1986) 1–8.
[10] A. Zindler, S.R. Hart, Chemical geodynamics, Annu. Rev. Earth Planet. Sci. 14 (1986) 493–571.
[11] D.R. Hilton, J. Barling, G.E. Wheller, Effect of shallow-level contamination on the helium isotope systematics of ocean-island lavas, Nature 373 (1995) 330–333.
[12] C.J. Allègre, Isotope geodynamics, Earth Planet. Sci. Lett. 86 (1987) 175–203.
[13] C.J. Allègre, E. Lewin, Isotopic systems and stirring times of the Earth's mantle, Earth Planet. Sci. Lett. 136 (1995) 629–646.
[14] B.L. Weaver, The origin of ocean island basalt end-member compositions: trace element and isotopic constraints, Earth Planet. Sci. Lett. 104 (1991) 381–397.
[15] C. Chauvel, A.W. Hofmann, P. Vidal, HIMU-EM: the French Polynesian connection, Earth Planet. Sci. Lett. 110 (1992) 99–119.
[16] B.B. Hanan, D.W. Graham, Lead and Helium evidence from oceanic basalts for a common deep source of mantle plumes, Science 272 (1996) 991–995.
[17] S.R. Hart, E.H. Hauri, L.A. Oschmann, J.A. Whitehead, Mantle plumes and entrainment: isotopic evidence, Science 256 (1992) 517–520.
[18] C. Class, S.L. Goldstein, Plume–lithosphere interactions in the ocean basins: constraints from the source mineralogy, Earth Planet. Sci. Lett. 150 (1997) 245–260.
[19] M.D. Kurz, W.J. Jenkins, J.-G. Schilling, S.R. Hart, Helium isotopic variation in the mantle beneath the central North Atlantic Ocean, Earth Planet. Sci. Lett. 58 (1982) 1–14.
[20] M.D. Kurz, A. Gulessarian, R.B. Moore, Isotopic variations within oceanic islands: He, Sr and Pb isotopes in basalts from São Miguel, Azores, Eos 71 (1990) 657.
[21] R.H. Kingsley, J.G. Schilling, Carbon in Mid-Atlantic Ridge basalt glasses from 28° to 63°N: evidence for a carbon-eriched Azores mantle plume, Earth Planet. Sci. Lett. 142 (1996) 175–189.
[22] A.A. Abdel-Monem, L.A. Fernandez, G.M. Boone, K–Ar ages from the eastern Azores group (Santa Maria, São Miguel and the Formigas Islands), Lithos 8 (1975) 247–254.
[23] L.A. Fernandez, Geology and petrology of the Nordeste volcanic complex, São Miguel, Azores: summary, Geol. Soc. Am. Bull. 91 (1980) 675–680.
[24] G. Feraud, I. Kaneoka, C.J. Allègre, K/Ar ages and stress pattern in the Azores: geodynamic implications, Earth Planet. Sci. Lett. 46 (1980) 275–286.
[25] R. Moore, Volcanic geology and eruption frequency, São Miguel, Azores, Bull. Volcanol. 52 (1990) 602–614.
[26] R.C. Mitchell-Thomé, Geology of the Middle Atlantic Islands, Gebruder Borntraeger, Berlin, Stuttgart, 1976, 382 pp.
[27] Z. França, M.H. Almeida, N. Wallenstein, Ocorrencia de xenolotos mantelicos numa lava da ilha do Pico (Açores), GAIA- Revista de Geociencias, Univ. Lisboa, 1995.
[28] M.D. Kurz, Cosmogenic helium in a terrestrial igneous rock, Nature 320 (1986) 435–439.
[29] T. Staudacher, C.J. Allègre, Terrestrial xenology, Earth Planet. Sci. Lett. 60 (1982) 389–406.
[30] M. Moreira, T. Staudacher, P. Sarda, J.-G. Schilling, C.J. Allègre, A primitive plume neon component in MORB: The Shona ridge-anomaly, South Atlantic (51–52°S), Earth Planet. Sci. Lett. 133 (1995) 367–377.
[31] T. Staudacher, P. Sarda, C.J. Allègre, Noble gas systematics of Réunion Island, Indian Ocean, Chem. Geol. 89 (1990) 1–17.

[32] D. Graham, J.G. Lupton, F. Albarède, M. Condomines, Extreme temporale homogeneity of Helium isotopes at Piton de la Fournaise, Réunion Island, Nature 347 (1990) 545–548.
[33] M.D. Kurz, T.C. Kenn, J.C. Lassiter, D.J. DePaolo, Helium isotopic evolution of Mauna Kea volcano: first results from the 1 km drill core, J. Geophys. Res. 101 (1996) 11781–11791.
[34] G. Manhès, J.-F. Minster, C.J. Allègre, Comparative U–Th–Pb and Rb–Sr study of the St Severin amphoterites: consequence for early solar system chronology, Earth Planet. Sci. Lett. 39 (1978) 14–24.
[35] E.J. Cantanzaro, T.J. Murphy, W.R. Shields, E.L. Garner, Absolute isotopic abundance ratios of common, equal-atom, and radiogenic lead isotopic standards, J. Res. Natl. Bur. Stand. 72A (1968) 261–267.
[36] M.D. Kurz, Noble gas isotopes in oceanic basalts: controversial constraints on mantle models, Miner. Assoc. Can. Short Course 19 (1991) 259–286.
[37] B. Dupré, B. Lambret, C.J. Allègre, Isotopic variations within a single oceanic island: the Terceira case, Nature 299 (1982) 620–622.
[38] S. Turner, C. Hawkesworth, N. Rogers, P. King, U–Th isotope disequilibria and ocean island basalt generation in the Azores, Chem. Geol. 139 (1997) 145–164.
[39] E.H. Hauri, T.P. Wagner, T.L. Grove, S.F. Foley, S.R. van der Laan, Experimental and natural partitioning of Th, U, Pb and other trace elements between garnet, clinopyroxene and basaltic melts, Chem. Geol. 117 (1234) (1994) 149–166.
[40] T. Staudacher, C.J. Allègre, Recycling of oceanic crust and sediments: the noble gas subduction barrier, Earth Planet. Sci. Lett. 89 (1988) 173–183.
[41] R. Searle, Tectonic pattern of the Azores spreading centre and triple junction, Earth Planet. Sci. Lett. 51 (1980) 415–434.
[42] C.J. Allègre, T. Staudacher, P. Sarda, Rare gas systematics, formation of the atmosphere, evolution and structure of the Earth's mantle, Earth Planet. Sci. Lett. 81 (1986) 127–150.
[43] T. Staudacher, P. Sarda, S.H. Richardson, C.J. Allègre, I. Sagna, L.V. Dmitriev, Noble gases in basalt glasses from a Mid-Atlantic ridge topographic high at 14ºN: geodynamic consequences, Earth Planet. Sci. Lett. 96 (1989) 119–133.
[44] M. Moreira, J. Kunz, C.J. Allègre, Rare gas systematics on popping rock: estimates of isotopic and elemental compositions in the upper mantle, Science 279 (1998) 1178–1181.
[45] M. Condomines, C. Hemond, C.J. Allègre, U–Th–Ra radioactive disequilibria and magmatic processes, Earth Planet. Sci. Lett. 90 (1988) 243–262.
[46] D.M. Pyle, The volume and residence time of magma beneath active volcanoes determined by decay-series disequilibria methods, Earth Planet. Sci. Lett. 112 (1992) 61–73.
[47] B. Dupré, C. Göpel, H. Bougault, Lead isotopic variations in old ocean crust near the Azores, Init. Reports DSDP 82 (1985) 497–500.
[48] E. Widom, R.W. Carlson, J.B. Gill, H.U. Schmincke, Th–Sr–Nd–Pb isotope and trace element evidence for the origin of the São Miguel, Azores, enriched mantle source, Chem. Geol. 140 (1997) 49–68.
[49] C.J. Hawkesworth, M.J. Norry, J.C. Roddick, R. Vollmer, 143Nd/144Nd and 87Sr/86Sr ratios from the Azores and their significance in LIL-element enriched mantle, Nature 280 (1979) 28–31.
[50] A.W. Hofmann, W.M. White, Mantle plumes from ancient oceanic crust, Earth Planet. Sci. Lett. 57 (1982) 21–436.
[51] C.J. Allègre, T. Staudacher, P. Sarda, M.D. Kurz, Constraints on evolution of Earth's mantle from rare gas systematics, Nature 303 (1983) 762–766.
[52] M. Moreira, C.J. Allègre, Rare gases in Mid Atlantic Ridge basalts near the Azores: injection of atmospheric rare gases in the mantle?, in prep.
[53] J.G. Schilling, Azores mantle blob: rare earth evidence, Earth Planet. Sci. Lett. 25 (1975) 103–115.
[54] W.M. White, J.G. Schilling, S.R. Hart, Evidence for the Azores mantle plume from strontium isotopes geochemistry of the Central North Atlantic, Nature 263 (1976) 659–663.
[55] B. Bourdon, C. Langmuir, A. Zindler, Ridge–hotspot interaction along the Mid-Atlantic Ridge between 37º30′ and 40º30′N: the U–Th disequilibrium evidence, Earth Planet. Sci. Lett. 142 (1996) 175–189.
[56] D. Yu, D. Fontignie, J.-G. Schilling, Mantle plume–ridge interaction in the Central North Atlantic: A Nd isotope study of Mid-Atlantic Ridge basalts from 30º to 50ºN, 146 (1997) 256–272.
[57] J. Freire Luis, J.M. Miranda, A. Galdeano, P. Patriat, J.C. Rossignol, L.A. Mendes Victor, The Azores triple junction evolution since 10 Ma from an aeromagnetic survey of the Mid Atlantic Ridge, Earth Planet. Sci. Lett. 125 (1994) 439–459.
[58] C.J. Allègre, E. Lewin, Chemical structure and history of the Earth: evidence from global non-linear inversion of isotopic data in a three box model, Earth Planet. Sci. Lett. 96 (1989) 61–88.
[59] W. Pegram, Development of continental lithospheric mantle as reflected in the chemistry of the Mesozoic Appalachian Tholeites, USA, Earth Planet. Sci. Lett. 97 (1990) 316–331.
[60] C.J. Hawkesworth, P.D. Kempton, N.W. Rogers, R.M. Ellam, P.W. Van Calsteren, Continental mantle lithosphere, and shallow level enrichment processes in the Earth's mantle, Earth Planet. Sci. Lett. 96 (1990) 256–268.
[61] J. Mahoney, A.P. LeRoex, Z. Peng, R.L. Fisher, J.H. Natland, Southwestern Limits of Indian Ocean Ridge Mantle and the Origin of Low 206Pb/204Pb Mid-Ocean Ridge Basalt: Isotope Systematics of the Central Southwest Indian Ridge (17º–50ºE), J. Geophys. Res. 97 (13) (1992) 19771–19790.
[62] T. Dunai, H. Baur, Helium, neon and argon systematics of the European subcontinental mantle: implications for its geochemical evolution, Geochim. Cosmochim. Acta 59 (1992) 2767–2784.
[63] M.R. Reid, D.W. Graham, Resolving lithospheric and sublithospheric contributions to helium isotope variations in

basalts from the Southwestern US, Earth Planet. Sci. Lett. 144 (12) (1996) 213–222.
[64] S.B. Shirey, J.F. Bender, C.H. Langmuir, Three-component isotopic heterogeneity near the Oceanographer transform, Mid-Atlantic Ridge, Nature 325 (1987) 217–223.
[65] L. Dosso, H. Bougault, J.-L. Joron, Geochemical morphology of the North Mid-Atlantic Ridge, 10º–24ºN: Trace element-isotope complementarity, Earth Planet. Sci. Lett. 120 (1993) 443–462.
[66] J. Pilot, C.-D. Werner, F. Haubrich, N. Baumann, Paleozoic and Proterozoic zircons from the Mid Atlantic Ridge, Nature 393 (1998) 676–679.
[67] V. Forjaz, A. Serralheiro, J.C. Nunes, Carta Vulcanologica dos Açores, Grupo Central, Universidade Dos Açores, 1st ed., Ponta Delgada, 1990.
[68] T. Staudacher, M. Moreira, C.J. Allègre, Heterogeneity and scatter of helium isotopic ratios in MORB, Mineral. Mag. 58A (1994) 874.
[69] S.R. Hart, A large-scale isotope anomaly in the Southern Hemisphere mantle, Nature 309 (1984) 753–757.
[70] B. Dupré, C.J. Allègre, Pb–Sr–Nd isotopic correlation and the chemistry of the north atlantic mantle, Nature 286 (1980) 17–22.
[71] B. Dupré, B. Lambret, D. Rousseau, C.J. Allègre, Limitations on the scale of mantle heterogeneities under oceanic ridges, Nature 294 (5841) (1981) 552–554.
[72] B. Hamelin, B. Dupré, C.J. Allègre, Lead–strontium isotopic variations along the East Pacific rise and the Mid-Atlantic Ridge: a comparative study, Earth Planet. Sci. Lett. 67 (1984) 340–350.
[73] E. Ito, W. White, C. Göpel, The O, Sr, Nd and Pb isotope geochemistry of MORB, Chem. Geol. 62 (1987) 157–176.
[74] P. Vidal, C. Chauvel, R. Brousse, Large mantle heterogeneity beneath French Polynesia, Nature 307 (1984) 536–538.
[75] E.H. Hauri, S.R. Hart, Re–Os isotope systematics of HIMU and EMII oceanic island basalts from the south Pacific Ocean, Earth Planet. Sci. Lett. 114 (1993) 353–371.
[76] J.D. Woodhead, Extreme HIMU in an oceanic setting: the geochemistry of Mangaia Island (Polynesia), and temporal evolution of the Cook-Austral hotspot, J. Volcanol. Geotherm. Res. 72 (1996) 1–19.

Pergamon

Geochimica et Cosmochimica Acta, Vol. 67, No. 19, pp. 3717–3733, 2003

0016-7037/03 $30.00 + .00

doi:10.1016/S0016-7037(03)00161-3

# Pb-Sr-He isotope and trace element geochemistry of the Cape Verde Archipelago

RÉGIS DOUCELANCE,[1,2,*] STÉPHANE ESCRIG,[1] MANUEL MOREIRA,[3,†] CLÉMENT GARIÉPY,[2] and MARK D. KURZ[3]

[1]Laboratoire de Géochimie et Cosmochimie (UMR 7579 CNRS), Institut de Physique du Globe de Paris, Université Denis Diderot Paris 7, 4 Place Jussieu, 75252 Paris cedex 05, France

[2]GEOTOP-UQAM-McGILL, CP 8888, Succursale Centre-Ville, Montréal, QC H3C 3P8, Canada

[3]Department of Marine Chemistry and Geochemistry, Woods Hole Oceanographic Institution, 360 Woods Hole Road, MS25, Woods Hole, MA 02543, USA

(*Received September* 13, 2002; revised 17 February 2003; *accepted in revised form February* 17, 2003)

**Abstract**—New lead, strontium and helium isotopic data, together with trace element concentrations, have been determined for basalts from the Cape Verde archipelago (Central Atlantic). Isotopic and chemical variations are observed at the scale of the archipelago and lead to the definition of two distinct groupings, in keeping with earlier studies. The Northern Islands (Santo Antão, São Vicente, São Nicolau and Sal) present Pb isotopic compositions below the Northern Hemisphere Reference Line (NHRL) (cf. Hart, 1984), unradiogenic Sr and relatively primitive $^4He/^3He$ ratios. In contrast, the Southern Islands (Fogo and Santiago) display Pb isotopes above the NHRL, moderately radiogenic Sr and MORB-like helium signatures. We propose that the dichotomy between the Northern and Southern Islands results from the presence of three isotopically distinct components in the source of the Cape Verde basalts: (1) recycled ~1.6-Ga oceanic crust (high $^{206}Pb/^{204}Pb$, low $^{87}Sr/^{86}Sr$ and high $^4He/^3He$); (2) lower mantle material (high $^3He$); and (3) subcontinental lithosphere (low $^{206}Pb/^{204}Pb$, high $^{87}Sr/^{86}Sr$ and moderately radiogenic $^4He/^3He$ ratios). The signature of the Northern Islands reflects mixing between recycled oceanic crust and lower mantle, to which small proportions of entrained depleted material from the local upper mantle are added. Basalts from the Southern Islands, however, require the addition of an enriched component thought to be subcontinental lithospheric material instead of depleted mantle. The subcontinental lithosphere may stem from delamination and subsequent incorporation into the Cape Verde plume, or may be remnant from delamination just before the opening of the Central Atlantic. Basalts from São Nicolau reflect the interaction with an additional component, which is identified as oceanic crustal material. 

## 1. INTRODUCTION

Isotopic variations in ocean island basalts (OIB) are now commonly interpreted as resulting from the mixtures between various components. These mixtures have several end-members (Zindler et al., 1982; Allègre and Turcotte, 1985; White, 1985; Zindler and Hart, 1986a; Allègre et al., 1986/1987), termed HIMU (for high $\mu$), EMI and EMII (for Enriched Mantle I and II) and DMM (for Depleted MORB Mantle) by Zindler and Hart (1986a). However, the exact nature of these end-members is still debated. The HIMU end-member is generally thought to represent recycling of subduction of ancient and altered oceanic crust (Hofmann and White, 1982; Allègre, 1987; Weaver, 1991; Chauvel et al., 1992; Thirlwall, 1997). Intermediate, HIMU-like signatures measured in some oceanic basalts (also termed "young" HIMU) are either explained by the mixture between DMM and HIMU material or by the presence of relatively young recycled oceanic crust (Thirlwall, 1997). The characteristics of EMI and EMII have been associated with old pelagic and/or terrigeneous sediments, recycled with, or without, oceanic crust (Allègre, 1987; Weaver, 1991; Chauvel et al., 1992) or related, in the case of EMI, to subcontinental lithospheric mantle material (Cohen and O'Nions, 1982; McKenzie and O'Nions, 1983). It has also been proposed that both HIMU and EM end-members result from intra-mantle metasomatic processes (Vollmer, 1983; Hart, 1988; Hawkesworth et al., 1990).

In comparison, rare gas systematics, notably He isotope signatures, provide good evidence for the involvement of lower mantle material in some OIB sources. Indeed, mid-ocean ridge basalts (MORB) display a quite constant $^4He/^3He$ ratio of 88,000 ± 5000 ($R/R_A = 8 \pm 1$; $R/R_A$ is the $^3He/^4He$ ratio normalized to the atmospheric value of $1.384 \times 10^{-6}$), corresponding to the mean value of the degassed upper mantle (Kurz et al., 1982; Allègre et al., 1995), whereas higher $R/R_A$ ratios measured in OIB (up to ~43 in Icelandic lavas, cf. Breddam and Kurz, 2001) reflect a relatively undegassed reservoir thought to be the lower mantle (Kurz et al., 1982). Lower $R/R_A$ measured in some EM- and HIMU-OIB are, however, a source of controversy. They are either attributed to the recycling of oceanic crust and/or sediments into the mantle, characterized by high $(U + Th)/^3He$ ratios, which were stored for some time at the 670-km boundary layer (Kurz et al., 1982; Graham et al., 1992; Hanyu and Kaneoka, 1997, Moreira et al., 1999), or to magma chamber contamination processes (Condomines et al., 1983; Zindler and Hart, 1986b; Hilton et al., 1995).

The study of different OIB archipelagos around the world is very useful in clarifying such problems. The first detailed geochemical study of the Cape Verde was that of Gerlach et al. (1988) who determined trace element concentrations and Sr-

* Author to whom correspondence should be addressed, at Laboratoire Magmas et Volcans, Université Blaise Pascal, CNRS (UMR 6524), Observatoire de Physique du Globe de Clermont-Ferrand, 5 Rue Kessler, 63038, Clermont-Ferrand cedex, France (doucelance@opgc.univ-bpclermont.fr).

† *Present address:* Laboratoire de Géochimie et Cosmochimie (UMR 7579 CNRS), Institut de Physique du Globe de Paris, Université Denis Diderot Paris 7, 4 Place Jussieu, 75252 Paris cedex 05, France.

Nd-Pb isotopic compositions of lavas from five islands. They pointed out differences between the Southern and Northern Islands, and interpreted them as reflecting the presence of three isotopically distinct end-members: (1) Depleted MORB Mantle (DMM); (2) a HIMU-like end-member; and (3) an EMI-like end-member. These results have been confirmed by the subsequent study of Davies et al. (1989) who presented a comparison between the Azores and Cape Verde archipelagos. Concerning the geodynamic context of lava generation, Gerlach et al. (1988) presented two different models. In the first, the EMI-like end-member is located at the base of the oceanic lithosphere and only contributes to magmatism in the Southern Islands; the HIMU-like end-member, supplied by the plume and possibly supplemented by "entrained" DMM material, explains the isotopic compositions of the Northern Islands. In the second model, the Cape Verde plume displays EMI-like characteristics and the HIMU end-member is present in the upper mantle as pyroxene-rich recycled oceanic crust, in a fashion similar to the marble cake mantle of Allègre and Turcotte (1986). The absence of EMI contributions in the Northern Islands would thus result from a smaller degree of partial melting.

Kokfelt et al. (1998) suggested an alternative model in which both the EMI- and HIMU-like end-members reside in the oceanic lithosphere above the non-melting Cape Verde mantle plume. Based on Sr, Nd and Pb isotopic compositions, U/Th measurements and trace element data, these authors proposed that: (1) the HIMU-like end-member corresponds to a so-called "young HIMU" component resulting from metasomatism by carbonatitic fluids of the oceanic crust associated with the degassing of the mantle just before the opening of the Atlantic ocean; and (2) the EMI end-member is related to delaminated subcontinental lithosphere. Jørgensen and Holm (2002), however, proposed the existence of two separate HIMU-like end-members within the Cape Verde plume to explain the isotopic signature of basalts and carbonatites sampled on São Vicente island.

Finally, Christensen et al. (2001) presented the first rare gas results (He and Ar) as well as Pb isotopic results for the two youngest islands of the archipelago: Fogo and Santo Antão. They confirmed the presence of a "young HIMU" end-member in the source of the Cape Verde magmas, but also argued for the involvement of lower mantle material in the Northern Islands to explain the moderately primitive He ratios of Santo Antão basalts ($^4He/^3He \sim 50{,}000$). Due to the small number of He and Pb data available from Fogo, they did not draw any conclusions in favour of such a lower mantle contribution in the Southern Islands, nor about the EMI-like end-member previously identified by Gerlach et al. (1988), Davies et al. (1989) and Kokfelt et al. (1998).

In this study we present new Pb, Sr and He analyses, together with trace element concentrations, for five islands of the Cape Verde Archipelago: Fogo, Santiago, São Vicente, São Nicolau and Sal (Fig. 1). Using time-integrated models, we calculate the isotopic composition for Pb, Sr and He of recycled oceanic crust, delaminated subcontinental lithosphere and lower mantle materials. We then consider the presence of these three components in the source of the Cape Verde basalts and discuss the geodynamic implications.

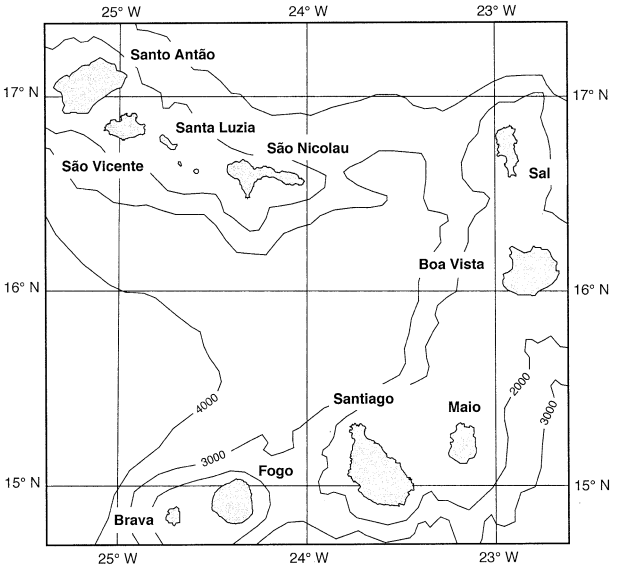


Fig. 1. Location map and sea-floor bathymetry of the Cape Verde archipelago, modified after Gerlach et al. (1988).

## 2. GEOGRAPHIC LOCATION, TECTONIC SETTING AND GEOLOGICAL DESCRIPTION

The Cape Verde Islands are located ~500 km to the west of Senegal, between latitudes 15 and 17°N. The archipelago is composed of 10 principal islands, which can be divided into two groups: (1) the Southern Islands of Brava, Fogo, Santiago and Maio; and (2) the Northern Islands of Santo Antão, São Vicente, Santa Luzia and São Nicolau, extending to the east with Sal and Boa Vista (Fig. 1). In the two groups, the alignment of islands is thought to be controlled by: (1) a deep structure (possibly an old oceanic ridge) present in this part of Atlantic since the Mesozoic (Klerkx and De Paepe, 1971); and (2) a transverse fracture zone (Le Pichon and Fox, 1971). The Cape Verde archipelago constitutes one of the highest oceanic plateaux, with an average depth of 2 km above the oceanic floor. Anomalous heat flow and geoid data cannot be explained by reheating of the oceanic lithosphere alone, implying the presence of a thermal plume (Courtney and White, 1986). Although the archipelago is located quite close to the African continent, its position relative to the continental slope does not suggest the presence of continental crust under the Cape Verde Islands (Klerkx et al., 1974).

The oldest submarine formations formed in the Jurassic (Klerkx et al., 1974). For exposed volcanic rocks on the islands, magmatic activity probably started in the Miocene for the youngest (Brava, Fogo, Santo Antão and São Vicente), and between the initial- and middle-parts of the Cenozoic for the others (Gerlach et al., 1988). Currently, volcanism is restricted to Brava and Fogo with the most recent eruption of the Fogo volcano occurring on April 3, 1995. There is a regional ageing of the Southern Islands from the west (Brava) to the east (Maio), consistent with the movement of the oceanic plate toward the northeast. However, due to its location near the pole of rotation of the African plate, the Cape Verde archipelago appears to have remained quite stationary relative to a fixed hotspot frame of reference (Duncan, 1980) for the last 20 Ma,

with a relative speed of ~12 mm/yr (Courtney and White, 1986).

Exposed magmatic units on all islands of the archipelago have a volcanic origin, except for rare, discrete carbonatite intrusives (Allègre et al., 1971; Hoernle et al., 2002). The lavas define a petrographic series ranging from nephelinites to phonolites (De Paepe et al., 1974; Klerkx et al., 1974). Some important calcareous deposits are also present on Sal, Boa Vista and Maio (Matos Alves et al., 1979; Gerlach et al., 1988). For this study, we analyzed lavas from Fogo, Santiago, São Vicente, São Nicolau and Sal which were collected in February 1998. Sample locations are illustrated in Figure 2.

### 3. ANALYTICAL PROCEDURE

Lead chemical separation was done using ~1 g of whole-rock powder, following the procedure of Manhès et al. (1978), in a clean room under controlled atmosphere. Total Pb blanks are <0.5 ng and show a common isotopic composition, making corrections in all cases negligible with respect to sample Pb contents. Lead isotopic ratios were measured on a VG354 thermal ionization mass spectrometer used in peak jumping mode; the instrument was calibrated against the NIST SRM981 standard (Catanzaro et al., 1968) yielding a statistical mass bias factor of 0.1 ± 0.03% per mass unit difference in the isotopic ratios. Additional values were obtained at the GEOTOP laboratory (Montréal, Canada) using a Micromass IsoProbe MC-ICP-MS operated in static mode. Chemical separation was performed with 10 $\mu$L column volume of AG1X8 resin (loading and washing in 0.8N HBr, elution in 6.2N HCl) on ~100 mg of the powdered samples; blanks were in the range of 100 to 150 pg and negligible. Tail corrections on the IsoProbe instrument were based on abundance sensitivity measurements of separate $^{204}$Pb and $^{208}$Pb isotope solutions instead of half-mass zeroes (Thirlwall, 2001, 2002). Mass fractionation was corrected for by using the Tl doping technique and an exponential law, assuming identical fractionation factors for both Pb and Tl. External reproducibility between the Pb measurements done on the TIMS and the MC-ICP-MS instruments was corrected for by adjusting the $^{205}$Tl/$^{203}$Tl ratio to 2.38884, thus yielding a mean of 0.91464 for the $^{207}$Pb/$^{206}$Pb ratio of NIST SRM981 (Catanzaro et al., 1968). Total reproducibility is better than 0.04% (2$\sigma$) per amu; it can be evaluated using samples F-02 (A and B) and F-15 (A and B) which were measured on both instruments. Samples F-08b (A and B), F-11 (A and B) and F-12 (A, B, and C) are duplicates of the total procedure developed in Montréal.

Strontium isotopic measurements were done also using the VG354 mass spectrometer after chemical separation using a Sr Spec Column (Pin and Bassin, 1992). Sr blank for the complete procedure was between 30 and 80 pg. Isotopic measurements were mass-fractionation-corrected using $^{86}$Sr/$^{88}$Sr = 0.1194 and normalized to $^{87}$Sr/$^{86}$Sr = 0.71025 for the NIST SRM987 standard. Total reproducibility, tested on replicate analyses of SRM987, was better than 0.002% (2$\sigma$). Some leaching experiments have also been performed on three basalts from São Vicente, by using hot 6N HCl over a period of 8 h (Dupré et al., 1982).

Helium analyses were performed on millimeter-sized olivine and pyroxene phenocrysts separated from fresh lavas. Measurements were done by crushing these materials, to avoid possible

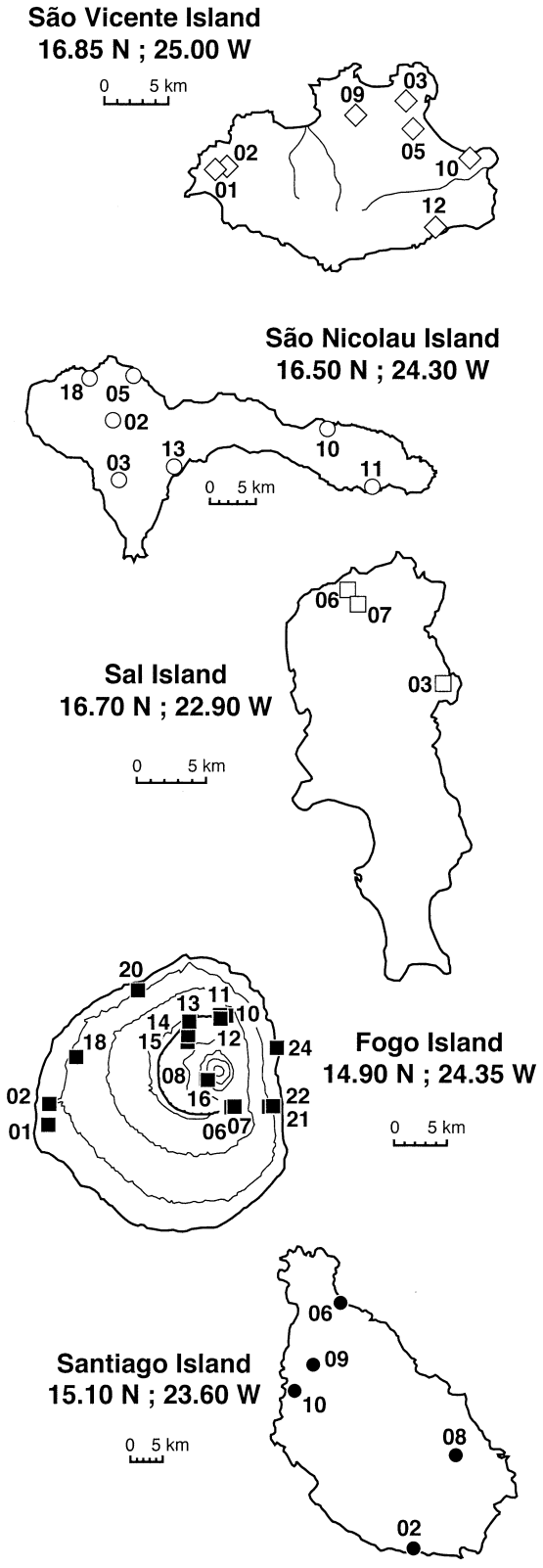


Fig. 2. Fogo, Santiago, São Vicente, São Nicolau and Sal island sampling maps.

Table 1. Major (%) and trace element (ppm) concentrations of samples from Cape Verde.

| | Fogo (F-) | | | | | | Santiago (ST-) | | | | |
|---|---|---|---|---|---|---|---|---|---|---|---|
| | 02 | 07 | 08 | 15 | 20 | 24 | 02 | 06 | 08 | 09 | 10 |
| $SiO_2$ | 41.59 | 42.24 | 42.47 | 42.14 | 40.65 | 41.42 | 42.96 | 38.08 | 42.91 | 39.45 | 41.66 |
| $Al_2O_3$ | 14.88 | 15.32 | 15.59 | 15.71 | 14.53 | 13.31 | 12.92 | 10.22 | 11.80 | 14.75 | 15.49 |
| $Fe_2O_3$ | 14.19 | 13.31 | 13.24 | 13.06 | 14.07 | 14.18 | 12.39 | 12.49 | 12.38 | 12.36 | 11.02 |
| MnO | 0.18 | 0.20 | 0.20 | 0.21 | 0.20 | 0.20 | 0.17 | 0.18 | 0.17 | 0.23 | 0.17 |
| MgO | 7.15 | 6.49 | 6.17 | 5.81 | 6.50 | 9.21 | 10.40 | 13.19 | 10.71 | 6.25 | 5.82 |
| CaO | 11.07 | 12.02 | 11.94 | 11.60 | 12.81 | 12.81 | 12.89 | 14.54 | 12.74 | 13.05 | 11.19 |
| $Na_2O$ | 4.41 | 3.75 | 3.89 | 4.00 | 3.61 | 3.08 | 2.82 | 3.16 | 1.89 | 3.34 | 2.67 |
| $K_2O$ | 2.18 | 2.60 | 2.74 | 2.77 | 2.39 | 1.92 | 1.23 | 2.08 | 1.34 | 1.78 | 2.91 |
| $TiO_2$ | 4.07 | 3.74 | 3.80 | 3.65 | 4.40 | 3.53 | 2.66 | 3.59 | 3.20 | 3.50 | 3.91 |
| $P_2O_5$ | 0.60 | 0.82 | 0.84 | 0.91 | 0.70 | 0.74 | 0.58 | 0.72 | 0.48 | 1.20 | 0.92 |
| Total | 100.32 | 100.49 | 100.88 | 99.86 | 99.86 | 100.40 | 99.02 | 98.25 | 97.62 | 95.91 | 95.76 |
| L.O.I. | — | — | — | — | — | — | 1.17 | 1.59 | 2.32 | 3.92 | 4.40 |
| Rb | 63 | 56 | 60 | 61 | 49 | 43 | 24 | 43 | 33 | 58 | 59 |
| Ba | 795 | 802 | 849 | 771 | 747 | 634 | 963 | 700 | 561 | 986 | 844 |
| Th | 4.5 | 5.1 | 5.7 | 5.6 | 4.1 | 4.0 | 5.0 | 6.3 | 4.6 | 15.4 | 8.5 |
| U | 0.97 | 1.05 | 1.19 | 1.25 | 0.96 | 0.88 | 1.14 | 1.36 | 0.92 | 4.71 | 2.06 |
| Nb | 83 | 84 | 90 | 89 | 77 | 67 | 69 | 81 | 62 | 165 | 112 |
| Ta | 6.57 | 6.38 | 7.04 | 7.20 | 6.30 | 5.24 | 4.70 | 5.64 | 4.39 | 12.10 | 9.00 |
| La | 45 | 56 | 59 | 57 | 49 | 47 | 51 | 58 | 45 | 132 | 87 |
| Ce | 98 | 124 | 131 | 124 | 110 | 100 | 102 | 117 | 89 | 252 | 175 |
| Pr | 11.6 | 14.8 | 15.7 | 15.4 | 14.0 | 13.1 | 12.1 | 14.0 | 11.1 | 29.3 | 20.7 |
| Nd | 47 | 57 | 63 | 64 | 58 | 54 | 48 | 58 | 44 | 115 | 81 |
| Sr | 929 | 1041 | 1066 | 1104 | 1014 | 893 | 930 | 824 | 910 | 2064 | 1652 |
| Sm | 9.1 | 10.8 | 11.4 | 11.3 | 10.8 | 10.0 | 8.7 | 10.3 | 8.9 | 19.4 | 14.0 |
| Zr | 330 | 338 | 357 | 357 | 356 | 281 | 236 | 326 | 285 | 502 | 437 |
| Eu | 2.84 | 3.41 | 3.70 | 3.64 | 3.70 | 3.25 | 2.93 | 3.10 | 2.61 | 5.72 | 4.37 |
| Gd | 6.74 | 8.78 | 9.06 | 9.41 | 8.78 | 8.18 | 6.95 | 7.17 | 6.47 | 14.10 | 11.00 |
| Tb | 0.98 | 1.22 | 1.33 | 1.25 | 1.25 | 1.09 | 0.98 | 1.05 | 0.97 | 1.99 | 1.49 |
| Dy | 5.00 | 6.12 | 6.49 | 6.33 | 6.47 | 5.70 | 4.81 | 5.51 | 4.86 | 9.81 | 7.63 |
| Ho | 0.868 | 1.020 | 1.030 | 1.120 | 1.060 | 0.973 | 0.820 | 0.888 | 0.884 | 1.670 | 1.350 |
| Er | 2.05 | 2.59 | 2.57 | 2.64 | 2.45 | 2.19 | 2.00 | 2.06 | 2.01 | 3.85 | 2.98 |
| Tm | 0.271 | 0.294 | 0.314 | 0.339 | 0.358 | 0.300 | 0.230 | 0.239 | 0.266 | 0.530 | 0.420 |
| Y | 23.4 | 29.1 | 29.9 | 31.0 | 29.5 | 27.2 | 22.1 | 24.6 | 25.0 | 44.5 | 34.7 |
| Yb | 1.81 | 2.17 | 2.12 | 2.27 | 1.96 | 1.80 | 1.47 | 1.35 | 1.43 | 2.88 | 2.39 |
| Lu | 0.251 | 0.290 | 0.310 | 0.308 | 0.284 | 0.256 | 0.230 | 0.233 | 0.233 | 0.453 | 0.307 |
| Co | 47 | 43 | 40 | 41 | 47 | 54 | 52 | 62 | 61 | 37 | 35 |
| Ni | 83 | 50 | 42 | 34 | 43 | 113 | 211 | 313 | 274 | 34 | 39 |

in situ radiogenic decay products or cosmogenic $^3He$ and to obtain the volcanic helium gas trapped in inclusions (Kurz et al., 1982; Kurz, 1986). Some samples were also melted under vacuum conditions to release the gases located in the matrix and evaluate the content of radiogenic and cosmogenic helium. Measurements were done in the Woods Hole Oceanographic Institution with an automated mass spectrometer; the total blank is typically 3 to $5 \times 10^{-11}$ $cm^3$ STP (Kurz et al., 1996).

Whole-rock major- and trace-element results were obtained from the Service d'Analyse des Roches et des Minéraux (SARM) at the Centre de Recherches Pétrographiques et Géochimiques (CRPG/Nancy). Major- and trace-element contents were determined by ICP-AES and ICP-MS, respectively, after alkaline melting with lithium borate and nitric acid dissolution. International standards as well as analytical procedures used in the CRPG laboratory at Nancy can be downloaded from the Web site at http://www.crpg.cnrs-nancy.fr/SARM/index.html.

## 4. MAJOR AND TRACE ELEMENT VARIATIONS

All samples have $SiO_2$ contents <45% (Table 1); they are mafic lavas corresponding to nephelinites, picro-basalts, basanites and tephrites. Such an abundance of mafic rocks was already noted by Klerkx et al. (1974) and Gerlach et al. (1988). The major element abundances do not define any significant variations as the samples are not strongly differentiated. However, the MgO contents are regionally lower for samples collected on the Southern Islands (5.81–13.19, mean = 7.97, compared to 10.10–19.97, mean = 13.14, for the Northern Islands) and, in a general way, samples from the Southern Islands display a more alkaline character than those from the Northern Islands.

The dichotomy suggested by major element abundances can be shown more clearly when considering trace elements. For example, Figure 3 presents a Th/Nb vs. Th/Tb plot where samples from the Northern and Southern Islands define two different trends. These can be explained by the melting of two distinct sources for Th, Nb and Tb (Joron and Treuil, 1989). Modeling based on São Nicolau and São Vicente samples, for which crystal fractionation is most probably only minimal (high and relatively constant Ni and Cr contents; Table 1), shows that variations of the Th/Nb and Th/Tb ratios can be reproduced by the batch melting of a harzburgite containing amphibole, phlogopite and ilmenite (Fig. 3; Table 2). Mineral

Table 1. (Continued)

| São Vicente (SV-) | | | | | | | São Nicolau (SN-) | | | | | | | Sal (S-) | | |
|---|---|---|---|---|---|---|---|---|---|---|---|---|---|---|---|---|
| 01 | 02 | 03 | 05 | 09 | 10 | 12 | 02 | 03 | 05 | 10 | 11 | 13 | 18 | 03 | 06 | 07 |
| 44.33 | 43.07 | 44.47 | 40.60 | 38.54 | 38.84 | 43.28 | 41.70 | 42.52 | 40.45 | 39.97 | 41.89 | 44.47 | 44.47 | 35.67 | 38.25 | 38.89 |
| 13.23 | 11.27 | 13.34 | 10.59 | 11.24 | 11.34 | 8.38 | 11.88 | 13.20 | 12.28 | 11.93 | 12.47 | 13.17 | 13.87 | 10.93 | 9.59 | 8.25 |
| 12.12 | 12.59 | 12.55 | 13.23 | 13.27 | 13.09 | 13.52 | 13.36 | 13.05 | 12.95 | 12.90 | 12.85 | 11.59 | 12.55 | 12.20 | 12.92 | 13.37 |
| 0.17 | 0.17 | 0.18 | 0.17 | 0.17 | 0.18 | 0.17 | 0.20 | 0.18 | 0.19 | 0.21 | 0.19 | 0.18 | 0.17 | 0.20 | 0.19 | 0.19 |
| 10.10 | 11.33 | 10.77 | 15.19 | 12.05 | 12.69 | 18.96 | 14.20 | 10.87 | 12.62 | 12.48 | 12.13 | 10.40 | 10.16 | 12.90 | 16.52 | 19.97 |
| 12.24 | 13.80 | 11.92 | 12.12 | 12.89 | 14.17 | 9.71 | 11.50 | 12.41 | 13.65 | 14.02 | 12.83 | 12.27 | 10.81 | 16.42 | 13.37 | 12.48 |
| 2.09 | 2.05 | 3.27 | 2.75 | 2.93 | 2.75 | 1.19 | 3.67 | 1.98 | 3.93 | 3.63 | 3.29 | 3.01 | 2.66 | 3.07 | 2.59 | 1.80 |
| 1.10 | 1.01 | 1.25 | 0.60 | 0.35 | 1.25 | 0.63 | 0.56 | 0.73 | 0.76 | 1.03 | 1.06 | 1.13 | 1.03 | 0.93 | 1.34 | 1.04 |
| 3.11 | 3.42 | 2.69 | 3.28 | 4.42 | 3.69 | 2.25 | 2.77 | 3.47 | 3.11 | 2.85 | 2.74 | 2.71 | 2.82 | 3.34 | 3.40 | 3.31 |
| 0.43 | 0.41 | 0.41 | 0.53 | 0.65 | 0.61 | 0.30 | 0.53 | 0.41 | 0.74 | 0.79 | 0.60 | 0.40 | 0.45 | 1.44 | 0.68 | 0.48 |
| 98.92 | 99.12 | 100.85 | 99.06 | 96.51 | 98.61 | 98.39 | 100.37 | 98.82 | 100.68 | 99.79 | 100.05 | 99.33 | 98.99 | 97.10 | 98.85 | 99.76 |
| 1.35 | 0.90 | — | 1.20 | 3.59 | 1.51 | 1.65 | — | 1.21 | — | 0.18 | — | 0.26 | 1.05 | 2.30 | 0.49 | 0.32 |
| 25 | 20 | 23 | 7 | 27 | 23 | 15 | 28 | 18 | 14 | 18 | 25 | 30 | 21 | 33 | 31 | 25 |
| 331 | 264 | 377 | 392 | 591 | 517 | 204 | 423 | 324 | 494 | 498 | 534 | 355 | 392 | 929 | 514 | 352 |
| 4.7 | 3.0 | 2.9 | 3.7 | 6.0 | 4.5 | 2.3 | 4.0 | 2.9 | 6.3 | 7.8 | 4.1 | 4.4 | 3.7 | 12.2 | 6.2 | 3.3 |
| 1.08 | 0.72 | 0.52 | 0.82 | 1.03 | 0.99 | 0.5 | 0.8 | 0.67 | 1.16 | 1.54 | 1.09 | 0.93 | 0.85 | 2.95 | 1.31 | 0.75 |
| 49 | 40 | 44 | 47 | 73 | 62 | 28 | 54 | 48 | 65 | 74 | 54 | 48 | 51 | 89 | 67 | 47 |
| 3.56 | 3.05 | 3.45 | 3.57 | 5.12 | 4.46 | 2.01 | 3.83 | 3.31 | 4.21 | 5.15 | 3.59 | 3.46 | 3.80 | 6.15 | 4.81 | 3.40 |
| 36 | 29 | 25 | 36 | 54 | 43 | 22 | 35 | 28 | 51 | 58 | 41 | 33 | 33 | 92 | 52 | 36 |
| 76 | 66 | 55 | 76 | 112 | 90 | 48 | 71 | 64 | 99 | 114 | 85 | 67 | 70 | 181 | 108 | 77 |
| 9.0 | 8.3 | 6.7 | 9.0 | 12.6 | 10.7 | 5.7 | 8.4 | 7.8 | 11.8 | 13.2 | 10.1 | 7.9 | 8.3 | 21.2 | 13.4 | 9.7 |
| 36 | 35 | 29 | 37 | 54 | 44 | 24 | 35 | 33 | 48 | 54 | 39 | 31 | 33 | 80 | 51 | 39 |
| 611 | 555 | 590 | 659 | 1026 | 786 | 348 | 611 | 653 | 866 | 876 | 775 | 544 | 614 | 1515 | 902 | 643 |
| 7.6 | 7.2 | 5.8 | 7.1 | 10.0 | 8.3 | 5.0 | 6.8 | 6.6 | 8.4 | 9.6 | 7.8 | 6.7 | 7.1 | 14.8 | 10.2 | 8.0 |
| 215 | 207 | 173 | 206 | 270 | 219 | 142 | 197 | 234 | 228 | 221 | 219 | 229 | 215 | 301 | 236 | 216 |
| 2.41 | 2.30 | 2.04 | 2.22 | 3.02 | 2.71 | 1.64 | 2.25 | 2.09 | 2.86 | 3.22 | 2.64 | 2.28 | 2.35 | 4.43 | 3.00 | 2.53 |
| 6.08 | 6.57 | 5.64 | 5.69 | 8.39 | 6.97 | 4.49 | 6.02 | 5.84 | 7.84 | 8.52 | 6.91 | 5.97 | 6.00 | 11.10 | 7.74 | 6.65 |
| 0.97 | 0.90 | 0.90 | 0.85 | 1.11 | 0.97 | 0.64 | 0.91 | 0.84 | 1.04 | 1.17 | 0.92 | 0.87 | 0.91 | 1.44 | 1.14 | 0.89 |
| 4.84 | 4.56 | 4.34 | 4.22 | 5.50 | 4.99 | 3.30 | 4.55 | 4.66 | 5.53 | 6.16 | 5.26 | 4.84 | 5.06 | 7.56 | 5.57 | 4.32 |
| 0.886 | 0.848 | 0.802 | 0.755 | 1.000 | 0.808 | 0.604 | 0.852 | 0.911 | 0.959 | 1.145 | 0.977 | 0.851 | 1.020 | 1.180 | 0.897 | 0.741 |
| 2.19 | 1.85 | 2.08 | 1.87 | 2.21 | 1.90 | 1.37 | 2.09 | 2.13 | 2.21 | 2.56 | 2.24 | 2.11 | 2.33 | 3.14 | 2.06 | 1.57 |
| 0.315 | 0.275 | 0.286 | 0.243 | 0.291 | 0.256 | 0.228 | 0.301 | 0.298 | 0.299 | 0.353 | 0.291 | 0.333 | 0.370 | 0.346 | 0.269 | 0.203 |
| 25.4 | 23.3 | 22.6 | 20.8 | 26.0 | 23.3 | 16.3 | 24.6 | 26.1 | 28.9 | 31.6 | 28.1 | 25.3 | 26.3 | 35.5 | 25.4 | 19.7 |
| 1.90 | 1.68 | 1.57 | 1.37 | 1.66 | 1.40 | 1.24 | 1.78 | 1.92 | 1.80 | 2.18 | 1.85 | 2.05 | 2.17 | 2.48 | 1.67 | 1.31 |
| 0.273 | 0.227 | 0.252 | 0.238 | 0.238 | 0.206 | 0.197 | 0.264 | 0.298 | 0.295 | 0.315 | 0.296 | 0.283 | 0.325 | 0.323 | 0.245 | 0.170 |
| 53 | 62 | 57 | 70 | 61 | 60 | 83 | 67 | 59 | 62 | 60 | 60 | 51 | 52 | 58 | 72 | 78 |
| 205 | 214 | 216 | 454 | 252 | 282 | 553 | 349 | 163 | 257 | 245 | 261 | 211 | 221 | 232 | 466 | 611 |

proportions that best fit the evolution of Th/Nb and Th/Tb ratios measured in samples from the Northern Islands are ol:opx:cpx:gt:amp:phlog:ilm = 77:16:1.5:3:0.25:0.75:1.5, for Th, Nb and Tb source contents of 0.09, 2.2 and 0.065 ppm, respectively, close to the reference Bulk Silicate Earth (McDonough and Sun, 1995). Class and Goldstein (1997) have developed the concept of an enrichment factor for trace elements. It corresponds to the concentration ratio, for a given element, between the sample with the lowest extent of partial melting and the sample with the highest one, in a series of cogenetic samples. Such enrichment factors were determined for the São Nicolau lavas: samples corresponding to the highest and lowest partial melting rate were chosen on the basis of Th vs. Nb contents. Figure 4 compares the enrichment factors thus calculated for São Nicolau with model values determined by Class and Goldstein (1997) for a harzburgite with amphibole, phlogopite and ilmenite. The overall agreement of factors for São Nicolau with those of Class and Golstein (1997), as well as the modeling presented in Figure 3, suggest that basalts from the Northern and Southern Islands may result from the melting of two distinct sources containing amphibole and phlogopite. This is comparable with the results of Gerlach et al. (1988) who interpreted positive trends between Rb and K abundances and $K_2O/TiO_2$ ratios in Cape Verde samples as reflecting phlogopite melting. The stability domain of such phases requires that melting occurred partly within the oceanic lithosphere.

Extended trace element patterns for the Fogo and Santiago samples (Figs. 5a and 5b) are similar to the EMI pattern defined by the mean composition of Tristan da Cunha volcanics (Le Roex et al., 1990; Cliff et al., 1991). In contrast, the Northern Island basalts display trace element enrichment with respect to primitive mantle (Figs. 5c–5e), similar to average Mangaia lavas (HIMU-like, cf. Woodhead, 1996) in Polynesia. These data are consistent with previous results and models (Gerlach et al., 1988; Davies et al., 1989) which showed the involvement of both EMI- and HIMU-like end-members in the source of the Cape Verde basalts. The low, but quite systematic, depletion which is observed for K relative to the lower mantle can be explained by the presence of a K-rich phase such as phlogopite in the source of the Cape Verde samples (Dupuy et al., 1988). However, Woodhead (1996) noted such a depletion was a common feature of ocean island basalts, and he interpreted this result as a graphic artefact due to the value of K chosen for normalization.

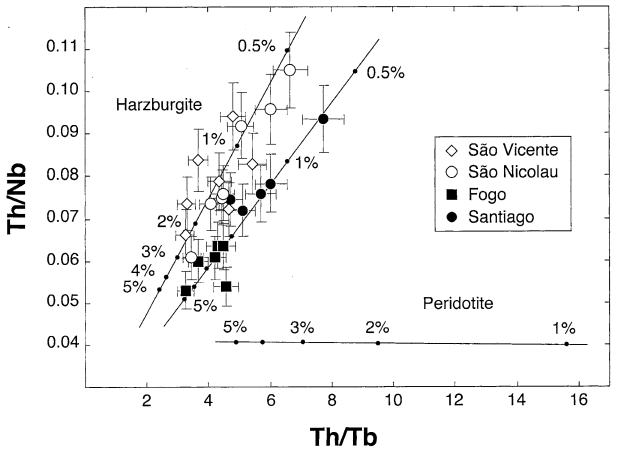


Fig. 3. Th/Nb vs. Th/Tb diagram for Cape Verde basalts in this study. Open symbols = Northern Islands; filled symbols = Southern Islands. Trace element data for São Vicente and São Nicolau samples are modeled by the batch melting of a harzburgite, containing amphibole, phlogopite and ilmenite in the proportion ol:opx:cpx:gt:amp:phlog:ilm = 77:16:1.5:3:1:1:0.5 with Th, Nb and Tb source concentrations of 0.09, 2.2 and 0.065 ppm, respectively. The expected trend for a peridotite (ol:opx:cpx:gt = 55:25:11:9) is also shown for comparison. The Th, Nb and Tb contents of the reference Bulk Silicate Earth are 0.0795, 0.658 and 0.099 ppm, respectively (McDonough and Sun, 1995). Fogo and Santiago results can be modeled either using the same mineralogy, but different source concentrations, or similar Th, Nb and Tb contents, but variable garnet, amphibole and ilmenite proportions.

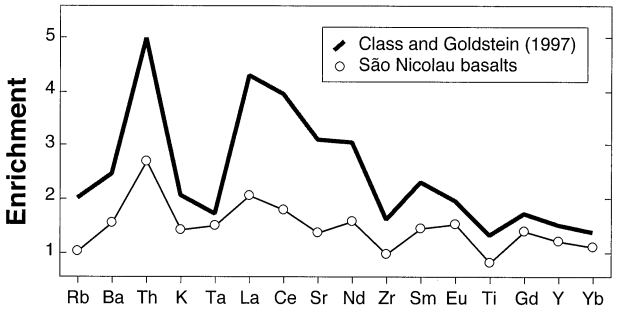


Fig. 4. Comparison between the enrichment factors of Class and Goldstein (1997) for a harzburgite with amphibole, phlogopite and ilmenite and values determined from São Nicolau basalts (see text for details).

## 5. LEAD-STRONTIUM-HELIUM ISOTOPE VARIATIONS

The variation ranges in Pb and Sr isotopic composition determined here (Table 3; Fig. 6) are of the same magnitude as those previously determined by Gerlach et al. (1988), Davies et al. (1989), Kokfelt et al. (1998), Christensen et al. (2001) and Jørgensen and Holm (2002). In parallel with the trace element signatures, the isotopic variations are related to the geographical position of the samples within the archipelago. Samples from the Southern Islands all have Pb isotopic compositions ($^{206}Pb/^{204}Pb$ = 18.883–19.398; $^{207}Pb/^{204}Pb$ = 15.530–15.580; and $^{208}Pb/^{204}Pb$ = 38.701–39.190) plotting above the NHRL (Hart, 1984), for $^{87}Sr/^{86}Sr$ ratios in the range of 0.70349 to 0.70379. In contrast, the samples from the Northern Islands all yield Pb isotope ratios plotting below the NHRL ($^{206}Pb/^{204}Pb$ = 19.187–19.692; $^{207}Pb/^{204}Pb$ = 15.564–15.619; and $^{208}Pb/^{204}Pb$ = 38.763–39.401) and $^{87}Sr/^{86}Sr$ ratios lower than the former, ranging from 0.70299 to 0.70336. Note that the São Nicolau samples appear to define a distinct alignment in the $^{208}Pb/^{204}Pb$ (Fig. 6a) and $^{87}Sr/^{86}Sr$ (Fig. 6c) vs. $^{206}Pb/^{204}Pb$ diagrams. This may also be the case for the three basalt samples from Sal, but there are insufficient samples to confirm this trend. Lastly, leaching experiments that have been performed on three São Vicente samples do not show significant variations between residues and bulk samples (Table 3).

Helium concentrations obtained from crushing experiments (Table 4; Fig. 7a) range from $0.6 \times 10^{-9}$ cm$^3$ STP/g in olivines from sample SV-05 (São Vicente) to $5.12 \times 10^{-8}$ cm$^3$ STP/g in olivines from sample F-07 (Fogo). $^4He/^3He$ isotopic ratios vary from 45,928 ($R/R_A$ = 15.73) to 522,824 ($R/R_A$ = 1.38) in SN-10 (São Nicolau) and ST-09 (Santiago) samples, respectively. Blank levels were significantly higher in Santiago samples compared to other islands (Table 4) and correspond to olivines and pyroxenes which yielded the most radiogenic He values (e.g., ST-06 and ST-09). The helium concentration obtained from the melting experiment completed after crushing of CPXs from sample ST-09 is $15.28 \times 10^{-8}$ cm$^3$ STP/g; the $^4He/^3He$ ratio is 4,128,819 ± 117,966 ($R/R_A$ = 0.18 ± 0.01), much more radiogenic than that of the crushed aliquot (Table 4). This strongly suggests in situ production of radiogenic $^4He$, thus this sample probably does not reflect the isotopic composition of its magma source. The "re-crush" experiment carried out on sample ST-06, which initially had a radiogenic $^4He/^3He$ value of 185,505 ± 38,054 ($R/R_A$ = 3.9 ± 0.8), yielded a $R/R_A$ value of 7.66 ± 2.77 (Table 4) which is consistent with other values determined for Santiago samples. However, the "melting" after crushing experiment carried out on olivines from this sample indicates the presence of cosmogenic $^3He$ (cf. left-hand portion of Fig. 7b) with a $^4He/^3He$ ratio of 24,741 ± 231 ($R/R_A$ = 29.20 ± 0.27). Figures 7c and 7d present replicates of crushing experiments for two samples (F-13 from Fogo and

Table 2. Partition coefficients.

| | Olivine | OPX | CPX | Garnet | Amphibole | Phlogopite | Ilmenite |
|---|---|---|---|---|---|---|---|
| Th | 0.00001 | 0.00003 | 0.03 | 0.0015 | 0.5 | 0.0014 | 0 |
| Nb | 0.0001 | 0.003 | 0.005 | 0.02 | 0.8 | 1.00 | 0.8 |
| Tb | 0.0028 | 0.012 | 0.57 | 0.705 | 0.635 | 0.03 | 0.14 |

$D^{Th}$ for olivine and OPX: Beattie (1993a); $D^{Th}$ (garnet): Beattie (1993b); $D^{Th}$ (phlogopite): La Tourette et al. (1995); $D^{Nb}$ (olivine and OPX): Kelemen et al. (1993); $D^{Tb}$ (olivine): Beattie (1993a), $D^{X}$ (ilmenite): Paster et al. (1974) except $D^{Nb}$: Irving (1978). All other partition coefficients can be found in Rollinson (1993), except $D^{Tb}$ (Olivine, OPX, amphibole and phlogopite) which were determined by linear interpolation with adjacent REE.

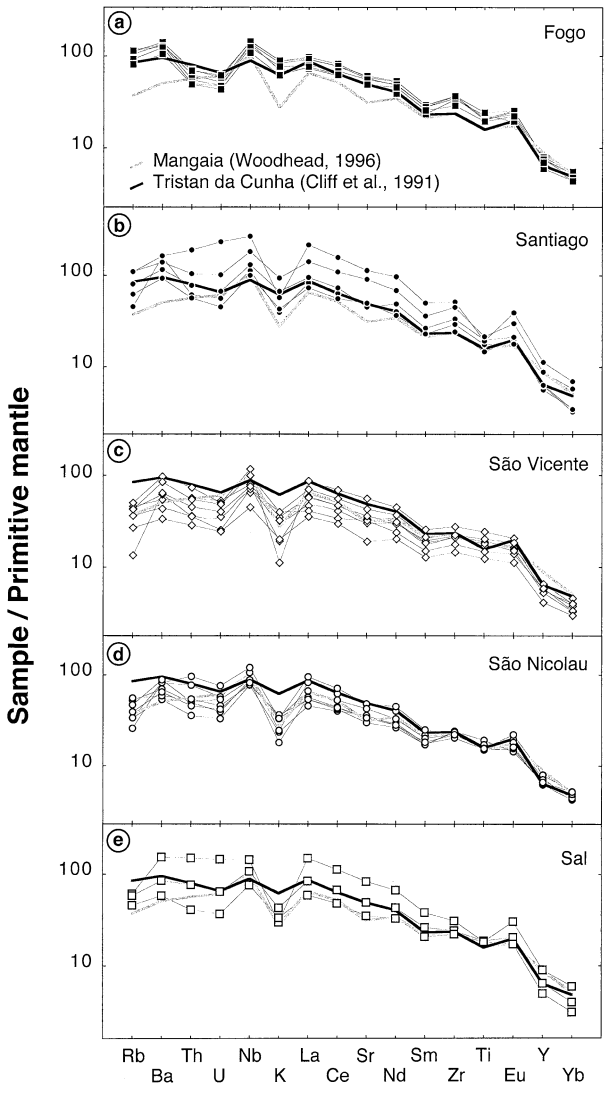


Fig. 5. Abundances of trace elements in samples from (a) Fogo, (b) Santiago, (c) São Vicente, (d) São Nicolau, and (e) Sal normalized to the primitive mantle values of Hofmann (1988).

S-07 from Sal) together with "melting" experiments. $^4He/^3He$ isotopic ratios (crushing) display reproducible values for olivines and pyroxenes.

The helium isotopic results for Cape Verde basalts clearly define two geographical groups (Fig. 7a). Fogo ($R/R_A$ = 7.90–8.40) and Santiago ($R/R_A$ = 7.66–8.31) in the Southern Islands have MORB-like compositions, whereas the Northern Island basalts have more primitive He isotopic compositions ($8.41 < R/R_A < 15.73$), with the exception of a single sample from Sal (S-06; Table 4) with $R/R_A$ = 6.98. The most primitive values ($R/R_A$ = 10.47–15.73) are found for São Nicolau basalts, which also plot out of the "Northern Island" trend for Pb isotopes (Fig. 6). The strong homogeneity in helium ratios measured in samples from Fogo island cannot be related to a sampling bias, as both pre- and post-caldera basalts covering a large surface area (Fig. 2) have been analyzed. Low helium ratios ($^4He/^3He$ down to 52,000; $R/R_A$ = 13.8) associated with relatively radiogenic lead ($^{206}Pb/^{204}Pb$ = 18.90–19.63; $^{207}Pb/^{204}Pb$ = 15.526–15.621; and $^{208}Pb/^{204}Pb$ = 38.694–39.272) were measured by Christensen et al. (2001) for the Northern Islands in their study of Santo Antão island. They were not able, however, to define the MORB-like helium signature for the Southern Islands because they only measured two samples from Fogo.

## 6. FINGERPRINTING MANTLE SOURCES

Modeling presented in section 4 based on trace element data may suggest that basalts from the Northern and Southern Islands mainly represent the partial melting in variable degrees of two distinct oceanic lithospheric sources. However, as trace element patterns (Fig. 5) and Sr-Pb-He isotope ratios (section 5) are also very similar to those of HIMU-like and EMI-like mantle end-members, we will interpret all the variations observed in this study in terms of mixing between components. This assumption is in agreement with the existence of positive trends between Th/Nb ratios and Pb isotopic compositions for both the Northern and Southern Islands of the Cape Verde archipelago (Fig. 8), which demonstrates that Th/Nb vs. Th/Tb variations here do not result solely from melting processes.

As pointed out by Gerlach et al. (1988), the fact that the isotopic signatures of samples from the Southern and Northern Islands barely overlap suggests that mantle source heterogeneities exist at the scale of ~100 to 200 km beneath the Cape Verde archipelago. In principle, linear correlations in Pb-Pb space can be interpreted as simple binary mixing between isotopically distinct reservoirs. In the Cape Verde archipelago three distinct groups are present (e.g., Fig. 6a), corresponding respectively to the Southern Islands, the Northern Islands and the São Nicolau basalts, which would require six end-members.

Figure 9 summarizes the Pb and Sr isotopic results obtained herein and compares them to a set of reference parameters, data from the literature and potential end-members. End-member labeled [1], sitting on the NHRL (Figs. 9a and 9b), is admittedly common to the Fogo-Santiago (Southern Islands) and São Vicente-Santo Antão (Northern Islands) trends. This end-member is also consistent with the Sr-Pb isotopic relationships (Fig. 9c); it has $^{206}Pb/^{204}Pb$ and $^{87}Sr/^{86}Sr$ ratios of ~19.75 and ~0.70333, respectively. The other end-members required to explain the data distribution (labeled [2] to [5] on Fig. 9) are: [2] $^{206}Pb/^{204}Pb < 18.80$ and $^{87}Sr/^{86}Sr > 0.7039$; [3] $^{206}Pb/^{204}Pb \sim 19.00$ and $^{87}Sr/^{86}Sr \sim 0.7028$; [4] $^{206}Pb/^{204}Pb \sim 19.35$ and $^{87}Sr/^{86}Sr \sim 0.7034$; [5] $^{206}Pb/^{204}Pb \sim 19.65$ and $^{87}Sr/^{86}Sr \sim 0.7028$.

We interpret the variations of the isotopic data in terms of five distinct components: recycled oceanic crust, lower mantle, subcontinental lithosphere, depleted mantle and oceanic crustal material. End-member [1] is thought to result from the mixture between 1.6-Ga recycled oceanic crust and lower mantle material, whereas end-member [2] is related to subcontinental lithospheric mantle: the mixing in variable proportions between these two end-members leads to the isotopic variations that are observed in the Southern Islands. End-member [3] corresponds to the locally depleted upper mantle; it explains, coupled with end-member [1], the variations found at São Vicente and Santo Antão (Northern Islands). We infer that end-member [4] is only slightly different from [1], as it also results from lower mantle

Table 3. Strontium and lead isotopic compositions of Cape Verde basalts.

| Sample | $^{87}Sr/^{86}Sr$ | $^{206}Pb/^{204}Pb$ | $^{207}Pb/^{204}Pb$ | $^{208}Pb/^{204}Pb$ |
|---|---|---|---|---|
| *Fogo* | | | | |
| F-01 | 0.703685 (18) | 19.105 (8) | 15.553 (9) | 38.884 (31) |
| F-02 (A) | 0.703723 (23) | 19.062 (11) | 15.563 (14) | 38.858 (47) |
| F-02 (B) | | 19.067 (8) | 15.571 (9) | 38.903 (31) |
| F-06 | 0.703738 (20) | 18.900 (8) | 15.539 (9) | 38.731 (31) |
| F-07 | 0.703789 (19) | 18.882 (11) | 15.530 (14) | 38.701 (46) |
| F-08a | 0.703734 (22) | 18.954 (8) | 15.563 (9) | 38.836 (31) |
| F-08b (A) | 0.703734 (22) | 18.936 (8) | 15.560 (9) | 38.818 (31) |
| F-08b (B) | | 18.937 (8) | 15.556 (9) | 38.810 (31) |
| F-10 | 0.703616 (24) | 19.133 (8) | 15.560 (9) | 38.917 (31) |
| F-11 (A) | 0.703665 (21) | 19.072 (8) | 15.567 (9) | 38.938 (31) |
| F-11 (B) | | 19.081 (8) | 15.565 (9) | 38.957 (31) |
| F-12 (A) | 0.703625 (20) | 19.144 (8) | 15.577 (9) | 38.974 (31) |
| F-12 (B) | | 19.139 (8) | 15.579 (9) | 38.973 (31) |
| F-12 (C) | | 19.145 (8) | 15.577 (9) | 38.978 (31) |
| F-13 | 0.703715 (19) | 19.109 (8) | 15.552 (9) | 38.901 (31) |
| F-14 | 0.703758 (19) | 18.935 (8) | 15.549 (9) | 38.772 (31) |
| F-15 (A) | 0.703738 (22) | 18.923 (11) | 15.544 (14) | 38.783 (47) |
| F-15 (B) | | 18.937 (8) | 15.558 (9) | 38.797 (31) |
| F-16 | 0.703764 (19) | 18.932 (8) | 15.537 (9) | 38.752 (31) |
| F-18 | 0.703546 (20) | 19.220 (8) | 15.563 (9) | 38.914 (31) |
| F-20 | 0.703722 (22) | 19.062 (11) | 15.548 (14) | 38.822 (47) |
| F-21 | 0.703727 (18) | 19.020 (8) | 15.554 (9) | 38.832 (31) |
| F-22 | 0.703656 (21) | 19.094 (8) | 15.561 (9) | 38.898 (31) |
| F-24 | 0.703761 (18) | 18.969 (11) | 15.562 (14) | 38.804 (47) |
| *Santiago* | | | | |
| ST-02 | 0.703486 (22) | 19.308 (12) | 15.567 (14) | 39.001 (47) |
| ST-06 | 0.703516 (19) | 19.374 (12) | 15.575 (14) | 39.097 (47) |
| ST-08 | | 19.398 (12) | 15.580 (14) | 39.190 (47) |
| ST-09 | 0.703510 (18) | 19.216 (12) | 15.549 (14) | 39.014 (47) |
| ST-10 | | 19.095 (11) | 15.539 (14) | 38.905 (47) |
| *São Vicente* | | | | |
| SV-01 | 0.703212 (21) | 19.639 (12) | 15.594 (14) | 39.361 (47) |
| SV-02 | 0.703284 (16) | 19.273 (12) | 15.619 (14) | 38.995 (47) |
| SV-02 L | 0.703222 (19) | | | |
| SV-03 | 0.703210 (20) | 19.187 (12) | 15.571 (14) | 38.763 (47) |
| SV-03 L | 0.703161 (20) | | | |
| SV-05 | 0.703256 (25) | 19.692 (12) | 15.610 (14) | 39.270 (47) |
| SV-09 | | 19.676 (12) | 15.618 (14) | 39.337 (47) |
| SV-10 | 0.703120 (20) | 19.357 (12) | 15.578 (14) | 38.964 (47) |
| SV-10 L | 0.703115 (21) | | | |
| SV-12 | 0.703279 (19) | 19.677 (12) | 15.608 (14) | 39.401 (47) |
| *São Nicolau* | | | | |
| SN-02 | 0.702990 (18) | 19.526 (12) | 15.603 (14) | 38.984 (47) |
| SN-03 | 0.703356 (20) | 19.406 (12) | 15.570 (14) | 38.946 (47) |
| SN-05 | 0.703067 (18) | 19.489 (12) | 15.573 (14) | 38.953 (47) |
| SN-10 | 0.703050 (16) | 19.538 (12) | 15.586 (14) | 38.964 (47) |
| SN-11 | 0.703130 (18) | 19.464 (12) | 15.580 (14) | 38.961 (47) |
| SN-13 | 0.703115 (15) | 19.472 (12) | 15.589 (14) | 38.981 (47) |
| SN-18 | 0.703222 (23) | 19.446 (12) | 15.580 (14) | 38.939 (47) |
| *Sal* | | | | |
| S-03 | 0.703131 (19) | 19.442 (12) | 15.575 (14) | 38.927 (47) |
| S-06 | | 19.360 (12) | 15.564 (14) | 38.990 (47) |
| S-07 | | 19.363 (12) | 15.582 (14) | 39.004 (47) |

Numbers in parentheses are $2\sigma$ errors refering to the last significant digits. Leached samples are suffixed "L".

material and recycled oceanic crust, the latter being younger (~1.1 Ga). Lastly, end-member [5] is interpreted as being oceanic crustal material with isotopic characteristics of unaltered Jurassic MORB. These last two end-members create the variations found at São Nicolau. Links between end-members [1] to [5] and the different components listed above will be discussed in detail in the following sections.

### 6.1. HIMU Signatures of the Northern Islands

Gerlach et al. (1988), Davies et al. (1989) and Christensen et al. (2001) investigated the nature of end-member [1]. These authors all concluded the presence of a HIMU or a "young HIMU" component made of ancient recycled oceanic crust. This scenario was modeled for Pb isotopes using a two-stage

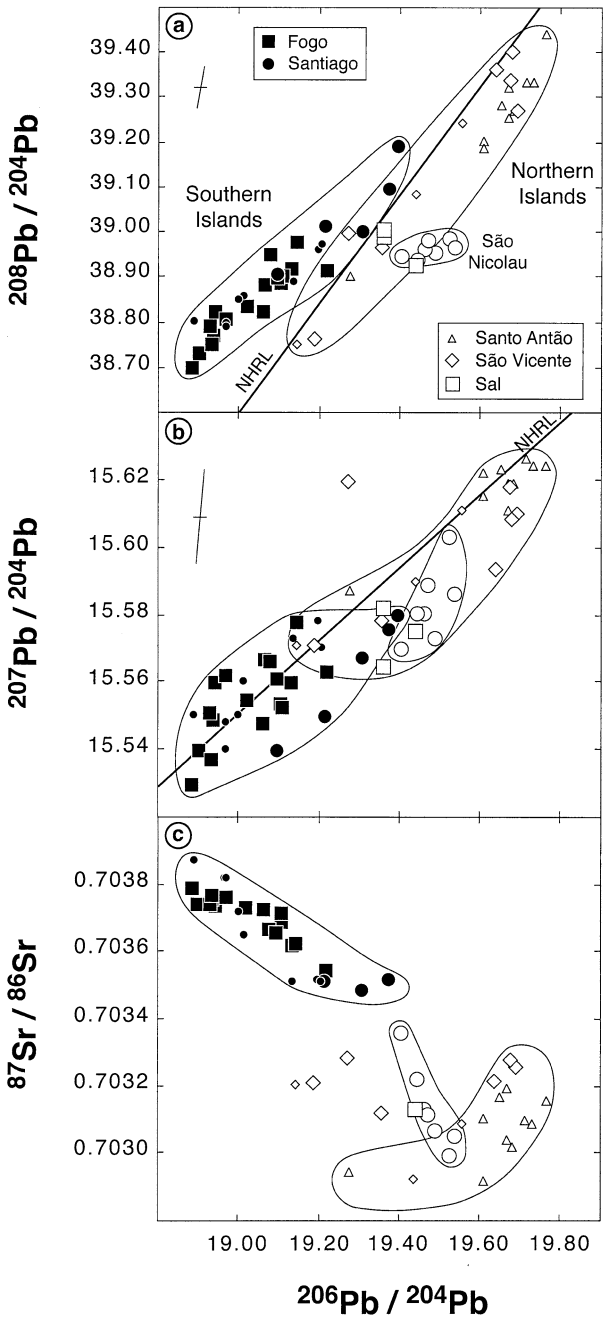


Fig. 6. (a) $^{208}Pb/^{204}Pb$, (b) $^{207}Pb/^{204}Pb$, and (c) $^{87}Sr/^{86}Sr$ vs. $^{206}Pb/^{204}Pb$ diagrams for Cape Verde samples. Large symbols identify results from this study; small symbols correspond to data in the literature (Gerlach et al., 1988). Open symbols = Northern Islands; filled symbols = Southern Islands. NHRL = Northern Hemisphere Reference Line (Hart, 1984). Typical $2\sigma$ analytical errors for Pb isotope ratios are shown in upper left hand corner.

model and the following parameters: recycled oceanic crust = 1 to 1.6 Ga; initial Canyon Diablo values; $\mu_1 \sim 8$, $\mu_2$ = mean $\mu$, $\kappa_1 \sim 3.8$, $\kappa_2 \sim 3.1$ and $T = 4.55$ Ga (Weaver, 1991; Chauvel et al., 1992; Thirlwall, 1997). The modeling does not yield appropriate Pb isotopic compositions for end-member [1]. As can be seen in Figure 9a, the recycled oceanic crust component displays, in the best case (i.e., for a recycling age of ~1.1 Ga), a $^{208}Pb/^{204}Pb$ ratio close to 39.0 for a $^{206}Pb/^{204}Pb$ of ~20.0. In other words, it has a $\Delta 8/4$ value ($\Delta 8/4$ is the deviation of the $^{208}Pb/^{204}Pb$ ratio relative to the NHRL for a given $^{206}Pb/^{204}Pb$, as defined by Hart, 1984) $< -69$, instead of –7 as predicted by the position of end-member [1]. Thus recycling of oceanic crust alone cannot result in the end-member common to the Fogo-Santiago and the São Vicente-Santo Antão trends, and mixing with another component is required to explain its isotopic composition. Mixing of recycled oceanic crust with Atlantic depleted MORB mantle (DMM) material will not increase the $\Delta 8/4$ value up to –7. This is because: (1) the DMM Pb isotopic composition has a $\Delta 8/4$ near zero; and (2) its involvement must be limited otherwise the $^{206}Pb/^{204}Pb$ ratio will not remain close to 20.0. In contrast, addition of materials such as sediments or lower mantle material would increase the $\Delta 8/4$ value as well as the $^{87}Sr/^{86}Sr$ ratio of end-member [1]. Recycled sediments (Weaver, 1991; Chauvel et al., 1992) display radiogenic $^{87}Sr/^{86}Sr$ ($\geq 0.710$), low $^{206}Pb/^{204}Pb$ ($\leq 18$) and high $\Delta 8/4$ ($>100$), whereas lower mantle material is expected to display an isotopic composition close to that of the Bulk Silicate Earth i.e., $^{87}Sr/^{86}Sr = 0.70462$, $^{206}Pb/^{204}Pb = 18.34$ and $^{208}Pb/^{204}Pb = 39.05$ ($\Delta 8/4 = 125$) (Allègre and Lewin, 1989). Evidence for the involvement of the lower mantle rather than recycled sediments in the source of the Cape Verde basalts is presented in section 6.2.

In an alternative scenario, Kokfelt et al. (1998) proposed that the HIMU end-member could correspond to subcontinental mantle that was metasomatized by carbonatitic fluids before the opening of the Atlantic Ocean. This model is supported by the presence of: (1) carbonatite intrusions on some Cape Verde islands (carbonatites are rare in oceanic settings and have only been found on the Canary and Cape Verde islands e.g., Allègre et al., 1971; Hoernle et al., 2002); and (2) the HIMU end-member in Cape Verde basalts has high U/Pb, U/Th and Zr/Hf ratios, which are typical features of carbonatites. However, Cape Verde carbonatites (Gerlach et al., 1988; Hoernle et al., 2002) do not yield Pb isotopic compositions corresponding to end-member [1] (Figs. 9a and 9b). Furthermore, Cape Verde basalts yield Zr/Hf ratios in the range of 36 to 59 (mean = 45; data from Gerlach et al., 1988, and Table 1). These are values similar to those reported by Turner et al. (1997) for the Azores archipelago (41–50; mean = 44) where no carbonatites occur. Higher Zr/Hf ratios, $\gg 50$ (Woodhead, 1996), would be expected if carbonatized mantle was present in the source of the Cape Verde basalts. In the same way, the lack of correlation between Zr/Hf and $^{206}Pb/^{204}Pb$ (figure not shown) excludes the involvement of a carbonatite-like component in the most radiogenic $^{206}Pb/^{204}Pb$ samples of the Cape Verde archipelago. Such a conclusion was also defended by Jørgensen and Holm (2002) in a recent study of São Vicente island. They showed that two distinct sources were required to explain the HIMU-like signature of basalt and carbonatite samples, even if carbonatitic fluids could affect some basalt compositions to a lesser extent.

The recycling of ~1.6-Ga-old oceanic crust with carbonate sediments was recently proposed by Hoernle et al. (2002) to explain major, trace element and isotopic variations in calcio-carbonatites (that is excluding dolomitic-carbonatites which may be secondary in origin) from the Cape Verde archipelago.

Table 4. Helium concentrations (in $10^{-8}$ cm$^3$ STP/g) and blank corrected isotopic ratios.

| Sample | | Weight (g) | $^4$He ($\times 10^{-8}$) | $R/R_A$ | $\sigma$ | $^4$He/$^3$He | $\sigma$ | % blank |
|---|---|---|---|---|---|---|---|---|
| *Fogo* | | | | | | | | |
| F-01 | Ol. | 0.297 | 0.70 | 8.53 | 0.09 | 84,706 | 894 | 2.4 |
| | CPX | 0.286 | 0.24 | 6.88 | 0.13 | 105,021 | 1984 | 7.3 |
| F-02 | Ol. | 0.346 | 0.33 | 7.90 | 0.12 | 91,519 | 1437 | 4.4 |
| | CPX | 0.328 | 0.75 | 7.91 | 0.09 | 91,322 | 1062 | 2.0 |
| | *mp* | 0.306 | 0.41 | 4.89 | 0.07 | 147,669 | 1992 | 4.0 |
| F-05 | Ol. | 0.186 | 0.69 | 7.53 | 0.09 | 95,955 | 1147 | 3.9 |
| | CPX | 0.057 | 1.01 | 8.56 | 0.19 | 84,409 | 1874 | 8.7 |
| F-07 | Ol. | 0.100 | 5.12 | 8.28 | 0.06 | 87,264 | 632 | 1.0 |
| | *mp* | 0.083 | 1.93 | 7.90 | 0.09 | 91,450 | 1019 | 3.1 |
| F-08 | Ol. | 0.088 | 2.67 | 8.06 | 0.10 | 89,646 | 1112 | 2.1 |
| | *mp* | 0.066 | 0.16 | 4.66 | 0.50 | 155,185 | 16,498 | 46.1 |
| F-11 | Ol. | 0.294 | 0.10 | 6.31 | 0.23 | 114,562 | 4087 | 16.6 |
| | *mp* | 0.262 | 0.13 | 8.44 | 0.32 | 85,609 | 3286 | 14.2 |
| | Ol. | 0.281 | 0.12 | 7.23 | 0.26 | 99,909 | 3550 | 14.7 |
| | | *Re-crush* | 0.04 | 9.54 | 0.85 | 75,746 | 6773 | 46.8 |
| | Ol. | 0.156 | 0.38 | 8.04 | 0.21 | 89,869 | 2347 | 8.5 |
| F-13 | Ol. | 0.126 | 0.30 | 7.76 | 0.29 | 93,147 | 3458 | 13.3 |
| | | *Re-crush* | 0.05 | 6.90 | 0.98 | 104,777 | 14,860 | 83.7 |
| | CPX | 0.211 | 0.89 | 7.74 | 0.11 | 93,352 | 1327 | 2.6 |
| | *mp* | 0.186 | 0.44 | 5.90 | 0.13 | 122,486 | 2762 | 6.2 |
| | CPX | 0.252 | 1.45 | 7.96 | 0.09 | 90,772 | 1026 | 1.4 |
| F-15 | Ol. | 0.083 | 4.39 | 8.15 | 0.07 | 88,677 | 762 | 1.4 |
| F-16 | Ol. | 0.076 | 4.58 | 8.24 | 0.08 | 87,687 | 851 | 1.4 |
| F-18 | Ol. | 0.244 | 1.49 | 7.91 | 0.06 | 91,346 | 693 | 1.4 |
| F-20 | Ol. | 0.171 | 0.36 | 8.40 | 0.14 | 86,068 | 1425 | 8.1 |
| F-21 | Ol. | 0.075 | 1.37 | 8.04 | 0.12 | 89,869 | 1341 | 4.9 |
| F-24 | Ol. | 0.163 | 1.23 | 7.76 | 0.10 | 93,135 | 1152 | 2.5 |
| *Santiago* | | | | | | | | |
| ST-02 | Ol. | 0.079 | 0.17 | 8.24 | 0.42 | 87,719 | 4515 | 38.5 |
| ST-06 | Ol. | 0.157 | 0.04 | 3.90 | 0.80 | 185,505 | 38,054 | 75.0 |
| | | *Re-crush* | 0.02 | 7.66 | 2.77 | 94,327 | 34,160 | 159.2 |
| | *mp* | 0.135 | 0.48 | 29.20 | 0.27 | 24,741 | 231 | 7.7 |
| ST-08 | Ol. | 0.193 | 0.19 | 8.31 | 0.23 | 86,917 | 2405 | 13.4 |
| | *mp* | 0.168 | 0.58 | 6.36 | 0.21 | 113,697 | 3686 | 5.2 |
| ST-09 | CPX | 0.095 | 0.11 | 1.38 | 0.51 | 522,824 | 192,938 | 47.6 |
| | *mp* | 0.075 | 15.28 | 0.18 | 0.01 | 4,128,819 | 117,966 | 0.4 |
| *São Vicente* | | | | | | | | |
| SV-01 | Ol. | 0.230 | 1.01 | 9.07 | 0.11 | 79,628 | 965 | 2.1 |
| | | *Re-crush* | 0.06 | 6.45 | 0.34 | 111,970 | 5865 | 34.3 |
| SV-02 | Ol. | 0.194 | 0.60 | 9.95 | 0.12 | 72,617 | 876 | 4.3 |
| | CPX | 0.211 | 0.25 | 9.07 | 0.18 | 79,663 | 1581 | 9.5 |
| | | *Re-crush* | 0.09 | 9.82 | 0.43 | 73,579 | 3222 | 25.8 |
| SV-03 | Ol. | 0.159 | 0.92 | 10.83 | 0.64 | 66,717 | 3943 | 3.4 |
| SV-05 | Ol. | 0.177 | 0.06 | 10.70 | 0.83 | 67,527 | 5238 | 48.4 |
| | | *Re-crush* | 0.02 | 10.81 | 1.52 | 66,840 | 9398 | 136.5 |
| SV-09 | Ol. | 0.161 | 0.64 | 11.08 | 0.18 | 65,211 | 1059 | 4.8 |
| SV-10 | Ol. | 0.092 | 0.43 | 12.27 | 0.77 | 58,887 | 3695 | 12.8 |
| SV-12 | Ol. | 0.097 | 1.41 | 8.41 | 0.13 | 85,905 | 1369 | 3.7 |
| *São Nicolau* | | | | | | | | |
| SN-02 | Ol. | 0.302 | 5.00 | 12.94 | 0.04 | 55,838 | 173 | 0.3 |
| | *mp* | 0.245 | 4.06 | 12.87 | 0.07 | 56,133 | 301 | 0.5 |
| SN-03 | Ol. | 0.173 | 0.41 | 14.03 | 0.20 | 51,515 | 742 | 7.1 |
| | | *Re-crush* | 0.02 | 10.87 | 1.87 | 66,447 | 11,421 | 132.2 |
| SN-05 | Ol. | 0.148 | 1.88 | 15.24 | 0.06 | 47,411 | 187 | 1.8 |
| SN-10 | Ol. | 0.257 | 2.33 | 15.73 | 0.09 | 45,928 | 251 | 0.8 |
| | | *Re-crush* | 0.29 | 15.58 | 0.19 | 46,367 | 571 | 6.7 |
| SN-11 | Ol. | 0.044 | 1.39 | 10.47 | 0.21 | 69,031 | 1359 | 8.1 |
| SN-13 | Ol. | 0.330 | 0.27 | 12.00 | 0.14 | 60,212 | 702 | 5.7 |
| *Sal* | | | | | | | | |
| S-03 | Ol. | 0.058 | 0.40 | 9.55 | 0.30 | 75,659 | 2377 | 21.5 |
| S-06 | Ol. | 0.280 | 1.03 | 6.98 | 0.05 | 103,590 | 772 | 1.7 |
| S-07 | Ol. | 0.237 | 0.94 | 9.97 | 0.12 | 72,486 | 880 | 2.2 |
| | | *Re-crush* | 0.34 | 9.74 | 0.13 | 74,175 | 952 | 6.2 |
| | *mp* | 0.200 | 2.52 | 42.64 | 0.16 | 16,947 | 64 | 1.0 |
| | Ol. | 0.166 | 1.56 | 9.98 | 0.13 | 72,416 | 973 | 1.9 |

$R/R_A$ is the $^3$He/$^4$He ratio normalized to the atmospheric value of $1.384 \times 10^{-6}$. Uncertainty in the helium concentrations is ~5%. The last column gives the percentages of $^4$He blank contribution, $\sim 5 \times 10^{-11}$ cm$^3$ STP, relative to sample content. Measurements were completed on olivine (Ol.) and clinopyroxene (CPX). "Re-crush" identifies samples which were crushed a second time, sequentially, in order to verify for complete extraction and identify any contributions from radiogenic helium. The experiments done by melting of remaining crushed powders are labeled "mp".

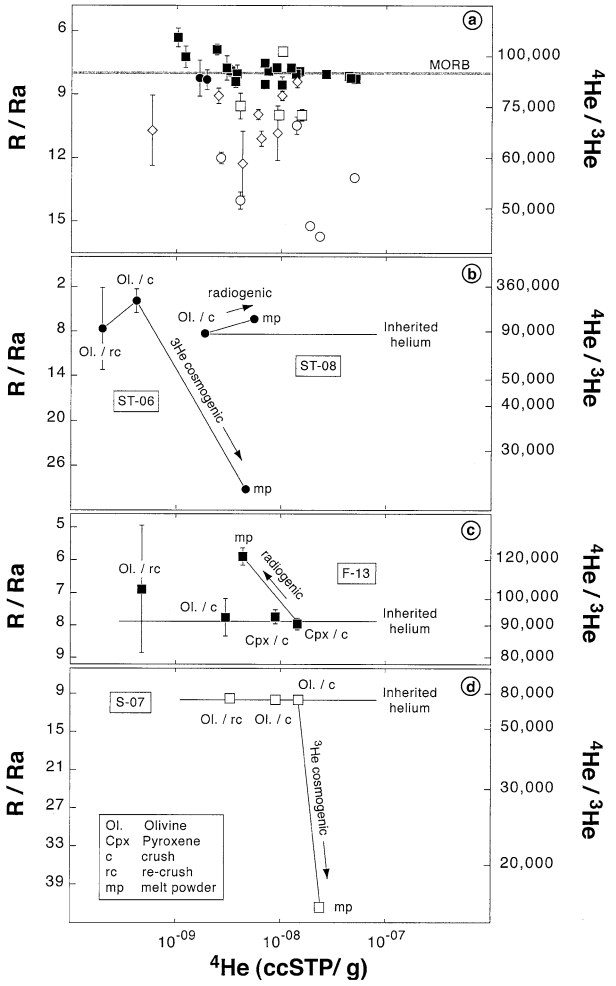


Fig. 7. Diagrams of $R/R_A$ (and absolute $^4He/^3He$) ratios vs. $^4He$ concentrations for studied Cape Verde basalts. (a) Results for all olivine and pyroxene separates from samples analyzed using the crushing protocol compared to the MORB reference composition; symbols as in Figure 6. (b-d) Results for olivines and pyroxenes from samples ST-06, ST-08, F-13 and S-07; key to symbols and analytical steps in (d). The crushing of olivines and pyroxenes from samples F-13 and S-07 yields similar $R/R_A$ ratios. This implies that the $^4He/^3He$ ratios obtained by crushing are representative of the magmatic values (inherited helium). Melt products (mp) indicate that excesses of radiogenic $^4He$ and cosmogenic $^3He$ are present in the samples.

In the following sections we, too, will use the figure of 1.6 Ga for the recycled oceanic crust component(s).

### 6.2. Lower Mantle Material in the Plume Source

The low $^4He/^3He$ ratios determined in basalts from the Northern Islands ($R/R_A$ up to 15.73) imply the involvement of a lower mantle component in the plume source. Mid-ocean ridge basalts have similar $^4He/^3He$ values of 88,000 ± 5000 ($R/R_A \sim 8 \pm 1$; cf. Kurz et al., 1982; Allègre et al., 1995) representative of the outgassed upper mantle; conversely, OIB values as low as 17,000 ($R/R_A \sim 43$; cf. Breddam and Kurz, 2001) are attributed to a relatively undegassed reservoir thought to be the lower mantle (Kurz et al., 1982).

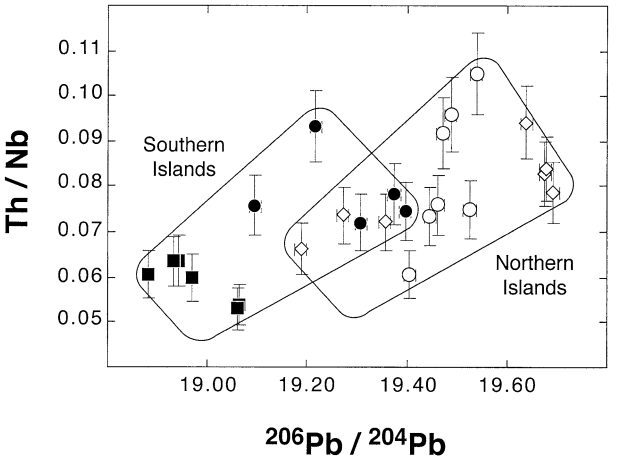


Fig. 8. Th/Nb vs. $^{206}Pb/^{204}Pb$ variations for Cape Verde samples. The two positive trends which are observed for basalts from the Northern and Southern Islands suggest that Th/Nb ratios do not reflect melting processes, but rather mixing between two distinct end-members.

We assume that present-day Pb and Sr isotope compositions of the lower mantle (LM) are similar to those of the Bulk Silicate Earth (BSE), reflecting binary mixing between BSE material and a fraction of depleted mantle. Mass balance calculations which are detailed in the Appendix lead to the following isotopic signature: $^{206}Pb/^{204}Pb = 18.30$, $^{207}Pb/^{204}Pb = 15.546$ ($\Delta 7/4 \sim 7$), $^{208}Pb/^{204}Pb = 38.97$ ($\Delta 8/4 \sim 120$) and $^{87}Sr/^{86}Sr = 0.70429$. This allows us to verify that the Pb and Sr isotopic compositions of end-member [1] can be explained by mixing between 1.6-Ga recycled oceanic crust and lower mantle material. Assuming that the 1.6-Ga recycled oceanic crust component (ROC) had $^{206}Pb/^{204}Pb = 21.17$, $^{207}Pb/^{204}Pb = 15.72$, $^{208}Pb/^{204}Pb = 39.92$ ($\mu_1 = 8$, $\mu_2 = 21$, $\kappa_1 = 3.8$ and $\kappa_2 = 3.05$) and $^{87}Sr/^{86}Sr = 0.70290$, solid-state mixing of ROC and LM in the proportion of 42:58 (with Pb contents of 0.2 and 0.3 ppm, and Sr contents of 20 and 60 ppm, respectively) yields Pb and Sr isotopic ratios close to those expected for end-member [1]: $^{206}Pb/^{204}Pb = 19.758$; $^{207}Pb/^{204}Pb = 15.636$ ($\Delta 7/4 = 0.3$); $^{208}Pb/^{204}Pb = 39.454$ ($\Delta 8/4 = -6.1$); and $^{87}Sr/^{86}Sr = 0.70334$.

In the same way, assuming a $^4He$ content of $1 \times 10^{-4}$ cm$^3$ STP/g (Allègre et al., 1986) and a $R/R_A \sim 43$ ($^4He/^3He = 16{,}800$) for lower mantle material as well as a $^4He$ production of $3 \times 10^{-5}$ cm$^3$ STP/g (cf. radioactive production equation in Moreira et al., 1999, with [U] = 0.09 ppm and Th/U = 3.03) and $R/R_A = 0$ for the recycled oceanic crust component, the mixture in the proportion of 42:58 yields a $^4He/^3He$ ratio of ~20,600 ($R/R_A \sim 35$) for end-member [1] (Fig. 10).

Lower mantle material is possibly entrained into plumes by viscous coupling from a boundary layer in a mass proportion which does not exceed 10% (Davaille, 1999). Recent numerical simulations by Farnetani et al. (2002) have shown that heterogeneities present in the source region of plumes evolve as narrow filaments while rising, but are not homogenized. End-member [1], however, presents a well-constrained signature for both Pb and Sr isotopes suggesting that proportions of recycled oceanic crust and lower mantle material are relatively constant over the time interval of the

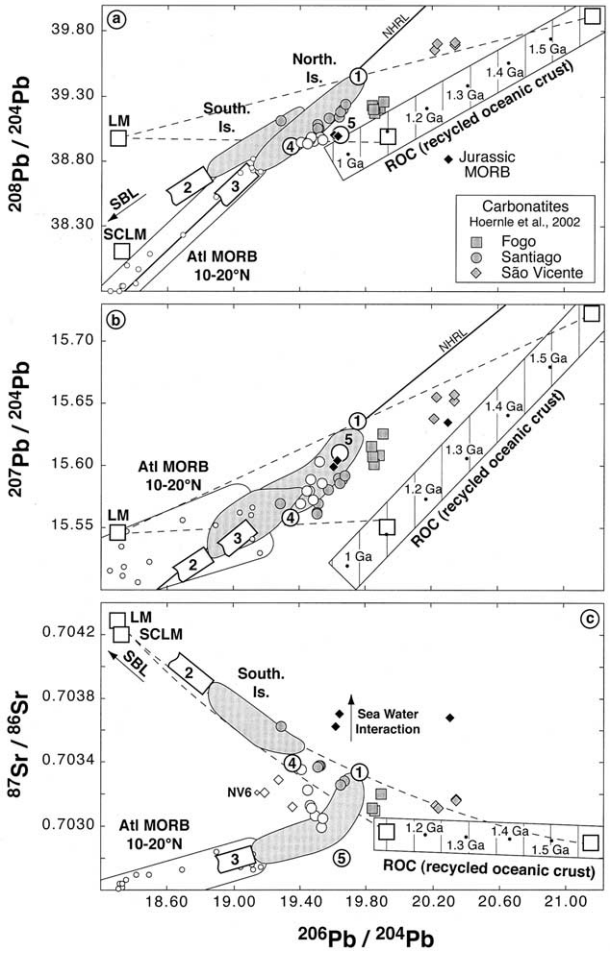


Fig. 9. Pb and Sr isotopic compositions of studied Cape Verde basalts in relation to potential end-members (labeled [1] to [5]) and data from the literature. (a) $^{208}Pb/^{204}Pb$ vs. $^{206}Pb/^{204}Pb$; (b) $^{207}Pb/^{204}Pb$ vs. $^{206}Pb/^{204}Pb$; and (c) $^{87}Sr/^{86}Sr$ vs. $^{206}Pb/^{204}Pb$ diagrams. Grey fields = data from the Southern and Northern Island groups (cf. Fig. 6). Large open circles = data for São Nicolau basalts. Small open circles = Atlantic MORB collected between latitudes 10 and 20°N (Dosso et al., 1993). Black diamonds = Jurassic MORB sampled on Santiago island (Gerlach et al., 1988). Grey symbols = carbonatites on the Fogo, Santiago and São Vicente islands (Hoernle et al., 2002). NHRL = Northern Hemisphere Reference Line of Hart (1984); LM = Lower Mantle (see Appendix for calculations); SCLM = SubContinental Lithospheric Mantle from Zartman and Haines (1988); and SBL = Smoky Butte Lamproites (Fraser et al., 1985/1986). Striped fields = Recycled Oceanic Crust (ROC), considering a two-stage model with $\mu_1 = 8$, $\mu_2 = 21$, $\kappa_1 = 3.8$, $\kappa_2 = 3.05$ and an age ranging from 1 to 1.6 Ga. End-member [1] is interpreted as resulting from the mixture between 1.6 Ga recycled oceanic crust and lower mantle material; end-members [2] and [3] correspond to subcontinental lithosphere and depleted local upper mantle, respectively; end-member [4] is also interpreted as resulting from the mixture between oceanic crust and lower mantle, but recycling age is younger (~1.1 Ga); end-member [5] is thought to be oceanic crustal material having isotopic characteristics of unaltered Jurassic MORB.

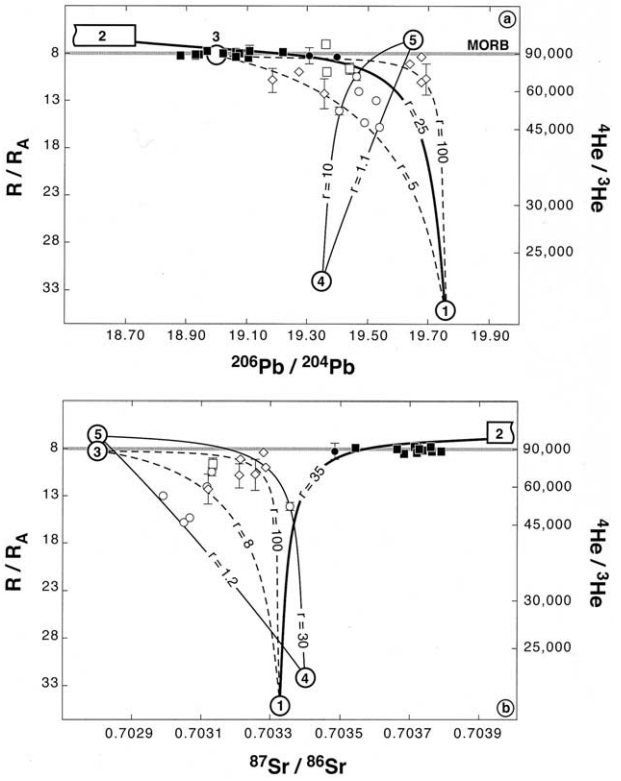


Fig. 10. (a) $R/R_A$ ($^4He/^3He$) vs. $^{206}Pb/^{204}Pb$; and (b) $R/R_A$ ($^4He/^3He$) vs. $^{87}Sr/^{86}Sr$ for Cape Verde samples (symbols as in Fig. 6). Potential end-members which allow observed isotopic variations to be explained for both the Northern and Southern Islands are labeled [1] to [5] (see Fig. 9). Also reported are the *r*-values (Langmuir et al., 1978) which determine the curvature of mixing lines: these are the $(He/Pb)_a/(He/Pb)_b$ and $(He/Sr)_a/(He/Sr)_b$ ratios between two end-members a and b.

samples analyzed by Gerlach et al. (1988) and this study. These constant proportions imply a two-stage history for Cape Verde basalts: firstly end-member [1] has to be generated, possibly in a magma chamber. Secondly, it is mixed in variable proportions with another component, whose identity depends on the group of islands which is considered. Consequently, the proportions of recycled oceanic crust and lower mantle material which are required to model the isotopic composition of end-member [1] (42:58) do not necessarily correspond to the proportions that are present in the Cape Verde plume.

It should be noted that recycling of oceanic crust is possibly accompanied by recycling of oceanic lithosphere (Moreira and Kurz, 2001). The latter has a low Pb content as well as an unradiogenic signature. Consideration of recycled oceanic crust (ROC) and lithosphere together instead of oceanic crust alone results in a less radiogenic Pb composition for the ROC component (Fig. 9); it also decreases the proportion of lower mantle material which is required to model the isotopic composition of end-member [1]. Nevertheless its $^4He/^3He$ ratio will remain low (close to 20,000) due to the high $^3He$ content of lower mantle material.

To summarize, we propose that end-member [1] corresponds to 1.6-Ga recycled oceanic crust, to which is added a fraction of lower mantle material. This model is in agreement with Christensen et al. (2001), who also proposed the involvement of recycled oceanic crust and lower mantle.

### 6.3. Subcontinental Lithospheric Material as the EMI End-Member

The trace element patterns for Fogo and Santiago are very similar to those of Tristan da Cunha lavas (Fig. 5), suggesting that end-member [2] is an EMI-like source. Gerlach et al. (1988) and Davies et al. (1989) explained this feature by the occurrence of subcontinental mantle beneath the Southern Islands. However, they did not address the question of whether such material was present beneath the Cape Verde archipelago as a passive heterogeneity or was supplied by the plume. In their study of Fogo, Kokfelt et al. (1998) also argued for a subcontinental origin of the EMI-like signature, proposing that it represented delaminated continental lithosphere left behind in the mantle during the early opening of the Atlantic, following the model of Cohen and O'Nions (1982) and McKenzie and O'Nions (1983). Finally, Christensen et al. (2001) also concluded that an EMI component must be present in the source of Southern Island basalts. Linking subcontinental lithosphere to end-member [2] is supported by the high Ba/La (7–23, mean = 14) and low La/Nb ratios (0.54–0.89, mean = 0.71) measured in Fogo and Santiago basalts (data from Gerlach et al., 1988, and this study). Furthermore, coupled with the fact that $^{143}Nd/^{144}Nd$ ratios measured in Fogo basalts are low (~0.51260, cf. Gerlach et al., 1988; Kokfelt et al., 1998), both Fogo and Santiago samples are aligned in Pb-Pb space (Figs. 9a and 9b) with the expected composition of the subcontinental lithosphere (Zartman and Haines, 1988) as well as with Smoky Butte lamproites (data from Fraser et al., 1985/1986) which are thought to sample this reservoir (Hawkesworth et al., 1990). Smoky Butte lamproites have been interpreted as sampling subcontinental lithosphere enriched by the introduction of small volumes of silicate melts. They can be modeled for Pb isotopes using a two-stage evolution where decreasing of the $\mu_2$ value relative to $\mu_1$ reflects the low U/Pb ratio in the enriching agent or the stabilization of low U/Pb phases (Fraser et al., 1985/1986). Their Pb isotopic compositions, however, plot quite far from the expected values of end-member [2], and do not agree with trace element data which suggest a high proportion of the EMI-like end-member relative to [1] in the source of the Southern Islands. Using a similar evolution ($\mu_2 <$ 7.5, cf. Fraser et al., 1985/1986) for a second stage between 1 and 2.5 Ga does not allow the generation of radiogenic Pb isotopic ratios ($^{206}Pb/^{204}Pb$ close to 18.5) which would remain aligned with those of Fogo and Santiago. Thus a more complex evolution where a decrease of the U/Pb ratio is followed by a more recent increase (Fraser et al., 1986/1986) has to be considered. In addition to unradiogenic Pb, Smoky Butte lamproites also display relatively high Sr values ($0.70587 < {}^{87}Sr/^{86}Sr < 0.70633$) which are consistent with Fogo and Santiago data (Fig. 9c). For helium isotopes, we refer to the recent study of Gautheron and Moreira (2002) who demonstrate the homogeneous signature of the subcontinental mantle with a mean $^4He/^3He$ ratio of 118,000 ± 15,500 ($R/R_A$ = 6.1 ± 0.9). Our measurements show lower values ($^4He/^3He \sim 90{,}000$) which certainly reflect mixing with the lower mantle material which makes up end-member [1]. It is surprising, however, to obtain the $^4He/^3He$ ratio of MORB, although this can be viewed in relation to Hawaiian postshield lavas which display MORB-like helium values (Kurz et al., 1996) but Sr and Pb isotopic signatures, demonstrating the involvement of sediments.

### 6.4. Mixing With Depleted Mantle Material

Albeit the least radiogenic samples from São Vicente and Santo Antão plot far from the depleted mantle value (DMM), the Northern Islands (excluding São Nicolau) point toward the composition of the nearest Atlantic MORB (10–20°N) in Pb-Pb space (Figs. 9a and 9b). The latter were interpreted as a mixture between a regional enriched component and DMM, but are not related to the Cape Verde plume (Dosso et al., 1993). Thus end-member [3] could represent locally depleted mantle material, as previously proposed by Gerlach et al. (1988) who argued that a minor DMM contribution would even explain the low Ba/La (6–16, mean = 11) and Ba/Nb (5–10, mean = 8) ratios measured in São Vicente and Santo Antão basalts.

It is, however, noteworthy that samples SV-02, SV-03, SV-10 and alkali basalt NV6 (Gerlach et al., 1988) from São Vicente display $^{87}Sr/^{86}Sr$ ratios higher than that expected from a DMM contribution (Fig. 9c). These four samples are all Quaternary or post-erosional basalts. Several authors have proposed that Hawaiian post-erosional lavas may not represent the plume itself, but rather the oceanic lithosphere (e.g., Chen and Frey, 1985; Lassiter et al., 2000). Low $^4He/^3He$ ratios measured for the three São Vicente basalts ($R/R_A$ = 9.95–12.27) do not allow us to rule out significant melt input from the plume. Leaching experiments that were performed on these basalts, which were all collected near the ocean shore (Fig. 2), argue against seawater alteration, as leaching residues have Sr signatures comparable with those of the bulk samples (Table 3). It is more likely that high Sr values, coupled with less radiogenic Pb, relative to other São Vicente samples result from interaction with Quaternary sedimentary deposits belonging, together with recent lavas, to the "Monte Verde" complex as defined by Serralheiro (1976) and Trindade et al. (2001), which is where samples SV-03 and SV-10 were collected. Alternatively, these basalts could reflect carbonatite assimilation, as has been recently proposed for some lavas from São Vicente by Jørgensen and Holm (2002).

### 6.5. São Nicolau: Evidence for Oceanic Crustal Material Assimilation?

The Pb and Sr isotopic compositions of basalts from São Nicolau show small but significant variations defining good correlations in both Pb-Pb and Sr-Pb spaces (Fig. 6). The alignment of the data suggests binary mixing of isotopically distinct end-members. The end-members must differ in isotopic compositions from those postulated for São Vicente and Santo Antão lavas. Trace element characteristics (HIMU-like) are, however, quite similar for all the Northern Islands (Fig. 5).

As end-member [4] plots on the São Vicente-Santo Antão trend on the $^{208}Pb/^{204}Pb$ vs. $^{206}Pb/^{204}Pb$ diagram (Fig. 9a), its isotopic composition may result from the mixture of 1.6-Ga recycled oceanic crust and lower mantle material, to which is added some local upper mantle (see sections 6.2 and 6.4). Addition of depleted material should result in a decrease of the Sr isotope signature. However, a more radiogenic value is observed relative to [1], thus dismissing such a hypothesis for

the origin for end-member [4]. With respect to the observations related to trace elements (Fig. 5), it is more likely that end-member [4] results from the mixture of ancient recycled oceanic crust and lower mantle material only. Its Pb and Sr isotopic composition can be modeled, for example, with a younger recycled oceanic crust of 1.1 Ga. Indeed, using similar characteristics for both recycled oceanic crust and lower mantle to that described in section 6.2, solid-state mixing in the proportion of 52:48 yields isotopic ratios close to those expected for end-member [4] i.e., $^{206}Pb/^{204}Pb \sim 19.30$, $^{207}Pb/^{204}Pb \sim 15.55$, $^{208}Pb/^{204}Pb \sim 39.00$ and $^{87}Sr/^{86}Sr \sim 0.7033$ (Fig. 9). This also results in a $^{4}He/^{3}He$ composition of 22,600 ($R/R_A \sim 32$), consistent with the low helium ratios measured in São Nicolau samples (Fig. 10).

In their study of the Cape Verde archipelago, Gerlach et al. (1988) analyzed Late Jurassic basalts from Santiago which were interpreted as N-type "normal" MORB (Gerlach et al., 1988; Mendes and Silva, 2001). Their initial $^{143}Nd/^{144}Nd$ ratios range from 0.51282 to 0.51288 and are close to those expected for Late Jurassic MORB. However, their initial Sr isotopic compositions (0.70284–0.70340) are more radiogenic than expected, and were interpreted to reflect seawater alteration. Pb isotopic compositions, although heterogeneous, are radiogenic with $^{206}Pb/^{204}Pb = 19.611$ to 20.303, $^{207}Pb/^{204}Pb = 15.599$ to 15.635 and $^{208}Pb/^{204}Pb = 38.820$ to 39.004; $\Delta 7/4$ and $\Delta 8/4$ values are close to –1.5 and –35 (or lower), respectively, thus similar to those expected for end-member [5]. The $^{87}Sr/^{86}Sr$ ratio of unaltered Jurassic MORB can be estimated from both the measured $^{143}Nd/^{144}Nd$ and the Sr-Nd correlation defined by Cape Verde basalts (Gerlach et al., 1988). This yields a value of ~0.7028 which, coupled with Pb isotopic compositions, corresponds to end-member [5] in the $^{87}Sr/^{86}Sr$ vs. $^{206}Pb/^{204}Pb$ diagram (Fig. 9c). Based on isotopic arguments, we thus propose that São Nicolau samples could reflect the mixing between end-member [4] and oceanic crustal material having an isotopic signature similar to that of unaltered Jurassic MORB, and forming the deeper part of the basement beneath the Cape Verde Islands. Inferring that end-member [5] indeed represents Late Jurassic MORB, its helium isotopic composition must be MORB-like, or radiogenic, due to degassing at the ridge and possible production of radioactive $^{4}He$ (Fig. 10).

## 7. GEOCHEMICAL AND DYNAMIC ASPECTS OF THE CAPE VERDE PLUME

Kokfelt et al. (1998) proposed that the Cape Verde plume provided heat but not a distinct magma source. Evidence for lower mantle material in the Northern Island basalts with low $^{4}He/^{3}He$ signatures argues against such a model. Instead, we consider, based on Sr, Pb and He isotopes, the involvement of at least two components at the source of the plume: recycled oceanic crust and lower mantle material.

The Southern Island basalts reflect preferential mixing of this material (recycled oceanic crust + lower mantle) with relatively high proportions of subcontinental lithosphere, yielding EMI-like trace element patterns, displacing isotopic compositions toward less radiogenic Pb and higher Sr, and compensating for the primitive He signature of the lower mantle. Conversely, the Northern Island samples present isotopic compositions and trace element patterns which are consistent with mixing between the two plume components and depleted material (Figs. 9 and 10).

Two distinct models can be proposed for the presence of the subcontinental lithospheric mantle (SCLM) component. In the first, the SCLM is present in the plume source: Gerlach et al. (1988) envisaged the storage of cold, dense subcontinental lithosphere at the 670-km discontinuity, the presence of whose signature is suppressed in the Northern Islands due to a lower degree of partial melting. In the second model, the SCLM is present in the oceanic lithosphere as a passive heterogeneity, and only the Southern Island basalts sample it. In such a case, the subcontinental lithosphere would have been recycled into the upper mantle by delamination during the opening of the Central Atlantic. One argument against model (1) is the necessity to preserve heterogeneities in the plume head: the SCLM on the one hand, recycled oceanic crust and lower mantle material on the other. However, a recent study has shown that heterogeneities initially present in the plume source are not homogenized during the ascent (Farnetani et al., 2002). Model (2) is also paradoxical; all samples from the Southern Islands (Fogo, Santiago as well as Maio, cf. Gerlach et al., 1988; Davies et al., 1989) present EMI-like characteristics, indicating that delaminated subcontinental lithosphere, although not sampled by the Northern Islands, occurs over a scale of at least ~150 km. This feature could be due to a tectonic control since the Northern and Southern Islands are related to different geological structures (see section 2).

The case of São Nicolau appears to be more problematic. Although basalts sampled on this island present trace element characteristics similar to those of São Vicente and Santo Antão, isotopic compositions for both Pb and Sr are significantly different. We propose that these compositions reflect mixing in constant proportions of ancient recycled oceanic crust (~1.1 Ga) and lower mantle, with assimilation of oceanic crustal material (Figs. 9 and 10). The involvement of recycled oceanic crust dating back to ~1.1 Ga, together with that of 1.6 Ga, has to be put in perspective with the source heterogeneity of the Cape Verde plume. Nevertheless, future analyses of new samples will help to ascertain the nature of the source components involved in São Nicolau volcanism.

Christensen et al. (2001) envisaged a source composition for Santo Antão similar to that proposed above (1.6-Ga recycled oceanic crust + lower mantle), although they suggested the presence of younger recycled oceanic crust (age not given), arguing that mixing of extreme HIMU (following the terminology of Thirlwall, 1997) and DMM material will not produce Pb isotopic compositions and $^{87}Sr/^{86}Sr$ ratios consistent with the most radiogenic samples of Santo Antão. They did not consider, however, that a lower mantle contribution would also increase $\Delta 7/4$ and $\Delta 8/4$ values and $^{87}Sr/^{86}Sr$ ratios without strongly decreasing the $^{206}Pb/^{204}Pb$. We thus think there is no clear evidence for the presence of a so-called "young HIMU" component in the source of Santo Antão basalts. Furthermore, the involvement of 1.6-Ga recycled oceanic crust in the source of the Cape Verde basalts is consistent with the model proposed by Hoernle et al. (2002) to explain the Sr and Pb isotopic compositions of Fogo, Santiago and São Vicente carbonatites. Christensen et al. (2001) also proposed two hypotheses to explain the primitive He signatures of Santo Antão samples, either by entrainement of lower mantle material or He migra-

tion. Our model favors the first proposition, as it requires the involvement of lower mantle material for Pb and Sr isotopes.

## 8. SUMMARY

Pb-Sr-He isotope data show intra-island variations that require at least five distinct end-members for the source of the Cape Verde basalts. We propose that the isotopic compositions measured in the Northern Island samples are best explained by the mixture of 1.6-Ga recycled oceanic crust and lower mantle material which is added in variable proportions to entrained upper mantle material during the plume ascent. We also show that compositions of the Southern Islands require the presence of recycled oceanic crust and lower mantle material, albeit isotopic signatures are dominated by another component, identified as the subcontinental lithospheric mantle. Results for São Nicolau basalts are only slightly different from those of other Northern Islands (Santo Antão and São Vicente); they suggest, however, the assimilation of oceanic crustal material with an isotopic signature similar to that of unaltered Jurassic MORB. The model developed here confirms the previous studies of Gerlach et al. (1988) and Davies et al. (1989) who argued for the presence of old, recycled oceanic crust and subcontinental lithospheric material in the source of the Cape Verde basalts. It also extends their conclusions since we provide arguments for the involvement of the lower mantle and propose that both the HIMU- and EMI-like end-members may be present in the plume. Our model disagrees, however, with the conclusions of Kokfelt et al. (1998) and Christensen et al. (2001). The former restrict the plume to a heat source; the latter propose a younger age for the recycled oceanic crust (young HIMU) as well as an absence of (or minor) contribution from entrained depleted material for Santo Antão island.

*Acknowledgments*—The authors thank C. J. Allègre, B. Bourdon, A. Davaille, C. Farnetani, C. H. Langmuir and P. Schiano for constructive discussions and suggestions on the manuscript. R.D. is grateful to A. Simonetti for skilled assistance during the MC-ICP-MS measurements. Helium analyses were performed with the help of J. Curtice. R.D. was supported by a Lavoisier postdoctoral fellowship and M.M. by a WHOI fellowship. F. van Wik de Vries helped us for the quality of the manuscript. This paper was improved by critical comments by D. W. Peate and two anonymous reviewers. This is IPGP contribution 1889.

*Associate editor:* M. A. Menzies

## REFERENCES

Allègre C. J. (1987) Isotope geodynamics. *Earth Planet. Sci. Lett.* **86,** 175–203.

Allègre C. J. and Turcotte D. L. (1985) Geodynamical mixing in the mesosphere boundary layer and the origin of oceanic islands. *Geophys. Res. Lett.* **12,** 207–210.

Allègre C. J. and Turcotte D. L. (1986) Implications of a two-component marble-cake mantle. *Nature* **323,** 123–127.

Allègre C. J. and Lewin E. (1989) Chemical structure and history of the Earth: Evidence from global non-linear inversion of isotopic data in a three box model. *Earth Planet. Sci. Lett.* **96,** 61–88.

Allègre C. J., Pineau F., Bernat M., and Javoy M. (1971) Evidence for the occurrence of carbonatites on the Cape Verde and Canary Islands. *Nature Phys. Sci.* **233,** 103–104.

Allègre C. J., Hart S. R., and Minster J. F. (1983) Chemical structure of the mantle and continents determined by inversion of Nd and Sr isotopic data, II. Numerical experiments and discussion. *Earth Planet. Sci. Lett.* **66,** 191–213.

Allègre C. J., Staudacher T., and Sarda P. (1986) Rare gas systematics: Formation of the atmosphere, evolution and structure of the earth's mantle. *Earth Planet. Sci. Lett.* **81,** 127–150.

Allègre C. J., Hamelin B., Provost A., and Dupré B. (1986/1987) Topology in isotopic multispace and origin of mantle chemical heterogeneities. *Earth Planet. Sci. Lett.* **81,** 319–337.

Allègre C. J., Moreira M., and Staudacher T. (1995) $^{4}He/^{3}He$ dispersion and mantle convection. *Geophys. Res. Lett.* **22,** 2325–2328.

Beattie P. (1993a) The generation of uranium series disequilibria by partial melting of spinel peridotite: Constraints from partitioning studies. *Earth Planet. Sci. Lett.* **117,** 379–391.

Beattie P. (1993b) Uranium-thorium disequilibria and partitioning on melting of garnet peridotite. *Nature* **363,** 63–65.

Breddam K. and Kurz M. D. (2001) Helium isotopic signatures of Icelandic alkaline lavas. *Eos: Trans. Am. Geophys. Union* **82,** 47.

Cantanzaro E. J., Murphy T. J., Shields W. R., and Garner E. L. (1968) Absolute isotopic abundance ratios of common, equal-Atom, and radiogenic lead isotopic standards. *J. Res. Natl. Bur. Stand.* **72A,** 261–267.

Chauvel C., Hofmann A. W., and Vidal P. (1992) HIMU-EM: The French Polynesian connection. *Earth Planet. Sci. Lett.* **110,** 99–119.

Chen C.-Y. and Frey F. A. (1985) Trace element and isotopic geochemistry of lavas from Haleakala Volcano, East Maui, Hawaii; implications for the origin of Hawaiian basalts. *J. Geophys. Res.* **90,** 8743–8768.

Christensen B. P., Holm P. M., Jambon A., and Wilson J. R. (2001) Helium, argon and lead isotopic composition of volcanics from Santo Antão and Fogo, Cape Verde Islands. *Chem. Geol.* **178,** 127–142.

Class C. and Goldstein S. L. (1997) Plume-lithosphere interactions in the ocean basins: Constraints from the source mineralogy. *Earth Planet. Sci. Lett.* **150,** 245–260.

Cliff R. A., Baker P. E., and Mateer N. J. (1991) Geochemistry of Inaccessible Island volcanics. *Earth Planet. Sci. Lett.* **92,** 251–260.

Cohen R. S. and O'Nions R. K. (1982) Identification of recycled continental material in the mantle from Sr, Nd and Pb isotope investigations. *Earth Planet. Sci. Lett.* **61,** 73–84.

Condomines M., Grönvold K., Hooker P. J., Muehlen-Bachs K., O'Nions R. K., Oskarsson N., and Oxburgh E. R. (1983) Helium, oxygen, strontium and neodymium isotopic relationships in Icelandic volcanic. *Earth Planet. Sci. Lett.* **66,** 125–136.

Courtney R. C. and White R. S. (1986) Anomalous heat flow and geoid across the Cape Verde Rise: Evidence for dynamic support from a thermal plume in the mantle. *Geophys. J. R. Astr. Soc.* **87,** 815–867.

Davaille A. (1999) Simultaneous generation of hotspots and superswells by convection in a heterogeneous planetary mantle. *Nature* **402,** 756–760.

Davies G. R., Norry M. J., Gerlach D. C., and Cliff R. A. (1989) A combined chemical and Pb-Sr-Nd isotope study of the Azores and Cape Verde hot-spots: The geodynamic implications. In *Magmatism in the Ocean Basins* (eds. A. D. Saunders and M. J. Norry). *Geol. Soc. Spec. Publ.* **42,** 231–255.

De Paepe P., Klerkx J., Hertogen J., and Plinke P. (1974) Oceanic tholeiites on the Cape Verde Islands: Petrochemical and geochemical evidence. *Earth Planet. Sci. Lett.* **22,** 347–354.

Dosso L., Bougault H., and Joron J.-L. (1993) Geochemical morphology of the North Mid-Atlantic Ridge, 10°-20°N: Trace element-isotope complementarity. *Earth Planet. Sci. Lett.* **120,** 443–462.

Duncan R. A. (1980) Hotspots in the southern ocean—An absolute frame of reference for motion of the Gondwana continents. *Tectonophysics* **74,** 29–42.

Dupré B., Lambret B., and Allègre C. J. (1982) Isotopic variations within a single island: The Terceira case. *Nature* **299,** 620–622.

Dupuy C., Barsczus H. G., Liotard J. M., and Dostal J. (1988) Trace element evidence for the origin of oceanic island basalts: An example from the Austral Islands (French Polynesia). *Contrib. Mineral. Petrol.* **98,** 293–302.

Farnetani C. G., Legras B., and Tackley P. J. (2002) Mixing and deformations in mantle plumes. *Earth Planet. Sci. Lett.* **196,** 1–15.

Fraser K. J., Hawkesworth C. J., Erlank A. J., Mitchell R. H., and Scott-Smith B. H. (1985/1986) Sr, Nd and Pb isotope and minor element geochemistry of lamproites and kimberlites. *Earth Planet. Sci. Lett.* **76,** 57–70.

Gautheron C. and Moreira M. (2002) Helium signature of the subcontinental mantle. *Earth Planet. Sci. Lett.* **199,** 39–47.

Gerlach D. C., Cliff R. A., Davies G. R., Norry M., and Hodgson N. (1988) Magma sources of the Cape Verdes archipelago: Isotopic and trace element constraints. *Geochim. Cosmochim. Acta* **52,** 2979–2992.

Graham D. W., Humphris S. E., Jenkins W. J., and Kurz M. D. (1992) Helium isotope geochemistry of some volcanic rocks from Saint Helena. *Earth Planet. Sci. Lett.* **110,** 121–131.

Hart S. R. (1984) A large-scale isotope anomaly in the Southern Hemisphere mantle. *Nature* **309,** 753–757.

Hart S. R. (1988) Heterogeneous mantle domains: Signatures, genesis and mixing chronology. *Earth Planet. Sci. Lett.* **90,** 273–296.

Hart S. R. and Zindler A. (1986) In search of a bulk Earth composition. *Chem. Geol.* **57,** 247–267.

Hanyu T. and Kaneoka I. (1997) The uniform and low $^{3}He/^{4}He$ ratios of HIMU basalts as evidence for their origin as recycled materials. *Nature* **390,** 273–276.

Hawkesworth C. J., Kempton P. D., Rogers N. W., Ellam R. M., and van Calsteren P. W. (1990) Continental mantle lithosphere and shallow level enrichment processes in the Earth's mantle. *Earth Planet. Sci. Lett.* **96,** 256–268.

Hilton D. R., Barling J., and Wheller G. E. (1995) Effects of shallow-level contamination on the helium isotope systematics of ocean-island lavas. *Nature* **373,** 330–333.

Hoernle K., Tilton G., Le Bas M. J., Duggen S., and Garbe-Schönberg D. (2002) Geochemistry of oceanic carbonatites compared with continental carbonatites: Mantle recycling of oceanic crustal carbonate. *Contrib. Mineral. Petrol.* **142,** 520–542.

Hofmann A. W. (1988) Chemical differentiation of the Earth: The relationship between mantle, continental crust and oceanic crust. *Earth Planet. Sci. Lett.* **90,** 297–314.

Hofmann A. W. and White W. M. (1982) Mantle plumes from ancient oceanic crust. *Earth Planet. Sci. Lett.* **57,** 421–436.

Irving A. J. (1978) A review of experimental studies of crystal/liquid trace element partitioning. *Geochim. Cosmochim. Acta* **42,** 743–770.

Jagoutz E., Palme H., Baddenhausen H., Blum K., Cendales M., Dreibus G., Spettel B., Lorentz V., and Wänke H. (1979) The abundance of major, minor and trace elements in the Earth's mantle as derived from primitive ultramafic nodules. In *Proc. 10th Lunar Planet. Sci. Conf.* pp. 2031–2050.

Jørgensen J. Ø. and Holm P. M. (2002) Temporal variation and carbonatite contamination in primitive ocean island volcanics from São Vicente, Cape Verde Islands. *Chem. Geol.* **192,** 249–267.

Joron J.-L. and Treuil M. (1989) Hygromagmaphile element distributions in oceanic basalts as fingerprints of partial melting and mantle heterogeneities: A specific approach and proposal of an identification and modelling method. In *Magmatism in the Ocean Basins* (eds. A. D. Saunders and M. J. Norry). *Geol. Soc. Spec. Publ.* **42,** 277–299.

Kelemen P. B., Shimizu N., and Dunn T. (1993) Relative depletion of niobium in some arc magmas and the continental crust: Partitioning of K, Nb, La and Ce during melt/rock interaction in the upper mantle. *Earth Planet. Sci. Lett.* **120,** 111–134.

Klerkx J. and De Paepe P. (1971) Cape Verde Islands: Evidence for a Mesozoic oceanic ridge. *Nature Phys. Sci.* **233,** 117–118.

Klerkx J., Deutsch S., and De Paepe P. (1974) Rubidium, strontium content and strontium isotopic composition of strongly alkalic basaltic rocks from the Cape Verde Islands. *Contrib. Mineral. Petrol.* **45,** 107–118.

Kokfelt T. F., Holm P. M., Hawkesworth C. J., and Peate D. W. (1998) A lithospheric mantle source for the Cape Verde Island magmatism: Trace element and isotopic evidence from the island of Fogo. *Min. Mag.* **62A,** 801–802.

Kurz M. D. (1986) Cosmogenic helium in a terrestrial igneous rock. *Nature* **320,** 435–439.

Kurz M. D., Jenkins W. J., Schilling J.-G., and Hart S. R. (1982) Helium isotopic variation in the mantle beneath the central North Atlantic Ocean. *Earth Planet. Sci. Lett.* **58,** 1–14.

Kurz M. D., Kenn T. C., Lassiter J. C., and DePaolo D. J. (1996) Helium isotopic evolution of Mauna Kea Volcano: First results from the 1 km drill core. *J. Geophys. Res.* **101,** 11781–11791.

Langmuir C. H., Vocke R. D., Hanson G. N., and Hart S. R. (1978) A general mixing equation with applications to Icelandic basalts. *Earth Planet. Sci. Lett.* **37,** 380–392.

Lassiter J. C., Hauri E. H., Reiners P. W., and Garcia M. O. (2000) Generation of Hawaiian post-erosional lavas by melting of a mixed lherzolite/pyroxenite source. *Earth Planet. Sci. Lett.* **178,** 269–284.

La Tourette T. Z., Hervig R. L., and Holloway J. R. (1995) Trace element partitioning between amphibole, phlogopite and basanite melt. *Earth Planet. Sci. Lett.* **135,** 13–30.

Le Pichon X. and Fox P. J. (1971) Marginal offsets, fractures zones and the early opening of the North Atlantic. *J. Geophys. Res.* **76,** 6294–6308.

Le Roex A. P., Cliff R. A., and Adair B. J. I. (1990) Tristan da Cunha, South Atlantic: Geochemistry and petrogenesis of a basanite-phonolite lava series. *J. Petrol.* **31,** 779–812.

Manhès G., Minster J.-F., and Allègre C. J. (1978) Comparative U-Th-Pb and Rb-Sr study of the St. Severin amphoterites: Consequence for early solar system chronology. *Earth Planet. Sci. Lett.* **39,** 14–24.

Matos Alves C. A., Macedo J. R., Silva L. C., Serralheiro A., and Peixoto A. F. (1979) Estudo geologico, petrologico e vulcanologico da Ihla de Santiago (Cabo Verde). *Garcia de Orta Sér. Geol. Lisboa.* **3,** 47–74.

McDonough W. F. and Sun S. S. (1995) The composition of the Earth. *Chem. Geol.* **120,** 223–253.

McKenzie D. and O'Nions R. K. (1983) Mantle reservoirs and ocean island basalts. *Nature* **301,** 229–231.

Mendes M. H. and Silva L. C. (2001) Xenolitos crustais nas ilhas de Cabo Verde: Caracteristicas petrograpicas e quimica mineral. In *VI Congresso de Geoquimica des Paises de Lingua Portuguesa, Universidade do Algarve, Faro,* pp. 153–156.

Moreira M. and Kurz M. D. (2001) Subducted oceanic lithosphere and the origin of the "high $\mu$" basalt helium isotopic signature. *Earth Planet. Sci. Lett.* **189,** 49–57.

Moreira M., Doucelance R., Kurz M. D., Dupré B., and Allègre C. J. (1999) Helium and lead isotope geochemistry of the Azores Archipelago. *Earth Planet. Sci. Lett.* **169,** 189–205.

Paster T. P., Schauwecker D. S., and Haskin L. A. (1974) The behaviour of some trace elements during solidification of the Skaergaard layered series. *Geochim. Cosmochim. Acta* **38,** 1549–1577.

Pin C. and Bassin C. (1992) Evaluation of a strontium-specific extraction chromatographic method for isotopic analysis in geological materials. *Anal. Chim. Acta* **269,** 249–255.

Rollinson H. (1993) *Using Geochemical Data: Evaluation, Presentation, Interpretation*. Longman Scientific & Technical, Essex, UK.

Serralheiro A. (1976) A geologia da ilha de Santiago. *Bol. Mus. Lab. Min. Geol. Fac. Ciênc. Lisboa* **14,** *2,* 218.

Thirlwall M. F. (1997) Pb isotopic and elemental evidence for OIB derivation from young HIMU mantle. *Chem. Geol.* **139,** 51–74.

Thirlwall M. F. (2001) Inappropriate tail corrections can cause large inaccuracy in isotope ratio analysis by MC-ICP-MS. *J. Anal. At. Spectrom.* **16,** 1121–1125.

Thirlwall M. F. (2002) Multicollector ICP-MS analysis of Pb isotopes using a $^{207}Pb$-$^{204}Pb$ double spike demonstrates up to 400 ppm/amu systematic errors in Tl-normalization. *Chem. Geol.* **184,** 255–279.

Trindade M. J., Munha J., and Mata J. (2001) Geoquimica das "lavas recentes" da ilha de S. Vicente (Cabo Verde): Evidencias para a existência de heterogeneidades mantélicas verticais e horizontais. In *VI Congresso de Geoquimica des Paises de Lingua Portuguesa, Universidade do Algarve, Faro,* pp. 197–200.

Turcotte D. L. and Schubert G. (1982) From direct integration of Table F, Appendix 2. In *Geodynamics: Applications of Continuum Physics to Geological Problems,* pp. 432–433. John Wiley, New York.

Turner S., Hawkesworth C., Rogers N., and King P. (1997) U-Th isotope disequilibria and ocean island basalt generation in the Azores. *Chem. Geol.* **139,** 145–164.

Vollmer R. (1983) Earth degassing, mantle metasomatism and isotopic evolution of the mantle. *Geology* **11,** 452–454.

Weaver B. L. (1991) The origin of ocean island basalt end-member compositions: Trace element and isotopic constraints. *Earth Planet. Sci. Lett.* **104,** 381–397.

White W. M. (1985) Sources of oceanic basalts: radiogenic isotopic evidence. *Geology* **13,** 115–118.

Woodhead J. D. (1996) Extreme HIMU in an oceanic setting: The geochemistry of Mangaia Island (Polynesia), and temporal evolution of the Cook-Austral hotspot. *J. Volcanol. Geotherm. Res.* **72,** 1–19.

Zartman R. E. and Haines S. M. (1988) The plumbotectonic model for Pb isotopic systematics among major terrestrial reservoirs—A case for bi-directional transport. *Geochim. Cosmochim. Acta* **52,** 1327–1339.

Zindler A. and Hart S. R. (1986a) Chemical geodynamics. *Ann. Rev. Earth Planet. Sci.* **14,** 493–571.

Zindler A. and Hart S. R. (1986b) Helium: Problematic primordial signals. *Earth Planet. Sci. Lett.* **79,** 1–8.

Zindler A., Jagoutz E., and Goldstein S. L. (1982) Nd, Sr and Pb isotopic systematics in a three-component mantle: A new perspective. *Nature* **298,** 519–523.

## APPENDIX

### Sr and Pb Isotopic Composition of the Lower Mantle

Complementarity between the continental crust (CC) and the depleted mantle (DM), with respect to the Bulk Silicate Earth (BE), is assumed. Following Allègre and Lewin (1989) the mass balance equations for isotopic pairs (radiogenic element X) and absolute concentrations (reference stable isotope $^{S}X$) are

$$\alpha^{X}_{BE} = \alpha^{X}_{CC} \cdot W^{X} + \alpha^{X}_{DM} \cdot (1-W^{X}) \quad \text{(A1)}$$

$$[^{S}X]_{BE} = \phi \cdot [^{S}X]_{CC} + (1-\phi) \cdot [^{S}X]_{DM} \quad \text{(A2)}$$

where $\alpha$ refers to the isotopic ratio, $W^{X}$ to the sialic index, which indicates the preferential affinity of an element for the continental crust (cf. Allègre and Lewin, 1989), and $\phi$ to the mass fraction of continental crust, using the value of Allègre and Lewin (1989) i.e., $\phi = 0.015$;

$$W^{X} = \phi \cdot [^{S}X]_{CC}/[^{S}X]_{BE} \quad \text{(A3)}$$

$$\phi = \text{mass}_{CC}/(\text{mass}_{DM} + \text{mass}_{CC}) \quad \text{(A4)}$$

where $\text{mass}_{DM}$ is the mass of depleted mantle and $\text{mass}_{CC}$ that of the continental crust.

Combination of Eqn. A1 to A4 yields the chemical ratio $[^{S}X]_{DM}/[^{S}X]_{BE}$. Since depletion affects a portion of the mantle that is greater than the upper mantle alone (Jagoutz et al., 1979; Allègre et al., 1983; Hart and Zindler, 1986), the lower mantle (LM) composition is represented by a mixture of depleted and Bulk Silicate Earth materials. Since oceanic crust and sediments potentially recycled into the lower mantle through subduction mainly sink at the base ($D''$ layer), the mass of recycled material into the lower mantle is considered negligible. In this model, mass balance equations for isotopic pairs and absolute concentrations are

$$\alpha^{X}_{LM} = \alpha^{X}_{BE} \cdot U^{X} + \alpha^{X}_{DM} \cdot (1-U^{X}) \quad \text{(A5)}$$

$$[^{S}X]_{LM} = f \cdot [^{S}X]_{DM} + (1-f) \cdot [^{S}X]_{BE} \quad \text{(A6)}$$

where $U^{X}$ is the proportion of BE material and $f$ the fraction of depleted mantle in the lower mantle. Then

$$U^{X} = (1-f) \cdot [^{S}X]_{BE}/[^{S}X]_{LM} \quad \text{(A7)}$$

$$f = (\text{mass}_{DM} - \text{mass}_{UM})/\text{mass}_{LM} = (\text{mass}_{DM} - \text{mass}_{UM})/(\text{mass}_{MM} - \text{mass}_{UM}) \quad \text{(A8)}$$

where $\text{mass}_{UM}$ is the mass of the upper mantle and $\text{mass}_{MM}$ the total mass of the mantle.

Eqn. A6 yields the chemical ratio $[^{S}X]_{LM}/[^{S}X]_{BE}$; combining Eqn. A5 and A7 leads to the isotopic composition of the lower mantle. Given that $\text{mass}_{UM}/\text{mass}_{MM} = 25.6\%$ (Turcotte and Schubert, 1982) and $\text{mass}_{DM}/\text{mass}_{MM} = 38.1\%$ (Allègre and Lewin, 1989), $f = 16.8\%$.

ELSEVIER

Chemical Geology 219 (2005) 93–113

CHEMICAL GEOLOGY
INCLUDING
ISOTOPE GEOSCIENCE

www.elsevier.com/locate/chemgeo

# Os isotope systematics in Fogo Island: Evidence for lower continental crust fragments under the Cape Verde Southern Islands

Stéphane Escrig[a,*], Régis Doucelance[b,c], Manuel Moreira[a], Claude Jean Allègre[a]

[a]*Laboratoire de Géochimie et Cosmochimie (UMR 7579 CNRS), Institut de Physique du Globe de Paris, Université Denis Diderot (Paris 7), 4 place Jussieu, 75252 Paris Cedex 05, France*
[b]*GEOTOP-UQAM-McGILL, Case postale 8888, Succursale Centre-ville, Montréal, Canada, Qc H3C 3P8*
[c]*Now at Laboratoire 'Magma et Volcans', Université Blaise-Pascal, CNRS (UMR 6524), Observatoire de Physique du Globe de Clermont-Ferrand, 5 rue Kessler, 63038 Clermont-Ferrand Cedex, France*

Received 17 June 2004; received in revised form 8 February 2005; accepted 15 February 2005

**Abstract**

Os and Nd isotopic ratios as well as major and trace element compositions have been measured in 17 mafic lavas from Fogo Island, Cape Verde. These new data complement a previous archipelago-scale study (Southern and Northern Islands) by Doucelance et al. [Doucelance, R., Escrig, S., Moreira, M., Gariépy, C., Kurz, M., 2003. Pb-Sr-He isotope and trace element geochemistry of the Cape Verde Archipelago. Geochim. Cosmochim. Acta, 67 (19), 3717-3733], in which major, trace element contents and Sr–Pb–He isotopic compositions of lavas were determined. We also report Os–Sr–Nd–Pb isotopic ratios of 2 carbonatites from Fogo.

Fogo mafic lavas have Os–Sr–Nd–Pb isotopic ratios that define correlations similar to those previously observed for the Cape Verde Southern Islands and interpreted to reflect a mixture between a moderate HIMU end-member ($^{206}Pb/^{204}Pb \sim 20$), common to the Northern and Southern Islands of the archipelago, and an EM1-like end-member. Similar isotopic correlations are observed within the different lava flows which requires that the two end-members are mixed during the lava differentiation at shallow depth. The increasing contribution of the enriched end-member through time in Fogo lavas confirms the shallow origin for the EM1 signature.

As with Pb, Sr and He, the Os and Nd isotopic compositions of the moderate HIMU end-member are explained by the mixing of 1.6 Ga recycled oceanic crust (ROC) and lower mantle material (LM) and interpreted to represent the Cape Verde mantle plume expression. For the EM1-like end-member, the high $^{187}Os/^{188}Os$ ratios that are measured in mafic lavas preclude the sub-continental lithospheric mantle from being its origin, as previously proposed based on trace element and Pb, Sr and Nd isotopic compositions. Our new isotopic and trace element data still indicate that the enriched component is

* Corresponding author. Department of Earth and Planetary Sciences, Harvard University, 20 Oxford Street, Cambridge, MA 02138, USA. Tel.: +1 617 496 6983.
*E-mail address:* escrig@eps.harvard.edu (S. Escrig).

0009-2541/$ - see front matter 
doi:10.1016/j.chemgeo.2005.02.011

related to continental lithospheric material incorporated in the oceanic lithosphere during the opening of the Atlantic Ocean but requires the involvement of lower continental crust fragments.


*Keywords:* Osmium; OIB; Cape Verde; Lower continental crust

## 1. Introduction

Systematic analysis of Sr–Nd–Pb isotopic compositions in oceanic island basalts (OIB) and mid-oceanic ridge basalts (MORB) has led to the identification of several mantle end-members with extreme locations in isotopic diagrams (Allègre and Turcotte, 1985; White, 1985; Zindler and Hart, 1986; Allègre et al., 1986/87) and termed DMM ('Depleted MORB Mantle'), HIMU ('high $^{238}U/^{204}Pb$'), EM1 and EM2 ('Enriched Mantle 1 and 2') by Zindler and Hart (1986). However, most of the oceanic islands have intermediate positions in the Sr–Nd–Pb isotopic diagrams, which suggest end-members having similar characteristics but less extreme isotopic compositions. The differences in end-member isotopic compositions are currently debated. For example, while the extreme HIMU end-member is generally associated with old (~2 Ga) and altered recycled oceanic crust, the moderate HIMU-like signature can be explained by the mixing of this old oceanic crust with another mantle component and also by the recycling of relatively younger oceanic crust ("young HIMU", cf. Thirlwall (1997)). In the same way, the EM1-like signature can have different origins such as intra-mantle metasomatism processes (Hart, 1988; Hawkesworth et al., 1990), recycling of sediments associated with ancient oceanic crust (Weaver, 1991; Chauvel et al., 1992) or sub-continental lithospheric mantle (Cohen and O'Nions, 1982; McKenzie and O'Nions, 1983). Lastly, it has to be noted that noble gas results, notably high $^{3}He/^{4}He$ ratios measured in some oceanic island basalts, provide arguments in favour of another mantle component: a relatively undegassed reservoir thought to be the lower mantle (LM) (Kurz et al., 1982).

The Re/Os isotopic system provides new information on the nature and the composition of mantle end-members. Re and Os are both highly siderophile and chalcophile and have been strongly depleted in the silicate Earth during the core formation. However, the upper mantle appears to have a broadly chondritic composition in such elements, supporting the model of a late veneer input during the Earth accretion (Allègre and Luck, 1980; Walker et al., 1996). During melting processes, Re behaves as a moderately incompatible element while Os is strongly compatible. Therefore, melting products such as crustal material have very high Re/Os relative to the residual mantle and rapidly develop high radiogenic $^{187}Os/^{188}Os$ by $\beta^-$ decay of $^{187}Re$ to $^{187}Os$ ($\lambda = 1.666 \times 10^{-11}$ yr$^{-1}$, cf. Smoliar et al. (1996)). Furthermore, ancient sub-continental lithospheric mantle has been depleted in Re relative to Os by the crust extraction and has a lower than primitive upper mantle $^{187}Os/^{188}Os$ value (Meisel et al., 1996). Therefore, the $^{187}Os/^{188}Os$ ratio appears to be sensitive to the presence in basaltic sources either of important amounts of recycled crustal material, having high $^{187}Os/^{188}Os$ ratio but low Os concentration, or small amounts of sub-continental lithospheric mantle, having subchondritic $^{187}Os/^{188}Os$ ratio and mantle-like concentration.

Previous studies of the Cape Verde archipelago based on trace elements and isotopic measurements (Sr, Nd, Pb, U/Th, He ratios) have shown relatively clear variations between the Northern and Southern Islands. Lavas from the Southern Islands display trace elements and isotopic compositions that support the involvement of sub-continental lithospheric mantle (SCLM) in their source (Gerlach et al., 1988; Davies et al., 1989; Kokfelt et al., 1998). This result has motivated our Os study of Fogo Island where the current volcanism of the Cape Verde archipelago occurs. We report the first isotopic Os analyses as well as new major, trace element and $^{143}Nd/^{144}Nd$ measurements on samples previously analyzed for Pb, Sr and He isotopes by Doucelance et al. (2003).

The Os and Nd isotopic compositions confirm that Fogo lavas result from the mixture between a moderate HIMU end-member ($^{206}Pb/^{204}Pb \sim 20$) and

an EM1-like end-member, as previously proposed (Gerlach et al., 1988; Davies et al., 1989; Kokfelt et al., 1998). Together with the major and trace element compositions, the isotopic data suggests the contribution of the EM1-like end-member occurred during magma differentiation. The Os compositions of Fogo lavas combined with the other isotopic systems indicate this end-member is lower continental crust fragments, possibly with sub-continental lithospheric mantle, stored within the oceanic lithosphere during the opening of the Atlantic Ocean.

## 2. Geological Setting and sample location

The Cape Verde Islands are located in the central Atlantic between latitudes 15° and 17° N. The archipelago consists of ten major islands separated into the Southern Islands (Brava, Fogo, Santiago and Maio) and the Northern Islands (Santo Antão, São Vicente, Santa Luzia and São Nicolau), which also include the Eastern Islands (Boa Vista and Sal) (Fig. 1). Summaries of the structure and geology of each island can be found in Matos Alves et al. (1979) and Gerlach et al. (1988).

Fogo Island is located in the southwest of the archipelago and forms the top of a large strato-volcano with a summit at 2829 m. A collapse caldera fills the northeast of the island and presently contains a more recent cone, inactive since the 18th century. Fogo is still a very active volcano with many smaller cones within the caldera associated with historic lava flows (1847, 1857, 1951, 1995) which erupted in the eastern part of the island (Day et al., 1999).

The 17 samples analyzed in this study were selected to span the whole volcanic series, from pre-caldera activity to the latest historic eruption in 1995. Samples F-01, -02, -18 and -20 are pre-caldera, coming from the western part of the island. F-11 and F-13, collected in the wall of the caldera, are syn- or post-caldera. Others (F-06, -07, -08, -10, -12, -14, -15, -16, -21, -22 and -24) are post-caldera and sample historic volcanism. Samples F-10 and -12 come from the 1785 lava flow, F-24 from the 1847, F-22 from the

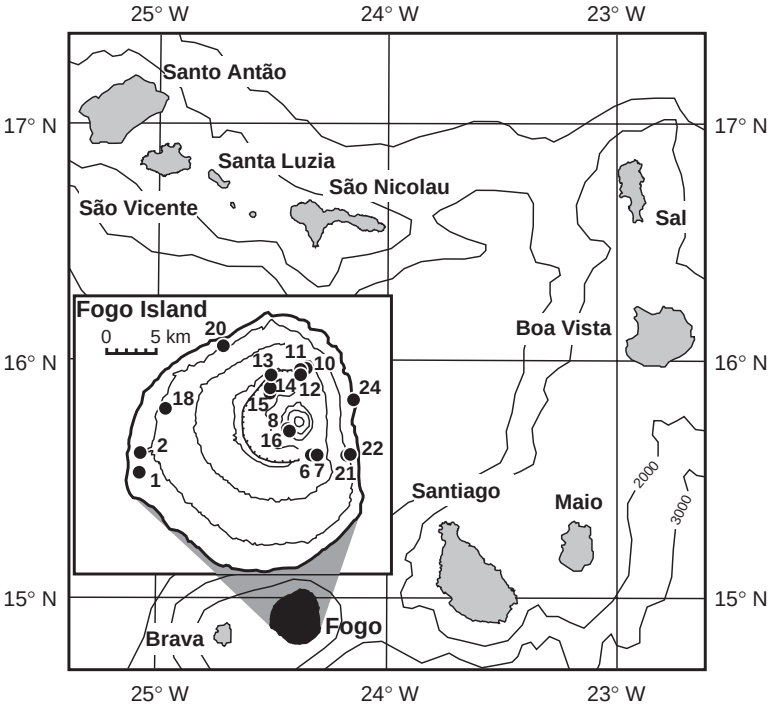


Fig. 1. Geographical location map and seafloor bathymetry of the Cape Verde archipelago including sampling map of Fogo modified after Doucelance et al. (2003).

1857, and F-06, -07 and -21 from the 1951, respectively. F-14 and -15 come from a separate lava flow also erupted in 1951. Lastly, F-08 and -16 sample the most recent volcanic activity of the island (1995). Sample locations are given in Table 2 and shown in Fig. 1. The two carbonatites were collected in the western part of the island during a previous sampling campaign (Hodgson, 1986). NF 43 is a brown fine-grained carbonatite; NF 44 is mottled, with brown rhombs in a white/grey matrix.

Table 1
Major (wt.%) and trace element (ppm) concentrations of basalts from Fogo, Cape Verde

| | F-01 | F-02* | F-06 | F-07* | F-08* | F-10 | F-11 | F-12 | F-13 | F-14 | F-15* | F-16 | F-18 | F-20* | F-21 | F-22 | F-24* |
|---|---|---|---|---|---|---|---|---|---|---|---|---|---|---|---|---|---|
| SiO2 | 39.63 | 41.59 | 41.72 | 42.24 | 42.47 | 42.18 | 39.26 | 41.49 | 41.13 | 42.60 | 42.14 | 42.35 | 42.08 | 40.65 | 41.10 | 42.92 | 41.42 |
| TiO2 | 4.39 | 4.07 | 3.83 | 3.74 | 3.80 | 3.73 | 3.64 | 3.77 | 4.01 | 3.67 | 3.65 | 3.83 | 3.07 | 4.40 | 4.01 | 3.34 | 3.53 |
| Al2O3 | 12.71 | 14.88 | 14.99 | 15.32 | 15.59 | 15.40 | 11.48 | 15.29 | 14.09 | 15.80 | 15.71 | 15.49 | 12.64 | 14.53 | 14.56 | 16.89 | 13.31 |
| Fe2O3 | 14.79 | 14.19 | 13.98 | 13.31 | 13.24 | 12.97 | 14.63 | 13.29 | 14.57 | 13.24 | 13.06 | 13.29 | 12.28 | 14.07 | 14.52 | 11.42 | 14.18 |
| MgO | 8.69 | 7.15 | 6.79 | 6.49 | 6.17 | 6.01 | 10.41 | 6.18 | 7.04 | 5.81 | 5.81 | 6.04 | 10.79 | 6.50 | 6.81 | 4.62 | 9.21 |
| CaO | 14.18 | 11.07 | 12.06 | 12.02 | 11.94 | 11.98 | 14.39 | 11.60 | 13.22 | 11.48 | 11.60 | 11.87 | 12.67 | 12.81 | 13.21 | 10.61 | 12.81 |
| Na2O | 2.86 | 4.41 | 3.55 | 3.75 | 3.89 | 4.35 | 3.01 | 4.31 | 3.34 | 3.98 | 4.00 | 3.83 | 3.62 | 3.61 | 3.44 | 5.33 | 3.08 |
| K2O | 1.75 | 2.18 | 2.47 | 2.60 | 2.74 | 2.88 | 0.39 | 2.89 | 1.86 | 2.75 | 2.77 | 2.69 | 1.96 | 2.39 | 2.28 | 3.50 | 1.92 |
| MnO | 0.19 | 0.18 | 0.19 | 0.20 | 0.20 | 0.21 | 0.19 | 0.21 | 0.20 | 0.20 | 0.21 | 0.20 | 0.20 | 0.20 | 0.21 | 0.22 | 0.20 |
| P2O5 | 0.59 | 0.60 | 0.83 | 0.82 | 0.84 | 0.91 | 0.77 | 0.87 | 0.64 | 0.89 | 0.91 | 0.81 | 0.71 | 0.70 | 0.79 | 0.95 | 0.74 |
| Total | 100.16 | 100.32 | 100.00 | 100.49 | 100.88 | 100.48 | 98.60 | 99.48 | 100.25 | 100.02 | 99.86 | 100.11 | 100.02 | 99.86 | 100.32 | 99.95 | 100.40 |
| | | | | | | | | | | | | | | | | | |
| V | 423 | 341 | 365 | 348 | 340 | 323 | 383 | 321 | 370 | 321 | 328 | 359 | 310 | 372 | 396. | 291 | 350 |
| Cr | 129 | 144 | 112 | 94 | 62 | 58 | 477 | 63 | 74 | 54 | 55 | 58 | 627 | 66 | 89 | 12 | 350 |
| Co | 54.6 | 47.2 | 46.3 | 42.8 | 40.3 | 36.6 | 60.0 | 40.4 | 48.0 | 38.5 | 40.6 | 42.4 | 52.1 | 46.9 | 47.1 | 30.2 | 53.6 |
| Ni | 93.3 | 82.9 | 58.3 | 50.4 | 41.6 | 40.5 | 161.6 | 49.0 | 55.8 | 32.0 | 33.9 | 46.3 | 220 | 43.0 | 52.6 | 17.5 | 113 |
| Cu | 119 | 94 | 93 | 72 | 69 | 63 | 91 | 71 | 86 | 67 | 58 | 420 | 74 | 81 | 67 | 62 | 101 |
| Zn | 132 | 149 | 148 | 149 | 151 | 133 | 133 | 135 | 135 | 147 | 155 | 171 | 125 | 155 | 146 | 150 | 135 |
| Ga | 23.3 | 23.8 | 24.8 | 24.8 | 24.7 | 23.7 | 21.7 | 23.4 | 22.5 | 25.1 | 25.9 | 25.8 | 20.8 | 25.1 | 24.6 | 24.8 | 22.4 |
| Rb | 44.1 | 62.6 | 54.1 | 56.0 | 60.1 | 64.4 | 36.1 | 62.4 | 47.9 | 61.7 | 61.1 | 62.6 | 54.9 | 49.4 | 51.8 | 81.0 | 43.4 |
| Sr | 827 | 929 | 1000 | 1041 | 1066 | 1126 | 681 | 1092 | 906 | 1095 | 1104 | 1068 | 1089 | 1014 | 971 | 1350 | 893 |
| Y | 25.6 | 23.4 | 27.9 | 29.1 | 29.9 | 30.0 | 26.6 | 29.4 | 27.1 | 30.8 | 31.0 | 30.5 | 26.0 | 29.5 | 29.7 | 33.5 | 27.2 |
| Zr | 299 | 330 | 325 | 338 | 357 | 356 | 289 | 342 | 291 | 370 | 357 | 364 | 290 | 356 | 335 | 436 | 281 |
| Nb | 51.5 | 83.0 | 80.7 | 84.1 | 90.0 | 94.0 | 48.4 | 91.4 | 57.7 | 93.1 | 88.5 | 91.6 | 63.3 | 76.6 | 77.8 | 119 | 66.9 |
| Cs | 0.40 | 0.64 | 0.58 | 0.68 | 0.74 | 0.76 | 0.42 | 0.70 | 0.47 | 0.65 | 0.71 | 0.67 | 0.60 | 0.56 | 0.58 | 0.92 | 0.64 |
| Ba | 560 | 795 | 768 | 802 | 849 | 878 | 319 | 877 | 682 | 831 | 771 | 847 | 733 | 747 | 720 | 1036 | 634.0 |
| La | 37.0 | 44.9 | 46.9 | 56.2 | 59.4 | 63.0 | 43.4 | 61.1 | 45.7 | 62.1 | 56.8 | 61.4 | 59.2 | 48.5 | 46.9 | 76.1 | 46.9 |
| Ce | 95.1 | 97.6 | 116.1 | 124.0 | 131.0 | 132.0 | 110.0 | 130.1 | 112.1 | 133.0 | 124.0 | 131.2 | 120.3 | 110.0 | 117.4 | 155.9 | 100.0 |
| Pr | 12.3 | 11.6 | 14.4 | 14.8 | 15.7 | 16.1 | 13.9 | 15.8 | 13.9 | 16.5 | 15.4 | 15.9 | 14.2 | 14.0 | 14.9 | 18.7 | 13.1 |
| Nd | 51.3 | 46.5 | 57.5 | 57.1 | 62.6 | 63.7 | 57.2 | 62.5 | 56.2 | 66.1 | 63.5 | 63.8 | 56.5 | 58.2 | 59.7 | 71.7 | 54.4 |
| Sm | 10.53 | 9.09 | 11.00 | 10.80 | 11.40 | 12.17 | 11.00 | 11.74 | 11.04 | 12.58 | 11.30 | 12.10 | 10.46 | 10.80 | 11.49 | 13.02 | 9.97 |
| Eu | 3.26 | 2.84 | 3.48 | 3.41 | 3.70 | 3.73 | 3.44 | 3.65 | 3.43 | 3.98 | 3.64 | 3.80 | 3.22 | 3.70 | 3.66 | 4.02 | 3.25 |
| Gd | 8.47 | 6.74 | 8.95 | 8.78 | 9.06 | 6.05 | 8.60 | 9.22 | 8.58 | 9.60 | 9.41 | 9.61 | 7.96 | 8.78 | 9.10 | 10.18 | 8.18 |
| Tb | 1.13 | 0.98 | 1.20 | 1.22 | 1.33 | 1.26 | 1.16 | 1.26 | 1.16 | 1.31 | 1.25 | 1.25 | 1.10 | 1.25 | 1.25 | 1.39 | 1.09 |
| Dy | 5.76 | 5.00 | 6.22 | 6.12 | 6.49 | 6.61 | 6.09 | 6.68 | 6.03 | 6.77 | 6.33 | 6.67 | 5.64 | 6.47 | 6.57 | 7.15 | 5.70 |
| Ho | 0.94 | 0.87 | 1.01 | 1.02 | 1.03 | 1.10 | 0.96 | 1.07 | 1.00 | 1.14 | 1.12 | 1.10 | 0.93 | 1.06 | 1.09 | 1.23 | 0.97 |
| Er | 2.26 | 2.05 | 2.51 | 2.59 | 2.57 | 2.72 | 2.32 | 2.71 | 2.54 | 2.84 | 2.64 | 2.76 | 2.37 | 2.45 | 2.71 | 3.10 | 2.19 |
| Tm | 0.31 | 0.27 | 0.34 | 0.29 | 0.31 | 0.37 | 0.31 | 0.35 | 0.33 | 0.37 | 0.34 | 0.36 | 0.29 | 0.36 | 0.35 | 0.41 | 0.30 |
| Yb | 1.74 | 1.81 | 2.03 | 2.17 | 2.12 | 2.28 | 1.77 | 2.06 | 1.94 | 2.25 | 2.27 | 2.24 | 1.74 | 1.96 | 2.05 | 2.49 | 1.80 |
| Lu | 0.25 | 0.25 | 0.29 | 0.29 | 0.31 | 0.32 | 0.26 | 0.32 | 0.29 | 0.33 | 0.31 | 0.32 | 0.26 | 0.28 | 0.30 | 0.35 | 0.26 |
| Hf | 7.66 | 7.73 | 7.41 | 7.39 | 8.10 | 7.99 | 6.82 | 7.53 | 7.15 | 8.27 | 7.99 | 8.20 | 6.34 | 9.04 | 7.79 | 8.46 | 6.57 |
| Ta | 4.95 | 6.57 | 6.25 | 6.38 | 7.04 | 7.53 | 4.46 | 7.15 | 5.26 | 7.32 | 7.20 | 7.07 | 5.63 | 6.30 | 6.05 | 8.95 | 5.24 |
| Pb | 2.50 | 2.57 | 4.02 | 3.50 | 3.74 | 3.88 | 3.11 | 3.90 | 3.50 | 4.25 | 4.09 | 6.07 | 3.61 | 3.03 | 3.36 | 6.14 | 3.36 |
| Th | 3.02 | 4.47 | 4.23 | 5.11 | 5.73 | 5.39 | 3.41 | 5.24 | 4.31 | 4.84 | 5.62 | 5.07 | 4.86 | 4.06 | 4.06 | 6.47 | 4.01 |
| U | 0.76 | 0.97 | 1.01 | 1.05 | 1.19 | 1.32 | 1.09 | 1.27 | 1.09 | 1.16 | 1.25 | 1.18 | 1.57 | 0.96 | 1.01 | 1.61 | 0.88 |

* From Doucelance et al. (2003).

## 3. Analytical techniques

Osmium, rhenium and neodymium analyses were performed on whole rocks, using the same powder crushed into an agate mortar. Re–Os analyses were done on 2–3 g samples. Osmium chemical separations including extraction and purification steps are described in detail elsewhere (Birck et al., 1997). Osmium and rhenium isotopic ratios were measured as $OsO_3^-$ and $ReO_4^-$ oxides on a Finnigan Mat 262 using negative thermal ionization and single-collection on an Ion Counting Multiplier. Os blanks ($n=5$) were on the average: $0.036 \pm 0.009$ pg/g with $^{187}Os/^{188}Os = 0.35 \pm 0.09$; Re blanks range from 1.3 to 2.3 pg/g (mean = 1.7 pg/g). Blank correction for the Os isotopic ratio ranges from 0.05% to 0.42% (Table 2). Measured ratios were also corrected for oxygen. Within-run $2\sigma$ precisions vary between 0.46% and 3.63% for the $^{187}Os/^{188}Os$ ratio. These values are larger than the total external reproducibility of 0.13% that was obtained on Os IPGP internal standards. It is consistent with the low Os concentration of samples and the lower signal intensity during acquisition. Replicate analyses of the $^{187}Os/^{188}Os$ ratio agree within 0.3–0.8%. Due to the low Os content and to the heterogeneous distribution of Os inside samples, replicate measurements of Os concentration display expected variations ranging from 3.9% to 10.7%.

Neodymium analyses were done on the same dissolved fraction used by Doucelance et al. (2003) for Sr analyses. Nd chemical separation is based on the procedure described in Richard et al. (1976). Neodymium measurements were performed in static multi-collection mode on a Finnigan Triton and corrected for mass discrimination using $^{144}Nd/^{146}Nd = 0.7219$. Lead and strontium analyses of carbonatites were performed following the procedure described for basalts in Doucelance et al. (2003).

Major and trace element compositions were measured by the "Service d'Analyses des Roches et des Mineraux" at CRPG/Nancy. Following alkaline melting with $LiBO_2$ and nitric acid dissolution, major abundances have been determined by ICP-AES with a precision better than 1% except for CaO, $Na_2O$, $K_2O$ and MnO (<2%) and $P_2O_5$ (<10%). Trace element composition were determined by ICP-MS with a precision better than 5% for most elements except for Pb (<20%), Cr and Cs (<15%) Ni, Lu and Tm (<10%), U (<8%), Dy and Th (<7%), Gd (6%) and Sr (<4%). Trace element data for international standards measured by the SARM are available on their web site (http://www.crpg.cnrs-nancy.fr/SARM/) and in Carignan et al. (2001).

## 4. Results

### 4.1. Major and trace element compositions

Whole-rock analyses of major and trace elements are reported in Table 1. Using the alkali–silica nomenclature, Fogo lavas are mostly basanites, tephrites and nephelinites. In comparison to the other Cape Verde islands, Fogo lavas (Fig. 2) have relatively high $Fe_2O_3$ (11.42–14.79 wt.%) and $TiO_2$ (3.07–4.40 wt.%) and low MgO content (4.6–10.8 wt.%) for a similar range of $SiO_2$ contents (39.26–42.92 wt.%). The trace element compositions show homogenous primitive mantle-normalized trace element patterns, similar to those from previous studies (Gerlach et al., 1988; Davies et al., 1989; Doucelance et al., 2003) and from Tristan da Cunha basalts (Cliff et al., 1991). These results confirm the EMI-like signature of Fogo lavas with relative depletion in Pb, Th and U and large enrichments for Ba, Nb, La and Rb.

The osmium concentrations range from 2.2 to 28.6 ppt (Table 2 and Fig. 2), among the lowest Os content measured in OIB, particularly in Atlantic archipelagos like the Azores and the Canary Islands (Hauri and Hart, 1993; Reisberg et al., 1993; Marcantonio et al., 1995; Roy-Barman and Allègre, 1995; Bennet et al., 1996; Hauri et al., 1996; Widom and Shirey, 1996; Lassiter and Hauri, 1998; Brandon et al., 1999; Widom et al., 1999; Schiano et al., 2001; Eisele et al., 2002). The rhenium concentrations vary from 281 to 1826 ppt.

### 4.2. Isotopic compositions

Except sample F-22, which has the lowest Os content together with the most radiogenic Os isotopic ratio (0.1548), Fogo lavas define a small range from 0.1323 to 0.1369 (Fig. 3). Compared to this range, the uncertainty on $^{187}Os/^{188}Os$ ratios (from 0.46% to 3.63%) appear to be relatively large. Nevertheless, the

Table 2
Sample locations and Os, Sr, Nd and Pb isotopic compositions of Fogo basalts and carbonatites

| Samples | Latitude E° | Longitude W° | Volc. unit | Re (ppt) | Os (ppt) | $^{187}Re/^{188}Os$ | $(^{187}Os/^{188}Os)_m$ | Blank correction (%) | $(^{187}Os/^{188}Os)_i$ | $^{87}Sr/^{86}Sr$ | $^{143}Nd/^{144}Nd$ | $^{206}Pb/^{204}Pb$ | $^{207}Pb/^{204}Pb$ | $^{208}Pb/^{204}Pb$ |
|---|---|---|---|---|---|---|---|---|---|---|---|---|---|---|
| *Basalts* | | | | | | | | | | | | | | |
| F-01 | 14°54′00 | 24°30′00 | Pre-caldera | 674 | 18.30 | 176.5 | 0.1334 (23) | 0.11 | | 0.703685 (18) | 0.512760 (4) | 19.105 (8) | 15.553 (9) | 38.884 (31) |
| F-02 | 14°55′04 | 24°29′57 | Pre-caldera | 488 | 18.72 | 125.1 | 0.1343 (23) | 0.29 | | 0.703723 (23) | 0.512727 (3) | 19.064 (14) | 15.567 (17) | 38.880 (56) |
| F-18 | 14°57′28 | 24°28′32 | Pre-caldera | 444 | 18.21 | 117.1 | 0.1323 (06) | 0.10 | | 0.703546 (20) | 0.512764 (3) | 19.220 (8) | 15.563 (9) | 38.914 (31) |
| F-20 | 14°00′53 | 24°25′18 | Pre-caldera | 955 | 11.61 | 394.8 | 0.1343 (08) | 0.07 | | 0.703722 (22) | 0.512735 (9) | 19.062 (11) | 15.548 (14) | 38.822 (47) |
| F-20b | 14°00′53 | 24°28′18 | Pre-caldera | | 12.06 | | 0.1343 (07) | 0.07 | | | | | | |
| F-11 | 14°59′39 | 24°20′54 | Caldera wall | 281 | 28.60 | 47.1 | 0.1331 (09) | 0.05 | | 0.703665 (21) | 0.512759 (3) | 19.077 (11) | 15.566 (9) | 38.947 (44) |
| F-13 | 14°59′19 | 24°22′40 | Caldera wall | 620 | 7.13 | 417.6 | 0.1352 (08) | 0.26 | | 0.703715 (19) | 0.512733 (9) | 19.109 (8) | 15.552 (9) | 38.901 (31) |
| F-10 | 14°59′42 | 24°20′40 | 1785 | 729 | 15.28 | 228.8 | 0.1330 (18) | 0.08 | | 0.703616 (24) | 0.512745 (4) | 19.133(8) | 15.560 (9) | 38.917 (31) |
| F-12 | 14°59′39 | 24°20′54 | 1785 | 456 | 16.32 | 134 | 0.1347 (14) | 0.07 | | 0.703625 (20) | 0.512758 (2) | 19.143 (13) | 15.577 (9) | 38.975 (31) |
| F-24 | 14°57′56 | 24°17′38 | 1847 | 714 | 20.03 | 172 | 0.1334 (07) | 0.40 | | 0.703761 (18) | 0.512728 (4) | 18.969 (11) | 15.562 (14) | 38.804 (47) |
| F-24b | 14°57′56 | 24°17′38 | 1847 | 553 | 18.90 | 141.1 | 0.1328 (09) | 0.38 | | | | | | |
| F-22 | 14°55′15 | 24°17′40 | 1857 | 961 | 2.20 | 2116.3 | 0.1548 (56) | 0.42 | | 0.703656 (21) | 0.512765 (3) | 19.094 (8) | 15.561 (9) | 38.898 (31) |
| F-06 | 14°54′56 | 24°20′23 | 1951 | 1826 | 9.98 | 878 | 0.1362 (16) | 0.12 | | 0.703738 (20) | 0.512726 (3) | 18.900 (8) | 15.539 (9) | 38.731 (31) |
| F-07 | 14°54′56 | 24°20′23 | 1951 | 667 | 7.07 | 471.2 | 0.1360 (09) | 0.09 | | 0.703789 (19) | 0.512722 (4) | 18.882 (11) | 15.530 (14) | 38.701 (46) |
| F-07b | 14°54′56 | 24°20′23 | 1951 | 543 | 6.79 | 368.7 | 0.1349 (12) | 0.07 | | | | | | |
| F-14 | 14°58′41 | 24°22′42 | 1951 | 494 | 8.12 | 291.8 | 0.1348 (13) | 0.14 | | 0.703758 (22) | 0.512725 (18) | 18.935 (8) | 15.549 (9) | 38.772 (31) |
| F-15 | 14°58′23 | 24°22′42 | 1951 | 973 | 5.75 | 812.9 | 0.1356 (10) | 0.10 | | 0.703738 (22) | 0.512728 (19) | 18.930 (11) | 15.551 (14) | 38.790 (56) |
| F-15b | 14°58′23 | 24°22′42 | 1951 | 868 | 6.45 | 645.9 | 0.1369 (17) | 0.09 | | | | | | |
| F-21 | 14°55′13 | 24°17′41 | 1951 | 1085 | 8.09 | 643.3 | 0.1336 (20) | 0.15 | | 0.703727 (18) | 0.512736 (2) | 19.020 (8) | 15.554 (9) | 38.832 (31) |
| F-16 | 14°56′19 | 24°21′38 | 1995 | 1081 | 4.79 | 1083.5 | 0.1358 (17) | 0.24 | | 0.703764 (19) | 0.512737 (4) | 18.932 (8) | 15.537 (9) | 38.752 (31) |
| F-08 | 14°56′23 | 24°21′40 | 1995 | 707 | 4.40 | 768.9 | 0.1358 (09) | 0.14 | | 0.703734 (22) | 0.512737 (5) | 18.937 (11) | 15.558 (9) | 38.814 (44) |
| *Carbonatites* | | | | | | | | | | | | | | |
| NF 43 | | | | 1623 | 22.87 | 343.1 | 0.1924 (20) | 0.16 | 0.1698 (39) | 0.703156 (16) | 0.512930 (6) | 19.865 (8) | 15.604 (9) | 39.208 (31) |
| NF 44 | | | | 481 | 12.60 | 184.4 | 0.1839 (24) | 0.22 | 0.1718 (48) | 0.703158 (20) | 0.512926 (3) | 19.866 (8) | 15.597 (9) | 39.189 (31) |

Numbers in parentheses are $2\sigma$ errors refering to the last digits. Samples ending with "b" are Re–Os duplicates. Sr and Pb ratios are from Doucelance et al. (2003). Mean values have been used in case of Pb duplicate analyses. $^{187}Os/^{188}Os$ ratios of carbonatites are corrected for Re decay using a mean age of 4 Ma.

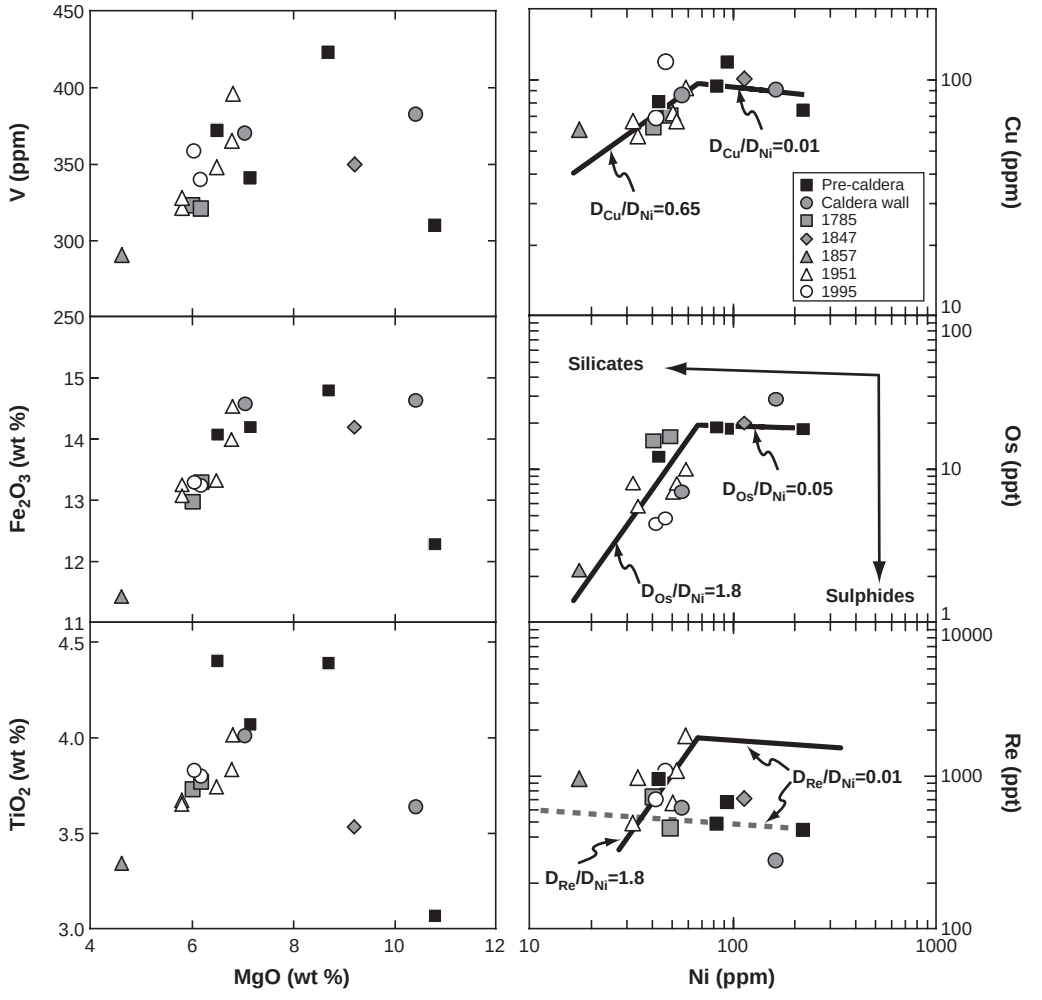


Fig. 2. Major and trace element variations of Fogo lavas. Though Fogo mafic lavas are not derived from a same parental magma, the $Fe_2O_3$–$TiO_2$–V–MgO variations suggest they have been differentiated first by crystallization of olivine and cpx and then by Fe–Ti oxide formation. The variations of Os and Cu versus Ni show that Fe–Ti oxide is a fractionating phase. Thick lines represent a fractional crystallization model starting from a primary melt with 220 ppm Ni, 18 ppt Os and 85 ppm Cu. The first step corresponds to an evolution with $D_{Os}/D_{Ni}=0.05$ and $D_{Cu}/D_{Ni}=0.01$. The second step begins at 65 ppm Ni with ratios of Os and Cu partition coefficients over that of Ni changed to $D_{Os}/D_{Ni}=1.8$ and $D_{Cu}/D_{Ni}=0.65$. The chalcophile property of Os and Cu supports that the change of their partition coefficients essentially reflects the formation of sulphides associated with Fe–Ti oxide formation. The overall negative trend in the Re vs. Ni diagram failed to be reproduced by a single-stage differentiation (dashed line) starting from the most primitive sample and a $D_{Re}/D_{Ni}$ as low a 0.01. The positive trend defined by the 1951–1995 lava flows can be reproduced by a two-step crystallisation model (thick line), starting at 220 ppm Ni and 1600 ppt Re with $D_{Re}/D_{Ni}=0.01$ and $D_{Re}/D_{Ni}=1.8$ below 65 ppm Ni, which support the chalcophile property of Re.

analytical scatter cannot account for all the variation observed and the overall positive trend with the inverse of $^{188}Os$ (Fig. 3). Global correlations with the other isotopic ratios (Fig. 4) support that the Os isotopic variation reflects the mixture between the two end-members previously identified. In addition, the correlations within flows between Os and Pb and Sr isotopic composition despite the fact that the samples are indistinguishable within the quoted uncertainties also confirms that the isotopic variations observed are real.

Fogo lavas have neodymium isotopic ratios ranging from 0.512718 to 0.512765. These isotopic ratios are similar to those previously measured for Fogo,

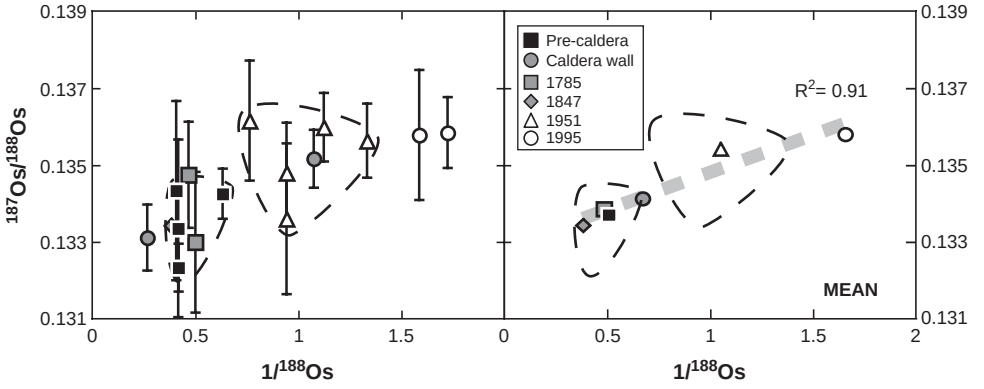


Fig. 3. $^{187}Os/^{188}Os$–$1/^{188}Os$ variation for Fogo lavas. Sample F-22 from 1857, which has the lowest Os content as well as the highest $^{187}Os/^{188}Os$ ratio, plots outside the range represented. Taken as a whole, Fogo lavas define a global positive trend, feature accentuated by the use of the average compositions as shown by the dashed grey line ($r^2$=0.91), which suggests a binary mixing. At the lava flow scale, basalts from the 1951 lava flows and pre-caldera group, which represent the most sampled groups, do not define any positive trend, implying that the intra-lava flow isotopic heterogeneity has been produced prior to the end of the differentiation. The lack of intra-lava flow relationship and the correlation at the volcano scale imply that the contribution of the radiogenic Os end-member occur during the magma differentiation.

after correction of Nd isotope ratios from Gerlach et al. (1988) for inter-laboratory bias (see Hoernle et al. (2002) for details).

Os–Sr–Nd–Pb compositions are also reported for two carbonatites from Fogo (Table 2). NF43 and NF44 have more radiogenic $^{187}Os/^{188}Os$ (0.1924 and 0.1839, respectively) than mafic lavas for concentrations of the same order (22.9 and 12.6 ppt, respectively). These radiogenic Os compositions are in agreement with those measured in carbonatites from the Canary Islands (Widom et al., 1999). Earlier works found ages of 3.4 ± 1.0 Ma (Lancelot and Allègre, 1974) and 4 Ma (Hoernle et al., 2002) for the Fogo carbonatites. In a $^{187}Os/^{188}Os$ vs. $^{187}Re/^{88}Os$ diagram, the two samples we analyzed yield an age of 3.2 ± 1.2 Ma, consistent with those previously proposed. Nevertheless, having no evidence of a common history for our two samples, the mean age of 4 Ma proposed by Hoernle et al. (2002) is used, leading to corrected $^{187}Os/^{188}Os$ ratios of 0.1698 ± 0.039 and 0.1718 ± 0.048 for NF43 and NF44, respectively. NF43 and NF44 also have very similar Sr–Nd–Pb isotopic compositions, identical within the uncertainty. The two carbonatites fall within the restricted range of previous analyses of carbonatites from Fogo (Gerlach et al., 1988; Hoernle et al., 2002). Their signature is less radiogenic than basaltic lavas for Sr isotopes ($^{87}Sr/^{86}Sr$=0.703158), but more radiogenic for Nd ($^{143}Nd/^{144}Nd$=0.512930) and Pb isotopes ($^{206}Pb/^{204}Pb$=19.868; $^{207}Pb/^{204}Pb$=15.599; $^{208}Pb/^{204}Pb$=39.201).

### 4.3. Isotopic variability within lava flows

The mafic lavas we analyzed correspond to at least six different volcanic series with different ages of eruption. The distinction of the different groups reveals an important isotopic variability within each lava flow. The two groups with more than two samples (i.e., 1951 and pre-caldera groups) have Os, Pb, Sr and Nd isotopic ratios that define binary mixing trends (Fig. 4). The basalts from 1951 have particularly low mean Os contents (~7.8 ppt), making them highly sensitive to post-differentiation contamination by radiogenic material. However, the inverse of Os contents of these samples does not correlate with $^{187}Os/^{188}Os$, indicating that they have not been significantly contaminated after differentiation (Fig. 3). Instead, the almost constant values of differentiation index associated with the isotopic variation implies that the mixture occurred prior to the end of magma differentiation and that the isotopic heterogeneity is preserved within the magma.

Pre-caldera samples define a linear correlation in $^{187}Os/^{188}Os$–$^{187}Re/^{188}Os$ diagram (not shown) that could represent either an isochron (395 ± 216 Ma and $(^{187}Os/^{188}Os)_0$=0.1317) or a binary mixture. The mixture hypothesis is supported by the correla-

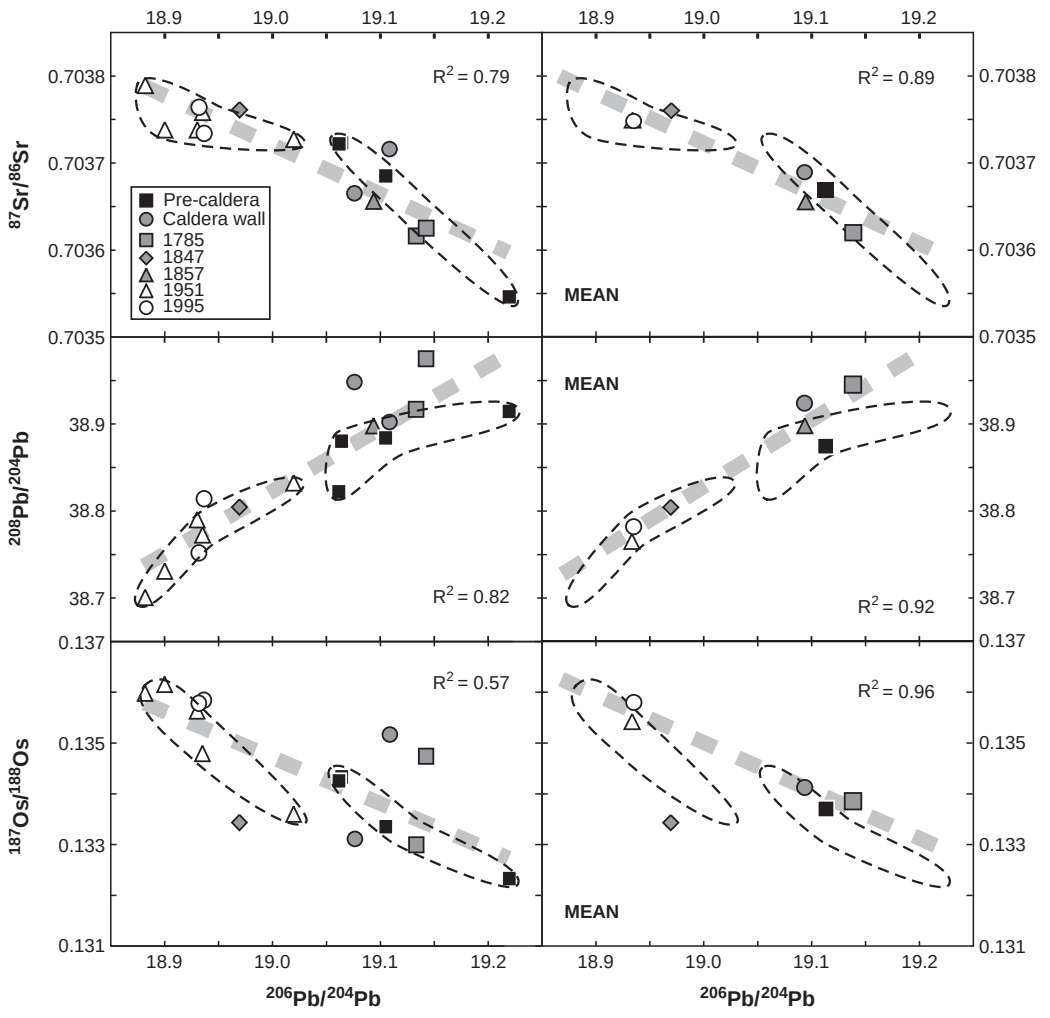


Fig. 4. $^{87}Sr/^{86}Sr$, $^{208}Pb/^{204}Pb$ and $^{187}Os/^{188}Os$ vs. $^{206}Pb/^{204}Pb$ variations of Fogo lavas. The 1951 lava flows and pre-caldera samples define trends in the isotopic diagrams (fields delimited by dashed lines) that are interpreted to reflect binary mixing. The entire dataset also defines correlations as shown by the thick dashed grey line, which represent the best-fit lines. Using the average isotopic compositions improves these correlations. Due to the $^{187}Os/^{188}Os$ scatter within a single lava flow, the best-fit curve in the $^{187}Os/^{188}Os$ vs. $^{206}Pb/^{204}Pb$ diagram is calculated using the lava flows which are sampled at least twice. The correlations defined by the average isotopic compositions are similar to the correlations within the 1951 and pre-caldera data, supporting a common origin for the intra-lava Os–Pb–Sr–Nd isotopic variations and the Fogo basalt isotopic evolution through time.

tions between the isotopic ratios and the incompatible element ratios such as Ba/Nb or Ba/La defined by the pre-caldera samples. Moreover, correlations between Sr–Nd–Pb isotopes indicate a binary mixture and, since the Os isotopes correlate with Sr–Nd–Pb, their variations should reflect the same mixture. Correcting Os isotopic compositions for post-eruption decay would reduce the Os variability within the pre-caldera group but would have no effect on the other isotopic ratios and remove the pre-caldera samples from the overall Pb–Os and Sr–Os correlations (Fig. 4).

The isotopic compositions of samples from the groups with two samples (Caldera wall and 1785 lava flow) do not define linear trends parallel to those defined by 1951's lava flows and pre-caldera samples. Without a more numerous sampling, discussing the origin of their intra-lava isotopic variability remains

somewhat speculative. Except for Os isotopic composition of sample F-22, the other isotopic compositions are within the range defined by the most numerous groups.

### 4.4. Temporal isotopic variations

The trends defined by the 1951 and pre-caldera groups are similar to those defined by the whole dataset, suggesting they reflect the same mixture. In order to study the temporal evolution of Fogo volcanism, we consider here the average isotopic compositions of each lava flow. As reported in Fig. 4, the average isotopic compositions define correlations, similar to those defined by the whole dataset, which can be explained by a mixture in variable proportions of two end-members. Due to their similarities in major, trace element and isotopic compositions, mafic lavas from the 1951 and 1995 lava flows can be interpreted to be representative of the current volcanism. Pre-caldera samples display Os, Pb, Sr and Nd ratios distinct from those measured in samples from the 1951–1995 lava flows (Fig. 4).

Except for one pre-caldera sample, the 1785 lava flow display the largest HIMU signature measured in this study and plot within the pre-caldera field. The sample from the 1847 lava flow plot within the 1951–1995 lava flow fields while the sample from the 1857 lava flow plot in the pre-caldera field (see Fig. 4). While the Pb, Sr and Nd isotopic compositions of the 1847 and 1857 samples are consistent with the correlations defined in the isotopic diagrams, these two samples have Os isotopic ratios plotting outside of the correlations defined by the other lava flows. The Os isotopic ratio of sample F-24 (1847 lava flow) is within the range defined by the other lava flows, suggesting that the deviation is caused by a sampling bias. Concerning the 1857 lava flow, sample F-22 has the lowest Os content measured in this study together with a high $^{187}Os/^{188}Os$ ratio (0.1548) that strongly differs from the isotopic compositions measured in other Fogo lavas. This feature strongly suggests that its Os isotopic composition reflect a post-differentiation contamination by radiogenic material such as old oceanic crust forming the sea floor.

Due to the short time interval between the 1847 and 1857 eruptions and to the isotopic scatter existing within the 1951 lava flow and the pre-caldera group, the two samples from the 1847 and 1857 lava flows could be grouped together. Such a grouping emphasizes the temporal isotopic evolution existing in the historic lava flows, starting from the moderate HIMU composition of the 1785 lava flow and pre-caldera group, toward the enriched composition (i.e. high $^{87}Sr/^{86}Sr$ and $^{187}Os/^{188}Os$ ratios and low $^{206}Pb/^{204}Pb$ and $^{143}Nd/^{144}Nd$ ratios) of the 1951–1995 lava flows, through the 1847 and 1857 lava flow compositions. A similar isotopic distinction has been previously observed in Fogo and Santiago basalts and interpreted as a temporal evolution of the proportions of the different end-members involved in the magmatic source (Gerlach et al., 1988).

## 5. Discussion

### 5.1. Re–Os behaviour during differentiation

Despite the fact that Fogo lavas belong to different lava series and derive from different parental magmas, their composition in major elements suggests that they have experienced similar episodes of differentiation. The evolution of the $TiO_2$, $Fe_2O_3$ and V contents relative to MgO (Fig. 2) supports a differentiation by fractional crystallization that may occur first by crystallization of olivine and clinopyroxene and later by crystallization of Fe–Ti oxides. The evolution of Os content with MgO and Ni contents is comparable to $TiO_2$ evolution (Fig. 2), with a change of slope at MgO = 7.1 wt.% and Ni = 65 ppm. Since the silicates have very low Os content, the decrease in Os suggests the formation and fractionation of sulphides (Burton et al., 2002). The similar evolution of Os and Cu (Fig. 2), both chalcophile elements, confirms that the increase of slope is related to sulphide formation enhanced by Fe–Ti oxide precipitation that induces a marked sulphur oversaturation in the melt. The bulk partition coefficient for Os can be estimated relative to that of Ni for the two steps of crystallization. A fractional crystallization model reproducing the Ni–Os trends is reported in Fig. 2, starting from a hypothetical primary melt with 220 ppm Ni, 18 ppt Os and 85 ppm Cu and $D_{Os}/D_{Ni} = 0.05$ and $D_{Cu}/D_{Ni} = 0.01$. At 65 ppm Ni, the ratios of Os and Cu partition coefficients over that of Ni increase signifi-

cantly to $D_{Os}/D_{Ni}=1.8$ and $D_{Cu}/D_{Ni}=0.65$. The estimation of bulk partition coefficient for Os is difficult because $D_{Ni}$ is changing during crystallization (Hart and Davis, 1978).

The high Re contents of Fogo lavas contrast with the low contents measured in Hawaiian subaerial lavas (<350 ppt), which have been attributed to reflect Re degassing during the eruption (Lassiter, 2003). Our dataset define an overall negative trend in the Re vs. Ni diagram which cannot be produced by a single-stage differentiation starting from the most primitive sample (Fig. 2). The positive trend defined by the 1951–1995 lava flows is similar to those defined in the other diagrams reported in Fig. 2, which suggests that sulphide formation has an significant effect on the evolution of Re content. Such a positive trend can be reproduced using a $D_{Re}/D_{Ni}$ equal to 1.8 for the second step of crystallization and the high Re content of F-06 requires a Re content up to 1600 ppt for the starting melt used for the first step. The dispersion of Fogo lavas in the Re vs. Ni diagram confirms that the different groups of samples identified above have to be derived from different parental magmas, with initial Re content as low as 150 and up to 1600 ppt for the recent lava flows. The high initial Re content required for the recent lava flows, which have the more enriched signature, suggests that the Re content is strongly influenced by the enriched component contribution. The initial Re content should be even higher if the magmas have encountered a significant degassing.

### 5.2. Origin of Fogo basalt isotopic variations

The correlations defined by the Os, Pb, Sr and Nd isotopic compositions of Fogo lavas support the existence of binary mixing between a moderate HIMU and an EM1-like end-member. The fact that these correlations are similar to the intra-lava flow trends defined by pre-caldera and 1951 groups (Fig. 4) suggests they reflect mixing of the same components. The existence of isotopic correlation within a single lava flow also implies that the mixture occurred after the magma formation and was not followed by an efficient homogenization.

The linear relationship observed between the mean $^{187}Os/^{188}Os$ and $1/^{188}Os$ ratios (Fig. 3) can be interpreted either as (1) the mixing of two end-members, one with high $^{187}Os/^{188}Os$ and low Os content and one with low $^{187}Os/^{188}Os$ and high Os content, or as (2) the addition of radiogenic material during or after the magma differentiation, which has a greater effect on the low Os content lava. The first hypothesis would imply that the measured Os concentrations directly reflect the proportion of mixing of the two end-members involved and should not correlate with indices of fractionation. However, it has been shown above that the Os content variation of Fogo basalts is consistent with differentiation processes, supporting the second hypothesis. Within a given lava flow the Os isotopes do not correlate with differentiation indices. This suggests that the contribution of the Os radiogenic end-member occurred prior to the end of the magma differentiation, producing an isotopic heterogeneity that is preserved in the magma, while differentiation has obscured the initial Os concentration variations.

To summarize, the combination of the different scales of variation imply that the enriched signature of Southern Cape Verde Islands is related to a shallow contamination. The enriched end-member has to interact with the magma during its differentiation and affect the Os–Pb–Sr–Nd isotopic compositions. This contribution can correspond either to the addition of another silicate melt with distinct isotopic composition or to the assimilation of surrounding lithologies.

The correlations defined by our dataset in the Sr–Nd–Pb isotopic diagrams (cf. Doucelance et al. (2003) and Figs. 5 and 6) are similar to those observed in previous studies of the Southern Islands (Gerlach et al., 1988; Davies et al., 1989; Kokfelt et al., 1998; Christensen et al., 2001). This feature strongly suggests that our isotopic dataset reflects similar mixtures of the same two end-members. The convergence of the Southern and Northern Island trends in the $^{208}Pb/^{204}Pb$–$^{206}Pb/^{204}Pb$ and $^{87}Sr/^{86}Sr$–$^{206}Pb/^{204}Pb$ isotopic diagrams toward high $^{206}Pb/^{204}Pb$ values have led to the identification of a common moderate HIMU end-member ($^{206}Pb/^{204}Pb \sim 20$, cf. Gerlach et al. (1988); Hoernle et al. (2002); Doucelance et al. (2003)) and two others: (a) an EM1-like end-member for the Southern Islands; (b) the local depleted mantle for the Northern Islands. On the basis of all the isotopic diagrams, the two end-members are identified in the Os isotopic diagrams. Using the

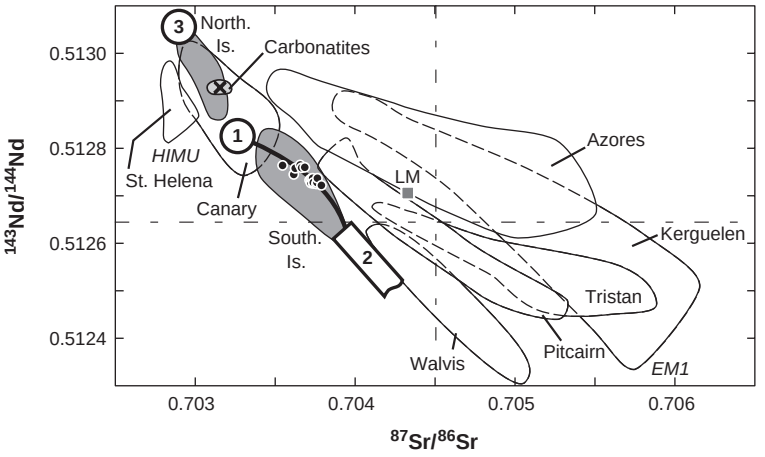


Fig. 5. $^{143}Nd/^{144}Nd$ vs. $^{87}Sr/^{86}Sr$ diagram for Cape Verde samples. Symbols correspond to Fogo samples which were analysed for Os: Circles=basalts; crosses=carbonatites. Grey fields=data from the Northern (Santo Antão, São Vicente, cf. Gerlach et al. (1988) and Southern Islands (Fogo: this study; Santiago: Gerlach et al. (1988)); Fogo carbonatites: this study and Hoernle et al. (2002). As basalts from Santiago show covariations between age and isotopic signature (Gerlach et al., 1988), only the latest volcanic series (Pico da Antonia formation) is plotted. The three Cape Verde end-members (see text for details) have the following compositions: for the common moderate HIMU end-member noted "1": $^{143}Nd/^{144}Nd=0.51281$ and $^{87}Sr/^{86}Sr=0.70334$; for the enriched end-member of the Southern Islands noted "2": $^{143}Nd/^{144}Nd=0.51262$ and $^{87}Sr/^{86}Sr=0.7040$; for the local depleted mantle end-member noted "3": $^{143}Nd/^{144}Nd=0.51305$ and $^{87}Sr/^{86}Sr=0.7028$. The mixing hyperbola is calculated using the following concentration ratios: $(Sr)_1/(Sr)_2=3.3$ and $(Nd)_1/(Nd)_2=3$. For comparison we report fields for Walvis ridge basalts (Richardson et al., 1982) and the following Atlantic islands: St. Helena (Chaffey et al., 1989), Azores (Widom and Shirey, 1996), Canary (Hoernle et al., 1991; Marcantonio et al., 1995) and Tristan da Cunha (White and Hofmann, 1982; Le Roex et al., 1990; Cliff et al., 1991). Samples from the Southern and Northern Islands define two distinct domains. The Northern Islands define a steep trend with low $^{87}Sr/^{86}Sr$ and radiogenic $^{143}Nd/^{144}Nd$, almost parallel to the trend defined by St. Helena basalts. In contrast, the Southern Islands define a trend significantly steeper than the classical mantle array from the lowest $^{143}Nd/^{144}Nd$ value of the Northern Islands toward unradiogenic $^{143}Nd/^{144}Nd$ and moderately radiogenic $^{87}Sr/^{86}Sr$ ratios. Also reported are fields for Pitcairn for which the EMI-like signature has been explained by sediment contribution in the source (Woodhead and Devey, 1993; Eisele et al., 2002) and Kerguelen islands (Dosso and Murthy, 1980; White and Hofmann, 1982; Weis et al., 1993). HIMU is for the extreme HIMU end-member; EM1 corresponds to the Enriched Mantle 1 (Zindler and Hart, 1986). LM=Lower Mantle. Its isotopic composition ($^{87}Sr/^{86}Sr=0.70429$ and $^{143}Nd/^{144}Nd=0.51272$) is calculated as resulting from the mixture of Bulk Silicate Earth material and ~17% of Depleted Mantle (See Doucelance et al. (2003) for details).

converging isotopic trends defined by the Southern and Northern Islands, the composition of the moderate HIMU end-member is estimated: $^{187}Os/^{188}Os\sim0.1325$, $^{206}Pb/^{204}Pb\sim19.76$, $^{87}Sr/^{86}Sr\sim0.70334$ and $^{143}Nd/^{144}Nd\sim0.51281$. The location of the EM1-like end-member in the isotopic diagrams is less constrained. However, using the isotopic correlations, a possible isotopic composition can be estimated: $^{206}Pb/^{204}Pb\sim18.60$, $^{87}Sr/^{86}Sr\sim0.7040$ and $^{143}Nd/^{144}Nd\sim0.51262$ and $^{187}Os/^{188}Os\sim0.1450$. This composition has been chosen to plot at the enriched extremity of the Southern Island field in the different isotopic diagrams and one should keep in mind during the following discussion that the actual composition of the enriched component is likely to be more extreme.

### 5.3. Nature of the enriched end-member

On the basis of trace elements and Sr–Nd–Pb compositions, previous studies have identified the EM1-like end-member of Southern Islands as the sub-continental lithospheric mantle (SCLM) (Gerlach et al., 1988; Davies et al., 1989; Kokfelt et al., 1998; Doucelance et al., 2003). It should be noted that evidence has also been shown that fragments of continental lithosphere may be located beneath the eastern Canary Islands (Hoernle et al., 1991; Hoernle, 1998; Widom et al., 1999). The radiogenic Os isotopic composition we determine for the enriched end-member is an unexpected feature for the sub-continental lithospheric mantle. Indeed, most of the ultramafic xenoliths sampling SCLM display partic-

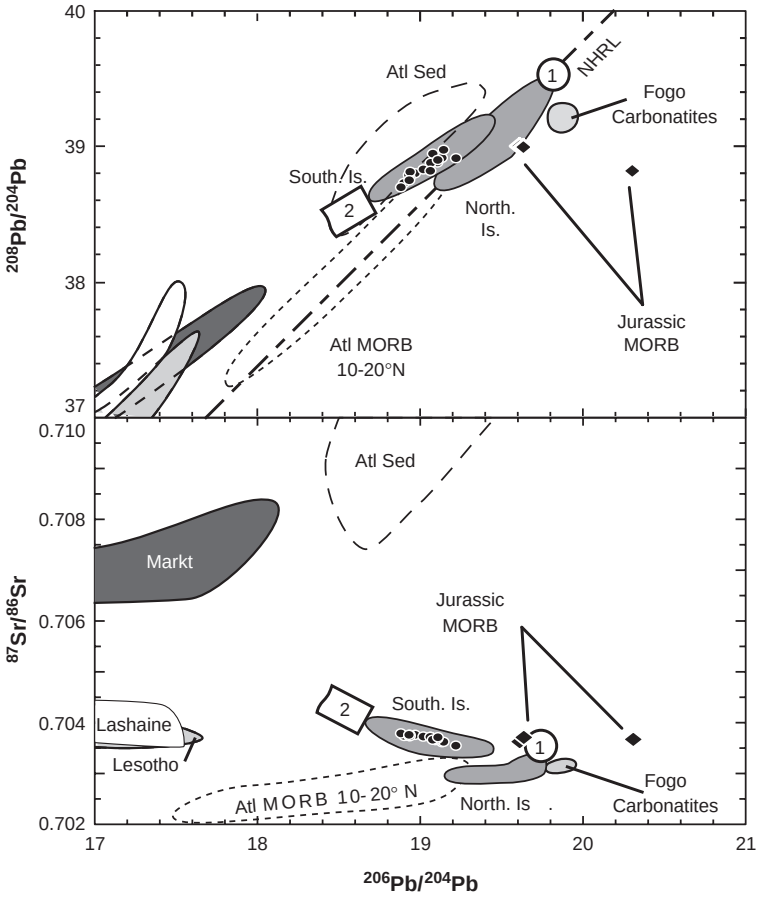


Fig. 6. $^{87}Sr/^{86}Sr$ and $^{208}Pb/^{204}Pb$ vs. $^{206}Pb/^{204}Pb$ diagram with potential candidates for the EM1-like end-member. Black circles correspond to Fogo samples analysed for Os. Black diamonds represent the local Jurassic MORB (Gerlach et al., 1988). Northern Islands (Santo Antão, São Vicente, cf. Gerlach et al. (1988)), Southern Islands (Fogo: this study; Santiago: Gerlach et al. (1988) and Fogo carbonatites (this study and Hoernle et al. (2002)) are reported as grey fields. The moderate HIMU and the EM1-like end-member compositions are plotted and labelled 1 and 2, respectively. The dashed fields are Atlantic sediments (White and Dupré, 1986; Hoernle et al., 1991; Hoernle, 1998) and the 10–20° N Atlantic MORB (Dosso et al., 1993). The dashed thick line represents the Northern Hemisphere Reference Line (Hart, 1984). Fields for the African lower continental crust (granulites from Lashaine, Lesotho and Markt groups (Rogers and Hawkesworth, 1982; Cohen et al., 1984; Huang et al., 1995) are also shown.

ularly unradiogenic $^{187}Os/^{188}Os$ ratios (average $^{187}Os/^{188}Os \approx 0.1214 \pm 0.0078$ ($1\sigma$)) (Walker et al., 1989; Carlson and Irving, 1994; Pearson et al., 1995; Chesley et al., 1999; Meisel et al., 2001; Schmidt and Snow, 2002). These low $^{187}Os/^{188}Os$ ratios reflect the evolution of a mantle reservoir with a low Re/Os due to the Re depletion associated with the crust extraction (Walker et al., 1989; Pearson et al., 1995). Even if some minerals have high Re/Os ratios and have developed radiogenic $^{187}Os/^{188}Os$ ratios with time, sulphides with low Re/Os dominate the Os budget of ultramafic xenoliths and impose an unradiogenic bulk composition (Burton et al., 1999; Burton et al., 2000). The $^{187}Os/^{188}Os$ ratios measured in ultramafic xenoliths remain less radiogenic than those measured in Cape Verde basalts and the value estimated for the enriched end-member.

The contribution of the enriched end-member may be related to different processes occurring at different steps of the magma evolution, such as (1) the mixture with oceanic lithosphere melted by the thermal effect associated with the mantle plume, (2) the assimilation

in a magmatic chamber of the surrounding rocks or (3) the interaction with the oceanic crust during the magma ascent. In the following section, we investigate the different possible contaminants that may interact with the magma, with the aim of explaining the radiogenic Os isotopic compositions of basalts. This contaminant must account for Pb–Sr–Nd isotopic and trace elements compositions that have previously led to propose it to be the sub-continental lithospheric mantle, i.e. the steep trend defined by the Cape Verde Southern Islands in the Sr–Nd isotopic diagram which differs from those defined by other oceanic islands (Fig. 5) and the elevated $^{208}Pb/^{204}Pb$ and $^{207}Pb/^{204}Pb$ ratios for a given $^{206}Pb/^{204}Pb$.

*5.3.1. Interaction with the volcanic pile*

On the basis of our sampling, the assimilation of ancient lavas forming the volcanic pile during the latest stage of the magma ascent or interaction with the underlying lava flows can be rejected. Indeed, the temporal isotopic variation shows that the younger the lavas are, the more they have an EM1-like signature, with higher $^{87}Sr/^{86}Sr$ and $^{187}Os/^{188}Os$ and lower $^{206}Pb/^{204}Pb$ ratios. Conversely, the oldest lavas display isotopic compositions closer to the moderate HIMU end-member and cannot account for the EM1-like contaminant. Invoking older lavas that may not be sampled in this study, located deeper in the edifice, does not provide a more satisfying explanation. While these lavas could have high $^{87}Sr/^{86}Sr$ and $^{187}Os/^{188}Os$ ratios produced by post-eruption decay, the low $^{206}Pb/^{204}Pb$ ratio of the EM1-like end-member, lower than the moderate HIMU end-member composition, could not be explained. The enriched signature has to be related to an end-member that has undergone an evolution with a low U/Pb ratio. Thus, the variation of the Os, Sr, Nd and Pb isotopic ratios is related to the assimilation of deeper material.

*5.3.2. Assimilation of oceanic crust or sediment*

For most of the Os analyses of OIB (Marcantonio et al., 1995; Widom and Shirey, 1996; Widom et al., 1999), samples with concentrations lower than 30 ppt display a large range of Os isotopic ratios, up to 0.195, which is interpreted as sediment or crustal material assimilation during the magma ascent. Concerning Fogo basalts, neither Jurassic MORB identified by Gerlach et al. (1988) on the Southern Islands nor actual Atlantic sediments can account for the end-member which displays $^{187}Os/^{188}Os \sim 0.1450$, $^{206}Pb/^{204}Pb \sim 18.60$, $^{87}Sr/^{86}Sr \sim 0.7040$ and $^{143}Nd/^{144}Nd \sim 0.51262$ (see Fig. 6). Jurassic MORB have the following isotopic compositions: $^{87}Sr/^{86}Sr = 0.703627 - 0.703707$, $^{143}Nd/^{143}Nd = 0.51306 - 0.51309$ and $^{206}Pb/204Pb = 19.61 - 20.30$; they are not consistent with the EM1-like end-member identified in the Southern Islands. Despite the fact that Atlantic sediments (White and Dupré, 1986; Hoernle et al., 1991; Hoernle, 1998) with the lowest $^{206}Pb/^{204}Pb$ ratios possess Pb isotopic compositions that can account for the EM1-like end-member, they have $^{87}Sr/^{86}Sr$ ratios that are too radiogenic, which precludes them to be the contaminant.

*5.3.3. Contribution of the underlying mantle*

The contribution of the depleted MORB mantle has been already proposed (Gerlach et al., 1988; Davies et al., 1989; Doucelance et al., 2003) to explain the isotopic variation of the Northern Island basalts. As shown in Fig. 6, the field of the 10–20° N Atlantic MORB (Dosso et al., 1993) plots in the continuity of the Northern Island trend. This is not the case for the Southern Islands, which precludes a similar contribution in the source of Fogo. Moreover, the fact that assimilation of depleted mantle by oceanic basalts leads to unradiogenic Os isotopic ratios and an increase of Os content (Widom et al., 1999) also argues against such a contribution.

The carbonatites found on the Cape Verde Islands provide evidence that metasomatic processes occur in the underlying mantle. The carbonatites analyzed preserve radiogenic $^{187}Os/^{188}Os$ ratios consistent with the enriched end-member but too elevated in Pb and too low in Sr isotopic ratios (Fig. 6). In addition, Fogo basalts do not display high CaO contents compared to Northern Island basalts, as would be expected with a carbonatitic contribution. Generally, the low $^{143}Nd/^{144}Nd$ together with moderate $^{87}Sr/^{86}Sr$ measured in oceanic island basalts are attributed to a mantle metasomatised by migration of small volume of partial melt (Hawkesworth et al., 1984). Since the local Jurassic MORB have depleted compositions (Gerlach et al., 1988), the convecting mantle that formed the oceanic lithosphere consisted of depleted MORB mantle. Subsequent metasomatism of the oceanic lithospheric mantle

cannot explain the low $^{143}Nd/^{144}Nd$ ratios of Southern Island basalts which require a long evolution with a low Sm/Nd ratio. The end-member responsible for the enriched signature of Southern Island lavas must thus be related to an ancient material located in the oceanic lithosphere.

*5.3.4. Fragments of continental lithosphere within the oceanic lithosphere*

As developed above, the trace element and Pb–Sr isotopic compositions of the Southern Island basalts are consistent with sub-continental lithospheric mantle as the origin of the enriched signature (Gerlach et al., 1988; Davies et al., 1989; Kokfelt et al., 1998; Doucelance et al., 2003) but the radiogenic $^{187}Os/^{188}Os$ ratios measured in Fogo lavas require a high Re/Os component that cannot be the sub-continental lithospheric mantle. In earlier works, lower continental crust has been proposed to explain the enriched compositions of the Cape Verde and Canary volcanic rocks (Hoernle et al., 1991; Hoernle, 1998; Hoernle et al., 2002). From an Os isotopic point of view, xenoliths sampling the lower continental crust have radiogenic isotopic ratios ranging from 0.179 to 1.814 (Esperança et al., 1997; Saal et al., 1998) and highly variable Sr–Nd–Pb isotopic compositions related to the age of their formation and of the following events of metamorphism (Rudnick, 1992). In a recent study, Jull and Kelemen (2001) have shown that lower crust delamination may occur in several geological settings such as arcs, volcanic rifted margins and continental areas that are undergoing extension or removal of the underlying upper mantle. The extension associated with the opening of the Atlantic Ocean represents a favourable setting for lower crustal delamination and the location of the Cape Verde plateau, close to the African continent, suggests that some lower continental fragments could have been stored into the oceanic lithosphere. The presence of continental crust fragments found by drilling in the Iberian abyssal plain (Whitmarsh et al., 1998) supports such an assumption.

The fact that our estimate of the enriched end-member Os isotopic composition ($^{187}Os/^{188}Os \sim 0.1450$) does not fall within the lower continental crust range of compositions suggests that it has a more extreme location in the isotopic diagrams, with higher $^{187}Os/^{188}Os$, $^{87}Sr/^{86}Sr$ ratios and lower $^{206}Pb/^{204}Pb$ and $^{143}Nd/^{144}Nd$ ratios. It should also be noted that, due to their low buoyancy, the upper lithospheric mantle and the lower part of the continental crust appears to be the most likely parts of the continental lithosphere to be delaminated (Kay and Mahlburg Kay, 1993). Because of the high contrast in Os content and Os isotopic ratios between the lower continental crust and the SCLM, a small amount of SCLM will significantly decrease the Os isotopic composition of the contaminant as well as increase its Os content. Thus, even a $^{187}Os/^{188}Os$ ratio close to 0.145 for the enriched contaminant would still be consistent with the lower continental crust if mixed with sub-continental lithospheric mantle.

The isotopic data available on the African granulites (Rogers and Hawkesworth, 1982; Cohen et al., 1984; Huang et al., 1995) show low $^{206}Pb/^{204}Pb$ ratios and unradiogenic $^{143}Nd/^{144}Nd$ associated with moderate $^{87}Sr/^{86}Sr$. In particular, the Markt group of granulite xenoliths from the margin of the Kaapvaal Craton have Sr–Nd–Pb isotopic compositions in good agreement with the correlations defined by our dataset (Fig. 6).

Incompatible trace element ratios also provide arguments in favour of the involvement of lower continental crust in the source of the Southern Islands. In a La/Ba vs. Nb/Ba plot (Fig. 7) the Southern and Northern Islands define two contiguous but distinct fields. Basalts from the Northern Islands define a trend toward high Nb/Ba and La/Ba values, consistent with a Depleted Mantle contribution. In contrast, the Southern Islands have lower La/Ba and Nb/Ba ratios and plot below the trend toward bulk continental crust values (Rudnick and Fountain, 1995) defined by the EM1-like basalts from the Atlantic Ocean (Humphris and Thompson, 1983; Le Roex, 1985; Weaver et al., 1987; Le Roex et al., 1990; Cliff et al., 1991) and from Pitcairn (Woodhead and Devey, 1993). The lack of correlation between trace element and isotopic ratios is related to the fact that our samples are derived from different parental magmas which have different fractionation and contamination histories. However, the Southern Islands trace element ratios support the involvement of a Ba-rich source in the Southern Islands, closer in composition to the granulites than to the bulk continental

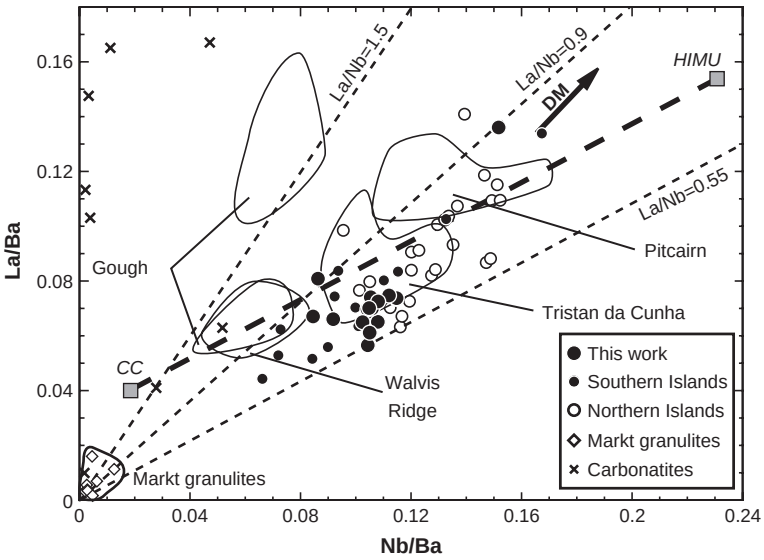


Fig. 7. La/Ba vs. Nb/Ba for Fogo basalts and samples from the whole archipelago with similar major element characteristics, Markt granulites (Huang et al., 1995) and Fogo carbonatites (Hoernle et al., 2002). CC=Continental Crust from (Rudnick and Fountain, 1995). The thick dashed line represents the mixture between (1) a continental crustal-derived sediment with an average crustal composition and (2) the extreme HIMU end-member (Weaver, 1991). For comparison, we also show fields for Gough Island (Le Roex, 1985; Weaver et al., 1987), Walvis ridge basalts (Humphris and Thompson, 1983), Tristan da Cunha (Le Roex et al., 1990; Cliff et al., 1991) and Pitcairn Islands (Woodhead and Devey, 1993; Eisele et al., 2002). Cape Verde Southern Island basalts have a low Nb/La ratio and define a rough trend toward granulite-like compositions while the other oceanic basalts reported trend toward the CC composition.

crust composition, more representative of sediment compositions.

The temporal isotopic evolution of Fogo and Santiago basalts shows that the enriched end-member contribution increases through time (this study and Gerlach et al. (1988)). This temporal evolution supports that the lower crust fragments are located at shallow depth in the oceanic lithosphere. The mafic compositions of Fogo lavas imply that the lower crustal material is totally assimilated by the magma or at least melts to a high degree. Combining all these features suggests that the enriched signature of the Cape Verde Southern Island basalts is produced by interaction of the magma with lower continental crust fragments present at shallow depth in the oceanic lithosphere, possibly within the crust. The location of the enriched end-member is consistent with the conclusions of previous studies of Canary and Cape Verde Islands, for which the presence of fragments of continental lithosphere within the oceanic lithosphere was proposed (Gerlach et al., 1988; Davies et al., 1989; Hoernle et al., 1991; Hoernle, 1998; Widom et al., 1999).

### 5.4. Nature of the moderate HIMU end-member

Previous studies have proposed various origins for the moderate HIMU-like signature (Gerlach et al., 1988; Davies et al., 1989; Kokfelt et al., 1998; Christensen et al., 2001; Doucelance et al., 2003). Gerlach et al. (1988) and Davies et al. (1989) have proposed two different models involving, for the Southern Islands, a mixture between a DMM-HIMU hybrid end-member and an EM1-like end-member. Both their models are based on an ancient recycled oceanic crust (ROC) present either as a major component in the ascending plume or as an ubiquitous small-scale heterogeneity in the depleted mantle. Kokfelt et al. (1998) and Christensen et al. (2001) have suggested alternative models based on a so-called “young HIMU”, having a HIMU-like trace element pattern but moderate Pb isotopic ratios. Kokfelt et al. (1998) proposed this end-member to be associated with carbonatitic fluids produced during metasomatic processes while Christensen et al. (2001) argued in favour of “young” recycled oceanic crust (age not given). Recently, Doucelance et al.

(2003) have shown that a "young HIMU" cannot explain the most radiogenic Pb compositions of the Northern Islands. Using the helium evidence for lower mantle involvement (Christensen et al., 2001; Doucelance et al., 2003), they model the Sr and Pb isotopic composition of the moderate HIMU end-member as a mixture of lower mantle material and 1.6 Ga recycled oceanic crust.

The Os isotopic composition of the moderate HIMU end-member is the less radiogenic of the two Fogo end-members, significantly lower than the extreme HIMU-like signature ($^{187}Os/^{188}Os \sim 0.155$) defined by samples from the Austral-Cook Islands (Hauri and Hart, 1993; Reisberg et al., 1993; Schiano et al., 2001) or than the St. Helena values (~0.145) (Reisberg et al., 1993).We will show that such an unradiogenic value is fully consistent with a mixture of lower mantle material and a 1.6 Ga recycled oceanic crust as it has been proposed on the basis of Pb–Sr–He isotopes. Using the correlations that are observed in the isotopic diagrams, we will also confirm that the HIMU-like end-member is not related to carbonatitic fluids.

*5.4.1. Rejecting carbonatites as the HIMU-like end-member*

If carbonatites are a common feature on continents, they are rare on oceanic islands (Allègre et al., 1971). Their origin is still discussed and we want to focus on their possible influence in the source of basalts. Recently, assimilation of carbonatites by the lavas has been proposed to explain trace element enrichment in some basaltic rocks erupted on São Vicente (Northern Islands, cf. Jorgensen and Holm (2002)). The Sr, Nd, Pb isotopic compositions of the two carbonatites reported in this work are similar to those previously analyzed (Gerlach et al., 1988; Hoernle et al., 2002). The locations in the different isotopic diagrams (Figs. 5, 6 and 8), with radiogenic $^{187}Os/^{188}Os$ and $^{208}Pb/^{204}Pb$ ratios that are too low relative to $^{206}Pb/^{204}Pb$ ratios preclude carbonatites from being the moderate HIMU end-member of Fogo

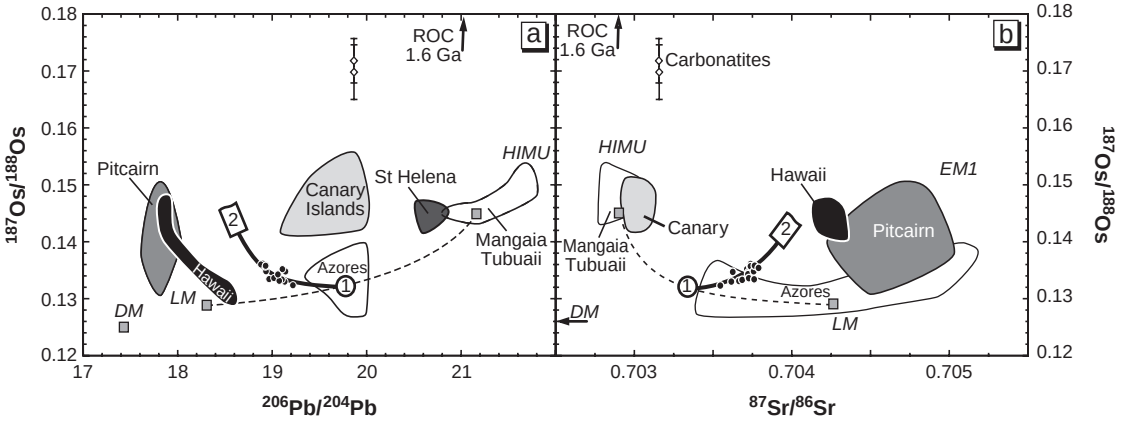


Fig. 8. (a) $^{187}Os/^{188}Os$ vs. $^{206}Pb/^{204}Pb$ and (b) $^{187}Os/^{188}Os$ vs. $^{87}Sr/^{86}Sr$ for Fogo samples. Black circles=basalts; open diamonds =carbonatites. LM=Lower Mantle; DM=Depleted Mantle; ROC=Recycled Oceanic Crust. HIMU is for the extreme HIMU end-member; EM1 corresponds to the Enriched Mantle 1 (Hauri and Hart, 1993; Reisberg et al., 1993). Also reported are fields for St Helena (Reisberg et al., 1993); Azores (Widom and Shirey, 1996); Canary Islands (with Os>45 ppt from Marcantonio et al. (1995) and those from Widom et al. (1999) thought to be representative of the plume); Hawaii (Hauri et al., 1996); Mangaia, Tubuaii (Hauri and Hart, 1993) and Pitcairn islands (Eisele et al., 2002). In comparison with the Azores and Canary Islands, Fogo lavas show less dispersion of the $^{187}Os/^{188}Os$ ratio relative to $^{206}Pb/^{204}Pb$ or $^{87}Sr/^{86}Sr$. This homogeneity does not reflect a sampling bias at the island scale since pre- and post-caldera samples have been analyzed. The $^{187}Os/^{188}Os$ variation is thought to reflect mixing effects. The locations of end-members "1" and "2" as well as concentration ratios used to calculate the mixing hyperbolas (plain curves) are computed to provide the best fit curves in the whole dataset. End-member "1": $^{187}Os/^{188}Os=0.1325$ $^{87}Sr/^{86}Sr=0.70334$; $^{206}Pb/^{204}Pb=19.76$; End-member "2": $^{187}Os/^{188}Os=0.1450$; $^{87}Sr/^{86}Sr=0.7040$, $^{206}Pb/^{204}Pb=18.60$; and $(Sr)_1/(Sr)_2=3.3$; $(Pb)_1/(Pb)_2=1$; $(Os)_1/(Os)_2=8.7$. The Os isotopic composition of 1.6 Ga recycled oceanic lithosphere is set at 0.145, by analogy with St. Helena and Mangaia basalts that have similar Pb isotopic compositions. Dashed curves represent mixing hyperbolas between this latter composition and that of the Lower Mantle (cf. Fig. 3 and Doucelance et al. (2003)). $(Sr)_{ROC}/(Sr)_{LM}=3$; $(Pb)_{ROC}/(Pb)_{LM}=1.33$; $(Os)_{ROC}/(Os)_{LM}=0.33$.

volcanism. The recent study of Cape Verde carbonatites by Hoernle et al. (2002) has shown that major and trace element as well as isotopic compositions of calcio-carbonatites located on Fogo, Brava, São Vicente and Santiago islands are consistent with metasomatic processes involving a low degree of melting of a recycled carbonated oceanic crust (1.6 Ga). However, the comparison of carbonatites and basalts from São Vicente has shown evidence of two separate HIMU sources located within the Cape Verde plume (Jorgensen and Holm, 2002). The high $^{187}Os/^{188}Os$ (up to 0.171) measured in carbonatites together with their Pb isotopic compositions are consistent with a HIMU source with high Re/Os for carbonatitic fluids distinct from the HIMU basaltic source and derived from 1.6 Ga ROC.

*5.4.2. Recycled oceanic crust and lower mantle material*

The presence of lower mantle material in the Cape Verde is supported by the high $^{3}He/^{4}He$ ratios measured in the Northern Island basalts by Christensen et al. (2001) and Doucelance et al. (2003). Despite the fact that Southern Island basalts tend toward the Cape Verde mantle plume composition in the Os–Pb–Sr–Nd isotopic diagrams, they do not display high $^{3}He/^{4}He$ ratios. This feature can be explained by the contribution of lower crustal material, which has low $^{3}He/^{4}He$, compensating for the primitive He signature.

The presence of lower mantle associated with recycled oceanic crust in the mantle plume is responsible for the unradiogenic Os isotopic composition of the moderate HIMU end-member, closer to the peridotitic mantle value (Roy-Barman and Allègre, 1994; Snow and Reisberg, 1995) than the extreme HIMU value (Hauri and Hart, 1993; Reisberg et al., 1993; Schiano et al., 2001). The lower mantle composition is thought to reflect the mixing of Bulk Silicate Earth material and depleted mantle in the proportion of 83:17 (Allègre and Lewin, 1989; Doucelance et al., 2003). The $^{187}Os/^{188}Os$ ratio of BSE (i.e. primitive mantle) has been estimated to $^{187}Os/^{188}Os \sim 0.1296 \pm 0.0008$ (Meisel et al., 2001), in good agreement with the chondrite compositions (Luck et al., 1980). Combined with the estimate of depleted mantle composition ($^{187}Os/^{188}Os \sim 0.125$) based on abyssal peridotites (Roy-Barman and Allègre, 1994; Snow and Reisberg, 1995), this yields a $^{187}Os/^{188}Os$ ratio close to 0.129 for the lower mantle, similar within the uncertainty to the BSE composition.

Estimating the Os isotopic evolution of recycled oceanic lithosphere remains a difficult task since it is composed of different layers (basalt, gabbro and depleted peridotite) with different Re/Os ratios and Os isotopic evolutions through time. Moreover the effects of melting and dehydration during subduction processes on the Re/Os ratios are not well enough constrained to enable precise and relevant calculations (Becker, 2000). Using an Os-evolution model of basalt with a low $^{187}Re/^{188}Os$ value of 50 (Widom et al., 1999) yields very radiogenic $^{187}Os/^{188}Os$ ratio of ~1.4 for 1.6 Ga recycled oceanic crust much more radiogenic than the extreme HIMU end-member. Hauri and Hart (1993) proposed the HIMU end-member corresponds to a mixture of recycled oceanic crust and mantle peridotite. The oceanic lithospheric mantle, which has a low $^{187}Re/^{188}Os$ ratio and a high Os content, would then lower the bulk $^{187}Os/^{188}Os$ of the recycled material. Due to the difference of Pb, Sr and Nd concentrations between oceanic crust and oceanic lithosphere peridotite, the latter would have a negligible effect on the Pb, Sr and Nd isotopic compositions.

In the case of the Cape Verde Islands, a 1.6 Ga recycled oceanic crust is associated with lower mantle material in the plume. Since the moderate HIMU end-member composition appears to be mainly dominated by the lower mantle material with high Os content and unradiogenic $^{187}Os/^{188}Os$ ratio, the Cape Verde lavas do not provide constraints on the composition of the 1.6 Ga recycled oceanic crust. However, by analogy with basalts from St. Helena (Reisberg et al., 1993) and Mangaia (Hauri and Hart, 1993; Schiano et al., 2001) with Pb isotopic compositions close to those calculated for a 1.6 Ga recycled oceanic crust, we estimate a $^{187}Os/^{188}Os$ ratio of 0.145 for the 1.6 Ga ROC melt-derived (Fig. 8). The mixture of such a component (1.6 Ga recycled oceanic crust and its residual mantle) with lower mantle material, illustrated in Fig. 8, reproduces the Os isotopic composition of the moderate HIMU end-member as proposed by Doucelance et al. (2003).

## 6. Conclusions

Our Os–Nd isotope dataset of Fogo lavas complements the work of Doucelance et al. (2003). The Sr–

Nd–Pb isotopic data show correlations similar to those previously observed between a moderate HIMU end-member and an EM1-like end-member. The correlations in the isotopic diagrams involving the Os and Nd isotopic ratios reflect the same mixing between the two end-members identified for the Southern Islands. The isotopic composition of the moderate HIMU end-member identified as the plume signature can be produced by the mixing of melts derived from 1.6 Ga recycled oceanic lithosphere and lower mantle material. The EM1-like end-member, previously identified as sub-continental lithospheric material on the basis of trace elements and Sr, Nd, Pb isotopic ratios, displays a radiogenic Os isotopic signature which requires the presence of a high Re/Os material. The temporal isotopic variation shows an increasing effect of the EM1-like end-member in the most recent lavas that supports the presence of the enriched end-member located at shallow depth in the oceanic lithosphere. The Os–Pb–Sr–Nd isotopic and trace element compositions of Fogo lavas lead to the identification of the contaminant as continental lithospheric fragments including lower continental crust, presently located under the Southern Islands and incorporated in the oceanic lithosphere during the Atlantic Ocean opening.

## Acknowledgements

This work would not have gone so far without the stimulating discussions with A.E. Saal, C.H. Langmuir and A. Bezos. We thank L. Reisberg and E. Widom for their constructive and helpful reviews. P. Agrinier generously gave us the two carbonatites. RD work at GEOTOP was supported by a Lavoisier post-doctoral fellowship. This is IPGP contribution 2034. **[RLR]**

## References

Allègre, C.J., Lewin, E., 1989. Chemical structure and history of the Earth: evidence from global non-linear inversion of isotopic data in a three-box model. Earth Planet. Sci. Lett. 96, 61–88.

Allègre, C.J., Luck, J.-M., 1980. Osmium isotopes as petrogenetic and geological tracers. Earth Planet. Sci. Lett. 48, 148–154.

Allègre, C.J., Turcotte, D.L., 1985. Geodynamical mixing in the mesosphere boundary layer and the origin of oceanic islands. Geophys. Res. Lett. 12, 207–210.

Allègre, C.J., Pineau, F., Bernat, M., Javoy, M., 1971. Evidence for the occurrence of carbonatites on the Cape Verde and Canary islands. Nature Phys. Sci. 233, 103–104.

Allègre, C.J., Hamelin, B., Provost, A., Dupré, B., 1986/87. Topology in isotopic multispace and origin of mantle chemical heterogeneities. Earth Planet. Sci. Lett., 81, 319–337.

Becker, H., 2000. Re–Os fractionation in eclogites and blueshcists and the implications for recycling of oceanic crust into the mantle. Earth Planet. Sci. Lett. 177, 287–300.

Bennet, V.C., East, T.M., Norman, M.D., 1996. Two mantle-plume components in Hawaiian picrites inferred from correlated Os–Pb isotopes. Nature 381, 221–224.

Birck, J.-L., Roy-Barman, M., Capmas, F., 1997. Re–Os isotopic measurements at the femtomole level in natural samples. Geostand. Newsl. 20, 19–27.

Brandon, A.D., Norman, M.D., Walker, R.J., Morgan, J.W., 1999. 1860s–1870s systematics of Hawaiian picrites. Earth Planet. Sci. Lett. 174, 25–42.

Burton, K.W., Schiano, P., Birck, J.-L., Allègre, C.J., 1999. Osmium isotope disequilibrium between mantle minerals in a spinel-lherzolite. Earth Planet. Sci. Lett. 172, 311–322.

Burton, K.W., et al., 2000. The distribution and behaviour of rhenium and osmium amongst mantle minerals and the age of the lithospheric mantle beneath Tanzania. Earth Planet. Sci. Lett. 183, 93–106.

Burton, K.W., et al., 2002. The compatibility of rhenium and osmium in natural olivine and their behaviour during mantle melting and basalt genesis. Earth Planet. Sci. Lett. 198, 63–76.

Carignan, J., Hild, P., Mevelle, G., Morel, J., Yeghichevan, D., 2001. Routine analyses of trace elements in geological samples using flow injection and low pressure on-line liquid chromatography coupled to ICP-MS: a study of reference materials BR, DR-N, UB-N, AN-G and GH. Geostand. Newsl. 25, 187–198.

Carlson, R.W., Irving, A.J., 1994. Depletion and enrichment history of subcontinental lithospheric mantle; an Os, Sr, Nd and Pb isotopic study of ultramafic xenoliths from the northwestern Wyoming Craton. Earth Planet. Sci. Lett. 126, 457–472.

Chaffey, D.J., Cliff, R.A., Wilson, B.M., 1989. Characterization of the St. Helena magma source. Geol. Soc. London Spec. Publ. 42, 257–276.

Chauvel, C., Hofmann, A.W., Vidal, P., 1992. HIMU-EM: the French Polynesian connection. Earth Planet. Sci. Lett. 110, 99–119.

Chesley, J.T., Rudnick, R.L., Lee, C.-T., 1999. Re–Os systematics of mantle xenoliths from the East African Rift: age, structure, and history of the Tanzanian craton. Geochim. Cosmochim. Acta 63 (7-8), 1203–1217.

Christensen, B.P., Holm, P.M., Jambon, A., Wilson, J.R., 2001. Helium, argon and lead isotopic composition of volcanics from Santo Antão and Fogo, Cape Verde Islands. Chem. Geol. 178, 127–142.

Cliff, R.A., Baker, P.E., Mateer, N.J., 1991. Geochemistry of inaccessible island volcanics. Chem. Geol. 92, 251–260.

Cohen, R.S., O'Nions, R.K., 1982. Identification of recycled continental material in the mantle from Sr, Nd and Pb isotope investigations. Earth Planet. Sci. Lett. 61, 73–84.

Cohen, R.S., O'Nions, R.K., Dawson, J.B., 1984. Isotope geochemistry of xenoliths from East Africa: implications for development of mantle reservoirs and their interaction. Earth Planet. Sci. Lett. 68, 209–220.

Davies, G.R., Norry, M.J., Gerlach, D.C., Cliff, R.A., 1989. A combined chemical and Pb–Sr–Nd isotope study of the Azores and Cape Verde hot-spots: the geodynamic implications, magmatism in the ocean basins. Geol. Soc. Spec. Publ. 42, 231–255.

Day, S.J., Heleno da Silva, S.I.N., Fonseca, J.F.B.D., 1999. A past giant lateral collapse and present-day flank instability of Fogo, Cape Verde Islands. J. Volcanol. Geotherm. Res. 94, 191–218.

Dosso, L., Murthy, V.R., 1980. A Nd isotopic study of the Kerguelen Islands; inferences on enriched oceanic mantle sources. Earth Planet. Sci. Lett. 48, 268–276.

Dosso, L., Bougault, H., Joron, J.-L., 1993. Geochemical morphology of the North Mid-Atlantic Ridge, 10°–20° N: trace element-isotopic complementarity. Earth Planet. Sci. Lett. 120, 443–462.

Doucelance, R., Escrig, S., Moreira, M., Gariépy, C., Kurz, M., 2003. Pb–Sr–He isotope and trace element geochemistry of the Cape Verde Archipelago. Geochim. Cosmochim. Acta 67 (19), 3717–3733.

Eisele, J., et al., 2002. The role of sediment recycling in EM-1 inferred from Os, Pb, Hf, Nd, Sr isotope and trace element systematics of the Pitcairn hotspot. Earth Planet. Sci. Lett. 196, 197–212.

Esperança, R.W., Carlson, R.W., Shirey, S.B., Smith, D., 1997. Dating crust-mantle separation: Re–Os isotopic study of mafic xenoliths from central Arizona. Geology 25, 651–654.

Gerlach, D.C., Cliff, R.A., Davies, G.R., Norry, M.J., Hodgson, N., 1988. Magma sources of the Cape Verdes archipelago: isotopic and trace element constraints. Geochim. Cosmochim. Acta 52, 2979–2992.

Hart, S.R., 1984. A large-scale isotope anomaly in the southern hemisphere mantle. Nature 309, 753–757.

Hart, S.R., 1988. Heterogeneous mantle domains: signatures, genesis and mixing chronologies. Earth Planet. Sci. Lett. 90, 273–296.

Hart, S.R., Davis, K.E., 1978. Nickel partitioning between olivine and silicate melt. Earth Planet. Sci. Lett. 40, 203–219.

Hauri, E.H., Hart, S.R., 1993. Re–Os isotope systematics of HIMU and EMII oceanic island basalts from the south Pacific Ocean. Earth Planet. Sci. Lett. 114, 353–371.

Hauri, E.H., Lassiter, J.C., DePaolo, D.J., 1996. Os isotope systematics of drilled lavas from Mauna Loa, Hawaii. J. Geophys. Res. 101, 11793–11806.

Hawkesworth, C.J., Rogers, N.W., VanCalsteren, P.W., Menzies, M.A., 1984. Mantle enrichment processes. Nature 311, 331–335.

Hawkesworth, C.J., Kempton, P.D., Rogers, N.W., Ellam, R.M., Van Calsteren, P.W., 1990. Continental mantle lithosphere and shallow level enrichment processes in the Earth's mantle. Earth Planet. Sci. Lett. 96, 256–268.

Hodgson, N., 1986. Carbonatites and associated rocks from the Cape Verde islands. Unpublished thesis Thesis, University of Leicester.

Hoernle, K., 1998. Geochemistry of Jurassic oceanic crust beneath Gran Canaria (Canary Islands): implications for crustal recycling and assimilation. J. Petrol. 39, 859–880.

Hoernle, K., Tilton, G., Schmincke, H.-U., 1991. Sr–Nd–Pb isotopic evolution of Gran Canaria: evidence for shallow enriched mantle beneath the Canary Islands. Earth Planet. Sci. Lett. 106, 44–63.

Hoernle, K., Tilton, G., Le Bas, M.J., Duggen, S., Garbe-Schönberg, D., 2002. Geochemistry of oceanic carbonatites compared with continental carbonatites: mantle recycling of oceanic crustal carbonate. Contrib. Mineral. Petrol. 142, 520–542.

Huang, Y.-M., Van Calsteren, P.W., Hawkesworth, C.J., 1995. The evolution of the lithosphere in southern Africa: a perspective on the basic granulite xenoliths from kimberlites in south Africa. Geochim. Cosmochim. Acta 59, 4905–4920.

Humphris, S.E., Thompson, G., 1983. Geochemistry of rare earth elements in basalts from the Walvis Ridge; implications for its origin and evolution. Earth Planet. Sci. Lett. 66, 223–242.

Jorgensen, J.O., Holm, P.M., 2002. Temporal variation and carbonatite contamination in primitive ocean island volcanics from Sao Vicente, Cape Verde Islands. Chem. Geol. 195, 249–267.

Jull, M., Kelemen, P.B., 2001. On the condition for lower crust convective instability. J. Geophys. Res. 106, 6423–6446.

Kay, R.W., Mahlburg Kay, S., 1993. Delamination and delamination magmatism. Tectonophysics 219, 177–189.

Kokfelt, T.F., Holm, P.M., Hawkesworth, C.J., Peate, D.W., 1998. A lithospheric mantle source for the Cape Verde Island magmatism: trace element and isotopic evidence from the island of Fogo. Min. Mag. 62A, 801–802.

Kurz, M., Jenkins, W.J., Schilling, J.G., Hart, S.R., 1982. Helium isotopic systematics of ocean islands and mantle heterogeneity. Nature 297, 43–47.

Lancelot, J.R., Allègre, C.J., 1974. Origin of carbonatitic magma in the light of the Pb–U–Th isotope system. Earth Planet. Sci. Lett. 22, 233–238.

Lassiter, J.C., 2003. Rhenium volatility in subaerial lavas: constraints from subaerial and submarine portions of the HSDP-2 Mauna Kea drillcore. Earth Planet. Sci. Lett. 214, 311–325.

Lassiter, J.C., Hauri, E.H., 1998. Osmium-isotope variations in Hawaiian lavas: evidence for recycled oceanic lithosphere in the Hawaiian plume. Earth Planet. Sci. Lett. 164, 483–496.

Le Roex, A.P., 1985. Geochemistry, mineralogy, and magmatic evolution of the basaltic and trachytic lavas from Gough Island, South Atlantic. J. Petrol. 26, 149–186.

Le Roex, A.P., Cliff, R., Adair, B., 1990. Tristan da Cunha, south Atlantic: geochemistry and petrogenesis of a basanite–phonolite lava series. J. Petrol. 31, 779–812.

Luck, J.M., Birck, J.L., Allègre, C.J., 1980. 187Re–187Os systematics in meteorites: early chronology of the solar system and the age of the Galaxy. Nature 283, 256–259.

Marcantonio, F., Zindler, A., Elliot, T., Staudigel, H., 1995. Os isotope systematics of La Palma, Canary islands: evidence for recycled crust in the mantle source of HIMU ocean islands. Earth Planet. Sci. Lett. 133, 397–410.

Matos Alves, C.A., Macedo, J.R., Silva, L.C., Serralheiro, A., Peixoto, A.F., 1979. Estudo geologico, petrologico e vulcanologico da Ihla de Santiago (Cabo Verde). Garcia de Orta, Sér. Geol. Lisboa 3, 9–27.

McKenzie, D., O'Nions, R.K., 1983. Mantle reservoirs and ocean island basalts. Nature 301, 229–231.

Meisel, T., Walker, R.J., Morgan, J.W., 1996. The osmium isotopic composition of the Earth's primitive upper mantle. Nature 383, 517–520.

Meisel, T., Walker, R.J., Irving, A.J., J.-P., L., 2001. Osmium isotopic compositions of mantle xenoliths: a global perspective. Geochim. Cosmochim. Acta 65, 1311–1323.

Pearson, D.G., Carlson, R.W., Shirey, S.B., Boyd, F.R., Nixon, P.H., 1995. Stabilisation of Archean lithospheric mantle: a Re–Os isotope study of peridotite xenoliths from the Kaapvaal craton. Earth Planet. Sci. Lett. 134, 341–357.

Reisberg, L., et al., 1993. Os isotope systematics in ocean island basalts. Earth Planet. Sci. Lett. 120, 149–167.

Richard, P., Shimizu, N., Allègre, C.J., 1976. 143Nd/146Nd, a natural tracer: an application to oceanic basalts. Earth Planet. Sci. Lett. 31, 269–278.

Richardson, S.H., Erlank, A.J., Duncan, A.R., Reid, D.L., 1982. Correlated Nd, Sr and Pb isotope variation in walvis ridge basalts and implications for evolution of their mantle source. Earth Planet. Sci. Lett. 59, 327–352.

Rogers, N.W., Hawkesworth, C.J., 1982. Proterozoic age and cumulate origin for granulite xenoliths, Lesotho. Nature 299, 409–413.

Roy-Barman, M., Allègre, C.J., 1994. $^{187}Os/^{186}Os$ ratios in mid-ocean ridge basalts and abyssal peridotites. Geochim. Cosmochim. Acta 58, 5043–5054.

Roy-Barman, M., Allègre, C.J., 1995. $^{187}Os/^{186}Os$ in oceanic island basalt: tracing oceanic crust recycling in the mantle. Earth Planet. Sci. Lett. 129, 145–161.

Rudnick, R.L., 1992. Samples of lower continental crust. In: Fountain, D.M., Arculus, R., Kay, R. (Eds.), The Continental Lower Crust. Elsevier, Amsterdam, pp. 269–316.

Rudnick, R.L., Fountain, D.M., 1995. Nature and composition of the continental crust: a lower crustal perspective. Rev. Geophys. 33, 267–309.

Saal, A.E., Rudnick, R.L., Ravizza, G.E., Hart, S.R., 1998. Re–Os isotope evidence for the composition, formation and age of the lower continental crust. Nature 393, 58–61.

Schiano, P., Burton, K.W., Dupré, B., Brick, J.-L., Allègre, C.J., 2001. Correlated Os–Pb–Nd–Sr isotopes in the Austral-Cook chain basalts: the nature of mantle components in plume sources. Earth Planet. Sci. Lett. 186, 353–371.

Schmidt, G., Snow, J.E., 2002. Os isotopes in mantle xenoliths from the Eifel volcanic field and the Vogelsberg (Germany): age constraints on the lithospheric mantle. Contrib. Mineral. Petrol. 143, 694–705.

Smoliar, M.I., Walker, R.J., Morgan, J.W., 1996. Re–Os ages of group IIA, IIIA, IVA and IVB iron meteorites. Science 271, 1099–1102.

Snow, J.E., Reisberg, L., 1995. Os isotopic systematics of the MORB mantle: results from altered abyssal peridotites. Earth Planet. Sci. Lett. 133, 411–421.

Thirlwall, M.F., 1997. Pb isotopic and elemental evidence for OIB derivation from young HIMU mantle. Chem. Geol. 139, 51–74.

Walker, R.J., Carlson, R.W., Shirey, S.B., Boyd, F.R., 1989. Os, Sr, Nd, and Pb isotope systematics of southern African peridotite xenoliths: implications for the chemical evolution of subcontinental mantle. Geochim. Cosmochim. Acta 53, 1583–1595.

Walker, R.J., Hanski, E., Vuollo, J., Lippo, J., 1996. The Os isotopic composition of Proterozoic upper mantle; evidence for chondritic upper mantle from the Outokumpu Ophiolite, Finland. Earth Planet. Sci. Lett. 141, 161–173.

Weaver, B., 1991. The origin of ocean island basalt end-member compositions: trace element and isotopic constraint. Earth Planet. Sci. Lett. 104, 381–397.

Weaver, B.L., Wood, D.A., Tarney, J., Joron, J.-L., 1987. Geochemistry of ocean island basalts from the South Atlantic; Ascension, Bouvet, St. Helena, Gough and Tristan da Cunha. Geol. Soc. London Spec. Publ. 30, 253–267.

Weis, D., Frey, F.A., Leyrit, H., Gautier, I., 1993. Kerguelen Archipelago revisited; geochemical and isotopic study of the Southeast Province lavas. Earth Planet. Sci. Lett. 118, 101–119.

White, W.M., 1985. Sources of oceanic basalts: radiogenic isotope evidence. Geology 13, 115–118.

White, W., Dupré, B., 1986. Sediment subduction and magma genesis in the Lesser Antilles; isotopic and trace element constraints. J. Geophys. Res. 91, 5927–5941.

White, W.M., Hofmann, A.W., 1982. Sr and Nd isotope geochemistry of oceanic basalts and mantle evolution. Nature 296, 821–825.

Whitmarsh, R.B., 1998. Drilling reveals transition from continental breakup to early magmatic crust. EOS Trans. Am. Geophys. Union 79 (14), 173–181.

Widom, E., Shirey, S.B., 1996. Os isotope systematics in the Azores: implications for mantle plume sources. Earth Planet. Sci. Lett. 142, 451–465.

Widom, E., Hoernle, K., Shirey, S.B., Schmincke, H.-U., 1999. Os isotope systematics in the Canary Islands and Madeira: lithospheric contamination and mantle plume signatures. J. Petrol. 40, 276–296.

Woodhead, J.D., Devey, C.W., 1993. Geochemistry of the Pitcairn seamounts: I. Source character and temporal trends. Earth Planet. Sci. Lett. 116, 81–99.

Zindler, A., Hart, S.R., 1986. Chemical geodynamics. Ann. Rev. Earth Planet. Sci. 14, 493–571.

Journal of Volcanology and Geothermal Research 176 (2008) 265–276

Contents lists available at ScienceDirect

Journal of Volcanology and Geothermal Research

journal homepage: www.elsevier.com/locate/jvolgeores

# Mantle plume heterogeneity versus shallow-level interactions: A case study, the São Nicolau Island, Cape Verde archipelago

Marc-Alban Millet *, Régis Doucelance, Pierre Schiano, Karine David, Chantal Bosq

*Laboratoire Magmas et Volcans, Observatoire de Physique du Globe de Clermont-Ferrand, 5, rue Kessler, 63038 Clermont-Ferrand Cedex, France*

ARTICLE INFO

*Article history:*
Received 8 August 2007
Accepted 3 April 2008
Available online 16 April 2008

*Keywords:*
OIB
isotope
mantle plume
Cape Verde archipelago
shallow-level interaction

ABSTRACT

We present new Sr–Nd–Pb isotopic data, as well as major- and trace-element concentrations, for 19 basaltic samples from São Nicolau Island, Cape Verde archipelago. Fine-scale study of the island argues in favor of mixing between four endmembers to explain isotopic variations of collected samples: 1) a radiogenic endmember ($^{87}Sr/^{86}Sr \sim 0.7034$; $^{143}Nd/^{144}Nd \sim 0.51285$; $^{206}Pb/^{204}Pb \sim 20.0$; $^{207}Pb/^{204}Pb \sim 15.65$; $^{208}Pb/^{204}Pb \sim 39.8$) representative of the Cape Verde plume deep source; 2) an unradiogenic endmember having isotopic compositions resembling those of Atlantic MORB dredged at the same latitude; 3) a low Sr–high Nd and Pb endmember identified as the Jurassic MORB basement of the archipelago; and 4) São Vicente-like Cape Verde carbonatites. Compositional and isotopic results show that most of the measured variations can be related to mixing of plume-derived melts with shallow-level reservoirs. Therefore the source heterogeneity of the Cape Verde plume is much smaller than the one sampled in basaltic samples. This observation illustrates how caution is required when interpreting global OIB data in terms of mantle topology without filtering from the contribution of shallow-level reservoirs.



## 1. Introduction

Oceanic Island Basalts (OIB) are widely accepted to be derived from partial melting of upwelling mantle plumes arising from the deep mantle. As plumes are the most efficient probe of mantle reservoirs, OIB have been extensively studied for the last 30 years in order to delineate the scale, nature and origin of chemical heterogeneities within the mantle and to assess mantle dynamics. The geochemical signature of OIB records is generally interpreted in terms of fingerprint of the proportions of components present in the deep source of basalts. However, erupted magmas may have undergone extensive modification of their initial composition by interaction with the surrounding environment during their ascent through the oceanic lithosphere and crust. Several interaction processes have been advocated in the literature, including i) Plume–Lithosphere Interaction (PLI) (Class and Goldstein, 1997; Lassiter et al., 2000); ii) Assimilation and Fractional Crystallization (AFC) (DePaolo, 1981; DePaolo, 1985); and iii) post-eruption seawater interaction (Dasch et al., 1973; Menzies and Seyfried, 1979; Dupré et al., 1982). Therefore, the question we address in this paper is how the OIB isotopic variability is representative of the heterogeneity of the deep source of plumes.

For this purpose, we focus on the Cape Verde islands, North Atlantic Ocean. Their volcanic origin is well described by Fogo historical eruptions (last eruption in April 1995) and has been associated with the presence of a seismically identified mantle plume (Montelli et al., 2006). Composed of 10 principal islands and some islets, the archipelago draws two distinct alignments: the Northern Islands with Santo Antão, São Vicente, Santa Luzia and São Nicolau on the one hand, and the Southern Islands with Brava, Fogo, Santiago and Maio on the other hand, extended to the East by Boa Vista and Sal (Fig. 1). Although close to the West African coasts, ~500 km away from the Senegal, the distance between the Cape Verde archipelago and the continental slope excludes the possibility of a continental basement for the archipelago. Nevertheless, some enriched material delaminated during rifting process could reside in the shallowest levels of the mantle as suggested for the Walvis Ridge (Class and LeRoex, 2006). Geochronological studies that have revealed large and overlapping ranges of activity for the different islands (Mitchell et al., 1983; Plesner et al., 2003; Madeira et al., 2005; Duprat et al., 2007) show no clear relationship between the age of volcanism and the location of the islands in the archipelago. However, historical volcanism is restricted to the western part of the archipelago and eastern islands are the most eroded, suggesting a regional westward ageing of islands. Basaltic samples collected on the Cape Verde islands present a large range of variations for major-, trace-element concentrations and Sr–Nd–Pb isotopic ratios (see archipelago-scale studies by Gerlach et al., 1988; Davies et al., 1989; Doucelance et al., 2003), in

* Corresponding author. School of Geography, Environment and Earth Sciences, Victoria University, PO Box 600, Wellington, New Zealand. Tel.: +64 4 463 5391; fax: +64 4 463 5186.
*E-mail address:* Marc-Alban.Millet@vuw.ac.nz (M.-A. Millet).

0377-0273/$ – see front matter © 2008 Elsevier B.V. All rights reserved.
doi:10.1016/j.jvolgeores.2008.04.003

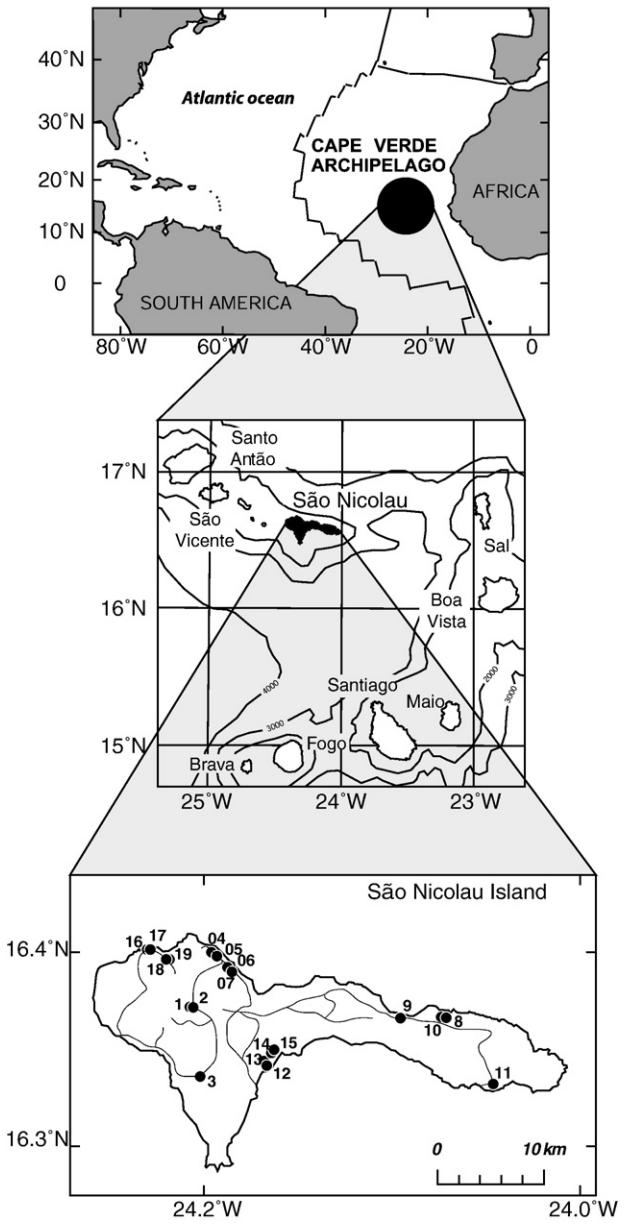


**Fig. 1.** Location of the Cape Verde archipelago and São Nicolau Island in the Atlantic Ocean. Map of sampling localities in the São Nicolau Island.

relation with their geographical location. For example, samples collected on the Southern Islands show Pb isotopic compositions plotting on the left of the Northern Hemisphere Reference Line (NHRL, see Hart, 1984), whereas samples from the Northern Islands fall on the right.

These variations have been first interpreted as resulting from mixing between 3 distinct endmembers with HIMU-, EM1- and DMM-like characteristics, following two alternative models (Gerlach et al., 1988; Davies et al., 1989). In the first model, the HIMU-like endmember is deep-seated in the plume source, along with likely entrained depleted mantle, whereas the EM1-like endmember, contributing to the Southern Island volcanism only, is located in the lithosphere. The second model involves an EM1-like plume, entraining HIMU and DMM endmembers from a marble cake-like upper mantle (Allègre and Turcotte, 1986).

Alternatively, Kokfelt et al. (1998) have proposed that the contribution of the Cape Verde plume is only thermal. For these authors, both EM1- and HIMU-like endmembers are of lithospheric origin. The HIMU-like endmember is interpreted as resulting from mantle degassing and carbonatitic metasomatism during opening of the Atlantic Ocean, whereas the EM1-like is derived from delamination of sub-continental lithosphere, also due to the opening of the Atlantic Ocean. However, rare gas data measured in Cape Verde samples (Christensen et al., 2001; Doucelance et al., 2003) and notably the moderately primitive He signatures that characterize samples from Santo Antão, São Vicente, São Nicolau and Sal ($^4He/^3He$ down to 50,000 in Santo Antão) suggest the involvement of an additional, deep-seated, plume-related component, identified as Lower Mantle (LM) material.

Finally, recent island-scale studies have revealed some Cape Verde basalts to have experienced shallow-level contamination, either by carbonatite (Jørgensen and Holm, 2002), or oceanic crustal material (i.e., Jurassic MORB basement, see Doucelance et al., 2003) or delaminated subcontinental EM1-like material left behind in the oceanic lithosphere after opening of the Atlantic ocean (Hoernle et al., 1991; Escrig et al., 2005), thus implying a minimum of 6 endmembers (and/or components; that is, HIMU, EM1, DMM, LM, carbonatites, Jurassic MORB basement) that could be involved in the isotopic signature of Cape Verde basaltic samples.

If part of the chemical and isotopic signature of Cape Verde basalts is inherited from shallow-level components (EM1 subcontinental material present in the oceanic lithosphere (Hoernle et al., 1991; Escrig et al., 2005) and Jurassic MORB basement (Doucelance et al., 2003)) and therefore does not represent the deep-seated source of the plume, there is no consensus about the depth of the other components recorded in the Cape Verde signature except lower mantle material. For instance, Holm et al., 2006 have suggested temporal variations in a Cape Verde heterogeneous mantle plume containing several components, whereas others (Gerlach et al., 1988; Davies et al., 1989; Doucelance et al., 2003) have proposed a homogeneous Cape Verde plume entraining components located in the oceanic lithosphere.

Here, we present a detailed study of São Nicolau Island, for which a limited set of samples was previously interpreted as recording the fingerprint of at least 4 isotopic endmembers; LM, HIMU, DMM and Jurassic MORB; among the 6 identified for the whole archipelago (Doucelance et al., 2003). We report new major-, trace-element concentrations and Sr–Nd–Pb isotope ratios measured for 19 basaltic samples covering most geological formations of the island, together with 3 late Jurassic MORB from Santiago. Our aim is threefold: (1) identifying the depth of the 4 components discussed above, (2) filtering the global geochemical signature of São Nicolau basalts from shallow-level processes in order to retrieve the pristine source information, and (3) using published Cape Verde data to generalize our results to the whole Cape Verde archipelago.

## 2. Analytical procedures

All samples were coarsely pound with a hydraulic press. Millimetric grains were then hand-picked under a binocular microscope, rinsed with tri-distilled water into an ultrasonic bath, before being gently crushed with an agate pestle–mortar set.

Major and trace-element contents were determined at the Magmas & Volcans laboratory (LMV) using Inductively Coupled Plasma-Atomic Emission Spectrometry (ICP-AES, Ultima-C instrument) and Inductively Coupled Plasma-Mass Spectrometry (ICP-MS, VG PQ2+ spectrometer), respectively. Analyses were performed on two aliquots from the same sample solution obtained by alkaline melting with lithium meta/tetraborate and nitric acid dissolution. Total external reproducibilities (including crushing) were evaluated by repeated measurements of samples; they are below 5% ($2\sigma$) for major elements (except for MgO which displays a reproducibility twice that of other elements) and below 7% ($2\sigma$) for trace elements, apart from Pb (20%).

Sr and Nd isotopes separations and measurements were also done at the LMV. 100 mg of sample powders were leached with hot 6 M HCl (5 ml, 100 °C) during 3 h (see Fig. 2 for optimization of the leaching time), acid-digested with a HF-HNO3 mixture and passed through the "cascade" column protocol (Sr Spec, True Spec and Ln Spec columns) described in Pin and Bassin (1992) and Pin et al. (1994). Total blanks (including leaching and HF-$HNO_3$ digestion) were <1 ng and <0.2 ng for Sr and Nd, respectively. All measurements were made in static mode on a Finnigan Triton thermo-ionization mass spectrometer (TIMS), with the virtual amplifier and double W filaments. Isotope ratios were mass-fractionation corrected with $^{86}Sr/^{88}Sr=0.1194$ and normalized to $^{87}Sr/^{86}Sr=0.71025$ for the NIST SRM987 standard; with $^{146}Nd/^{144}Nd=0.7219$ and normalized to $^{143}Nd/^{144}Nd=0.51196$ for the Rennes-AMES standard. Repeated analyses of the two standards during the course of the study gave $^{87}Sr/^{86}Sr=0.710250\pm15$ ($2\sigma$, $n=16$) and $^{143}Nd/^{144}Nd=0.511961\pm6$ ($2\sigma$, $n=8$), in agreement with long-term reproducibilities: $^{87}Sr/^{86}Sr=0.710254\pm23$ ($2\sigma$, $n=76$) and $^{143}Nd/^{144}Nd=0.511959\pm9$ ($2\sigma$, $n=120$). All sample duplicates fall within these errorbars.

Pb isotopes were separated from whole-rock sample powders (~500 mg) at LMV following the procedure of Manhès et al. (1978). Total blanks (including acid digestion) were all about 90 pg. Measurements were performed at ENS Lyon on a Nu Plasma MC-ICP-MS in static mode. Mass discrimination was monitored using the Tl doping technique and an exponential law. The $^{205}Tl/^{203}Tl$ ratio was set to 2.3892 in order to adjust measured NIST SRM981 standard values to those of Doucelance and Manhès (2001) recalculated at $^{208}Pb/^{206}Pb=2.1677$ ($^{207}Pb/^{206}Pb=0.91488$ and $^{204}Pb/^{206}Pb=0.059027$, cf. Thirlwall, 2002). NIST SRM981 standards, as well as aliquots of a single sample solution, were reproducible at the 200-ppm level for each $^{20X}Pb/^{204}Pb$ ratio ($2\sigma$, $n=24$). Total external reproducibilities based on the replicate analyze (including crushing) of sample SN01 are consistent with this value. Two samples previously measured by Doucelance et al. (2003) were re-analyzed. No difference was observed in isotopic compositions within errorbars; therefore no correction was applied to previous São Nicolau data (Doucelance et al., 2003) used for comparison. Light leaching (1 h, 6 M HCl, room temperature) of these two same samples also gave identical results compared to previous data, precluding Pb contamination of rock powders during sampling and crushing.

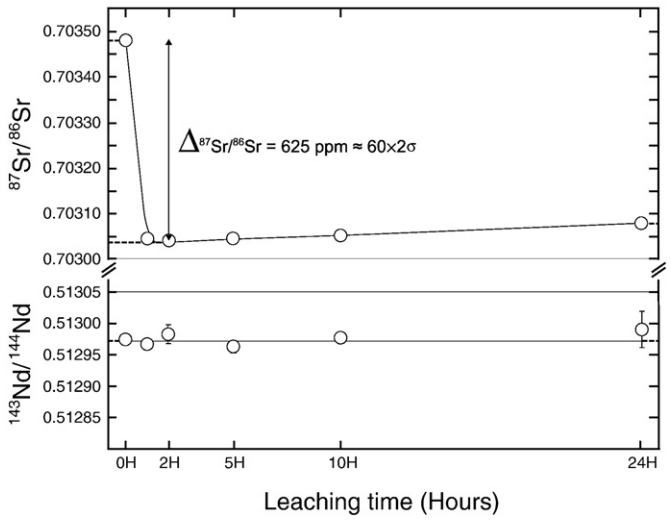


**Fig. 2.** Optimization of the leaching time of altered basaltic samples in hot HCl 6 M (illustrated here with sample SN15) and Sr–Nd isotopic signature. The Sr isotopic ratio first decreases to a minimal value (reached after 2–3 h of leaching) before going toward more radiogenic values with time. This final increase cannot be related to the exhaustion of an unradiogenic magmatic phase in the sample powder as the Nd isotopes ratio (uncontaminated by seawater) is constant throughout the entire leaching experiment. It is attributed to progressive recontamination of the residue by the leachate.

## 3. Results

### 3.1. Major- and trace-element variations

All samples have $SiO_2$ contents between 39 and 47 wt.% (Table 1) for MgO contents ranging from 5 to 15%. They include melanephelinites, picrobasalts, subalkali basalts and tephrites, classified according to the alkali–silica nomenclature. With regard to previous studies (Gunn and Watkins, 1976; Macedo, 1989; Mazarovich et al., 1990; Duprat et al., 2007), they show a relatively restricted range of compositions and plot towards the least differentiated values in major-element variation diagrams (Fig. 3), except for sample SN19. Compositional variations for major elements in lavas from Cape Verde islands can be accounted for by fractional crystallization of an olivine–clinopyroxene assemblage (Duprat et al., 2007), as illustrated by the decrease of CaO towards less magnesian compositions.

Primitive mantle-normalized trace-element patterns of São Nicolau samples (Fig. 4; see Table 1 for values) show sub-parallel shapes and display a limited range of variations, indicating little influence of fractional crystallization differentiation, in agreement with the restricted range of major-element compositions. The patterns are typical of OIB with enriched concentrations in the most incompatible elements and Pb negative anomalies (Fig. 4). They also display the K negative anomalies which is a distinctive feature of all OIB (represented by Mangaia basalts; Woodhead, 1996) with a HIMU-type isotopic signature.

Nb/U ratios display a large range of variation, from typical oceanic basalt values (47 ± 10) up to values of 73.

### 3.2. Sr–Nd–Pb isotope variations

$^{87}Sr/^{86}Sr$ and $^{143}Nd/^{144}Nd$ isotopic ratios measured for São Nicolau samples display small ranges of variations from 0.702974 to 0.703108 and from 0.512949 to 0.512997, respectively (Table 1). In a $^{143}Nd/^{144}Nd$ vs. $^{87}Sr/^{86}Sr$ diagram (Fig. 5), datapoints draw a single binary trend consistent with the isotopic fields previously defined for basalts from the Northern Islands (Gerlach et al., 1988; Jørgensen and Holm, 2002; Doucelance et al., 2003; Holm et al., 2006). They plot amongst the most depleted lavas (lowest Sr and highest Nd isotopic ratios) of the Cape Verde archipelago, arguing for the involvement in high proportions of a depleted component in their genesis.

São Nicolau samples have also restricted ranges of variations for Pb isotopes relative to all other islands from the Northern islands, with $^{206}Pb/^{204}Pb=19.357–19.667$, $^{207}Pb/^{204}Pb=15.570–15.615$, and $^{208}Pb/^{204}Pb=38.875–39.164$ (Table 1). They plot to the right of the NHRL (Hart, 1984) in a $^{208}Pb/^{204}Pb$ vs. $^{206}Pb/^{204}Pb$ diagram (Fig. 6), as it is the case for all samples from the Northern Islands. A detailed inspection of the $^{87}Sr/^{86}Sr$, $^{143}Nd/^{144}Nd$ and $^{208}Pb/^{204}Pb$ vs. $^{206}Pb/^{204}Pb$ isotope variation diagrams reveals that São Nicolau samples define two distinct subsets. Most datapoints present $^{206}Pb/^{204}Pb$ ratios <19.6, in agreement with previously published data (Doucelance et al., 2003), whereas two samples (SN07 and SN09) show more radiogenic Pb compositions towards the direction of Fogo (or São Vicente) carbonatites (Fig. 6). The three Jurassic MORB samples from Santiago display a restricted range of variations for Sr–Nd–Pb isotopic ratios with $^{87}Sr/^{86}Sr=0.702891–0.702972$, $^{143}Nd/^{144}Nd=0.513118–0.513167$, and $^{206}Pb/^{204}Pb=19.382–19.417$ (Table 1). They are slightly less radiogenic for Sr and Pb (and more radiogenic for Nd) than those previously measured by Gerlach et al. (1988). Although differences for Sr results are partly related to the leaching procedure (not operated by these authors), the variability of the Pb and Nd Jurassic MORB compositions may result from shallow-level processes that have

**Table 1**
Major-, trace-elements and isotopes ratios for 19 São Nicolau samples and 3 Jurassic MORB from Santiago Island

| Sample name | SN01 | SN02 | SN03 | SN04 | SN05 | SN06 | SN07 | SN08 | SN09 | SN10 | SN11 |
|---|---|---|---|---|---|---|---|---|---|---|---|
| Location | São Nicolau | São Nicolau | São Nicolau | São Nicolau | São Nicolau | São Nicolau | São Nicolau | São Nicolau | São Nicolau | São Nicolau | São Nicolau |
| $SiO_2$ | 41.01 | 41.70 | 42.52 | 39.35 | 40.45 | 39.79 | 43.38 | 43.06 | 42.22 | 39.88 | 42.02 |
| $Al_2O_3$ | 11.24 | 11.88 | 13.20 | 11.71 | 12.28 | 11.03 | 13.90 | 12.70 | 11.01 | 11.80 | 12.29 |
| $Fe_2O_3$ | 13.55 | 13.36 | 13.05 | 13.14 | 12.95 | 13.04 | 12.63 | 12.76 | 12.29 | 12.93 | 12.89 |
| MnO | 0.20 | 0.20 | 0.18 | 0.20 | 0.19 | 0.19 | 0.21 | 0.19 | 0.17 | 0.21 | 0.20 |
| MgO | 15.09 | 14.20 | 10.87 | 12.44 | 12.62 | 13.13 | 8.21 | 12.22 | 12.06 | 12.50 | 12.15 |
| CaO | 11.31 | 11.50 | 12.41 | 13.24 | 13.65 | 13.17 | 11.97 | 12.26 | 12.27 | 14.05 | 12.88 |
| $Na_2O$ | 3.57 | 3.67 | 1.98 | 3.75 | 3.93 | 2.65 | 3.90 | 2.89 | 2.62 | 3.67 | 3.27 |
| $K_2O$ | 0.67 | 0.56 | 0.73 | 0.77 | 0.76 | 0.66 | 1.02 | 1.08 | 0.52 | 1.08 | 1.09 |
| $TiO_2$ | 2.88 | 2.77 | 3.47 | 3.42 | 3.11 | 3.91 | 3.51 | 2.81 | 3.20 | 2.90 | 2.81 |
| $P_2O_5$ | 0.61 | 0.53 | 0.41 | 0.91 | 0.74 | 0.84 | 0.75 | 0.52 | 0.50 | 0.85 | 0.68 |
| LOI | 0.03 | −0.30 | 1.14 | −0.06 | −0.86 | 1.97 | 0.92 | 0.41 | 1.16 | −0.42 | 0.11 |
| Total | 100.16 | 100.07 | 99.96 | 98.86 | 99.82 | 100.39 | 100.39 | 100.90 | 98.02 | 99.43 | 100.39 |
| Rb | 23.8 | 27.9 | 17.9 | 25.33 | 13.4 | 13.8 | 15.6 | 24.7 | 10.5 | 18.3 | 25.6 |
| Ba | 465 | 438 | 342 | 613 | 522 | 520 | 552 | 388 | 383 | 511 | 557 |
| Th | 3.9 | 3.8 | 2.8 | 5.3 | 5.9 | 4.8 | 5.4 | 3.11 | 3.4 | 7.7 | 4.1 |
| U | 0.85 | 0.82 | 0.69 | 1.16 | 1.17 | 1.10 | 1.47 | 0.76 | 0.80 | 1.54 | 1.11 |
| Nb | 56 | 57 | 51 | 68 | 69 | 69 | 71 | 41 | 45 | 74 | 54 |
| K | 5570 | 4647 | 6057 | 638é | 6306 | 5515 | 8437 | 8945 | 4327 | 8933 | 9024 |
| La | 35 | 35 | 30 | 51 | 53 | 48 | 50 | 29 | 37 | 60 | 42 |
| Ce | 70 | 71 | 67 | 103 | 104 | 99 | 102 | 61 | 77 | 116 | 87 |
| Pb | 0.97 | 2.31 | 1.95 | 2.32 | 2.73 | 2.66 | 2.70 | 1.37 | 2.02 | 2.91 | 2.28 |
| Pr | 8.6 | 8.6 | 8.5 | 12.5 | 12.6 | 12.2 | 12.4 | 7.4 | 9.3 | 13.5 | 10.4 |
| Nd | 34 | 359 | 35 | 49 | 49 | 49 | 49 | 30 | 37 | 54 | 41 |
| Sr | 604 | 602 | 654 | 835 | 851 | 797 | 953 | 570 | 672 | 879 | 774 |
| Sm | 7.1 | 6.7 | 7.0 | 9.8 | 9.1 | 9.5 | 10.2 | 6.7 | 7.6 | 10.1 | 8.4 |
| Hf | 4.42 | 4.52 | 5.31 | 5.20 | 5.09 | 5.65 | 6.79 | 3.66 | 4.53 | 4.84 | 4.52 |
| Zr | 192 | 196 | 239 | 230 | 229 | 262 | 324 | 159 | 195 | 220 | 216 |
| Eu | 2.28 | 2.29 | 2.25 | 3.03 | 2.98 | 2.96 | 3.27 | 2.26 | 2.51 | 3.29 | 2.72 |
| Gd | 6.69 | 6.58 | 6.55 | 8.75 | 8.47 | 8.30 | 8.46 | 5.89 | 6.43 | 8.51 | 7.24 |
| Tb | 0.95 | 0.94 | 0.92 | 1.18 | 1.12 | 1.11 | 1.22 | 0.88 | 0.92 | 1.20 | 1.00 |
| Dy | 4.98 | 4.81 | 4.98 | 6.14 | 5.89 | 5.83 | 6.90 | 5.01 | 5.08 | 6.39 | 5.56 |
| Ho | 0.91 | 0.90 | 0.96 | 1.12 | 1.03 | 1.04 | 1.28 | 0.93 | 0.90 | 1.17 | 1.03 |
| Er | 2.20 | 2.17 | 2.33 | 2.66 | 2.43 | 2.48 | 3.08 | 2.21 | 2.05 | 2.69 | 2.41 |
| Y | 24 | 24 | 26 | 29 | 28 | 28 | 36 | 27 | 26 | 32 | 29 |
| Tm | 0.29 | 0.31 | 0.33 | 0.34 | 0.33 | 0.31 | 0.41 | 0.28 | 0.26 | 0.36 | 0.31 |
| Yb | 1.78 | 1.82 | 2.08 | 2.09 | 1.96 | 1.90 | 2.65 | 1.78 | 1.60 | 2.24 | 1.98 |
| Lu | 0.25 | 0.27 | 0.32 | 0.29 | 0.30 | 0.26 | 0.40 | 0.26 | 0.23 | 0.32 | 0.30 |
| $^{87}Sr/^{86}Sr$ | 0.702974 | 0.702981 | 0.702985 | 0.703016 | 0.703029 | 0.703036 | 0.703041 | 0.703019 | 0.703083 | 0.702986 | 0.703073 |
| $^{143}Nd/^{144}Nd$ | 0.512993 | 0.512982 | 0.512987 | 0.512974 | 0.512963 | 0.512949 | 0.512972 | 0.512997 | 0.512949 | 0.512973 | 0.512951 |
| $^{206}Pb/^{204}Pb$ | 19.515 | 19.515 | 19.406 | 19.534 | 19.489 | 19.451 | 19.667 | 19.357 | 19.652 | 19.538 | 19.464 |
| $^{207}Pb/^{204}Pb$ | 15.609 | 15.604 | 15.570 | 15.605 | 15.573 | 15.611 | 15.615 | 15.594 | 15.615 | 15.586 | 15.580 |
| $^{208}Pb/^{204}Pb$ | 39.010 | 38.998 | 38.946 | 39.058 | 38.953 | 39.024 | 39.164 | 38.875 | 39.151 | 38.964 | 38.961 |

Sr isotope values correspond to leached samples.

affected the local oceanic crust (Sm/Nd and mostly U/Pb fractionation) for the last 120 Myr.

## 4. Discussion

Previous Cape Verde studies have concluded to the presence of at least 5 endmembers (corresponding to 6 components) to explain measured Sr–Nd–Pb–Os–He isotopic compositions of basaltic samples. These are: [1] a radiogenic Pb endmember located on the NHRL with Sr–Nd isotopic compositions intermediate between those of basalts from the Northern and Southern Islands and relatively primitive/unradiogenic $^4He/^3He$ ratios, [2] an enriched endmember specific to samples from the Southern Islands, [3] a depleted endmember specific to basalts from the Northern Islands, [4] an endmember which isotopic composition resembles that of Fogo and São Vicente carbonatites, and [5] an endmember with an composition similar to that of Jurassic MORB samples from Santiago Island (Gerlach et al., 1988; Davies et al., 1989; Christensen et al., 2001; Hoernle et al., 2002; Jørgensen and Holm, 2002; Doucelance et al., 2003; Escrig et al., 2005; Holm et al., 2006).

Mixing trends between endmembers presented above are controlled by the geographical location of islands in the archipelago illustrated in Fig. 7. Basalts collected in the Northern Islands (Santo Antão, São Vicente and São Nicolau) reflect the mixing between the endmember [1] and material having isotopic characteristics similar to those of 10–20° North Atlantic MORB, DMM-like [3], (Dosso et al. (1993) for North Atlantic data). Endmember [1] shows HIMU-like characteristics and relatively primitive/unradiogenic and is therefore modeled as a mixture of recycled oceanic crust [ROC] and lower mantle material [LM]. Furthermore, assimilation of carbonatites [4] has been evidenced for some São Vicente (Jørgensen and Holm, 2002) and Santo Antão lavas (Holm et al., 2006), whereas São Nicolau samples have recorded assimilation of unaltered Jurassic MORB [5] forming the deep basement of the Cape Verde archipelago (Doucelance et al., 2003). Conversely, samples from the Southern Islands (Fogo, Santiago and Maio) have been interpreted by the mixing of a common endmember to all islands (termed [1] in Fig. 7), with an EM1-like endmember corresponding to subcontinental lithospheric mantle (SCLM) [2]. However, new data for Santo Antão Island by (Holm et al., 2006) displaced the endmember [1] toward more radiogenic Pb compositions along the NHRL with consequences that will be discussed later in this paper.

Although displaying a narrow range of isotopic variations, our new dataset is consistent with previous observations and models proposed for the Northern Islands. This is illustrated in a $^{208}Pb/^{204}Pb$ vs. $^{206}Pb/$

| SN12 | SN13 | SN14 | SN15 | SN16 | SN17 | SN18 | SN19 | S16 | S17 | S56 |
|---|---|---|---|---|---|---|---|---|---|---|
| São Nicolau | São Nicolau | São Nicolau | São Nicolau | São Nicolau | São Nicolau | São Nicolau | São Nicolau | Santiago | Santiago | Santiago |
| 39.36 | 44.60 | 39.70 | 39.50 | 40.74 | 39.57 | 44.30 | 46.73 | 46.704 | 46.208 | 47.022 |
| 11.07 | 13.03 | 10.80 | 11.21 | 11.90 | 11.93 | 13.64 | 16.74 | 15.054 | 14.931 | 15.257 |
| 12.43 | 11.72 | 12.65 | 12.60 | 13.42 | 13.24 | 12.57 | 10.57 | 10.115 | 9.759 | 9.991 |
| 0.18 | 0.18 | 0.19 | 0.19 | 0.19 | 0.18 | 0.18 | 0.19 | 0.188 | 0.169 | 0.172 |
| 12.39 | 10.47 | 12.73 | 12.40 | 12.88 | 11.37 | 10.22 | 5.01 | 7.628 | 7.018 | 7.419 |
| 11.65 | 12.21 | 12.45 | 12.80 | 12.63 | 11.94 | 10.71 | 8.70 | 12.379 | 12.648 | 12.301 |
| 3.37 | 3.15 | 2.25 | 2.07 | 2.24 | 3.03 | 2.66 | 4.52 | 3.098 | 3.372 | 3.204 |
| 1.82 | 1.16 | 0.63 | 0.84 | 0.86 | 0.84 | 1.04 | 2.01 | 0.574 | 0.29 | 0.66 |
| 3.67 | 2.77 | 3.78 | 3.75 | 4.29 | 4.37 | 2.88 | 2.67 | 0.853 | 0.837 | 0.854 |
| 0.63 | 0.43 | 0.70 | 0.74 | 0.51 | 0.57 | 0.49 | 0.59 | 0.075 | 0.068 | 0.068 |
| 0.02 | 0.49 | 3.69 | 4.36 | 3.78 | 1.24 | 1.44 | 1.55 | 3.383 | 4.857 | 3.298 |
| 96.59 | 100.21 | 99.57 | 100.46 | 103.45 | 98.28 | 100.12 | 99.29 | 100.05 | 100.16 | 100.25 |
| 36.78 | 30.8 | 9.3 | 8.9 | 10.8 | 7.4 | 21.9 | 54.3 | 17.7 | 7.0 | 20.1 |
| 573.17 | 369 | 628 | 554.06 | 538 | 606 | 405 | 613 | 28 | 17 | 26 |
| 3.96 | 4.4 | 4.1 | 4.2 | 3.6 | 4.1 | 3.7 | 7.0 | 7.3 | 1.3 | 3.828 |
| 0.96 | 0.95 | 0.99 | 1.05 | 0.93 | 0.98 | 0.88 | 1.83 | 0.14 | 0.03 | 0.11 |
| 67.90 | 49 | 65 | 68 | 61 | 68 | 52 | 76 | 1.9 | 1.8 | 1.7 |
| 1510.75 | 9603 | 5251 | 6944 | 7126 | 6985 | 8613 | 16,719 | 476.3 | 2406 | 5477 |
| 39.87 | 35 | 37 | 38 | 32 | 36 | 34 | 50 | 1.18 | 1.12 | 1.10 |
| 82.66 | 69 | 78 | 79 | 67 | 73 | 70 | 95 | 4.04 | 3.86 | 3.72 |
| 1.90 | 2.29 | 1.57 | 1.59 | 1.20 | 2.02 | 2.39 | 4.37 | 1.543 | 1.569 | 1.463 |
| 10.13 | 8.1 | 9.7 | 9.6 | 8.3 | 9.1 | 8.4 | 10.8 | 0.75 | 0.73 | 0.70 |
| 40.88 | 32 | 39 | 39 | 34 | 38 | 34 | 41 | 4.6 | 4.3 | 4.1 |
| 717.52 | 555 | 752 | 787 | 739 | 723 | 636 | 774 | 77 | 91 | 74 |
| 8.56 | 6.9 | 8.2 | 8.1 | 7.4 | 8.0 | 7.2 | 8.0 | 2.07 | 1.81 | 1.72 |
| 5.99 | 5.24 | 6.16 | 5.86 | 5.40 | 5.97 | 5.04 | 6.78 | 1.19 | 1.21 | 1.24 |
| 260.46 | 233 | 257 | 251 | 216 | 239 | 223 | 335 | 51 | 46 | 47 |
| 2.72 | 2.32 | 2.63 | 2.59 | 2.37 | 2.47 | 2.38 | 2.53 | 0.86 | 0.71 | 0.72 |
| 7.12 | 6.25 | 6.78 | 6.72 | 6.24 | 6.77 | 6.29 | 6.78 | 3.11 | 2.75 | 2.65 |
| 0.99 | 0.92 | 0.97 | 0.95 | 0.89 | 0.96 | 0.95 | 1.03 | 0.59 | 0.53 | 0.49 |
| 5.44 | 5.11 | 5.28 | 5.18 | 4.88 | 5.30 | 5.38 | 6.06 | 3.94 | 3.64 | 3.44 |
| 0.97 | 0.92 | 0.95 | 0.93 | 0.88 | 0.95 | 1.06 | 1.15 | 0.86 | 0.78 | 0.76 |
| 2.22 | 2.28 | 2.23 | 2.17 | 2.02 | 2.16 | 2.54 | 2.96 | 2.57 | 2.38 | 2.21 |
| 27.33 | 27 | 27 | 27 | 25 | 26 | 28 | 32 | 27 | 25 | 22 |
| 0.29 | 0.33 | 0.28 | 0.28 | 0.25 | 0.26 | 0.36 | 0.40 | 0.39 | 0.37 | 0.34 |
| 1.81 | 2.09 | 1.76 | 1.72 | 1.56 | 1.65 | 2.21 | 2.62 | 2.62 | 2.53 | 2.40 |
| 0.26 | 0.29 | 0.26 | 0.26 | 0.22 | 0.24 | 0.33 | 0.39 | 0.40 | 0.38 | 0.38 |
| 0.703108 | 0.703045 | 0.703059 | 0.703039 | 0.70306 | 0.703008 | 0.70303 | 0.703023 | 0.702891 | 0.702972 | 0.702893 |
| 0.512962 | 0.512961 | 0.51297 | 0.512974 | 0.512966 | 0.512967 | 0.512965 | 0.512968 | 0.513135 | 0.513118 | 0.513167 |
| 19.437 | 19.472 | 19.433 | 19.440 | 19.491 | 19.502 | 19.450 | 19.476 | 19.382 | 19.405 | 19.417 |
| 15.600 | 15.589 | 15.599 | 15.604 | 15.606 | 15.605 | 15.594 | 15.597 | 15.591 | 15.595 | 15.593 |
| 38.994 | 38.981 | 38.985 | 39.004 | 39.087 | 39.092 | 38.996 | 39.016 | 39.156 | 39.051 | 39.093 |

$^{204}$Pb isotope variation diagram (Fig. 7a) for which mixing trends are represented by straight lines. Most São Nicolau datapoints define a mixing line (hereafter called the first mixing process) joining (i) the endmember discussed above [1] and modeled here with the mixing of 1.5 Gyr recycled oceanic crust ($^{206}$Pb/$^{204}$Pb ~ 21.26 and $^{208}$Pb/$^{204}$Pb ~ 40.3; cf. Chauvel et al., 1992) and lower mantle material ($^{206}$Pb/$^{204}$Pb ~ 18.3 and $^{208}$Pb/$^{204}$Pb ~ 39.0; cf. Doucelance et al., 2003), and (ii) an unradiogenic endmember ($^{206}$Pb/$^{204}$Pb ~ 18.5 and $^{208}$Pb/$^{204}$Pb ~ 38.0) similar in composition with Atlantic MORB dredged between 10 and 20°N (Dosso et al., 1993). Other samples fall outside of this mixing line. Two datapoints (SN07 and SN09) display higher negative Δ8/4 values for more radiogenic $^{206}$Pb/$^{204}$Pb ratios, plotting in direction of Fogo and/or São Vicente carbonatites (second mixing process toward endmember [4]), whereas a third group of samples define a less steep trend towards compositions measured for some Jurassic MORB (third mixing process toward endmember [5]). These three mixing trends are also drawn in a $^{143}$Nd/$^{144}$Nd vs. $^{206}$Pb/$^{204}$Pb isotope variation diagram (Fig. 7b) even if Pb/Nd ratios corresponding to each endmember have to be known (which is not the case) to precisely plot mixing hyperbolas. They indeed show distinct directions in this diagram, whereas they appear to be nearly parallel in the Pb–Pb (Fig. 7a). Fig. 7c shows São Nicolau samples in the $^{207}$Pb*/$^{206}$Pb* vs. $^{208}$Pb/$^{206}$Pb*, which offers the advantage of better scattering typical mantle components, and in which mixing are also represented by straight lines. In this diagram, the three mixing trends identified above are nearly perpendicular and clearly separated from one another.

The restricted range of isotopic compositions of our dataset prevents us to discuss more thoroughly the isotopic composition of the endmembers. However, still remain some questions that need to be addressed to fully understand the processes at the origin of these endmembers; in particular, what is their depth of origin. In the following, we use trace-elements and isotopes ratios measured in our samples to show that São Nicolau geochemical signature can be explained by multi-stage, shallow-level mixing with several components. Then, we try to generalize this conclusion to the regional trends before speculating about the Cape Verde plume source composition.

### *4.1. Superficial components as the origin of São Nicolau isotopic variability?*

The identification of endmember [6] with Jurassic MORB collected on Santiago Island implies the third mixing trend discussed above to represent superficial contamination of the ascending melts by the

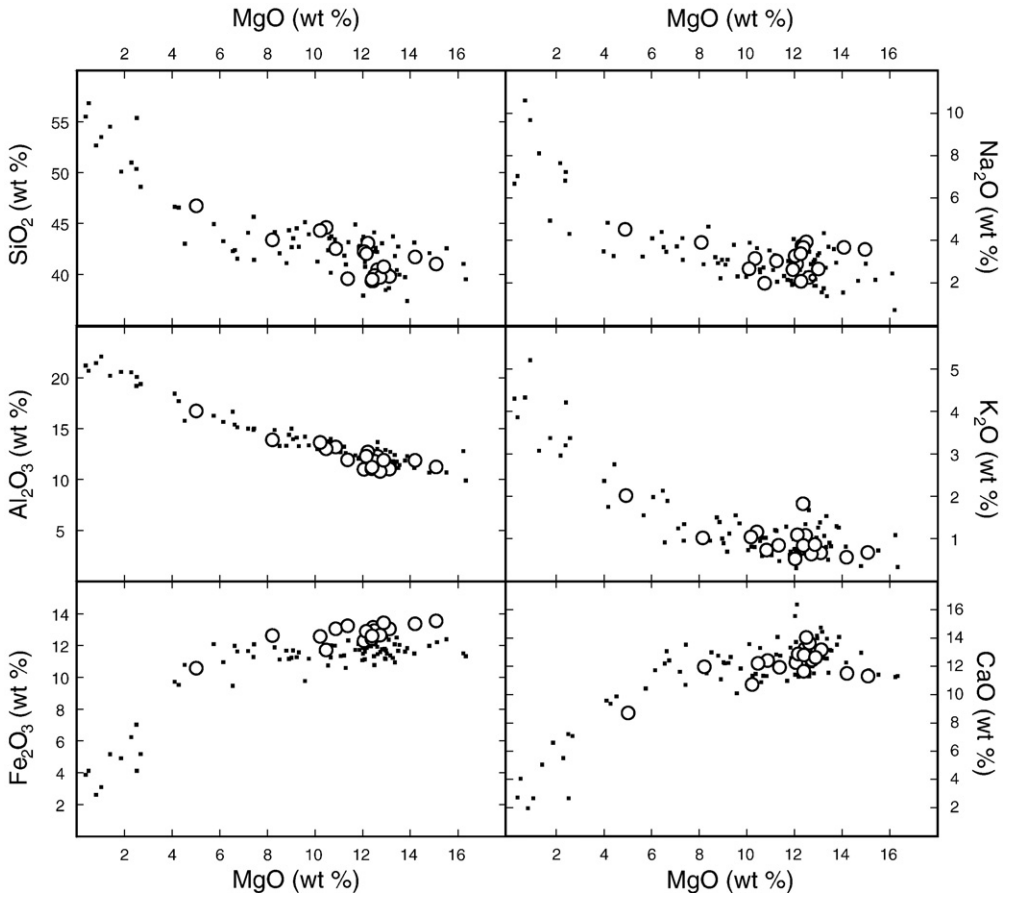


**Fig. 3.** Variations of some major elements along with MgO weight content in samples from São Nicolau Island. Large open circles: this study; small filled squares: literature data (Gunn and Watkins, 1976; Macedo, 1989; Mazarovich et al., 1990; Duprat et al., 2007).

oceanic basement of the Cape Verde archipelago. The required Sr isotopic ratio of the contaminant is obtained in MORB samples only after the leaching procedure, suggesting that the mixing process is likely to take place in the unaltered part of the oceanic crust.

More puzzling is the origin of the second mixing trend displacing samples SN07 and SN09 towards the isotopic compositions of carbonatites (Note that a carbonatite dyke was reported on São Nicolau by Kogarko (1993) — cf. sample 506). This observation is supported by two São Nicolau samples only, but it seems to be a regional feature of the Northern Islands, as the composition of some basalts from both São Vicente and Santo Antão islands (Jørgensen and Holm, 2002; Holm et al., 2006) is also shifted towards those of carbonatites.

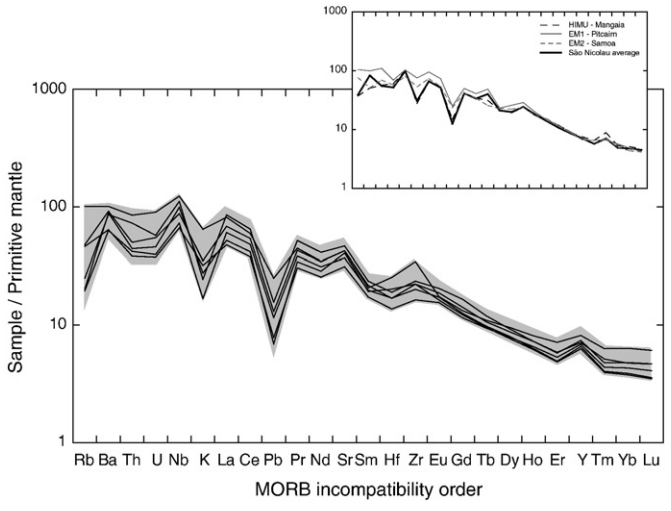


**Fig. 4.** Incompatible trace-element patterns (normalized to primitive mantle, Hofmann, 1988) of some representative São Nicolau samples. Comparison of the average of the basalts with characteristic patterns of extreme OIB endmembers EM1 (average of Tristan basalts, Gibson et al., 2005), EM2 (average of Malumalu volcanics, Workman et al., 2004), and HIMU (average of Mangaia samples, Woodhead, 1996).

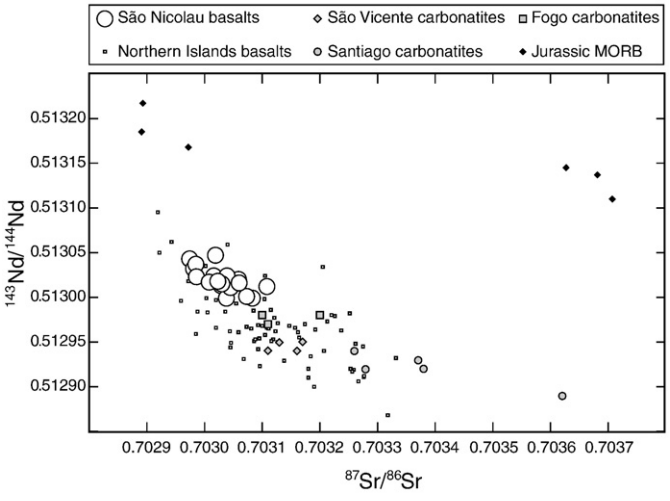


**Fig. 5.** $^{143}Nd/^{144}Nd$ vs. $^{87}Sr/^{86}Sr$ diagram for some Cape Verde volcanics. São Nicolau data: this study; Northern Islands (São Vicente, Santo Antao): (Gerlach et al., 1988; Christensen et al., 2001; Jørgensen and Holm, 2002; Doucelance et al., 2003; Holm et al., 2006), Jurassic MORB: Gerlach et al. (1988) and this study; Carbonatites: Gerlach et al. (1988), Hoernle et al. (2002). Samples from the São Nicolau Island plot within the Northern Island field, and have amongst the depleted values of this group of islands.

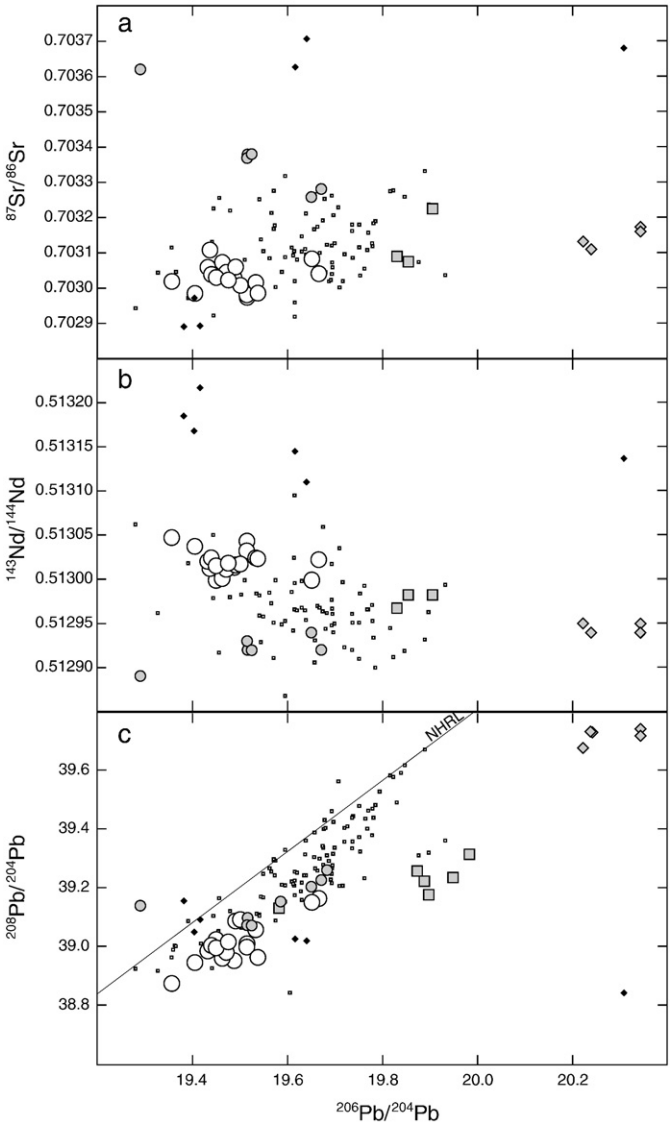


**Fig. 6.** Plot of $^{87}Sr/^{86}Sr$ (a), $^{143}Nd/^{144}Nd$ (b), $^{208}Pb/^{204}Pb$ (c) vs. $^{206}Pb/^{204}Pb$ isotopes ratios for São Nicolau samples. Symbols as in Fig. 5 and are bigger than errorbars. Most of our samples plot at $^{206}Pb/^{204}Pb < 19.6$, whereas two samples are plotting distinctly from this group, toward Fogo or São Vicente carbonatites (age-corrected data from Gerlach et al. (1988) and Hoernle et al. (2002)).

Interpretation of the mixing process in terms of depth location, however, is uncertain. It could represent assimilation of shallow carbonatites, or mixing with a carbonatitic component located deeply in the Capverdean plume source. Note that only 2 samples out of 19 seem to be affected by such carbonatite contamination. On the one hand, this scarcity could indicate that the mixing process is not of important magnitude, and hence that the carbonatitic component is volumetrically small. Such a feature would be more likely representative of a shallow assimilation of carbonatite rather than mixing with a plume-related carbonatitic component, which would affect the totality of the sample set. On the other hand, this observation could only be the result of a sampling bias. Nevertheless, samples SN07 and SN09 (and, to a lesser extent, SN04, see Fig. 7c) plot on the same trend than intermediate volcanics from São Vicente (see Fig. 6c), previously interpreted as shallow-level contamination by carbonatites (Jørgensen and Holm, 2002). This suggests that they are the consequence of the same process, albeit with less important involvement of carbonatitic material as they plot closer to the field of the Northern Islands.

Consequently we favor a shallow origin for carbonatite mixing. Such an origin is in agreement with conclusions by Kogarko (1993) relative to Cape Verde magnesiocarbonatites on the basis that their major-element compositions were similar to partial melts of carbonated peridotite at lithospheric depths. In the same way, Doucelance et al. (2007) recently proposed that Cape Verde carbonatites occur as a result of plume-induced partial melting of carbonatitic metasomatized oceanic lithosphere to explain measured Sr–Nd–He–C isotope systematics of Cape Verde carbonatites.

Let us now discuss the first mixing trend between (i) a HIMU-like Pb ($^{206}Pb/^{204}Pb \sim 20.0$; $^{207}Pb/^{204}Pb \sim 15.65$; $^{208}Pb/^{204}Pb \sim 39.8$), unradiogenic He ($^{4}He/^{3}He \sim 20{,}500$) endmember (termed [1]) and (ii)

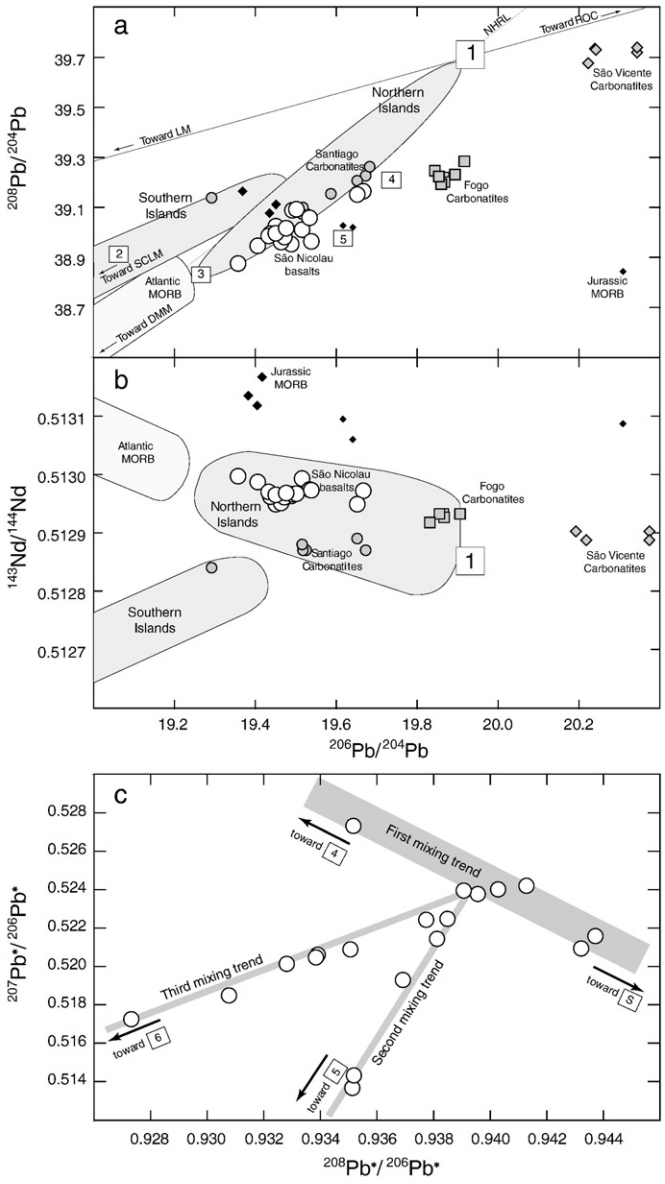


**Fig. 7.** Interpretation diagram of isotopic results for São Nicolau basaltic samples. Cape Verde samples from localities other than São Nicolau Island are represented by Northern and Southern Islands fields, other symbols as in Fig. 5. Components and endmembers involved in the isotopic variability (ROC: Recycled Oceanic Crust 1.5 Gyr Chauvel et al., 1992; LM: Lower Mantle Doucelance et al., 2003; DMM: Depleted Mantle Material; SCLM: Subcontinental lithospheric mantle; 1: Radiogenic Pb endmember to the Northern Islands; 2: Specific endmember to the Southern Islands; 3: Specific endmember to the Northern Islands; 4: Fogo or São Vicente carbonatites (age-corrected data from Gerlach et al., 1988; Hoernle et al., 2002); 5: Jurassic MORB (Gerlach et al., 1988; this study)) are plotted at a representative composition, although they could be more extreme. Endmember noted [1] also represents the composition of the Cape Verde plume source. Errorbars for raw data are within the size of datapoints (Fig. 7a and b).

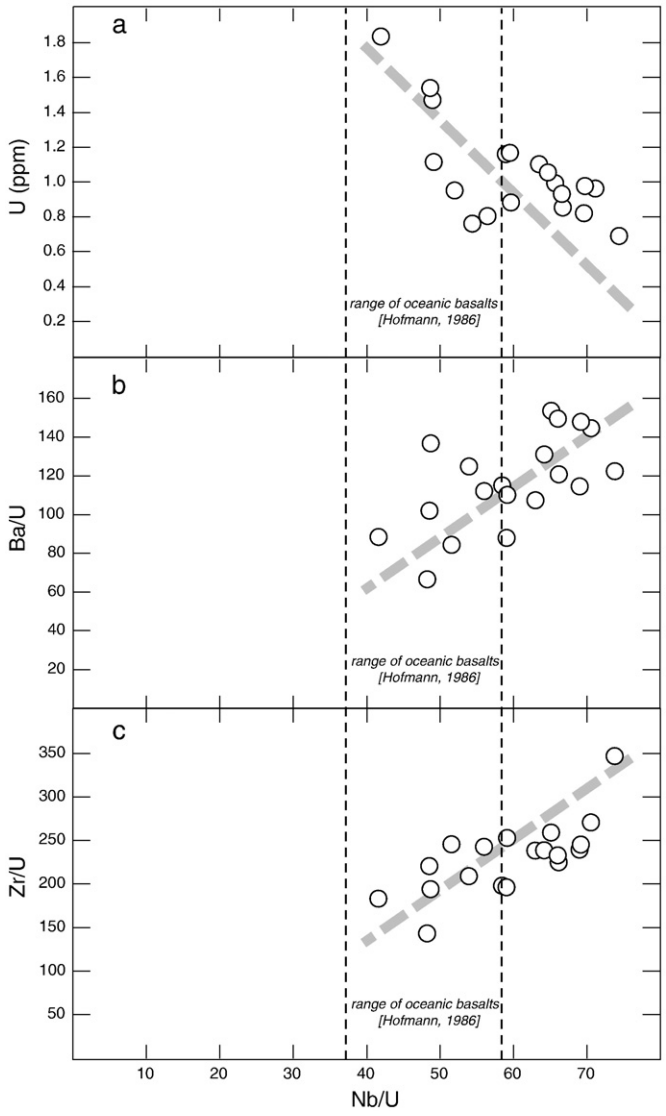


**Fig. 8.** (a) Nb/U vs. U diagram in basaltic samples from São Nicolau Island. The negative correlation observed in those samples can either be related (i) to a lesser incompatibility of Nb relative to U in a magmatic process, or to (ii) mixing between a high U–normal Nb/U endmember and a low U–high Nb/U endmember. The elevated Nb/U signature is also associated with high Ba/U (b) and Zr/U (c) ratios, suggesting enrichments in Nb, Ba and Zr relative to U.

North Atlantic MORB-like compositions [3]. Unradiogenic (primitive) $^4He/^3He$ values are generally interpreted as tracing a relatively undegassed reservoir thought to be the lower mantle (Kurz et al., 1982). They therefore imply the Pb radiogenic endmember to be deep-seated in the Cape Verde plume source. On the contrary, two options can be proposed for the depleted endmember: (i) the oceanic lithosphere, or (ii) viscously entrained asthenospheric material. Following Class and Goldstein (1997), depletions in Rb, Ba, K and Ta for São Nicolau basalts would be expected in case of underlying oceanic lithosphere assimilation. However, such trace-element characteristics could also be interpreted as "ghost" amphibole or phlogopite signature in ancient, recycled lithospheric material during subduction (Gurenko et al., 2006).

Additional constraints on this problem are given by the trace-element characteristics of São Nicolau basalts. These have Nb/U ratios ranging from 41 up to 73, which is clearly distinguishable from the average values of MORB and OIB (47 ± 10: Hofmann et al., 1986; 50 ± 14 Sims and DePaolo, 1997). According to Hofmann et al. (1986), Nb and U have identical bulk partition coefficients during oceanic basalts melting, and display contrasting ratios in oceanic basalts and in the estimates of the primitive mantle and the continental crust. They thus can distinguish between mantle enrichments which have produced oceanic basalt sources and sources derived from the continental crust or the primitive mantle.

Nb/U ratios for São Nicolau basalts correlate negatively when plotted against U concentrations (Fig. 8a). This relationship could at first glance indicate a lesser incompatibility of Nb relative to U, implying thus that Nb/U do not directly reflect the long-term characteristics of São Nicolau sources. However, such a hypothesis is based on the assumption that São Nicolau basalts are cogenetic in the sense that they correspond to partial melts from a source of uniform composition, a hypothesis which is not supported by the isotopic variations indicating a heterogeneous source for São Nicolau basalts. An alternative hypothesis is that the relationship reflects a mixing process between an endmember with normal OIB-like Nb/U values and an endmember with high Nb/U values. Following this hypothesis, the endmember with OIB-like Nb/U values is likely to be the Cape Verde plume source whereas two candidates need to be considered on the basis of the isotope systematics, for the high Nb/U endmember. These are the oceanic lithosphere and the entrained asthenospheric material.

This high Nb/U signature is also associated with high (Ba, Zr)/(Th, U) compared to depleted mantle values (Ba/U and Zr/U represented in Fig. 8b and c), suggesting enrichment in Nb, Ba and Zr. Such enrichments can hardly be reconciled with the hypothesis of asthenospheric material (i.e., depleted mantle source with a MORB-like value), nevertheless such ratios can be found in the oceanic lithosphere, as it generally contains amphibole and/or phlogopite, two minerals known to have affinities with Ba, Nb and Zr (LaTourette et al., 1995; Halliday et al., 1995). It has to be noted, however, that this signature is not associated with similar K and Rb enrichments, two elements also enriched within amphibole and/or phlogopite. High values of the Rb/U ratio are indeed restricted to the high Nb/U lavas but no reliable trend is observed between these two ratios, neither with K/U. Nevertheless, Rb and K do not correlate with Th (contrary to other elements), indicating perturbation due to sample weathering.

Two scenarios can thus be envisioned. The high Nb/U endmember is located in the local underlying lithosphere, recently metasomatized (either at mid-ocean ridges, Class and Goldstein, 1997; or by first plume melts, Lundstrom et al., 2003), or the high Nb/U values reflect the involvement of subducted recycled lithosphere with a ghost phlogopite–amphibole signature (Gurenko et al., 2006) in the plume. One expectation of the model of Gurenko et al. (2006) is coherent information between Nb/U ratios and isotope compositions as they

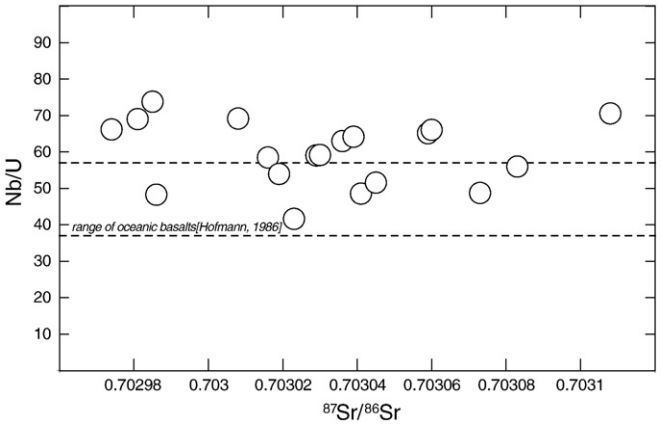


**Fig. 9.** Nb/U vs. $^{87}Sr/^{86}Sr$ diagram for São Nicolau samples. No correlation can be observed between those two parameters and values of the Nb/U ratio in the represented samples are extremely scattered compared to the mantle range defined by Hofmann et al. (1986).

both behave as effective source tracers. However, no covariations between isotope ratios and Nb/U is observed ($^{87}Sr/^{86}Sr$ in Fig. 9), and thus support that the first mixing trend is the consequence of the assimilation by plume melts of the underlying lithosphere containing dispersed amphibole–phlogopite. The sampling of these minerals at variable degrees of melting could be the cause of the high Nb/U ratios.

A similar two-step model was proposed by Lundstrom et al. (2003) for lavas from eastern Canary Islands. In the first stage, the local lithosphere is contaminated with amphibole/phlogopite veins crystallizing from ascending plume melts. The metasomatized lithosphere is then assimilated by subsequent ascending melts, implying that the isotopic signature of high Nb/U lavas could represent plume heterogeneity. Nevertheless, this model is supported by indications in some samples of amphibole/phlogopite fractionation, which are absent in São Nicolau samples. Moreover, amphibole/phlogopite veins have to be sufficiently enriched in Sr, Nd and Pb to account for plume heterogeneity. This can be the case for Sr and Nd, but not for Pb which is highly incompatible in amphibole and phlogopite (Halliday et al., 1995). Thus these two minerals will not be important contributors to the Pb budget of samples. Consequently, we favor a shallow origin for the Cape Verde depleted component [3].

A melting-mixing model has been then carried out in order to compute the weight fraction of lithosphere needed to account for isotope variations recorded by São Nicolau samples. We decided to focus on Pb and Nd data only, Sr contents being potentially perturbed by seawater interaction (uncontaminated Sr contents cannot be retrieved with the leaching technique). The model is a two-step model with, first, continuous fractional melting of the metasomatized lithosphere (mineralogy is ol:72, opx: 21.5, cpx: 3, gt: 1, amph: 0.8, phlog: 1.7; partition coefficients from Halliday et al. (1995) and reference therein; [Pb]=20 ppb, $^{206}Pb/^{204}Pb$=19; [Nd]=1.1 ppm, $^{143}Nd/^{144}Nd$=0.51305), and second, mixing with pristine plume melts ([Pb]=1 ppm, $^{206}Pb/^{204}Pb$=20; [Nd]=30 ppm, $^{143}Nd/^{144}Nd$=0.51285). Results show that 32 to 40% of lithospheric melts (~1.3% partial melting) can account for the isotopic variations.

It should be noted that Nb/U vs. U variations are explained in terms of a simple binary mixing process whereas isotopes ratios point to three different mixing processes and four endmembers. However, Jurassic MORB (or carbonatites) assimilation is likely to occur at crustal levels through a coupled assimilation–fractional crystallization (AFC) process. As São Nicolau basalts are not strongly differentiated, the AFC process is likely to be subordinate to the first mixing process expressed – in isotopes diagram between endmembers [1] and [3] (Fig. 9) – which therefore can be seen as the isotope equivalent of the Nb/U versus U mixing trend.

In summary, converging trace-elements and isotopic signatures in São Nicolau basalts can be explained by mixing of pristine plume melts with three different superficial components (Jurassic MORB basement, carbonatite and underlying oceanic lithosphere). If assimilation of carbonatites and Jurassic MORB is a process of limited magnitude that affects only a small subset of the samples, interaction with the underlying lithosphere appears as the main contamination process that controls the geochemical signature of São Nicolau basalts.

### 4.2. Generalization to the regional trends

As discussed above, isotopic variations of São Nicolau basalts can be explained by mixing between plume melts with constant compositions and superficial components. In the following, we evaluate if this interpretation can be extrapolated to the isotope ratios variations measured for lavas from the other islands of the Cape Verde archipelago.

At the archipelago scale, isotopic variations define two regional trends, the Southern Island trend between the endmember [1] and subcontinental lithosphere [2], and the Northern Island trend between endmember [1] and Atlantic MORB [3], which corresponds to the first trend identified in São Nicolau samples. In order to discuss those regional features, we will focus only on data unaffected by carbonatite and/or Jurassic MORB assimilation and with $SiO_2$ contents <50 wt.%. Our selection then takes into account (i) all samples from Santiago and Fogo regarding the Southern Islands (Gerlach et al., 1988; Escrig et al., 2005) and; (ii) 7 samples from São Nicolau (this study); all the analyses by (Gerlach et al., 1988); old volcanics (OV) from São Vicente (Jørgensen and Holm, 2002); and Santo Antão data except 10 from Holm et al. (2006) for the Northern Islands.

Samples from the Northern Islands have Nb/U values (as well as high (Ba, Zr)/(Th, U)) ranging from 30 to 100 and are uncorrelated with isotope. Two samples have Nb/U values that are well below the normal range for MORB and OIB (Hofmann et al., 1986). Such low values are usually linked to the involvement of continental material, an hypothesis in disagreement with isotopes ratios measured in the Northern Islands, or could indicate that the lavas have experienced phlogopite and/or amphibole fractionation, as proposed by Lundstrom et al. (2003). However, such fractionation would be of limited extent as only 2 samples over all volcanics from the Northern Islands show this signature, being thus not able to account for plume-related lithosphere metasomatism at the archipelago scale.

It has also to be noted that shallow-level interaction between plume melts and the local underlying oceanic lithosphere does not definitely rule out the involvement of entrained depleted material (Holm et al., 2006) or depleted subducted material (Gurenko et al., 2006), as their signature would be hidden by shallowest processes.

The exact location of endmembers [2] and [3], specific to Southern and Northern Islands respectively, at shallow levels (sampling via assimilation) or deeper in the plume source (sampling by partial melting) would lead to contrasted relationships between the various geochemical tools. In the case of assimilation, broad correlations between the different geochemical tools witnessing assimilation and mixing process are expected, whereas a location in the plume should lead to a decoupling of major- or trace-element contents and isotopic ratios due to partial melting. Fig. 10 presents $Na_2O$ contents vs. $^{87}Sr/^{86}Sr$ isotopic ratios for Cape Verde basalts, restricting datapoints to samples unaffected by assimilation of Jurassic MORB and/or carbonatites. Datapoints distribute into 2 broad distinct trends corresponding to samples from the Northern Islands, on the one hand, and samples from the Southern Islands on the other hand. In details, basalts from Santo Antão, São Vicente and São Nicolau present negatively correlated $Na_2O$ contents and $^{87}Sr/^{86}Sr$ ratios, whereas samples from Fogo and Santiago display a positive relationship. Such a coupled evolution of a differentiation index ($Na_2O$ content) with a source tracer like $^{87}Sr/^{86}Sr$ argues in favor of syn- or post-differentiation mixing processes in the final fingerprint of Cape Verde basalt geochemical signatures.

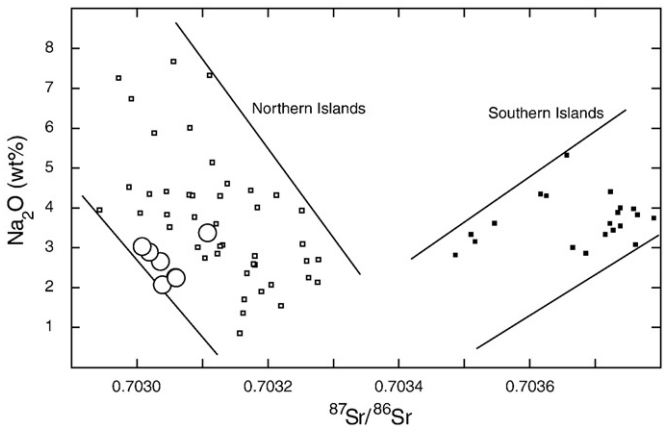


**Fig. 10.** Plot of $Na_2O$ weight content vs. Sr isotopes ratio for both groups of Cape Verde islands. Covariation between those variables indicates that both magmatic differentiation and mixing occurs simultaneously. This is best interpreted in terms of a shallow-level mixing rather than deep source heterogeneity.

### 4.3. Isotopic signature of the Cape Verde plume source

As discussed previously, the detailed study of elemental and isotopic compositions of São Nicolau basalts together with previous analyzes for Santo Antão and São Vicente lavas (Gerlach et al., 1988; Jørgensen and Holm, 2002; Doucelance et al., 2003; Holm et al., 2006) indicates that chemical variabilities observed for basalts from the Northern Islands are related to multi-component assimilation at a shallow level. An identical conclusion was reached by Escrig et al. (2005) for the origin of the binary mixing trends defined by samples from the Southern Islands in isotope variation diagrams. They interpreted the Sr–Nd–Pb–Os compositions of Fogo basalts as results of the mixing between (i) a HIMU-like endmember associated with the Cape Verde plume source (similar to the endmember [1] discussed for the Northern Islands, see Section IV.1) and (ii) a EM1-like endmember, identified as subcontinental lithospheric material left behind in the oceanic lithosphere after opening of the Atlantic ocean. Such a conclusion is mainly based on the time-dependent evolution of mixing as the youngest samples being closer to the EM1-like endmember. This observation suggests a shallow-level location of the EM1-like endmember, which is more likely assimilated during melt ascent through the oceanic lithosphere than present in the deep plume source. Indeed, the progressive recharge of a magma chamber that was not totally emptied by previous eruptions will result in mixing of older batches that have already suffered assimilation with pristine melts; this will thus result in the generation of melts with intermediate isotopic signatures, evolving with time towards the contaminant (wallrock) endmember. Furthermore Fogo basalts show a clear relationship between $Na_2O$ contents and Sr isotopic ratios (Fig. 10) tracing syn- or post-differentiation processes.

We also noted earlier in this manuscript that the recent extension of the Northern Island filed toward more radiogenic Pb compositions and lower Nd values (Holm et al., 2006). Consequently the endmember [1] cannot be considered as common to the two groups of islands anymore (as it was the case in Doucelance et al., 2003). Indeed, the Southern Islands trend starts from a point that plots within the Northern Islands field (Fig. 7). This implies that melts from the Southern Island have been modified by interaction with the metazomatized Atlantic oceanic lithosphere (Northern Islands mixing) before acquiring their EM1 signature. This allows us to locate the EM1-like component identified by previous authors in the upper levels of the lithosphere underlying the Cape Verde archipelago, in agreement with previous conclusions from Hoernle et al. (1991).

From observations and models related to both groups of islands, we thereby propose that most of the isotopic variability registered in basaltic samples from the Cape Verde archipelago is resulting from shallow-level interactions between unradiogenic $^4He/^3He$, HIMU-like Sr–Nd–Pb, plume-related melts ($^{87}Sr/^{86}Sr \sim 0.7034$; $^{143}Nd/^{144}Nd \sim 0.51285$; $^{206}Pb/^{204}Pb \sim 20.0$; $^{207}Pb/^{204}Pb \sim 15.65$; $^{208}Pb/^{204}Pb \sim 39.8$; $^4He/^3He \sim 20{,}500$) and various components associated with the oceanic lithosphere (subcontinental lithosphere, carbonatite and Jurassic MORB).

This conclusion implies that the deep source of the Cape Verde plume has remained nearly constant over the span of time covered by samples used in this study (~10 Myr). Such constancy in the plume source composition is somewhat not exceptional. As an example, the Reunion plume melts have been recording the same composition for the last 60 millions of years (Peng and Mahoney, 1995). For the Cape Verde plume, whose source is supposed to be heterogeneous (i.e., best explained by a mixture of lower mantle material and recycled oceanic crust), this suggests almost constant partial melting degrees resulting in constant proportions of both components.

Turning to the control of the isotopic variability of basalts by shallow-level processes, this may be related to the geographical position of the Cape Verde archipelago. Its location over an old and very thick lithosphere (Cazenave et al., 1988) allows plume melts to interact with it. Additionally, a thick lithosphere is limiting the range of melting depths and by consequence the range of partial melting degrees.

## 5. Concluding remarks and general considerations

New measurements for major-, trace-elements and Sr–Nd–Pb isotope ratios have been carried out for 19 samples from São Nicolau Island, Cape Verde archipelago. Isotopic results are in agreement with previously published data for basalts from the Northern Cape Verde Islands (Santo Antão and São Vicente), although the range of variations appears to be more limited. They also show variations of the (Nb, Ba, Zr)/(Th, U) ratio that indicates involvement of a reservoir containing amphibole and/or phlogopite. We interpret this signature as shallow-level mixing between plume-related melts with a HIMU-like Sr–Nd–Pb isotopic composition ($^{87}Sr/^{86}Sr \sim 0.7034$; $^{143}Nd/^{144}Nd \sim 0.51285$; $^{206}Pb/^{204}Pb \sim 20.0$; $^{207}Pb/^{204}Pb \sim 15.65$; $^{208}Pb/^{204}Pb \sim 39.8$) and 3 superficial components: (1) oceanic lithosphere, (2) carbonatites, and (3) Jurassic MORB (the last 2 components being associated with the oceanic lithosphere). Despite the lack of unambiguous data, the converging signatures presented in this contribution coupled to previous conclusions invoking an AFC process for Santiago and Fogo basalts (Hoernle et al., 1991; Escrig et al., 2005), lead us to infer that the isotopic variability registered by basaltic samples from the whole Cape Verde archipelago might not be source-related, but rather associated with shallow-level processes.

Sampling of the oceanic stratigraphy during interactions has already been observed by Thirlwall et al. (1997) and Widom et al. (1999) in the nearby Canary archipelago where they propose that lavas are contaminated by lithospheric mantle, oceanic crust and overlying sediments during ascent. In addition, isotopic variations toward an enriched endmember in samples from Walvis Ridge (Gibson et al., 2005), Madeira (Geldmacher and Hoernle, 2000), Oceanographer Fracture Zone (Shirey et al., 1987) and the recently discovered Godzilla seamount (Geldmacher et al., 2008) have also been interpreted in terms of shallow-level mixing with continental material delaminated during the opening of the Atlantic Ocean. This show that oceanic lithosphere plays an important role in controlling the geochemical signature of OIB as it can both influence their pristine major-trace elements compositions via its age/thickness (Ellam, 1992; Haase, 1996) and be a source of isotopic variability.

Identification of these shallow-level interactions is however hardened by the similarity of isotopic compositions of contaminants and classical mantle endmembers (EM1, EM2, DMM, HIMU, see Zindler and Hart, 1986). Indeed, the local underlying oceanic lithosphere resembles the depleted upper mantle and could be confused with entrained asthenospheric mantle; Sub-continental lithospheric mantle, delaminated into the Cape Verde Jurassic lithosphere in this case study, can be recycled via mantle plumes after thermal erosion of continental roots and sinking into the mantle, moreover, they also have Sr–Nd–Pb isotopic compositions in agreement with recycled sediments. Finally, Cape Verde carbonatites have fairly radiogenic Pb isotopic compositions coupled with depleted Sr and Nd isotopes, similar to a HIMU endmember. Therefore, island-scale studies of oceanic basalts taking into account major- and trace-element information coupled with isotopic signatures are mandatory to filter the deep source information from the shallow-level signature.

The diversity of isotopic compositions for contaminants and their important influence on the isotopic variability of Cape Verde volcanics and from other localities such as Tristan da Cunha/Walvis ridge (Gibson et al., 2005), Comores archipelago (Späth et al., 1996; Class and Goldstein, 1997), Pitcairn seamounts (Woodhead and Devey, 1993) suggest that mantle isotopic variability, usually assumed to be identical to the one measured in OIB, could be less important. Notably this may have implications on studies that use convergence of isotopic mixing trends to define a common component to all OIB (FOZO: Hart et al., 1992; Hauri et al., 1994; Jackson et al., 2007; PHEM: Farley et al.,

1992; C: Hanan and Graham, 1996) without deciphering the part of the isotopic signature that comes from shallow-level interactions.

## Acknowledgements

The authors wish to thank Ivan Vlastelic for stimulating discussions, Philippe Telouk for help with MC-ICP-MS analyses in ENS Lyon, Monica Handler and Ken Koga for correcting the English. We also acknowledge Margaret Mangan for editorship as well as two anonymous reviewers for helpful comments that greatly improved the manuscript.

## References

Allègre, C.J., Turcotte, D.L., 1986. Implications of a two-component marble-cake mantle. Nature 323, 123–127.
Cazenave, A., Dominh, K., Rabinowicz, M., Ceuleneer, G., 1988. Geoid and depth anomalies over ocean swells and troughs: evidence of an increasing trend of the geoid to depth ratio with age of plate. J. Geophys. Res. 93, 8064–8077.
Chauvel, C., Hofmann, A.W., Vidal, P., 1992). HIMU-EM: the French Polynesian connection. Earth Planet. Sci. Lett. 110, 99–119.
Christensen, B.P., Holm, P.M., Jambon, A., Wilson, J.R., 2001. Helium, argon and lead isotopic composition of volcanics from Santo Antão and Fogo, Cape Verde Islands. Chem. Geol. 178, 127–142.
Class, C., Goldstein, S.L., 1997. Plume–lithosphere interactions in the ocean basins: constraints from the source mineralogy. Earth Planet. Sci. Lett. 150, 245–260.
Class, C., LeRoex, A.P., 2006. Continental material in the shallow oceanic mantle — how does it get there? Geology 34, 129–132.
Dasch, E.J., Hedge, C.E., Dymond, J., 1973. Effect of sea water interaction on strontium isotope composition of deep-sea basalts. Earth. Planet. Sci. Lett. 19, 177–183.
Davies, G.R., Norry, M., Gerlach, D.C., Cliff, R.A., 1989. A combined chemical and Pb–Sr–Nd isotope study of the Azores and Cape Verde hotspots: the geodynamic implications. In: Saunders, A.D., Norry, M.J. (Eds.), Magmatism in the Ocean Basins. Geol. Soc. Spec. Publ., London, pp. 231–255.
DePaolo, D.J., 1981. Trace element and isotopic effects of combined wallrock assimilation and fractional crystallization. Earth Planet. Sci. Lett. 53, 189–202.
DePaolo, D.J., 1985. Isotopic studies of processes in mafic magma chambers: I. The Kiglapait Intrusion. J. Petrol. 26, 925–951.
Dosso, L., Bougault, H., Joron, J.-L., 1993. Geochemical morphology of the North Mid-Atlantic Ridge, 10°–20°N: trace element–isotope complementarity. Earth Planet. Sci. Lett. 120, 443–462.
Doucelance, R., Manhès, G., 2001. Reevaluation of precise lead isotope measurements by thermal ionization mass spectrometry: comparison with determinations by plasma source mass spectrometry. Chem. Geol. 176, 361–377.
Doucelance, R., Escrig, S., Moreira, M., Gariépy, C., Kurz, M.D., 2003. Pb–Sr–He isotope and traces element geochemistry of Cape Verde archipelago. Geochim. Cosmochim. Acta 67, 3717–3733.
Doucelance, R., Mata, J., Moreira, M., Silva, L.C., 2007. Isotopes evidence for the origin of Cape Verde oceanic carbonatites. 17th V.M. Goldschmidt Conf. Geochim. Cosmochim. Acta 71 (15), A233.
Duprat, H.I., Friis, J., Holm, P.M., Grandvuinet, T., Sorrensen, R.V., 2007. The volcanic and geochemical development of São Nicolau, Cape Verde Islands: constraints from field and $^{40}Ar/^{39}Ar$ evidence. J. Volcanol. Geotherm. Res. 162, 1–19.
Dupré, B., Lambert, B., Allègre, C.J., 1982. Isotopic variations within a single island: the Terceira case. Nature 620–622.
Ellam, R., 1992. Lithospheric thickness as a control on basalt geochemistry. Geology 20, 153–156.
Escrig, S., Doucelance, R., Moreira, M., Allègre, C.J., 2005. Os isotope systematics in Fogo basalts: evidence for lower continental crust residing in the oceanic lithosphere beneath the Cape Verde Islands. Chem. Geol. 219, 93–113.
Farley, K.A., Natland, J.H., Craig, H., 1992. Binary mixing of enriched and undegassed (primitive?) mantle components (He, Sr, Nd, Pb) in Samoan lavas. Earth and Planet. Sci. Lett. 111, 183–199.
Geldmacher, J., Hoernle, K., 2000. The 72 Ma geochemical evolution of the Madeira hotspot (eastern North Atlantic): recycling of Paleozoic (≤500 Ma) oceanic lithosphere. Earth and Planet. Sci. Lett. 183, 73–92.
Geldmacher, J., Hoernle, K., Klügel, A., van den Bogaard, P., Bindeman, I., 2008. Geochemistry of a new enriched mantle type locality in the Northern hemisphere: implications for the origin of the EM-1 source. Earth and Planet. Sci. Lett. 265, 167–182.
Gerlach, D.C., Cliff, R.A., Davies, G.R., Norry, M., Hodgson, N., 1988. Magma sources of the Cape Verde archipelago: isotopic and trace elements constraints. Geochim. Cosmochim. Acta 52, 2979–2992.
Gibson, S.A., Thompson, R.N., Day, J.A., Humphris, S.E., Dickin, A.P., 2005. Melt-generation processes associated with the Tristan mantle plume: constraints on the origin of EM-1. Earth and Planet. Sci. Lett. 237, 744–767.
Gunn, B.M., Watkins, N.D., 1976. Geochemistry of the Cape Verde Islands and Fernandio de Noronha. Bull. Geol. Soc. Am. 87, 1089–1100.
Gurenko, A.A., Hoernle, K.A., Hauff, F., Schmincke, H.-U., Han, D., Miura, Y.N., Kaneoka, I., 2006. Major, trace element and Nd–Sr–Pb–O–He–Ar isotope signatures of shield stage lavas from the central and western Canary Islands: insights into mantle and crustal processes. Chem. Geol. 233, 75–112.
Haase, K., 1996. The relationship between the oceanic lithosphere and the composition of oceanic magmas: constraints on partial melting, mantle sources and the thermal structures of the plates. Earth and Planet. Sci. Lett. 144, 75–92.
Halliday, A.N., Lee, D.C., Tommasini, S., Davies, G.R., Paslick, C.R., Fitton, J.G., James, D.E., 1995. Incompatible trace elements in OIB and MORB and source enrichments in the sub-oceanic mantle. Earth and Planet. Sci. Lett. 133, 379–395.
Hanan, B.B., Graham, D.W., 1996. Lead and helium isotopic evidence from oceanic basalts for a common deep source of mantle plumes. Science 272, 991–995.
Hart, S.R., 1984. Large-scale isotope anomaly in the Southern Hemisphere mantle. Nature 309, 753–757.
Hart, S.R., Hauri, E.H., Oschmann, L.A., Whitehead, J.A., 1992. Mantle plumes and entrainment: isotopic evidence. Science 256, 517–520.
Hauri, E.H., Whitehead, J.A., Hart, S.R., 1994. Fluid dynamic and geochemical aspects of entrainment in mantle plumes. J. Geophys. Res. 99, 24275–24300.
Hoernle, K., Tilton, G., Schmincke, H.-U., 1991. Sr–Nd–Pb isotopic evolution of Gran Canaria: Evidence for shallow enriched mantle beneath the Canary Islands. Earth and Planet. Sci. Lett. 106, 44–63.
Hoernle, K., Tilton, G., Bas, M.J.L., Duggen, S., Garbe-Schönberg, D., 2002. Geochemistry of oceanic carbonatites compared with continental carbonatites: mantle recycling of oceanic crustal carbonate. Contrib. Mineral. Petrol. 142, 520–542.
Hofmann, A.W., 1988. Chemical differentiation of the Earth: the relationship between mantle, continental crust and oceanic crust. Earth and Planet. Sci. Lett. 90, 297–314.
Hofmann, A.W., Jochum, K.P., Seufert, M., White, W.M., 1986. Nb and Pb in oceanic basalts: new constraints on mantle evolution. Earth and Planet. Sci. Lett. 79, 33–45.
Holm, P.M., Wilson, J.R., Christensen, B.P., Hansen, L., Hansen, S.L., Hein, K.M., Mortensen, A.K., Pedersen, R., Plesner, S., Runge, M.K., 2006. Sampling the Cape Verde mantle plume: evolution of melt composition on Santo Antão, Cape Verde Islands. J. Petrol. 47, 145–189.
Jackson, M.G., Kurz, M.D., Hart, S.R., Workman, R.H., 2007. New Samoan lavas from Ofu Island reveal an hemispherically heterogeneous high $^{3}He/^{4}He$ mantle. Earth and Planet. Sci. Lett. 264, 360–374.
Jørgensen, J.Ø., Holm, P.M., 2002. Temporal variation and carbonatite contamination in primitive ocean island volcanics from São Vicente, Cape Verde Islands. Chem. Geol. 192, 249–267.
Kogarko, L.N., 1993. Geochemical characteristics of oceanic carbonatites from the Cape Verde Islands. S. Afr. J. Geol. 96, 119–125.
Kokfelt, T.F., Holm, P.M., Hawkesworth, C.J., Peate, D.W., 1998. A lithospheric mantle source for the Cape Verde island magmatism: trace element and isotopic evidence from the island of Fogo. Min. Mag. 62A, 801–802.
Kurz, M.D., Jenkins, W.J., Schilling, J.-G., Hart, S.R., 1982. Helium isotopic variation in the mantle beneath the central North Atlantic Ocean. Earth Planet. Sci. Lett. 58, 1–14.
Lassiter, J.C., Hauri, E.H., Reiners, P.W., Garcia, M.O., 2000. Generation of Hawaiian post-erosional lavas by melting of a mixed lherzolite/pyroxenite source. Earth Planet. Sci. Lett. 178, 269–284.
LaTourette, T.Z., Hervig, R.L., Holloway, J.R., 1995. Trace element partitioning between amphibole, phlogopite and basanite melt. Earth and Planet. Sci. Lett. 135, 13–30.
Lundstrom, C.C., Hoernle, K.A., Gill, J., 2003. U-series disequilibria in volcanic rocks from the Canary Islands: plume versus lithospheric melting. Geochim. Cosmochim. Acta 67, 4153–4177.
Macedo, J., 1989. In: Orta, G.d. (Ed.), Petrologia e geoquímica de lavas da ilha de S. Nicolau (arquipélago de Cabo Verde). Série Geológica, Lisboa, vol. 12, pp. 1–20.
Madeira, J., Munha, J., Tassinari, C., Mata, J., Silveira, A.B.d., Martins, S., 2005. K/Ar ages of carbonatites from the island of Fogo (Cape Verde). VIII Congresso de Geoquimica dos Paises de Lingua Portuguesa, pp. 475–478.
Manhès, G., Minster, J.-F., Allègre, C.J., 1978. Comparative U–Th–Pb and Rb–Sr study of the St-Séverin amphoterites: consequence for early solar system chronology. Earth and Planet. Sci. Lett. 39, 14–24.
Mazarovich, A.O., Frikh-Kar, D.I., Kogarko, L.N., Koporulin, V.I., Rikhter, A.V., Akhmetev, M.A., Zolotarev, B.P., 1990. Tectonics and Magmatism of the Cape Verde Islands. Nauka, Moscow. 246 pp.
Menzies, M., Seyfried, W.E., 1979. Basalt–seawater interaction: trace element and strontium isotopic variations in experimentally altered glassy basalt. Earth Planet. Sci. Lett. 44, 463–472.
Mitchell, J.G., Bas, M.J.L., Zielonka, J., Furnes, H., 1983. On dating the magmatism of Maio, Cape Verde Islands. Earth Planet. Sci. Lett. 64, 61–76.
Montelli, R., Nolet, G., Dahlen, F.A., Masters, G., 2006. A catalogue of deep mantle plumes: new results from finite-frequency tomography. Geochem. Geophys. Geosyst. 7, Q11007. doi:10.1029/2006GC001248.
Peng, Z.X., Mahoney, J.J., 1995. Drillhole lavas from the northwestern Deccan Traps, and the evolution of Réunion hotspot mantle. Earth and Planet. Sci. Lett. 134, 169–185.
Pin, C., Bassin, C., 1992. Evaluation of a strontium-specific extraction chromatographic method for isotopic analysis in geological materials. Anal. Chim. Acta 269, 249–255.
Pin, C., Briot, D., Bassin, C., Poitrasson, F., 1994. Concomitant separation of strontium and samarium–neodymium for isotopic analysis in silicate samples, based on specific extraction chromatography. Anal. Chim. Acta 298, 209–217.
Plesner, S., Holm, P.M., Wilson, J.R., 2003. $^{40}Ar–^{39}Ar$ geochronology of Santo Antao, Cape Verde Islands. J. Volcanol. Geotherm. Res. 120, 103–121.
Shirey, S.B., Bender, J.F., Langmuir, C.H., 1987. Three-component isotopic heterogeneity near the oceanographer Transform, Mid-Atlantic ridge. Nature 325, 217–223.
Sims, K.W.W., DePaolo, D.J., 1997. Inferences about mantle magma sources from incompatible element concentration ratios in oceanic basalts. Geochim. Cosmochim. Acta 61, 765–784.
Späth, A., Roex, A.P., Le, Duncan, R.A., 1996. The geochemistry of lavas from the Comores archipelago, Western Indian ocean: Petrogenesis and mantle source region characteristics. J. Petrol. 37, 961–991.

Thirlwall, M.F., 2002. Multicollector ICP-MS analysis of Pb isotopes using a $^{207}Pb$–$^{204}Pb$ double spike demonstrates up to 400 ppm/amu systematic errors in Tl-normalization. Chem. Geol. 184, 255–279.

Thirlwall, M.F., Jenkins, C., Vroon, P.Z., Mattey, D.P., 1997. Crustal interaction during construction of ocean islands: Pb–Sr–Nd–O isotope geochemistry of the shield basalts of Gran Canaria, Canary Islands. Chem. Geol. 135, 235–262.

Widom, E., Hoernle, K.A., Shirey, S.B., Schmincke, H.-U., 1999. Os isotope systematics in the Canary Islands and Madeira: lithospheric contamination and mantle plume signatures. J. Petrol. 40, 279–296.

Woodhead, J.D., 1996. HIMU in an oceanic setting: the geochemistry of Mangaia Island (Polynesia) and temporal evolution of the Cook–Austral hotspot. J. Volcanol. Geotherm. Res. 72, 1–19.

Woodhead, J.D., Devey, C.W., 1993. Geochemistry of the Pitcairn seamount, 1: source character and temporal trends. Earth Planet. Sci. Lett. 116, 81–99.

Workman, R.K., Hart, S.R., Jackson, M., Regelous, M., Farley, K.A., Blusztajn, J., Kurz, M.D., Staudigel, H., 2004. Recycled metasomatized lithosphere as the origin of the Enriched Mantle II (EM2) end-member: evidence from the Samoan Volcanic Chain. Geochem. Geophys. Geosyst. 5. doi:10.1029/2003GC000623.

Zindler, A., Hart, S.R., 1986. Chemical geodynamics. Annu. Rev. Earth. Planet. Sci. 14, 493–571.

Chemical Geology 265 (2009) 289–302

Contents lists available at ScienceDirect

Chemical Geology

journal homepage: www.elsevier.com/locate/chemgeo

# Reconsidering the origins of isotopic variations in Ocean Island Basalts: Insights from fine-scale study of São Jorge Island, Azores archipelago

Marc-Alban Millet [a,*], Régis Doucelance [a], Joel A. Baker [b], Pierre Schiano [a]

[a] Laboratoire Magmas et Volcans, Université Blaise Pascal, OPGC, CNRS, IRD, 5, rue Kessler, 63038 Clermont-Ferrand Cedex, France
[b] School of Geography, Environment and Earth Sciences, Victoria University of Wellington, PO Box 600, Wellington, New Zealand

ARTICLE INFO

*Article history:*
Received 26 September 2008
Received in revised form 30 March 2009
Accepted 4 April 2009

Editor: R.L. Rudnick

*Keywords:*
OIB
Isotope
Mantle plume
Mixing trends
Azores archipelago
Shallow-level interaction

ABSTRACT

New major and trace element and Sr–Nd–Pb isotope data have been determined for 21 basaltic samples from São Jorge Island, Azores archipelago. Samples can be separated into two groups best identified in a plot of $^{208}Pb/^{204}Pb$ versus $^{206}Pb/^{204}Pb$ where they form two sub-parallel mixing arrays. Lavas from the old (Topo) formation have lower $^{208}Pb/^{204}Pb$ for a given $^{206}Pb/^{204}Pb$ and more radiogenic Sr than samples from intermediate (Rosais) and young (Manadas) formations. Topo samples also tend to have higher MgO contents and lower incompatible trace element concentrations. Both Pb mixing arrays can be related to mixing of plume melts having a HIMU-like Pb isotope signature with two depleted components. One depleted component is best seen in analyses of Topo samples and is interpreted to represent upper mantle material from the nearby Mid-Atlantic ridge. The second depleted component has Sr–Nd–Pb isotopic characteristics similar to E-MORB and resides in the oceanic crust basement under São Jorge. Pb isotope analyses of lavas from São Jorge make it possible to re-define the Terceira end-member of the Azores archipelago, moving its composition to more radiogenic Pb with $^{206}Pb/^{204}Pb \sim 20.51$, $^{207}Pb/^{204}Pb \sim 15.67$ and $^{208}Pb/^{204}Pb \sim 39.56$, at $^{143}Nd/^{144}Nd \sim 0.51295$ and $^{87}Sr/^{86}Sr \sim 0.70375$. Extending the interpretations made for the origins of the São Jorge isotopic mixing arrays to other islands from the Azores archipelago (Pico, Faial, Terceira and São Miguel), we show that most of the isotopic variability recorded by Azores magmas can be related to mixing of plume melts with two distinct and homogeneous signatures as well as several other components dispersed in the shallow mantle/lithosphere under the Azores. This illustrates how caution is required when interpreting ocean island basalt isotopic data as reflecting their deep mantle plume source, and subsequently for constraining mantle topology.



## 1. Introduction

Extensive measurements of radiogenic isotope ratios (Sr, Nd, Pb and, to a lesser extent, Hf and Os) in oceanic basalts have provided major constraints on mantle geodynamic models. Based on the assumption that these isotope ratios are representative of their deep mantle sources, studies of Ocean Island Basalts (OIB) and Mid-Ocean Ridge Basalts (MORB) have helped define the nature of mantle end-members and length-scales of mantle heterogeneities. On a global scale, this has led to the identification of mantle end-members with extreme compositions termed DMM, EM1, EM2 and HIMU (Zindler et al., 1982; Allègre and Turcotte, 1985; Zindler and Hart, 1986; Allègre et al., 1986/1987). Apart from the Depleted MORB Mantle (DMM) component, all other end-members have been defined solely on the basis of OIB data. EM1 has the isotopic composition with the most extreme (highest) $^{87}Sr/^{86}Sr$ and lowest $^{206}Pb/^{204}Pb$ defined by analyses of Pitcairn seamounts (Woodhead and Devey, 1993; Eisele et al., 2002), EM2 shows the most radiogenic Sr at intermediate Pb measured in samples from the Samoan volcanic chain (Jackson et al., 2007a), and HIMU corresponds to samples with the most radiogenic Pb analysed from Mangaïa Island (Woodhead, 1996). An additional end-member, corresponding to the intercept of converging mixing trends in Sr–Nd–Pb isotope variation diagrams and thus displaying intermediate $^{87}Sr/^{86}Sr$, $^{143}Nd/^{144}Nd$ and $^{206}Pb/^{204}Pb$ ratios, is also currently proposed (FOZO: Hart et al., 1992; Farley et al., 1992; Hauri et al., 1994; C: Hanan and Graham, 1996; Jackson et al., 2007b; PHEM). It also has high $^{3}He/^{4}He$ ratios and is thought to be common to all oceanic basalts. If the existence of the four extreme end–members (DMM, EM1, EM2, HIMU) is now accepted (although the nature of their origin and the existence of additional extreme end-members is still a matter of debate), the idea of a common end-member remains questionable. Indeed, mixing trends observed for OIB at local (island) and/or regional scales (archipelago) may either reflect different proportions of various components present in upwelling mantle plumes, or shallow-level interaction processes during magma ascent. Consequently, deciphering the exact origin of isotopic trends in OIB is required before isotopic variations can be

* Corresponding author. Present address: School of Geography, Environment and Earth Sciences, Victoria University of Wellington, PO Box 600, Wellington, New Zealand. Tel.: +64 4 463 5391; fax: +64 4 463 5186.
*E-mail address:* marc-alban.millet@vuw.ac.nz (M.-A. Millet).

0009-2541/$ – see front matter © 2009 Elsevier B.V. All rights reserved.
doi:10.1016/j.chemgeo.2009.04.005

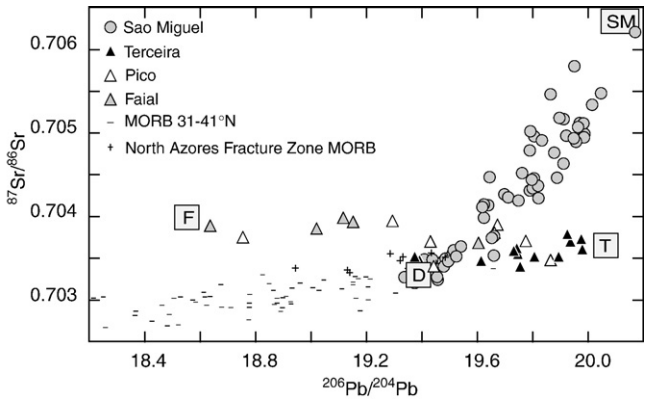


**Fig. 1.** Map of the Azores archipelago with the age of the oldest subaerial volcanic activity on each island shown.

interpreted as deep mantle heterogeneities occurring on a global scale.

Shallow-level magma interactions can include several processes occurring at different levels within the oceanic lithosphere. From surface to source, the geochemistry of plume magmas can be altered by post-eruption seawater and/or meteoric water interaction at the surface or near-surface, by Assimilation and Fractional Crystallization (AFC) during storage in magma chambers at crustal depths, or via Plume–Lithosphere Interactions (PLI) during melt ascent through the local lithosphere. Identification of isotopic variations related to shallow-level interactions in Comores (Späth et al., 1996; Class and Goldstein, 1997), Cape Verde archipelago (Doucelance et al., 2003; Escrig et al., 2005; Millet et al., 2008) and Canary Islands (Hoernle et al., 1991; Thirlwall et al., 1997; Widom et al., 1999) show that such processes are common when volcanic activity is situated on very old oceanic floor (>120 Ma).

The objective of this work is to examine potential shallow-level magma interactions that can be observed in a different geodynamical setting compared to Comores, Cape Verdes or Canary Islands. The focus of this paper is on São Jorge Island, Azores archipelago, located on young oceanic lithosphere and close to the mid-Atlantic ridge. We present major and trace element data and Sr–Nd–Pb isotope ratios for 21 basaltic samples. We first consider geochemical variations that are observed at the scale of the island in an attempt to resolve information related to deep source heterogeneities versus those due to shallow-level interactions. Then, we speculate about the implications of the São Jorge Island dataset on the processes responsible for the geochemical variability in other islands from the Azores archipelago in order to: (a) assess the origin of the fine-scale variability of volcanic rocks from other Azores islands and (b) define the true isotopic fingerprint of the Azores mantle plume.

## 2. Geographic location and previous studies

The Azores archipelago (Fig. 1) comprises nine islands of volcanic origin, representing the emerged part of a large oceanic plateau that extends on both sides of the Mid-Atlantic Ridge (MAR). The islands can be divided in three geographical groups: (1) the Occidental Group, located to the west of the MAR, that comprises Corvo and Flores Islands; (2) the Central Group, to the east of the MAR, formed by Terceira, Graciosa, Pico, Faial and São Jorge Islands; and (3) the Oriental Group, to the east of the Central Group, with São Miguel and Santa Maria. Subaerial volcanic activity started on Santa Maria ~8 Myr ago (Abdel-Monem et al., 1975) and five islands have recorded historical eruptions, the last one occurring on Faial in 1957. Recent tomographic studies have proposed that the volcanic activity is associated with the presence of a mantle plume starting from the core-mantle boundary (Montelli et al., 2004; Montelli et al., 2006). Using a similar method, Yang et al. (2006) also observed a plume shaped thermal anomaly in the upper mantle beneath the Azores. Nonetheless it should be noted that Van der Hilst and De Hoop (2005) have questioned the theoretical background of finite frequency tomography.

São Jorge is located in the middle of the Central Group, between Terceira (to the northeast) and Pico/Faial (to the south), and is ~200 km east of the MAR. The island has an elongated shape, inherited from fissural volcanism, sub-parallel to the Terceira rift (located~20 km north), and sub-perpendicular to the MAR. São Jorge comprises three geological formations characterizing different periods of volcanic activity (Fig. 2). The Topo formation crops out in the east of the island,

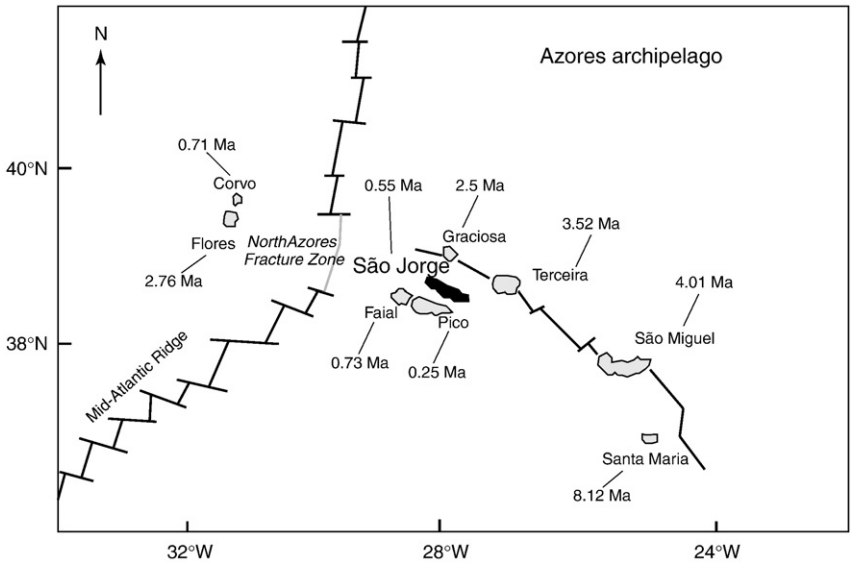


**Fig. 2.** Detailed map of São Jorge Island annotated with sampling locations. The island can be divided into three different geological complexes corresponding to distinct periods of volcanic activity: (1) Topo: westernmost and oldest formation; (2) Rosais: easternmost and intermediate complex; and (3) Manadas: central and site of the most recent (historical) volcanic activity.

and is the oldest formation with published ages ranging from ~550 kyr to 1.32 Myr (K–Ar method, Feraud et al., 1980; Hildenbrand et al., 2008). Subsequent periods of volcanic activity are represented by the Rosais (intermediate — western part of the island) and Manadas (young — central part of the island) complexes, and date from few 100 kyr to historical volcanic activity (last eruption in 1808). The lack of systematic age progression precludes lava emplacement to be solely controlled by movement of the underlying tectonic plate toward the east.

Large geochemical variations have been recorded at both intra-island and archipelago scales (White et al., 1976; Hawkesworth et al., 1979; Dupré et al., 1982; Davies et al., 1989; Widom and Shirey, 1996; Turner et al., 1997; Widom et al., 1997; Moreira et al., 1999; Schaefer et al., 2002; Widom and Farquhar, 2003; Madureira et al., 2005; Beier et al., 2007; Elliott et al., 2007; Turner et al., 2007). From an isotopic perspective, Azores basalts appear to have contributions from 4 end-members (Fig. 3):

- The first end-member (SM) corresponds to the most radiogenic Pb measured in samples from São Miguel Island. It plots to the left of the Northern Hemisphere Reference Line (NHRL; Hart, 1984), and displays enriched Sr–Nd isotope ratios. The origin of this end-member has been the debate of many studies with proposed models ranging from shallow, delaminated metasomatized lithospheric mantle (Widom et al., 1997; 2nd scenario from Moreira et al., 1999; Widom and Farquhar, 2003) to recycled material intrinsic to the Azores mantle plume (Turner et al., 1997; 1st scenario from Moreira et al., 1999; Beier et al., 2007; Elliott et al., 2007). The most recent studies also showed that neither delaminated SCLM nor sediments display the adequate isotopic signature to account for this end-member.
- The second end-member (T), defined by Terceira samples, also has radiogenic Pb, but falls to the right of the NHRL. Sr and Nd isotope ratios are intermediate with regard to the OIB global range of variations ($^{87}Sr/^{86}Sr \sim 0.7037$; $^{143}Nd/^{144}Nd \sim 0.51295$). Negative Δ7/4 recorded for Terceira end-member (Dupré et al., 1982; Turner et al., 1997; Moreira et al., 1999) is usually considered an indicator of a young HIMU component (Thirlwall, 1997). However, coupled high $^{3}He/^{4}He$ (~11.5 $R_A$) and excesses in $^{20}Ne$ and $^{21}Ne$ compared to MORB values (Moreira et al., 1999; Madureira et al., 2005) in Terceira samples are unlikely for such a component and suggest that this end-member is a more complex component rather than the signature of a single, young HIMU, end-member.
- Samples from São Miguel and Terceira Islands define two specific trends that join at depleted values of Sr–Nd–Pb isotopes, defining a third end-member (D), common to all islands. In detail, this end-member plots in the field of local MORB (31–41°N, data from Dosso et al., 1999). It has consequently been associated with the upper mantle sampled along the MAR at the latitude of the Azores archipelago (Turner et al., 1997, Moreira et al., 1999).
- Faial lavas define another trend starting from the Terceira end-member toward less radiogenic Pb (to the left of the NHRL) and slightly enriched Sr–Nd isotopes. This defines a fourth component (F), whose nature has still to be addressed. However, recent studies have shown that Faïal lavas are associated with very unradiogenic Os ($^{187}Os/^{188}Os \sim 0.11$) as well as the heaviest B isotope data (Schaefer et al., 2002; Turner et al., 2007), arguing for the involvement of an old fluid-and-melt-depleted component.

Samples from Pico show strong similarities with Faial lavas (apart from a couple of basalts that display intermediate characteristics between Terceira and Faial), indicating that the two trends associated with these islands might be genetically linked. Basalts from other localities (Corvo, Flores, Graciosa, and Santa Maria) also plot at intermediate positions between Terceira and Faial trends. However, the relatively small number of analysed samples prevents a definitive conclusion about their geographical grouping.

It should be noted that 3 of the 4 end-members described above belong to the Central Group of islands, and therefore are only separated spatially by a length-scale of 40 to 100 km. This suggests that their marked differences in isotopic composition may represent small-scale heterogeneity of the Azores mantle plume. Conversely, this could also reflect the presence of shallow contaminants in the upper mantle underneath the Azores archipelago.

## 3. Analytical procedures

All samples were coarsely crushed with a hydraulic press. Millimetre-sized grains were then hand-picked under a binocular microscope, rinsed with triply-distilled water in an ultrasonic bath, before being gently crushed with an agate mortar and pestle.

Major and trace element contents were determined at the *Service d'Analyses des Roches et des Minéraux* (SARM) at CRPG Nancy. Powder-rock samples were fused along with lithium borate before being dissolved in dilute nitric acid/hydrogen peroxide. Solutions were then aliquoted for measurements on ICP-AES for major elements and ICP-MS for trace elements. A detailed description of the procedure can be found in Carignan et al. (2001). Additional information about methods and analytical reproducibility can be also found at http://helium.crpg.cnrs-nancy.fr/SARM/analyses/roches.html, duplicates measurements for 2 samples can be found in appendices).

Sr and Nd chemical separations and isotope measurements were carried at the Laboratoire Magmas et Volcans in Clermont–Ferrand (LMV). Approximately 100 mg of sample powder was leached with hot 6 M HCl (5 mL, 100 °C) during 3 h following the procedures described in Millet et al. (2008), acid-digested with HF-$HNO_3$, and

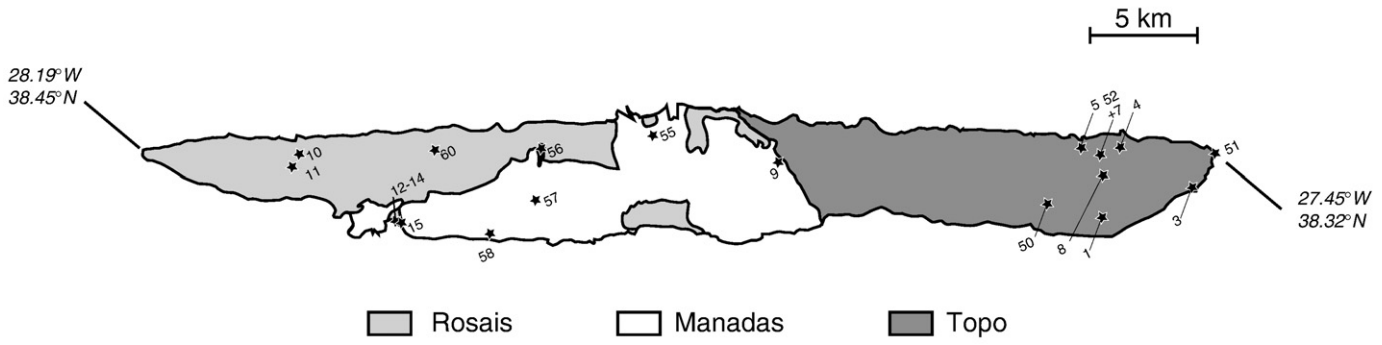


**Fig. 3.** $^{87}Sr/^{86}Sr$ versus $^{206}Pb/^{204}Pb$ diagram illustrating previously published data on Pico/Faial, Terceira and São Miguel islands, together with isotopic end-members (SM, T, D and F) used to describe the range of isotopic variations measured in basalts from the Azores archipelago.

passed through the "cascade" column protocol (Sr Spec, TRU Spec and Ln Spec columns) described in Pin and Bassin (1992) and Pin et al. (1994). Total procedural blanks (including leaching and HF-$HNO_3$ digestion) were <0.5 ng and <0.2 ng for Sr and Nd, respectively. All isotope measurements were made in static mode on a Finnigan Triton thermal ionization mass spectrometer (TIMS), utilising the virtual amplifier and loading Sr and Nd onto double W filaments. Sr isotope ratios were mass-fractionation-corrected to $^{86}Sr/^{88}Sr = 0.1194$ and normalized to $^{87}Sr/^{86}Sr = 0.71025$ for the NIST SRM987 standard. Nd isotope ratios were mass-fractionation-corrected to $^{146}Nd/^{144}Nd = 0.7219$ and normalized to $^{143}Nd/^{144}Nd = 0.51196$ for the Rennes-AMES standard. Repeated analyses of the two standards during the course of the study gave $^{87}Sr/^{86}Sr = 0.710250 \pm 15$ ($2\sigma$, $n = 16$) and $^{143}Nd/^{144}Nd = 0.511961 \pm 6$ ($2\sigma$, $n = 8$), in agreement with 2008 long-term reproducibility in this laboratory i.e., $^{87}Sr/^{86}Sr = 0.710245 \pm 6$ ($2\sigma$, $n = 38$) and $^{143}Nd/^{144}Nd = 0.511959 \pm 6$ ($2\sigma$, $n = 27$). Measurements of the LaJolla Nd standard during the course of this study gave $0.511845 \pm 3$ ($2\sigma$, $n = 4$). All sample duplicates reproduced within these estimates of external reproducibility (see appendices).

Pb isotope measurements were made on whole-rock sample powders (~100 mg) at the Geochemistry Laboratory of Victoria University of Wellington, New Zealand. Chemical separation was carried out in cleaned pipette tip columns filled with ~0.2 mL of AG1-X8 resin (100–200 mesh). Sample loading and elution of matrix was carried out in 0.8 M HBr, and Pb collection was undertaken in 2 mL of 7 M HCl. Total procedural Pb blanks (including acid digestion) were ca. 10 pg. Pb isotope measurements were performed on a Nu Plasma MC-ICP-MS in static mode. Mass discrimination was corrected by standard bracketing of samples with NBS-981 using values of Baker et al. (2004). Accuracy and reproducibility of Pb isotope measurements were assessed by repeated measurements of JB2 standard ($n = 8$) and yielded $18.342 \pm 170$ ppm, $15.561 \pm 250$ ppm and $38.275 \pm 290$ ppm for $^{206}Pb/^{204}Pb$, $^{207}Pb/^{204}Pb$ and $^{208}Pb/^{204}Pb$, respectively. All sample duplicates fall inside these uncertainties.

## 4. Results

### 4.1. Major and trace element variations

Samples from São Jorge that were analyzed during the course of this study all have MgO>4 wt.%, with $SiO_2$ ranging from 44 to 48 wt.% (Table 1). The samples are all subalkaline basalts in the total alkalis — silica nomenclature, apart from the three most differentiated samples, which are hawaiites and basanites. All samples also show low LOI (loss on ignition) contents <1 wt.%, except for SJ01 (~2%) and SJ05 (4.5%). SJ05 is considered too weathered to truly represent its initial composition and is not considered further in this study.

Major element variations as a function of MgO content are shown in Fig. 4. Topo samples (older) are on average more primitive (MgO>8 wt.%) than samples from the intermediate and recent Rosais and Manadas complexes (primitive to slightly differentiated with MgO = 4 to 11 wt.%). This difference reflects the continuous fractional crystallization of principally olivine and clinopyroxene, as illustrated by the CaO decrease and increase of $Al_2O_3/CaO$ ratio with decreasing MgO. In addition, lower $TiO_2$ contents for samples with MgO<5 wt.% suggest the onset of titanomagnetite fractionation.

Trace element patterns normalized to primitive mantle (Hofmann, 1988) show similar patterns (Fig. 5) to HIMU basalts (average of Mangaia samples: Woodhead, 1996), most notably depletions in the most incompatible elements, negative anomalies in K and Pb, and moderate enrichments in Nb, Ba and Y. Patterns of selected samples from each geological formation show a progressive, time-related, enrichment in highly incompatible elements, as shown by strong variations of $(La/Yb)_N = 5.5–13$, and to a lesser extent La/Sm and Rb/Sr. Such enrichments are not observed for moderately incompatible elements, as exemplified by the $(Gd/Yb)_N$ ratio which is nearly constant in all samples (= 2.5 to 3.0).

Variations of major element contents as well as ratios of both trace and major elements are coupled with Th contents (Fig. 6). Notably, MgO and Th co-variations (Fig. 6a) indicate that Th is a robust differentiation index. This also suggests that variations of $(La/Yb)_N$ ratios (Fig. 6d) are, in part, related to olivine and clinopyroxene fractionation. Variations related to extent of melting, although less important, are also observed as shown by the range of Th content at constant MgO.

### 4.2. Sr–Nd–Pb isotope variations

Pb isotope ratios measured in São Jorge basalts (Table 1) show marked variations in $^{206}Pb/^{204}Pb$ (19.347 to 20.511) with rather limited $^{207}Pb/^{204}Pb$ and $^{208}Pb/^{204}Pb$ variations (15.626 to 15.673 and 39.050 to 39.564, respectively). Nearly all samples plot to the right of the NHRL in both $^{208}Pb/^{204}Pb$ versus $^{206}Pb/^{204}Pb$ (Fig. 7a) and $^{207}Pb/^{204}Pb$ versus $^{206}Pb/^{204}Pb$ (Fig. 7b) diagrams, overlapping the Terceira trend, but also extending it to significantly more radiogenic Pb (20.511 against 20.027 for the $^{206}Pb/^{204}Pb$ ratio). In detail, most samples lie on two sub-parallel trends (Rosais/Manadas complexes; Topo samples) in the $^{208}Pb/^{204}Pb$ versus $^{206}Pb/^{204}Pb$ diagram, with the Rosais and Manadas samples having higher $^{208}Pb/^{204}Pb$ for a given $^{206}Pb/^{204}Pb$. Such a clear difference between these two trends, however, is not observed when considering the $^{207}Pb/^{204}Pb$, suggesting the difference between the two trends is related to a component with recently fractionated for the Th/U ratios. Samples SJ01 (Topo formation) and SJ11 (Rosais complex) do not fall on the São Jorge trends in the $^{207}Pb/^{204}Pb$ versus $^{206}Pb/^{204}Pb$ diagram (Fig. 7b), suggesting a different and possibly more complex history for these two magmas.

The Pb isotope difference between Topo and Rosais/Manadas samples can also be observed in the $^{143}Nd/^{144}Nd$ versus $^{87}Sr/^{86}Sr$ diagram, in which they form two sub-perpendicular trends (Fig. 8). Older samples (Topo) have higher and rather constant Sr isotope ratios (0.703705 to 0.703765) with variable $^{143}Nd/^{144}Nd$ (0.512900 to 0.512983; note most of this variation is largely due to sample SJ01 (that is also anomalous for its high $^{207}Pb/^{204}Pb$ ratio compared to all other samples, see above and Fig. 7b) and SJ04. Conversely, younger lavas (Manadas and Rosais) display lower and more variable $^{87}Sr/^{86}Sr$ (0.703399 to 0.703638) at almost constant $^{143}Nd/^{144}Nd$ (0.512914 to 0.512940).

It should also be noted that samples from the Manadas formation are characterized by lower $^{87}Sr/^{86}Sr$ than Rosais basalts, indicating a temporal decrease of the $^{87}Sr/^{86}Sr$ of magmas erupted at Sao Jorge.

### 4.3. Comparison with previous data

Three historical lavas from the Manadas complex (one sample from 1808 and two samples from 1580) were previously analyzed for major and trace elements and Sr–Nd–Pb isotopes by Turner et al. (1997). Major and trace element data from this previous study are in good agreement with our measurements; the three historical Manadas basalts (Turner et al., 1997) plot on the differentiation trend defined by our samples and have similar concentrations to those of our samples from the 1580 and 1808 lava flows. However, comparison between isotopic data of the two datasets is more problematic. While Sr isotope ratios measured for the three historical Manadas samples (Turner et al., 1997) are broadly consistent with our Sr isotope dataset for Manadas lavas, previously published $^{143}Nd/^{144}Nd$ values are highly variable (0.51283; 0.51284; 0.51297) compared to the range recorded by our samples ($0.512926 \pm 14$; $2\sigma$, $n = 7$). In the case of Pb isotopes, the two analyses (Turner et al., 1997) of samples from the 1580 eruption display significantly different values as compared to one another and with our analysis (sample SJ15). Similarly to these observations, Elliott et al. (2007) noted some discrepancies between Pb isotope data for Pico and São Miguel

**Table 1**
Major-, trace-elements and isotopes ratios for 21 samples of the São Jorge island.

| Sample | SJ01 | SJ03 | SJ04 | SJ05 | SJ07 | SJ08 | SJ50 | SJ51 | SJ52 | SJ10 | SJ11 | SJ12 | SJ13 | SJ14 | SJ09 | SJ15 | SJ55 | SJ56 | SJ57 | SJ58 | SJ60 |
|---|---|---|---|---|---|---|---|---|---|---|---|---|---|---|---|---|---|---|---|---|---|
| Formation | Topo | Topo | Topo | Topo | Topo | Topo | Topo | Topo | Topo | Rosais | Rosais | Rosais | Rosais | Rosais | Manadas | Manadas | Manadas | Manadas | Manadas | Manadas | Manadas |
| Latitude (°N) | 38.54 | 38.54 | 38.57 | 38.57 | 38.57 | 38.56 | 38.57 | 38.57 | 38.57 | 38.72 | 38.72 | 38.68 | 38.68 | 38.68 | 38.63 | 38.68 | 38.68 | 38.69 | 38.67 | 38.67 | 38.71 |
| Longitude (°E) | −27.78 | −27.76 | −27.80 | −27.82 | −27.82 | −27.82 | −27.86 | −27.86 | −27.82 | −28.23 | −28.24 | −28.20 | −28.20 | −28.20 | −27.98 | −28.20 | −28.05 | −28.11 | −28.12 | −28.16 | −28.17 |
| $SiO_2$ | 45.07 | 45.37 | 45.66 | 42.46 | 44.12 | 44.87 | 45.10 | 45.29 | 44.35 | 46.32 | 45.15 | 45.33 | 45.74 | 44.38 | 45.29 | 45.24 | 44.80 | 46.12 | 48.64 | 44.90 | 45.65 |
| $TiO_2$ | 3.25 | 3.26 | 3.33 | 3.35 | 3.76 | 3.66 | 3.21 | 2.71 | 3.78 | 3.46 | 3.06 | 3.08 | 3.60 | 3.91 | 3.64 | 3.32 | 3.78 | 3.88 | 2.97 | 3.97 | 3.15 |
| $Al_2O_3$ | 15.53 | 14.50 | 13.94 | 15.08 | 14.43 | 15.04 | 13.90 | 12.46 | 14.53 | 16.69 | 13.64 | 14.79 | 15.33 | 14.97 | 15.50 | 15.81 | 16.10 | 16.54 | 16.94 | 16.29 | 13.79 |
| $Fe_2O_3$ | 11.58 | 11.87 | 11.51 | 13.38 | 12.83 | 12.90 | 11.88 | 12.41 | 12.86 | 10.30 | 12.56 | 12.69 | 12.46 | 13.25 | 12.65 | 12.23 | 12.68 | 13.81 | 11.36 | 13.82 | 12.25 |
| MnO | 0.17 | 0.17 | 0.17 | 0.18 | 0.18 | 0.18 | 0.19 | 0.16 | 0.18 | 0.14 | 0.17 | 0.17 | 0.17 | 0.18 | 0.18 | 0.17 | 0.17 | 0.20 | 0.19 | 0.18 | 0.17 |
| MgO | 8.24 | 8.58 | 9.99 | 8.95 | 8.45 | 7.97 | 8.84 | 11.99 | 8.20 | 6.27 | 10.52 | 8.72 | 6.81 | 7.35 | 7.12 | 6.97 | 6.61 | 5.35 | 4.53 | 6.81 | 10.89 |
| CaO | 9.32 | 10.39 | 10.21 | 8.31 | 10.38 | 9.96 | 10.29 | 11.50 | 10.41 | 10.66 | 11.03 | 10.38 | 9.47 | 10.15 | 9.93 | 10.39 | 9.27 | 8.48 | 8.05 | 9.42 | 11.58 |
| $Na_2O$ | 2.23 | 3.18 | 2.91 | 2.10 | 2.98 | 2.96 | 3.06 | 2.19 | 3.21 | 2.94 | 2.76 | 2.81 | 3.67 | 3.19 | 3.10 | 3.42 | 3.58 | 3.87 | 4.56 | 3.59 | 2.53 |
| $K_2O$ | 1.16 | 1.03 | 1.00 | 0.57 | 1.04 | 0.90 | 1.23 | 0.46 | 1.08 | 1.07 | 0.84 | 0.85 | 1.22 | 1.07 | 0.91 | 0.87 | 1.24 | 1.46 | 1.83 | 1.23 | 0.80 |
| $P_2O_5$ | 0.55 | 0.52 | 0.53 | 0.49 | 0.56 | 0.46 | 0.60 | 0.26 | 0.56 | 0.59 | 0.41 | 0.45 | 0.77 | 0.60 | 0.69 | 0.59 | 0.71 | 0.95 | 0.95 | 0.72 | 0.43 |
| LOI | 2.23 | −0.31 | −0.02 | 4.48 | 0.25 | −0.15 | 0.32 | −0.53 | −0.05 | 0.33 | −0.59 | −0.34 | −0.65 | −0.45 | 0.08 | −0.30 | −0.36 | −0.44 | −0.68 | −0.82 | −0.67 |
| Total | 99.31 | 98.56 | 99.23 | 99.34 | 98.97 | 98.75 | 98.61 | 98.90 | 99.10 | 98.76 | 99.55 | 98.93 | 98.58 | 98.60 | 99.09 | 98.70 | 98.57 | 100.22 | 99.33 | 100.10 | 100.55 |
| Rb | 21 | 22 | 22 | 9 | 20 | 16 | 26 | 8 | 21 | 17 | 17 | 17 | 26 | 21 | 15 | 16 | 26 | 31 | 40 | 23 | 16 |
| Ba | 329 | 270 | 282 | 272 | 270 | 239 | 313 | 134 | 267 | 278 | 235 | 228 | 315 | 301 | 302 | 234 | 329 | 370 | 416 | 301 | 205 |
| Th | 3.8 | 3 | 3.2 | 3.1 | 2.5 | 2.4 | 3.7 | 1.3 | 2.6 | 3.4 | 2.5 | 2.6 | 4.33 | 3.3 | 3.5 | 2.3 | 3.7 | 3.9 | 5.8 | 3.3 | 2.4 |
| Nb | 46 | 38 | 46 | 40 | 42 | 34 | 48 | 19 | 41 | 45 | 35 | 33 | 55 | 46 | 51 | 34 | 54 | 62 | 75 | 51 | 34 |
| U | 1.26 | 1.05 | 1.08 | 1.00 | 1.00 | 0.91 | 1.31 | 0.52 | 0.98 | 1.33 | 0.85 | 0.84 | 1.55 | 1.15 | 1.30 | 0.81 | 1.30 | 1.35 | 1.93 | 1.14 | 0.82 |
| La | 38 | 30 | 33 | 34 | 30 | 26 | 36 | 15 | 29 | 33 | 27 | 26 | 43 | 35 | 40 | 25 | 39 | 46 | 55 | 36 | 25 |
| Ce | 80 | 65 | 69 | 59 | 65 | 56 | 75 | 33 | 65 | 73 | 59 | 57 | 93 | 75 | 8 | 57 | 84 | 98 | 116 | 79 | 56 |
| Pb | 2.24 | 2.13 | 1.93 | 1.64 | 1.95 | 1.52 | 3.54 | 0.99 | 1.90 | 1.72 | 1.48 | 1.33 | 2.25 | 1.82 | 1.80 | 1.55 | 2.03 | 2.14 | 2.95 | 1.95 | 1.22 |
| Pr | 9.7 | 8.3 | 8.7 | 8.9 | 8.4 | 7.5 | 9.3 | 4.6 | 8.5 | 9.3 | 7.4 | 7.4 | 11.7 | 9.5 | 10.6 | 7.4 | 10.7 | 12.5 | 14.3 | 10.2 | 7.3 |
| Nd | 40 | 36 | 36 | 39 | 36 | 33 | 38 | 21 | 36 | 39 | 31 | 32 | 49 | 40 | 45 | 32 | 45 | 52 | 59 | 44 | 31 |
| Sr | 507 | 587 | 567 | 464 | 657 | 737 | 601 | 418 | 661 | 639 | 598 | 474 | 749 | 715 | 667 | 570 | 769 | 834 | 824 | 786 | 560 |
| Sm | 8.2 | 8.1 | 7.7 | 8.8 | 8.3 | 7.6 | 8.2 | 5.4 | 8.4 | 8.5 | 6.9 | 7.2 | 10.5 | 8.7 | 9.5 | 7.4 | 9.5 | 10.9 | 11.7 | 9.4 | 7.0 |
| Hf | 6.08 | 5.49 | 5.73 | 6 | 5.82 | 4.97 | 5.87 | 3.62 | 5.94 | 6.55 | 4.58 | 5.09 | 7.07 | 5.49 | 7.14 | 4.85 | 6.84 | 7.34 | 8.38 | 6.10 | 5.11 |
| Zr | 260 | 231 | 240 | 255 | 262 | 210 | 262 | 141 | 260 | 293 | 195 | 209 | 324 | 232 | 317 | 210 | 305 | 357 | 413 | 279 | 225 |
| Eu | 2.63 | 2.63 | 2.50 | 2.89 | 2.83 | 2.53 | 2.53 | 1.91 | 2.75 | 2.84 | 2.26 | 2.35 | 3.33 | 2.82 | 3.13 | 2.52 | 3.10 | 3.46 | 3.59 | 3.08 | 2.28 |
| Gd | 7.36 | 7.50 | 7.01 | 8.38 | 8.05 | 7.20 | 7.20 | 5.59 | 7.90 | 7.64 | 6.40 | 6.68 | 9.15 | 7.84 | 8.66 | 7.03 | 8.49 | 9.55 | 10.10 | 8.39 | 6.45 |
| Tb | 1.04 | 1.10 | 1.01 | 1.26 | 1.15 | 1.04 | 1.05 | 0.84 | 1.15 | 1.08 | 0.93 | 0.96 | 1.28 | 1.10 | 1.23 | 1.01 | 1.22 | 1.32 | 1.40 | 1.18 | 0.94 |
| Dy | 5.57 | 5.92 | 5.50 | 6.80 | 6.31 | 5.83 | 5.72 | 4.73 | 6.41 | 5.97 | 5.03 | 5.45 | 6.80 | 5.94 | 6.69 | 5.63 | 6.57 | 7.04 | 7.40 | 6.28 | 4.96 |
| Ho | 0.99 | 1.08 | 0.98 | 1.21 | 1.14 | 1.04 | 1.04 | 0.86 | 1.12 | 1.05 | 0.91 | 0.96 | 1.21 | 1.08 | 1.18 | 1.00 | 1.16 | 1.23 | 1.31 | 1.10 | 0.90 |
| Er | 2.62 | 2.80 | 2.63 | 3.18 | 2.95 | 2.68 | 2.68 | 2.16 | 2.87 | 2.68 | 2.32 | 2.45 | 3.05 | 2.71 | 3.06 | 2.57 | 2.95 | 3.10 | 3.37 | 2.78 | 2.28 |
| Y | 28 | 29 | 27 | 35 | 33 | 28 | 27 | 24 | 31 | 29 | 26 | 25 | 33 | 28 | 33 | 27 | 32 | 37 | 39 | 32 | 26 |
| Tm | 0.36 | 0.38 | 0.34 | 0.43 | 0.39 | 0.35 | 0.35 | 0.29 | 0.38 | 0.37 | 0.31 | 0.33 | 0.42 | 0.35 | 0.40 | 0.34 | 0.39 | 0.42 | 0.46 | 0.37 | 0.31 |
| Yb | 2.28 | 2.37 | 2.15 | 2.63 | 2.41 | 2.18 | 2.30 | 1.77 | 2.44 | 2.31 | 1.92 | 2.08 | 2.57 | 2.20 | 2.52 | 2.19 | 2.47 | 2.62 | 2.90 | 2.36 | 1.90 |
| Lu | 0.33 | 0.35 | 0.33 | 0.40 | 0.35 | 0.32 | 0.35 | 0.26 | 0.36 | 0.34 | 0.28 | 0.31 | 0.38 | 0.33 | 0.38 | 0.32 | 0.36 | 0.39 | 0.43 | 0.34 | 0.28 |
| Cu | 44 | 37 | 45 | 34 | 40 | 34 | 44 | 46 | 46 | 31 | 54 | 45 | 28 | 30 | 28 | 28 | 33 | 22 | 19 | 23 | 24 |
| Co | 44 | 45 | 47 | 48 | 52 | 46 | 44 | 61 | 48 | 45 | 58 | 48 | 40 | 46 | 44 | 43 | 44 | 39 | 31 | 47 | 59 |
| Ni | 180 | 147 | 218 | 169 | 131 | 108 | 142 | 234 | 118 | 100 | 202 | 166 | 87 | 79 | 82 | 82 | 71 | 27 | 27 | 65 | 186 |
| Cr | 380 | 300 | 442 | 334 | 274 | 206 | 323 | 617 | 254 | 228 | 377 | 198 | 173 | 171 | 111 | 168 | 80 | 20 | 25 | 89 | 426 |
| $^{87}Sr/^{86}Sr$ | 0.703743 | 0.703733 | 0.703705 | 0.703715 | 0.703752 | 0.703765 | 0.703761 | 0.703742 | 0.703745 | 0.703426 | 0.703638 | 0.703562 | 0.703606 | 0.703632 | 0.703399 | 0.703421 | 0.703437 | 0.703412 | 0.703435 | 0.703438 | 0.703504 |
| $^{143}Nd/^{144}Nd$ | 0.512900 | 0.512963 | 0.512924 | 0.512983 | 0.512959 | 0.512976 | 0.512956 | 0.512980 | 0.512955 | 0.512923 | 0.512914 | 0.512927 | 0.512927 | 0.512924 | 0.512922 | 0.512940 | 0.512925 | 0.512924 | 0.512921 | 0.512921 | 0.512930 |
| $^{206}Pb/^{204}Pb$ | 19.347 | 19.861 | 19.800 | 20.047 | 20.511 | 20.276 | 20.177 | 20.127 | 20.507 | 19.972 | 19.776 | 19.793 | 20.134 | 20.186 | 19.896 | 19.993 | 20.001 | 19.959 | 19.959 | 19.850 | 19.874 |
| $^{207}Pb/^{204}Pb$ | 15.626 | 15.631 | 15.626 | 15.627 | 15.673 | 15.653 | 15.647 | 15.639 | 15.667 | 15.636 | 15.643 | 15.621 | 15.638 | 15.654 | 15.624 | 15.637 | 15.637 | 15.632 | 15.632 | 15.627 | 15.628 |
| $^{208}Pb/^{204}Pb$ | 39.059 | 39.084 | 39.196 | 39.121 | 39.564 | 39.402 | 39.364 | 39.194 | 39.556 | 39.414 | 39.274 | 39.266 | 39.481 | 39.496 | 39.334 | 39.364 | 39.450 | 39.408 | 39.406 | 39.320 | 39.310 |

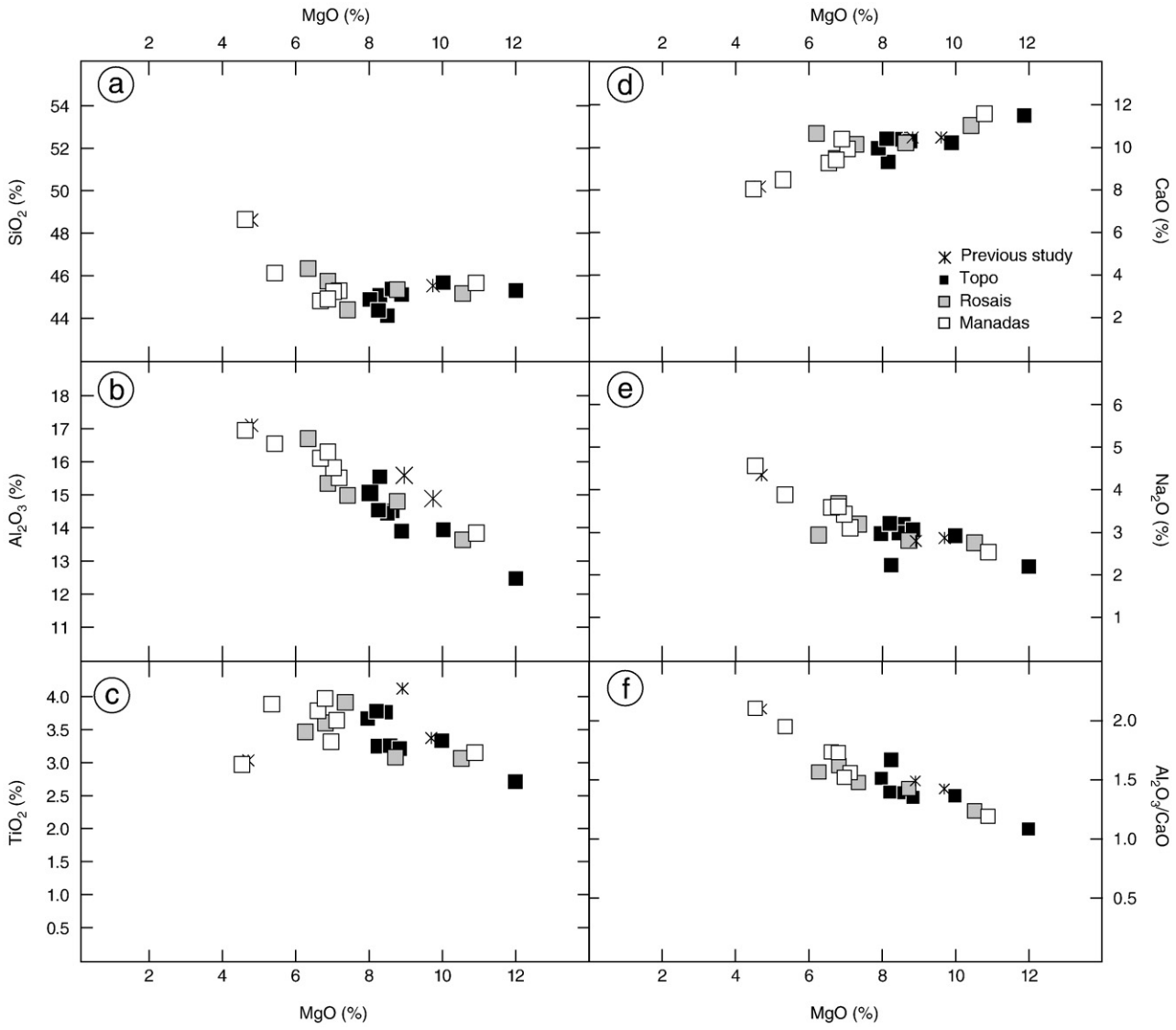


**Fig. 4.** Variations of major elements with MgO contents in São Jorge lavas. Systematic decrease of CaO together with increasing $Al_2O_3$/CaO indicate fractional crystallization of olivine and clinopyroxene. Samples from Topo complex are more primitive on average than Rosais and Manadas lavas.

samples. Given these inconsistencies, we decided not to include any data measured by Turner and co-workers on any island. Nevertheless, their interpretations and conclusions will be discussed on the basis of the remaining data from the literature.

## 5. Intra-island variability

In this section, we describe the variations delineated by São Jorge basalts in isotope variation diagrams. Notably, we identify local end-members and discuss them with respect to previous isotopic studies of the Azores archipelago.

### *5.1. São Jorge end-members*

The two trends defined by São Jorge samples in isotope variation diagrams, as well as the distinct composition of SJ01 and SJ11 (see Section 4.2 and Figs. 7a,b and 8) require at least four end-members. Their proposed compositions are shown in Fig. 9 and will be discussed in more detail in the following section. However, it is important to note that these defined compositions are arbitrary; they could be more extreme than shown in Fig. 9, provided they are on the same mixing trends.

In the $^{207}Pb/^{204}Pb$ versus $^{206}Pb/^{204}Pb$ diagram, all São Jorge samples with the exception of SJ01 and SJ11 plot on a well-defined mixing trend that overlaps the Terceira trend and extend it to more radiogenic Pb ($^{206}Pb/^{204}Pb \sim 20.51$ and $^{207}Pb/^{204}Pb \sim 15.67$), defining end-member 1 (Fig. 9b). This end-member has a negative $\Delta 7/4$ value of about −4.7, and a $^{87}Sr/^{86}Sr$ ratio close to 0.70375 (Fig. 9c), and in other ocean island settings has been interpreted as reflecting a young HIMU-like mantle component (Thirlwall, 1997).

In the $^{208}Pb/^{204}Pb$ versus $^{206}Pb/^{204}Pb$ diagrams (Fig. 9a), São Jorge basalts define two distinct mixing trends, perhaps eminating from end-member 1. A detailed look at Fig. 9c shows the lack of any trend for Rosais and Manadas lavas, which are rather shifted toward less radiogenic Sr isotope ratios. Hence, the pseudo-alignement of Rosais and Manadas samples in Fig. 9a is rather the consequence of a small vertical scatter than the signature of an independent mixing process. In detail, samples from Topo plot on a trend from end-member 1 to less radiogenic values of $^{87}Sr/^{86}Sr \sim 0.70345$, $^{206}Pb/^{204}Pb \sim 19.25$ and $^{208}Pb/^{204}Pb \sim 38.75$, similar to those of local MORB (31–41°N, data from Dosso et al., 1999) and defining end-member 3. Samples from Rosais and Manadas complexes are intermediate between end-member 1 and less radiogenic $^{206}Pb/^{204}Pb \sim 19.25$ and $^{208}Pb/^{204}Pb \sim 39.35$ values coupled to unradiogenic Sr (~0.70330),

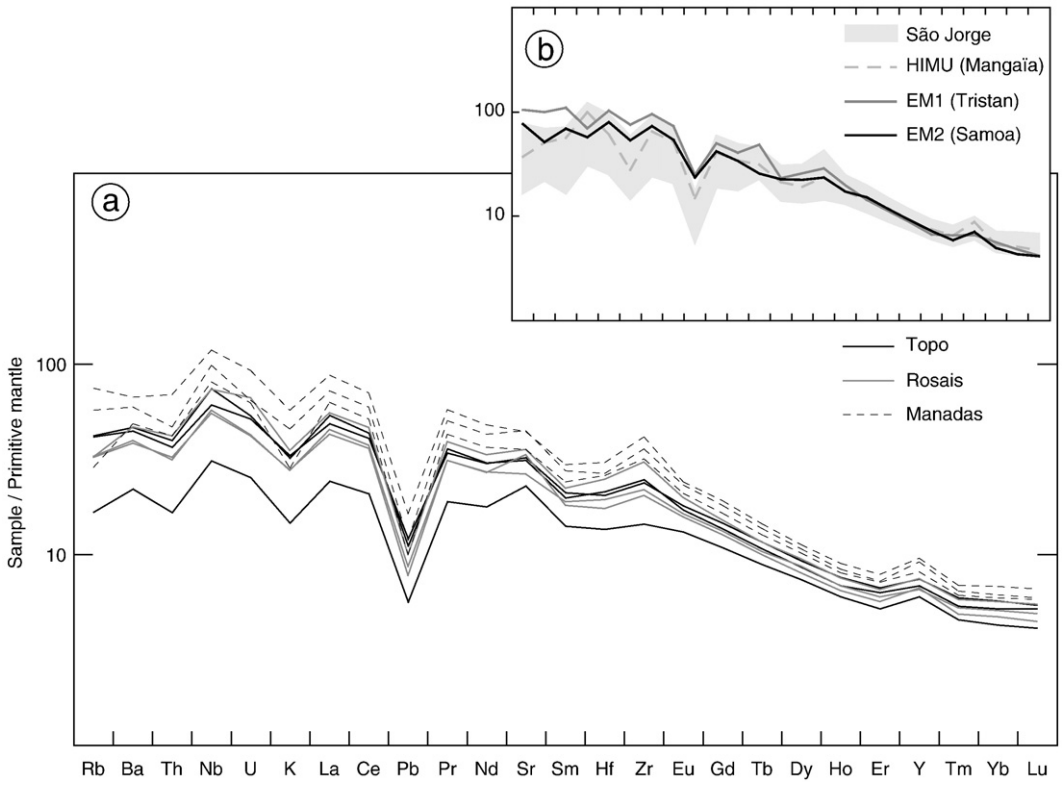


**Fig. 5.** Abundances of trace elements in representative São Jorge lavas normalized to primitive mantle values (Hofmann, 1988). Inset on the top-right of the figure shows a comparison between the general pattern of São Jorge lavas and patterns for extreme OIB end-members EM1, EM2 and HIMU.

characteristic of end-member 2. Closer examination of Fig. 9c reveals that samples from the Manadas and Rosais formations may actually diverge from various proportions of the Topo mixing line (end-members 1 + 3) toward end-member 2. Isotopic ratios determined for end-member 2 resemble those measured in a MORB sample collected on the Mid-Atlantic Ridge at 43°N (Kamenetsky et al., 1998).

As noted above, samples SJ01 and SJ11 plot outside the São Jorge mixing trend in the $^{207}Pb/^{204}Pb$ versus $^{206}Pb/^{204}Pb$ diagram (Fig. 9b). These two basalts have Sr–Nd–Pb isotopic compositions falling in the field of Faïal volcanics (to the left of the NHRL). These samples require a further end-member 4, the composition of which is similar to the unradiogenic end of Faial trend. The influence of end-member 4 in Sao Jorge is limited to samples SJ01 and SJ11 only, hence discussion about its nature will be addressed in the section dealing with isotopic variations at the archipelago scale.

### 5.2. Geochemical evolution of São Jorge volcanism

The main temporal geochemical change of São Jorge Island volcanism is the difference observed between basalts from Topo and younger samples from Manadas and Rosais formations. One could argue that this difference reflects melting of another component in plume source, potentially a pyroxenitic or eclogitic lithology that could also generate the observed enrichment in $(La/Yb)_N$ ratio. However, a garnet bearing lithology (i.e. eclogite) can be rejected due to the lack of variation of the Gd/Yb ratio in São Jorge lavas. In addition, although a pyroxenitic component certainly plays a role in the generation of São Jorge lavas, variable extent of melting of such component in the plume cannot be invoked as the reason for the observed variations. If so, the most radiogenic samples for Pb isotopes (i.e. the most HIMU-like) would be expected to have the highest $(La/Yb)_N$ ratio, whereas they are amongst the lowest and no strong correlation is observed between $^{206}Pb/^{204}Pb$ and $(La/Yb)_N$. Nevertheless, because Rosais and Manadas samples have isotopic compositions that differ from Topo lavas, it is likely that they are mixed with a component that also display $(La/Yb)_N$ potentially deriving from a pyroxenitic source.

The difference between samples from those complexes is best expressed in the $^{208}Pb/^{204}Pb$ versus $^{206}Pb/^{204}Pb$ diagram (Fig. 9a) where these two populations of basalts broadly delineate two sub-parallel trends as samples from Manadas/Rosais have higher $^{208}Pb/^{204}Pb$ for a given $^{206}Pb/^{204}Pb$ than the older Topo basalts. One way to quantify such an offset between the two sample populations is to compute the shortest distance between each sample and the best-fit line for Topo samples (slope = 0.6517, intercept = 26.17, $r^2 = 0.84$, with the exception of sample SJ01 as it does not plot with other Topo samples to the right of the NHRL, but falls in the field of Faïal lavas) in the $^{208}Pb/^{204}Pb$ versus $^{206}Pb/^{204}Pb$ plot. This offset, designated here as $\Delta_{SJ}$, is a linear combination of two Pb isotope ratios and consequently is also behaving as a source tracer. It quantifies the scattering of any São Jorge lavas around the main alignment formed by the samples in this diagram. Slight changes of the reference line slope do not affect strongly observed covariations.

Fig. 10 shows variations of $\Delta_{SJ}$ with $^{143}Nd/^{144}Nd$, MgO, $Al_2O_3$, $Al_2O_3/CaO$. Samples from the Manadas and Rosais formations have positive $\Delta_{SJ}$, associated with low MgO and $^{143}Nd/^{144}Nd$, and high $Al_2O_3$. Samples from both groups are aligned on the same trend in plots of $\Delta_{SJ}$ against these chemical and isotopic data. This suggests that isotopic and chemical variations in São Jorge basalts are resulting from processes involving: (i) mixing (attested by the Pb–Nd isotope variations) with a component that has an isotopic composition similar to E-MORB (end-member 2, see Section 5.1), and (ii) magmatic differentiation (attested by the major elements contents and ratio) that are related to olivine and clinopyroxene crystallization. All samples collected along the island seem to be affected as even Topo samples show important range of variation along $\Delta_{SJ}$, only youngest samples seem to be shifted toward higher values of this parameter. Such a combination of processes is typical of magma chamber

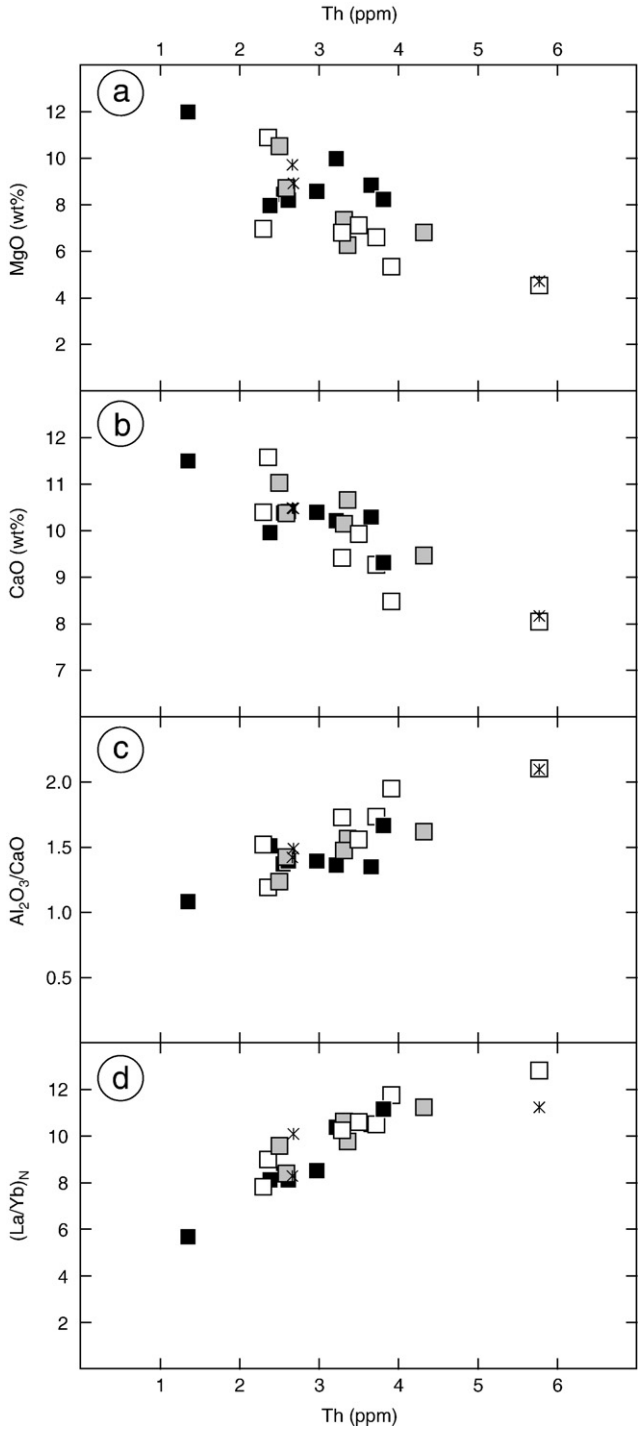


**Fig. 6.** Variations of (a) MgO, (b) CaO, (c) $Al_2O_3/CaO$ and (d) $(La/Yb)_N$ with Th contents for São Jorge lavas. Systematic relationships that are observed indicate that fractionation of olivine and clinopyroxene are the main source of variation of the $(La/Yb)_N$ ratio. Symbols as in Fig. 4. Normalized values for La and Yb are taken from Hofmann (1988).

processes where assimilation of wall-rock material occurs during fractional crystallization (AFC). As a consequence, the geochemical variations between the different formations of São Jorge Island are not interpreted to be related to heterogeneity of the Azores mantle plume, but rather to AFC processes in the oceanic crust basement beneath São Jorge. Moreover, they take place all along the volcanic history of Sao Jorge island as samples from all volcanic complexes show covariations of trace elements and isotopes ratios with the $\Delta_{SJ}$ parameter.

It may seem somewhat paradoxical that the basement of São Jorge (>10 Myr; Cannat et al., 1999), which is interpreted in this study to

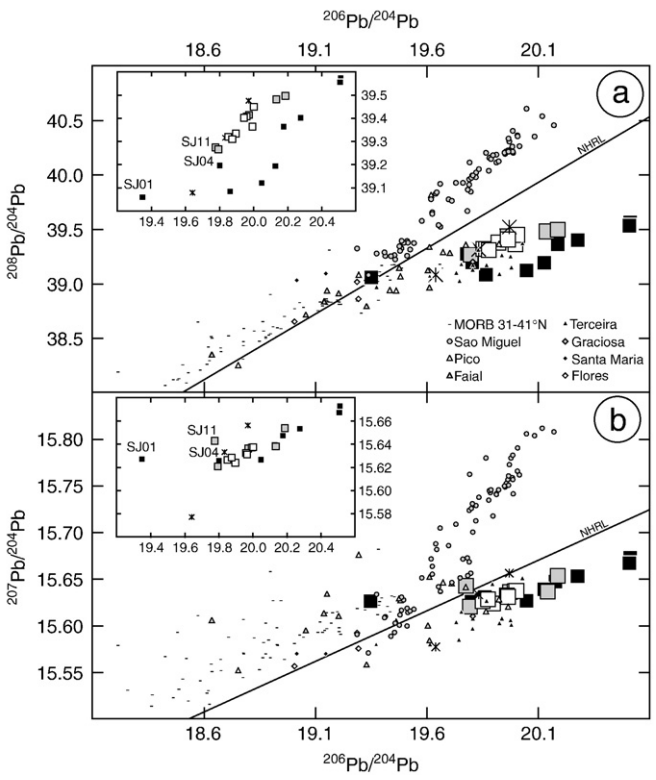


**Fig. 7.** (a) $^{208}Pb/^{204}Pb$ versus $^{206}Pb/^{204}Pb$ and (b) $^{207}Pb/^{204}Pb$ versus $^{206}Pb/^{204}Pb$ diagrams for Azores basalts and Atlantic MORB collected at latitudes 31°–41°N. Symbols for São Jorge volcanics are as in Fig. 4 and bigger than errorbars. Samples from the Topo complex, on the one hand, and Rosais–Manadas formations, on the other hand, define two sub-parallel trends in the $^{208}Pb/^{204}Pb$ versus $^{206}Pb/^{204}Pb$ diagram, whereas no difference can be observed in the $^{207}Pb/^{204}Pb$ versus $^{206}Pb/^{204}Pb$ plot. Note that two samples (SJ01 and SJ11) fall outside of the São Jorge trend in this last diagram.

being assimilated, shows an isotopic composition similar to that of an E-MORB, which reflects the actual interaction between the Azores mantle plume and the Mid-Atlantic Ridge. However, the Azores oceanic plateau started to be created around 50 Myr ago (Searle, 1980), suggesting that MORB with similar compositions have been produced in the area over long time making this the most probable locally available crustal assimilant.

### 5.3. Origin of the depleted end-member involved in Topo lavas

As discussed above, samples from the Topo complex appear to be less influenced by crustal contamination. Because their scatter around

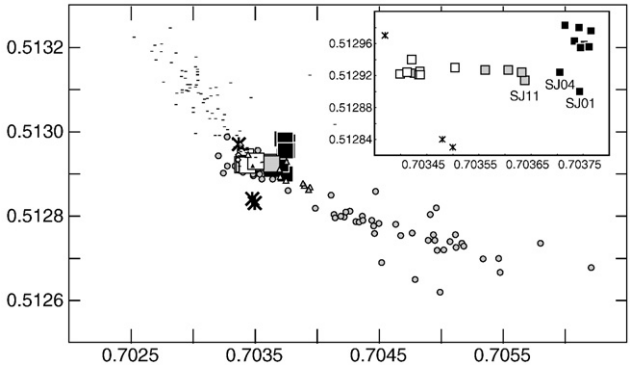


**Fig. 8.** Sr–Nd isotope compositions of Azores samples. Symbols are as in Fig. 6 and bigger than errorbars. Samples from Rosais and Manadas complexes show variable $^{87}Sr/^{86}Sr$ ratios at relatively constant $^{143}Nd/^{144}Nd$ values. Conversely, samples from Topo have variable Nd isotope compositions at near constant Sr isotope ratios.

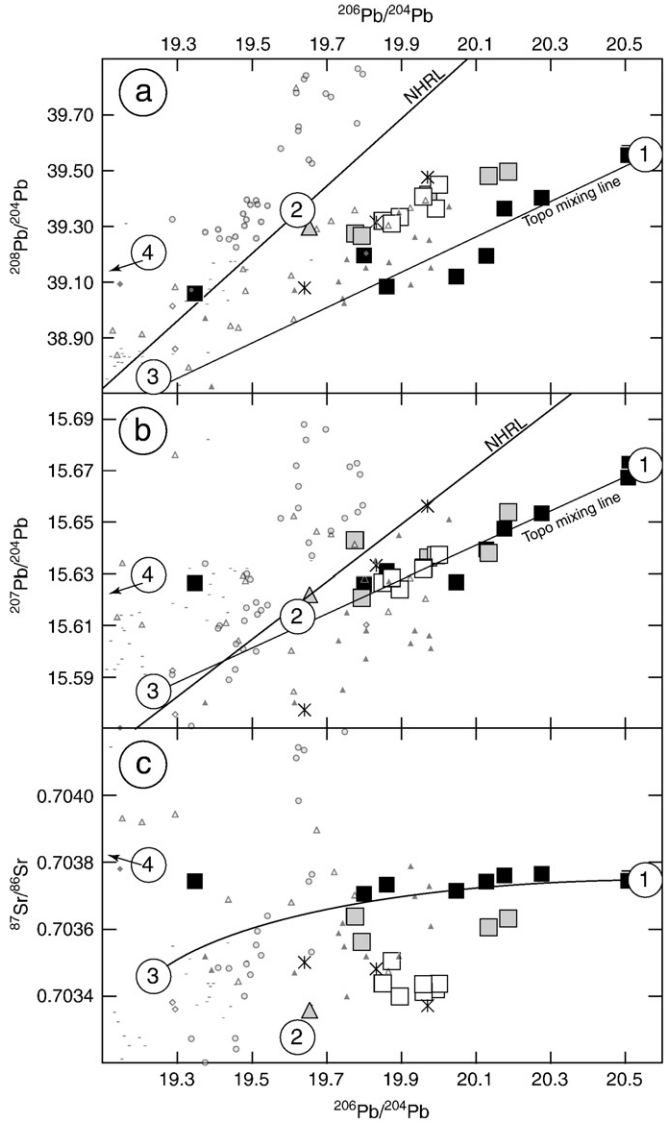


**Fig. 9.** Locations of the four end-members needed to account for the isotopic variability of São Jorge basalts in (a) $^{208}Pb/^{204}Pb$ versus $^{206}Pb/^{204}Pb$, (b) $^{207}Pb/^{204}Pb$ versus $^{206}Pb/^{204}Pb$, and (c) $^{87}Sr/^{86}Sr$ versus $^{206}Pb/^{204}Pb$ isotope variation diagrams. Symbols are as in preceding figures and bigger than errorbars. The large shaded triangle represents the composition of an E-MORB sample collected in the latitude of the Azores archipelago (data from Kamenetsky et al., 1998).

the best-fit line is rather small, mixing lines defined by those samples in the different isotope variation diagrams reflect a process occurring before interaction with the oceanic basement. We now consider the origin of the depleted end-member 3.

If we assume end-member 3 to correspond to a single component, two distinct models can be envisaged for its location in the mantle and its nature. As a plume-supplied component, it could correspond to recycled oceanic lithosphere, as was proposed by Schaefer et al. (2002) and Turner et al. (2007) to explain isotopic compositions of volcanics from Faial Island. Conversely this component could have a shallow origin resulting from the interaction of the Azores mantle plume with the Mid-Atlantic ridge. From an isotopic perspective, these two models lead to distinct compositions. Recycled oceanic lithosphere should indeed display slightly more depleted isotopic compositions than material from the Atlantic ridge as incompatible elements have been segregated out of the former for at least a few hundred millions of years. In any case, the composition of the depleted end-member lies on the Topo mixing line. Extrapolation of this line toward less radiogenic Pb in the $^{208}Pb/^{204}Pb$ versus $^{206}Pb/^{204}Pb$ diagram (Fig. 9a) intersects the field of MORB samples collected in the North Azores Fracture Zone (data from Dosso et al., 1999) at $^{206}Pb/^{204}Pb \sim 19.2–19.3$. As the North Azores Fracture Zone is located in the extension of São Jorge Island at a distance of ~200 km (Fig. 1), this strongly favours the interaction between the Azores mantle plume and the Mid-Atlantic Ridge for the origin of the depleted end-member 3.

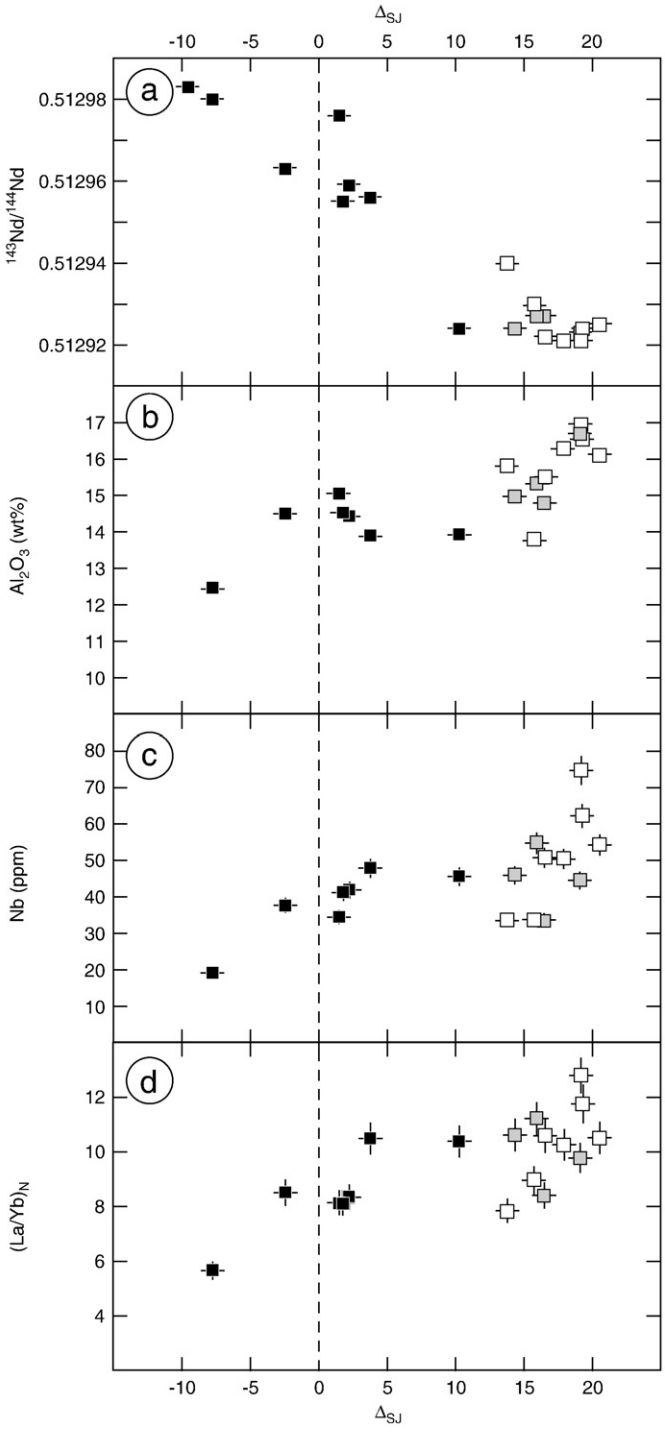


**Fig. 10.** Variations of major and trace element contents as well as major, trace element and isotope ratios with the $\Delta_{SJ}$ parameter (see text for details). Co-variations recorded between (a) $^{143}Nd/^{144}Nd$, (b) MgO, (c) $Al_2O_3$, (d) $(La/Yb)_N$ and the $\Delta_{SJ}$ parameter indicate that magmatic differentiation and mixing occurs simultaneously, mostly affecting Rosais and Manadas samples. The component responsible for isotopic variations is therefore most likely assimilated during an AFC process.

## 6. Reconsidering the isotopic variability of Azores basalts

In previous sections, we have shown that the isotopic variability of São Jorge samples is essentially controlled by two mixing processes: (1) all samples result from mixing between a young HIMU-like end-member and a depleted component sampled at the North Azores Fracture Zone; (2) some samples, in particular, intermediate and young volcanics of Rosais and Manadas formations are furthermore progressively contaminated by the oceanic crustal basement that has a composition similar to that of E-MORB. The second mixing process does, however, generate quite small isotope variations compared to the range of isotopic variations that are observed for the whole archipelago and subordinate to the more important process of interaction between the Azores mantle plume and the MAR. Therefore, in the following we focus on the identification of (i) the signature of the MAR in Azores basalts and (ii) the genetic links between the three regional isotopic trends defined by Terceira/São Jorge, Pico/Faial and São Miguel basalts, respectively (see Section 2).

### 6.1. Influence of the Mid-Atlantic Ridge

Samples from São Miguel and Terceira/São Jorge are represented in a Δ8/4 versus $^{206}Pb/^{204}Pb$ diagram in Fig. 11. Regression lines computed for the two groups intersect in the field of MORB sampled at the North Azores Fracture Zone, in agreement with observation made by Moreira et al. (1999) using a He–Pb isotope correlations as well as the He–Ne isotope study of Madureira et al. (2005). This suggests that lavas from those two islands share a common depleted component that is related to the MAR and, therefore, not intrinsic to the Azores mantle plume.

Alternatively, Beier et al. (2007) have proposed that lavas from the Sete Cidades complex of São Miguel, which are the most isotopically depleted from this island, were linked with a FOZO-like component (Hart et al., 1992; Stracke et al., 2005). They also reject an interaction with the mid-Atlantic ridge, arguing that MORB have generally too low Th/U, U/Pb and Th/Pb ratios. Samples from this portion of the MAR have not been measured for U, Th and Pb concentrations (Dosso et al., 1999). However, they show enrichments in highly incompatible elements that suggest plausible elevated (U, Th)/Pb ratios. Moreover, FOZO-like components should have unradiogenic He isotope ratios, which is not observed in this case as the two alignments join at a MORB-like $^{3}He/^{4}He$ values (Moreira et al., 1999).

Consequently, we favour the involvement of a depleted component related to the MAR in the genesis of Azores basalts. This component is therefore located at a shallow level. Nevertheless it has to be noted that this does not necessarily imply an interaction with the ridge

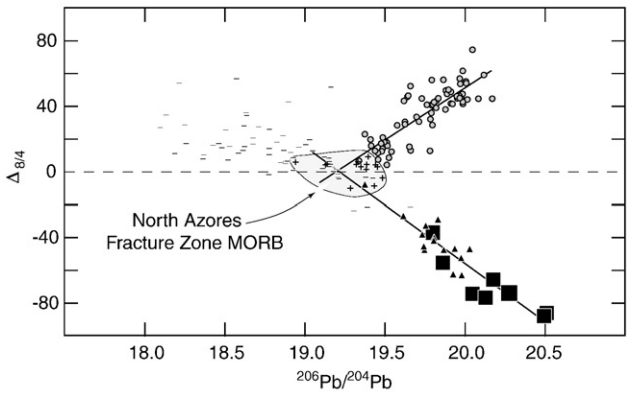


**Fig. 11.** Regression trends for São Jorge–Terceira basalts, on the one hand, and São Miguel lavas, on the other hand, in a Δ8/4 versus $^{206}Pb/^{204}Pb$ diagram. Symbols are as in preceding figures. Intersection of the two regression lines in the field of MORB collected in the North Azores Fracture Zone suggests that the common component involved in the genesis of basalts from these three islands is related to the Mid-Atlantic ridge.

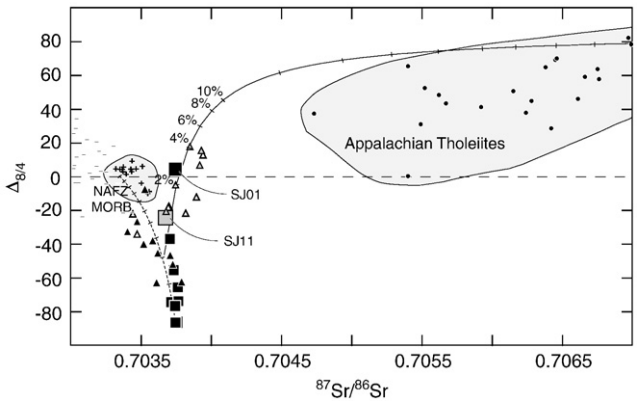


**Fig. 12.** Mixing relationships between São Jorge–Terceira samples and Pico–Faial lavas in the Δ8/4 versus $^{87}Sr/^{86}Sr$ diagram. Symbols are as in preceding figures. The Faial alignment intersects the São Jorge–Terceira trend at intermediate locations thus indicating a late occurrence in the mixing chronology. Mixing curves are calculated assuming a low degree partial melting of oceanic depleted lithosphere (for São Jorge–Terceira samples) and delaminated continental lithosphere (for Pico–Faial lavas) with a composition similar to that of Appalachian Tholeiites (Pegram, 1990). Tick marks on mixing curves are every 10% if not specified. See text for details of mixing models.

system. Indeed, compositional similarities of the depleted end-member observed in Terceira, São Jorge and São Miguel lavas with MORB from the North Azores Fracture Zone (located in the middle of the Azores archipelago) is more indicative of a genetic link rather than identical components. Another alternative scenario would then be interaction with the underlying oceanic lithosphere, created some millions years ago along the MAR, during plume ascent.

Hyperbola corresponding to the mixing between a pristine OIB melt (with an isotopic composition equal to that of the São Jorge radiogenic Pb end-member) and small-degree lithospheric melts have been computed in order to test this last model. Satisfactory results are obtained for an oceanic lithosphere mineralogy of ol:0.65; opx:0.15; cpx:0.15; sp:0.05 (melting mode: 0.05; 0.05; 0.45; 0.45) containing 7.7, 0.6 and 0.01 ppm of Sr, Nd and Pb, assuming an accumulated fractional melting process with a melting degree of 0.3% (Fig. 12). Most isotopically depleted samples require ~40% assimilation of those melts to account for their composition. Variations of the degree of melting only slightly affect the hyperbola curvature in such a way that melting degrees ranging from 0.1 to 1% allow reproducing the dispersion of data points around the plotted 0.3% model. Such model nevertheless raises the question of the ability of the local oceanic lithosphere to contaminate plume melts. Assuming that the base of the lithosphere is located around 50 km depth (~1.5 GPa), its solidus should be around 1340 °C (Gudfinnsson and Presnall, 2000). As the temperature excess of the Azores plume is around 100 °C (Yang et al., 2006), the base of the lithosphere should be no colder than 1240 °C in order for it to melt in anhydrous conditions. However, Bourdon et al. (2005) have proposed that the Azores local lithosphere contains small proportions of volatiles that could help to reduce this crude estimate.

### 6.2. Genesis of the Pico/Faial alignment

Previous studies have shown that the two trends defined by Pico/Faial samples, on the one hand, and Terceira samples, on the other hand, shared a common end-member with moderately elevated Pb isotope ratios ($^{206}Pb/^{204}Pb$ ~20). Our results significantly shift this common end-member toward more radiogenic, HIMU-like, compositions. Doing so, it modifies the relative arrangement of those two alignments and provides further constraints on the nature of end-member 4 (see Fig. 9 for location).

Representation of samples from Pico/Faial and Terceira/São Jorge in a Δ8/4 versus $^{87}Sr/^{86}Sr$ diagram (Fig. 12) best expresses the new insights our data provides with respect to the isotopic variability of the

Azores mantle plume. Samples from the Pico/Faial group define a trend that originates from the Terceira/São Jorge alignment at radiogenic Pb with $\Delta 8/4 \sim -40$ toward positive $\Delta 8/4$ values and more radiogenic Sr. This argues for the following chronological evolution: (1) mixing in variable proportions of end-members 1 and 3 accounts for variations measured in Terceira/São Jorge samples; (2) followed by a second mixing process that involves end-member 4 that generates compositions determined for Pico/Faial lavas. Consequently, the new data from São Jorge Island presented here suggests that the component responsible for slightly enriched values of Pico/Faial is located at a shallow level and is not intrinsic to the Azores mantle plume because addition of the enriched component occurs after interaction of the Azores mantle plume with depleted upper mantle. This model is different to previous models that proposed recycling of a fluid- and melt-depleted oceanic lithosphere to explain the isotopic variations of the Azores basalts (Schaefer et al., 2002; Turner et al., 2007).

A possible candidate for the shallow end-member 4, is subcontinental lithospheric mantle material delaminated during the opening of the Atlantic Ocean. Such material generally has positive $\Delta 8/4$ and $\Delta 7/4$ values, as well as slightly enriched Sr–Nd isotopic signatures, which are all characteristics of Pico/Faial basalts. Such a signature has been identified in the signature of many oceanic basalts sampled in the Atlantic Ocean such as Walvis Ridge (Richardson et al., 1982; Gibson et al., 2005), Fernando de Noronha (Gerlach et al., 1987), Cape Verde (Hoernle et al., 1991, Doucelance et al., 2003; Escrig et al., 2005), North Oceanographer Transform Fault (Shirey et al., 1987) and Godzilla seamount (Geldmacher et al., 2008).

The nearest subcontinental material from the Azores is located under the Appalachian chain, Northern America. Tholeiites from this region display an isotopic composition (Pegram, 1990) that is compatible with end-member 4 (Fig. 12). Bulk assimilation of such material during magma ascent can be modelled assuming Sr, Nd and Pb contents of 10, 2 and 0.4 ppm, respectively (mixed into a pristine OIB melt containing 465, 38 and 1.45 ppm of those elements). Such values are close to the ones proposed by Zartman and Haines (1988) and imply ~75% of SCLM assimilation, which seems unreasonably elevated. However, it is plausible that small degree melting of the SCLM body occurs during assimilation. A first-order model to this process can be constructed with an enriched mantle mineralogy of ol:0.55; opx:0.25; cpx:0.15; sp:0.05 (partition coefficients from Halliday et al. (1995) and references therein) containing 10 ppm Sr, 1.7 ppm Nd and 0.18 ppm Pb. Assuming accumulated fractional modal melting (melting mode: 0.05; 0.05; 0.45; 0.45), a 0.5% partial melt would be sufficiently enriched to generate an adequate mixing hyperbola (OIB end-member identical to the bulk assimilation model) and only 4% mass fraction would be enough to account for the most enriched isotopic composition recorded in Faial samples.

Pico and Faial lavas are also characterized by very unradiogenic Os isotope ratios, and $d^{11}B$ and $d^{18}O$ values higher and lower, respectively, than MORB, as well as slightly elevated Nb/B ratios (Schaefer et al., 2002; Turner et al., 2007). While subcontinental mantle is known to have unradiogenic Os isotopes (Shirey and Walker, 1998), the oxygen and boron signatures are more problematic. Indeed, oxygen isotope ratios of subcontinental mantle are supposed to be identical to that of the MORB mantle (Mattey et al., 1994) and no data have yet been reported for B isotopes. Nevertheless, a low $d^{18}O$ signature has been measured in a São Jorge sample (Turner et al., 2007) and it is also a characteristic of HIMU basalts (Eiler et al., 1997). Consequently, it is likely that the lower than MORB oxygen isotope signature measured by Turner et al. (2007) is related to the São Jorge mantle source rather than to end-member 4. Finally, Nb/B ratios as elevated as the ones measured in Faial have been reported in samples from Fernando de Noronha (Ryan et al., 1996). Although these samples have not been measured for radiogenic isotope ratios, lavas from this locality have been interpreted as being contaminated by delaminated subcontinental material, suggesting a similar process is possible under Pico and Faial Islands.

Given the enriched isotopic signature is mostly restricted to Pico and Faial Islands (undetected in Terceira basalts), the volume of the fragment of delaminated subcontinental material (end-member 4) can be estimated. If we assume that Pico and Faial subaerial volcanics represent a volume of 300 km3 and that all this volume is contaminated at 4% (worst case scenario), then the SCLM fragment needs to be ~4200 km3. This represent a box of 60 km length, 35 km width and only 2 km height that therefore would easily fit at the bottom of the lithosphere in between the islands of São Jorge, Faial and Pico.

## 7. The dual signature of the Azores mantle plume

In the previous sections, we have considered the relative importance of isotopic variations measured in Azores basalts that are related to the plume source compared to that which we interpret to represent shallow-level interactions. As a result of this filtering, from the four end-members needed at the archipelago scale, only the São Jorge (end-member 1) and São Miguel (end-member SM) radiogenic Pb isotope compositions are considered to be intrinsic to the Azores mantle plume. Such a dual plume composition is unusual, especially as no apparent mixing lines seem to join those two plume-related radiogenic Pb end-members. In the following, we model the isotopic and trace-element composition of São Jorge source melts in order to investigate this feature and speculate about on recycling processes.

Recent studies have proposed that the São Miguel enriched end-member comprises recycled enriched basaltic material (Elliott et al., 2007; Beier et al., 2007), thus implying that São Miguel basalts with the most radiogenic Pb are sampling a pure component rather than a mix of physically distinct lithologies in the Azores mantle plume. On the contrary, the nature of the São Jorge source is slightly more puzzling. Its Pb isotopic composition appears to indicate the influence of a young, HIMU-like, component (Thirlwall, 1997: i.e., radiogenic Pb, negative $\Delta 8/4$ and $\Delta 7/4$ values), yet its Sr–Nd isotope ratios do not support such an origin. For example, HIMU OIB with $^{206}Pb/^{204}Pb$ ratios around 20.5 such as those found at St Helena Island display $^{87}Sr/^{86}Sr = 0.7028$, significantly lower than the value of ~0.7037 recorded in Topo lavas. Such a difference cannot be accounted for by assuming a more extreme Pb isotopes ratios for the São Jorge end-member as the slope of the São Jorge trend in the Sr–Pb diagram is sub-parallel to the *x*-axis. Therefore, the radiogenic Pb and moderate Sr isotope signature is a characteristic of the São Jorge source rather than the result of a sampling bias.

HIMU sources in oceanic volcanism are often linked to the recycling of altered oceanic crust (Weaver, 1991; Chauvel et al., 1992; Hofmann, 1997; Stracke et al., 2003). Alteration is invoked to raise the U content of the oceanic crust, as well as its Sr isotopic ratio, as seawater is characterized by a more elevated $^{87}Sr/^{86}Sr$ than mantle. Hence one could imagine an extremely altered oceanic crust to account for the São Jorge unusual HIMU signature for Sr isotopes. Nevertheless, if such a signature was related to extensive oceanic crust alteration prior to subduction, it would be expected that other HIMU sources would display such enrichments. To the contrary, OIB end-members with $^{206}Pb/^{204}Pb > 20.5$ usually display $^{87}Sr/^{86}Sr < 0.703$ (Stracke et al., 2005). Therefore, the São Jorge source is unlikely to result from the recycling and ageing of a single package of altered oceanic crust and mixing of different lithologies present in the plume has to be considered.

The elevated Pb isotope signature of São Jorge basalts, as well as the lower than MORB $d^{18}O$ value recorded by Turner et al. (2007) argue for high proportions of recycled altered oceanic crust in their source. The São Miguel component, also intrinsic to the Azores plume, displays enriched Sr–Nd isotope signatures and radiogenic Pb. Consequently, we propose that the São Jorge end-member results from mixing between recycled altered oceanic crust and material at the origin of the São Miguel end-member. Using worksheets provided by Stracke et al. (2003) in order to compute chemical parameters of the altered oceanic crust, we find that mixing of (1) an igneous crust

that was composed of 30% N-MORB (value from Sun and McDonough, 1989), 20% altered MORB (Staudigel et al., 1996) and 50% gabbro (sample 735B, Hart et al., 1999), and recycled ~1.85 Gyr ago with (2) the São Miguel component (as defined by Beier et al., 2007) in the mass proportions 0.89–0.11 makes it possible to model the São Jorge source fingerprint (see appendix for details). Assuming this result, we also find that ~1.7% accumulated fractional melting in the garnet stability field is needed in order to reproduce the trace-element pattern of the most primitive São Jorge basalt by partial melting.

Doing so, we have assumed a near-perfect solid-state mixing between the recycled oceanic crustal material and the São Miguel component. However, the process by which the two components are mixed is unconstrained. The São Jorge source could either be a fragment of recycled oceanic crust that was slightly enriched before its subduction, much like models by Beier et al. (2007) and Elliott et al. (2007) for the São Miguel component, or the mixing could take place in the deep source of the plume or even during upwelling. Numerical models from Farnetani et al. (2002) would tend to dismiss the later hypothesis hence promoting the idea of an early enrichment.

Turning to the heterogeneity of the Azores mantle plume, this result suggests that the influence of the São Miguel component might be more regional than previously thought. Moreover, this would also show that the Azores mantle plume is an example of varying degrees of enrichment of recycled oceanic crust in OIB sources.

## 8. Summary and conclusions

New major and trace element and Sr–Nd–Pb isotope ratio measurements have been carried out for 21 samples from São Jorge Island. Isotopic results show the extension of the previously measured range of variations for Terceira Island toward more radiogenic Pb ratios, with negative Δ7/4 and Δ8/4 values, implying the influence of a HIMU-like component in the source of the Azores mantle plume.

At the island scale, samples from the oldest complex (Topo) define a mixing line between the HIMU-like component and a depleted end-member whose composition corresponds to that of MORB samples from the mid-Atlantic ridge (MAR) collected along the North Azores Fracture Zone (NAFZ; the nearest fracture zone from São Jorge). This mixing is interpreted as resulting from the interaction of plume-derived melts with a shallow depleted component. Intermediate and recent geological formations (Rosais and Manadas) have a more complex history, deriving from various proportions of the HIMU-NAFZ mixing line toward an end-member with the composition of an E-MORB. The influence of this last end-member is linked to olivine and clinopyroxene differentiation and is therefore thought to occur at oceanic crustal level and be generated during AFC processes.

At the archipelago scale, lavas from São Jorge Island plot on the same alignment as Terceira samples. Best-fit lines for these two islands and São Miguel basalts intercept in the field of NAFZ MORB, suggesting the influence of a MAR-related depleted component is a regional characteristic of the Azores archipelago. Such a conclusion is in agreement with the He–Pb isotope study of Moreira et al. (1999). Our new values also allow us to address the issue of the small-scale heterogeneity of the Azores mantle plume, illustrated by the contrasting isotopic signatures of Pico/Faial and Terceira Islands. Extension of the Terceira trend toward more radiogenic Pb values imply that the Pico/Faial alignment do not sample the very radiogenic Pb but rather originate from a proportion of mixing of the Terceira/São Jorge trend. Our preferred interpretation for this trend is the contamination of plume-derived melts by a subcontinental mantle fragment, delaminated during the opening of the Atlantic Ocean. Influence of this component is mostly restricted to Pico and Faial islands but affects also two samples from São Jorge, suggesting a length scale of the order of the tens of kilometres.

Those results necessitate serious reconsideration of the Azores plume compositional heterogeneity. Indeed, from the four end-members needed to explain the regional-scale variations, only two of them are likely to be deep-seated in the plume (São Miguel enriched component and São Jorge HIMU-like end-member). Speculation about the Sr isotopic ratios of São Jorge mantle source shows that it cannot be explained by the single involvement of recycled oceanic crust. On the contrary, mixing of such component with 11% in mass of the São Miguel component is required to account for trace elements and isotope ratios.

Two general conclusions can be drawn from this study. First, the present dataset highlights the influence of shallow-level interaction as a major agent of isotopic variability in OIB, even when volcanic activity is occurring over young lithosphere such as in the case of the Azores archipelago. Coupled to previous studies where the oceanic lithosphere is much older and thicker (Canary Islands: Hoernle et al., 1991; Comores: Späth et al., 1996; Class and Goldstein, 1997; Thirlwall et al., 1997; Widom et al., 1999; Cape Verde archipelago: Doucelance et al., 2003; Escrig et al., 2005; Millet et al., 2008), this illustrates how caution is required when interpreting the isotopic variations measured in OIB in the framework of chemical geodynamics. Second, modeling of the São Jorge end-member composition suggests a possible genetic link between the São Miguel enriched composition and the source of basalts from other Azores islands. This implies that the São Miguel composition might not be the consequence of a peculiar set of recycling parameters. In our view, the two isotopic fingerprints of the Azores mantle plume would represent the recycling of variously enriched oceanic crust material. This would suggest that recycling of OIB melts (Beier et al., 2007) or underplated basalts (Elliott et al., 2007) together with MORB-like crust could be of wider influence in the genesis of HIMU-like sources than hitherto thought.

## Acknowledgements

The authors are much indebted to Manuel Moreira who provided the samples. We also would like to thank Monica Handler and Ivan Vlastelic for insightful discussions as well as Chantal Bosq and Alex McCoy-West who helped us in the clean lab. Finally, careful editing by Roberta Rudnick and comments by two anonymous reviewers greatly improved the quality of the manuscript.

## Appendix: modeling of São Jorge radiogenic Pb end-member

Major- and trace-elements data for duplicate measurements of some São Jorge samples.

| | SJ 11 | | SJ 58 A | |
|---|---|---|---|---|
| $SiO_2$ | 44.80 | 45.50 | 45.65 | 44.15 |
| $TiO_2$ | 3.03 | 3.09 | 3.80 | 4.14 |
| $Al_2O_3$ | 13.59 | 13.69 | 16.42 | 16.15 |
| $Fe_2O_3$ | 12.45 | 12.68 | 13.04 | 14.60 |
| MnO | 0.17 | 0.17 | 0.18 | 0.18 |
| MgO | 10.44 | 10.60 | 6.56 | 7.05 |
| CaO | 10.99 | 11.06 | 9.40 | 9.44 |
| $Na_2O$ | 2.74 | 2.77 | 3.73 | 3.46 |
| $K_2O$ | 0.84 | 0.85 | 1.28 | 1.18 |
| $P_2O_5$ | 0.41 | 0.41 | 0.76 | 0.68 |
| LOI | −0.52 | −0.66 | −0.76 | −0.87 |
| Total | 98.94 | 100.15 | 100.05 | 100.15 |
| Rb | 17 | 18 | 25 | 22 |
| Ba | 227 | 244 | 319 | 283 |
| Th | 2.5 | 2.5 | 3.5 | 3.1 |
| Nb | 34 | 36 | 53 | 48 |
| U | 0.85 | 0.85 | 1.21 | 1.06 |
| La | 27 | 28 | 39 | 33 |
| Ce | 57 | 60 | 83 | 75 |
| Pb | 1.5 | 1.5 | 2.0 | 1.9 |
| Pr | 7.4 | 7.5 | 10.8 | 9.6 |
| Nd | 30 | 33 | 46 | 41 |
| Sr | 566 | 630 | 822 | 749 |
| Sm | 6.7 | 7.1 | 9.9 | 8.9 |
| Hf | 4.5 | 4.7 | 6.4 | 5.8 |

**Appendix** (*continued*)

| | SJ 11 | | SJ 58 A | |
|---|---|---|---|---|
| Zr | 181 | 209 | 296 | 262 |
| Eu | 2.2 | 2.3 | 3.2 | 2.9 |
| Gd | 6.3 | 6.5 | 8.7 | 8.1 |
| Tb | 0.91 | 0.95 | 1.23 | 1.14 |
| Dy | 4.9 | 5.1 | 6.6 | 6.0 |
| Ho | 0.89 | 0.92 | 1.15 | 1.05 |
| Er | 2.3 | 2.4 | 2.9 | 2.7 |
| Y | 24 | 28 | 33 | 30 |
| Tm | 0.30 | 0.32 | 0.39 | 0.36 |
| Yb | 1.9 | 2.0 | 2.5 | 2.3 |
| Lu | 0.27 | 0.28 | 0.35 | 0.33 |
| Cu | 50 | 59 | 25 | 21 |
| Co | 52 | 65 | 46 | 48 |
| Ni | 181 | 223 | 63 | 66 |
| Cr | 351 | 403 | 86 | 92 |

Sr–Nd–Pb isotopes ratios of duplicates measurements for some São Jorge lavas.

| Sample | $^{143}Nd/^{144}Nd$ | $^{87}Sr/^{86}Sr$ | $^{206}Pb/^{204}Pb$ | $^{207}Pb/^{204}Pb$ | $^{208}Pb/^{204}Pb$ |
|---|---|---|---|---|---|
| SJ 11 | 0.512914 ± 7 | 0.703638 ± 11 | 19.777 ± 3 | 15.645 ± 4 | 39.280 ± 11 |
| | 0.512913 ± 7 | 0.703644 ± 11 | 19.776 ± 3 | 15.643 ± 4 | 39.274 ± 11 |
| SJ 51 | 0.512990 ± 12 | 0.703742 ± 9 | 20.124 ± 3 | 15.641 ± 4 | 39.198 ± 11 |
| | 0.512971 ± 12 | 0.703743 ± 12 | 20.127 ± 3 | 15.639 ± 4 | 39.194 ± 11 |
| SJ 58 | 0.512921 ± 8 | 0.703439 ± 11 | 19.858 ± 3 | 15.628 ± 4 | 39.322 ± 11 |
| | 0.512923 ± 8 | 0.703436 ± 12 | 19.842 ± 3 | 15.625 ± 4 | 39.318 ± 11 |

All calculations have been performed using two Excel spreadsheets provided by Stracke et al. (2003) with their paper, i.e. "basalt + sediment recycling.xls" for isotopes and "TE_OIBmelts.xls" for trace-element compositions, respectively. Both spreadsheets computes the geochemical signature of recycled oceanic crust by a two-stage model. Modeling stages account for the evolution of the geochemical characteristics before (stage 1) and after (stage 2) subduction zone processing. Details are given in the following.

Trace-element contents of altered oceanic crust (before subduction) were calculated as the sum of 30% N-MORB (value from Sun and McDonough, 1989), 20% altered MORB (Staudigel et al., 1996) and 50% Gabbro (sample 735B, Hart et al., 1999). Subduction processing was accounted for by removing elements according to mobility coefficients (values from Kogiso et al., 1997). Recycled crust (after subduction) was then mixed in mass proportions 0.05–0.95 with depleted mantle (composition identical to that proposed by Workman and Hart, 2005).

Turning to the isotopic fingerprint of the subducted crust, Pb ratios have been computed using radioactive decay equations between 4.55 and 1.85 Ga (recycling time) with $\mu_1 = 8.15$, $\kappa_1 = 3.00$ and Canyon Diablo (Tatsumoto et al., 1973) as the initial composition ($\mu = {}^{238}U/{}^{204}Pb$; $\kappa = {}^{232}Th/{}^{238}U$). Regarding Sr–Nd isotope ratios, it is assumed that the oceanic crust was generated 2 Ga ago by a mantle source that would produce MORB samples with $^{87}Sr/^{86}Sr = 0.7025$ and $^{143}Nd/^{144}Nd = 0.51335$ as present-day ratios. Seawater alteration was taken into account by exchanging 5% of Sr with a composition equal to 0.7047 (that of seawater at the time of recycling).

Evolution of recycled crust after subduction processing is entirely controlled by mobilities of elements. Hence, in order to fit measured data, all variables have to be adapted for the first stage of evolution. This is especially true for the $^{232}Th/^{238}U$ ratio that is set to a low value of 3.00 in the first stage. Such a value fails to reproduce the present-day $^{206}Pb/^{204}Pb$ ratio of MORB. As a comparison, Chauvel et al. (1992) modeled the HIMU-like, Mangaia end-member with a $\kappa_1$ value of 3.8. On the contrary, the post-subduction $\kappa_2$ value used in this study is set to 3.57, reflecting more efficient extraction of U than Th in during slab dehydration, whereas Chauvel et al. (1992) decrease this value down to 3.2. Those considerations outline the variability of chemical fractionation that can occur during recycling processes and justify our lower-than-expected $\kappa_1$ value in order to compensate the rigidity of the post-subduction stage modeling.

The trace-element pattern of melt corresponding to São Jorge radiogenic Pb end-member is finally computed as the 1.7% accumulated fractional melting of the recycled oceanic crust + ambient mantle source, mixed with 11% in mass of the São Miguel component (data from Beier et al., 2007). Partial melting was thought to occur in the garnet stability field (ol:0.5; opx:0.26; cpx:0.2; gt:0.04) with the following melting mode: ol:0.1; opx:0.15; cpx:0.3; gt:0.45. Partition coefficients used for melting are those proposed by Stracke et al. (2003) in their spreadsheets. Trace-element contents of the most primitive sample of São Jorge Island were reproduced with a tolerance of ±20% for all elements measured in our samples apart from Pb (+24%), Eu (−31%) and Gd (−28%).

## References


Abdel-Monem, A.A., Fernandez, L.A., Boone, G.M., 1975. K–Ar ages from the eastern Azores group (Santa Maria, São Miguel and the Formigas Islands). Lithos 8 (4), 247–254.

Allègre, C.J., Hamelin, B., Provost, A., Dupré, B., 1986/1987. Topology in isotopic multispace and origin of mantle chemical heterogeneities. Earth Planet. Sci. Lett. 81, 319–337.

Allègre, C.J., Turcotte, D.L., 1985. Geodynamical mixing in the mesosphere boundary layer and the origin of oceanic islands. Geophys. Res. Lett. 12, 207–210.

Baker, J., Peate, D., Waight, T., Meyzen, C., 2004. Pb isotopic analysis of standards and samples using a $^{207}Pb$–$^{204}Pb$ double spike and thallium to correct for mass bias with a double-focusing MC-ICP-MS. Chem. Geol. 211, 275–303.

Beier, C., Stracke, A., Haase, K.M., 2007. The peculiar geochemical signatures of São Miguel (Azores) lavas: metasomatised or recycled mantle sources? Earth Planet. Sci. Lett. 259 (1–2), 186–199.

Bourdon, B., Turner, S.P., Ribe, N.M., 2005. Partial melting and upwelling rates beneath the Azores from a U-series isotope perspective. Earth Planet. Sci. Lett. 239, 42–56.

Carignan, J., Hild, P., Mevelle, G., Morel, J., Yeghicheyan, D., 2001. Routine analyses of trace element in geological samples using flow injection and low pressure on-line liquid chromatography coupled to ICP-MS: a study of geochemical reference materials BR, DR-N, UB-N, AN-G and GH. Geostand. Newsl. 25, 187–198.

Cannat, M., et al., 1999. Mid-Atlantic Ridge-Azores hotspot interactions: along-axis migration of a hotspot-derived event of enhanced magmatism 10 to 4 Ma ago. Earth Planet. Sci. Lett. 173 (3), 257–269.

Chauvel, C., Hofmann, A.W., Vidal, P., 1992. HIMU-EM: the French Polynesian connection. Earth Planet. Sci. Lett. 110, 99–119.

Class, C., Goldstein, S.L., 1997. Plume-lithosphere interactions in the ocean basins: constraints from the source mineralogy. Earth Planet. Sci. Lett. 150, 245–260.

Davies, G.R., Norry, M., Gerlach, D.C., Cliff, R.A., 1989. A combined chemical and Pb–Sr–Nd isotope study of the Azores and Cape Verde hotspots: the geodynamic implications. In: A.D. Saunders and M.J. Norry (Editors), magmatism in the ocean basins. Geol. Soc. Spec. Publ. Lond. 231–255.

Dosso, L., et al., 1999. The age and distribution of mantle heterogeneity along the Mid-Atlantic Ridge (31–41°N). Earth Planet. Sci. Lett. 170 (3), 269–286.

Doucelance, R., Escrig, S., Moreira, M., Gariépy, C., Kurz, M.D., 2003. Pb–Sr–He isotope and traces element geochemistry of Cape Verde archipelago. Geochim. Cosmochim. Acta 67, 3717–3733.

Dupré, B., Lambert, B., Allègre, C.J., 1982. Isotopic variations within a single island : the Terceira case. Nature 620–622.

Eiler, J.M., et al., 1997. Oxygen isotope variations in ocean island basalt phenocrysts. Geochim. Cosmochim. Acta 61 (11), 2281–2293.

Eisele, J., et al., 2002. The role of sediment recycling in EM-1 inferred from Os, Pb, Hf, Nd, Sr isotope and trace element systematics of the Pitcairn hotspot. Earth Planet. Sci. Lett. 196, 197–212.

Elliott, T., Blichert-Toft, J., Heumann, A., Koetsier, G., Forjaz, V., 2007. The origin of enriched mantle beneath São Miguel, Azores. Geochim. Cosmochim. Acta 71 (1), 219–240.

Escrig, S., Doucelance, R., Moreira, M., Allègre, C.J., 2005. Os isotope systematics in Fogo basalts: evidence for lower continental crust residing in the oceanic lithosphere beneath the Cape Verde Islands. Chem. Geol. 219, 93–113.

Farley, K.A., Natland, J.H., Craig, H., 1992. Binary mixing of enriched and undegassed (primitive?) mantle components (He, Sr, Nd, Pb) in Samoan lavas. Earth Planet. Sci. Lett. 111, 183–199.

Farnetani, C.G., Legras, B., Tackley, P.J., 2002. Mixing and deformations in mantle plumes. Earth Planet. Sci. Lett. 196, 1–15.

Feraud, G., Kaneoka, I., Allègre, C.J., 1980. K/Ar ages and stress pattern in the Azores: geodynamic implications. Earth Planet. Sci. Lett. 46, 275–286.

Geldmacher, J., Hoernle, K., Klugel, A., van den Bogaard, P., Bindeman, I., 2008. Geochemistry of a new enriched mantle type locality in the northern hemisphere: implications for the origin of the EM-I source. Earth Planet. Sci. Lett. 265 (1–2), 167–182.

Gerlach, D.C., Stormer Jr, J.C., Mueller, P.A., 1987. Isotopic geochemistry of Fernando de Noronha. Earth Planet. Sci. Lett. 85 (1–3), 129–144.

Gibson, S.A., Thompson, R.N., Day, J.A., Humphris, S.E., Dickin, A.P., 2005. Melt-generation processes associated with the Tristan mantle plume: constraints on the origin of EM-1. Earth Planet. Sci. Lett. 237 (3–4), 744–767.

Gudfinnsson, G.H., Presnall, D.C., 2000. Melting behaviour of model lherzolite in the system $CaO–MgO–Al_2O_3–SiO_2–FeO$ at 0.7–2.8 GPa. J. Petrol. 41 (8), 1241–1269.

Halliday, A.N., Lee, D.C., Tommasini, S., Davies, G.R., Paslick, C.R., Fitton, J.G., James, D.E., 1995. Incompatible trace elements in OIB and MORB and source enrichments in the sub-oceanic mantle. Earth Planet. Sci. Lett. 133, 379–395.

Hanan, B.B., Graham, D.W., 1996. Lead and helium isotope evidence from oceanic basalts for a common deep source of mantle plumes. Science 272 (5264), 991–995.
Hart, S.R., 1984. Large-scale isotope anomaly in the Southern Hemisphere mantle. Nature 309, 753–757.
Hart, S.R., Blusztajn, J., Dick, H.J.B., Meyer, P.S., Muehlenbachs, K., 1999. The fingerprint of seawater circulation in a 500-meter section of ocean crust gabbros. Geochim. Cosmochim. Acta 63 (23–24), 4059–4080.
Hart, S.R., Hauri, E.H., Oschmann, L.A., Whitehead, J.A., 1992. Mantle plumes and entrainment: isotopic evidence. Science 256, 517–520.
Hauri, E.H., Whitehead, J.A., Hart, S.R., 1994. Fluid dynamic and geochemical aspects of entrainment in mantle plumes. J. Geophys. Res. 99, 24275–24300.
Hawkesworth, C.J., Norry, M.J., Roddick, J.C., Vollmer, R., 1979. $^{143}Nd/^{144}Nd$ and $^{87}Sr/^{86}Sr$ ratios from the Azores and their significance in LIL-element enriched mantle. Nature 280, 28–31.
Hildenbrand, A., Madureira, P., Ornela Marques, F., Cruz, I., Henry, B., Silva, P., 2008. Multi stage evolution of a sub-aerial volcanic ridge over the last 1.3 Myr: S. Jorge Island, Azores Triple Junction. Earth Planet. Sci. Lett. 273 (3–4), 289–298.
Hoernle, K., Tilton, G., Schmincke, H.-U., 1991. Sr–Nd–Pb isotopic evolution of Gran Canaria: evidence for shallow enriched mantle beneath the Canary Islands. Earth Planet. Sci. Lett. 106, 44–63.
Hofmann, A.W., 1988. Chemical differentiation of the Earth: the relationship between mantle, continental crust and oceanic crust. Earth Planet. Sci. Lett. 90, 297–314.
Hofmann, A.W., 1997. Mantle geochemistry: the message from oceanic volcanism. Nature 385, 219–229.
Jackson, M.G., et al., 2007a. The return of subducted continental crust in Samoan lavas. Nature 448 (7154), 684–687.
Jackson, M.G., Kurz, M.D., Hart, S.R., Workman, R.K., 2007b. New Samoan lavas from Ofu Island reveal a hemispherically heterogeneous high 3He/4He mantle. Earth Planet. Sci. Lett. 264 (3–4), 360–374.
Kamenetsky, V.S., et al., 1998. Calcic melt inclusions in primitive olivine at 43∞N MAR: evidence for melt-rock reaction/melting involving clinopyroxene-rich lithologies during MORB generation. Earth Planet. Sci. Lett. 160 (1–2), 115–132.
Kogiso, T., Tatsumi, Y., Nakano, S., 1997. Trace element transport during dehydration processes in the subducted oceanic crust: 1. Experiments and implications for the origin of ocean island basalts. Earth Planet. Sci. Lett. 148 (1–2), 193–205.
Madureira, P., Moreira, M., Mata, J., Allègre, C.J., 2005. Primitive neon isotopes in Terceira Island (Azores archipelago). Earth Planet. Sci. Lett. 233 (3–4), 429–440.
Mattey, D., Lowry, D., Macpherson, C., 1994. Oxygen isotope composition of mantle peridotite. Earth Planet. Sci. Lett. 128 (3–4), 231–241.
Millet, M.-A., Doucelance, R., Schiano, P., David, K., Bosq, C., 2008. Mantle plume heterogeneity versus shallow-level interactions: a case study, the São Nicolau Island, Cape Verde archipelago. J. Volcanol. Geotherm. Res. 176 (2), 265–276.
Montelli, R., et al., 2004. Finite-frequency tomography reveals a variety of plumes in the mantle. Science 303 (5656), 338–343.
Montelli, R., Nolet, G., Dahlen, F.A., Masters, G., 2006. A catalogue of deep mantle plumes: new results from finite-frequency tomography. Geochem. Geophys. Geosyst. 7, Q11007. doi:10.1029/2006GC001248.
Moreira, M., Doucelance, R., Kurz, M.D., Dupré, B., Allègre, C.J., 1999. Helium and lead isotope geochemistry of the Azores Archipelago. Earth Planet. Sci. Lett. 169, 189–205.
Pegram, W., 1990. Development of continental lithospheric mantle as reflected in the chemistry of the Mesozoic Appalachian Tholeites. Earth Planet. Sci. Lett. 97, 316–331.
Pin, C., Bassin, C., 1992. Evaluation of a strontium-specific extraction chromatographic method for isotopic analysis in geological materials. Anal. Chim. Acta 269, 249–255.
Pin, C., Briot, D., Bassin, C., Poitrasson, F., 1994. Concomitant separation of strontium and samarium-neodymium for isotopic analysis in silicate samples, based on specific extraction chromatography. Anal. Chim. Acta 298 (2), 209–217.
Richardson, S.H., Erlank, A.J., Duncan, A.R., Reid, D.L., 1982. Correlated Nd, Sr and Pb isotope variation in Walvis Ridge basalts and implications for the evolution of their mantle source. Earth Planet. Sci. Lett. 59, 327–342.
Ryan, J.G., Leeman, W.P., Morris, J.D., Langmuir, C.H., 1996. The boron systematics of intraplate lavas: implications for crust and mantle evolution. Geochim. Cosmochim. Acta 60 (3), 415–422.
Schaefer, B.F., Turner, S., Parkinson, I., Rogers, N., Hawkesworth, C., 2002. Evidence for recycled Archaean oceanic mantle lithosphere in the Azores plume. Nature 420, 304–307.
Searle, R., 1980. Tectonic pattern of the Azores spreading centre and triple junction. Earth Planet. Sci. Lett. 51 (2), 415–434.
Shirey, S.B., Bender, J.F., Langmuir, C.H., 1987. Three-component isotopic heterogeneity near the oceanographer transform, Mid-Atlantic ridge. Nature 325, 217–223.
Shirey, S.B., Walker, R.J., 1998. The Re-Os isotope system in cosmochemistry and high-temperature geochemistry. Annu. Rev. Earth Planet. Sci. 26, 423–500.
Späth, A., Roex, A.P.L., Duncan, R.A., 1996. The geochemistry of lavas from the Comores archipelago, Western Indian ocean: petrogenesis and mantle source region characteristics. J. Petrol. 37, 961–991.
Staudigel, H., Plank, T., White, W.M., Schmincke, H.U., 1996. Geochemical fluxes during seafloor alteration of the basaltic upper crust: DSDP sites 417 and 418. In: Bebout, D.W.S.G.E., Kirby, S.H., Platt, J.P. (Eds.), Subduction: Top to Bottom. Geophys. Monogr. Ser. AGU, Washington, D.C., pp. 19–38.
Stracke, A., Bizimis, M., Salters, V.J.M., 2003. Recycling oceanic crust: quantitative constraints. Geochem. Geophys. Geosys. 4.
Stracke, A., Hofmann, A.W., Hart, S.R., 2005. FOZO, HIMU and the rest of the mantle zoo. Geochem. Geophys. Geosys. 6.
Sun, S.s., McDonough, W.F., 1989. Chemical and isotopic systematics of oceanic basalts: implications for mantle composition and processes. Special Publications, vol. 42(1). Geological Society, London, pp. 313–345.
Tatsumoto, M., Knight, R.J., Allegre, C.J., 1973. Time differences in the formation of meteorites as determined from the ratio of lead-207 to lead-206. Science 180 (4092), 1279–1283.
Thirlwall, M.F., 1997. Pb isotopic and elemental evidence for OIB derivation from young HIMU mantle. Chem. Geol. 139 (1–4), 51–74.
Thirlwall, M.F., Jenkins, C., Vroon, P.Z., Mattey, D.P., 1997. Crustal interaction during construction of ocean islands: Pb–Sr–Nd–O isotope geochemistry of the shield basalts of Gran Canaria, Canary Islands. Chem. Geol. 135 (3–4), 233–262.
Turner, S., Hawkesworth, C., Rogers, N., King, P., 1997. U–Th isotope disequilibria and ocean island basalt generation in the Azores. Chem. Geol. 139 (1–4), 145–164.
Turner, S., Tonarini, S., Bindeman, I., Leeman, W.P., Schaefer, B.F., 2007. Boron and oxygen isotope evidence for recycling of subducted components over the past 2.5 Gyr. Nature 447, 702–705.
Van der Hilst, R.D., De Hoop, M.V., 2005. Banana-doughnut kernels and mantle tomography. Geophys. J. Int. 163, 956–961.
Weaver, B.L., 1991. The origin of ocean island basalt end-member compositions: trace element and isotopic constraints. Earth Planet. Sci. Lett. 104 (2–4), 381–397.
White, W.M., Tapia, M.D.M., Schilling, J.-G., 1976. The petrology and geochemistry of the Azores Islands. Contrib. Mineral. Petrol. 69, 201–213.
Widom, E., Carlson, R.W., Gill, J.B., Schmincke, H.-U., 1997. Th–Sr–Nd–Pb isotope and trace element evidence for the origin of the Sao Miguel, Azores, enriched mantle source. Chem. Geol. 140 (1), 49–68.
Widom, E., Farquhar, J., 2003. Oxygen isotope signatures in olivines from São Miguel (Azores) basalts: implications for crustal and mantle processes. Chem. Geol. 193 (3–4), 237–255.
Widom, E., Hoernle, K.A., Shirey, S.B., Schmincke, H.-U., 1999. Os isotope systematics in the Canary Islands and Madeira: lithospheric contamination and mantle plume signatures. J. Petrol. 40, 279–296.
Widom, E., Shirey, S.B., 1996. Os isotope systematics in the Azores: implications for mantle plume sources. Earth Planet. Sci. Lett. 142 (3–4), 451–465.
Woodhead, J.D., 1996. HIMU in an oceanic setting: the geochemistry of Mangaia Island (Polynesia) and temporal evolution of the Cook–Austral hotspot. J. Volcanol. Geotherm. Res. 72, 1–19.
Woodhead, J.D., Devey, C.W., 1993. Geochemistry of the Pitcairn seamount, 1: source character and temporal trends. Earth Planet. Sci. Lett. 116, 81–99.
Workman, R.K., Hart, S.R., 2005. Major and trace element composition of the depleted MORB mantle (DMM). Earth Planet. Sci. Lett. 231 (1–2), 53–72.
Yang, T., Shen, Y., van der Lee, S., Solomon, S.C., Hung, S.-H., 2006. Upper mantle structure beneath the Azores hotspot from finite-frequency seismic tomography. Earth Planet. Sci. Lett. 250, 11–26.
Zartman, R.E., Haines, S.M., 1988. The plumbotectonic model for Pb isotopic systematics among major terrestrial reservoirs—a case for bi-directional transport. Geochim. Cosmochim. Acta 52 (6), 1327–1339.
Zindler, A., Hart, S.R., 1986. Chemical geodynamics. Ann. Rev. Earth Planet. Sci. Lett. 14, 493–571.
Zindler, A., Jagoutz, E., Goldstein, S.L., 1982. Nd, Sr, and Pb isotopic systematics in a three component mantle: a new perspective. Nature 298, 519–523.

Chemical Geology 334 (2012) 44–61

Contents lists available at SciVerse ScienceDirect

Chemical Geology

journal homepage: www.elsevier.com/locate/chemgeo

# Geochemical temporal evolution of Brava Island magmatism: Constraints on the variability of Cape Verde mantle sources and on carbonatite–silicate magma link

Cyntia Mourão [a,b,*], João Mata [a,b], Régis Doucelance [c,d,e], José Madeira [a,f,g], Marc-Alban Millet [h,i], Manuel Moreira [j]

[a] Faculdade de Ciências da Universidade de Lisboa, Departamento de Geologia (GeoFCUL), Campo Grande, C6, 1749-016 Lisboa, Portugal
[b] Centro de Geologia da Universidade de Lisboa (CeGUL), Campo Grande, C6, 1749-016 Lisboa, Portugal
[c] Clermont Université, Université Blaise Pascal, Laboratoire Magmas et Volcans, BP 10448, F-63000 Clermont-Ferrand, France
[d] CNRS, UMR 6524, LMV, F-63038 Clermont-Ferrand, France
[e] IRD, R 163, LMV, F-63038 Clermont-Ferrand, France
[f] LATTEX — Laboratório de Tectonofísica e Tectónica Experimental, 1749-016 Lisboa, Portugal
[g] IDL — Instituto D. Luís, 1250-102 Lisboa, Portugal
[h] Origins Laboratory, Department of the Geophysical Sciences, University of Chicago, 5734 South Ellis Avenue, Chicago, IL 60637, USA
[i] Enrico Fermi Institute, 5734 South Ellis Avenue, Chicago, IL 60637, USA
[j] Laboratoire de Géochimie et Cosmochimie (UMR 7579 CNRS), Institut de Physique du Globe de Paris, Université Paris 7, 4 place Jussieu, 75252 Paris cedex, France

ARTICLE INFO

*Article history:*
Received 8 June 2011
Received in revised form 14 August 2012
Accepted 23 September 2012
Available online 29 September 2012

Editor: L. Reisberg

*Keywords:*
Cape Verde archipelago
Alkaline magmas
Carbonatites
Recycled components
Mantle plume
Sr–Nd–Pb isotopes

ABSTRACT

Elemental and isotopic (Sr, Nd and Pb) analyses of silicate and carbonatite rocks from Brava, the southernmost island of the Cape Verde archipelago, are reported here to assess the nature, origin and location of the main contributors to magma composition and to evaluate the chemical evolution of magma through time. In contrast to other islands of the archipelago where a continuous range is usually observed, Brava is clearly characterized by two groups of distinct isotopic compositions. Rocks from the Upper Unit (<0.5 Ma) are less Nd- and Pb-radiogenic and more Sr-radiogenic than rocks belonging to the Basal Complex (~3 to 1.4 Ma), which are also characterized by more unradiogenic He signatures. Here, the chemistry of the Basal Complex is mainly explained by the mixing of a high-μ (HIMU)-type local end-member, which represents an ancient (~1.3 Ga) recycled oceanic crust, with the lower mantle. For the Upper Unit, elemental and isotopic signatures suggest the involvement of an additional local end-member akin to the EM1-type. Such differences in the contributing end-members to the Upper Unit and Basal Complex sources mirror those usually assigned to the southern and northern Cape Verde islands, respectively. This temporal evolution is discussed in light of plume interaction with a shallow EM1-type domain, which is considered to represent the subcontinental lithosphere floating in the asthenosphere. Brava carbonatites define two distinct groups with similar isotopic ranges as those observed for the coeval alkaline silicate rocks. This observation suggests that, in each of the volcano-stratigraphic units, carbonatite and silicate magmas are ultimately derived from the same sources. We propose that calciocarbonatites from either the Basal Complex or the Upper Unit resulted from nephelinite–carbonatite liquid immiscibility, while the subordinate Basal Complex magnesiocarbonatites represent residual liquids after calcite fractionation from carbonatite magma.



## 1. Introduction

In contrast with continental basalts, oceanic magmas cross relatively young/un-enriched lithospheres, as well as crustal sections dominated by mafic/ultramafic lithotypes with relatively high *solidus* temperatures. Although shallow-level interaction processes have been shown to affect the composition of ascending oceanic magmas (e.g., Woodhead et al., 1993; Class and Goldstein, 1997; Millet et al., 2008, 2009; Martins et al., 2010), they undoubtedly offer a better image of the sub-lithospheric mantle than their continental counterparts. Therefore, the study of oceanic basalts is of utmost importance to characterize the composition and understand the evolution of the Earth's mantle and constrain the residence sites of the so-called mantle components (e.g., White, 1985; Zindler and Hart, 1986; Hofmann, 2003; Stracke et al., 2005; Jackson and Dasgupta, 2008; Collerson et al., 2010).

The volcanically active Cape Verde archipelago (Eastern Central Atlantic Ocean) exhibits significant inter-island isotopic variations when compared with most oceanic archipelagos. Previous studies have revealed two geographical/geochemical groups, with a strong contrast between the southern and northern islands (Gerlach et al., 1988; Davies et al., 1989; Christensen et al., 2001; Doucelance et

* Corresponding author at: Faculdade de Ciências da Universidade de Lisboa, Departamento de Geologia (GeoFCUL), Campo Grande, C6, 1749-016 Lisboa, Portugal. Tel.: +351 217500000; fax: +351 217500119.
*E-mail address:* ccmourao@fc.ul.pt (C. Mourão).

0009-2541/$ – see front matter © 2012 Elsevier B.V. All rights reserved.
http://dx.doi.org/10.1016/j.chemgeo.2012.09.031

al., 2003; Escrig et al., 2005; Holm et al., 2006; Millet et al., 2008; Barker et al., 2009, 2010; Martins et al., 2010). According to these authors, volcanic rocks from the southern islands are less Nd- and Pb-radiogenic and more Sr-radiogenic than those from the northern islands, which are also characterized by more unradiogenic He signatures. Such a distinction is also evident in the $^{208}Pb/^{204}Pb$ vs. $^{206}Pb/^{204}Pb$ diagram. While the northern islands tend to plot along the Northern Hemisphere Reference Line (NHRL; Hart, 1984), the southern islands are positioned above the NHRL. Such differences have mainly been explained by distinct contributions from HIMU ("high μ" = high time-integrated $^{238}U/^{204}Pb$), EM1 (enriched mantle 1), and DMM (depleted mid ocean ridge basalt — MORB-mantle) mantle components and the lower mantle, making Cape Verde an interesting place to study the mixing mechanisms between those components. The contribution of FOZO has been proposed by Barker et al. (2009).

Brava is the southernmost island of the Cape Verde archipelago. From the geochemical data presented by Mourão et al. (2010), Madeira et al. (2010), Hildner et al. (2011) and Mourão et al. (2012), it can be inferred that some Brava silicate rocks display characteristics distinct from those considered typical of the southern islands. Namely, some rocks are markedly more radiogenic in terms of $^{206}Pb/^{204}Pb$ and $^{143}Nd/^{144}Nd$, present more unradiogenic He isotope compositions and are significantly enriched in Nb and Ta relative to the light rare-earth (LREE) and other high field strength (HFSE) elements, conferring some affinity with the northern islands. This finding suggests that Brava magmatism samples a larger number of mantle components than the other individual Cape Verde islands. Thus, the study of that island offers an opportunity to better understand the mixing mechanisms of the mantle components referred to above.

In addition, Brava is known by the occurrence of magnesio- and calciocarbonatites (Madeira et al., 2010; Mourão et al., 2010) that offers the opportunity to address the genetic processes that originated these two types of carbonatites and to discuss the possible existence of co-magmatism between them and with the associated silicate rocks. Moreover, data from Hoernle et al. (2002) and Mourão et al. (2010) demonstrate that Brava's extrusive carbonatites are isotopically distinct from those occurring in other islands of the archipelago (see also Doucelance et al., 2010).

In this study, we report elemental and Sr–Nd–Pb isotopic data of silicate and carbonatite rocks from Brava Island. Our work aims to: 1) evaluate the geochemical temporal evolution of magmatism at Brava Island; 2) identify the mantle components of Brava magmas and assess the origin and residence sites of the HIMU- and EM1-type Brava end-members; 3) better understand the causes of isotope variability at the Cape Verde archipelago; and 4) evaluate the possible genetic link between Brava carbonatites and the temporally/spatially associated silicate rocks.

## 2. Geological setting

The Cape Verde archipelago (15–17°N, 23–26°W) is located 600 to 900 km off the West African coast and consists of 10 major islands (Fig. 1). It is situated on the Cape Verde Rise, which is a 2.2 km-high, 1400–1600 km-wide swell occurring in a region where the oceanic lithosphere is 120 to 140 Ma old (Williams et al., 1990; Müller et al., 2008).

The islands are flanked by smaller than expected flexural moats that suggest an upward-acting subsurface load that counteracts downward flexure due to surface volcanic loading (Ali et al., 2003). This finding, along with the coincidence of Cape Verde with bathymetric, gravimetric and heat flow anomalies (e.g., Dash et al., 1976; Courtney and White, 1986), has been interpreted by Crough (1978) as resulting from lithosphere impingement by a mantle plume, which explains why the transition zone at the Cape Verde region is up to ≈30 km thinner than that of the ambient mantle (Vinnik et al., 2012). The genesis of Cape Verde from a mantle plume anchored at the deepest levels of the lower mantle seems to be supported by both seismic tomography studies (Montelli et al., 2006; Zhao, 2007; Forte et al., 2010) and unradiogenic He isotopic signatures (Christensen et al., 2001; Doucelance et al., 2003; Mata et al., 2010; Mourão et al., 2012) obtained from silicate and carbonatite rocks ($^4He/^3He$ down to 46,022 and 46,616, respectively; R/Ra up to 15.7 and 15.5; Ra corresponds to the atmospheric $^3He/^4He$ value of $1.384\times10^{-6}$ and R the measured ratio).

The emerged alkaline magmatic rocks range in age from 25.6 Ma (Sal Island; Torres et al., 2002) to the present (latest eruption in 1995 at Fogo Island). However, the K–Ar age resetting of late Jurassic MORBs at 40–50 Ma suggests that plume-related magmatism may have started some 15–25 Ma before the genesis of the most ancient alkaline outcropping rocks (Mitchell et al., 1983).

The lack of a typical linear distribution of islands (Fig. 1) and a simple age progression of volcanism at Cape Verde primarily reflects the fact that the archipelago is close to the rotation pole of the slowly drifting African plate (Pollitz, 1991; Holm et al., 2008). Such spatial distribution of the islands was also interpreted as resulting from mantle melting in three distinct channels (Holm et al., 2008) or from deep fracture control on magma emplacement (e.g., Le Pichon and Fox, 1971; Torres et al., 2010). Brava (64 $km^2$) is the westernmost island of the southern alignment (Fig. 1) and is located 18 km west of the neighboring Fogo Island. These islands are separated by a channel with depths in excess of 1400 m, where a volcanic cone field was revealed by multibeam bathymetry and backscatter data. The same techniques also revealed a growing 3-km tall seamount volcano (Cadamosto) to the southwest of Brava (Masson et al., 2008; Grevemeyer et al., 2010; see also Barker et al., 2012 for a geochemical study of Cadamosto).

Three major outcropping volcano-stratigraphic units have been identified on Brava Island by Madeira et al. (2010) (Fig. 1). The Lower Unit (2 to 3 Ma) is composed of an uplifted nephelinite/ankaramite sequence that includes pillow lavas, pillow breccias and hyaloclastites and is cut by abundant dikes. This unit represents the upper part of the submarine seamount precursor of the island. A subvolcanic plutonic complex (Middle Unit: 2.0 to 1.4 Ma) intrudes on the Lower Unit and includes nepheline syenites, urtites, ijolites, melteigites, pyroxenites, and carbonatites, probably formed in magma chambers related to a volcanic phase that is no longer preserved. The younger volcanic sequence (Upper Unit < 0.5 Ma) rests on an important erosional discontinuity truncating the Basal Complex (Lower and Middle units) that developed between 1.4 and ~0.5 Ma ago. This mainly phonolitic sequence is dominated by products of explosive volcanism generated by phreatomagmatic and phreatoplinian eruptions as well as extrusion of domes and lava flows. Rare mafic products, predominantly of nephelinitic composition, and extrusive carbonatites are also present (Mourão et al., 2010). The occurrence of pillow lavas and hyaloclastites up to 400 m above the present sea level and raised Upper Pleistocene (~106 Ka) beaches indicates a continuous uplift of Brava at rates between 0.2 and 0.4 mm/a, which is mainly explained by the crustal emplacement of magma bodies (Madeira et al., 2010; Ramalho et al., 2010).

## 3. Analytical procedures

Sampling was conducted to obtain a set of rocks representative of all volcano-stratigraphic units cropping out at Brava as well as their main magmatic lithotypes. The sampling locations are shown in Supplementary material S1.

After reducing samples of 1–2 kg to centimeter-sized chips in a hydraulic press, the freshest pieces were selected, coarsely pounded using a jaw crusher, and powdered in an agate swing mill.

Major and trace element compositions were performed at Activation Laboratories Ltd. (Canada). Samples were prepared and analyzed in a batch system. Each batch also contained a method reagent blank, certified reference materials and sample duplicates. The samples were mixed with

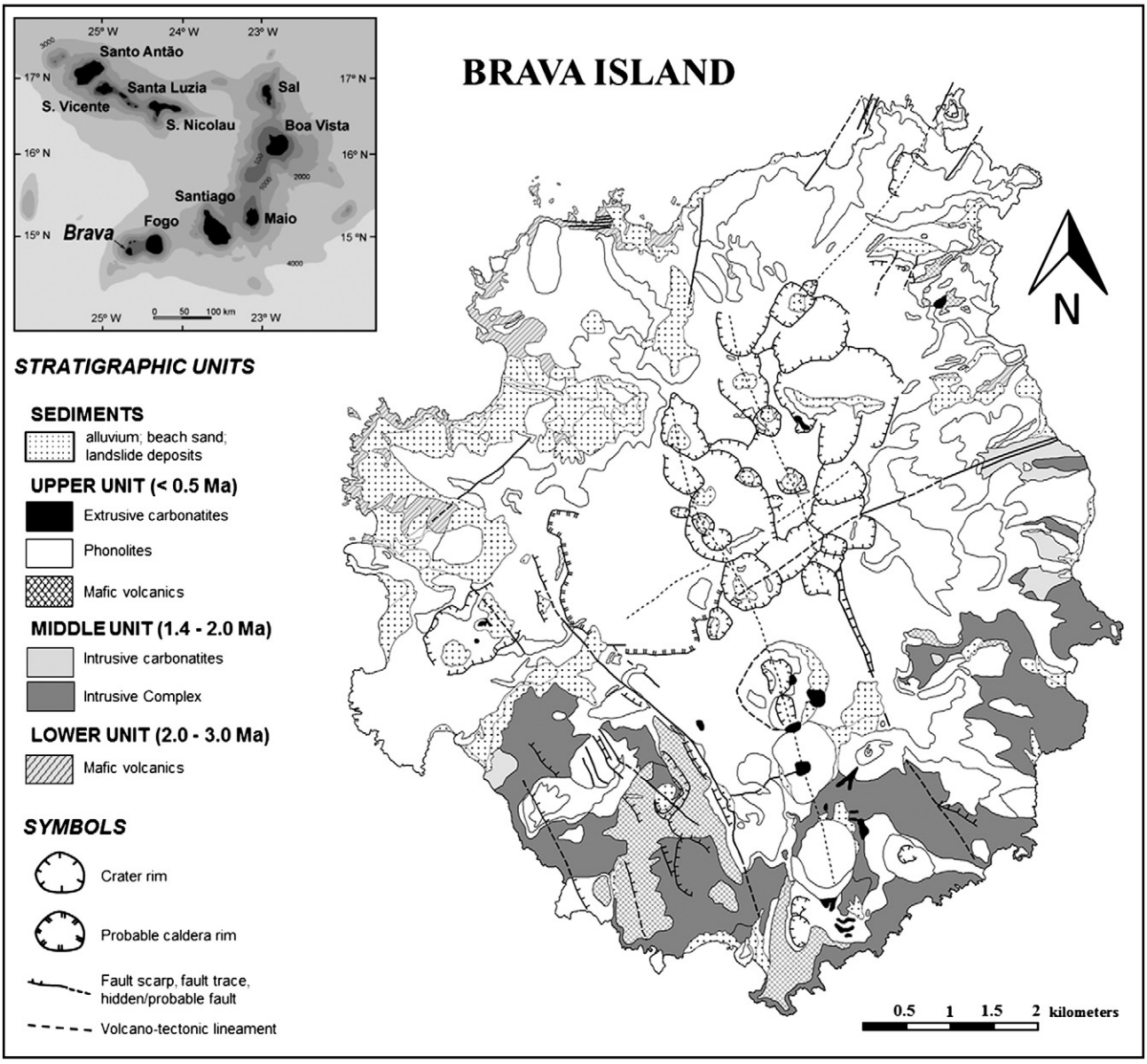


**Fig. 1.** Location of Brava in Cape Verde archipelago (inset) and geological sketch representing main stratigraphic units and structures. Simplified from Madeira et al. (2010).

a flux of lithium metaborate and lithium tetraborate and then fused in an induction furnace. The obtained melt was immediately poured into a solution of 5% nitric acid containing an internal standard and mixed continuously until completely dissolved (~30 min).

Major oxide content was analyzed using inductively coupled plasma-optical emission spectrometry (ICP-OES) using a Thermo Jarrell-Ash ENVIRO II ICP and/or Spectro Cirros ICP. Trace element contents were obtained using inductively coupled plasma-mass spectrometry (ICP-MS) on a Perkin Elmer SCIEX ELAN 6000, 6100 or 9000 ICP/MS (with the exception of Sc, V, Ba and Sr, which were obtained by ICP-OES). Fluorine was analyzed using the ion-selective electrode technique (ISE), and $CO_2$ was determined by coulometry. For ICP-OES and ICP-MS analyses, calibration was performed using seven prepared USGS and CANMET certified reference materials. One of the seven standards was used during the analysis of every group of 10 samples to monitor instrumental drift.

Duplicate measurements of samples give an estimate of the total reproducibility of our analyses. The reproducibility is better than 3 relative-% for major element contents (i.e., $SiO_2$, $TiO_2$, $Al_2O_3$, $Fe_2O_3$, MnO, MgO, CaO, $Na_2O$, $K_2O$ and $P_2O_5$), 7 relative-% for rare earth elements, 5 relative-% for elements that are generally highly incompatible in an oceanic context (i.e., Rb, Ba, U and Th), and 6 relative-% for $CO_2$. See Supplementary material (S2) for analyses of standard reference materials and detection limits for each element. Additional information on the analytical procedures can be found at http://www.actlabs.com.

Sr–Nd–Pb isotopic analyses were also performed on representative silicate and carbonatite powdered whole-rock samples including nephelinites, melilite nephelinites and one basanite from the Lower Unit, nepheline syenites and magnesiocarbonatites from the Middle Unit and nephelinites, phonotephrites and phonolites from the Upper Unit.

For Sr and Nd, the whole-rock silicate samples (100 mg) were leached with hot 6 M HCl (3 ml, 75 °C) for 3 h, while the carbonatite samples were treated with distilled water (75 °C for 3 h). After removal of the supernatant and drying of the samples at 75 °C on hot plates, dissolution of the residue was performed in Savillex beakers with a mixture of 2 ml HF (29 M) + 0.5 ml $HNO_3$ (14 M) at 75 °C for 24 h (Savillex

closed). A mixture of 0.2 ml $HClO_4$ (12 M) + 3 ml $HNO_3$ (7 M) was added to dissolve any residual fluorides. This mixture was first evaporated on a hot plate (at 50 °C for 3 days and 95 °C for 6 h) and then in an epiradiator (for 2 h), which was followed by the addition of 5 ml of distilled HCl (6 M) at 75 °C for 24 h and additional drying of the samples at 65 °C on hot plates. The residue was recovered in 10 ml HCl (1.25 M) and centrifuged for 10 min. Sr and Nd separations were performed with the "cascade" column procedure (Sr Spec, True Spec and Ln Spec columns) described by Pin and Bassin (1992) and Pin et al. (1994) after most of the iron was removed through an AG50X4 column. A mixture of $HNO_3$ (5 M) + HF (0.1 M) was used to collect Sr and REE. Sr and Nd blanks for the complete procedure were <0.5 ng and <0.2 ng, respectively. To test for possible seawater contamination, four samples of leached and unleached powders were analyzed, as were the leachates from the above-mentioned leaching process (see Section 5.1; Table 3).

Sr–Nd isotopic measurements were performed at the Laboratoire Magmas et Volcans (Clermont-Ferrand, France) using a Finnigan Triton mass spectrometer (TIMS) equipped with nine Faraday detectors and operating in the static multicollection mode with relay matrix rotation (also called virtual amplifier). Sr samples were loaded on double W filaments with 1 μl $H_3PO_4$ (3 M), and Nd samples were loaded on the same type of filaments with 1 μl $H_3PO_4$ (1 M). $^{87}Sr/^{86}Sr$ measurements were mass-fractionation-corrected to $^{86}Sr/^{88}Sr = 0.1194$ and normalized to $^{87}Sr/^{86}Sr = 0.71025$ for the NIST SRM987 standard after correcting for $^{87}Rb$ interference. Nd isotopic ratios were mass-fractionation-corrected to $^{146}Nd/^{144}Nd = 0.7219$ and normalized to $^{143}Nd/^{144}Nd = 0.51196$ for the Rennes-AMES standard (Chauvel and Blichert-Toft, 2001). Repeated analyses of the two standards yielded $^{87}Sr/^{86}Sr = 0.710246 \pm 0.000005$ (2σ, n = 16) and $^{143}Nd/^{144}Nd = 0.511961 \pm 0.000007$ (2σ, n = 12). A typical run consisted of at least nine blocks of ten cycles to allow a full rotation of the virtual amplifier system.

For Pb analyses, we followed the procedure described in Manhès et al. (1978) and Millet et al. (2009). Dissolution was performed for 150 mg of unleached powdered sample material in Savillex beakers in a mixture of 3 ml HF (29 M) + 0.3 ml $HNO_3$ (16 M) at 100 °C for 24 h (Savillex closed). Then, 3 ml HBr (8 M) was added to induce the formation of soluble lead bromide, which allowed the nearly total recovery of Pb from the residue. The mixture was evaporated on a hot plate (at 75 °C) followed by the addition of 6 ml of diluted HBr (0.8 M) at 50 °C for 12 h. Chemical separation was conducted using clean pipette tip columns filled with ~0.2 ml of AG1-X8 resin (100–200 mesh). Sample loading and elution of the matrix were performed in 0.8 M HBr, and Pb collection was undertaken in 2 ml of 7 M HCl. Total procedural Pb blanks (including acid digestion) were ~15 pg.

Pb isotopic measurements were performed at the School of Geography, Environment and Earth Sciences of Victoria University (Wellington, New Zealand), on an Nu Plasma MC-ICP-MS. Mass discrimination was corrected using sample-standard bracketing of samples with NBS981 with admitted values of $^{206}Pb/^{204}Pb = 16.9416$, $^{207}Pb/^{204}Pb = 15.5000$ and $^{208}Pb/^{204}Pb = 36.7262$ (Baker et al., 2004). The accuracy of Pb isotopic measurements was assessed by analysis of the JB2 rock standard. The average values thus obtained were $^{206}Pb/^{204}Pb = 18.3423$, $^{207}Pb/^{204}Pb = 15.5614$ and $^{208}Pb/^{204}Pb = 38.2760$, within the error of Baker et al. (2004). Reproducibility of the mass spectrometric measurement was assessed with repeated measurements of the JB2 standard (2σ, n = 11) and yielded 136 ppm, 205 ppm and 223 ppm for $^{206}Pb/^{204}Pb$, $^{207}Pb/^{204}Pb$ and $^{208}Pb/^{204}Pb$, respectively. All sample duplicates fell within these uncertainties.

## 4. Results

This paper is part of a project that previously produced elemental and isotopic (Sr and Nd) results for Brava Island (Doucelance et al., 2010; Madeira et al., 2010; Mourão et al., 2010). These data, as well as new elemental (70 samples) and isotopic (Sr and Nd: 25 samples; Pb: 30 samples) data, are presented in Tables 1 and 2 and in Supplementary material S3.

### 4.1. Major and trace element compositions and rock systematics

Major and trace element data of selected samples are reported in Table 1. Silicate rocks from Brava are alkaline, with ultrabasic to intermediate compositions ($SiO_2$ = 35.91 to 57.84 wt.% on an anhydrous basis). Mafic volcanic rocks from the Lower Unit are highly $SiO_2$-undersaturated, and almost all of these samples plot in the basanite and foidite fields ($SiO_2$ = 36.70 to 44.73 wt.%; Fig. 2A). Following the IUGS classification (Le Maître, 2002), these samples predominantly include melilite nephelinites (normative larnite up to 8.6 wt.%), melanephelinites, nephelinites and basanites. The intrusive Middle Unit consists of an association of alkaline silicate rocks and carbonatites, the former spanning ultramafic (pyroxenites) to salic rocks (nepheline-syenites), through melteigite–ijolite–urtite types. The Upper Unit is typically bimodal. The melanocratic pole (basic and ultrabasic; $SiO_2$ < 46.09 wt.%) is composed of nephelinites (normative nepheline up to 27.4%; normative olivine up to 24.2%), basanites, tephrites and phonotephrites while meso-leucocratic rocks (basic and intermediate; $SiO_2$ = 45.96 to 57.84 wt.%) include nephelinites (or phonolitic nephelinites following the nomenclature of Cox et al., 1979) and phonolites (Fig. 2A). These nephelinites are distinct from melanocratic varieties as they lack normative olivine.

Carbonatitic rocks present a large range of CaO and MgO documenting the occurrence of two groups (Fig. 2B): calciocarbonatites (sövites and alvikites) with high CaO (>37 wt.%) and low MgO (<6 wt.%), and magnesiocarbonatites with lower CaO (<32 wt.%) and higher MgO (>15 wt.%). Calciocarbonatite rocks are represented in the Upper and Middle units, while magnesiocarbonatites occur only in the Middle Unit.

With more than 90% of its area covered by phonolitic rocks, it is unarguable that magmatic evolution processes were more important at Brava than in the majority of Cape Verde islands. Despite the fact that the study of these processes is beyond the scope of this paper, we emphasize that the wide concentration range of transition elements and magnesium is compatible with the earliest fractionation of olivine and clinopyroxene (Ni<20 to 360 ppm; Cr<5 to 1030 ppm; and Mg# = 12 to 74). It should be noted, however, that some of the highest Mg# values and Ni and Cr contents were obtained in highly porphyric rocks and, therefore, argue in favor of the occurrence of cumulative processes.

As may be expected from their highly $SiO_2$-undersaturated character, even the least evolved volcanic rocks and dikes from Brava show a high abundance of the elements thought to be incompatible during mantle processes (see Fig. 3 and Table 1). In addition, rare earth element (REE) patterns (Fig. 4) are strongly fractionated; the samples representative of relatively primitive magmas (Ni>100 ppm) present chondrite normalized La/Yb>13.90. Furthermore, chondrite normalized Tb/Yb ratios (>2.59) for the same set of samples suggest the presence of garnet as a residual phase during partial melting (e.g., George and Rogers, 2002). Nepheline syenites and phonolites, the most evolved silicate rocks from Brava, are strongly enriched in some LILE (e.g., Cs, Rb, Ba and K) and HFSE (e.g., Zr and Hf) but are depleted in Ti compared with coeval (*s.l.*) mafic rocks (Fig. 3).

Carbonatites are often highly enriched in some incompatible elements (e.g., Ba up to 6851 ppm; La up to 1080 ppm; Sr down to 2151 ppm) and present significant Zr, Hf and Ti negative anomalies on multi-element normalized plots (Fig. 5; Table 1; Supplementary material S3). REE patterns distinguish between magnesio- and calciocarbonatites, with the latter presenting somewhat concave upward patterns (Fig. 5), reflecting dissimilar chondrite-normalized Gd/Yb ratios (magnesiocarbonatites: 7.04 ± 0.94, 2σ; calciocarbonatites: 3.07 ± 1.67, 2σ).

**Table 1**
Major (wt.%) and trace element (ppm) analyses of representative samples of silicate rocks and magnesium carbonatites from Brava Island. All elemental analyses, including of intrusive and extrusive calciocarbonatites, are listed in Supplemental material S3.

| Sample | Lower unit | | Middle unit | | | | | | Upper unit | | | |
|---|---|---|---|---|---|---|---|---|---|---|---|---|
| | Melilite nephelinite | | Clino-pyroxenite | Ijolite *s.l.* | Nepheline syenite | | Magnesiocarbonatite | | Nephelinite | Tephrite | Phonolites *s.l.* | |
| | CY173 | CY174 | CY55 | CY178 | CY154 | CY48 | CY110 | CY111 | CY31 | CY45 | CY205 | CY27 |
| *Major elements (wt.%)* | | | | | | | | | | | | |
| $SiO_2$ | 39.23 | 38.27 | 36.20 | 35.12 | 45.02 | 52.51 | 1.47 | 1.58 | 38.08 | 42.05 | 46.65 | 50.41 |
| $TiO_2$ | 4.453 | 5.033 | 5.528 | 2.885 | 1.292 | 0.394 | 0.013 | 0.154 | 4.255 | 3.429 | 1.982 | 0.404 |
| $Al_2O_3$ | 11.49 | 11.89 | 8.30 | 15.88 | 21.38 | 16.93 | 0.14 | 0.32 | 13.03 | 14.93 | 18.51 | 21.46 |
| $Fe_2O_3^t$ | 15.01 | 15.10 | 19.79 | 9.59 | 5.72 | 7.47 | 4.03 | 8.11 | 12.99 | 11.20 | 7.56 | 3.40 |
| MnO | 0.208 | 0.201 | 0.247 | 0.271 | 0.201 | 0.374 | 0.584 | 0.612 | 0.215 | 0.201 | 0.192 | 0.199 |
| MgO | 8.38 | 6.97 | 10.91 | 2.71 | 1.49 | 0.20 | 16.44 | 16.78 | 6.44 | 5.54 | 2.30 | 0.95 |
| CaO | 13.73 | 13.65 | 14.37 | 14.01 | 7.13 | 4.68 | 30.66 | 28.88 | 12.91 | 10.75 | 6.86 | 2.87 |
| $Na_2O$ | 3.12 | 2.85 | 1.64 | 8.49 | 9.66 | 8.55 | 0.08 | 0.15 | 5.06 | 3.98 | 7.97 | 10.28 |
| $K_2O$ | 1.15 | 1.40 | 0.95 | 2.65 | 4.75 | 5.66 | 0.08 | 0.22 | 1.21 | 1.71 | 3.74 | 6.99 |
| $P_2O_5$ | 0.63 | 0.76 | 0.07 | 1.44 | 0.39 | 0.17 | 3.89 | 3.25 | 1.10 | 0.59 | 0.50 | 0.17 |
| $CO_2$ | n.a. | n.a. | n.a. | n.a. | n.a. | n.a. | 43.1 | 40.8 | n.a. | n.a. | n.a. | n.a. |
| F | n.a. | n.a. | n.a. | n.a. | n.a. | n.a. | 0.35 | 0.23 | n.a. | n.a. | n.a. | n.a. |
| LOI | 3.33 | 4.40 | 0.29 | 5.44 | 3.44 | 3.60 | 40.97 | 38.1 | 3.47 | 4.41 | 3.90 | 3.23 |
| Total | 100.70 | 100.50 | 98.29 | 98.49 | 100.50 | 100.50 | 98.35 | 98.17 | 98.77 | 98.80 | 100.20 | 100.30 |
| Mg# | 56.62 | 51.90 | 55.35 | 43.22 | 41.19 | 7.22 | 88.99 | 80.39 | 53.68 | 55.45 | 44.99 | 44.49 |
| *Trace elements (ppm)* | | | | | | | | | | | | |
| Sc | 30 | 26 | 52 | 1 | 2 | 3 | 2 | 3.1 | 18 | 21 | 5 | 1 |
| V | 431 | 488 | 504 | 319 | 179 | 136 | 9 | 59 | 416 | 313 | 212 | 63 |
| Cr | 228 | 50 | <5 | <5 | <5 | <5 | <5 | <5 | 28 | 92 | <5 | <5 |
| Co | 57 | 59 | 74 | 10 | 5 | 2 | 5 | 17 | 42 | 27 | 14 | <1 |
| Ni | 200 | 140 | 90 | 40 | <20 | <20 | <20 | <20 | 80 | 80 | <20 | <20 |
| Cu | 130 | 100 | 90 | 20 | 10 | <10 | <10 | <10 | 70 | 60 | 20 | <10 |
| Zn | 230 | 240 | 180 | 200 | 100 | 200 | 40 | 80 | 220 | 200 | 180 | 140 |
| Ga | 23 | 24 | 20 | 20 | 31 | 54 | 4 | 6 | 24 | 28 | 30 | 33 |
| Ge | 1.4 | 1.4 | 1.5 | 1.4 | 1.1 | 1.1 | <0.5 | <0.5 | 1.5 | 1.5 | 1.2 | 1.0 |
| Rb | 21 | 25 | 9 | 70 | 125 | 210 | 4 | 8 | 40 | 63 | 46 | 205 |
| Sr | 1082 | 687 | 388 | 1812 | 1347 | 1604 | 4959 | 6076 | 1423 | 1201 | 1056 | 1012 |
| Y | 34.7 | 34.6 | 22.9 | 56.0 | 21.3 | 19.0 | 67.4 | 55.7 | 35.4 | 31.1 | 28.5 | 21.7 |
| Zr | 309 | 292 | 258 | 476 | 508 | 2640 | 71 | 76 | 313 | 351 | 452 | 682 |
| Nb | 70.5 | 67.1 | 42.2 | 195.0 | 130.0 | 783.0 | 5.6 | 37.6 | 80.3 | 83.3 | 106.0 | 95.6 |
| Cs | 0.2 | 0.3 | <0.1 | 0.4 | 0.4 | 4.2 | <0.1 | 0.1 | 0.6 | 1.0 | 1.4 | 1.9 |
| Ba | 475 | 514 | 304 | 414 | 1815 | 424 | 75 | 70 | 916 | 1593 | 1696 | 2095 |
| La | 57.6 | 58.7 | 47.9 | 113.0 | 41.2 | 10.2 | 159 | 148 | 69.7 | 63.6 | 77.7 | 59.6 |
| Ce | 124.0 | 125.0 | 104.0 | 229.0 | 92.9 | 20.0 | 397 | 373 | 147.0 | 126.0 | 147.0 | 99.4 |
| Pr | 14.6 | 14.9 | 12.3 | 27.8 | 11.0 | 2.1 | 51.5 | 48.8 | 17.0 | 13.9 | 15.6 | 8.9 |
| Nd | 59.6 | 62.7 | 50.2 | 104.0 | 41.7 | 7.1 | 225 | 211 | 67.9 | 54.7 | 53.8 | 27.5 |
| Sm | 11.9 | 12.5 | 9.6 | 18.8 | 7.3 | 1.3 | 40.6 | 38.2 | 12.5 | 9.8 | 8.9 | 4.1 |
| Eu | 3.90 | 4.17 | 3.22 | 6.28 | 2.35 | 0.49 | 12.3 | 11.4 | 4.03 | 3.33 | 2.81 | 1.35 |
| Gd | 11.3 | 11.9 | 8.3 | 16.9 | 5.9 | 1.5 | 30.6 | 27.6 | 11.5 | 9.4 | 6.9 | 3.0 |
| Tb | 1.55 | 1.58 | 1.18 | 2.41 | 0.88 | 0.31 | 4.06 | 3.65 | 1.52 | 1.26 | 1.03 | 0.56 |
| Dy | 7.58 | 7.85 | 5.72 | 12.30 | 4.56 | 2.40 | 17.8 | 15.7 | 7.51 | 6.30 | 5.53 | 3.51 |
| Ho | 1.31 | 1.33 | 0.94 | 2.10 | 0.76 | 0.58 | 2.76 | 2.38 | 1.28 | 1.12 | 0.97 | 0.71 |
| Er | 3.32 | 3.27 | 2.36 | 5.41 | 2.16 | 2.18 | 6.27 | 5.2 | 3.27 | 2.94 | 2.65 | 2.27 |
| Tm | 0.438 | 0.429 | 0.294 | 0.688 | 0.301 | 0.462 | 0.699 | 0.589 | 0.432 | 0.400 | 0.381 | 0.362 |
| Yb | 2.58 | 2.50 | 1.67 | 3.75 | 2.03 | 3.88 | 3.51 | 2.84 | 2.44 | 2.35 | 2.33 | 2.44 |
| Lu | 0.354 | 0.335 | 0.223 | 0.521 | 0.354 | 0.722 | 0.423 | 0.332 | 0.342 | 0.320 | 0.330 | 0.382 |
| Hf | 7.9 | 7.4 | 8.5 | 10.4 | 9.4 | 37.5 | 1 | 1.1 | 7.4 | 7.8 | 7.9 | 10.4 |
| Ta | 4.77 | 4.73 | 2.46 | 12.40 | 5.01 | 4.16 | 2.86 | 22.5 | 6.04 | 4.96 | 4.61 | 2.43 |
| Th | 4.75 | 5.19 | 2.21 | 3.74 | 1.87 | 1.80 | 4.12 | 3.07 | 4.82 | 6.49 | 8.91 | 11.80 |
| U | 1.41 | 1.23 | 0.75 | 1.92 | 0.50 | 3.82 | 4.19 | 24.3 | 2.56 | 1.81 | 1.28 | 1.74 |

n.a., not analyzed; Mg# = $[Mg^{2+}/(Mg^{2+}+Fe^{2+})]*100$. For silicate rocks, $Fe^{3+}/Fe^{2+}$ ratios were calculated as recommended by Middlemost (1989) for different rock types. For carbonatitic rocks, Mg# was calculated assuming all Fe as $Fe^{2+}$.

### 4.2. Sr–Nd–Pb isotopic composition

Sr, Nd and Pb isotopic ratios obtained on representative samples from Brava are presented in Table 2 and shown in Fig. 6, where, for comparison, they are plotted in conjunction with the fields defined by silicate rocks from the northern and southern Cape Verde islands. Recently published, but not discussed, Brava analyses by Hildner et al. (2011) are also plotted. No significant difference is observed between the two data sets. Hereafter, the discussion will be based on the data presented in Table 2.

Considering the young age of the rocks (<3 Ma) and the low decay constants for the Rb–Sr and Sm–Nd isotope systems, radiogenic ingrowth is not considered significant and the data are presented and discussed without age correction. For example, sample CY-8 (1.99 ± 0.09 Ma; Madeira et al., 2010) presents initial $^{87}Sr/^{86}Sr = 0.703311$ and $^{143}Nd/^{144}Nd = 0.512909$ which, within error, are indistinguishable from those presented in Table 2. Due to the absence of accurate Pb elemental analyses, we are not able to estimate the initial Pb isotope ratios. If the ratios for silicate rocks are expected to be identical, within error, to the measured values, the initial values of at least some of the carbonatites must be significantly lower (second decimal place) due to their high U and Th contents (up to 24.3 and 32.1 ppm, respectively) and the high U/Pb and Th/Pb ratios reported by Hoernle et al. (2002) for Cape Verde carbonatites.

**Table 2**
Sr–Nd–Pb isotopic composition of Lower, Middle and Upper units from Brava Island.

| | $^{87}Sr/^{86}Sr$ | $^{143}Nd/^{144}Nd$ | $^{206}Pb/^{204}Pb$ | $^{207}Pb/^{204}Pb$ | $^{208}Pb/^{204}Pb$ | $^{208}Pb^*/^{206}Pb^*$ | $\kappa_{Pb}$ | $\kappa$ |
|---|---|---|---|---|---|---|---|---|
| *Lower unit* | | | | | | | | |
| Mafic rocks | | | | | | | | |
| CY-8 | 0.703315 (6) | 0.512911 (5) | 20.017 (1) | 15.620 (1) | 39.194 (4) | 0.907 | 3.69 | 3.54 |
| CY-11 | 0.703281 (14) | 0.512906 (3) | 20.251 (2) | 15.645 (2) | 39.364 (5) | 0.904 | 3.67 | 3.20 |
| CY-19 | 0.703315 (6) | 0.512903 (5) | 19.873 (2) | 15.616 (1) | 39.153 (4) | 0.916 | 3.72 | 3.46 |
| CY-25 | 0.703183 (6) | 0.512909 (3) | 19.634 (2) | 15.607 (1) | 39.084 (4) | 0.930 | 3.78 | 1.63 |
| CY-82 | 0.703251 (6) | 0.512898 (5) | 19.792 (2) | 15.611 (2) | 39.190 (5) | 0.926 | 3.76 | 4.05 |
| CY-165 | 0.703352 (7) | 0.512915 (5) | 19.847 (1) | 15.615 (1) | 39.131 (3) | 0.916 | 3.72 | 4.63 |
| CY-174 | 0.703274 (7) | 0.512905 (4) | 20.020 (1) | 15.613 (1) | 39.205 (3) | 0.908 | 3.69 | 4.36 |
| *Middle unit* | | | | | | | | |
| Nepheline syenite | | | | | | | | |
| CY-39 | 0.703377 (7) | 0.512905 (6) | 19.905 (1) | 15.631 (5) | 39.224 (4) | 0.920 | 3.74 | 2.79 |
| CY-148 | 0.703354 (7) | 0.512912 (8) | 19.937 (2) | 15.630 (2) | 39.216 (5) | 0.916 | 3.72 | 4.83 |
| CY-154 | 0.703348 (7) | 0.512910 (4) | 19.947 (2) | 15.631 (2) | 39.213 (4) | 0.915 | 3.72 | 3.86 |
| CY-179 | 0.703372 (8) | 0.512913 (3) | 19.988 (2) | 15.639 (2) | 39.266 (5) | 0.917 | 3.72 | 0.54 |
| Intrusive calciocarbonatites | | | | | | | | |
| BR-15 | 0.703340 (12) | 0.512908 (7) | 19.761 (1) | 15.623 (1) | 39.073 (3) | 0.918 | 3.73 | 6.87 |
| BR-23 | 0.703356 (8) | 0.512911 (6) | 19.828 (2) | 15.615 (2) | 39.144 (9) | 0.919 | 3.73 | 0.65 |
| Intrusive magnesiocarbonatites | | | | | | | | |
| CY-114 | 0.703401 (7) | 0.512897 (5) | 20.004 (2) | 15.630 (2) | 39.268 (5) | 0.915 | 3.72 | 6.43 |
| CY-115 | 0.703346 (6) | 0.512893 (3) | 20.147 (1) | 15.647 (5) | 39.282 (4) | 0.905 | 3.67 | 2.05 |
| CY-117 | 0.703396 (7) | 0.512899 (4) | 20.040 (1) | 15.633 (1) | 39.247 (3) | 0.910 | 3.70 | 0.51 |
| *Upper unit* | | | | | | | | |
| Mafic rocks | | | | | | | | |
| CY-31 | 0.703631 (8) | 0.512783 (5) | 19.464 (1) | 15.589 (1) | 39.154 (4) | 0.953 | 3.87 | 1.95 |
| CY-32 | 0.703701 (7) | 0.512776 (4) | 19.254 (2) | 15.568 (1) | 39.038 (3) | 0.961 | 3.90 | 4.70 |
| CY-99 | 0.703621 (8) | 0.512795 (6) | 19.556 (1) | 15.587 (1) | 39.133 (4) | 0.942 | 3.83 | 4.70 |
| CY-200 | 0.703631 (6) | 0.512788 (6) | 19.430 (1) | 15.588 (1) | 39.134 (3) | 0.954 | 3.88 | 4.80 |
| Phonolites *s.l.* | | | | | | | | |
| CY-27 | 0.703602 (6) | 0.512807 (6) | 19.433 (1) | 15.594 (1) | 39.144 (3) | 0.955 | 3.88 | 7.01 |
| CY-80 | 0.703654 (7) | 0.512790 (13) | 19.359 (2) | 15.584 (2) | 39.115 (4) | 0.959 | 3.89 | 3.00 |
| CY-138 | 0.703662 (7) | 0.512801 (7) | 19.622 (1) | 15.596 (1) | 39.226 (2) | 0.945 | 3.84 | 3.31 |
| CY-188 | 0.703668 (8) | 0.512783 (4) | 19.257 (1) | 15.570 (1) | 39.037 (3) | 0.961 | 3.90 | 3.02 |
| CY-193 | 0.703582 (6) | 0.512800 (6) | 19.555 (3) | 15.593 (3) | 39.175 (8) | 0.946 | 3.84 | 3.79 |
| CY-197 | 0.703571 (7) | 0.512806 (4) | 19.655 (2) | 15.598 (2) | 39.209 (7) | 0.941 | 3.82 | 5.26 |
| CY-215 | 0.703682 (6) | 0.512767 (6) | 19.393 (1) | 15.578 (1) | 39.102 (4) | 0.954 | 3.88 | 5.09 |
| Extrusive calciocarbonatites | | | | | | | | |
| CY-95 | 0.703595 (6) | 0.512792 (5) | 19.657 (2) | 15.602 (1) | 39.250 (4) | 0.944 | 3.84 | 6.42 |
| CY-222 | 0.703557 (7) | 0.512816 (8) | 19.677 (1) | 15.596 (1) | 39.243 (4) | 0.942 | 3.83 | 14.22 |
| CY-238 | 0.703580 (6) | 0.512801 (6) | 19.660 (1) | 15.603 (1) | 39.258 (3) | 0.945 | 3.84 | 7.56 |

Sr and Nd isotopic ratios for samples BR-15 and BR-23 are from Doucelance et al. (2010).
Numbers in parentheses are within run 2σ errors referring to the last significant digits.
$^{208}Pb^*/^{206}Pb^* = [(^{208}Pb/^{204}Pb)meas - (^{208}Pb/^{204}Pb)_{CD}]/ [(^{206}Pb/^{204}Pb)meas - (^{206}Pb/^{204}Pb)_{CD}]$, where *meas* denotes measured and *CD* is the Pb isotopic composition in Canyon Diablo troilite ($^{206}Pb/^{204}Pb = 9.3066$ and $^{208}Pb/^{204}Pb = 29.475$; Chen and Wasserburg, 1983).
$\kappa_{Pb} = (^{208}Pb^*/^{206}Pb^*)\ [(e^{(\lambda 238T)} - 1)/(e^{(\lambda 232T)} - 1)]$, where λ238 and λ232 are decay constants of $^{238}Pb$ ($1.55 \times 10{-}10\ yr^{-1}$) and $^{232}Th$ ($4.95 \times 10{-}11\ yr^{-1}$), respectively, T = 4.55 Ga (Galer and O'Nions, 1985; Allègre et al., 1986).
κ: $^{232}Th/^{238}U$ atomic ratio derived from elemental Th and U concentrations.

In contrast to the other Cape Verde islands where a continuous range is usually observed in the $^{143}Nd/^{144}Nd$ vs. $^{87}Sr/^{86}Sr$ diagram, Brava is clearly characterized by two distinct groups of isotopic compositions (Fig. 6A). Silicate rocks from the Upper Unit show $^{87}Sr/^{86}Sr$ ratios between 0.703571 and 0.703701 and $^{143}Nd/^{144}Nd$ ratios between 0.512767 and 0.512807, typical of the silicate rocks cropping out from the southern islands. In contrast, the Lower and Middle units (hereafter referred to as the Basal Complex) display more radiogenic Nd (0.512898–0.512915) isotopic compositions, similar to those characterizing silicate rocks from the northern islands. However, their $^{87}Sr/^{86}Sr$ (0.703183–0.703377) are in the range where the northern and southern island fields overlap. This finding indicates that silicate magmas from the Basal Complex were derived from sources with lower time-integrated Rb/Sr and Nd/Sm ratios than those from the Upper Unit and most samples from the other southern islands.

Pb isotopic ratios are also quite distinct between stratigraphic units. The older units have higher $^{206}Pb/^{204}Pb$ (19.634–20.251) and $^{207}Pb/^{204}Pb$ (15.607–15.645) than the Upper Unit (19.254–19.655 and 15.568–15.598, respectively). However, $^{208}Pb/^{204}Pb$ values show similar ranges of variation in the Basal Complex and the Upper Unit (39.084–39.364 and 39.037–39.226, respectively). This observation indicates that throughout Brava's evolution, magmatism has sampled sources with similar time-integrated Th/Pb ratios but distinct U/Pb ratios (Fig. 6B and C).

It should also be emphasized that Brava Pb isotopic compositions are somewhat different from those displayed by other Cape Verde islands. Although most samples from the Upper Unit lie within the southern island silicate field, some samples present higher Pb-radiogenic values and extend the range of isotopic composition towards the northern islands. Therefore, this study confirms that the radiogenic end of the southern islands' compositional trend starts from a point plotting in the field of the northern islands, as observed by Millet et al. (2008). In contrast to what is observed for silicate volcanics from other southern islands (Fogo, Santiago and Maio; see Gerlach et al., 1988; Doucelance et al., 2003), all samples from the Basal Complex plot below the North Hemisphere Reference Line (NHRL; Hart, 1984) (Δ7/4 down to −4.9; Δ8/4 down to −74.7; where $\Delta 7/4 = (^{207}Pb/^{204}Pb)_{measured} - (^{207}Pb/^{204}Pb)_{NHRL}$ and $(^{206}Pb/^{204}Pb)_{NHRL} = 0.1084$

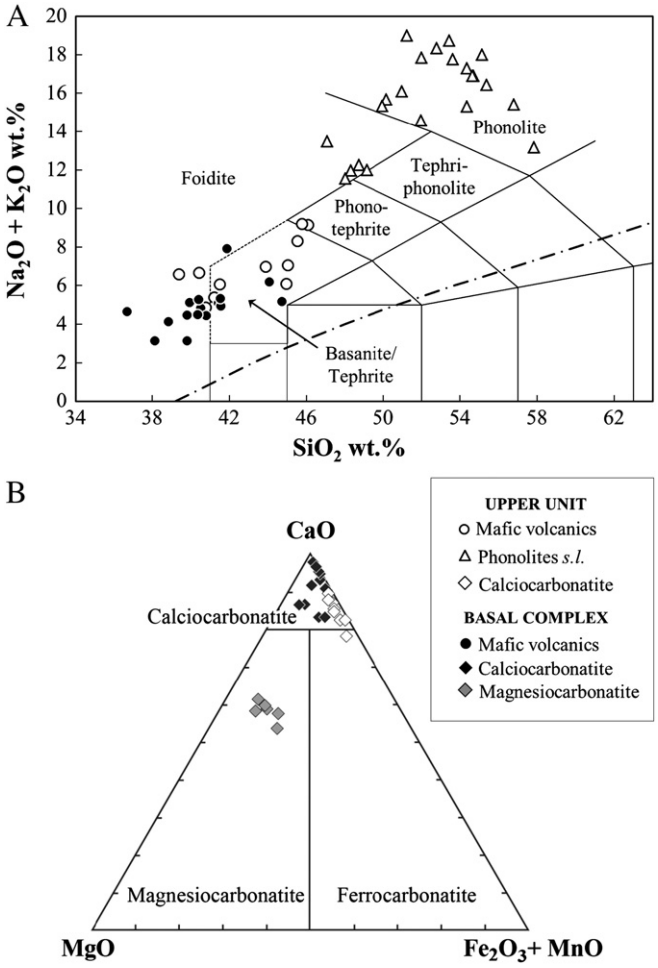


**Fig. 2.** (A) Total alkali-silica (TAS) diagram (Le Maître, 2002) for the Lower and Upper volcanics (see Section 4.1). The thick dashed line is a compositional divider between alkaline and subalkaline volcanics (MacDonald, 1968). The normative content of olivine (Ol), albite (Ab) and nepheline (Ne) was used to correctly classify samples plotted in the "foidite" and "basanite/tephrite" fields. Nephelinites: >20% normative Ne; melanephelinites: <20% normative Ne and 0–5% normative Ab; basanites: >10% normative Ol; tephrite: <10% normative Ol. Intrusive rocks from the Middle Unit (see text for details) were not plotted in this diagram designed for classification of volcanic rocks. However, we note that, if plotted, the intrusive rocks would also depict a bimodal distribution. (B) Plot of carbonatites from Brava in the diagram proposed by Woolley and Kempe (1989). Calciocarbonatites from the Upper Unit are extrusives. The other plotted carbonatites are intrusives. Oxides expressed in wt.%.

$(^{206}Pb/^{204}Pb) + 13.491$; $\Delta 8/4 = (^{208}Pb/^{204}Pb)_{measured} - (^{208}Pb/^{204}Pb)_{NHRL}$ and $(^{208}Pb/^{204}Pb)_{NHRL} = 1.209\ (^{206}Pb/^{204}Pb) + 15.627$; see Hart, 1984). Furthermore, these samples form a trend with a significantly less steep slope compared to northern island silicate volcanics, extending towards the most radiogenic $^{206}Pb/^{204}Pb$ signature (20.251) ever reported for silicate rocks in the Cape Verde archipelago and close to the highest $^{206}Pb/^{204}Pb$ reported for Cape Verde carbonatites (20.408; Hoernle et al., 2002). It is interesting to note that the neighboring Cadamosto seamount presents chemical characteristics akin to those of the Basal Complex, thus also presenting greater affinities with the northern islands (Barker et al., 2012).

Cape Verde carbonatites are considered isotopically distinct from silicate lithotypes and usually present more radiogenic $^{206}Pb/^{204}Pb$ and $^{187}Os/^{188}Os$ than associated silicate rocks (Hoernle et al., 2002; Jørgensen and Holm, 2002; Escrig et al., 2005). In contrast to the other islands, Brava carbonatites are characterized by isotopic ratios (Table 2) similar to those described above for the coeval silicate rocks, also defining two distinct areas in the Sr–Nd–Pb isotope space as a function of age (Fig. 6).

## 5. Discussion

### 5.1. Assessing the role of exogenous contributions

Some caution is needed in interpreting OIB composition. In fact, exogenous contributions, such as assimilation during fractional crystallization (AFC; DePaolo, 1981) at crustal depths and/or post-eruption hydrothermal/meteoric alteration, may constrain the composition of magmatic rocks, as demonstrated for Cape Verde (e.g., Jørgensen and Holm, 2002; Millet et al., 2008; Barker et al., 2010). Therefore, before attributing isotopic variations to mantle source heterogeneities, it is important to evaluate potential chemical changes caused by exogenous interactions.

Silicate rocks from the Upper Unit display a significant range of $SiO_2$ content (39.39 to 57.84 wt.%), but they are characterized by near-constant $^{87}Sr/^{86}Sr$ ($0.703637 \pm 0.000082$, $2\sigma$) and $^{143}Nd/^{144}Nd$ ($0.512791 \pm 0.000025$, $2\sigma$) ratios relative to the range of variation shown by silicate rocks from the other Cape Verde islands. This observation indicates that the lithological variation within this unit is primarily a consequence of fractional crystallization from relatively homogeneous parent magma.

In contrast, in the Sr–Nd isotopic space (Fig. 6A), silicate samples from the Basal Complex develop a quasi-horizontal trend characterized by high and variable $^{87}Sr/^{86}Sr$ at relatively constant $^{143}Nd/^{144}Nd$, resulting in the plot of some of the Brava samples completely outside of the fields defined by silicate rocks from Cape Verde islands. Hildner et al. (2011) and Barker et al. (2012) described similar trends for the neighboring Brava Island and Cadamosto seamount, respectively. For the seamount, Barker et al. (2012) concluded that the high $^{87}Sr/^{86}Sr$, and also $\delta^{16}O$ and $\delta^{34}S$, resulted from assimilation of oceanic sediments (anhydrite included), explaining, for example, that samples with the highest $\delta^{16}O$ and $^{87}Sr/^{86}Sr$ are also characterized by high $SiO_2$ content.

The Sr, Nd and Pb isotopic compositions of likely crustal contaminants, such as the oceanic crust basement (Gerlach et al., 1988; Janney and Castillo, 2001; Millet et al., 2008) on which the Cape Verde islands were constructed, and local recent sediments (Hoernle et al., 1991) seem to be clearly distinct from those required to explain the composition of the studied rocks. For example, in contrast to what is observed, contamination by the altered oceanic crust would lead to the concomitant increase in $^{87}Sr/^{86}Sr$ and $^{143}Nd/^{144}Nd$ (Fig. 6A). Although the panoply of potential contaminants is huge and its entire compositional range is poorly constrained, making it difficult to completely eliminate the possibility of crustal (*s.l.*) contamination, we note that there is no systematic isotopic variation with differentiation indexes. In fact, for Brava's Lower Unit volcanics, $SiO_2$ (36.70 to 44.73 wt.%) and $^{87}Sr/^{86}Sr$ (0.703183 to 0.703352) do not observe a positive correlation (Fig. 7A), demonstrating that the observed geochemical variation cannot be ascribed to AFC processes. This finding suggests that the high $^{87}Sr/^{86}Sr$ for a given $^{143}Nd/^{144}Nd$ results at least in part from post-magmatic alteration by Nd-depleted and Sr-enriched seawater (see, for example, Shields and Veizer, 2002). This percept receives some support from the fact that at least some of the volcanic rocks of the Basal Complex clearly erupted in a submarine environment during the seamount stage of the island development (Madeira et al., 2010). Moreover, some samples are characterized by the presence of non-negligible amounts of low-temperature minerals, such as carbonates, hydroxides and phyllosilicates and by a higher scatter of Cs and Rb as compared with the behavior of the high field strength elements on the variation diagrams (not shown).

To fully answer this question, we analyzed both leached and unleached samples as well as the leachates of the more Sr-radiogenic submarine samples (CY-11 and CY-165; Table 3). The results show that their leachates are characterized by higher $^{87}Sr/^{86}Sr$ than leached or

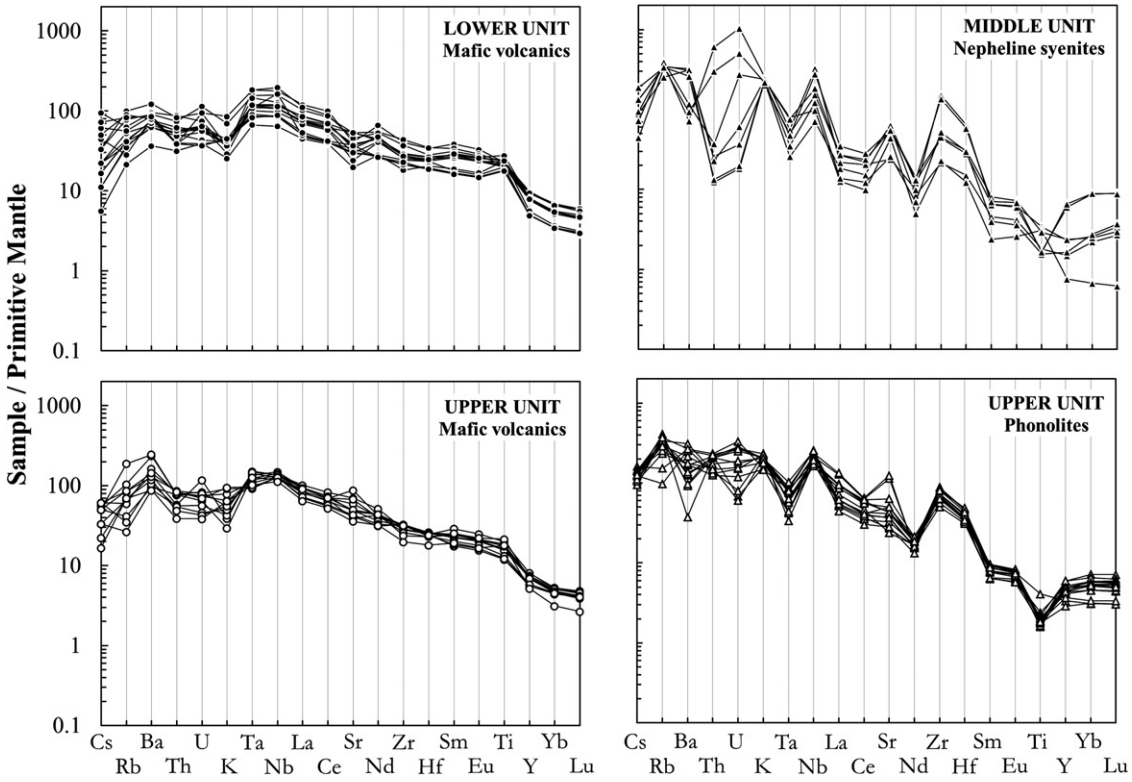


**Fig. 3.** Primitive-mantle-normalized trace elements patterns for mafic rocks from the Lower Unit, nepheline syenites from the Middle Unit, and mafic rocks and phonolites from the Upper Unit. Normalizing values are from Palme and O'Neill (2003).

unleached samples, demonstrating the occurrence of post-magmatic additions to be consistent with seawater. However, all samples were leached in order to reduce/eliminate the effect of such alteration on isotopic compositions. Taking into account that leaching was performed using the same procedure than Millet et al. (2008), which presumably erased completely the effect of seawater alteration,

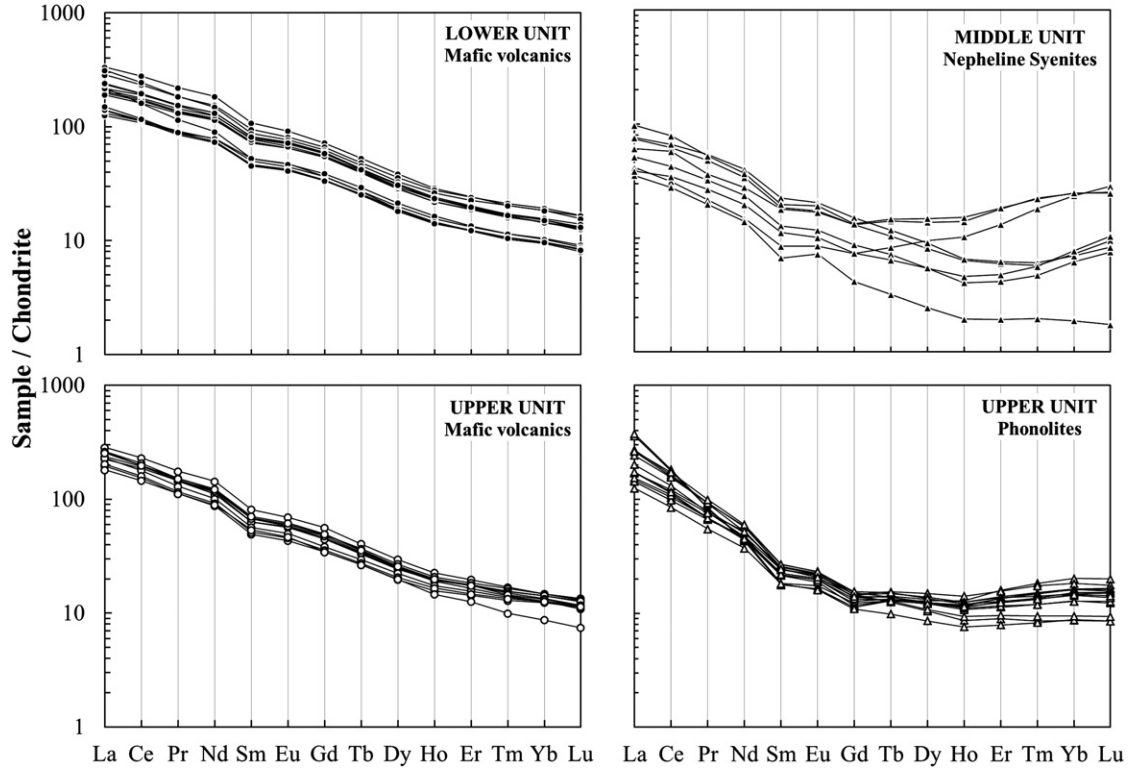


**Fig. 4.** Chondrite-normalized rare earth elements for mafic rocks from the Lower Unit, nepheline syenites and carbonatites from the Middle Unit, and mafic rocks and phonolites from the Upper Units. Normalizing values are from Palme and O'Neill (2003).

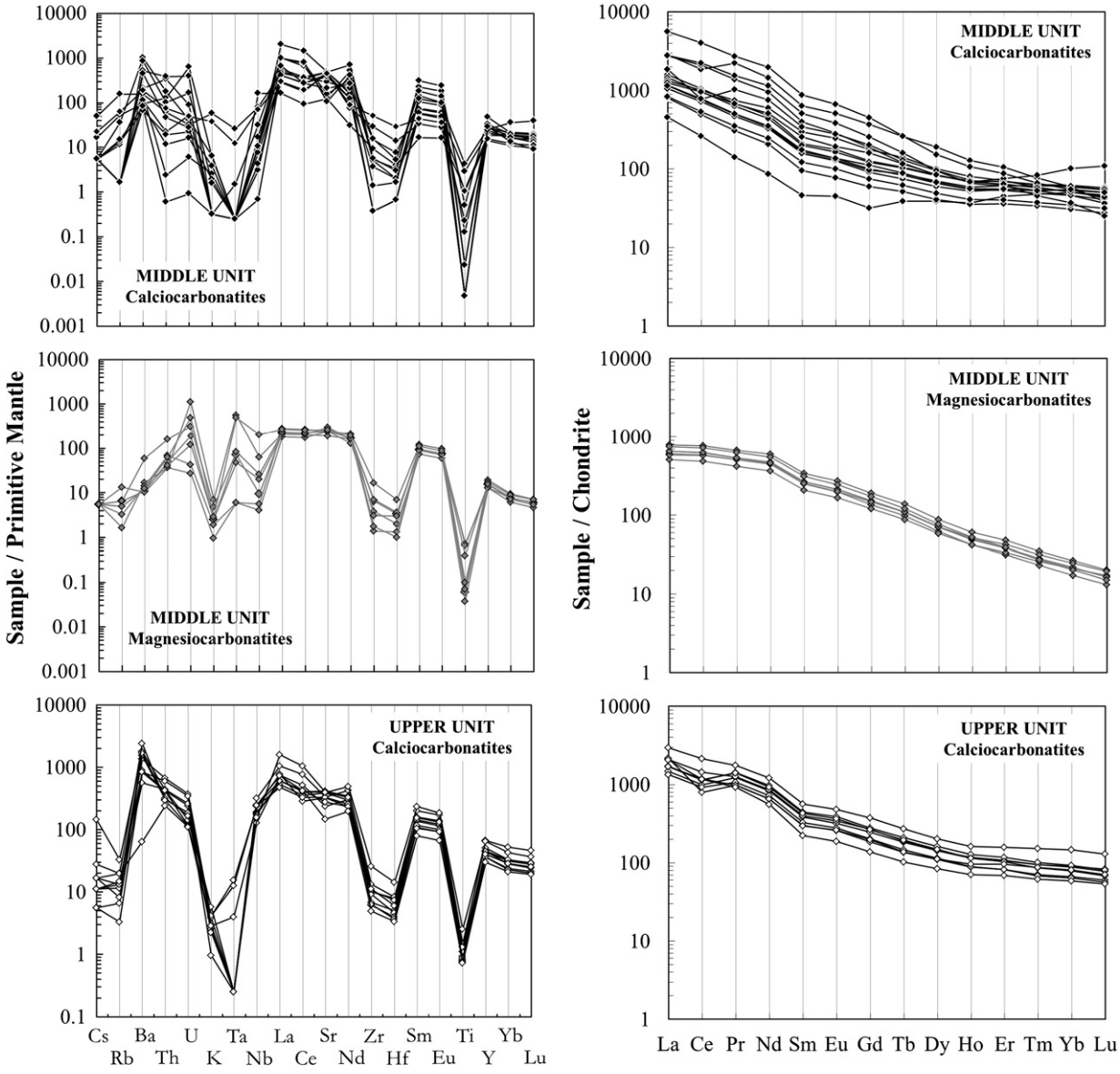


**Fig. 5.** Primitive-mantle-normalized trace element patterns and chondrite normalized rare earth elements for calcio- and magnesiocarbonatites from the Middle and Upper units. Normalizing values are from Palme and O'Neill (2003).

we would expect that analyzed samples mirror magmatic compositions, although that exogenous process cannot be completely discarded as a constrainer of the $^{87}Sr/^{86}Sr$ ratios of the volcanics from the Lower Unit. Consequently, the Sr isotopic signature of these rocks will not be considered when discussing petrogenetic processes.

We stress that seawater, characterized by negligible amounts of Nd ($<5.61\times10^{-6}$ ppm; Rickli et al., 2009), is not able to induce significant alteration in the $^{143}Nd/^{144}Nd$ of rocks with which it interacts. In contrast, it has been demonstrated that during rock alteration by seawater, no significant Pb additions occur (Chauvel et al., 1992; Kelley et al., 2003). Moreover, the young age of the studied rocks (<3 Ma; Madeira et al., 2010) makes it highly improbable that hypothetical U, Th, and Sm modifications have any effect, by radiogenic in-growth, on the Pb and Nd isotopic compositions, given that these isotopic systems are characterized by low decay constants.

Two nepheline syenite samples (CY-39 and CY-179) also present relatively high $^{87}Sr/^{86}Sr$ for a given $^{143}Nd/^{144}Nd$, contributing to the aforementioned sub-horizontal trend that distinguishes the Basal Complex from both the Upper Unit and the usual trends depicted by the Cape Verde islands. For these samples, the values obtained from unleached samples and leachates are identical, within error, showing that, for nepheline syenites, interaction with seawater did not play a significant role in the $^{87}Sr/^{86}Sr$ ratios (Table 3). For this lithotype, Sr isotopes tend to correlate positively with $SiO_2$ content, pointing to the occurrence of AFC processes, as proposed by Barker et al. (2012) to the neighboring Cadamosto seamount (Fig. 7B).

### 5.2. Identifying the Brava compositional end-members

Pb isotope linear arrays such as the ones presented by Brava (Fig. 6B and C) reflect either secondary isochrons or binary mixing lines (e.g., Chase, 1981). If the $^{207}Pb/^{204}Pb$-$^{206}Pb/^{204}Pb$ regression lines defined by Brava's Basal Complex and Upper Unit are mantle isochrones, this same situation should also be observed for the linear arrays in the $^{208}Pb/^{204}Pb$-$^{206}Pb/^{204}Pb$ space. Because during melting, Th is more incompatible than U (see Blundy and Wood, 2003 for a review), the source $\kappa$ ($^{232}Th/^{238}U$) values inferred from the measured Th and U concentrations should be higher than the time-integrated Th/U ratios calculated from $^{208}Pb^*/^{206}Pb^*$ ratios ($\kappa_{Pb}$; Galer and O'Nions, 1985). In contrast to the prediction, some Brava samples $\kappa$ were smaller than

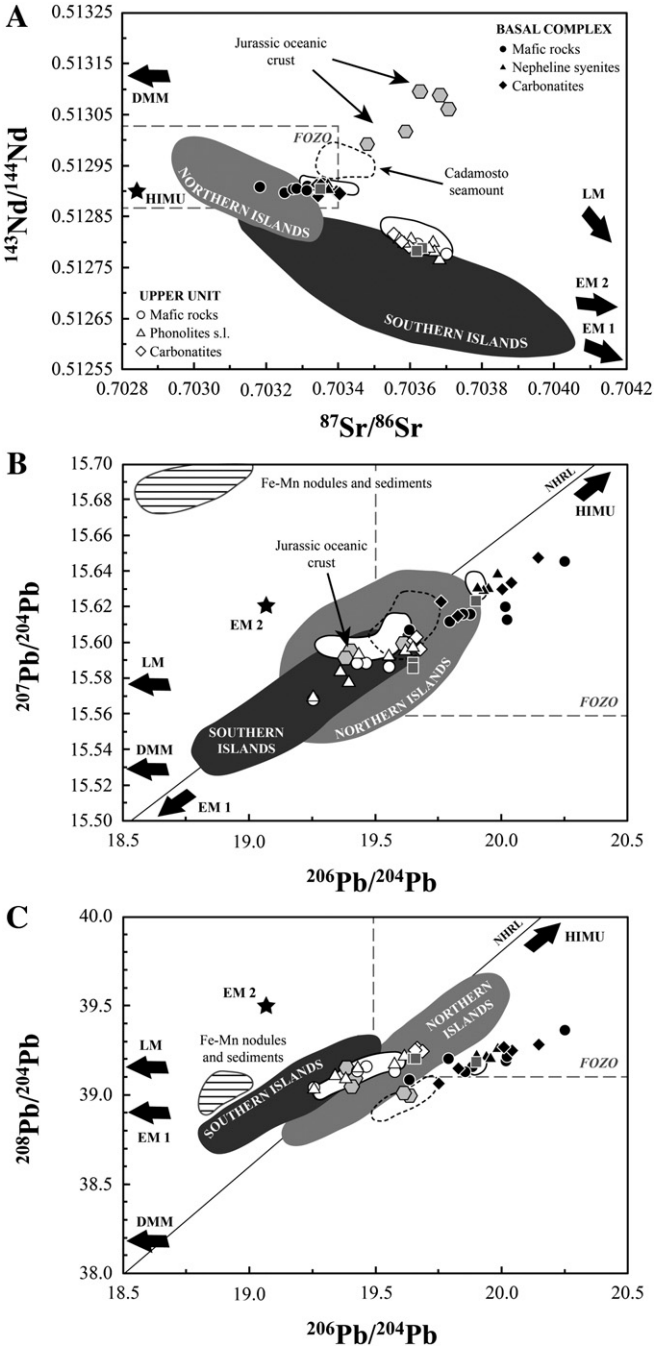


**Fig. 6.** Sr–Nd–Pb isotopic compositions for Brava intrusive and extrusive rocks. (A) $^{143}Nd/^{144}Nd$ vs. $^{87}Sr/^{86}Sr$; (B) $^{207}Pb/^{204}Pb$ vs. $^{206}Pb/^{204}Pb$; and (C) $^{208}Pb/^{204}Pb$ vs. $^{206}Pb/^{204}Pb$. Data sources: Northern Islands (Santo Antão, São Vicente and São Nicolau: Jørgensen and Holm, 2002; Holm et al., 2006; Millet et al., 2008) and Southern Islands (Fogo and Santiago: Doucelance et al., 2003; Escrig et al., 2005; Barker et al., 2010; Martins et al., 2010). Shown for comparison are Brava silicate data (basalts and phonolites; white fields) from Hildner et al. (2011), carbonatite data (gray squares) from Hoernle et al. (2002), and Cadamosto Seamount samples from Barker et al. (2012). Jurassic ocean crust (gray hexagon), exposed on Cape Verde (Gerlach et al., 1988; Janney and Castillo, 2001; Millet et al., 2008), and Atlantic Fe–Mn nodules and sediments from DSDP Hole 397 (Hoernle et al., 1991; Abouchami et al., 1999), are shown where appropriate. The solid black line represents the Northern Hemisphere Reference Line (NHRL; Hart, 1984). When possible, the more extreme compositions of HIMU, EM1 and EM2 mantle components are shown (Stracke et al., 2003). FOZO field data from Stracke et al. (2005) are also shown. The LM (lower mantle) and DMM (Depleted Mantle MORB) compositions are from Doucelance et al. (2003) and Workman and Hart (2005), respectively.

$\kappa_{Pb}$ (Table 2). Considering the errors associated with Th and U analyses (see Section 3) and the fact that samples with relatively low $\kappa$ values differed only slightly from $\kappa_{Pb}$, we cannot completely discard the

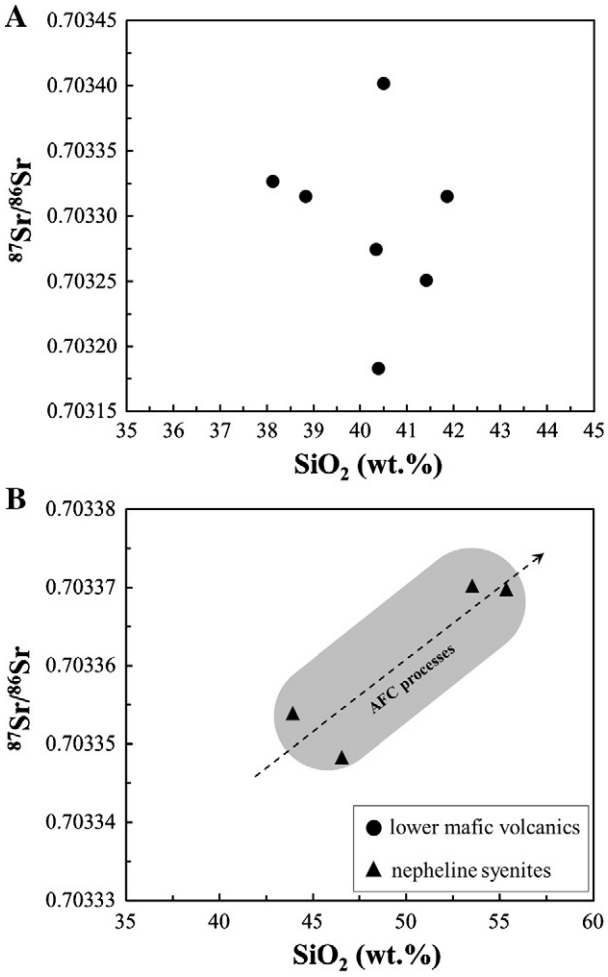


**Fig. 7.** Plot of $^{87}Sr/^{86}Sr$ vs. $SiO_2$ for the lower mafic volcanics (A) and nepheline syenites (B) from the Brava's Basal Complex. While for the submarine mafic rocks, no correlation is observed between Sr isotopic ratio and silica content, these variables are positively correlated to the plutonic felsic rocks, suggesting that the role of AFC processes is not negligible.

hypothesis that low $\kappa$ values did not result from analytical incertitude. However, taking into account the $^{87}Sr/^{86}Sr$-$^{143}Nd/^{144}Nd$ (Fig. 6A) and the $^{143}Nd/^{144}Nd$–$^{206}Pb/^{204}Pb$ (Fig. 8B) linear arrays, we consider that the Pb arrays are unlikely to represent secondary isochrons and most probably represent mixing lines between different local end-members (see Abouchami et al., 2000).

Among the most commonly discussed mantle end-members and components, FOZO has the closest Sr–Nd–Pb isotopic composition relative to Brava magmatic rocks from the Basal Complex. Although not very well defined, FOZO has the approximate range for $^{87}Sr/^{86}Sr$ of 0.7028–0.7034, $^{143}Nd/^{144}Nd$ of 0.51287–0.51303, $^{206}Pb/^{204}Pb$ of 19.5–20.5, $^{207}Pb/^{204}Pb$ of 15.56–15.71 and $^{208}Pb/^{204}Pb$ of 39.1–40.0 (cf. Table 2; Stracke et al., 2005). This observation may suggest that such magmas sampled FOZO-dominated sources. Although other compositions can be inferred for FOZO (see Hart et al., 1992; Hauri et

**Table 3**
Sr isotopic results comparing compositions of unleached and leached samples with leachates.

| Samples | Lithology | Unleached | Leached | Leachate |
|---|---|---|---|---|
| | | $^{87}Sr/^{86}Sr$ | $^{87}Sr/^{86}Sr$ | $^{87}Sr/^{86}Sr$ |
| CY-11 | Melilite nephelinite | 0.703752 (5) | 0.703281 (14) | 0.704067 (7) |
| CY-165 | Foidite | 0.703560 (6) | 0.703352 (7) | 0.703636 (9) |
| CY-39 | Nepheline syenite | 0.703377 (5) | 0.703377 (7) | 0.703376 (12) |
| CY-179 | Nepheline syenite | 0.703410 (8) | 0.703372 (8) | 0.703417 (8) |

Numbers in parentheses are within run 2σ errors referring to the last significant digits.

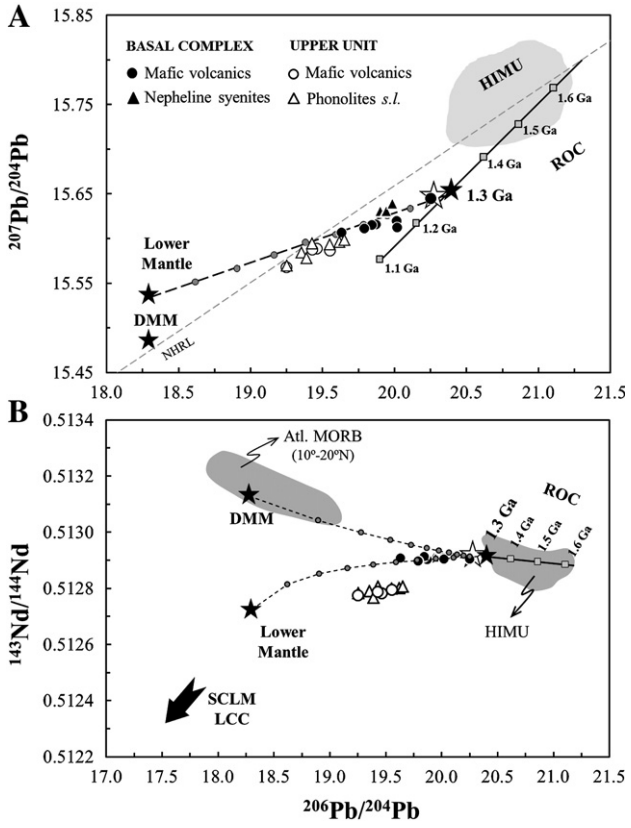


**Fig. 8.** Variation of $^{207}Pb/^{204}Pb$ (A) and $^{143}Nd/^{144}Nd$ (B) vs. $^{206}Pb/^{204}Pb$ for the Basal Complex and the Upper Unit. Recycled oceanic crust (ROC) was modeled using a two-stage model with $\mu_1 = 8.1$, $\mu_2 = 20.5$, $\kappa_1 = 3.8$ and $\kappa_2 = 3.075$, and an age ranging from 1.3 to 1.6 Ga (see Supplementary material S4). White star represents mixing of ROC and lower mantle (LM) at a proportion of 90:10. Tick marks on mixing curves indicate every 10%. Data source: HIMU (St. Helen and Tubuai) from GEOROC; Atlantic MORB (10°–20°N) from Dosso et al. (1993); depleted mantle MORB (DMM) from Workman and Hart (2005); and lower mantle from Doucelance et al. (2003).

al., 1994), this component is usually considered to be characterized by low $^4He/^3He$ (<24,085; R/Ra > 30, Hart et al., 1992; Ballentine et al., 2002; Jackson et al., 2009). These values are at odds with the observed values for Brava carbonatites ($^4He/^3He \sim 61{,}223$, R/Ra < 11.80) and silicate volcanics ($^4He/^3He > 55{,}580$, R/Ra < 13) (Mourão et al., 2012).

For Cape Verde, the presence of an HIMU-like component has been repeatedly suggested (e.g., Gerlach et al., 1988; Doucelance et al., 2003; Holm et al., 2006; Millet et al., 2008). In a $^{207}Pb/^{204}Pb$ vs. $^{206}Pb/^{204}Pb$ diagram (Fig. 6B), Brava samples exhibit a linear trend that overlaps the southern and northern island fields, extends into more radiogenic Pb ($^{206}Pb/^{204}Pb = 20.25$ and $^{207}Pb/^{204}Pb = 15.65$) and defines a local end-member compositionally close to an HIMU-type component, which is more important for the Basal Complex rocks.

The Pb isotopic composition of the HIMU-like end-member was modeled assuming that it is dominated by ancient recycled ocean crust (ROC) as proposed elsewhere for the HIMU mantle end-member (e.g., Weaver, 1991; Chauvel et al., 1992; Stracke et al., 2003) (Fig. 8). The above-mentioned isotopic signature of the most Pb-radiogenic sample, which plots at the radiogenic end of the Brava trend, was used to constrain the age of the recycling process. Taking this into account, we propose a two-stage evolution model that considers 1.3 Ga as the recycling age of the altered oceanic crust, i.e., as the age of the U–Pb fractionation responsible for the positioning of Brava samples clearly to the right of the Geochron (see Supplementary material S4 for calculation details). This age is also compatible with negative values of Δ7/4 (~−7.7) characterizing the presumably high $^{206}Pb/^{204}Pb$ local end-member. In fact, the archetypes of HIMU-type basalts (Mangaia, Tubuai; Santa Helena) all lie on the NHRL (Chaffey et al., 1989; Chauvel et al., 1992), and even if the Brava linear trend has no age significance, negative Δ7/4 values have been interpreted as implying a younger recycling age than 1.5 to 2 Ga required by classical HIMU (Thirlwall, 1997) (see also Fig. 8A).

The HIMU-like end-member alone cannot explain the range of Nd–Pb isotopic variations recorded in the Basal Complex. In fact, the $^{143}Nd/^{144}Nd$ vs. $^{206}Pb/^{204}Pb$ plot (Fig. 8B) shows that rocks from this complex develop a trend that, departing from the 1.3 Ga ROC, extends toward significantly less radiogenic Pb isotope signatures. As a working hypothesis, this trend can be interpreted as the result of mixing with one of the following contributors: Lower Mantle (LM), Sub-Continental Lithospheric Mantle (SCLM), Lower Continental Crust (LCC) or even DMM, if slightly different parent–daughter element ratios were considered in the calculation of the HIMU–DMM mixing line.

HIMU-type rocks are elsewhere characterized by quite uniform radiogenic He isotopic signatures ($^4He/^3He = 103{,}220$ to 120,424, R/Ra = 6 to 7) that are in agreement with the theoretically expected high time-integrated $(U+Th)/^3He$ of ancient recycled oceanic crust (e.g., Hanyu and Kaneoka, 1997; Hanyu et al., 1999; Moreira and Kurz, 2001; Parai et al., 2009). However, Mourão et al. (2012) measured R/Ra values up to 12.85 ($^4He/^3He$ down to 56,229) in samples from the Basal Complex, which clearly suggest the involvement of an additional component with a highly unradiogenic He signature. This component cannot be assigned to the SCLM (R/Ra ≤ 8; Gautheron et al., 2005; Czuppon et al., 2009), the LCC (R/Ra ≈ 0; Ballentine and Burnard, 2002) or the DMM inferred from the N-type MORB (R/Ra 8 ± 1; e.g., Allègre et al., 1995; Graham, 2002). Consequently, we suggest that mixing of the lower mantle with ROC is the best explanation for the isotope variability of the Basal Complex. A ROC/LM mixture at a proportion of 90:10 closely matches the multi-isotope characteristics of the most Pb-radiogenic sample of the Basal Complex (see Supplementary material S4 for calculations). This observation and seismic data (Montelli et al., 2006; Zhao, 2007; Forte et al., 2010) strongly suggest that the aging environment of the recycled oceanic crust lies at the deepest levels of the mantle.

We emphasize that a contribution of depleted material, isotopically similar to the Atlantic N-MORB, as has been proposed to explain the isotopic signature of volcanics from the northern islands (Gerlach et al., 1988; Doucelance et al., 2003; Holm et al., 2006; Barker et al., 2010) is not mandatory, also considering the relatively Nd-unradiogenic signatures of Brava Basal Complex compared with some of the northern islands (Fig. 6A).

The samples from the Upper Unit are clearly more Sr-radiogenic and Nd-unradiogenic than those from the Basal Complex. They are also characterized by lower $^{206}Pb/^{204}Pb$ and higher $^{208}Pb/^{204}Pb$ for a given $^{206}Pb/^{204}Pb$ than their older counterparts (Figs. 6 and 8). These findings suggest a source with lower time-integrated Sm/Nd and U/Pb, coupled with higher Th/Pb and Rb/Sr ratios, than the source of the Basal Complex rocks. Moreover, Ba/Nb ratios that characterize mafic rocks from the Upper Unit (mean = 12.3 ± 4.4, 2σ) are higher than the mean value of 7.7 ± 1.9 (2σ) that characterizes the mafic volcanic rocks from the Basal Complex. Such elemental signatures argue in favor of the additional involvement of an enriched-mantle, EM1-like source for the Upper Unit (see Weaver, 1991).

Models for the EM1 signature in the southern Cape Verde islands suggested the presence of ancient recycled pelagic sediments, delaminated subcontinental lithospheric mantle (SCLM) and/or lower continental crust (Gerlach et al., 1988; Doucelance et al., 2003; Escrig et al., 2005; Martins et al., 2010). The applicability of these models to Brava Island is very difficult to assess, given the significant heterogeneity of the candidates and the diluted character of the EM1-type component present in the studied rocks (Fig. 9).

In fact, magmatic provinces where the EM1 signature is more evident (e.g., Pitcairn: Eisele et al., 2002; Walvis Ridge: Salters and Sachi-Kocher, 2010) present Pb isotopic signatures that extend to values above the

NHRL (Pitcairn: Δ8/4 up to 206; Δ7/4 up to 8.26; Walvis Ridge: Δ8/4 up to 140; Δ7/4 up to 9.62) in opposition to Brava where only a few samples from the Upper Unit are marginally above the NHRL (Δ8/4 up to 13; Δ7/4 up to −0.328; see Table 2 and Hildner et al., 2011).

Lodge and Helffrich (2006) described distinct mantle flow patterns beneath the northern and southern Cape Verde islands, suggesting that magmas spread from separate melting loci. According to Barker et al. (2010), this could explain the dichotomic distribution of the EM1-type signatures, that are absent on the northern islands but characterize the southern islands. For those authors, this reflects the mantle plume azimuthal heterogeneity, and the EM1 component constitutes a sheared plume heterogeneity formed from the ancient recycled oceanic crust package, a hypothesis that, in our opinion, may favor the sediment-recycling model.

As previously described (e.g., Ben Othman et al., 1989,Weaver, 1991; Stracke et al., 2003), the elemental characteristics of recycled marine sediments suggest that, over time, they develop low $^{143}Nd/^{144}Nd$ and $^{206}Pb/^{204}Pb$ and high $^{87}Sr/^{86}Sr$ and $^{208}Pb^*/^{206}Pb^*$. In general, these characteristics match those attributed to the EM1 mantle component. However, as emphasized by Porter and White (2009) through the assessment of elemental flux into the deep mantle, sediments after processing at subduction zones do not have compositions capable of long-term evolution toward Sr–Nd–Pb isotopic signatures similar to the EM1 component. For example, none of the deep-recycled sediments can evolve to compositions less radiogenic than $\varepsilon_{Nd} \approx +2.5$, when Pitcairn and Walvis Ridge are characterized by $\varepsilon_{Nd}$ down to −5.9 and −4.7, respectively (e.g., Eisele et al., 2002; Salters and Sachi-Kocher, 2010). In addition, for the Brava Upper Unit, the role of sediments seems to be denied by the lack of Nb/U ratios significantly lower than the average mantle value (see Porter and White, 2009) or Nb and Ce negative anomalies, which are sometimes linked to the contribution of a small proportion of sediment to mantle sources (e.g., Plank and Langmuir, 1998; Eisele et al., 2002; Huang et al., 2005; Class and le Roex, 2008).

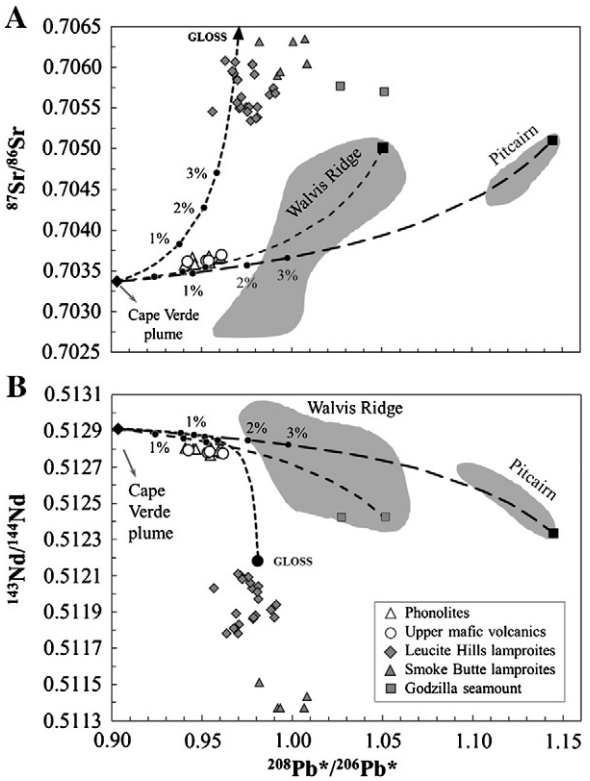


**Fig. 9.** $^{87}Sr/^{86}Sr$ vs. $^{208}Pb^*/^{206}Pb^*$ (A) and $^{143}Nd/^{144}Nd$ vs. $^{208}Pb^*/^{206}Pb^*$ (B) diagrams. The small EM1-type component makes any of the most plausible contributors here difficult; they are typified by 1) the most Sr-radiogenic compositions of Walvis Ridge (Salters and Sachi-Kocher, 2010) and Pitcairn (Eisele et al., 2002), which were assumed by these authors as the result of the incorporation of ancient recycled sediment into the mantle source(s); 2) the Global Subducting Sediment (GLOSS) defined by Plank and Langmuir (1998); 3) the composition of lamproites from Leucite Hills (Mirnejad and Bell, 2006) and Smoky Butte (Fraser et al., 1985) as well as of Godzilla seamount (Geldmacher et al., 2008), which was considered a proxy of SCLM. Note the extreme variability of these hypothetical representatives of the EM1 component.

Based on the geochemistry of lavas from the southern Cape Verde islands, many authors suggested that EM1-type signatures resulted from the interaction of the ascending plume with continental lithosphere megaliths produced by delamination during the opening of the Atlantic Ocean (Gerlach et al., 1988; Kokfelt et al., 1998; Doucelance et al., 2003; Escrig et al., 2005; Millet et al., 2008; O'Reilly et al., 2009; Martins et al., 2010). This proposal recently received independent support from studies reporting 1) the existence of a zone characterized by anomalously high S-wave propagation velocities beneath the Cape Verde archipelago, reaching 100 km in depth (Begg et al., 2009), i.e., below the typical depth of the oceanic lithosphere in the region; 2) sulfides in highly depleted mantle xenoliths occurring in the Cape Verde lavas, which present Proterozoic and Archean Re-depletion model ages mirroring those of the main tectonic events that took place at the Atlantic margins of the West African Craton and Brazil (Coltorti et al., 2010); and 3) evidence of kimberlitic metasomatism affecting mantle (lherzolites and harzburgites) xenoliths (Bonadiman et al., 2005). These observations support the existence of continental lithosphere remnants in the region, conferring plausibility to the aforementioned geochemical studies and suggesting their role in the origin of EM1-type signatures for source from the Cape Verde Islands.

We note that, due to their origin, subsequent evolution and very long-term isolation from convective motion, both SCLM and lower continental crust are thought to be characterized by extreme chemical variability. This makes the option for one of these specific lithospheric reservoirs as contributors to the Cape Verde sources a difficult decision, leaving room for the possible contribution of SCLM and lower continental crust, as proposed by Escrig et al. (2005) for Fogo Island.

Escrig et al. (2005) and Millet et al. (2008) presented strong evidence for the residence of such continental megaliths within the Cape Verde oceanic lithosphere. Applying a similar model to Brava, we expected that these megaliths contributed to magmatic composition throughout the island's evolution. From this perspective, a temporal evolution could be envisaged where the continental lithosphere role diminishes/vanishes with progressive exhaustion of the less refractory/more fertile (i.e., metasomatized) domains, due to the interaction with the ascending hot plume magmas. However, the opposite is observed for Brava where the most ancient rocks (Basal Complex) do not provide evidence for significant continental lithosphere contribution, in contrast to the volcanics from the Upper Unit. Considering the observed temporal evolution of Brava, we propose that in the Cape Verde region at least some of the continental megaliths are not attached to the oceanic lithosphere but instead float and move within the asthenosphere at a level that is likely determined by density constraints (see also Coltorti et al., 2010).

### *5.3. On the genesis of Brava carbonatite: the role of liquid immiscibility and fractional crystallization*

One interesting characteristic of Brava Island is the occurrence of carbonatites at different stages of island development. In fact, carbonatites are known either on the Basal Complex, where they intrude the Lower Unit volcanics, or on the Upper Unit, where they present volcanic explosive and effusive facies. The dominant type is calciocarbonatite, but an important magnesiocarbonatite outcrop is known at Ferreiros beach (southern coast) intruding nepheline syenites.

As emphasized above, Brava Island carbonatites present isotopic ratios that are bracketed by those characterizing coeval silicate

rocks, suggesting that these two types of rocks are ultimately derived from similar sources.

*5.3.1. Magnesiocarbonatites*

Experimental work has demonstrated that magnesiocarbonatites can be produced at appropriate depths (>2 GPa) by very low degrees of partial melting of $CO_2$-rich mantle lithologies (e.g., Dalton and Wood, 1993; Wyllie and Lee, 1998; Lee et al., 2000; Foley et al., 2009). Experimental attempts to reproduce Mg-rich compositions by immiscibility have failed (e.g., Dasgupta et al., 2006) and extreme fractional crystallization of carbonated silicate magmas is not a reasonable mechanism to produce Mg-rich carbonatite magmas comparable to those from Brava (Mg#>80).

Considering the similar isotopic ratios of magnesiocarbonatites and coeval silicate rocks of the Basal Complex, there is room for the hypothesis that both types of magmas are a direct result of partial melting of the same source. Taking into account a progressive increase of partial melting degree, a continuous gradation from carbonatitic to various types of silicate melts can be generated from $CO_2$-enriched mantle sources (e.g., Wyllie and Huang, 1975; Dalton and Presnall, 1998; Gudfinnsson and Presnall, 2005). As such, Brava magnesiocarbonatite magma could have resulted from a smaller degree of partial melting than their silicate counterparts. These carbonatites are characterized by Mg# (80 to 90 wt.%; see Supplementary material S3) similar to those obtained experimentally by melting of carbonated peridotites (Mg# = 76 to 88; Foley et al., 2009) but clearly higher than those resulting from carbonated eclogite sources (Mg# = 61 to 69; Dasgupta et al., 2006) which eliminates carbonated eclogite as a source of Brava magnesiocarbonatites and confers plausibility to an origin by melting of carbonated peridotite. However, these carbonatites are also characterized by very low Ni (<20 ppm) and Cr (<5 ppm) content and cannot be considered representative of melts in equilibrium with a peridotitic mantle-residual paragenesis (see Foley et al., 2009).

We are left with two hypotheses: the volumetrically subordinated magnesiocarbonatites represent a residual melt originated by calcite fractionation of carbonatic magma, as proposed by de Ignacio et al. (2012) for São Vicente Island, or these magnesiocarbonatites resulted from post-magmatic dolomitization steaming from secondary processes, following the models by Hoernle et al. (2002) for Cape Verde and Bouabdellah et al. (2010) for Morocco.

Using alizarine as a staining product (Friedman, 1959), we found no textural evidence for calcite replacement by dolomite on magnesiocarbonatites. Moreover, the reported enrichment of Cape Verde magnesiocarbonatites relative to their calcium counterparts in elements (e.g., LREE; Th, U, Nb and Ta) compatible with accessory phases resistant to alteration (Hoernle et al., 2002), is not observed or conspicuous for Brava. Although this question can only be unequivocally solved through the use of carbon and oxygen isotopes, these data strongly suggest that such a model is not applicable to Brava.

Some calciocarbonatites present textures indicating calcite accumulation, which suggest that the de Ignacio's model (see above) can be applied to the present case. However, we note that magnesiocarbonatites have, for example, slightly higher $^{206}Pb/^{204}Pb$ (20.004–20.147 vs. 19.761–19.828), $^{208}Pb/^{204}Pb$ (39.247–39.282 vs. 39.073–39.144) and La/Yb for a given La (Fig. 10A) than the coeval calciocarbonatites (see Table 2, Supplementary material S3). This finding indicates that the analyzed samples of the two types of carbonatites are not strictly comagmatic and that if magnesiocarbonatites are the result of calcite fractionation, the resultant calcite cumulates were not analyzed.

*5.3.2. Calciocarbonatites*

Several authors have proposed the hypothesis that carbonatites can result from extreme fractionation of carbonated silicate magmas (e.g., Veksler et al., 1998; Verhulst et al., 2000). In the present case, such genetic models are not denied by the fact that intrusive calciocarbonatites present isotopic signatures in the range of those characterizing the silicate rocks of the Basal Complex. Carbonatites and highly undersaturated silicate rocks are known as carriers of numerous exotic minerals (e.g., Hogarth, 1989), with some as important repositories of trace elements (e.g., Chakhmouradian, 2006). Their partition coefficients are poorly known, making quantitative and even qualitative assessment of processes such as crystal fractionation, extremely difficult. However, for the stoichiometric elements in the more abundant mineral phases, the operation of such a process must imply neat liquid lines of descent linking silicate and carbonatite magma compositions. This is not the case for Brava, as clearly indicated by the CaO vs. MgO diagram (Fig. 10B) and this finding strongly suggest that extreme crystal fractionation affecting carbonated silicate magmas does not explain the genesis of these carbonatites.

Considering the identical isotopic ratios of Basal Complex calciocarbonatites and their silicate counterparts, two other models are plausible: wallrock reaction (Dalton and Wood, 1993; Lee and Wyllie, 2000; see below) and silicate-carbonatite liquid immiscibility.

Experimental data (see above) have shown that calciocarbonatites are not a product of partial melting of mantle lithologies. However, on ascent, magnesiocarbonatite magmas produced by a very low degree of partial melting tend to react with lherzolitic and harzburgitic wallrocks to produce calciocarbonatite magmas and transform the wallrocks into wherlite (Dalton and Wood, 1993; Lee and Wyllie, 2000; Xu et al., 2007). Considering that magnesiocarbonatites

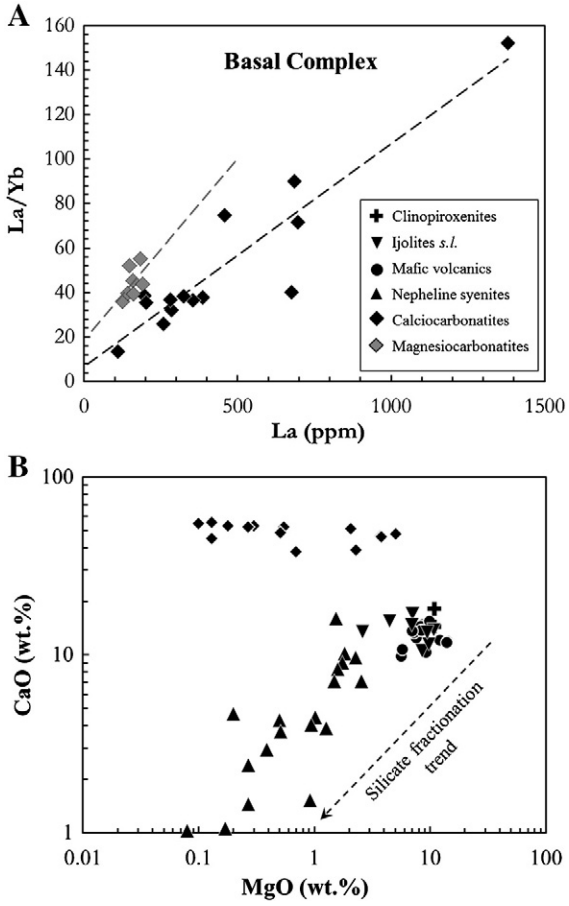


**Fig. 10.** (A) La versus La/Yb plot for intrusive carbonatites from the Basal Complex showing that, for a given La content, calciocarbonatites present lower La/Yb ratios than magnesiocarbonatites. (B) Variation of CaO with MgO in carbonatite and associated silicate rocks from Brava's Basal Complex. While silicate trend can be explained by fractional crystallization, this process cannot account for the genesis of carbonatites as a differentiation product of the silicate rocks.

generated by this process are highly enriched in incompatible elements, their isotopic ratios (e.g., $^{143}Nd/^{144}Nd$ and $^{206}Pb/^{204}Pb$) are relatively insensitive to interaction with a depleted mantle matrix. As such, the similarity of isotope ratios between coeval carbonatite and silicate rocks cannot be used to deny that hypothesis.

Carbonatites, nephelinites and nepheline syenites from Brava's Basal Complex are plotted in Fig. 11 along with the 0.8 GPa *solvus* defined by Kjarsgaard and Hamilton (1988) and the 2 to 3 GPa experimental data of Dasgupta et al. (2006). The positioning of the studied rocks is compatible with an immiscibility process producing conjugate nephelinites and carbonatites. Nevertheless, it should be noted that experimentally produced immiscible carbonatite liquids are characterized, similar to the Brava liquids, by low alkali content (<5 wt.%) but significantly higher aluminosilicate content ($SiO_2 + Al_2O_3 > \sim 10$ wt.%) than those of the studied rocks (e.g., Brooker and Kjarsgaard, 2010 and references therein). This finding could be viewed as an argument against the immiscibility model. However, as emphasized by Brooker and Kjarsgaard (2010), fractionation of silicate minerals and the release of alkali-rich fenitizing fluids would deplete immiscibility-generated carbonatite magma in alkalis, silica and alumina. Moreover, the operation of immiscibility is supported by the relative trace element partitioning between silicate and carbonatite liquids (Fig. 12). In fact, relative to the nephelinitic rocks, the calciocarbonatites are highly depleted in K, Rb, Zr, Hf, Nb, Ta and Ti, but enriched in Sr and Ba. This observation is in agreement with the experimental partition coefficients determined by Veksler et al. (1998) for pressures below 0.1 GPa. However, these authors reported carbonatite/nephelinite partition coefficients for REEs lower than 1, which is inconsistent with observations from Brava. The fact that REEs are enriched in carbonatites relative to the conjugated silicate magmas can be explained by considering that immiscibility occurred at significantly higher pressures (0.6 GPa; Hamilton et al., 1989), which is in greater agreement with the plot along the 0.8 GPa *solvus* (Fig. 11). Additionally, the marked negative anomalies in Ti and P are explained by the role of subsequent fractionation of Fe–Ti oxides and apatite, which are mineral phases identified in some of the rocks.

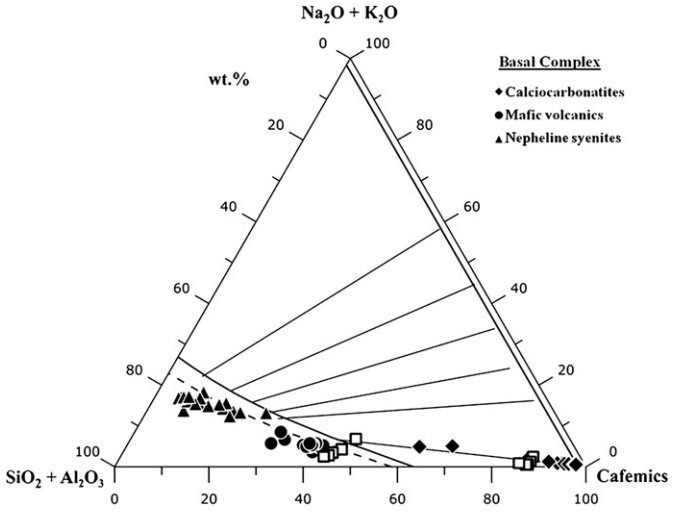


**Fig. 11.** Projection of rock compositions from the Basal Complex in the $(SiO_2 + Al_2O_3) - (Na_2O + K_2O) - Cafemics$ ($CaO + FeO + MgO + MnO$) diagram; the topology of the carbonate–silicate liquid immiscibility experimental system (Kjarsgaard and Hamilton, 1988) is also presented. Open squares are the compositions of carbonate- and silicate-rich conjugate melts from Dasgupta et al. (2006). The *solvus* at 0.5 GPa (bold continuous line) and at 0.8 GPa (dashed line) as well as the experimentally determined tie-lines for different carbonatite–silicate conjugate liquids are shown. This diagram supports the occurrence of an immiscibility process to explain the origin of calciocarbonatites from the Basal complex. For comparison with extrusive silicate and carbonatite rocks from the Upper Unit, see Fig. 11 in Mourão et al. (2010). The composition of some nephelinites can be observed to have conjugate carbonatitic liquids plotting very close to the Cafemic corner.

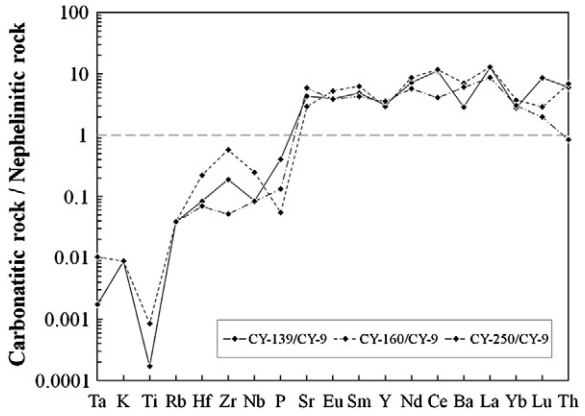


**Fig. 12.** Enrichment/depletion factors for selected elements of representative intrusive calciocarbonatites with respect to the composition of a nephelinitic rock from the Lower Unit (sample CY-9), plotting closest to the *solvus* and to the end of the tie line drawn in Fig. 11 The elements are arranged taking into account the experimental partition coefficients during silicate–carbonatite immiscibility processes (Hamilton et al., 1989; Veksler et al., 1998).

Considering the positioning of silicate rocks and carbonatites relatively to the solvus (Fig. 11) and the elemental fractionation depicted by Fig. 12, we consider that the genesis of the calciocarbonatites from Brava Basal Complex is better explained by the immiscibility model.

Similarly, Mourão et al. (2010) proposed a nephelinite–carbonatite immiscibility process to explain the genesis of Brava extrusive carbonatites from the Upper Unit. Their model was based on three considerations: 1) the intimate temporal/spatial association of carbonatites and nephelinitic rocks, 2) the comparison of their major element compositions with the results of immiscibility experimental data, and 3) carbonatite/nephelinite trace element enrichment/depletion factors. Table 2 and Fig. 6 show the similarity of the Sr–Nd–Pb isotopic signatures between carbonatites and the associated silicate rocks and reinforce the proposed model (extrusive carbonatites: $^{87}Sr/^{86}Sr = 0.703557–0.703595$, $^{143}Nd/^{144}Nd = 0.512792–0.512816$, $^{206}Pb/^{204}Pb = 19.657–19.677$; silicate rocks: $^{87}Sr/^{86}Sr = 0.703571–0.703701$, $^{143}Nd/^{144}Nd = 0.512767–0.512807$, $^{206}Pb/^{204}Pb = 19.254–19.655$). Immiscibility was also invoked for other Cape Verde occurrences by Kogarko (1993) and de Ignacio et al. (2012).

### 5.3.3. The origin of carbon

The origin of carbon needed to explain the occurrence of Brava's carbonatites is beyond the scope of this paper. Consequently, this issue is treated only briefly.

Proposed models range from a deep origin (involving or not recycled crustal carbon; cf. Hoernle et al., 2002; Mata et al., 2010; Mourão et al., 2012), to a shallow one, with the Cape Verde mantle plume only providing the heat necessary to melt the carbonated domains of the oceanic lithosphere (Doucelance et al., 2010). As mentioned above, Brava carbonatites present not only isotopic characteristics distinct from those of the other Cape Verde carbonatites but also isotopic characteristics similar to those of the coeval silicate rocks, suggesting that the genetic mechanisms associated with other Cape Verde carbonatites may not apply to those occurring in Brava.

Mourão et al. (2012) demonstrated that Brava Basal Complex carbonatites are characterized by a primary low $^4He/^{40}Ar^*$ ratio ($\leq 0.3$), where $^{40}Ar^*$ stands for $^{40}Ar$ concentration corrected for atmospheric contamination. This was considered incompatible with recycling of crustal components. In fact, after processing at subduction zones, those components would be characterized by low K/U (down to <1000; Becker et al., 2000; Lassiter, 2004) as opposed to the K/U of approximately 110,000 and 62,000 needed to reach the low $^4He/^{40}Ar^*$ in 1.6 and 4.5 Ga, respectively (see Mourão et al., 2012). This reasoning makes the applicability of models invoking the recycling of crustal carbon to Brava Basal

Complex carbonatites implausible and supports the involvement of a very long-term isolated reservoir (lower mantle) on the genesis of these rocks. The existence in the mantle of reservoirs isolated for some 4.45 Ga received recent support from a new interpretation of the $^{129}Xe$ excess of OIB relative to air (Mukhopadhyay, 2012). Interestingly, as shown by Mata et al. (2010), one of the Brava carbonatites is also characterized by $^{129}Xe$ excess ($^{129}Xe/^{130}Xe = 6.71$).

Upper Unit extrusive carbonatites were considered the result of immiscibility processes from a carbonated silicate melt whose composition reflects the partial melting of plume material and posterior mixing with continental lithosphere melts. At least part of the carbon involved comes from the same reservoir proposed for the oldest carbonatites, although we cannot exclude some carbon contribution from the continental lithosphere.

## 6. Summary and further implications

Brava, the southernmost island of Cape Verde, is atypical in the archipelago geology/geochemistry. In fact, in opposition to the other islands for which a continuous intra-island isotopic range is usually observed, Brava is characterized by two distinct groups in the Sr–Nd–Pb isotopic space(s). Rocks from the Upper Unit (<0.5 Ma) present characteristics akin to those defined by southern Cape Verde islands, whereas the Basal Complex (2 to 3 Ma) signatures are more similar to those of the northern islands (Fig. 6). Moreover, on the $^{208}Pb/^{204}Pb$ vs. $^{206}Pb/^{204}Pb$ diagram (Fig. 6C) Brava rocks form a significantly less steep trend than the one reported for other Cape Verde islands.

The proposed petrogenetic model for the geochemical and lithological variability of Brava magmatic rocks is synthesized in Fig. 13.

The isotopic variability of the Basal Complex is here mainly explained by mixing of the lower mantle with a dominant HIMU-type local end-member, considered to represent ancient (~1.3 Ga) recycled oceanic crust (ROC). The presence of an HIMU-type component in the Cape Verde sources is well-known and is considered to be better sampled by magma erupting in the northern islands (e.g., Gerlach et al., 1988; Doucelance et al., 2003; Holm et al., 2006). Notably, the most radiogenic $^{206}Pb/^{204}Pb$ signature (20.251) ever found in the Cape Verde silicate rocks is reported here for one of the lavas from the Basal Complex. The HIMU-type and lower mantle materials, including the carbon needed for the carbonatites, are considered to have been carried to the upper mantle by the Cape Verde plume, which, according to seismic tomographic (Montelli et al., 2006; Zhao, 2007; Forte et al., 2010) and noble gas data (Christensen et al., 2001; Doucelance et al., 2003; Mata et al., 2010; Mourão et al., 2012), is probably anchored in the deepest levels of the lower mantle. However, it should be noted that the ROC age modeled here for Brava (1.3 Ga) is slightly different than what was calculated for some of the other islands of the archipelago (≥1.5 Ga; Gerlach et al., 1988; Hoernle et al., 2002; Doucelance et al., 2003; Millet et al., 2008) but identical to that proposed by Holm et al. (2006) for Santo Antão Island. In addition, the ROC/lower mantle proportions obtained in this study for Brava (see Section 5.2 and Supplementary material S4) are distinct from those calculated by Doucelance et al. (2003) and Millet et al. (2008) for other Cape Verde islands. These differences point to the heterogeneous character of the Cape Verde mantle plume. This observation is not surprising given that high-resolution numerical simulations demonstrate that mantle plumes sample

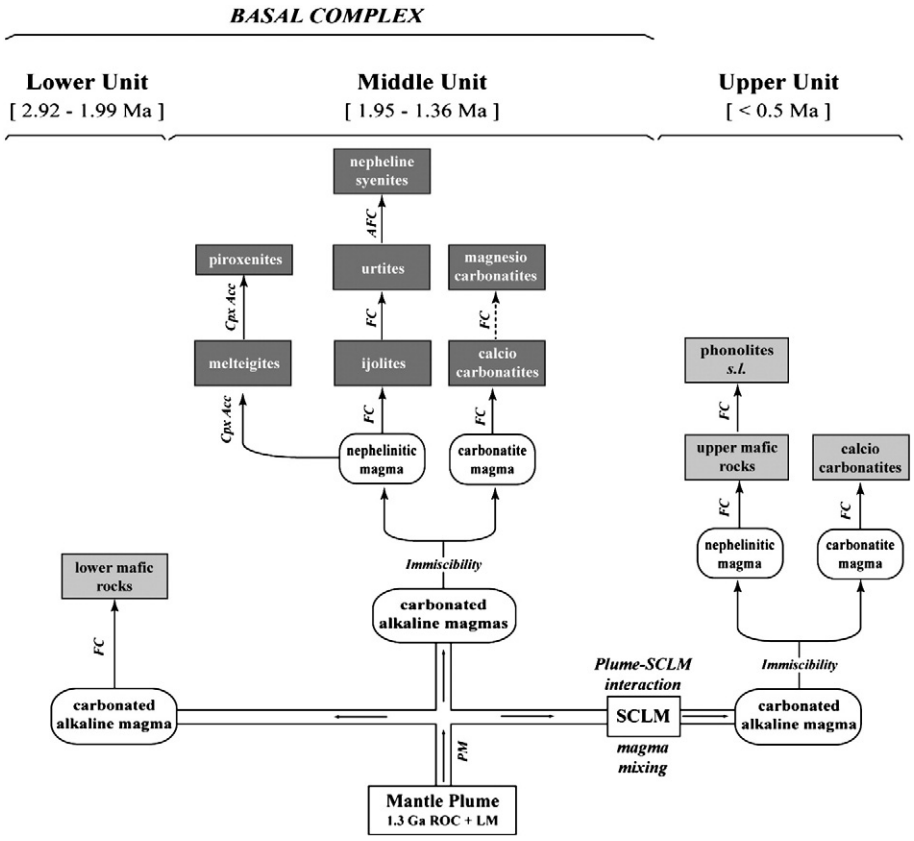


**Fig. 13.** Schematic illustration of the proposed scenario for the genesis and evolution of magmas at the origin of the three Brava Island volcanostratigraphic units. The "lower" and "upper" mafic volcanics include nephelinites, melilite nephelinites, basanites, foidites, tephrites and phonotephrites. The "phonolites *s.l.*" include phonolites and nepheline phonolites. *PM*, *FC*, *Acc* and *AFC* stand for *Partial Melting*, *Fractional Crystallization*, *Accumulation* and *Assimilation and Fractional Crystallization* processes, respectively. SCLM, subcontinental lithospheric mantle; ROC, ancient recycled oceanic crust; LM, lower mantle; Cpx, clinopyroxene; Cal, calcite. Dark gray boxes: intrusive rocks; light gray boxes: extrusive rocks. As shown, even though magnesiocarbonatites of the Middle Unit are considered representative of a liquid residue left after calcite accumulation, they cannot be considered strictly comagmatic with the outcropping calciocarbonatites.

their source heterogeneities and carry them to the Earth's shallower levels without significant homogenization (Farnetani and Hofmann, 2009).

An additional local end-member was required to explain the variability of the Upper Unit. Such an end-member presents elemental and isotopic characteristics allowing its assignment to an EM1-type composition, as described for the other southern islands. The assignment, based on lava chemistry, of a specific precursor to the EM1 signature (pelagic sediments vs. SCLM vs. Lower Continental Crust) is difficult given the extreme heterogeneity of these materials and their diluted contribution to Brava magmas. However, based on independent data, a contribution of continental lithosphere is favored via mixing of plume melts with melts from continental megaliths left behind during the Atlantic opening. Taking into account the absence of evidence of such an EM1-type component contribution to the Brava Basal complex, we propose that those megaliths float on the asthenosphere (Section 5.2; see also Coltorti et al., 2010).

Brava carbonatites are peculiar in their isotopic composition. Whereas other Cape Verde occurrences define a common field in the Sr–Nd–Pb space independent of their geographical location and the chemistry of the associated silicate rocks, Brava occurrences define two distinct groups with similar isotopic ranges as those observed for the coeval alkaline silicate rocks. This observation suggests that Brava carbonatites result from genetic mechanisms distinct from those responsible for the other Cape Verde occurrences. Calciocarbonatites from both the Basal Complex and the Upper Unit are considered the result of nephelinite–carbonatite liquid immiscibility, affecting carbonated silicate magma generated by low degrees of partial melting of the ascending plume, whose composition is dominated by ROC and entrained lower mantle. From constraints, such as REE partitioning between the two magma types, immiscibility occurred at pressures $\geq$0.6 GPa. If we assume that crustal thickness under Brava is similar to that of neighboring Fogo Island (~15 km; Lodge and Helffrich, 2006), then immiscibility occurred in the upper levels of the mantle. We suggest that the genesis of the subordinate Basal Complex magnesiocarbonatites represent residual liquids after calcite fractionation from carbonatite magma and are not the product of secondary processes. We emphasize that Brava magnesiocarbonatites are characterized by chemical signatures more akin to HIMU-type magmas than those reported by Hoernle et al. (2002) for magnesiocarbonatites from other Cape Verde islands, to which they assigned EM1-type signatures.

Brava presents isotopic and elemental characteristics typical of both the southern and northern islands and calls into question the clear geochemical distinction between the two groups characteristic of the Cape Verde islands that have been accepted by most authors since Gerlach et al. (1988). This finding is further supported by the possible presence of SCLM relicts beneath Sal, one of the northern islands (Bonadiman et al., 2005; Begg et al., 2009; Coltorti et al., 2010), by the EM1-type fingerprints which, according to Torres et al. (2010), are identifiable by two Sal lavas, and the absence of EM1 signatures in the Cadamosto seamount near Brava (Barker et al., 2012).

Supplementary data to this article can be found online at http://dx.doi.org/10.1016/j.chemgeo.2012.09.031.

## Acknowledgments

This work was supported by FCT/FEDER through project PLINT (POCTI/CTA/45802/2002) and a PhD scholarship (SFRH/BD/39493/2007) for C. Mourão, and by FCT through the Pest-OE/CTE/UI0263/2011 projects. We wish to thank L. Celestino Silva for his help and insight at many stages of this project, namely in petrographic studies and in preparation of the field campaigns, and to S. Martins for stimulating discussions on the geochemistry of Cape Verde. A. Brum da Silveira is thanked for his help during field work. We also acknowledge Fundação Calouste Gulbenkian, which supported C. Mourão's travel/accommodation expenses and made her analytical work at the Laboratoire de Magmas et Volcans (France) possible. The authors are grateful to C. Bosq for skilled assistance during the chemical separation of Sr and Nd and to D. Auclair for maintaining the TIMS in top condition. Joel Baker is acknowledged for providing access to the geochemistry laboratory at Victoria University of Wellington. We also thank Editor L. Reisberb, P.M. Holm, Jörg Geldmacher and an anonymous reviewer for the helpful criticism and suggestions, which highly improved the quality of the present manuscript.

## References

Abouchami, W., Galer, S.J.G., Koschinsky, A., 1999. Pb and Nd isotopes in NE Atlantic Fe–Mn crusts: proxies for trace metal paleosources and paleocean circulation. Geochimica et Cosmochimica Acta 63, 1489–1505.

Abouchami, W., Galer, S.J.G., Hofmann, A.W., 2000. High precision lead isotope systematics of lavas from the Hawaiian Scientific Drilling Project. Chemical Geology 169, 187–209.

Ali, M.Y., Watts, A.B., Hill, I., 2003. A seismic reflection profile study of lithospheric flexure in the vicinity of the Cape Verde Islands. Journal of Geophysical Research 108, 2239. http://dx.doi.org/10.1029/2002JB002155.

Allègre, C.J., Dupré, B., Lewin, E., 1986. Thorium/Uranium ratio of the Earth. Chemical Geology 56, 219–227.

Allègre, C.J., Moreira, M., Staudacher, T., 1995. $^{4}He/^{3}He$ dispersion and mantle convection. Geophysical Research Letters 22, 2325–2328.

Baker, J., Peate, D., Waight, T., Meyzen, C., 2004. Pb isotopic analysis of standards and samples using a $^{207}Pb$–$^{204}Pb$ double spike and thallium to correct for mass bias with a double-focusing MC-ICP-MS. Chemical Geology 211, 275–303.

Ballentine, C.J., Burnard, P.G., 2002. Production, release and transport of noble gases in the continental crust. Reviews in Mineralogy and Geochemistry 47, 481–538.

Ballentine, C.J., van Keken, P.E., Porcelli, D., Hauri, E.H., 2002. Numerical models, geochemistry and the zero–paradox noble-gas mantle. Philosophical Transactions of the Royal Society of London, Series A: Mathematical, Physical and Engineering Sciences 360, 2611–2631.

Barker, A.K., Holm, P.M., Peate, D.W., Baker, J.A., 2009. Geochemical stratigraphy of submarine lavas (3–5 Ma) from the Flamengos Valley, Santiago, Southern Cape Verde Islands. Journal of Petrology 50, 169–193.

Barker, A., Holm, P., Peate, D., Baker, J., 2010. A 5 million year record of compositional variations in mantle sources to magmatism on Santiago, southern Cape Verde archipelago. Contributions to Mineralogy and Petrology 160, 133–154.

Barker, A., Troll, V., Ellam, R., Hansteen, T., Harris, C., Stillman, C., Andersson, A., 2012. Magmatic evolution of the Cadamosto Seamount, Cape Verde: beyond the spatial extent of EM1. Contributions to Mineralogy and Petrology 163, 949–965.

Becker, H., Jochum, K.P., Carlson, R.W., 2000. Trace element fractionation during dehydration of eclogites from high-pressure terranes and the implications for element fluxes in subduction zones. Chemical Geology 163, 65–99.

Begg, G.C., Griffin, W.L., Natapov, L.M., O'Reilly, S.Y., Grand, S.P., O'Neill, C.J., Hronsky, J.M.A., Djomani, Y.P., Swain, C.J., Deen, T., Bowden, P., 2009. The lithospheric architecture of Africa: seismic tomography, mantle petrology, and tectonic evolution. Geosphere 5, 23–50.

Ben Othman, D., White, W.M., Patchett, J., 1989. The geochemistry of marine sediments, island arc magma genesis, and crust–mantle recycling. Earth and Planetary Science Letters 94, 1–21.

Blundy, J., Wood, B., 2003. Partitioning of trace elements between crystals and melts. Earth and Planetary Science Letters 210, 383–397.

Bonadiman, C., Beccaluva, L., Coltorti, M., Siena, F., 2005. Kimberlite-like metasomatism and 'garnet signature' in spinel-peridotite xenoliths from Sal, Cape Verde Archipelago: relics of a subcontinental mantle domain within the Atlantic Oceanic lithosphere? Journal of Petrology 46, 2465–2493.

Bouabdellah, M., Hoernle, K., Kchit, A., Duggen, S., Hauff, F., Klügel, A., Lowry, D., Beaudoin, G., 2010. Petrogenesis of the Eocene Tamazert continental carbonatites (Central High Atlas, Morocco): implications for a common source for the Tamazert and Canary and Cape Verde Island carbonatites. Journal of Petrology 51, 1655–1686.

Brooker, R.A., Kjarsgaard, B.A., 2010. Silicate–carbonate liquid immiscibility and phase relations in the system $SiO_2$–$Na_2O$–$Al_2O_3$–CaO–$CO_2$ at 0.1–2.5 GPa with applications to carbonatite genesis. Journal of Petrology 52, 1281–1305.

Chaffey, D.J., Cliff, R.A., Wilson, B.M., 1989. Characterization of the St. Helena source. In: Saunders, A.J., Norry, M.J. (Eds.), Magmatism in the ocean basins: Geological society special publication, pp. 257–276.

Chakhmouradian, A.R., 2006. High-field-strength elements in carbonatitic rocks: geochemistry, crystal chemistry and significance for constraining the sources of carbonatites. Chemical Geology 235, 138–160.

Chase, C.G., 1981. Oceanic island Pb: two-stage histories and mantle evolution. Earth and Planetary Science Letters 52, 277–284.

Chauvel, C., Blichert-Toft, J., 2001. A hafnium isotope and trace element perspective on melting of the depleted mantle. Earth and Planetary Science Letters 190, 137–151.

Chauvel, C., Hofmann, A.W., Vidal, P., 1992. HIMU-EM: the French Polynesian connection. Earth and Planetary Science Letters 110, 99–119.

Chen, C.Y., Wasserburg, G.J., 1983. The least radiogenic Pb in iron meteorites, Fourteenth Lunar and Planetary Science Conference, Houston, Texas. pp. 103–104.

Christensen, B.P., Holm, P.M., Jambon, A., Wilson, J.R., 2001. Helium, argon and lead isotopic composition of volcanics from Santo Antão and Fogo, Cape Verde Islands. Chemical Geology 178, 127–142.

Class, C., Goldstein, S.L., 1997. Plume–lithosphere interactions in the ocean basins: constraints from the source mineralogy. Earth and Planetary Science Letters 150, 245–260.
Class, C., le Roex, A.P., 2008. Ce anomalies in Gough Island lavas — trace element characteristics of a recycled sediment component. Earth and Planetary Science Letters 265, 475–486.
Collerson, K.D., Williams, Q., Ewart, A.E., Murphy, D.T., 2010. Origin of HIMU and EM-1 domains sampled by ocean island basalts, kimberlites and carbonatites: the role of $CO_2$-fluxed lower mantle melting in thermochemical upwellings. Physics of the Earth and Planetary Interiors 181, 112–131.
Coltorti, M., Bonadiman, C., O'Reilly, S.Y., Griffin, W.L., Pearson, N.J., 2010. Buoyant ancient continental mantle embedded in oceanic lithosphere (Sal Island, Cape Verde Archipelago). Lithos 120, 223–233.
Courtney, R.C., White, R.S., 1986. Anomalous heat flow and geoid across the Cape Verde Rise: evidence for dynamic support from a thermal plume in the mantle. Geophysical Journal of the Royal Astronomical Society 87, 815–867.
Cox, K.G., Bell, J.D., Pankhurst, R.J., 1979. The interpretation of igneous rocks. George Allen & Unwin, London . 450 pp.
Crough, S.T., 1978. Thermal origin of mid-plate hot-spot swells. Geophysical Journal of the Royal Astronomical Society 55, 451–469.
Czuppon, G., Matsumoto, T., Handler, M.R., Matsuda, J.-I., 2009. Noble gases in spinel peridotite xenoliths from Mt Quincan, North Queensland, Australia: undisturbed MORB-type noble gases in the subcontinental lithospheric mantle. Chemical Geology 266, 19–28.
Dalton, J.A., Presnall, D.C., 1998. The continuum of primary carbonatitic–kimberlitic melt compositions in equilibrium with lherzolite: data from the system CaO–MgO–$Al_2O_3$–$SiO_2$–$CO_2$ at 6 GPa. Journal of Petrology 39, 1953–1964.
Dalton, J.A., Wood, B.J., 1993. The compositions of primary carbonate melts and their evolution through wallrock reaction in the mantle. Earth and Planetary Science Letters 119, 511–525.
Dasgupta, R., Hirschmann, M.M., Stalker, K., 2006. Immiscible transition from carbonate-rich to silicate-rich melts in the 3 GPa melting interval of eclogite + $CO_2$ and genesis of silica-undersaturated ocean island lavas. Journal of Petrology 47, 647–671.
Dash, B.P., Ball, M.M., King, G.A., Butler, L.W., Rona, P.A., 1976. Geophysical investigation of the Cape Verde archipelago. Journal of Geophysical Research 81, 5249–5259.
Davies, G.R., Cliff, R.A., Norry, M.J., Gerlach, D.C., 1989. A combined chemical and Pb–Sr–Nd isotope study of the Azores and Cape Verde hot-spots: the geodynamic implications. Geological Society, London, Special Publications 42, 231–255.
de Ignacio, C., Muñoz, M., Sagredo, J., 2012. Carbonatites and associated nephelinites from São Vicente, Cape Verde Islands. Mineralogical magazine 76, 311–355.
DePaolo, D.J., 1981. Trace element and isotopic effects of combined wallrock assimilation and fractional crystallization. Earth and Planetary Science Letters 53, 189–202.
Dosso, L., Bougault, H., Joron, J.-L., 1993. Geochemical morphology of the North Mid-Atlantic Ridge, 10°-24°N: trace element-isotope complementarity. Earth and Planetary Science Letters 120, 443–462.
Doucelance, R., Escrig, S., Moreira, M., Gariépy, C., Kurz, M.D., 2003. Pb–Sr–He isotope and trace element geochemistry of the Cape Verde Archipelago. Geochimica et Cosmochimica Acta 67, 3717–3733.
Doucelance, R., Hammouda, T., Moreira, M., Martins, J.C., 2010. Geochemical constraints on depth of origin of oceanic carbonatites: the Cape Verde case. Geochimica et Cosmochimica Acta 74, 7261–7282.
Eisele, J., Sharma, M., Galer, S.J.G., Blichert-Toft, J., Devey, C.W., Hofmann, A.W., 2002. The role of sediment recycling in EM-1 inferred from Os, Pb, Hf, Nd, Sr isotope and trace element systematics of the Pitcairn hotspot. Earth and Planetary Science Letters 196, 197–212.
Escrig, S., Doucelance, R., Moreira, M., Allègre, C.J., 2005. Os isotope systematics in Fogo Island: evidence for lower continental crust fragments under the Cape Verde Southern Islands. Chemical Geology 219, 93–113.
Farnetani, C.G., Hofmann, A.W., 2009. Dynamics and internal structure of a lower mantle plume conduit. Earth and Planetary Science Letters 282, 314–322.
Foley, S.F., Yaxley, G.M., Rosenthal, A., Buhre, S., Kiseeva, E.S., Rapp, R.P., Jacob, D.E., 2009. The composition of near-solidus melts of peridotite in the presence of $CO_2$ and $H_2O$ between 40 and 60 kbar. Lithos 112, 274–283.
Forte, A.M., Quéré, S., Moucha, R., Simmons, N.A., Grand, S.P., Mitrovica, J.X., Rowley, D.B., 2010. Joint seismic-geodynamic-mineral physical modelling of African geodynamics: a reconciliation of deep-mantle convection with surface geophysical constraints. Earth and Planetary Science Letters 295, 329–341.
Fraser, K.J., Hawkesworth, C.J., Erlank, A.J., Mitchell, R.H., Scott-Smith, B.H., 1985. Sr, Nd and Pb isotope and minor element geochemistry of lamproites and kimberlites. Earth and Planetary Science Letters 76, 57–70.
Friedman, G.M., 1959. Identification of carbonate minerals by staining methods. Journal of Sedimentary Research 29, 87–97.
Galer, S.J.G., O'Nions, R.K., 1985. Residence time of thorium, uranium and lead in the mantle with implications for mantle convection. Nature 316, 778–782.
Gautheron, C., Moreira, M., Allègre, C., 2005. He, Ne and Ar composition of the European lithospheric mantle. Chemical Geology 217, 97–112.
Geldmacher, J., Hoernle, K., Klügel, A., van den Bogaard, P., Bindeman, I., 2008. Geochemistry of a new enriched mantle type locality in the northern hemisphere: Implications for the origin of the EM-I source. Earth and Planetary Science Letters 265, 167–182.
George, R.M., Rogers, N.W., 2002. Plume dynamics beneath the African plate inferred from the geochemistry of the Tertiary basalts of southern Ethiopia. Contributions to Mineralogy and Petrology 144, 286–304.
Gerlach, D.C., Cliff, R.A., Davies, G.R., Norry, M., Hodgson, N., 1988. Magma sources of the Cape Verdes archipelago: isotopic and trace element constraints. Geochimica et Cosmochimica Acta 52, 2979–2992.
Graham, D.W., 2002. Noble gas isotope geochemistry of mid-ocean ridge and ocean island basalts: characterization of mantle source reservoirs. Reviews in Mineralogy and Geochemistry 47, 247–317.
Grevemeyer, I., Helffrich, G., Faria, B., Booth-Rea, G., Schnabel, M., Weinrebe, W., 2010. Seismic activity at Cadamosto seamount near Fogo Island, Cape Verdes — formation of a new ocean island? Geophysical Journal International 180, 552–558.
Gudfinnsson, G.H., Presnall, D.C., 2005. Continuous gradations among primary carbonatitic, kimberlitic, melilititic, basaltic, picritic, and komatiitic melts in equilibrium with garnet lherzolite at 3–8 GPa. Journal of Petrology 46, 1645–1659.
Hamilton, D.L., Bedson, P., Esson, J., 1989. The behaviour of trace elements in the evolution of carbonatites. In: Bell, K. (Ed.), Carbonatites: genesis and evolution. Unwin Hyman, London, pp. 405–427.
Hanyu, T., Kaneoka, I., 1997. The uniform and low $^3He/^4He$ ratios of HIMU basalts as evidence for their origin as recycled materials. Nature 390, 273–276.
Hanyu, T., Kaneoka, I., Nagao, K., 1999. Noble gas study of HIMU and EM ocean island basalts in the Polynesian region. Geochimica et Cosmochimica Acta 63, 1181–1201.
Hart, S.R., 1984. A large-scale isotope anomaly in the Southern Hemisphere mantle. Nature 309, 753–757.
Hart, S.R., Hauri, E.H., Oschmann, L.A., Whitehead, J.A., 1992. Mantle plumes and entrainment: isotopic evidence. Science 256, 517–520.
Hauri, E.H., Whitehead, J.A., Hart, S.R., 1994. Fluid dynamic and geochemical aspects of entrainment in mantle plumes. Journal of Geophysical Research 99, 24275–24300.
Hildner, E., Klügel, A., Hauff, F., 2011. Magma storage and ascent during the 1995 eruption of Fogo, Cape Verde Archipelago. Contributions to Mineralogy and Petrology 1–22.
Hoernle, K., Tilton, G., Schmincke, H.-U., 1991. Sr–Nd–Pb isotopic evolution of Gran Canaria: evidence for shallow enriched mantle beneath the Canary Islands. Earth and Planetary Science Letters 106, 44–63.
Hoernle, K., Tilton, G., Le Bas, M., Duggen, S., Garbe-Schönberg, D., 2002. Geochemistry of oceanic carbonatites compared with continental carbonatites: mantle recycling of oceanic crustal carbonate. Contributions to Mineralogy and Petrology 142, 520–542.
Hofmann, A.W., 2003. Sampling mantle heterogeneity through oceanic basalts: isotopes and trace elements. In: Heinrich, D.H., Karl, K.T. (Eds.), Treatise on geochemistry. Pergamon, Oxford, pp. 61–101.
Hogarth, D.D., 1989. Pyrochlore, apatite and amphibole: distinctive minerals in carbonatite. In: Bell, K. (Ed.), Carbonatites: genesis and evolution. Unwin Hyman, London, pp. 105–148.
Holm, P.M., Wilson, J.R., Christensen, B.P., Hansen, L., Hansen, S.L., Hein, K.M., Mortensen, A.K., Pedersen, R., Plesner, S., Runge, M.K., 2006. Sampling the Cape Verde mantle plume: evolution of melt compositions on Santo Antão, Cape Verde Islands. Journal of Petrology 47, 145–189.
Holm, P.M., Grandvuinet, T., Friis, J., Wilson, J.R., Barker, A.K., Plesner, S., 2008. An $^{40}Ar$-$^{39}Ar$ study of the Cape Verde hot spot: temporal evolution in a semistationary plate environment. Journal of Geophysical Research 113, 1–22.
Huang, S., Frey, F.A., Blichert-Toft, J., Fodor, R.V., Bauer, G.R., Xu, G., 2005. Enriched components in the Hawaiian plume: evidence from Kahoolawe Volcano, Hawaii. Geochemistry, Geophysics, Geosystems 6, Q11006. http://dx.doi.org/10.1029/2005gc001012.
Jackson, M.G., Dasgupta, R., 2008. Compositions of HIMU, EM1, and EM2 from global trends between radiogenic isotopes and major elements in ocean island basalts. Earth and Planetary Science Letters 276, 175–186.
Jackson, M.G., Kurz, M.D., Hart, S.R., 2009. Helium and neon isotopes in phenocrysts from Samoan lavas: evidence for heterogeneity in the terrestrial high $^3He/^4He$ mantle. Earth and Planetary Science Letters 287, 519–528.
Janney, P.E., Castillo, P.R., 2001. Geochemistry of the oldest Atlantic oceanic crust suggests mantle plume involvement in the early history of the central Atlantic Ocean. Earth and Planetary Science Letters 192, 291–302.
Jørgensen, J.Ø., Holm, P.M., 2002. Temporal variation and carbonatite contamination in primitive ocean island volcanics from São Vicente, Cape Verde Islands. Chemical Geology 192, 249–267.
Kelley, K.A., Plank, T., Ludden, J., Staudigel, H., 2003. Composition of altered oceanic crust at ODP Sites 801 and 1149. Geochemistry, Geophysics, Geosystems 4, 8910. http://dx.doi.org/10.1029/2002GC000435.
Kjarsgaard, B.A., Hamilton, D.L., 1988. Liquid immiscibility and the origin of alkali-poor carbonatites. Mineralogical Magazine 52, 43–55.
Kogarko, L., 1993. Geochemical characteristics of oceanic carbonatites from the Cape Verde Islands. South African Journal of Geology 96, 119–125.
Kokfelt, T.F., Holm, P.M., Hawkesworth, C.J., Peate, D.W., 1998. A lithospheric mantle source for the Cape Verde Island magmatism: trace element and isotopic evidence from the island of Fogo. Mineralogical Magazine. Goldschmidt, pp. 801–802.
Lassiter, J.C., 2004. Role of recycled oceanic crust in the potassium and argon budget of the Earth: toward a resolution of the "missing argon" problem. Geochemistry, Geophysics, Geosystems 5, Q11012. http://dx.doi.org/10.1029/2004GC000711.
Le Maître, R.W., 2002. Igneous rocks. A classification and glossary of terms. Recommendations of the International Union of Geological Sciences Subcommission on the systematics of igneous rocks. Cambridge University Press, Cambridge . 236 pp.
Le Pichon, X., Fox, P.J., 1971. Marginal offsets, fracture zones, and the early opening of the North Atlantic. Journal of Geophysical Research 76, 6294–6308.
Lee, W.J., Wyllie, P.J., 2000. The system CaO–MgO–$SiO_2$–$CO_2$ at 1 GPa, metasomatic wehrlites, and primary carbonatite magmas. Contributions to Mineralogy and Petrology 138, 214–228.
Lee, W.J., Fanelli, M.F., Cava, N., Wyllie, P.J., 2000. Calciocarbonatite and magnesiocarbonatite rocks and magmas represented in the system CaO–MgO–$CO_2$–$H_2O$ at 0.2 GPa. Mineralogy and Petrology 68, 225–256.

Lodge, A., Helffrich, G., 2006. Depleted swell root beneath the Cape Verde Islands. Geology 34, 449–452.
MacDonald, G.A., 1968. Composition and origin of Hawaiian lavas. Geological Society of America Memoir 116, 477–522.
Madeira, J., Mata, J., Mourão, C., Brum da Silveira, A., Martins, S., Ramalho, R., Hoffmann, D.L., 2010. Volcano-stratigraphic and structural evolution of Brava Island (Cape Verde) based on $^{40}Ar/^{39}Ar$, U–Th and field constraints. Journal of Volcanology and Geothermal Research 196, 219–235.
Manhès, G., Minster, J.F., Allègre, C.J., 1978. Comparative uranium–thorium–lead and rubidium–strontium study of the Saint Sèverin amphoterite: consequences for early solar system chronology. Earth and Planetary Science Letters 39, 14–24.
Martins, S., Mata, J., Munhá, J., Mendes, M., Maerschalk, C., Caldeira, R., Mattielli, N., 2010. Chemical and mineralogical evidence of the occurrence of mantle metasomatism by carbonate-rich melts in an oceanic environment (Santiago Island, Cape Verde). Mineralogy and Petrology 99, 43–65.
Masson, D.G., Le Bas, T.P., Grevemeyer, I., Weinrebe, W., 2008. Flank collapse and large-scale landsliding in the Cape Verde Islands, off West Africa. Geochemistry, Geophysics, Geosystems 9, Q07015. http://dx.doi.org/10.1029/2008gc001983.
Mata, J., Moreira, M., Doucelance, R., Ader, M., Silva, L.C., 2010. Noble gas and carbon isotopic signatures of Cape Verde oceanic carbonatites: implications for carbon provenance. Earth and Planetary Science Letters 291, 70–83.
Middlemost, E.A.K., 1989. Iron oxidation ratios, norms and the classification of volcanic rocks. Chemical Geology 77, 19–26.
Millet, M.-A., Doucelance, R., Schiano, P., David, K., Bosq, C., 2008. Mantle plume heterogeneity versus shallow-level interactions: a case study, the São Nicolau Island, Cape Verde archipelago. Journal of Volcanology and Geothermal Research 176, 265–276.
Millet, M.-A., Doucelance, R., Baker, J.A., Schiano, P., 2009. Reconsidering the origins of isotopic variations in ocean island basalts: insights from fine-scale study of São Jorge Island, Azores archipelago. Chemical Geology 265, 289–302.
Mirnejad, H., Bell, K., 2006. Origin and source evolution of the Leucite Hills lamproites: evidence from Sr–Nd–Pb–O isotopic compositions. Journal of Petrology 47, 2463–2489.
Mitchell, J.G., Le Bas, M.J., Zielonka, J., Furnes, H., 1983. On dating the magmatism of Maio, Cape Verde Islands. Earth and Planetary Science Letters 64, 61–76.
Montelli, R., Nolet, G., Dahlen, F.A., Masters, G., 2006. A catalogue of deep mantle plumes: new results from finite-frequency tomography. Geochemistry, Geophysics, Geosystems 7, Q11007. http://dx.doi.org/10.1029/2006GC001248.
Moreira, M., Kurz, M.D., 2001. Subducted oceanic lithosphere and the origin of the "high-μ" basalt helium isotopic signature. Earth and Planetary Science Letters 189, 49–57.
Mourão, C., Mata, J., Doucelance, R., Madeira, J., Silveira, A.B.D., Silva, L.C., Moreira, M., 2010. Quaternary extrusive calciocarbonatite volcanism on Brava Island (Cape Verde): a nephelinite–carbonatite immiscibility product. Journal of African Earth Sciences 56, 59–74.
Mourão, C., Moreira, M., Mata, J., Raquin, A., Madeira, J., 2012. Primary and secondary processes constraining the noble gas isotopic signatures of carbonatites and silicate rocks from Brava Island: evidence for a lower mantle origin of the Cape Verde plume. Contributions to Mineralogy and Petrology 163, 995–1009.
Mukhopadhyay, S., 2012. Early differentiation and volatile accretion recorded in deep-mantle neon and xenon. Nature 486, 101–104.
Müller, R.D., Sdrolias, M., Gaina, C., Roest, W.R., 2008. Age, spreading rates, and spreading asymmetry of the world's ocean crust. Geochemistry, Geophysics, Geosystems 9, Q04006. http://dx.doi.org/10.1029/2007GC001743.
O'Reilly, S.Y., Zhang, M., Griffin, W.L., Begg, G., Hronsky, J., 2009. Ultradeep continental roots and their oceanic remnants: a solution to the geochemical "mantle reservoir" problem? Lithos 112, 1043–1054.
Palme, H., O'Neill, H.S.C., 2003. Cosmochemical estimates of mantle composition. In: Holland, H.D., Turekian, Karl K. (Eds.), Treatise on geochemistry. Elsevier Ltd., USA, pp. 1–38.
Parai, R., Mukhopadhyay, S., Lassiter, J.C., 2009. New constraints on the HIMU mantle from neon and helium isotopic compositions of basalts from the Cook–Austral Islands. Earth and Planetary Science Letters 277, 253–261.
Pin, C., Bassin, C., 1992. Evaluation of a strontium-specific extraction chromatographic method for isotopic analysis in geological materials. Analytica Chimica Acta 269, 249–255.
Pin, C., Briot, D., Bassin, C., Poitrasson, F., 1994. Concomitant separation of strontium and samarium-neodymium for isotopic analysis in silicate samples, based on specific extraction chromatography. Analytica Chimica Acta 298, 209–217.
Plank, T., Langmuir, C.H., 1998. The chemical composition of subducting sediment and its consequences for the crust and mantle. Chemical Geology 145, 325–394.
Pollitz, F.F., 1991. Two-stage model of African absolute motion during the last 30 million years. Tectonophysics 194, 91–106.
Porter, K.A., White, W.M., 2009. Deep mantle subduction flux. Geochemistry, Geophysics, Geosystems 10, Q12016. http://dx.doi.org/10.1029/2009GC002656.
Ramalho, R., Helffrich, G., Schmidt, D.N., Vance, D., 2010. Tracers of uplift and subsidence in the Cape Verde archipelago. Journal of the Geological Society 167, 519–538.
Rickli, J., Frank, M., Halliday, A.N., 2009. The hafnium–neodymium isotopic composition of Atlantic seawater. Earth and Planetary Science Letters 280, 118–127.
Salters, V.J.M., Sachi-Kocher, A., 2010. An ancient metasomatic source for the Walvis Ridge basalts. Chemical Geology 273, 151–167.
Shields, G., Veizer, J., 2002. Precambrian marine carbonate isotope database: version 1.1. Geochemistry, Geophysics, Geosystems 3, 1031. http://dx.doi.org/10.1029/2001gc000266.
Stracke, A., Bizimis, M., Salters, V.J.M., 2003. Recycling oceanic crust: quantitative constraints. Geochemistry, Geophysics, Geosystems 4, 8003. http://dx.doi.org/10.1029/2001gc000223.
Stracke, A., Hofmann, A.W., Hart, S.R., 2005. FOZO, HIMU, and the rest of the mantle zoo. Geochemistry, Geophysics, Geosystems 6, Q05007. http://dx.doi.org/10.1029/2004gc000824.
Thirlwall, M.F., 1997. Pb isotopic and elemental evidence for OIB derivation from young HIMU mantle. Chemical Geology 139, 51–74.
Torres, P., Silva, L.C., Serralheiro, A., Tassinari, C.C.G., Munhá, J., 2002. Enquadramento geocronológico pelo método K/Ar das principais sequências vulcano estratigráficas da Ilha do Sal - Cabo Verde. Garcia de Orta: Série de Geologia 18, 9–13.
Torres, P., Silva, L.C.D., Munhá, J., Caldeira, R., Mata, J., Tassinari, C.C.G., 2010. Petrology and geochemistry of lavas from Sal Island: implications for the variability of the Cape Verde magmatism. Comunicações Geológicas, Tomo 97, 35–62.
Veksler, I.V., Petibon, C., Jenner, G.A., Dorfman, A.M., Dingwell, D.B., 1998. Trace Element partitioning in immiscible silicate–carbonate liquid systems: an initial experimental study using a centrifuge autoclave. Journal of Petrology 39, 2095–2104.
Verhulst, A., Balaganskaya, E., Kirnarsky, Y., Demaiffe, D., 2000. Petrological and geochemical (trace elements and Sr–Nd isotopes) characteristics of the Paleozoic Kovdor ultramafic, alkaline and carbonatite intrusion (Kola Peninsula, NW Russia). Lithos 51, 1–25.
Vinnik, L., Silveira, G., Kiselev, S., Farra, V., Weber, M., Stutzmann, E., 2012. Cape Verde hotspot from the upper crust to the top of the lower mantle. Earth and Planetary Science Letters 319–320, 259–268.
Weaver, B.L., 1991. The origin of ocean island basalt end-member compositions: trace element and isotopic constraints. Earth and Planetary Science Letters 104, 381–397.
White, W.M., 1985. Sources of oceanic basalts: radiogenic isotopic evidence. Geology 13, 115–118.
Williams, C.A., Hill, I.A., Young, R., White, R.S., 1990. Fracture zones across the Cape Verde Rise, NE Atlantic. Journal of the Geological Society 147, 851–857.
Woodhead, J.D., Greenwood, P., Harmon, R.S., Stoffers, P., 1993. Oxygen isotope evidence for recycled crust in the source of EM-type ocean island basalts. Nature 362, 809–813.
Woolley, A.R., Kempe, D.R.C., 1989. Carbonatites: nomenclature, average chemical compositions, and element distribution. In: Bell, K. (Ed.), Carbonatites: genesis and evolution. Unwin Hyman, London, pp. 1–14.
Workman, R.K., Hart, S.R., 2005. Major and trace element composition of the depleted MORB mantle (DMM). Earth and Planetary Science Letters 231, 53–72.
Wyllie, P.J., Huang, W.-L., 1975. Influence of mantle $CO_2$ in the generation of carbonatites and kimberlites. Nature 257, 297–299.
Wyllie, P.J., Lee, W.-J., 1998. Model system controls on conditions for formation of magnesiocarbonatite and calciocarbonatite magmas from the mantle. Journal of Petrology 39, 1885–1893.
Xu, C., Campbell, I.H., Allen, C.M., Huang, Z., Qi, L., Zhang, H., Zhang, G., 2007. Flat rare earth element patterns as an indicator of cumulate processes in the Lesser Qinling carbonatites, China. Lithos 95, 267–278.
Zhao, D., 2007. Seismic images under 60 hotspots: search for mantle plumes. Gondwana Research 12, 335–355.
Zindler, A., Hart, S., 1986. Chemical geodynamics. Annual Review of Earth and Planetary Sciences 14, 493–571.

Available online at www.sciencedirect.com
SCIENCE DIRECT®
Geochimica et Cosmochimica Acta 70 (2006) 723–741
Geochimica
www.elsevier.com/locate/gca

# Multi-stage mixing in subduction zones: Application to Merapi volcano (Java island, Sunda arc)

Vinciane Debaille [a], Régis Doucelance [a,*], Dominique Weis [b,1], Pierre Schiano [a]

[a] *Laboratoire Magmas et Volcans, OPGC-Université Blaise Pascal-CNRS, 5 rue Kessler, 63038 Clermont-Ferrand Cedex, France*
[b] *Département des Sciences de la Terre et de l'Environnement, Université Libre de Bruxelles, CP 160/02, 1050 Brussels, Belgium*

Received 28 April 2005; accepted in revised form 29 September 2005

**Abstract**

Many studies have argued for the contribution of at least three components, namely the mantle wedge, the subducted oceanic crust, and its sediment cover, to describe the geochemistry of island arc volcanics. However, isotope correlations reflecting a simple binary mixing can be observed at the scale of a single arc island or volcano. Here we investigate the possibility that these trends reflect pseudo-binary mixing relationships in a three-component system. We present a simplified, two-stage model for the systematic isotope modelling of a cogenetic suite of arc lavas. This includes metasomatism of portions of the mantle wedge by hydrous phases released from the downgoing oceanic crust, and sediments, followed by progressive mixing and melting. A consequence of this model is that it leads to a two end-member mixing process from the mantle wedge, oceanic crust, and sediment components. To solve the model we reduce it to a step-by-step procedure combined with a Monte-Carlo simulation. The procedure consists of: (i) producing a large number of random values on each variable of the model; (ii) using the computed values to calculate the isotopic compositions of lavas; and (iii) comparing the obtained isotopic compositions with measured data. Applied to a new set of Sr, Nd, and Pb isotope data for volcanics (basalts, basaltic andesites, trachybasalts, and basaltic trachyandesites) from Merapi volcano (Java island, Sunda arc), the model successfully reproduces the binary mixing relationships previously documented for the medium-K and high-K lava series from this volcano, thus giving further support to the hypothesis that this distinction is inherited from the primary magmas and primarily reflects a property of the mantle source. The results allow identification of a set of numerical values for bulk partition coefficients (solid/hydrous fluid, and solid/$H_2O$-rich melt) and variables (e.g., the mass ratio between the metasomatizing phase and the mantle wedge), which can be used for quantitative arc-lava petrogenetic calculations. They also require a direct relationship between dehydration of the slab and melting of the metasomatized mantle wedge. Finally, our evaluation shows that for isotope modelling of the Merapi lavas, the two-stage procedure is controlled more by the considered source components (mantle wedge, oceanic crust, sediments, and their derivatives) than by the various processes involved (dehydration, melting, and mixing).


## 1. Introduction

Geochemical characteristics of island-arc basalts (IAB) are consistent with derivation by partial melting of portions of the upper mantle that have been enriched in water and incompatible elements due to interaction with a $H_2O$-rich phase released from subducted oceanic lithosphere (e.g., Gill, 1981). The trace-element characteristics of IAB (depletion of high field strength elements, HFSE, relative to the large ion lithophile elements, LILE) reflect this enrichment process (e.g., Perfit et al., 1980; Saunders et al., 1980; Arculus and Powell, 1986; McCulloch and Gamble, 1991). The enrichment process operates on mantle sources which are believed to be depleted peridotites, comparable to the source of mid-ocean ridge basalts (MORB). However, some arc magmas have been proposed to form by melting non-peridotite sources, such as ocean island basalt (OIB)-type source (Morris and Hart, 1983; Ito and

* Corresponding author. Fax: +33 4 73 34 67 44.
*E-mail address:* doucelance@opgc.univ-bpclermont.fr (R. Doucelance).
[1] Pacific Centre for Isotopic and Geochemical Research, Department of Earth and Ocean Sciences, University of British Columbia, Vancouver, Canada V6T 1Z4.

0016-7037/$ - see front matter © 2005 Elsevier Inc. All rights reserved.
doi:10.1016/j.gca.2005.09.021

Stern, 1986), subducted crust (Kay, 1978; Defant and Drummond, 1990), deep crust (Pichler and Zeil, 1972), and lower crustal or shallow upper mantle clinopyroxene-rich cumulates (Schiano et al., 2000). In addition, although coupled metasomatism and fluxed melting of peridotites in the mantle wedge is believed to be the dominant process by which primary arc magmas form and acquire their distinctive geochemical signature (e.g., McCulloch and Gamble, 1991; Stolper and Newman, 1994), important aspects of this process remain somewhat hypothetical.

In particular it is still not clear whether the high concentrations of LILE elements in arc lavas directly reflect their relative solubilities in slab-derived hydrous fluids (Tatsumi et al., 1986; Keppler, 1996), or are controlled by the subducted sediment input (Plank and Langmuir, 1993). In fact some of the geochemical characteristics of IAB, particularly their high Pb isotope ratios (Kay, 1978; White, 1985), high Sr isotope ratios (Perfit et al., 1980; McLennan and Taylor, 1981; White and Patchett, 1984; Hawkesworth et al., 1993) and the presence of $^{10}$Be (Tera et al., 1986), are attributed to recycled sediment contributions to the lava source. However, it has been shown that the geochemical characteristics of some arc lavas, for example from the Kamchatka arc (Kersting and Arculus, 1995), do not require the presence of recycled sediments in their source. In any case, it is still a matter of debate how reliably recycled sediment contributions to the source can be distinguished from crustal contamination during shallow level fractional crystallization. Finally, subduction zones act as a dynamic system, in which motion rate of the slab may vary in time, and variation in the sediment accumulation rate on the oceanic floor may modify the potential sediment supply to the subduction zone (Alves et al., 1999). The extent to which the observed compositional variations among arc volcanics reflect the above influences remains poorly understood.

Many authors have argued for the contribution of three components, namely the mantle wedge, the subducted basaltic ocean crust and its sediment cover, to account for the geochemistry of arc basalts (e.g. Kay, 1980; Ellam and Hawkesworth, 1988; Miller et al., 1994; Turner et al., 1996). However, even if arc lavas do not define an overall trend on isotope variation diagrams such as the "mantle-array" for MORB and OIB, correlations reflecting a simple binary mixing can be observed at the scale of a single arc island or volcano (e.g., Ellam and Hawkesworth, 1988; Turner et al., 1997; Turner and Foden, 2001). This observation seems, at first sight, to challenge the variety of physical processes and element fluxes that could be involved in the generation of arc magmas, as well as the number of potential sources. It suggests the predominance of two sources linked by a simple process of mixing. An alternative explanation is that the correlations for arc lavas are pseudo-binary mixing lines, formed by mixing of three or more components, as documented for basalts from some mid-ocean ridge regions (Hanan et al., 1986; Schilling et al., 1992; Douglass and Schilling, 2000).

In this paper, we present a two-stage model for the systematic isotope modelling of a cogenetic suite of arc lavas. The first stage of the model considers metasomatism of portions of the mantle wedge by hydrous fluids and/or melts derived from dehydration and/or melting reactions in the down-going altered oceanic crust and sediments. These processes lead to the definition of two end-members, namely the portions of mantle wedge metasomatized by the oceanic crust-derived phase and those metasomatized by the sediment-derived phase. The second stage of the model concerns progressive mixing of the two end-members thus defined. An important consequence of this two-stage model is that it leads to a two end-member mixing process from three distinct components (the mantle wedge, the subducted, altered oceanic crust, and sediments). For the purpose of testing, we apply the model to a new set of isotopic data (Sr, Nd, and Pb) for volcanics from Merapi volcano (Java island, Sunda arc), combining step-by-step calculations with a Monte-Carlo approach. Merapi volcano is almost ideally suited to be a case study for several reasons. Geochemical characteristics of the lavas might be ascribed to variable amounts of recycled oceanic crust and sediments in the source (McDermott and Hawkesworth, 1991; Alves et al., 1999; Turner and Foden, 2001; Gertisser and Keller, 2003a), contamination by the overlying basement does not significantly affect their whole-rock isotopic compositions and compositional correlations reflecting binary mixing relationships are documented (Alves et al., 1999; Gertisser and Keller, 2003a). The results show that the multi-stage model proposed here can reproduce the binary mixing trends defined by Merapi lavas. They also give a set of numerical values for bulk partition coefficients (solid/hydrous fluid, and solid/$H_2O$-rich melt) and parameters such as the mass ratio between the metasomatizing phase and the mantle wedge, which can be used for quantitative arc-lava petrogenetic calculations.

## 2. Role of subducted oceanic crust and sediments in arc lava petrogenesis

Evaluation of the influence of dehydration/melting of slab components on the generation of arc lavas is limited by imperfect knowledge of parameters such as the thermal structure of the upper mantle beneath volcanic arcs (e.g., Tatsumi et al., 1983) and the mineralogy of the subducted materials. Two parts of the descending slab can potentially play an important role in arc magma genesis: the altered oceanic crust and its sediment cover (Fig. 1).

Correctly assessing the contribution of the subducted oceanic crust, either as hydrated fluids or as silicate melts, to source regions of arc volcanics has been the subject of several studies (e.g., Kay, 1980; Perfit et al., 1980; Wyllie, 1982; Von Drach et al., 1986; Tatsumi et al., 1986; Woodhead, 1989; Davies and Stevenson, 1992; Schiano et al., 1995; Elliot et al., 1997; Yogodzinski and Kelemen,

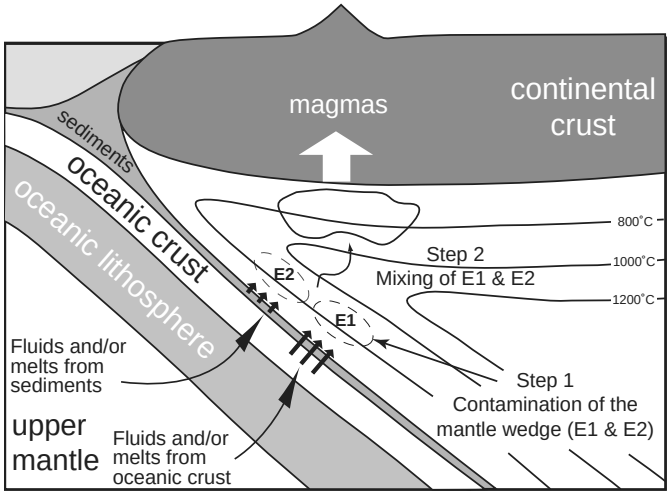


Fig. 1. Schematic cross section of the mantle wedge beneath a subduction zone illustrating the model of formation of arc lavas discussed in the text. Stage 1 considers metasomatism of the mantle wedge by fluids and/or melts derived by dehydration and/or melting processes in the down-going altered oceanic crust and sediments. Stage 2 considers progressive mixing of the two distinct end-members E1 and E2: E1, the portions of mantle wedge metasomatized by the phase issued from the subducted oceanic crust, and E2, the portions of mantle wedge metasomatized by the phase issued from the subducted sediments.

1998). Direct partial melting of the oceanic crust, thought to generate geochemically distinct andesitic lavas (Kay, 1978; Defant and Drummond, 1990), is generally restricted to young subduction/collision zones, incipient subduction, or post-collisional regimes, during thermal re-equilibration following cessation of subduction (e.g., Peacock, 1990; Davies and Stevenson, 1992; Peacock et al., 1994; Iwamori, 1998). Direct evidence for slab melting is given by the study of olivine-hosted melt inclusions in xenoliths from sub-arc mantle regions, which sample $H_2O$-rich silicate melt phases whose chemistry indicates an origin by very low degrees of melting of the subducted oceanic crust (Schiano et al., 1995). The aqueous fluid and/or silicate melt phase released from the subducted oceanic crust is generally considered to induce coupled metasomatism and fluxed melting of peridotites in the mantle wedge (e.g., Nicholls and Ringwood, 1973; Tatsumi et al., 1986). An alternative is that the phase does not directly trigger melting of the mantle wedge, as it reacts with the overlying peridotites that are then dragged downward above the subducting slab by the viscous coupling between the mantle wedge and the rigid slab (Tatsumi and Kogiso, 1997).

Subducted sediments, if present, can also be dehydrated and/or melted. Experiments indicate that melting of pelagic sediments occurs at a slightly lower temperature than wet gabbro (Nichols et al., 1994), thus sediment melting and subducted gabbroic crust dehydration can occur at the same temperature. This observation can be linked to the deduction of Plank and Langmuir (1993) that in many subduction zones the proportion of silicate melts released by subducted sediments is much more important than altered oceanic crust.

### 2.1. Behaviour of trace elements during dehydration and melting

When the descending plate, capped with hydrated oceanic crust and sediments, is warmed up by the surrounding mantle, high T/high P metamorphism takes place. Dehydration governed by the breakdown of hydrous phases, and possibly by the melting of descending material occurs at particular depths (Fig. 1). The resulting fluids and melts released from the slab act as an important means of mass transfer from the slab to the mantle wedge and are often invoked in order to explain many of the geochemical characteristics of arc magmas. However, assessing the exact influence of such mass transfer on island-arc characteristics requires precise evaluation of the chemical behaviour of elements in the released phase. As discussed below, behaviour of trace elements during dehydration and melting processes is directly related to their mobility and solid/melt partition coefficients, respectively.

#### 2.1.1. Relationship between slab-derived fluids and melts

Evidence for the identity and composition of the phase(s) released from subducted oceanic lithosphere is mostly indirect, based primarily on the chemical compositions of erupted arc lavas and mineral/fluid partitioning experiments that provide insight into the compositional characteristics of slab-derived fluids. Therefore there are still some aspects of the processes that transport the elements from the slab to the sources of arc lavas which remain somewhat hypothetical. For example, unambiguous characterization of the primary phase (fluid and/or melt) has proven to be difficult. Some authors have proposed complete miscibility between hydrous fluids and silicate melts at upper mantle P–T conditions (Bureau and Keppler, 1999), whereas others have suggested partial miscibility, broadly controlled by the amount of Cl in the fluid (Ayers and Eggler, 1995). The amount of dissolved silica in aqueous fluids at these temperatures and pressures does not have a major effect on mineral-aqueous fluid partitioning of trace elements (Keppler, 1996), because it is mainly controlled by the crystal chemistry of the residual phase (Stalder et al., 1998). Thus, only small differences in trace-element partitioning between aqueous fluids and silicate melts are expected, except perhaps for Th, Be, and Nb (Jonhson and Plank, 1999), and the geochemical signature left by the fluids will not be distinctly different from that of silicate melts (Ayers and Eggler, 1995). However, in the following investigations we will still separate the slab-derived metasomatic phase into (i) hydrous fluids and (ii) silicate melts.

#### 2.1.2. Dehydration

Transport of a trace element ($x$) during dehydration is related to its ability to be dissolved into aqueous fluids. The mobility ($M^x$) of $x$ can thus be expressed as the amount of $x$ lost during dehydration divided by its initial value (Tatsumi et al., 1986)

$$M^x = \frac{C_o^x - C_{\text{run}}^x}{C_o^x}, \quad (2.1)$$

where $C_{\text{run}}^x$ is the concentration of element $x$ after dehydration, and $C_o^x$, its initial concentration in the slab components (oceanic crust and sediments).

Assuming an equilibrium-state dehydration process, the mass balance equation gives

$$C_o^x = f \times C_{\text{fluids}}^x + (1-f) \times C_{\text{run}}^x, \quad (2.2)$$

where $f$ is the weight fraction of hydrous fluids extracted from the slab components and $C_{\text{fluids}}^x$ the concentration of element $x$ into these fluids.

By rearranging Eqs. (2.1 and 2.2) we obtain

$$C_{\text{fluids}}^x = \frac{C_o^x}{f} \times [1 - (1-f) \times (1 - M^x)]. \quad (2.3)$$

A fundamental assumption underlying the use of radiogenic (e.g., Sr, Nd, and Pb) isotopes is that dehydration processes do not fractionate them. Thus, the isotopic composition of long-lived isotopes of heavy elements in slab-derived fluids ($\alpha_{\text{fluids}}^x$) and subducted materials ($\alpha_o^x$) should be the same

$$\alpha_{\text{fluids}}^x = \alpha_o^x. \quad (2.4)$$

*2.1.3. Melting*

The behaviour of trace element $x$ during melting is expressed by the bulk solid/melt partition coefficient ($D^x$)

$$D^x = \frac{C_{\text{solid}}^x}{C_{\text{melt}}^x}, \quad (2.5)$$

where $C_{\text{solid}}^x$ and $C_{\text{melt}}^x$ are the concentrations of element $x$ in the slab components and silicate melts, respectively.

Assuming equilibrium-state melting, the mass balance equation gives the initial concentration ($C_o^x$) of element $x$ in the subducted materials

$$C_o^x = F \times C_{\text{melt}}^x + (1-F) \times C_{\text{solid}}^x, \quad (2.6)$$

where $F$ is the melt fraction.

Thus, combining Eqs. (2.5 and 2.6), the equation for the concentration of trace element $x$ in a silicate melt is

$$C_{\text{melt}}^x = \frac{C_o^x}{D^x + F \times (1 - D^x)}. \quad (2.7)$$

As in the case of dehydration, long-lived isotopes of heavy elements are not fractionated during melting; isotopic compositions of slab-derived melts ($\alpha_{\text{melt}}{}^x$) are thus in equilibrium with their source

$$\alpha_{\text{melt}}^x = \alpha_o^x, \quad (2.8)$$

where $\alpha_o^x$ is the isotopic composition of the subducted materials.

## 3. Modelling procedure

Important features of IAB isotope compositions, which should be explained by any global subduction zone model, are the binary mixing relationships that can be observed at the scale of a single island or volcano (e.g., Ellam and Hawkesworth, 1988; Turner et al., 1997; Turner and Foden, 2001; Alves et al., 2002). To address this characteristic, we use the following two-stage model to approximate the formation of arc magmas (Fig. 2).

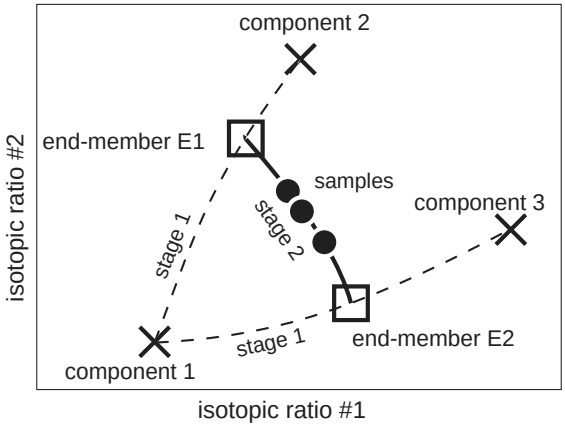


Fig. 2. Isotope diagram showing a hypothetical curved data array resulting from mixing of the two end-members E1 and E2 in a three component system, referred to as a pseudo-binary mixing array.

In the first stage, metasomatism of the mantle wedge by hydrous fluids and/or silicate melts derived from dehydration and/or melting reactions in the down-going slab generates two distinct end-members: E1, the portion of mantle wedge metasomatized by melts/fluids issued from the subducted oceanic crust, and E2, the portion of mantle wedge metasomatized by melts/fluids issued from the subducted sediments. An important observation to be made is that this first stage reduces the three involved components (mantle wedge, oceanic crust, and sediments) to two end-members.

In the second stage, after some unspecified period of time, the two end-members (E1 and E2) are mixed and melted to generate arc lavas.

It should be noted that contamination via assimilation of continental crust through the assimilation-fractional crystallization model (AFC, DePaolo, 1981) could also affect the isotopic composition of arc magmas. How reliably such shallow-level crustal contamination may be distinguished from recycled sediment contributions to the magma source is still a matter of debate (e.g., Davidson, 1987; Davidson et al., 2005).

A recent study of Merapi samples by Chadwick et al. (2005) has provided evidence for crustal influence at the mineral scale. However, in the case of Java, a significant role of the crustal contamination on the whole-rock isotopic compositions was previously dismissed (Alves et al., 1999, 2002; Gertisser and Keller, 2003a). For this reason, and also because there are subduction zones which do not have a continental basement, we decided not to consider crustal contamination in our modelling.

### 3.1. Mathematical formulation

#### 3.1.1. Dehydration and melting of subducted materials

Using Eqs. (2.3 and 2.7), we obtain the concentration ($C^x_{OC/SED}$) of element $x$ in the melts/fluids originating from melting/dehydration of subducted oceanic crust ($C^x_{OC}$) and sediments ($C^x_{SED}$)

$$C^x_{OC/SED} = \frac{Tm}{Tm+1} \times C^x_{melt} + \frac{1}{Tm+1} \times C^x_{fluid}, \quad (3.1)$$

where $Tm$ is the mass ratio between melts and hydrous fluids issued from melting and dehydration reactions in the slab.

From the definition of the mass ratio $Rm$ between the slab-derived melts/fluids and the mantle wedge, we can determine the concentration of element $x$ ($C^x_{end\text{-}member}$) in the end-members E1 and E2 (the mantle wedge contaminated by melts/fluids issued from subducted oceanic crust and sediments, respectively)

$$C^x_{end\text{-}member} = \frac{Rm}{Rm+1} \times C^x_{OC/SED} + \frac{1}{Rm+1} \times C^x_{MW}, \quad (3.2)$$

where $C^x_{MW}$ is the concentration of element $x$ in the mantle wedge.

For the isotopic compositions of E1 and E2, we consider Eqs. (2.4 and 2.8) and use a complete formulation of mixing, to take into account potentially large differences in isotopic compositions between slab-derived melts/fluids and the mantle wedge

$$\alpha^x_{end\text{-}member} = \gamma_\alpha \times \alpha^x_o + (1-\gamma_\alpha) \times \alpha^x_{MW}, \quad (3.3)$$

where $\alpha^x_{MW}$ is the isotopic composition of the mantle wedge and $\gamma_\alpha$ the mass fraction of the normalizing isotope for the isotopic ratios $\alpha^x_{end\text{-}member}$, $\alpha^x_o$, and $\alpha^x_{MW}$

$$\gamma_\alpha = \frac{\dfrac{Rm \times C^x_{OC/SED}}{1+\left(\sum_{i=1}^{n} \frac{a_i}{b} \times \frac{Ma_i}{M_b}\right)_{OC/SED}}}{\dfrac{Rm \times C^x_{OC/SED}}{1+\left(\sum_{i=1}^{n} \frac{a_i}{b} \times \frac{Ma_i}{M_b}\right)_{OC/SED}} + \dfrac{C^x_{MW}}{1+\left(\sum_{i=1}^{n} \frac{a_i}{b} \times \frac{Ma_i}{M_b}\right)_{MW}}}, \quad (3.4)$$

where $\left(\sum_{i=1}^{n} a_i/b \times M_{a_i}/M_b\right)_{OC/SED}$ and $\left(\sum_{i=1}^{n} a_i/b \times M_{a_i}/M_b\right)_{MW}$ correspond to the isotopic compositions of slab-derived melts/fluids and the mantle wedge, respectively, weighted by the ratios of molar masses. For instance, this gives for Pb

$$\frac{^{206}Pb}{^{204}Pb} \times \frac{M_{^{206}Pb}}{M_{^{204}Pb}} + \frac{^{207}Pb}{^{204}Pb} \times \frac{M_{^{207}Pb}}{M_{^{204}Pb}} + \frac{^{208}Pb}{^{204}Pb} \times \frac{M_{^{208}Pb}}{M_{^{204}Pb}}. \quad (3.5)$$

#### 3.1.2. Mixing of end-members

Given the concentrations and isotopic compositions of end-members E1 and E2, isotopic compositions of lavas resulting from various proportions of mixing between E1 and E2 can therefore be estimated from

$$\alpha^x_{lavas} = \gamma_E \times \alpha^x_{E1} + (1-\gamma_E) \times \alpha^x_{E2}, \quad (3.6)$$

where $\gamma_E$ is the mass fraction of the normalizing isotope for the isotopic ratios $\alpha^x_{lavas}$, $\alpha^x_{E1}$, and $\alpha^x_{E2}$.

For this mixing stage we assume a similar behaviour of trace elements during melting of the two end-members E1 and E2. In other words, most trace elements have effective partition coefficients in the two melting processes that are approximately the same.

### 3.2. Model solution

Here we restrict our method to systematic Sr, Nd, and Pb isotope modelling of a suite of arc lavas (such as in the Merapi case; cf. Section 5). Therefore the two-stage model developed in Section 3 leads to a system described by 16 equations. These are, for each end-member (E1 and E2), the mixing equations related to the three concentrations (Sr, Nd, and Pb) and the five isotopic ratios ($^{87}Sr/^{86}Sr$, $^{143}Nd/^{144}Nd$, $^{206}Pb/^{204}Pb$, $^{207}Pb/^{204}Pb$, and $^{208}Pb/^{204}Pb$).

#### 3.2.1. Step-by-step calculation and Monte-Carlo approach

To solve equations of the model and thus give an estimation of the mobility and bulk solid/melt partition coefficients for Sr, Nd, and Pb in oceanic crust and sediments, we combine a step-by-step calculation with a Monte-Carlo simulation. The procedure consists of: (i) producing a large number of random values on each variable of the model, given realistic ranges of variations; (ii) using the computed values to calculate the isotopic compositions of lavas for $\gamma_E$ comprised between 0 and 1 (cf. Eq. (3.6)); and (iii) comparing the obtained isotopic compositions with a true dataset (i.e., measured on natural samples), to retain or otherwise the inputted values. The calculation is repeated 1,000,000 times for statistical considerations.

#### 3.2.2. Comparison between modelled and natural isotopic compositions

Testing the isotope compositions obtained from the Monte-Carlo simulation is done by evaluating the fit to measured data in isotope variation diagrams ($^{143}Nd/^{144}Nd$ vs. $^{87}Sr/^{86}Sr$, $^{87}Sr/^{86}Sr$ vs. $^{206}Pb/^{204}Pb$, $^{143}Nd/^{144}Nd$ vs. $^{206}Pb/^{204}Pb$, $^{207}Pb/^{204}Pb$ vs. $^{206}Pb/^{204}Pb$, and $^{208}Pb/^{204}Pb$ vs. $^{206}Pb/^{204}Pb$). For this, we calculate the distance (Dist) in a least-square sense between hyperbolae corresponding to mixing of the end-members E1 and E2 and measured data in a five dimensional space corresponding to the five isotope ratios used. However, as the level of geochemical significance is not the same for all isotopic systems (for example, $^{207}Pb/^{204}Pb$ displays weak variations due to the near extinction of $^{235}U$ but is measured with an analytical precision similar to that of $^{206}Pb/^{204}Pb$; therefore, treating the two ratios equally would obviously amount to overestimation of the $^{207}Pb/^{204}Pb$ information), we do not consider raw data but apply a factor designed to weigh all isotopic tracers equivalently. This weighting factor ($R$) is comparable in essence to that used by Allègre et al. (1986/1987) in their isotope multispace analysis, and corresponds to the ratio of the total range for the set of samples over the minimum difference between two samples above

which they are considered as significantly different (i.e., the $2\sigma$ external reproducibility of standard measurements, see Table 1).

Mathematically, the distance between modelled and measured data is given by

$$\mathrm{Dist} = \sum_{1}^{n}\left[\sum_{1}^{5}\left(\alpha_j^M - \alpha_j^C\right)^2 \times (R_j/\sigma_j)^2\right]^{(1/2)}, \quad (3.7)$$

where $n$ is the number of samples used for comparison; $\alpha_j^M$ is the measure of the isotopic ratio considered ($^{87}Sr/^{86}Sr$, $^{143}Nd/^{144}Nd$, $^{206}Pb/^{204}Pb$, $^{207}Pb/^{204}Pb$ or $^{208}Pb/^{204}Pb$) and $\alpha_j^C$ its calculated value; $\sigma_j$ is the standard deviation of the measured dataset, and $R_j$ the weighting factor for a given isotopic ratio.

It should be noted that the distance (Dist) is not calculated, but is considered as infinite when at least one of the two end-members E1 and E2 falls within the range of variations of the measured samples.

### 3.2.3. Best solution

The smallest distance ($\mathrm{Dist_{min}}$) calculated among the set of 1,000,000 combinations defines the best solution; i.e., the combination of data that minimizes the difference between modelled compositions and measured data. We should, however, be aware that this best solution does not guarantee that all data will lie closely along the corresponding mixing hyperbola, thus requiring visual comparison between the hyperbola and the data in isotope variation diagrams.

A way to evaluate how reliable the best combination is is to consider the minimum distance ($D_{2\sigma}$) between measured data and the theoretical mixing curve above which they are considered as indistinguishable, i.e. within the analytical error ($2\sigma$), and to compare this distance with the calculated distance (Dist)

$$D_{2\sigma} = \sum_{1}^{n}\left[\sum_{1}^{5}(2\times\sigma_{\mathrm{ext}}^j)^2 \times (R_j/\sigma_j)^2\right]^{(1/2)}, \quad (3.8)$$

where $\sigma_{\mathrm{ext}}^j$ is the $1\sigma$ external reproducibility of the isotopic ratio considered ($^{87}Sr/^{86}Sr$, $^{143}Nd/^{144}Nd$, $^{206}Pb/^{204}Pb$, $^{207}Pb/^{204}Pb$ or $^{208}Pb/^{204}Pb$) (see also Table 1).

### 3.2.4. Graphic representations

Distances calculated from the combinations of inputted values other than the best solution give further information on the model. In particular comparison between results of the best solution and those obtained for the 2nd, 3rd, ..., $n$th smallest distances may be useful. We thus represent all combinations by using histograms of the model parameters (Fig. 3). However, we do not attribute an identical weight to all computed values of a given parameter: we attribute the ratio of the smallest total distance ($\mathrm{Dist_{min}}$) over the distance of the considered combination (Dist) as a weighting factor. This provides a weight of 1 for parameters of the best solution, and a weight inversely proportional to their distance for parameters of the other combinations (a weight of 0 is thus attributed to solutions with E1 and/or E2 falling within the range of variations of the measured samples). In other words, the less the modelled hyperbola fits the measured data, the less the corresponding parameters influence the shape of the histograms.

### 3.2.5. Reproducibility of the approach

To test the reproducibility of the procedure, we have twice repeated the injection of 1,000,000 randomly selected combinations (with the same ranges of variations) into the model and mixing equations. Results are illustrated in Fig. 3 in histograms of best solution-normalized parameters. The good agreement observed between the two simulations demonstrates the reproducibility of the total approach.

## 4. A priori variables

A total of 44 variables is used in the model (Table 2). They can be divided into three different categories: (i) 24 variables related to components; (ii) 8 variables related to

Table 1
Data normalization (Range of isotopic variations $\Delta$, $1\sigma$ external reproducibility of standard measurements $\sigma_{\mathrm{ext}}$ and weighting factor $R = \Delta/2\sigma_{\mathrm{ext}}$ for each tracer) calculated for the Merapi medium-K and high-K lava series isotope dataset

| | $^{87}Sr/^{86}Sr$ | $^{143}Nd/^{144}Nd$ | $^{206}Pb/^{204}Pb$ | $^{207}Pb/^{204}Pb$ | $^{208}Pb/^{204}Pb$ |
|---|---|---|---|---|---|
| *Medium-K series* | | | | | |
| Minimum value | 0.705043 | 0.512687 | 18.738 | 15.680 | 39.093 |
| Maximum value | 0.705876 | 0.512770 | 18.818 | 15.697 | 39.218 |
| Variation ($\Delta$) | 0.000833 | 0.000083 | 0.080 | 0.017 | 0.125 |
| $\sigma_{\mathrm{ext}}$ | 0.000011 | 0.000012 | 0.003 | 0.003 | 0.008 |
| $R$ | 39.09 | 3.45 | 11.80 | 2.74 | 8.28 |
| *High-K series* | | | | | |
| Minimum value | 0.705341 | 0.512676 | 18.737 | 15.676 | 39.084 |
| Maximum value | 0.705763 | 0.512782 | 18.768 | 15.696 | 39.158 |
| Variation ($\Delta$) | 0.000422 | 0.000106 | 0.031 | 0.020 | 0.074 |
| $\sigma_{\mathrm{ext}}$ | 0.000011 | 0.000012 | 0.003 | 0.003 | 0.008 |
| $R$ | 19.81 | 4.41 | 4.57 | 3.23 | 4.90 |

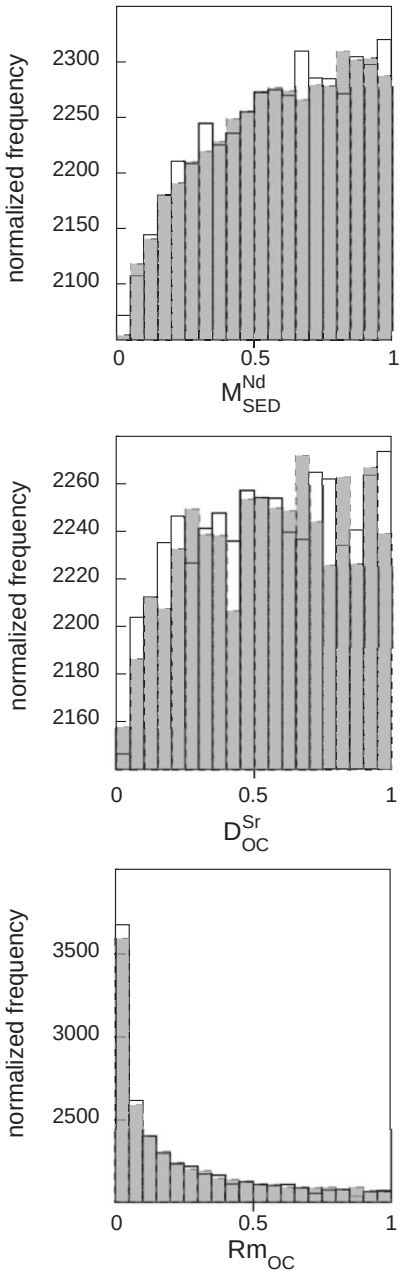


Fig. 3. Comparison of histograms of the best-solution normalized parameters $M^{Nd}_{SED}$ (Nd mobility coefficient during sediment dehydration), $D^{Sr}_{OC}$ (Sr bulk solid/melt partition coefficient during oceanic crust melting) and $Rm_{OC}$ (mass ratio between melts/fluids released by subducted oceanic crust and the mantle wedge) obtained from two inputs of 1,000,000 randomly selected combinations (with the same ranges of variations) into the model equations for the medium-K series from Merapi Volcano. The good agreement observed between the two simulations demonstrates the reproducibility of the total approach.

dehydration and melting processes; and (iii) 12 variables related to behaviour of elements.

### 4.1. Variables related to components

These correspond to the Sr, Nd, and Pb concentrations and $^{87}Sr/^{86}Sr$, $^{143}Nd/^{144}Nd$, $^{206}Pb/^{204}Pb$, $^{207}Pb/^{204}Pb$, and $^{208}Pb/^{204}Pb$ ratios of the mantle wedge, oceanic crust and sediment components. These variables can be considered as well constrained since their values can be deduced from direct measurements of natural samples, such as Oceanic Drilling Project (ODP) samples for the oceanic crust and sediments and MORB for the mantle wedge. Note, however, that the Sr, Nd, and Pb concentrations of the mantle wedge inferred from MORB measurements have to be corrected for partial melting.

### 4.2. Variables related to dehydration and melting processes

These correspond to the melt fractions and dehydration rates of oceanic crust and sediments, the mass ratios between silicate melts and hydrous fluids in the $H_2O$-rich released phase, and the mass ratios between the released phase and the mantle wedge. While some of these variables are poorly constrained, others, including the weight fractions of hydrous fluids extracted from the slab (Peacock, 1990) and the degree of partial melting of both oceanic crust and sediments (Jonhson and Plank, 1999; Nichols et al., 1994), are known with a relatively high degree of confidence.

### 4.3. Variables related to behaviour of elements during slab dehydration and melting

These correspond to the respective mobility and bulk partition coefficients of Sr, Nd, and Pb in the subducted oceanic crust and sediments. These variables represent unknowns in the model. In practice, however, we assume an incompatible behaviour (i.e., a bulk partition coefficient between 0 and 1) for the three elements during melting of the two slab components.

### 4.4. Ranges of errors

A constant relative error of 100% is adopted for unconstrained variables (unknowns) in the model. For example, mobility and bulk partition coefficients are randomly extracted from intervals equal to $0.5 \pm 0.5$. Conversely, maximum errors of 10% are assumed for well-constrained variables (parameters). Among the 44 variables of the model, 28 can thus be considered as parameters and 16 as unknowns (Table 2). Therefore, the system to be solved through a step-by-step procedure comprises 16 equations for 16 unknowns.

## 5. Case study: Merapi volcano, Java island, Sunda arc

In the following sections, we apply parts of the simplified model of arc-lava genesis described above to a new set of Sr, Nd, and Pb isotope data on volcanics from Merapi volcano. The point of this application is to emphasize the different aspects of our approach and examine values of the parameters (for example, bulk partition coefficients, mobility coefficients, and slab-derived melt/fluid ratios)

Table 2
List of the variables used in the model

| Variable | | Mean value | Variation | % error |
|---|---|---|---|---|
| $MW^{87}$ | $^{87}Sr/^{86}Sr$ of mantle wedge | 0.702925 | 0.000095 | 0.014 |
| $MW^{143}$ | $^{143}Nd/^{144}Nd$ of mantle wedge | 0.513070 | 0.000013 | 0.003 |
| $MW^{206}$ | $^{206}Pb/^{204}Pb$ of mantle wedge | 17.923 | 0.038 | 0.21 |
| $MW^{207}$ | $^{206}Pb/^{204}Pb$ of mantle wedge | 15.488 | 0.021 | 0.13 |
| $MW^{208}$ | $^{206}Pb/^{204}Pb$ of mantle wedge | 37.776 | 0.05 | 0.13 |
| $MW^{Sr}$ | Sr concentration of mantle wedge | 15.0 | 1.5 | 10 |
| $MW^{Nd}$ | Nd concentration of mantle wedge | 1.0 | 0.1 | 10 |
| $MW^{Pb}$ | Pb concentration of mantle wedge | 0.065 | 0.006 | 9.23 |
| $OC^{87}$ | $^{87}Sr/^{86}Sr$ of subducted oceanic crust | 0.703450 | 0.000753 | 0.11 |
| $OC^{143}$ | $^{143}Nd/^{144}Nd$ of subducted oceanic crust | 0.512949 | 0.000094 | 0.02 |
| $OC^{206}$ | $^{206}Pb/^{204}Pb$ of subducted oceanic crust | 18.610 | 0.560 | 3.01 |
| $OC^{207}$ | $^{207}Pb/^{204}Pb$ of subducted oceanic crust | 15.576 | 0.085 | 0.54 |
| $OC^{208}$ | $^{208}Pb/^{204}Pb$ of subducted oceanic crust | 38.645 | 0.685 | 1.77 |
| $OC^{Sr}$ | Sr concentration of subducted oceanic crust | 125.0 | 12.5 | 10 |
| $OC^{Nd}$ | Nd concentration of subducted oceanic crust | 11.0 | 1.1 | 10 |
| $OC^{Pb}$ | Pb concentration of subducted oceanic crust | 0.2 | 0.02 | 10 |
| $SED^{87}$ | $^{87}Sr/^{86}Sr$ of subducted sediments | 0.711348 | 0.005472 | 0.77 |
| $SED^{143}$ | $^{143}Nd/^{144}Nd$ of subducted sediments | 0.512391 | 0.000286 | 0.05 |
| $SED^{206}$ | $^{206}Pb/^{204}Pb$ of subducted sediments | 18.904 | 0.086 | 0.45 |
| $SED^{207}$ | $^{207}Pb/^{204}Pb$ of subducted sediments | 15.719 | 0.022 | 0.14 |
| $SED^{208}$ | $^{208}Pb/^{204}Pb$ of subducted sediments | 39.273 | 0.055 | 0.14 |
| $SED^{Sr}$ | Sr concentration of subducted sediments | 220.0 | 22 | 10 |
| $SED^{Nd}$ | Nd concentration of subducted sediments | 33.0 | 3.3 | 10 |
| $SED^{Pb}$ | Pb concentration of subducted sediments | 25.0 | 2.5 | 10 |
| $M^{Sr}_{OC}$ | Mobility of Sr in subducted oceanic crust | 0.5 | 0.5 | 100 |
| $M^{Nd}_{OC}$ | Mobility of Nd in subducted oceanic crust | 0.5 | 0.5 | 100 |
| $M^{Pb}_{OC}$ | Mobility of Pb in subducted oceanic crust | 0.5 | 0.5 | 100 |
| $D^{Sr}_{OC}$ | Partition coefficient of Sr in subducted oceanic crust | 0.5 | 0.5 | 100 |
| $D^{Nd}_{OC}$ | Partition coefficient of Nd in subducted oceanic crust | 0.5 | 0.5 | 100 |
| $D^{Pb}_{OC}$ | Partition coefficient of Pb in subducted oceanic crust | 0.5 | 0.5 | 100 |
| $M^{Sr}_{SED}$ | Mobility of Sr in subducted sediments | 0.5 | 0.5 | 100 |
| $M^{Nd}_{SED}$ | Mobility of Nd in subducted sediments | 0.5 | 0.5 | 100 |
| $M^{Pb}_{SED}$ | Mobility of Pb in subducted sediments | 0.5 | 0.5 | 100 |
| $D^{Sr}_{SED}$ | Partition coefficient of Sr in subducted sediments | 0.5 | 0.5 | 100 |
| $D^{Nd}_{SED}$ | Partition coefficient of Nd in subducted sediments | 0.5 | 0.5 | 100 |
| $D^{Pb}_{SED}$ | partition coefficient of Pb in subducted sediments | 0.5 | 0.5 | 100 |
| $Rm_{OC}$ | Mass of fluids released by subducted oceanic crust/ mass of mantle wedge | 0.5 | 0.5 | 100 |
| $Rm_{SED}$ | Mass of fluids released by subducted sediments/ mass of mantle wedge | 0.5 | 0.5 | 100 |
| $f_{OC}$ | Dehydration rate of subducted oceanic crust | 0.015 | 0.0015 | 10 |
| $f_{SED}$ | Dehydration rate of subducted sediments | 0.015 | 0.0015 | 10 |
| $F_{OC}$ | Partial melting degree of subducted oceanic crust | 0.15 | 0.015 | 10 |
| $F_{SED}$ | Partial melting degree of subducted sediments | 0.015 | 0.0015 | 10 |
| $\frac{Tm_{OC}}{Tm_{OC}+1}$ | $Tm_{OC}$ = mass of melts/mass of hydrated fluids from subducted oceanic crust | 0.5 | 0.5 | 100 |
| $\frac{Tm_{SED}}{Tm_{SED}+1}$ | $Tm_{SED}$ = mass of melts/mass of hydrated fluids from subducted sediments | 0.5 | 0.5 | 100 |

Data source: Mantle wedge, Dosso et al. (1988); oceanic crust, Weis and Frey (1996); sediments, Ben Othman et al. (1989); Plank and Langmuir (1998); Hemming and McLennan (2001).

that can account for the isotopic arrays found in arc volcanoes.

### 5.1. Geological setting

Merapi volcano has been built up in the central part of Java island over the last $650 \pm 250$ kyr (Camus et al., 2000). Its activity, related to the northward subduction of the Indo-Australian plate beneath the Eurasian plate (Hamilton, 1979; Turner and Foden, 2001), is characterized by semi-continuous lava extrusions producing summit domes and periodic collapse events triggering pyroclastic flows (Camus et al., 2000). Although an overall isotopic trend has been documented for Merapi volcanics (e.g., Gertisser and Keller, 2003a), three distinct components are generally considered for their source. These are the mantle wedge, the subducted oceanic crust and its sediment cover (McDermott and Hawkesworth, 1991; Alves et al., 1999; Turner and Foden, 2001; Gertisser and Keller, 2003a). In addition, even though a slight role for shallow-level crustal contamination has been envisioned (Turner and Foden, 2001; Chadwick et al., 2005), this process has not significantly changed the isotopic characteristics of erupted whole rocks in the region (Alves et al., 1999; Gertisser and Keller, 2003a) and thus it will not be considered in the following discussion.

### 5.2. Major and isotope analyses

#### 5.2.1. Analytical procedures

All samples were coarse-crushed in a hydraulic piston crusher before being reduced to powder in an agate shatterbox. Major-element concentrations were measured by ICP-AES, at the Service d'Analyse des Roches et des Minéraux (SARM, CRPG/Nancy) with a precision better than 1% except for MnO, CaO, and $Na_2O$ (<2%) and $TiO_2$ and $P_2O_5$ (<5%). Standards and reproducibilities can be downloaded from the SARM website at http://www.crpg.cnrs-nancy.fr/SARM.

Sr isotope ratios were measured by TIMS at the Pacific Centre for Isotopic and Geochemical Research (PCIGR/Vancouver), whereas isotopic composition measurements of Nd and Pb were made by MC-ICP-MS at the Université Libre de Bruxelles (ULB). Sr, Nd, and Pb were separated using the chemical procedure described in Weis and Frey (1991) and Weis et al. (2005). Prior to dissolution, samples were leached several times during a 15 mn period with 6N HCl in an ultrasonic bath to remove any secondary contamination. The mean weight loss during leaching was 34%. Total blank values were negligible (< 1 ng) for each element with respect to sample abundances (> 60,000, 200, and 3000 ng for Sr, Pb, and Nd, respectively).

Sr was measured dynamically and corrected for mass discrimination to $^{86}Sr/^{88}Sr = 0.1194$. Seven analyses of the SRM987 NIST standard performed during the course of the study give a mean $^{87}Sr/^{86}Sr$ value of $0.710247 \pm 24$ ($2\sigma$). The total external reproducibility based on measurements of replicates (crushing, chemical separation, and mass spectrometric run, cf. samples MP 231 a and b and MP 304 a and b) is better than 30 ppm.

Nd was measured dynamically and corrected for potential Ce and Sm interferences by monitoring $^{140}Ce$ and $^{147}Sm$, respectively. Mass discrimination was normalized to $^{146}Nd/^{144}Nd = 0.7219$. The $^{143}Nd/^{144}Nd$ mean value obtained for the Rennes standard (Chauvel and Blichert-Toft, 2001), analysed every two samples, was $0.511927 \pm 24$ ($2\sigma$, $n = 16$). The total external reproducibility based on the replicate sample analyses (crushing, chemical separation, and mass spectrometric run) is better than 47 ppm.

Pb isotope measurements were made statically. Mass discrimination was corrected for by using the Tl doping technique, assuming the same fractionation effect between Tl and Pb and $^{203}Tl/^{205}Tl = 2.3885$ (Weis et al., 2005). Isobaric interference between $^{204}Hg$ and $^{204}Pb$ was controlled by monitoring $^{202}Hg$. Repeated analyses ($n = 28$) of the SRM981 NIST standard (200 ppb Pb diluted with 50 ppb Tl in 0.05 M $HNO_3$), measured every two samples, give mean values of $16.941 \pm 6$ ($2\sigma$), $15.497 \pm 6$ ($2\sigma$) and $37.717 \pm 15$ ($2\sigma$) for $^{206}Pb/^{204}Pb$, $^{207}Pb/^{204}Pb$, and $^{208}Pb/^{204}Pb$, respectively. The total external reproducibility based on the replicate sample analyses (crushing, chemical separation, and mass spectrometric run) is better than 400 ppm.

#### 5.2.2. Major-element and isotope results

Twenty samples (see Berthommier (1990) for locations) were analyzed in this study. They all have $SiO_2$ contents between 48 and 55% wt, MgO between 2.5 and 4.8% wt, and ($Na_2O + K_2O$) between 3.7 and 5.8% wt (Table 3 and Fig. 4); they correspond to basalts, basaltic andesites, trachybasalts, and basaltic trachyandesites. The 20 samples span the period between 400 kyr ago and recent flows. Consequently, Sr, Nd, and Pb isotopic compositions were not corrected for radioactive decay of Rb, Sm, U, and Th. Isotope data are given in Table 4 and illustrated in Fig. 5. They are in agreement for Sr and Nd isotopes with

Table 3
Major-element concentrations for samples from Merapi volcano

| | Series | $SiO_2$ | $Al_2O_3$ | $Fe_2O_3$ | MnO | MgO | CaO | $Na_2O$ | $K_2O$ | $TiO_2$ | $P_2O_5$ | LOI | Total |
|---|---|---|---|---|---|---|---|---|---|---|---|---|---|
| MP 1 | MK | 53.6 | 19.0 | 8.36 | 0.18 | 2.67 | 8.77 | 3.41 | 2.05 | 0.77 | 0.32 | 0.74 | 99.87 |
| MP 14 | MK | 53.7 | 19.1 | 8.66 | 0.17 | 3.15 | 9.01 | 3.33 | 1.54 | 0.78 | 0.26 | 0.21 | 99.91 |
| MP 21 | MK | 48.3 | 19.9 | 10.40 | 0.16 | 3.77 | 10.30 | 2.68 | 1.00 | 1.01 | 0.27 | 2.10 | 99.89 |
| MP 29 | HK | 52.0 | 19.0 | 9.36 | 0.18 | 3.65 | 9.27 | 3.21 | 1.63 | 0.86 | 0.27 | 0.48 | 99.91 |
| MP 41 | HK | 54.1 | 18.6 | 8.59 | 0.19 | 2.75 | 7.99 | 3.60 | 1.81 | 0.83 | 0.28 | 1.15 | 99.89 |
| MP 42 | HK | 54.3 | 18.7 | 8.18 | 0.18 | 2.73 | 8.43 | 3.71 | 1.87 | 0.83 | 0.29 | 0.59 | 99.81 |
| MP 43 | MK | 55.3 | 18.7 | 8.18 | 0.16 | 2.76 | 8.39 | 3.50 | 1.76 | 0.85 | 0.27 | −0.02 | 99.87 |
| MP 63 | MK | 48.5 | 19.6 | 10.60 | 0.19 | 4.82 | 9.16 | 2.70 | 1.15 | 0.90 | 0.25 | 2.21 | 100.08 |
| MP 65 | MK | 49.7 | 19.3 | 10.80 | 0.16 | 3.17 | 9.28 | 2.82 | 1.91 | 1.00 | 0.28 | 1.55 | 99.97 |
| MP 84-g | HK | 55.2 | 19.5 | 7.82 | 0.19 | 2.47 | 8.52 | 3.68 | 2.15 | 0.73 | 0.29 | −0.21 | 100.55 |
| MP 84-1 | HK | 54.9 | 19.2 | 7.82 | 0.19 | 2.50 | 8.52 | 3.65 | 2.12 | 0.73 | 0.30 | −0.03 | 99.93 |
| MP 88 | MK | 55.1 | 18.7 | 7.91 | 0.18 | 2.65 | 8.25 | 3.56 | 1.86 | 0.83 | 0.27 | 0.33 | 99.64 |
| MP 93 | MK | 55.2 | 19.0 | 7.10 | 0.17 | 2.68 | 7.61 | 3.32 | 1.57 | 0.62 | 0.22 | 2.39 | 99.88 |
| MP 231 | MK | 49.1 | 20.1 | 9.36 | 0.15 | 3.94 | 10.80 | 2.87 | 1.25 | 0.79 | 0.21 | 1.68 | 100.25 |
| MP 232 | MK | 49.3 | 19.2 | 10.00 | 0.15 | 4.51 | 10.20 | 2.93 | 1.44 | 0.86 | 0.24 | 1.14 | 99.97 |
| MP 243 | MK | 52.7 | 18.3 | 9.15 | 0.20 | 4.00 | 9.01 | 2.98 | 1.40 | 0.84 | NA | NA | 98.58 |
| MP 288 | MK | 54.1 | 18.8 | 8.73 | 0.17 | 3.46 | 8.74 | 3.44 | 1.75 | 0.90 | 0.29 | −0.02 | 100.38 |
| MP 297 | HK | 51.6 | 18.4 | 9.44 | 0.21 | 4.06 | 9.75 | 3.30 | 1.80 | 0.94 | NA | NA | 99.50 |
| MP 304 | HK | 52.4 | 19.2 | 9.26 | 0.19 | 3.53 | 9.42 | 3.37 | 2.07 | 0.89 | 0.27 | −0.19 | 100.60 |
| MP 305 | HK | 52.2 | 19.0 | 9.23 | 0.18 | 3.51 | 9.40 | 3.33 | 2.09 | 0.87 | 0.24 | −0.15 | 100.05 |
| MP 307 | MK | 54.6 | 19.2 | 8.27 | 0.19 | 2.84 | 8.64 | 3.56 | 1.71 | 0.79 | 0.27 | −0.07 | 100.07 |

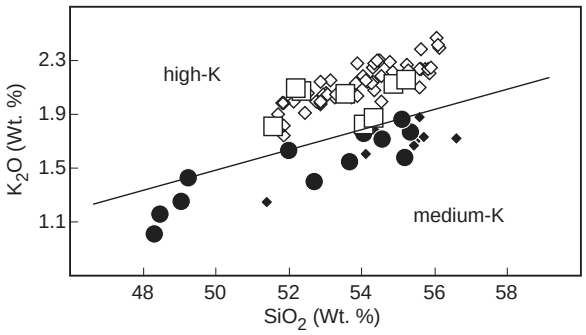


Fig. 4. Plot of $K_2O$ vs. $SiO_2$ for Merapi lavas. Black symbols correspond to the medium-K lava series (circles: this study; diamonds: Gertisser and Keller, 2003a,b). White symbols are for the high-K lava series (squares: this study; diamonds: Gertisser and Keller, 2003a,b). Classification after Le Maitre et al. (1989).

previous values for lavas from Merapi volcano (McDermott and Hawkesworth, 1991; Turner and Foden, 2001; Gertisser and Keller, 2003a), but they extend towards more radiogenic $^{206}Pb/^{204}Pb$ values than those previously reported by Gertisser and Keller (2003a). Although the samples display a small range of variations ($^{87}Sr/^{86}Sr = 0.705043$–$0.705876$, $^{143}Nd/^{144}Nd = 0.512676$–$0.512782$, $^{206}Pb/^{204}Pb = 18.7374$–$18.8180$, $^{207}Pb/^{204}Pb = 15.6760$–$15.6975$, $^{208}Pb/^{204}Pb = 39.0845$–$39.2176$) relative to the entire range displayed by arc lavas, overall they define clear isotopic trends on variation diagrams. More precisely, the data define two sub-parallel trends (Fig. 5C), which correspond to the Medium-K (basalts and basaltic andesites) and High-K (trachybasalts and basaltic trachyandesites) series of Gertisser and Keller (2003a) (see also Fig. 4). These authors have proposed that this distinction is inherited from the primary parental magmas and clearly reflects a property of the mantle sources, such as variable contribution of subducted sediments, rather than the product of high-level differentiation or contamination processes.

Below we will consider the two series separately. First, we apply our method to the medium-K series, because it has a greater number of data, defines clear binary mixing relationships and is thus better suited for petrogenetic modelling. We then consider the high-K series for comparison.

### 5.3. Range of variations of variables

The 44 variables used in the model are listed in Table 2, together with their ranges of variations.

#### 5.3.1. Variables related to the mantle wedge, oceanic crust, and sediment components

Sr, Nd, and Pb isotopic compositions of the mantle wedge beneath Merapi volcano are obtained from a set of MORB samples from the South East Indian Ridge (SEIR; Dosso et al., 1988), the nearest ridge to the Indonesian Arc, away from the influence of the Kerguelen and Amsterdam/St. Paul hotspots. The Sr, Nd, and Pb concentrations of the mantle wedge are also estimated from the SEIR MORB, after removing the effect of partial melting using a batch melting process with a melt fraction of 10% (Klein and Langmuir, 1987; Hofmann, 1988; Schiano et al., 1993). Isotopic ratios and concentrations for the oceanic crust and sediments are taken from the mean values for samples collected during the Ocean Drilling Project (ODP) in the Wharton Basin (Weis and Frey, 1996) and in the Indian Ocean (100°–120°E and 0°–20°S; see

Table 4
Strontium, neodymium, and lead isotope data for samples from Merapi volcano

| | $^{87}S/^{86}Sr \pm 2\sigma_m$ | $^{143}Nd/^{144}Nd \pm 2\sigma_m$ | $^{206}Pb/^{204}Pb \pm 2\sigma_m$ | $^{207}Pb/^{204}Pb \pm 2\sigma_m$ | $^{208}Pb/^{204}Pb \pm 2\sigma_m$ |
|---|---|---|---|---|---|
| MP1 | 0.705763 ± 6 | 0.512726 ± 10 | 18.7677 ± 7 | 15.6907 ± 6 | 39.1519 ± 34 |
| MP 14 | 0.705156 ± 5 | 0.512735 ± 10 | 18.7513 ± 6 | 15.6805 ± 6 | 39.1078 ± 40 |
| MP 21 | 0.705435 ± 8 | 0.512747 ± 9 | 18.8099 ± 7 | 15.6969 ± 8 | 39.2105 ± 32 |
| MP 29 | 0.705531 ± 3 | 0.512724 ± 14 | 18.7858 ± 6 | 15.6910 ± 5 | 39.1684 ± 38 |
| MP 41 | 0.705356 ± 5 | 0.512769 ± 8 | 18.7408 ± 7 | 15.6760 ± 7 | 39.0845 ± 34 |
| MP 42 | 0.705341 ± 7 | 0.512782 ± 10 | 18.7374 ± 7 | 15.6778 ± 7 | 39.0906 ± 41 |
| MP 43 | 0.705221 ± 5 | 0.512764 ± 12 | 18.7595 ± 10 | 15.6847 ± 9 | 39.1257 ± 46 |
| MP 63 | 0.705480 ± 7 | 0.512741 ± 13 | 18.7921 ± 8 | 15.6908 ± 9 | 39.1682 ± 30 |
| MP 84-g | 0.705748 ± 7 | 0.512713 ± 12 | 18.7592 ± 7 | 15.6835 ± 6 | 39.1214 ± 24 |
| MP 84-1 | 0.705755 ± 4 | 0.512700 ± 9 | 18.7601 ± 18 | 15.6849 ± 23 | 39.1341 ± 73 |
| MP 88 | 0.705179 ± 5 | 0.512757 ± 9 | 18.7544 ± 7 | 15.6843 ± 7 | 39.1224 ± 22 |
| MP 93 | 0.705115 ± 5 | 0.512770 ± 7 | 18.7570 ± 6 | 15.6840 ± 6 | 39.1172 ± 43 |
| MP 231 a | 0.705816 ± 6 | 0.512727 ± 13 | 18.8180 ± 9 | 15.6972 ± 9 | 39.2165 ± 61 |
| MP 231 b | 0.705821 ± 6 | 0.512706 ± 16 | 18.8110 ± 28 | 15.6937 ± 27 | 39.2008 ± 81 |
| MP 232 | 0.705876 ± 6 | 0.512687 ± 20 | 18.8183 ± 6 | 15.6975 ± 5 | 39.2176 ± 22 |
| MP 243 | 0.705128 ± 9 | 0.512769 ± 9 | 18.7606 ± 9 | 15.6881 ± 8 | 39.1332 ± 24 |
| MP 288 | 0.705043 ± 5 | 0.512750 ± 10 | 18.7383 ± 9 | 15.6813 ± 11 | 39.0935 ± 34 |
| MP 297 | 0.705647 ± 6 | 0.512676 ± 10 | 18.7467 ± 15 | 15.6787 ± 13 | 39.1015 ± 38 |
| MP 304 a | 0.705688 ± 4 | 0.512704 ± 13 | 18.7674 ± 10 | 15.6960 ± 11 | 39.1579 ± 38 |
| MP 304 b | 0.705667 ± 5 | 0.512710 ± 12 | 18.7613 ± 15 | 15.6910 ± 13 | 39.1440 ± 43 |
| MP 305 | 0.705646 ± 3 | 0.512693 ± 13 | 18.7563 ± 13 | 15.6854 ± 14 | 39.1231 ± 48 |
| MP 307 | 0.705411 ± 7 | 0.512745 ± 9 | 18.7756 ± 5 | 15.6886 ± 5 | 39.1518 ± 20 |

$2\sigma_m$ is the internal reproducibility. Duplicate analyses are indicated by letters a and b.

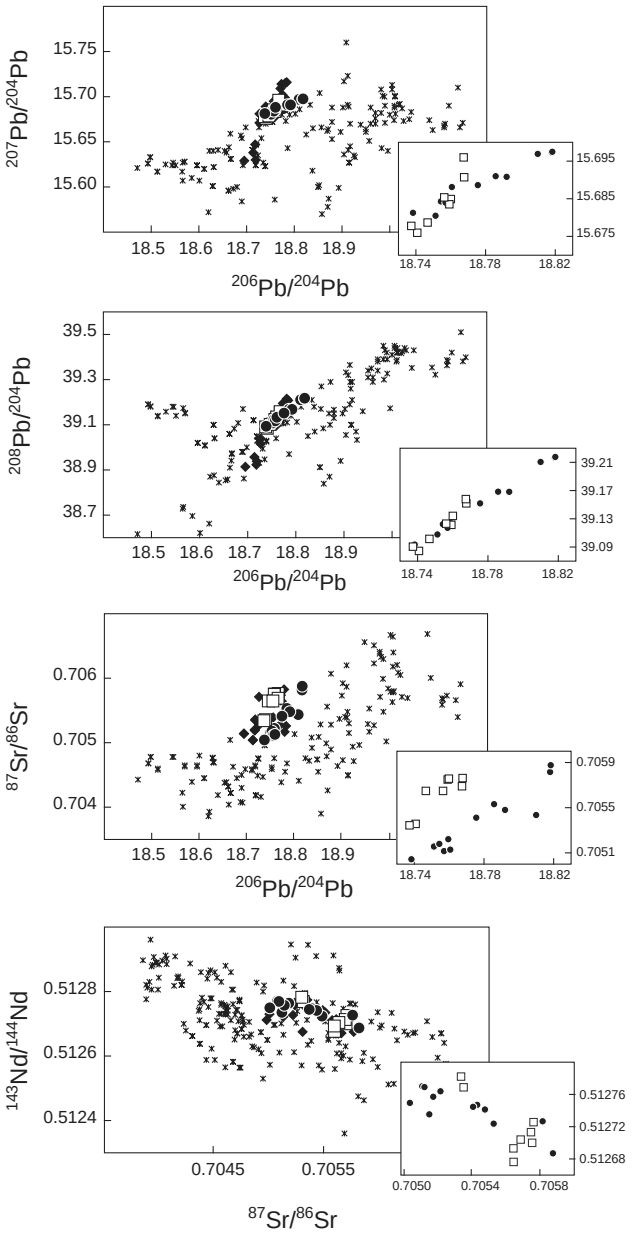


Fig. 5. $^{207}Pb/^{204}Pb$ vs. $^{206}Pb/^{204}Pb$, $^{208}Pb/^{204}Pb$ vs. $^{206}Pb/^{204}Pb$, $^{87}Sr/^{86}Sr$ vs. $^{206}Pb/^{204}Pb$ and $^{143}Nd/^{144}Nd$ vs. $^{87}Sr/^{86}Sr$ for Merapi lavas. Black circles: medium-K series from Merapi (this study); squares: high-K series from Merapi (this study); black diamonds: Merapi lavas (Gertisser and Keller, 2003a); crosses: Sunda arc lavas (Edwards et al., 1991, 1993, 1994; Gerbe et al., 1992 ; Gill and Williams, 1990; Hoogewerff et al., 1997; McDermott and Hawkesworth, 1991; Stolz et al., 1990; Turner and Foden, 2001; Turner et al., 2003; Varekamp et al., 1989; Varne and Foden, 1986; Woodhead et al., 2001).

compilation in Ben Othman et al., 1989; Plank and Langmuir, 1998; Hemming and McLennan, 2001), respectively.

The sample populations used to estimate the mean isotopic values of the components show relatively small variations in $^{87}Sr/^{86}Sr$, $^{143}Nd/^{144}Nd$, $^{206}Pb/^{204}Pb$, $^{207}Pb/^{204}Pb$, and $^{208}Pb/^{204}Pb$ ratios. We thus consider the ranges of variations of these populations as ranges of errors of the parameters. Practically, values of the 5 isotopic ratios are randomly computed, independently from each other. For sediments, however, this procedure cannot be carried out because clear binary relationships are observed between the different isotopic tracers (cf. Ben Othman et al., 1989; Plank and Langmuir, 1998; Hemming and McLennan, 2001). As an alternative, we randomly select a $^{206}Pb/^{204}Pb$ value and then we re-calculate the ranges of variations from which $^{87}Sr/^{86}Sr$, $^{143}Nd/^{144}Nd$, $^{207}Pb/^{204}Pb$, and $^{208}Pb/^{204}Pb$ ratios can be extracted, using the correlations in isotopic diagrams.

For trace-element concentrations of the components we use an arbitrary range of errors of 10%.

### 5.3.2. Variables related to dehydration and melting processes

For subducted sediments, an average degree of partial melting of 15% is assumed based on the experiments of Jonhson and Plank (1999). Nichols et al. (1994) have shown that the melt productivity (i.e., the amount of melt for a given $\Delta T$) for sediments is much higher than for oceanic crustal material. Accordingly, we postulate a factor of 10 between the average melting degrees of the two slab components. Coupled with the fact that the melt fractions are parameters (i.e., well-constrained variables with errors of 10%) of the model, partial melting degrees of $1.50 \pm 0.15\%$ and $15.0 \pm 0.5\%$ are thus chosen for the oceanic crust and sediments, respectively.

Based on the studies of Peacock (1990) and Tatsumi and Kogiso (1997), values of $1.50 \pm 0.15\%$ (10% relative error) for weight fractions of hydrous fluids extracted from both down-going oceanic crust and sediments are considered plausible and are used in subsequent modelling. In contrast, there is, to our knowledge, no estimate of the mass ratios ($Tm_{OC}$ and $Tm_{SED}$, see Table 2) between melts and fluids released from the oceanic crust and sediments in the literature. Thus we consider $Tm$ values between 0 and $+\infty$. Practically, we define the $Tm/(Tm+1)$ ratio and set its range of variations between 0 and 1 ($0.5 \pm 0.5$, 100% relative error) for both the oceanic crust and sediments. Finally, a value of 1 ($Rm = 0.5 \pm 0.5$; 100% relative error) represents a reasonable upper limit for mass ratios $Rm_{OC}$ and $Rm_{SED}$ between the slab component-derived melts/fluids and the mantle wedge. Note that $Tm_{OC}$, $Tm_{SED}$, $Rm_{OC}$, and $Rm_{SED}$ correspond to unknowns in the model.

### 5.3.3. Variables related to behaviour of elements

Bulk solid/melt partition and mobility coefficients for Sr, Nd, and Pb during melting and dehydration of oceanic crust and sedimentary materials also represent unknowns (100% relative errors) of the model. However, it seems realistic to suppose that Sr, Nd, and Pb behave as incompatible elements during partial melting of the subducted components. A value of $0.5 \pm 0.5$ is thus attributed to all bulk partition and mobility coefficients.

## 6. Discussion

In this section, we evaluate the results of our modelling of the medium-K lava series from Merapi volcano.

First, we consider values of the parameters obtained for the best solution. The whole set of random combinations is then assessed through examination of histograms of the model parameters. Finally, we compare the results with those obtained for the high-K lava series from Merapi volcano.

### 6.1. The best solution

The Dist value for the best solution of our modelling (i.e., the solution that minimizes the distance between measured data and the computed mixing hyperbola, see Section 3.2.2 and Eq. (3.7)) is $<2\sigma$ (i.e., $<D_{2\sigma}$). The corresponding

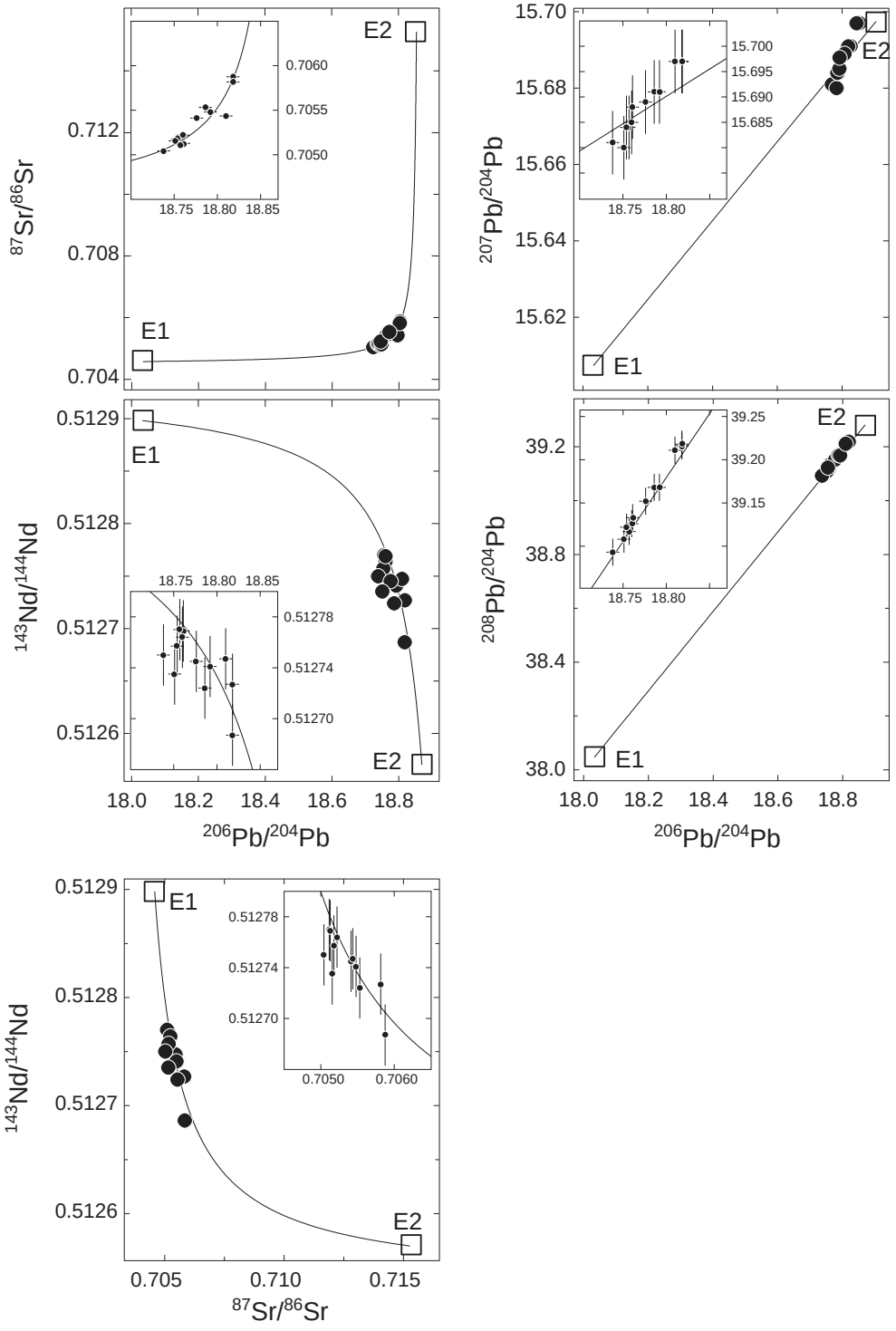


Fig. 6. Isotope diagrams comparing the mixing hyperbola computed for the best solution of our modelling in five-dimensional isotopic space with data for the medium-K lava series from Merapi volcano. Inserts show the error bars ($2\sigma$).

mixing hyperbola between the two end-members E1 and E2 generated in the first stage of the model (metasomatism of the mantle wedge by $H_2O$-rich phases released from the subducted oceanic crust and sediments) is reported in Fig. 6, together with isotopic data for the medium-K series. The good agreement observed between the calculated curve and the data gives additional support to our assumption that isotopic compositions of the medium-K lava series from Merapi volcano define a pseudo-binary mixing line formed by mixing three distinct components in a multi-stage process. Furthermore, it should be noted that direct binary mixing of the involved components (given the same isotopic and elemental characteristics of the best solution of our model) cannot account for the data (Fig. 7).

Values of the unknowns for the best solution of the model are displayed in Figs. 8A–C (in grey). They include (i) mobility ($M^x$) and bulk solid/melt partition ($D^x$) coefficients for Sr, Nd, and Pb in the subducted oceanic crust and sediments (i.e., the behaviour parameters during dehydration and melting processes); and (ii) melt/fluid mass ratios ($Tm$) in the slab-derived hydrous phase and the mass ratio ($Rm$) between this released phase and the mantle wedge (i.e., the proportions of the involved parts).

From Figs. 8A–C, several features of the best solution are immediately apparent. First, the inferred mobility coefficients for Sr, Nd, and Pb during sediment dehydration are relatively high, $\geqslant 50\%$. This challenges experimental studies that suggest low mobility coefficients ($<20\%$) for Sr and Nd (Aizawa et al., 1999). In contrast, during dehydration of the oceanic crust, the inferred mobility coefficient for the REE Nd is very low relative to those for Sr and Pb, as already noted by Tatsumi and Kogiso (1997). But in our case, Sr is more mobile than Pb, contrary to the observations of Tatsumi and Kogiso (1997). Second, highly contrasted Sr–Nd–Pb incompatibility orders are obtained during melting of the slab components; the order of trace-element incompatibility is $D_{Nd} \leqslant D_{Sr} < D_{Pb}$ during sediment melting and $D_{Sr} < D_{Pb} \approx D_{Nd}$ during oceanic crust melting. This is a clear indication of distinct proportions of the residual phases in the two components or of the presence of distinct residual phases. Note also that a comparable behaviour between LREE (Ce, Nd) and Pb during partial melting of oceanic crust is in agreement with the bulk partition coefficients during the generation of MORB (Hofmann, 1997). A third feature is the minor role for the mantle wedge relative to the slab-derived melt/fluid phase, as indicated by the $Rm_{OC}$ and $Rm_{SED}$ ratios $>0.8$. Also there is a significant difference in the ratios between melts and fluids released from the subducted oceanic crust ($Tm_{OC}/(Tm_{OC}+1)$ $\sim 0.3$) and sediments ($Tm_{SED}/(Tm_{SED}+1)$ $\sim 0.7$). The metasomatic phase issued from the oceanic crust is thus more hydrous than that from the sediments, in agreement with the lower melting temperature for sediments (Nichols et al., 1994).

### 6.2. Histograms of the model parameters

The entire set of 1,000,000 combinations, represented as histograms of the model parameters weighted by the $Dist_{min}/Dist$ ratio (see Section 3.2.4), is also shown in Figs. 8A–C. A high peak in these histograms could reflect a small number of solutions with a high weighting (i.e., that fit the data well), or a large number of solutions with a small weighting. The former hypothesis is supported by the fact that the weighted histograms and raw histograms of combinations with $Dist < 1.5 \times D_{2\sigma}$ (115 combinations) have comparable shapes (Fig. 9).

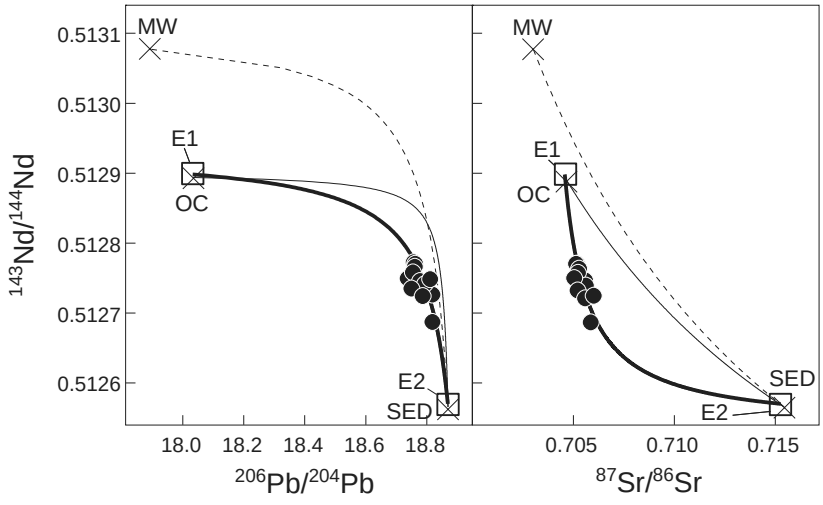


Fig. 7. Plots of $^{143}Nd/^{144}Nd$ vs. $^{206}Pb/^{204}Pb$ and $^{87}Sr/^{86}Sr$ comparing pseudo-binary mixing hyperbola computed for the best solution of the medium-K lava series modelling and direct binary mixing of the three involved components (mantle wedge, MW; subducted oceanic crust, OC; and subducted sediments, SED) having the isotopic and elemental characteristics of the best solution. Medium-K lava series: black circles; end-members (E1 and E2): squares; components: crosses; mixing between E1 and E2: thick black line; mixing between OC and SED: thin line; mixing between MW and SED: dashed line.

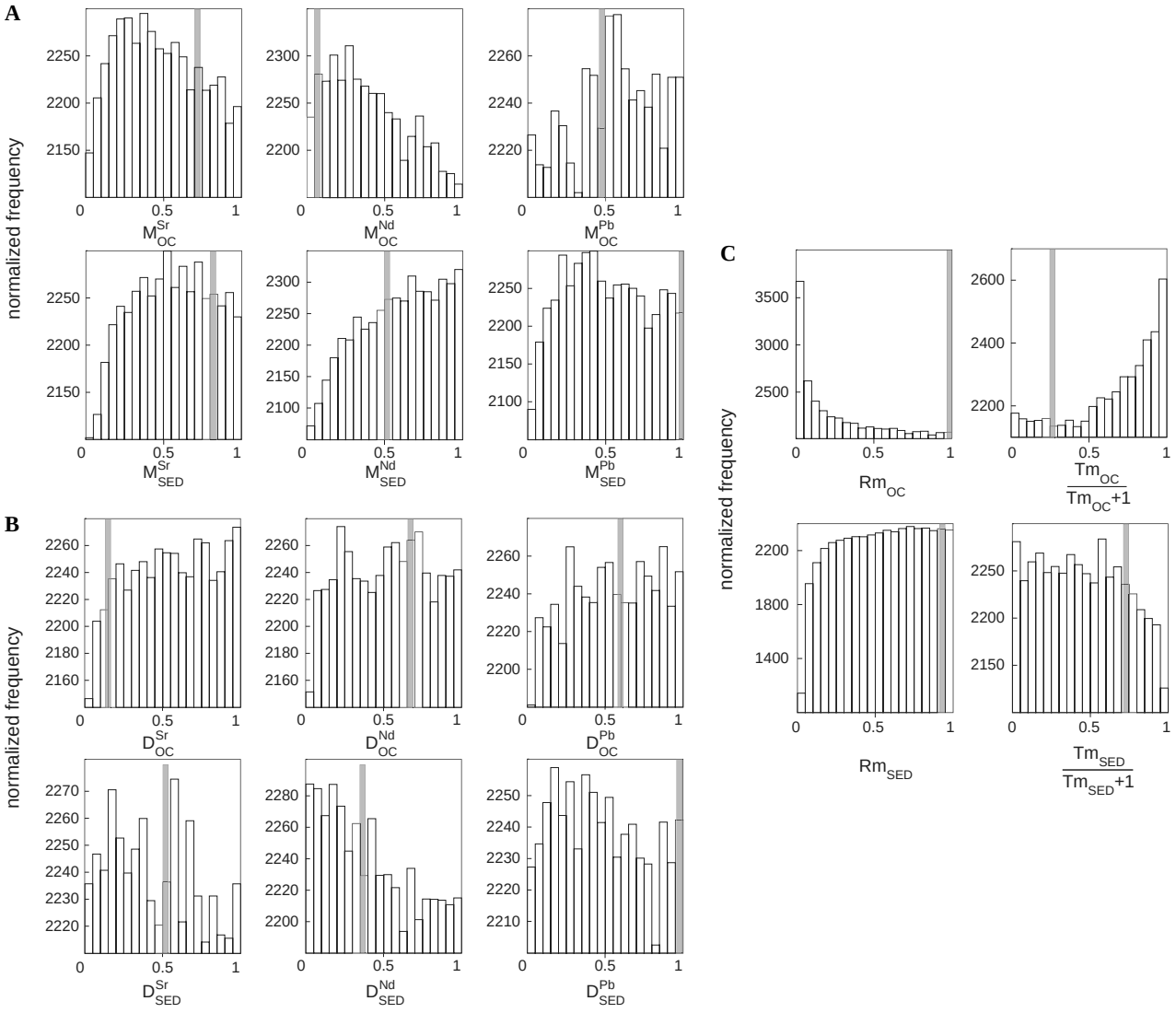


Fig. 8. Histograms of the best-solution normalized model parameters obtained for the Merapi medium-K lava series modelling. (A) Mobility ($M^x$); (B) bulk solid/melt partition ($D^x$) coefficients for Sr, Nd, and Pb in the subducted oceanic crust and sediments; (C) Melt/fluid mass ratios ($Tm$) in the slab-derived hydrous phase and mass ratio ($Rm$) between this released phase and the mantle wedge. Also shown in grey are the values of the parameters for the best solution of the model.

Although many histograms of the model parameters do not show a "single-peaked" distribution, they generally allow identification of a predominant value or range of values. For example, a maximum peak around 20% is clearly discernible for the Nd mobility coefficient $M^{Nd}_{OC}$ during oceanic crust dehydration (Fig. 8A). Conversely, mass ratios between melts/fluids released by subducted sediments and the mantle wedge ($Rm_{SED}$) display an almost flat distribution between 10 and 100% (Fig. 8C). This is a clear indication that contrary to $M^{Nd}_{OC}$, $Rm_{SED}$ values do not greatly influence calculation of our model of arc-lava genesis nor, consequently mixing hyperbolae between end-members E1 and E2. Identification of the predominant values leads to the characterization of the most appropriate average combination. An important feature of this average combination is the change in Sr, Nd and Pb behaviour during dehydration of the two subducted components; during oceanic crust dehydration the mobility sequence is $M^{Nd}_{OC} \approx M^{Sr}_{OC} < M^{Pb}_{OC}$, whereas $M^{Pb}_{SED} < M^{Sr}_{SED} < M^{Nd}_{SED}$ during sediment dehydration. In contrast, histograms for Sr, Nd, and Pb bulk solid/melt partition coefficients show small-scale fluctuations that preclude identification of any predominant value, except for the $D^{Nd}_{SED}$ and $D^{Pb}_{SED}$ histograms which suggest an incompatible behaviour of Nd and Pb during sediment melting. Significantly, $Rm$ and $Tm$ mass ratios determined for the average combination distinguish oceanic crust from sediments. Maximum values observed for $Rm_{OC}$ (<10%) and $Rm_{SED}$ (between 10 and 100%) highlight a major contribution of down-going sediments to the metasomatizing phase, and comparison between $Tm_{OC}$ and $Tm_{SED}$ histograms emphasizes the hydrous character of the oceanic crust-derived phase relative

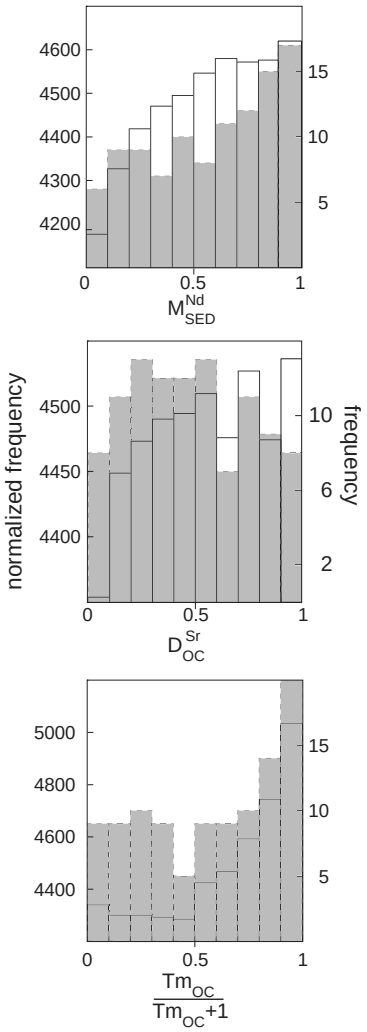


Fig. 9. Comparison of the best-solution normalized histograms of model parameters shown in Fig. 8 (left *Y*-axis) with the raw histograms (grey; right *Y*-axis) of the combinations having a total distance between modelled mixing hyperbolae and measured data less than $1.5\times\ D_{2\sigma}$ (115 combinations).

to that released from sediments. It should also be noted that, although the amount of the oceanic-crust derived phase is subordinate to that from sediments, its value is precisely characterized, indicating that $Rm_{OC}$ acts as a major parameter of our model.

An additional important observation to be made is that the oceanic crust and sediments show well-defined, but complementary, *Rm* and *Tm* histograms (Fig. 8C). In this context, the absence of precise constraints on most of the mobility and bulk partition coefficients demonstrates that our two-stage procedure for isotope modelling of a cogenetic suite of arc lavas is more controlled by the involved components (mantle wedge, oceanic crust, sediments and their derivatives) than the various processes (dehydration, melting, and mixing).

It should be noted that, while the majority of the principal values defining the average combination are consistent with values of the best solution, some show significant differences, for example the Sr, Nd, and Pb mobility coefficients during oceanic crust and sediment dehydration and the mass ratio between melt and fluid from the oceanic crust. The differences illustrate the fact that a combination cannot provide a unique solution for the model. Several combinations of inputted values can account for the same arc lava data. These combinations do not differ in just one variable, but in all of them; i.e., any modification of an unconstrained variable (unknown) would induce some change in all the others. In the Merapi lava suites unknowns in the model relate to the melting and dehydration processes (see Section 5.3). This suggests that the two processes are closely related and influence each other, in agreement with previous studies that suggest a correlation between the degree of melting in arc settings and the amount of $H_2O$ in the source (Stolper and Newman, 1994).

Such a balancing mechanism can also occur at the scale of the parameters of one process only. For example a decreasing degree of partial melting is balanced by a decrease in the computed bulk solid/melt partition coefficients (i.e., elements are more incompatible). Similarly, a lower mobility coefficient for an element results in a higher dehydration rate. As a consequence of these associations there is no simple relationship between unconstrained variables of our model. This is illustrated by the absence of binary correlations between these variables, when the 115 combinations with Dist $< 1.5\times D_{2\sigma}$ used to construct raw histograms of Fig. 9 are considered.

### 6.3. Origin of the high-K lava series from Merapi volcano

According to Gertisser and Keller (2003a), the distinction between high-K and medium-K lava series in Merapi is primary and reflects a variable contribution of subducted sediments in their mantle sources, rather than shallow-level processes. To illustrate this hypothesis, and as an independent test of our procedure, we applied a simplified version of the modelling to the data of the high-K lava series. We adopted a calculation in which the inputted values of the variables are assumed to be identical to those found for the best solution of the medium-K lava series modelling, except for the sediment-related variables (isotope ratios and trace-element concentrations) which are randomly produced. Then the step-by-step calculation and Monte-Carlo simulation of the procedure led to the characterization of the new end-member E2 and mixing hyperbola between E1 and E2. Again, a best solution can be defined, which minimizes the distance between modelled compositions and the high-K lava data. Fig. 10 shows isotope diagrams comparing the computed mixing hyperbolae for the best solution (with Dist $< D_{2\sigma}$) and the data. The overall isotopic trend for the high-K lava series is reproduced, to a close approximation, by the calculated hyperbolae. Results for the sedimentary materials are poorly different concerning the isotope ratios (except a lesser radiogenic $^{206}Pb/^{204}Pb$), but greater Sr and Nd and lower Pb concentrations essentially

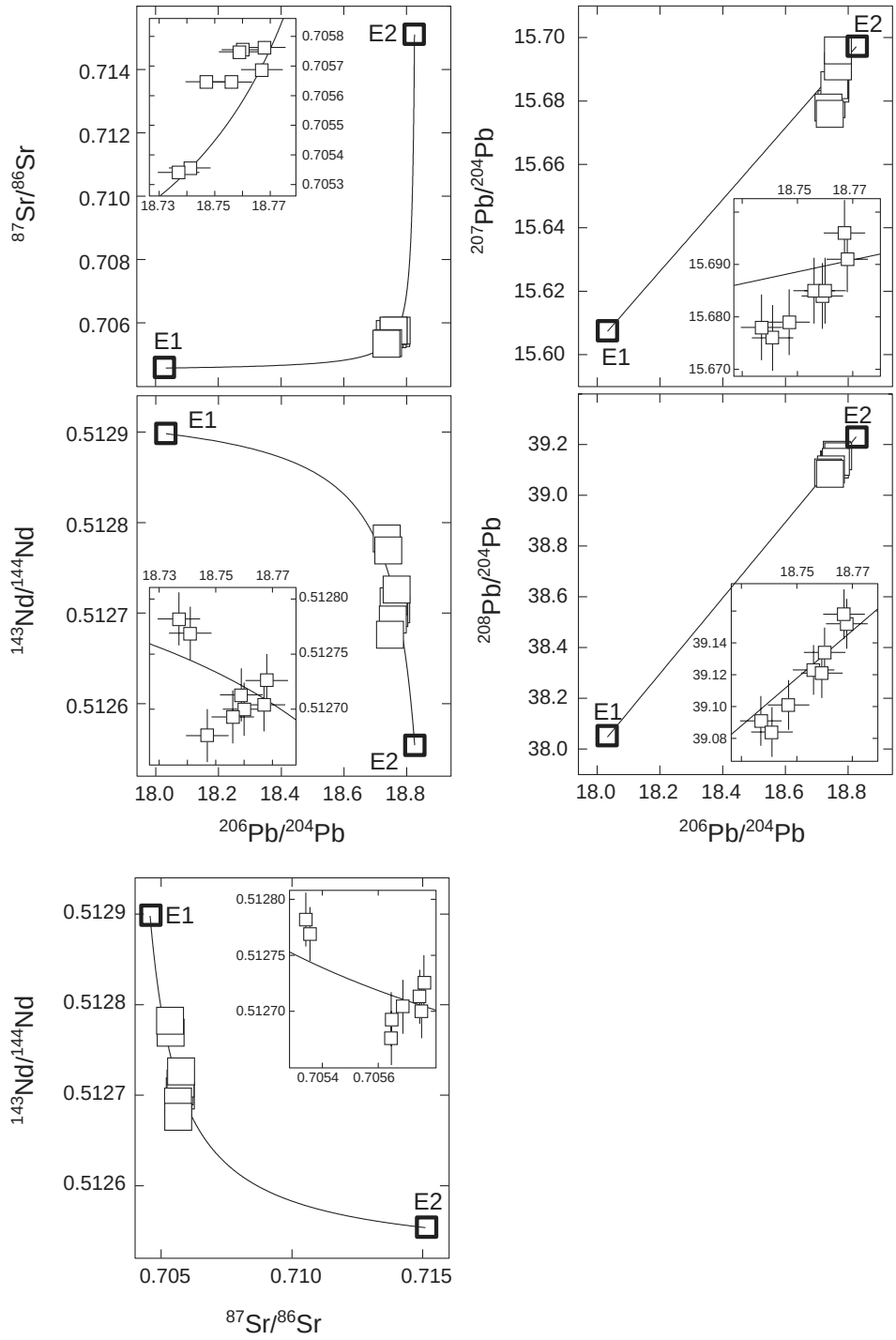


Fig. 10. Isotope diagrams comparing the mixing hyperbola computed for the best solution of a simplified version of the modelling in the five-dimensional isotopic space and data for the high-K lava series from Merapi volcano. Inserts show the error bars ($2\sigma$). For this modelling, we have adopted a calculation in which the inputted values of the variables are assumed to be identical to those found for the best solution of the medium-K lava series modelling, except for the sediment-related variables (isotope ratios and trace-element concentrations) which are randomly produced.

explain the dichotomy between the two series. This result gives further support to the hypothesis that compositional differences between the two series encountered at Merapi volcano are mainly inherited from source heterogeneities related to variable contribution of subducted sediments. It also indicates that the system is extremely sensitive to chemical variations in the sedimentary input.

## 7. Summary

The simplified model of formation of arc lavas described in this study, namely metasomatism of portions of the mantle wedge followed by progressive mixing and melting, is applied successfully to sequences of volcanics from Merapi volcano. The results require a direct relationship

between dehydration of the slab and melting of the metasomatized mantle wedge.

The most important feature of the model is that it generates pseudo-binary mixing trends in isotope diagrams; i.e., the two end-members of these trends do not represent physical components of a subduction zone, but mixtures of derivatives from slab dehydration and melting processes. This feature could reconcile two apparently contradictory observations in some arc settings, namely the evidence from correlations in isotope diagrams that simple binary mixing could generate the range of compositions of arc lavas and the variety of physical processes and potential sources that could be involved in the generation of arc magmas. A corollary to this feature is that caution is required before assessing isotopic compositions of arc lava mantle source components from the isotopic arrays of arc lavas.

## Acknowledgments

We thank Claude Maerschalk for his help during preparation and analyses of the samples and Eric Lewin and Ariel Provost for discussion. R.D. and P.S. are also indebted to the Earth Sciences Master 1 students who helped clarify and shape calculations. F. van Wik de Vries helped us for the quality of the manuscript. This paper was improved by critical comments by R. Ellam and R. Gertisser.

*Associate editor:* Bernard Marty

## References

Aizawa, Y., Tastumi, Y., Yamada, H., 1999. Element transport by dehydration of subducted sediments: implication for arc and ocean island magmatism. *The Island Arc* **8**, 38–46.

Allègre, C.J., Hamelin, B., Provost, A., Dupré, B., 1986/1987. Topology in isotopic multispace and origin of mantle chemical heterogeneities. *Earth Planet. Sci. Lett.* **81**, 319–337.

Alves, S., Schiano, P., Allègre, C.J., 1999. Rhenium–Osmium isotopic investigation of Java subduction zone lavas. *Earth Planet. Sci. Lett.* **168**, 65–77.

Alves, S., Schiano, P., Capmas, F., Allègre, C.J., 2002. Osmium isotope binary mixing arrays in arc volcanism. *Earth Planet. Sci. Lett.* **198**, 355–369.

Arculus, R.J., Powell, R., 1986. Source component mixing in the regions of arc magma generation. *J. Geophys. Res.* **91**, 5913–5926.

Ayers, J.C., Eggler, D.H., 1995. Partitioning of elements between silicate melt and $H_2O$-NaCl fluids at 1.5 and 2.0 GPA pressure; implications for mantle metasomatism. *Geochim. Cosmoschim. Acta* **59**, 4237–4246.

Ben Othman, D., White, W.M., Patchett, J., 1989. The geochemistry of marine sediments, island arc genesis, and crust-mantle recycling. *Earth Planet. Sci. Lett.* **94**, 1–21.

Berthommier P.-C., 1990. Etude volcanologique du Merapi (Centre Java). Téphrostratigraphie et chronologie. Mécanismes éruptifs. Unpublished thesis, University of Clermont-Ferrand.

Bureau, H., Keppler, H., 1999. Complete miscibility between silicate melts and hydrous fluids in the upper mantle: experimental evidence and geochemical implications. *Earth Planet. Sci. Lett.* **165**, 187–196.

Camus, G., Gourgaud, A., Mossand-Berthommier, P.-C., Vincent, P.-M., 2000. Merapi (Central Java, Indonesia): an outline of the structural and magmatological evolution, with a special emphasis to the major pyroclastic events. *J. Volcanol. Geotherm. Res.* **100**, 139–163.

Chadwick, J.P., Troll, V.R., Ginibre, C., Morgan, D., Gertisser, R., Waight, T., Davidson, J.P., 2005. Magma crust interaction at Merapi volcano, Java, Indonesia: insights from crystal isotope stratigraphy. *Geophys. Res. Abstr.* **7**, 06958.

Chauvel, C., Blichert-Toft, J., 2001. A Hafnium isotope and trace element perspective on melting of the depleted mantle. *Earth Planet. Sci. Lett.* **190**, 137–151.

Davidson, J.P., 1987. Crustal contamination versus subduction zone enrichment: examples from the lesser Antilles and implications for mantle source compositions of island arc volcanic rocks. *Geochim. Cosmochim. Acta* **51**, 2185–2198.

Davidson, J.P., Hora, J.M., Garrison, J.M., Dungan, M.A., 2005. Crustal forensics in arc magmas. *J. Volc. Geotherm. Res.* **140**, 157–170.

Davies, J.H., Stevenson, D.J., 1992. Physical model of source region of subduction zone volcanics. *J. Geophys. Res.* **97**, 2037–2070.

Defant, M.J., Drummond, M.S., 1990. Derivation of some modern arc magmas by melting of young subducted lithosphere. *Nature* **347**, 662–665.

DePaolo, D.J., 1981. Trace element and isotopic effect of combined wallrock assimilation and fractional crystallization. *Earth Planet. Sci. Lett.* **53**, 189–202.

Dosso, L., Bougault, H., Beuzart, P., Calvez, J.-Y., Joron, J.-L., 1988. The geochemical structure of the South-East Indian Ridge. *Earth Planet. Sci. Lett.* **88**, 47–59.

Douglass, J., Schilling, J.-G., 2000. Systematics of three-component, pseudo-binary mixing lines in 2D isotope ratio space representations and implications for mantle plume-ridge interaction. *Chem. Geol.* **163**, 1–23.

Edwards, C.M.H., Menzies, M.A., Thirlwall, M.F., 1991. Evidence from Muriah, Indonesia, for the interplay of supra-subduction zone and intraplate processes in the genesis of potassic alkaline magmas. *J. Petrol.* **32**, 555–592.

Edwards, C.M.H., Morris, J.D., Thirlwall, M.F., 1993. Separating mantle from slab signatures in arc lavas using B/Be and radiogenic isotope systematics. *Nature* **362**, 530–533.

Edwards, C.M.H., Menzies, M.A., Thirlwall, M.F., Morris, J.D., Leeman, W.P., Harmon, R.S., 1994. The transition to potassic alkaline volcanism in island arcs: the ringgit-beser complex, East Java, Indonesia. *J. Petrol.* **35**, 1557–1595.

Ellam, R.M., Hawkesworth, C.J., 1988. Elemental and isotopic variations in subduction related basalts: evidence for a three component model. *Contrib. Mineral. Petrol.* **98**, 72–80.

Elliot, T., Plank, T., Zindler, A., White, W., Bourdon, B., 1997. Element transport from slab to volcanic front at the Mariana arc. *J. Geophys. Res.* **102**, 14,991–15,019.

Gerbe, M.-C., Gourgaud, A., Sigmarsson, O., Harmon, R.S., Joron, J.-L., Provost, A., 1992. Mineralogical and geochemical evolution of the 1982–83 Galunggung eruption (Indonesia). *Bull. Volcanol.* **54**, 284–298.

Gertisser, R., Keller, J., 2003a. Trace element and Sr, Nd, Pb and O isotope variations in medium-K and high-K volcanic rocks from Merapi volcano, central Java, Indonesia: Evidence for the involvement of subducted sediments in Sunda arcs magma genesis. *J. Petrol.* **44**, 457–489.

Gertisser, R., Keller, J., 2003b. Temporal variations in magma composition at Merapi Volcano (Central Java, Indonesia): magmatic cycles during the past 2000 years of explosive activity. *J. Volc. Geotherm. Res.* **123**, 1–23.

Gill, J.B., 1981. *Orogenic andesites and plate tectonics*. Springer, New York, 390 pp.

Gill, J.B., Williams, R.W., 1990. Th isotope and U-series studies of subduction related volcanic rocks. *Geochim. Cosmochim. Acta* **54**, 1427–1442.

Hamilton, W., 1979. Tectonics of the Indonesian Region. *U.S. Geol. Survey Prof. Paper* **1078**, 1–345.

Hanan, B.B., Kingsley, R.H., Schilling, J.-G., 1986. Pb isotope evidence in the South Atlantic for migrating ridge-hotspot interactions. *Nature* **322**, 137–144.

Hawkesworth, C.J., Gallagher, K., Hergt, J.M., McDermott, F., 1993. Mantle and slab contributions in arc magmas. *Annu. Rev. Earth Planet. Sci.* **21**, 175–204.

Hemming, S.R., McLennan, S.M., 2001. Pb isotope compositions of modern deep sea turbidites. *Earth Planet Sci. Lett.* **184**, 489–503.

Hofmann, A.W., 1988. Mantle reservoirs. In: Origin of the Earth., Lunar and Planetary Institute, *LPI Contribution* **681**, pp. 33–34.

Hofmann, A.W., 1997. Mantle geochemistry: the message from oceanic volcanism. *Nature* **385**, 219–229.

Hoogewerff, J., Van Bergen, M.J., Vroon, P.Z., Hertogen, J., Wordel, R., Sneyers, A., Nasution, A., Varekamp, J.C., Moens, H.L.E., Mouchel, G., 1997. U series, Sr-Nd-Pb isotope and trace element systematics across an active island arc-continent collision zone: implications for element transfer at the slab-wedge interface. *Geochim. Cosmochim. Acta* **61**, 1057–1072.

Ito, E., Stern, R.J., 1986. Oxygen-isotopic and Strontium-isotopic investigations of subduction zone volcanism ; The case of the volcano arc and the Marianas island-arc. *Earth Planet. Sci. Lett.* **76**, 312–320.

Iwamori, H., 1998. Transportation of H2O and melting in subduction zones. *Earth Planet. Sci. Lett.* **160**, 65–80.

Jonhson, M.C., Plank, T., 1999. Dehydration and melting experiments constrain the fate of subducted sediment. *Geochem. Geophys. Geosyst.* **1**: 1999GC000014.

Kay, R.W., 1978. Aleutian magnesian andesites: Melts from subducted Pacific Ocean crust. *J. Volcanol. Geotherm. Res.* **4**, 117–132.

Kay, R.W., 1980. Volcanic arc magmas: implications of a melting-mixing model for element recycling in the crust-upper mantle system. *J. Geol.* **88**, 497–522.

Keppler, H., 1996. Constraints from partitioning experiments on the composition of subduction-zone fluids. *Nature* **380**, 237–240.

Kersting, A.B., Arculus, R.J., 1995. Pb isotope composition of Klyuchevskoy volcano, Kamchatka and North Pacific sediments: implications for magma genesis and crustal recycling in the Kamchatkan arc. *Earth Planet. Sci. Lett.* **136**, 133–148.

Klein, E.M., Langmuir, C.H., 1987. Global correlations of ocean ridge basalt chemistry with axial depth and crustal thickness. *J. Geophys. Res.* **92**, 8089–8115.

Le Maitre, R.W., Bateman, P., Dudek, A., Keller, J., Lameyer Le Bas, M.J., Sabine, P.A., Schmid, R., Sorensen, H., Streckeisen, A., Woolley, A.R., Zanettin, B., 1989. *A Classification of Igneous Rocks and Glossary of Terms*. Blackwell, Oxford.

McCulloch, M.T., Gamble, J.A., 1991. Geochemical and geodynamical constraint on subduction zone magmatism. *Earth Planet. Sci. Lett.* **102**, 358–374.

McDermott, F., Hawkesworth, C.J., 1991. Th, Pb and Sr isotope variations in young island arc volcanics and oceanic sediments. *Earth Planet. Sci. Lett.* **104**, 1–15.

McLennan, S.M., Taylor, S.R., 1981. Role of subducted sediments in island-arc magmatism: constraints from REE patterns. *Earth Planet. Sci. Lett.* **54**, 423–430.

Miller, D.M., Goldstein, S.L., Langmuir, C.H., 1994. Cerium/lead and lead isotope ratios in arc magmas and the enrichment of lead in the continents. *Nature* **368**, 514–520.

Morris, J.D., Hart, S.R., 1983. Isotopic and incompatible element constraints on the genesis of island arc volcanics from Cold Bay and Amak Island, Aleutians, and implications for mantle structure. *Geochim. Cosmochim. Acta* **47**, 2015–2030.

Nicholls, I.A., Ringwood, A.E., 1973. Effect of water on olivine stability in tholeiites and the production of silica saturated magmas in the island arc environment. *J. Geol.* **81**, 285–300.

Nichols, G.T., Wyllie, P.J., Stern, C.R., 1994. Subduction zone melting of pelagic sediments constrained by melting experiments. *Nature* **371**, 785–788.

Peacock, S.M., 1990. Fluid processes in subduction zones. *Science* **248**, 329–337.

Peacock, S.M., Rushmer, T., Thompson, A.B., 1994. Partial melting of subducting oceanic crust. *Earth Planet. Sci. Lett.* **121**, 227–244.

Perfit, M.R., Gust, D.A., Bence, A.E., Arculus, R.J., Taylor, S.R., 1980. Chemical characteristics of island-arc basalts: implications for mantle sources. *Chem. Geol.* **30**, 227–256.

Pichler, H., Zeil, V.W., 1972. The Cenozoic rhyolite-andesite association of Chilean Andes. *Bull. Volcanol.* **35**, 424–552.

Plank, T., Langmuir, C.H., 1993. Tracing trace elements from sediment input to volcanic output at subduction zones. *Nature* **362**, 739–743.

Plank, T., Langmuir, C.H., 1998. The chemical composition of subducted sediment and its consequences for the crust and mantle. *Chem. Geol.* **145**, 325–394.

Saunders, A.D., Tarney, J., Weaver, S.D., 1980. Transverse geochemical variations across the Antarctic peninsula: implications for the genesis of calc-alkaline magmas. *Earth Planet. Sci. Lett.* **46**, 344–360.

Schiano, P., Allègre, C.J., Dupré, B., Lewin, E., Joron, J.-L., 1993. Variability of trace elements in basaltic suites. *Earth Planet. Sci. Lett.* **119**, 37–51.

Schiano, P., Clocchiatti, R., Shimizu, N., Maury, R.C., Jochum, K.P., Hofmann, A.W., 1995. Hydrous, silica-rich melts in the sub-arc mantle and their relationship with erupted lavas. *Nature* **377**, 595–600.

Schiano, P., Clocchiatti, R., Bourdon, B., Burton, K.W., Thellier, B., 2000. The composition of melt inclusions in minerals at the garnet-spinel transition zone. *Earth Planet. Sci. Lett.* **174**, 375–383.

Schilling, J.-G., Kingsley, R.H., Hanan, B.B., McCully, B.L., 1992. Nd–Sr–Pb isotopic variations along the Gulf of Aden: evidence for Afar mantle plume-continental lithosphere interaction. *J. Geophys. Res.* **97**, 10927–10966.

Stalder, R., Foley, S.F., Brey, G.P., Horn, I., 1998. Mineral-aqueous fluid partitioning of trace elements at 900–1200 °C and 3.0–5.7 GPa: New experimental data for garnet, clinopyroxene, and rutile, and implications for mantle metasomatism. *Geochim. Cosmochim. Acta* **62**, 1781–1801.

Stolper, E., Newman, S., 1994. The role of water in the petrogenesis of Mariana trough magmas. *Earth Planet. Sci. Lett.* **121**, 293–325.

Stolz, A.J., Varne, R., Davies, G.R., Wheller, G.E., Doden, J.D., 1990. Magma source components in an arc-continent collision zone: the Flores-lembata sector, Sunda arc, Indonesia. *Contrib. Mineral. Petrol.* **105**, 585–601.

Tatsumi, Y., Kogiso, T., 1997. Trace element transport during dehydration processes in the subducted oceanic crust: 2.Origin of chemical and physical characteristics in arc magmatism. *Earth Planet. Sci. Lett.* **148**, 207–221.

Tatsumi, Y., Sakuyama, M., Fukuyama, H., Kushiro, I., 1983. Generation of arc basalt magmas and thermal structure of the mantle wedge in subduction zones. *J. Geophys. Res.* **88**, 5815–5825.

Tatsumi, Y., Hamilton, D.L., Nesbitt, R.W., 1986. Chemical characteristics of fluid phase released from a subducted lithosphere and origin of arc magmas: Evidence from high-pressure experiments and natural rocks. *J. Volcanol. Geotherm. Res.* **29**, 293–309.

Tera, F., Brow, L., Morris, J., Selwyn Sacks, I., Klein, J., Middleton, R., 1986. Sediment incorporation in island-arc magmas: Inferences from 10Be. *Geochim. Cosmochim. Acta* **50**, 535–550.

Turner, S.P., Foden, J.D., 2001. U, Th and Ra disequilibria, Sr, Nd and Pb isotope and trace element variations in Sunda arc Lavas: predominance of a subducted sediment component. *Contrib. Mineral. Petrol.* **142**, 43–57.

Turner, S.P., Hawkesworth, C., van Calsteren, P., Heath, E., Macdonald, R., Black, S., 1996. U-series isotopes and destructive plate margin magma genesis in the Lesser Antilles. *Earth Planet. Sci. Lett.* **142**, 191–207.

Turner, S.P., Hawkesworth, C., Rogers, N., Bartlett, J., Worthington, T., Hergt, J., Pearce, J., Smith, I., 1997. $^{238}U/^{230}Th$ disequilibria, magma petrogenesis, and fluxes rates beneath the depleted Tonga-Kermadec island arc. *Geochim. Cosmochim. Acta* **61**, 4855–4884.

Turner, S.P., Foden, J.D., George, R.M., Evans, P., Varne, R., Elburg, M.A., Jenner, G.A., 2003. Rates and processes of potassic magma evolution beneath Sangeang Api volcano, East Sunda Arc, Indonesia. *J. Petrol.* **44**, 491–515.

Varekamp, J.C., Van Bergen, M.J., Vroon, P.Z., Poorter, R.P.E., Wirakusumah, A.D., Erfan, R.D., Suharyono, K., Sriwana, T., 1989. Volcanism and tectonics in the eastern Sunda Arc, Indonesia. *Netherlands J. Sea Res.* **24**, 303–312.

Varne, R., Foden, J.D., 1986. Geochemical and isotopic systematics of Eastern Sunda Arc volcanics: implications for mantle sources and mantle mixing processes the origin of arcs. In: Wezel, F.-C. (Ed.), *The Origin of Arcs*. Elsevier, Amsterdam, pp. 159–189.

Von Drach, V., Marsh, B.D., Wasserburg, G.J., 1986. Nd and Sr isotopes in the Aleutians: multicomponent parenthood of island-arc magmas. *Contrib. Mineral. Petrol.* **92**, 13–34.

Weis D., Frey F.A., 1991. Isotope geochemistry of Ninetyeast Ridge basalt: Sr, Nd and Pb evidence for the involvement of the Kerguelen hot spot, In: Weissel, J., Peirce, J., Taylor, E., Alt, J. (Eds), *Proc. ODP Sci. Research*, **121**, Ocean Drilling Program, College Station, TX, pp. 591–610.

Weis, D., Frey, F.A., 1996. Role of the Kerguelen plume in generating the eastern Indian Ocean seafloor. *J. Geophys. Res.* **101**, 13831–13849.

Weis, D., Kieffer, B., Maerschalk, C., Pretorius, W., Barling, J., 2005. High-precision Pr-Sr-Nd-Hf isotopic characterization of USGS BHVO-1 and BHVO-2 reference materials. *Geochem. Geophys. Geosyst.*. doi:10.1029/2004GC000852.

White, W.M., 1985. Sources of oceanic basalts: radiogenic isotopic evidence. *Geology* **13**, 115–118.

White, W.M., Patchett, P.J., 1984. Hf-Nd-Sr isotopes and incompatible element abundances in island arcs: implications for magma origins and crust-mantle evolution. *Earth Planet. Sci. Lett.* **67**, 167–185.

Woodhead, J.D., 1989. Geochemistry of the Marian arc (Western Pacific): Source composition and processes. *Chem. Geol.* **76**, 1–24.

Woodhead, J.D., Hergt, J.M., Davidson, J.P., Eggins, S.M., 2001. Hafnium isotope evidence for conservative element mobility during subduction zone processes. *Earth Planet. Sci. Lett.* **192**, 331–346.

Wyllie, P.J., 1982. Subduction products according to experimental prediction. *Geol. Soc. Am. Bull.* **93**, 468–476.

Yogodzinski, G.M., Kelemen, P.B., 1998. Slab melting in the Aleutians: implications of an ion probe study of clinopyroxene in primitive adakite and basalt. *Earth Planet. Sci. Lett.* **158**, 53–65.

Lithos 123 (2011) 73–91

Contents lists available at ScienceDirect

Lithos

journal homepage: www.elsevier.com/locate/lithos

# Geochemistry and petrogenesis of high-K "sanukitoids" from the Bulai pluton, Central Limpopo Belt, South Africa: Implications for geodynamic changes at the Archaean–Proterozoic boundary

Oscar Laurent [a,b,c,*], Hervé Martin [a,b,c], Régis Doucelance [a,b,c], Jean-François Moyen [b,c,d], Jean-Louis Paquette [a,b,c]

[a] Clermont Université, Université Blaise Pascal, Laboratoire Magmas et Volcans, BP 10448, F-63000 Clermont-Ferrand, France
[b] CNRS, UMR6524, LMV, F-63038 Clermont-Ferrand, France
[c] IRD, R 163, LMV, F-63038 Clermont-Ferrand, France
[d] Département de Géologie, Université Jean Monnet, 23 rue du Docteur Paul Michelon 42023 Saint-Étienne, France

ARTICLE INFO

*Article history:*
Received 30 April 2010
Accepted 3 December 2010
Available online 25 December 2010

*Keywords:*
Archaean–Proterozoic boundary
Sanukitoids
Bulai pluton
Mantle metasomatism
Subducted sediments
Geochemical modelling

ABSTRACT

The Neoarchaean Bulai pluton is a magmatic complex intrusive in the Central Zone of the Limpopo Belt (Limpopo Province, South Africa). It is made up of large volumes of porphyritic granodiorites with subordinate enclaves and dykes of monzodioritic, enderbitic and granitic compositions. New U–Pb LA-ICP-MS dating on zircon yield pluton-emplacement ages ranging between 2.58 and 2.61 Ga. The whole pluton underwent a high-grade thermal overprint at ~2.0 Ga, which did not affect the whole-rock compositions for most of the major and trace-elements, as suggested by a Sm–Nd isochron built up with 16 samples and yielding an age consistent with U–Pb dating.

The whole-rock major- and trace-element compositions evidence that the Bulai pluton belongs to a high-K, calc-alkaline to shoshonitic suite, as well as unequivocal affinities with "high-Ti" sanukitoids. Monzodioritic enclaves and enderbites have both "juvenile" affinities and a strongly enriched signature in terms of incompatible trace elements (LREE, HFSE and LILE), pointing to an enriched mantle source. Based on trace-element compositions, we propose the metasomatic agent at their origin to be a melt deriving from terrigenous sediments. We therefore suggest a two-step petrogenetic model for the Bulai pluton: (1) a liquid produced by melting of subducted terrigenous sediments is consumed by reactions with mantle peridotite, producing a metasomatic assemblage; (2) low-degree melting of this metasomatized mantle gives rise to Bulai mafic magmas. Such a model is supported by geochemical modelling and is consistent with previous studies concluding that sanukitoids result from interactions between slab melts and the overlying mantle wedge.

Before 2.5 Ga, melting of hydrous subducted metabasalts produced large volumes of TTG (Tonalite–Trondhjemite–Granodiorite) forming most of the volume of Archaean continental crust. By constrast, our geochemical study failed in demonstrating any significant role played by melting of subducted metabasalts, which points to lower thermal regimes as metasediments melt at lower temperature than metabasalts. This suggests that the geodynamic changes that took place at the Archaean–Proterozoic transition and witnessed by sanukitoid-related rocks are mainly the result of progressive and global cooling of Earth. On the other hand, melting of subducted detrital material is uncommon during the Archaean, which would also indicate that significant recycling of continental material within the mantle roughly began at the Archaean–Proterozoic transition.



## 1. Introduction

The Archaean–Proterozoic transition corresponds to a fundamental change in global geodynamic mechanisms. During the Archaean, partial melting of hydrous garnet- and amphibole-bearing metabasalts gave rise to tonalite–trondhjemite–granodiorite (TTG) series (e.g. Barker and Arth, 1976; Condie, 1981; Ellam and Hawkesworth 1988; Martin, 1986, 1987, 1993; Rapp et al., 1991; Smithies, 2000; review in Martin et al., 2005), that volumetrically represent most of Archaean continental crust. On the contrary, since the beginning of Proterozoic until now, juvenile magmas identified as typical arc series (BADR for basalt–andesite–dacite–rhyolite) are generated in subduction settings by partial melting of the mantle wedge peridotite, previously enriched by slab-derived fluids (e.g. Arculus, 1994;

* Corresponding author. Clermont Université, Université Blaise Pascal, Laboratoire Magmas et Volcans, BP 10448, F-63000 Clermont-Ferrand, France. Tel.: +33 47334 6891.
*E-mail address:* o.laurent@opgc.univ-bpclermont.fr (O. Laurent).

0024-4937/$ – see front matter © 2010 Elsevier B.V. All rights reserved.
doi:10.1016/j.lithos.2010.12.009

McCulloch and Gamble, 1991; Tatsumi, 1989; Tatsumi et al., 1986). In other words, at the Archaean–Proterozoic transition, the source of juvenile continental crust changed from metabasalt to mantle peridotite.

In many Archaean cratons, the transition between both mechanisms is witnessed by specific rocks, generally referred as late-Archaean sanukitoids (Martin et al., 2005, 2009; Shirey and Hanson, 1984; Smithies and Champion, 2000; Stern, 1989; Stern and Hanson, 1991). They are made up of significant volumes of high-Mg dioritic, monzodioritic and granodioritic plutons that mostly emplaced between 2.9 and 2.5 Ga. The transitional characteristic of these plutons is not only temporal, but also compositional, as they share geochemical affinities with both Archaean TTGs (high LREE and low HREE contents resulting in highly fractionated REE patterns) and modern BADR series (calc-alkaline differentiation trends, high $K_2O$, LILE and transition element contents).

Most studies investigating the petrogenesis of sanukitoids concluded that their transitional characteristics result from interactions (hybridization) between a peridotite and a felsic, TTG-like melt (e.g. Heilimo et al., 2010; Martin et al., 2005, 2009; Shirey and Hanson, 1984; Smithies and Champion, 1999, 2000; Stern, 1989). These conclusions are strongly supported by experimental interactions between peridotite and hydrous silicic and/or sodic magmas giving rise to an ultramafic residue and liquids with composition closely resembling that of sanukitoids (Prouteau et al., 2001; Rapp et al., 1999, 2003, 2010). However, the detailed relationships between these two components remain unclear. Their interaction can be achieved by two distinct scenarios: i) a one-stage process, in which the TTG liquid reacts with peridotite to give a sanukitoid liquid in equilibrium with an ultramafic solid; ii) a two-stage model, in which the TTG magma is totally consumed by metasomatic reactions with the peridotite. In this case, these interactions produce a metasomatized mantle, which subsequent melting can give rise to sanukitoids.

The geodynamic setting where sanukitoids are generated is still a matter of debate. Interactions between felsic melt and peridotite are easily achieved in subduction zones where hydrous basalts (which melting at depth can generate TTG magmas) are overlain by the mantle wedge (Defant and Drummond, 1990; Martin, 1994, 1999; Martin et al., 2005, 2009). However, sanukitoids can be also generated in a subduction environment, where the peridotite is enriched in fluid-mobile elements provided by slab dehydration (Halla, 2005; Kamber et al., 2002; Stern and Hanson 1991). Furthermore, interactions between sanukitoid parental magma and continental crust during emplacement (AFC, mixing and induced melting) would be a key process in the differentiation and evolution of sanukitoid suites (Martin et al., 2009; Moyen et al., 1997; Stevenson et al., 1999).

In this paper, we focused on the Bulai pluton, a composite sanukitoid-like complex which emplaced ~2.6 Ga ago (Barton et al., 1994; Kröner et al., 1999; Zeh et al., 2007) within the Central Zone of the Limpopo Belt, in South Africa. The goal of this study is twofold: 1) we characterize the Bulai pluton as a whole in terms of petrography, timing of emplacement and whole-rock geochemistry; and 2) we investigate the petrogenesis of the "juvenile" component of this pluton (i.e. the mafic facies) in order to discuss the geodynamic setting in which it was generated and its implications for the petrogenetic changes that took place at the Archaean–Proterozoic boundary.

## 2. Geological setting

### 2.1. The Limpopo Belt

The Limpopo Belt (Fig. 1) is a ~650 km-long and ~200 km-wide high-grade granulitic terrane, outcropping in South Africa, Zimbabwe and Botswana. It corresponds to a complex Himalayan-type orogenic belt, which results from the continental collision between two Archaean blocks: the Zimbabwe craton to the North and the Kaapvaal craton to the South (e.g. Barton and Van Reenen, 1992; Holzer et al., 1998; Roering et al., 1992).

The Limpopo Belt is divided into three lithological domains separated by large shear zones (e.g. Van Reenen et al., 1992): the Central Zone is bordered by the Northern Marginal Zone (NMZ) and

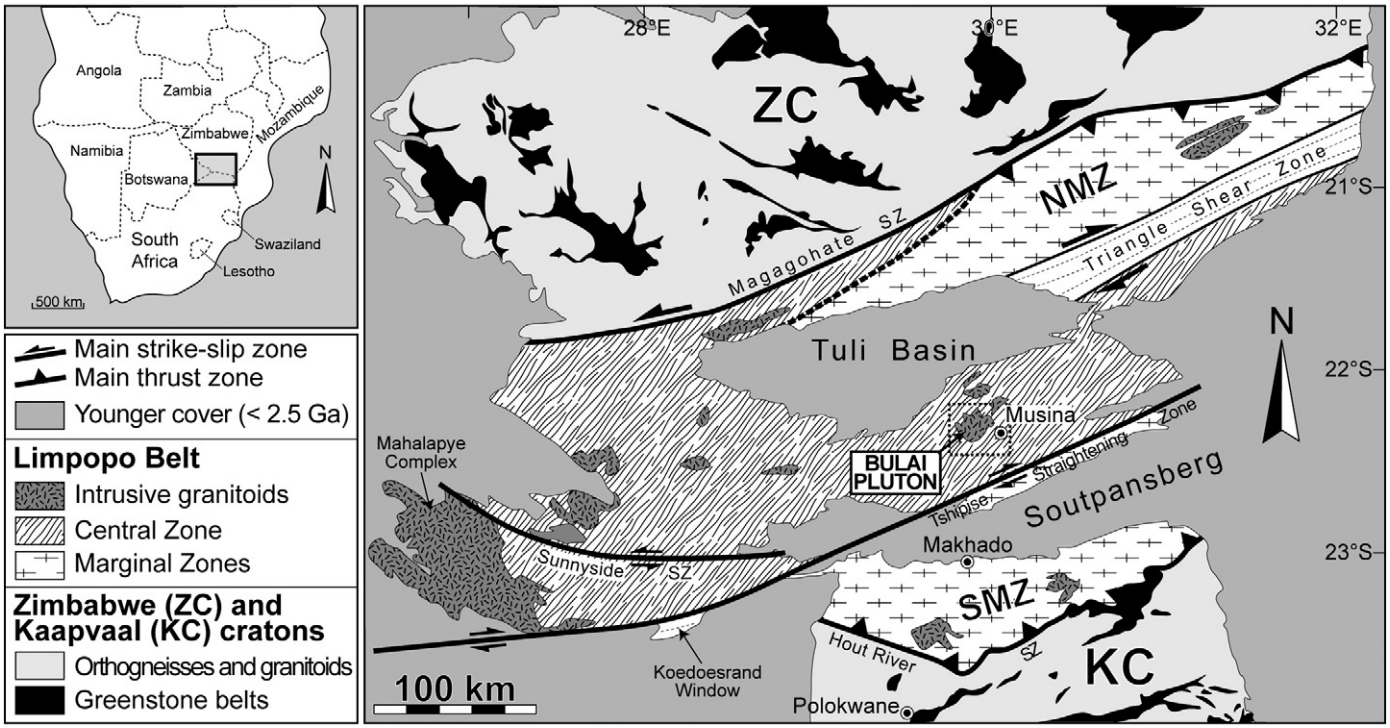


**Fig. 1.** Regional sketch map of the Limpopo Belt (modified after Boshoff et al., 2006; Van Reenen et al., 2008). SZ = shear zone; NMZ = Northern Marginal Zone; SMZ = Southern Marginal Zone; the dashed box represents the geographic area covered by Fig. 2.

the Southern Marginal Zone (SMZ) (Fig. 1). The Marginal Zones consist of large volumes of orthogneisses assumed to represent mainly reworked material of the neighbour craton (e.g. Kreissig et al., 2000), whereas the Central Zone is a very complex and highly deformed assemblage of miscellaneous lithologies which are unrelated with the two cratons (Roering et al., 1992).

### 2.2. The Central Zone of the Limpopo Belt

Most of the Central Zone consists of metapelites, paragneisses, marbles, mafic granulites, quartzites and BIFs, all affected by high-grade granulitic metamorphism (e.g. Van Reenen et al., 1992), and generally referred to as the Beit Bridge Complex (BBC). The age of the BBC still remains imprecise: its maximum age (3258 ± 11 Ma; Barton and Sergeev, 1997) is given by detrital zircons in a quartzite layer, while a minimum age of 2200 Ma has been deduced from carbon isotope study in metacarbonate units coupled with U–Th–Pb SHRIMP data (Buick et al., 2003).

In the Central Zone, the banded and migmatitic Sand River Gneisses correspond to large volumes of TTGs (e.g. Hofmann et al., 1998; Kröner et al., 1998, 1999), associated with mafic to ultramafic bodies (the Messina Layered Intrusion; Barton et al., 1979; Barton, 1996). U–Pb and Pb–Pb dating on separated zircons yield ages in the range 3314–3167 Ma (Jaeckel et al., 1997; Kröner et al., 1999; Retief et al., 1990; Tsunogae and Yurimoto, 1995; Zeh et al., 2007). Moreover, a complex patchwork of tonalitic, granitic and granodioritic magmas emplaced in the Central Zone all over the Neoarchaean, between 2750 and 2550 Ma (e.g. Jaeckel et al., 1997; Kröner et al., 1999). They include sheets and lenses of grey gneisses (e.g. Alldays, Regina, Verbaard, Zanzibar gneisses) and leucocratic, garnet-bearing patches and veins referred as Singelele gneisses. The Bulai pluton is the biggest of these late-Archaean intrusions.

The rocks of the Central Zone underwent three distinct metamorphic (M) granulite-facies and deformation (D) events:

i. A first episode $M_1/D_1$ took place at ~3.14 Ga (Holzer et al., 1998; Zeh et al., 2007), which induced the anatexis of the Sand River Gneisses.
ii. A second episode $M_2/D_2$ is considered as being roughly coeval with the late-Archaean magmatic event (e.g. Barton and Van Reenen, 1992; Barton et al., 1994; Holzer et al., 1998; Zeh et al., 2007). Millonig et al. (2008) determined the peak conditions of $M_2$ at 830–860 °C, 8–9 kbar and concluded from U–Pb dating of monazite that this event took place at 2644 ± 8 Ma.
iii. Petrological and geochronological data evidence a Palaeoproterozoic (1.97–2.03 Ga) $M_3/D_3$ high-grade tectono-metamorphic overprint (e.g. Barton et al., 1994; Boshoff et al., 2006; Buick et al., 2006; Holzer et al., 1998; Jaeckel et al., 1997; Kröner et al., 1999; Van Reenen et al., 2004; Zeh et al., 2004, 2007). *P–T* estimates for the Messina area point to a clockwise path with a first metamorphic peak at 780 °C and 9–10 kbar followed by a second one at 830 °C and 8 kbar (Zeh et al., 2004).

## 3. The Bulai Pluton

### 3.1. General features and previous work

The Bulai pluton outcrops in the Central zone as a discontinuous set of magmatic bodies, the main massif (Fig. 2) lying a few kilometres to the North-West of Musina. Based on structural and petrographic data, Holzer (1995) demonstrated that this intrusion slightly postdates the Neoarchaean metamorphic overprint $M_2/D_2$, but that subsequently, it underwent static recrystallization during the ~2.0 Ga tectono-metamorphic event $M_3/D_3$. The BBC thrusted over the Bulai Pluton during $M_3/D_3$ as evidenced by the Ha-Tshansi high-grade shear zone (Holzer et al., 1998; Millonig et al., 2008; Fig. 2).

The Bulai pluton has long been considered as a chronological key marker for the understanding of the geological evolution of the Musina area. Barton et al. (1994) performed U–Pb ID-TIMS analyses on zircons from two samples. They obtained two ages of 2605 ± 2 Ma (enderbitic facies) and 2572 ± 4 Ma (granitic facies). Kröner et al. (1999) investigated another enderbitic sample by stepwise evaporation of four zircon grains, which yielded a minimum $^{207}Pb/^{206}Pb$ age of 2587.1 ± 0.4 Ma. Finally, Zeh et al. (2007) carried out LA-ICP-MS analyses on zircons from a granite sample that gave a concordant age of 2612 ± 7 Ma.

Besides dating works, few authors paid attention to the petrogenesis of the Bulai pluton. Bahnemann (1973) described the whole pluton in terms of remobilised basement, whereas Watkeys (1984) proposed that Bulai represents a monzonitic I-type intrusion. Holzer (1995) interpreted the geochemical variability of the Bulai suite in terms of fractional crystallization but did not investigate the source of the primary mafic magma. On the other hand, Zeh et al. (2007)

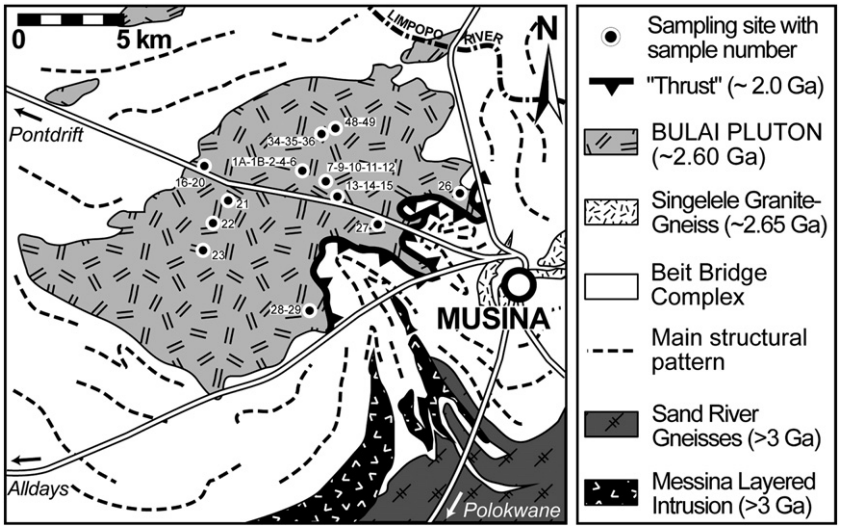


**Fig. 2.** Schematic geological map of the study area (modified after Millonig et al., 2008). Black dots represent the sampling localities and corresponding sample numbers.

calculated an Hf model age of 3220 ± 60 Ma for a granite sample whose zircons were dated at 2612 ± 7 Ma and concluded that the granitic melt originated from recycling of an old crustal source.

### 3.2. Structural and petrographic data

We focused our field work and sampling along the Musina-Pontdrift road and the "Three Sisters" area, on farm Boston 152 MS (Fig. 2). Here, we summarize the main petrographic features only; a more detailed description is available in Holzer (1995).

In the Bulai pluton, the most widespread rock type is a reddish porphyritic granodiorite (Fig. 3a). The phenocrysts are 3–6 cm K-feldspar crystals, which usually draw a strong magmatic fabric. The K-feldspar phenocrysts are enclosed in a fine- to medium-grained matrix made of quartz, plagioclase (~$An_{30}$), K-feldspar and disseminated aggregates of fine-grained mafic minerals (pargasitic hornblende and biotite together with subordinated amounts of magnetite, ilmenite and apatite). Zircon and epidote (including allanite) can be also abundant. There is little or no evidence for deformation at the grain-size scale, and the alignment of K-feldspars phenocrysts and some quartz ribbons are likely magmatic in origin. Holzer (1995) already noticed that the matrix displays a polygonal granoblastic texture (Fig. 3b) while quartz and K-feldspars megacrysts show annealing features rather than deformation.

The Bulai pluton contains two kinds of enclaves: 1) large (1–10 m) xenoliths of the country rocks (metapelites from the BBC, Singelele gneiss; Fig. 3c); and 2) small (<30 cm), fine-grained (<1 mm) Microgranular Mafic Enclaves (MMEs) always stretched along the magmatic fabric of the porphyritic granodiorite. Their edges are relatively sharp and K-feldspar euhedral phenocrysts often straddle the boundary of the MME (Fig. 3d), thus indicating that they were mechanically introduced into it. This implies that both the granodiorite and the MMEs were co-magmatic phases. In addition, many mafic fine-grained dykes intrude the granodiorite (Fig. 3e); they also display co-magmatic features such as diffuse or irregular footwalls and delamination (as previously detailed by Watkeys and Armstrong, 1985). Finally, leucogranitic and tonalitic bodies and dykes (Fig. 3f) are often associated with the granodiorite.

MMEs and mafic dykes display dioritic to monzodioritic mineral assemblages. Plagioclase (~$An_{32}$) and pargasitic hornblende generally form most of the volume of the rock, associated with abundant biotite, magnetite, ilmenite and apatite together with subordinated amounts

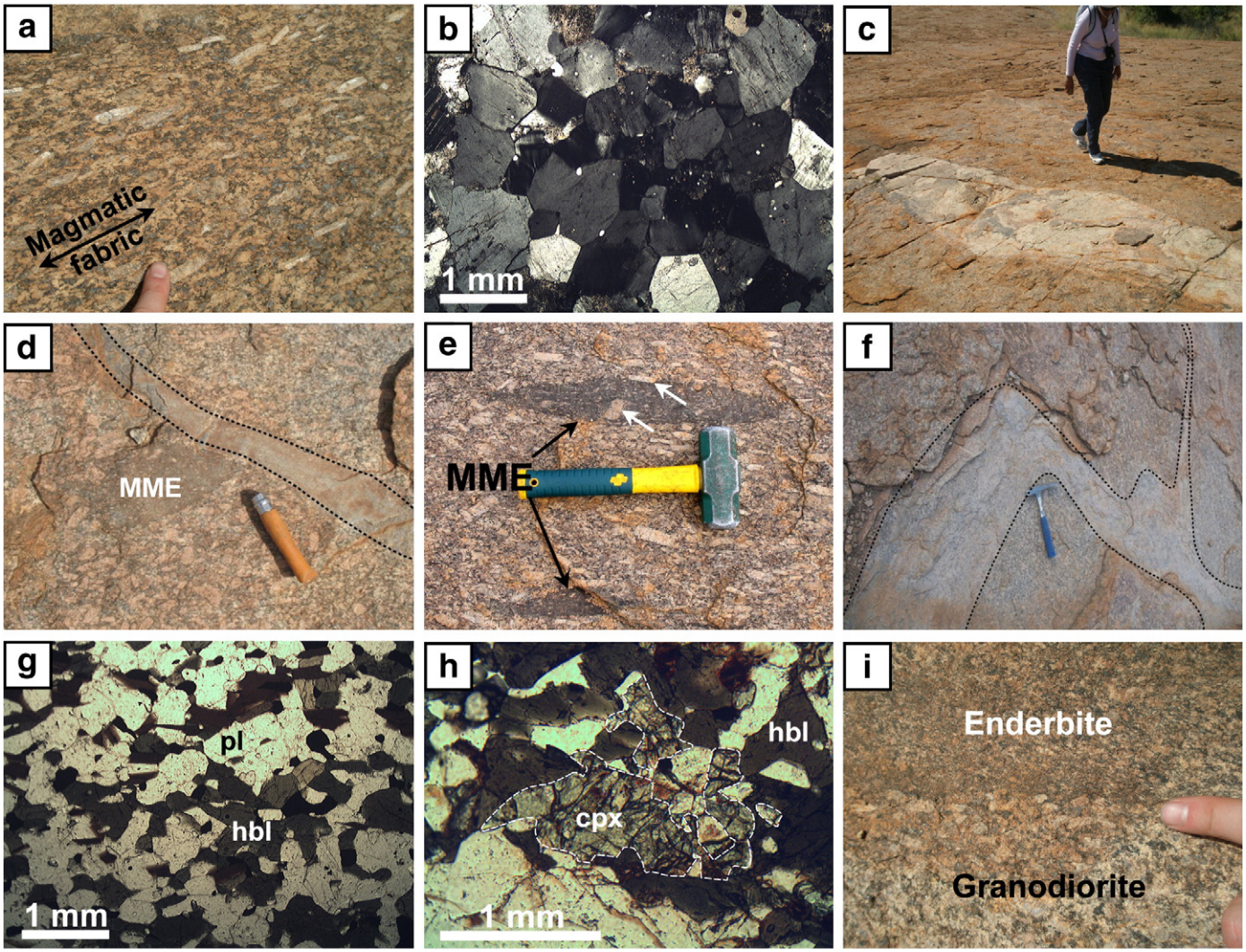


**Fig. 3.** Field relationships and rock textures of the Bulai pluton. (a) Typical porphyritic granodiorite where the preferential orientation of the K-feldspar phenocrysts draws a magmatic flow fabric. (b) Photomicrograph of porphyritic granodiorite BUL-4 showing the polygonal texture of the quartzo-feldspathic matrix. (c) Large angular xenolith of Singelele-type granite–gneiss. (d) Mafic dyke cross-cutting both the porphyritic granodiorite and a Microgranular Mafic Enclave (MME). (e) Typical MMEs stretched along the magmatic fabric; white arrows indicate K-feldspars phenocrysts that were introduced mechanically within the enclaves. (f) Leucogranite dyke intruding the granodiorite. (g) Photomicrograph of MME BUL-2, showing a granoblastic, equigranular texture, rich in plagioclase (pl) and hornblende (hbl). (h) Photomicrograph of enderbite BUL-36: clinopyroxene (cpx) in a hornblende- (hbl) and quartz-bearing matrix. (i) Sharp contact between the granodiorite and an enderbite enclave.

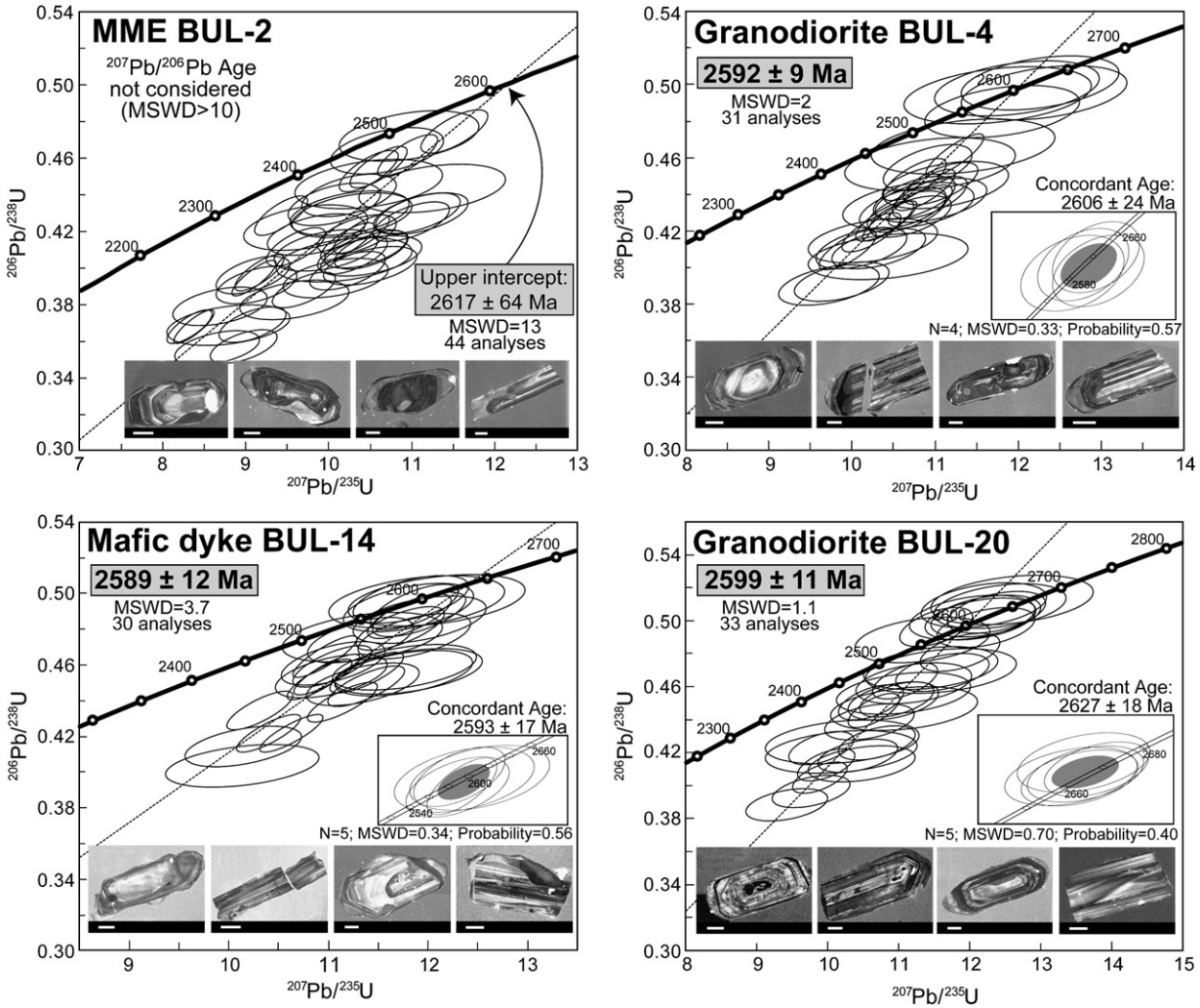


**Fig. 4.** Results of LA-ICP-MS analyses of single zircon grains from 4 samples of the Bulai pluton represented in Concordia diagrams (analyses with ≤15% discordance). Each ellipse represents one analytical spot. The size and shape of the ellipses are defined by analytical uncertainties on $^{206}Pb/^{238}U$, $^{207}Pb/^{235}U$ and their correlation coefficient. For each sample, the concordant age as well as the weighted average of the $^{207}Pb/^{206}Pb$ ages (grey box) are given, except for BUL-2 (no concordant analyses, scattered data) for which the upper intercept is indicated. Examples of cathodoluminescence of zircons from each sample are also shown (scale bars are 50 μm).

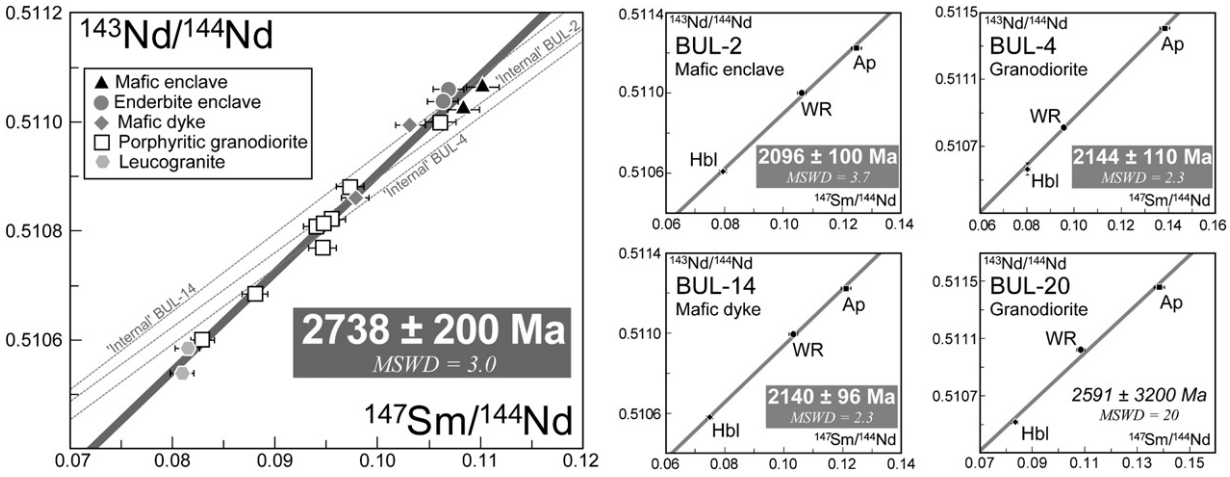


**Fig. 5.** (a) Sm–Nd isochron (thick grey line) established with 16 whole-rock samples from the Bulai pluton. In spite of a large error, the Sm–Nd age is consistent with the U–Pb age. The grey dashed lines represent "internal" isochrons detailed in Fig. 5b (BUL-20 is not reported). (b) Sm–Nd "internal" isochrons for the 4 samples dated by U–Pb on zircon. Each isochron is drawn from whole-rock (WR), hornblende (Hbl) and apatite (Ap) compositions. These isochrons systematically yield ages about ~2.0 Ga (except for BUL-20 which is meaningless) similar with the one of the $M_3/D_3$ structural-metamorphic overprint. Error bars are 2σ in all diagrams.

of quartz and orthoclase. These rocks often present a granoblastic texture, very similar to that of the matrix of porphyritic granodiorites (Fig. 3g).

Enderbites, charnockites and charno-enderbites were reported as part of the Bulai complex (Barton et al., 1994; Holzer, 1995; Watkeys, 1984). In the studied area, these facies outcrop as enclaves (as large as a hundred metres) within the porphyritic granodiorite. They differ from the other facies by the presence of clinopyroxene within large clusters of hornblende, quartz and oxides (Fig. 3h). Sub-euhedral small crystals (<0.5 mm) of orthopyroxene are also present in the matrix. Although these rocks appear as enclaves within the granodiorite with relatively sharp contacts between both rock types (Fig. 3i), their chemical features suggest that they belong to the Bulai suite (see Section 4). Thus, we consider that they represent early mafic intrusions rather than reworked basement.

In summary, field and petrographic data show that the Bulai pluton is a composite body, as many sanukitoids. The different facies share a homogeneous mineralogical assemblage and represent different cogenetic and coexisting magmas. Furthermore, the pluton did not undergo any subsolidus deformation but an episode of late static recrystallization represented by granoblastic textures and annealing developed during the ~2.0 Ga ($M_3/D_3$) metamorphic event. Consequently, the magmatic textures are relatively well preserved, and witness remnants of the petrography of sanukitoids such as a speckled appearance given by the numerous mafic aggregates and ubiquity of rounded mafic enclaves.

## 4. Geochemical characteristics of the Bulai pluton

Twenty-seven fresh samples representative of the different facies (12 porphyritic granodiorites, 3 MMEs, 4 enderbites, 5 mafic dykes and 3 leucogranite dykes) were selected for geochemical analyses. Descriptions of sample preparation and analytical techniques are given in the Appendix.

### 4.1. U–Pb and Sm–Nd dating

Four samples were selected for geochronological work: granodiorites BUL-4 and BUL-20, MME BUL-2 and mafic dyke BUL-14. Zircons were extracted for U–Pb *in situ* analysis by LA-ICP-MS, while separate hornblendes and apatites were analysed by TIMS in order to draw Sm–Nd internal isochrons. A whole-rock Sm–Nd isochron has also been built using 16 samples.

Zircons are often rounded, or display long prismatic shapes with rounded ends; they are generally light to medium brown. All grains exhibit complex internal oscillatory zoning (see Fig. 4), probably of igneous origin. Results of U–Pb dating are available as Supplementary Data and synthetized in Fig. 4. In all samples, analyses plot along a Discordia: most of the data points are less than 25% discordant, and few zircon analyses are concordant. $^{207}Pb/^{206}Pb$ ages were calculated only with analyses having a discordance ≤15%. Granodiorite BUL-4 gives a discordant age (31 analyses) of 2592 ± 9 Ma (2σ; MSWD = 2), identical within error to the concordant age (4 analyses; 2606 ± 24 Ma, 2σ; MSWD = 0.33). Granodiorite BUL-20 yields an age of 2599 ± 11 Ma (33 analyses, 2σ; MSWD = 1.05) that is slightly younger than the concordant age of 2627 ± 18 Ma (4 analyses, 2σ; MSWD = 0.7). Finally, the monzodiorite dyke BUL-14 provides an age of 2589 ± 12 Ma (30 analyses, 2σ; MSWD = 3.7) identical to the concordant age of 2593 ± 17 Ma (5 analyses, 2σ; MSWD = 0.34).

On the contrary, the age of the monzodiorite enclave BUL-2 is poorly constrained, as we did not obtain concordant analyses and the data set fails in defining a Discordia line. However, the upper intercept of the rough trend defined by 44 analyses yields an age of 2617 ± 64 Ma (2σ; MSWD = 13) which is in good agreement with the ages provided by the three other samples.

We interpret these ages as being those of zircon crystallization and consequently of Bulai pluton cooling and emplacement. These ages are similar to those already published (Barton et al., 1994; Kröner et al., 1999; Zeh et al., 2007), thus corroborating that the Bulai pluton emplaced between 2.58 and 2.61 Ga. In addition, all the measured

**Table 1**
Sm–Nd isotopic compositions measured in both whole rock (WR) and mineral fractions (Ap = apatite; Hbl = hornblende) of the Bulai samples, and calculations of initial isotopic signature ($^{143}Nd/^{144}Nd$ at 2.6 Ga; $\varepsilon_{Nd}$) and model ages ($T_{CHUR}$).

| Sample | Facies | Type | $^{147}Sm/^{144}Nd$ | ±2σ | $^{143}Nd/^{144}Nd$ | ±2σ | $^{143}Nd/^{144}Nd_{T=2.6\ Ga}$ | ±2σ | $\varepsilon_{Nd}$ | ±2σ | $T_{CHUR}$[a] (Ga) | ±2σ |
|---|---|---|---|---|---|---|---|---|---|---|---|---|
| BUL-1A | MME | WR | 0.1102 | 0.0016 | 0.511065 | 0.000004 | 0.50918 | 0.00005 | −0.34 | 0.89 | 2.78 | 0.05 |
| BUL-2 | MME | WR | 0.1061 | 0.0015 | 0.511000 | 0.000006 | 0.50918 | 0.00004 | −0.26 | 0.86 | 2.76 | 0.05 |
| | | WR[b] | 0.1061 | 0.0016 | 0.510998 | 0.000005 | 0.50918 | 0.00004 | −0.29 | 0.86 | 2.77 | 0.05 |
| | | Ap | 0.1247 | 0.0018 | 0.511224 | 0.000010 | | | | | | |
| | | Hbl | 0.0794 | 0.0011 | 0.510609 | 0.000010 | | | | | | |
| BUL-34 | Enderbite | WR | 0.1065 | 0.0015 | 0.511040 | 0.000004 | 0.50921 | 0.00004 | +0.42 | 0.86 | 2.71 | 0.05 |
| BUL-35 | Enderbite | WR | 0.1063 | 0.0015 | 0.511039 | 0.000006 | 0.50922 | 0.00004 | +0.44 | 0.86 | 2.71 | 0.05 |
| BUL-11 | “Lamprophyre” | WR | 0.0973 | 0.0014 | 0.510882 | 0.000004 | 0.50921 | 0.00004 | +0.40 | 0.79 | 2.70 | 0.04 |
| BUL-14 | “Lamprophyre” | WR | 0.1031 | 0.0015 | 0.510995 | 0.000010 | 0.50923 | 0.00004 | +0.64 | 0.85 | 2.69 | 0.05 |
| | | Ap | 0.1210 | 0.0017 | 0.511223 | 0.000010 | | | | | | |
| | | Hbl | 0.0748 | 0.0011 | 0.510580 | 0.000010 | | | | | | |
| BUL-4 | Granodiorite | WR | 0.0955 | 0.0014 | 0.510817 | 0.000005 | 0.50918 | 0.00004 | −0.26 | 0.77 | 2.75 | 0.04 |
| | | WR[b] | 0.0953 | 0.0013 | 0.510819 | 0.000006 | 0.50918 | 0.00004 | −0.17 | 0.76 | 2.74 | 0.04 |
| | | Ap | 0.1382 | 0.0020 | 0.511406 | 0.000010 | | | | | | |
| | | Hbl | 0.0801 | 0.0012 | 0.510567 | 0.000036 | | | | | | |
| BUL-10 | Granodiorite | WR | 0.0949 | 0.0013 | 0.510817 | 0.000004 | 0.50919 | 0.00004 | −0.07 | 0.77 | 2.73 | 0.04 |
| BUL-16 | Granodiorite | WR | 0.0946 | 0.0013 | 0.510769 | 0.000004 | 0.50915 | 0.00004 | −0.91 | 0.76 | 2.80 | 0.04 |
| BUL-20 | Granodiorite | WR | 0.1083 | 0.0015 | 0.511024 | 0.000005 | 0.50917 | 0.00004 | −0.53 | 0.87 | 2.79 | 0.05 |
| | | WR[b] | 0.1084 | 0.0015 | 0.511021 | 0.000006 | 0.50916 | 0.00004 | −0.62 | 0.87 | 2.80 | 0.05 |
| | | Ap | 0.1384 | 0.0020 | 0.511460 | 0.000010 | | | | | | |
| | | Hbl | 0.0834 | 0.0012 | 0.510516 | 0.000010 | | | | | | |
| BUL-21 | Granodiorite | WR | 0.0941 | 0.0013 | 0.510809 | 0.000004 | 0.50920 | 0.00004 | +0.06 | 0.76 | 2.72 | 0.04 |
| BUL-22 | Granodiorite | WR | 0.0829 | 0.0012 | 0.510600 | 0.000005 | 0.50918 | 0.00003 | −0.31 | 0.67 | 2.74 | 0.03 |
| BUL-23 | Granodiorite | WR | 0.0880 | 0.0012 | 0.510685 | 0.000005 | 0.50918 | 0.00004 | −0.35 | 0.71 | 2.75 | 0.03 |
| BUL-27 | Granodiorite | WR | 0.0978 | 0.0014 | 0.510862 | 0.000005 | 0.50919 | 0.00004 | −0.16 | 0.79 | 2.75 | 0.04 |
| BUL-12 | Leucogranite | WR | 0.0819 | 0.0012 | 0.510599 | 0.000004 | 0.50920 | 0.00003 | +0.04 | 0.66 | 2.71 | 0.03 |
| BUL-26 | Leucogranite | WR | 0.0825 | 0.0012 | 0.510562 | 0.000005 | 0.50915 | 0.00003 | −0.91 | 0.67 | 2.78 | 0.03 |

[a] CHUR model from Jacobsen and Wasserburg (1984).
[b] Sample duplicates.

ages fall in the same range, inside the analytical error bars; thus, following Zeh et al. (2007), we consider that the Bulai pluton emplaced within a short period of time.

It is noteworthy that none of the analysed zircon crystals recorded the $M_3/D_3$ thermal overprint. Indeed, we never obtained near-concordant Palaeoproterozoic ages, and the Discordia lines point to the origin of the plot and not to ~2.0 Ga. Consequently, the discordance seems a result of continuous Pb loss rather than of any perturbation of the U–Pb system by the late recrystallization event.

Results of Sm–Nd analyses are summarized in Table 1 and Sm–Nd isochrons are presented in Fig. 5. The internal isochrons are relatively well defined (MSWD = 1.8–3.3), excepted for BUL-20 (MSWD = 20). They give Palaeoproterozoic ages ranging between 1.99 and 2.37 Ga, which are systematically younger than the U–Pb zircon ages. On the other hand, the external isochron exclusively built from whole rocks, in spite of some scatter (MSWD = 3.1), provides a significantly older Archaean $^{147}Sm/^{143}Nd$ age of 2738 ± 200 Ma, in agreement with the U–Pb range of 2577–2610 Ma. Consequently, we interpret the whole-rock isochron as dating the crystallization of the Bulai pluton, which also means that the Sm–Nd system remained closed at the whole-rock scale. By contrast, the Palaeoproterozoic ages obtained by internal isochrons demonstrate that individual minerals behaved as open systems for Sm–Nd isotopes. We interpret these ages as being those of the $M_3/D_3$ tectono-metamorphic event.

In summary, isotopic re-equilibration took place at the grain-size scale during the Palaeoproterozoic granulite metamorphism, but the whole-rock isotopic composition of our samples remained unchanged. Consequently, the chemistry of the Bulai whole-rocks is considered as representative of that of their parental magma. Such an extrapolation is reasonable for major and most trace elements. However, one must keep in mind that most "mobile" elements, such as Cs, Rb, Ba, U and Pb, are likely to have undergone greater perturbations than Sm and Nd. Thus, the whole-rock compositions in "mobile" elements will be considered with a more critical point of view for any petrogenetic interpretation.

### 4.2. Major element geochemistry

Whole-rock analyses of the Bulai pluton are reported in Table 2. All samples plot along a calc-alkaline trend in the Na–K–Ca triangle (Barker and Arth, 1976) and cover the fields of granodiorite and quartz-monzonite in the feldspar triangle (An–Ab–Or, O'Connor, 1965) (Fig. 6). These characteristics clearly highlight that these rocks differ from the Archaean TTG series. In Harker diagrams (Fig. 6), data plot along linear trends: typically, all oxides are negatively correlated with $SiO_2$, except $K_2O$ that displays a slightly positive correlation. In the $K_2O$ vs. $SiO_2$ diagram, all data plot in the high-K calc-alkaline to shoshonitic fields of Le Maître (1989).

The porphyritic granodiorites are $SiO_2$-rich (60.52–67.29 wt.%), with high $Na_2O + K_2O$ (6.94–7.90 wt.%) and $K_2O/Na_2O > 1$. They are slightly metaluminous (A/NK ~1.6; A/NK = molecular ratio Al/(Na + K), and A/CNK = 0.91–1.05; A/CNK = molecular ratio Al/(Ca + Na + K)), iron- and magnesium-rich ($FeO_T + MgO$ = 4.54–7.76 wt.%) and have relatively high Mg# (38–45) for such $SiO_2$-rich rocks. Leucogranites are $SiO_2$-richer (71.48–74.36 wt.%) with high $Na_2O + K_2O$ (7.46–8.44); contrarily to granodiorites they are peraluminous (A/CNK > 1). They significantly differ from the granodiorites by their lower $FeO_T + MgO$ (1.41–2.76 wt.%) but like them they have relatively high Mg# (42–43).

Among the mafic facies, enderbites and mafic dykes roughly display the same range of $SiO_2$ content (52.05–54.32 and 52.54–58.42 wt.%, respectively), whilst silica contents of MME are even lower (46.11–48.82 wt.%). Their Mg# (28–51) varies in the same range as in granodiorites and leucogranites, which can be accounted for by the relatively high $FeO_T$ contents (6.03–12.33 wt.%) compared to MgO. Both MME and enderbites are metaluminous (A/NK ~1.95 and A/CNK < 0.83) and alkali-rich ($K_2O + Na_2O$ = 5.28–6.66), but they are less potassic than the granodiorites ($K_2O/Na_2O$ = 0.61–0.77). Mafic dykes show contrasted compositions and they can be divided into a "lamprophyre" group ($K_2O/Na_2O$ = 1.29–1.47) and a more "sodic" group ($K_2O/Na_2O$ = 0.53–0.63), both being $Al_2O_3$-rich (16.75–20.81 wt.%). In addition, all mafic facies have high $TiO_2$ (1.07–2.89 wt.%) and $P_2O_5$ (0.35–1.79 wt.%) contents.

Fig. 6 also shows that Bulai samples plot within the compositional field of the "high-Ti sanukitoids" as defined by Martin et al. (2009). It is noteworthy that the 3 "sodic" dykes often plot far away from the sub-linear correlation defined by the other facies. Consequently, they probably do not belong to the Bulai suite and will not be considered in any further detail.

### 4.3. Trace elements

The trace element composition of Bulai rocks is presented in primitive mantle-normalized multi-element diagrams and also as chondrite-normalized REE patterns (Fig. 7). The most characteristic feature of the Bulai suite is its high content in all incompatible elements. From this point of view they clearly look like "high-Ti sanukitoids" (Martin et al., 2009) as already noticed on the basis of major elements. Another characteristic of these rocks is that they present parallel REE patterns, the amount of REE being negatively correlated with $SiO_2$ content (Fig. 8). In particular, the mafic facies exhibit extreme enrichment in LREE ($La_N$ = 169–313). However, the steepness of the REE patterns increases with the degree of differentiation of the magma (Fig. 8). All rocks display a negative Eu anomaly ($Eu_N/Eu^*$ = 0.52–0.96; $Eu^* = [Sm_N + Gd_N]/2$) except the leucogranites which have $Eu_N/Eu^* > 1.44$.

Alike REE, Nb is negatively correlated with $SiO_2$ (Fig. 8). In spite of high concentrations (up to 45.6 ppm in MMEs), it displays a typical negative anomaly which increases with differentiation: $Nb_N/Nb^*$ ($Nb^* = [K_N + La_N]/2$) ranges from 0.31 in MMEs to 0.03 in leucogranites. Similarly, all samples show a Ti negative anomaly. Zr contents are high (up to 1128 ppm) when compared with TTG (~135 ppm), BADR (~171 ppm) and sanukitoids (~237 ppm).

Bulai rocks are also rich in LILE: Rb, Ba and K are more than 2 orders of magnitude-richer than the primitive mantle (Fig. 7). However, when compared with other Archaean plutonic rocks, they are less enriched in LILE. For instance, the average $Rb_N/La_N$ is lower than 1.5 in Bulai rocks, whereas it is 2.3 in TTG. The Bulai pluton also shows a strong, negative Sr anomaly: Sr/Nd is typically below 10, which is significantly lower than in classical sanukitoids (12–21) or average TTGs (~22; values from Martin et al., 2009). All these observations must be moderated for the "lamprophyre" dykes that have high Rb, Ba, K and Sr contents compared with other mafic rocks (Fig. 7) and are not valid for leucogranites that show high $Rb_N/La_N$ (2.3–7.4) and no negative Sr anomaly.

Transition element contents are also negatively correlated with $SiO_2$. They have low values in leucogranites, moderate ones in granodiorites, whereas mafic facies are rich in Cr (41–109 ppm), Ni (30–43 ppm) and V (126–178 ppm). These compositions are like those of high-Ti sanukitoids that, for a silica content of 58 wt.%, have Cr ~58 ppm, Ni ~36 ppm and V ~127 ppm (Martin et al., 2009).

### 4.4. Nd isotopes

$^{143}Nd/^{144}Nd$ initial ratios and model ages of selected Bulai samples were calculated using the present-day values for the CHUR reservoir ($^{143}Nd/^{144}Nd$ = 0.512638 and $^{147}Sm/^{144}Nd$ = 0.1967; Jacobsen and Wasserburg, 1984). All the studied samples have identical $^{143}Nd/^{144}Nd$ initial ratios and $\varepsilon_{Nd(T=2.6\ Ga)}$ (within error), regardless of the facies (Table 1; Fig. 9a): $\varepsilon_{Nd}$ varies between −0.91 and +0.64 (between −1.5 and +1.5 when error bars are taken into account). Similarly, $T_{CHUR}$ ranges from 2.69 to 2.80 Ga, which is only 0.1–0.2 Ga older than the magmatic U–Pb age. These results are consistent with data obtained for Neoarchaean magmatism in

**Table 2**
Whole-rock major (wt.%) and trace (ppm) element compositions of samples from the Bulai pluton.

| | BUL-1A | BUL-2 | BUL-48 | BUL-34 | BUL-35 | BUL-36 | BUL-49 | BUL-11 | BUL-14 | BUL-6 | BUL-7 | BUL-9 |
|---|---|---|---|---|---|---|---|---|---|---|---|---|
| Facies | MME | | | Enderbite | | | | Mafic dyke | | | | |
| *Major elements (wt.%)* | | | | | | | | | | | | |
| $SiO_2$ | 46.11 | 48.26 | 48.82 | 52.87 | 54.32 | 52.05 | 53.96 | 52.54 | 58.42 | 54.05 | 54.90 | 55.50 |
| $TiO_2$ | 2.89 | 2.34 | 2.05 | 1.70 | 1.65 | 1.81 | 1.51 | 1.81 | 1.42 | 2.33 | 1.08 | 1.07 |
| $Al_2O_3$ | 16.24 | 17.34 | 17.45 | 16.48 | 16.54 | 16.70 | 16.89 | 18.42 | 16.75 | 19.09 | 20.80 | 20.10 |
| $FeO_T$[a] | 12.33 | 10.27 | 8.14 | 8.14 | 7.32 | 6.81 | 7.52 | 6.96 | 6.03 | 6.88 | 6.56 | 6.87 |
| MnO | 0.14 | 0.12 | 0.11 | 0.10 | 0.10 | 0.10 | 0.12 | 0.12 | 0.06 | 0.05 | 0.05 | 0.05 |
| MgO | 3.75 | 3.59 | 3.82 | 3.85 | 3.39 | 3.95 | 3.32 | 2.56 | 1.94 | 2.35 | 1.52 | 1.36 |
| CaO | 8.10 | 8.01 | 6.75 | 7.28 | 6.58 | 7.60 | 6.47 | 5.88 | 4.40 | 5.28 | 5.41 | 5.15 |
| $Na_2O$ | 3.52 | 3.88 | 3.63 | 3.42 | 3.46 | 3.27 | 3.69 | 3.60 | 3.31 | 4.42 | 4.94 | 4.72 |
| $K_2O$ | 2.70 | 2.48 | 2.73 | 2.12 | 2.45 | 2.01 | 2.97 | 4.63 | 4.88 | 2.80 | 2.60 | 2.96 |
| $P_2O_5$ | 1.79 | 1.42 | 0.99 | 0.84 | 0.76 | 0.96 | 0.79 | 0.99 | 0.73 | 0.72 | 0.37 | 0.35 |
| LOI[b] | 0.5 | 0.5 | 1.9 | 0.7 | 0.7 | 0.5 | 1.0 | 0.8 | 0.8 | 0.7 | 0.7 | 0.7 |
| Total | 98.08 | 98.21 | 96.41 | 97.52 | 97.29 | 95.78 | 98.25 | 98.32 | 98.74 | 97.67 | 97.91 | 97.83 |
| Mg#[c] | 40 | 41 | 48 | 51 | 51 | 50 | 51 | 42 | 39 | 40 | 32 | 28 |
| *Trace elements (ppm)* | | | | | | | | | | | | |
| V | 178 | 157 | 165 | 142 | 126 | 149 | 134 | 119 | 96 | 126 | 101 | 109 |
| Cr[d] | 62 | 41 | 109 | 103 | 89 | 109 | 55 | 21 | 27 | <d.l.[e] | <d.l. | <d.l. |
| Ni | 32 | 31 | 43 | 37 | 30 | 35 | 37 | 23 | 19 | 14 | 9 | 10 |
| Rb | 59 | 67 | 90 | 54 | 46 | 50 | 83 | 109 | 88 | 92 | 70 | 76 |
| Sr | 691 | 794 | 510 | 637 | 597 | 662 | 537 | 1405 | 987 | 547 | 699 | 710 |
| Y | 86 | 71 | 45 | 51 | 49 | 42 | 39 | 38 | 40 | 16 | 15 | 13 |
| Zr | 697 | 939 | 767 | 554 | 769 | 608 | 514 | 661 | 505 | 1128 | 923 | 813 |
| Nb | 45.6 | 38.1 | 24.3 | 26.1 | 24.9 | 25.1 | 21.2 | 24.2 | 20.9 | 23.8 | 10.1 | 11.2 |
| Ba | 1337 | 1340 | 949 | 1304 | 1515 | 1209 | 1063 | 4407 | 2322 | 1723 | 1191 | 1442 |
| La | 197.0 | 202.7 | 152.3 | 127.4 | 141.8 | 127.5 | 109.4 | 171.2 | 125.9 | 81.9 | 77.4 | 75.9 |
| Ce | 448.3 | 435.8 | 329.3 | 280.3 | 305.0 | 278.1 | 246.6 | 286.0 | 269.2 | 153.1 | 139.1 | 132.4 |
| Pr | 58.58 | 54.97 | 38.52 | 33.76 | 35.22 | 32.62 | 30.82 | 38.38 | 33.63 | 18.59 | 15.54 | 14.76 |
| Nd | 245.1 | 216.2 | 147.0 | 140.0 | 142.1 | 128.5 | 121.7 | 150.7 | 130.1 | 70.0 | 59.3 | 54.0 |
| Sm | 40.63 | 35.75 | 22.79 | 23.49 | 22.93 | 20.01 | 19.55 | 23.16 | 21.94 | 10.21 | 8.41 | 7.89 |
| Eu | 5.51 | 5.43 | 3.43 | 4.05 | 3.96 | 3.74 | 3.78 | 5.42 | 4.54 | 2.59 | 2.91 | 2.93 |
| Gd | 30.73 | 25.88 | 15.80 | 17.36 | 16.63 | 14.62 | 13.46 | 16.09 | 15.52 | 7.08 | 5.87 | 5.31 |
| Tb | 4.03 | 3.31 | 2.12 | 2.41 | 2.29 | 1.81 | 1.78 | 1.88 | 1.90 | 0.83 | 0.70 | 0.64 |
| Dy | 17.89 | 15.08 | 9.69 | 11.15 | 10.21 | 8.63 | 8.08 | 8.14 | 8.74 | 3.48 | 3.05 | 2.75 |
| Ho | 3.22 | 2.61 | 1.50 | 1.83 | 1.69 | 1.40 | 1.28 | 1.32 | 1.38 | 0.60 | 0.51 | 0.48 |
| Er | 7.54 | 6.26 | 3.72 | 4.38 | 4.09 | 3.43 | 3.16 | 3.12 | 3.40 | 1.45 | 1.35 | 1.13 |
| Tm | 1.03 | 0.86 | 0.50 | 0.58 | 0.54 | 0.47 | 0.44 | 0.45 | 0.50 | 0.18 | 0.18 | 0.16 |
| Yb | 5.86 | 4.77 | 2.74 | 3.24 | 3.08 | 2.78 | 2.51 | 2.71 | 2.92 | 1.06 | 1.13 | 1.02 |
| Lu | 0.72 | 0.63 | 0.40 | 0.43 | 0.43 | 0.38 | 0.34 | 0.35 | 0.41 | 0.13 | 0.16 | 0.14 |
| Hf | 16.1 | 21.9 | 19.3 | 13.8 | 17.5 | 14.5 | 12.7 | 12.5 | 12.3 | 23.7 | 19.7 | 17.6 |
| Ta | 2.2 | 1.7 | 0.9 | 0.9 | 1.0 | 0.9 | 1.0 | 1.3 | 1.0 | 1.0 | 0.4 | 0.6 |
| Pb | 2.6 | 3.6 | 5.9 | 3.9 | 4.0 | 3.4 | 3.8 | 2.8 | 4.4 | 1.7 | 2.1 | 1.9 |
| Th | 8.9 | 14.7 | 25.1 | 15.1 | 15.1 | 14.9 | 19.0 | 7.3 | 9.2 | 3.3 | 2.6 | 2.7 |
| U | 2.1 | 2.4 | 2.1 | 0.7 | 1.0 | 0.8 | 1.6 | 2.2 | 1.0 | 1.1 | 1.1 | 1.0 |

[a] All iron recalculated in FeO.
[b] LOI = Loss of ignition.
[c] Mg# = [Mg/(Mg + $Fe^{II}$)] (molar).
[d] Cr recalculated in ppm from analysis of $Cr_2O_3$ (in wt.%).
[e] <d.l. = below detection limit.

the Northern Marginal Zone (Berger et al., 1995) and the Francistown greenstone belt (Southern Zimbabwe Craton; Zhai et al., 2006). They are not in agreement with the results of Zeh et al. (2007) that calculated an Hf model age of 3.22 ± 0.06 Ga for granite sample Bu1 and concluded that it represents melting of older crustal material. However, this assumption lies on a unique sample and may not be reliable for the whole pluton. Our self-consistent data set for initial isotopic compositions rather suggests that the signature of the Bulai pluton is apparently "juvenile" (Fig. 9b).

## 5. Discussion: petrogenesis of the Bulai mafic facies

Many chemical characteristics of the mafic facies of the Bulai pluton show that they originated more or less directly from the mantle (see below). Unravelling their petrogenesis should provide constraints about the geodynamic environment in which the mantle melted, thus, we will focus only on the origin of the less differentiated end-member of the Bulai suite in the following discussion.

### 5.1. Magma source

MMEs, enderbites and mafic dykes share low silica contents (46–58 wt.%) and high $FeO_T$ + MgO (8–16 wt.%), together with relatively high Mg# (40–50) and high transition-element contents. These characteristics, coupled to "juvenile" isotopic signatures, indicate that a mantle component played a prominent role in their genesis. On the other hand, they are rich in all incompatible elements. This could result from crustal contamination during or after magma emplacement. However, the very high LREE and HFSE contents of mafic facies (e.g. up to 200 ppm La; 450 ppm Ce; 45 ppm Nb; 85 ppm Y) would require a contaminant even richer in these elements, which was not sampled until now in the Central Zone of the Limpopo belt. Moreover, the negative correlation between $SiO_2$ and incompatible trace elements (Fig. 8) as well as the absence of correlation between $SiO_2$ and $\varepsilon_{Nd(T=2.6\ Ga)}$ (Fig. 9a), preclude any significant contamination by older continental crust.

The accumulation of accessory phases preferentially incorporating some trace elements (e.g. allanite for LREE and Th, apatite for Sr and

| | BUL-1B | BUL-4 | BUL-10 | BUL-15 | BUL-16 | BUL-20 | BUL-21 | BUL-22 | BUL-23 | BUL-27 | BUL-28 | BUL-29 | BUL-12 | BUL-13 | BUL-26 |
|---|---|---|---|---|---|---|---|---|---|---|---|---|---|---|---|
| Facies | Porphyritic granodiorite | | | | | | | | | | | | Leucogranite dyke | | |
| *Major elements (wt.%)* | | | | | | | | | | | | | | | |
| $SiO_2$ | 62.80 | 60.52 | 61.80 | 62.00 | 67.07 | 66.74 | 63.52 | 67.29 | 65.30 | 63.29 | 65.23 | 66.26 | 71.50 | 72.60 | 74.36 |
| $TiO_2$ | 0.95 | 1.20 | 1.11 | 1.09 | 0.68 | 0.73 | 0.91 | 0.64 | 0.76 | 1.01 | 0.83 | 0.78 | 0.38 | 0.18 | 0.21 |
| $Al_2O_3$ | 16.30 | 16.08 | 16.30 | 16.10 | 15.21 | 14.94 | 15.78 | 15.56 | 16.11 | 15.41 | 15.64 | 15.19 | 14.40 | 14.58 | 13.54 |
| $FeO_T$[a] | 4.71 | 5.82 | 5.53 | 5.62 | 3.60 | 3.73 | 4.93 | 3.45 | 3.85 | 5.15 | 4.38 | 4.23 | 2.02 | 1.04 | 1.03 |
| MnO | 0.05 | 0.06 | 0.06 | 0.06 | 0.03 | 0.04 | 0.06 | 0.03 | 0.04 | 0.06 | 0.05 | 0.05 | 0.02 | 0.02 | 0.01 |
| MgO | 1.46 | 1.94 | 1.79 | 1.79 | 1.51 | 1.50 | 1.70 | 1.09 | 1.39 | 1.71 | 1.42 | 1.38 | 0.74 | 0.40 | 0.38 |
| CaO | 3.97 | 4.64 | 4.36 | 4.13 | 3.19 | 3.62 | 3.84 | 2.60 | 3.39 | 3.82 | 3.55 | 3.57 | 2.27 | 1.74 | 1.52 |
| $Na_2O$ | 3.26 | 3.33 | 3.50 | 3.43 | 3.13 | 3.15 | 3.45 | 2.96 | 3.32 | 3.17 | 3.38 | 3.42 | 2.86 | 3.34 | 2.60 |
| $K_2O$ | 4.44 | 3.89 | 3.44 | 3.85 | 4.02 | 3.98 | 3.93 | 4.87 | 4.58 | 4.33 | 3.99 | 3.56 | 4.60 | 5.24 | 5.84 |
| $P_2O_5$ | 0.57 | 0.72 | 0.54 | 0.53 | 0.28 | 0.27 | 0.44 | 0.29 | 0.29 | 0.46 | 0.35 | 0.31 | 0.14 | 0.08 | 0.07 |
| LOI[b] | 0.5 | 0.6 | 0.5 | 0.4 | 0.6 | 0.5 | 0.5 | 0.6 | 0.2 | 0.6 | 0.4 | 0.5 | 0.5 | 0.5 | 0.2 |
| Total | 98.96 | 97.80 | 98.88 | 98.94 | 99.32 | 99.21 | 99.06 | 99.38 | 99.24 | 99.01 | 99.23 | 99.25 | 98.44 | 98.72 | 99.77 |
| Mg#[c] | 38 | 40 | 39 | 39 | 45 | 44 | 41 | 39 | 42 | 40 | 39 | 39 | 42 | 43 | 42 |
| *Trace elements (ppm)* | | | | | | | | | | | | | | | |
| V | 64 | 84 | 79 | 75 | 54 | 58 | 75 | 50 | 56 | 74 | 59 | 62 | 28 | 17 | 22 |
| Cr[d] | 14 | <d.l. | 21 | 14 | 27 | 21 | 21 | 21 | 27 | 27 | 21 | 27 | <d.l. | <d.l. | 14 |
| Ni | 14 | 16 | 15 | 17 | 18 | 17 | 19 | 13 | 14 | 19 | 14 | 14 | 5 | 2 | 3 |
| Rb | 102 | 98 | 101 | 93 | 97 | 91 | 101 | 101 | 102 | 95 | 106 | 104 | 95 | 196 | 124 |
| Sr | 741 | 710 | 621 | 589 | 372 | 463 | 498 | 382 | 460 | 506 | 371 | 340 | 504 | 230 | 214 |
| Y | 32 | 39 | 25 | 33 | 11 | 30 | 26 | 11 | 16 | 33 | 24 | 27 | 5 | 6 | 4 |
| Zr | 437 | 582 | 670 | 505 | 233 | 300 | 403 | 325 | 413 | 420 | 417 | 374 | 205 | 114 | 131 |
| Nb | 14.2 | 16.8 | 15.6 | 16.6 | 9.1 | 14.2 | 13.9 | 6.8 | 10.6 | 16.8 | 15.0 | 16.3 | 4.0 | 3.6 | 2.9 |
| Ba | 2577 | 2076 | 1631 | 1554 | 1277 | 1208 | 1399 | 1409 | 1441 | 1580 | 1150 | 1006 | 1956 | 897 | 622 |
| La | 84.3 | 154.7 | 119.1 | 135.4 | 59.7 | 76.7 | 101.0 | 78.2 | 94.3 | 129.4 | 80.0 | 125.3 | 45.1 | 28.4 | 30.0 |
| Ce | 175.9 | 301.3 | 233.4 | 250.8 | 114.7 | 169.8 | 201.2 | 145.1 | 180.9 | 255.2 | 156.5 | 236.5 | 74.4 | 42.2 | 48.9 |
| Pr | 21.63 | 35.55 | 27.41 | 30.66 | 13.37 | 21.06 | 23.54 | 16.12 | 19.96 | 29.31 | 18.42 | 26.06 | 7.62 | 4.31 | 5.01 |
| Nd | 86.8 | 136.4 | 105.3 | 111.4 | 49.1 | 77.7 | 86.0 | 55.1 | 68.5 | 106.9 | 68.0 | 90.6 | 26.0 | 15.0 | 15.6 |
| Sm | 14.71 | 20.62 | 15.11 | 17.43 | 7.56 | 13.47 | 13.74 | 7.58 | 9.87 | 16.66 | 11.45 | 13.64 | 3.46 | 2.31 | 2.14 |
| Eu | 3.35 | 3.67 | 3.05 | 3.37 | 1.90 | 2.42 | 2.81 | 2.07 | 2.30 | 3.03 | 2.19 | 2.11 | 1.97 | 1.19 | 0.85 |
| Gd | 11.08 | 14.91 | 10.46 | 12.30 | 5.13 | 9.25 | 9.53 | 4.98 | 6.49 | 11.58 | 8.11 | 9.57 | 2.24 | 1.59 | 1.30 |
| Tb | 1.52 | 1.89 | 1.28 | 1.53 | 0.58 | 1.25 | 1.17 | 0.56 | 0.78 | 1.49 | 1.08 | 1.23 | 0.24 | 0.22 | 0.13 |
| Dy | 6.79 | 8.42 | 5.50 | 6.94 | 2.39 | 5.98 | 5.48 | 2.35 | 3.53 | 6.86 | 4.94 | 5.37 | 1.06 | 1.08 | 0.72 |
| Ho | 1.25 | 1.45 | 0.92 | 1.14 | 0.37 | 1.02 | 0.88 | 0.37 | 0.58 | 1.14 | 0.84 | 0.91 | 0.17 | 0.19 | 0.11 |
| Er | 2.85 | 3.44 | 2.29 | 2.73 | 0.87 | 2.58 | 2.15 | 0.90 | 1.42 | 2.79 | 2.11 | 2.29 | 0.40 | 0.48 | 0.28 |
| Tm | 0.39 | 0.47 | 0.32 | 0.41 | 0.12 | 0.38 | 0.32 | 0.12 | 0.19 | 0.40 | 0.31 | 0.31 | 0.05 | 0.08 | 0.05 |
| Yb | 2.08 | 2.59 | 1.88 | 2.23 | 0.67 | 2.10 | 1.79 | 0.72 | 1.09 | 2.29 | 1.66 | 1.73 | 0.39 | 0.40 | 0.26 |
| Lu | 0.27 | 0.34 | 0.26 | 0.31 | 0.09 | 0.28 | 0.26 | 0.11 | 0.16 | 0.32 | 0.23 | 0.23 | 0.05 | 0.07 | 0.05 |
| Hf | 10.2 | 13.5 | 15.8 | 12.9 | 6.5 | 8.1 | 10.4 | 8.7 | 10.3 | 11.1 | 10.9 | 10.3 | 5.0 | 3.6 | 4.2 |
| Ta | 0.6 | 0.7 | 0.8 | 0.8 | 0.4 | 1.1 | 0.6 | 0.2 | 0.5 | 0.8 | 0.6 | 0.6 | 0.1 | 0.2 | 0.2 |
| Pb | 2.6 | 6.2 | 4.4 | 7.0 | 5.7 | 5.7 | 6.7 | 4.1 | 5.0 | 6.3 | 5.5 | 8.6 | 5.1 | 3.5 | 3.3 |
| Th | 5.1 | 28.5 | 18.7 | 24.9 | 23.4 | 25.7 | 21.1 | 11.4 | 21.0 | 33.5 | 20.5 | 39.4 | 24.2 | 6.2 | 45.4 |
| U | 1.2 | 1.8 | 1.9 | 2.1 | 1.3 | 1.5 | 2.3 | 1.4 | 1.7 | 1.4 | 2.8 | 3.0 | 1.1 | 0.9 | 2.2 |

MREE, zircon for Zr and HREE) could also account for the enrichment of these rocks. However, this would imply that the mafic facies are at least partly cumulates, while field relationships and petrographic observations show that they derive from the crystallization of magmatic liquids.

Therefore, the great enrichment in incompatible trace elements is necessarily inherited from the source of the Bulai less-differentiated magmas. Thus, the mantle source of the mafic facies must have been previously enriched by a metasomatic event.

### 5.2. Nature of the metasomatic agent

Two distinct metasomatic endmembers can account for mantle enrichment: (1) an aqueous fluid and (2) a hydrous melt. The Bulai mafic magmas are enriched in HFSE such as Nb (up to 46 ppm) and Ti (up to 1.73 wt.%). Due to their high $Kd_{HFSE}^{rock/fluid}$, these elements cannot be significantly dissolved and carried by fluids (e.g. Audétat and Keppler, 2005; Brenan et al., 1994, 1995; McCulloch and Gamble, 1991; Tatsumi et al., 1986; Tropper and Manning, 2005). Consequently, the high HFSE content of Bulai mafic magmas precludes a prominent role played by fluid metasomatism. By contrast, felsic melts can transport and transfer Nb and Ti into the mantle source (Brenan et al., 1995) because of their low $Kd_{HFSE}^{rock/magma}$. This is frequently invoked to account for the HFSE abundance (Nb>20 ppm) in some mantle derived arc volcanics such as Nb-enriched basalts (NEB) (Defant et al., 1992; Reagan and Gill, 1989; Sajona et al., 1996). In addition, petrological experiments have demonstrated that a hydrous melt is much more efficient as a metasomatic agent than an aqueous fluid (Brenan et al., 1995; Hermann and Rubatto, 2009; Prouteau et al., 2001), which accounts for the extreme enrichment in all incompatible trace elements in the Bulai mafics.

### 5.3. Origin of the metasomatic agent

The Bulai mafic magmas share unequivocal affinities with high-Ti sanukitoids. Therefore, it is reasonable to assume that they could

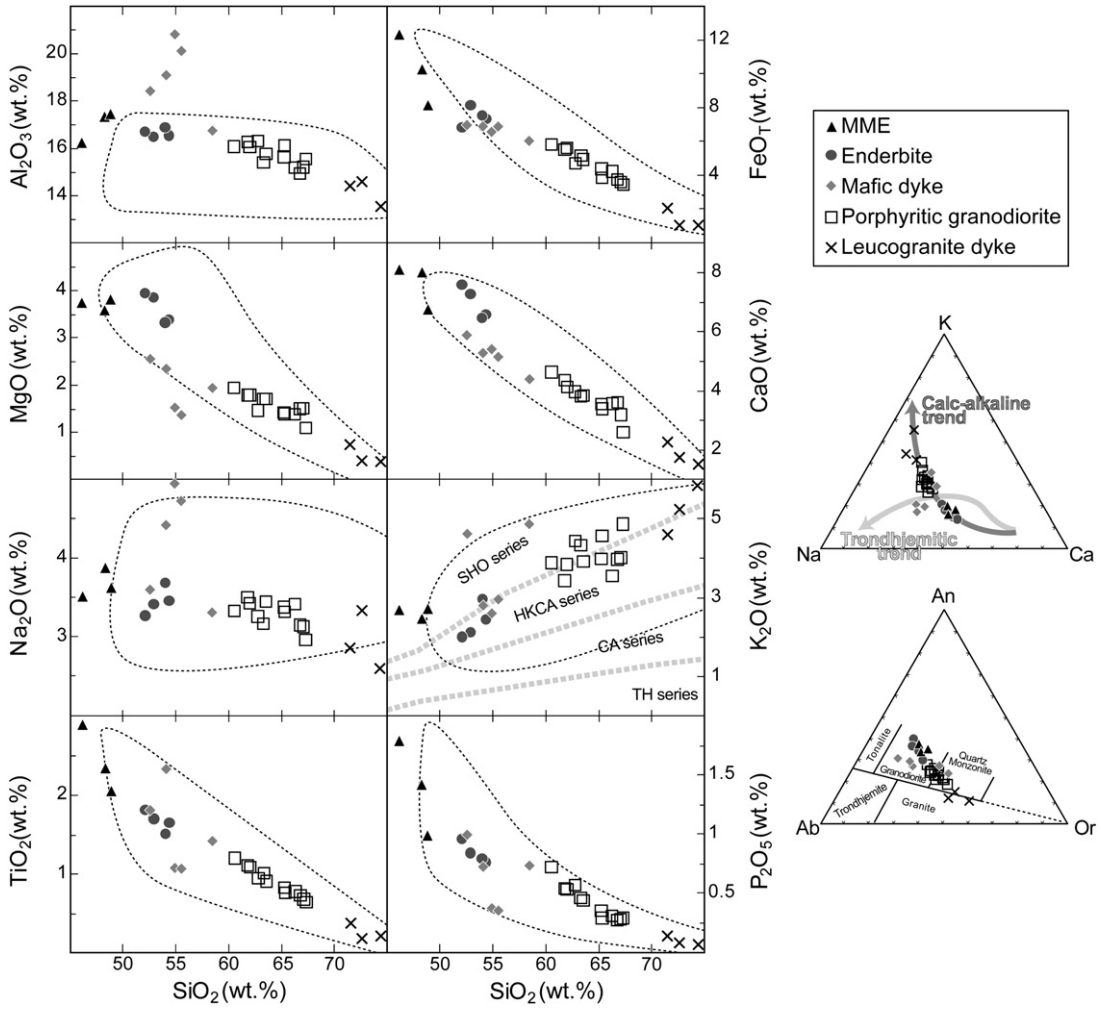


**Fig. 6.** Major element characteristics of the Bulai rocks presented in Harker diagrams, Na–K–Ca triangle (Barker and Arth, 1976) and feldspar triangle (An–Ab–Or, O'Connor, 1965). The most important features are: (i) samples plot along calc-alkaline trends and show no affinity with TTG series; (ii) all elements but $K_2O$, are negatively correlated with $SiO_2$. In addition, the compositional variability of the Bulai suite overlaps the field of "high-Ti sanukitoids" (dashed areas, Martin et al., 2009). Fields in the $K_2O$ vs. $SiO_2$ diagram are from Le Maître (1989); TH = tholeiitic; CA = calc-alkaline; HKCA = high-K calc-alkaline; SHO = shoshonitic.

derive from a mantle source hybridized with TTGs. This hypothesis is supported by the fact that the Bulai rocks (high Nb/Y>0.5 and La/Yb>33) plot within the field of melts derived from a mantle source enriched by TTG liquids in the Nb/Y vs. La/Yb discrimination diagram (Martin et al., 2009) (Fig. 10).

However, this mechanism alone cannot account for some geochemical features of the Bulai pluton. Indeed, it fails in explaining the Sr depletion with respect to LREE (Sr/Nd = 3–10). The strongest Sr negative anomalies are found in the less differentiated magmas (MMEs), and consequently preclude Sr depletion by plagioclase fractionation during late fractional crystallization. Another possibility would be that plagioclase was a stable residual phase during mantle melting. A first-order calculation shows that switch of Sr/Nd from 22 (average value of Archaean TTG) to 3 is only achieved if 25% plagioclase remain in the residue when assuming $Kd_{Sr/LREE}^{plag/magma}$ ~20 (Adam and Green, 2006) and $Kd_{Sr/LREE}^{mineral/magma}$ ~1 for all other minerals. This appears totally unrealistic for an ultramafic assemblage. As a consequence, the only possibility for the Sr negative anomaly consists in having an already "Sr-depleted" mantle source.

Among the geological materials bearing a Sr negative anomaly, terrigenous sediments are by far the most common (Plank and Langmuir, 1998). Furthermore, experimental melting of natural pelagic clays produces melts with subchondritic Sr/Nd (e.g. Johnson and Plank, 1999). We compiled the major- and trace-element compositions of 66 samples (shales, pelites and greywackes) from the neighbouring of the Limpopo Belt (Dominion Group, Witwatersrand and Ventersdorp Supergroups: Wronciewicz and Condie, 1987; Jahn and Condie 1995; Bushwa: Fedo et al., 1996), referred SATS [South African Terrigenous Sediments] database in the rest of this study. They show extremely low Sr/Nd (average: 2.4 ± 0.4) as well as Nb, Eu and Ti negative anomalies, such as the Bulai magmas.

Involvement of sediments in Bulai magma genesis would not only account for Sr depletion, but would also explain the $K_2O$ richness of the mafic magmas. Indeed, terrigeneous sediments typically have high K/Na, and consequently, their melting would produce melts with higher K/Na than TTGs. In addition, sediments are also rich in HFSE, especially in Nb (Plank and Langmuir, 1998), which results in low Zr/Nb ratios in volcanic rocks having a significant sedimentary component in their source (e.g. Vroon et al., 1993). These considerations are illustrated by plots of Sr/Nd vs. K/Na and Zr/Nb, in which Bulai mafics plot within the compositional range of mixtures between the depleted mantle and magmatic liquids derived from sediment melting (Fig. 11). This is particulary true for MMEs and enderbites, whereas petrogenesis of "lamprophyre" dykes might involve a component with higher Sr/Nd and K/Na.

Finally, Fig. 12 shows that both the low Sr/Nb and the Nd isotopic composition of Bulai MMEs and enderbites can be satisfactorily reproduced by mixing a depleted mantle composition with ancient terrigeneous sediments from the Kaapvaal Craton. However, as previously noticed, the compositions of the lamprophyric mafic

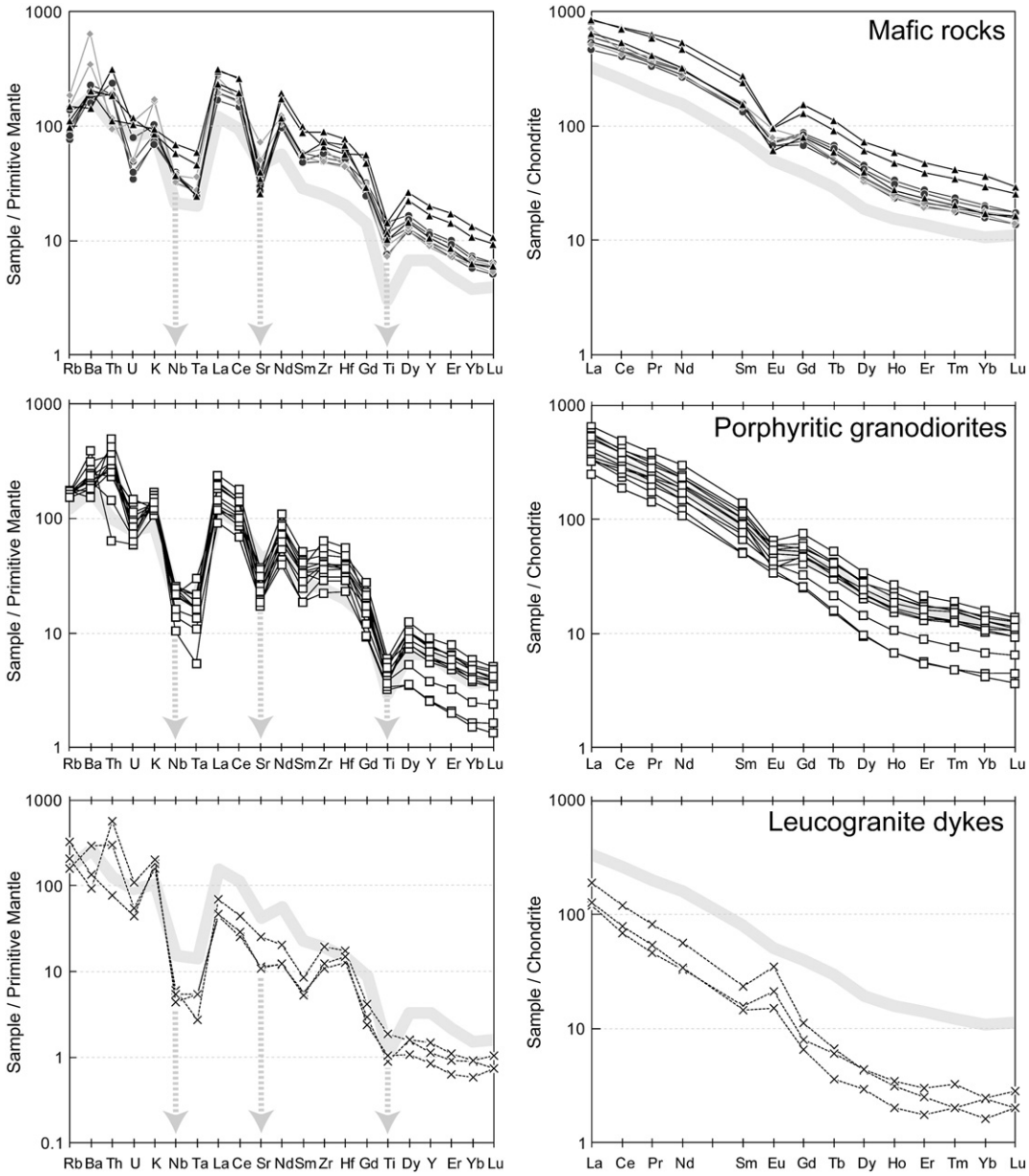


**Fig. 7.** Trace element compositions of the Bulai samples presented in primitive mantle-normalized trace elements patterns (left-hand side) and chondrite-normalized REE concentrations (right-hand side). Normalization values are from McDonough and Sun (1995). In all diagrams, the light grey pattern represents the average composition of "high-Ti sanukitoids" (Martin et al., 2009). Arrows indicate typical negative spikes in Nb(–Ta), Sr and Ti. Symbols are as in Fig. 6. The "sodic" mafic dykes (see Section 4.2) are not represented.

dykes imply the presence of a high-Sr/Nb component in their source, such as an aqueous fluid. This hypothesis can account for their higher K, Sr and Ba contents with respect to MMEs and enderbites, and has already been proposed for late-Archaean alkaline dykes emplaced in the Musina area (Watkeys and Armstrong, 1985).

In conclusion, we propose that the Bulai mafic magmas, and in particular the MMEs and enderbites, derive from a mantle source previously enriched in trace elements by a liquid formed by partial melting of terrigeneous sediments. Melting of detrital material and subsequent interaction with the mantle imply that sediments are located beneath a thick mantle slice, which can be easily achieved in subduction environments. This hypothesis is supported by the fact that the compositions of the Bulai mafic magmas are close to those of modern arc volcanics, which petrogenesis involves subducted sediments (Fig. 13). This is particularly obvious in discrimination plots such as Th/Yb vs. Ba/La (Woodhead et al., 2001) and U/Th vs. Th (Hawkesworth et al., 1997). The low U/Th of the Bulai mafic magmas can result from preferential removal of U over Th during granulite-facies metamorphism, but this process cannot account for their high Th/Yb relative to "classical" arc volcanics, as Th is more mobile than Yb. Consequently, we consider that these geochemical signatures rather reflect source processes than post-magmatic perturbations.

### 5.4. Geochemical modelling

A quantitative, geochemical modelling has been performed in order to reproduce the chemical characteristics of both MME and enderbite. Modelling follows the three successive steps described in Martin et al. (2009). (1) The composition of a felsic magma is calculated by the batch melting (equation from Shaw, 1970) of a virtual terrigenous sediment which composition falls within the SATS database (Table 3), using a degree of melting of 20% and partition coefficients from Johnson and Plank (1999). (2) Melt obtained at step 1 is then mixed with depleted mantle material (using DM composition from Workman and Hart, 2005). The composition of the metasomatized mantle $C_{mm}$ is obtained using a simple mass balance

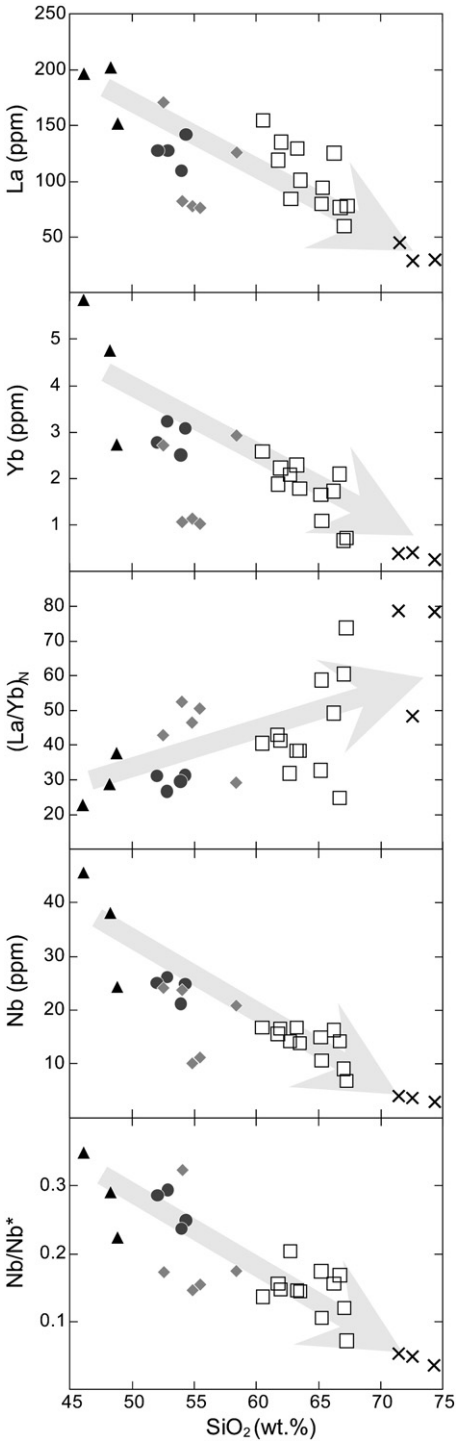


**Fig. 8.** Harker plots for La, Yb, $(La/Yb)_N$ (primitive mantle-normalized ratio), Nb and Nb/Nb* ($Nb^* = (K_N + La_N)/2$) in the Bulai rocks. These diagrams evidence the negative correlation between $SiO_2$ and LREE (La), HREE (Yb) as well as HFSE (Nb). The Nb negative anomaly (Nb/Nb*) also increases with the silica content, whereas the fractionation of the REE show the reverse behaviour. Symbols are as in Fig. 6.

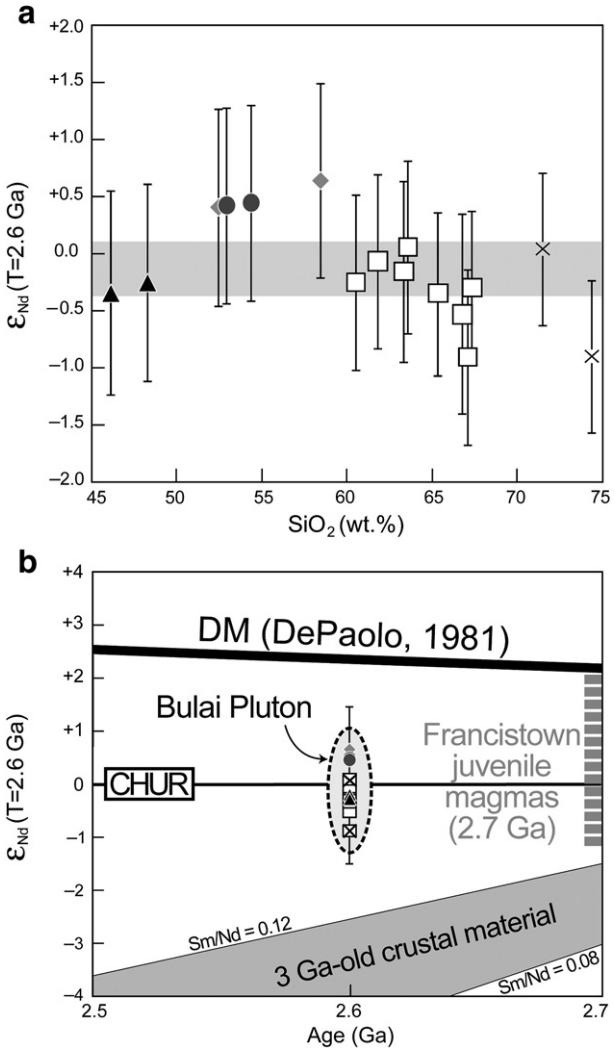


**Fig. 9.** $^{143}Nd/^{144}Nd$ initial isotopic compositions of the Bulai rocks. (a) $\varepsilon_{Nd(T=2.6\ Ga)}$ vs. $SiO_2$ diagram showing the "juvenile" character ($-1.5 < \varepsilon_{Nd} < +1.5$) of all the rocks from the Bulai suite, regardless of their silica content. The error bars are 2σ uncertainty and the grey field represents the weighted average of all analyses. (b) Plot of $\varepsilon_{Nd}$ vs. age. The isotopic signature of the Bulai samples is similar to the one of the Francistown juvenile TTGs and sanukitoids (Zhai et al., 2006), and far from the one of a virtual "pristine" crustal component extracted from the DM at 3 Ga (light grey field). Symbols are as in Fig. 6.

calculation $C_{mm} = a.C_{melt} + (1-a).C_m$ where $a$ is the percentage of felsic melt added to the mantle, $C_m$ the composition of the depleted mantle and $C_{melt}$ the composition of the felsic melt. (3) Batch melting (~5%) of the metasomatized mantle gives rise to Bulai magmas. Step 3 calculations are made using a Monte-Carlo-type numerical simulation. Input data are randomly chosen among ±20%, ±25% and ±50% intervals for degree of melting, partition coefficients (based on values from Adam and Green, 2006) and initial contents ($C_{mm}$), respectively. We consider a large uncertainty for $C_{mm}$ because it is directly influenced by that of sediment-derived melts, which variability is poorly constrained given the wide range of published partition coefficients for melting of subducted sediments as well as uncertainties about melting rates. Calculations were repeated $N = 10^5$ times in order to statistically span the whole range of possibility. Results are synthetized in multi-element diagrams (Fig. 14).

Results show that the final enrichment in incompatible trace elements is closely related to the $F_M/a$ ratio, as already noticed for sanukitoids (Martin et al., 2009). The best fit is found for low values of $F_M/a$ (0.1–0.15), and the model that yields the best match between calculated and observed compositions (Fig. 14a) is obtained for $F_M = 5 \pm 1\%$ and $a = 0.4$ ($F_M/a$ ~0.125). According to Martin et al. (2009), low $F_M/a$ results in lowering MgO and increasing FeO and $TiO_2$ contents in the final melt, thus decreasing Mg#, which is consistent with the Fe- and Ti-richness of the mafic magmas of Bulai pluton, as well as with their moderate Mg# (38–51).

High degrees of metasomatism ($a$) might appear unrealistic, but when applied to natural systems, the high computed melt:rock ratio (~0.67) could represent propagation of subducted-sediment-derived

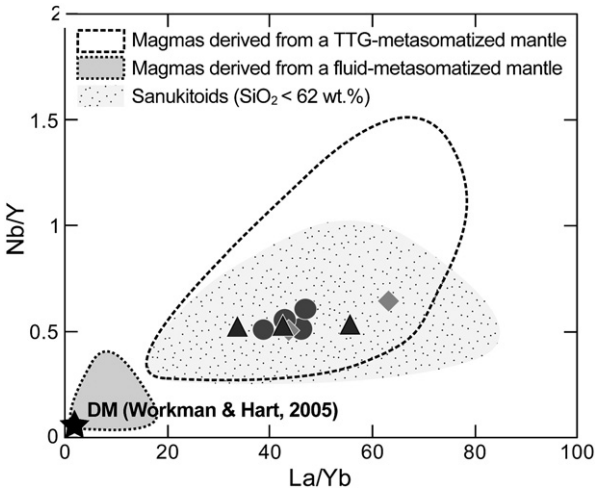


**Fig. 10.** Nb/Y vs. La/Yb diagram, discriminating magmas generated by melting of a mantle metasomatized by fluids (grey field) or by felsic melts (dashed field). Fields are from Martin et al. (2009). The Bulai mafic samples have high Nb/Y and La/Yb ratios, similar to those of mafic sanukitoids, which is in agreement with melt-induced metasomatism. Symbols are as in Fig. 6.

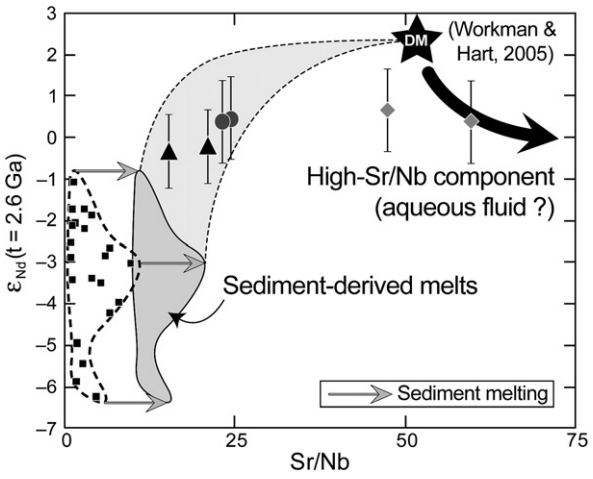


**Fig. 12.** Plot of $\varepsilon_{Nd}$ values (calculated at 2.6 Ga) vs. Sr/Nb. The compositions of sediment-derived melts at 2.6 Ga were calculated using the isotopic and trace element compositions of Archaean pelites from the Kaapvaal craton (black squares; Jahn and Condie, 1995) and Kds from Johnson and Plank (1999). MMEs (triangles) and enderbites (circles) plot within the mixing field (light grey, dashed area) between the resulting compositions and the depleted mantle, whereas "lamprophyres" (diamonds) point towards a high-Sr/Nb component which is probably an aqueous fluid. DM values are from Workman and Hart (2005) for Sr and Nb and De Paolo (1981) for $\varepsilon_{Nd}$.

melts in small conduits, such that interaction with the mantle is extensive at the walls. Alternatively, if the sediment-derived melt was richer in incompatible elements, the degree of metasomatism needed to reach sufficient enrichment of the source would be lower. Similarly, low melting degree of the mantle ($F_M$) is questionable because physical extraction of ~5% melt is difficult. However, the produced liquids must have a low viscosity given their low silica contents (46–53 wt.% for MMEs and enderbites) that would trigger their extraction from the residual peridotite. It is also possible that Bulai MMEs and enderbites could have underwent a small extent of fractional crystallization that contributed to lower transition-element contents, Mg#, and to enrich the residual liquid in incompatible elements. In this case and for a same source composition, a higher melting rate $F_M$ would account for the trace element concentrations of the "primary" magma.

In addition, without residual phlogopite (up to 10 wt.%), the computed melts do not reproduce the relative depletion of LILE (Rb, Ba, and K) with respect to LREE observed in the Bulai mafics (Fig. 14b). Several experiments demonstrated that interactions between a silicic hydrous melt and a mantle peridotite consume olivine and melt and produce a metasomatic, orthopyroxene-, pargasite- and phlogopite-bearing assemblage (Prouteau et al., 2001; Rapp et al., 1999, 2003, 2010; Sen and Dunn, 1994). Comparison of trace-element partition coefficients between pargasite and phlogopite (values from Adam and Green, 2006) reveals that REE, HFSE and Sr concentrate in pargasite ($Kd_i^{parg/phl} > 2$) during crystallization of both phases, whereas LILE are the only elements to be preferentially partitioned into phlogopite ($Kd_i^{parg/phl} < 0.1$). In addition, pargasitic amphibole is the first phase to melt in a metasomatic assemblage, at 980–1000 °C (Schmidt and Poli, 1998). Therefore, a liquid produced by low degrees of melting of an amphibole- and phlogopite-bearing peridotite/pyroxenite will be enriched in LREE relative to LILE because amphibole is the main melt-producing phase (Rogers and Saunders, 1989), which is fully consistent with our geochemical modelling. Interestingly, incongruent melting of amphibole produces clinopyroxene, garnet and melt (Dalpé and Baker, 2000; Francis and Ludden, 1995). In such a case, garnet can remain stable over degrees of melting sufficiently wide to generate the fractionated REE patterns observed in Bulai, that do not appear when garnet lacks into the residue (Fig. 14b).

Nevertheless, it must be kept in mind that the LILE are much more "mobile" than the LREE, such as the misfit between calculated and observed composition without residual phlogopite might also be the result of partitioning between LILE and LREE during granulite-facies

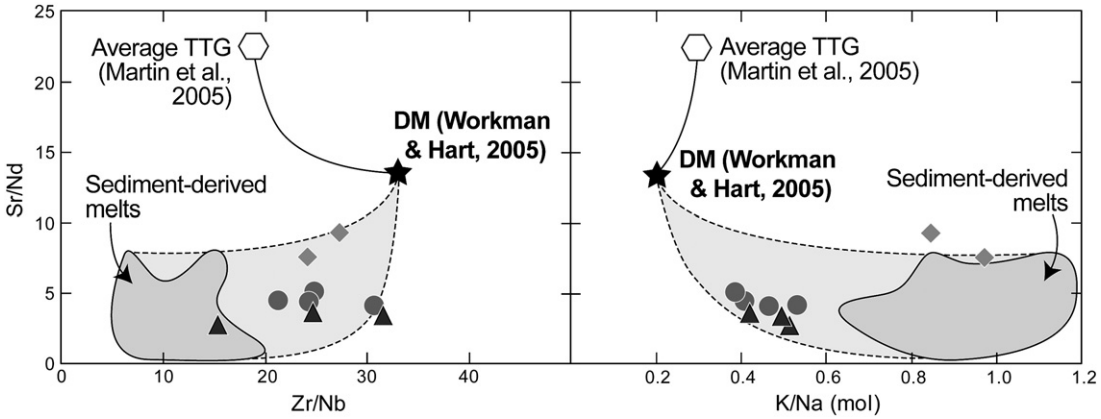


**Fig. 11.** Plots of Sr/Nd vs. K/Na (molar) and Zr/Nb. MMEs and enderbites plot within the compositional range of mixtures between depleted mantle (DM) and sediment-derived melts (light grey, dashed area). However, the petrogenesis of "lamprophyres" needs a component with higher Sr/Nd, such as an aqueous fluid. The compositional range of sediment-derived melts was calculated using batch melting of SATS (references in text), for degrees of melting ranging from 0.1 to 0.3, with partition coefficients from Johnson and Plank (1999). Symbols are as in Fig. 6.

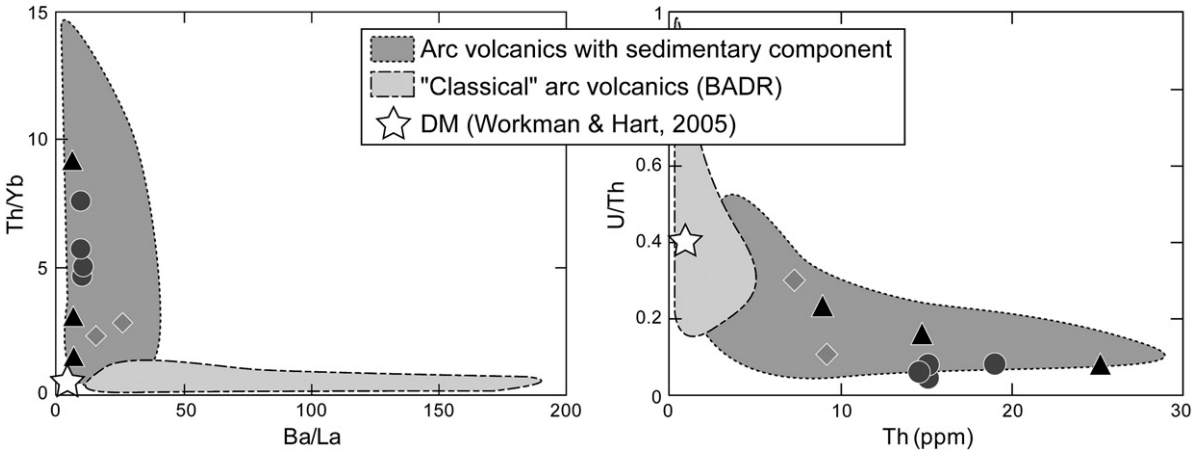


**Fig. 13.** Discrimination plots for modern arc volcanics between "classical" series (derived from a fluid-metasomatized mantle source; light grey field) and magmas with a sediment-derived magmatic component in their source (dark grey field). The mafic samples from Bulai belong to the latter group. Fields are from Woodhead et al. (2001) for Th/Yb vs. Ba/La and Hawkesworth et al. (1997) for U/Th vs. Th. Symbols are as in Fig. 6.

metamorphism. Indeed, Rb, Ba and K might have been at least partially re-equilibrated during the Palaeoproterozoic overprint whereas the LREE behaved as "refractory" elements (see Section 4.1). As a consequence, we consider that the relative depletion of LILE relative to LREE in the Bulai mafics is related either to source or to post-magmatic processes, both mechanisms being not mutually exclusive.

In conclusion, the petrogenetic model that best reproduces the trace element composition of the Bulai mafic magmas consists in a three-stage scenario: (1) Subducted terrigeneous sediments partially melt, producing a hydrous, silica-rich magma. (2) This felsic magma ascents through the mantle wedge and reacts with the peridotite inducing the crystallization of phlogopite, pargasitic amphibole, and probably orthopyroxene. (3) Low-degree melting of this metasomatized mantle gives rise to Bulai mafic magmas.

Given the relatively high $\varepsilon_{Nd}$ of Bulai magmas compared with sediments, the time range between mantle metasomatism and mantle melting was necessary short, such that the Nd isotopic signature of sediment melts imprinted to the mantle did not evolve towards "crustal" values. Consequently, the Bulai magmas were probably generated during a unique geodynamic event (enrichment of the mantle during subduction, immediately followed by melting of the hybrid peridotite).

**Table 3**
Trace-element composition of the sedimentary source used for geochemical modelling and compositional range of the SATS database.

| | Source (ppm) | SATS (ppm) |
|---|---|---|
| Rb | 72 | 10–240 |
| Ba | 1000 | 99–1450 |
| Th | 6 | 2–24 |
| K | 20,000 | 1400–64590 |
| Nb | 7 | 0.5–23 |
| La | 40 | 6–88 |
| Ce | 96 | 11–210 |
| Sr | 67 | 3–166 |
| Nd | 50 | 5–83 |
| Sm | 10 | 1–14 |
| Zr | 210 | 44–388 |
| Eu | 2.5 | 0.4–3.1 |
| Gd | 10.5 | 2–13 |
| Ti | 6200 | 1440–14500 |
| Dy | 10[a] | |
| Y | 54 | 14–69 |
| Er | 5.7[a] | |
| Yb | 5 | 1.3–6.5 |

[a] Values for Dy and Er were determined by linear interpolation with adjacent REE in chondrite-normalized patterns.

## 6. Geodynamic implications

### 6.1. Regional considerations

The petrogenetic model developed for the Bulai pluton is in good agreement with previous geodynamic models that proposed the existence of a Neoarchaean continental active margin to account for the juvenile magmatism of the Central and the Northern Marginal Zones of the Limpopo Belt (Berger and Rollinson, 1997; Berger et al., 1995; Watkeys and Armstrong, 1985; Zeh et al., 2007). The absence of any Neoarchaean juvenile TTG in the Central Zone led Zeh et al. (2007) to the conclusion that the slab did not melt but dehydrated. The resulting fluid-enriched mantle would be the source of the lamprophyres that cross-cut the Bulai pluton (Watkeys and Armstrong, 1985). Our results failed in demonstrating significant melting of subducted metabasalts, but evidenced a fluid component in the source of the "lamprophyre" mafic dykes (see Section 5.3). However, we also show that the MMEs and enderbites from Bulai derive from a mantle source previously enriched by a sediment-derived melt, thus implying that at least the sedimentary component of the slab underwent significant melting.

### 6.2. Comparison of the Bulai pluton with TTGs and sanukitoids

The Bulai pluton shares unequivocal characteristics with high-Ti sanukitoids (i.e., high $K_2O$, $TiO_2$, $FeO_T$, LREE and HFSE contents). At the same time, it also presents distinct features such as relative depletion of LILE and Sr relative to LREE. Furthermore, sanukitoids are supposed to derive from a mantle enriched by TTG-like melts (Heilimo et al., 2010; Martin et al., 2005, 2009; Shirey and Hanson, 1984; Smithies and Champion, 1999, 2000; Stern, 1989), whereas the genesis of Bulai rather implies melting of subducted terrigenous sediments. Consequently, the Bulai pluton obviously belongs to the sanukitoid group (in terms of petrogenetic processes) but differs by the unusual involvement of a sedimentary component in its source.

During Archaean times, melting of the subducted oceanic crust (= hydrated metabasalts) at relatively shallow depth generated important volumes of TTGs, which formed most of the volume of the archaic juvenile continental crust. The production rate of TTG magmas progressively decreased in the course of Archaean times, as witnessed by their secular compositional variations (Martin and Moyen, 2002; Smithies, 2000; Smithies and Champion, 2000). This

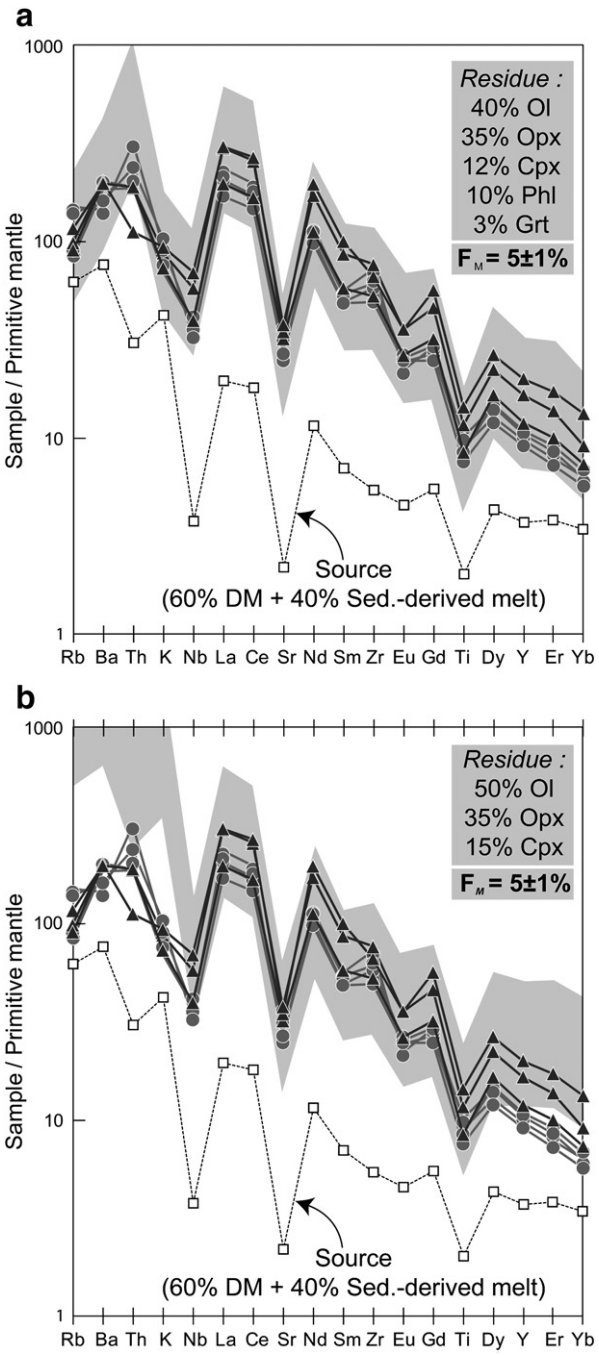


**Fig. 14.** Results of the geochemical Monte-Carlo modelling reported as primitive mantle-normalized trace elements patterns. The bulk source composition (60% DM + 40% liquid derived from 20% melting of sediment) is represented (dashed pattern) together with the composition of the MMEs (triangles) and enderbites (circles). The calculated melt compositions are represented by the light grey field. (a) Calculated melt compositions for 5 ± 1% melting of the source, with a residue composed by 45% olivine + 30% opx + 12% cpx + 10% phlogopite + 3% garnet. The range of possible melt compositions well fits the range of observed trace element patterns of the Bulai mafic magmas. (b) Calculated melt compositions for 5 ± 1% melting of the source, with a simple lherzolitic residue (50% olivine + 35% opx + 15% cpx). The resulting melt compositions do not reproduce the low LILE and HREE compositions of the Bulai mafics. Normalization values are from McDonough and Sun (1995).

evolution results in a progressively more efficient hybridization with the mantle wedge (secular increase of Mg#), and in parallel, a regular decrease of the melt:rock (peridotite) ratio. Finally, this ratio became so low that almost the whole volume of TTG melt was consumed during interaction with mantle, generating the hybrid source of sanukitoids *s.s.* (Shirey and Hanson, 1984; Stern, 1989; Smithies and Champion, 1999, 2000; Rapp et al., 1999; Martin et al., 2005, 2009).

In the case of sanukitoids, the temperature along the slab was high enough to allow metabasalt melting, such that sediments (if present) contributed to only subordinate proportion of felsic melt. In the case of Bulai, the sediment signature appears more prominently because of the lack of melting of metabasalts, which points to lower thermal regimes. Indeed, the wet solidus of terrigeneous sediments is 50–100 °C lower than that of hydrous metabasalts at slab pressures (2.5–4 GPa) (Green, and Hermann, 2001; Johnson and Plank, 1999; and Nichols et al., 1994; Fig. 15). In such a scenario, the temporal link which accounts for the successive relationship between TTG, Sanukitoid and Bulai lithologies is the progressive and global cooling of Earth, as previously proposed by Martin and Moyen (2002) and Martin et al. (2009).

Therefore, the Archaean–Proterozoic boundary represents a "threshold" in the cooling history of the Earth (Fig. 15). It marks the moment when the heat flow was still high enough to induce melting of the subducted oceanic crust, but sufficiently low to generate very small amounts of slab melts that were entirely consumed by hybridation with overlying mantle wedge.

### 6.3. Involvement of terrigeneous sediments

In modern subduction zones, melting of subducted sediments is a quite common feature (e.g. Duggen et al., 2007; Hawkesworth et al., 1997; Tatsumi, 2001; Turner and Foden, 2001). Conversely, there is little if no evidence for subducted sediment melting during Archaean times, although hydrous sediments are a more fertile lithology than metabasalts (e.g. Nichols et al., 1994).

The amount of sediments on the ocean floor depends on the age of the oceanic crust (a very young seafloor can be devoid of any sedimentary cover). Due to higher internal heat production, it is classically considered that Archaean plates moved faster than today (Hargraves, 1986), which leads to the conclusion that the oceanic crust was young when it began to enter in subduction, such that it was unable to carry large volumes of sediments with respect to its modern equivalent.

On the other hand, the thickness of the sedimentary layer above the seafloor is correlated to the volume of sediments produced by erosion of continents, which directly depends on the continental surface. All crustal growth models agree that the latter increased during the Archaean, so it can be proposed that ~2.6 Ga ago, the amount of sediments accumulated onto the ocean floor and being subducted became sufficient for significantly contributing to the genesis of arc magmas. This scenario is consistent with the work of Condie (1989) which demonstrated that Proterozoic lavas derive from a mantle source less depleted in incompatible trace elements than late-Archaean ones (2.5–3.5 Ga) due to recycling of continental sediments into the mantle just after the rapid late-Archaean crustal growth.

In conclusion, the Bulai magmas point to the initiation during the late-Archaean of a change in global mass transfers, with a progressively more important role played by erosion and sedimentation processes and recycling of detrital material into the mantle.

## 7. Summary and conclusions

The late-Archaean Bulai pluton emplaced between 2.58 and 2.61 Ga within the supracrustal sequence of the Beit Bridge Complex and is formed by large volumes of granodioritic magma associated with mafic enclaves (MMEs, enderbites) and dykes together with leucogranitic batches. The Bulai rocks were affected by extensive annealing and open-system behaviour of individual minerals during the Palaeoproterozoic $M_3/D_3$ metamorphic overprint ~2.0 Ga ago.

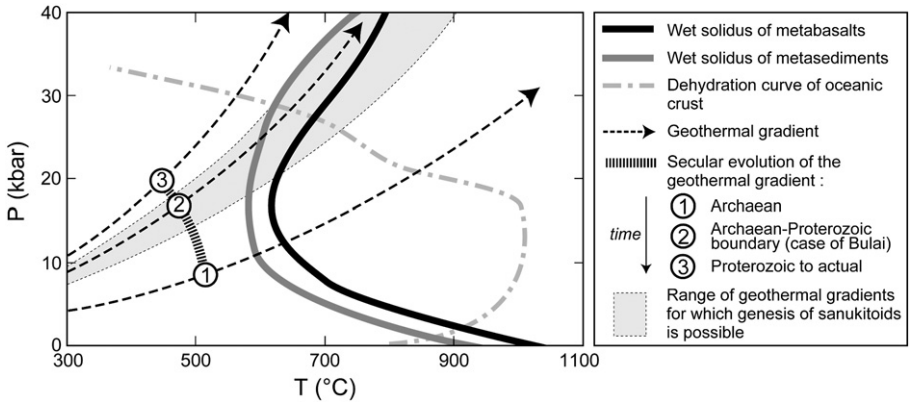


**Fig. 15.** Sketch *P–T* diagram illustrating the secular evolution of the geothermal gradient along the Benioff plane in subduction zones, and related petrogenetic processes (modified after Martin, 1999; Martin et al., 2009). During the Archaean (1), high melting rates of metabasalts produced large volumes of TTG magmas due to the elevated geothermal gradient. At the Archaean–Proterozoic boundary, the geotherm is too low to induce high melting degrees of the metabasalts, such that TTG subsequently interact with the mantle wedge, producing sanukitoids (light grey field). In the case of Bulai (2), the geothermal gradient is too low to induce melting of metabasalts, but metasediments are mobilized as they melt at lower temperatures (wet solidus after Nichols et al., 1994). Since the Proterozoic until now (3), the slab is too cold to melt anymore. As a result, the oceanic crust reaches its dehydration curve before its wet solidus and the mantle wedge is only enriched by aqueous fluids.

However, Nd isotopes demonstrate that chemical and isotopic re-equilibration took place at the grain-size scale, but did not affect the whole-rock samples, which thus preserve the major and trace element compositions of their parental magma.

The geochemical study of the Bulai pluton evidences that the whole suite belongs to the high-K calc-alkaline series and shares unequivocal features with "high-Ti sanukitoids". In particular, all facies are rich in $K_2O$, HFSE, LREE, together with "juvenile" affinities in terms of initial $^{143}Nd/^{144}Nd$ isotopic compositions. However, the Bulai pluton distinguishes by significantly original features such as extreme enrichment in all incompatible trace elements and low LILE/LREE ratios such as Sr/Nd.

Petrogenetic investigations carried out on the most mafic facies of the pluton reveal that a sedimentary component played a significant role during their genesis: a melt deriving from subducted terrigenous material was consumed by metasomatic reactions with mantle peridotite. Geochemical modelling evidences that low-degree melting of the metasomatized mantle produces virtual liquids that match the composition of the Bulai mafics.

These results have several geodynamical implications:

1. Subduction and collision took place 2.7–2.6 Ga ago in the Limpopo area, and the mantle wedge enriched by slab components, typically melts derived from the sedimentary layer, contributed to high-K calc-alkaline magmatism.
2. From a broader perspective, the petrogenetic model developed for Bulai (and sanukitoids in general) is consistent with the global and progressive cooling of Earth: a) During Archaean times, the terrestrial heat production was high enough to allow high melting rates of subducted hydrous metabasalts to produce TTG magmas; b) At the Archaean–Proterozoic boundary, the Earth heat production and the efficiency of slab-melting had both declined, such that slab-melts were almost totally consumed in reaction with mantle peridotite, thus producing Archaean sanukitoids. In addition, lower geothermal gradients favoured sediment rather than basalt melting (e.g. in the case of Bulai); c) After 2.5 Ga, Earth's heat production became too low and subducted slabs do not melt anymore but rather dehydrate, thus producing the fluid-metasomatized mantle source of classical calc-alkaline arc magmas.
3. Sediment involvement in juvenile crustal magma genesis was seldom in Archaean times. The significant role played by sediments in Bulai pluton genesis therefore indicates a change in global mass transfers, with a progressively more important role played by erosion and sedimentation processes and recycling of detrital material into the mantle.

Supplementary materials related to this article can be found online at doi:10.1016/j.lithos.2010.12.009.

## Acknowledgements

This project is funded by a NRF/CNRS Scientific Cooperation program PICS number 4828 and by international CNRS !Khure program co-operated between France and South Africa. We very much appreciated constructive comments from B. Bonin as well as from an anonymous reviewer together with those of the editorial staff, which significantly contributed to improve the original manuscript. We also wish to thank C. Bosq and M. Besairie for support during sample preparation, as well as the Department of Geology of the Stellenbosch University for fieldwork assistance.

## Appendix 1. Analytical techniques

### *1.1. Sample preparation*

1–3 kg samples were reduced in chips in a jaw crusher and then powdered in an agate swing mill. For each sample, a first crushing run was conducted to pre-contaminate the agate mill. The separation of about 20 mg of hornblende, apatite and zircon was carried out on 4 samples (BUL-2, BUL-4, BUL-14 and BUL-20).

### *1.2. Major and trace element analysis*

Major element concentrations were determined by ICP-AES and trace elements by ICP-MS from 20 g of rock powder for each sample, at ACME Laboratories in Vancouver, Canada. Six analyses of the standard SO-18 were realized during the same analytical session than our samples. They are accurate to <1% relative for all elements, and are consistent with the expected values for this standard. Duplicate measurements of two granodiorite samples give an estimate of the total reproducibility of these analyses. The results show that the reproducibility is better than 4% relative for major elements and generally better than 8% for trace elements, except for Tm (8–10%), Zr and Hf (12–17%). Three blanks display measured values typically under detection limits for all major and trace elements. A detailed description of the procedure and additional information about methods and analytical reproducibility can be also found at http://www.acmelab.com.

### 1.3. Sm–Nd analyses

Sm–Nd isotopic analyses were carried on ~100 and ~20 mg for whole-rock powder and separated minerals, respectively. Acid-digestion was performed in Teflon vessel (Savillex®) using a 4:1 $HF:HNO_3$ mixture, except for apatite that was totally dissolved in $HNO_3$. Sm and Nd chemical separation was realized through the "cascade" column protocol (AG50-X4, TRU Spec and Ln Spec columns) following the procedure described in Pin et al. (1994). Total procedure blanks are generally <0.5 ng for Nd.

Sm–Nd concentrations and the $^{147}Sm/^{144}Nd$ ratio were determined by isotopic dilution, using a $^{150}Nd$–$^{149}Sm$ spike. All isotope measurements were performed at the Laboratoire Magmas et Volcans in Clermont-Ferrand, France. Nd isotopes were measured using a Thermo-Finnigan Triton thermal ionization mass spectrometer (TIMS), loaded onto double W filaments. Sm isotopes were measured using a fully automated VG54E mass spectrometer, loaded onto simple Ta filaments. Nd isotope ratios were mass-fractionation-corrected to $^{146}Nd/^{144}Nd = 0.7219$ using an exponential law, and normalized to $^{143}Nd/^{144}Nd = 0.5121$ for the JNDi-1 standard. Repeated analyses of the standard during the course of the study gave $^{143}Nd/^{144}Nd = 0.512097 \pm 5$ ($2\sigma$, $n = 12$). All sample duplicates reproduced within these estimates of reproducibility (see Table 2). In addition, $^{143}Nd/^{144}Nd$ isochrons were built using the Isoplot v.3.70 software of Ludwig (2008).

### 1.4. U–Pb dating

U–Pb dating on separated zircons was realized at the Laboratoire Magmas et Volcans in Clermont-Ferrand, France. After setting between 17 and 23 grains by sample in an epoxy mount, cathodoluminescence (CL) images were obtained prior to analysis, using a Jeol JSM-5910 LV scanning electron microscope (SEM) in order to characterize internal structures of individual grains and choose potential targets for *in situ* analyses. Laser ablation ICP-MS zircon U–Pb analyses were conducted on an Agilent 7500cs ICP-MS equipped with a 193-nm Resonetics M-50E laser system. The synthetic silicate glass NIST 610 was used to calibrate the performances of the ICP-MS, in particular to maximize the signal of $^{238}U$ and minimize the oxide rate (<1%). Natural zircon standards 91500 and JG1 were used for analysis, 2 analyses of the standard 91500 being realized each 9 sample runs and 2 analyses of JG1 being made at the beginning and the end of each analytical session. The analyses were performed with a spot size of 20 to 26 μm, and a frequency of 4 to 5 Hz. Information about data acquisition is provided in Tiepolo (2003). Raw signals in $^{238}U$, $^{235}U$, $^{207}Pb$ and $^{206}Pb$ were treated with the GLITTER program (van Achterbergh et al., 2001) to calculate $^{206}Pb/^{238}U$, $^{207}Pb/^{235}U$ and $^{207}Pb/^{206}Pb$ ratios. Measured ratios in standard zircon 91500 in the course of the analytical session were used to calculate correction factors. Calculation of $^{207}Pb/^{206}Pb$ ages and building Concordia plots were realized using the Isoplot v.3.70 software of Ludwig (2008).

## References


Adam, J., Green, T.H., 2006. Trace element partitioning between mica- and amphibole-bearing garnet lherzolite and hydrous basanitic melt: 1. Experimental results and the investigation of controls on partitioning behavior. Contributions to Mineralogy and Petrology 152 (1), 1–17.

Arculus, R.J., 1994. Aspects of magma genesis in arcs. Lithos 33, 189–208.

Audétat, A., Keppler, H., 2005. Solubility of rutile in subduction zone fluids, as determined by experiments in the hydrothermal diamond anvil cell. Earth and Planetary Science Letters 232, 393–402.

Bahnemann, K.P., 1973. The origin of the Singelele Granite Gneiss, near Messina, northern Transvaal. Special Publication of the Geological Society of South Africa 3, 235–244.

Barker, F., Arth, J.G., 1976. Generation of trondhjemitic-tonalitic liquids and Archaean bimodal trondhjémite-basalt suites. Geology 4 (10), 596–600.

Barton, J.M., 1996. The Messina layered intrusion, Limpopo Belt, South Africa: an example of in-situ contamination of an Archean anorthosite complex by continental crust. Precambrian Research 78, 139–150.

Barton, J.M., Sergeev, S., 1997. High precision, U-Pb analyses of single grains of zircon from quartzite in the Beitbridge Group yield a discordia. South African Journal of Geology 100, 37–42.

Barton, J.M., Van Reenen, D.D., 1992. When was the Limpopo orogeny? Precambrian Research 55, 7–16.

Barton, J.M., Fripp, R.E.P., Horrocks, P., McLean, N., 1979. The geology, age and tectonic setting of the Messina Layered Intrusion, Limpopo Mobile Belt, Southern Africa. American Journal of Science 279, 1108–1134.

Barton, J.M., Holzer, L., Kamber, B., Doig, R., Kramers, J.D., Nyfeler, D., 1994. Discrete metamorphic events in the Limpopo Belt, southern Africa: implications for the application of P-T paths in complex metamorphic terrains. Geology 22, 1035–1038.

Berger, M., Rollinson, H., 1997. Isotopic and geochemical evidence for crust-mantle interaction during late Archaean crustal growth. Geochimica et Cosmochimica Acta 61 (22), 4809–4829.

Berger, M., Kramers, J.D., Nägler, T.F., 1995. An Archaean high grade province adjacent to a granite greenstone terrain: geochemistry and geochronology of charnoenderbites in the Northern Marginal Zone of the Limpopo Belt, Southern Africa and genetic models. Schweizerische Mineralogische und Petrographische Mitteilungen 75, 17–42.

Boshoff, R., Van Reenen, D.D., Smit, C.A., Perchuk, L.L., Kramers, J.D., Armstrong, R., 2006. Geologic history of the Central Zone of the Limpopo Complex: the West Alldays Area. Journal of Geology 114, 699–716.

Brenan, J.M., Shaw, H.F., Ryerson, F.J., Phinney, D.L., 1994. Rutile-aqueous fluid partitioning of Nb, Ta, Hf, Zr, U and Th: implications for high field strength element depletions in island-arc basalts. Earth and Planetary Science Letters 128, 327–339.

Brenan, J.M., Shaw, H.F., Ryerson, F.J., Phinney, D.L., 1995. Mineral-aqueous fluid partitioning of trace elements at 900 °C and 2.0 GPa: constraints on the trace element chemistry of mantle and deep crustal fluids. Geochimica et Cosmochimica Acta 59, 3331–3350.

Buick, I.S., Williams, I.S., Gibson, R.L., Cartwright, I., Miller, J.A., 2003. Carbon and U-Pb evidence for a Palaeoproterozoic crustal component in the Central Zone of the Limpopo Belt, South Africa. Journal of the Geological Society of London 160 (4), 601–612.

Buick, I.S., Hermann, J., Williams, I.S., Gibson, R.G., Rubatto, D., 2006. A SHRIMP U–Pb and LA-ICP-MS trace element study of the petrogenesis of garnet–cordierite–orthoamphibole gneisses from the Central Zone of the Limpopo belt, South Africa. Lithos 88, 150–172.

Condie, K.C., 1981. Archaean Greenstone Belts. In: Windley, B.F. (Ed.), Developments in Precambrian Geology, vol. 3. 434 pp.

Condie, K.C., 1989. Geochemical changes in basalts and andesites across the Archean-Proterozoic boundary: identification and significance. Lithos 23 (1–2), 1–18.

Dalpé, C., Baker, D.R., 2000. Experimental investigation of large-ion-lithophile-element-, high-field-strength-element- and rare-earth-element-partitioning between calcic amphibole and basaltic melt: the effects of pressure and oxygen fugacity. Contributions to Mineralogy and Petrology 140, 233–250.

De Paolo, D.J., 1981. A neodymium and strontium isotopic study of the Mesozoic calc-alkaline granitic batholiths of the Sierra Nevada and peninsular ranges, California. Journal of Geophysical Research 86 (B11), 10470–10488.

Defant, M.J., Drummond, M.S., 1990. A model for trondhjemite-tonalite-dacite genesis and crustal growth via slab melting: Archaean to modern comparisons. Journal of Geophysical Research 95 (B-13), 21503–21521.

Defant, M.J., Jackson, T.E., Drummond, M.S., De Boer, J.Z., Bellon, H., Feigenson, M.D., Maury, R.C., Stewart, R.H., 1992. The geochemistry of young volcanism throughout western Panama and southeastern Costa Rica: an overview. Journal of the Geological Society of London 149 (4), 569–579.

Duggen, S., Portnyagin, M., Baker, J., Ulfbeck, D., Hoernle, K., Garbe-Schönberg, D., Grassineau, N., 2007. Drastic shift in lava geochemistry in the volcanic-front to rear-arc region of the Southern Kamchatkan subduction zone: evidence for the transition from slab surface dehydration to sediment melting. Earth and Planetary Science Letters 71, 452–480.

Ellam, R.M., Hawkesworth, C.J., 1988. Is average continental crust generated at subduction zones? Geology 16, 314–317.

Fedo, C.M., Eriksson, K.A., Krogstad, E.J., 1996. Geochemistry of shales from the Archean (3.0 Ga) Bushwa Greenstone Belt, Zimbabwe: implications for provenance and source-area weathering. Geochimica et Cosmochimica Acta 60 (10), 1751–1763.

Francis, D., Ludden, J., 1995. The signature of amphibole in mafic alkaline lavas, a study in the Northern Canadian Cordillera. Journal of Petrology 36, 1171–1191.

Halla, J., 2005. Late Archean high-Mg granitoids (sanukitoids) in the southern Karelian domain, eastern Finland: Pb and Nd isotopic constraints on crust-mantle interactions. Lithos 79 (1–2), 161–178.

Hargraves, R.B., 1986. Faster spreading or greater ridge length in the Archean? Geology 14 (9), 750–752.

Hawkesworth, C.J., Turner, S.P., McDermott, F., Peate, D.W., Van Calsteren, P., 1997. U–Th isotopes in arc magmas: implications for element transfer from the subducted crust. Science 276, 551–555.

Heilimo, E., Halla, J., Hölttä, P., 2010. Discrimination and origin of the sanukitoid series: geochemical constraints from the Neoarchean western Karelian Province (Finland). Lithos 115, 27–39.

Hermann, J., Green, D.H., 2001. Experimental constraints on high pressure melting in subducted crust. Earth and Planetary Science Letters 188, 149–168.

Hermann, J., Rubatto, D., 2009. Accessory phase control on the trace element signature of sediment melts in subduction zones. Chemical Geology 265, 512–526.

Hofmann, A.W., Kröner, A., Brandl, G., 1998. Field relationships of mid- to late-Archean high-grade gneisses of igneous and sedimentary parentage in the Sand River, Central Zone of the Limpopo Belt, South Africa. South African Journal of Geology 101, 185–200.

Holzer L., 1995. The magmatic petrology of the Bulai Pluton and the tectonometamorphic overprint at 2.0 Ga. in the Central Zone of the Limpopo Belt (Messina-Beitbridge area, Southern Africa). Unpublished MSc. Thesis, Université de Berne.
Holzer, L., Frei, R., Barton, J.M., Kramers, J.D., 1998. Unraveling the record of successive high-grade events in the Central Zone of the Limpopo Belt using Pb single phase dating of metamorphic minerals. Precambrian Research 87, 87–115.
Jacobsen, S.B., Wasserburg, G.J., 1984. Sm-Nd isotopic evolution of chondrites and achondrites, II. Earth and Planetary Science Letters 67 (2), 137–150.
Jaeckel, P., Kröner, A., Kamo, S.L., Brandl, G., Wendt, J.I., 1997. Late Archean to early Proterozoic granitoid magmatism and high-grade metamorphism in the central Limpopo Belt, South Africa. Journal of the Geological Society of London 154, 25–44.
Jahn, B., Condie, K.C., 1995. Evolution of the Kaapvaal Craton as viewed from geochemical and Sm-Nd isotopic analyses of intracratonic pelites. Geochimica et Cosmochimica Acta 59 (11), 2239–2258.
Johnson, M.C., Plank, T., 1999. Dehydration and melting experiments constrain the fate of subducted sediments. Geochemistry, Geophysics, Geosystems 1, 1007. doi:10.1029/1999GC000014.
Kamber, B.S., Ewart, A., Collerson, K.D., Bruce, M.C., McDonald, G.D., 2002. Fluid-mobile trace element constraints on the role of slab melting and implications for Archaean crustal growth models. Contributions to Mineralogy and Petrology 144, 38–56.
Kreissig, K., Nagler, T.F., Kramers, J.D., Van Reenen, D.D., Smit, C.A., 2000. An isotopic and geochemical study of the Kaapvaal Craton and the Southern Marginal Zone of the Limpopo Belt: are they juxtaposed terranes? Lithos 50, 1–25.
Kröner, A., Jaeckel, P., Hofmann, A.W., Nemchin, A.A., Brandl, G., 1998. Field relationships and age of supracrustal Beit Bridge Complex and associated granitoid gneisses in the Central Zone of the Limpopo Belt, South Africa. South African Journal of Geology 101, 201–213.
Kröner, A., Jaeckel, P., Brandl, G., Nemchin, A.A., Pidgeon, R.T., 1999. Single zircon ages for granitoid gneisses in the Central Zone of the Limpopo Belt, Southern Africa and geodynamic significance. Precambrian Research 93, 299–337.
Le Maître, R.W., 1989. A Classification of Igneous Rocks and Glossary of Terms, Recommandations of the International Union of Geological Sciences, Subcommission on the systematics of Igneous Rocks1st edition. Blackwell, Oxford. 193 pp.
Ludwig, K., 2008. Isoplot 3.70, A Geochronological Toolkit for Microsoft Excel. Berkeley Geochronology Central Special Publication No. 4. 76 pp.
Martin, H., 1986. Effect of steeper Archaean geothermal gradient on geochemistry of subduction-zone magmas. Geology 14, 753–756.
Martin, H., 1987. Petrogenesis of Archaean trondhjemites, tonalites and granodiorites from Eastern Finland: major and trace element geochemistry. Journal of Petrology 28, 921–953.
Martin, H., 1993. The mechanisms of petrogenesis of the Archaean continental crust, comparison with modern processes. Lithos 30, 373–388.
Martin, H., 1994. The Archaean grey gneisses and the genesis of continental crust. In: Condie, K.C. (Ed.), Archaean crustal evolution: Developments in Precambrian Geology, vol. 11, pp. 205–260.
Martin, H., 1999. Adakite magmas: modern analogs of Archaean granitoids. Lithos 46, 411–429.
Martin, H., Moyen, J.F., 2002. Secular changes in TTG composition as markers of the progressive cooling of the Earth. Geology 30 (4), 319–322.
Martin, H., Smithies, R., Rapp, R.P., Moyen, J.F., Champion, D., 2005. An overview of adakite, TTG, and sanukitoid: relationships and some implications for crustal evolution. Lithos 79 (1–2), 1–24.
Martin, H., Moyen, J.F., Rapp, R.P., 2009. The sanukitoid series: magmatism at the Archaean–Proterozoic transition. Earth and Environmental Science Transactions of the Royal Society of Edinburgh 100 (1–2), 15–33.
McCulloch, M.T., Gamble, J.A., 1991. Geochemical and geodynamical contraints on subduction zone magmatism. Earth and Planetary Science Letters 102, 358–374.
McDonough, W.F., Sun, S.S., 1995. The composition of the Earth. Chemical Geology 120 (3–4), 223–253.
Millonig, L., Zeh, A., Gerdes, A., Klemd, R., 2008. Neoarchaean high-grade metamorphism in the Central Zone of the Limpopo Belt (South Africa): combined petrological and geochronological evidence from the Bulai pluton. Lithos 103 (3–4), 333–351.
Moyen, J.F., Martin, H., Jayananda, M., 1997. Origine du granite fini-Archéen de Closepet (Inde du Sud): apports de la modélisation géochimique du comportement des éléments en traces. Comptes-Rendus de l'Académie des Sciences de Paris 325, 659–664.
Nichols, G.T., Wyllie, P.J., Stern, C.R., 1994. Subduction zone melting of pelagic sediments constrained by melting experiments. Nature 371, 785–788.
O'Connor, J.T., 1965. A Classification for Quartz-rich Igneous Rocks Based on Feldspar Ratios. US Geological Survey professional paper 525-B, pp. 79–84.
Pin, C., Briot, D., Bassin, C., Poitrasson, F., 1994. Concomitant separation of strontium and samarium-neodymium for isotopic analysis in silicate samples, based on specific extraction chromatography. Anlytica Chimica Acta 298 (2), 209–217.
Plank, T., Langmuir, C.H., 1998. The chemical composition of subducted sediments and its consequence for the crust and mantle. Chemical Geology 145, 325–394.
Prouteau, G., Scaillet, B., Pichavant, M., Maury, R., 2001. Evidence for mantle metasomatism by hydrous silicic melts derived from subducted oceanic crust. Nature 410, 197–200.
Rapp, R.P., Watson, E.B., Miller, C.F., 1991. Partial melting of amphibolite/eclogite and the origin of Archaean trondhjemites and tonalites. Precambrian Research 51, 1–25.
Rapp, R.P., Shimizu, N., Norman, M.D., Applegate, G.S., 1999. Reaction between slab-derived melts and peridotite in the mantle wedge: experimental constraints at 3.8 GPa. Chemical Geology 160, 335–356.
Rapp, R.P., Shimizu, N., Norman, M.D., 2003. Growth of early continental crust by partial melting of eclogite. Nature 425, 605–609.
Rapp, R.P., Norman, M.D., Laporte, D., Yaxley, G.M., Martin, H., Foley, S.F., 2010. Continent formation in the Archean and chemical evolution of the Cratonic lithosphere: melt–rock reaction experiments at 3–4 GPa and petrogenesis of Archean Mg-Diorites (Sanukitoids). Journal of Petrology 51 (6), 1237–1266.
Reagan, M.K., Gill, J.B., 1989. Coexisting calcalkaline and high-niobium basalts from Turrialba volcano, Costa Rica: implications for residual titanates in arc magma sources. Journal of Geophysical Research 94, 4619–4633.
Retief, E.A., Compston, W., Armstrong, R.A., Williams, I.S., 1990. Characteristics and preliminary U–Pb ages of zircons from Limpopo Belt lithologies. Abstract volume, Limpopo Workshop, Rand Afrikaans University, Johannesburg, South Africa, pp. 95–99.
Roering, C., Van Reenen, D.D., Smit, C.A., Barton, J.M., De Beer, J.H., De Wit, M.J., Stettler, E.H., Van Schalkwyk, J.F., Stevens, G., Pretorius, S., 1992. Tectonic model for the evolution of the Limpopo Belt. Precambrian Research 55, 539–552.
Rogers, G., Saunders, A.D., 1989. Magnesian Andesites from Mexico, Chile and the Aleutian Islands: Implications for Magmatism Associated with Ridge–Trench Collisions. In: Crawford, A.J. (Ed.), Boninites and Related Rocks. Unwin Hyman, London, pp. 416–445.
Sajona, F.G., Maury, R.C., Bellon, H., Cotten, J., Defant, M., 1996. High field strength element enrichment of Pliocene–Pleistocene island arc basalts, Zamboanga Peninsula, Western Mindanao (Philippines). Journal of Petrology 37 (3), 693–726.
Schmidt, M.W., Poli, S., 1998. Experimentally based water budgets for dehydrating slabs and consequences for arc magma generation. Earth and Planetary Science Letters 163 (1–4), 361–379.
Sen, C., Dunn, T., 1994. Experimental modal metasomatism of a spinel lherzolite and the production of amphibole-bearing peridotite. Contributions to Mineralogy and Petrology 119, 422–432.
Shaw, D.M., 1970. Trace element fractionation during anatexis. Geochimica et Cosmochimica Acta 34, 237–243.
Shirey, S.B., Hanson, G.N., 1984. Mantle-derived Archaean monzodiorites and trachyandesites. Nature 310, 222–224.
Smithies, R.H., 2000. The Archaean tonalite–trondhjemite–granodiorite (TTG) series is not an analogue of Cenozoic adakite. Earth and Planetary Science Letters 182, 115–125.
Smithies, R.H., Champion, D.C., 1999. High-Mg diorite from the Archaean Pilbara Craton; anorogenic magmas derived from a subduction-modified mantle. Geological Survey of Western Australia, Annual Review, pp. 45–59.
Smithies, R.H., Champion, D.C., 2000. The Archaean high-Mg diorite suite: links to Tonalite–Trondhjemite–Granodiorite magmatism and implications for early Archaean crustal growth. Journal of Petrology 41 (12), 1653–1671.
Stern R.A., 1989. Petrogenesis of Archaean sanukitoid suite. PhD thesis, State University of New York at Stony Brook, 275 pp.
Stern, R.A., Hanson, G.N., 1991. Archaean High-Mg granodiorites: a derivative of light rare earth enriched monzodiorites of mantle origin. Journal of Petrology 32, 201–238.
Stevenson, R., Henry, P., Gariépy, C., 1999. Assimilation-fractional crystallization origin of Archaean sanukitoid suites: Western Superior Province, Canada. Precambrian Research 96, 83–99.
Tatsumi, Y., 1989. Migration of fluid phases and genesis of basalt magmas in subduction zones. Journal of Geophysical Research 94, 4697–4707.
Tatsumi, Y., 2001. Geochemical modeling of partial melting of subducting sediments and subsequent melt-mantle interaction: Generation of high-Mg andesites in the Setouchi volcanic belt, southwest Japan. Geology 29 (4), 323–326.
Tatsumi, Y., Hamilton, D.L., Nesbitt, R.W., 1986. Chemical characteristics of fluid phase released from a subducted lithosphere and origin of arc magmas: evidence from high-pressure experiments and natural rocks. Journal of Volcanology and Geothermal Research 29, 293–309.
Tiepolo, M., 2003. In situ Pb geochronology of zircon with laser ablation–inductively coupled plasma–sector field mass spectrometry. Chemical Geology 199 (1–2), 159–177.
Tropper, P., Manning, C.E., 2005. Very low solubility of rutile in $H_2O$ at high pressure and temperature, and its implications for Ti mobility insubduction zones. American Mineralogist 90, 502–505.
Tsunogae, T., Yurimoto, H., 1995. Single zircon U–Pb geochronology of the Limpopo Belt by secondary ion mass spectrometry. Geochemical Journal 29, 197–205.
Turner, S., Foden, J., 2001. U, Th and Ra disequilibria, Sr, Nd and Pb isotope and trace element variations in Sunda arc lavas: predominance of a subducted sediment component. Contributions to Mineralogy and Petrology 142 (1), 43–57.
Van Achterbergh, E., Ryan, C., Jackson, S., Griffin, W.L., 2001. Appendix 3 Data Reduction Software for LA-ICP-MS in Laser-Ablation-ICPMS in the Earth Sciences. In: Sylvester, P. (Ed.), Mineralogical Association of Canada Short Course, vol. 29, pp. 239–243.
Van Reenen, D.D., Roering, C., Ashwal, L.D., De Wit, M.J., 1992. Regional geological setting of the Limpopo Belt. Precambrian Research 55, 1–5.
Van Reenen, D.D., Perchuk, L.L., Smit, C.A., Varlamov, D.A., Boshoff, R., Huizenga, J.M., Gerya, T.V., 2004. Structural and P–T evolution of a major cross fold in the Central Zone of the Limpopo High Grade Terrane. Journal of Petrology 45, 1413–1439.
Van Reenen, D.D., Boshoff, R., Smit, C.A., Perchuk, L.L., Kramers, J.D., McCourt, S., Armstrong, R.A., 2008. Geochronological problems related to polymétamorphism in the Limpopo Complex, South Africa. Gondwana Research 14, 644–662.
Vroon, P.Z., Van Bergen, M.J., White, W.M., Varekamp, J.C., 1993. Sr-Nd-Pb Isotope systematics of the Banda Arc, Indonesia: combined subduction and assimilation of continental material. Journal of Geophysical Research 98, 22349–22366.
Watkeys M.K., 1984. The Precambrian geology of the Limpopo Belt north and west of Messina. PhD thesis, University of Witwatersrand, Johannesburg, 349 pp.
Watkeys, M.K., Armstrong, R.A., 1985. The importance of being alkaline–deformed late Archean lamprophyric dykes, Central Zone, Limpopo Belt. Transactions Geological Society of South Africa 88, 195–206.

Woodhead, J.D., Hergt, J.M., Davidson, J.P., Eggins, S.M., 2001. Hafnium isotope evidence for 'conservative' element mobility during subduction zone processes. Earth and Planetary Science Letters 192, 331–346.
Workman, R.K., Hart, S.R., 2005. Major and trace element composition of the depleted MORB mantle (DMM). Earth and Planetary Science Letters 231 (1–2), 53–72.
Wronciewicz, D.J., Condie, K.C., 1987. Geochemistry of Archaean shales from the Witwatersrand Supergroup, South Africa: Source-area weathering and provenance. Geochimica et Cosmochimica Acta 51, 2401–2416.
Zeh, A., Klemd, R., Buhlmann, S., Barton, J.M., 2004. Pro-and retrograde P–T evolution of granulites of the Beit Bridge Complex (Limpopo Belt, South Africa); constraints from quantitative phase diagrams and geotectonic implications. Journal of Metamorphic Geology 22, 79–95.
Zeh, A., Gerdes, A., Klemd, R., Barton, J.M., 2007. Archaean to Proterozoic crustal evolution in the Central Zone of the Limpopo Belt (South Africa-Botswana): constraints from combined U–Pb and Lu–Hf isotope analyses of zircon. Journal of Petrology 48, 1605–1639.
Zhai, M., Kampunzu, A.B., Modisi, M.P., Bagai, Z., 2006. Sr and Nd isotope systematics of the Francistown plutonic rocks, Botswana: implications for Neoarchean crustal evolution of the Zimbabwe craton. Geologische Rundschau 95, 355–369.

# Diversity in Earth's early felsic crust: Paleoarchean peraluminous granites of the Barberton Greenstone Belt

Cynthia J.M.G. Sanchez-Garrido[1,3,4,5], Gary Stevens[1], Richard A. Armstrong[2], Jean-François Moyen[4,5,6], Hervé Martin[3,4,5], and Régis Doucelance[3,4,5]

[1]Center for Crustal Petrology, Department of Earth Sciences, University of Stellenbosch, South Africa Private Bag X-1, Matieland 7602, South Africa

[2]Research School of Earth Sciences, Australian National University, Canberra A.C.T. 0200, Australia

[3]Clermont Université, Université Blaise Pascal, Laboratoire Magmas et Volcans, BP 10448, F-63000 Clermont-Ferrand, France

[4]Centre National de la Recherche Scientifique, UMR 6524, LMV Laboratoire Magmas et Volcans, F-63038 Clermont-Ferrand, France

[5]Institut de Recherche pour le Développement, R 163, LMV (Laboratoire Magmas et Volcans), F-63038 Clermont-Ferrand, France

[6]Université Jean-Monnet, Laboratoire Magmas et Volcans, Département de Géologie 23 rue du Docteur Michelon, 42023 Saint Etienne, France

## ABSTRACT

**Earth's oldest preserved granitoid crust dates back to the Paleoarchean and consists predominantly of sodic tonalite-trondhjemite-granodiorite (TTG) granitoids that arose through the partial melting of hydrated metabasalts. In contrast, granites (sensu stricto) typically appear relatively late in the plutonic record of the old cratons. However, the existence of Hadean zircons with mineral inclusion suites that are consistent with crystallization from peraluminous granitic magmas indicates that granitic rocks formed part of the earliest felsic crust; although we have direct evidence, this earliest felsic crust is not preserved. Here we present evidence of an unusual variety of markedly low-CaO, $K_2O$-rich, rutile-bearing, peraluminous granite and rhyolite that was produced concurrently with TTG magmas during three magmatic cycles in the Barberton Greenstone Belt (BGB), southern Africa. This material is not preserved as in situ rock units, but occurs as clasts within a younger conglomerate. Within these rocks, plagioclase feldspar is a rare inclusion in zircon, relative to alkali feldspar, and has low anorthite contents (An < 15%), attesting to the primary nature of the low-Ca signature of the magmas. This, along with Eu/Eu* ~ 1, high $K_2O$ and Sr content, as well as the peraluminous character of the magmas, is a consequence of phengite melting in a metagraywacke source at pressures in excess of those of plagioclase stability. This process contributed to each episode of continental crustal growth through the Paleoarchean to Mesoarchean in the BGB, despite leaving no plutonic record at the typical mid-crustal level of exposure that the TTG plutons around the belt represent.**

## INTRODUCTION

The most common Archean granitoids, the tonalite-trondhjemite-granodiorites (TTGs), acquire their leucocratic, mildly peraluminous and sodic nature, as well as their characteristically low heavy rare earth element (HREE) contents and steep REE patterns, from the high-pressure melting of hydrous metamafic rocks, either in the garnet-amphibolite (Martin, 1986; Foley et al., 2002) or eclogite facies (Rapp et al., 2003). Archean potassic granites, however, are mostly regarded as the result of remelting of this early felsic sodic crust, forming true potassic granites at a late stage of cratonic evolution. This interpretation is largely supported by the geology of Archean terrains, where granitic plutons tend to be late and postdate early sodic gneisses of TTG composition. This is the case in the well-preserved Paleoarchean–Mesoarchean BGB, southern Africa (Fig. 1A), where continental crust grew during three episodes of TTG magmatism, 3538–3509 Ma, 3470–3443 Ma, and 3290–3216 Ma (Kamo and Davis, 1994; Schoene et al., 2008; de Ronde and de Wit, 1994; Kisters et al., 2010) (Fig. 1B), and where the youngest episode coincides with the amalgamation of distinct northwest and southeast terranes within the greenstone belt (e.g., de Wit et al., 1992). Potassic granitoid plutonism in the BGB occurred between 3236 and ca. 3100 Ma and is represented by the Usutu suite (Schoene and Bowring, 2010), the Dalmein pluton (Lana et al., 2010), and the granodiorite-monzogranite-syenogranite (GMS) batholiths (Schoene et al., 2008; de Ronde and de Wit, 1994). Thus it coincides with or follows the ca. 3210 Ma terrane amalgamation (Fig. 1B) (Lowe, 1994; Moyen et al., 2006). One exception to this is granitic (sensu stricto) clasts that are older than most of the TTG plutons associated with the BGB (Kröner and Compston, 1988). They have been documented within the basal conglomerate of the Moodies Group, a coarse clastic sedimentary succession formed between 3225 and 3215 Ma (Lowe, 1999). In this study, we examined more than 110 granitic clasts from 6 exposures of this basal conglomerate within the Eureka syncline (Fig. 1A), in order to understand their petrogenesis and the significance thereof for early continental crust formation.

## RESULTS

The clasts sampled in this study typically display either pristine magmatic textures (Figs. 1C and 1D), ranging from granophyric to porphyric, characterized by quartz and feldspar phenocrysts, or volcaniclastic textures, also with quartz and alkali feldspar as phenocrysts. This demonstrates that the magmas crystallized at shallow depth or erupted at the surface. Most of the clasts have peraluminous granitic compositions (0.97 < A/CNK < 1.83) [A/CNK—molecular Al/(Ca + Na + K)] (Fig. 2D) and display a wide range of $SiO_2$ content (63.13–76.62 wt%). They are rich in $K_2O$ (3.78–9.02 wt%), poor in CaO (0.02–1.37 wt%), and consequently differ substantially from BGB TTGs (Figs. 2A, 2B), which are peraluminous to metaluminous (A/CNK average ~1.00) (Fig. 2D), have low $K_2O$ (average 1.93 wt%), and relatively high CaO (average 2.85 wt%) contents (Table DR1 in the GSA Data Repository[1]). The granitic (sensu stricto) clasts are relatively Sr rich (12–330 ppm) and Rb poor (32–153 ppm); their light REE patterns are fractionated while their HREE ends are relatively flat with a slightly negative Eu anomaly (Fig. 2E).

Zircons from four of the clasts were analyzed for oxygen isotope compositions by sensitive high-resolution ion microprobe (SHRIMP) at the Research School of Earth Sciences of the Australian National University (ANU). The zircon's $\delta^{18}O$ values range from 4.90‰ to 5.91‰ (standard mean ocean water) (Fig. 1H; Table DR2). The zircons contain inclusions of quartz, alkali feldspar, plagioclase, biotite, monazite, apatite, rutile, and ilmenite that are scattered throughout the magmatic oscillatory

[1]GSA Data Repository item 2011282, Tables DR1–DR4 and Figures DR1 and DR2, is available online at www.geosociety.org/pubs/ft2011.htm, or on request from editing@geosociety.org or Documents Secretary, GSA, P.O. Box 9140, Boulder, CO 80301, USA.

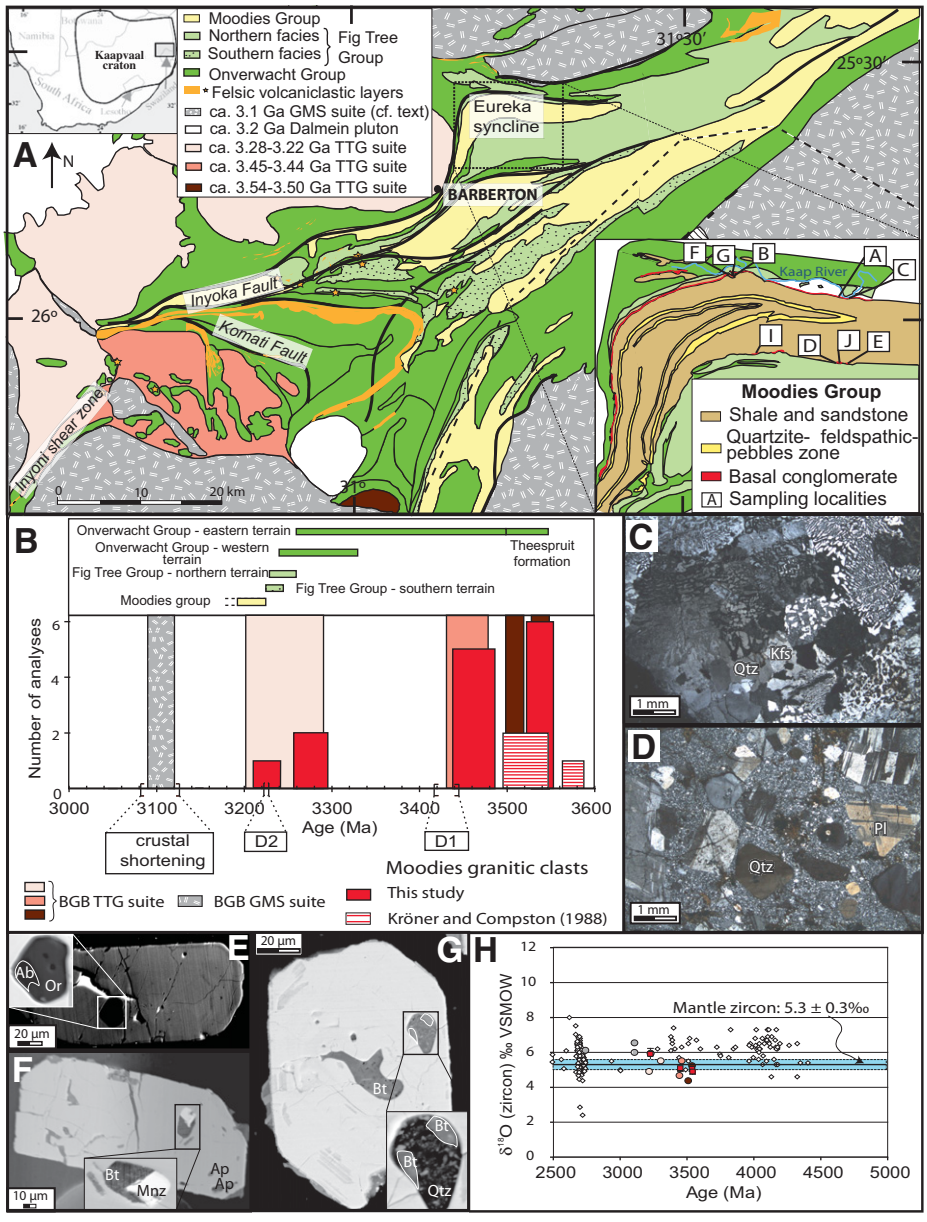


**Figure 1. Summary of key geological information relevant to genesis of granitic clasts in Moodies Group basal conglomerate. A: Simplified geological map highlighting stratigraphy of Barberton Greenstone Belt (BGB), southern Africa, and ages of tonalite-trondhjemite-granodiorite (TTG) and younger granitic rocks. Felsic volcaniclastic layers similar to those from which granite clasts were possibly eroded are highlighted in orange. Average compositions for northern and southern facies of Fig Tree Group are provided in Table DR1 (see footnote 1). Inset is geological map of Eureka syncline with sample locations. B: Histogram representing crystallization age frequency in granitic clasts (this study; Kröner and Compston, 1988) (2σ age uncertainty). Only data from clasts where crystallization age is unambiguous have been included. Major tectonic events affecting BGB are represented along age axis. D1 event has been proposed to record processes within an active oceanic arc margin (de Ronde and de Wit, 1994; de Wit et al., 1992; Lowe, 1999); D2 event represents terrain amalgamation during accretionary orogeny. The 3126–3084 Ma event likely represents transcurrent shearing in an intraplate compressional context (de Ronde and de Wit, 1994) accompanied by substantial mantle heat addition to base of crust and widespread granitic magmatism, represented mostly by granodiorite-monzogranite-syenogranite (GMS) suite. C: Crossed-polarized light (CPL) image of typical mineral texture in representative sample of medium-grained micrographic granite (C33). Rock is characterized by micrographic K-feldspar (Kfs) and quartz (Qtz) intergrowths. These are interpreted to represent quench crystallization products. D: Typical mineral textures (in CPL) from representative rhyolitic clast (B25). This rock is quartz–K-feldspar–plagioclase–phyric rhyolite with rounded quartz phenocrysts, abundant large euhedral K-feldspar phenocrysts, and smaller euhedral plagioclase (Pl) phenocrysts. Matrix consists of fine-grained quartz, K-feldspar, and muscovite interpreted to represent recrystallized glass. E: Cathodoluminescence image of zircon (C30-Zr6) with plagioclase (albite, Ab) ($An_1$-$Ab_{94}$-$Or_5$; An—anorthite; Or—orthoclase) and K-feldspar (Or) inclusions ($Ab_2$-$Or_{98}$) crosscutting magmatic zoning. F: Scanning electron microscope (SEM) image of zircon (B17-Zr6) with monazite (Mnz), biotite (Bt), and apatite (Ap) inclusions. G: SEM image of zircon (C14-Zr4) with polymineralic quartz-biotite-plagioclase inclusions. H: Evolution of $\delta^{18}O$ (‰; VSMOW—Vienna standard mean ocean water) in zircons from Moodies granites as function of time, compared to those from BGB TTGs (King, 2001) and other Archean granitoids (white diamonds). Legend is identical to that in D.**

zoned crystals. (Table DR3; Figs. 1E–1G). The inclusion suite is considered to reflect the assemblage present in the magma during zircon crystallization. Polymineralic quartz-feldspar-mica inclusions are interpreted to represent former melt inclusions.

SHRIMP U/Pb dating of zircons from 22 clasts was undertaken at ANU (Table DR4). No inherited cores were identified in cathodoluminescence images of the zircons (Fig. DR1). The data and ages are plotted on representative concordia diagrams (Fig. DR1); the upper intercept dates are interpreted as crystallization ages. A subset of the ages obtained is consistent with the single-zircon evaporation ages (3570 ± 6 Ma to 3474 ± 35 Ma) of Kröner and Compston (1988). In addition, the ages obtained in this study cluster in three groups that were not identified in previous works: 3519–3554 Ma, 3438–3486 Ma, and 3210–3295 Ma (Fig. 1B). There is no correlation between age group and clast rock type (e.g., crystal tuff, granite, rhyolite); however, these age ranges correlate perfectly with periods of TTG magmatism in the BGB (Fig. 1B).

## DISCUSSION

The key characteristic of these granites is their low CaO content, coupled with their high $Na_2O + K_2O$, which could either be a primary magmatic feature or due to postcrystallization alteration. However, several lines of evidence argue in favor of the preservation of the primary magmatic chemical and mineralogical characteristics in the granites. (1) Alkali feldspar and quartz are significantly more abundant than plagioclase as single mineral inclusions within zircon. This is consistent with zircon crystallization from a low CaO magma, as plagioclase would commonly be the first tectosilicate to crystallize in peraluminous magmas with average CaO contents (e.g., Clemens and Wall, 1981). (2) Where plagioclase inclusions in

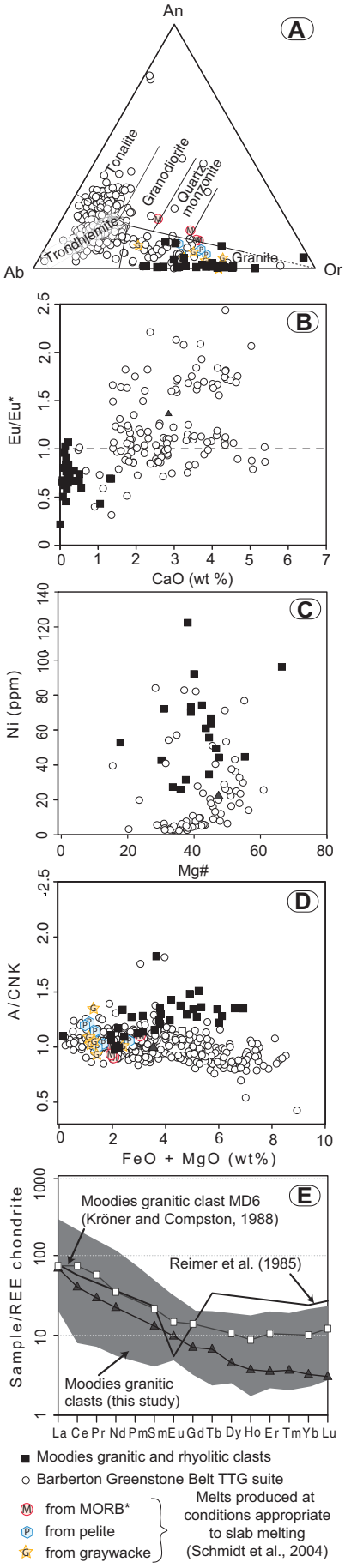


**Figure 2. Summary of pertinent geochemical features of granitic clasts compared to Barberton Greenstone Belt (BGB) tonalite-trondhjemite-granodiorite (TTG). Experimental melt compositions from Schmidt et al. (2004) are also plotted for reference. A: Feldspar ternary diagram showing K-rich and CaO-poor nature of clasts compared to dominant TTG suite. B: Eu/Eu* versus CaO (excluding three outliers included in Table DR1; see footnote 1). C: Ni versus Mg# plot highlighting high Ni content of clasts relative to TTG. D: Maficity versus A/CNK [molecular Al/(Ca + Na + K)] plot (excluding two outliers) demonstrating that clasts are peraluminous and that A/CNK is positively correlated with maficity. E: Rare earth element (REE) plot showing that average of BGB TTG (gray triangle) is more depleted in heavy REEs than are the granites of the Moodies Group (gray field). Strong Eu anomaly found in study by Reimer et al. (1985) has proved impossible to duplicate in this study or in study by Kröner and Compston (1988) (as shown by MD6 sample). MORB—mid-oceanic ridge basalt.**

zircon do exist (3 have been confirmed in >300 inclusions investigated), their composition is albitic, with $An_{15}$ being the most Ca-rich plagioclase recorded (Table DR3). In contrast, the first plagioclase to crystallize in typical S-type granites would be $An_{40–50}$ (e.g., Clemens and Wall, 1984). (3) The primary magmatic character of the clasts is also supported by the fact that, in the most Ca-rich rocks, plagioclase occasionally displays magmatic oscillatory zoning of Ca content. (4) CaO-poor samples that have the lowest A/CNK values (≤1.1) contain monazite as both a matrix accessory mineral and as inclusions in zircon. Addition of even minor amounts of CaO to these magmas would have resulted in an insufficiently peraluminous composition unable to support monazite stability (Montel, 1993).

All this evidence supports the conclusion that the low CaO character of the clasts is not due to postcrystallization alteration, but is a primary magmatic feature. Consequently, these rocks represent an as-yet undocumented variety of low-CaO peraluminous granite.

The contemporaneous formation of granitic and TTG magmas in the BGB may indicate a petrogenetic link between the two magmas types. In such a scenario, the high $K_2O$ and very low CaO contents of the granitic magma (Fig. 2A) can only be potentially accounted for if they represent either residual liquids from TTG fractional crystallization or liquids produced by low-degree partial melting of a TTG source. Both options would require separation of the magma from essentially all of the plagioclase in the system, which is inconsistent with the lack of significant negative Eu anomaly in the granites (Fig. 2B). Removal of almost all the CaO in the system by Ca-rich ferromagnesian minerals is similarly unlikely, as the Cr and Ni contents of the granites are high (typically as high as the highest TTGs for Cr and as much as four times higher for Ni), and neither clinopyroxene nor amphibole are likely to be stable in the peraluminous and K-rich magma compositions documented here.

Thus, the perfect correlation between the crystallization ages of the TTG plutons and those of these granitic magmas results from the concurrent partial melting of different sources, most likely as a consequence of the same geodynamic process.

The granites documented here share many characteristics with granites generated through anatexis of metasedimentary rocks, including the positive correlation between A/CNK and maficity (Fig. 2D), the K/Na range and variability, the Mg# range, and the close positive correlation between Fe + Mg and Ti. However, they also differ from typical S-types granites by their exceptionally low CaO contents, suggesting that they may represent a uniquely Archean type of magma formed via a unique petrogenetic process. The decoupling between low CaO concentrations and high Sr and Eu values demands a source that contains significant CaO, yet undergoes melting via a mechanism that keeps CaO in the residuum without producing a strong negative Eu anomaly; more specifically, the source has to be an originally plagioclase-rich sediment that melted at a pressure in excess of the plagioclase stability field. High-pressure melting is also supported by their negative Ti anomaly, and their high Zr/Sm and low Nb/Ta ratios, reflecting the presence of residual rutile during melting (John et al., 2010), i.e., at pressures >1.5 GPa at 850 °C (e.g., Patiño Douce and Johnston, 1991). The Ni and Cr contents of the granites are substantially higher than those of S-type granites, indicating the enrichment of these elements in the source. In addition, the average Rb contents of the granites are relatively low but within the range displayed by S-type granites, interpreted to reflect the low Rb content of the source. The $\delta^{18}O$ values of the zircon crystallized from the granites are similar to those of the zircon formed in TTG rocks of the same age (King, 2001). This precludes a significant volume of high $\delta^{18}O$ clay minerals in the source protolith. This is not inconsistent with the peraluminous character of the rocks, as this simply reflects the melting of biotite and does not require a clay-bearing source.

Collectively, this information indicates that the granitic magmas were generated at pressures in excess of plagioclase stability, by low-degree partial melting of an Rb-poor, Ni- and Cr-rich, quartz + mica–bearing source, the protolith of which was plagioclase rich before eclogite facies metamorphism. This leads us to propose an eclogite facies metagraywacke source

derived from relatively unweathered TTG material or from felsic to intermediate volcaniclastic rocks. In both cases, a component of mafic and/or ultramafic greenstone material is required to account for the Ni and Cr values.

Little relevant experimental information exists on the melting of eclogite facies K-rich sources. However, an investigation at 3–5 GPa by Schmidt et al. (2004) showed that, under high-pressure conditions, phengite is the stable $K_2O$-bearing phase in both mafic and metasedimentary sources. When the experiments are conducted sufficiently close to the phengite solidus (i.e., before significant contributions to the melt from garnet- or clinopyroxene-consuming reactions), the melt compositions produced from the metagraywacke source are similar to those of the granites described in this study (e.g., Table DR1; Fig. 2A), and are consistent with the minimum temperature estimate of magma formation calculated from the zircon saturation temperatures of ~855 °C (Baker et al., 2002) (Table DR1).

## CONCLUSIONS

Granitic (sensu stricto) magmatism occurred concurrently with each of the three episodes of TTG magmatism in the BGB. However, the granites and the TTGs are not genetically related, and formed via the synchronous melting of contrasting sources. The same high-pressure conditions of anatexis required by the TTG geochemical characteristics are also required to account for the chemistry of the granites. Consequently, we conclude that the peraluminous granite magmas were generated by high-pressure (in excess of plagioclase stability) anatexis of a phengite-bearing metagraywacke. They thus represent a potentially uniquely Archean variety of S-type granite that formed as a consequence of sedimentary rocks being dragged down the subduction channel and melting at pressures probably >2 GPa. The very low CaO signature documented in this study, in conjunction with the Sr and $SiO_2$ contents of the rocks, suggests a unique type of magma that has not previously been reported in the Archean rock record. This signature appears to be restricted to the Paleoarchean and Mesoarchean, reflecting the interaction of subducting or foundering crust with a hotter mantle than has existed subsequently on Earth. In essence, these rocks could be an early Earth equivalent of S-type granites. In the BGB this Paleoarchean and Mesoarchean granitic magmatism appears to have produced only eruptive and high-level plutonic rocks; it does not appear to have produced plutons at the mid-crustal levels at which many TTG plutons have intruded. Such superficially emplaced rocks would be vulnerable to erosion, thus accounting for their lack of preservation. The southern facies of the predominantly volcaniclastic Fig Tree Group (Fig. 1A; Table DR1) is characterized by very low average CaO (0.05 wt%) and high $K_2O$ (3.98 wt%) contents. This is much more consistent with this volcano-sedimentary succession having been derived from the granite magmatism described herein than by eruptive TTG magmas. Thus, we suggest that potassic granitic magmatism contributed fundamentally to the development of the BGB rock record. The Moodies Group granitic clasts, by virtue of the fact that only fresh material would have survived to be deposited as clasts, provided us with the opportunity to make these unique insights.


## ACKNOWLEDGMENTS

Stevens acknowledges National Research Foundation (NRF, South Africa) funding through the SARChI program. Stevens, Moyen, and Martin acknowledge joint Centre National de la Recherche Scientifique and NRF funding. We thank J. Clemens, M. de Wit, B. Schoene, D. Champion, A. Patiño-Douce, and W. Collins for their very helpful reviews of earlier versions of the manuscript.


## REFERENCES CITED


Baker, D.R., Conte, A.M., Freda, C., and Ottolini, L., 2002, The effects of halogens on Zr diffusion and zircon dissolution in hydrous metaluminous granitic melts: Contributions to Mineralogy and Petrology, v. 142, p. 666–678, doi:10.1007/s00410-001-0328-3.

Clemens, J.D., and Wall, V.J., 1981, Crystallization and origin of some peraluminous (S-type) granitic magmas: Canadian Mineralogist, v. 19, p. 111–131.

Clemens, J.D., and Wall, V.J., 1984, Origin and evolution of a peraluminous silicic ignimbrite suite: The Violet Town Volcanics: Contributions to Mineralogy and Petrology, v. 88, p. 354–371, doi:10.1007/BF00376761.

de Ronde, C.E.J., and de Wit, M.J., 1994, Tectonic history of the Barberton greenstone belt, South Africa: 490 million years of Archean crustal evolution: Tectonics, v. 13, p. 983–1005, doi:10.1029/94TC00353.

de Wit, M.J., Roering, C., Hart, R.J., Armstrong, R.A., de Ronde, C.E.J., Green, R.W.E., Tredoux, M., Peberdy, E., and Hart, R.A., 1992, Formation of an Archaean continent: Nature, v. 357, p. 553–562, doi:10.1038/357553a0.

Foley, S., Tiepolo, M., and Vannucci, R., 2002, Growth of early continental crust controlled by melting of amphibolite in subduction zones: Nature, v. 417, p. 837–840, doi:10.1038/nature00799.

John, T., Klemd, R., Klemme, S., Pfänder, J.A., Hoffmann, J.E., and Gao, J., 2010, Nb-Ta fractionation by partial melting at the titanite–rutile transition: Contributions to Mineralogy and Petrology, v. 161, p. 35–45, doi:10.1007/s00410-010-0520-4.

Kamo, S.L., and Davis, D.W., 1994, Reassessment of Archean crustal development in the Barberton Mountain Land, South Africa, based on U-Pb dating: Tectonics, v. 13, p. 167–192, doi:10.1029/93TC02254.

King, E.M., 2001, Oxygen isotope study of magmatic source and alteration of granitic rocks in the western United States and the Superior Province, Canada [Ph.D. thesis]: Madison, University of Wisconsin, 224 p.

Kisters, A.F.M., Belcher, R.W., Poujol, M., and Dziggel, A., 2010, Continental growth and convergence-related arc plutonism in the Mesoarchaean: Evidence from the Barberton granitoid-greenstone terrain, South Africa: Precambrian Research, v. 178, p. 15–26, doi:10.1016/j.precamres.2010.01.002.

Kröner, A., and Compston, W., 1988, Ion microprobe ages of zircons from early Archaean granite pebbles and greywacke, Barberton greenstone belt, southern Africa: Precambrian Research, v. 38, p. 367–380, doi:10.1016/0301-9268(88)90034-4.

Lana, C., Tohver, E., and Cawood, P., 2010, Quantifying rates of dome-and-keel formation in the Barberton granitoid-greenstone belt, South Africa: Precambrian Research, v. 177, p. 199–211, doi:10.1016/j.precamres.2009.12.001.

Lowe, D.R., 1994, Accretionary history of the Archean Barberton Greenstone Belt (3.55–3.22 Ga), southern Africa: Geology, v. 22, p. 1099–1102, doi:10.1130/0091-7613(1994)022<1099:AHOTAB>2.3.CO;2.

Lowe, D.R., 1999, Geologic evolution of the Barberton greenstone belt and vicinity, *in* Lowe, D.R., and Byerly, G.R., eds., Geologic evolution of the Barberton greenstone belt, South Africa: Geological Society of America Special Paper 329, p. 287–213, doi:10.1130/0-8137-2329-9.287.

Martin, H., 1986, Effect of steeper Archean geothermal gradient on geochemistry of subduction-zone magmas: Geology, v. 14, p. 753–756, doi:10.1130/0091-7613(1986)14<753:EOSAGG>2.0.CO;2.

Montel, J.-M., 1993, A model for monazite/melt equilibrium and application to the generation of granitic magmas: Chemical Geology, v. 110, p. 127–146, doi:10.1016/0009-2541(93)90250-M.

Moyen, J.-F., Stevens, G., and Kisters, A., 2006, Record of mid-Archaean subduction from metamorphism in the Barberton terrain, South Africa: Nature, v. 442, p. 559–562, doi:10.1038/nature04972.

Patiño Douce, A.E., and Johnston, A.D., 1991, Phase equilibria and melt productivity in the pelitic system: Implications for the origin of peraluminous granitoids and aluminous granulites: Contributions to Mineralogy and Petrology, v. 107, p. 202–218, doi:10.1007/BF00310707.

Rapp, R.P., Shimizu, N., and Norman, M.D., 2003, Growth of early continental crust by partial melting of eclogite: Nature, v. 425, p. 605–609, doi:10.1038/nature02031.

Reimer, O., Condie, K.C., Schneider, G., and Georgia, A., 1985, Petrography and geochemistry of granitoid and metamorphite pebbles from the early Archaean Moodies Group, Barberton Mountainland/South Africa: Precambrian Research, v. 29, p. 383–404, doi:10.1016/0301-9268(85)90044-0.

Schmidt, M.W., Vielzeuf, D., and Auzanneau, E., 2004, Melting and dissolution of subducting crust at high pressures: The key role of white mica: Earth and Planetary Science Letters, v. 228, p. 65–84, doi:10.1016/j.epsl.2004.09.020.

Schoene, B., and Bowring, S.A., 2010, Rates and mechanisms of Mesoarchean magmatic arc construction, eastern Kaapvaal craton, Swaziland: Geological Society of America Bulletin, v. 122, p. 408–429, doi:10.1130/B26501.1.

Schoene, B., de Wit, M.J., and Bowring, S.A., 2008, Mesoarchean assembly and stabilization of the eastern Kaapvaal craton: A structural-thermochronological perspective: Tectonics, v. 27, TC5010, doi:10.1029/2008TC002267.



Manuscript received 22 February 2011
Revised manuscript received 10 May 2011
Manuscript accepted 16 May 2011

Printed in USA

Precambrian Research 227 (2013) 186–203

Contents lists available at SciVerse ScienceDirect

Precambrian Research

journal homepage: www.elsevier.com/locate/precamres

# Differentiation of the late-Archaean sanukitoid series and some implications for crustal growth: Insights from geochemical modelling on the Bulai pluton, Central Limpopo Belt, South Africa

Oscar Laurent[a,b,c,*], Régis Doucelance[a,b,c], Hervé Martin[a,b,c], Jean-François Moyen[b,c,d]

[a] Clermont Université, Université Blaise Pascal, Laboratoire Magmas et Volcans, BP 10448, F-63000 Clermont-Ferrand, France
[b] CNRS, UMR6524, LMV, F-63038 Clermont-Ferrand, France
[c] IRD, R 163, LMV, F-63038 Clermont-Ferrand, France
[d] Département de Géologie, Université Jean Monnet, 23 rue du Docteur Paul Michelon, 42023 Saint-Étienne, France

ARTICLE INFO

*Article history:*
Received 27 September 2011
Received in revised form 14 July 2012
Accepted 21 July 2012
Available online 1 August 2012

*Keywords:*
Sanukitoid series
Granitoids
Geochemical modelling
Differentiation
Crustal growth

ABSTRACT

The late-Archaean (~2.59 Ga) Bulai pluton from North-Eastern South Africa mostly consists in granodioritic rocks and subordinate amounts of mafic lithologies, mainly monzodiorites, both belonging to the sanukitoid series. Many lines of evidence point to a genetic link between these two components, such as similar mineralogical assemblages, parallel trace-element patterns and isotopic homogeneity. The nature of this genetic link has been investigated using semi-quantitative geochemical modelling.

Several models reproduce the geochemistry of the Bulai granodiorites, including magma mixing, crystallization from a primary magma and partial melting of mafic rocks. Pure mixing between two magmas that are highly contrasted in terms of geochemistry and physical properties is of doubtful reliability in generating massive volumes of homogeneous hybrid magma. Thus, the models that best fit the data involve either equilibrium or fractional crystallization from a mafic mantle-derived magma, coupled with increasing amounts of mixing with felsic melt in course of differentiation. Alternatively, melts computed by dehydration melting of monzodiorites (incongruent melting of biotite) are also similar in composition to the most differentiated Bulai granodiorites ($SiO_2$ > 65 wt.%). However, formation of the least differentiated granodiorites ($SiO_2$ < 65 wt.%) by such a process requires unrealistic melting conditions. Rather, they would result from entrainment of the (mafic) residual solid after melting.

The widespread differentiated rocks of the sanukitoid suite were probably derived from differentiation of mafic mantle-derived melts (sanukitoids *s.s.*), either as residual liquids (crystallization and mixing) or partial melts. Thus, the presence of pre-existing differentiated crust is not a requirement to the generation of these granitoids that therefore can be considered as a juvenile addition to the crust. In addition, the composition of the sanukitoid series matches the one of some post-Archaean, high-K calc-alkaline suites of late-orogenic affinity, as well as the average composition of the continental crust. As a result, growth and differentiation of the crust since the end of the Archaean were likely accommodated by similar processes that gave rise to the sanukitoid series and post-Archaean high-K calc-alkaline granitoids.



## 1. Introduction

The Archaean-Proterozoic transition represents a fundamental change in the petrogenetic and geodynamic processes of crustal growth on Earth (Condie, 1989; Kemp and Hawkesworth, 2003; Taylor, 1987; Taylor and McLennan, 1995). The Archaean continental crust is characterized by the emplacement of magmas belonging to the Tonalite–Trondhjemite–Granodiorite (TTG) series that are sodic granitoids ($K_2O/Na_2O$ < 1) generated by partial melting of hydrous garnet- and amphibole-bearing metabasalts (e.g. Barker and Arth, 1976; Condie, 1981; Martin, 1986, 1993; Martin et al., 2005; Rapp et al., 1991; Smithies, 2000). By contrast, most modern, calc-alkaline granitoids are potassic ($K_2O/Na_2O$ > 1) and bear a mantle-derived component: it is widely accepted that the latter derived from melting of mantle peridotite variously enriched in incompatible elements by prior subduction processes (e.g. Barbarin, 1999; Condie, 1997; Kemp and Hawkesworth, 2003; Liégeois et al., 1998; Pitcher, 1987; Schmidt and Poli, 1998; Tatsumi, 1989).

The transition between both granitoid types is recorded by the Late-Archaean sanukitoid series that shares geochemical features with both TTGs and modern calc-alkaline granitoids. They consist

* Corresponding author at: Clermont Université, Université Blaise Pascal, Laboratoire Magmas et Volcans, BP 10448, F-63000 Clermont-Ferrand, France. Tel.: +33 47334 6891.
*E-mail address:* o.laurent@opgc.univ-bpclermont.fr (O. Laurent).

0301-9268/$ – see front matter © 2012 Elsevier B.V. All rights reserved.
http://dx.doi.org/10.1016/j.precamres.2012.07.004

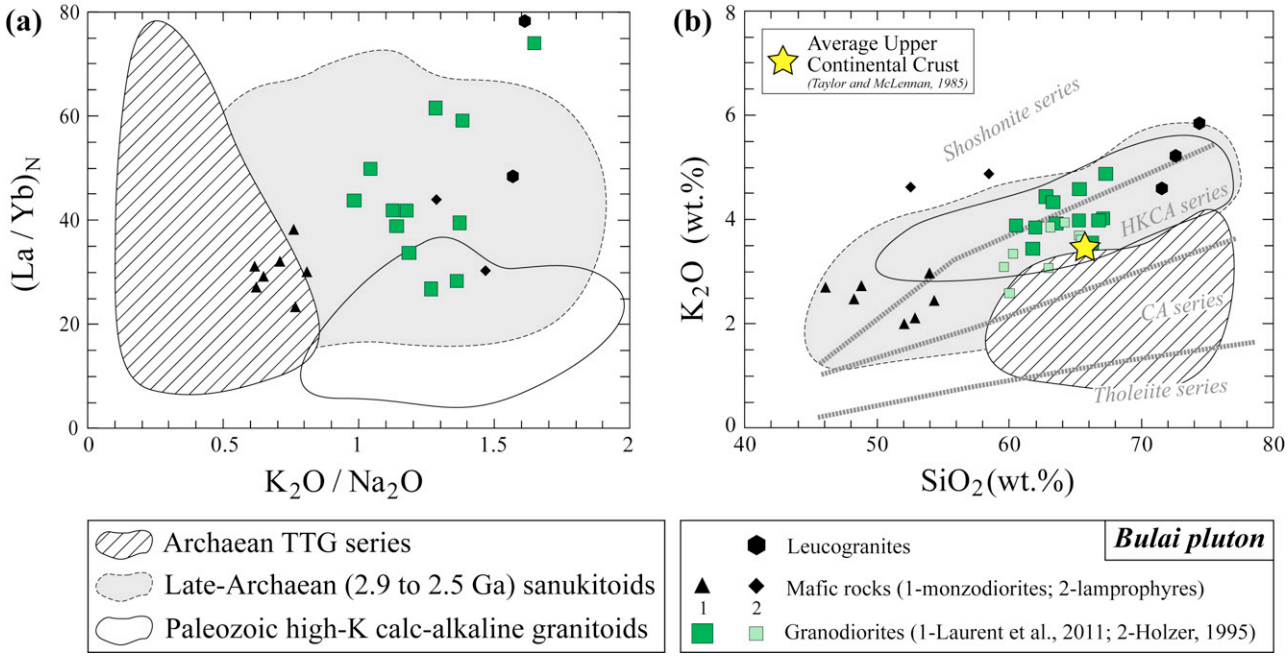


**Fig. 1.** Comparison between the compositions of Archaean TTGs, late-Archaean sanukitoids and modern (Palaeozoic) high-K calc-alkaline granitoids. Samples from the Bulai pluton, which is the focus of this study, are also plotted and fall within the field of late-Archaean sanukitoids. (a) REE fractionation (expressed as La/Yb ratio normalized to chondritic value from McDonough and Sun, 1995) plotted vs. $K_2O/Na_2O$ ratio. (b) Harker plot for $K_2O$, labeled with differentiation series as defined by Peccerillo and Taylor (1976). Note that the sanukitoid field (and samples from the Bulai pluton) straddles the boundary between high-K calc-alkaline and shoshonite series. Data for TTGs, sanukitoids and Palaeozoic granitoids are from author's databases (available on request).

in post-tectonic and composite complexes of plutonic rocks characterized by high Mg#, Ni and Cr contents as well as richness in LILE and LREE leading to highly fractionated REE patterns (Martin et al., 2005, 2010; Shirey and Hanson, 1984; Smithies and Champion, 2000; Stern et al., 1989; Stern and Hanson, 1991; Fig. 1a). As defined by Heilimo et al. (2010) and Martin et al. (2010), the sanukitoid series covers a wide compositional range from mafic diorites and monzodiorites (~50 wt.% $SiO_2$ and up to 9 wt.% MgO), which represent sanukitoids *sensu stricto* (Shirey and Hanson, 1984; Stern et al., 1989), to granodiorites and granites (up to ~70 wt.% $SiO_2$ and down to ~1 wt.% MgO). Both mafic and felsic components share similar trace-element features. The 'juvenile' mafic component has been well-studied both geochemically and experimentally; it is assumed to result from strong hybridization of a mantle peridotite with a felsic melt, the latter being either derived from metabasalts (Heilimo et al., 2010; Martin et al., 2005, 2010; Shirey and Hanson, 1984; Smithies and Champion, 2000; Rapp et al., 1999, 2010) or metasediments (Laurent et al., 2011; Smithies et al., 2004).

However, in general, the volumetrically dominant rocks of sanukitoid complexes are not the mantle-derived ones but rather the granitoids (Lobach-Zhuchenko et al., 2005; Martin et al., 2010; Moyen et al., 2001; Stern and Hanson, 1991; Stevenson et al., 1999). The petrogenetic processes responsible for the origin of these "differentiated sanukitoids" are poorly constrainted with respect to their mafic counterparts. Moyen et al. (2001) argued that the Closepet sanukitoids of Southern India result from magma mixing between mantle- and crust-derived melts. By contrast, differentiation of the sanukitoid suite of the Superior Province is thought to have resulted from fractional crystallization (Stern and Hanson, 1991), possibly coupled with crustal assimilation (Stevenson et al., 1999). These hypotheses were not investigated further, and need refinement in order to understand the differentiation mechanism of the sanukitoid series from a global point of view.

Moreover, the petrogenesis of "differentiated sanukitoids" may also have critical implications for crustal growth and differentiation. Indeed, understanding how the continental crust grew and differentiated into felsic upper crust and more mafic lower crust, are still pendent questions. The composition of "differentiated sanukitoids" generally matches that of modern, metaluminous high-K calc-alkaline granitoids, both being similar to that of the Upper Continental Crust (Fig. 1b). Therefore, addressing sanukitoid petrogenesis appears as a key issue for understanding the processes of continental crust extraction from the mantle since ~2.5 Ga and for deciphering why they differ from Archaean ones.

This paper focuses on the ~2.6 Ga-old Bulai pluton, a sanukitoid complex intrusive within the Central Zone of the Limpopo Belt in North-Eastern South Africa. The composition of the main, granodioritic, phase of this pluton is very typical of late-Archaean sanukitoids (Fig. 1b). The "juvenile" mafic component of the Bulai pluton has already been investigated (Laurent et al., 2011), while more felsic rocks were less studied. This is the reason why the present paper complementary focuses on the petrogenesis of differentiated rocks of the Bulai suite (in particular, quartz-monzonites and granodiorites with $SiO_2$ = 60–70 wt.%). Their genesis through magma mixing, fractional crystallization, coupled or not with crustal assimilation, and partial melting of mafic rocks in the lower crust was tested using semi-quantitative, forward and multi-element geochemical modelling.

## 2. The Bulai pluton: an overview

The Bulai pluton is intrusive within the Central Zone (CZ) of the high-grade Limpopo mobile belt, a Neoarchaean to Palaeoproterozoic terrane separating the Zimbabwe Craton to the North from the Kaapvaal Craton to the South (Figs. 2 and 3). The CZ is made up of grey gneisses of TTG composition (the polymetamorphic Sand River gneisses) and supracrustal lithologies of the Beit Bridge Complex (mainly metapelites, with subordinate quartzite, BIF and mafic meta-volcanics). Both formed between ~3.33 and ~2.65 Ga, and underwent at least two granulite-facies metamorphic overprints at ~2.65 and ~2.0 Ga (for detailed description and review, see Roering et al., 1992; Holzer et al., 1998; Zeh et al., 2007, 2009; Van Reenen

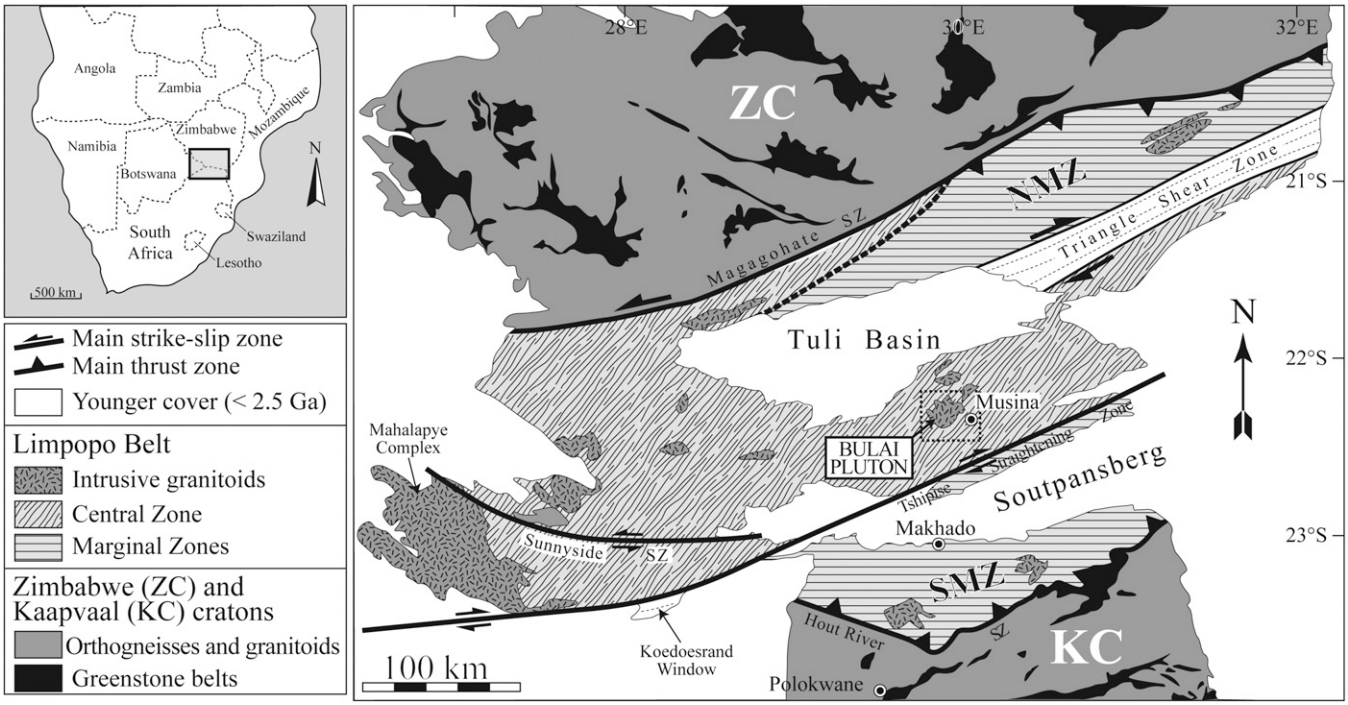


**Fig. 2.** Regional sketch map of the Limpopo Belt and adjacent cratons (after Laurent et al., 2011). The dashed square represents the area covered by Fig. 3. NMZ, Northern Marginal Zone; SMZ, Southern Marginal Zone.

et al., 2008; and references therein). The Bulai pluton is intrusive within the Beit Bridge Complex, and relationships between both are detailed in Holzer (1995), Holzer et al. (1998), Millonig et al. (2008) and Laurent et al. (2011). U–Pb and Pb–Pb dating on separated zircons indicates that intrusion of the Bulai pluton occurred between 2.61 and 2.58 Ga (Barton et al., 1994; Kröner et al., 1999; Laurent et al., 2011; Zeh et al., 2007), i.e. just after the Archaean granulite-facies metamorphic event and associated deformation.

A detailed description of the magmatic petrology of the Bulai is given in Holzer (1995). The main phase of the pluton is represented by K-feldspar porphyritic granitoids, herein referred as "granodiorites" even if their modal composition ranges from monzonite to quartz-monzonite and granodiorite. They are systematically associated with subordinate amounts of mafic rocks (mainly monzodiorites), either pyroxene-free or pyroxene-bearing (the latter being locally referred to as 'enderbites', i.e. Opx-bearing tonalites, even if they are rather jotunites, i.e. Opx-bearing monzodiorites) that occur either as large bodies (>100 m) or as small, rounded

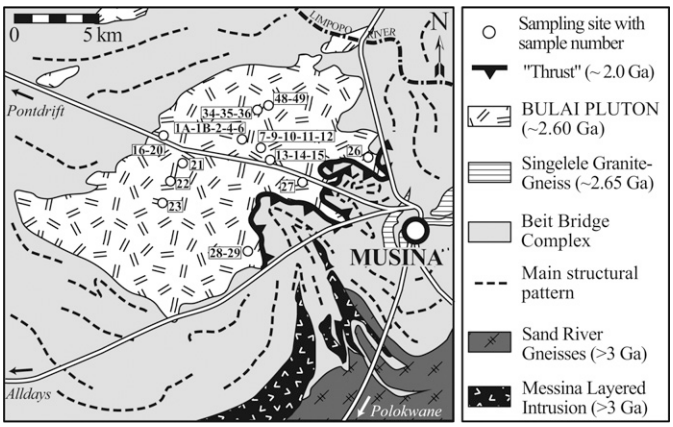


**Fig. 3.** Geological map of the Musina area focused on the Bulai pluton and indicating sampling localities (after Millonig et al., 2008).

Microgranular Mafic Enclaves (MMEs) comagmatic with the granodiorites. On the other hand, small bodies of leucogranite are locally associated with the porphyritic granodiorite, whereas late mafic dykes and pegmatites crosscut the whole pluton.

The porphyritic granodiorite and associated mafic rocks share a common mineralogical assemblage of quartz, sodic plagioclase, K-feldspar, Ca-rich amphibole, biotite, magnetite and ilmenite together with apatite, zircon and allanite as accessory phases. Monzodiorites sometimes contain both clino- and orthopyroxene, partly replaced by amphibole and biotite (respectively).

Geochemical characteristics of the Bulai pluton, in terms of major, trace elements and Nd isotopes, were investigated in detail by Laurent et al. (2011), whilst key features are summarized in Fig. 4 (see figure caption for more information). In terms of previous petrogenetic modelling, Laurent et al. (2011) recently interpreted the whole-rock geochemistry of MME and enderbites as inherited from a hybrid source rock: a mantle peridotite metasomatized by sediment-derived felsic melts. In particular, these rocks bear chemical features typical of both the mantle (high $FeO_T$, MgO, Ni–Cr–V contents) and a crustal component (extremely high LILE, LREE and HFSE contents) of typical terrigenous affinity (extremely high K, Zr, Nb, Th, REE contents and low Sr/Nd).

## 3. Petrogenesis of the Bulai granodiorites: starting hypotheses

Several lines of evidence point to a strong cogenetic link between the porphyritic granodiorites and the monzodiorites. Field relationships (magmatic enclaves, diffuse boundaries and other mingling features) as well as geochronology demonstrate the comagmatic and coeval characters of these rocks. In addition, they share a common mineral assemblage, parallel trace-element patterns and an identical initial Nd isotopic signature (Fig. 4). Four distinct petrogenetic processes are commonly proposed to account for these observations in other high-K calc-alkaline suites (including Archaean sanukitoids). These are:

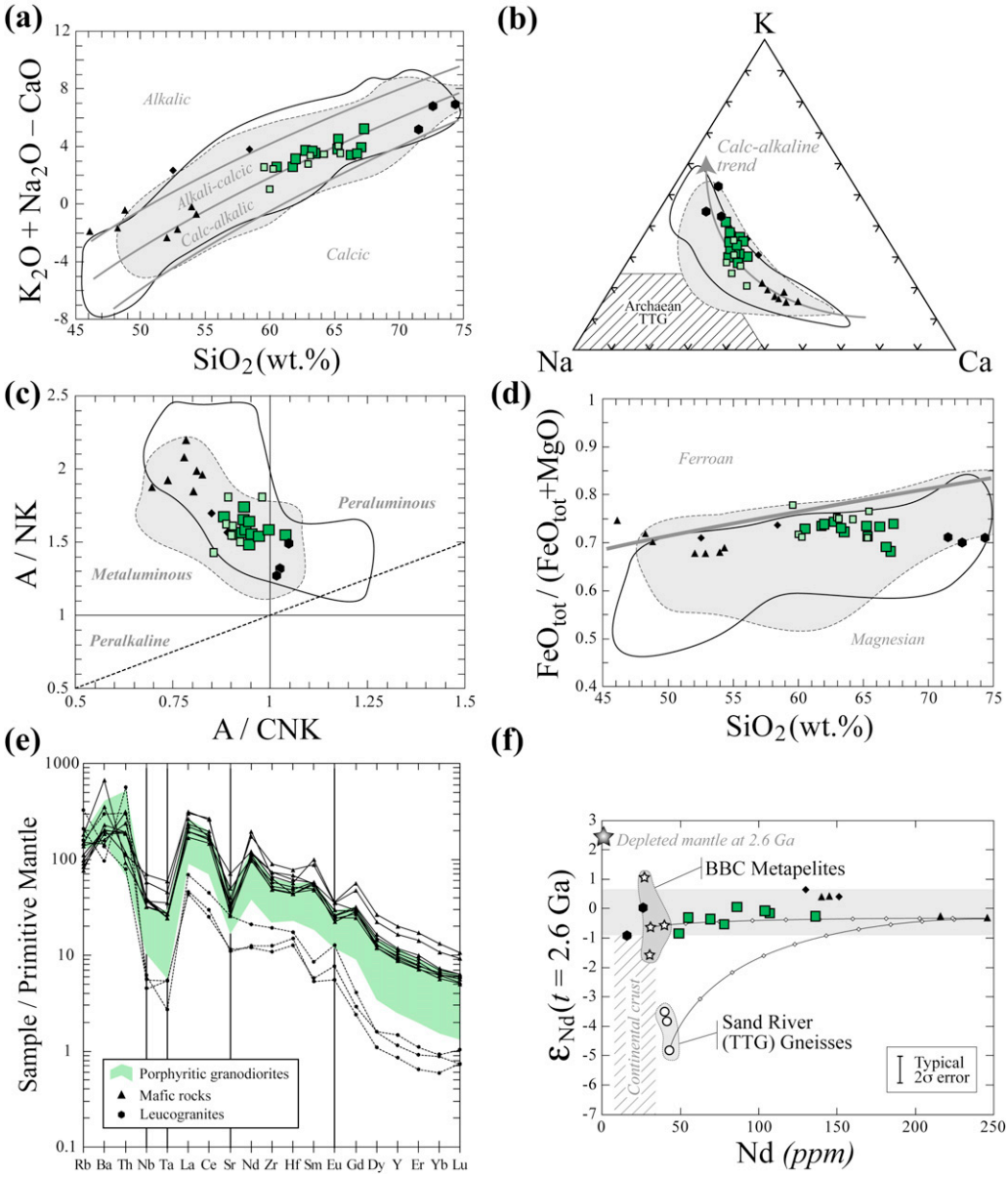


**Fig. 4.** Geochemical characteristics of the Bulai pluton expressed as (a) $K_2O + Na_2O$–CaO (MALI index) vs. $SiO_2$ (Frost et al., 2001); (b) Na–K–Ca triangle (the calc-alkaline trend is from Barker and Arth, 1976 and the TTG field from Martin, 1999); (c) A/NK vs. A/CNK plot (Shand, 1943); (d) $FeO_{tot}/(FeO_{tot} + MgO)$ vs. $SiO_2$ (Frost et al., 2001); (e) primitive mantle-normalized multi-element patterns (normalization values are from the "pyrolite silicate earth" of McDonough and Sun, 1995) and (f) plot of $\varepsilon_{Nd}$ at 2.6 Ga vs. Nd concentration (data for BBC metapelites and Sand River Gneisses are from Harris et al., 1987; isotopic composition of the depleted mantle was calculated from the equation of DePaolo, 1981 and the range of Nd concentrations in the continental crust was taken from Rudnick and Gao, 2003). Symbols and fields are as in Fig. 1. The Bulai suite covers a wide range of silica contents, from the MMEs to the leucogranites, and belongs to a calc-alkaline differentiation trend. Most samples are metaluminous, except the leucogranites (slightly peraluminous) and belong to the magnesian group defined by Frost et al. (2001). Granodiorites and mafic rocks show very similar, parallel trace-element patterns. The field of porphyritic granodiorites is systematically intermediate between that of monzodiorites and of leucogranites (except for scattered values of Ba and Th). Homogeneous initial $^{143}Nd/^{144}Nd$ signature measured for all rock of the Bulai suite provide further support for a strong genetic link between all rock types.

(1) Binary mixing between felsic and mafic magmas (Clemens et al., 2009; Janoušek et al., 2004; Moyen et al., 2001; Słaby and Martin, 2008; Zhang et al., 2011)
(2) Crystallization (either fractional or at equilibrium) of a primary magma similar in composition to the mafic rocks of the Bulai suite (Holzer, 1995). Stern and Hanson (1991) considered fractional crystallization as the single differentiation process accounting for the origin of the sanukitoid suite of the Roaring River Complex (Superior Province);
(3) 'Open-system' fractional crystallization coupled with assimilation of, or mixing with, felsic material (AFC: Assimilation – Fractional Crystallization, or MFC: Mixing plus Fractional Crystallization). Stevenson et al. (1999) proposed that such a mechanism could have given rise to silicic rocks of the sanukitoid series in the Superior Province. This process is also assumed to account for the genesis of some modern I-type, calc-alkaline granitoid batholiths (Barbarin, 2005; Christophides et al., 2007; Karsli et al., 2007; Poli and Tommasini, 1999) and high-Mg andesites similar in composition to late-Archaean sanukitoids (Tatsumi, 2008);
(4) Partial melting of rocks similar in composition to the Bulai mafic lithologies, which are amphibole- and biotite-bearing such that they can undergo significant dehydration melting. Roberts and Clemens (1993), followed by Roberts et al. (2000) and Chen and Jahn (2004), proposed that this might be a reliable petrogenetic process for most high-K calc-alkaline rocks.

**Table 1**
Major- and trace-element compositions of materials used as end-members for geochemical modeling. The 'Type' row indicates the sources of the data. For all the data, concentrations of major oxides have been recalculated on anhydrous basis.

| Facies<br>Type | AD19-93[a] | MME<br>Average[b] | Enderbite<br>Average[b] | 'Primary' PGd.<br>Calculated[c] | Felsic PGd.<br>BUL-22[b] | Leucogranite<br>BUL-26[b] | Metapelite<br>Average[d] |
|---|---|---|---|---|---|---|---|
| *Major oxides (wt.%)* | | | | | | | |
| $SiO_2$ | *50.99* | 49.42 | 55.22 | 59.00 | 68.13 | 74.69 | 66.84 |
| $TiO_2$ | *1.26* | 2.39 | 1.79 | 1.44 | 0.65 | 0.21 | 0.60 |
| $Al_2O_3$ | *19.47* | 17.76 | 17.25 | 16.88 | 15.75 | 13.6 | 17.93 |
| $FeO_T$[e] | *9.74* | 10.51 | 7.72 | 7.39 | 3.49 | 1.04 | 5.22 |
| MgO | *4.54* | 3.76 | 3.88 | 2.45 | 1.10 | 0.38 | 3.60 |
| CaO | *7.43* | 8.20 | 7.45 | 5.22 | 2.66 | 1.53 | 1.90 |
| $Na_2O$ | *3.78* | 3.97 | 3.52 | 3.88 | 3.00 | 2.61 | 1.72 |
| $K_2O$ | *2.33* | 2.54 | 2.28 | 2.97 | 4.93 | 5.87 | 2.10 |
| $P_2O_5$ | *0.46* | 1.45 | 0.89 | 0.77 | 0.29 | 0.07 | 0.09 |
| *Trace elements (ppm)* | | | | | | | |
| Sc | | 20 | 18 | 12 | 3 | <1[f] | 15 |
| V | | 157 | 140 | 95 | 50 | 22 | 107 |
| Rb | | 67 | 50 | 86 | 101 | 124 | 74 |
| Sr | | 794 | 632 | 810 | 382 | 214 | 74 |
| Y | | 71 | 47 | 42 | 11 | 4 | 32 |
| Zr | | 939 | 644 | 680 | 325 | 131 | 157 |
| Nb | | 38 | 25 | 17 | 7 | 3 | 12 |
| Ba | | 1340 | 1343 | 1800 | 1409 | 622 | 439 |
| La | | 203 | 132 | 170 | 78 | 30 | 35 |
| Ce | | 436 | 288 | 320 | 145 | 49 | 66 |
| Nd | | 216 | 137 | 140 | 55 | 16 | 24 |
| Sm | | 35.8 | 22.1 | 22 | 7.6 | 2.1 | 4.7 |
| Eu | | 5.4 | 3.9 | 4.0 | 2.1 | 0.9 | 1.1 |
| Gd | | 25.9 | 16.2 | 15.0 | 5.0 | 1.3 | 4.5 |
| Dy | | 15.1 | 10.0 | 9.0 | 2.4 | 0.7 | 4.8 |
| Er | | 6.26 | 3.97 | 3.60 | 0.90 | 0.28 | 2.75 |
| Yb | | 4.77 | 2.75 | 3.00 | 0.72 | 0.26 | 2.62 |
| Lu | | 0.63 | 0.35 | 0.40 | 0.11 | 0.05 | 0.42 |
| Hf | | 22 | 15 | 15 | 9 | 4 | 5 |
| Ta | | 1.7 | 0.9 | 0.8 | 0.2 | 0.2 | 0.8 |
| Th | | 15 | 15 | 20 | 11 | 45 | 13 |

[a] High-K hornblende–biotite gabbro from the Sierra Nevada Batholith (California, USA; starting composition in experimental study of Sisson et al., 2005).
[b] Samples or average of several samples from Laurent et al. (2011).
[c] Calculated from linear regression (element = a.$SiO_2$ + b) at 59 wt.% $SiO_2$ on the basis of data from Laurent et al. (2011) for REE, Sc, Hf and Ta; and Laurent et al. (2011) as well as Holzer (1995) for other elements.
[d] Average of several samples from Boryta and Condie (1990).
[e] All iron recalculated in FeO.
[f] Value below detection limit (=1 ppm). An arbitrary value of 0.5 ppm has been assumed for modeling.

In the following section, we will test these four petrogenetic hypotheses using semi-quantitative, multi-element geochemical modelling.

## 4. Geochemical modelling

### 4.1. Model 1: magma mixing

This model is based on the assumption that the Bulai granodiorites represent perfect mixing between a mafic end-member and a felsic one, their geochemical variability resulting only from different mixing proportions. For this purpose, we used a classical mass-balance equation expressed as $C_L^i = X_m \times C_m^i + (1 - X_m) \times C_f^i$ where $C_L^i$ is the concentration of element $i$ in the 'hybrid' liquid, $C_m^i$ and $C_f^i$ the concentration of the element $i$ in the mafic and felsic end-members respectively, and $X_m$ the mass fraction of mafic melt. Sample BUL-26 is the most differentiated leucogranite and has been thus chosen as representative of the felsic end-member, while two distinct mafic end-members were considered: the average composition of MMEs and enderbites. Their compositions are reported in Table 1.

In details, modelling proceeded in two successive steps:

(1) The first step of the model is based on major element behaviour. For each sample, the composition of hybrid melt is calculated for mass fractions of mafic melt $X_m$ ranging from 0 to 100% (by steps of 1%). Modelled compositions are then compared to the real composition of the sample using a least-square calculation ($S^2 = \sum (C_L^i - C_S^i)^2/(\sigma_{C_S^i})^2$, where $C_S^i$ is the concentration of major element $i$ in the sample, and $\sigma_{C_S^i}$ the standard deviation determined for concentrations of major element $i$ from all samples). The 'best' $X_m$ value is the one resulting in the lowest $S^2$.
(2) The trace element composition of each sample is recalculated using the $X_m$ value obtained at step 1, and is then normalized to the measured composition. A perfect match would result in a normalized value (noted $C_n$) of 1 for all elements.

Results of modelling for step 1 are summarized in Table 2. Independently of the chosen mafic end-member, $X_m$ values vary by a factor 2 in order to account for the geochemical variability of Bulai granodiorites. They range from 0.26–0.33 for the most felsic granodiorite (BUL-22) to 0.52–0.66 for the least evolved one (BUL-04). Results of trace-element modelling (step 2) are reported in Fig. 5 as $C_n$ plots. A first-order comparison shows that results do not significantly differ when considering a MME-like or a enderbite-like end-member. Both result in general flat patterns, $C_n$ being comprised in the range $1 \pm 0.3$ (MME end-member) and $0.8 \pm 0.2$ (enderbite end-member) for most elements. Only Ba and Th are systematically too low or too high. This may result from the choice of sample BUL-26 as the felsic end-member that displays exceptionally high Th and low Ba contents (45.4 and 622 ppm, respectively).

**Table 2**
Results of the magma mixing model for major elements. For a given mafic end-member (MME and enderbite) and a given felsic end-member (BUL-26; compositions reported in Table 3) $X_{MB}$ represents the calculated mass fraction of mafic melt needed to account for the major-element composition of each sample. $S^2$ is the sum of square residuals divided by the squared standard deviation for all major oxides (see Section 3.2 for explanation).

| Mafic end-member | MME | | Enderbite | |
|---|---|---|---|---|
| | $X_{MB}$ | $S^2$ | $X_{MB}$ | $S^2$ |
| *Granodiorite sample* | | | | |
| BUL-1B | 0.45 | *16* | 0.52 | *22* |
| BUL-4 | 0.51 | *2.7* | 0.60 | *11* |
| BUL-10 | 0.49 | *12* | 0.57 | *17* |
| BUL-15 | 0.47 | *7.7* | 0.55 | *14* |
| BUL-16 | 0.30 | *8.5* | 0.36 | *5.5* |
| BUL-20 | 0.32 | *7.4* | 0.38 | *4.6* |
| BUL-21 | 0.42 | *10* | 0.49 | *13* |
| BUL-22 | 0.24 | *7.2* | 0.28 | *8.6* |
| BUL-23 | 0.33 | *13* | 0.39 | *15* |
| BUL-27 | 0.40 | *2.6* | 0.47 | *5.9* |
| BUL-28 | 0.36 | *11* | 0.42 | *13* |
| BUL-29 | 0.35 | *15* | 0.41 | *16* |

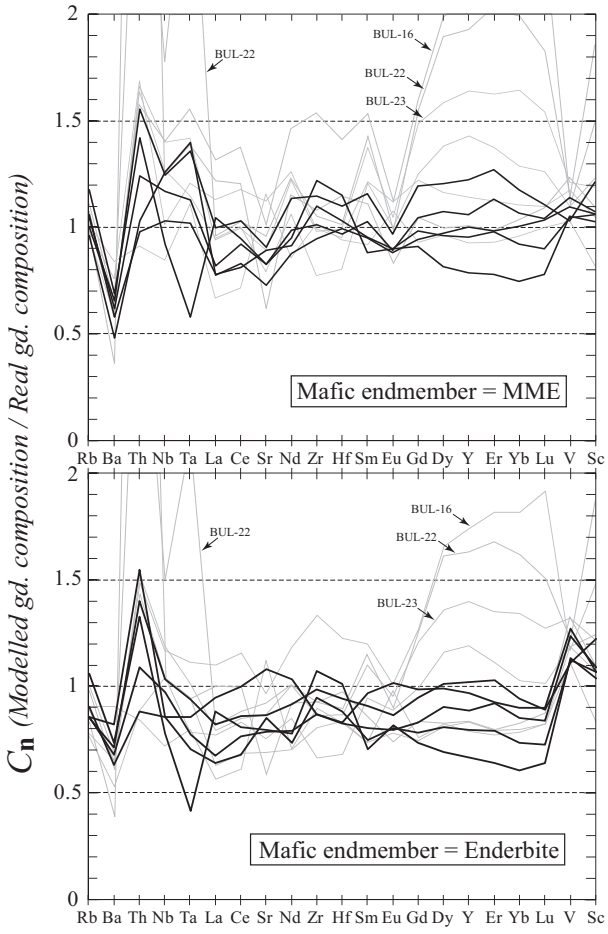


**Fig. 5.** Results of binary mixing model for trace elements. For each tested mafic end-member, we have plotted the calculated compositions of granodiorites (gd.) normalized to the measured values. Black thick lines represent the 5 granodiorite samples that yielded the best $S^2$ from major-element regression with a given mafic endmember, other samples being represented by thin grey lines. See text for a detailed description.

In details, among the twelve studied samples, only three granodiorites (BUL-16, BUL-22 and BUL-23) show very inconsistent patterns. They have very high $C_n$ for (Nb–)Ta, Y, HREE (Gd–Lu) and to a lesser extent for Sc. These discrepancies between modelled and natural compositions result from a slightly different trace-element signature (lower Nb, Ta, Y and HREE concentrations) compared with other granodiorites (see also Section 4.5).

### 4.2. Model 2: fractional or equilibrium crystallization (FC–EC)

Modelling is based on Monte-Carlo simulations. The program computes a large number of melt compositions (typically $N = 10{,}000$) using partition coefficients chosen randomly in an appropriate range, depending on the modelled composition of the liquid (Table 3), for each element at each run. In details, there are two successive steps:

(1) Derivation of the least evolved granodiorite from mafic compositions (modelled with partition coefficients for 'mafic' liquids);
(2) Derivation of the most evolved granodiorite from the least evolved one (modelled with partition coefficients for 'intermediate' liquids).

For both steps, cumulate modal compositions have been computed using mass balance calculations on major elements (algorithm XLFRAC, Stormer and Nicholls, 1978). This calculation is based on the fact that in major-element multi-dimensional space, the initial liquid, the cumulate and the differentiated liquid plot along a straight line. Based on a least-squares approach, the algorithm calculates the modal composition of the solid as well as the melt fraction *F*. Input data are the compositions of parent melt, differentiated melt and mineral phases. The latter are reported in Table 4. We chose the average composition of both MMEs and enderbites as representative of those of the mafic parent magma. For the compositions of daughter melts, we used the most extreme compositions of the granodiorite trend. The most evolved granodiorite is represented by sample BUL-22 (68.1 wt.% $SiO_2$) of Laurent et al. (2011). The least evolved granodiorite ($SiO_2$ = 59.6 wt.%) is sample 93_024 of Holzer (1995), but it lacks REE, Ta and Sc measurements. Therefore, we calculated the major- and the trace-element composition of a virtual primary granodiorite using linear correlations observed in most Harker diagrams, for a $SiO_2$ content of 59.0 wt.%. All compositions are reported in Table 1.

Resuts of mass-balance calculations are reported in Table 5. All cumulates are dominated by plagioclase, amphibole and biotite with subordinate amounts of ilmenite, magnetite and apatite. For the first step with a starting composition represented by average enderbite, computation has been performed using two distinct cumulates, one being amphibole-bearing (Cm02) and the other one containing pyroxenes (Cm03) (see Table 5). A cumulate including both minerals has not been considered, albeit they coexist in enderbite samples, because they cannot crystallize simultaneously. This conclusion is supported by the observation of reaction textures between both minerals (amphibole replacing clinopyroxene, in particular).

Consistency of the computed modal composition of cumulates has been tested in the light of experimental work of Sisson et al. (2005). These authors performed melting experiments on a high-K calc-alkaline gabbro (AD19-93) with a composition comparable to that of the Bulai mafic samples (Table 1). At temperatures between 800 and 900 °C, they showed that such a mafic, high-K composition yields ~15–35% melt, in equilibrium with a mineral assemblage dominated by plagioclase, amphibole and biotite. The most important observations are that (1) melt compositions encompass those of Bulai granodiorites (60–70 wt.% $SiO_2$); (2) melt proportions (17–34%) are consistent with residual melt fractions

**Table 3**
Partition coefficients used in geochemical modelling. The composition of the liquid exerts a strong control on the value of a partition coefficient for an element *i* in a given mineral. As a result, for each element and each mineral, 3 ranges of partition coefficients were selected that respectively correspond to 'mafic', 'intermediate' and 'felsic' liquids. All values were compiled from the GERM database (see http://earthref.org for references) using partition coefficients in calc-alkaline rocks including basalts, basaltic andesites ('mafic' compositions), andesites, dacites ('intermediate' compositions) and rhyolites ('felsic' compositions). Obvious outliers were excluded. Italic values for quartz are arbitrary; when no data were available for a given melt composition, we assumed that partition coefficient were the same than for other compositions.

| Mineral | Allanite | | Amphibole | | Apatite | | Biotite | | Clinopyroxene | | Ilmenite | | K-Feldspar | | Magnetite | | Orthopyroxene | | Plagioclase | | Quartz | | Zircon | |
|---|---|---|---|---|---|---|---|---|---|---|---|---|---|---|---|---|---|---|---|---|---|---|---|---|
| | Min | Max | Min | Max | Min | Max | Min | Max | Min | Max | Min | Max | Min | Max | Min | Max | Min | Max | Min | Max | Min | Max | Min | Max |
| *Partition coefficients in MAFIC liquids ($SiO_2$ < 60 wt.%)* | | | | | | | | | | | | | | | | | | | | | | | | |
| Rb | 0.02 | 0.2 | 0.1 | 0.5 | 0 | 0.003 | 2.5 | 4 | 0.003 | 0.03 | 0.0001 | 0.025 | 0.3 | 3 | 0.01 | 0.15 | 0.001 | 0.03 | 0.02 | 0.15 | *0.001* | *0.01* | 0.1 | 4 |
| Ba | 1 | 12 | 0.05 | 0.15 | 0.05 | 0.12 | 6 | 12 | 0.001 | 0.03 | 0.0001 | 0.02 | 2 | 15 | 0.01 | 0.5 | 0 | 0.05 | 0.05 | 0.4 | *0.001* | *0.01* | 0.1 | 4 |
| Th | 150 | 700 | 0.02 | 0.2 | 0.5 | 1 | 0.01 | 0.3 | 0.001 | 0.012 | 0.01 | 0.05 | 0.01 | 0.03 | 0.01 | 0.2 | 0.001 | 0.01 | 0.05 | 0.2 | *0.001* | *0.01* | 5 | 65 |
| Nb | 0.2 | 3.5 | 0.05 | 1 | 0.001 | 0.004 | 1 | 7.5 | 0.003 | 0.03 | 0.5 | 2.5 | 0.01 | 0.15 | 0.01 | 0.7 | 0.003 | 0.1 | 0.02 | 0.1 | *0.001* | *0.01* | 10 | 50 |
| Ta | 0.2 | 3.5 | 0.05 | 0.35 | 0.001 | 0.003 | 1 | 7.5 | 0.01 | 0.3 | 1 | 5 | 0.001 | 0.01 | 0.01 | 0.8 | 0.01 | 0.1 | 0.02 | 0.2 | *0.001* | *0.01* | 10 | 50 |
| La | 800 | 2500 | 0.05 | 0.4 | 1 | 10 | 0.02 | 0.4 | 0.02 | 0.2 | 0.005 | 0.1 | 0.07 | 0.15 | 0.003 | 0.07 | 0.002 | 0.015 | 0.075 | 0.25 | *0.001* | *0.01* | 1 | 10 |
| Ce | 600 | 2300 | 0.15 | 0.45 | 2 | 12 | 0.03 | 0.35 | 0.03 | 0.25 | 0.006 | 0.11 | 0.03 | 0.08 | 0.01 | 0.2 | 0.001 | 0.025 | 0.025 | 0.175 | *0.001* | *0.01* | 2 | 20 |
| Sr | 0.5 | 2 | 0.1 | 0.5 | 1 | 3 | 0.1 | 0.55 | 0.04 | 0.16 | 0.0001 | 0.02 | 1 | 5 | 0.005 | 0.03 | 0.002 | 0.02 | 1 | 2.75 | *0.001* | *0.01* | 1 | 20 |
| Nd | 250 | 1500 | 0.2 | 0.8 | 4 | 14 | 0.03 | 0.3 | 0.1 | 0.5 | 0.0075 | 0.14 | 0.02 | 0.06 | 0.02 | 0.25 | 0.003 | 0.03 | 0.02 | 0.14 | *0.001* | *0.01* | 1 | 8 |
| Zr | 0.1 | 0.3 | 0.1 | 0.6 | 0.025 | 0.1 | 0.07 | 0.75 | 0.02 | 0.25 | 0.05 | 0.28 | 0.01 | 0.4 | 0.01 | 0.1 | 0.01 | 0.07 | 0.002 | 0.014 | *0.001* | *0.01* | 300 | 3000 |
| Hf | 5 | 25 | 0.05 | 0.6 | 0.01 | 0.05 | 0.1 | 1 | 0.1 | 0.35 | 0.05 | 0.5 | 0.02 | 0.05 | 0.05 | 0.5 | 0.01 | 0.15 | 0.005 | 0.03 | *0.001* | *0.01* | 300 | 3000 |
| Sm | 100 | 900 | 0.25 | 1.75 | 4 | 15 | 0.025 | 0.35 | 0.1 | 0.8 | 0.01 | 0.2 | 0.015 | 0.045 | 0.02 | 0.3 | 0.01 | 0.11 | 0.015 | 0.11 | *0.001* | *0.01* | 5 | 20 |
| Eu | 10 | 120 | 0.2 | 1.5 | 2 | 10 | 0.03 | 0.5 | 0.25 | 0.75 | 0.01 | 0.1 | 1.5 | 7.5 | 0.01 | 0.075 | 0.01 | 0.1 | 0.05 | 0.8 | *0.001* | *0.01* | 0.5 | 10 |
| Gd | 30 | 450 | 0.3 | 2 | 3 | 17 | 0.04 | 0.45 | 0.3 | 0.9 | 0.01 | 0.2 | 0.01 | 0.035 | 0.01 | 0.3 | 0.02 | 0.15 | 0.025 | 0.07 | *0.001* | *0.01* | 15 | 35 |
| Dy | 10 | 100 | 0.3 | 2 | 3 | 15 | 0.05 | 0.5 | 0.4 | 1 | 0.01 | 0.1 | 0.01 | 0.03 | 0.01 | 0.3 | 0.025 | 0.3 | 0.015 | 0.055 | *0.001* | *0.01* | 25 | 60 |
| Y | 20 | 100 | 0.6 | 2 | 1 | 5 | 0.1 | 0.75 | 0.2 | 1.2 | 0.005 | 0.05 | 0.01 | 0.1 | 0.01 | 0.2 | 0.1 | 0.5 | 0.01 | 0.04 | *0.001* | *0.01* | 10 | 150 |
| Er | 4 | 45 | 0.25 | 1.6 | 2 | 13 | 0.075 | 0.5 | 0.3 | 0.9 | 0.01 | 0.13 | 0.01 | 0.04 | 0.01 | 0.3 | 0.025 | 0.25 | 0.005 | 0.05 | *0.001* | *0.01* | 50 | 220 |
| Yb | 2 | 30 | 0.4 | 1.6 | 1 | 8.5 | 0.1 | 0.6 | 0.2 | 0.9 | 0.01 | 0.17 | 0.015 | 0.045 | 0.015 | 0.25 | 0.05 | 0.5 | 0.002 | 0.045 | *0.001* | *0.01* | 75 | 400 |
| Lu | 1.5 | 30 | 0.2 | 1.3 | 1 | 5 | 0.25 | 0.75 | 0.3 | 1 | 0.03 | 0.2 | 0.015 | 0.05 | 0.015 | 0.15 | 0.075 | 0.75 | 0.005 | 0.05 | *0.001* | *0.01* | 100 | 500 |
| V | 0.1 | 10 | 1.5 | 10 | 0.1 | 1 | 1 | 10 | 0.5 | 5 | 5 | 25 | 0.05 | 0.25 | 5 | 45 | 0.5 | 2.5 | 0.01 | 0.45 | *0.001* | *0.01* | 0.01 | 1 |
| Sc | 50 | 65 | 2 | 10 | 0.2 | 0.5 | 5 | 17 | 1.5 | 15 | 0.5 | 2 | 0.01 | 0.04 | 0.5 | 5 | 0.5 | 5 | 0.01 | 0.1 | *0.001* | *0.01* | 50 | 80 |
| *Partition coefficients in INTERMEDIATE liquids (60 < $SiO_2$ < 70 wt.%)* | | | | | | | | | | | | | | | | | | | | | | | | |
| Rb | 0.02 | 0.2 | 0.05 | 0.33 | 0 | 0.003 | 2.5 | 4 | 0.03 | 0.05 | 0.001 | 0.025 | 0.3 | 3 | 0.01 | 0.15 | 0.01 | 0.06 | 0.03 | 0.2 | *0.001* | *0.01* | 0.1 | 4 |
| Ba | 1 | 12 | 0.08 | 0.3 | 0.05 | 0.45 | 6 | 12 | 0.08 | 0.5 | 0.001 | 0.02 | 2 | 15 | 0.01 | 0.5 | 0.003 | 0.07 | 0.1 | 0.5 | *0.001* | *0.01* | 0.1 | 4 |
| Th | 150 | 700 | 0.05 | 0.23 | 0.4 | 1.3 | 0.01 | 0.3 | 0.1 | 0.3 | 0.05 | 0.1 | 0.01 | 0.03 | 0.01 | 0.2 | 0.05 | 0.2 | 0.01 | 0.04 | *0.001* | *0.01* | 5 | 65 |
| Nb | 0.2 | 3.5 | 0.5 | 1.5 | 0.001 | 0.002 | 1 | 7.5 | 0.05 | 0.8 | 5 | 25 | 0.01 | 0.15 | 0.04 | 0.2 | 0.01 | 0.7 | 0.025 | 0.25 | *0.001* | *0.01* | 10 | 50 |
| Ta | 0.2 | 3.5 | 0.15 | 0.45 | 0.001 | 0.003 | 1 | 7.5 | 0.1 | 0.6 | 5 | 25 | 0.001 | 0.01 | 0.03 | 0.3 | 0.03 | 0.25 | 0.02 | 0.1 | *0.001* | *0.01* | 10 | 50 |
| La | 800 | 2500 | 0.1 | 0.6 | 4 | 15 | 0.02 | 0.4 | 0.5 | 3 | 0.015 | 0.3 | 0.07 | 0.15 | 0.05 | 0.5 | 0.003 | 0.1 | 0.1 | 0.4 | *0.001* | *0.01* | 1 | 10 |
| Ce | 600 | 2300 | 0.2 | 0.8 | 8.5 | 20 | 0.03 | 0.35 | 0.6 | 4 | 0.02 | 0.5 | 0.03 | 0.08 | 0.1 | 0.5 | 0.01 | 0.05 | 0.1 | 0.3 | *0.001* | *0.01* | 2 | 20 |
| Sr | 0.5 | 2 | 0.1 | 0.5 | 3 | 6 | 0.1 | 0.55 | 0.15 | 0.55 | 0.002 | 0.02 | 1 | 5 | 0.01 | 0.05 | 0.005 | 0.05 | 1.5 | 5 | *0.001* | *0.01* | 1 | 20 |
| Nd | 250 | 1500 | 0.5 | 1.5 | 10 | 40 | 0.03 | 0.3 | 0.75 | 5 | 0.03 | 0.6 | 0.02 | 0.06 | 0.2 | 0.6 | 0.015 | 0.15 | 0.05 | 0.25 | *0.001* | *0.01* | 1 | 8 |
| Zr | 0.1 | 0.3 | 0.2 | 1.5 | 0.05 | 1 | 0.07 | 0.75 | 0.15 | 0.8 | 0.3 | 3 | 0.01 | 0.4 | 0.04 | 0.4 | 0.02 | 0.12 | 0.01 | 0.15 | *0.001* | *0.01* | 300 | 3000 |
| Hf | 5 | 25 | 0.3 | 1 | 0.01 | 1 | 0.1 | 1 | 0.2 | 1 | 0.1 | 3 | 0.02 | 0.05 | 0.07 | 0.7 | 0.02 | 0.2 | 0.01 | 0.07 | *0.001* | *0.01* | 300 | 3000 |
| Sm | 100 | 900 | 0.75 | 2.5 | 15 | 50 | 0.025 | 0.35 | 1 | 8 | 0.05 | 1 | 0.015 | 0.045 | 0.3 | 0.75 | 0.015 | 0.3 | 0.04 | 0.2 | *0.001* | *0.01* | 5 | 20 |
| Eu | 10 | 120 | 1 | 2 | 12 | 25 | 0.03 | 0.5 | 1.5 | 8 | 0.03 | 0.5 | 1.5 | 7.5 | 0.2 | 0.5 | 0.02 | 0.3 | 0.25 | 1.5 | *0.001* | *0.01* | 0.5 | 10 |
| Gd | 30 | 450 | 1 | 3 | 15 | 75 | 0.04 | 0.45 | 1 | 6 | 0.05 | 1 | 0.01 | 0.035 | 0.3 | 0.75 | 0.025 | 0.3 | 0.03 | 0.11 | *0.001* | *0.01* | 15 | 35 |
| Dy | 10 | 100 | 1.5 | 3 | 10 | 45 | 0.05 | 0.5 | 2 | 8 | 0.02 | 0.8 | 0.01 | 0.03 | 0.25 | 0.6 | 0.05 | 0.5 | 0.02 | 0.1 | *0.001* | *0.01* | 25 | 60 |
| Y | 20 | 100 | 1.75 | 3.5 | 3 | 30 | 0.1 | 0.75 | 2 | 6 | 0.05 | 0.1 | 0.01 | 0.1 | 0.015 | 0.75 | 0.2 | 0.75 | 0.015 | 0.15 | *0.001* | *0.01* | 10 | 150 |
| Er | 4 | 45 | 1.25 | 2.5 | 10 | 35 | 0.075 | 0.5 | 1 | 7 | 0.02 | 0.7 | 0.01 | 0.04 | 0.2 | 0.5 | 0.05 | 0.5 | 0.01 | 0.08 | *0.001* | *0.01* | 50 | 220 |
| Yb | 2 | 30 | 1 | 2 | 6 | 20 | 0.1 | 0.6 | 2 | 7 | 0.01 | 0.5 | 0.015 | 0.045 | 0.1 | 0.5 | 0.15 | 0.65 | 0.005 | 0.075 | *0.001* | *0.01* | 75 | 400 |
| Lu | 1.5 | 30 | 0.9 | 2 | 4 | 16 | 0.25 | 0.75 | 2 | 7 | 0.01 | 0.5 | 0.015 | 0.05 | 0.2 | 0.45 | 0.3 | 0.85 | 0.01 | 0.08 | *0.001* | *0.01* | 100 | 500 |
| V | 0.1 | 10 | 3 | 10 | 0.1 | 1 | 1 | 10 | 1 | 5 | 7 | 40 | 0.05 | 0.25 | 10 | 50 | 0.75 | 3 | 0.05 | 0.5 | *0.001* | *0.01* | 0.01 | 1 |
| Sc | 50 | 65 | 5 | 15 | 0.2 | 0.5 | 5 | 17 | 3 | 20 | 1 | 15 | 0.01 | 0.04 | 1 | 15 | 2 | 15 | 0.01 | 0.1 | *0.001* | *0.01* | 50 | 80 |
| *Partition coefficients in FELSIC liquids ($SiO_2$ > 70 wt.%)* | | | | | | | | | | | | | | | | | | | | | | | | |
| Rb | 0.02 | 0.2 | 0.01 | 0.3 | 0.001 | 0.01 | 2 | 5 | 0.03 | 0.05 | 0.01 | 0.05 | 0.3 | 3 | 0.01 | 0.05 | 0.02 | 0.05 | 0.04 | 0.3 | *0.001* | *0.01* | 0.1 | 4 |
| Ba | 1 | 12 | 0.1 | 0.6 | 0.1 | 0.75 | 4.5 | 12 | 0.08 | 0.5 | 0.01 | 0.05 | 2 | 15 | 0.01 | 0.05 | 0.05 | 0.25 | 0.5 | 1.5 | *0.001* | *0.01* | 0.1 | 4 |
| Th | 300 | 600 | 0.15 | 0.3 | 0.5 | 2 | 0.5 | 1.5 | 0.1 | 0.3 | 0.1 | 0.5 | 0.01 | 0.03 | 0.02 | 0.3 | 0.1 | 0.3 | 0.01 | 0.06 | *0.001* | *0.01* | 5 | 65 |
| Nb | 0.1 | 2 | 1 | 5 | 0.01 | 0.1 | 2 | 10 | 0.05 | 0.8 | 40 | 80 | 0.01 | 0.15 | 0.5 | 2.5 | 0.3 | 0.8 | 0.05 | 0.6 | *0.001* | *0.01* | 10 | 50 |
| Ta | 1.5 | 5 | 0.2 | 0.5 | 0.01 | 0.1 | 2 | 10 | 0.1 | 0.6 | 20 | 100 | 0.001 | 0.01 | 0.75 | 3 | 0.1 | 0.75 | 0.02 | 0.06 | *0.001* | *0.01* | 10 | 50 |

Table 3 (*Continued*)

| Mineral | Allanite | | Amphibole | | Apatite | | Biotite | | Clinopyroxene | | Ilmenite | | K-Feldspar | | Magnetite | | Orthopyroxene | | Plagioclase | | Quartz | | Zircon | |
|---|---|---|---|---|---|---|---|---|---|---|---|---|---|---|---|---|---|---|---|---|---|---|---|---|
| | Min | Max | Min | Max | Min | Max | Min | Max | Min | Max | Min | Max | Min | Max | Min | Max | Min | Max | Min | Max | Min | Max | Min | Max |
| La | 800 | 3000 | 0.25 | 1.25 | 5 | 35 | 1 | 4 | 0.5 | 3 | 0.5 | 5 | 0.07 | 0.15 | 0.2 | 2 | 0.05 | 0.75 | 0.15 | 0.45 | *0.001* | *0.01* | 1 | 10 |
| Ce | 600 | 2500 | 0.5 | 2 | 10 | 45 | 0.25 | 3 | 0.6 | 4 | 1 | 8 | 0.03 | 0.08 | 0.5 | 2.5 | 0.075 | 1 | 0.15 | 0.35 | *0.001* | *0.01* | 2 | 20 |
| Sr | 0.5 | 2 | 0.1 | 1.3 | 5 | 10 | 0.1 | 0.45 | 0.15 | 0.55 | 0.05 | 0.75 | 1 | 5 | 0.01 | 0.07 | 0.01 | 0.15 | 3 | 6 | *0.001* | *0.01* | 1 | 20 |
| Nd | 400 | 1900 | 2 | 7 | 30 | 60 | 0.2 | 2.5 | 0.75 | 5 | 1 | 8 | 0.02 | 0.06 | 0.75 | 5 | 0.1 | 1 | 0.1 | 0.3 | *0.001* | *0.01* | 1 | 8 |
| Zr | 0.1 | 0.3 | 0.4 | 1 | 0.1 | 1.5 | 0.2 | 1.5 | 0.15 | 0.8 | 0.5 | 10 | 0.01 | 0.4 | 0.1 | 0.8 | 0.03 | 0.15 | 0.04 | 0.25 | *0.001* | *0.01* | 300 | 3000 |
| Hf | 5 | 30 | 0.5 | 1 | 0.1 | 1.5 | 0.4 | 0.9 | 0.2 | 1 | 0.5 | 3 | 0.02 | 0.05 | 0.2 | 2 | 0.05 | 0.25 | 0.03 | 0.3 | *0.001* | *0.01* | 300 | 3000 |
| Sm | 200 | 1000 | 3 | 10 | 25 | 75 | 0.25 | 2 | 1 | 8 | 2 | 10 | 0.015 | 0.045 | 0.5 | 4 | 0.1 | 1.5 | 0.05 | 0.2 | *0.001* | *0.01* | 5 | 20 |
| Eu | 80 | 120 | 2 | 6 | 20 | 30 | 0.1 | 1 | 1.5 | 8 | 0.3 | 3 | 1.5 | 7.5 | 0.1 | 2 | 0.1 | 1.5 | 2 | 6 | *0.001* | *0.01* | 0.5 | 10 |
| Gd | 130 | 500 | 5 | 12 | 40 | 90 | 0.1 | 1 | 1 | 6 | 3 | 8 | 0.01 | 0.035 | 0.5 | 4 | 0.3 | 1.75 | 0.05 | 0.15 | *0.001* | *0.01* | 15 | 35 |
| Dy | 100 | 150 | 6 | 13 | 30 | 60 | 0.1 | 1.2 | 2 | 8 | 1 | 5 | 0.01 | 0.03 | 0.4 | 3.5 | 0.5 | 3.25 | 0.07 | 0.18 | *0.001* | *0.01* | 25 | 60 |
| Y | 20 | 100 | 3 | 10 | 10 | 40 | 1 | 2.5 | 2 | 6 | 0.15 | 0.5 | 0.01 | 0.1 | 0.1 | 2 | 0.5 | 1.2 | 0.025 | 0.2 | *0.001* | *0.01* | 10 | 150 |
| Er | 40 | 100 | 5 | 12 | 20 | 45 | 0.1 | 0.6 | 1 | 7 | 0.75 | 4 | 0.01 | 0.04 | 0.3 | 3 | 0.5 | 2 | 0.05 | 0.1 | *0.001* | *0.01* | 50 | 220 |
| Yb | 8 | 50 | 3.5 | 8 | 15 | 25 | 0.1 | 0.7 | 2 | 7 | 0.5 | 4 | 0.015 | 0.045 | 0.25 | 2 | 0.75 | 2.5 | 0.025 | 0.09 | *0.001* | *0.01* | 75 | 400 |
| Lu | 7 | 45 | 2 | 6 | 7.5 | 21 | 0.3 | 0.8 | 2 | 7 | 0.7 | 4 | 0.015 | 0.05 | 0.2 | 1.7 | 0.9 | 3 | 0.02 | 0.1 | *0.001* | *0.01* | 100 | 500 |
| V | 0.1 | 10 | 3 | 10 | 0.1 | 1 | 1 | 10 | 1 | 5 | 7 | 80 | 0.05 | 0.25 | 10 | 130 | 2 | 10 | 0.05 | 0.5 | *0.001* | *0.01* | 0.01 | 1 |
| Sc | 50 | 65 | 5 | 15 | 0.2 | 0.5 | 5 | 17 | 3 | 20 | 1 | 15 | 0.01 | 0.04 | 1 | 15 | 30 | 120 | 0.01 | 0.1 | *0.001* | *0.01* | 50 | 80 |

predicted by calculations (15–36% when compiled for both steps); (3) the mineral phases in the experiments of Sisson et al. (2005) are the same as in the computed assemblages and (4) their relative modal proportions are similar (e.g. ~50% plagioclase, 30–40% of amphibole + biotite, <10% of apatite and Fe–Ti oxides). Consequently, the computed cumulate compositions are consistent with experimental data.

Finally, Bulai granodiorites contain accessory phases such as allanite and zircon that appear as euhedral crystals in inclusion within major minerals. This means that they formed early in the magma and, consequently, played a significant role in trace-element fractionation. Due to their low modal proportions, mass-balance calculations based on major elements do not allow us to constrain their abundance. Therefore, small amounts (<0.2% modal) of both zircon and allanite were arbitrary taken into account for trace-element modelling.

The effect of fractional crystallization (FC) on trace elements was modelled using the Rayleigh equation ($C_L^i = C_0^i \times F^{D^i - 1}$ where $C_0^i$ and $C_L^i$ are the concentrations of element $i$ in the parent and daughter melts respectively, $F$ the melt fraction and $D^i$ the global partition coefficient for element $i$). For equilibrium crystallization (EC), we used the equation of Shaw (1970) originally formulated for equilibrium melting processes, but equally applicable to crystallization ones.

Fig. 6 presents the results of FC–EC models for the first crystallization step. Compositions of the computed melts are similar for both crystallization mechanisms. The modelled liquids fail in reproducing the composition of the calculated 'primary' granodiorite when the parental magma has a MME composition (Fig. 6a). In particular, REE and Nb–Ta contents are far too high. An enderbitic parental liquid seems to be more suitable. Its differentiation roughly accounts for all trace element contents especially when the amphibole-bearing cumulate (Cm02) is considered: in this case, the shape of the natural pattern is well reproduced by the modelled liquids (Fig. 6b).

Results for the second step (differentiation from the 'primary' granodiorite to the most evolved one) are presented in Fig. 7. There are no significant differences between the melts computed by EC and FC. Both reasonably well fit the composition of the most evolved granodiorite, with the exception of the REE fractionation: La/Yb is too low in the models, because of higher calculated HREE contents than in the samples. In addition, samples BUL-16, BUL-22 and BUL-23 are clearly different in composition with respect to the other granodiorites, as stated for the mixing model (see Section 4.1). Their trace-element signatures can be accounted for neither by FC, nor by EC: in particular, Nb–Ta, Y and HREE of these 3 samples are lower than in the calculated residual melts.

### 4.3. Model 3: crystallization coupled with assimilation (E–FCA)

'Open-system' crystallization was simulated using the equation of decoupled Fractional Crystallization and Assimilation (FCA) proposed by Cribb and Barton (1996). The FCA equation was here adapted to model decoupled Equilibrium Crystallization and Assimilation (ECA) by replacing for FC term in the original formulation of Cribb and Barton (1996) by a EC term, which is the equation of Shaw (1970). We applied the same differentiation sequence as used for Model 2 (see Section 4.2), with identical datasets of partition coefficients (Table 3) and modal compositions of cumulates (Table 5).

Three putative assimilated materials (also termed 'contaminants' hereafter) are spatially associated with Bulai granodiorites: metapelites of the Beit Bridge Complex (BBC), the Sand River TTG gneisses and the Bulai leucogranites. In order to account for the isotopic homogeneity of the whole Bulai suite, the assimilated

**Table 4**
Major-element compositions of rock-forming minerals in Bulai samples. For each mineral, we calculated the average composition (re-calculated on anhydrous basis) from several analyses (*N* is the number of analyses). Compositions were determined by in situ analyses on carbon-coated, polished thin sections (~30 μm) using the Cameca SX100 electron microprobe of the Laboratoire Magmas et Volcans in Clermont-Ferrand (standard operating conditions: 15 kV accelerating voltage; 10 s counting time by element and a beam current of 20 nA).

| Mineral | Ap | Amph | Bt | Cpx | Ilm | Kfs | Mt | Opx | Plag |
|---|---|---|---|---|---|---|---|---|---|
| *N* | *10* | *25* | *31* | *23* | *6* | *18* | *7* | *38* | *42* |
| *Major oxides (wt.%)* | | | | | | | | | |
| $SiO_2$ | 0.27 | 43.71 | 39.08 | 51.77 | 0.03 | 64.62 | 0.04 | 52.65 | 60.39 |
| $TiO_2$ | 0.00 | 2.08 | 4.86 | 0.25 | 41.64 | 0.05 | 0.03 | 0.09 | 0.00 |
| $Al_2O_3$ | 0.00 | 11.03 | 14.49 | 2.46 | 0.06 | 18.76 | 0.15 | 1.19 | 24.93 |
| $FeO_T$[a] | 0.08 | 16.09 | 15.86 | 10.62 | 58.19 | 0.04 | 99.75 | 25.06 | 0.12 |
| MgO | 0.00 | 11.60 | 15.07 | 12.75 | 0.00 | 0.00 | 0.00 | 20.31 | 0.00 |
| CaO | 56.28 | 12.00 | 0.01 | 21.60 | 0.03 | 0.06 | 0.03 | 0.66 | 7.00 |
| $Na_2O$ | 0.00 | 1.72 | 0.13 | 0.55 | 0.04 | 1.05 | 0.00 | 0.02 | 7.26 |
| $K_2O$ | 0.00 | 1.79 | 10.50 | 0.00 | 0.00 | 15.41 | 0.00 | 0.01 | 0.30 |
| $P_2O_5$ | 43.37 | 0.00 | 0.00 | 0.00 | 0.00 | 0.00 | 0.00 | 0.00 | 0.00 |

Mineral abbreviations: Ap, apatite; Amph, amphibole; Bt, biotite; Cpx, clinopyroxene; Ilm, ilmenite; Kfs, K-feldspar; Mt, magnetite; Opx, orthopyroxene; Plag, plagioclase feldspar.

[a] All iron measured as FeO.

material would necessarily have the same $\varepsilon_{Nd}$ as the parental liquid at 2.6 Ga, i.e. almost chondritic values. Fig. 4f shows that the Bulai leucogranites and the BBC metapelites fulfil this requirement, whereas the $\varepsilon_{Nd}$ values of the Sand River Gneisses are too low to be considered as suitable contaminants. The major- and trace-element compositions of the assimilated materials tested in the models are presented in Table 1.

For each parental liquid and each contaminant, the calculations were performed for different values of crystallization rate ($1-F$) and assimilation rate ($R = M_a/M_c$, i.e. the mass ratio between assimilated material and crystallized material). The compositional ranges of FCA–ECA computed liquids whose compositions best fit those of real granodiorites, are presented in Figs. 8 and 9 for the first and second steps of the modelling, respectively. Results show that there are no chemical differences between the liquids modelled by the two different mechanisms. Computed liquids better match the composition of the calculated 'primary' granodiorite than for 'closed-system' FC or EC models (see Section 4.2), whatever the parental melt considered (Fig. 8). Moreover, computed values of $1-F$ are lower than for crystallization models without assimilation. *R* values are low (0.1–0.2) for enderbite parental melts, whereas they are higher (0.4–0.5) when MME is considered as starting material.

**Table 5**
Best modal compositions of fractionated solids obtained by mass-balance calculations between parent and daughter compositions using XLFRAC algorithm (Stormer and Nicholls, 1978). $\Sigma R^2$ is the sum of the squared differences for all major oxides between calculated and natural compositions, and $1-F$ gives the crystallization rate.

| Initial composition | MME | Enderbite | | Mafic PGd. |
|---|---|---|---|---|
| Final composition | Mafic PGd. | Mafic PGd. | | Felsic PGd. |
| | Cm-01 | Cm-02 | Cm-03 | Cm-04 |
| Allanite[a] | 0.05 | 0.05 | 0.05 | 0.08 |
| Amphibole | 15 | 39.3 | 0 | 12.2 |
| Apatite | 6.5 | 3 | 3.2 | 3.3 |
| Biotite | 15.2 | 6 | 18 | 16.5 |
| Clinopyroxene | 0 | 0 | 17 | 0 |
| Ilmenite | 4.7 | 2 | 3.8 | 2.4 |
| K-Feldspar | 0 | 0 | 0 | 0 |
| Magnetite | 7.5 | 0.6 | 0 | 5.3 |
| Orthopyroxene | 0 | 0 | 3.3 | 0 |
| Plagioclase | 51 | 49 | 54.5 | 60 |
| Zircon[a] | 0.08 | 0.08 | 0.08 | 0.15 |
| $\Sigma R^2$ | 0.77 | 0.35 | 0.41 | 0.10 |
| $1-F$ | 0.75 | 0.40 | 0.47 | 0.42 |

[a] Trace amounts of zircon and allanite has been added to the fractionated solids to account for their presence as early crystals in the Bulai samples (see text for details).

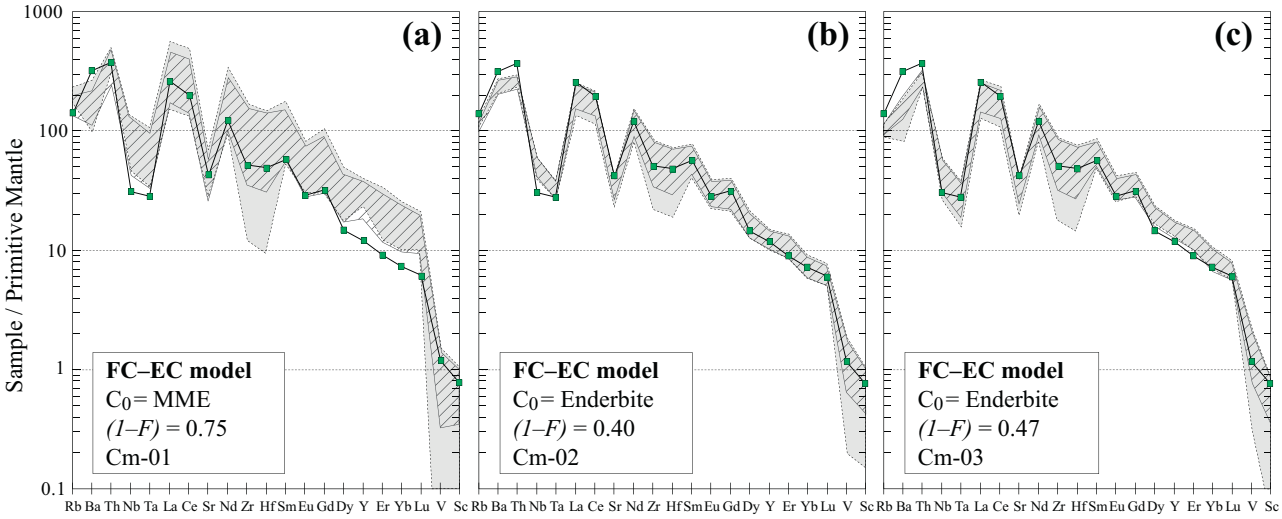


**Fig. 6.** Primitive mantle-normalized trace-element patterns for Monte-Carlo models of crystallization from mafic compositions (Step 1). The grey and hatched fields represent the compositional range of liquids calculated by fractional crystallization (FC) and equilibrium crystallization (EC), respectively. (a), (b) and (c) correspond to various initial compositions ($C_0$; see Table 1), crystallization rates ($1-F$) and cumulate compositions (Cm-0X; see Table 5) are indicated in the caption. The bold pattern with green squares represents the expected final composition of the liquid, i.e. the calculated 'primary' granodiorite. See text for a detailed description. (For interpretation of the references to colour in this figure legend, the reader is referred to the web version of this article.)

**Table 6**
Summary of parameters used for modelling of the partial melting sequence (see Section 3.4 for details).

| Source rock | Enderbite | | | | | | | | MME | | | | | | | |
|---|---|---|---|---|---|---|---|---|---|---|---|---|---|---|---|---|
| Step | Step 1[a] | | Step 2[b] | | | Step 3[c] | | | Step 1[a] | | Step 2[b] | | | Step 3[c] | | |
| $F$ | 0.15 | | 0.144 | | | *0.1*[d] | | | 0.12 | | 0.216 | | | *0.1*[d] | | |
| $F_T$ | 0.15 | | 0.294 | | | *0.394* | | | 0.12 | | 0.336 | | | *0.436* | | |
| | $X_0$ | $p_i$ | $X_1$ | $p_i$ | $T_i$ | $X_2$ | $p_i$ | $T_i$ | $X_0$ | $p_i$ | $X_1$ | $p_i$ | $T_i$ | $X_2$ | $p_i$ | $T_i$ |
| Allanite | 0.05 | | 0.05 | | | 0.05 | | | 0.05 | | 0.05 | | | 0.05 | | |
| Amphibole | 17 | | 20 | | 0.4 | 34.5 | 0.5 | | 18 | | 20.5 | | 0.4 | 44.5 | 0.5 | |
| Apatite | 3 | | 4 | | | 4.5 | | | 3 | | 3.5 | | | 4.5 | | |
| Biotite | 10 | | 12 | 0.5 | | 0 | | | 16 | | 18 | 0.5 | | 0 | | |
| Cpx | 5 | | 6 | | | 7 | | 0.6 | 0 | | 0 | | | 0 | | 0.6 |
| Ilmenite | 2 | | 2.5 | | | 2.9 | | | 3 | | 3.5 | | | 4.5 | | |
| KFs | 5 | 0.33 | 0 | | | 0 | | | 4 | 0.33 | 0 | | | 0 | | |
| Magnetite | 3 | | 3.5 | | | 4 | | | 4 | | 4.5 | | | 5.7 | | |
| Opx | 3 | | 3.5 | | | 4 | | 0.2 | 0 | | 0 | | | 0 | | 0.2 |
| Plagioclase | 47 | 0.33 | 48.5 | 0.5 | | 43 | 0.5 | | 48 | 0.33 | 50 | 0.5 | | 40.8 | 0.5 | |
| Quartz | 5 | 0.33 | 0 | | | 0 | | | 4 | 0.33 | 0 | | | 0 | | |
| Zircon | 0.08 | | 0.08 | | | 0.08 | | | 0.08 | | 0.08 | | | 0.08 | | |

$X_0$: initial modal composition (in %) of the source rock calculated by mass-balance between major-element compositions of whole-rock and mineral phases. $X_1$, $X_2$: modal compositions (in %) of residual solids at the onset of Steps 2 and 3, respectively. Mass fractions are re-calculated from values at the end of the prior step. $p_i$: relative proportions of phases contributing to the melt. $T_i$: relative proportions of phases produced by incongruent melting (the relative proportion of liquid produced is $1-[\Sigma T_i]$). $F$: mass fraction of liquid at the end of the melting step with respect to the onset of the given step, calculated to account for exhaustion of one or several melt-producing phases. $F_T$ is the total amount of melt with respect to the initial source rock.

[a] Step 1: Equilibrium, non-modal melting of quartz, K-feldspar and plagioclase in eutectic proportions.
[b] Step 2: Incongruent melting of biotite and plagioclase to produce amphibole and melt.
[c] Step 3: Incongruent melting of amphibole and plagioclase to produce melt and pyroxenes.
[d] An arbitrary value of $F=0.1$ was applied for the last melting step.

This modelling also shows that, except minor discrepancies for Rb, Ba and Th, leucogranite BUL-26 (rather than metapelite) is the contaminant that better matches the composition of the 'primary' granodiorite (Fig. 8). In particular, Sr, Nb, Ta and HREE concentrations are better reproduced. Concerning the second step, the liquids generated when assimilation of leucogranite is taken into account also well fit the composition of felsic granodiorites (Fig. 9). By contrast, the melt compositions computed using metapelite assimilation are slightly too rich in HREE compared with analytical data. Importantly, contribution of assimilation is greater than for the first differentiation step, as values of the parameter $R$ are significantly higher (0.5–0.75). Finally, as already observed for FC and EC models, the trace-element compositions of granodiorites BUL-16, BUL-22 and BUL-23 cannot be explained by E–FCA models, even when high assimilation rates ($R>0.75$) are taken into account.

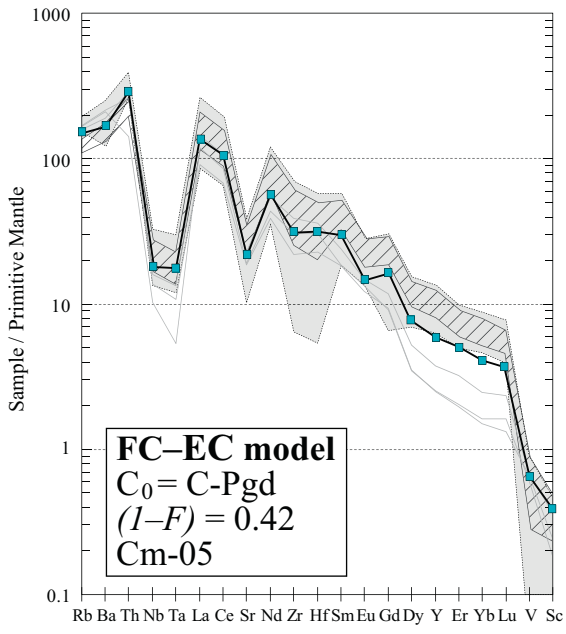


**Fig. 7.** Primitive mantle-normalized trace-element patterns for Monte-Carlo models of crystallization from the calculated 'primary' granodiorite (C-Pgd). Signification of fields and parameters in the caption are the same as Fig. 6. The bold pattern with blue squares is the expected final composition of the liquid represented by a felsic granodiorite (sample BUL-20 of Laurent et al., 2011). The light grey patterns represent the compositions of samples BUL-16, BUL-22 and BUL-23 that have a distinctive geochemical signature (see text for details). (For interpretation of the references to colour in this figure legend, the reader is referred to the web version of this article.)

### 4.4. Model 4: partial melting of mafic rocks

In this section, derivation of the Bulai granodiorites by partial melting of mafic rocks, similar in composition either to MME or enderbites (Table 1) has been tested. Melting is a sequential process involving successive exhaustion of different mineral phases, therefore we inferred a melting sequence for high-K, amphibole- and biotite-bearing mafic rocks. Experimental results have shown that three successive melting steps can be distinguished. (1) There are no available data below 825 °C, but so close to the solidus, it is likely that melting produces a 'minimum melt' by consuming quartz, K-feldspar and plagioclase in eutectic proportions. (2) Experimental melting runs by Sisson et al. (2005) on starting composition AD19-93 (Table 3) showed that melt and amphibole proportions increase with temperature between 825 and 950 °C, whereas plagioclase and biotite contents decrease. This suggests that biotite and plagioclase melt incongruently to produce amphibole and melt, as already proposed by Helz (1976). (3) After exhaustion of biotite, the melting reaction is derived from experimental work on amphibolite systems (e.g. Beard and Lofgren, 1991; Rapp and Watson, 1995). According to these studies, incongruent melting of plagioclase and amphibole occurs to produce melt as well as ortho- and clinopyroxene. Equilibrium melting at the first step was modelled with the equations of Shaw (1970), while formulation of Hertogen and Gijbels (1976) was used for incongruent melting at subsequent steps. The melting parameters (proportions of phases that contribute to the melt, or formed by peritectic reactions) were estimated for the second and third steps from experiments of Sisson et al. (2005) and Beard and Lofgren (1991), respectively. All parameters are detailed in Table 6. Similarly to crystallization models, a

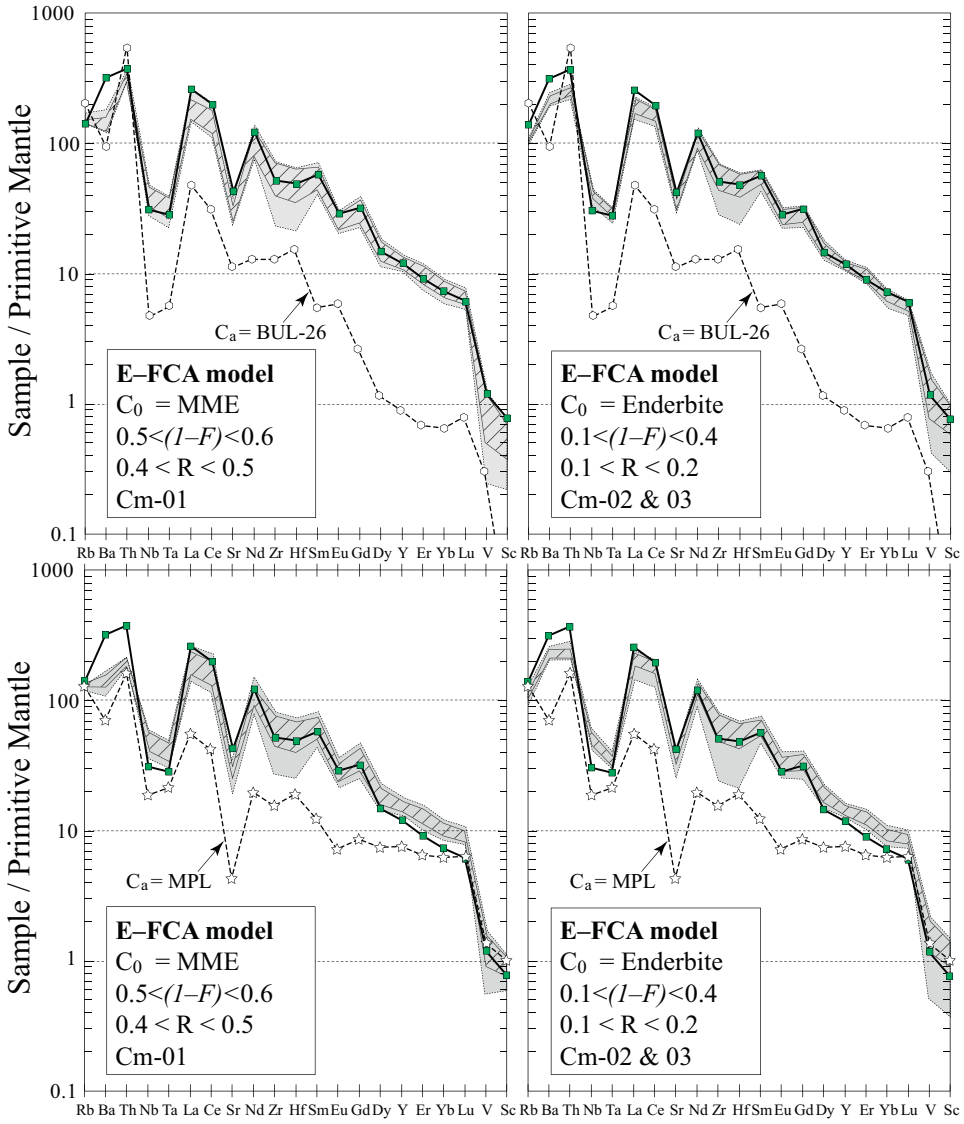


**Fig. 8.** Primitive mantle-normalized trace-element patterns for Monte-Carlo models of crystallization from mafic compositions (Step 1) coupled with assimilation. Signification of fields and parameters in the caption are the same as Fig. 6. *R* is the mass ratio between assimilated material and crystallized solid. The composition of the assimilated material is also represented (BUL-26, Bulai leucogranite; MPL, metapelites; see Table 1). The bold pattern with green squares represents the expected final composition of the liquid, i.e. the calculated 'primary' granodiorite. See text for a detailed description. (For interpretation of the references to colour in this figure legend, the reader is referred to the web version of this article.)

Monte-Carlo approach has been applied, with random selection of partition coefficients in appropriate ranges for each step (see Section 4.2 and Table 3). The same mineral compositions were used as for crystallization models (Table 4).

Modelling does not show conclusive results when considering MME as the source. The calculations generally predict HFSE (Nb–Ta, Y) and HREE (Gd–Yb) concentrations that are too high or global shapes of trace-element patterns that are not consistent with those of Bulai granodiorites (Fig. 10). By contrast, modelling with an enderbite source shows an excellent fit between calculated compositions and natural samples for the second melting step. The third melting step is actually not required: it results in less consistent trace-element patterns, notably for Rb, Ba and HREE (Fig. 10). Consequently, melting of mafic rocks similar to the Bulai enderbites, with a mass fraction of liquid comprised between 15 and 30% (calculated *F* at the onset and end of the second step; see Table 6) produces liquids with trace-element concentrations that closely match those of Bulai granodiorites. Finally, it must be noted that the compositions of low-(Nb, Ta, Y, HREE) samples BUL-16, BUL-22 and BUL-23 are not reproduced by any of the melting models.

### 4.5. Origin of low-(Nb, Ta, Y, HREE) granodiorites and leucogranite

The composition of samples BUL-16, BUL-22 and BUL-23 is accounted for by neither magma mixing between mafic and felsic liquids, nor E–FCA, nor partial melting. These three samples represent differentiated granodiorites (65.9–68.1 wt.% $SiO_2$) that have slightly different trace-element signatures than all other samples. In particular, they show more fractionated REE patterns, lower Nb–Ta and Y concentrations with conversely higher Sr/HFSE ratios and no negative Eu anomaly. Such geochemical characteristics, to some extent, resemble those of the Bulai leucogranites. As a result, we propose that they represent mixing between the latter and "classical" granodiorites. Fig. 11 provides further support for such a model. In selected trace-element diagrams, samples BUL-16, BUL-22 and BUL-23 plot along broad mixing curves between the average composition of Bulai leucogranites on the one hand, and the average composition of "classical" granodiorites on the other hand.

Concerning the leucogranites, they could derive either (1) from extreme fractionation of granodioritic liquids or (2) from

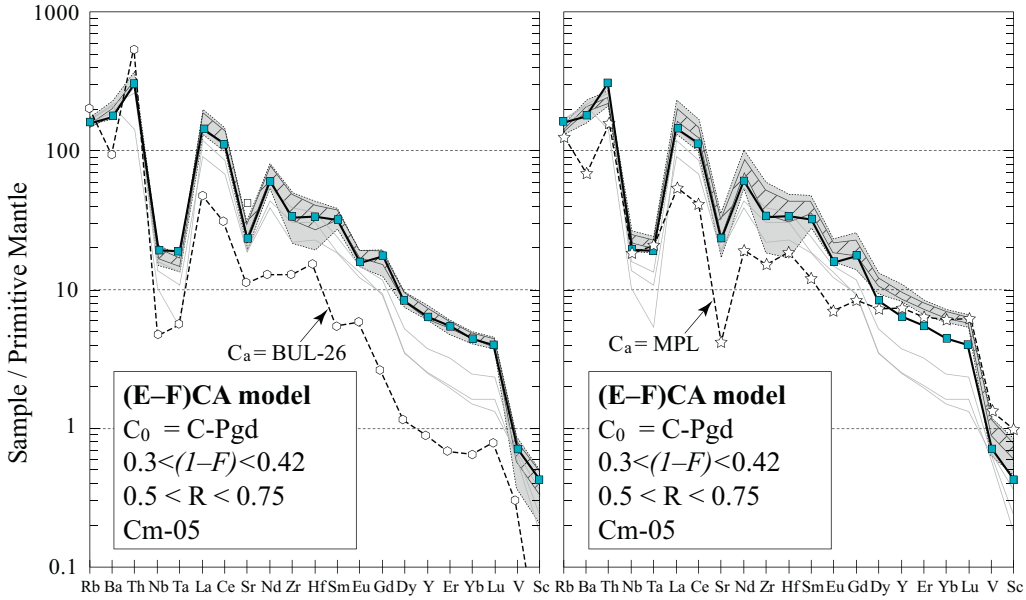


**Fig. 9.** Primitive mantle-normalized trace-element patterns for Monte-Carlo models of crystallization from the calculated 'primary' granodiorite (C-Pgd; Step 2) coupled with assimilation. Signification of fields and parameters in the caption are the same as Figs. 6 and 8. The composition of the assimilated material is also represented (same labels as Fig. 8). The bold pattern with blue squares is the expected final composition of the liquid represented by a felsic granodiorite (sample BUL-20 of Laurent et al., 2011). The light grey patterns represent the compositions of samples BUL-16, BUL-22 and BUL-23. (For interpretation of the references to colour in this figure legend, the reader is referred to the web version of this article.)

low-degree melting of the mafic rocks. The first hypothesis can be ruled out: indeed, the trace-element patterns of leucogranites show no negative Sr anomaly and a slight, positive Eu anomaly (Fig. 4e). Such features are unlikely to characterize a melt that differentiated through plagioclase fractionation, which is typical for such I-type granitoids. By contrast, they are consistent with melting of plagioclase together with quartz and K-feldspar, as assumed at the onset of the melting model (see Section 4.4). Moreover, in this case, computed melts show trace-element concentrations close to that of leucogranites (Fig. 10, to be compared with trace-element patterns of leucogranites in Fig. 4e). As a result, we suggest that the latter generated through low-degree (<10%) partial melting of the Bulai enderbites.

## 5. Discussion

### 5.1. Discrimination between petrogenetic models

The modelling presented here does not highlight a single mechanism responsible for the origin of Bulai granodiorites. Indeed, from a geochemical point of view, the isotopic, major- and trace-element signatures of these rocks can be acquired either by magma mixing, fractional crystallization with or without assimilation, or by partial melting of mafic rocks (see Fig. 11 and Section 4). The aim of this section is to establish whether one of these hypotheses appears more robust and reliable than the others.

If magma mixing is retained as the main petrogenetic process responsible for the genesis of Bulai granodiorites, it would have been efficient enough to have given rise to significant volumes (approximately, several tens of $km^3$) of relatively homogeneous, hybrid granodioritic magma. However, in the case of the Bulai pluton, both end-members contrast strongly in terms of chemical composition and by extension, viscosity (e.g. Poli et al., 1996; Sparks and Marshall, 1986). This limits their ability to mix at pluton scale (Barbarin, 2005; Jellinek and Kerr, 1999), and would rather produce mingling relationships (e.g. mafic enclaves) that are ubiquitous in the Bulai pluton. Consequently, these observations show that magma mixing cannot be the unique process accounting for the genesis of the granodiorites.

All EC and FC models require relatively high degrees of crystallization (>40%) that would make physical extraction of the cumulate difficult: for >35% crystals, gravity-controlled processes such as cumulate settling are no longer efficient (Fernandez and Gasquet, 1994). Nevertheless, a combination of E–FC with assimilation seems to be a reliable alternative. Indeed, E–FCA models generally yield much better results than E–FC or mixing models, and assimilation leads to lower, and more realistic, calculated degree of crystallization. In the case of Bulai, we showed that the match between modelled and natural composition is better when assimilation of leucogranite is considered instead of metapelite. As granodiorites and leucogranites are coeval and comagmatic, we consider that Mixing plus Fractional Crystallization (MFC; cf. Christophides et al., 2007; Poli et al., 1996), rather than E–FCA, likely occurred. Such a process is indeed potentially more efficient than E–FCA. In the latter case, a fraction of the energy dissipated by the crystallizing magma (latent heat) is required to melt the solid contaminant, which is not the case for MFC processes (Thompson et al., 2002).

In addition, Christophides et al. (2007) highlighted that during the early stages of mafic–felsic magma interaction, strong thermal and viscosity contrasts between both liquids may inhibit significant mixing such that crystallization processes would prevail. However, as the mafic melt evolves toward more silicic compositions, the rheological contrast progressively decreases and mixing becomes more viable. Similar behaviour is noticed in our numerical simulations: the value of $R$ (mass ratio between assimilated and crystallized materials) increases between Step 1 (0.1–0.5) and Step 2 (0.5–0.75). Subsequently, as MFC processes produce evolved granodioritic magmas ($SiO_2$ > 65 wt.%), mixing with granitic melt becomes increasingly efficient such that it could be the single mechanism that produced the more differentiated samples BUL-16, BUL-22 and BUL-23 (see Section 4.5 and Fig. 11).

On the other hand, modelling also showed that 15–30% partial melting of monzodioritic rocks similar to the Bulai enderbites could account for the geochemical characteristics of the

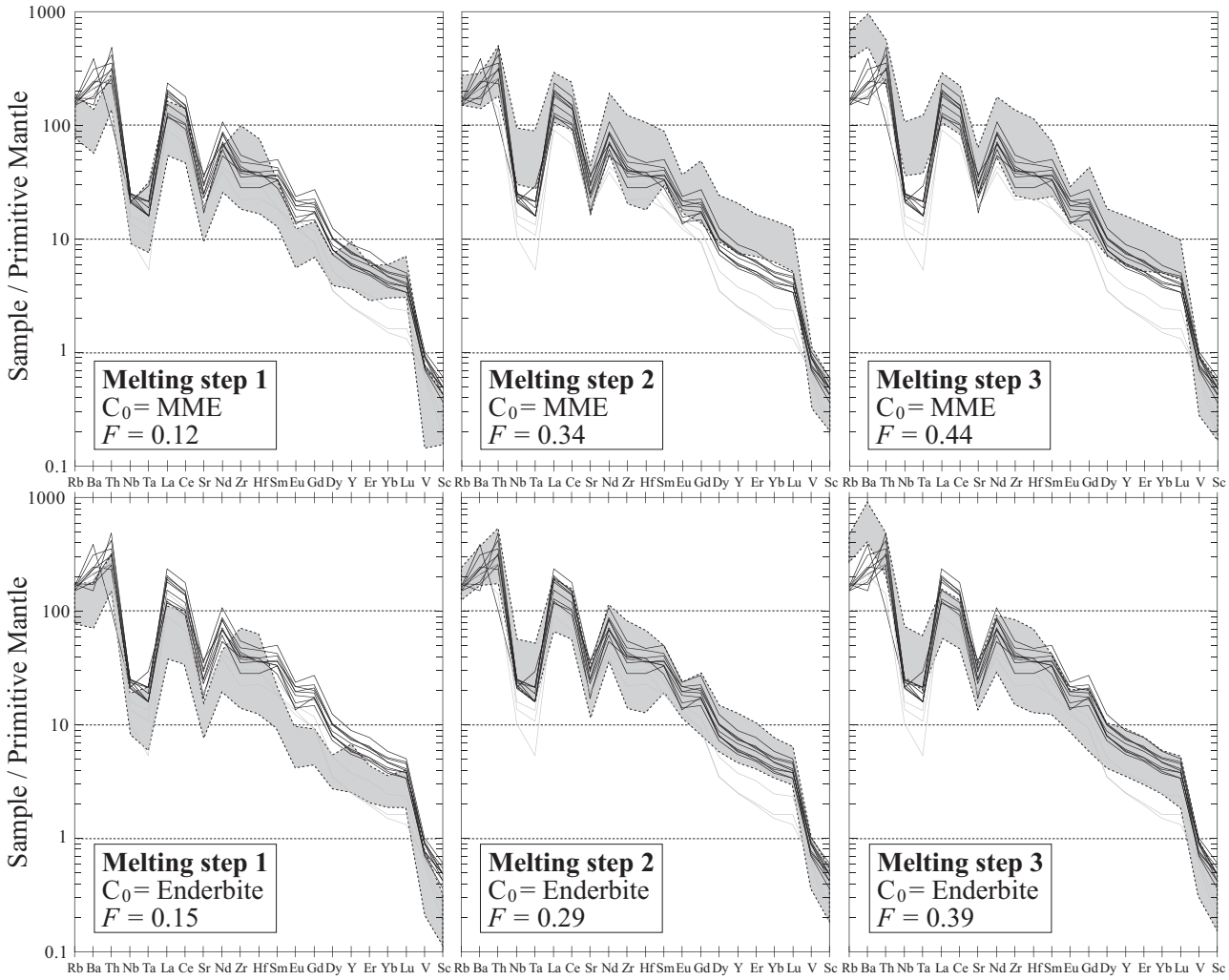


**Fig. 10.** Primitive mantle-normalized trace-element patterns for the Bulai granodiorites (black patterns) as well as Monte-Carlo models of partial melting following the melting sequence described in Section 4.4. Models were tested for source rocks represented by MME and enderbites (upper and lower part, respectively). The grey field represents the compositional range of computed liquids with the melting rate (*F*) indicated in the caption for the three successive melting steps (see Table 6 and text for explanation). The light grey patterns represent the compositions of samples BUL-16, BUL-22 and BUL-23. Note that the best fit is obtained for the Step 2 of enderbite melting.

granodiorites. The experiments of Sisson et al. (2005) showed that the amount of liquid is strongly dependant on temperature and $fO_2$ conditions. The oxygen fugacity of the magma that crystallized to form the Bulai granodiorites was probably above the Ni–NiO (NNO) buffer as magnetite is the main Fe–Ti oxide (e.g. Naney, 1983). For $fO_2$ = +3.5 △NNO, melting produces only 23% melt at 925 °C (Sisson et al., 2005). As a consequence, the genesis of the least evolved granodiorites ($F \sim 30\%$; see Section 4.4) by partial melting of mafic rocks would have required unrealistic temperatures (~1000 °C). Furthermore, stability of amphibole, a mineral that generally appears as an euhedral phase, indicates that the initial granodioritic melt contained up to 6 wt.% $H_2O$ (Bogaerts et al., 2006; Costa et al., 2004; Naney, 1983). Typically, for temperatures above 900 °C, the $H_2O$ content of a melt produced by dehydration melting of mafic rocks would not exceed 4 wt.% (Clemens and Watkins, 2001; Scaillet et al., 1998), thus precluding derivation of the least-evolved granodiorites by such a process.

Therefore, genesis of the least evolved granodiorites (<65 wt.% $SiO_2$) via melting of mafic rocks requires unrealistic $T$–$fO_2$–$H_2O$ melting conditions. Nevertheless, this process could have produced differentiated liquids ($SiO_2$ > 65 wt.%). In this case, the geochemical characteristics of the least evolved granodiorites could result from incomplete separation of the residual source material, a process that has already been invoked to account for geochemical variability of S-type granitoids (Chappell et al., 1987; Stevens et al., 2007; Villaros et al., 2009) and could equally be applied to I-type ones.

We tested this model by calculating the major-element composition of virtual residual solids produced by partial melting of the Bulai mafic rocks that could be entrained by granitoid melt. Mineral compositions are similar as used in crystallization and melting models (Table 4), whereas modal proportions are derived from experiments by Sisson et al. (2005). In Harker diagrams, the granodiorite trend closely fits the mixing line between a "pristine" granitoid melt (similar to the most evolved granodiorites with $SiO_2$ ~68 wt.%) and the calculated residual solids (Fig. 12). The geochemical diversity of the Bulai granodiorites might therefore result from various proportions (0 to ~35 wt.%) of entrained material from the melting region. Such a process would also produce linear variations of trace elements as a function of $SiO_2$, as it is observed for Bulai pluton (Laurent et al., 2011). In this case, entrainment of accessory phases from the source would be of key importance in generating linear variations in Th, LREE (allanite), MREE, Sr (apatite), HREE, Zr and Y (zircon). Finally, this hypothesis is supported by occurrence of mafic clusters in Bulai granodiorites, containing the same minerals as the expected residual solids (amphibole + biotite + plagioclase ± Fe–Ti oxides, apatite, allanite, zircon). However, in the case of Bulai, even the most mafic

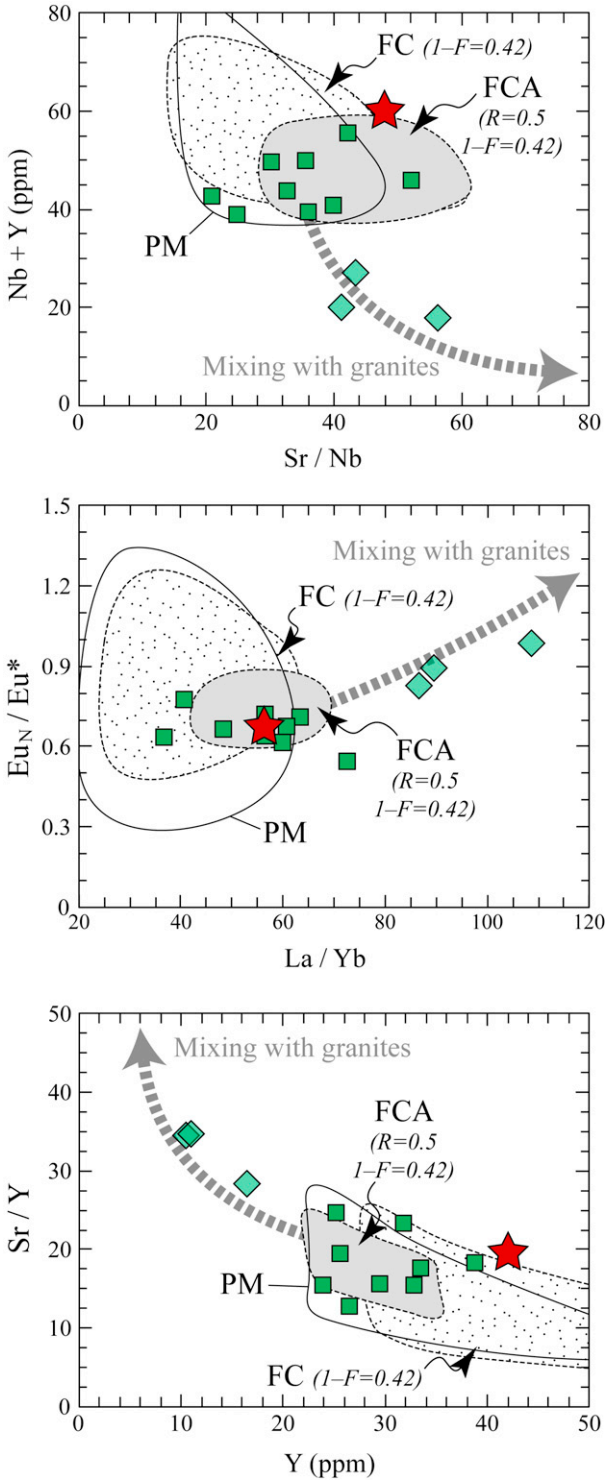


**Fig. 11.** Trace-element diagrams for the Bulai granodiorites and Monte-Carlo models of: (i) fractional crystallization (FC; dotted fields) for Step 2; (ii) fractional crystallization coupled with assimilation of leucogranite (FCA; grey fields) for Step 2 and (iii) partial melting of enderbite (PM), second melting step. Model envelopes are contoured for 95% of the data. The red star represents the compositions of calculated 'primary' granodiorite (see Table 1 and Section 5.2), the dark green squares the ones of the 'classical' Bulai granodiorites and the light green diamonds those of samples BUL-16, BUL-22 and BUL-23. The grey dashed arrows represent mixing curves between average composition of granodiorites and average composition of leucogranites (not represented). $Eu^* = (Sm_N + Gd_N)/2$. (For interpretation of the references to colour in this figure legend, the reader is referred to the web version of this article.)

granodiorites do not contain as much as 35% of mafic clusters, questioning the validity of this model. As a result, it may not be fully relevant for the genesis of the Bulai granodiorites, but could account for the one of other sanukitoid suites.

To conclude, the genesis of Bulai granodiorites might result from two distinct scenarios:

(1) Wet, mafic mantle-derived melts roughly similar in composition to the Bulai enderbites intruded in the crust. Their crystallization supplied fluids and latent heat that triggered low-degree melting of surrounding crustal rocks (either pre-existing mafic rocks or meta-sedimentary material) to produce leucogranite. This liquid subsequently mixed with the continuously crystallizing mafic melt to form the least evolved granodioritic magma (step 1 of Section 4.3). The magma then evolved in turn by MFC (step 2 of Section 4.3) and, as rheological contrast with leucogranitic melt decreased, magma mixing became increasingly efficient to give rise to the observed range of granodiorite compositions. This process is summarized in Fig. 13a.

(2) Instead of evolving by MFC, the mafic magma would have crystallized at mid-crustal depths to form amphibole- and biotite-bearing high-K mafic rocks. Continuous injection of voluminous mafic liquids provided heat and fluids to induce 15–20% dehydration melting of these monzodiorites. The resulting granodioritic liquid (~67 wt.% $SiO_2$) was not extracted as a body of completely molten magma, but rather contained solid assemblages of residual character. Transfer and subsequent emplacement of magma batches, with various proportions of entrained crystals from the source, yielded the geochemical range of Bulai granodiorites. This model is summarized in Fig. 13b. Because the mafic clusters in Bulai granodiorites cannot be unequivocally interpreted as reflecting entrained material, this model is less constrained than the first one and, consequently, less likely.

Both scenarios are comparable to the model of a "Deep Crustal Hot Zone" (Annen et al., 2006) that implies differentiation of mafic material in the lower crust, triggered by continuous injection of wet mantle-derived melts. As a result, whatever the mechanism considered to explain the origin of Bulai granodiorites, it probably occurred at relatively high depth (20–30 km) in the crust. This accounts for the absence of cumulative material in the Bulai pluton as well as the subordinate amount of exposed mafic rocks with respect to the granitoids. In this perspective, granodiorite magmas were extracted to emplace as relatively homogeneous magma batches. This hypothesis is consistent with the idea that granitoid plutons likely represent incrementally emplaced, small magmatic bodies rather than large long-lived magma chambers (Glazner et al., 2004).

### 5.2. Implications for the differentiation of sanukitoid series

Former studies on the petrogenesis of "differentiated sanukitoids" generally highlighted a single process at the origin of these rocks: either FC (Stern and Hanson, 1991), or AFC (Stevenson et al., 1999) or binary magma mixing (Moyen et al., 2001). The present study points out that interplay of multiple processes, involving the crystallization of wet, mantle-derived magma and mixing with felsic melts in increasing amounts during differentiation, is the most appropriate petrogenetic mechanism for these rocks. Such a model is very similar to the one of Tatsumi (2008) that studied the differentiation of Phanerozoic high-Mg andesites, similar in composition to Archaean sanukitoid suites. He suggested that the most silicic lavas result from 'self-mixing' between the primary, mantle-derived mafic ones and their differentiation products.

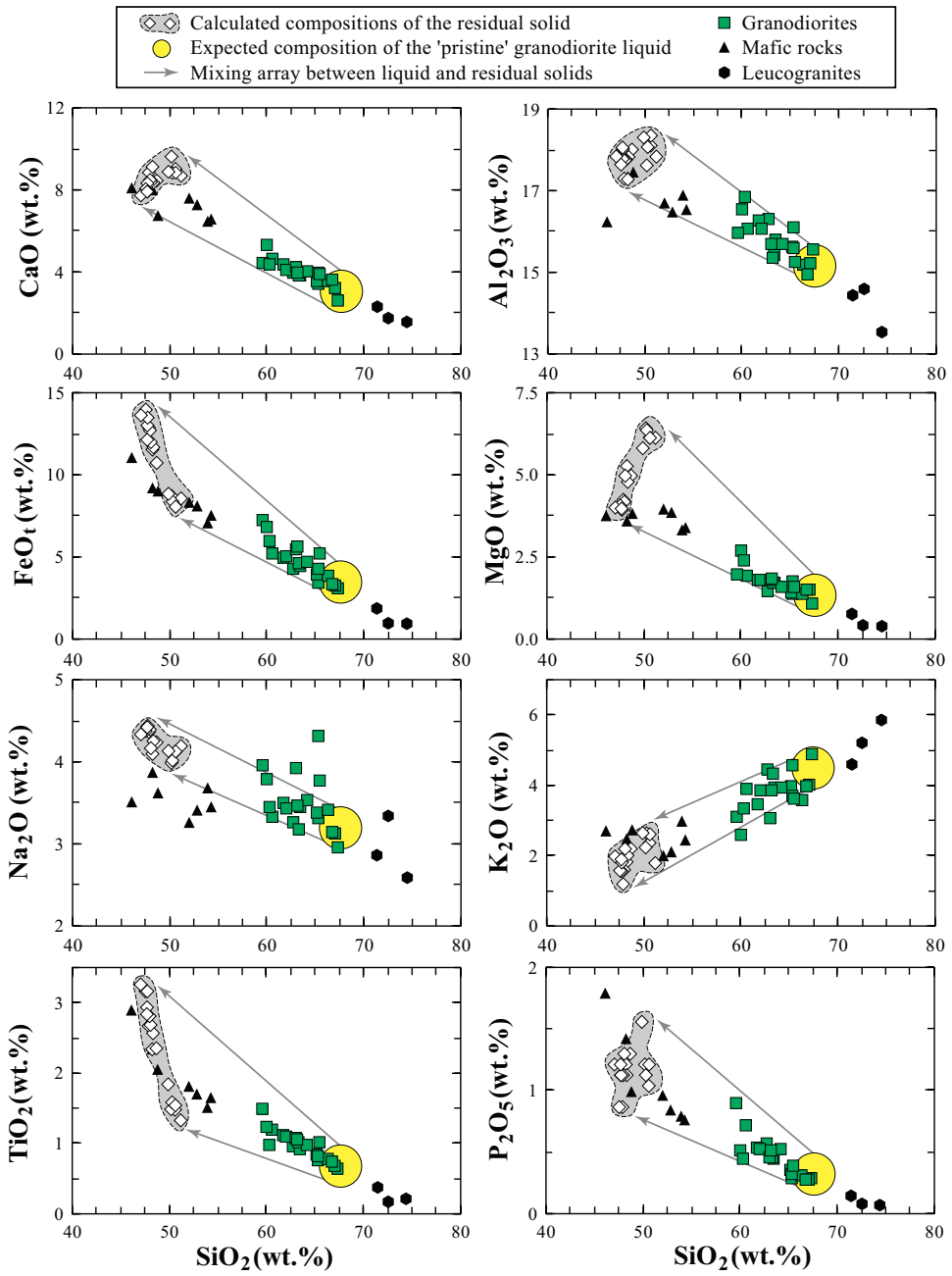


**Fig. 12.** Major-element compositions of the Bulai rocks plotted in Harker diagrams (major oxides vs. $SiO_2$). By contrast with Figs. 1 and 4, no distinction has been made between analyses of Holzer (1995) and Laurent et al. (2011). The compositions of the residual solids were calculated from modal compositions in experiments of Sisson et al. (2005) as well as mineral compositions measured in the Bulai samples (Table 4). The granodiorites plot along a well-defined trend included within the mixing field between a virtual 'pristine' liquid (yellow circle) and those residual solid compositions. (For interpretation of the references to colour in this figure legend, the reader is referred to the web version of this article.)

Dehydration partial melting of mafic rocks is an alternative process, but cannot account for the composition of the least evolved granodiorites (<65% $SiO_2$) which genesis requires unrealistic melting conditions. By contrast, their chemical features would result from entrainment of residual solids within pristine, most evolved granodiorites (>65% $SiO_2$). This is consistent with recent studies suggesting that the chemical variations of I-type granitoids, comparable in many aspects to the late-Archaean "differentiated sanukitoids", could result from entrainment of peritectic phases (Clemens et al., 2011).

Both petrogenetic models for "differentiated sanukitoids" imply the presence of a wet mafic magma that evolves through differentiation controlled by plagioclase + (Ca-)amphibole + biotite-bearing solids. All sanukitoid complexes bear this mafic end-member and share the same mineralogical assemblage as the Bulai suite. It is therefore plausible that most sanukitoid complexes evolved through the same mechanisms as proposed in this study. These models, involving "closed-system" processes, adequately explain the isotopic homogeneity generally observed throughout many sanukitoid suites. Correlatively, the succession of geological events that built these suites likely took place within a relatively short time range so that isotopic homogeneity was preserved. Consequently, mantle melting and subsequent evolution of the resulting mafic melt, either by MFC or partial melting, necessarily belong to the same geodynamic event and within a short time span (ca. < 100 Ma).

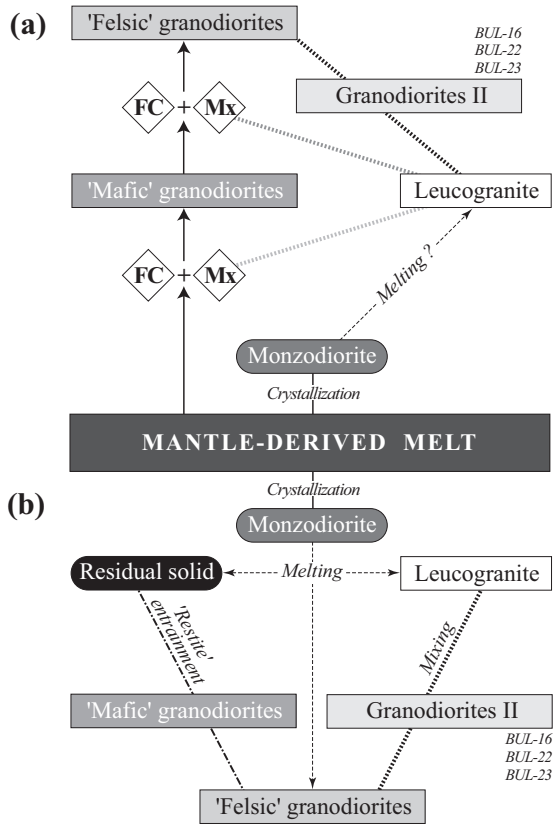


**Fig. 13.** Synthetic sketch of the models developed for the petrogenesis of the Bulai granitoids: (a) 'MFC' processes dominated by fractional crystallization (FC) and mixing (Mx); (b) processes dominated by dehydration melting of mafic rocks. Rectangles indicate liquid components, rounded rectangles are solid components. Thick dashed lines represent hybridation processes (i.e. mixing and mingling), the darker the line, the more efficient the hybridation. Thin dashed arrows represent dehydration melting. 'Mafic' and 'felsic' granodiorites correspond to liquids with $SiO_2$ < 65 wt.% and >65 wt.%, respectively. Granodiorites II correspond to samples BUL-16, BUL-22 and BUL-23 that probably result from 'pure' mixing between an average granodiorite composition and the leucogranitic melt (see Section 4.5 and Fig. 11 for details).

### 5.3. Implications for the growth and differentiation of the continental crust

The geochemical signature of I-type granitoids, including the sanukitoid series, is generally believed to reflect hybridization between mantle- and crust-derived components (e.g. Barbarin, 1999; Patiño-Douce, 1999). Scenarios developed in this paper show that the genesis of silicic magmas ($SiO_2$ > 60 wt.%) of the sanukitoid series mainly rely on the differentiation of a mantle-derived mafic component and thus, does not necessary require the existence of pre-existing silica-rich continental crust. Consequently, this shows that the 'hybrid' signature of these granitoids is inherited from the primary, mafic end-member itself, as already suggested by Clemens et al. (2009). This argues for a hybridation event that took place in mantle levels, consistently with the petrogenetic models developed for mafic members of the series involving interactions between felsic melts and mantle peridotite (Heilimo et al., 2010; Laurent et al., 2011; Martin et al., 2005, 2010; Rapp et al., 1999, 2010; Shirey and Hanson, 1984; Smithies and Champion, 2000).

Such conclusions imply that most sanukitoid complexes can be regarded as significant juvenile additions to the crust. The contribution to crustal growth is particularly obvious considering that a large peak of juvenile magmatism occurred at ~2.7 Ga (Condie, 1998; Condie and Aster, 2010), i.e. the average age of emplacement of sanukitoid series worldwide. On the other hand, it is noteworthy that "differentiated sanukitoids" share unequivocal affinities with some post-Archaean, metaluminous I-type granitoids, in particular the late-orogenic high-K calc-alkaline suites. This is particularly obvious in terms of major-element geochemistry (Figs. 1b and 4a–d), but also in terms of petrographic features. Therefore, the genetic model developed in this paper for "differentiated sanukitoids" might be extended to some high-K calc-alkaline batholiths. Such a conclusion is supported by the development of similar models for these rocks, involving differentiation (crystallization or melting) of an initial mantle-derived component together with interactions with felsic melts (e.g. Christophides et al., 2007; Clemens et al., 2009; Janoušek et al., 2000; Karsli et al., 2007; Roberts et al., 2000). As a result, high-K calc-alkaline magmatism, in general, might have significantly contributed to crustal growth since the end of Archaean.

In addition, the petrogenetic model developed for felsic rocks of the sanukitoid series can be extrapolated, not only to the growth, but also to the differentiation of the continental crust. Indeed, the compositional range of Bulai "differentiated sanukitoids" closely matches that of the estimated *upper* crust (e.g. Fig. 1b for $SiO_2$ and $K_2O$). Furthermore, Kelemen (1995) noticed that the *bulk* crust is similar in composition to high-Mg andesites (HMA), or low-silica adakites (LSA) that are considered to be the modern counterparts of Archaean, "mafic" sanukitoids *s.s.* (Martin et al., 2005). The parallel between bulk and upper crust in the one hand, and the sanukitoid series on the other hand, shows that both systems might have experienced similar differentiation processes.

From this perspective, the global intermediate (i.e. andesitic) composition of the crust is inherited from its primary, mantle-derived component of sanukitoid-like composition (Kelemen, 1995; Tatsumi, 2008). The subsequent differentiation of the mantle-derived component gives rise to a stratified crust: the segregated liquids emplaced in its upper part while the fractionated solids remain at depth. As shown in our models, the latter are always dominated by plagioclase and amphibole, representing gabbroic lithologies which *P*-wave velocities (6.5–7.0 km $s^{-1}$) would match the velocities measured in the lower crust (e.g. Rudnick and Fountain, 1995). Additionally, the Bulai granodiorites are enriched in very incompatible elements (Rb, Ba, Th, U, K) with respect to the parental melts. This also accounts for the chemical stratification of the crust, as these elements are enriched in the upper part compared with deeper levels (Rudnick and Fountain, 1995; Rudnick and Gao, 2003).

Obviously, the continental crust did not acquire its present-day structure during a single and global differentiation event, and it rather represents the integration of a long-lasting process. Based on the previous assumption that the late-Archaean sanukitoid series and post-Archaean high-K calc-alkaline series share similar differentiation processes, then the genesis and evolution of the continental crust towards a differentiated structure likely occurred continuously since the end of the Archaean. As a result, high-K calc-alkaline magmatism, in general, accounts for both growth and differentiation of the continental crust since the end of the Archaean. In terms of petrogenetic mechanisms, it is not that different compared with Archaean times during which melting of hydrous, amphibole-bearing metabasalts produced the silicic rocks (generally >60 wt.% $SiO_2$) of the TTG series (e.g. Barker and Arth, 1976; Condie, 1981; Martin, 1986, 1993; Martin et al., 2005; Moyen, 2011; Rapp et al., 1991; Smithies, 2000). However, during the Archaean, this mafic component was purely mantle-derived, while in the case of sanukitoids and post-Archaean, high-K calc-alkaline suites, it derives from an enriched mantle source and thus, is hybrid between mantle and crust compositions. From this point of view, the global changes at the Archaean-Proterozoic transition, marked by the emplacement of the first high-K calc-alkaline rocks (i.e. sanukitoid series), reflect inter alia the onset of recycling of continental material within the mantle (Laurent et al., 2011).

## 6. Summary and conclusions

The results and interpretations of our geochemical modelling of the Bulai pluton highlight the following conclusions:

(1) From a strict geochemical point of view, modelling is not an effective petrogenetic discriminator because it shows that the compositions of Bulai granodiorites could result either from magma mixing, or FCA processes or from partial melting of mafic rocks. This highlights the importance of constraining results of geochemical modelling with other geological evidence.
(2) The Bulai granodiorites formed either by Mixing plus Fractional Crystallization (MFC) of an initial, hydrous mantle-derived melt or, less likely, by dehydration melting of mafic rocks compositionally similar to the latter and subsequent entrainment of residual material. Silicic melts involved in MFC processes are similar in composition to the Bulai leucogranites. Both petrogenetic processes would have taken place at relatively high depth in the crust, followed by upward transfer and emplacement of granodioritic melts at shallower levels.
(3) These models are relevant for the origin of late-Archaean granitoids of the sanukitoid series, as well as some post-Archaean and generally late-orogenic high-K calc-alkaline complexes that share geochemical and petrographic features with the Bulai pluton.
(4) The petrogenetic models always imply the differentiation of a juvenile mantle-derived component and give rise to granitoid liquids that match the composition of the present-day upper continental crust. So, in relation with the previous conclusion, this shows that protracted high-K calc-alkaline magmatism since the Archaean-Proterozoic transition significantly contributed to crustal growth and differentiation.

## Acknowledgements

This project is funded by a NRF/CNRS Scientific Cooperation program PICS number 4828 and by international CNRS !Khure program co-operated between France and South Africa. We are indebted to R.H. Smithies and an anonymous reviewer for their detailed and critical comments that significantly improved the original manuscript. Many colleagues are thanked for fruitful discussion throughout the development of the ideas presented in this paper, especially J.D. Clemens, E. Słaby, V. Janoušek and A. Villaros. Modelling was performed using MatLab® software version 7.0 (R14), and Y. Guéhenneux is greatly acknowledged for his support during computing. We also wish to thank J.L. Devidal for his analytical skills and assistance during microprobe sessions.

## References

Annen, J., Blundy, J.D., Sparks, S.J., 2006. The genesis of intermediate and silicic magmas in deep crustal hot zones. Journal of Petrology 47 (3), 505–539.
Barbarin, B., 1999. A review of the relationships between granitoid types, their origins and their geodynamic environments. Lithos 46, 605–626.
Barbarin, B., 2005. Mafic magmatic enclaves and mafic rocks associated with some granitoids of the central Sierra Nevada batholith California: nature, origin, and relations with the hosts. Lithos 80 (1–4), 155–177.
Barker, F., Arth, J.G., 1976. Generation of trondhjemitic–tonalitic liquids and Archaean bimodal trondhjémite-basalt suites. Geology 4 (10), 596–600.
Barton, J.M., Holzer, L., Kamber, B., Doig, R., Kramers, J.D., Nyfeler, D., 1994. Discrete metamorphic events in the Limpopo Belt, southern Africa: implications for the application of *P–T* paths in complex metamorphic terrains. Geology 22, 1035–1038.
Beard, J.S., Lofgren, G.E., 1991. Dehydration melting and water-saturated melting of basaltic and andesitic greenstones and amphibolites at 1, 3 and 6.9 kbar. Journal of Petrology 32 (2), 365–401.
Bogaerts, M., Scaillet, B., Vander Auwera, J., 2006. Phase equilibria of the Lyngdal granodiorite (Norway): implications for the origin of metaluminous ferroan granitoids. Journal of Petrology 47 (12), 2405–2431.
Boryta, M., Condie, K.C., 1990. Geochemistry and origin of the Archaean Beit Bridge complex, Limpopo Belt, South Africa. Journal of the Geological Society 147, 229–239.
Chappell, B.W., White, A.J.R., Wyborn, D., 1987. The importance of residual source material (restite) in granite petrogenesis. Journal of Petrology 28 (6), 1111–1138.
Chen, B., Jahn, B., 2004. Genesis of post-collisional granitoids and basement nature of the Junggar Terrane, NW China; Nd–Sr isotope and trace element evidence. Journal of Asian Earth Sciences 23, 691–703.
Christophides, G., Perugini, D., Koroneos, A., Soldatos, T., Poli, G., Eleftheriadis, G., Del Moro, A., Neiva, A.M., 2007. Interplay between geochemistry and magma dynamics during magma interaction: an example from the Sithonia Plutonic Complex (NE Greece). Lithos 95, 243–266.
Clemens, J.D., Darbyshire, D.P.F., Flinders, J., 2009. Sources of post-orogenic calcalkaline magmas: the Arrochar and Garabal Hill–Glen Fyne complexes, Scotland. Lithos 112, 524–542.
Clemens, J.D., Stevens, G., Farina, F., 2011. The enigmatic sources of I-type granites and the clinopyroxene–ilmenite connexion. Lithos 126, 174–181.
Clemens, J.D., Watkins, J.M., 2001. The fluid regime of high-temperature metamorphism during granitoid magma genesis. Contributions to Mineralogy and Petrology 140, 600–606.
Condie, K.C., 1981. Archaean greenstone belts. In: Windley, B.F. (Ed.), Developments in Precambrian Geology 3, 434.
Condie, K.C., 1989. Geochemical changes in basalts and andesites across the Archean-Proterozoic boundary: identification and significance. Lithos 23 (1–2), 1–18.
Condie, K.C., 1997. Plate Tectonics and Crustal Evolution. Butterworth-Heinemann, Oxford, UK.
Condie, K.C., 1998. Episodic continental growth and supercontinents: a mantle avalanche connection? Earth and Planetary Science Letters 163, 97–108.
Condie, K.C., Aster, R.C., 2010. Episodic zircon age spectra of orogenic granitoids: the supercontinent connection and continental growth. Precambrian Research 180, 227–236.
Costa, F., Scaillet, B., Pichavant, M., 2004. Petrological and experimental constraints on the pre-eruptive conditions of Holocene dacite from Volcán San Pedro (36°S, Chilean Andes) and the importance of sulphur in silicic subduction-related magmas. Journal of Petrology 45, 855–881.
Cribb, J.W., Barton, M., 1996. Goechemical effects of decoupled fractional crystallization and crustal assimilation. Lithos 37, 293–307.
DePaolo, D.J., 1981. Trace element and isotopic effects of combined wallrock assimilation and fractional crystallization. Earth and Planetary Science Letters 53, 189–202.
Fernandez, A., Gasquet, D., 1994. Relative rheological evolution of chemically contrasted coeval magmas: example of the Tichka plutonic complex (Morocco). Contributions to Mineralogy and Petrology 116, 316–326.
Frost, B.R., Barnes, C.G., Collins, W.J., Arculus, R.J., Ellis, D.J., Frost, C.D., 2001. A geochemical classification for granitic rocks. Journal of Petrology 42, 2033–2048.
Glazner, A.F., Bartley, J.M., Coleman, D.S., Gray, W., Taylor, Z.T., 2004. Are plutons assembled over millions of years by amalgamation from small magma chambers? GSA Today 14, 4–11.
Harris, N.B.W, Hawkesworth, C.J., Van Calsteren, P., McDermott, F., 1987. Evolution of continental crust in southern Africa. Earth and Planetary Science Letters 83, 85–93.
Heilimo, E., Halla, J., Hölttä, P., 2010. Discrimination and origin of the sanukitoid series: geochemical constraints from the Neoarchean western Karelian Province (Finland). Lithos 115, 27–39.
Helz, R., 1976. Phase relations of basalts in their melting ranges at $PH_2O = 5$ kb. Part 2. Melt compositions. Journal of Petrology 17, 139–193.
Hertogen, J., Gijbels, R., 1976. Calculation of trace element fractionation during partial melting. Geochimica et Cosmichimica Acta 40, 313–322.
Holzer, L., 1995. The magmatic petrology of the Bulai Pluton and the tectonometamorphic overprint at 2.0 Ga in the Central Zone of the Limpopo Belt (Messina-Beitbridge area, Southern Africa). Unpublished M.Sc. Thesis. Université de Berne.
Holzer, L., Frei, R., Barton, J.M., Kramers, J.D., 1998. Unraveling the record of successive high-grade events in the Central Zone of the Limpopo Belt using Pb single phase dating of metamorphic minerals. Precambrian Research 87, 87–115.
Janoušek, V., Braithwaite, C.J.R., Bowes, D.R., Gerdes, A., 2004. Magma-mixing in the genesis of Hercynian calc-alkaline granitoids: an integrated petrographic and geochemical study of the Sázava intrusion, Central Bohemian Pluton, Czech Republic. Lithos 78, 67–99.
Janoušek, V., Bowes, D.R., Rogers, G., Farrow, C.M., Jelínek, E., 2000. Modelling diverse processes in the petrogenesis of a composite batholith: the Central Bohemian Pluton, Central European Hercynides. Journal of Petrology 41, 511–543.
Jellinek, A.M., Kerr, R.C., 1999. Mixing and compositional stratification produced by natural convection. 2. Applications to the differentiation of basaltic and silicic magma chambers and komatiite lava flows. Journal of Geophysical Research 104 B4, 7203–7218.
Karsli, O., Chen, B., Aydin, F., Şen, C., 2007. Geochemical and Sr–Nd–Pb isotopic compositions of the Eocene Dölek and Sariçiçek Plutons Eastern Turkey: implications for magma interaction in the genesis of high-K calc-alkaline granitoids in a post-collision extensional setting. Lithos 98, 67–96.
Kelemen, P.B., 1995. Genesis of high Mg# andesites and the continental crust. Contributions to Mineralogy and Petrology 120, 1–19.
Kemp, A.I.S., Hawkesworth, C.J., 2003. Granitic perspectives on the generation and secular evolution of the continental crust. In: Rudnick, R.L. (Ed.), The Crust. Treatise on Geochemistry. Elsevier-Pergamon, Oxford, pp. 349–410.

Kröner, A., Jaeckel, P., Brandl, G., Nemchin, A.A., Pidgeon, R.T., 1999. Single zircon ages for granitoid gneisses in the Central Zone of the Limpopo Belt Southern Africa and geodynamic significance. Precambrian Research 93, 299–337.
Laurent, O., Martin, H., Doucelance, R., Moyen, J.F., Paquette, J.L., 2011. Geochemistry and petrogenesis of high-K "sanukitoids" from the Bulai pluton, Central Limpopo Belt South Africa: implications for geodynamic changes at the Archaean-Proterozoic boundary. Lithos 123 (1–4), 73–91.
Liégeois, J.P., Navez, J., Hertogen, J., Black, R., 1998. Contrasting origin of post-collisional high-K calc-alkaline and shoshonitic versus alkaline and peralkaline granitoids The use of sliding normalization. Lithos 45, 1–28.
Lobach-Zhuchenko, S.B., Rollinson, H.R., Chekulaev, V.P., Arestova, N.A., Kovalenko, A.V., Ivanikov, V.V., Guseva, N.S., Sergeev, S.A., Matukov, D.I., Jarvis, K.E., 2005. The Archaean sanukitoid series of the Baltic Shield: geological setting, geochemical characteristics and implications for their origin. Lithos 79, 107–128.
McDonough, W.F., Sun, S.S., 1995. The composition of the Earth. Chemical Geology 120 (3–4), 223–253.
Martin, H., 1986. Effect of steeper Archaean geothermal gradient on geochemistry of subduction-zone magmas. Geology 14, 753–756.
Martin, H., 1993. The mechanisms of petrogenesis of the Archaean continental crust, comparison with modern processes. Lithos 30, 373–388.
Martin, H., 1999. Adakite magmas: modern analogs of Archaean granitoids. Lithos 46, 411–429.
Martin, H., Moyen, J.F., Rapp, R.P., 2010. The sanukitoid series: magmatism at the Archaean-Proterozoic transition. Earth and Environmental Science. Transactions of the Royal Society of Edinburgh 100 (1–2), 15–33.
Martin, H., Smithies, R., Rapp, R.P., Moyen, J.F., Champion, D., 2005. An overview of adakite, TTG, and sanukitoid: relationships and some implications for crustal evolution. Lithos 79 (1–2), 1–24.
Millonig, L., Zeh, A., Gerdes, A., Klemd, R., 2008. Neoarchaean high-grade metamorphism in the Central Zone of the Limpopo Belt (South Africa): combined petrological and geochronological evidence from the Bulai pluton. Lithos 103 (3–4), 333–351.
Moyen, J.F., Martin, H., Jayananda, M., 2001. Multi-element geochemical modelling of crust–mantle interactions during late-Archaean crustal growth: the Closepet granite (South India). Precambrian Research 112, 87–105.
Moyen, J.F., 2011. The composite Archaean grey gneisses: petrological significance, and evidence for a non-unique tectonic setting for Archaean crustal growth. Lithos 123, 21–36.
Naney, M.T., 1983. Phase equilibria of rock-forming ferromagnesian silicates in granitic systems. American Journal of Science 283, 993–1033.
Patiño-Douce, A.E., 1999. What do experiments tell us about the relative contributions of crust and mantle to the origin of granitic magmas? Geological Society, London 168, 55–75 (Special Publications).
Peccerillo, A., Taylor, S.R., 1976. Geochemistry of Eocene calc-alkaline volcanic rocks from the Kastamonu area Northern Turkey. Contributions to Mineralogy and Petrology 58 (1), 63–81.
Pitcher, W.S., 1987. Granites and yet more granites forty years on. Geologische Rundschau 76, 51–79.
Poli, G., Tommasini, S., 1999. Geochemical modelling of acid–basic magma interaction in the Sardinia–Corsica Batholith: the case study of Sarrabus, southeastern Sardinia, Italy. Lithos 46, 552–571.
Poli, G., Tommasini, S., Halliday, A.N., 1996. Trace elements and isotopic exchange during acid–basic magma interaction processes. Transactions of the Royal Society of Edinburgh, Earth Sciences 87, 225–232.
Rapp, R.P., Norman, M.D., Laporte, D., Yaxley, G.M., Martin, H., Foley, S.F., 2010. Continent formation in the Archean and chemical evolution of the cratonic lithosphere: melt–rock reaction experiments at 3–4 GPa and petrogenesis of Archean Mg-diorites (Sanukitoids). Journal of Petrology 51 (6), 1237–1266.
Rapp, R.P., Shimizu, N., Norman, M.D., Applegate, G.S., 1999. Reaction between slab-derived melts and peridotite in the mantle wedge: experimental constraints at 3.8 GPa. Chemical Geology 160, 335–356.
Rapp, R.P., Watson, E.B., 1995. Dehydration melting of metabasalt at 8–32 kbar: implications for continental growth and crust-mantle recycling. Journal of Petrology 36 (4), 891–931.
Rapp, R.P., Watson, E.B., Miller, C.F., 1991. Partial melting of amphibolite/eclogite and the origin of Archaean trondhjemites and tonalites. Precambrian Research 51, 1–25.
Roberts, M.P., Clemens, J.D., 1993. Origin of high-potassium, calc-alkaline, I-type granitoids. Geology 21, 825–828.
Roberts, M.P., Pin, C., Clemens, J.D., Paquette, J.L., 2000. Petrogenesis of mafic to felsic plutonic rocks associations: the calc-alkaline Quérigut Complex, French Pyrenees. Journal of Petrology 41, 809–844.
Roering, C., Van Reenen, D.D., Smit, C.A., Barton, J.M., De Beer, J.H., De Wit, M.J., Stettler, E.H., Van Schalkwyk, J.F., Stevens, G., Pretorius, S., 1992. Tectonic model for the evolution of the Limpopo Belt. Precambrian Research 55, 539–552.
Rudnick, R.L., Fountain, D.M., 1995. Nature and composition of the continental crust: a lower crustal perspective. Reviews of Geophysics 33 (3), 267–309.
Rudnick, R.L., Gao, S., 2003. Composition of the continental crust. In: Rudnick, R.L. (Ed.), The Crust. Treatise on Geochemistry. Elsevier-Pergamon, Oxford, pp. 1–64.
Scaillet, B., Holtz, F., Pichavant, M., 1998. Phase equilibrium constraints on the viscosity of silicic magmas. 1. Volcanic–plutonic association. Journal of Geophysical Research 103, 27257–27266.
Schmidt, M.W., Poli, S., 1998. Experimentally based water budgets for dehydrating slabs and consequences for arc magma generation. Earth and Planetary Science Letters 163 (1–4), 361–379.
Shand, S.J., 1943. Eruptive Rocks: Their Genesis, Composition, Classification, and Their Relations to Ore-deposits. Wiley, New York, p. 444.
Shaw, D.M., 1970. Trace element fractionation during anatexis. Geochimica et Cosmochimica Acta 34, 237–243.
Shirey, S.B., Hanson, G.N., 1984. Mantle-derived Archaean monzodiorites and trachyandesites. Nature 310, 222–224.
Sisson, T., Ratajeski, K., Hankins, W., Glazner, A., 2005. Voluminous granitic magmas from common basaltic sources. Contributions to Mineralogy and Petrology 148, 635–661.
Słaby, E., Martin, H., 2008. Mafic and Felsic magma interaction in granites: the Hercynian Karkonosze Pluton (Sudetes, Bohemian Massif). Journal of Petrology 49 (2), 353–391.
Smithies, R.H., 2000. The Archaean tonalite–trondhjemite–granodiorite (TTG) series is not an analogue of Cenozoic adakite. Earth and Planetary Science Letters 182, 115–125.
Smithies, R.H., Champion, D.C., Sun, S.S., 2004. Evidence for Early LREE-enriched mantle source regions: diverse magmas from the c. 3.0 Ga Mallina Basin, Pilbara Craton, NW Australia. Journal of Petrology 45 (8), 1515–1537.
Smithies, R.H., Champion, D.C., 2000. The Archaean high-Mg diorite suite: links to Tonalite–Trondhjemite–Granodiorite magmatism and implications for early Archaean crustal growth. Journal of Petrology 41 (12), 1653–1671.
Sparks, R.S.J., Marshall, L.A., 1986. Thermal and mechanical constraints on mixing between mafic and silicic magmas. Journal of Volcanology and Geothermal Research 29, 99–124.
Stern, R.A., Hanson, G.N., Shirey, S.B., 1989. Petrogenesis of mantle-derived LILE-enriched Archean monzodiorites and trachyandesites (sanukitoids) in southwestern Superior Province. Canadian Journal of Earth Science 26, 1688–1712.
Stern, R.A., Hanson, G.N., 1991. Archaean high-Mg granodiorites: a derivative of light rare earth enriched monzodiorites of mantle origin. Journal of Petrology 32, 201–238.
Stevens, G., Villaros, A., Moyen, J.F., 2007. Selective peritectic garnet entrainment as the origin of geochemical diversity in S-type granites. Geology 35 (1), 9–12.
Stevenson, R., Henry, P., Gariépy, C., 1999. Assimilation-fractional crystallization origin of Archaean sanukitoid suites: Western Superior Province, Canada. Precambrian Research 96, 83–99.
Stormer, J.C., Nicholls, J., 1978. XLFRAC: a program for the interactive testing of magmatic differentiation models. Computers and Geosciences 4 (2), 143–159.
Tatsumi, Y., 1989. Migration of fluid phases and genesis of basalt magmas in subduction zones. Journal of Geophysical Research 94, 4697–4707.
Tatsumi, Y., 2008. Making continental crust: the sanukitoid connection. Chinese Science Bulletin 53 (11), 1620–1633.
Taylor, S.R., 1987. Geochemical and petrological significance of the Archaean–Proterozoic boundary. In: Pharaoh, T.C., Beckinsale, R.D., Rickard, D. (Eds.), Geochemistry and Mineralization of Proterozoic Volcanic Suites. Geological Society Special Publication No. 33, pp. 3–8.
Taylor, S.R., McLennan, S.M., 1995. The geochemical evolution of the continental crust. Reviews of Geophysics 33 (2), 241–265.
Thompson, A.B., Matile, L., Ulmer, P., 2002. Some thermal constraints on crustal assimilation during fractionation of hydrous, mantle-derived magmas with examples from central alpine batholiths. Journal of Petrology 43 (3), 403–422.
Van Reenen, D.D., Boshoff, R., Smit, C.A., Perchuk, L.L., Kramers, J.D., McCourt, S., Armstrong, R.A., 2008. Geochronological problems related to polymétamorphism in the Limpopo Complex, South Africa. Gondwana Research 14, 644–662.
Villaros, A., Stevens, G., Moyen, J.F., Buick, I., 2009. The trace-element compositions of S-type granites: evidence for disequilibrium melting and accessory phase entrainment in the source. Contributions to Mineralogy and Petrology 158 (4), 543–561.
Zeh, A., Gerdes, A., Klemd, R., Barton, J.M., 2007. Archean to proterozoic crustal evolution in the central zone of the limpopo belt (South Africa-Botswana): constraints from combined U–Pb and Lu–Hf isotope analyses of zircon. Journal of Petrology 48, 1605–1639.
Zeh, A., Gerdes, A., Barton, J.M., 2009. Archean accretion and crustal evolution of the Kalahari Craton-the zircon age and Hf isotope record of granitic rocks from Barberton/Swaziland to the Francistown arc. Journal of Petrology 50 (5), 933–966.
Zhang, X., Mao, Q., Zhang, H., Zhai, M., Yang, Y., Hu, Z., 2011. Mafic and felsic magma interaction during the construction of high-K calc-alkaline plutons within a metacratonic passive margin: the Early Permian Guyang batholith from the northern North China Craton. Lithos 125 (1–2), 569–591.

Precambrian Research 230 (2013) 209–226

Contents lists available at SciVerse ScienceDirect

Precambrian Research

journal homepage: www.elsevier.com/locate/precamres

# LA-ICP-MS dating of zircons from Meso- and Neoarchean granitoids of the Pietersburg block (South Africa): Crustal evolution at the northern margin of the Kaapvaal craton

Oscar Laurent[a,b,c,*], Jean-Louis Paquette[a,b,c], Hervé Martin[a,b,c], Régis Doucelance[a,b,c], Jean-François Moyen[b,c,d]

[a] Clermont Université, Université Blaise Pascal, Laboratoire Magmas et Volcans, BP 10448, F-63000 Clermont-Ferrand, France
[b] CNRS, UMR6524, LMV, F-63038 Clermont-Ferrand, France
[c] IRD, R 163, LMV, F-63038 Clermont-Ferrand, France
[d] Département de Géologie, Université Jean Monnet, 23 rue du Docteur Paul Michelon, 42023 Saint-Étienne, France

ARTICLE INFO

*Article history:*
Received 14 June 2012
Received in revised form 7 February 2013
Accepted 25 February 2013
Available online xxx

*Keywords:*
U–Pb dating
Zircon
LA-ICP-MS
Kaapvaal craton
Granitoids
Archean crust evolution

ABSTRACT

In order to unravel the late-Archean magmatic evolution of the northern Kaapvaal craton, we performed LA-ICP-MS U–Pb isotopic analyses on zircon grains from 15 granitoid samples of the Pietersburg block, including tonalitic and granodioritic gneisses (TTG) as well as weakly to not deformed high-K monzogranites, granodiorites and diorites.

Our new age data, coupled to already published results, show that the Pietersburg block is schematically made up of two lithologically and chronologically distinct domains, namely (1) gneiss units that cover most of the surface of this terrane and comprising the formerly defined Goudplaats, Hout River, Groot Letaba gneisses as well as the so-called "Duiwelskloof batholith", where crust formation and reworking took place between 3350 and 2840 Ma; and (2) late-stage high-K plutons and batholiths that emplaced at ~2780 Ma and ~2690 Ma.

In details, the tectono-magmatic evolution of the Pietersburg block can be divided into five successive episodes: (1) The first crust-forming event is related to the emplacement of juvenile TTG magmas in the range 3150–3350 Ma. In our dataset, it is only represented by inherited zircon cores from younger granitoids; (2) Two TTG samples from the Goudplaats–Hout River gneiss unit and the Duiwelskloof area yielded emplacement ages of ~2950 Ma. This magmatic event is very widespread in the whole Pietersburg block, and we propose that it represents an important period of crustal growth linked with the accretion of the Pietersburg block to the northern edge of the older nucleus (ca. 3600–3100 Ma) of the Kaapvaal craton; (3) We obtained an intrusion age of ~2840 Ma for two samples of high-K biotite-bearing granites that are intimately associated with, and probably formed by melting of, the ~2950 Ma-old TTGs. Thus, this episode represents an important event of crust reworking that is likely associated with a long-lasting deformation event; (4) Further intracrustal melting led to the development of large batholiths of high-K biotite granites (e.g. Turfloop batholith) and their satellite intrusions, the latter being represented by one of our samples dated at ~2780 Ma; (5) The intrusion of high-K calc-alkaline granitoids of possible mixed crust-mantle origin (Mashashane, Matlala, Moletsi and Matok plutons) took place at ~2690 Ma. They are likely associated with collision between the Pietersburg block and the Central Zone of the Limpopo Belt, together with localized strain along shear zones (e.g. Hout River shear zone) and granulite-facies metamorphism that both occurred in the same time.



## 1. Introduction

Located in Southern Africa, the Archean Kaapvaal craton (Fig. 1) is one of the oldest, well-exposed continental blocks on Earth. Schematically, its growth proceeded in three steps: (1) formation of a stable nucleus between ~3600 and ~3100 Ma followed by (2) magmatic and tectonic accretion along the northern and western margins of the craton between ~3100 and ~2600 Ma and (3) collision with the Zimbabwe craton to the north, giving rise to

* Corresponding author at: Clermont Université, Université Blaise Pascal, Laboratoire Magmas et Volcans, BP 10448, F-63000 Clermont-Ferrand, France. Tel.: +33 047334 6891.
*E-mail addresses:* o.laurent@opgc.univ-bpclermont.fr, oscarlaurent86@gmail.com (O. Laurent).

0301-9268/$ – see front matter © 2013 Elsevier B.V. All rights reserved.
http://dx.doi.org/10.1016/j.precamres.2013.02.009

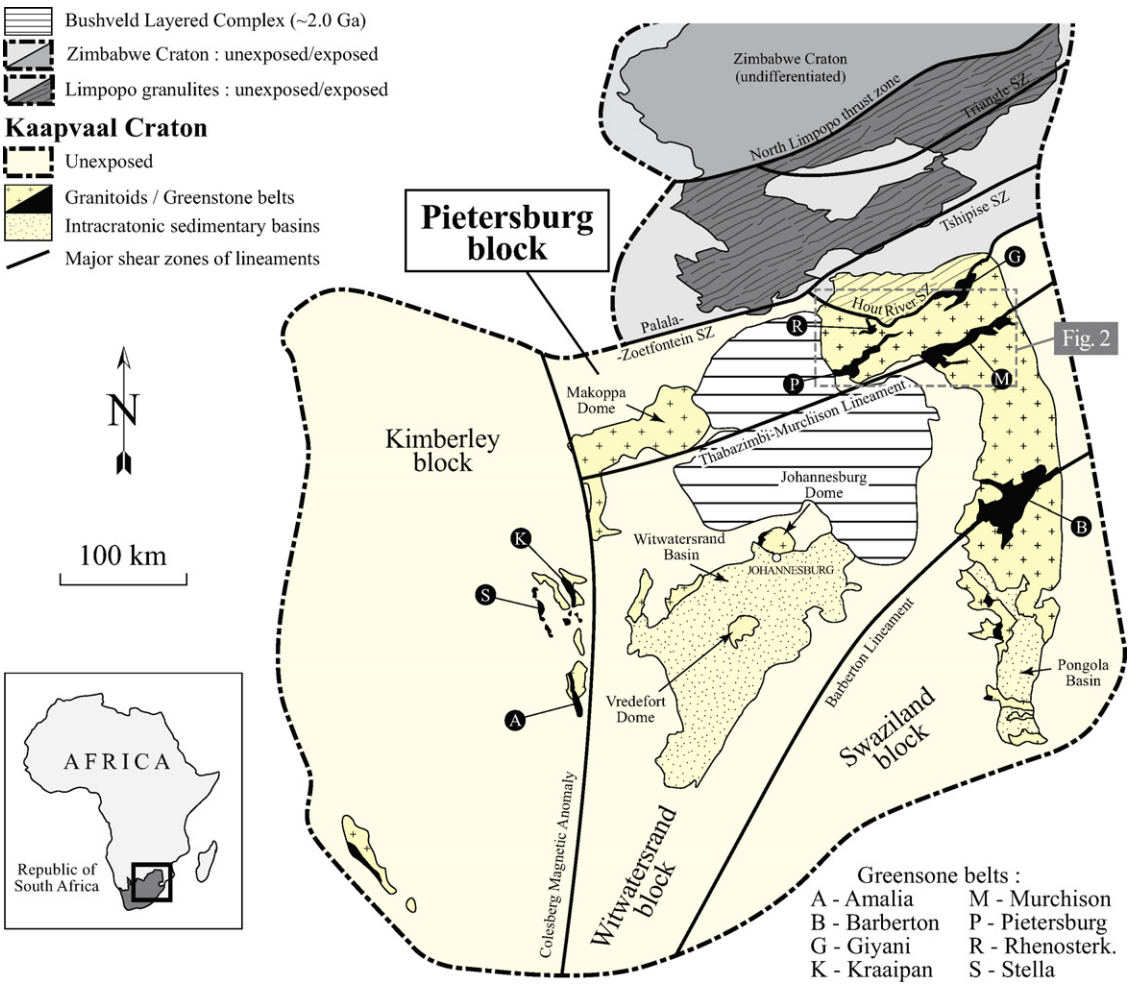


**Fig. 1.** Sketch geological map (after Eglington and Armstrong, 2004) detailing the different structural domains of the Kaapvaal craton and highlighting the position of the Pietersburg block. The area covered by Fig. 2 is represented by the gray rectangle.

the high-grade (granulite-facies) Limpopo mobile belt (e.g. de Wit et al., 1992a; Poujol et al., 2003; Roering et al., 1992; van Reenen et al., 1987).

The architecture and geological history of the Palaeoarchaean nucleus were extensively studied in terms of geochronology, isotopic geochemistry and metamorphic geology (e.g. Armstrong et al., 1990; Kamo and Davis, 1994; Kröner et al., 1991, 1996; Moyen et al., 2006; Sanchez-Garrido et al., 2011; Zeh et al., 2009). Similarly, the tectonic evolution of the Limpopo belt is presently well understood: it results from collision between the Kaapvaal and Zimbabwe craton during Neoarchean times (2650–2600 Ma), followed by a Paleoproterozoic (~2000 Ma) tectonic reworking (Kramers et al., 2006; Kramers and Houri, 2011; van Reenen et al., 2008). By contrast, the evolution of the Kaapvaal craton during Meso- and Neoarchaeantimes is still under debate (e.g. Brandl et al., 2006). This is especially true for the architecture and crustal evolution of its western and northern edges, which require further investigation, in particular in the so-called Pietersburg block (Eglington and Armstrong, 2004; Fig. 1). This terrane is located between the Witwatersrand block and the Central Zone of the Limpopo Belt (Fig. 1). It is bounded to the south by the Thabazimbi-Murchison Lineament (de Wit et al., 1992a; Good and de Wit, 1997), and to the North by the Palala–Zoetfontein Shear Zone (Fig. 1). The Pietersburg block comprises a high-grade (granulite-facies) domain to the North (the Southern Marginal Zone of the Limpopo belt) and a low-grade one (greenschist to lower amphibolites-facies) to the South (Kramers et al., 2001, 2006; Kreissig et al., 2000; van Reenen et al., 1987; Zeh et al., 2009). Both domains are separated by the Hout River shear zone (Figs. 1 and 2). They consist of volumetrically subordinated volcano-sedimentary remnants (i.e. greenstone belts) framed by orthogneiss and granitoids.

Recent Hf–Nd isotopic studies showed that the continental crust of the Pietersburg block has been extracted from the mantle between 3300 and 2950 Ma (Kreissig et al., 2000; Zeh et al., 2009). However, the scarce data presently available on this terrane clearly indicate that crust formation did not take place as a single even but rather results from several magmatic pulses that spread between ~3300 and ~2600 Ma (Brandl and Kröner, 1993; Henderson et al., 2000; Kreissig et al., 2001; Kröner et al., 2000; Zeh et al., 2009). Nevertheless, very little is known about the detailed tectono-magmatic evolution of the crust in the Pietersburg terrane because of insufficient geochronological data. Furthermore, most ages were obtained using zircon dissolution techniques (i.e. ID-TIMS or Pb–Pb stepwise evaporation), which are unable to resolve complex age patterns within single grains, in contrast with in situ techniques (e.g. Whitehouse et al., 1999). Finally, some granitoids and gneiss units lack any reliable age data and consequently, their geological significance in the late-Archean evolution of the Pietersburg terrane is unconstrained so far.

Consequently, this paper aims to provide new time constraints on the evolution of the Pietersburg terrane using in situ LA-ICP-MS

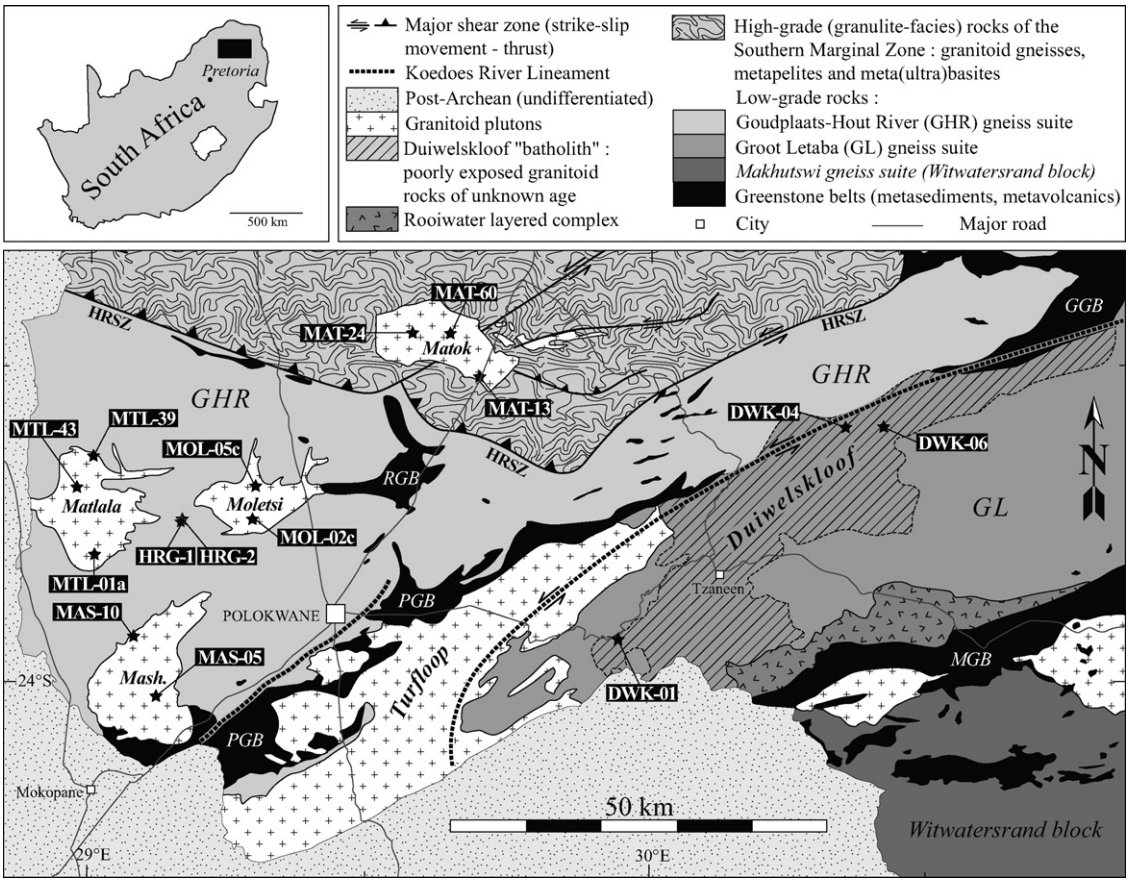


**Fig. 2.** Geological map of the Pietersburg block in the Polokwane area (after Robb et al., 2006; Smit et al., 2001; Zeh et al., 2009 and 1:50,000[e] geological maps: Brandl, 1986, 1987). Sample locations (with sample name) are represented by black stars. GGB = Giyani greenstone belt; MGB = Murchison greenstone belt; PGB = Pietersburg greenstone belt; RGB = Rhenosterkoppies greenstone belt; HRSZ = Hout River shear zone.

dating on separated zircons from granitoids. The goal of this paper is twofold: (1) dating several samples for each unit or pluton, in order to unravel its particular magmatic evolution and (2) from a broader perspective, studying the spatial and temporal distributions of granitoid magmatism in the Pietersburg block, and addressing its implications for the architecture and evolution of this terrane during the Meso- and Neoarchean. In order to achieve these tasks, we investigated the age of 15 samples selected within a range of granitoid types, from both "basement" gneiss units and late-stage plutons.

## 2. Geological setting

The Pietersburg block (as defined by Eglington and Armstrong, 2004) is also referred to as the Murchison–Northern Kaapvaal terrane (Zeh et al., 2009). It is located in the northernmost part of the Kaapvaal craton and lies between the Witwatersrand block and the Limpopo mobile belt (Fig. 1). It is bounded to the South by the Thabazimbi–Murchison Lineament and to the North by the Palala–Zoetfontein Shear Zone (Anhaeusser, 2006; de Wit et al., 1992b; Good and de Wit, 1997; Fig. 1). The Pietersburg block, which also extends to the West in Botswana (Gaborone granite suite, Makoppa Dome), is made up of three distinct domains (Fig. 2): (1) granite-gneiss terrains; (2) greenstone belts and (3) granulite-facies rocks of the Southern Marginal Zone (SMZ) of the Limpopo belt. The three domains are described separately in the following.

(1) The granite-gneisses are the wider spread lithologies and are mainly made up of felsic layered orthogneisses, including the Groot Letaba and Goudplaats–Hout River gneissic suites. Both consist of several generations of variously deformed and migmatized trondhjemites, tonalites and granodiorites (TTG) associated with minor amphibolites (Robb et al., 2006). All these rocks display a pervasive vertical foliation that regionally lies in an ENE-trending direction. If the age of the protoliths can be as old as 3333 Ma (Brandl and Kröner, 1993), it appears that they emplaced episodically until the end of the Archean (Brandl and Kröner, 1993; Kröner et al., 2000; Zeh et al., 2009), pointing to a complex, polycyclic history (Robb et al., 2006) that remains unconstrained so far. The gneisses were intruded by post-tectonic plutons (Mashashane, Matlala, Moletsi granites; Brandl, 1986) and batholiths (Duiwelskloof leucogranite, Turfloop granite; Brandl, 1987), from which the only available ages are ~2780 Ma for the Turfloop batholith and ~2690 Ma for the Mashashane pluton (de Wit et al., 1993; Henderson et al., 2000; Kröner et al., 2000; Zeh et al., 2009).

(2) South of the Hout River shear zone (Fig. 2), the Pietersburg block also includes several supracrustal sequences: the Murchison, Giyani, Pietersburg and Rhenosterkoppies greenstone belts. They mostly consist in low-grade (greenschist to lower amphibolites facies) metasedimentary rocks (conglomerates, quartzites, shales, cherts and BIF) associated with volcanic sequences ranging from basalts and komatiites to intermediate and felsic lavas (Brandl et al., 2006). The Murchison greenstone belt has a keel morphology with maximum depths up to 9–12 km (de Beer et al., 1984) while the other sequences consist of very thin (0.4–1.8 km; Kleywegt et al., 1987; Stettler et al., 1988), subhorizontal slices (Brandl et al., 2006). All greenstone belts are elongated in a ENE–WSW

direction, parallel to the structural framework of the gneiss units. The age of felsic lavas ranges between ~3200 and ~2880 Ma, with a maximum in volcanic activity at 2950–2970 Ma (Brandl and Kröner, 1993; Brandl et al., 1996; Kröner et al., 2000; Poujol et al., 1996; Poujol, 2001). On the other hand, deposition of detrital sequences and subsequent metamorphism took place between 2880 and 2690 Ma (Zeh and Gerdes, 2012).

(3) The Hout River shear zone (Fig. 2) separates the latter two domains from the Southern Marginal Zone (SMZ) of the Limpopo Belt. The SMZ consists of two main lithological units: (i) migmatitic orthogneisses (locally referred to as the Bavianskloof gneisses, even if they are part of the Goudplaats–Hout River unit; Kramers et al., 2006) and (ii) metapelites together within minor mafic rocks and BIFs, locally referred to as the "Bandelierkop complex" (Kramers et al., 2006). Both units are highly deformed, high-grade (granulite-facies) counterparts of the previously described granite-gneiss and greenstone belts, respectively (du Toit et al., 1983; Mason, 1973; van Reenen and Hollister, 1988). Indeed, major-, trace elements and Hf–Nd isotopes of rocks from both sides of the Hout River shear zone show that they belong to the same 3200 to 2990 Ma-old crustal material (Kreissig et al., 2000; Zeh et al., 2009). The geological evolution of the SMZ has been extensively studied because it belongs to the Limpopo Belt that could possibly represent one of the oldest examples of continent-continent collision on Earth (Roering et al., 1992). The first tectono-metamorphic event related to this orogeny is associated with crustal thickening and prograde metamorphism ($M_1$) associated with top-to-the-North thrusting ($D_1$) along low-dipping shear zones, now mostly preserved in the low-grade greenstones south of the Hout River shear zone (Barton and Van Reenen, 1992; de Wit et al., 1992a, 1993; Smit et al., 1992; van Reenen and Smit, 1996). The age of $D_1$ thrusting was bracketed between 2700 and 2760 Ma (Passeraub et al., 1999), while $M_1$ peak metamorphism took place at 2691 ± 7 Ma (Kreissig et al., 2001). The conditions of metamorphism did not exceed the lower amphibolite facies south of the Hout River shear zone ($T \leq 600$ °C; de Wit et al., 1992a; Passeraub et al., 1999; Perchuk et al., 2000b,c) but reached granulite-facies conditions in the SMZ, with peak conditions up to 1000 °C and maximum pressure of 9.5 kbar (Belyanin et al., 2012; Perchuk et al., 1996; Stevens and Van Reenen, 1992; Tsunogae et al., 2004; van Reenen et al., 1987). Subsequent exhumation of the granulites was accommodated by southward thrusting along the steeply north-dipping Hout River shear zone ($D_2$; Kreissig et al., 2001; Smit et al., 1992; van Reenen et al., 2011). The *P–T* conditions evolved to $M_2$ conditions of 850 °C and 7–8 kbar (Perchuk et al., 2000a,c; Stevens and Van Reenen, 1992), followed by a retrograde path down to final $M_3$ conditions of 500–600 °C and 4–5 kbar in the SMZ granulites (Perchuk et al., 1996, 2000a; Smit et al., 2001; Tsunogae et al., 2004; van Reenen, 1986; van Reenen et al., 2011). The $M_3$ conditions are accompanied by strike-slip movement along $D_3$, E–W trending mylonitic shear zones (Smit et al., 2001).

It is now fairly well established that the Pietersburg block accreted to the northern margin of the Kaapvaal craton nucleus (Anhaeusser, 2006; de Wit et al., 1992a; Poujol et al., 2003; Zeh et al., 2009) between 2920 and 2970 Ma (Block et al., 2013) and was subsequently affected by collision with a crustal block located northwards (either the Central Zone of the Limpopo belt or the Zimbabwe craton) between 2700 and 2600 Ma (e.g. de Wit et al., 1992a; Kreissig et al., 2001; van Reenen et al., 1987; Zeh et al., 2009). By contrast, the tectono-magmatic evolution of the Pietersburg block before and between those two events is still under debate.

## 3. Description of granitoid plutons and units

Most of the descriptions presented in this section are based on our own structural and petrographic observations carried out during a fieldwork and sampling campaign in the Pietersburg block.

### 3.1. Matok Igneous Complex (MIC)

The Matok Igneous Complex (MIC) intrudes the granulite-facies rocks of the SMZ north of the Hout River shear zone (Fig. 2) and consists of medium to high-K calc-alkaline, metaluminous plutonic rocks. The MIC can be subdivided into three main magmatic phases: (1) fine-grained, dark, generally clino- and orthopyroxene-bearing diorites ("enderbites" of Barton et al., 1992; Bohlender et al., 1992) (Fig. 3a); (2) white to pinkish gray, medium-grained porphyritic granodiorites (Fig. 3a) that are either pyroxene-free or pyroxene-bearing (the latter being termed "charno-enderbites" by Barton et al., 1992; Bohlender et al., 1992) and (3) biotite monzogranites displaying a wide range of textures and grain sizes (Fig. 3b). Volumetrically, the MIC consists of equal proportions of diorites, mostly restricted to its northern part, and of granodiorites and monzogranites that principally outcrop to the south (Barton et al., 1992; Bohlender, 1991; Bohlender et al., 1992).

Barton et al. (1992) obtained U–Pb TIMS upper intercept ages of 2671 ± 2 Ma for the "charno-enderbites" and of ~2664 Ma for the granodiorites. Those ages only rely on few data: the age of charno-enderbites is constrained by a single, concordant analysis and the one of granodiorites is based on three slightly discordant analyses.

### 3.2. Mashashane, Matlala, Moletsi plutons

These plutons intruded the western part of the Goudplaats–Hout River gneiss suite (Fig. 2). In most studies, they are usually referred to as the "2650 Ma granitoids", owing to their post-tectonic nature (Brandl, 1986; de Wit et al., 1993; Robb et al., 2006). However, to date, only two U–Pb zircon ages were published: 2679 ± 7 Ma for the Mashashane pluton (Zeh et al., 2009; LA-ICP-MS) and 2687 ± 2 Ma for a "post-tectonic granite" that intruded sediments of the Pietersburg greenstone belt at the southeastern edge of the Mashashane pluton (de Wit et al., 1993; TIMS).

All three plutons consist of high-K calc-alkaline and metaluminous plutonic rocks, most of them being coarse-grained biotite monzogranites (Fig. 3c). They contain enclaves of hornblende-biotite granodiorites and quartz-monzodiorites, which have sizes of a few cm to several hundreds of meters. In all plutons, the rock-forming minerals are undeformed, thus preserving typical magmatic textures and supporting their post-tectonic character.

### 3.3. Duiwelskloof batholith

The Duiwelskloof batholith is mapped as an elongated ENE-trending leucogranite body (>50 km in length and up to 15 km in width) that lies between the Pietersburg and Murchison greenstone belts (Fig. 2). It is poorly known mainly because of the bad outcropping conditions: when exposed, rocks are generally strongly weathered.

The Duiwelskloof batholith perhaps represents the eastern continuation of the Turfloop batholith (Fig. 2). The latter was dated by several independent methods (U–Pb on zircon and titanite, Sm–Nd and Rb–Sr on whole rocks) at ~2775 Ma (Henderson et al., 2000; Kröner et al., 2000; Zeh et al., 2009), whereas no data exists for the Duiwelskloof batholith. Alike the Turfloop batholith, the most widespread facies in the Duiwelskloof batholith consists of a medium-grained, equigranular biotite granite. However, while the Turfloop batholith is a continuous and well-circumscribed

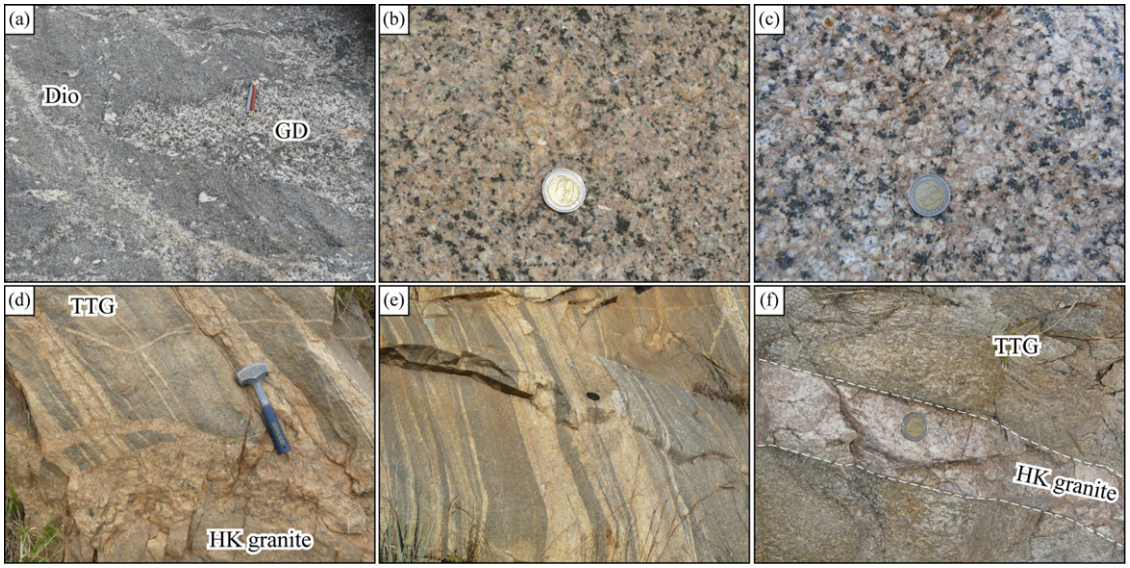


**Fig. 3.** Selected field pictures presenting the granitoids of the Pietersburg block investigated in this study: (a) mingling relationships between dark, fine-grained pyroxene-bearing diorite (Dio) and lighter, coarser-grained pyroxene-free granodiorite (GD) in the Matok Igneous Complex; (b) a variety of pink monzogranite in the Matok Igneous Complex; (c) typical monzogranite of the Mashashane pluton (very similar to that of the Matlala and Moletsi plutons); (d) high-K (HK) biotite-bearing granite cross-cutting the foliation of low-K orthogneisses (TTG) in the Duiwelskloof "batholith"; (e) typical banding of TTG gray gneisses of the Goudplaats–Hout River unit; (f) dike of high-K (HK) biotite-bearing granite intruding homogeneous, foliated TTG gneiss in the Goudplaats–Hout River unit.

intrusion, the Duiwelskloof batholith is much more complex and heterogeneous. It is made up of discontinuous magmatic bodies, separated from each other by gray gneisses of TTG affinity (Robb et al., 2006) (Fig. 3d). The TTGs probably belong to the Groot Letaba gneiss suite, from which geochronological investigations provided ages ranging between 3171 ± 6 Ma (Brandl and Kröner, 1993; Pb–Pb zircon evaporation) and 2784 ± 8 Ma (Zeh et al., 2009; U–Pb zircon, LA-ICP-MS). In some outcrops, several generations of biotite granites are cross-cutting each other, indicating that the Duiwelskloof area is characterized by a protracted and relatively long-lived magmatic activity.

### 3.4. Goudplaats–Hout River gneiss suite

The Goudplaats–Hout River gneiss suites lies north of the Pietersburg greenstone belt, in both sides of the Hout River shear zone (Fig. 2). This unit consists of several lithologies: (1) biotite-bearing, sodic tonalitic, trondhjemitic and granodioritic (TTG) gneisses, generally strongly deformed and sometimes migmatized (Fig. 3e); (2) dikes, small bodies and lenses of equigranular potassic and peraluminous biotite granites, weakly or not deformed (Fig. 3f); (3) medium-grained amphibolites and (4) a dense network of pegmatites, the two latter lithologies being volumetrically subordinated.

Because of the poor quality of exposures, the Goudplaats–Hout River gneiss suite has not been extensively investigated. However, U–Pb dating of several samples of Goudplaats–Hout River gneisses yielded ages that scatter between 3333 ± 5 Ma and 2885 ± 4 Ma (Brandl and Kröner, 1993; Pb–Pb zircon evaporation and Kröner et al., 2000; TIMS).

## 4. U–Pb dating

### 4.1. Analytical techniques and data processing

Sample preparation and U–Pb dating were both carried out at the Laboratoire Magmas et Volcans in Clermont-Ferrand. Selected samples weighting 3–10 kg were pulverized with a jaw crusher and subsequently sieved to a grain size <315 μm. Heavy minerals were concentrated with a Wilfley shaking table, followed by magnetic separation and heavy liquid techniques (using methylene iodide with density of ~3.3). Finally, ~25 grains by sample were hand-picked under a binocular microscope, set in an epoxy mount and polished. In all samples studied, zircon grains are relatively large, having sizes in the range 100–300 μm.

Prior to U–Pb dating, cathodoluminescence (CL) images were obtained using a Jeol JSM-5910 LV scanning electron microscope (SEM). Laser ablation ICP-MS U–Pb analyses were conducted on an Agilent 7500cs quadrupole ICP-MS attached to a 193-nm Resonetics M-50E laser system. Laser was fired using a spot size of 26 μm, a fluency of 9 J cm$^{-2}$ and a repetition rate of 3 Hz. The analyses were performed in a two-volume Laurin Technic ablation cell where the sampled material is carried into He and subsequently mixed with $N_2$ and Ar before injection into the plasma source of the ICP-MS. The synthetic silicate glass NIST 612 was used for ICP-MS tuning (sensitivity, mass off-set calibration and minimization of the oxidation rate, monitored using the $UO_2$/U ratio) prior to each analytical session. Data were acquired during ~30 s background measurement followed by ~60 s of sample ablation and ~30 s of wash-out delay. Raw signals in $^{204}$(Hg + Pb), $^{206}$Pb, $^{207}$Pb and $^{238}$U were acquired using a peak integration time of 10 ms, the mean time resolution of the data being ~130 ms. The carrier gas contains detectable amounts of $^{204}$Hg (~1000 cps) that results in a large isobaric interference on $^{204}$Pb, and the analytical accuracy of the quadrupole ICP-MS is not sufficient to distinguish low amounts of $^{204}$Pb from the background signal of $^{204}$Hg. As a result, no correction for common Pb was possible and the analyses that visibly contain common Pb (higher intensity on mass $^{204}$(Hg + Pb) than the average background value from the carrier gas) were simply eliminated. Standard zircon GJ-1 was used as a primary reference material, while standard zircon 91500 was used as a secondary reference material, i.e. treated as unknown to independently control the accuracy of the corrections. We obtained a mean Concordia age of 1065.7 ± 3.6 Ma (MSWD = 0.84; $N$ = 33) for standard 91500 (complete datasets and Concordia plots for standard zircons are available in the Supplementary Material associated with the article). A table summarizing the analytical conditions can be also found in Supplementary Material.

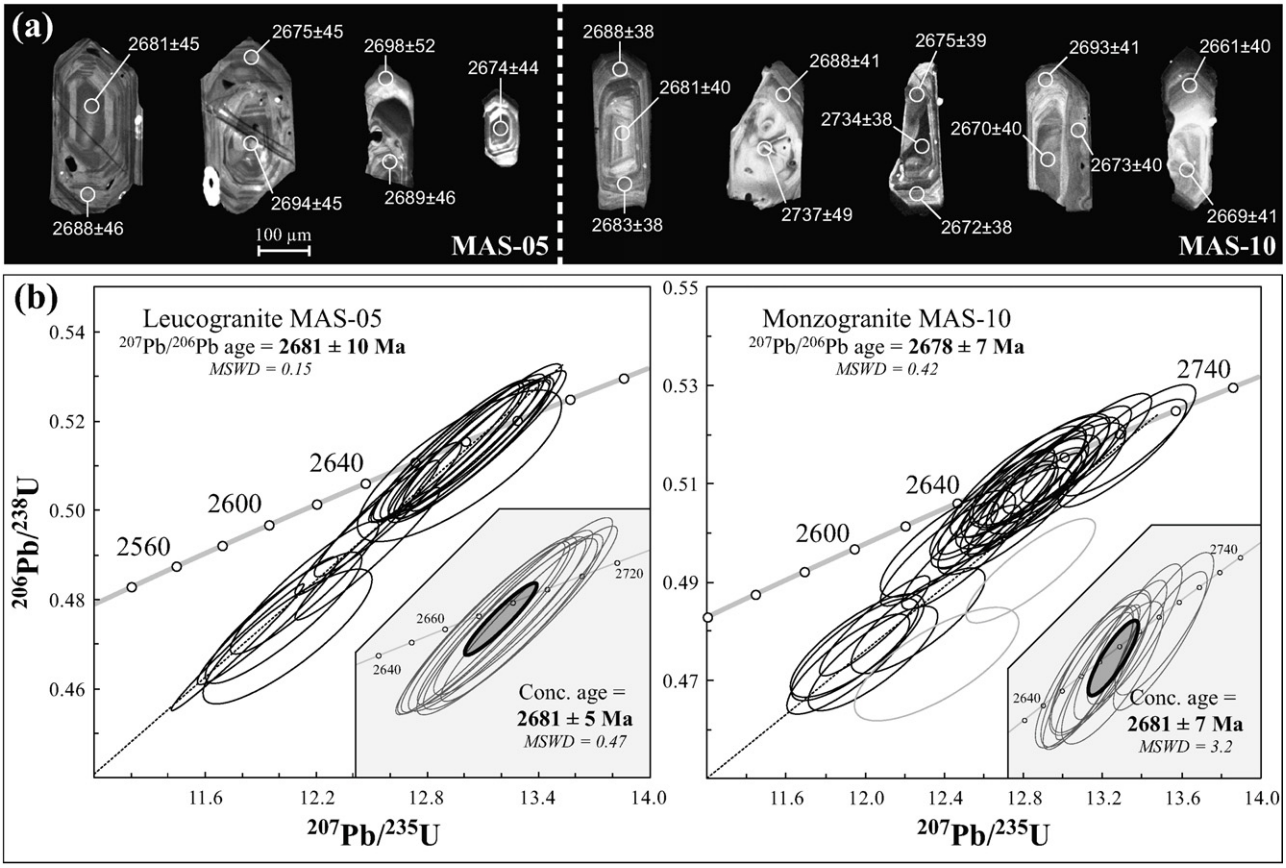


**Fig. 4.** (a) CL pictures of selected zircon grains from samples of the Mashashane pluton. The circles represent the position of laser spots used for age determination, and the associated values are the resulting $^{207}Pb/^{206}Pb$ age (in Ma) and its uncertainty (2σ). (b) Concordia plots ($^{206}Pb/^{238}U$ vs. $^{207}Pb/^{235}U$) for data obtained on samples from the Mashashane pluton. Light gray ellipses represent analyses that were not used to calculate the $^{207}Pb/^{206}Pb$ age. The insert on the bottom right is a close-up on the Concordia showing the analyses used for the calculation of the Concordia (Conc.) age. Error ellipses are 2σ.

Data reduction was carried out using the GLITTER® software (van Achterbergh et al., 2001). For each spot analysis, the time-resolved signals of single isotope and isotope ratios (which generally comprises 400–500 cycles of measurements) were examined carefully for signal perturbations reflecting the presence of common Pb (e.g. analysis of tiny inclusions), important Pb loss or mixing of different age domains. Analyses containing common Pb (see above) and characterized by more than 5–15% discordance (depending on the sample) were systematically discarded. The ratios $^{207}Pb/^{206}Pb$, $^{206}Pb/^{238}U$, and $^{207}Pb/^{235}U$ (the latter being obtained from $^{207}Pb/^{238}U$ using $^{238}U/^{235}U = 137.88$) and their uncertainties were calculated after correction of raw signals for elemental fractionation and instrumental mass discrimination using classical standard bracketing (GJ-1 reference material). External reproducibility of standard measurements was propagated in the error calculation by quadratic addition following Horstwood et al. (2003). Th, U and Pb concentrations were calibrated relative to the certified contents of standard GJ-1. The whole dataset is available as Supplementary Material.

Subsequent age calculations and Concordia plots were realized using the software package Isoplot v.4.10 (Ludwig, 2008). After data reduction, the remaining dataset consists of concordant to slightly discordant analyses, on the basis of which two different ages were determined: (1) a concordant age (referred to as "Concordia age" in the following), calculated using individual analyses having identical $^{206}Pb/^{238}U$ and $^{207}Pb/^{235}U$ ages (for details about the calculation of age and uncertainties, see Ludwig, 1998) and (2) a discordant age that is the average of all individual $^{207}Pb/^{206}Pb$ ages for this sample, weighted according to their internal 2σ error (referred to as "average $^{207}Pb/^{206}Pb$ age" in the following). Both of them are presented for purposes of comparison, in the text and in Figs. 2–7. The uncertainties of Concordia ages are 2σ, while the errors of average $^{207}Pb/^{206}Pb$ ages are quoted with 95% confidence (i.e. 1.96σ; see Ludwig, 2008 for more details).

### 4.2. Results

Table 1 is a list of the samples dated in this study, which includes rock types, mineral compositions as well as localities and GPS coordinates of sampling sites.

#### 4.2.1. Mashashane pluton

Two samples from the Mashashane pluton have been dated: a hornblende-biotite monzogranite (MAS-10) and a pink leucogranite (MAS-05). The zircon grains from MAS-05 have sizes ranging between 100 and 400 µm. They are euhedral, prismatic and range from colorless and transparent to dark pinkish. In addition, they display a well-developed oscillatory zoning free of complex internal structures (Fig. 4a). 19 analyses carried out on 15 crystals give an average $^{207}Pb/^{206}Pb$ age of 2681 ± 10 Ma, whereas the 9 concordant spots yield a Concordia age of 2681 ± 5 Ma (MSWD = 0.47) (Fig. 4b).

Zircons from MAS-10 are ~300 µm long, transparent and light pink. They exhibit continuous oscillatory zoning, albeit somewhat complex in some cases (Fig. 4a). 32 spot analyses from 12 grains give an average $^{207}Pb/^{206}Pb$ age of 2681 ± 7 Ma, identical to the Concordia age of 2681 ± 7 Ma (MSWD = 3.2) yielded by 10 analyses (Fig. 4b). Two analyses (MAS10-09-2 and

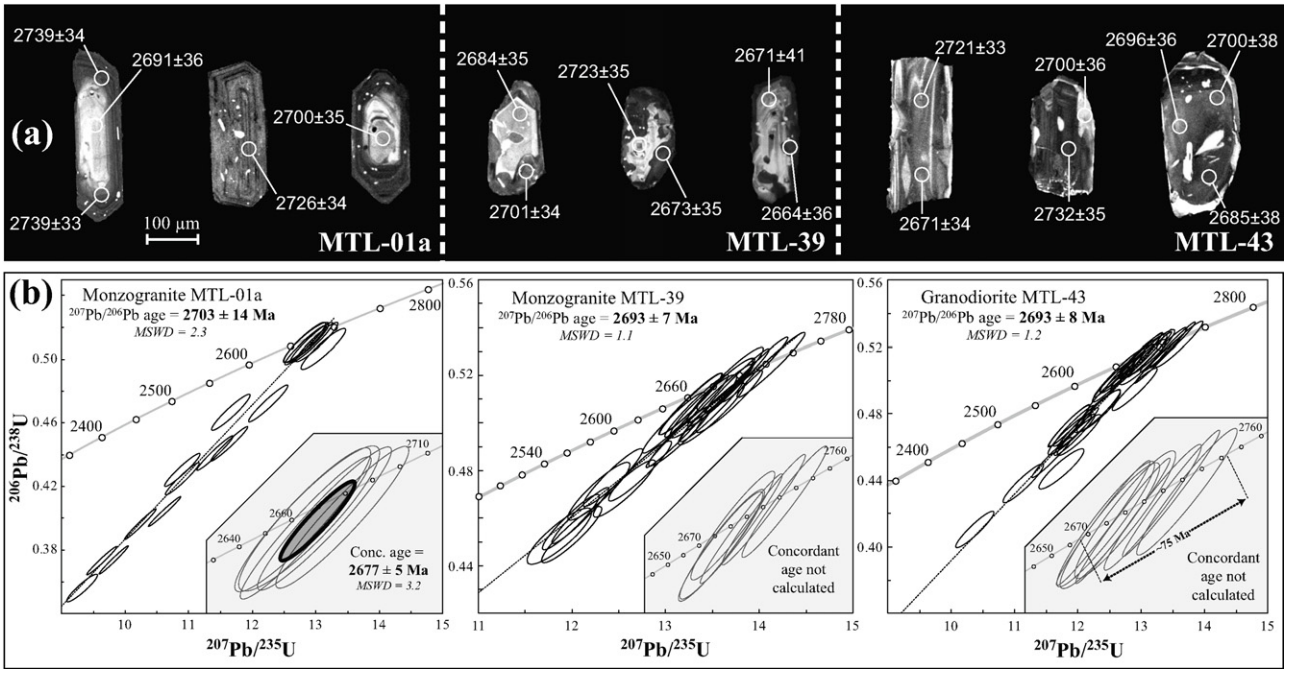


**Fig. 5.** (a) CL pictures of selected zircon grains from samples of the Matlala pluton. The circles represent the position of laser spots used for age determination, and the associated values are the resulting $^{207}Pb/^{206}Pb$ age (in Ma) and its uncertainty (2σ). (b) Concordia plots ($^{206}Pb/^{238}U$ vs. $^{207}Pb/^{235}U$) for data obtained on samples from the Matlala pluton. The insert on the bottom right is a close-up on the Concordia showing the analyses used for the calculation of the Concordia (Conc.) age. Error ellipses are 2σ.

MAS10-10-1) yield significantly older individual $^{207}Pb/^{206}Pb$ ages of 2737 ± 49 Ma and 2734 ± 38 Ma, respectively. When these two points are removed from age calculation, the $^{207}Pb/^{206}Pb$ age becomes 2678 ± 7 Ma (Fig. 4b), which is undistinguishable from the former one.

*4.2.2. Matlala pluton*

Three Matlala samples were dated: a pink (MTL-01a) and a gray (MTL-39) biotite monzogranites together with a medium-grained, dark gray, hornblende-biotite granodiorite (MTL-43).

Zircons of MTL-01a are euhedral to subhedral prismatic crystals (aspect ratio <4) and pinkish to brownish in color. Most grains contain small inclusions, mostly apatite (Fig. 5a). Oscillatory zoning is common but not systematic. 17 analyses carried out on 13 zircon grains provide highly discordant data (Fig. 5b) resulting in an average $^{207}Pb/^{206}Pb$ age of 2703 ± 14 Ma. On the other hand, 5 concordant analyses yield a significantly younger Concordia age of 2677 ± 5 Ma (MSWD = 3.2) (Fig. 5b).

Zircons from MTL-39 are dark pink, subhedral to anhedral, with typical rounded shapes. CL images reveal their rather complex internal structure, which consists of a bright, oscillatory zoned core that is strongly corroded and embayed is always overgrown by a darker, unzoned rim (Fig. 5a). 18 core analyses and 7 rim analyses were obtained from 16 grains. The cores are always U-poor (<100 ppm) whereas the rims are richer in U (> 100 ppm). However, age data fail to discriminate between both domains as individual $^{207}Pb/^{206}Pb$ ages obtained from the cores and rims overlap. All together, they give an average of 2693 ± 7 Ma (MSWD = 1.1) (Fig. 5b). The individual $^{207}Pb/^{206}Pb$ ages are somewhat scattered (Fig. 3b), ranging between 2729 ± 34 Ma and 2664 ± 38 Ma. Because of this scatter, we failed to obtain any Concordia age for sample MTL-39 (Fig. 5b).

MTL-43 contains zircon grains that are usually subhedral, colorless to pinkish and brownish. Inclusions are frequent and the grains exhibit irregular internal zoning, either oscillatory or patchy (Fig. 5a). 26 analyses from 18 grains were used for age calculation. The individual $^{207}Pb/^{206}Pb$ ages show the same scatter (from 2665 ± 34 Ma to 2732 ± 35 Ma) and the same average value (2693 ± 8 Ma; MSWD = 1.2) as zircons from sample MTL-39 (Fig. 5b). Multiple analyses of the same zircon domain can yield age variations >100 Ma (including uncertainties), and 8 concordant analyses encompass ~75 Ma (Fig. 5b) such that no Concordia age was obtained.

*4.2.3. Moletsi pluton*

From the Moletsi pluton, a coarse-grained, pinkish gray biotite monzogranite (MOL-05c) and a medium-grained, porphyritic biotite monzogranite (MOL-02c) have been dated.

The zircons of MOL-02c appear as euhedral, long-prismatic crystals which length ranges from 100 to 300 μm, some ones being as long as 500 μm (Fig. 6a). They are light pink to light brown and usually display a regular oscillatory zoning. The 19 spots carried out on 14 grains give an average $^{207}Pb/^{206}Pb$ age of 2688 ± 10 Ma (MSWD = 0.19), which is identical within error to the Concordia age of 2684 ± 5 Ma (MSWD = 1.12) obtained from 8 analyses (Fig. 6b).

Zircons from MOL-05c are light to dark brown, long to short prismatic (aspect ratio ranging from 1.5 to 4). Their zoning can be complex, either oscillatory or irregular (Fig. 6a). A total of 28 spot analyses, obtained from 16 zircon grains, yield an average $^{207}Pb/^{206}Pb$ age of 2685 ± 7 Ma (MSWD = 0.31) (Fig. 6b). This age is undistinguishable from the Concordia age of 2684 ± 4 Ma (MSWD = 4.0) calculated on the basis of 10 analyses (Fig. 6b). It must be noted that two analyses performed in heavily fractured zircon domains yield significantly older $^{207}Pb/^{206}Pb$ ages of 2748 ± 38 Ma (analysis MOL05c-23-1) and 2764 ± 37 Ma (analysis MOL05c-22-2). These two analyses were not taken into account for the age calculations.

*4.2.4. Matok Igneous Complex*

One sample of each of the three magmatic phases of the Matok Igneous Complex has been dated: a hornblende-biotite porphyritic granodiorite (MAT-13), a pink porphyritic biotite monzogranite (MAT-24) and a fine-grained, dark pyroxene-bearing diorite (MAT-60).

**Table 1**
Nature, mineralogy, sampling localities and GPS co-ordinates of granitoid samples dated in this study.

| Pluton/Unit | Sample | Rock type[a] | Rock-forming minerals[b] | Minor and accessory minerals[b] | Locality | GPS Co-ordinates | |
|---|---|---|---|---|---|---|---|
| | | | | | | Lat. S | Long. E |
| Mashashane | MAS-05 | Monzogranite | Qz, Kfs, Pl, Bt | Mag, Ep, Ap, Ttn, Zrn, Aln | Along railway 1.5 km W of Lunsklip station | 24°01′33″ | 29°07′02″ |
| | MAS-10 | Granodiorite | Pl, Qz, Kfs, Bt, Hbl | Ilm, Mag, Ap, Ttn, Zrn, Aln | Along track 2 km W of Ga-Mashashane | 23°56′34″ | 29°04′27″ |
| Matlala | MTL-01a | Monzogranite | Qz, Kfs, Pl, Bt | Mag, Ttn, Ep, Ap, Zrn, Aln | Bottom of hill 1.5 km SW of Ga-Madietane | 23°49′11″ | 28°59′58″ |
| | MTL-39 | Monzogranite | Qz, Pl, Kfs, Bt | Mag, Ttn, Ep, Ap, Zrn, Aln | Along tarred road just opposite to Tibanefo | 23°38′36″ | 29°01′09″ |
| | MTL-43 | Granodiorite | Pl, Qz, Kfs, Hbl, Bt | Ilm, Mag, Cpx, Ap, Ttn, Zrn, Aln | Along track 0.5 km E of Ntlolane | 23°43′20″ | 28°59′11″ |
| Matok | MAT-13 | Granodiorite | Pl, Qz, Kfs, Bt, Hbl | Ilm, Mag, Ep, Ap, Ttn, Zrn, Aln | Loose quarry along N1 road south of Mphakane | 23°31′31″ | 29°42′12″ |
| | MAT-24 | Monzogranite | Qz, Kfs, Pl, Bt | Ilm, Ttn, Ap, Ep, Zrn, Aln | Along track 10 km W of Sekakene | 23°26′42″ | 29°35′10″ |
| | MAT-60 | (Qz-Monzo)Diorite (Enderbite[c]) | Pl, Bt, Cpx, Qz, Opx, Kfs | Ilm, Mag, Ap, Zrn, Aln | Bed of the Sand River | 23°26′35″ | 29°38′27″ |
| Moletsi | MOL-02c | Monzogranite | Qz, Pl, Kfs, Bt | Ilm, Mag, Ttn, Ap, Zrn, Aln | Small hill in Koloti, 2 km N of R567 road | 23°44′53″ | 29°18′43″ |
| | MOL-05c | Monzogranite | Qz, Kfs, Pl, Bt | Mag, Ilm, Ep, Ap, Ttn, Zrn, Aln | Large pavement W of Mahwibitswane | 23°43′03″ | 29°18′18″ |
| Duiwelskloof | DWK-01 | Monzogranite | Qz, Kfs, Pl, Bt | Mag, Ilm, Ap, Zrn | Along R528 road 0.5 km E of Haenertsburg | 23°56′26″ | 29°56′53″ |
| | DWK-04 | Granodiorite (gneiss) | Qz, Pl, Kfs, Bt | Ilm, Mag, Ap, Zrn, Aln | Along tarred road down the Modjadji Nature Reserve | 23°36′43″ | 30°19′44″ |
| | DWK-06 | Monzogranite | Qz, Kfs, Pl, Bt | Mag, Ilm, Ap, Zrn | Along track 3.5 km SE of Ga-Matshwi | 23°36′24″ | 30°23′37″ |
| Hout River | HRG-1 | Tonalite (gneiss) | Pl, Qz, Bt, Kfs | Ilm, Mag, Ap, Zrn, Aln | Bed of the Kalkspruit River, 1 km SE of Lepotlako | 23°47′33″ | 29°07′39″ |
| | HRG-2 | Monzogranite | Qz, Kfs, Pl, Bt | Mag, Ap, Zrn, Aln | | 23°47′34″ | 29°07′43″ |

[a] After QAPF modal classification of Streckeisen (1974).
[b] Mineral abbreviations after Whitney and Evans (2010); minerals are classified from most abundant to less abundant.
[c] The term "enderbite" refers to the nomenclature used by Bohlender et al. (1992) and Barton et al. (1992).

Zircons from granodiorite MAT-13 are subhedral and long-prismatic, transparent, colorless to light pink and have sizes in the range 200–400 μm. Their internal zoning is rather complex, albeit sometimes oscillatory. Small inclusions of apatite are common (Fig. 7a). The 27 analyses performed on 17 zircon grains yield an average $^{207}Pb/^{206}Pb$ age of 2688 ± 8 Ma (MSWD = 0.85), which is identical to the Concordia age of 2679 ± 4 Ma (MSWD = 3.7) calculated on the basis of 9 analyses (Fig. 7b). It must be noted that the Concordia age display a high MSWD which we interpret as reflecting a relative spread (over ~60 Ma) of individual concordant ages.

In monzogranite MAT-24, zircons are euhedral, with an aspect ratio that ranges from 2 to 4. They are brown with a regular, oscillatory zoning and also contain apatite inclusions (Fig. 7a). 27 analyses from 18 zircon grains give an average $^{207}Pb/^{206}Pb$ age of 2679 ± 9 Ma (MSWD = 0.37), identical to the Concordia age of 2676 ± 6 Ma (MSWD = 7.0) obtained from 10 analyses (Fig. 7b). Two grains reveal rounded CL-bright zones, which are surrounded by CL-dark rims (grain #1 of Fig. 7a). One of these cores yielded a very discordant $^{207}Pb/^{206}Pb$ age of 2939 ± 44 Ma (analysis MAT24-23-01), while the second gave a concordant age of ~2727 Ma (analysis MAT24-07-01; see Fig. 7a).

The diorite MAT-60 contains smaller zircons (<250 μm) than in all other Matok samples, which are commonly long-prismatic (aspect ratio ~3), transparent and colorless. They reveal a concentric, oscillatory zoning that is locally more irregular, patchy or cloudy (Fig. 7a). 25 grains supplied a total of 40 analyses, all of them being concordant to sub-concordant and yielding an average $^{207}Pb/^{206}Pb$ age of 2686 ± 7 Ma (MSWD = 0.22), identical to a Concordia age of 2683 ± 3 Ma (MSWD = 3.6) obtained from 13 analyses (Fig. 7b).

#### 4.2.5. Duiwelskloof batholith

Three samples of the Duiwelskloof batholith were dated: two equigranular, medium-grained biotite granites (DWK-01 and DWK-06) and one of gneissic and slightly migmatized biotite granodiorite (DWK-04).

Sample DWK-01 contains a heterogeneous zircon population (Fig. 8a): (1) some grains are euhedral to subhedral with an aspect ratio ranging from 2 to 4; generally they are light to dark pink; (2) other grains are smaller (<150 μm) with anhedral, locally angular shapes. Moreover, some grains display simple, oscillatory zoning, whereas others bear a relatively bright and regularly zoned core, surrounded by dark overgrowths. On the basis of CL brightness two generations of rims can be identified in some grains (e.g. grain #3 of sample DWK-01 in Fig. 8a). Finally, owing to their angular shape and sharp edges that cross-cut the internal zoning, some crystals have been interpreted as xenocrysts. This textural heterogeneity is reflected by the age distribution. The 24 spot analyses obtained from 13 zircon grains cluster in three age groups (Fig. 8b): (1) 18 analyses yielded an average $^{207}Pb/^{206}Pb$ age of 2841 ± 10 Ma (MSWD = 0.25), which is identical to the 2840 ± 4 Ma (MSWD = 0.65) Concordia age (7 analyses). (2) 4 analyses, including a sub-concordant one, give an older average $^{207}Pb/^{206}Pb$ age of 2936 ± 21 Ma (MSWD = 0.13); (3) two analyses of zircon cores (DWK01-06-01 and DWK01-07-01) provided significantly older individual $^{207}Pb/^{206}Pb$ ages of 3119 ± 44 and 3124 ± 45 Ma. It is noteworthy that a single zircon grain can have recorded these three events. This is the case of grain DWK01-07 (grain #3 in Fig. 8a), the core of which is 3119 ± 44 Ma-old while its inner rim was dated at 2932 ± 44 Ma and its outer rim at 2864 ± 43 Ma.

Zircons of the gneissic granodiorite sample DWK-04 are much less heterogeneous than that of DWK-01. The grains are generally ≤200 μm, dark pink and transparent, long-prismatic with an aspect ratio ≥3 and up to 5 (Fig. 8a). For age calculation, we used 17 analyses from 9 zircon grains. 14 analyses give an average

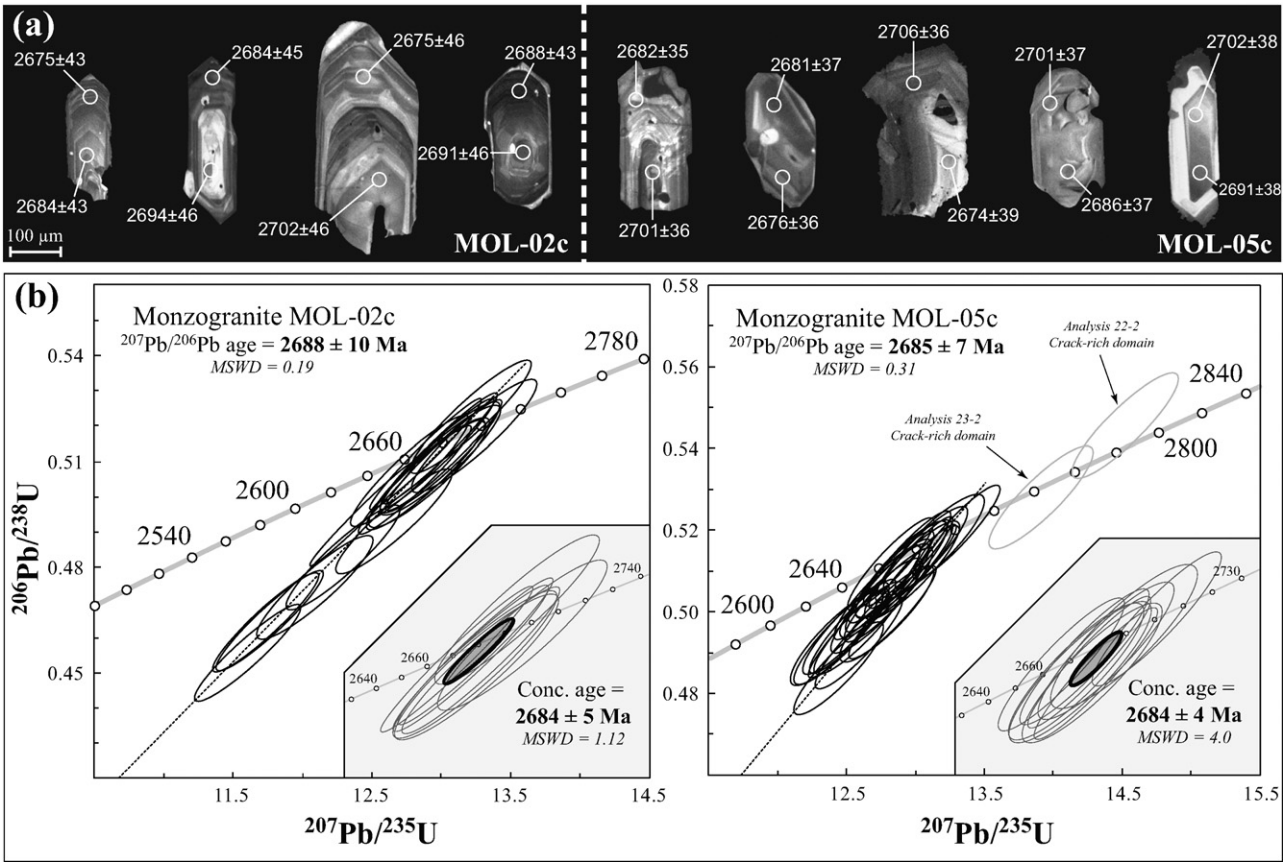


**Fig. 6.** (a) CL pictures of selected zircon grains from samples of the Moletsi pluton. The circles represent the position of laser spots used for age determination, and the associated values are the resulting $^{207}Pb/^{206}Pb$ age (in Ma) and its uncertainty (2σ). (b) Concordia plots ($^{206}Pb/^{238}U$ vs. $^{207}Pb/^{235}U$) for data obtained on samples from the Moletsi pluton. Light gray ellipses represent analyses that were not used to calculate the $^{207}Pb/^{206}Pb$ age. The insert on the bottom right is a close-up on the Concordia showing the analyses used for the calculation of the Concordia (Conc.) age. Error ellipses are 2σ.

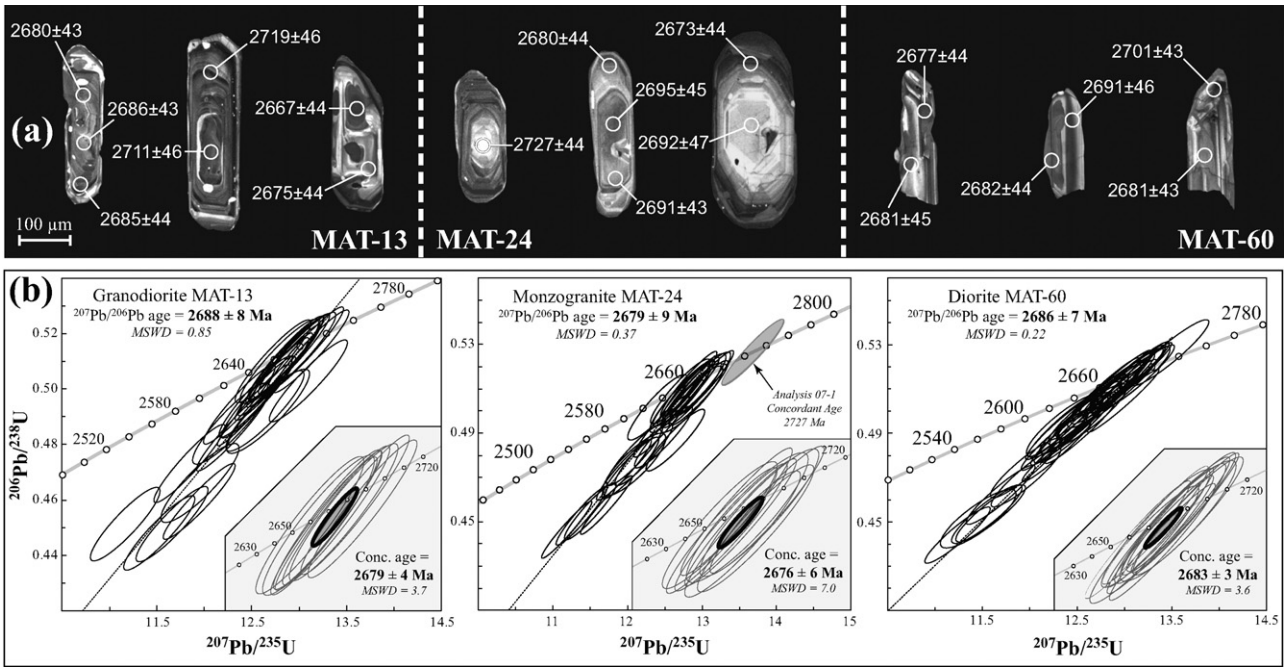


**Fig. 7.** (a) CL pictures of selected zircon grains from samples of the Matok Igneous Complex. The circles represent the position of laser spots used for age determination, and the associated values are the resulting $^{207}Pb/^{206}Pb$ age (in Ma) and its uncertainty (2σ). (b) Concordia plots ($^{206}Pb/^{238}U$ vs. $^{207}Pb/^{235}U$) for data obtained on samples from the Matok Igneous Complex. Light gray ellipses represent analyses that were not used to calculate the $^{207}Pb/^{206}Pb$ age. The insert on the bottom right is a close-up on the Concordia showing the analyses used for the calculation of the Concordia (Conc.) age. Error ellipses are 2σ.

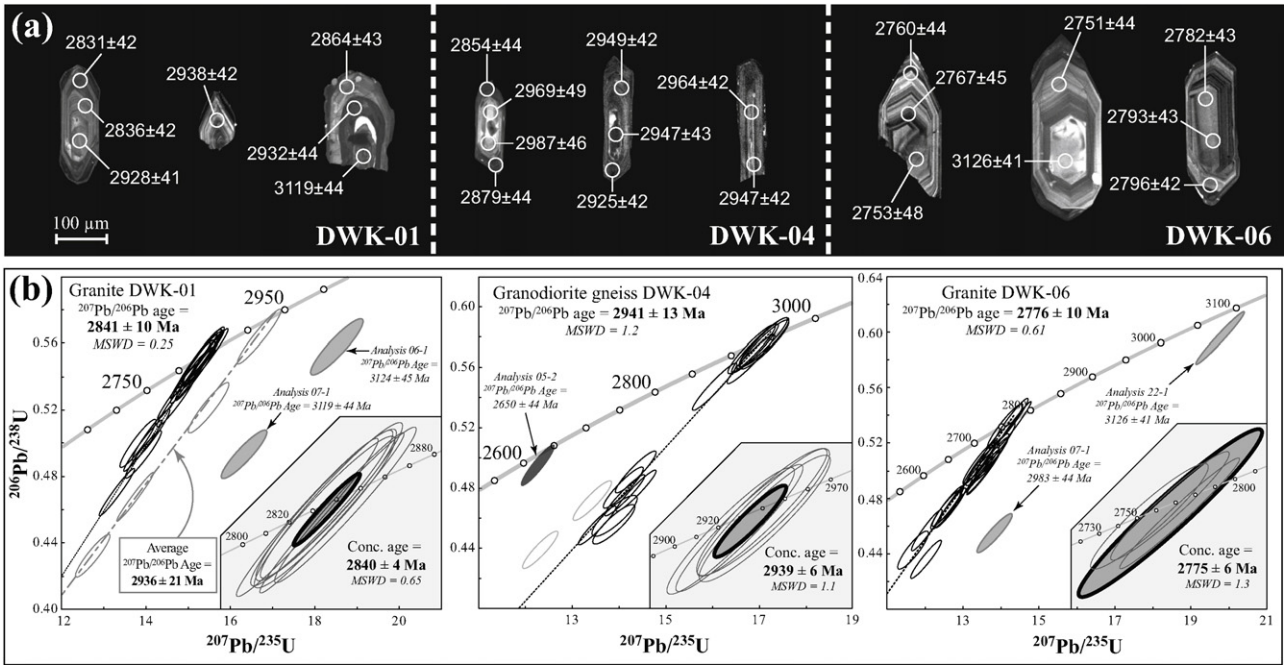


**Fig. 8.** (a) CL pictures of selected zircon grains from samples of the Duiwelskloof batholith. The circles represent the position of laser spots used for age determination, and the associated values are the resulting $^{207}Pb/^{206}Pb$ age (in Ma) and its uncertainty (2σ). (b) Concordia plots ($^{206}Pb/^{238}U$ vs. $^{207}Pb/^{235}U$) for data obtained on samples from the Duiwelskloof batholith. Light gray ellipses were not used to calculate the $^{207}Pb/^{206}Pb$ age and filled gray ellipses are inherited analyses. The insert on the bottom right is a close-up on the Concordia showing the analyses used for the calculation of the Concordia (Conc.) age. Error ellipses are 2σ.

$^{207}Pb/^{206}Pb$ age of 2941 ± 13 Ma (MSWD = 1.2), which is identical to the Concordia age of 2939 ± 6 Ma (MSWD = 1.1), calculated on the basis of 5 analyses (Fig. 8b). In contrast, two discordant analyses (DWK04-01-3 and DWK04-01-4) result in an average $^{207}Pb/^{206}Pb$ age of 2866 ± 31 Ma, while a sub-concordant analysis (DWK04-05-2) yields an individual $^{207}Pb/^{206}Pb$ age of 2650 ± 44 Ma.

In the granite DWK-06 zircon crystals are short-prismatic and light pink to light brown in color. They do not display any complex internal structure but a systematic and well-developed oscillatory zoning (Fig. 8a), excepted for two grains that contain a bright core (DWK06-22, grain #2 in Fig. 8a, and DWK06-07). 19 analyses from 12 zircon grains provide an average $^{207}Pb/^{206}Pb$ age of 2776 ± 10 Ma (MSWD = 0.61) similar to the Concordia age of 2775 ± 6 Ma (MSWD = 1.3) calculated from 3 spots (Fig. 8b). The two bright cores yield older individual $^{207}Pb/^{206}Pb$ ages: 2983 ± 44 Ma (analysis DWK06-07-01) and 3126 ± 41 Ma (analysis DWK06-22-01).

#### 4.2.6. Goudplaats–Hout River Gneisses

Two samples of the Goudplaats–Hout River Gneisses were dated: a pinkish, medium-grained migmatitic biotite gneiss, tonalitic in composition (HRG-1) and a fine-grained pink biotite granite (HRG-2) that intrudes HRG-1.

Zircons crystals extracted from HRG-1 are transparent, colorless to light pinkish and have a heterogeneous size distribution (50–250 µm). All are euhedral with an aspect ratio from 1.5 to 4 and exhibit regular oscillatory zoning (Fig. 9a). Only one grain displays a bright rounded core (Fig. 9a, grain #2). Age data were determined on the basis of 15 analyses obtained from 11 zircon grains. No Concordia age has been obtained, Nevertheless, 11 discordant analyses give an average $^{207}Pb/^{206}Pb$ age of 2953 ± 13 Ma (MSWD = 0.44) (Fig. 9b). Three spots (HRG-1-07-1; HRG-1-09-2 and HRG-1-22-2) were excluded from the calculation as they yield significantly younger $^{207}Pb/^{206}Pb$ ages (weighted average of 2889 ± 25 Ma). The rounded core of zircon #2 in Fig. 9a (analysis HRG-1-09-1) has a sub-concordant age of 3125 ± 45 Ma (Fig. 9b).

Granite HRG-2 contains pinkish zircons with subhedral to euhedral shapes and a regular oscillatory zoning (Fig. 9a). Some grains contain very bright cores surrounded by gray rims (see grains #1, #4 and #5 of sample HRG-2 in Fig. 9a). 22 spot analyses from 15 grains are concordant to moderately discordant with an average $^{207}Pb/^{206}Pb$ age of 2836 ± 11 Ma (MSWD = 0.52), which is undistinguishable from the Concordia age of 2833 ± 5 Ma (MSWD = 2.0) obtained from 6 analyses (Fig. 9b). Two sub-concordant cores (HRG-2-15-1 and HRG-2-21-1; see grains #4 and #5 on Fig. 9a) yield significantly older individual $^{207}Pb/^{206}Pb$ ages of 2966 ± 44 Ma and 2959 ± 43 Ma (Fig. 9b). Similarly, the analysis of the bright core of grain #1 in Fig. 7a (analysis HRG-2-04-1) gives an even older concordant age of ~3190 Ma (Fig. 9b). In addition, 3 analyses present older $^{207}Pb/^{206}Pb$ ages between ~2895 and ~2950 Ma, one being sub-concordant at 2914 ± 43 Ma (Fig. 9b).

## 5. Discussion

### 5.1. Interpretation of age data

Table 2 summarizes the ages or groups of ages obtained for each sample. Their significance is discussed in the following, from the oldest to the youngest.

#### 5.1.1. Goudplaats–Hout River Gneisses (ca. 3350–2840 Ma)

Samples HRG-1 and HRG-2 provided three age clusters: (1) 3100–3200 Ma, (2) ~2950 Ma and (3) ~2830 Ma (see Table 2 and Fig. 10). The oldest ages yielded by both samples (~3125 Ma in HRG-1; ~3190 Ma in HRG-2) are from zircon cores. These ages are slightly younger than the oldest ages obtained so far from this gneiss unit, namely: (1) emplacement ages of 3333 ± 5 Ma (Brandl and Kröner, 1993) and 3282.6 ± 0.4 Ma (Kröner et al., 2000) for two migmatitic gneisses; and (2) ages peaks at 3210–3260 Ma and ~3350 Ma for detrital zircons from the Pietersburg greenstone belt (Zeh and Gerdes, 2012), the provenance of which is likely to be, at least partly, the Goudplaats–Hout River gneisses. Thus, we interpret

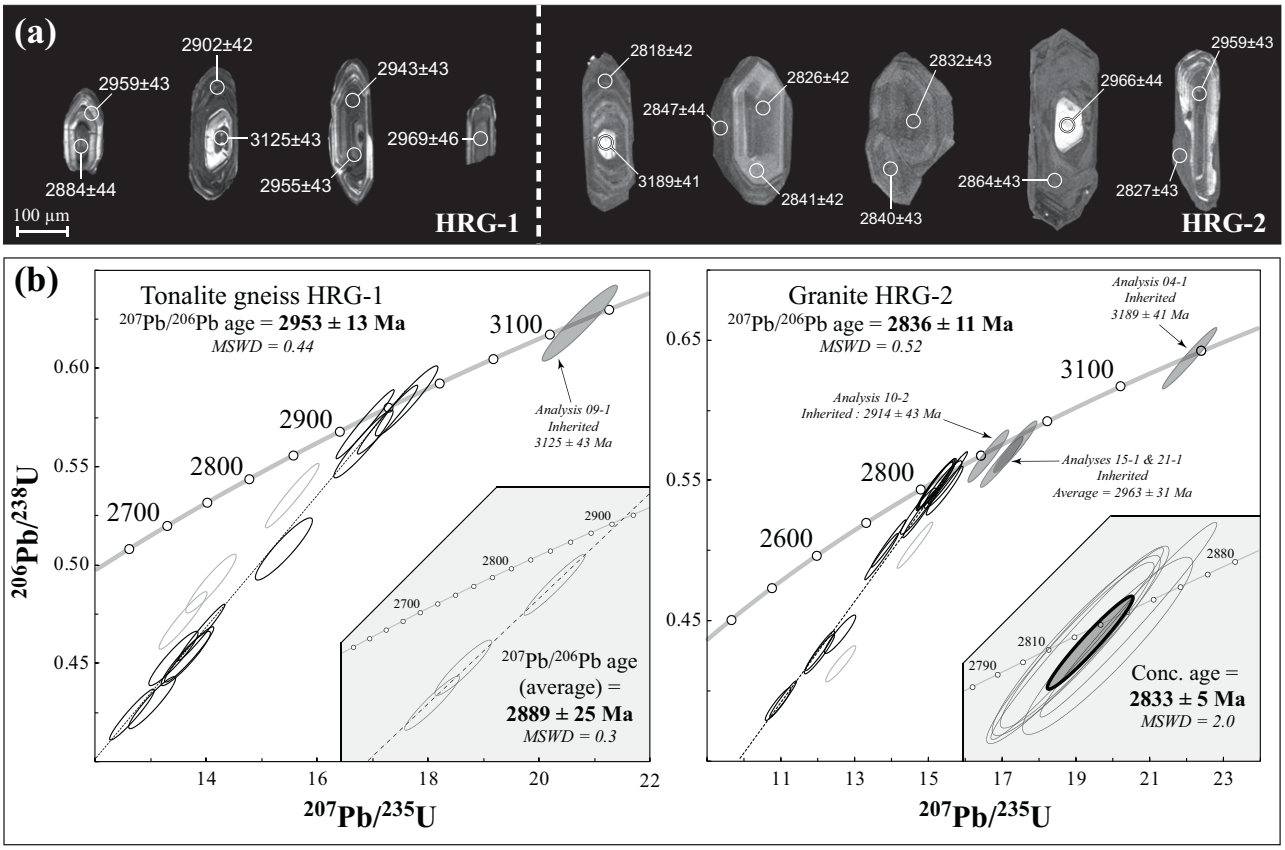


**Fig. 9.** (a) CL pictures of selected zircon grains from samples of the Goudplaats–Hout River gneisses. The circles represent the position of laser spots used for age determination, and the associated values are the resulting $^{207}Pb/^{206}Pb$ age (in Ma) and its uncertainty (2σ). (b) Concordia plots ($^{206}Pb/^{238}U$ vs. $^{207}Pb/^{235}U$) for data obtained on samples from the Hout River gneisses. Light gray ellipses represent analyses that were not used to calculate the $^{207}Pb/^{206}Pb$ age, and filled gray ellipses are inherited analyses. The insert on the bottom right is a close-up on the Concordia showing the analyses used for the calculation of the Concordia (Conc.) age. Error ellipses are 2σ.

**Table 2**
Summary of U–Pb dating results on granitoid samples from the Pietersburg block and their preferred interpretation.

| Unit | Sample | Age (Ma) | ±2σ | Type[a] | Interpretation |
|---|---|---|---|---|---|
| Matok Igneous Complex | MAT-13 | 2688 | 8 | Pb/Pb WA | Intrusion |
| | MAT-24 | 2679 | 9 | Pb/Pb WA | Intrusion |
| | MAT-60 | 2686 | 7 | Pb/Pb WA | Intrusion |
| Matlala Pluton | MTL-01a | 2677 | 5 | Conc. | Intrusion |
| | MTL-39 | 2693 | 7 | Pb/Pb WA | Intrusion |
| | MTL-43 | 2693 | 8 | Pb/Pb WA | Intrusion |
| Mashashane Pluton | MAS-05 | 2681 | 10 | Pb/Pb WA | Intrusion |
| | MAS-10 | 2678 | 7 | Pb/Pb WA | Intrusion |
| Moletsi Pluton | MOL-02c | 2688 | 10 | Pb/Pb WA | Intrusion |
| | MOL-05c | 2685 | 7 | Pb/Pb WA | Intrusion |
| Goudplaats-Hout River Gneiss | HRG-1 | 2889 | 25 | Pb/Pb WA | *Metamorphic* |
| | | 2953 | 13 | Pb/Pb WA | Intrusion |
| | | 3125 | 43 | Pb/Pb Ind. | *Inheritance* |
| | HRG-2 | 2836 | 11 | Pb/Pb WA | Intrusion |
| | | 2941 | 25 | Pb/Pb WA | *Inheritance* |
| | | 3189 | 41 | Pb/Pb Ind. | *Inheritance* |
| Duiwelskloof "batholith" | DWK-01 | 2841 | 10 | Pb/Pb WA | Intrusion |
| | | 2936 | 21 | Pb/Pb WA | *Inheritance* |
| | | 3121 | 32 | Pb/Pb Ind. | *Inheritance* |
| | DWK-04 | 2650 | 44 | Pb/Pb Ind. | *Metamorphic* |
| | | 2866 | 31 | Pb/Pb WA | *Metamorphic* |
| | | 2941 | 13 | Pb/Pb WA | Intrusion |
| | DWK-06 | 2776 | 10 | Pb/Pb WA | Intrusion |
| | | 2983 | 44 | Pb/Pb Ind. | *Inheritance* |
| | | 3126 | 41 | Pb/Pb Ind. | *Inheritance* |

[a] The "Type" column indicates how the age was calculated: "Pb/Pb WA" refers to a weighted average of individual $^{207}Pb/^{206}Pb$ ages of all analyses for this sample; "Pb/Pb Ind." refers to the $^{207}Pb/^{206}Pb$ age of a single spot analysis; "Conc." refers to a Concordia age.

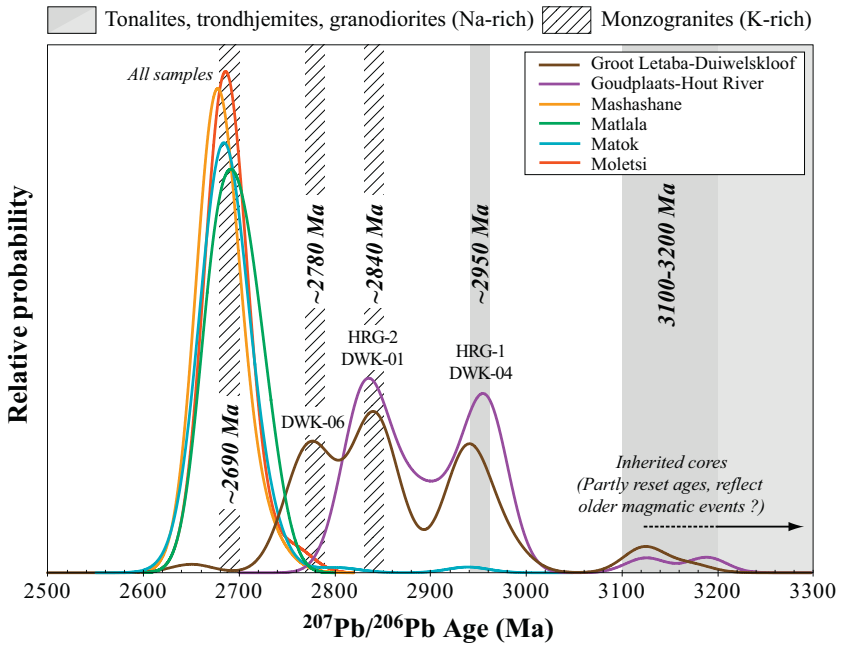


**Fig. 10.** Relative probability density plot of $^{207}Pb/^{206}Pb$ ages obtained from each granitoid pluton or gneiss unit dated in this study. For the Mashashane, Matlala, Matok and Moletsi plutons, all samples from each pluton have been considered, whereas distinction between samples has been made for the Goudplaats–Hout River and Groot Letaba–Duiwelskloof gneiss units. The gray and hatched areas represent the ages of the five successive magmatic events defined by the results of this study and respectively correspond to Na-rich (TTG) or K-rich (granites) magmatism (see Section 5).

our 3100–3200 Ma ages as inherited and recording an older magmatic event that took place between 3350 Ma and 3210 Ma. Subsequently, owing to a partial resetting of the U–Pb system during magmatic or metamorphic events, these ages shifted toward younger ages.

The average $^{207}Pb/^{206}Pb$ age of 2953 ± 13 Ma recorded by 11 zircon analyses of the tonalitic gneiss HRG-1 is consistent with the ages previously obtained from the Pietersburg greenstone belt: (1) pre- to syn-tectonic granitoids adjacent to sediments of the belt gave an age of 2958 ± 2 Ma (de Wit et al., 1993); (2) in these sediments, detrital zircons provide a major age peak at ~2950 Ma (de Wit et al., 1993; Zeh and Gerdes, 2012) and (3) the extrusion of the Ysterberg felsic lavas took place at 2949 ± 2 Ma (Kröner et al., 2000). As a result, we consider the age of 2953 ± 13 Ma as that of the emplacement of the tonalitic protolith of sample HRG-1 and, furthermore, of a major magmatic event in the Goudplaats–Hout River suite and the adjacent Pietersburg greenstone belt. On the other hand, we interpret the average $^{207}Pb/^{206}Pb$ age of 2889 ± 25 Ma measured on three zircon grains from HRG-1 as due to (1) a metamorphic overprint (presumably linked to the migmatization of the tonalitic gneisses), (2) partial resetting during the late magmatic event(s), or (3) mixed ages between the two main groups at ~2950 and ~2840 Ma.

Sample HRG-2 gives a well-constrained average $^{207}Pb/^{206}Pb$ age of 2836 ± 11 Ma that is identical within error to the Concordia age. We therefore interpret this age as being that of the granite intrusion, which is consistent with relative chronology as the granite HRG-2 intrudes the tonalitic gneiss HRG-1. Nevertheless, 5 analyses recorded individual $^{207}Pb/^{206}Pb$ ages ranging from 2895 ± 42 Ma to 2966 ± 44 Ma; this range is closely similar to that measured in HRG-1. We interpret this in terms of inheritance: HRG-2 preserved the memory of a precursor, the composition and history of which were similar to HRG-1 ones.

It is noteworthy that Brandl and Kröner (1993) obtained ages of ~2890 Ma for two samples of the Goudplaats–Hout River gneisses (a tonalitic gneiss and an associated discordant leucosome). These ages were obtained by the zircon evaporation technique such that these data may represent mixtures between 2950 and 2840 Ma, i.e. the ages of the main magmatic events in the Goudplaats–Hout River gneiss suite.

### 5.1.2. Duiwelskloof "batholith" (ca. 3210–2770 Ma)

All the investigated samples of the Duiwelskloof batholith are undeformed and preserved their original magmatic texture, except DWK-04 that underwent deformation and migmatization. Consequently, it appears that DWK-04 emplaced before the other components of the "batholith", which is corroborated by our dating. Indeed, we consider that its average $^{207}Pb/^{206}Pb$ age of 2941 ± 13 Ma represents the crystallization age of its granodiorite protolith. On the other hand, both biotite granites DWK-01 and DWK-06 provided younger average $^{207}Pb/^{206}Pb$ ages of 2841 ± 10 Ma and 2776 ± 10 Ma, respectively, which we interpret as being the age of their intrusion.

Cores from DWK-01 and DWK-06 zircons provide two groups of ages: (1) the first one is represented by two individual $^{207}Pb/^{206}Pb$ ages of 2936 ± 21 Ma (DWK-01) and 2983 ± 44 Ma (DWK-06), which likely witness significant inheritance from an older material similar to the granodiorite gneiss DWK-04 (emplaced at 2941 ± 13 Ma); (2) the second one encompass even older ages of 3124 ± 45 Ma (DWK-01) and 3126 ± 41 Ma (DWK-06). Zeh et al. (2009) already published similar ages of ~3120 Ma for zircons from a granite south of the Duiwelskloof "batholith". However, these ages are slightly younger than the oldest ages published so far for the area, i.e. an intrusion age of 3170.5 ± 0.3 Ma for a migmatitic gneiss south of the Giyani greenstone belt (Kröner et al., 2000). Such a discrepancy is very similar to that observed for the Goudplaats–Hout River gneiss unit. As a result, the oldest inherited zircons from the Duiwelskloof "batholith" possibly crystallized at 3170–3210 Ma and subsequently underwent a partial resetting of their U–Pb system while reworked during younger magmatic events. The same process is also considered as accounting for two young individual ages (~2650 Ma and ~2870 Ma) measured in sample DWK-04.

*5.1.3. Mashashane, Matlala, and Moletsi plutons (2670–2700 Ma)*

Compared with the Goudplaats–Hout River Gneisses and the Duiwelskloof "batholith", the age pattern for the Mashashane, Matlala and Moletsi plutons is simpler. Indeed, zircons from these granitoids do not record any complex internal structure (no inherited cores, no metamorphic overgrowth) and all age data cluster around a unique value. As a result, we considered the average $^{207}Pb/^{206}Pb$ age as representative of the crystallization age for each sample (summary in Table 2) and thus, that these massifs emplaced between 2670 and 2700 Ma (weighted average of all analyses = 2689 ± 3 Ma). This is consistent with similar ages of 2679 ± 7 Ma for the Uitloop granite that is part of the Mashashane pluton (Zeh et al., 2009) and of 2689 ± 2 Ma for a post-tectonic granite intruding meta-sediments of the Pietersburg greenstone belt (de Wit et al., 1993).

This convergence of ages suffers a single exception. Indeed, the Matlala granite (MTL-01a) shows significant difference between the Concordia age of 2677 ± 5 Ma and the average $^{207}Pb/^{206}Pb$ age of 2703 ± 14 Ma. Due to the poor quality of its zircon data, the average $^{207}Pb/^{206}Pb$ age includes up to 17% discordant analyses (see Supplementary Material), such that we consider that the Concordia age of 2677 ± 5 Ma better represents the granite intrusion age. Importantly, in all Matlala samples, the measured individual $^{207}Pb/^{206}Pb$ ages are rather scattered and, similarly, concordant ages may range over more than 75 Ma when errors are taken into account. However, there is no correlation between the age and the part of the crystal (core or rim) that have been analyzed. Matlala zircons differ from those of other studied rocks by the fact that they are notably rich in apatite inclusions (Fig. 5a). Consequently, we interpret their older ages as due to a minor contribution of common Pb owing to a mixed analysis of zircon and apatite, such that we consider the scatter of $^{207}Pb/^{206}Pb$ ages as an artifact and do not consider it for any geological interpretation. Nevertheless, this artifact does not significantly alter the age data, because the calculated average $^{207}Pb/^{206}Pb$ ages of samples MTL-43 and MTL-39 are identical within error to that of other samples from the Mashashane, Moletsi and Matok plutons.

*5.1.4. Matok Igneous Complex (~2685 Ma)*

Alike Mashashane, Matlala and Moletsi plutons, the Matok Igneous Complex displays a limited scatter of individual $^{207}Pb/^{206}Pb$ ages around 2685 Ma, which we interpret as the age of emplacement. A granite sample from the Matok Igneous Complex has been recently dated by Zeh et al. (2009) and gave a similar age of 2679 ± 7 Ma (U–Pb, LA-ICP-MS on zircon). Importantly, all these ages are slightly older than the U–Pb ages of 2664 to 2671 Ma previously published by Barton et al. (1992) for Matok granodiorites and "enderbites", respectively. Therefore, it appears that the Matok Igneous Complex is slightly (10–30 Ma) older than previously thought, so that it is coeval with the Matlala, Mashashane and Moletsi plutons that intruded on the other side of the Hout River shear zone.

*5.2. Implications for the architecture of the Pietersburg block*

The 2776 ± 10 Ma intrusion age obtained for leucogranite DWK-06 from the Duiwelskloof "batholith" appears as undistinguishable from the ages published on different facies of the Turfloop batholith, including porphyritic granodiorite (2777 ± 10 Ma and 2763 ± 15 Ma, Henderson et al., 2000) as well as biotite monzogranite (2765 ± 7 Ma, Kröner et al., 2000 and 2782 ± 13 Ma, Zeh et al., 2009). Therefore, it is likely that, at least, parts of the Duiwelskloof "batholith" actually correspond to the eastward continuation (or satellite intrusions) of the Turfloop batholith, as previously suggested by Henderson et al. (2000). On the other hand, the older ages measured in Duiwelskloof samples DWK-01 and DWK-04 indicate that other parts of the Duiwelskloof "batholith" underwent a more complex history. In other words, the Duiwelskloof "batholith" does not represent a single individual and continuous granitoid body, as initially mapped by Brandl (1987). This body was assumed to intrude the surrounding Groot Letaba gneiss unit that outcrops between the Pietersburg and the Murchison greenstone belts (see Fig. 2). However, Kröner et al. (2000) dated a quartzo-feldspathic orthogneiss of the Groot Letaba unit at $2953^{+68}_{-61}$ Ma, age that is similar to that of DWK-04. Similarly, Zeh et al. (2009) reported ages of 2839 ± 8 Ma and 2784 ± 8 Ma for samples of the Groot Letaba unit that are respectively equivalent to those of samples DWK-01 and DWK-06. Consequently, it appears that both the Duiwelskloof and Groot Letaba granitoids underwent the same history, i.e. succession of three magmatic events at ~2950 Ma, ~2840 Ma and ~2780 Ma. Therefore, it appears that the denomination of "batholith" is no longer relevant for rocks of the Duiwelskloof area, which must be considered as belonging to the same unit as the Groot Letaba gneisses. We propose to rename this unit the "Groot Letaba–Duiwelskloof gneiss unit".

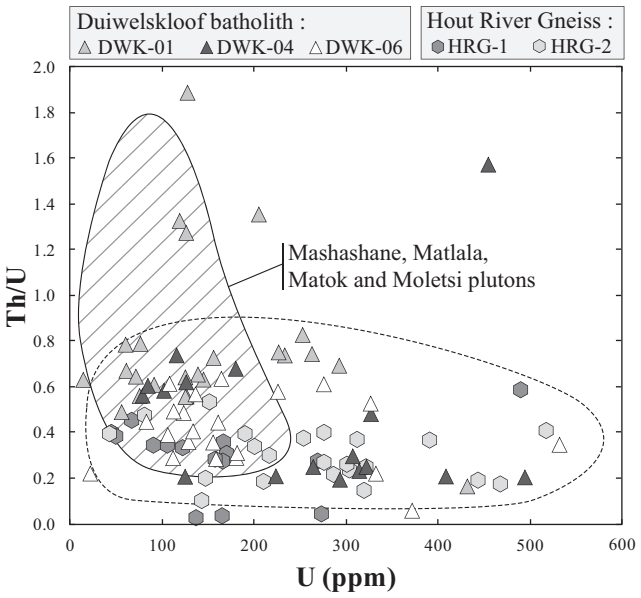


**Fig. 11.** Th/U vs. U diagrams expressing the chemical compositions of the dated zircons for (1) the Goudplaats–Hout River and Groot Letaba–Duiwelskloof units (symbols) and (2) the Mashashane, Matlala, Matok and Moletsi plutons (hatched field).

Furthermore, the ages measured in Duiwelskloof rocks not only correlate with those of the Groot Letaba gneisses but also with those of the Goudplaats–Hout River gneisses. As shown in Fig. 10, the Goudplaats–Hout River gneiss unit in one hand and the Groot Letaba–Duiwelskloof gneiss unit on the other hand, show the same three peaks of granitoid emplacement (or inheritance) at 3100–3200 Ma, ~2950 Ma and ~2840 Ma. In addition, samples from both domains not only have similar ages, but also display the same petrographic features. Specifically, DWK-04 and HRG-1 are migmatitic orthogneisses, whereas DWK-01 and HRG-2 are undeformed and equigranular biotite granites. Moreover, Goudplaats–Hout River and Groot Letaba–Duiwelskloof zircons are characterized by highly variable U concentrations (10–550 ppm) and typical magmatic Th/U ratios ranging from 0.1 to 0.8 (Fig. 11). Consequently, it clearly appears that the distinction between both gneiss units is somewhat artificial, such that they must be regarded jointly as the basement of the whole Pietersburg block, which underwent a common, polycyclic history with emplacement of granitoids at >3100 Ma (likely in the range 3150–3350 Ma), ~2950 Ma and ~2840 Ma.

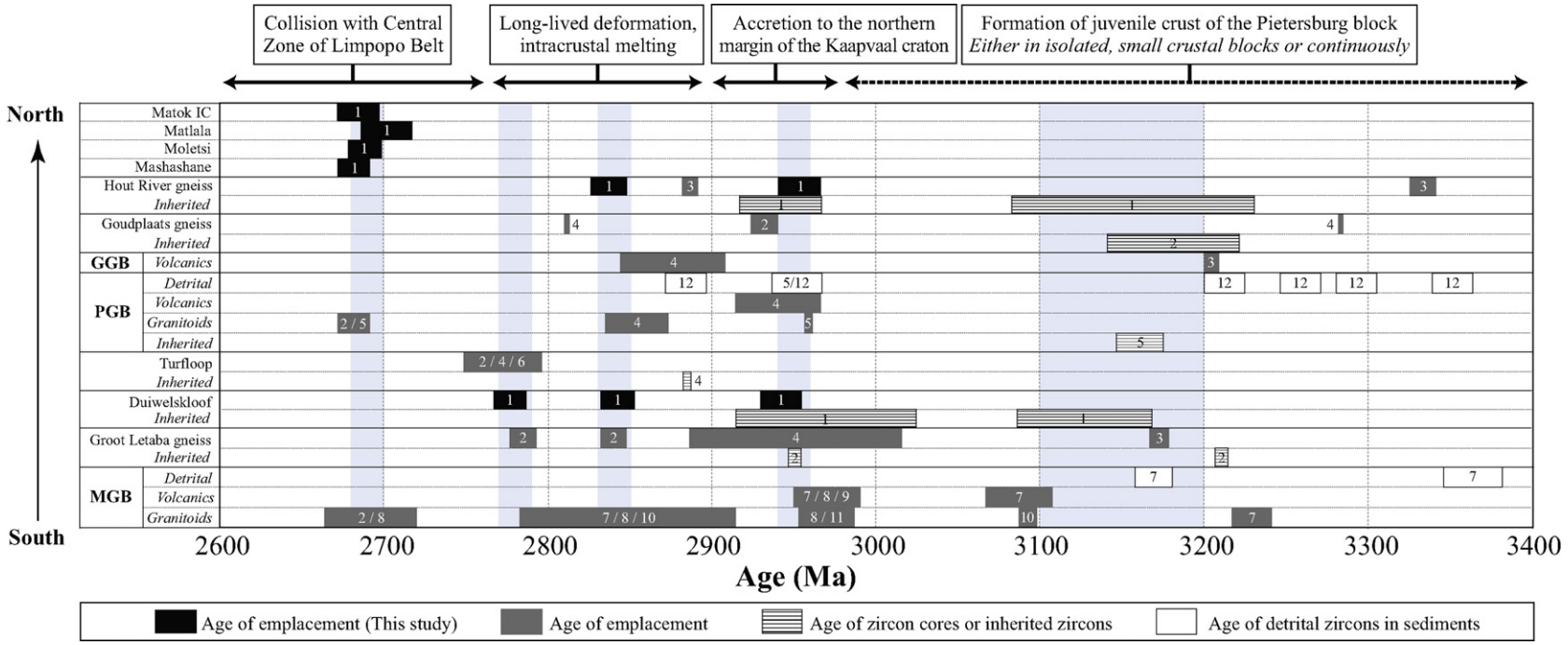


**Fig. 12.** Timeline for ages published so far in the northern Kaapvaal craton. Data are organized according to the geographic/structural position of dated samples, from south (bottom) to north (top). The light blue stripes refer to the five age clusters of Fig. 10. The timing of the main geological events related to the evolution of the Pietersburg block is also outlined (see text for details). Digits label the source of data: (1) This study U–Pb LA Zrn; (2) Zeh et al. (2009) U–Pb LA Zrn; (3) Brandl and Kröner (1993) Pb–Pb Evap Zrn; (4a) Kröner et al. (2000) Pb–Pb Evap Zrn; (4b) Kröner et al. (2000) U–Pb ID Zrn; (5) de Wit et al. (1993) U–Pb ID Zrn; (6) Henderson et al. (2000) U–Pb ID Zrn and Ttn; (7) Poujol (1996) U–Pb ID Zrn; (8) Poujol (2001) U–Pb ID Zrn; (9) Brandl et al. (1996) U–Pb ID Zrn; (10) Poujol and Robb (1999) U–Pb ID Zrn; (11) Poujol (1997) U–Pb ID Zrn; (12) Zeh and Gerdes (2012) U–Pb LA Zrn (ID = isotopic dilution; LA = laser ablation; Evap = zircon evaporation technique; Zrn = zircon; Ttn = titanite).

Our results demonstrate that the Pietersburg block evolved through two distinct geological periods, the first one corresponding to the formation and evolution of gneiss units between ~3350 Ma and ~2840 Ma, and the second one related to the intrusion of large, post-tectonic K-rich granitoid plutons and batholiths between ~2780 and ~2690 Ma. Such a scenario is not consistent with that proposed by Kröner et al. (2000), who considered that the Pietersburg block formed between 2900 and 2800 Ma by welding of small individual crustal slivers. Indeed, Fig. 10 clearly shows that the two gneiss units of the Pietersburg block basement underwent a common geological history at least from ~2950 Ma (and possibly as early as 3200 Ma).

### 5.3. Magmatic evolution of the Pietersburg block

Based on our results, the magmatic evolution of the Pietersburg block can be divided into 5 successive magmatic events, the chronology of which is highlighted in Fig. 10 and can be summarized as follows:

(1) 3100–3200 Ma – This range of ages is that of inherited zircons and cores from the Goudplaats–Hout River and Groot Letaba–Duiwelskloof gneiss units. As discussed earlier, they might be partly reset and consequently represent several episodes of granitoid emplacement between 3170 and 3350 Ma. The scarce petrographic and geochemical data available (Kröner et al., 2000) show that these granitoids are of TTG affinity.
(2) ~2950 Ma – This age is that of HRG-1 and DWK-04 protolith, it has also been recorded by inherited zircons from HRG-2, DWK-01 and DWK-06. Both HRG-1 and DWK-04 are typical sodic TTGs, such that the ~2950 Ma event can be considered as a period of TTG intrusion.
(3) ~2840 Ma – This is the age of emplacement of the monzogranites HRG-2 and DWK-01, which intrude the older TTGs. By contrast with TTG, these monzogranites are likely richer in K because of their higher K-feldspar content.
(4) ~2780 Ma – That is the emplacement age of leucogranite DWK-06 as well as of the Turfloop batholith (Henderson et al., 2000; Kröner et al., 2000; Zeh et al., 2009). Both are K-rich monzogranites (Henderson et al., 2000).
(5) ~2690 Ma – This age corresponds to the emplacement of granitoids north of the Pietersburg greenstone belt (Mashashane, Matlala and Moletsi plutons) and in the SMZ (Matok Igneous Complex). These granitoids are also K-rich but, when compared with the 2840 and 2780 Ma monzogranites, they display a wider compositional range from diorites to granodiorites and monzogranites.

The evolution outlined above also evidences that a major change in the magmatic activity took place between 2840 and 2950 Ma (Fig. 10). Indeed, at that time, the nature of granitoids shifted from sodic TTGs, which emplaced between ~3350 and ~2950 Ma, toward K-richer lithologies that emplaced between ~2840 Ma and ~2690 Ma. Moreover, Kreissig et al. (2000) performed a Nd isotope systematic study on a large variety of rocks from the Pietersburg block. All gave model ages ranging between 2950 and 3200 Ma, which overlap the age range of the sodic TTGs. As a result, this compositional change from TTGs to more potassic granites likely reflects a major transition between juvenile magmatism and crust recycling in the Pietersburg block.

### 5.4. Links between age data and the geological evolution of the Pietersburg block

The five age peaks highlighted in Fig. 10 are compared with available ages published so far from the Pietersburg block in the timeline of Fig. 12. These data are discussed to assess the geological evolution of this terrane.

#### 5.4.1. 3350–3100 Ma: Juvenile crust formation

Nd and Hf isotopic studies (Kreissig et al., 2000; Zeh et al., 2009; Zeh and Gerdes, 2012), have shown that juvenile crust formation in the Pietersburg block took place between 2950 and 3350 Ma. This time span coincides with that of TTG magmatism as deduced from U–Pb dating (this study as well as Brandl and Kröner, 1993; Kröner et al., 2000; Zeh et al., 2009). However, age data older than 3100 Ma are somewhat scattered (Fig. 12): Kröner et al. (2000) measured an age of ~3171 Ma in a sample of the Groot Letaba–Duiwelskloof gneisses, and dated a deformed granitoid from the Goudplaats–Hout River unit at ~3283 Ma. From the same unit, Brandl and Kröner (1993) reported an emplacement age of ~3333 Ma. Moreover, detrital zircons from the Pietersburg greenstone belt recorded several age peaks at ~3290, ~3260, ~3210 and ~3170 Ma (Zeh and Gerdes, 2012). These observations either indicate that (1) TTG juvenile magmatism took place more or less continuously over ~200 Ma between 3350 and 3170 Ma or that (2) >3100 Ma-old crust of the Pietersburg terrane is made up of several discrete, small blocks that underwent different geological histories before amalgamating (as proposed by Brandl and Kröner, 1993; Kröner et al., 2000).

#### 5.4.2. ~2950 Ma: crust formation during accretion of the Pietersburg block with the Kaapvaal craton

The data presented in this paper, together with previous work by de Wit et al. (1993), Kröner et al. (2000), Zeh et al. (2009) and Zeh and Gerdes (2012), point to a major episode of TTG magmatism at ~2950 Ma, in both the Groot Letaba–Duiwelskloof and the Goudplaats–Hout River gneiss units. In addition, Zeh and Gerdes (2012) analyzed Hf isotopes in zircons from sediments of the Pietersburg belt; most of them have positive $\varepsilon_{Hf}$ (from 0 up to +4), which indicates the juvenile character of this magmatic event. However, few analyses show negative $\varepsilon_{Hf}$ values (down to −4), indicating a significant role played by recycling of older material (Zeh and Gerdes, 2012). This later conclusion is fully consistent with the presence of inherited cores and grains with ages >3100 Ma within the ~2950 Ma-old granitoids (e.g. sample HRG-1).

Importantly, ~2950 Ma is also the age of an important magmatic event in the Murchison greenstone belt (Fig. 12). Indeed, in this area, (1) TTG genesis and intrusion, (2) associated volcanism in the Rubbervale formation and (3) intrusion of the mafic magmas of the Rooiwater Complex took place at 2950–2970 Ma (Brandl et al., 1996; Poujol, 1997, 2001; Poujol et al., 1996). The Murchison belt outcrops along a major suture zone that separates the Pietersburg block, to the North, from the Witwatersrand block, to the South (Fig. 1; Anhaeusser, 2006; de Wit et al., 1992a; Eglington and Armstrong, 2004; Poujol et al., 2003). Recently, Block et al. (2013) proposed that this geometry results from oblique collision between the Pietersburg block and the northern margin of the Kaapvaal craton nucleus at 2970–2900 Ma. Following this interpretation, we propose that the ~2950 Ma magmatic event recorded throughout the whole Pietersburg block is related to its accretion to the northern edge of the Kaapvaal craton.

#### 5.4.3. 2950–2780 Ma: crust reworking associated with long-lasting deformation

In the Goudplaats–Hout River and Groot Letaba–Duiwelskloof gneiss units, the K-rich biotite-bearing monzogranites (i.e. HRG-2, DWK-01, DWK-06) emplaced during two distinct episodes at ~2840 Ma and ~2780 Ma. In Archean terranes worldwide, such granites are generated by recycling of the TTG basement (e.g. Moyen, 2011; Moyen et al., 2003; Sylvester, 1994). Such a scenario has already been proposed by Henderson et al. (2000) to

account for the genesis of the ~2780 Ma-old Turfloop granitoids. Field data also support this interpretation: the TTG gneisses display migmatitic textures, attesting that they underwent anatexis, and the leucosomes are monzogranitic in composition. In addition, the K-rich granites contain inherited zircon cores recording ages of ~2950 Ma and >3100 Ma, i.e. the intrusion age inferred for the TTGs. Thus, all lines of evidence indicate that the K-rich monzogranites derived, at least partly, by partial melting of older TTG. This interpretation corroborates that the period between 2950 and 2840 Ma corresponds to a major geodynamic change from mostly juvenile, TTG magmatism to significant recycling of older crust (see Section 5.3).

On the other hand, these episodes of crust recycling were likely associated with a deformation event which took place between 2950 and 2780 Ma. Indeed, the ~2950 Ma-old granitoids are always more complexly and intensely deformed than the ~2840 Ma-old ones, while those emplaced at ~2780 Ma preserved their undeformed magmatic textures. Consistently, Kröner et al. (2000) already noticed the syntectonic character of the volcanics and granitoids emplaced ~2850 Ma ago in the Pietersburg block. Such a long-lasting deformation event has also been evidenced in the Murchison belt by Jaguin et al. (2012). These authors considered that the NW–SE directed shortening, related to the convergence between the Pietersburg block and the northern edge of the Kaapvaal craton, presumably continued over ~200 Ma even after accretion of both crustal segments at ~2950 Ma.

#### *5.4.4. 2750–2650 Ma: mixed crust-mantle contribution during collision with the Limpopo belt*

The granitoids that emplaced ~2685 Ma ago (Mashashane, Matlala, Moletsi plutons and Matok Igneous Complex) specifically intruded close to the Hout River shear zone (Figs. 2 and 12) and thus, put further time constraints on the exhumation rates of the SMZ granulites. Indeed, according to our age data, the emplacement of these granitoids is coeval with 2691 ± 7 Ma-old granulite-facies metamorphism in the SMZ (Kreissig et al., 2001). If this age actually reflects the *P–T* peak of high-grade metamorphism, then the Matok pluton emplaced at conditions up to 9.5 kbar and 1000 °C (at least, in granulite-facies conditions). By contrast, the Mashashane, Moletsi and Matlala plutons, which emplaced to the south of the Hout River shear zone, recorded pressures < 6 kbar and temperatures <600 °C (from maximal *P–T* conditions inferred for the footwall Kaapvaal craton by Kreissig et al., 2001; Perchuk et al., 2000b,c). The juxtaposition, at the same crustal level, of two terranes with such contrasted *P–T* conditions at ~2690 Ma requires that the exhumation of the SMZ granulites (and the Matok Igneous Complex) along the Hout River shear zone necessarily lasted over a relatively long time span *after* the emplacement of the granitoids. Such an interpretation is in good agreement with of the scenario proposed by Kreissig et al. (2001), who assumed that the tectonic activity along the Hout River shear zone lasted between 2700 and 2600 Ma.

The ~2690 Ma-old plutons are made up of high-K calc-alkaline granitoids, which suggests that recycling of older crust played an important role in their genesis. This conclusion is supported by the $\varepsilon_{Hf}$ values of ca. −3 reported by Zeh et al. (2009) for the Uitloop granite (part of the Mashashane pluton) and the Matok Igneous Complex. However, some features of the granitoids testify that a mantle component could also have contributed to their petrogenesis: they are hornblende- and locally pyroxene-bearing granitoids, systematically associated with intermediate to mafic rocks (i.e. diorites), the zircons of which never show any inheritance from older crustal material. Moreover, as shown in Fig. 11 and contrarily to TTG and older K-rich granites of the Pietersburg block, the zircons of these granitoids display a more limited spread of U concentrations (10–250 ppm) and more scattered Th/U ratios (0.2–1.8), pointing to a different origin. This possible mixed crustal- and mantle-like signature of the ~2690 Ma-old granitoids depicts them as late- to post-orogenic magmas (e.g. Barbarin, 1999; Bonin, 2004). Thus, the age of their emplacement likely witnesses the end of a major collisional event in the Pietersburg block. Following Zeh et al. (2009), we tentatively propose that this event is linked to the collision between the Pietersburg block and the Central Zone of the Limpopo Belt located northwards, which resulted in a major tectono-metamorphic event between ~2760 and ~2600 Ma as well as massive granitoid emplacement at ~2690 Ma.

## 6. Summary and conclusions

The U–Pb dating of zircon grains from granitoids of the Pietersburg block (northern Kaapvaal craton) provide new insights on both the architecture of this terrane and its magmatic evolution. The new age dataset presented in this paper shows that the latter can be subdivided into five distinct phases, each one being related to a particular episode of the geological evolution of the Pietersburg block:

(1) Inherited zircon cores from the Goudplaats–Hout River and Groot Letaba–Duiwelskloof gneiss units display ages ranging from 3200 to 3100 Ma, which we interpret as inherited ages from older magmatic events (3100–3350 Ma) that have been partly reset subsequently. This magmatic episode represents the first juvenile crust-forming episode in the Pietersburg block, which consisted in the genesis of TTG magmas.
(2) Two TTG gneiss samples from the Goudplaats–Hout River (HRG-1) and Groot Letaba–Duiwelskloof (DWK-04) units yielded emplacement ages of ~2950 Ma, which we interpret as reflecting a second major episode of juvenile crust formation linked to the accretion of the Pietersburg block to the northern edge of the older Kaapvaal craton nucleus, along a suture zone now represented by the Murchison greenstone belt.
(3) Subsequently, the juvenile TTG crust of the Pietersburg block has been reworked and melted, thus giving rise to the high-K biotite-bearing granites that emplaced ~2840 Ma ago (HRG-2, DWK-01). These latter recorded significant inheritance from older phases (i.e. TTG emplaced at ~2950 Ma and >3100 Ma). This episode of crustal recycling took place during ongoing, N–S-directed convergence that resulted in a long-lasting deformation event (2950–2780 Ma).
(4) ~2780 Ma ago, further melting of the old TTGs gave rise to the large Turfloop batholith. It is likely that satellite intrusions of this batholith also emplaced in the surrounding Groot Letaba–Duiwelskloof gneiss unit (sample DWK-06).
(5) Finally, the Pietersburg block likely collided with the Central Zone of the Limpopo belt, which resulted in further deformation, granulite-facies metamorphism in the SMZ and massive granitoid magmatism ~2690 Ma ago (high-K calc-alkaline Mashashane, Matlala and Moletsi plutons as well as Matok Igneous Complex). These granitoids were generated by melting of both a crustal and a mantle source, which demonstrates that both crustal recycling and juvenile magmatism operated simultaneously at that time.

## Acknowledgements

The work presented in this article is part of a project that was funded by a NRF/CNRS Scientific Cooperation program PICS number 4828 and by international program !Khure, both co-operated between France and South Africa. J.H. Bédard is acknowledged for his comments on an earlier draft of this manuscript, as well as R.R. Parrish for his editorial skills and support. Thorough and

constructive reviews by A. Zeh and D. Van Reenen were very much appreciated and greatly improved the original manuscript. This work also benefited from helpful discussion with many colleagues, especially J. Jaguin, M. Poujol and S. Block. J.M. Hénot is acknowledged for his skillful support during SEM analytical sessions. We are also grateful to the University of Stellenbosch (South Africa) for fieldwork assistance and funding, and in particular to G. Stevens.

## Appendix A. Supplementary data

Supplementary data associated with this article can be found, in the online version, at http://dx.doi.org/10.1016/j.precamres.2013.02.009.

## References

Anhaeusser, C.R., 2006. A reevaluation of Archean intracratonic terrane boundaries on the Kaapvaal Craton, South Africa: collisional suture zones? In: Reimold, W.U., Gibbson, R. (Eds.), Processes on the Early Earth. Geological Society of America Special Publications, 405, pp. 315–332.

Armstrong, R.A., Compston, W., de Wit, M.J., Williams, I.S., 1990. The stratigraphy of the 3.5–3.2 Ga Barberton greenstone belt revisited: a single zircon ion microprobe study. Earth and Planetary Science Letters 101, 90–106.

Barbarin, B., 1999. A review of the relationships between granitoid types, their origins and their geodynamic environments. Lithos 46, 605–626.

Barton Jr., J.M., Van Reenen, D.D., 1992. When was the Limpopo Orogeny? Precambrian Research 55 (1–4), 7–16.

Barton Jr., J.M., Doig, R., Smith, C.B., Bohlender, F., Van Reenen, D.D., 1992. Isotopic and REE characteristics of the intrusive charnoenderbite and enderbite geographically associated with the Matok Pluton, Limpopo Belt, southern Africa. Precambrian Research 55 (1–4), 451–467.

Belyanin, G.A., Rajesh, H.M., Sajeev, K., van Reenen, D.D., 2012. Ultrahigh-temperature metamorphism from an unusual corundum + orthopyroxene intergrowth bearing Al–Mg granulite from the Southern Marginal Zone, Limpopo Complex, South Africa. Contributions to Mineralogy and Petrology 164 (3), 457–475.

Block, S., Moyen, J.-F., Zeh, A., Poujol, M., Jaguin, J., Paquette, J.-L., 2013. The Murchison Greenstone Belt. South Africa: accreted slivers with contrasting metamorphic conditions. Precambrian Research 227, 77–98.

Bohlender, F., 1991. Igneous and metamorphic charnockitic rocks associated with the Matok pluton and their significance in the Limpopo orogeny. Ph.D. Thesis. Rand Afrikaans University, Johannesburg, South Africa.

Bohlender, F., Van Reenen, D.D., Barton Jr., J.M., 1992. Evidence for metamorphic and igneous charnockites in the Southern Marginal Zone of the Limpopo Belt. Precambrian Research 55 (1–4), 429–449.

Bonin, B., 2004. Do coeval mafic and felsic magmas in post-collisional to within-plate regimes necessarily imply two contrasting, mantle and crustal, sources? A review. Lithos 78, 1–24.

Brandl, G., 1986. The geology of the Pietersburg area. Explanation of the geological map of South Africa, scale 1:250000, sheet 2328. Ed. by the Geological Survey of South Africa.

Brandl, G., 1987. The geology of the Tzaneen area. Explanation of the geological map of South Africa, scale 1:250000, sheet 2330. Ed. by the Geological Survey of South Africa.

Brandl, G., Kröner, A., 1993. Preliminary results of single zircon studies from various archaean rocks of the northeastern Transvaal. In: Ext. Abstr. 16th International Colloquium of African Geology, Mbabane, Swaziland, pp. 54–56.

Brandl, G., Cloete, M., Anhaeusser, C.R., 2006. Archean greenstone belts. In: Johnson, M.R., Anhaeusser, C.R., Thomas, R.J. (Eds.), the Geology of South Africa. Geological Society of South Africa, Johannesburg/Council for Geoscience, Pretoria, pp. 9–56.

Brandl, G., Jaeckel, P., Kröner, A., 1996. Single zircon age for the felsic Rubbervale Formation, Murchison greenstone belt, South Africa. South African Journal of Geology 99 (3), 229–234.

de Beer, J.H., Stettler, E.H., Duvenhage, A.W.A., Joubert, S.J., de Raath, C.J., 1984. Gravity and geoelectrical studies of the Murchison greenstone belt, South Africa. South African Journal of Geology 87, 347–359.

de Wit, M.J., Armstrong, R.A., Kamo, S.L., Erlank, A.J., 1993. Gold-bearing sediments in the Pietersburg greenstone belt: age equivalents of the Witwatersrand Supergroup sediments, South Africa. Economic Geology 88, 1242–1252.

de Wit, M.J., Jones, M.G., Buchanan, D.L., 1992b. The geology and tectonic evolution of the Pietersburg Greenstone Belt, South Africa. Precambrian Research 55, 111–122.

de Wit, M.J., Roering, C., Hart, R.J., Armstrong, R.A., de Ronde, R.E.J., Green, R.W., Tredoux, M., et al., 1992a. Formation of an Archaean continent. Nature 357, 553–562.

du Toit, M.C., Van Reenen, D.D., Roering, C., 1983. Some aspects of the geology, structure and metamorphism of the Southern marginal zone of the Limpopo metamorphic complex. Special Publication of the Geological Society of South Africa 8, 121–142.

Eglington, B.M., Armstrong, R.A., 2004. The Kaapvaal Craton and adjacent orogens, southern Africa: a geochronological database and overview of the geological development of the craton. South African Journal of Geology 107, 13–32.

Good, N., de Wit, M.J., 1997. The Thabazimbi-Murchison Lineament of the Kaapvaal Craton, South Africa: 2700 Ma of episodic deformation. Journal of the Geological Society, London 154, 93–97.

Henderson, D.R., Long, L.E., Barton Jr., J.M., 2000. Isotopic ages and chemical and isotopic composition of the Archaean Turfloop Batholith, Pietersburg granite-greenstone terrane, Kaapvaal Craton, South Africa. South African Journal of Geology 103 (1), 38–46.

Horstwood, M.S.A., Foster, G.L., Parrish, R.R., Noble, S.R., Nowell, G.M., 2003. Common-Pb corrected *in situ* U–Pb accessory mineral geochronology by LA-MC-ICP-MS. Journal of Analytical Atomic Spectrometry 18 (8), 837–846.

Jaguin, J., Gapais, D., Poujol, M., Boulvais, P., Moyen, J.-F., 2012. the Murchison Greenstone Belt (South Africa): a General Tectonic Framework. South African Journal of Geology 115 (1), 65–76.

Kamo, S.L., Davis, D.W., 1994. Reassessment of Archean crustal development in the Barberton Mountain Land, South Africa, based on U-Pb dating. Tectonics 13 (1), 167–192.

Kleywegt, R.J., de Beer, J.H., Stettler, E.H., Brandl, G., Duvenhage, W.A., Day, R.W., 1987. The structure of the Giyani greenstone belt, as derived from geophysical studies. South African Journal of Geology 90, 282–295.

Kramers, J.D., Kreissig, J., Jones, M.Q.W., 2001. Crustal heat production and style of metamorphism: a comparison between to Archaean high-grade provinces in the Limpopo Belt, South Africa. Precambrian Research 112, 149–163.

Kramers, J.D., McCourt, S., van Reenen, D.D., 2006. The Limpopo Belt. In: Johnson, M.R., Anhaeusser, C.R., Thomas, R.J. (Eds.), The Geology of South Africa. Geological Society of South Africa, Johannesburg/Council for Geoscience, Pretoria, pp. 209–236.

Kramers, J.D., Houri, H., 2011. The geochronology of the Limpopo Complex: a controversy solved. In: van Reenen, D.D., Kramers, J.D., McCourt, S., Perchuk, L.L. (Eds.), Origin and evolution of Precambrian High-Grade Gneiss Terranes, with Special Emphasis on the Limpopo Complex of Southern Africa. Geological Society of America, Memoir 207, pp. 85–106.

Kreissig, K., Holzer, L., Frei, R., Villa, I.M., Kramers, J.D., Smit, C.A., Van Reenen, D.D., 2001. Geochronology of the Hout River Shear Zone and the metamorphism in the Southern Marginal Zone of the Limpopo Belt, Southern Africa. Precambrian Research 109, 145–173.

Kreissig, K., Nägler, T.F., Kramers, J.D., Van Reenen, D.D., Smit, C.A., 2000. An isotopic and geochemical study of the northern Kaapvaal Craton and the Southern Marginal Zone of the Limpopo Belt: are they juxtaposed terranes? Lithos 50, 1–25.

Kröner, A., Byerly, G.R., Lowe, D.R., 1991. Chronology of early Archean granite-greenstone evolution in the Barberton Moutain Land, South Africa, based on precise dating by single grain zircon evaporation. Earth and Planetary Science Letters 103, 41–54.

Kröner, A., Hegner, E., Wendt, J.I., Byerly, G.R., 1996. The oldest part of the Barberton granitoid-greenstone terrain, South Africa: evidence for crust formation at 3. 5 and 3.7 Ga. Precambrian Research 78, 105–124.

Kröner, A., Jaeckel, P., Brandl, G., 2000. Single zircon ages for felsic to intermediate rocks from the Pietersburg and Giyani greenstone belts and bordering granitoid orthogneisses, northern Kaapvaal Craton, South Africa. Journal of African Earth Sciences 30 (4), 773–793.

Ludwig, K.R., 1998. On the treatment of concordant uranium-lead ages. Geochimica et Cosmochimica Acta 62, 665–676.

Ludwig, K.R., 2008. Isoplot 3.70, A Geochronological Toolkit for Microsoft Excel. Berkeley Geochronology Central Special Publication No. 4, 76 pp.

Mason, R., 1973. The Limpopo Mobile Belt—Southern Africa. Philosophical Transactions of the Royal Society of London. Series A 273, 463–485.

Moyen, J.-F., 2011. The composite Archaean grey gneisses: petrological significance, and evidence for a non-unique tectonic setting for Archaean crustal growth. Lithos 123 (1–4), 21–36.

Moyen, J.-F., Martin, H., Jayananda, M., Auvray, B., 2003. Late Archaean granites: a typology based on the Dharwar Craton (India). Precambrian Research 127, 103–123.

Moyen, J.-F., Stevens, G., Kisters, A., 2006. Record of mid-Archaean subduction from metamorphism in the Barberton terrain, South Africa. Nature 442 (3), 559–562.

Passeraub, M., Wüst, T., Kreissig, K., Smit, C.A., Kramers, J.D., 1999. Structure, metamorphism and geochronology of the Rhenosterkoppies Greenstone Belt, Northern Province, South Africa. South African Journal of Geology 102, 323–334.

Perchuk, L.L., Gerya, T.V., Van Reenen, D.D., Krotov, A.V., Safonov, O.G., Smit, C.A., Shur, M.Y., 2000c. Comparative petrology and metamorphic evolution of the Limpopo (South Africa) and Lapland (Fennoscandia) high-grade terrains. Mineralogy and Petrology 69 (1), 69–107.

Perchuk, L.L., Gerya, T.V., van Reenen, D.D., Safonov, O.G., Smit, C.A., 1996. The Limpopo Metamorphic Belt, South Africa: 2. Decompression and cooling regimes of granulites and adjacent rocks of the Kaapvaal Craton. Petrology 4, 571–599.

Perchuk, L.L., Gerya, T.V., van Reenen, D.D., Krotov, A.V., Safonov, O.G., Smit, C.A., Shur, M.Y., 2000a. Comparative petrology and metamorphic evolution of the Limpopo (South Africa) and Lapland (Fennoscandia) high-grade terrains. Mineralogy and Petrology 69, 69–107.

Perchuk, L.L., Gerya, T.V., van Reenen, D.D., Smit, C.A., Krotov, A.V., 2000b. P-T paths and tectonic evolution of shear zones separating high-grade terrains from cratons: examples from Kola Peninsula (Russia) and Limpopo Region (South Africa). Mineralogy and Petrology 69 (1–2), 109–142.

Poujol, M., 1997. Étude U–Pb et Pb–Pb de la Murchison greenstone belt et du bassin aurifère d'Evander, Afrique du Sud: implications pour l'évolution du Kaapvaal Craton. Ph.D. Thesis. Université de Montpellier, 247 pp.

Poujol, M., 2001. U–Pb isotopic evidence for episodic granitoid emplacement in the Murchison greenstone belt, South Africa. Journal of African Earth Sciences 33 (1), 155–163.

Poujol, M., Robb, L.J., 1999. New U–Pb zircon ages on gneisses and pegmatite from south of the Murchison greenstone belt, South Africa. South African Journal of Geology 102 (2), 93–97.

Poujol, M., Robb, L.J., Anhaeusser, C.R., Gericke, B., 2003. A review of the geochronological constraints on the evolution of the Kaapvaal Craton, South Africa. Precambrian Research 127 (1–3), 181–213.

Poujol, M., Robb, L.J., Respaut, J.-P., Anhaeusser, C.R., 1996. 3.07–2.97 Ga greenstone belt formation in the northeastern Kaapvaal Craton: implications for the origin of the Witwatersrand Basin. Economic Geology 91, 1455–1461.

Robb, L.J., Brandl, G., Anhaeusser, C.R., Poujol, M., 2006. Archean granitoid intrusions. In: Johnson, M.R., Anhaeusser, C.R., Thomas, R.J. (Eds.), The Geology of South Africa. Geological Society of South Africa, Johannesburg/Council for Geoscience, Pretoria, pp. 57–94.

Roering, C., Van Reenen, D.D., Smit, C.A., Barton Jr., J.M., de Beer, J.H., de Wit, M.J., Stettler, E.H., et al., 1992. Tectonic model for the evolution of the Limpopo Belt. Precambrian Research 55, 539–552.

Sanchez-Garrido, C.J.M.G., Stevens, G., Armstrong, R.A., Moyen, J.-F., Martin, H., Doucelance, R., 2011. Diversity in Earth's early felsic crust: Paleoarchean peraluminous granites of the Barberton Greenstone Belt. Geology 39 (10), 963–966.

Smit, C.A., Roering, C., Van Reenen, D.D., 1992. The structural framework of the southern margin of the Limpopo Belt, South Africa. Precambrian Research 55 (1–4), 51–67.

Smit, C.A., Van Reenen, D.D., Gerya, T.V., Perchuk, L.L., 2001. P–T conditions of decompression of the Limpopo high-grade terrane: record from shear zones. Journal of Metamorphic Geology 19, 249–268.

Stettler, E.H., du Plessis, J.G., de Beer, J.H., 1988. The structure of the Pietersburg greenstone belt, South Africa, as derived from geophysics. South African Journal of Geology 91, 292–303.

Stevens, G., Van Reenen, D.D., 1992. Constraints on the form of the P–T loop in the Southern Marginal Zone of the Limpopo Belt, South Africa. Precambrian Research 55 (1–4), 279–296.

Streckeisen, A., 1974. Classification and nomenclature of plutonic rocks: recommendations of the IUGS subcommission on the systematics of Igneous Rocks. Geologische Rundschau 63 (2), 773–786.

Sylvester, P.J., 1994. Archaean granite plutons. In: Condie, K.C. (Ed.), Archaean Crustal Evolution. Developments in Precambrian Geology, vol. 11. Elsevier, Amsterdam, pp. 261–314.

Tsunogae, T., Miyano, T., Van Reenen, D.D., Smit, C.A., 2004. Ultrahigh temperature metamorphism of the Southern Marginal Zone of the Archean Limpopo Belt, South Africa. Journal of Mineralogical and Petrological Sciences 99, 213–224.

van Achterbergh, E., Ryan, C., Jackson, S., Griffin, W.L., 2001. Appendix 3 data reduction software for LA-ICP-MS in Laser-Ablation-ICPMS in the Earth Sciences. In: Sylvester, P. (Ed.), Mineralogical Association of Canada Short Course, vol. 29. , pp. 239–243.

van Reenen, D.D., 1986. Hydration of cordierite and hypersthene and a description of the retrograde orthoamphibole isograd in the Limpopo belt, South Africa. American Mineralogist 71, 900–915.

van Reenen, D.D., Hollister, L.S., 1988. Fluid inclusions in hydrated granulite facies rocks, Southern Marginal Zone of the Limpopo Belt, South Africa. Geochimica et Cosmochimica Acta 52, 1057–1064.

van Reenen, D.D., Smit, C.A., 1996. The Limpopo Metamorphic Belt, South Africa: 1. Geological Setting and relationship of the Granulite Complex with the Kaapvaal and Zimbabwe Cratons. Petrology 4 (6), 562–570.

van Reenen, D.D., Barton Jr., J.M., Roering, C., Smit, C.A., Van Schalkwyk, J.F., 1987. Deep crustal response to continental collision: the Limpopo belt of southern Africa. Geology 15, 11–14.

van Reenen, D.D., Smit, C.A., Perchuk, L.L., Roering, C., Boshoff, R., 2011. Thrust exhumation of the Neoarchean ultrahigh-temperature Southern Marginal Zone, Limpopo Complex: convergence of decompression-cooling paths in the hanging wall and prograde P-T paths in the footwall. In: van Reenen, D.D., Kramers, J.D., McCourt, S., Perchuk, L.L. (Eds.), Origin and Evolution of Precambrian High-Grade Gneiss Terranes, with Special Emphasis on the Limpopo Complex of Southern Africa. Geological Society of America, Memoir 207, pp. 189–212.

van Reenen, D.D., Boshoff, R., Smit, C.A., Perchuk, L.L., Kramers, J.D., McCourt, S., Armstrong, R.A., 2008. Geochronological problems related to polymetamorphism in the Limpopo Complex. South Africa. Gondwana Research 14, 644–662.

Whitehouse, M.J., Kamber, B.S., Moorbath, S., 1999. Age significance of U–Th–Pb zircon data from early Archaean rocks of west Greenland–a reassessment based on combined ion-microprobe and imaging studies. Chemical Geology 160 (3), 201–224.

Whitney, D.L., Evans, B.W., 2010. Abbreviations for names of rock-forming minerals. American Mineralogist 95, 185–187.

Zeh, A., Gerdes, A., 2012. U–Pb and Hf isotope record of detrital zircons from gold-bearing sediments of the Pietersburg Greenstone Belt (South Africa)—is there a common provenance with the Witwatersrand basin? Precambrian Research 204–205, 46–56.

Zeh, A., Gerdes, A., Barton Jr., J.M., 2009. Archean accretion and crustal evolution of the Kalahari Craton—the Zircon age and Hf isotope record of granitic rocks from Barberton/Swaziland to the Francistown Arc. Journal of Petrology 50, 933–966.

Lithos 196–197 (2014) 131–149

Contents lists available at ScienceDirect

Lithos

journal homepage: www.elsevier.com/locate/lithos

# Contrasting petrogenesis of Mg–K and Fe–K granitoids and implications for post-collisional magmatism: Case study from the Late-Archean Matok pluton (Pietersburg block, South Africa)

O. Laurent [a,b,c,*], M. Rapopo [d], G. Stevens [d], J.F. Moyen [b,c,e], H. Martin [a,b,c], R. Doucelance [a,b,c], C. Bosq [a,b,c]

[a] Clermont Université, Université Blaise Pascal, Laboratoire Magmas et Volcans, BP 10448, F-63000 Clermont-Ferrand, France
[b] CNRS, UMR6524, LMV, F-63038 Clermont-Ferrand, France
[c] IRD, R 163, LMV, F-63038 Clermont-Ferrand, France
[d] Department of Geology, University of Stellenbosch, Private Bag X-1, Matieland 7602, South Africa
[e] Département de Géologie, Université Jean Monnet, 23 Rue du Docteur Paul Michelon, 42023 Saint-Étienne, France

ARTICLE INFO

*Article history:*
Received 30 October 2013
Accepted 3 March 2014
Available online 11 March 2014

*Keywords:*
Fe–K granitoids
Post-collisional magmatism
Sanukitoids
Lithosphere reworking
Kaapvaal Craton
Matok pluton

ABSTRACT

This study investigates the origin of the 2.69 Ga-old Matok pluton, emplaced in the Pietersburg block, northern Kaapvaal Craton (South Africa), forthwith after a major tectono-metamorphic event ascribed to continent–continent collision. The Matok pluton consists of diorites, granodiorites and monzogranites. Petrography and whole-rock major- and trace element compositions of the Matok samples are similar to those of post-collisional Fe–K suites, which are very common in Proterozoic terranes. These granitoids are particularly rich in $FeO_t$, $TiO_2$, $P_2O_5$, span a wide range of $SiO_2$ contents and display elevated concentrations in $K_2O$, Ba, HFSE and REE, with moderately fractionated REE patterns.

All samples of the Matok pluton have unradionegic Nd isotopic compositions ($\varepsilon_{Nd(2.69\ Ga)} = -2.7$ to $-4.6$), but only a few monzogranite samples derive from reworking of older crust. Crustal contamination of basaltic melt cannot explain either the observed compositions. Most of the suite rather fractionated from a common mafic parent, either by partial melting or crystallization. Geochemical modeling shows that this parent magma or source rock is basaltic in composition, intermediate between calc-alkaline and tholeiitic groups, and enriched in incompatible trace elements with respect to the primitive mantle. It ultimately derives from the involvement of two distinct mantle sources: (1) enriched, sub-continental lithospheric mantle, which was metasomatized by sedimentary material derived from local crust of the Pietersburg block, <0.3 Ga before the pluton emplacement; and (2) asthenospheric mantle.

This model accounts for the differences between Fe–K suites, such as the Matok pluton, and Mg–K suites, such as sanukitoids, the origin of which only requires metasomatized mantle. We propose that the most appropriate geodynamic setting for the interaction between enriched lithospheric and asthenospheric mantle sources is an episode of "lithospheric reworking" (through slab breakoff, retreat or sub-continental mantle delamination) in response to continental collision. Depending on the relative contribution of the two mantle sources in this environment, the resulting magmas can show a wide range of compositions from Fe–K to Mg–K end-members. From a regional point of view, this conclusion supports that the Kaapvaal Craton and the Central Zone of the Limpopo Belt were amalgamated between 2.80 and 2.75 Ga owing to continent–continent collision.



## 1. Introduction

Continent–continent collision is soon followed (<0.1 Ga) by the emplacement of large volumes of granitoids, referred to as "post-collisional" (e.g. Bonin, 2004; Liégeois et al., 1998), which possibly represents up to 40% of the global granitoid record (Roberts and Clemens, 1993). Several previous reviews pointed out that these magmas are peraluminous to metaluminous, high-K calc-alkaline granitoids, the petrogenesis of the metaluminous ones involving both mantle and crustal components (Barbarin, 1999; Bonin, 2004; Clemens et al., 2009; Kemp and Hawkesworth, 2003; Liégeois et al., 1998). These magmas are (1) common since late-Archean times, as the 3.0- to 2.5 Ga-old sanukitoid suites belong to this group

* Corresponding author at: Department of Mineralogy, Institute of Geosciences, Johan Wolfgang Goethe-Universität, Altenhöferallee 1, D-60438 Frankfurt am Main, Germany. Tel.: +33 47334 6891.
*E-mail address:* laurent@em.uni-frankfurt.de (O. Laurent).

http://dx.doi.org/10.1016/j.lithos.2014.03.006
0024-4937/

(Fowler and Rollinson, 2012; Halla et al., 2009; Martin et al., 2009), and (2) possibly represent a significant juvenile addition to the continental crust (Clemens et al., 2009; Laurent et al., 2013b). Therefore, the study of post-collisional granitoids is of primary importance to unravel the nature and tectonic setting of crustal growth processes for the past 3.0 Ga.

Several studies have highlighted the fact that post-collisional granitoids are compositionally diverse and can be separated into two distinct groups, namely "magnesio-potassic" (Mg–K) and "ferro-potassic" (Fe–K). This is the case for both late-Archean granitoids, such as those of the Karelian part of the Baltic shield where Mg-rich sanukitoid suites coexist with Fe-rich counterparts (Mikkola et al., 2011), and Phanerozoic examples, such as the coexisting Fe- and Mg-rich suites in the crystalline massifs of Western Alps (Bonin, 2004; Debon and Lemmet, 1999). Both Mg- and Fe-rich groups are alkali-calcic to calc-alkaline and metaluminous in composition; they differ on the basis of their $FeO_t$/MgO ratio, $Al_2O_3$, $K_2O$ and some trace element contents. The petrogenesis of Mg–K suites is fairly well understood: for example, sanukitoids are believed to be derived from the interaction, at mantle levels, between peridotite and a component rich in incompatible elements, either a fluid or melt derived from metabasalts or metasediments (e.g. Fowler and Rollinson, 2012; Halla, 2005; Halla et al., 2009; Heilimo et al., 2010; Laurent et al., 2011; Lobach-Zhuchenko et al., 2008; Martin et al., 2009; Moyen et al., 2003; Rapp et al., 2010).

In contrast, Fe–K magmatic associations are faintly defined and their petrogenesis is still a matter of debate. Although they have been reported from late-Archean to Phanerozoic domains, they are particularly abundant in Proterozoic terranes, in particular in the Sveconorwegian area (Bogaerts et al., 2003, 2006; Demaiffe et al., 1990; Vander Auwera et al., 2003, 2007, 2011) and Western Africa (Ferré et al., 1998; Kouankap Nono et al., 2010; Tagne-Kamga, 2003) where they were extensively studied. Despite this considerable interest, there is no consensus on their origin, which is ascribed to melting of either juvenile lower crust (e.g. Duchesne et al., 2010; Skridlaite et al., 2003), old felsic crustal lithologies (e.g. Tagne-Kamga, 2003) or metasomatized mantle (e.g. Ferré et al., 1998). In addition, there is no existing model able to simultaneously explain (1) the similar post-collisional nature of both Fe–K and Mg–K suites; (2) their close temporal and spatial association in some terranes; and (3) their petrographic and geochemical differences.

Here we present a study of the Matok pluton, which is a 2.69 Ga-old magmatic complex intrusive in the Pietersburg block at the northern margin of the Kaapvaal Craton in South Africa. Whole-rock geochemistry (major-, trace elements and Sm–Nd isotopes) highlights the affinity of Matok pluton with other Fe–K suites worldwide. The aim of this article is to (1) unravel the petrogenesis of the Matok pluton and (2) compare it to that of sanukitoids, in order to propose a geodynamic model that concurrently accounts for (1) the differences between Mg–K and Fe–K suites and (2) their common post-collisional nature.

## 2. Geological setting

The Pietersburg block is the northernmost terrane of the Archean Kaapvaal Craton of southern Africa. It lies between the Witwatersrand block to the South and the Central Zone of the Limpopo Belt to the North (Fig. 1), from which it is separated by the Thabazimbi–Murchison Lineament and the Palala–Zoetfontein and Tshiphise Shear Zones, respectively (de Wit et al., 1992; Eglington and Armstrong, 2004; Zeh et al., 2009). Lithologies at the level of exposure can be separated into four different groups (Fig. 2a):

(1) the Goudplaats–Hout River and Groot Letaba–Duiwelskloof gneiss units are made up of trondhjemitic to granodioritic orthogneisses (TTG), as well as subordinate granites, amphibolites and pegmatites (Laurent et al., 2013b; Robb et al., 2006; Zeh et al., 2009). Magmatic precursors of the TTG gneisses emplaced during several discrete episodes at ~3.34, ~3.21, ~3.19, ~2.95 and ~2.84 Ga (e.g. Kröner et al., 2000; Laurent et al., 2013b; Zeh et al., 2009).

(2) the Giyani, Murchison, Pietersburg and Rhenosterkoppies greenstone belts consist of greenschist- to lower amphibolite-facies, ultramafic to felsic lavas and metasedimentary rocks (Brandl et al., 2006). U–Pb dating on felsic volcanic rocks provided ages in the range 3.1–2.8 Ga (Brandl et al., 1996; Kröner et al., 2000; Poujol et al., 1996).

(3) granulites of the Southern Marginal Zone (SMZ; Fig. 1, 2a), which crop out to the North of the Hout River Shear Zone, are made up of two lithologies: the Baviaanskloof and Bandelierkop complexes. They are interpreted to represent the high-grade counterparts of the gneiss units and greenstone belts mentioned above, respectively (Kramers et al., 2006; Kreissig et al., 2000; Zeh et al., 2009).

(4) Post-tectonic, high-K calc-alkaline granitoids of the Turfloop, Mashashane, Matlala, Matok and Moletsi plutons intruded all other lithologies (Robb et al., 2006). The age of the Turfloop batholith is ~2.78 Ga (Henderson et al., 2000; Kröner et al., 2000; Laurent et al., 2013b; Zeh et al., 2009) while other plutons, including the Matok one, emplaced at ~2.69 Ga (Laurent et al., 2013b; Zeh et al., 2009).

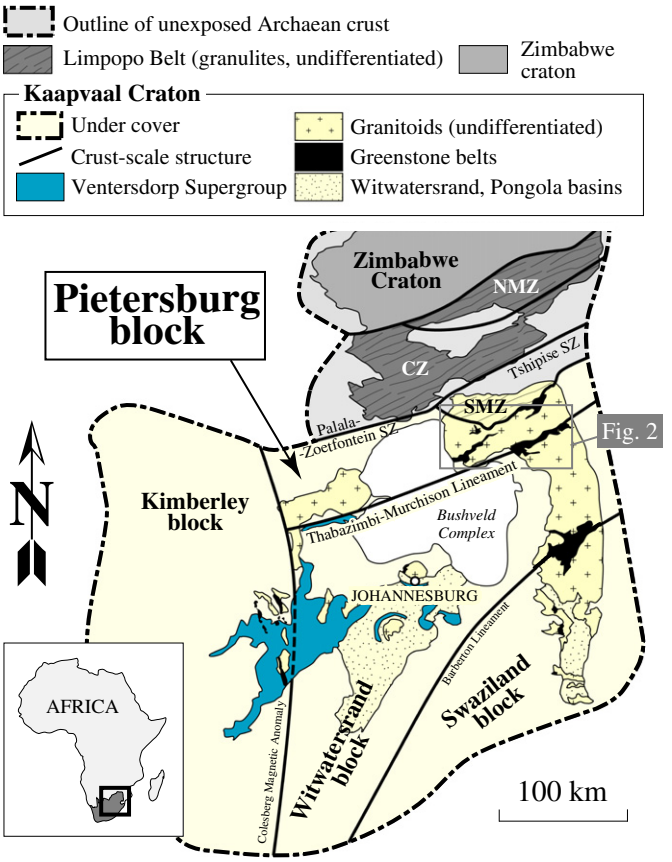


**Fig. 1.** Sketch of geological map (after Eglington and Armstrong, 2004) detailing the different structural domains of the Kaapvaal craton. The position of the Pietersburg block and the Ventersdorp supergroup are highlighted. The gray rectangle represents the study area. NMZ, CZ and SMZ refer to the three structural domains of the Limpopo Belt, i.e. Northern Marginal Zone, Central Zone and Southern Marginal Zone, respectively.

Age and isotopic constraints point to crust formation in the Pietersburg block between 3.3 and 2.9 Ga (Kreissig et al., 2000; Zeh et al., 2009, 2013). Several authors proposed that the >3.0 Ga-old

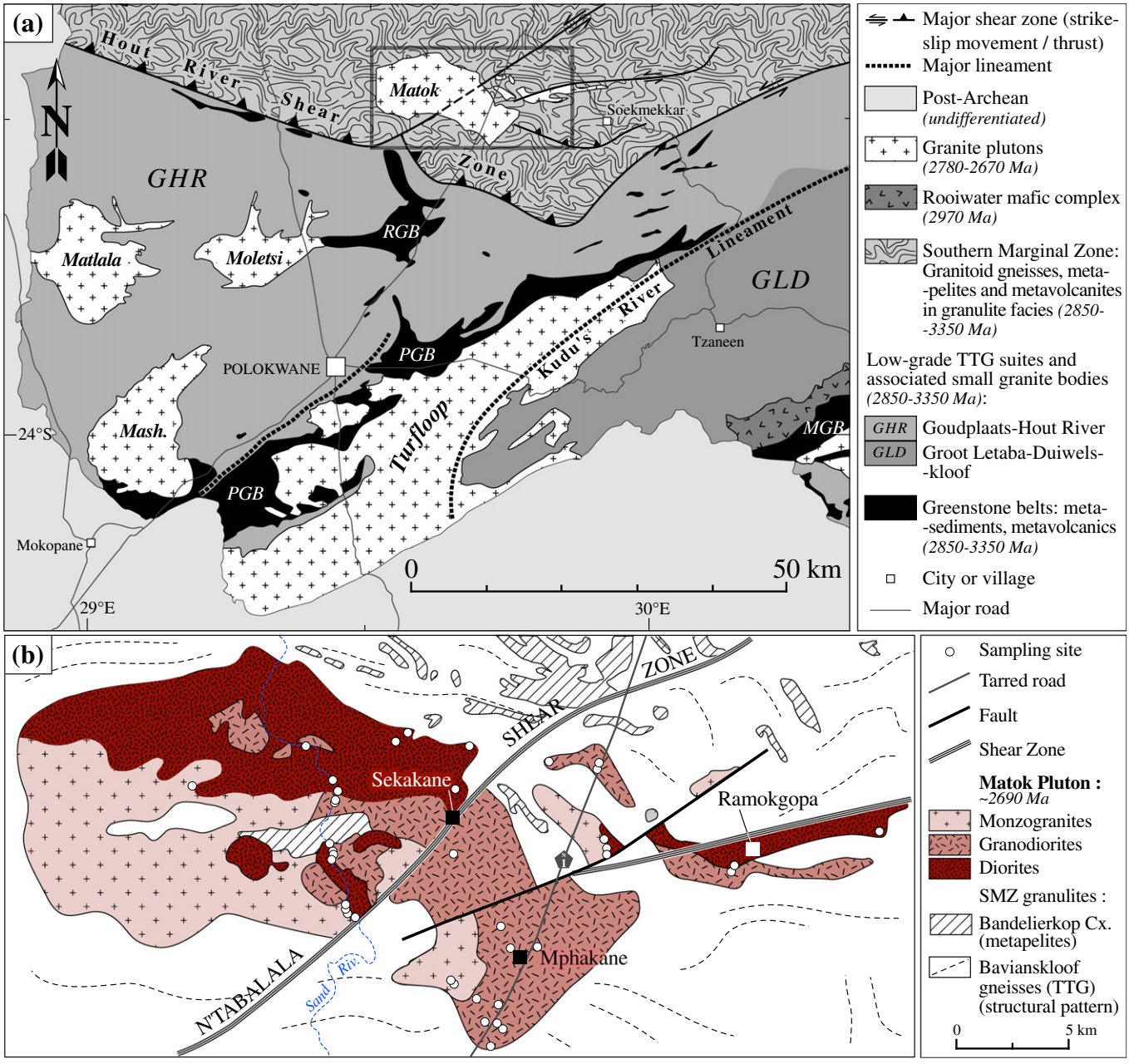


**Fig. 2.** (a) Geological sketch map of the Pietersburg block, modified after Robb et al. (2006). MGB = Murchison greenstone belt; PGB = Pietersburg greenstone belt; RGB = Rhenosterkoppies greenstone belt; (b) Geological map of the Matok pluton, modified after Bohlender (1991) according to our field observations.

crust accreted to the northern margin of the Palaeoarchaean nucleus of the Kaapvaal Craton at ~2.95 Ga (Block et al., 2013; Laurent et al., 2013b; Zeh et al., 2009, 2013). Crust deformation and associated reworking took place between 2.85 and 2.69 Ga (Henderson et al., 2000; Laurent et al., 2013b; Zeh et al., 2009). A major tectono-metamorphic event subsequently occurred around 2.7 Ga, possibly reflecting collision with the Zimbabwe Craton (de Wit et al., 1992; Roering et al., 1992; van Reenen et al., 1987). Structures associated to this event are top-to-the-North thrusts (Smit et al., 1992; van Reenen and Smit, 1996), largely overprinted by strike-slip and top-to-the-South reverse shear zones such as the Hout River Shear Zone (Kreissig et al., 2001; Smit et al., 2001). Peak metamorphism in the SMZ granulites reached medium-P (8.5–9.5 kbar), high-temperature (~850 °C) conditions (Nicoli et al., in press; Stevens and van Reenen, 1992; van Reenen et al., 1987) at ~2.71 Ga (Nicoli et al., in press). The Matok pluton is intrusive within the SMZ a few kilometers north of the Hout River shear zone (Fig. 2b). The different phases of the pluton emplaced at ~2.69 Ga (Laurent et al., 2013b). This age is similar to that of monazite from a metapelitic granulite sample obtained by Kreissig et al. (2001), which these authors interpret as the age of peak metamorphism but that more probably reflects (fluid-induced) re-equilibration owing to the intrusion of the Matok pluton.

## 3. Geology of the Matok pluton

The Matok pluton is a composite magmatic complex, formed by a main intrusive body up to ~25 km long and ~10 km wide, associated with smaller satellite stocks (Fig. 2b). Up to 12 varieties of plutonic rocks were recognized (Barton et al., 1992; Bohlender et al., 1992), which, according to our field observations, can be grouped into three main rock types:

(1) Dark, generally equigranular and fine- to medium-grained (1–5 mm) diorites (Fig. 3a). They are made up of plagioclase

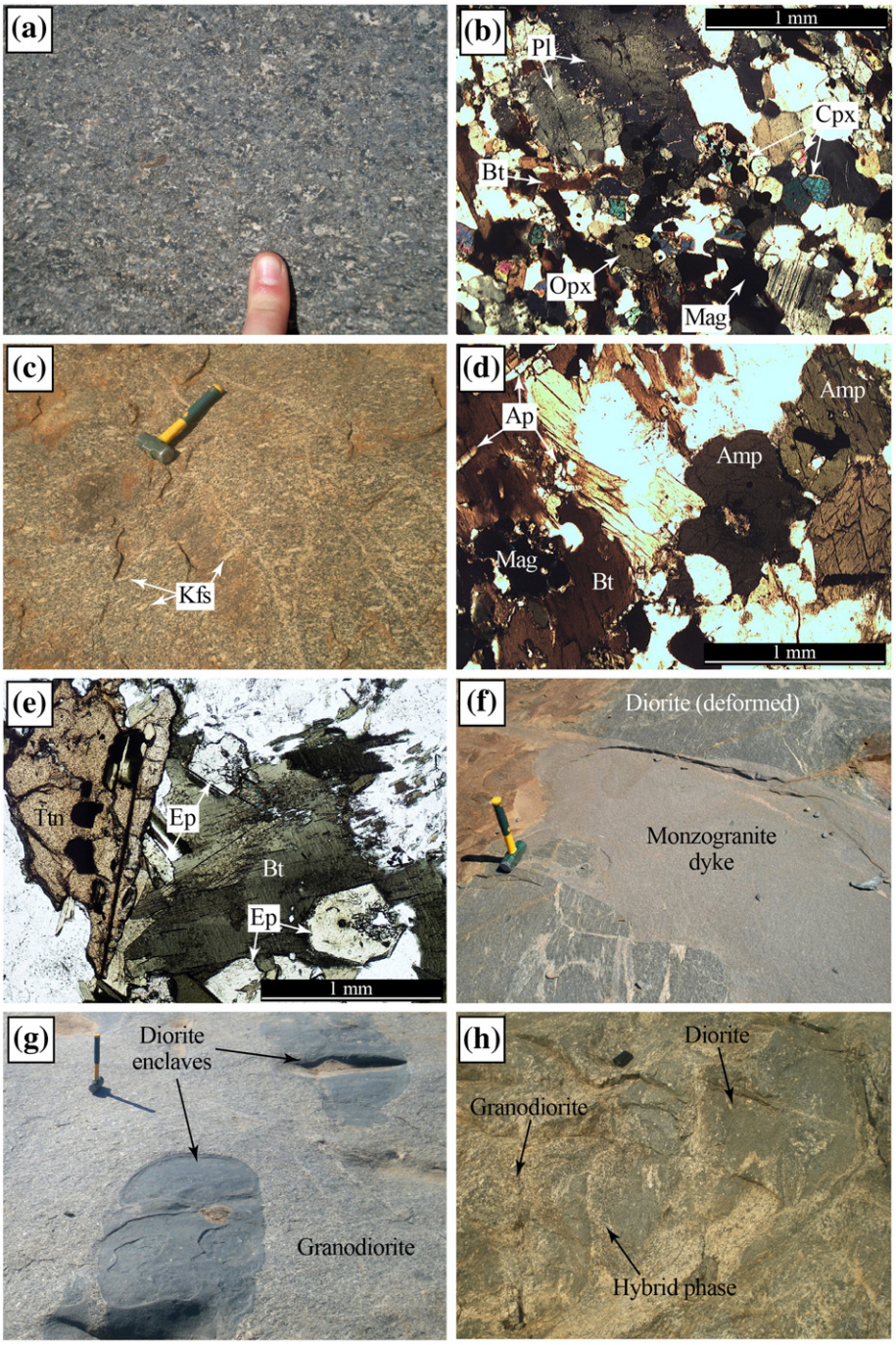


**Fig. 3.** Geology and petrography of the Matok pluton. (a) Typical dark, fine-grained and equigranular diorite; (b) photomicrograph of diorite MAT-17; (c) Typical texture of the porphyritic granodiorite; (d) Photomicrograph of granodiorite MAT-59 showing amphibole–biotite mafic clusters; (e) Photomicrograph of granodiorite MAT-13 showing biotite-epidote-titanite mafic clusters; (f) Homogeneous monzogranite dyke cross-cutting deformed diorite in a late-magmatic shear zone; (g) Rounded diorite enclaves enclosed within porphyritic granodiorite; (h) Mingling relationships between diorite and granodiorite.

($An_{20-25}$, generally >50% modal) together with clino- and orthopyroxene (up to 15% modal; Fig. 3b). The minerals coexist with subordinate amounts of anhedral biotite, orthoclase and quartz as well as accessory apatite, zircon, magnetite, ilmenite, sulfides and primary carbonates. The main mineral assemblage (Pl + Opx + Cpx) is characteristic of water-poor and relatively reduced magma (Bogaerts et al., 2006; Dall'Agnol et al., 1999; Frost and Frost, 1997). Frequently, clino- and orthopyroxene are replaced by amphibole (hastingsite and Fe-pargasite) and biotite, which sometimes results in a complete pseudomorphosis. This suggests that water activity and $fO_2$ increased during magma crystallization.

(2) Medium- to coarse-grained and generally porphyritic granodiorites (Fig. 3c). They contain large (1–5 cm) phenocrysts of orthoclase with occasional rapakivi textures, within a matrix (0.5–1 cm) of alkali feldspar, oligoclase ($An_{15-20}$) and quartz. Mafic clusters are made up of amphibole (hastingsite and Fe-pargasite) and biotite together with abundant accessory minerals (apatite, allanite, zircon, ilmenite, magnetite; Fig. 3d). Occasionally, amphibole contains relict cores of diopside.

**Table 1**
Whole-rock major- and trace element compositions of representative samples of each magmatic phase of the Matok pluton.

| Sample | MAT-17 | MAT-19 | MAT-46 | MAT-05 | MAT-06 | MAT-40 | MAT-11 | MAT-13 | MAT-03 | MAT-59 | MAT-36 | MAT-63 | MAT-63 | MAT-32 |
|---|---|---|---|---|---|---|---|---|---|---|---|---|---|---|
| Type | Diorite | Diorite | Diorite | Diorite | Diorite (enclave) | Diorite (enclave) | Granodiorite | Granodiorite | Granodiorite | Granodiorite | Granodiorite | Granite | Granite | Granite |
| *Major elements (wt.%)* | | | | | | | | | | | | | | |
| $SiO_2$ | 53.71 | 58.87 | 61.50 | 61.80 | 63.01 | 65.40 | 61.70 | 63.40 | 65.93 | 67.51 | 70.39 | 73.64 | 74.22 | 74.75 |
| $TiO_2$ | 1.94 | 1.90 | 2.02 | 1.63 | 1.41 | 1.26 | 1.39 | 1.06 | 1.23 | 0.99 | 0.81 | 0.37 | 0.38 | 0.29 |
| $Al_2O_3$ | 14.91 | 14.09 | 13.28 | 14.24 | 13.96 | 13.79 | 14.18 | 14.47 | 13.64 | 13.75 | 13.28 | 13.31 | 12.93 | 12.85 |
| $Fe_2O_3$ | 9.00 | 8.95 | 8.88 | 7.24 | 6.93 | 5.90 | 7.36 | 6.02 | 5.95 | 5.07 | 3.99 | 2.07 | 2.12 | 1.80 |
| MnO | 0.14 | 0.12 | 0.10 | 0.09 | 0.09 | 0.08 | 0.09 | 0.08 | 0.07 | 0.07 | 0.06 | 0.03 | 0.02 | 0.03 |
| MgO | 4.61 | 2.44 | 2.09 | 2.07 | 1.86 | 1.17 | 2.73 | 2.15 | 1.51 | 1.31 | 0.74 | 0.42 | 0.45 | 0.30 |
| CaO | 6.96 | 5.36 | 4.70 | 4.40 | 3.75 | 2.61 | 4.24 | 3.89 | 3.27 | 3.14 | 1.86 | 1.03 | 1.09 | 0.82 |
| $Na_2O$ | 3.42 | 3.79 | 3.83 | 3.80 | 3.79 | 3.24 | 4.07 | 3.88 | 3.55 | 3.90 | 3.84 | 3.66 | 3.26 | 3.63 |
| $K_2O$ | 1.91 | 1.48 | 1.63 | 2.38 | 2.74 | 4.49 | 2.67 | 3.16 | 3.32 | 3.16 | 3.71 | 4.58 | 4.82 | 4.88 |
| $P_2O_5$ | 0.91 | 0.77 | 0.80 | 0.80 | 0.75 | 0.38 | 0.62 | 0.49 | 0.47 | 0.34 | 0.25 | 0.19 | 0.13 | 0.10 |
| LOI | 2.1 | 1.7 | 0.9 | 1.1 | 1.2 | 1.2 | 0.6 | 1.0 | 0.6 | 0.4 | 0.6 | 0.5 | 0.4 | 0.4 |
| Total | 99.61 | 99.47 | 99.73 | 99.55 | 99.49 | 99.52 | 99.65 | 99.6 | 99.54 | 99.64 | 99.53 | 99.8 | 99.82 | 99.85 |
| *Trace elements (ppm)* | | | | | | | | | | | | | | |
| Sc | 18 | 19 | 23 | 14 | 15 | 11 | 14 | 13 | 12 | 11 | 9 | 3 | 2 | 4 |
| V | 170 | 156 | 181 | 135 | 109 | 96 | 116 | 89 | 91 | 83 | 47 | 37 | 24 | 23 |
| Cr[a] | 183 | n.d. | n.d. | 43 | n.d. | n.d. | n.d. | 57 | n.d. | n.d. | n.d. | n.d. | n.d. | 9 |
| Co[a] | 24 | n.d. | n.d. | 15 | n.d. | n.d. | n.d. | 10 | n.d. | n.d. | n.d. | n.d. | n.d. | 3 |
| Ni[a] | 102 | n.d. | n.d. | 20 | n.d. | n.d. | n.d. | 22 | n.d. | n.d. | n.d. | n.d. | n.d. | 4 |
| Rb | 66 | 26 | 68 | 61 | 81 | 115 | 110 | 124 | 105 | 67 | 67 | 176 | 128 | 223 |
| Sr | 752 | 740 | 479 | 514 | 450 | 435 | 498 | 488 | 487 | 409 | 408 | 173 | 208 | 146 |
| Y | 39 | 62 | 68 | 69 | 42 | 67 | 50 | 50 | 50 | 52 | 51 | 23 | 11 | 41 |
| Zr | 223 | 738 | 474 | 651 | 573 | 826 | 453 | 441 | 576 | 503 | 600 | 245 | 266 | 230 |
| Nb | 17.6 | 28.9 | 37.6 | 27.7 | 23.7 | 30.0 | 18.9 | 22.2 | 24.3 | 21.0 | 24.8 | 13.7 | 4.7 | 14.4 |
| Ba | 635 | 1116 | 490 | 978 | 975 | 1650 | 631 | 992 | 1308 | 1232 | 2144 | 698 | 803 | 667 |
| La | 50.3 | 97.7 | 43.8 | 78.1 | 64.4 | 92.4 | 56.1 | 60.6 | 76.6 | 77.9 | 128.9 | 44.3 | 67.3 | 48.4 |
| Ce | 117 | 226 | 121 | 221 | 162 | 249 | 126 | 148 | 189 | 171 | 267 | 93 | 115 | 121 |
| Pr | 14.7 | 28.8 | 18.0 | 24.4 | 17.2 | 26.3 | 16.5 | 18.7 | 20.9 | 21.1 | 31.3 | 11.1 | 12.7 | 13.7 |
| Nd | 60.4 | 114 | 82.0 | 95.7 | 68.3 | 105 | 68.0 | 74.2 | 81.7 | 82.4 | 110 | 41.3 | 41.1 | 49.5 |
| Sm | 10.6 | 18.6 | 16.3 | 16.8 | 12.2 | 17.5 | 12.1 | 12.5 | 13.7 | 13.9 | 16.5 | 6.5 | 4.9 | 8.7 |
| Eu | 2.48 | 3.70 | 2.47 | 3.28 | 1.64 | 2.65 | 2.01 | 2.39 | 2.30 | 2.18 | 3.12 | 0.91 | 1.35 | 1.15 |
| Gd | 9.7 | 15.3 | 15.1 | 14.3 | 10.6 | 14.4 | 10.5 | 10.6 | 11.1 | 11.4 | 12.7 | 4.8 | 3.2 | 7.1 |
| Tb | 1.45 | 2.34 | 2.36 | 2.25 | 1.57 | 2.28 | 1.65 | 1.60 | 1.73 | 1.79 | 1.91 | 0.79 | 0.42 | 1.21 |
| Dy | 8.22 | 12.25 | 13.19 | 11.89 | 8.44 | 12.49 | 9.04 | 9.01 | 9.24 | 9.76 | 9.95 | 4.42 | 2.06 | 7.03 |
| Ho | 1.48 | 2.28 | 2.49 | 2.36 | 1.57 | 2.39 | 1.69 | 1.73 | 1.72 | 1.85 | 1.82 | 0.85 | 0.35 | 1.43 |
| Er | 3.91 | 6.09 | 6.63 | 6.41 | 4.48 | 6.68 | 4.58 | 5.09 | 4.8 | 5.14 | 5.21 | 2.37 | 0.97 | 4.07 |
| Tm | 0.58 | 0.92 | 0.96 | 0.98 | 0.68 | 1.02 | 0.69 | 0.86 | 0.73 | 0.75 | 0.78 | 0.38 | 0.15 | 0.64 |
| Yb | 3.66 | 5.43 | 5.34 | 5.9 | 4.08 | 5.98 | 4.17 | 5.66 | 4.23 | 4.32 | 4.71 | 2.14 | 0.89 | 3.97 |
| Lu | 0.54 | 0.79 | 0.78 | 0.87 | 0.63 | 0.89 | 0.62 | 0.86 | 0.64 | 0.62 | 0.69 | 0.3 | 0.14 | 0.58 |
| Hf | 5.2 | 18 | 11.5 | 15.8 | 14.1 | 20.8 | 11.3 | 11.4 | 13.7 | 12.4 | 15.7 | 6.9 | 6.8 | 7.3 |
| Ta | 0.9 | 1.1 | 1.7 | 1.3 | 1.1 | 1.3 | 0.7 | 1.6 | 1.2 | 0.8 | 1.0 | 0.7 | 0.3 | 1.1 |
| Th | 1.3 | 2.5 | 0.6 | 1.6 | 5.3 | 7.0 | 2.6 | 5.4 | 6.9 | 2.1 | 6.7 | 5.7 | 3.9 | 9.4 |
| U | 0.3 | 0.6 | 0.5 | 0.4 | 0.6 | 0.8 | 0.9 | 1.7 | 0.7 | 0.4 | 0.4 | 0.5 | 0.5 | 1.8 |

[a] Cr, Co and Ni concentrations are not considered (no data; n.d.) except for samples that were crushed in an agate mill (see Analytical procedures for details).

In turn, it is replaced in some samples by an assemblage of biotite + epidote + quartz + oxides (Fig. 3e). This reaction likely took place above the solidus, as the pistachite content ($Fe^{3+}/[Al + Fe^{3+}]$) of epidote is 0.25–0.33 (Rapopo, 2010), which reflects its magmatic origin (Evans and Vance, 1987; Sial et al., 2008; Zen and Hammarstrom, 1984). Large (up to 2 mm) euhedral titanite crystals (Fig. 3e) are common, albeit their modal content is correlated to that of epidote. Greater amounts of amphibole, biotite and epidote in the granodiorites than in the diorites point to higher $H_2O$ contents (>5 wt.%; Bogaerts et al., 2006; Dall'Agnol et al., 1999) and more oxidized conditions. Specifically, the coexistence of biotite, epidote and titanite indicates that $fO_2$ was above the NNO buffer during crystallization of this assemblage (Sial et al., 2008; Wones, 1989).

(3) biotite-bearing monzogranites (Fig. 3f) showing a wide range of textures, from coarse- to fine-grained, equigranular to porphyritic and biotite-rich to hololeucocratic. Mineral assemblages are dominated by quartz, orthoclase and sodic plagioclase ($An_{5-15}$). Biotite is the only mafic mineral in the rocks, while epidote, titanite, magnetite, apatite and zircon are common accessories.

The different phases of the Matok pluton show compelling evidence for comagmatism and magma mingling. Diorites frequently occur as rounded enclaves (0.1–100 m) within more felsic rocks (Fig. 3g). The largest enclaves show pillowed shapes and are sometimes injected by veinlets and phenocrysts (quartz, K-feldspar) from the felsic host magma. In addition, contacts between the different phases are often irregular and/or gradational (Fig. 3h). The pluton locally contains xenoliths of the surrounding granulites (Barton et al., 1992; Bohlender et al., 1992; Kreissig et al., 2000). In general, they consist of 0.1–10 m sized angular enclaves, but a plurikilometric enclave of the Bandelierkop metapelites crops out near the center of the pluton (Kreissig et al., 2000; Fig. 2b). Because of its size, this enclave unlikely represents a xenolith and rather reflects that the Matok represents a number of successively emplaced, individual magma batches, locally separated by wallrock bodies (Rapopo, 2010). At a few outcrops, these granitoids are intensely deformed, especially along the N'Tabalala shear zone (Bohlender et al., 1992; Kreissig et al., 2000; Figs. 2b and 3f).

## 4. Whole-rock geochemistry

### 4.1. Major elements

On the basis of their major element composition (Table 1), and according to the classification of Frost et al. (2001), the Matok samples are calc-alkaline, mostly metaluminous granitoids, except the monzogranites that are slightly peraluminous (Fig. 4a,b). They straddle the boundaries between the ferroan and magnesian fields in the diagram of FeO* ($FeO_t/[FeO_t + MgO]$) vs. $SiO_2$ (Fig. 4c), and between the ferroan and calc-alkaline domains in the ternary AFM diagram (Fig. 4d).

All major oxides except the alkalis ($Na_2O$ and $K_2O$) are negatively correlated with $SiO_2$ in Harker diagrams (Fig. 5). The samples

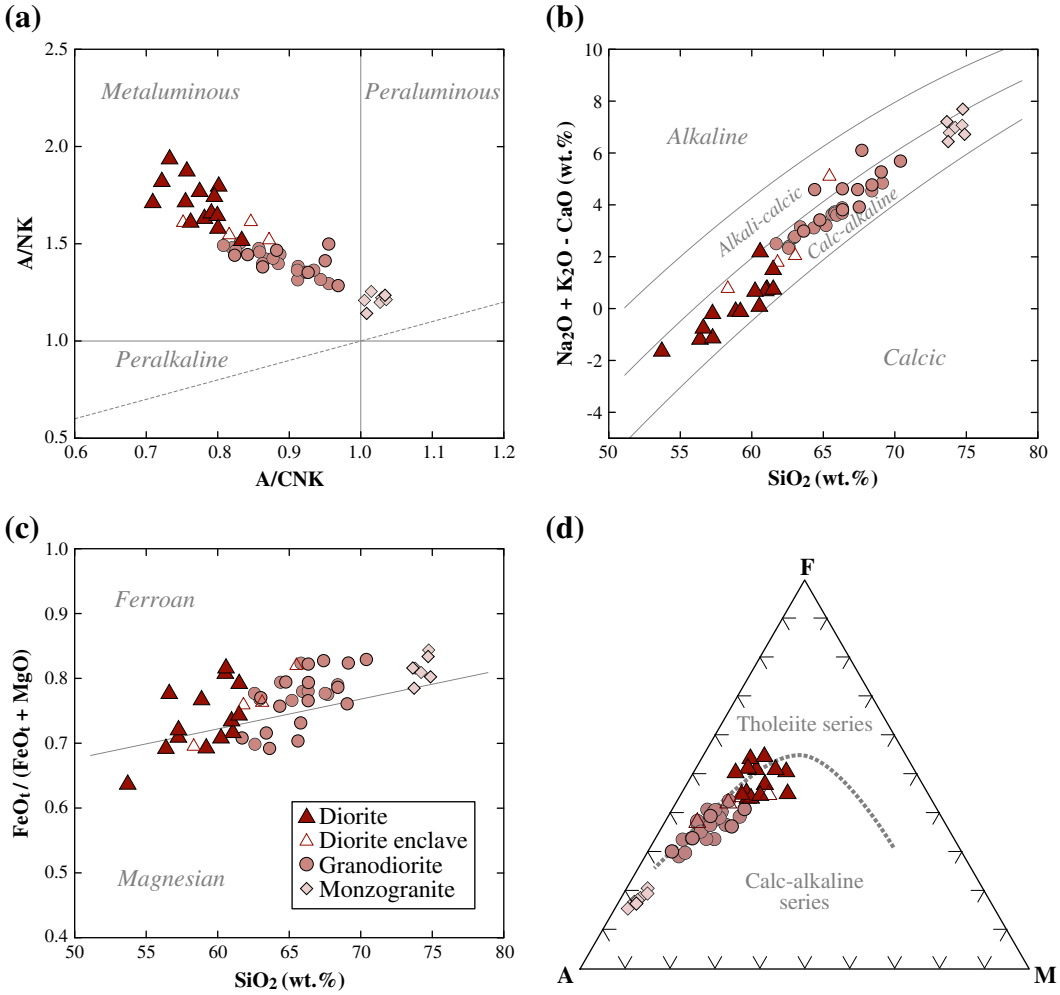


**Fig. 4.** Samples of the Matok pluton plotted in (a–c) classification diagrams proposed by Frost et al. (2001) and (d) in the AFM diagram of Kuno (1968).

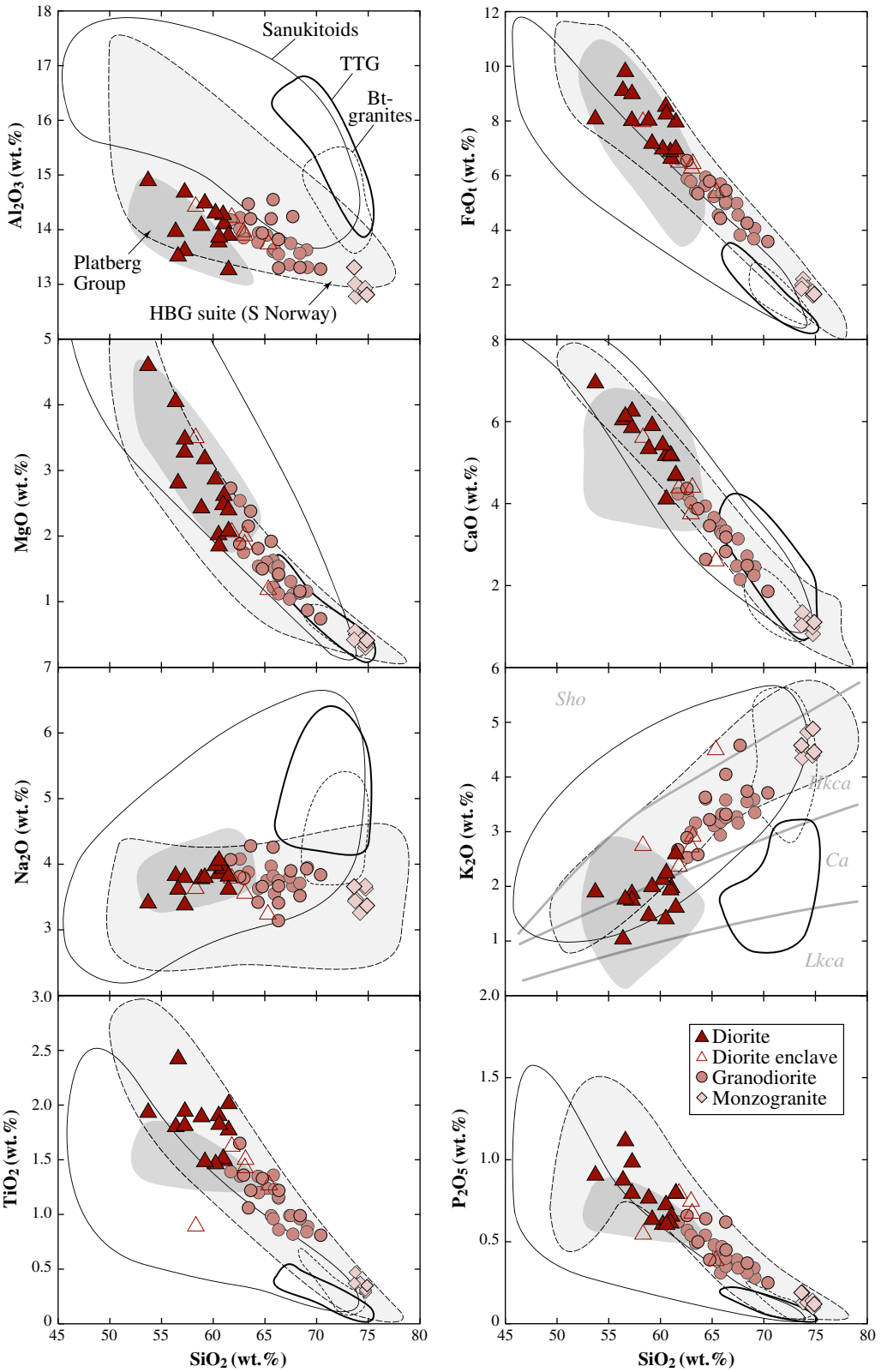


**Fig. 5.** Samples of the Matok pluton plotted in Harker diagrams. Fields in the $K_2O$ vs. $SiO_2$ diagram are after Peccerillo and Taylor (1976) (Sho = shoshonitic; Hkca = high-K calc-alkaline; Ca = calc-alkaline; Lkca = low-K calc-alkaline). Data for lavas of the Platberg Group (Ventersdorp Supergroup; gray field) are from Crow and Condie (1988), Nelson et al. (1992) and Altermann and Lenhardt (2012). Data for the HBG suite of southern Norway (light gray dashed field) are from Demaiffe et al. (1990) and Vander Auwera et al. (2003). Data for sanukitoids (thin black line) are from the database of Martin et al. (2009). Data for TTGs (thick black line) and biotite-bearing granites (dashed line) of the Pietersburg block are from Henderson et al. (2000), Kreissig et al. (2000) and Laurent et al. (in revision).

encompass a wide range of $SiO_2$ contents (53–75 wt.%), from mafic and intermediate diorites (<62 wt.% $SiO_2$) to silica-rich monzogranites. They show low $Al_2O_3$ contents, (12 to 15 wt.%) at any level of differentiation. MgO concentrations are moderate and range from 5.0 wt.% in the diorites down to 0.5 wt.% in the granites. Contrastingly, $FeO_t$ contents are high (1.5–10 wt.%), leading to low Mg# (from 0.25 in the

monzogranites to 0.50 in the diorites). CaO concentrations range from 7 wt.% in the diorites down to <1 wt.% in the monzogranites. $K_2O$ contents spread between 1 wt.% in the most mafic samples and 5 wt.% in monzogranites, which corresponds to medium- to high-K calc-alkaline affinities, whereas $Na_2O$ concentrations are less variable (3.0–4.5 wt.%). Finally, diorites and granodiorites are very rich in

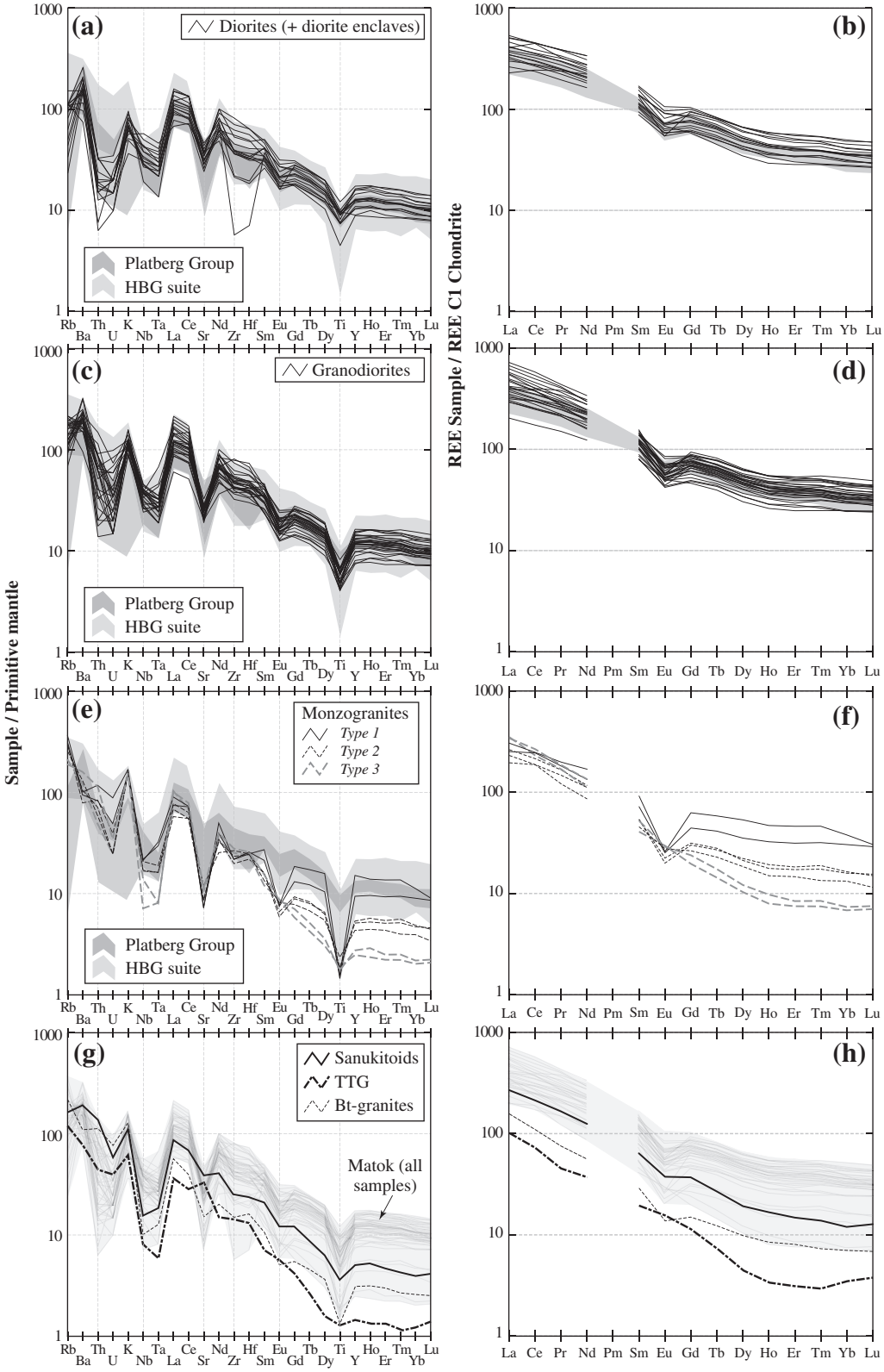


**Fig. 6.** Multi-element and REE patterns of diorites (a–b), granodiorites (c–d) and monzogranites (e–f) from the Matok pluton, compared with lavas from the Platberg Group (data from Altermann and Lenhardt, 2012; Crow and Condie, 1988; Nelson et al., 1992), the HBG Fe–K suite of southern Norway (Demaiffe et al., 1990; Vander Auwera et al., 2003) and average composition of other typical Archean plutonic rocks (g–h), i.e. TTGs and biotite-bearing granites of the Pietersburg block (data from Henderson et al., 2000; Kreissig et al., 2000; Laurent et al., in revision) and worldwide sanukitoids (database of Martin et al., 2009). Normalization values are the 'pyrolite silicate Earth' for the primitive mantle, and C1 chrondrites (McDonough and Sun, 1995).

**Table 2**
Sm–Nd isotopic compositions measured in whole-rock samples of the Matok pluton.

| Sample | Rock type | $^{147}Sm/^{144}Nd$ | ±2σ | $^{143}Nd/^{144}Nd$ | ±2σ | $(^{143}Nd/^{144}Nd)_i$[a] | ±2σ | $\varepsilon_{Nd}$[b] | ±2σ | $T_{DM}$[c] (Ga) |
|---|---|---|---|---|---|---|---|---|---|---|
| MAT-05 | Diorite (enclave) | 0.111 | 0.001 | 0.51094 | 0.00001 | 0.50897 | 0.00002 | −3.6 | 0.8 | 3.14 |
| MAT-13 | Granodiorite | 0.108 | 0.001 | 0.51093 | 0.00001 | 0.50901 | 0.00002 | −2.8 | 0.8 | 3.07 |
| MAT-17 | Diorite | 0.111 | 0.001 | 0.51096 | 0.00001 | 0.50900 | 0.00002 | −3.0 | 0.8 | 3.10 |
| MAT-21b | Granodiorite | 0.094 | 0.001 | 0.51064 | 0.00001 | 0.50898 | 0.00002 | −3.5 | 0.8 | 3.07 |
| MAT-24 | Monzogranite | 0.091 | 0.001 | 0.51060 | 0.00001 | 0.50900 | 0.00002 | −3.1 | 0.8 | 3.03 |
| MAT-28 | Diorite | 0.103 | 0.001 | 0.51079 | 0.00001 | 0.50896 | 0.00002 | −3.8 | 0.8 | 3.12 |
| MAT-32 | Monzogranite | 0.108 | 0.001 | 0.51083 | 0.00001 | 0.50892 | 0.00002 | −4.6 | 0.8 | 3.21 |
| MAT-34 | Granodiorite | 0.075 | 0.001 | 0.51033 | 0.00001 | 0.50899 | 0.00002 | −3.2 | 0.8 | 3.00 |
| MAT-60 | Diorite | 0.109 | 0.001 | 0.51092 | 0.00001 | 0.50899 | 0.00002 | −3.3 | 0.8 | 3.11 |
| MAT-62 | Granodiorite | 0.113 | 0.001 | 0.51100 | 0.00001 | 0.50899 | 0.00002 | −3.2 | 0.8 | 3.12 |
| MAT-66 | Diorite | 0.108 | 0.001 | 0.51089 | 0.00001 | 0.50898 | 0.00002 | −3.4 | 0.8 | 3.12 |
| MAT-70 | Diorite | 0.106 | 0.001 | 0.51090 | 0.00001 | 0.50902 | 0.00002 | −2.7 | 0.8 | 3.05 |

[a] Initial isotopic composition calculated considering radioactive decay only, and using $\lambda = 6.54 \cdot 10^{12}\ a^{-1}$.
[b] $\varepsilon_{Nd}$ calculated using the CHUR model of Jacobsen and Wasserburg, 1984.
[c] DM model age graphically estimated by intersection between the evolution line of the sample and the DM curve calculated from the equation of dePaolo, 1981.

both $TiO_2$ and $P_2O_5$ (1.0–2.5 and 0.4–1.2 wt.%, respectively), while they are only 0.25 and 0.1 wt.% in the monzogranites, respectively.

### 4.2. Trace elements

Trace element concentrations (Table 1) are reported in primitive mantle-normalized multi-element diagrams and chondrite-normalized REE patterns (Fig. 6). A notable feature of these patterns is their high enrichment in all elements with respect to normalizing values (1 to 3 orders of magnitude for most elements, regardless of the $SiO_2$ content of the rocks) as well as classic negative anomalies in Nb–Ta, Ti as well as Sr ($Sr_N/Nd_N$ = 0.1–0.8) and Eu. All rock types also bear less common troughs in Th and U, which are nevertheless more pronounced in the diorites ($Th_N/Rb_N$ = 0.05–0.2) than in more felsic rocks ($Th_N/Rb_N$ = 0.1–1.2).

The comparison between trace element patterns of diorites and granodiorites points out that the latter, in addition to the less pronounced Th–U anomalies, have higher Rb concentrations and lower Sr ones (Fig. 6a,c). Apart from these exceptions, the trace element contents of diorites and granodiorites are closely similar, characterized by richness in HFSE (Nb = 15–35 ppm; Zr = 400–850 ppm; Y = 40–75 ppm), Ba (>1000 ppm) as well as REE (La = 50–120 ppm; Gd = 7–17 ppm; Yb = 4–7 ppm) with moderately fractionated patterns ($La_N/Yb_N$ = 8–14) and negative Eu anomalies ($Eu_N/Eu^*$ = 0.3–0.8).

In contrast, monzogranites can be separated into three groups on the basis of their trace element signatures (Fig. 6e–f): (1) "Type 1", with trace element contents comparable to that of granodiorites and diorites, with the exception of higher Rb, Th, U as well as more pronounced negatives anomalies in Ba, Sr, Eu and Ti; (2) "Type 2", which only differs from Type 1 by lower Nb, Ta and HREE contents; and (3) "Type 3", with even lower Nb–Ta contents and more fractionated REE patterns ($La_N/Yb_N$ ~50) than any other rock type, owing to very low HREE concentrations (Yb < 1 ppm). "Type 3" samples also have no negative Eu anomaly and less pronounced Ti and Sr troughs.

### 4.3. Sm–Nd isotopes

Sm–Nd isotopic data are presented in Table 2. All Matok samples define a poorly constrained (MSWD = 7.1) Sm–Nd "isochron" (Fig. 7a), but the calculated age of 2662 ± 250 Ma is consistent with U–Pb dating (~2685 Ma; Laurent et al., 2013b). This consistency indicates that the Sm–Nd isotopic system has not been disturbed by post-crystallization events in the Matok samples. All the initial $^{143}Nd/^{144}Nd$ ratios were calculated using the average U–Pb age of 2685 Ma. They result in negative $\varepsilon_{Nd}$ values (Fig. 7b), ranging between −2.7 and −3.8 (±0.8, 2σ uncertainty of all $\varepsilon_{Nd}$ values), except for monzogranite MAT-32 that is even less radiogenic ($\varepsilon_{Nd}$ = −4.6). Such values are comparable to those obtained by Barton et al. (1992), which range between −2.1 and −4.3 (±1.0). Even though the samples investigated for Sm–Nd isotopes span the whole silica range of the magmatic suite,

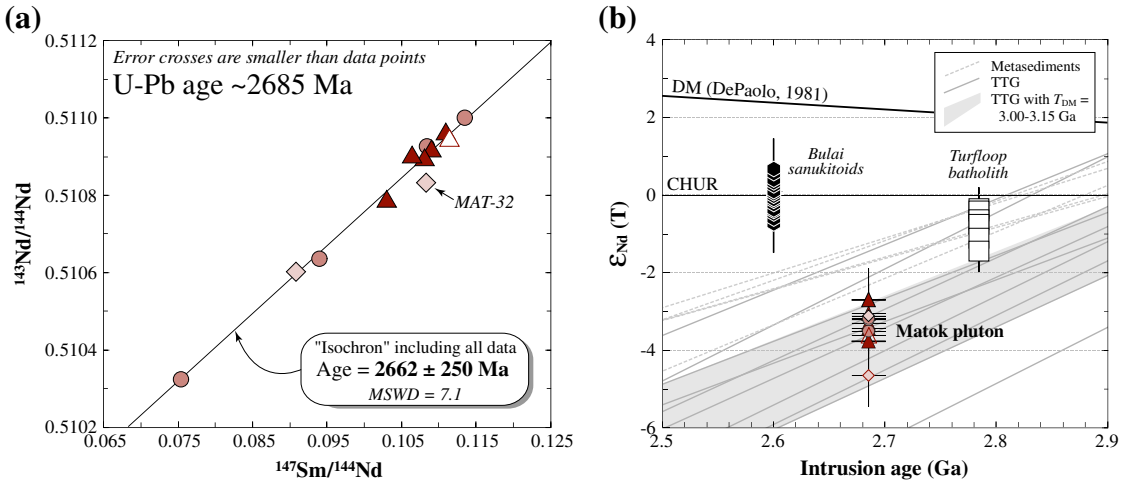


**Fig. 7.** (a) Sm–Nd whole-rock isochrons for samples of the Matok pluton; and (b) initial Nd isotopic signature, expressed as $\varepsilon_{Nd}$ at 2685 Ma, compared with other Archean plutonic rocks of the area (data from Barton et al., 1992; Kreissig et al., 2000 for TTG and metasediments; Henderson et al., 2000 for the Turfloop batholith and Laurent et al., 2011 for Bulai sanukitoids). Symbols are as in Figs. 4 and 5.

the initial isotopic compositions do not show any clear variation against $SiO_2$: all $\varepsilon_{Nd}$ are identical within error range, providing a weighted average of $-3.3 \pm 0.2$ (MSWD = 1.6).

It must be noted that local TTGs have $\varepsilon_{Nd\ (2685\ Ma)}$ values ranging from −1.5 to −6.6, most of the samples clustering around −4.0 (Barton et al., 1992; Kreissig et al., 2000). In other words, the Nd isotopic signature of the Matok granitoids is roughly similar to that of the local continental crust at the time they emplaced (Fig. 7b). Consistently, the model ages obtained on most TTG samples of the Pietersburg block fall within the range 3.00–3.15 Ga (Fig. 7b), which is identical to that of samples from the Matok pluton (3.00–3.21 Ga; Table 2).

## 5. Classification issues and comparison with other rock types

According to Moyen et al. (2003), the three most common types of late-Archean granitoids are TTGs, biotite-bearing granites and sanukitoids. In Figs. 5 and 6, the major- and trace element contents of the Matok samples are compared to the compositions of these three groups, using data from the surrounding Pietersburg block for TTGs and biotite-bearing granites, and literature data for sanukitoids worldwide in order to address a more global comparison. In some aspects, especially regarding their trace element contents, the Matok monzogranites are akin to biotite-bearing granites, although they are slightly richer in $TiO_2$ and $P_2O_5$ and contain less $Al_2O_3$ and $Na_2O$. In contrast, diorites and granodiorites are related to neither typical Archean TTGs, nor biotite-bearing granites, because of their low $SiO_2$, $Al_2O_3$, $Na_2O$ and Sr contents and their richness in REE and HFSE. These rocks share several similarities with sanukitoid suites, such as metaluminous compositions, great range in $SiO_2$, elevated $FeO_t + MgO$ and high incompatible trace element contents.

On the other hand, when compared with typical sanukitoids, Matok diorites and granodiorites turn out to be poorer in $Al_2O_3$, $K_2O$, Rb, Ba, Th and richer in $FeO_t$, $TiO_2$ (even with respect to the so-called "high-Ti sanukitoids"; Martin et al., 2009) and $P_2O_5$ (Fig. 5). They also display a more prominent negative Eu anomaly and less fractionated REE patterns owing to higher HREE contents (Fig. 6). The latter characteristics make the Matok rocks akin to ferroan, "A-type" granites that are notably rich in $FeO_t$, $TiO_2$, $P_2O_5$, REE and HFSE with moderately fractionated REE patterns and pronounced Eu–Sr negative anomalies (Anderson and Bender, 1989; Dall'Agnol and Oliveira, 2007; Eby, 1992; Frost and Frost, 1997; Rämö and Haapala, 1995; Whalen et al., 1987).

As a result, the Matok granitoids can be regarded as compositionally intermediate between sanukitoids and ferroan, "A-type" granites. In this matter, they are closely similar to the so-called "ferro-potassic" (Fe–K) suites that are widespread in Proterozoic terranes, for example in Algeria (Peucat et al., 2005), Antarctica (D'Souza et al., 2006), Australia (Smithies et al., 2011), Cameroon (Kouankap Nono et al., 2010; Tagne-Kamga, 2003), Nigeria (Ferré et al., 1998), Norway (Bogaerts et al., 2003; Demaiffe et al., 1990; Vander Auwera et al., 2003, 2007, 2011) and Poland (Duchesne et al., 2010; Skridlaite et al., 2003). In particular, the major- and trace element composition of samples from the Matok pluton overlap those of the 1.0–0.9 Ga-old Hornblende-Biotite Granitoid (HBG) suite and associated mafic rocks of the Sveconorwegian province in southern Norway (Vander Auwera et al., 2011; Figs. 5 and 6).

Such Fe-rich magmas were also documented in Neoarchean terranes, for example, in the North Atlantic Craton (Steenfelt et al., 2005), the Baltic Shield (Mikkola et al., 2011) and the North China Craton (Jahn et al., 1988). Although all these granitoids show higher $FeO_t/(FeO_t + MgO)$ than average sanukitoids, they are generally less ferroan and more aluminous than the Matok pluton, showing that a continuum exists between Fe–K suites and sanukitoids. It is indeed clear on Fig. 5 that sanukitoids, the HBG suite and the Matok samples define a compositional range, especially regarding $Al_2O_3$, $FeO_t$ and MgO contents, between low-Al, ferroan magmas, and high-Al, magnesian ones.

From a local point of view, diorites from the Matok pluton are close in composition to the basalts and basaltic andesites from the ca. 2710 Ma-old Platberg group of the Ventersdorp supergroup (Figs. 5 and 6), a large (>$10^6$ km$^2$) volcano-sedimentary basin that crops out in northern and central South Africa (van der Westhuizen et al., 2006; Fig. 1). The Platberg lavas are therefore compositional counterparts of the Matok granitoids, emplaced at surface level ~20 Ma earlier.

## 6. Discussion

### 6.1. Contribution of pre-existing crust and the origin of monzogranites

Petrogenetic studies carried out so far on the Matok granitoids concluded that they derive from reworking of felsic continental crust. This conclusion is mainly based on the observation that their initial isotope composition (Sr, Nd, Pb and Hf) overlaps that of the surrounding Goudplaats–Hout River TTG gneisses (Barton et al., 1992; Zeh et al., 2009). These gneisses are mostly trondhjemitic and granodioritic with usually >65 wt.% $SiO_2$ (Barton et al., 1992; Kreissig et al., 2000; Kröner et al., 2000; Laurent et al., in revision). Partial melting of such rocks would invariably generate magma with $SiO_2$ = 67–80 wt.% and $FeO_t + MgO < 5$ wt.% (Singh and Johannes, 1996; Skjerlie and Johnston, 1996; Watkins et al., 2007). Clearly, this cannot have given rise to the granodiorites and diorites that are poorer in silica (53–70 wt.% $SiO_2$) and more mafic (4–14 wt.% $FeO_t + MgO$), unless these rocks are considered as crystal cumulates formed through fractionation of the TTG-derived melt. This is inconsistent with (1) field and petrographic observations indicating that granodiorites and diorites were magmatic liquids (see Section 3 and Fig. 3), and (2) the Mg# (0.3–0.5) and transition element contents (V = 50–200 ppm) of these rocks that are too low to represent that of cumulates.

Another way to explain both the high $FeO_t + MgO$ and unradiogenic Nd isotope compositions of Matok diorites and granodiorites would be crustal contamination of mantle-derived basalt. Fig. 8 shows that the Nd isotopic composition of the diorites and granodiorites

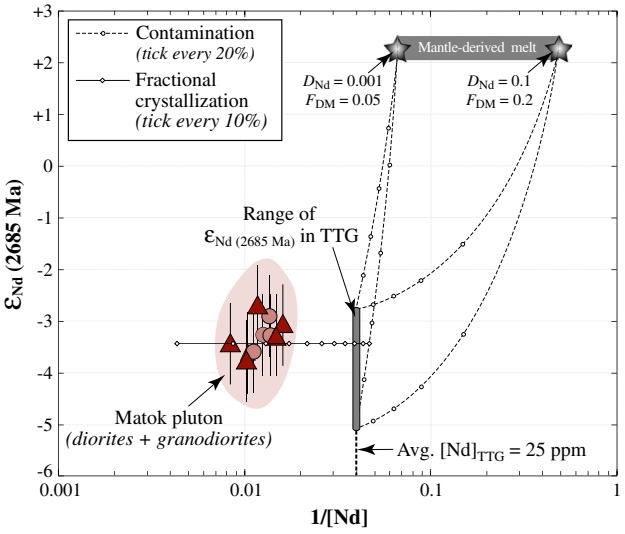


**Fig. 8.** Plot of $\varepsilon_{Nd}$ at 2685 Ma as a function of 1/[Nd], showing contamination curves (dashed lines) between two extreme Nd compositions of mafic, mantle-derived melts and local TTGs (elemental and isotope data from Kreissig et al., 2000). The two compositions of the mafic melts (stars) were modeled by batch melting (equation of Shaw, 1976) of a depleted mantle source (Nd = 0.58 ppm; Workman and Hart, 2005; $\varepsilon_{Nd\ (2685\ Ma)} = +2.25$ calculated using the equation of dePaolo, 1981) for extreme values of melt fractions ($F_{DM}$) and global distribution coefficients ($D_{Nd}$). The isotopic compositions of the diorites and granodiorites of the Matok pluton (symbols as in Figs. 4 and 5) are adequately reproduced by 25 to 65% contamination of the mafic melt (depending on the extreme composition chosen as representative of the initial magma) by TTG rocks with $\varepsilon_{Nd\ (2685\ Ma)}$ of ca. −5, but their high Nd concentrations requires >70% fractionation assuming $D_{Nd} = 0$ (fractional crystallization trend, solid line).

is successfully reproduced by contamination of a basaltic melt ($\varepsilon_{Nd\ (2685\ Ma)} = +2.25$) by 25% to 65% (depending on the Nd concentration of the basalt) of least radiogenic TTGs of the Pietersburg block ($\varepsilon_{Nd\ (2685\ Ma)} = -5$). However, such contamination cannot account for the high Nd (and other incompatible element) contents of the rocks, unless assuming very high degrees (70–90%) of subsequent fractional crystallization with Nd behaving as a perfectly incompatible element ($D_{Nd} = 0$; Fig. 8), both values being highly unrealistic. Therefore, Matok diorites and granodiorites derive neither from melting, nor from assimilation of felsic continental crust. Interestingly, Crow and Condie (1988) reached the same conclusion for the Platberg lavas of the Ventersdorp Supergroup, whose compositions are similar to those of the Matok diorites (Figs. 5 and 6).

On the other hand, it is possible that melting of pre-existing TTGs played a role in the genesis of the more felsic monzogranites (73–75 wt. $SiO_2$; 2–3 wt.% $FeO_t + MgO$). In terms of major elements, the latter are moreover close in composition to local biotite-bearing granites (Fig. 5) that derived from melting of older felsic gneisses (Kreissig et al., 2000; Henderson et al., 2000; Laurent et al., 2013b, in revision). Nevertheless, when trace elements are considered, this comparison only stands true for the so-called "Type 3" monzogranites, while "Type 1" and "Type 2" have less fractionated REE patterns, deeper Eu–Sr anomalies, and higher Nb–Ta contents than biotite-bearing granites (Fig. 6e–f). This observation indicates that Matok monzogranites unlikely result from a single petrogenetic mechanism. Specifically, the trace element pattern of "Type 1" monzogranites is very similar to that of the Matok diorites and granodiorites (Fig. 6e–f), except huge negative anomalies in Sr, Eu, Ti, to a lesser extent Ba, and less fractionated REE patterns ($La_N/Yb_N$ <10). Such characteristics are consistent with an origin through high degrees of differentiation from the diorites and granodiorites, with fractionation of plagioclase, Ti-rich phases (ilmenite, titanite) and LREE-rich apatite. We thus propose that the Matok monzogranites result from the interplay of two different petrogenetic processes, namely (1) melting of local TTG crust, and (2) extreme differentiation from diorites and granodiorites. These two mechanisms are respectively represented by "Type 3" and "Type 1" monzogranites. Interactions between granitic magmas generated from both mechanisms could have produced some hybrid phases, such as "Type 2" monzogranites showing intermediate trace element compositions (Fig. 6e–f).

### 6.2. A common mafic parent for diorites and granodiorites

As long as they derive from neither melting of TTG crust, nor from crustal contamination of a basaltic melt, the granodiorites and diorites from Matok necessarily derive from different degrees of differentiation of a common mafic parent. Consistently, many authors who have studied the petrogenesis of such Fe–K magmas have concluded that they fractionated from a mafic component in the lower crust, either by melting or crystallization (Bogaerts et al., 2006; D'Souza et al., 2006; Duchesne et al., 2010; Skridlaite et al., 2003; Tagne-Kamga, 2003; Vander Auwera et al., 2003, 2007). The nature and composition of the Matok parent has been investigated through the study of the diorites, which are the most primitive end-member of the suite. A review of experimental studies of phase relationships in mafic systems under crustal conditions (3–10 kbar; Beard and Lofgren, 1991; Longhi et al., 1999; Rapp and Watson, 1995; Sisson et al., 2005; Tatsumi and Suzuki, 2009; Wolf and Wyllie, 1994) shows that melts with major element compositions similar to those of the Matok diorites are produced at high temperatures (950–1100 °C), high melt proportions (25–65%) and $H_2O$-poor (<2 wt.%) compositions. The inferred temperatures are consistent with those calculated from $P_2O_5$ contents of the diorites using the apatite saturation thermometer (Watson and Harrison, 1983), which are comprised between 978 and 1072 °C. Furthermore, the primary mineral assemblage of Matok diorites consists of Pl + Opx + Cpx (see Section 3). This mineralogy is typical of water-poor magma and is systematically present in equilibrium with the melt in the experiments mentioned above. Experimental data thus indicate that the diorites plausibly represent magmas derived from high-temperature differentiation of a relatively water-poor mafic parent.

In the Pietersburg block, the parent could be represented by tholeiitic amphibolites, which are common both in the greenstone belts and as bodies of various sizes embedded in TTG gneisses (Brandl et al., 2006; Kreissig et al., 2000; Robb et al., 2006). The phase relationships derived from the experiments of Tatsumi and Suzuki (2009) were used to calculate the trace element contents of the liquids generated from such a parental composition, either by melting or crystallization. Fig. 9 shows that the computed compositions do not match those of the Matok diorites regardless of the differentiation mechanism. In particular, the concentration of HFSE (Nb, Ta, Zr and Hf), LREE and Sr, as well as $La_N/Yb_N$ ratios, are too low in the modeled melts.

Hence, it appears that the Matok parent is not present at the level of exposure, such that we modeled its composition from that of the diorites. This modeling is based on a single assumption: the range of diorite compositions results only from different degrees of differentiation of the same mafic parent, with a constant fractionating assemblage. Calculations were applied to both major- and trace elements; details about the models and results are presented in Table 3 and Fig. 10, respectively. In terms of major elements, the parent is a subalkaline basalt intermediate between tholeiitic and calc-alkaline groups ($FeO_t/MgO = 1.83$). It plausibly represents a pristine mantle melt ($FeO_t + MgO > 15$ wt.%). The composition of the solid residue is consistent with a fractionating assemblage dominated by Pl + Opx + Cpx (Table 3), which is in line with experimental constraints. Regarding trace elements, the patterns of the calculated parent have the same shape as those of Matok diorites (identical $La_N/Yb_N$ ratio, similar Nb–Ta and Th negative anomalies), except less pronounced or absent Sr–Eu negative anomalies (Fig. 10). It is also close in composition to gabbronorites of the Fe–K HBG suite of southern Norway (Fig. 10),

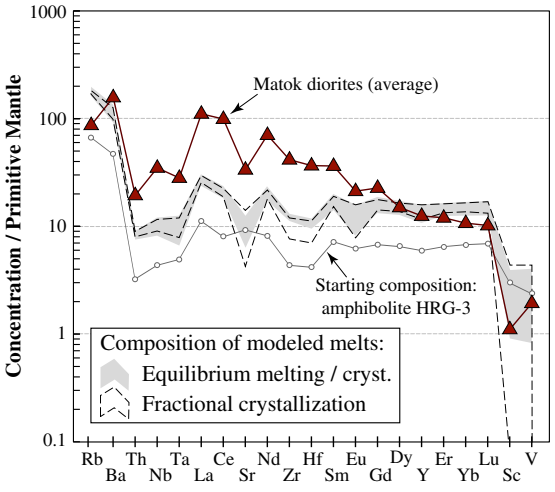


**Fig. 9.** Multi-element diagram with concentrations normalized to primitive mantle (McDonough and Sun, 1995) where the average trace element composition of the Matok diorites are compared to that of liquids derived from fractionation of tholeiitic amphibolites from the northern Kaapvaal craton. The latter were calculated using either the batch melting equation $C_0 = C_L \cdot [F + D \cdot (1 - F)]$ of Shaw (1976) for both equilibrium melting and equilibrium crystallization or the Rayleigh equation $C_0 = C_L / F^{D-1}$ for fractional crystallization. The starting composition is represented by amphibolite sample HRG-3 (major- and trace element composition reported in Supplementary Material). Fractionating minerals (60% plagioclase + 20% clinopyroxene + 10% orthopyroxene + 8% ilmenite + 2% magnetite) as well as the mass fraction of liquid ($F = 0.35$) were derived from experimental run HG385 of Tatsumi and Suzuki (2009). The result of the model is a range of possible compositions, rather than a unique value, because we used a range of possible partition coefficients (Kd) from a minimum value to a maximum one (see Table 3 in Laurent et al., 2013a for details and values).

**Table 3**
Modeling carried out on 8 major elements to calculate the composition of the parental component ($C_0$) from which the Matok diorites fractionated.

| | Most mafic diorite (MAT-17) | Most felsic diorite (MAT-05) | Parental component | Solid calculated by mass balance | Solid calculated using compositions of minerals | | | | | |
|---|---|---|---|---|---|---|---|---|---|---|
| | $C_{Dio}$ | | $C_0$[a] | $C_S$[a] | Bulk[b] | Pl[c] | Cpx | Opx | Mag | Ilm |
| | $F = 0.65$ | $F = 0.25$ | | | 1 | 0.6 | 0.2 | 0.14 | 0.02 | 0.04 |
| *Major oxides (wt.%)*[d] | | | | | | | | | | |
| $SiO_2$ | 56.21 | 63.82 | 54.54 | 51.45 | 51.30 | 56.0 | 52.5 | 51.2 | 0.9 | 0.3 |
| $TiO_2$ | 2.03 | 1.68 | 2.11 | 2.25 | 2.14 | 0 | 0.2 | 0.1 | 7.3 | 49 |
| $Al_2O_3$ | 15.60 | 14.71 | 15.80 | 16.16 | 16.72 | 27.0 | 1.4 | 0.7 | 6.1 | 0.5 |
| $FeO_t$[e] | 8.48 | 6.73 | 8.86 | 9.57 | 10.81 | 0.0 | 14.0 | 30.7 | 84.7 | 50 |
| MgO | 4.82 | 2.14 | 5.41 | 6.50 | 4.66 | 0.0 | 11.9 | 16.2 | 0.5 | 0 |
| CaO | 7.28 | 4.54 | 7.88 | 9.00 | 9.70 | 9.5 | 19.4 | 0.8 | 0.5 | 0.2 |
| $Na_2O$ | 3.58 | 3.92 | 3.50 | 3.36 | 3.51 | 5.6 | 0.6 | 0.3 | 0 | 0 |
| $K_2O$ | 2.00 | 2.46 | 1.90 | 1.71 | 0.60 | 1.0 | 0 | 0 | 0 | 0 |

[a] $C_0$ and $C_S$ have been calculated using a simple mass balance equation $C_0 = F \cdot C_{Dio} + (1 - F) \cdot C_S$ where $F$ is the melt fraction, $C_{Dio}$ the composition of a diorite sample and $C_S$ that of the residual solid assemblage (cumulate or restite). We solved the equation for both $C_0$ and $C_S$ considering that the range of diorite compositions derives from 25 to 65% of fractionation from the parental component ($F = 0.25$ for $C_{Dio}$ = most felsic diorite; $F = 0.65$ for $C_{Dio}$ = most mafic diorite), as pointed out by experimental studies (see text for explanation) and in agreement with linear trends in Harker plots of Fig. 5.

[b] Bulk composition of a hypothetical solid residual assemblage calculated using mineral proportions (indicated under the mineral name) deduced from experiments of Tatsumi and Suzuki (2009) and average mineral compositions measured in the Matok samples by Rapopo (2010), except for plagioclase. It must be noted that this composition is very close to that calculated from mass balance modeling ($C_S$), except that it has a too high $FeO_t$/MgO ratio. This may indicate that pyroxenes crystallized in the residual liquids (i.e. the diorites) had higher Fe/Mg than those which crystallized earlier in the residue or cumulate.

[c] Composition of the most Ca-rich plagioclase crystal (~$An_{50}$) in equilibrium with Fe–K melt in the experimental study of Bogaerts et al. (2006).

[d] All compositions are calculated on anhydrous basis, without MnO and $P_2O_5$.

[e] All iron is expressed as FeO.

believed to be the parental magmas of the whole series (Vander Auwera et al., 2007). It must be noted that calculations based on crystallization and melting models yield similar results (Fig. 10): then, it is not possible to discriminate between either of these two mechanisms.

### 6.3. Involvement of "enriched" mantle and comparison with sanukitoids

In spite of lower absolute concentrations than in the Matok samples, incompatible trace element contents of their calculated parent magma or source rock are still 5 to 70 times higher than in the primitive mantle (Fig. 10). Such high concentrations preclude derivation of the mafic parent from a non-enriched mantle source. Indeed, the incompatible element contents of a partial melt derived from primitive mantle compositions (McDonough and Sun, 1995) would approach those of the calculated parent only for melt fractions in the range 0–5% (using bulk distribution coefficients of Workman and Hart (2005), which is unrealistically low. Moreover, such a process would not account for the "crustal signature", i.e. high $La_N/Yb_N$ and negative Th–Nb–Ta anomalies, that characterize the pattern of the calculated parent (Fig. 10). Therefore, the mantle source from which the latter derived had to already be enriched in incompatible elements, owing to prior hybridization with a crustal component. This is consistent with the conclusions of several authors who proposed that Fe–K suites possibly derived from melting of a metasomatized, lithospheric mantle source, or lower crustal material derived from it (Ferré et al., 1998; Vander Auwera et al., 2003, 2011).

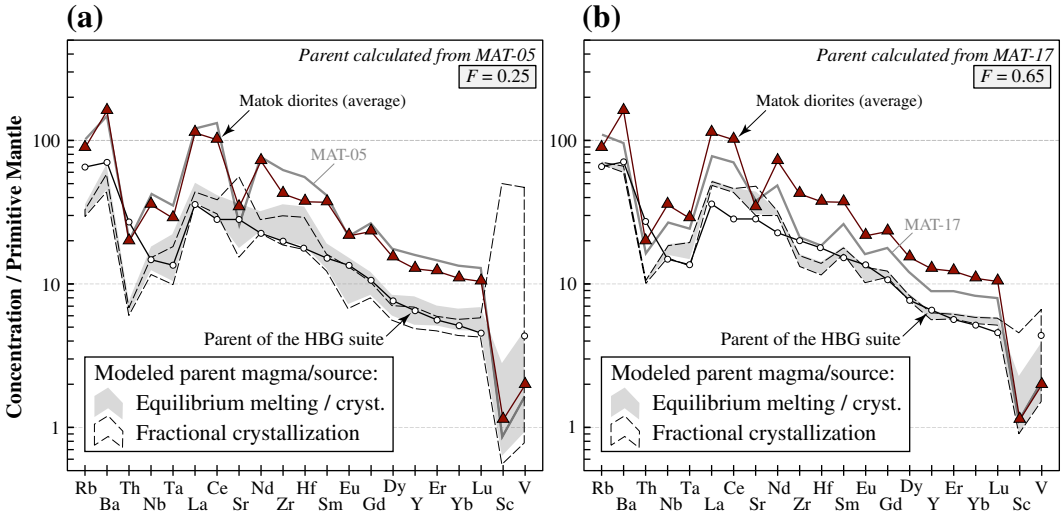


**Fig. 10.** Multi-element diagrams with concentrations normalized to primitive mantle (McDonough and Sun, 1995) showing the calculated trace element composition of the parental component from which the Matok diorites fractionated. The composition of the parent magma, or source rock, has been calculated using either the equation $C_0 = C_L \cdot [F + D \cdot (1 - F)]$ of Shaw (1976) for equilibrium melting/crystallization; or the Rayleigh equation $C_0 = C_L / F^{D-1}$ for fractional crystallization. The same approach has been used as for major elements, i.e. that we considered the Matok diorites as all derived from differentiation of a similar parent magma or source rock, with the same fractionating assemblage (see Table 3). Specifically, the composition of the parent $C_0$ has been calculated using (a) the most felsic diorite (MAT-05) as $C_L$, with $F = 0.25$; and (b) the most mafic diorite (MAT-17) as $C_L$, with $F = 0.65$. Fractionating minerals and mineral proportions are the same as presented in Table 3, and we used ranges of partition coefficients Kd (resulting in a range of possible compositions) as described in Fig. 9. The composition of the parental component is fairly similar in both cases, demonstrating the robustness of the model. The average composition of the Matok diorites are represented for comparison, as well as that of the gabbronorite sample VDA9912 of the HBG Fe–K suite of southern Norway (white circles), modeled as the parent of the whole series (Vander Auwera et al., 2007).

Fig. 7b shows that $\varepsilon_{Nd}$ of the Matok pluton was the same as that of samples of the Pietersburg block TTGs at the time of emplacement, which, as demonstrated earlier, does not result from crustal contamination. In addition, when compared with average upper continental crust, the Pietersburg block is characterized by its exceptionally low Th and U contents (Kramers et al., 2001). The Matok diorites are characterized by unusual Th–U negative anomalies in multi-element patterns, which is not either a result of crustal contamination as it tends to attenuate towards more felsic compositions (Fig. 6). Both lines of evidence support that the agent responsible for metasomatism of the mantle source region was derived from local crust. In the Pietersburg block, three main lithologies older than the Matok pluton could potentially have metasomatized the mantle: (1) TTG gneisses; (2) 2.78 to 2.84 Ga-old biotite-bearing granites and (3) sedimentary rocks. Fig. 11 compares some trace element ratios of these lithologies with those of the Matok diorites. We specifically selected incompatible element ratios that are not significantly fractionated during mantle melting and subsequent magma differentiation (i.e. K/Th; Nb/La; Gd/Y and Zr/Sm), such that they can be considered as reasonably representative of source compositions. These diagrams clearly display that the Matok diorite compositions fairly match those of sedimentary rocks rather than TTG or biotite-bearing granites.

On the other hand, modeling based on Nd isotopes (Fig. 12) shows that $\varepsilon_{Nd}$ values of the Matok diorites are inconsistent with a mantle-enrichment having taken place prior to ~3.0 Ga. Indeed, this would have required a crustal component with suprachondritic Nd isotope signature at the time of metasomatism (Fig. 12). This is very unlikely, especially if this crustal component is represented by meta-sedimentary rocks. Therefore, we propose that the mantle source of the Matok diorites and their parent has been metasomatized by sedimentary material (or fluids/melts derived from it) originating from the local crust of the Pietersburg block, between ~3.0 and ~2.7 Ga. Importantly, Barton et al. (1996) concluded from the study of the ~2.0 Ga-old Schiel alkaline complex, which emplaced ~50 km to the northeast of the Matok pluton, that the mantle lithosphere beneath the Pietersburg block underwent enrichment in incompatible elements between ~2.8 and ~2.6 Ga. Similarly, Crow and Condie (1988) and Nelson et al. (1992) concluded that a <3.0 Ga-old enriched mantle source was involved in the source of the Platberg lavas from the Ventersdorp Supergroup, which are compositionally similar to the Matok diorites (see Section 5) and emplaced over a vast area (Fig. 1). This indicates that extensive mantle enrichment took place beneath the northern edge of the Kaapvaal Craton during the Neoarchean.

A consequence of this model is that the petrogenesis of the Matok pluton (Fe–K suite) and sanukitoids (Mg–K suites) both require the interaction, at mantle levels, of peridotite with a felsic component rich in incompatible elements. Therefore, one can wonder why the two magma types show subtle, but systematic, chemical differences. When compared with sanukitoids, Fe–K suites generally have higher $FeO_t/MgO$ and lower $Al_2O_3$, LILE contents and $La_N/Yb_N$ (Figs. 5 and 6). These discrepancies are unlikely to result from a difference in the

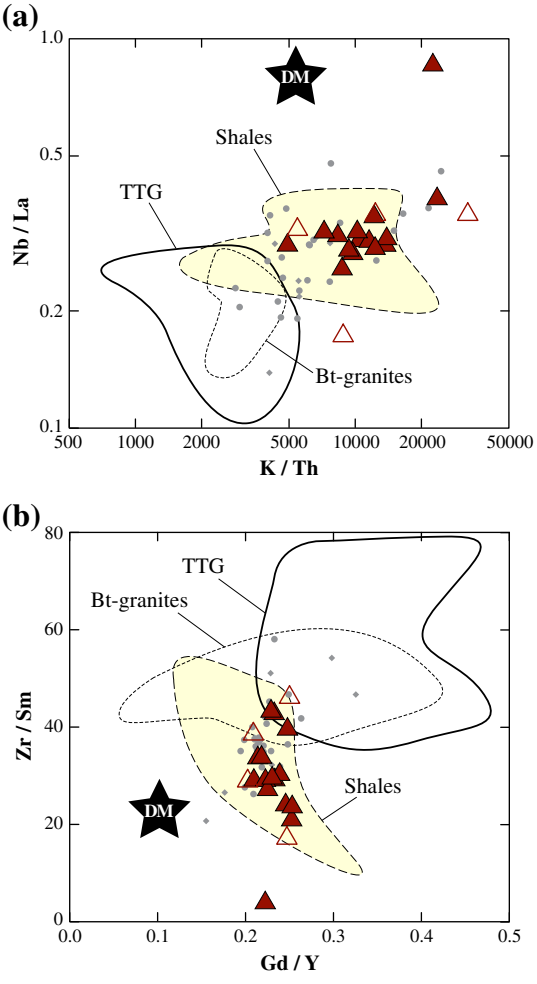


**Fig. 11.** Plots of selected minor- and trace element ratios that are not significantly fractionated during mantle melting and differentiation of mafic melts: (a) Nb/La vs. $K_{ppm}/Th$ and (b) Zr/Sm vs. Gd/Y. The Matok diorites are represented by red triangles, granodiorites by gray circles and monzogranites by gray diamonds. The composition of the diorites overlap that of detrital sedimentary rocks from the Pietersburg block (data from Kreissig et al., 2000) for both diagrams, while minor- and trace element ratios in TTGs (data from Kreissig et al., 2000; Kröner et al., 2000; Laurent et al., in revision) and biotite-bearing granites (data from Henderson et al., 2000; Kröner et al., 2000; Laurent et al., in revision) are different.

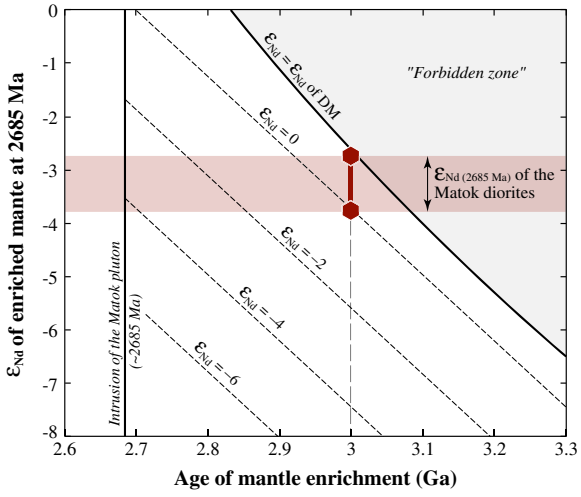


**Fig. 12.** Isotopic composition at 2685 Ma of several, virtual enriched mantle sources, each one represented by a line (dashed or solid). The different sources were obtained by mixing between 80% depleted mantle (DM) and 20% of a crustal component, which had different possible $\varepsilon_{Nd}$ values at the time of mixing, i.e. between −6 and 0 (dashed lines) or that of DM (thick black curve). For instance, mixing at 2.9 Ga of DM with a crustal component showing $\varepsilon_{Nd(2.9\ Ga)} = -6$ would result in a hybrid mantle with $\varepsilon_{Nd} = -8$ at 2685 Ma. The composition of the hybrid mantle at the time of enrichment was calculated assuming $[Nd]_{DM} = 0.58$ ppm (Workman and Hart, 2005), [Nd] = 30 ppm for the crustal component (average of metasediments from the Pietersburg block; Kreissig et al., 2000) and $\varepsilon_{Nd}$ of DM calculated by the equation of dePaolo (1981). The isotopic composition of the mixture at 2685 Ma was calculated considering radioactive decay only, using an average $^{147}Sm/^{144}Nd$ of 0.105 ("crustal average" of the Pietersburg block calculated using all data from Henderson et al., 2000; Kreissig et al., 2000, Laurent et al., in revision and this study). If mantle metasomatism took place at 3.0 Ga, then the crustal component would have had $\varepsilon_{Nd}$ comprised between 0 and that of DM (thick red line bounded by the two symbols) to account for the isotope composition of the Matok diorites at 2685 Ma.

**Table 4**
Results of the mixing model (1:1) between average composition of sanukitoids and that of Depleted Archean Tholeiites for 8 major elements.

| | Depleted Archean tholeiite (Condie, 1981) | Average sanukitoids (Martin et al., 2009) | Mixing product[a] | Calculated parent of the Matok suite | RD[b] (%) |
|---|---|---|---|---|---|
| Mixing proportions | 0.5 | 0.5 | | | |
| *Major oxides (wt.%)*[c] | | | | | |
| $SiO_2$ | 50.22 | 58.49 | 54.36 | 54.54 | 0.3 |
| $TiO_2$ | 0.94 | 1.22 | 1.08 | 2.11 | 64.5[e] |
| $Al_2O_3$ | 15.51 | 16.36 | 15.93 | 15.80 | 0.8 |
| $FeO_t$[d] | 11.82 | 7.56 | 9.69 | 8.86 | 8.9 |
| MgO | 7.53 | 3.42 | 5.48 | 5.41 | 1.2 |
| CaO | 11.61 | 5.60 | 8.60 | 7.88 | 8.7 |
| $Na_2O$ | 2.15 | 4.12 | 3.14 | 3.50 | 10.8 |
| $K_2O$ | 0.22 | 3.23 | 1.72 | 1.90 | 9.9 |

[a] Calculated by mass balance.
[b] RD = relative difference (in %) between the calculated mixing product and the calculated composition of the parent of the Matok suite (see Table 3). For all elements except $TiO_2$ (see footnote e") all RDs are ≤10%.
[c] All compositions calculated on anhydrous basis.
[d] All iron expressed as FeO.
[e] $TiO_2$ contents in the parent were probably over-estimated, explaining the high RD for this element. Because the behavior of $TiO_2$ is likely to be controlled by accessory ilmenite, late saturation or early exhaustion of this phase during crystallization or melting, respectively, would result in a kink in the differentiation trend from the parent towards the Matok diorites. In such case, the model used to determine the composition of the parent, based on linear interpolation, would not be applicable to $TiO_2$.

nature of metasomatic agents because sanukitoids themselves derive from interactions between mantle peridotite and a range of "enriched" components, such as $CO_2$-rich brines (Lobach-Zhuchenko et al., 2008), carbonatites (Steenfelt et al., 2005), TTG-like melts (Heilimo et al., 2010; Martin et al., 2009; Rapp et al., 2010) as well as sediment-derived fluids (Halla, 2005) or magmas (Laurent et al., 2011). In addition, differences in the degree of mantle melting ($F$), the intensity of metasomatism ($a$) and their relative importance ("$F/a$" ratio of Martin et al., 2009) does not account either for the observed differences. Indeed, Martin et al. (2009) demonstrated that decreasing $F/a$ results in an increase of both $FeO_t$/MgO ratios and incompatible element concentrations in the melt produced from the hybrid source. In contrast, Fe–K suites have higher $FeO_t$/MgO ratios than sanukitoids, but lower contents in the most incompatible elements (e.g. Rb, Ba, Th, K).

Alternatively, Fe–K and Mg–K suites could derive from a similar source (metasomatized mantle) but with different melting conditions, especially regarding pressure ($P$) and temperature ($T$). This possibility has been proposed by Debon and Lemmet (1999) to account for the dichotomy between both granitoid types in the late-Paleozoic crystalline massifs of the Western Alps. They concluded that lower $T$ and $P$ conditions in the source of Fe–K suites respectively prevent (1) melting of Mg-rich minerals and (2) garnet stability, producing melts with high $FeO_t$/MgO and low $La_N/Yb_N$. To explore this hypothesis, we compared the composition of experimental melts obtained in three studies of phase relationships in metasomatized peridotite, two at low $P$ and $T$ (1.0–1.5 GPa, 900–1075 °C; Conceicão and Green, 2004; Prouteau et al., 2001) and one at high $P$ and $T$ (3.0–3.8 GPa, 1100–1200 °C; Rapp et al., 2010). This comparison highlights that (1) melts in both sets of experiments do not show any clear dichotomy between each other in terms of $FeO_t$/MgO ratios (0.33–0.75); and (2) $Al_2O_3$ contents of melts in low $P$–$T$ experiments are much higher (17–20 wt.%) than those of melts in high $P$–$T$ ones (10–15 wt.%), which are in equilibrium with garnet and would thus have higher $La_N/Yb_N$. Both lines of evidence are in contradiction with the observed differences between Fe–K suites and sanukitoids and thus discard the role played by $P$ and $T$ in the origin of these differences. On the other hand, different $fO_2$ and water activities in the source region would be another way to explain the different $FeO_t$/MgO ratios and $Al_2O_3$ contents between both groups (Fe–K suites having a less oxidized, less hydrous source), but would hardly account for differences in their trace element systematics.

The involvement of a distinct source component (in addition to metasomatized mantle) in the genesis of Fe–K suites would rather be able to explain the differences. As pointed out in Section 5, the composition of Fe–K suites is intermediate between those of sanukitoids and "A-type" granites. A popular model for the genesis of "A-type" granites is the fractionation of tholeiitic, mafic sources in the lower crust (e.g. Anderson and Bender, 1989; Clemens et al., 1986; Dall'Agnol et al., 1999; Eby, 1992; Frost and Frost, 1997). Thus, such tholeiitic mafic material could have been involved in the genesis of the Matok pluton. Importantly, Archean tholeiites (data from Condie, 1981) have notably higher $FeO_t$/MgO ratios, as well as lower $Al_2O_3$, $La_N/Yb_N$ and LILE than sanukitoids, which adequately explain the differences between the latter and Fe–K suites. Thereby, a simple 1:1 mixture between average sanukitoid compositions and depleted Archean tholeiites (Condie, 1981) reasonably fits with the calculated parent of the Matok diorites, for major- (Table 4) and most trace elements (Fig. 13). The only exception is the $TiO_2$ content, which presumably results from an overestimation of $TiO_2$ in the calculated parent (see Table 4 for details). Consequently, we propose that Fe–K suites result from the interaction of two components: a sanukitoid one (derived from enriched mantle lithosphere) and a tholeiitic one (derived from mantle asthenosphere). The interaction would take

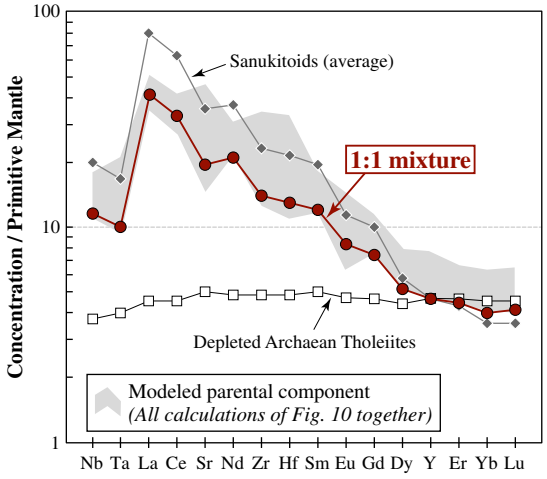


**Fig. 13.** Multi-element diagram for "immobile" elements with concentrations normalized to primitive mantle (McDonough and Sun, 1995) showing the results of binary mixing model (1:1) between average composition of sanukitoids (Martin et al., 2009; gray diamonds) and that of depleted Archean tholeiites (Condie, 1981; white squares). The trace element patterns and concentrations of the calculated mixture (red circles) reasonably match those of the calculated parental component of the Matok diorites.

place either by magma mixing (at lower crustal or mantle levels), through mechanical source mixing into the mantle, or else by modification of the lithospheric mantle by percolating tholeiitic melts. It is worthwhile noting that this petrogenetic model is consistent with the observed compositional spectrum from Fe–K suites to sanukitoids (see Section 5). This range of compositions would simply result from different degrees of interaction between the enriched, lithosperic mantle end-member, and the asthenospheric one.

### 6.4. Global and local geodynamic implications

The geodynamic environment where the Fe–K suites formed must be discussed in the light of the following constraints, fixed all along the above discussion: (1) the lithospheric mantle source region must have been extensively metasomatized by crustal material; (2) this metasomatized mantle and asthenospheric mantle, or their melting products, must have somehow interacted with each other; (3) both events must have taken place in a relatively short time span. This succession of events could be explained by considering a mantle plume impinging at the base of recently enriched continental lithosphere. However, it does not account for the systematic post-collisional nature of Fe–K suites, as it would imply that plume upwelling always takes place both at the right place, i.e. beneath a collisional belt, and the right time, i.e. forthwith after collision, which is unlikely. In contrast, "lithospheric reworking" at the end of continent–continent collision is a more appropriate setting to generate these magmas. Geological constraints and numerical models have indeed shown that continental collision is followed by either (1) breakoff or rollback of the subducting plate, owing to an increase in tensional stress resulting from the collision (e.g. Coulon et al., 2002; Davies and von Blanckenburg, 1995; Duretz and Gerya, 2013; Keskin et al., 2008; Magni et al., 2013; van Hunen and Allen, 2011); or (2) delamination of sub-continental mantle in response to rheological contrasts of the lithosphere between the two colliding blocks (e.g. Black and Liégeois, 1993; Liégeois et al., 1998). These situations are illustrated in the conceptual scenario of Fig. 14, and, importantly, all of them gather the required constraints.

First, mantle enrichment takes place through subduction (Fig. 14a) and is shortly followed in time by continental collision (Fig. 14b). Collision triggers either slab breakoff, slab retreat or sub-continental mantle delamination, depending on the local, thermo-mechanical characteristics of the system. In particular, contrasts in the thermal structure of colliding lithospheres favors sub-continental mantle delamination (Black and Liégeois, 1993), while the rheology contrast between crust and lithospheric mantle controls the fate of the subducted plate, i.e. the occurrence of either slab breakoff or retreat (Duretz and Gerya, 2013; Magni et al., 2013; van Hunen and Allen, 2011). Regardless of the mechanism(s) responsible for this "lithospheric reworking", the consequence is always the same, i.e. the inflow of hot, asthenospheric mantle at the base of the crust and its interaction with colder, metasomatized sub-continental lithospheric mantle, forming the mantle source region of Fe–K suites (Fig. 14c).

We consider that the scenario described in Fig. 14 not only explains the genesis of Fe–K suites, but also that of Mg–K magmas, as well as the relationship between them. Indeed, Mg–K granitoids are also post-collisional in character (Bonin, 2004; Debon and Lemmet, 1999; Fowler and Rollinson, 2012; Laurent et al., 2013a; Liégeois et al., 1998) and can be equally generated in the proposed environment. Depending on (1) the nature of the enriched mantle component, (2) the depth, temperature and degree of melting of the asthenosphere, as well as (3) the respective contribution of both sources, the resulting magmas can range from calc-alkaline to tholeiitic or truly alkaline. Again, this accounts for the continuous compositional range between Fe–K magmas (e.g. the Matok pluton), and granitoids derived from enriched mantle only, such as Mg–K sanukitoids (see Section 5).

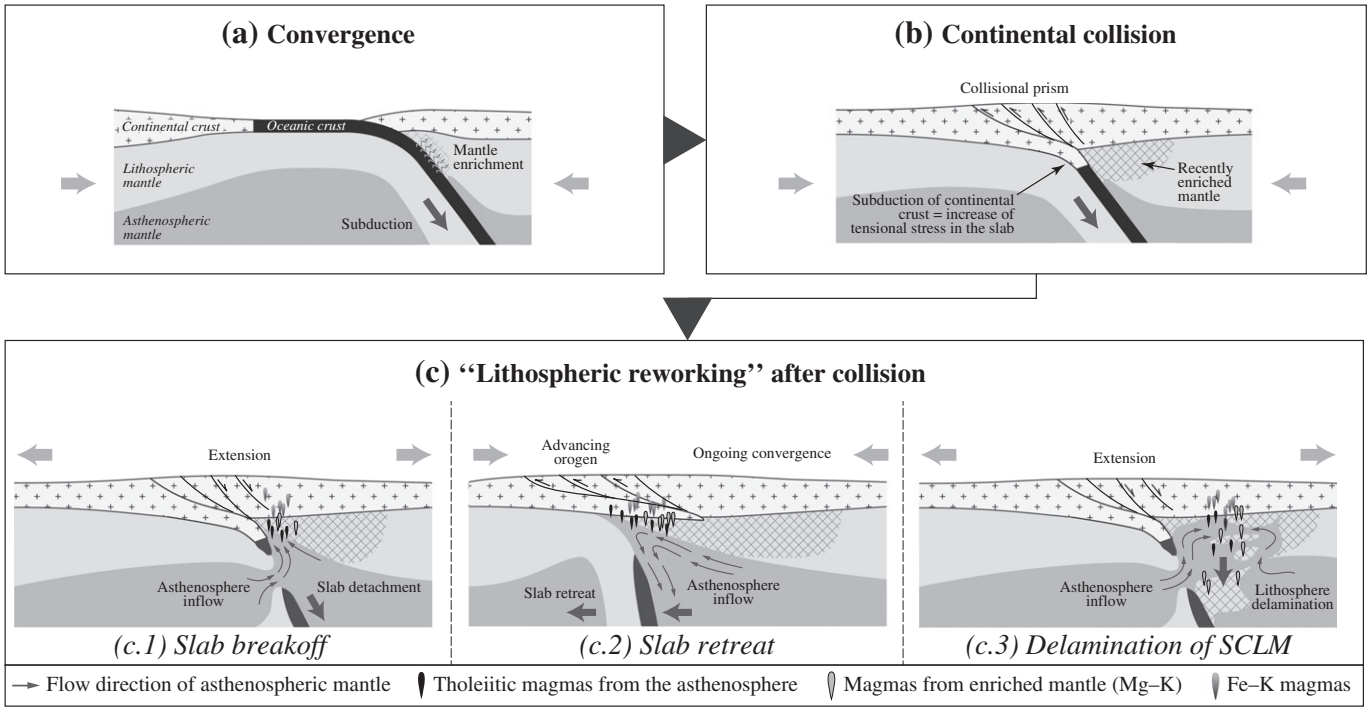


**Fig. 14.** Schematic cartoon illustrating the geodynamic evolution inferred to account for the origin of both Mg–K and Fe–K magmatic suites: (a) During basin closure and subduction along a continental active margin, the slab releases "enriched" components (fluids, melts derived from sedimentary or igneous material) that interact with the overlying mantle and modify its composition. (b) During continent–continent collision, subduction of continental material and the buoyancy contrast between continental and oceanic crusts leads to an increase of tensional stress within the subducted slab. (c) The consequence of collision is the reworking of the orogenic lithosphere that, depending on its thermo-mechanical characteristics (see text for details), proceeds either by (1) breakoff of the subducted slab; (2) retreat ("rollback") of the lithospheric mantle in the subducted plate; or (3) delamination of the sub-continental (enriched) lithospheric mantle (SCLM) beneath the upper plate. All mechanisms induce an inflow of mantle asthenosphere beneath the orogenic prism, the resulting thermal anomaly triggering the partial fusion of both recently enriched lithospheric mantle (possibly giving rise to Mg–K magmas such as sanukitoids) and the asthenosphere, which is the context required for the generation of Fe–K magmas. The models proposed in (c) are adapted from Black and Liégeois (1993), Duretz and Gerya (2013) and Magni et al. (2013).

Furthermore, it is worthwhile noting that when both types of granitoids coexist in a given area, Fe–K ones emplaced few tens of Ma after Mg–K ones. This has been documented in both Archean terranes (e.g. Mikkola et al., 2011) and post-Archean domains (e.g. Bonin, 2004; Debon and Lemmet, 1999). This is also consistent with the model presented in Fig. 14: asthenospheric upwelling would first trigger heating and partial melting of the sub-continental enriched mantle lithosphere (Fig. 14c), which gives rise to Mg–K magmas. Subsequent mixing of the two different mantle sources (lithospheric and asthenospheric) and/or their melting products generates Fe–K magmas a few tens of Ma later.

The petrogenetic model inferred for post-collisional magmas has also important implications for the Neoarchean evolution of the Pietersburg block, in which the Matok pluton emplaced. It indeed requires that subduction followed by continent–continent collision and "lithospheric reworking" took place prior to the genesis of the Matok magmas. Zeh et al. (2013) recently proposed that amalgamation of the Pietersburg block to the northern margin of the Paleoarchean nucleus of the Kaapvaal craton took place in response to subduction and "cordilleran-type" collision. The collision event would have taken place around 2.95 Ga according to age data from the Murchison greenstone belt, assumed to represent the "suture" zone (Block et al., 2013; Zeh et al., 2009, 2013). This is >250 Ma older than the Matok pluton, while according to numerical and geological models, the time lapse between continental collision and slab breakoff or retreat is generally one order of magnitude smaller (Coulon et al., 2002; Duretz and Gerya, 2013; Keskin et al., 2008; van Hunen and Allen, 2011). Therefore, the genesis of the Matok pluton cannot be related to this event, and implies that the Pietersburg block was involved in a younger continent–continent collision. We propose that this younger event corresponds to amalgamation with the northward-located Central Zone of the Limpopo Belt, between 2.75 and 2.80 Ga and after a period of south-verging subduction. The latter is required to produce the extensive metasomatized mantle source involved in the petrogenesis of several Neoarchean to Proterozoic magmatic associations of the area, including the Matok pluton and the Ventersdorp Supergroup and the Platberg lavas of the Ventersdorp Supergroup (see Section 6.3). Continent–continent collision between 2.80 and 2.75 Ga is supported by compression structures, such as north-verging thrusts, as well as large volumes of high-K anatectic granites, such as the Turfloop batholith, both dated in this time span throughout the Pietersburg block (Henderson et al., 2000; Laurent et al., 2013b; Passeraub et al., 1999; Robb et al., 2006; Smit et al., 1992). Furthermore, Block et al. (2013) also reported a concordant monazite U–Pb age of ~2.75 Ga from metasediments of the Murchison greenstone belt, which could be related to reactivation of the ~2.95 Ga-old "suture" during the younger collision event.

If this interpretation is correct, then slab breakoff, retreat or sub-continental mantle delamination are expected to have taken place between 2.75 and 2.70 Ga. This perfectly accounts for granulite-facies metamorphism in the SMZ, newly dated at ~2.71 Ga (Nicoli et al., in press). Indeed, steady-state crustal thickening cannot be at the origin of this high-temperature event, because of the low content of heat-producing elements in the Pietersburg block (Kramers et al., 2001). Asthenosphere upwelling, in response to post-collisional lithospheric reworking, provides the required external heat source, through both conduction and underplating of mafic magmas. Furthermore, slab detachment or sub-continental mantle delamination is associated with a thermal and isostatic uplift of the overlying crust, as well as extension tectonics (Black and Liégeois, 1993; Davies and von Blanckenburg, 1995; Duretz and Gerya, 2013; Magni et al., 2013; Rogers et al., 2002). This is very consistent with "exhumation" of the SMZ granulites along the Hout River Shear Zone starting at ~2.7 Ga (Kreissig et al., 2001) and the associated switch from compression to extension. The advent of an extensional tectonic regime also accounts for the emplacement of significant volumes of granitoid magmas throughout the whole Pietersburg block at ~2.69 Ga (Matok and associated granitoids of similar age; Laurent et al., 2013b; Zeh et al., 2009), and eventually to the deposition of the Transvaal basin from ~2.65 Ga.

## 7. Summary and conclusions

The 2.69 Ga-old Matok pluton is intrusive in the Pietersburg block in northern South Africa. It consists of a magmatic suite made up of metaluminous, medium- to high-K calc-alkaline and Fe-rich diorites, granodiorites and monzogranites. These rocks are comparable in many aspects to sanukitoid magmas that are widespread in late-Archean provinces. However, the Matok samples differ from sanukitoids because of lower $Al_2O_3$, $K_2O$, Rb, Ba and Th contents as well as higher $FeO_t$/MgO ratios, less fractionated REE patterns and stronger Eu–Sr negative anomalies. These differences indicate that the Matok pluton is rather akin to ferro-potassic (Fe–K) magmatic suites that are common in many Precambrian terranes and which are intermediate in composition between sanukitoids and truly alkaline, "A-type" granites.

The Fe–K Matok magmatic suite likely evolved by differentiation without any contribution of pre-existing crust, except in the case of monzogranites: the latter would indeed derive from interactions, in various proportions, between highly evolved magmas of the Matok suite and granitic melts derived from reworking of local crust. Based on whole-rock geochemistry, we demonstrated that the composition of the Matok diorites and granodiorites results neither from crustal contamination of mantle-derived melts, nor from differentiation of mafic material derived from a non-enriched mantle. In contrast, their genesis is well accounted for by differentiation of a mafic parent, the petrogenesis of which requires two contrasted mantle sources, namely:

(1) an enriched, sub-continental lithospheric mantle, which was metasomatized by fluids or magmas extracted from subducted sedimentary components derived from local crust of the Pietersburg block no more than 0.3 Ga prior to the emplacement of the Matok pluton;
(2) an asthenospheric mantle.

The involvement of these two contrasted mantle sources appears as the only way to explain the differences between Fe–K suites such as the Matok pluton and Mg–K sanukitoids, the petrogenesis of which only requires metasomatized mantle.

We propose that the most adequate geodynamic setting for the interaction between both mantle sources and/or their melting products is a post-subduction, late-collisional context, where reworking of the lithosphere takes place by slab breakoff, retreat or sub-continental mantle delamination. This model accounts for the post-collisional nature of both Mg–K and Fe–K magmas. It explains at the same time their close spatial and temporal association in some terranes of late-Archean to Phanerozoic age, their petrographic and geochemical differences, as well as the continuous range of compositions between each other.

From a regional point of view, our model supports that the Pietersburg block was amalgamated to the Central Zone of the Limpopo Belt between 2.80 and 2.75 Ga owing to continent–continent collision. This conclusion reconciles several puzzling aspects of the geological record in the Pietersburg block.

Supplementary data to this article can be found online at http://dx.doi.org/10.1016/j.lithos.2014.03.006.

## Acknowledgments

This study benefited from several funding sources: a NRF/CNRS Scientific Cooperation program PICS number 4828, the international program!Khure co-operated between France and South Africa, as well as research and travel grants from the University of Stellenbosch (South Africa) and Région Auvergne (France). Helpful discussion with many colleagues contributed to developing the models and ideas presented in this article, especially E. Heilimo, regarding sanukitoids,

and A. Zeh, for regional geology. Detailed and constructive reviews by J.C. Duchesne and P. Mikkola, as well as editorial handling and comments by N. Eby, helped us to greatly improve the original manuscript and were therefore much appreciated. We would like to acknowledge J. Halla, B. Bonin and J.H. Bédard for their comments and discussion about an earlier version of this manuscript. We are also grateful to D. Auclair for her support during TIMS analyses. Most diagrams were plotted using the GCDKit software v3.00 (Janoušek et al., 2006).

## Appendix A. Analytical procedures

Whole-rock analyses were performed on rock powder with grain size <10 μm. Hand samples weighing 1–5 kg were reduced to chips within a jaw crusher and powdered in a tungsten swing mill at the University of Stellensboch (South Africa). Using tungsten mills possibly induces contamination in transition elements such as Cr, Co and Ni. For this reason, the concentration of these elements in the Matok samples was not considered for any petrogenetic interpretation, except for 11 samples crushed in an agate swing mill at Laboratoire Magmas et Volcans, in Clermont-Ferrand (France).

### *A.1. Major elements*

Major-element compositions were analyzed at ACME Laboratories in Vancouver (Canada). 200 mg of rock powder were mixed with $LiBO_2$, molten and subsequently dissolved in 14 N $HNO_3$. The resulting solution was diluted and analyzed by ICP-AES. Multiple analyses of international standard SO-2 and sample replicates indicate that reproducibility is better than 1% relative for all major elements. Supplementary information on analytical procedures can be found at www.acmelabs.com.

### *A.2. Trace elements*

Trace-element analyses were performed by ICP-MS at ACME Laboratories in Vancouver (Canada), on the same diluted solutions as for major elements. Precious and base metals, including Pb, were analyzed after a simple digestion in aqua regia. Such a procedure yields unrealistically low Pb values, presumably because of incomplete dissolution. Therefore, Pb concentrations of our samples were not taken into account for any petrogenetic interpretation. Standard as well as sample replicates show that external reproducibility is generally better than 5% relative for most trace elements. Total procedure blanks are below detection levels for all the elements considered.

### *A.3. Sm–Nd isotopes*

Sample preparation and analyses for Sm–Nd isotopes were conducted at Laboratoire Magmas et Volcans in Clermont-Ferrand (France). 100 mg of sample were dissolved following a classic HF-$HNO_3$-$HClO_4$-HCl digestion procedure in screw-top Teflon vessel (Savillex®) on hot plates (75–125 °C). Additional HF–$HNO_3$ digestion was performed at 210 °C for 3 days in high-pressure bombs, in order to dissolve refractory phases like zircon. Sm and Nd chemical separation was realized through the "cascade" column protocol (AG50-X4, TRU Spec and Ln Spec columns) following the procedure described in Pin et al. (1994). The $^{147}Sm/^{144}Nd$ ratio of the samples was determined by isotopic dilution, using a $^{150}Nd$–$^{149}Sm$ mixed spike ($^{150}Nd/^{144}Nd = 105.12$; $^{149}Sm/^{147}Sm = 411.7$). Measurements were performed at the Laboratoire Magmas et Volcans in Clermont-Ferrand, using a Thermo-Finnigan Triton thermal ionization mass spectrometer (TIMS). Nd and Sm were loaded onto double W and Re filaments, respectively. Raw signals of Nd ($^{143}Nd$, $^{144}Nd$, $^{145}Nd$, $^{146}Nd$ and $^{150}Nd$) and Sm ($^{147}Sm$, $^{149}Sm$ and $^{152}Sm$) were acquired using multi-collector static mode. Raw Nd and Sm isotope ratios were mass-fractionation-corrected to $^{146}Nd/^{144}Nd = 0.7219$ and $^{152}Sm/^{147}Sm = 1.783135$ using an exponential law. The obtained isotopic Nd ratios were also corrected using a standard normalization, with respect to the reference value of $^{143}Nd/^{144}Nd = 0.5121$ for the JNDi-1 Nd standard. Repeated analyses of standards gave $^{143}Nd/^{144}Nd = 0.512101 \pm 5$ ($2\sigma$, Standard JNDi-1, $N = 8$) and $^{152}Sm/^{147}Sm = 1.78316 \pm 4$ ($2\sigma$, in-house standard Sm-IC, $N = 8$). All sample duplicates show identical values within these estimates of external reproducibility. Total procedure blanks are <0.25 ng for both Sm and Nd.

## References

Altermann, W., Lenhardt, N., 2012. The volcano-sedimentary succession of the Archean Sodium Group, Ventersdorp Supergroup, South Africa: volcanology, sedimentology and geochemistry. Precambrian Research 214–215, 60–81.
Anderson, J.L., Bender, E.E., 1989. Nature and origin of Proterozoic A-type granitic magmatism in the southwestern United States of America. Lithos 23, 19–52.
Barbarin, B., 1999. A review of the relationships between granitoid types, their origins and their geodynamic environments. Lithos 46, 605–626.
Barton Jr., J.M., Doig, R., Smith, C.B., Bohlender, F., van Reenen, D.D., 1992. Isotopic and REE characteristics of the intrusive charnoenderbite and enderbite geographically associated with the Matok Pluton, Limpopo Belt, southern Africa. Precambrian Research 55 (1–4), 451–467.
Barton, J.M., Barton, E.S., Smith, C.B., 1996. Petrography, age and origin of the Schiel alkaline complex, northern Transvaal, South Africa. Journal of African Earth Sciences 22 (2), 133–145.
Beard, J.S., Lofgren, G.E., 1991. Dehydration melting and water-saturated melting of basaltic and andesitic greenstones and amphibolites at 1, 3 and 6.9 kbar. Journal of Petrology 32 (2), 365–401.
Black, R., Liégeois, J.-P., 1993. Cratons, mobile belts, alkaline rocks and continental lithospheric mantle: the Pan-African testimony. Journal of the Geological Society of London 150, 89–98.
Block, S., Moyen, J.-F., Zeh, A., Poujol, M., Jaguin, J., Paquette, J.-L., 2013. The Murchison Greenstone Belt, South Africa: accreted slivers with contrasting metamorphic conditions. Precambrian Research 227, 77–98.
Bogaerts, M., Scaillet, B., Liégeois, J.-P., Vander Auwera, J., 2003. Petrology and geochemistry of the Lyndgal granodiorite (Southern Norway) and the role of fractional crystallization in the genesis of Proterozoic ferro-potassic A-type granites. Precambrian Research 124, 149–184.
Bogaerts, M., Scaillet, B., Vander Auwera, J., 2006. Phase equilibria of the Lyngdal granodiorite (Norway): implications for the origin of metaluminous ferroan granitoids. Journal of Petrology 47 (12), 2405–2431.
Bohlender, F., 1991. Igneous and metamorphic charnockitic rocks associated with the Matok pluton and their significance in the Limpopo orogeny. (Ph.D. thesis) Rand Afrikaans University, Johannesburg, South Africa.
Bohlender, F., Van Reenen, D.D., Barton Jr., J.M., 1992. Evidence for metamorphic and igneous charnockites in the Southern Marginal Zone of the Limpopo Belt. Precambrian Research 55 (1–4), 429–449.
Bonin, B., 2004. Do coeval mafic and felsic magmas in post-collisional to within-plate regimes necessarily imply two contrasting, mantle and crustal, sources? A review. Lithos 78, 1–24.
Brandl, G., Jaeckel, P., Kröner, A., 1996. Single zircon age for the felsic Rubbervale Formation, Murchison greenstone belt, South Africa. South African Journal of Geology 99 (3), 229–234.
Brandl, G., Cloete, M., Anhaeusser, C.R., 2006. Archean greenstone belts. In: Johnson, M.R., Anhaeusser, C.R., Thomas, R.J. (Eds.), The Geology of South Africa. Geological Society of South Africa, Johannesburg/Council for Geoscience, Pretoria, pp. 9–56.
Clemens, J.D., Holloway, J.R., White, A.J.R., 1986. Origin of the A-type granite: experimental constraints. AmeriCanadian Mineralogist 71, 317–324.
Clemens, J.D., Darbyshire, D.P.F., Flinders, J., 2009. Sources of post-orogenic calcalkaline magmas: the Arrochar and Garabal Hill–Glen Fyne complexes, Scotland. Lithos 112, 524–542.
Conceicão, R.V., Green, D.H., 2004. Derivation of potassic (shoshonitic) magmas by decompression melting of phlogopite + pargasite lherzolite. Lithos 72, 209–229.
Condie, K.C., 1981. Archaean Greenstone Belts. Elsevier (434 pp.).
Coulon, C., Megartsi, M., Fourcade, S., Maury, R.C., Bellon, H., Louni-Hacini, A., Cotten, J., Coutelle, A., Hermitte, D., 2002. Post-collisional transition from calc-alkaline to alkaline volcanism during the Neogene in Oranie (Algeria): magmatic expression of a slab breakoff. Lithos 62 (3–4), 87–110.
Crow, C., Condie, K.C., 1988. Geochemistry and origin of the late Archean volcanics from the Ventersdorp Supergroup, South Africa. Precambrian Research 42, 19–37.
Dall'Agnol, R., Oliveira, D.C., 2007. Oxidized, magnetite-series, rapakivi-type granites of Carajas, Brazil: Implications for classification and petrogenesis of A-type granites. Lithos 93, 215–233.
Dall'Agnol, R., Scaillet, B., Pichavant, M., 1999. An experimental study of a Lower Proterozoic A-type granite from the Eastern Amazonian Craton, Brazil. Journal of Petrology 40 (11), 1673–1698.
Davies, J.H., von Blanckenburg, F., 1995. Slab breakoff: a model of lithosphere detachment and its test in the magmatism and deformation of collisional orogens. Earth and Planetary Science Letters 129 (1–4), 85–102.
de Wit, M.J., Roering, C., Hart, R.J., Armstrong, R.A., de Ronde, R.E.J., Green, R.W., Tredoux, M., et al., 1992. Formation of an Archaean continent. Nature 357, 553–562.

Debon, F., Lemmet, M., 1999. Evolution of Fe/Mg Ratios in Late Variscan plutonic rocks from the external crystalline massif of the alps (France, Italy, Switzerland). Journal of Petrology 40 (7), 1151–1185.
Demaiffe, D., Bingen, B., Wertz, P., Hertogen, J., 1990. Geochemistry of the Lyngdal hyperites (SW Norway): comparison with the monzonorites associated with the Rogaland anorthosite complex. Lithos 24, 237–250.
dePaolo, D.J., 1981. A neodymium and strontium isotopic study of the Mesozoic calc-alkaline granitic batholiths of the Sierra Nevada and Peninsular Ranges, California. Journal of Geophysical Research 86 (B11), 10470–10488.
D'Souza, M.J., Keshava Prasad, A.V., Ravindra, R., 2006. Genesis of ferropotassic A-type granitoids of Mühlig-Hofmannfjella, Central Dronning Maud Land, East Antarctica. In: Fütterer, D.K., Damaske, D., Kleinschmidt, G., Miller, H., Tessensohn, F. (Eds.), Antarctica: Contributions to Global Earth Sciences. Springer, Berlin, Heidelberg, New York, pp. 45–54.
Duchesne, J.C., Martin, H., Baginski, B., Wiszniewska, J., Vander, Auwera J., 2010. The origin of ferroan-potassic A-type granitoids: the case of the hornblende-biotite granite suite of the Mesoproterozoic Mazury complex, northeastern Poland. Canadian Mineralogist 48 (4), 947–968.
Duretz, T., Gerya, T.V., 2013. Slab detachment during continental collision: Influence of crustal rheology and interactions with lithospheric delamination. Tectonophysics 602, 124–140.
Eby, G.N., 1992. Chemical subdivision of the A-type granitoids: petrogenesis and tectonic implications. Geology 20, 641–644.
Eglington, B.M., Armstrong, R.A., 2004. The Kaapvaal Craton and adjacent orogens, southern Africa: a geochronological database and overview of the geological development of the craton. South African Journal of Geology 107, 13–32.
Evans, B.W., Vance, J.A., 1987. Epidote phenocrysts in dacitic dikes, Boulder County, Colorado. Contributions to Mineralogy and Petrology 96, 178–185.
Ferré, E.C., Caby, R., Peucat, J.J., Capdevila, R., Monié, P., 1998. Pan-African, post-collisional, ferro-potassic granite and quartz–monzonite plutons of Eastern Nigeria. Lithos 45, 255–279.
Fowler, M., Rollinson, H.R., 2012. Phanerozoic sanukitoids from Caledonian Scotland: implications for Archaean subduction. Geology 40 (12), 1079–1082.
Frost, C.D., Frost, B.R., 1997. Reduced rapakivi-type granites: the tholeiite connection. Geology 25, 647–650.
Frost, B.R., Barnes, C.G., Collins, W.J., Arculus, R.J., Ellis, D.J., Frost, C.D., 2001. A geochemical classification for granitic rocks. Journal of Petrology 42, 2033–2048.
Halla, J., 2005. Late Archean high-Mg granitoids (sanukitoids) in the southern Karelian domain, eastern Finland: Pb and Nd isotopic constraints on crust–mantle interactions. Lithos 79 (1–2), 161–178.
Halla, J., van Hunen, J., Heilimo, E., Hölttä, P., 2009. Geochemical and numerical constraints on Neoarchaean plate tectonics. Precambrian Research 174, 155–162.
Heilimo, E., Halla, J., Hölttä, P., 2010. Discrimination and origin of the sanukitoid series: geochemical constraints from the Neoarchean western Karelian Province (Finland). Lithos 115, 27–39.
Henderson, D.R., Long, L.E., Barton Jr., J.M., 2000. Isotopic ages and chemical and isotopic composition of the Archaean Turfloop Batholith, Pietersburg granite-greenstone terrane, Kaapvaal Craton, South Africa. South African Journal of Geology 103 (1), 38–46.
Jacobsen, S.B., Wasserburg, G.J., 1984. Sm–Nd isotopic evolution of chondrites and achondrites, II. Earth and Planetary Science Letters 67 (2), 137–150.
Jahn, B.M., Auvray, B., Shen, Q.H., Liu, D.Y., Zhang, Z.Q., Dong, Y.J., Ye, X.J., Zhang, Q.Z., Cornichet, J., Macé, J., 1988. Archaean crustal evolution in China: the Taishan complex, and evidence for juvenile crustal addition from long-term depleted mantle. Precambrian Research 38, 381–403.
Janoušek, V., Farrow, C.M., Erban, V., 2006. Interpretation of whole-rock geochemical data in igneous geochemistry: introducing Geochemical Data Toolkit (GCDkit). Journal of Petrology 47, 1255–1259.
Kemp, A.I.S., Hawkesworth, C.J., 2003. Granitic perspectives on the generation and secular evolution of the continental crust. In: Rudnick, R.L. (Ed.), The Crust. Treatise on Geochemistry. Elsevier-Pergamon, Oxford, pp. 349–410.
Keskin, M., Genç, Ş.C., Tüysüz, O., 2008. Petrology and geochemistry of post-collisional Middle Eocene volcanic units in North-Central Turkey: evidence for magma generation by slab breakoff following the closure of the Northern Neotethys Ocean. Lithos 104, 267–305.
Kouankap Nono, G.D., Nzenti, J.P., Suh, C.E., Ganno, S., 2010. Geochemistry of ferriferous, high-K calc-alkaline granitoids from the Banefo-Mvoutsaha Massif (NE Bafoussam), Central Domain of the Pan-African Fold Belt, Cameroon. Open Geology Journal 4, 15–28.
Kramers, J.D., Kreissig, K., Jones, M.Q.W., 2001. Crustal heat production and style of metamorphism: a comparison between two Archaean high-grade provinces in the Limpopo belt, South Africa. Precambrian Research 112, 149–163.
Kramers, J.D., McCourt, S., van Reenen, D.D., 2006. The Limpopo Belt. In: Johnson, M.R., Anhaeusser, C.R., Thomas, R.J. (Eds.), The Geology of South Africa. Geological Society of South Africa, Johannesburg/Council for Geoscience, Pretoria, pp. 209–236.
Kreissig, K., Nagler, T.F., Kramers, J.D., Van Reenen, D.D., Smit, C.A., 2000. An isotopic and geochemical study of the Kaapvaal Craton and the Southern Marginal Zone of the Limpopo Belt: are they juxtaposed terranes? Lithos 50, 1–25.
Kreissig, K., Holzer, L., Frei, R., Villa, I.M., Kramers, J.D., Smit, C.A., van Reenen, D.D., 2001. Geochronology of the Hout River Shear Zone and the metamorphism in the Southern Marginal Zone of the Limpopo Belt, Southern Africa. Precambrian Research 109, 145–173.
Kröner, A., Jaeckel, P., Brandl, G., 2000. Single zircon ages for felsic to intermediate rocks from the Pietersburg and Giyani greenstone belts and bordering granitoid orthogneisses, northern Kaapvaal Craton, South Africa. Journal of African Earth Sciences 30 (4), 773–793.
Kuno, H., 1968. Differentiation of basalt magmas. In: Hess, H.H., Poldervaart, A.A. (Eds.), Basalts: The Poldervaart Treatise on Rocks of Basaltic Composition, 2. Interscience, New York, pp. 623–688.
Laurent, O., Martin, H., Doucelance, R., Moyen, J.-F., Paquette, J.-L., 2011. Geochemistry and petrogenesis of high-K "sanukitoids" from the Bulai pluton, Central Limpopo Belt, South Africa: implications for geodynamic changes at the Archaean–Proterozoic boundary. Lithos 123, 73–91.
Laurent, O., Doucelance, R., Martin, H., Moyen, J.F., 2013a. Differentiation of the late-Archaean sanukitoid series and some implications for crustal growth: insights from geochemical modelling on the Bulai pluton, Central Limpopo Belt, South Africa. Precambrian Research 227, 186–203.
Laurent, O., Paquette, J.-L., Martin, H., Doucelance, R., Moyen, J.F., 2013b. LA-ICP-MS dating of zircons from Meso- and Neoarchean granitoids of the Pietersburg block (South Africa): crustal evolution at the northern margin of the Kaapvaal craton. Precambrian Research 230, 209–226.
Laurent O., Martin H., Moyen J.F., Doucelance R., in revision. The diversity and evolution of late-Archaean granitoids: evidence for the onset of "modern-style" plate tectonics between 3.0 and 2.5 Ga. Submitted to Lithos and accepted with moderate revisions.
Liégeois, J.P., Navez, J., Hertogen, J., Black, R., 1998. Contrasting origin of post-collisional high-K calc-alkaline and shoshonitic versus alkaline and peralkaline granitoids. The use of sliding normalization. Lithos 45, 1–28.
Lobach-Zhuchenko, S.B., Rollinson, H., Chekulaev, V.P., Savatenkov, V.M., Kovalenko, A.V., Martin, H., Guseva, N.S., Arestova, N.A., 2008. Petrology of a Late Archaean, highly potassic, sanukitoid pluton from the Baltic Shield: insights into Late Archaean mantle metasomatism. Journal of Petrology 49 (3), 393–420.
Longhi, J., Vander Auwera, J., Fram, M., Duchesne, J.C., 1999. Some phase equilibrium constraints on the origin of Proterozoic (Massif) anorthosites and related rocks. Journal of Petrology 40 (2), 339–362.
Magni, V., Faccenna, C., van Hunen, J., Funiciello, F., 2013. Delamination vs. break-off: the fate of continental collision. Geophysical Research Letters 40, 285–289.
Martin, H., Moyen, J.F., Rapp, R.P., 2009. The sanukitoid series: magmatism at the Archaean–Proterozoic transition. Earth and Environmental Sciences Transactions of the Royal Society of Edinburgh 100 (1–2), 15–33.
McDonough, W.F., Sun, S.S., 1995. The composition of the Earth. Chemical Geology 120 (3–4), 223–253.
Mikkola, P., Huhma, H., Heilimo, E., Whitehouse, M., 2011. Archean crustal evolution of the Suomussalmi district as part of the Kianta Complex, Karelia: constraints from geochemistry and isotopes of granitoids. Lithos 125, 287–307.
Moyen, J.F., Martin, H., Jayananda, M., Auvray, B., 2003. Late Archaean granites: a typology based on the Dharwar Craton (India). Precambrian Research 127, 103–123.
Nelson, D.R., Trendall, A.F., de Laeter, J.R., Grobler, N.J., Fletcher, I.R., 1992. A comparative studies of the geochemical and isotopic systematics of late Archean flood basalts from the Pilbara and Kaapvaal cratons. Precambrian Research 54, 231–256.
Nicoli, G., Stevens, S., Buick, I.S., Moyen, J.F., 2014. A comment on "Ultrahigh-temperature metamorphism from an usual corundum + orthopyroxene intergrowth bearing Al-Mg granulite from the Southern Marginal Zone, Limpopo Complex, South Africa" by Belyanin et al. Contributions to Mineralogy and Petrology (in press).
Passeraub, M., Wüst, T., Kreissig, K., Smit, C.A., Kramers, J.D., 1999. Structure, metamorphism and geochronology of the Rhenosterkoppies Greenstone Belt, Northern Province, South Africa. South African Journal of Geology 102, 323–334.
Peccerillo, A., Taylor, S.R., 1976. Geochemistry of Eocene calc-alkaline volcanic rocks from the Kastamonu area, Northern Turkey. Contributions to Mineralogy and Petrology 58 (1), 63–81.
Peucat, J.J., Capdevila, R., Drareni, A., Mahdjoub, Y., Kahouri, M., 2005. The Eglab massif in the West African Craton (Algeria), an original segment of the Eburnean orogenic belt: petrology, geochemistry and geochronology. Precambrian Research 136, 309–352.
Pin, C., Briot, D., Bassin, C., Poitrasson, F., 1994. Concomitant separation of strontium and samarium–neodymium for isotopic analysis in silicate samples, based on specific extraction chromatography. Analytica Chimica Acta 298 (2), 209–217.
Poujol, M., Robb, L.J., Respaut, J.-P., Anhaeusser, C.R., 1996. 3.07–2.97 Ga greenstone belt formation in the northeastern Kaapvaal Craton: implications for the origin of the Witwatersrand Basin. Economical Geology 91, 1455–1461.
Prouteau, G., Scaillet, B., Pichavant, M., Maury, R., 2001. Evidence for mantle metasomatism by hydrous silicic melts derived from subducted oceanic crust. Nature 410, 197–200.
Rämö, O.T., Haapala, I., 1995. One hundred years of rapakivi granite. Mineralogy and Petrology 52, 129–185.
Rapopo, M., 2010. Petrogenesis of the Matok pluton, South Africa: implications on the heat source that induced regional metamorphism in the Southern Marginal Zone of the Limpopo Belt. (MSc. thesis) University of Stellenbosch, South Africa.
Rapp, R.P., Watson, E.B., 1995. Dehydration melting of metabasalt at 8–32 kbar: Implications for continental growth and crust–mantle recycling. Journal of Petrology 36 (4), 891–931.
Rapp, R.P., Norman, M.D., Laporte, D., Yaxley, G.M., Martin, H., Foley, S.F., 2010. Continent formation in the Archean and chemical evolution of the cratonic lithosphere: melt–rock reaction experiments at 3–4 GPa and petrogenesis of Archean Mg-diorites (sanukitoids). Journal of Petrology 51 (6), 1237–1266.
Robb, L.J., Brandl, G., Anhaeusser, C.R., Poujol, M., 2006. Archean granitoid intrusions. In: Johnson, M.R., Anhaeusser, C.R., Thomas, R.J. (Eds.), The Geology of South Africa. Geological Society of South Africa, Johannesburg/Council for Geoscience, Pretoria, pp. 57–94.
Roberts, M.P., Clemens, J.D., 1993. Origin of high-potassium, calc-alkaline, I-type granitoids. Geology 21, 825–828.
Roering, C., van Reenen, D.D., Smit, C.A., Barton, J.M., de Beer, J.H., de Wit, M.J., Stettler, E.H., van Schalkwyk, J.F., Stevens, G., Pretorius, S., 1992. Tectonic model for the evolution of the Limpopo Belt. Precambrian Research 55, 539–552.

Rogers, R.D., Karason, H., van der Hilst, R.D., 2002. Epeirogenic uplift above a detached slab in northern Central America. Geology 30 (11), 1031–1034.
Shaw, D.M., 1976. Trace element fractionation during anatexis. Geochimica et Cosmochimica Acta 34, 237–243.
Sial, A.N., Vasconcelos, P.M., Ferreira, V.P., Pessoa, R.R., Brasilino, R.G., Morais Neto, J.M., 2008. Geochronological and mineralogical constraints on depth of emplacement and ascension rates of epidote-bearing magmas from northeastern Brazil. Lithos 105, 225–238.
Singh, J., Johannes, W., 1996. Dehydration melting of tonalites. 2. Compositions of melts and solids. Contributions to Mineralogy and Petrology 125, 26–44.
Sisson, T., Ratajeski, K., Hankins, W., Glazner, A., 2005. Voluminous granitic magmas from common basaltic sources. Contributions to Mineralogy and Petrology 148, 635–661.
Skjerlie, K.P., Johnston, A.D., 1996. Vapour-absent melting from 10 to 20 kbar of crustal rocks that contain multiple hydrous phases: implications for anatexis in the deep to very deep continental crust and active continental margins. Journal of Petrology 37, 661–691.
Skridlaite, G., Wiszniewska, J., Duchesne, J.C., 2003. Ferro-potassic A-type granites and related rocks in NE Poland and S Lithuania: west of the East European Craton. Precambrian Research 124, 305–326.
Smit, C.A., Roering, C., van Reenen, D.D., 1992. The structural framework of the southern margin of the Limpopo Belt, South Africa. Precambrian Research 55 (1–4), 51–67.
Smit, C.A., van Reenen, D.D., Gerya, T.V., Perchuk, L.L., 2001. P–T conditions of decompression of the Limpopo high-grade terrane: record from shear zones. Journal of Metamorphic Geology 19, 249–268.
Smithies, R.H., Howard, H.M., Evins, P.M., Kirkland, C.L., Kelsey, D.E., Hand, M., Wingate, M.T.D., Collins, A.S., Belousova, E., 2011. High-temperature granite magmatism, crust–mantle interaction and the mesoproterozoic intracontinental evolution of the Musgrave Province, Central Australia. Journal of Petrology 52 (5), 931–958.
Steenfelt, A., Garde, A.A., Moyen, J.-F., 2005. Mantle wedge involvement in the petrogenesis of Archaean grey gneisses in West Greenland. Lithos 79, 207–228.
Stevens, G., van Reenen, D.D., 1992. Constraints on the form of the P–T loop in the Southern Marginal Zone of the Limpopo Belt, South Africa. Precambrian Research 55 (1–4), 279–296.
Tagne-Kamga, G., 2003. Petrogenesis of the Neoproterozoic Ngondo Plutonic complex (Cameroon, west central Africa): a case of late-collisional ferro-potassic magmatism. Journal of African Earth Sciences 36, 149–171.
Tatsumi, Y., Suzuki, T., 2009. Tholeiitic vs. calc-alkalic differentiation and evolution of arc crust: constraints from melting experiments on a basalt from the Izu–Bonin–Mariana Arc. Journal of Petrology 50 (8), 1575–1603.
van der Westhuizen, W.A., de Bruiyn, H., Meintjes, P.G., 2006. The Ventersdorp Supergroup. In: Johnson, M.R., Anhaeusser, C.R., Thomas, R.J. (Eds.), The Geology of South Africa. Geological Society of South Africa, Johannesburg/Council for Geoscience, Pretoria, pp. 187–208.
van Hunen, J., Allen, M.B., 2011. Continental collision and slab break-off: a comparison of 3-D numerical models with observations. Earth and Planetary Science Letters 302 (1–2), 27–37.
van Reenen, D.D., Smit, C.A., 1996. The Limpopo Metamorphic Belt, South Africa: 1. Geological setting and relationship of the granulite complex with the Kaapvaal and Zimbabwe Cratons. Petrology 4 (6), 562–570.
van Reenen, D.D., Barton Jr., J.M., Roering, C., Smit, C.A., van Schalkwyk, J.F., 1987. Deep crustal response to continental collision: the Limpopo belt of southern Africa. Geology 15, 11–14.
Vander Auwera, J., Bogaerts, M., Liégeois, J.P., Demaiffe, D., Wilmart, E., Bolle, O., Duchesne, J.C., 2003. Derivation of the 1.0–0.9 Ga ferro-potassic A-type granitoids of southern Norway by extreme differentiation from basic magmas. Precambrian Research 124, 107–148.
Vander Auwera, J., Bogaerts, M., Bolle, O., Longhi, J., 2007. Genesis of intermediate igneous rocks at the end of the Sveconorwegian (Grenvillian) orogeny (S Norway) and their contribution to intracrustal differentiation. Contributions to Mineralogy and Petrology 156, 721–743.
Vander Auwera, J., Bolle, O., Bingen, B., Liégeois, J.-P., Bogaerts, M., Duchesne, J.-C., de Waele, B., Longhi, J., 2011. Sveconorwegian massif-type anorthosites and related granitoids result from post-collisional melting of a continental arc root. Earth Science Reviews 107, 375–397.
Watkins, J.M., Clemens, J.D., Treloar, P.J., 2007. Archaean TTGs as sources of younger granitic magmas: melting of sodic metatonalites at 0.6–1.2 GPa. Contributions to Mineralogy and Petrology 154, 91–110.
Watson, E.B., Harrison, T.M., 1983. Zircon saturation revisited: temperature and composition effects in a variety of crustal magma types. Earth and Planetary Science Letters 64, 295–304.
Whalen, J.B., Currie, K.L., Chappell, B.W., 1987. A-type granite: geochemical characteristics, discrimination and petrogenesis. Contributions to Mineralogy and Petrology 95, 407–419.
Wolf, M.B., Wyllie, P.J., 1994. Dehydration–melting of amphibolite at 10 kbar: the effects of temperature and time. Contributions to Mineralogy and Petrology 115, 369–383.
Wones, D.R., 1989. Significance of the assemblage titanite + magnetite + quartz in granitic rocks. American Mineralogist 74, 744–749.
Workman, R.K., Hart, S.R., 2005. Major and trace element composition of the depleted MORB mantle (DMM). Earth and Planetary Science Letters 231 (1–2), 53–72.
Zeh, A., Gerdes, A., Barton Jr., J.M., 2009. Archean accretion and crustal evolution of the Kalahari Craton—the zircon age and Hf isotope record of granitic rocks from Barberton/Swaziland to the Francistown Arc. Journal of Petrology 50, 933–966.
Zeh, A., Jaguin, J., Poujol, M., Boulvais, P., Block, S., Paquette, J.-L., 2013. Juvenile crust formation in the northeastern Kaapvaal Craton at 2.97 Ga—implications for Archean terrane accretion, and the source of the Pietersburg gold. Precambrian Research 233, 20–43.
Zen, E., Hammarstrom, J.M., 1984. Magmatic epidote and its petrologic significance. Geology 12, 515–518.

Lithos 205 (2014) 208–235

Contents lists available at ScienceDirect

Lithos

journal homepage: www.elsevier.com/locate/lithos

Invited review article

# The diversity and evolution of late-Archean granitoids: Evidence for the onset of "modern-style" plate tectonics between 3.0 and 2.5 Ga

O. Laurent [a,b,c,*], H. Martin [a,b,c], J.F. Moyen [a,b,c,d], R. Doucelance [a,b,c]

[a] Clermont Université, Université Blaise Pascal, Laboratoire Magmas et Volcans, BP 10448, F-63000 Clermont-Ferrand, France
[b] CNRS, UMR6524, LMV, F-63038 Clermont-Ferrand, France
[c] IRD, R 163, LMV, F-63038 Clermont-Ferrand, France
[d] Département de Géologie, Université Jean Monnet, 23 rue du Docteur Paul Michelon, 42023 Saint-Étienne, France

ARTICLE INFO

*Article history:*
Received 11 December 2013
Accepted 15 June 2014
Available online 24 June 2014

*Keywords:*
Archean–Proterozoic transition
Continental crust
Granitoids
Geochemistry
Geodynamics
Plate tectonics

ABSTRACT

The end of the Archean aeon (3.0–2.5 Ga) was a period of fundamental change in many aspects of the geological record. In Archean cratons, this timespan is marked by a considerable diversification in both the nature and petrogenesis of granitoid rocks. In this article, we review the nature, petrogenesis and global evolution of late-Archean granitoids and discuss their geodynamic significance.

Late-Archean granitoids can be classified into four groups: (1) volumetrically-dominant and juvenile tonalites, trondhjemites and granodiorites (TTGs), whose geochemistry is consistent with an origin through partial melting of meta-igneous mafic rocks at various pressures; (2) Mg-, Fe- and K-rich, metaluminous (monzo)diorites and granodiorites, referred to as sanukitoids s.l., which derive primarily from hybridization between mantle peridotite and a component rich in incompatible elements; (3) peraluminous and K-rich biotite- and two-mica granites, formed through melting of older crustal lithologies (TTGs and meta-sediments, respectively); and (4) hybrid high-K granites with mixed characteristics from the first three groups.

The chronology of granitoid emplacement in late-Archean times is different from one craton to another but, in general, follows a very specific two-stage sequence: (1) a long period (0.2–0.5 Ga) of TTG emplacement; (2) a shorter period (0.02–0.15 Ga) during which all other granitoid types were generated. We propose that this sequence represents the first global subduction–collision cycle in the Earth's history. Although possibly present in the geological record prior to 3.0 Ga, such mechanisms became progressively prevalent on a planetary scale only between 3.0 and 2.5 Ga, indicating that the late-Archean geodynamic changes resulted from the global initiation of "modern-style" plate tectonics. The Archean–Proterozoic transition thus represents a major change in the mechanisms of the Earth's heat loss: before 3.0–2.5 Ga, it took place by large-scale magmatic differentiation characterized by generation of proto-continents that underwent crustal maturation locally, but without obvious cyclic activity on a planetary scale. After this, heat loss became accommodated by plate tectonics and global Wilson subduction–collision cycles. These changes were the consequence of the Earth's cooling, which in turn controlled a number of different parameters locally (thickness, temperature, volume and rheology of the crust). This explains why the changes took place over a short timespan (~0.5 Ga) relative to the Earth's history, but at different times and with different characteristics from one craton to another.



**Contents**

1. Introduction . . . 209
2. The diversity of late-Archean granitoids: a petrogenetic classification . . . 210
 2.1. TTGs . . . 210
  2.1.1. Geology and petrography . . . 211
  2.1.2. Key geochemical features . . . 211

* Corresponding author at: Department of Mineralogy, Institute of Geosciences, Johann Wolfgang Goethe-University, Altenhöferallee 1, 60438 Frankfurt-am-Main, Germany. Tel.: +49 69 798 40133.
*E-mail addresses:* laurent@em.uni-frankfurt.de, oscarlaurent86@gmail.com (O. Laurent).

http://dx.doi.org/10.1016/j.lithos.2014.06.012
0024-4937/

2.1.3. Petrogenesis . . . 211
2.2. Sanukitoids s.l. . . . 211
2.2.1. Geology and petrography . . . 215
2.2.2. Key geochemical features . . . 215
2.2.3. Petrogenesis . . . 217
2.3. Biotite- and two-mica granites . . . 218
2.3.1. Geology and petrography . . . 218
2.3.2. Key geochemical features . . . 219
2.3.3. Petrogenesis . . . 219
2.4. Hybrid granitoids . . . 219
2.4.1. Geology and petrography . . . 220
2.4.2. Key geochemical features . . . 220
2.4.3. Petrogenesis . . . 221
2.5. A synthetic classification diagram . . . 221
3. Late-Archean crustal evolution: a two-stage sequence . . . 221
3.1. Evidence from geochronology . . . 221
3.2. Evidence from isotope data . . . 223
4. Geodynamic implications: late-Archean granitoid evolution reflecting subduction and continental collision . . . 223
4.1. First stage: genesis of TTGs . . . 223
4.1.1. Possible geodynamic environments . . . 223
4.1.2. Late-Archean TTGs formed in a subduction setting: geometric and geochemical constraints . . . 223
4.1.3. The meaning of "subduction" . . . 225
4.2. Second stage: genesis of sanukitoids s.l., biotite-, two-mica granites and hybrids . . . 225
4.2.1. Possible geodynamic environments . . . 225
4.2.2. Continent–continent collision: analogy with post-Archean collisional granitoids . . . 225
4.2.3. The meaning of "continent–continent collision" . . . 227
4.3. A global geodynamic model . . . 227
5. The onset of "modern-style" plate tectonics . . . 228
5.1. Comparison with Eo- to Mesoarchean granitoids . . . 228
5.2. Support from other geological evidence . . . 229
5.3. Possible origins of the changes . . . 229
6. Summary and concluding remarks . . . 230
Acknowledgements . . . 230
Appendix A. Supplementary data . . . 230
References . . . 231

## 1. Introduction

The temporal changes in the mechanisms of continental crust extraction from the mantle are a consequence of the Earth's cooling and differentiation. The genesis of continental material started very early in the Earth's history, as demonstrated by the Hadean ages (4.0–4.4 Ga) of the Acasta gneisses (north-western Canada; Bowring and Williams, 1999; Iizuka et al., 2006) and the Jack Hills zircons (Western Australia; Wilde et al., 2001). Continental crust has been formed continuously from that time, but both the growth rates and mechanisms have changed over time. The most important changes took place between 3.0 and 2.5 Ga, at the very end of the Archean aeon. Indeed, >50% of the present-day continental volume formed prior to 2.5 Ga (Armstrong, 1981; Belousova et al., 2010; Dhuime et al., 2011; Guitreau et al., 2012; Kramers and Tolstikhin, 1997; Reymer and Schubert, 1984; Taylor and McLennan, 1985, 1995) and the Archean continental crust differs from the present day one in terms of petrographic and chemical compositions (Condie, 1981, 1989; Keller and Schoene, 2012; Kemp and Hawkesworth, 2003; Martin, 1987; Taylor and McLennan, 1985, 1995), *P–T* conditions of metamorphic provinces (Brown, 2006; Percival, 1994), geometry and lithology of volcano-sedimentary basins (Condie, 1981; Taylor, 1987; Veizer and McKenzie, 2003), and structures and rheology (Cagnard et al., 2011; Chardon et al., 2009; Thébaud and Rey, 2013). Consequently, the end of the Archean has long been regarded as a period of fundamental geodynamic changes (Condie and O'Neill, 2010; Taylor and McLennan, 1995; Windley, 1984), but the nature and origin of the changes are still controversial.

Schematically, an Archean crustal segment consists of three contrasting lithologies: (i) the so-called "grey gneisses", a complex, deformed and often migmatitic assemblage of meta-sedimentary and meta-igneous rocks, whose major components (Moyen, 2011) are low-K granitoid gneisses of the tonalite–trondhjemite–granodiorite ("TTG"; Jahn et al., 1981) series; (ii) supracrustal, meta-volcanic and meta-sedimentary rocks (generally recording greenschist- to amphibolite-facies metamorphism) forming the so-called greenstone belts; and (iii) late and generally high-K granitoid plutons and batholiths, typically intruding the two former lithologies. These granitoids generally represent the last Archean geological event in every craton worldwide (Condie, 1981; Heilimo et al., 2011; Martin, 1993; Moyen et al., 2003; Sylvester, 1994). Although this event is diachronous from one craton to another, it took place between 3.0 and 2.5 Ga ago on a planetary scale, and was followed by a ca. 0.25 Ga-long global magmatic shutdown (Condie et al., 2009). Therefore the late-Archean high-K granitic magmatism appears to be related to the final stabilization of the Archean cratonic lithosphere, which testifies to the geodynamic changes of that period.

Late-Archean granitoids cover a wide range of petrographic and mineralogical compositions (e.g. Champion and Sheraton, 1997; Champion and Smithies, 1999; Dall'Agnol et al., 2006; Feng and Kerrich, 1992; Frost et al., 1998; Kampunzu et al., 2003; Käpyaho et al., 2006; Mikkola et al., 2011b; Moyen et al., 2003; Sage et al., 1996; Schofield et al., 2010; Sylvester, 1994; Yang et al., 2008). The most commonly described groups are (i) high-K calc-alkaline, slightly peraluminous (A/CNK = 1.0–1.1) biotite-bearing granites, and (ii) metaluminous (A/CNK < 1.0), Mg- and K-rich (Mg# > 0.45; 1.5 < $K_2O$ < 6.0 wt.%)

rocks of the sanukitoid suite (monzodiorites, monzogabbros and their differentiated products). Both groups were found in almost all Archean terranes worldwide, but show some internal heterogeneity and complexity (e.g. Laurent et al., 2011; Martin et al., 2009; Meyer et al., 1994; Moyen et al., 2003; Sage et al., 1996; Whalen et al., 2004). Other, less common granitoid types, such as two-mica peraluminous (A/CNK > 1.1) leucogranites and metaluminous to peralkaline syenites and "A-type" granites, were also found in some cratons. Recent work reports other late-Archean granitoids which cannot be ascribed to any of these groups, either because of mixed characteristics (Almeida et al., 2010; Jayananda et al., 2006; Mikkola et al., 2011a,2011b; Prabhakar et al., 2009) or local particularities (Laurent et al., 2014; Steenfelt et al., 2005). On the other hand, TTGs are not restricted to early Archean times; they also represent a large fraction of the granitoids emplaced between 3.0 and 2.5 Ga, adding even more complexity to the late-Archean granitoid record.

Several studies have been conducted locally in order to identify, in a given cratonic area, the composition of the source and the processes that led to the genesis of late-Archean granitoids, as well as their temporal evolution (e.g. Almeida et al., 2013; Champion and Sheraton, 1997; Feng and Kerrich, 1992; Halla et al., 2009; Hill et al., 1992; Jahn et al., 1988; Jayananda et al., 2000; Käpyaho et al., 2006; Mikkola et al., 2011b; Moyen et al., 2001; Oliveira et al., 2011; Percival et al., 2006; Smithies and Champion, 2000; Whalen et al., 2004). However, despite efforts to formally define and classify late-Archean granitoids (e.g. Heilimo et al., 2010; Martin et al., 2009; Moyen et al., 2003), there is a lack of global perspective about the significance of this particular magmatism: the origin of granitoid diversity and the reason why they all were emplaced over a short timespan across all the cratons remain unclear. The present review aims to address these issues by proposing a schematic classification of late-Archean granitoids based on their petrogenesis. This classification is mainly supported by examples from the Archean granitoid basement of South Africa, where the transition from Archean to Proterozoic is well exposed between the Zimbabwe and Kaapvaal cratons (Pietersburg block and Limpopo mobile belt). Late-Archean granitoids from this area, as well as from most Archean cratons worldwide, are characterized by a very specific temporal evolution on which we base our attempt to decipher both the nature and origin of the geodynamic changes that took place between 3.0 and 2.5 Ga.

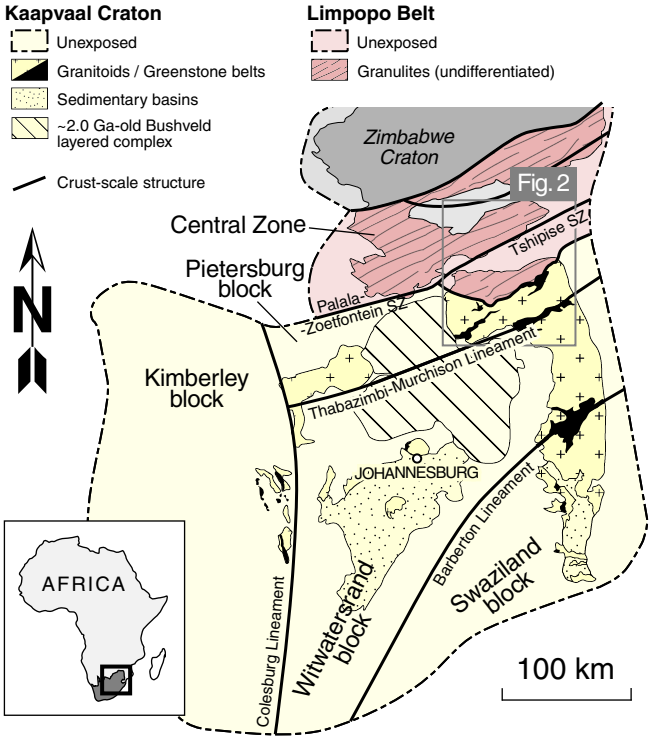


**Fig. 1.** Schematic geological map of the Kaapvaal Craton (yellow) and the Limpopo Belt (red) of southern Africa, after Eglington and Armstrong (2004) and Poujol et al. (2003). The grey rectangle represents the area covered by Fig. 2.

## 2. The diversity of late-Archean granitoids: a petrogenetic classification

Compiling published data in order to establish a global "descriptive" classification of late-Archean granitoids (i.e. based on petrography and/or geochemistry) is a difficult task, severely hindered by (i) the internal variability of each group, owing to local conditions and to the potentially heterogeneous composition of available sources; (ii) local terminologies that make comparisons difficult; and (iii) the frequent compositional overlap between the different groups. Therefore, in this paper we propose to build a classification for late-Archean granitoids based on both the nature of their sources and mechanisms of their petrogenesis. As such, it should theoretically not be used prior to careful petrogenetic modelling, although in most cases the granitoids belonging to a given group share several unique characteristics in terms of petrography and/or geochemistry, making them easy to identify.

This "genetic" typology is based on a review of available data and models (see summary in Table 1). These discriminate late-Archean granitoids into four different groups:

(1) sodic granitoids (TTGs) derived from melting of hydrous metabasalts at various depths;
(2) sanukitoids s.l., i.e. magmas resulting from interactions between the mantle and a component rich in incompatible elements, and their differentiated products;
(3) biotite- and two-mica granites generated by partial melting of pre-existing, felsic continental crust;
(4) hybrid granitoids, generally granodiorites and granites, formed through interaction (e.g. metasomatism, mingling, mixing) between magmas or sources of any of the former three groups.

In the following, we review the key geological and geochemical traits of each group as well as their petrogenesis, based on examples from the northern Kaapvaal craton and the Limpopo Belt (South Africa). The northernmost part of the Kaapvaal craton, known as the Pietersburg block (Fig. 1; de Wit et al., 1992; Eglington and Armstrong, 2004; Zeh et al., 2009), was tectonically and magmatically accreted between 3.1 and 2.7 Ga to the northern margin of a 3.6–3.2 Ga-old nucleus of continental crust (Block et al., 2013; de Wit et al., 1992; Eglington and Armstrong, 2004; Laurent et al., 2013b; Poujol et al., 2003; Zeh et al., 2009, 2013), now represented by the Swaziland and Witwatersrand blocks (Fig. 1). Subsequently, collision between the Kaapvaal and Zimbabwe cratons resulted in the formation of the Limpopo mobile belt between 2.7 and 2.5 Ga, with reactivation at, or continuation until, ca. 2.0 Ga (Barton et al., 2006; de Wit et al., 1992; Eriksson et al., 2009; Kramers and Houri, 2011; Kramers et al., 2006; Roering et al., 1992; van Reenen et al., 1987; Zeh et al., 2009 and references therein). Therefore, the Pietersburg block and Limpopo Belt consist of a portion of Archean crust formed over ~1 Ga across the Archean–Proterozoic boundary and intruded by large volumes of 3.1 to 2.6 Ga-old granitoid rocks (Fig. 2; Laurent et al., 2013b; Poujol et al., 2003; Zeh et al., 2009), which make it ideal for illustrating the present study.

### 2.1. TTGs

TTGs are the dominant lithology of Archean crust, and consist of silicic, plagioclase-rich plutonic rocks (tonalites, trondhjemites and granodiorites) with a sodic composition ($K_2O/Na_2O < 1$) and resulting from differentiation of tholeiitic and hydrous mafic rocks (for recent and detailed review about TTGs see Halla et al., 2009; Moyen, 2011; Moyen and Martin, 2012; Martin et al., 2014). TTGs are ubiquitous and

abundant in all Archean cratons, even in <3.0 Ga-old terranes where they are still the volumetrically dominant rock type (Table 1). For example more than half the surface of the Pietersburg block, in South Africa, consists of grey gneisses, themselves largely made up of TTGs (Fig. 2).

#### 2.1.1. Geology and petrography

In the field TTGs consist either of several banded, deformed and/or migmatized magmatic phases intruding each other (Fig. 3a), or of a single, homogeneous orthogneiss (Fig. 3b). In some places TTGs can form well-defined plutons where the rocks are weakly- to un-deformed, for instance around the Murchison greenstone belt in the Pietersburg block (Fig. 2; Baderoukwe and Maranda intrusions; Poujol et al., 1996; Poujol, 2001).

TTGs are typically characterized by high modal contents of sodic plagioclase and quartz with respect to alkali feldspar. For example, TTGs of the Pietersburg block consist of fine- to medium-grained (1–5 mm) trondhjemites and granodiorites, made up of an assemblage of sodic ($An_{15-30}$) plagioclase (~50%), quartz (~30%) and biotite (5–15%), with subordinate K-feldspar (<5%). Accessory minerals are magnetite, apatite, epidote (pistacite and/or allanite) and zircon. No hornblende was indentified in TTGs from the Pietersburg block, although in other places it can be present in the most mafic rocks (Moyen and Martin, 2012).

#### 2.1.2. Key geochemical features

The major-element geochemistry of TTGs is well represented by samples from the Pietersburg block in South Africa (Table 2; Fig. 4). TTGs are calcic to calc-alkaline, slightly peraluminous ($1.0 \leq A/CNK \leq 1.1$) silica-rich magmatic rocks ($65 \leq SiO_2 \leq 75$ wt.%) with low contents of ferromagnesian oxides ($FeO_t + MgO + MnO + TiO_2 \leq 5$ wt.%; Fig. 4a–c). Typically, they are K-poor and Na-rich, leading to low $K_2O/Na_2O$ ratios ($\leq 0.5$; Fig. 4b). CaO contents range from 1 to 5 wt.%, resulting in moderate $CaO/(Na_2O + K_2O)$ ratios (Fig. 4d).

Contrastingly, trace element contents in TTGs show significant variations depending on the pressure at which their meta-basaltic source melted. This issue has been discussed in detail by Almeida et al. (2011), Halla et al. (2009), Moyen (2011) and Moyen and Martin (2012). They broadly range between a "high-HREE" or "low-pressure" end-member (high HREE–Y and low Sr contents) and a "low-HREE" or "high-pressure" one (low HREE–Y and high Sr contents). It has been proposed that late-Archean TTGs (<3.0 Ga-old) are richer in Sr and poorer in Y–HREE than the older TTGs (Champion and Smithies, 2007; Martin and Moyen, 2002), thus belonging to the "high-pressure" group. This is well illustrated by the composition of the Pietersburg TTGs (Table 2; Fig. 5). These are moderately rich in incompatible elements (1 to 10 times the primitive mantle values), with negative Nb and Ta anomalies, a positive Sr anomaly and a typically fractionated REE pattern (Fig. 5a), due to low HREE concentrations ($Yb \leq 1.5$ ppm; $La_N/Yb_N > 30$). Y contents are also low ($\leq 10$ ppm), leading to high Sr/Y (20–200; Fig. 5b). TTGs also show moderate contents in HFSE ($1 \leq Nb \leq 7$ ppm; $45 \leq Zr \leq 245$ ppm) and REE, and are poor in transition elements ($V < 20$ ppm; Fig. 5c–d). Their REE patterns generally lack any significant Eu anomaly (Fig. 5d).

On the other hand, some studies also reported "low-" and "medium-pressure" TTGs of late-Archean age, for example in the Amazonian craton (Almeida et al., 2011; Althoff et al., 2000), the Baltic shield (Halla et al., 2009; Mikkola et al., 2011b) and the Superior Province (Feng and Kerrich, 1992; Sage et al., 1996; Whalen et al., 2002), with higher Y contents, flatter HREE profiles, as well as lower Sr and $Al_2O_3$ contents than "high-pressure" TTGs. This shows that the late-Archean period represents a diversification of TTG magmatism rather than a strict evolution towards the "high-pressure" group. However, it must be noted that in all the cases mentioned above, the "low-pressure" TTGs proper are clearly subordinate in volume with respect to "medium-" and "high-pressure" TTGs.

#### 2.1.3. Petrogenesis

It is widely accepted that TTGs were generated by differentiation of a basaltic parent, either by partial melting (e.g. Atherton and Petford, 1993; Barker and Arth, 1976; Ellam and Hawkesworth, 1988; Foley et al., 2002; Martin, 1986, 1987, 1994; Martin and Moyen, 2002; Martin et al., 2014; Rapp et al., 1991, 2003) or fractional crystallization (e.g. Kamber et al., 2002; Kleinhanns et al., 2003). Moyen and Martin (2012) stressed out that a number of observations are at odds with fractional crystallization (notably the lack of any mafic and intermediate phases in TTG suites), pointing to partial melting of a meta-basalt, leaving a garnet amphibolitic or eclogitic residue, as a more likely origin. This hypothesis is consistent with the major element geochemistry of the Pietersburg block TTG samples (Fig. 6).

The internal diversity within Archean TTGs could have resulted from subsequent subordinate fractional crystallization (Martin, 1987), but recent studies have shown that it depends primarily on the pressure and temperature conditions of melting (Almeida et al., 2011; Halla et al., 2009; Moyen, 2011; Moyen and Martin, 2012; Moyen and Stevens, 2006). Many late-Archean TTGs display high Sr and low Y–HREE contents (Table 2; Fig. 5), thus belonging to the "high-" and "medium-pressure" groups of Moyen (2011). Such magmas derived from melting of metabasaltic sources at $\geq 10$ kbar, which roughly corresponds to depths >35 km. Such conditions allow for the presence of garnet in the residue, accounting for low HREE contents, whilst being beyond the stability field of plagioclase, explaining the TTGs' richness in $Al_2O_3$, CaO and Sr and the lack of negative Eu anomaly. As noted above, a small fraction of late-Archean TTGs show low Sr, $Al_2O_3$ and CaO contents and less fractionated REE patterns, locally with a negative Eu anomaly (e.g. Almeida et al., 2011; Althoff et al., 2000; Halla et al., 2009), which pinpoints melting at shallow levels in the plagioclase stability field and a garnet-free or garnet-poor residue.

### 2.2. Sanukitoids s.l.

This group encompasses a wide diversity of rocks, which share a common petrogenesis: they derive partially or totally from interactions between a mantle peridotite and a component rich in incompatible elements. This includes the sanukitoids s.s., first described in the Superior Province (Bédard, 1996; Shirey and Hanson, 1984; Stern and Hanson, 1991; Stevenson et al., 1999; Sutcliffe et al., 1990) and recently redefined on the basis of geochemical criteria by Heilimo et al. (2010) and Martin et al. (2005, 2009). Those were further described in most late-Archean terranes (see Table 1), including the Slave Craton (Davis and Hegner, 1992), the Wyoming Province (Frost et al., 1998), the Baltic shield (Bibikova et al., 2005; Halla, 2005; Halla et al., 2009; Heilimo et al., 2010; Käpyaho et al., 2006; Kovalenko et al., 2005; Lobach-Zhuchenko et al., 2005, 2008; Samsonov et al., 2005), the Dharwar Craton of South India (Jayananda et al., 1995; Krogstad et al., 1995; Moyen et al., 2001, 2003; Sarvothaman, 2001), the North China Craton (Jahn et al., 1988; Wang et al., 2009; Yang et al., 2008), the Pilbara Craton in Western Australia (Smithies and Champion, 1999a, 2000), the Amazonian Craton (Althoff, 1996; Leite et al., 2004; Medeiros and Dall'Agnol, 1988; Oliveira et al., 2009) and southern Africa (Kampunzu et al., 2003; Laurent et al., 2011; Zhai et al., 2006).

This group also includes other late-Archean rocks that differ from sanukitoids s.s. in compositional detail, but whose petrogenesis is very similar (see Section 2.2.2). Such rocks were described as quartz diorites in the North Atlantic Craton (Steenfelt et al., 2005) and the Baltic shield (Mikkola et al., 2011b), as well as "syenite–quartz monzonite–granite suite" in the Superior Province (Feng and Kerrich, 1992; Sage et al., 1996) and includes the Matok pluton in the northern Kaapvaal craton (Laurent et al., 2014). All these granitoids are collectively grouped here under the term of "sanukitoids sensu lato (s.l.)".

Sanukitoids s.l. generally represent a minor, albeit ubiquitous, component of late-Archean terranes (roughly <15% in surface). For instance, in the northern Kaapvaal craton and the Limpopo Belt, this group is only

**Table 1**
A list of examples of the four late-Archean granitoid types discussed in the present review, from most cratonic areas worldwide. This table is non-exhaustive and only reports examples for which a comparison could be made on the basis of sufficient criteria (mostly based on petrography, whole-rock geochemistry and petrogenesis). The comparison is somewhat hypothetical for some terranes, because of the lack of geochemical data (particularly for the Slave and Zimbabwe Cratons).

| | TTG | | Sanukitoids s.l. | | Biotite- and two-mica granites | | "Hybrid" granitoids | | |
|---|---|---|---|---|---|---|---|---|---|
| | Name | Age[a] (Ga) | Name | Age (Ga) | Name | Age (Ga) | Name | Age (Ga) | Ref.[b] |
| Kaapvaal (±Limpopo) | • Goudplaats–Hout River unit<br>• Groot-Letaba Duiwelskloof unit<br>• Baderoukwe, Malati Pump, Maranda intrusions | [3.40]<br>3.30–2.85 | • Matok pluton<br>(• Bulai pluton) | ~2.69<br>(~2.60) | • Turfloop and Lekkersmaak batholith<br>• Various intrusions embedded in TTG gneisses | 2.84–2.77 | • Mashashane, Mashishimale, Matlala, Moletsi plutons | ~2.69 | [1] to [8] |
| Amazonian craton (Carajás Province) | • Arco Verde, Caracol, Mariazinha tonalites<br>• Agua Fria, Mogno trondhjemites | 3.00–2.84 | • Rio Maria suite | ~2.87 | • Mata Surrão, Xinguara granites | 2.87–2.86 | • Guarantã suite | 2.87–2.86 | [9] to [14] |
| Baltic Shield | • Various trondhjemites, tonalites and granodiorites (many local names) | [3.10]<br>2.95–2.74 | • Amindomaoja, Arola, Bergaul, Bolshozero, Chalka, Elmus, Hautavaara, Hizhjärvi, Ilomantsinjärvi, Jalonvaara, Kaapinsalmi, Kaartojärvet, Koitere, Kuittila, Kurgelampi, Kuusamo, Lieksa, Loso, Nilsiä, Njuk, Panozero, Peuravaara, Purnu, Sharavalampi, Siikalahti, Sjargozero, Sysmanjärvi, Tulos, Voloma plutons<br>• Lentiira and Riihivaara "quartz diorites" | 2.74–2.68 | • Katajavaara, Konivaara, Pieni Tuomaanjärvi intrusions (Kuhmo district)<br>• Vaamankallio leucogranite + leucosomes (Suomussalmi district) | 2.70–2.68 | • Leucogranite–granodiorite suite (Kuhmo district) | 2.72–2.68 | [15] to [24] |
| Dharwar | • Peninsular gneisses<br>• Krishnagiri tonalites<br>• Gneisses in the Hutti–Gurgunta area | 3.00–2.55 | • Dod gneisses<br>• Bisanattam granitoid<br>• Mafic phases of Closepet batholith | ~2.55 | • Bangalore leucogranite<br>• Kadiri, Krishnagiri, Lepakshi, Madanapalle, Nandi hills granites<br>• Kolar granodiorite<br>• Guramkonda, Vendodu granites | 2.54–2.51 | • Felsic phases of Closepet batholith<br>• Arsikere–Banavara and Chitradurga–Jampalnaikankote–Hosdurga granites<br>• "Transitional TTG" in the Hutti–Gurgunta area | 2.62–2.52 | [25] to [30] |
| East European (Ukrainian Shield) | • Granitoids of the West Azov group<br>• Parts of the Obitochnen Complex | [3.25]<br>3.12–2.91 | • Osipenkovskii massif<br>• Parts of the Obitochnen Complex | 2.92–2.86 | | | | | [31] |
| Madagascar | • Nosy Boraha suite | [3.35]<br>3.15–2.75 | • Masoala suite (very heterogeneous, different granitoid phases with characteristics of all three groups) | | | | | 2.54–2.51 | [32] |
| North Atlantic | • Disko Bugt, Fiskefjord, Ikkattoq gneisses, Âta tonalite | 3.20–2.80 | • Disko Bugt diorites<br>• Qeqertaussaq diorite | 3.00–2.80 | • Qôrqut granite<br>• Rodebay granodiorite? | ~2.55 | | | [33], [34] |

| | | | | | | | | | |
|---|---|---|---|---|---|---|---|---|---|
| North China | • Taishan granitoid gneisses<br>• Eastern Hebei gneisses<br>• Fuping Complex | 2.75–2.55 | • Taishan diorites<br>• Zhong Tian Men granodiorites<br>• Hornblendites and diorites of Anziling, Jiekouling, Qinhuangdao plutons | 2.55–2.52 | • Monzogranites of Qinhuangdao pluton<br>• Some granites of the Wutai Complex | 2.55–2.44 | • Granodiorites of Anziling, Jiekouling, Qinhuangdao plutons<br>• Some granites of the Wutai Complex | 2.55–2.52 | [35] to [38] |
| Pilbara | • Unnamed tonalitic, trondhjemitic and granodioritic gneisses | 3.26–2.99 | • Peewah suite: Peewah and Wallareenya granodiorites, Geemas, Jallogoonina, Jones Wells, Malindra, Nr. 1 and Toweranna stocks | ~2.95 | • Unnamed monzo- and syenogranites | 2.94–2.93 | • Portree Complex | ~2.95 | [39] |
| Slave | • Banded gneisses | [3.5] 3.10–2.65 | • Part of the "Type I" granitoids<br>• Concession and Defeat suites | 2.63–2.60 | • "Type II" granitoids<br>• Morose and Prosperous suites | 2.60–2.58 | • Part of the "Type I" granitoids | 2.63–2.60 | [40], [41] |
| Superior Province | • Lac Flavrian, Bourlamaque, Round Lake complexes (Abitibi Subp.)<br>• Tonalites, trondhjemites, granodiorites (Wabigoon Subp.)<br>• Gutcher Lake, Hawk Lake, Jubilee Lake suites (Wawa Subp.) | 2.89–2.70 | • Abitibi, Mattachewan batholiths, Lebel and Otto stocks (Abitibi Subp.)<br>• Stormer Lake and Okanse Lake plutons (Berens River Subp.)<br>• Lac Fréchette and Lac Rémigny complexes (Pontiac Subp.)<br>• Barnum, Blalock, Burchell Lake, Lappé, Penassen Lake suites (Quetico Subp.)<br>• Mafic phases of the KMGS suite, Jackfish Lake, Lac des Îles, plutons, Eye-Dashwa, Norway Lake, Roaring River, van Nostrand suites (Wabigoon Subp.)<br>• Dickenson Lake, Kabenung Lake, Maskinonge Lake, Troupe Lake stocks (Abitibi Subp.) | 2.72–2.69 | • GMG granite suite (Pontiac Subp.)<br>• Ghost Lake batholith (Sioux Lookout terrane)<br>• Granites and granodiorites (Wabigoon Subprovince) | 2.69–2.65 | • Watabeag batholith, Garrison stock (Abitibi Subp.)<br>• Granodiorites of the KMGS suite (Wabigoon Subp.)<br>• Hermann Lake stock (Wawa Subp.) | 2.69–2.68 | [42] to [49] |
| Wyoming Province | • Banded gneisses of the Washakie block, Native Lake gneisses | [3.35] 2.95–2.80 | • Louis Lake batholith<br>• Mafic phases of the Bridger batholith | 2.67–2.63 | • Bears Ears, Middle Mountain, New Fork Lake, South Pass granites | ~2.55 | • Felsic phases of the Bridger batholith | ~2.67 | [50], [51] |
| Yilgarn | • Banded gneiss and migmatite | [3.20–2.75] | • "Mafic" granitoids (Eastern Goldfields): Lawlers, Liberty, Maori Queen, Mt. Lucky, Porphyry plutons | ~2.66 | • "Low-Ca granites" | ~2.66 | • "High-Ca granites" (=Transitional TTG) (Eastern Goldfields)<br>• "High-HFSE" and "syenitic" granitoids (Eastern Goldfields) | 2.69–2.66 | [52] to [54] |
| Zimbabwe | • "TTGs" of the Tati-Selkirk suite<br>• Mashaba tonalite, Umwindsi gneiss, Shamvaian clasts | [3.20] 3.00–2.70 | • "Sanukitoids" of the Tati-Selkirk suite | 2.70–2.65 | • Chillimanzi suite?<br>• "Potassic granites" of the Tati-Selkirk suite | 2.67–2.60 | | | [55] to [58] |

[a] Ages between brackets are ages of oldest crust in the area of late-Archaean granitoid intrusions, either from inherited zircon grains in younger granitoids or Nd–Hf model ages.

[b] Reference list: [1] Henderson et al., 2000; [2] Jaguin et al., 2012; [3] Kröner et al., 2000; [4] Laurent et al., 2011; [5] Laurent et al., 2013a; [6] Laurent et al., 2013b; [7] Laurent et al., 2014; [8] Zeh et al., 2009; [9] Almeida et al., 2010; [10] Almeida et al., 2011; [11] Almeida et al., 2013; [12] Althoff et al., 2000; [13] Leite et al., 2004; [14] Oliveira et al., 2009; [15] Bibikova et al., 2005; [16] Halla, 2005; [17] Halla et al., 2009; [18] Heilimo et al., 2010; [19] Heilimo et al., 2011; [20] Käpyaho et al., 2006; [21] Kovalenko et al., 2005; [22] Lobach-Zhuchenko et al., 2005; [23] Lobach-Zhuchenko et al., 2008; [24] Mikkola et al., 2011b; [25] Jayananda et al., 1995; [26] Jayananda et al., 2006; [27] Moyen et al., 2001; [28] Moyen et al., 2003; [29] Prabhakar et al., 2009; [30] Vijaya Kumar et al., 2011; [31] Bibikova et al., 2008; [32] Schofield et al., 2010; [33] Garde, 1997; [34] Steenfelt et al., 2005; [35] Jahn et al., 1988; [36] Liu et al., 2004; [37] Wang et al., 2009; [38] Yang et al., 2008; [39] Smithies and Champion, 2000; [40] Davis and Bleeker, 1999; [41] Davis and Hegner, 1992; [42] Breaks and Moore, 1992; [43] Feng and Kerrich, 1992; [44] Sage et al., 1996; [45] Stern et al., 1989; [46] Stern and Hanson, 1991; [47] Stevenson et al., 1999; [48] Sutcliffe et al., 1990; [49] Whalen et al., 2004; [50] Frost et al., 1998; [51] Frost et al., 2006; [52] Cassidy et al., 1991; [53] Champion and Sheraton, 1997; [54] Champion and Smithies, 2003; [55] Bagai et al., 2002; [56] Jelsma et al., 1996; [57] Kampunzu et al., 2003; [58] Zhai et al., 2006.

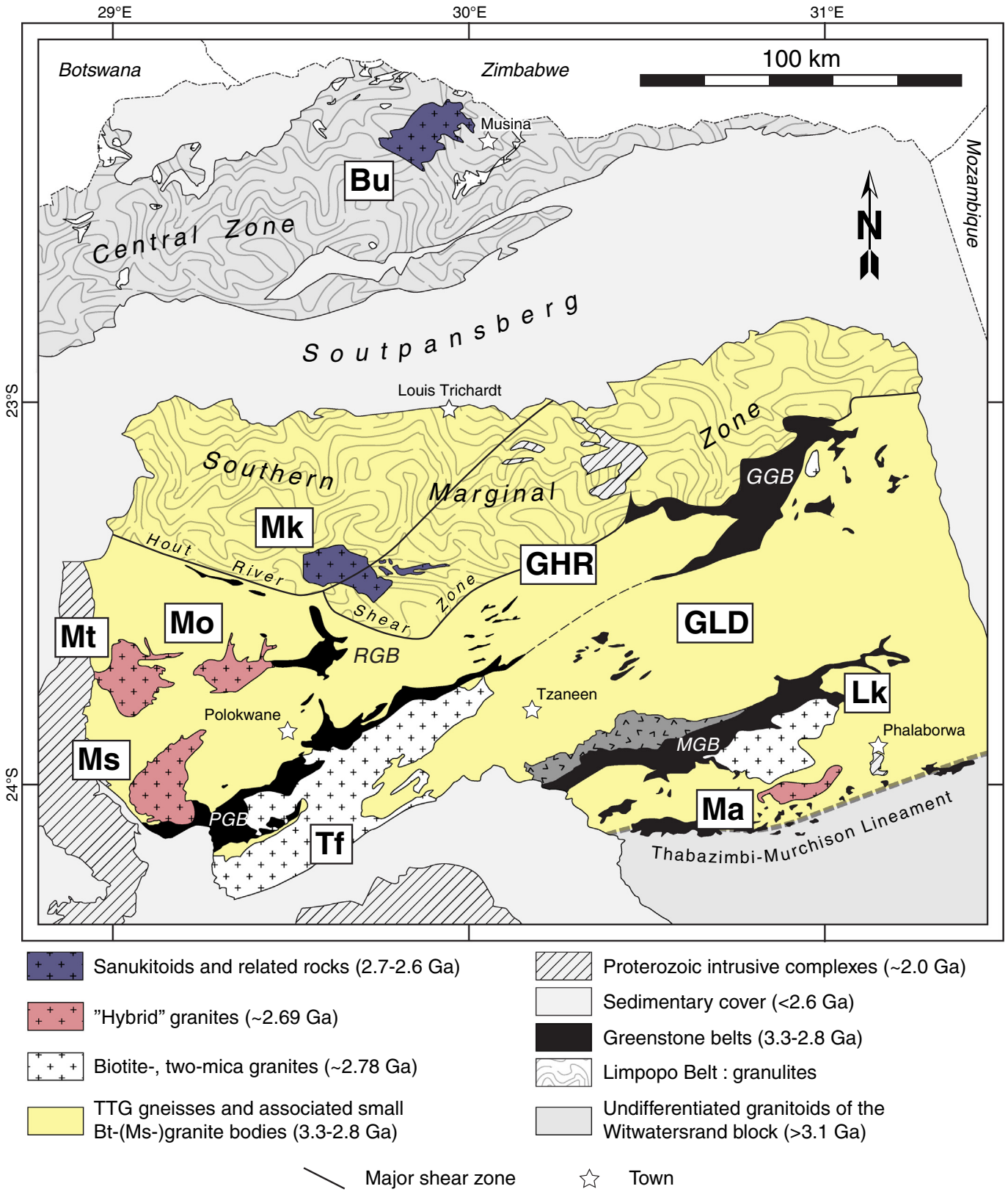


**Fig. 2.** Spatial distribution of the different late-Archean granitoid groups in the Pietersburg block and part of the Central Zone of the Limpopo Belt in South Africa (after Kramers et al., 2006; Laurent et al., 2013b and Robb et al., 2006). The abbreviations refer to the granitoid plutons or units described in this study: Bu = Bulai; GHR = Goudplaats–Hout River gneiss suite; GLD = Groot Letaba–Duiwelskloof gneiss unit; Lk = Lekkersmaak; Ma = Mashishimale; Mk = Matok; Ms = Mashashane; Mt = Matlala; Mo = Moletsi; Tf = Turfloop. Also abbreviated are the names of the Giyani (GGB), Murchison (MGB), Pietersburg (PGB) and Rhenosterkoppies (RGB) greenstone belts.

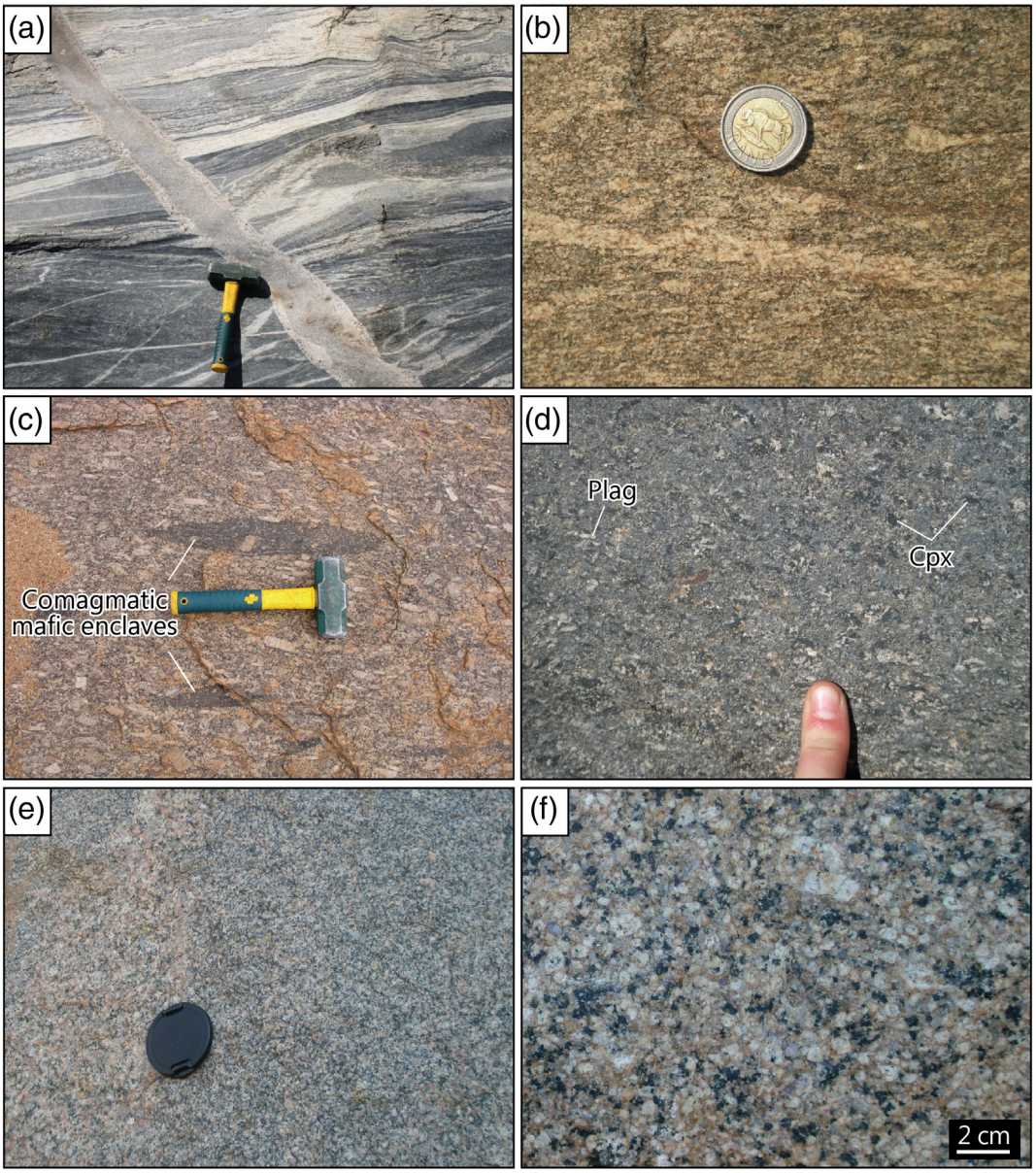


**Fig. 3.** Field photographs showing examples of late-Archean granitoids from the Pietersburg block and the Central Zone of the Limpopo Belt: TTGs, with (a) typically polyphased outcrop of highly deformed and partly migmatitic orthogneisses of TTG composition (Goudplaats–Hout River gneiss unit); and (b) example of homogeneous, foliated and unmigmatized granodioritic gneiss (Groot Letaba–Duiwelskloof gneiss unit); Sanukitoids s.l., with (c) K-feldspar porphyritic, relatively dark granodiorite, containing comagmatic mafic enclaves of monzodioritic composition (Bulai pluton); and (d) dark, fine-grained (monzo)diorite containing phenocrysts of plagioclase (Plag) and clinopyroxene (Cpx) (Matok pluton); (e) Biotite- and two-mica granites: homogeneous, equigranular biotite-bearing monzogranite (Turfloop batholith); (f) Hybrid granites: heterogeneous, coarse-grained and porphyritic monzogranite (Mashashane pluton).

represented by two intrusions, the Bulai and Matok plutons (Laurent et al., 2011, 2014; Fig. 2).

*2.2.1. Geology and petrography*

Sanukitoids are syn- to post-tectonic intrusions, ranging from well-foliated to undeformed. They most often consist of composite magmatic complexes: for instance, the dominant phase of the Bulai and Matok plutons is a porphyritic granodiorite (Fig. 3c) associated with abundant mafic bodies of quartz-(monzo)diorite (Fig. 3d), whose size ranges from small microgranular magmatic enclaves (MME) to bodies several kilometres in size. In some areas, the latter locally form individual and monogenic stocks, for instance in the Superior Province (Sage et al., 1996; Stevenson et al., 1999), the North China craton (Wang et al., 2009), the Pilbara craton (Smithies and Champion, 2000) or the Baltic shield (Heilimo et al., 2010). Some sanukitoid intrusions are also associated with lamprophyre dykes and/or ultrapotassic rocks (Laurent et al., 2011; Lobach-Zhuchenko et al., 2005; Mikkola et al., 2011a). Granites s.s. are invariably scarce.

The granodiorites often contain large (1–6 cm) K-feldspar phenocrysts within a medium-grained (0.1–1 cm) matrix made up of plagioclase ($An_{20–35}$), quartz, and very characteristic mafic aggregates of biotite and amphibole. Ortho- and clinopyroxene are relatively common, especially in the mafic clots where they occur as relict cores within biotite and amphibole. Magnetite, ilmenite, apatite, zircon, allanite and, locally, titanite are abundant accessory phases.

*2.2.2. Key geochemical features*

A number of definitions based on strict geochemical criteria have already been proposed for sanukitoids s.s. The original one only considered LILE- and LREE-rich diorites with high Mg# (>0.6; e.g. Stern et al., 1989), but it has since been widened to include their differentiated products (granodiorites and granites of the "sanukitoid suite"; Heilimo

**Table 2**
Average major- and trace-element compositions of the four types of late-Archean granitoids in the Pietersburg block and the Central Zone of the Limpopo Belt (South Africa).

| | TTG | | Sanukitoids s.l. | | Biotite- and two-mica granites | | Hybrid granites | |
|---|---|---|---|---|---|---|---|---|
| | *N* = 23 | | *N* = 77 | | *N* = 34 | | *N* = 104 | |
| | Average | *St. dev.* | Average | *St. dev.* | Average | *St. dev.* | Average | *St. dev.* |
| *Major elements (wt.%)* | | | | | | | | |
| $SiO_2$ | **71.20** | *2.12* | **63.57** | *6.43* | **72.54** | *1.59* | **70.65** | *3.82* |
| $TiO_2$ | **0.26** | *0.11* | **1.22** | *0.55* | **0.26** | *0.14* | **0.61** | *0.33* |
| $Al_2O_3$ | **15.42** | *0.74* | **14.48** | *1.26* | **14.42** | *0.48* | **13.36** | *0.60* |
| $FeO_t$ | **1.63** | *0.75* | **5.52** | *2.24* | **1.30** | *0.49* | **2.98** | *1.57* |
| MnO | **0.03** | *0.01* | **0.08** | *0.04* | **0.02** | *0.01* | **0.05** | *0.03* |
| MgO | **0.66** | *0.36* | **1.89** | *1.03* | **0.44** | *0.23* | **0.89** | *0.80* |
| CaO | **2.37** | *0.75* | **3.93** | *1.75* | **1.34** | *0.37* | **1.82** | *1.10* |
| $Na_2O$ | **5.37** | *0.61* | **3.60** | *0.31* | **4.36** | *0.37* | **3.86** | *0.33* |
| $K_2O$ | **1.77** | *0.66* | **3.32** | *1.05* | **4.07** | *0.72* | **4.26** | *0.88* |
| $P_2O_5$ | **0.11** | *0.05* | **0.54** | *0.31* | **0.10** | *0.06* | **0.22** | *0.15* |
| A/NK | **1.44** | *0.14* | **1.54** | *0.22* | **1.25** | *0.07* | **1.23** | *0.14* |
| A/CNK | **1.03** | *0.04* | **0.88** | *0.09* | **1.03** | *0.03* | **0.94** | *0.06* |
| $K_2O/Na_2O$ | **0.34** | *0.15* | **0.95** | *0.37* | **0.95** | *0.22* | **1.12** | *0.27* |
| *Trace elements (ppm)* | | | | | | | | |
| Cs | **4.1** | *2.8* | **1.1** | *1.0* | **5.1** | *4.1* | **7.3** | *3.8* |
| Rb | **71** | *37* | **90** | *39* | **155** | *53* | **186** | *57* |
| Ba | **532** | *243* | **1292** | *542* | **751** | *237* | **795** | *255* |
| Nb | **5.1** | *1.8* | **20.5** | *7.8* | **7.3** | *3.9* | **19.6** | *5.9* |
| Sr | **638** | *241* | **527** | *202* | **254** | *128* | **251** | *122* |
| Zr | **151** | *53* | **475** | *190* | **155** | *92* | **332** | *150* |
| Y | **8** | *4* | **44** | *18* | **15** | *11* | **44** | *14* |
| La | **24.2** | *11.1* | **86.8** | *36.0* | **40.8** | *25.2* | **70.9** | *24.0* |
| Ce | **47.6** | *21.9* | **186.3** | *74.0* | **74.2** | *45.7* | **145.1** | *45.8* |
| Pr | **4.58** | *1.72* | **22.79** | *9.28* | **7.64** | *4.75* | **17.05** | *5.69* |
| Nd | **18.6** | *7.9* | **88.6** | *37.9* | **27.7** | *16.8* | **62.1** | *20.9* |
| Sm | **3.01** | *1.23* | **14.43** | *6.18* | **4.56** | *2.33* | **10.64** | *3.63* |
| Eu | **0.88** | *0.31* | **2.81** | *1.03* | **0.69** | *0.25* | **1.66** | *0.73* |
| Gd | **2.27** | *0.91* | **11.26** | *4.66* | **3.19** | *1.51* | **8.96** | *3.19* |
| Tb | **0.30** | *0.13* | **1.64** | *0.66* | **0.49** | *0.24* | **1.38** | *0.47* |
| Dy | **1.31** | *0.56* | **8.50** | *3.35* | **2.74** | *1.57* | **7.78** | *2.66* |
| Ho | **0.24** | *0.10* | **1.57** | *0.65* | **0.53** | *0.34* | **1.55** | *0.54* |
| Er | **0.62** | *0.27* | **4.23** | *1.81* | **1.52** | *1.06* | **4.58** | *1.57* |
| Tm | **0.08** | *0.03* | **0.63** | *0.28* | **0.22** | *0.16* | **0.67** | *0.22* |
| Yb | **0.65** | *0.43* | **3.73** | *1.65* | **1.33** | *0.96* | **4.41** | *1.47* |
| Lu | **0.09** | *0.06* | **0.54** | *0.24* | **0.20** | *0.14* | **0.64** | *0.21* |
| Hf | **4.0** | *1.2* | **11.7** | *4.3* | **4.8** | *2.3* | **9.0** | *3.6* |
| Ta | **0.27** | *0.12* | **0.97** | *0.41* | **0.52** | *0.42* | **1.24** | *0.40* |
| Th | **3.7** | *1.5* | **8.9** | *9.6* | **10.9** | *4.6* | **10.3** | *4.5* |
| U | **1.0** | *0.4* | **1.0** | *0.7* | **2.1** | *1.3* | **2.5** | *1.2* |
| Pb | **13.4** | *4.5* | *n.d.* | *n.d.* | **25.8** | *5.6* | **21.4** | *5.6* |
| Sc | **3** | *1* | **12** | *6* | **3** | *1* | **8** | *5* |
| V | **16** | *2* | **98** | *48* | **8** | *7* | **53** | *33* |
| Cr | **13** | *6* | **79** | *49* | **11** | *6* | **29** | *38* |
| Co | **3** | *1* | **19** | *15* | **2** | *1* | **7** | *6* |
| Ni | **5** | *1* | **32** | *25* | **5** | *5* | **15** | *16* |
| Ga | **19** | *2* | **20** | *3* | **18** | *2* | **21** | *3* |
| Ba/Rb | **8.8** | *5.6* | **17.9** | *11.7* | **5.3** | *2.4* | **5.1** | *3.3* |
| Sr/Y | **94.9** | *56.0* | **15.3** | *13.4* | **28.5** | *25.4* | **6.0** | *3.3* |
| Nb/Ta | **19.5** | *7.7* | **22.0** | *4.8* | **19.7** | *10.8* | **17.0** | *5.0* |
| Lu/Hf | **0.021** | *0.010* | **0.050** | *0.038* | **0.057** | *0.072* | **0.076** | *0.026* |
| $(La/Yb)_N$ | **31.5** | *13.4* | **22.1** | *17.7* | **32.6** | *21.6* | **11.8** | *5.9* |
| $Eu_N/Eu^*$ | **1.10** | *0.32* | **0.73** | *0.27* | **0.62** | *0.23* | **0.51** | *0.13* |

et al., 2010; Martin et al., 2005) as well as the "high-Ti" sanukitoids (Martin et al., 2009), also referred to as "Closepet-type" granitoids (Moyen et al., 2003), which are distinctively rich in $FeO_t$, $TiO_2$ and other HFSE. Our group of sanukitoids s.l. is even looser, as it also comprises granitoids that do not match all the criteria proposed by these definitions. However, they are all demonstrably formed by similar processes as sanukitoids s.s., i.e. through interaction at mantle level between peridotite and an incompatible element-rich component.

All sanukitoids s.l. share several key geochemical characteristics. They are calc-alkaline to alkali-calcic, metaluminous ($0.7 \leq A/CNK \leq 1.0$) granitoids characterized by a large range of $SiO_2$ contents, extending down to mafic compositions ($45 \leq SiO_2 \leq 70$ wt.%), in contrast with other late-Archean granitoids (Fig. 4a–b). They are potassic, with variable $K_2O$ contents ($1.5 \leq K_2O \leq 5.0$ wt.%) leading to a wide range of $K_2O/Na_2O$ ratios, albeit generally $\geq 0.5$ (Table 2; Fig. 4b). Such rocks are typically characterized by high contents of ferromagnesian oxides ($5 \leq FeO_t + MgO + MnO + TiO_2 \leq 25$ wt.%) and CaO (Fig. 4c–d).

Primitive mantle-normalized trace element patterns of sanukitoids s.l. are relatively similar to those of TTGs, notably characterized by negative anomalies in Nb–Ta, but shifted to higher concentrations in all incompatible elements (Fig. 5a). These rocks are typically rich in Ba (generally >1000 ppm) and Sr (generally >400 ppm), which results in high Ba/Rb and Sr/Y ratios (Fig. 5b), and also have high contents in transition elements such as V (>50 ppm; Fig. 5c), Ni (15–200 ppm) and Cr (20–500 ppm). This dual geochemical character, i.e. richness in both "crustal" and "mantle" elements, is a unique and very typical feature

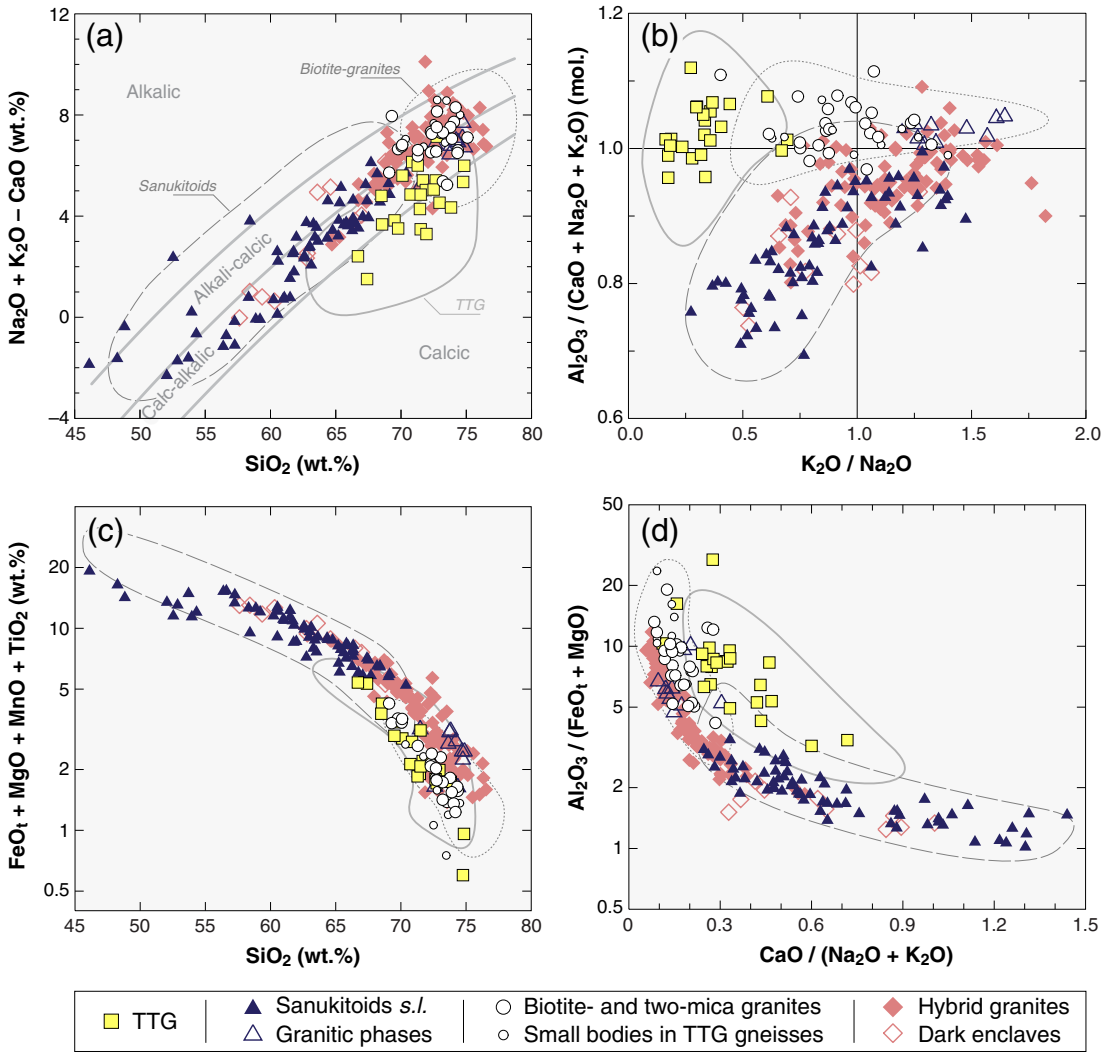


**Fig. 4.** Major-element geochemistry of the four groups of late-Archaean granitoids, illustrated with examples from the Pietersburg block and the Limpopo Belt (symbols) as well as literature data (fields; compilations from Martin et al., 2009; Moyen, 2011; Moyen and Martin, 2012). (a) MALI index ($[Na_2O + K_2O]$–CaO) vs. $SiO_2$ diagram of Frost et al. (2001); (b) A/CNK (molar $Al_2O_3/[CaO + Na_2O + K_2O]$ ratio) vs. $K_2O/Na_2O$ ratio; (c) sum of "mafic" oxides ($FeO_t + MgO + MnO + TiO_2$) vs. $SiO_2$; and (d) $Al_2O_3/(FeO_t + MgO)$ ratio vs. $CaO/(Na_2O + K_2O)$ ratio.

of all sanukitoids s.l. Some of them, such as the Bulai and Matok granitoids, are very rich not only in Ba and Sr, but also in other incompatible elements such as REE and HFSE ($\Sigma REE \geq 250$ ppm; $20 \leq Y \leq 70$ ppm; $300 \leq Zr \leq 1000$ ppm; Table 2; Fig. 5c,d), a typical feature of the "high-Ti" sanukitoids (Martin et al., 2009; Moyen et al., 2003). Thereby, some sanukitoids s.l. display a Sr negative anomaly in multi-element patterns (Fig. 5a), owing to a greater enrichment in REEs than Sr with respect to primitive mantle compositions. Sanukitoids s.l. show a wide range of $La_N/Yb_N$ ratios (10–75, but most often >25), and a variable Eu anomaly ($0.5 \leq Eu_N/Eu^* \leq 1.0$; Fig. 5d).

*2.2.3. Petrogenesis*

Experimental and geochemical constraints show that sanukitoids s.s. result from interaction between mantle peridotite and a component rich in incompatible elements, most often a TTG melt (Almeida et al., 2013; Dey et al., 2012; Halla et al., 2009; Heilimo et al., 2010; Martin et al., 2009; Moyen et al., 2001, 2003; Oliveira et al., 2011; Rapp et al., 1999, 2010; Smithies and Champion, 2000; Stern and Hanson, 1991). Geochemical variability of sanukitoids s.l. would result either from (i) different petrogenetic processes at mantle levels, especially regarding the physical conditions of the metasomatic interactions (*P*, *T* and relative volume of peridotite and contaminant; Martin et al., 2009; Mikkola et al., 2011b; Rapp et al., 1999, 2010), and/or (ii) the nature and composition of the metasomatic agent that could be represented, in addition to TTG melts, by $H_2O$- or $CO_2$-rich brines (Lobach-Zhuchenko et al., 2008; Stern et al., 1989), fluids or melts derived from sediments (Halla, 2005; King et al., 1998; Laurent et al., 2011; Mikkola et al., 2011b; Wang et al., 2009), or even alkaline melts (Heilimo et al., 2010) and carbonatites (Steenfelt et al., 2005). In the case of sanukitoids s.l. showing notably high $FeO_t/MgO$ ratios, low $Al_2O_3$ and flat HREE profiles, such as the Matok pluton from the Pietersburg block (Figs. 2, 4 and 5) and other granitoids reported from different cratons (Jahn et al., 1988; Mikkola et al., 2011b; Steenfelt et al., 2005), asthenospheric mantle could also have played a role as a source component (Laurent et al., 2014).

On the other hand, the widespread felsic rocks of sanukitoid suites (i.e. granodiorites) derive from differentiation of the most mafic magmas, regardless of the nature and source of the latter, by fractionation of amphibole- and plagioclase-rich solids with little or no involvement of pre-existing felsic crust (Bédard, 1996; Laurent et al., 2013a; Lobach-Zhuchenko et al., 2005, 2008; Oliveira et al., 2010; Stern and Hanson, 1991). Therefore, most of the chemical variability in sanukitoids s.l. (including the felsic rocks) results from mantle processes, as described above, rather than reflecting contamination at shallower levels of emplacement. This legitimates the identity of sanukitoids s.l. which, although compositionally diverse, are all related

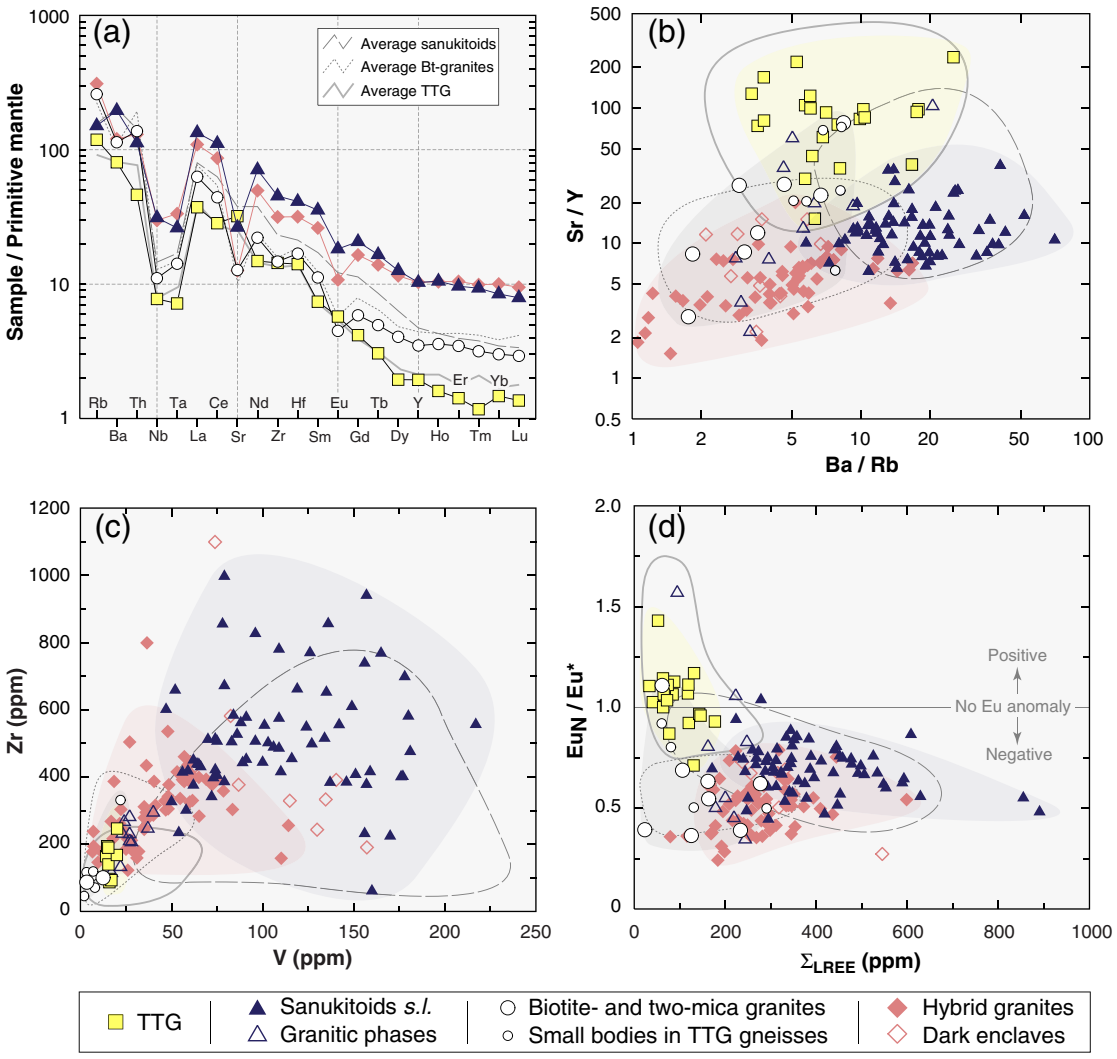


**Fig. 5.** Trace-element geochemistry of the four groups of late-Archaean granitoids, illustrated with examples from the Pietersburg block and the Limpopo Belt (symbols) as well as literature data (fields; compilations from Martin et al., 2009; Moyen, 2011; Moyen and Martin, 2012). (a) Multi-element patterns of average composition for each group, normalized to primitive mantle concentrations ("Pyrolite Silicate Earth" of McDonough and Sun, 1995); (b) Sr/Y vs. Ba/Rb ratios; (c) HFSE (represented by Zr) vs. transition element (represented by V) concentrations; and (d) amplitude of the Eu anomaly ($Eu_N$ = Eu concentrations normalized to C1 chondrites; McDonough and Sun, 1995; $Eu^* = \sqrt{Sm_N \cdot Gd_N}$) vs. sum of light rare earth elements (ΣLREE = La + Ce + Nd).

somehow to interactions between peridotite and incompatible element-rich components at mantle levels.

### 2.3. Biotite- and two-mica granites

This group basically consists of "purely crustal-derived" granites (i.e. generated by melting of grey gneisses: TTGs ± metasediments). They are widespread in every Archean craton (Sylvester, 1994; see Table 1), including the Superior Province (Breaks and Moore, 1992; Feng and Kerrich, 1992), the Slave Craton (Davis and Hegner, 1992), the Wyoming Province (Frost et al., 1998, 2006), the Baltic Shield (Käpyaho et al., 2006; Martin and Querré, 1984; Mikkola et al., 2011b), the Dharwar Craton of South India (Dey et al., 2012, 2014; Jayananda et al., 2006; Moyen et al., 2001, 2003; Vijaya Kumar et al., 2011), the North China Craton (Jahn et al., 1988; Liu et al., 2004; Yang et al., 2008), the Pilbara and Yilgarn Cratons in Western Australia (Champion and Sheraton, 1997; Champion and Smithies, 1999, 2007), the Amazonian Craton (Almeida et al., 2010, 2013; Althoff et al., 2000; Leite et al., 2004), the Tanzania Craton (Mshiu and Maboko, 2012) and the Kaapvaal Craton (Henderson et al., 2000; Meyer et al., 1994; this study).

After TTGs, biotite- and two-mica granites are the second most widespread lithology in late-Archean terranes (e.g. Moyen et al., 2003; Sylvester, 1994). For instance, they are largely exposed in the Pietersburg block as large plutons or batholiths (Turfloop and Lekkersmaak granites; Fig. 2) or occur as diffuse sheets, small bodies and dykes intrusive in, and intimately associated with, the TTGs of the Goudplaats–Hout River and Groot Letaba–Duiwelskloof gneiss units (Laurent et al., 2013b; Robb et al., 2006).

#### 2.3.1. Geology and petrography

Texturally, the biotite- and two-mica granites usually consist of homogeneous, grey to pink, equigranular granites and leucogranites whose grain size ranges from 0.1 to 0.5 cm (Fig. 3e). Some porphyritic varieties do occur, but are generally largely subordinate (e.g. in the Turfloop batholith of the Pietersburg block; Henderson et al., 2000; Kröner et al., 2000). Like sanukitoids, they are generally late- to post-tectonic and show variable levels of deformation from one area to another. Their modal composition is fairly constant, with ~30% K-

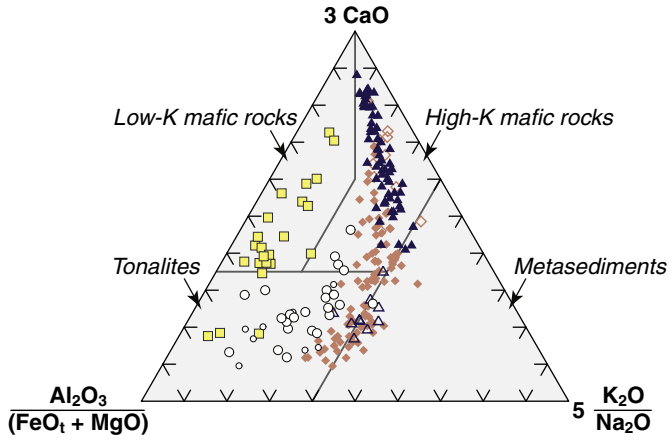


**Fig. 6.** Ternary diagram $Al_2O_3/(FeO_t + MgO)$; 3 * CaO; 5 * ($K_2O/Na_2O$) on which the composition of late-Archean granitoids from the Pietersburg block and Limpopo Belt is plotted (symbols as in Figs. 4 and 5). The multiplication factors were only added for scaling purposes. The fields represent the composition of melts derived from a range of potential sources (tonalites, metasediments, low- and high-K mafic rocks), determined using the major-element compositions of experimental studies: Patiño-Douce and Beard (1995), Singh and Johannes (1996), Skjerlie and Johnston (1996), Watkins et al. (2007) for tonalites; Patiño-Douce and Beard (1996), Patiño-Douce and Johnston (1991), Vielzeuf and Holloway (1988) for metasediments; Beard and Lofgren (1991), Rapp et al. (1999), Rapp and Watson (1995), Wolf and Wyllie (1994) for low-K mafic rocks and Sisson et al. (2005) for high-K mafic rocks.

feldspar, ~30% sodic plagioclase ($An_{5-15}$), and ~30% quartz; the other major mineral phases are biotite, and in places primary muscovite. For instance, in South Africa, most of the Lekkersmaak pluton (Jaguin et al., 2012) as well as some phases of the Turfloop batholith (Henderson et al., 2000; Kröner et al., 2000) are two-mica granites. Accessory phases are ilmenite, magnetite, apatite, zircon, allanite and, locally, pistacite. Exceptionally, the two-mica phases also bear Al-rich minerals such as cordierite, garnet and tourmaline, and are associated with rare metal-bearing (e.g. Sn and Li) pegmatite fields (e.g. Breaks and Moore, 1992; Feng and Kerrich, 1992; Frost et al., 1998; Kinny, 2000).

*2.3.2. Key geochemical features*

As shown by examples from South Africa (Table 2; Fig. 4a–c), typical chemical characteristics of biotite- and two-mica granites are their high silica contents ($68 \leq SiO_2 \leq 75$ wt.%), peraluminous affinity ($A/CNK \geq 1.0$), low amounts of ferromagnesian oxides ($1 \leq FeO_t + MgO + MnO + TiO_2 \leq 4$ wt.%), and a clear potassic signature, with $K_2O$ of ~4 wt.% resulting in $K_2O/Na_2O$ ratios >0.5. Low CaO concentrations (<2 wt.%) and moderate $Al_2O_3$ contents lead to low $CaO/(Na_2O + K_2O)$ and high $Al_2O_3/(FeO_t + MgO)$ ratios (Fig. 4d).

The trace element geochemistry of biotite- and two-mica granites from the Pietersburg block in South Africa is fairly representative of the whole group. Their primitive mantle normalized patterns are similar to those of TTGs, except for higher contents in highly incompatible elements (see Table 2) such as Rb (average = 155 ppm) and Th (average = 11 ppm), systematic negative Ba and Sr anomalies and higher concentrations in Y–HREE (Fig. 5a). Thus, such granites have lower Ba/Rb and Sr/Y ratios than TTGs (Fig. 5b). Both HFSE and transition element contents are low (Zr < 265 ppm; V < 20 ppm; Table 2; Fig. 5d), and their REE contents are moderate, with variously fractionated REE patterns ($15 \leq La_N/Yb_N \leq 65$ for most samples) but significant negative Eu anomalies ($Eu_N/Eu^* \sim 0.5$; Fig. 5d).

*2.3.3. Petrogenesis*

In all Archean cratons worldwide, including the Kaapvaal Craton, slightly peraluminous, potassic and calc-alkaline biotite-bearing granites are described as partial melts of older felsic crust, especially TTGs (e.g. Almeida et al., 2013; Althoff et al., 2000; Dey et al., 2012; Feng and Kerrich, 1992; Frost et al., 2006; Henderson et al., 2000; Moyen et al., 2001, 2003; Mshiu and Maboko, 2012; Sylvester, 1994; Vijaya Kumar et al., 2011; Whalen et al., 2004). Major element compositions of such granites are consistent with this model, matching the composition of experimental melts derived from tonalites (Fig. 6). Furthermore, these rocks are equivalent to the potassic granite subgroup of Archean grey gneisses defined by Moyen (2011), which he interpreted as partial melts of sodic TTGs at crustal pressure (<10 kbar). A plagioclase-rich and garnet-free residue accounts for the low Ba/Rb and Sr/Y ratios and negative Eu anomalies of these granites.

As pointed out by Watkins et al. (2007), most TTGs are too sodic to produce the large volumes of late-Archean potassic granites. Therefore, these authors proposed an alternative hypothesis, assuming that these granites could derive ultimately from a highly metasomatized, K-rich mantle source. Nevertheless, their very silicic nature, the absence of intermediate to mafic phases and the lack of geochemical affinities with sanukitoids s.l. (Figs. 4 and 5), which definitely derive from such an enriched mantle source, are at odds with this model. Moreover, the $K_2O$ contents of melts produced experimentally by partial melting of low-K TTGs range from 2 to 6 wt.% at 70–75 wt.% $SiO_2$ (Patiño-Douce and Beard, 1995; Singh and Johannes, 1996; Skjerlie and Johnston, 1996; Watkins et al., 2007), with an average $K_2O$ content of 3.8 wt.%, which is comparable to that of biotite- and two-mica granites in the Pietersburg block (4.1 wt.%; Table 2). On the other hand, melting of metagreywackes and metapelites would provide an additional source of $K_2O$: the two-mica-bearing late-Archean granites, such as the Lekkersmaak pluton in South Africa, show A/CNK values >1.1 similar to that of post-Archean S-type granites, pointing to the contribution of such a metasedimentary source (e.g. Breaks and Moore, 1992; Jaguin et al., 2012; Jahn et al., 1988). Therefore, we consider that late-Archean biotite- and two-mica granites derive from variable contributions of two distinct crustal sources, i.e. sodic orthogneisses (TTGs) and paragneisses (metasediments).

*2.4. Hybrid granitoids*

Late-Archean granitoids with hybrid characteristics were identified from most cratons. These formed through interaction (e.g. metasomatism, mingling, mixing) between magmas or sources of any of the previously defined groups. They form an extremely heterogeneous family that cannot be defined on geochemical criteria alone, because sources and petrogenetic mechanisms differ from one place to another. They most commonly result from interactions between sanukitoids s.l. and biotite- or two-mica granites, for example the Mashashane, Mashishimale, Matlala and Moletsi plutons of the Pietersburg block (Fig. 2), as well as several granitoids in the Superior Province (Stevenson et al., 1999; Whalen et al., 2004) and the Dharwar craton of southern India (Jayananda et al., 2006; Moyen et al., 2001). Some relatively common granodiorites and monzogranites, which are clearly too mafic to represent pristine crustal melts, also fall into this category (e.g. "high-Ca" granites of the Yilgarn Craton; Champion and Sheraton, 1997). In addition, this family includes all granitoids recognized as being hybrids between TTGs and sanukitoids or biotite-bearing granites, i.e. the so-called "Transitional TTGs" from the Yilgarn Craton (Champion and Smithies, 2003) and the Dharwar Craton (Dey et al., 2012; Jayananda et al., 2006; Prabhakar et al., 2009) as well as monzonite–granodiorite–granite suites of the Amazonian Craton (Almeida et al., 2010, 2013) and Superior Province (Feng and Kerrich, 1992). The rare Archean alkaline granites and syenites (Champion and Sheraton, 1997; Corfu et al., 1989; Feio et al., 2012; Mikkola et al., 2011a; Sage et al., 1996; Smithies and Champion, 1999b) may also be akin to this group, as they presumably derived from a lower crustal,

metasomatized basaltic source (Smithies and Champion, 1999b, 2000).

The global distribution of hybrid granitoids is very heterogeneous. They are not reported in every late-Archean craton, and where they do occur, they can represent either a very small volume (e.g. in the Kuhmo district of the Baltic shield; Mikkola et al., 2011b) or a significant crustal component, like in the Pietersburg block in South Africa where they form several large granitic plutons (Fig. 2).

*2.4.1. Geology and petrography*

In general, late-Archean hybrid granitoids are well-defined plutons, like in the Pietersburg block (Fig. 2). They generally consist of composite magmatic complexes where, in contrast to the sanukitoids, the monzogranitic phases largely prevail over granodiorites and diorites. For example, in the northern Kaapvaal craton, the latter are restricted to scarce, small (<1 m) enclaves enclosed within the dominant coarse-grained (0.5–2 cm), equigranular to porphyritic monzogranites (Fig. 3f). In other areas, granodioritic phases can be more abundant (e.g. Almeida et al., 2010; Champion and Smithies, 2003) but there, too, mafic rocks are scarce or even absent, and clearly distinguish these intrusions from sanukitoids s.l.

Most often, the dominant monzogranites consist of sodic plagioclase ($An_{5–20}$) (~30%), K-feldspar (~30%), quartz (~25%), with biotite (<15%) as the dominant mafic mineral. They differ from classic biotite- and two-mica granites by the absence of primary muscovite, their greater richness in biotite and the presence of magmatic epidote (pistacite), which is ubiquitous in hybrid granitoids from the Pietersburg block in South Africa as well as in the Amazonian and Dharwar Cratons (Almeida et al., 2010, 2013; Jayananda et al., 2006). Hornblende is generally rare or only present as relics: some monzogranites from the Pietersburg block contain cm-sized mafic clots, interpreted as pseudomorphs of early amphibole crystals into biotite + epidote assemblages (Laurent, 2012), a characteristic also reported from hybrid granitoids of the Dharwar Craton (Jayananda et al., 2006). Accessory minerals are magnetite, ilmenite, apatite, titanite and allanite.

*2.4.2. Key geochemical features*

There is no systematic geochemistry of hybrid granitoids, because the different components that are involved in their genesis differ from one craton to another. Nevertheless, as reported by all authors, they are typically intermediate in composition between the granitoids from the other three groups (Almeida et al., 2010, 2013; Champion and Sheraton, 1997; Champion and Smithies, 2003; Jayananda et al., 2006; Moyen et al., 2001). For example, the Mashashane, Mashishimale, Matlala and Moletsi monzogranites from the Pietersburg block resemble biotite- and two-mica granites in being calc-alkaline to alkali-calcic, silica-rich rocks ($SiO_2$ > 68 wt.%), with high $K_2O/Na_2O$

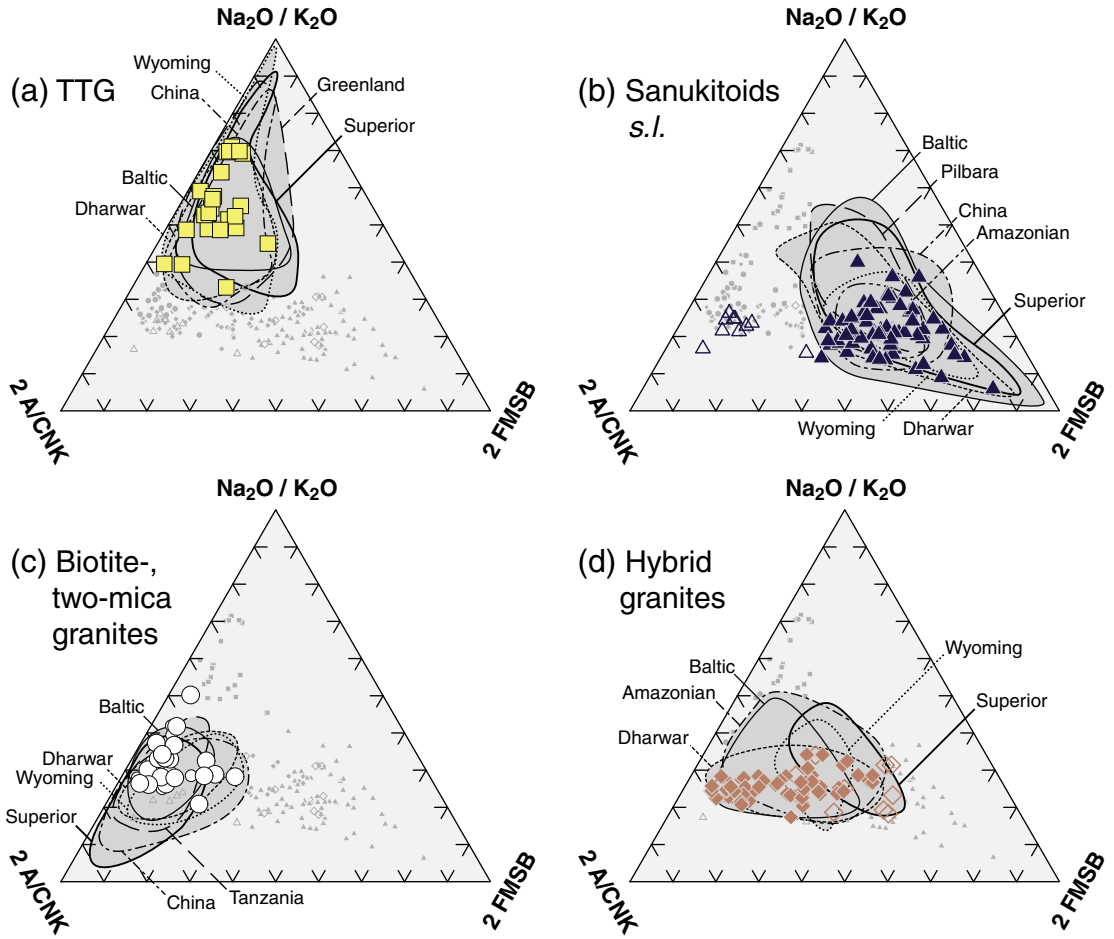


**Fig. 7.** Proposed ternary classification diagram for late-Archean granitoids: 2 * A/CNK (molar $Al_2O_3/[CaO + Na_2O + K_2O]$ ratio); $Na_2O/K_2O$ ratio; 2 * $(FeOt + MgO)_{wt.\%}$ * $(Sr + Ba)_{wt.\%}$ (=FMSB). The multiplication factors were only added for scaling purposes. Examples of each group of late-Archean granitoids were plotted on the diagram, including samples from the Pietersburg block and the Limpopo Belt in South Africa (symbols) as well as 7 other cratons worldwide (for references, see Table 2). This diagram can be used as a petrogenetic indicator, each pole representing an end-member source of late-Archean granitoids: (1) pre-existing crustal rocks (pole A/CNK); (2) low-K mafic rocks (pole $Na_2O/K_2O$); and (3) a LILE-rich, metasomatized mantle (pole FMSB). The hybrid granitoids plot in the convergence area of the other three groups. See text for details.

ratios (0.5–1.5) (Table 2; Fig. 4a–b). However, they are poorer in Al ($12 \leq Al_2O_3 \leq 14$ wt.%) and richer in ferromagnesian oxides ($1 \leq FeO_t + MgO + MnO + TiO_2 \leq 7$ wt.%; Fig. 4c) leading to metaluminous affinities ($0.85 \leq A/CNK \leq 1.05$; Fig. 4b) and lower $Al_2O_3/(FeO_t + MgO)$ ratios (Fig. 4d), which is more typical of sanukitoids s.l.

The same observation can be made for trace elements. Trace element patterns of hybrid granites are similar to those of biotite- and two-mica granites in their high Rb, Th contents (Table 2) and negative Ba, Sr anomalies (Fig. 5a), as well as their Ba/Rb ratios (Fig. 5b). However, like sanukitoids, they are also very rich in REE and HFSE (Fig. 5c–d), which results in lower Sr/Y ratios than in any other granitoid type (Fig. 5b). Zr and V contents are also intermediate between those of sanukitoids s.l. and high-Al granites (Table 2; Fig. 5c). Due to high HREE contents ($3.0 \leq Yb \leq 10.4$ ppm), REE patterns are moderately fractionated ($5.0 \leq La_N/Yb_N \leq 17.6$) and have a marked negative Eu anomaly ($0.2 \leq Eu_N/Eu^* \leq 0.7$; Fig. 5d).

#### 2.4.3. Petrogenesis

Fig. 6 shows that the major-element composition of hybrid granitoids does not unambiguously point to an origin through melting of a single crustal lithology. Most authors that have studied such granites worldwide therefore propose a mixed origin, which basically involves any of the magma or sources of the previously defined groups: mixing between a differentiated sanukitoid magma and a TTG liquid (Almeida et al., 2010), contamination of melts originating from the lower mafic crust by an older crustal component (Jayananda et al., 2006; Smithies and Champion, 2000), hybridization of TTG magmas by enriched mantle (Feng and Kerrich, 1992; Prabhakar et al., 2009) or a complex interplay of these different mechanisms (Champion and Sheraton, 1997). In the Pietersburg block, the hybrid granites are akin to both sanukitoid suites (high $FeO_t + MgO + MnO + TiO_2$ as well as high REE and HFSE contents; Figs. 4c, 5), and biotite- and two-mica granites (low CaO/$[Na_2O + K_2O]$, similar Rb, Ba, Th contents and $K_2O/Na_2O$; Figs. 4, 5). Therefore, in that case, they likely originate from interactions between felsic magmas derived from the differentiation of sanukitoids and crustal melts (similar in composition to biotite- and two-mica granites). This model is supported by structural and textural evidence of magma interaction (magma mingling, rapakivi textured feldspars and quartz ocelli; Laurent, 2012; heterogeneity in zircon populations and compositions; Laurent et al., 2013b), as well as variable Nd–Hf isotope compositions in hybrid granitoids ($\varepsilon_{Nd} = 0$ to $-5$; Laurent, 2012) compared with sanukitoids s.l. ($\varepsilon_{Nd} = -3$ to $-4$; Laurent et al., 2014).

### 2.5. A synthetic classification diagram

The review presented above pinpoints the involvement of three end-member petrogenetic processes in the origin of late-Archean granites. We therefore propose to use a synthetic ternary diagram for purposes of classification, in which each pole represents a key geochemical characteristic of granitoids produced through one of these processes (Fig. 7):

(1) **$Na_2O/K_2O$** for melting of meta-igneous mafic rocks with low to moderate $K_2O$ contents;
(2) **FMSB** ($[FeO_t + MgO]_{wt.\%} * [Sr + Ba]_{wt.\%}$) for the interactions between peridotite and components rich in incompatible elements (in particular LILE); and
(3) **A/CNK** for melting of Al-rich, felsic crustal lithologies (TTGs, metasediments).

We plotted the composition of late-Archean granitoids from South Africa together with those from other Archean cratons worldwide in this ternary diagram (Fig. 7). Three important observations can be made: (i) all members of a given group show relatively similar compositions regardless of their geographic origin, highlighting the relevance of the classification; (ii) the diagram is fairly effective at discriminating late-Archean granitoids, as the different groups are clearly distinct from each other: TTGs trend towards the $Na_2O/K_2O$ pole, whilst biotite- and two-mica granites plot close to the A/CNK pole and sanukitoids s.l. are concentrated around the FMSB end-member; (iii) there is however a significant overlap between the different granitoid groups, especially in the central part of the ternary diagram where they all converge towards the field of hybrid granitoids, a problem obviously inherent in the petrogenesis of the latter. This issue further emphasizes that there is a compositional continuum between the four granitoid groups defined here and that, therefore, many samples actually represent magmas derived from relative contributions of the three end-members. Likewise, this illustrates that this diagram must be used in addition to other, classical geochemical projections, and cannot substitute careful petrogenetic modelling.

## 3. Late-Archean crustal evolution: a two-stage sequence

### 3.1. Evidence from geochronology

It has long been demonstrated that during the Neoarchean, emplacement of dominantly granitic and potassic magmas followed the massive formation of sodic TTGs in most Archean cratons

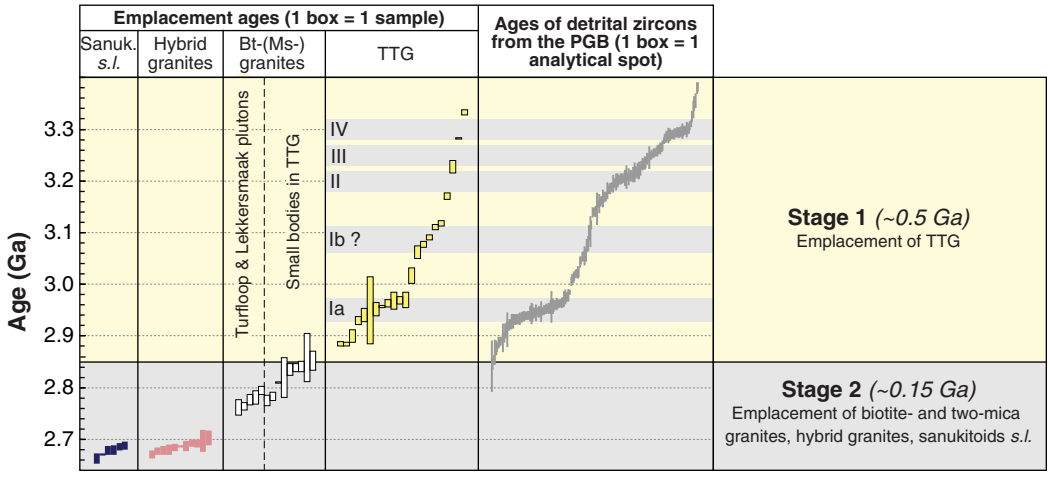


**Fig. 8.** Compilation of (1) U–Pb and Pb–Pb emplacement ages obtained for the four granitoid groups in the Pietersburg block (data from Brandl and Kröner, 1993; Brandl et al., 1996; de Wit et al., 1993; Henderson et al., 2000; Kröner et al., 2000; Laurent et al., 2013b; Poujol, 1997, 2001; Poujol and Robb, 1999; Zeh et al., 2009, 2013) — the different groups are colour-coded as in Figs. 4 to 7; and (2) all age data from detrital zircons in the Pietersburg greenstone belt (PGB; grey boxes) (Zeh and Gerdes, 2012). See text for discussion.

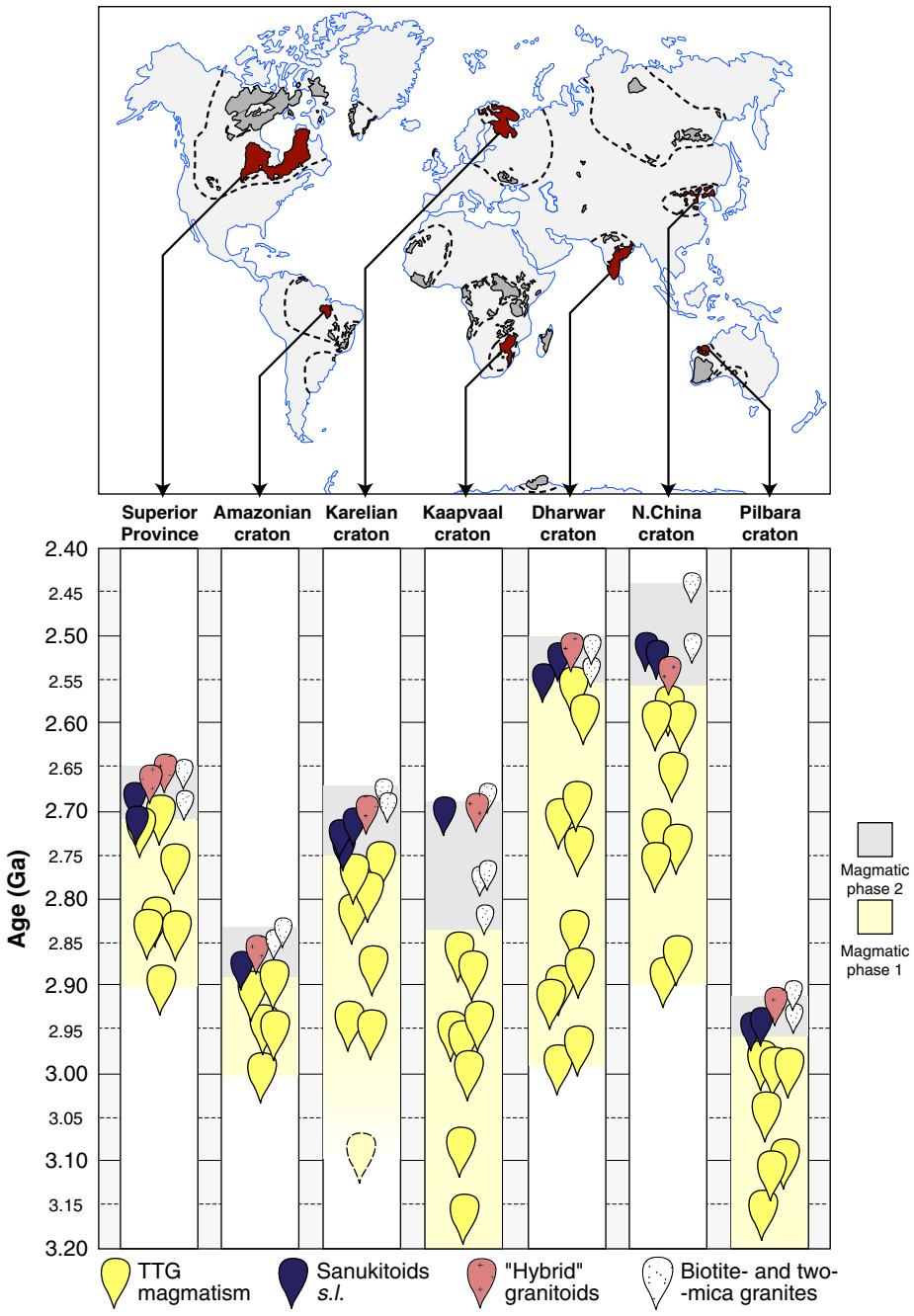


**Fig. 9.** Top: map of exposed Archean crust (after Bleeker, 2003) in grey, and selected cratons of interest (in red) where the late-Archean granitoid evolution is well documented. Bottom: for each one of these areas, simplified age distribution for the four groups of late-Archean granitoids defined in this study (modified and completed after Heilimo et al., 2011). The same sequence is systematically repeated in every terrane, with a preliminary, long-lasting period of TTG emplacement (Phase 1) and a subsequent, much shorter time during which all the other three groups are emplaced together or in rapid succession (Phase 2). For references and interpretation, see text and Table 1.

(e.g. Almeida et al., 2013; Champion and Smithies, 2003; Condie, 1981; Heilimo et al., 2011; Jahn et al., 1988; Martin and Querré, 1984; Moyen et al., 2003; Sylvester, 1994). Such an evolution is well illustrated by a compilation of emplacement ages obtained from all granitoid rocks of the Pietersburg block (Fig. 8). According to these data, the temporal evolution of late-Archean granitoid magmatism in this area took place in two main stages:

(1) Between 3.30 and 2.85 Ga, a long period of almost exclusively TTG magmatism was recorded by emplacement ages from the gneiss units. The ages of detrital zircons from sediments in the Pietersburg greenstone belt span this whole range (Fig. 8), indicating that TTG emplacement was more or less continuous during that period, but Zeh and Gerdes (2012) identified discrete episodes of more intense magmatic activity at ~3.30, ~3.25, ~3.20, ~3.10 and ~2.95 Ga (Fig. 7).

(2) Between 2.84 and 2.69 Ga, a briefer period during which all other types of granitoids were generated. Firstly, small masses of biotite- and two-mica granites intruded TTGs at 2.84 Ga; this event was followed, 2.75 to 2.79 Ga-ago, by the formation of the compositionally similar, but larger Turfloop and Lekkersmaak batholiths. All the hybrid granites were then emplaced within a very short time span at around 2.69 Ga, together with the sanukitoids s.l. of the Matok pluton and coeval with another major episode of crustal anatexis (e.g. Kreissig et al., 2000; Taylor et al., 2014).

Fig. 9 shows that there is a striking similarity between this emplacement sequence in the northern Kaapvaal Craton and granitoid evolution in other Archean terranes worldwide. Initially there is a long period (up to 0.5 Ga, but generally in the range of 0.2–0.3 Ga) of almost exclusive TTG magmatism, building up large volumes of felsic continental crust. Immediately after TTG emplacement, and within a shorter timespan (~0.05 Ga on average), the whole range of high-K granitoids (sanukitoids s.l., biotite-and two mica-bearing granites, hybrid granites) is generated and emplaced.

The planetary scale of this event is highlighted by the fact that, in most cratons, it took place at the end of Archean aeon, between 3.0 and 2.5 Ga (Fig. 9). However, a comparative scrutiny of the evolution shows two main temporal differences from one craton to another:

(1) The absolute lengths of the two magmatic stages vary widely from one region to another. Extreme examples are the Amazonian Craton, where the episode of TTG emplacement lasted ~0.1 Ga, and the second magmatic stage less than 30 Ma (Fig. 9), and the Kaapvaal Craton, in which these two events spanned over ~0.50 and ~0.15 Ga, respectively (Figs. 8 and 9). However, the relative duration of the two stages was identical in both cases.
(2) The transition from one magmatic stage to the other took place at very different times globally (as early as ~2.95 Ga in the Pilbara Craton, but as late as ~2.55 Ga in the Dharwar and North China cratons; Fig. 9), highlighting the diachronic character of late-Archean magmatism, as already discussed by Almeida et al. (2013), Heilimo et al. (2011) and Champion and Smithies (2003).

### 3.2. Evidence from isotope data

The temporal evolution of late-Archean granitoid magmatism is recorded not only by the geochronology, but also by Hf-Nd isotope systematics. Fig. 10 shows the evolution of initial isotope compositions of Hf (zircon) and Nd (whole-rock) in granitoids in the northern Kaapvaal Craton. The first magmatic stage (3.33–2.85 Ga) is characterized by positive $\varepsilon_{Hf}$ values in zircons from TTGs ($\varepsilon_{Hf}(t) = 0$ to $+5$; Fig. 10a), as well as a close similarity between magmatic ages of TTGs (2.85–3.33 Ga; Fig. 8) and their Nd model ages (2.95–3.30 Ga; Fig. 10b). Both lines of evidence unequivocally indicate that this was a period of juvenile magmatism and therefore of continental crust extraction from the mantle. In contrast, granitoids emplaced during the second stage (biotite- and two-mica granites, sanukitoids s.l. and hybrid granites) clearly show more scattered and more evolved, "enriched" signatures ($\varepsilon_{Nd}(t) = 0$ to $-5$; $\varepsilon_{Hf}(t) = +2$ to $-5$), pointing to significant reworking and recycling processes. In other words, the geological history of the Pietersburg block is characterized by long-lasting, intense juvenile crust formation and ended up with the recycling of this preexisting crust.

A review of available whole-rock Nd isotope data from late-Archean granitoids in four reasonably well-documented cratons (Baltic Shield, North China Craton, East Dharwar Craton and Superior Province; after Dey, 2013) shows that this evolution is systematic (Fig. 11). The first stage of the magmatic sequence defined in Section 3.1 is characterized either by (i) emplacement of juvenile TTGs, having dominantly positive $\varepsilon_{Nd}(t)$, over a long period; or (ii) major crust-forming events depicted by Nd model ages of TTGs ranging over that time span (Fig. 11). In comparison, the much shorter second magmatic stage is always associated with greater variability of Nd isotope compositions (up to 10 epsilon units; Fig. 11) and obvious involvement of older crustal components in granitoid sources (highly negative $\varepsilon_{Nd}(t)$).

According to the petrogenetic model of TTGs described in Section 2.1.3, new crust was formed during the first magmatic stage in two successive steps: (i) melting of the mantle to produce tholeiitic mafic rocks; and (ii) the subsequent melting of the latter, giving rise to the TTGs. The homogeneously high Hf–Nd isotope compositions and the wide spread of model ages over this long timespan indicate that mafic rocks were being continuously generated from the mantle and subsequently re-melted to produce TTGs over several hundreds of Ma, and that the length of time between the two steps remained relatively short throughout this period. In sharp contrast, the isotopic signature of the second stage points to the coeval involvement of mantle sources (many sanukitoids have positive $\varepsilon_{Nd}(t)$; Fig. 11) and recycling of the continental crust generated during the first stage. This second stage has a greater diversity of sources and petrogenetic mechanisms, which can be separated into three categories: (i) melting of an "enriched" mantle, to generate mafic magmas which subsequently differentiated to give rise to sanukitoid (s.l.) suites; (ii) melting of pre-existing crustal rocks (mostly TTGs and minor metasediments) to produce biotite- and two-mica granites; (iii) interaction between magma types from (i) and (ii) (or their sources) to generate the hybrid granitoids. Crustal recycling may therefore have resulted either from direct intracrustal melting (producing biotite- and two-mica granites) or introduction of crustal-derived material into the mantle, forming the metasomatized mantle source of the sanukitoids s.l. and explaining why some of them have relatively evolved isotopic signatures (Figs. 10 and 11).

## 4. Geodynamic implications: late-Archean granitoid evolution reflecting subduction and continental collision

### 4.1. First stage: genesis of TTGs

#### 4.1.1. Possible geodynamic environments

The geochemical diversity of TTGs, which is the main component of Archean crust, indicates that these were generated by melting of metabasalt at various depths, which can be achieved in several different geodynamic settings (see Moyen, 2011; Moyen and Martin, 2012 for review). These include (i) subduction-like settings in which subducted meta-basalts (oceanic crust or plateaus) melted due to higher Archean geothermal gradients (e.g. Defant and Drummond, 1990; Martin, 1986, 1987, 1999; Martin and Moyen, 2002; Martin et al., 2014; Rapp et al., 2003); (ii) tectonic environments unrelated to plate boundaries, such as the progressive maturation of an oceanic plateau above a long-lived mantle plume (e.g. Bédard, 2006, 2013; Bédard et al., 2003; Smithies, 2000; Willbold et al., 2009; Zegers and van Keken, 2001) and (iii) intermediate scenarios, such as delamination at the base of a magmatically or tectonically over-thickened (>30 km) mafic crust (e.g. Bédard et al., 2003; Johnson et al., 2013; Moyen, 2011; van Thienen et al., 2004). Here, we propose that subduction is arguably the most plausible geodynamic environment to explain the genesis of TTGs in the first stage of the late-Archean granitoid evolution.

#### 4.1.2. Late-Archean TTGs formed in a subduction setting: geometric and geochemical constraints

As discussed earlier, most of late-Archean (<3.0 Ga-old) TTGs are Sr-rich and Y–HREE-poor, thus corresponding to the "low-HREE" group of Halla et al. (2009) and the "medium-" to "high-pressure" groups of Moyen (2011), which these authors consider as having been generated at pressures >1.0 GPa (i.e. at depths >35 km). Such melting is unlikely to have taken place in the crust, especially in the Archean context where a higher heat flux from the mantle resulted in a weaker crust, unable to sustain thicknesses >30 km (England and Bickle, 1984; Johnson et al., 2013; Rey and Coltice, 2008). Thus, the genesis of these magmas requires that (hydrous) mafic rocks were somehow introduced deep into the mantle.

This requirement is easily achieved in the context of a subduction setting. It may also be fulfilled by other scenarios, though, especially if the base of the mafic crust becomes gravitationally unstable owing to

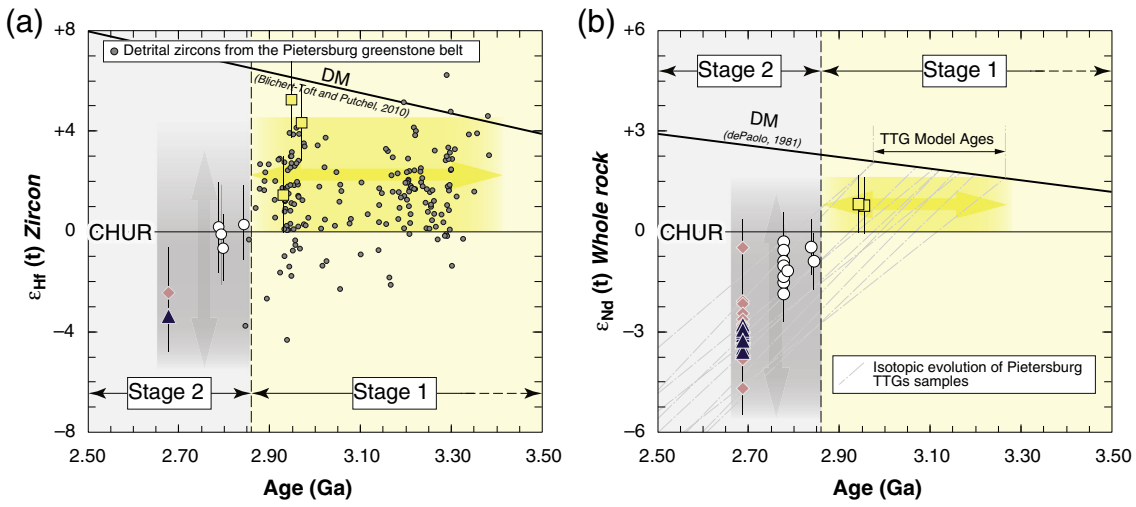


**Fig. 10.** Hf–Nd isotopic evolution of late-Archean granitoids in the Pietersburg block (symbols as in Figs. 4 to 7): (a) $\varepsilon_{Hf}(t)$ of zircon vs. age diagram for samples investigated by Zeh et al. (2009, 2013) (one symbol = average of several LA-MC-ICPMS zircon analyses, typically ~15) and individual analyses of detrital zircon grains from sediments of the Pietersburg greenstone belts (grey circles; Zeh and Gerdes, 2012). DM model is after Blichert-Toft and Putchel (2010); (b) $\varepsilon_{Nd}(t)$ of whole rock vs. age diagram (data from Henderson et al., 2000; Laurent, 2012 and Laurent et al., 2014); the dashed grey lines represent the isotopic evolution of TTG samples for which no absolute age is available (data from Kreissig et al., 2000). The two stages of the magmatic evolution defined on geochronological grounds in Section 3.1 and Fig. 8 are also shown (yellow and grey areas). Note that Stage 1 corresponds to (i) a long period of suprachondritic Hf isotope composition and (ii) a major crust-forming event as witnessed by TTG model ages, whereas Hf–Nd signatures are more scattered and evolve towards negative values during Stage 2.

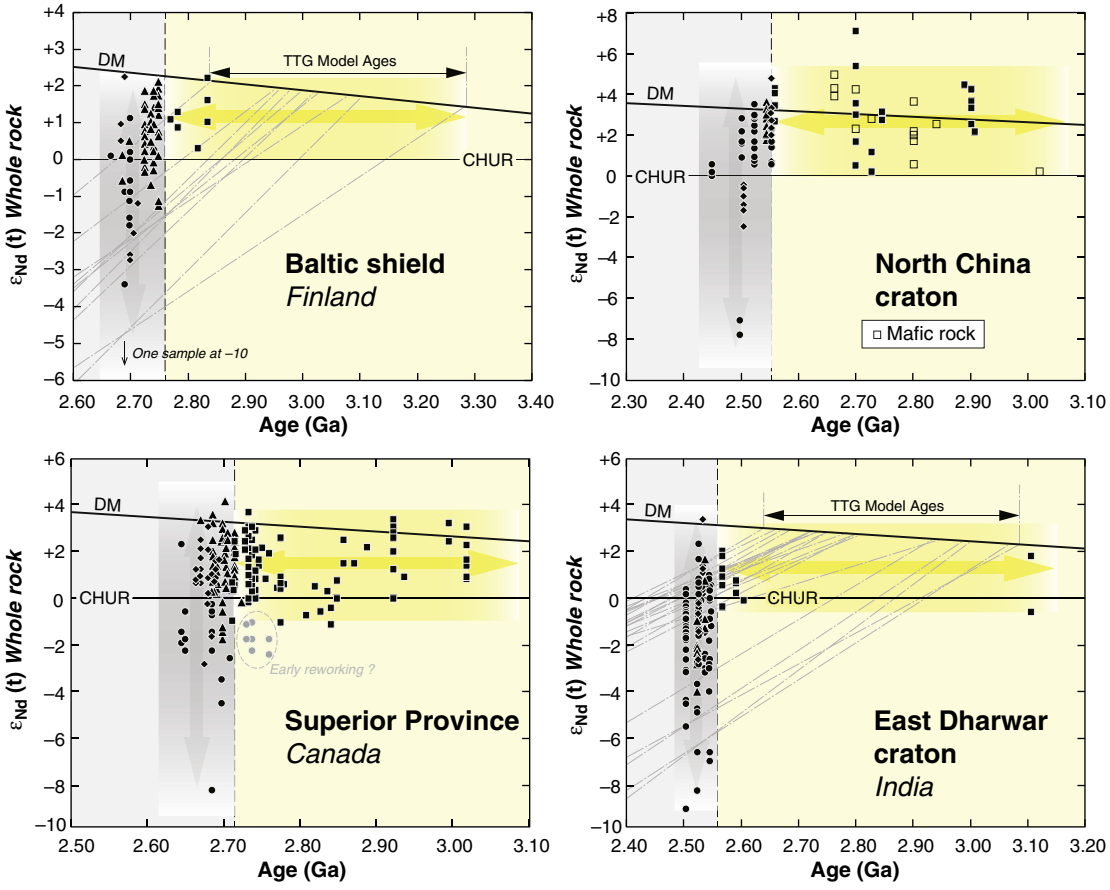


**Fig. 11.** Compilation of $\varepsilon_{Nd}(t)$ of whole rocks vs. age diagram for late-Archean granitoids in four different regions. Each sample is assigned to one of the four groups of our classification: TTGs (squares), sanukitoids s.l. (triangles), biotite- and two-mica granites (circles) and hybrid granites (diamonds). The grey dashed lines represent the isotopic evolution of TTG samples for which no absolute age is available. The two stages of the magmatic evolution are as in Fig. 9. The isotopic evolution is comparable to that of late-Archean granitoids in the Pietersburg block (Fig. 10), as the first stage (yellowish fields) is characterized either by emplacement of juvenile TTGs (and coeval mafic rocks) or represents a protracted period of crust formation (Nd model ages), whereas the second stage (greyish fields) shows much more scatter over a shorter timespan, and overall a salient trend towards more negative $\varepsilon_{Nd}(t)$. Modified and completed after Dey (2013); for references, see Table 1.

the formation of eclogites at depth. Formation of an eclogitic root can be due to partial melting of mafic material at the base of an oceanic crust or plateau, producing garnet- and pyroxene-bearing residues (e.g. Bédard, 2006; Zegers and van Keken, 2001). However, such delaminated residues would consist of anhydrous and refractory material, which is unlikely to melt any further and thus yield the great volumes of TTG observed in late Archean cratons. Alternatively, delamination can take place "spontaneously" if the mafic crust is thick enough for eclogitic assemblages to be stable at its base, but this can take place only if the crust has a komatiitic composition (>21 wt.% MgO; Johnson et al., 2013), whilst the source of TTGs is basaltic rather than komatiitic. The only way to generate "medium-" and "high-pressure" TTGs by melting delaminated mafic rocks is therefore to consider a tectonically over-thickened (i.e. gravitationally unstable) basaltic crust (Moyen, 2011).

Although plausible to explain the origin of TTGs as such, this possibility is challenged by the whole evolution of late-Archean granitoids, and in particular the subsequent emplacement of sanukitoids (s.l.) during the second stage of the magmatic sequence. Sanukitoids were generated by interactions between mantle peridotite and LILE-, LREE-rich material (see Sections 2.2.3 and 3.2). Such material had to be water-rich in order to account for the generally high $H_2O$ contents of the "primary" sanukitoid magmas (Laurent et al., 2013a; Lobach-Zhuchenko et al., 2008; Oliveira et al., 2009, 2010). Delaminated basalts would not be rich enough in incompatible elements and water to represent such material. Alternatively, melting of delaminated basaltic rocks might have produced LILE-, LREE-rich and hydrous TTGs, which in turn were responsible for metasomatism in the surrounding mantle. In that case, sanukitoids would be expected to have been produced at any time together with TTGs, in response to the successive events of mantle re-enrichment by delamination of lower crustal material. Instead, the evolution of late-Archean granitoids shows that sanukitoids s.l. are rather associated with biotite-, two-mica and hybrid granites and largely restricted to the second stage of the magmatic evolution (see Section 3 and Figs. 8 to 11).

Moreover, many authors proposed that the mantle source of some sanukitoids s.l. interacted with sediments, or sediment-derived fluids/melts (Halla, 2005; King et al., 1998; Laurent et al., 2011, 2014; Lobach-Zhuchenko et al., 2008; Mikkola et al., 2011b), which are most easily introduced to mantle depth by subduction. Delamination of supracrustal material could be an alternative to subduction (e.g. Bédard, 2013), but such buoyant material would be hard to transfer to lower crustal depths even considering a classical convective overturn. And if so, it is unlikely that it would survive its transfer through a hot, convective and certainly partially molten crust. Finally, the radiogenic isotope signature of many sanukitoids (Fig. 11) indicates that the interactions between mantle and enriched components took place shortly (<0.3 Ga and most often <0.1 Ga) before emplacement (Halla, 2005; Käpyaho et al., 2006; Kovalenko et al., 2005; Laurent et al., 2011, 2014; Shirey and Hanson, 1984). This supports the hypothesis that sanukitoid genesis took place soon after a subduction event.

Importantly, the presence of "low-pressure" (Sr- and Al-poor, Y- and HREE-rich) TTGs in the late-Archean geological record (Almeida et al., 2011; Feng and Kerrich, 1992; Halla et al., 2009; Whalen et al., 2002; see Section 2.1.3) does not preclude a convergent plate setting. As proposed by several authors, subduction can take place in an "intra-oceanic" setting, e.g. beneath a thick oceanic plateau (Almeida et al., 2011, 2013; Halla et al., 2009; Heilimo et al., 2010). This particular setting would adequately account for the coexistence, and even the co-magmatic character in some cases (Almeida et al., 2011), of "low-pressure" and "high-pressure" TTGs. The latter thus represent "slab melts", whilst the former originated through partial melting at the base of the thick, overlying mafic pile heated up by thermal conduction and advection.

#### 4.1.3. The meaning of "subduction"

The conclusion that late-Archean TTGs formed in a "subduction" environment does not imply necessarily that those "subduction" zones were similar to present-day situations (i.e. a long-lived, continuous slab regularly plunging along an active margin several thousands of kilometres long), neither that they were the driving force of plate tectonics at that time. Moyen and van Hunen (2012) proposed that, unlike the present-day situation, an Archean subducted slab could not have been stable, but would have been subjected to frequent break-off, leading to the episodic sinking of basaltic fragments into the mantle. Such a process is a possible scenario for the late-Archean period and would typically result in several pulses of TTG magmatism, as seen in the Pietersburg block (Zeh and Gerdes, 2012; see Section 3.1 and Fig. 8) and several other terranes of that age (Figs. 9 and 11). Likewise, if one considers melting of subducted oceanic plateaus, the episodic production of the latter would account for successive pulses of TTG magmatism (Martin et al., 2014).

On the other hand, if late-Archean subduction was actually an unstable, transient process, then it was probably unable to drive plate tectonics efficiently (Moyen and van Hunen, 2012; O'Neill et al., 2007b; Sizova et al., 2010; van Hunen and van den Berg, 2008). Recently, Bédard et al. (2013) proposed a solution to this paradox proposing that nuclei of continental crust were actually the active tectonic agent, drifting in response to the entrainment of their stiff mantle keel in mantle convection currents. At their leading edges, such drifting proto-cratons would override oceanic, mafic crust or plateaus, which in turn would be buried deep in the mantle and eventually melt to produce "medium-" to "high-pressure" TTGs; a scenario equivalent to subduction from a geometric (and geochemical) point of view.

### 4.2. Second stage: genesis of sanukitoids s.l., biotite-, two-mica granites and hybrids

#### 4.2.1. Possible geodynamic environments

In all late-Archean terranes the granitoids emplaced during the second magmatic stage (sanukitoids s.l., biotite- and two-mica granites, hybrid granitoids) result from different degrees of interaction between two main source end-members: (i) the local continental crust and (ii) mantle peridotite metasomatically enriched in incompatible elements. This implies that both geochemical reservoirs were associated geometrically, and requires a thermal anomaly to account for their coeval melting. There are two different geodynamic environments which fit these constraints: (i) an event of terrane accretion (i.e. continental collision) where crustal thickening followed by slab breakoff, retreat or lithospheric delamination provides the required heat source (Dey et al., 2014; Feng and Kerrich, 1992; Halla et al., 2009; Heilimo et al., 2010; Laurent et al., 2013a, 2014; Mikkola et al., 2011b; Smithies et al., 2007; Whalen et al., 2004), or (ii) an intraplate setting, where the lithosphere is affected by a thermal event such as plume upwelling (Jayananda et al., 2000) or rifting and break-up of a stable continent (Smithies and Champion, 2000). Following most authors, we prefer the model of terrane amalgamation and continental collision, as discussed below.

#### 4.2.2. Continent–continent collision: analogy with post-Archean collisional granitoids

Clearly, the range of granitoids formed during the second stage of the late-Archean evolution are more akin to those formed in post-Archean collisional settings than intraplate environments. Indeed, calc-alkaline, K-rich granitoids generated in syn- to late-collisional contexts of <2.5 Ga-old orogens also derive from the respective contribution of local crust and metasomatized lithospheric mantle, whilst granitoids formed in purely intraplate settings are invariably alkaline and less diverse (Bonin, 2004; Clemens et al., 2009; Debon and Lemmet, 1999; Downes et al., 1997; Ferré et al., 1998; Frost et al., 2001; Harris et al., 1986; Liégeois et al., 1998; Turner et al., 1992). For

instance, Cenozoic magmatism in the Himalayas is characterized by the coexistence of high-K granitoids generated by melting of local crust (either metasediments for the High Himalayan Leucogranites or meta-igneous lithologies for calc-alkaline granitoids; e.g. Aikman et al., 2012; Chung et al., 2003; Guo and Wilson, 2012; Harrison et al., 1997, 1999; Le Fort et al., 1987; Reichardt et al., 2010; Zeng et al., 2011) and high-K calc-alkaline, shoshonitic to ultrapotassic, mafic and intermediate volcanics, derived from metasomatized phlogopite- and/or amphibole-bearing mantle peridotite (e.g. Gao et al., 2010; Mahéo et al., 2009; Miller et al., 1999; Williams et al., 2004; Xu et al., 2001; Zhao et al., 2009).

In order to support this analogy, we present here a comparison of the granitoids emplaced during the second stage of the late-Archean magmatic evolution with Paleozoic granitoids from the French Massif Central (FMC). There, erosion has exposed the mid-crustal levels of the Variscan orogenic belt and in particular, huge amounts of Carboniferous syn- to late-collisional granitoids. These granitoids can be classified into three groups (Fig. 12):

(1) Low $FeO_t$ + MgO (<10 wt.%) peraluminous muscovite- or cordierite-bearing granites, with moderate incompatible element contents (e.g. Couturié, 1977; Ledru et al., 2001; Turpin et al., 1990). All were generated by partial melting of a crustal (generally meta-sedimentary) source (Barbey et al., 1999; Williamson et al., 1992, 1997).
(2) High $FeO_t$ + MgO, metaluminous, intermediate to mafic ($SiO_2$ = 45–60 wt.%) monzo- and syenodiorites, rich in K and incompatible elements ($4 \leq K_2O \leq 9$ wt.%), locally referred to as "vaugnerites" (Aït-Malek, 1997; Couzinié et al., 2014; Galán et al., 1997; Gardien et al., 2011; Ledru et al., 2001; Michon, 1987; Montel and Weisbrod, 1986; Solgadi et al., 2007). Their genesis requires an enriched mantle source (e.g. Agranier, 2001; Couzinié et al., 2014; Debon and Lemmet, 1999; von Raumer et al., 2013).
(3) "Sub-alkaline" granites, which are K-rich, generally amphibole-bearing granitoids containing abundant microgranular mafic enclaves (e.g. Didier et al., 1989; Solgadi et al., 2007). These granitoids are believed to result from mixing or mingling of the previous two groups (Downes et al., 1997; Solgadi et al., 2007) which gave rise to a great variety of hybrid and heterogeneous phases.

As shown in Fig. 12, the composition of these three groups of granitoids from the FMC overlaps those of granitoids emplaced during the second stage of the late-Archean granitoid evolution. The "vaugnerites" are the richest in both ferromagnesian oxides and incompatible elements, thus displaying the same features as sanukitoids s.l. On the other hand, FMC peraluminous granites are comparable to late-Archean biotite- and two-mica granites, in the sense that they derive from similar petrogenetic processes, i.e. melting of the dominant crustal lithologies (which are mostly TTGs in Archean terrains and metasediments in post-Archean orogens, thus accounting for the limited occurrence of two-mica granites before 2.5 Ga). In addition, a variety of granitoids range between these two end-members, i.e. the late-Archean hybrid granitoids and the late Carboniferous "sub-alkaline" ones. Therefore, it can be reasonably concluded that the granitoids which characterize the second magmatic stage of the late-Archean evolution were generated in a syn- to late-collisional geodynamic environment.

This hypothesis is also supported by isotope data from late-Archean granitoids: the second stage of the magmatic evolution is indeed marked by a greater diversity of initial Nd–Hf isotope signatures than the first one, and notably of a spread towards less radiogenic compositions (see Figs. 9 and 11 and Section 3.2). In the post-Archean record, such distinct isotopic evolutions are generally observed when a convergent (i.e. subduction) environment turns into continental collision, for

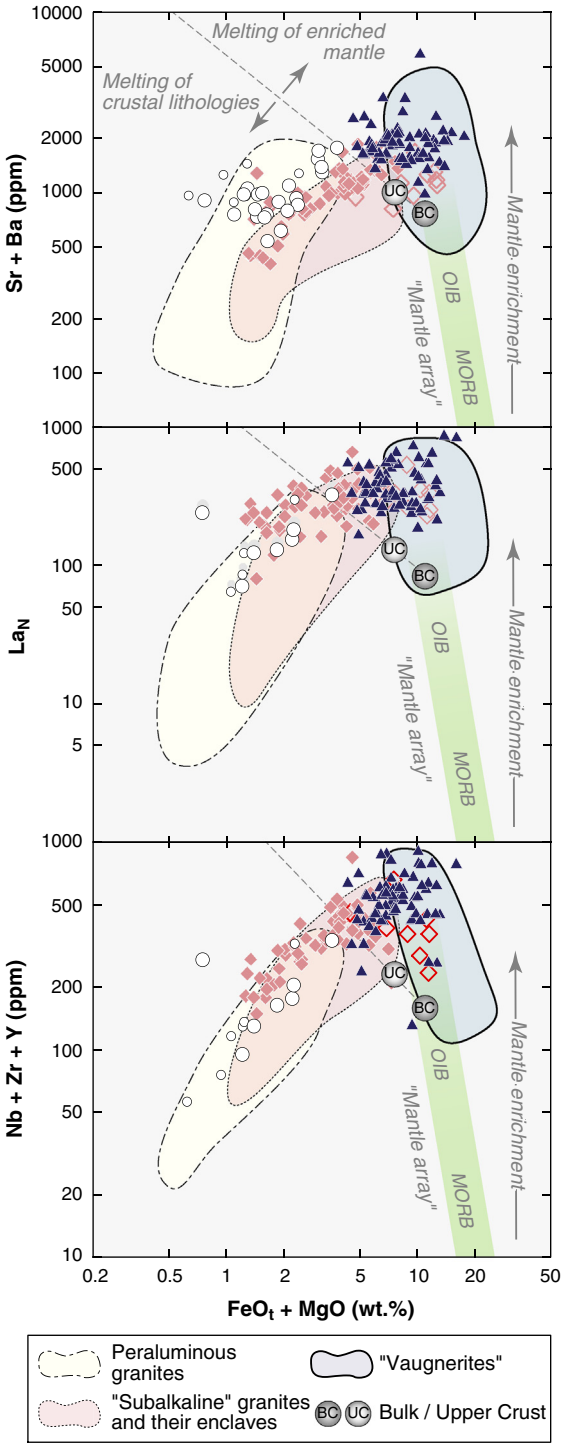


**Fig. 12.** Plots of incompatible element contents (Sr + Ba; La concentrations normalized to C1 chondrite value of McDonough and Sun, 1995; and sum of HFSE = Nb + Zr + Y) plotted as a function of $FeO_t$ + MgO (wt.%) concentrations. These plots illustrate the similarity between post-Archean, late-collisional granitoid associations (represented by the three groups of late-Variscan granitoids of the French Massif Central (FMC): "vaugnerites", peraluminous granites, "subalkaline" granites — coloured fields; database available on request), and the late-Archean granitoids emplaced during the second stage of the magmatic evolution discussed in Section 3: sanukitoids s.l., biotite-bearing granites and hybrid granitoids (represented by samples from the Pietersburg block; symbols as in Figs. 4 to 7). The composition of the average bulk and upper continental crust (data from Rudnick and Gao, 2003) as well as the composition of mantle-derived magmas (MORB and OIB) are also presented for comparison. The dashed line separating compositions of magmas derived from crustal- and enriched mantle sources is qualitatively represented by the "intracrustal" differentiation trend, i.e. the line joining the upper- and bulk crustal compositions.

example in the Lachlan fold belt in SE Australia (e.g. Hawkesworth et al., 2010; Kemp et al., 2009) or the Kohistan area in Pakistan (Bouilhol et al., 2013). The drift towards less radiogenic Nd–Hf isotope compositions is also very consistent with an increase in reworking and recycling processes, respectively associated with thickening of the crust during collision (genesis of biotite- and two-mica granites) and melting of "enriched" mantle sources with low Sm/Nd and Lu/Hf ratios during the post-collisional stage.

Finally, sanukitoids s.l., biotite-, two-mica granites and hybrid phases are either coeval or emplaced within a short time span immediately after the waning of TTG magmatism. This very specific evolution took place on a planetary scale between 3.0 and 2.5 Ga, but at slightly different times from one craton to another (see Section 3.1). If the activity of mantle plumes was at the origin of these granitoids, then plume upwelling would have taken place at different times from place to place, but always immediately after a period of TTG magmatism, which is implausible. Moreover, there is a strong structural control on granitoid emplacement during the second stage: magmas specifically intrude along crustal-scale structures (Champion and Sheraton, 1997; Jayananda et al., 1995; Moyen et al., 2001), at the boundaries between distinct crustal domains (Bibikova et al., 2005; Heilimo et al., 2010; Lobach-Zhuchenko et al., 2005; van Kranendonk et al., 2007) and/or in association with regional tectono-metamorphic overprints (Laurent et al., 2011, 2014). In addition, in a given cratonic area, late-Archean granulites are generally coeval with the granitoids emplaced during the second stage of the magmatic evolution (Percival, 1994). All lines of evidence thus support the granitoids being spatially and temporally associated with terrane amalgamation rather than a plume or rifting event.

#### 4.2.3. The meaning of "continent–continent collision"

The terminology of "continent–continent collision" that we use here has a very general meaning and refers primarily to the amalgamation of two continental blocks. Continental collision can be accommodated by different orogenic styles, including retreating or advancing plate boundaries followed by collision proper, which can itself take place and evolve according to different scenarios (such as slab retreat, break-off, or ongoing convergence and formation of an orogenic plateau) depending on the thermo-mechanical conditions of the system (Cawood et al., 2009; Duretz and Gerya, 2013; Vanderhaeghe, 2010; and references therein). These different possibilities vary primarily in terms of geothermal gradients, kinematics, deformation patterns and extent of crustal thickening (which can be limited, for example in the case of a "hot" or retreating orogen). Nevertheless, we emphasize here that the common factor in all these scenarios is the involvement of both metasomatized mantle and crustal lithologies in the genesis of granitoid magmas, irrespective of the geometry of the system and the heat source at the origin of crust and lithospheric mantle melting.

### 4.3. A global geodynamic model

The above evidence points to the evolution of late-Archean granitoids recording an episode of subduction (first stage) and subsequent continent–continent collision (second stage). This conclusion is consistent with those of previous studies focusing on the diversity of late-Archean granitoids in a given cratonic area (Almeida et al., 2011, 2013; Dey et al., 2014; Feng and Kerrich, 1992; Halla et al., 2009; Käpyaho et al., 2006; Moyen et al., 2003; Smithies and Champion, 2000; Whalen et al., 2004) and with reviews of geodynamic evolution in individual Archean terranes (Percival et al., 2006; Smithies et al., 2007; van Kranendonk et al., 2007). Hence, a tentative, generic geodynamic evolution for late-Archean terranes is proposed in Fig. 13. During the first stage, subduction takes place with possible episodic break-off and foundering of "rafts" of basaltic oceanic crust and/or oceanic plateaus (Fig. 13a). This leads to (i) several pulses of juvenile TTG magmatism over a long period of time and (ii) metasomatism of the overlying "mantle wedge" by fluids or melts derived from metabasalts (i.e. TTGs) and/or crust-derived, terrigenous sediments. Subduction can take place either along a pre-existing, Paleoarchean continental nucleus (e.g. in the northern Kaapvaal Craton) or in an "intra-oceanic" setting, for instance beneath a thick and recent oceanic plateau (Almeida et al., 2011, 2013; Halla et al., 2009) (Fig. 13a; see also Section 4.1). Ultimately, this first stage leads to the closure of an oceanic basin and welding of two (proto)continental blocks (continental collision). At that stage, sanukitoids s.l. can be generated by significant interaction between the last TTG melts and peridotite, whilst thickening of the crust triggers its partial melting, giving rise to biotite- and two-mica granites (Fig. 13b). Sanukitoid s.l. can also be emplaced during the late- to post-collisional period owing to thermal relaxation and extension, which induce melting of the previously enriched lithospheric mantle (Fig. 13c). Slab break-off, slab retreat or lithosphere delamination, which is likely to take place in the late- to post-collisional stages (e.g. Bonin, 2004; Duretz and Gerya, 2013; Liégeois et al., 1998; van Hunen and Allen, 2011;

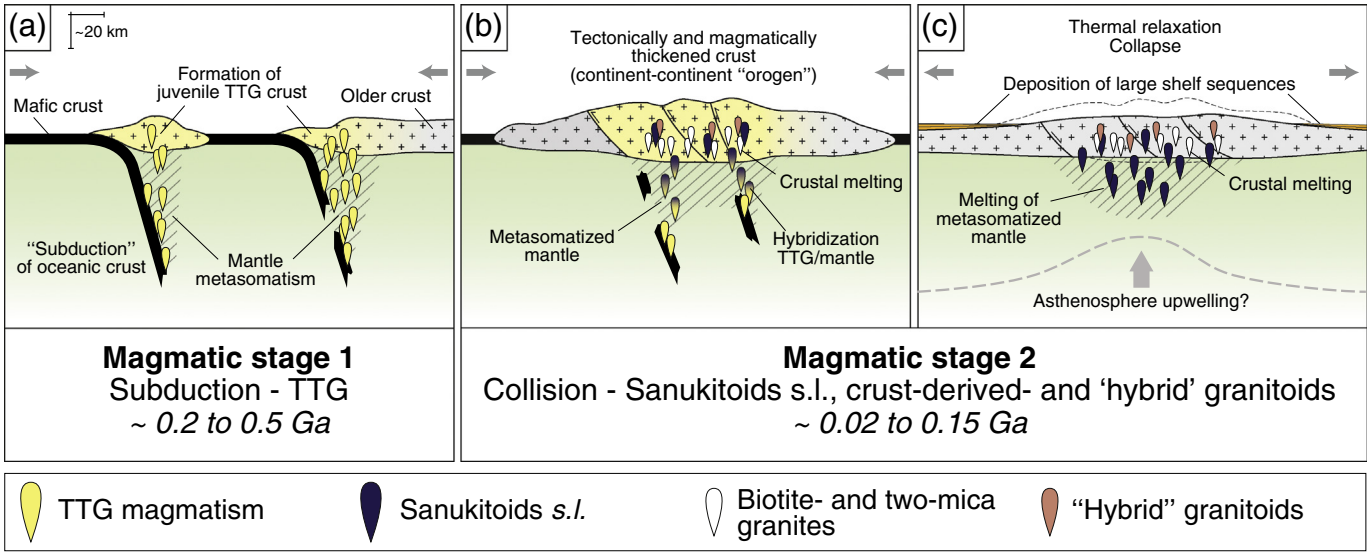


**Fig. 13.** Synthetic, conceptual cartoon illustrating the proposed geodynamic environment corresponding to the evolution of late-Archean granitoids, i.e. a subduction–collision sequence. See text for discussion.

Vanderhaeghe, 2010), has been consistently proposed as tectonic triggers for the generation of sanukitoids s.l. (Almeida et al., 2013; Halla et al., 2009; Laurent et al., 2014; Lobach-Zhuchenko et al., 2008; Mikkola et al., 2011b; Whalen et al., 2004). The resulting thermal anomaly can also promote further crustal anatexis. During both syn- (Fig. 13b) and late-collisional (Fig. 13c) periods, interaction between sanukitoids s.l. and crust-derived melts potentially generates a wide spectrum of hybrid granitoids.

Depending on local conditions, such as the composition of the sources involved in magma genesis, the nature of the resulting granitoids can vary from one craton to another. This reliably explains (i) why some granitoid types are more common in certain cratons than others, and (ii) the internal differences within each group from distinct terranes. On the other hand, as shown in Fig. 13b–c, the granitoids related to the second magmatic stage can be generated at different periods during continent-continent collision, adequately explaining the differences in the relative and absolute chronology of granitoid emplacement from one craton to another. Furthermore, the geometry of the system and orogenic style are also likely to play a role. For instance, the Pietersburg block is believed to have formed as a "Cordilleran" convergent margin, with successive accretion of microcontinents at the northern edge of the Kaapvaal craton (e.g. Zeh et al., 2013). In this context, a protracted period of crustal reworking and mantle enrichment would be expected, explaining the long duration of the second stage (~0.15 Ga) relative to other cratons (see Figs. 8 and 9).

## 5. The onset of "modern-style" plate tectonics

### 5.1. Comparison with Eo- to Mesoarchean granitoids

A two-stage evolution of granitoid magmatism, from dominant TTG magmas to the emplacement of high-K granites, has also been reported in some early Archean terranes: (i) the area of the Barberton greenstone belt (southeastern Kaapvaal Craton; see Fig. 1) between ~3.55 and ~3.09 Ga (Clemens et al., 2010; Kamo and Davis, 1994; Sanchez-Garrido et al., 2011; Yearron, 2003; Zeh et al., 2009); (ii) the North Atlantic Craton (Greenland) between ~3.85 and ~3.50 Ga (Friend and Nutman, 2005; Nutman et al., 2007, 2013); and (iii) the East Pilbara Craton (NW Australia) between ~3.50 and ~3.25 Ga (Barley and Pickard, 1999; Bickle et al., 1989; van Kranendonk et al., 2007).

For each region, when these granitoids are plotted in the ternary synthetic classification diagram (see Fig. 7 and Section 2.5), the oldest granitoids match the "TTG field", whilst the youngest one show more diversity (Fig. 14). In the case of the East Pilbara (Fig. 14a) and SW Greenland (Fig. 14b), these "second-stage" granitoids spread between the fields of the biotite- and two-mica granites, on one hand, and that of the TTGs, on the other hand. However, both terranes strikingly lack a sanukitoid s.l. component (Fig. 14a–b), and are therefore not equivalent to late-Archean domains. The situation is rather different in the Barberton area where some samples of the ~3.1 Ga-old Granite–Monzogranite–Syenite (GMS) suite plot within the field of sanukitoids s.l. (Fig. 14c). Although these samples are subordinate in volume, they possibly depict the involvement of enriched mantle sources, which is consistent with the proposed occurrence of a ≥3.23 Ga-old subduction event in this area (Moyen et al., 2006). Therefore, the evolution of granitoids in the Barberton region possibly results from successive subduction and collision, thus representing an early example of the late-Archean magmatic sequence described in this review.

However, to our knowledge, the diversity of granitoids reported in the Barberton area has no older equivalent. This means that the typical late Archean granitoid evolution as described here is either lacking, or very unusual, in terranes older than 3.0 Ga. In contrast, and despite some local differences, it took place in almost every Archean craton between 3.0 and 2.5 Ga. Since this magmatic evolution is very similar

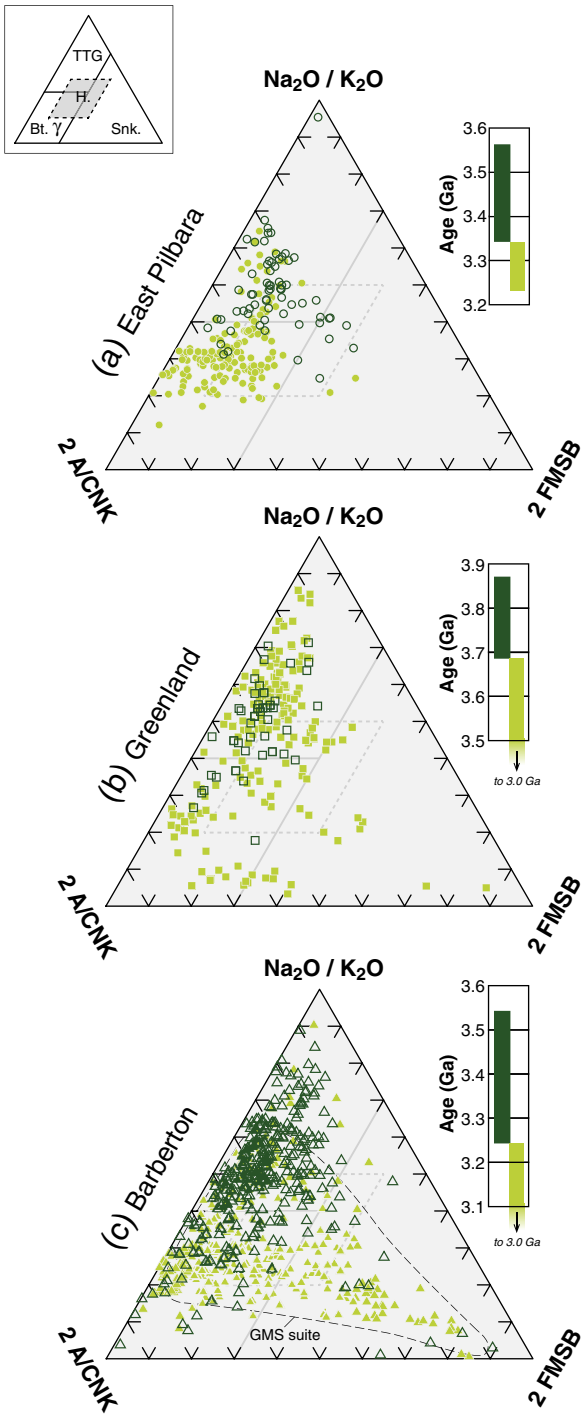


**Fig. 14.** Comparison of early Archean (>3.0 Ga-old) granitoids with the fields of late-Archean (3.0–2.5 Ga) granitoids (inset in the top left corner; Snk. = sanukitoids s.l., Bt. γ = biotite- and two-mica granites, H. = hybrids) in the synthetic classification diagram of Fig. 7 (see also Section 2.5). Early Archean data are from three different Paleo- to Mesoarchean terranes in which a secular evolution of granitoid compositions has been reported: (a) the East Pilbara Craton, NW Australia; (b) SW Greenland; (c) the area of the Barberton Greenstone Belt, South Africa. In a given area, granitoids are classified into two groups: (i) "early" granitoids (open dark green symbols) and (ii) "late" granitoids (filled light green symbols) on the basis of published models for crustal evolution in these terranes. The adjacent timelines indicate the approximate age range for each group. In (c), the dashed field encloses samples of the Granite–Monzogranite–Syenite (GMS) suite of the Barberton region. Data are from published or personal databases (Moyen, 2011; Moyen and Martin, 2012; J.F. Moyen).

to that of modern subduction–collision settings (see Section 4), it can be concluded that such geodynamic mechanisms have only been operating globally since 3.0 Ga. Thus, whilst subduction and continental collision could have taken place before 3.0 Ga as discrete events in both space and time, it is only from the late-Archean that global plate tectonics were characterized by a cyclic pattern of successive assembly and break-up of continental masses, with the late-Archean evolution being the very first of these cycles.

### 5.2. Support from other geological evidence

Our interpretation of the late-Archean granitoid evolution is supported independently: (i) the chemistry of continental basalts changed across the Archean–Proterozoic boundary, reflecting an evolution towards LILE-richer mantle sources (Condie, 1989; Keller and Schoene, 2012; Smithies et al., 2004, 2007), which is consistent with the initiation of crustal recycling into the mantle owing to either rising volumes of continental crust or increasingly efficient subduction processes; (ii) Hf and O isotopic compositions of detrital and magmatic zircons indicate changes in crustal growth rates and granitoid sources at 3.0–2.5 Ga, interpreted as the onset of subduction- and collision-driven continental recycling (Dhuime et al., 2011; Valley et al., 2005); (iii) Shirey and Richardson (2011) noted that lithospheric inclusions in diamond crystals changed from peridotitic to peridotitic and eclogitic at ~3.0 Ga, interpreted as reflecting the initiation of subduction and collision processes; (iv) the appearance of shelf sequences and mature sediments in supracrustal lithologies, typical of Wilson cycles, at the end of the Archean (Veizer and McKenzie, 2003) and (v) the style of crustal deformation changed from the late Archean to the middle Proterozoic, with an increasing number of orogenic belts characterized by predominantly horizontal deformation and focused high-strain zones (Cagnard et al., 2011; Chardon et al., 2009; Smithies et al., 2007).

In addition, Wilson cycles are characterized by a global balance between crustal formation and crustal recycling into the mantle, such that the net continental growth is presently close to zero (Cawood et al., 2009; Clift and Vannucchi, 2004; Clift et al., 2009; Hawkesworth et al., 2010; Scholl and von Huene, 2009). Many studies pointed out that the crustal growth rate significantly decreased between 3.0 and 2.0 Ga ago, i.e. by the end of the Archean (Dhuime et al., 2011; Guitreau, 2012; Kramers and Tolstikhin, 1997; Taylor and McLennan, 1985, 1995), confirming that modern Wilson cycles were not operating efficiently prior to that. This observation is also supported by the present study (see Section 3.2), which shows that late-Archean granitoids derived largely from crustal recycling processes (intracrustal melting; introduction of crustal-derived material and formation of metasomatized mantle; see also Figs. 10 and 11). Hence, the geodynamic changes at the Archean–Proterozoic transition also correspond to a major shift in the balance between growth and recycling rates of the continental crust.

### 5.3. Possible origins of the changes

Because of the higher heat flux from the mantle, Archean oceanic crust was thicker, more buoyant and less coupled to the underlying convective mantle (e.g. Abbott et al., 1994; Hargraves, 1986; O'Neill et al., 2007a,b; van Thienen et al., 2004). This must have resulted in smaller-scale, less coherent and "weaker" Archean subduction, unable to drive plate tectonic processes and Wilson cycles efficiently as it presently does (Moyen and Martin, 2012; O'Neill et al., 2007b; Sizova et al., 2010; Moyen and van Hunen, 2012; van Hunen and van den Berg, 2008; see also Section 4.1.3). Abbott et al. (1994) proposed that, besides its composition, the thickness and temperature of oceanic crust exert a first-order control on its capacity to subduct. They concluded that modern, steep subduction geometry could only be achieved with a relatively thin (<10 km), cold crust (Fig. 15a). They calculated that most oceanic crust reached the 10 km thickness threshold between ~2.5 and ~2.0 Ga (Fig. 15a), thus "modern" behaviour could not be adopted until the very end of the Archean. This threshold would actually have been reached somewhat earlier (~3.0 Ga) considering that komatiites associated with basalts in the oceanic crust would have significantly decreased its buoyancy (Barbey and Martin, 1987; Johnson et al., 2013; Martin et al., 2014). Alternatively, Hargraves (1986) proposed that a higher heat production in the early Earth could have been accommodated by increasing the ridge length rather than the thickness of oceanic crust. In this case, the size of oceanic plates would have been smaller than today (de Wit and Hart, 1993; Lagabrielle et al., 1997), and the geometry of subduction systems different. If this was the case, then the establishment of "modern-style", stable subduction zones by the end of the Archean reflects a progressive increase in oceanic plate size.

The emergence of continental collision and the increasing importance of reworking processes at the end of the Archean are due to an evolution of both the volume and thermo-mechanical characteristics of continental crust. Firstly, a trivial but fundamental parameter is that, before being able to recycle continental crust, a significant volume of this crust must already exist. Hence, the late-Archean period follows a long period of predominantly juvenile magmatism (Dhuime et al., 2011; Guitreau, 2012; Kramers and Tolstikhin, 1997; Taylor and McLennan, 1985, 1995; Fig. 15b) and thus marks the moment when the volume of the continental blocks became sufficient for them to be welded to each other to form collisional belts, and undergo significant internal differentiation (producing large amounts of anatectic granite, i.e. biotite- and two-mica granites). Secondly, these mechanisms depend not only on the volume of continental crust, but also on its ability to thicken and to maintain thickening during a sufficiently long time for the recycling mechanisms to start and develop. In other words, continental crust must be stiff enough for deformation to be focused along sub-linear orogenic belts. England and Bickle (1984) and Rey and Coltice (2008) proposed that due to higher Archean heat flux, the continental crust was weaker and unable to sustain thicknesses >30 km, such that collision between crustal blocks did not result in the formation of collisional belts at plate boundaries. Instead, deformation of Archean continental crust was dominated by volume forces, coaxial shortening and lateral flow rather than sustainable vertical thickening (Chardon et al., 2009; Choukroune et al., 1995; England and Bickle, 1984; Rey and Coltice, 2008; Thébaud and Rey, 2013). Specifically, Rey and Coltice (2008) proposed that the continental crust was too hot and weak to sustain high topographic anomalies (>2 km) until 2.5 Ga ago (Fig. 15c). Therefore, collisional orogens would have become stable only from 3.0 to 2.5 Ga (Fig. 15c).

Importantly, the strength of the crust, and thus its capacity to sustain high topography, has important implications for hypsometry. It has been proposed that continental emersion was not significant until the late-Archean (Flament et al., 2008; Rey and Coltice, 2008), resulting in a major obstacle to the establishment of effective sedimentary cycles before ~3.0 Ga. The absence of thick sedimentary deposits on the oceanic crust (coupled to less efficient subduction processes) implies that the recycling of sediments into the mantle remained negligible until that time. The emergence of sanukitoids s.l., some of which required a sediment-metasomatized mantle source (Halla, 2005; King et al., 1998; Laurent et al., 2011, 2014; Lobach-Zhuchenko et al., 2008; Mikkola et al., 2011b), is therefore a good chronological marker of the onset of crustal recycling into the mantle.

To summarize, the establishment of "modern-style" subduction–collision mechanisms depended on several different parameters, namely the thickness, temperature, composition and rheology of oceanic and continental crusts as well as the net volume of continental material. However, as noted by Moyen and Martin (2012), the single mechanism that controls all these parameters is the evolution of the Earth's thermal regime. This global control over a number of local parameters adequately accounts for the ambiguous nature of the late-Archean geodynamic changes: they follow a global scheme (similar magmatic evolution in

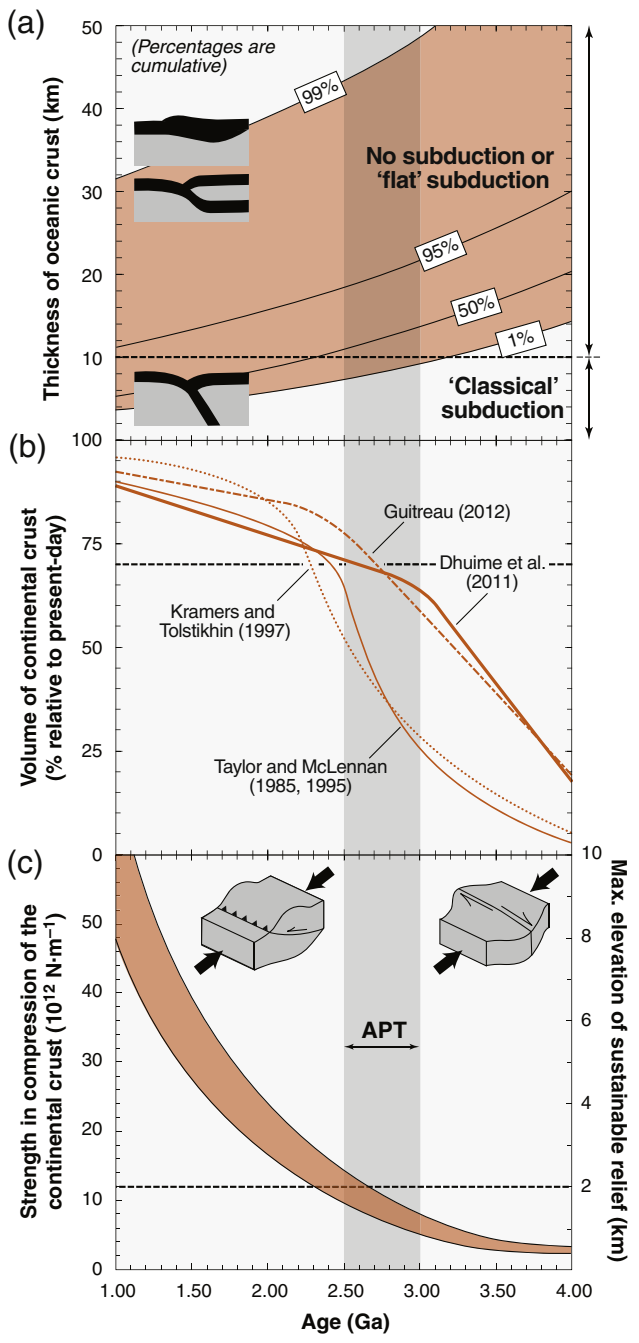


**Fig. 15.** Evolution of some key properties of the oceanic and continental crusts between 4.0 and 1.0 Ga, being possible causes for the onset of "modern-style" plate tectonics during the Archean–Proterozoic Transition (APT): (a) progressive thinning of the oceanic crust through time, according to thermal models (modified after Abbott et al., 1994). Between 2.0 and 3.0 Ga, ~50% of oceanic crust became thinner than 10 km, the "threshold" below which "classic" subduction is stable; (b) several models of crustal growth, all predicting that at the end of the Archean, ~70% of the present-day volume of continental crust was already formed. This highlights the switch from dominantly juvenile to dominantly recycling processes at that time; (c) stiffening of the continental crust through time, as a result of its cooling. The compressive strength of the crust increased significantly (by a factor of 2) during the last 0.5 Ga of the Archean, so that at the end of this period it was able to sustain positive topographic anomalies of >2 km, i.e., collisional orogens (modified after Rey and Coltice, 2008). See text for discussion.

every craton, within a relatively short time span on a planetary scale) but with local characteristics (different ages from one craton to another; diversity in magma sources and relative chronology).

## 6. Summary and concluding remarks

This review shows that 3.0- to 2.5 Ga-old granitoids are very diverse, in relation to the TTG-dominated magmatic record of >3.0 Ga. These late-Archean granitoids can be separated into four groups:

(1) TTGs, i.e. volumetrically dominant low-K tonalites, trondhjemites and granodiorites, which were generated from melting of hydrous, meta-igneous mafic rocks. Melting took place principally at great depth (>35 km);
(2) Sanukitoids s.l., i.e. (Fe + Mg)- and K-rich magmas (monzodiorites, monzogabbros and their differentiation products) derived from interaction between mantle peridotite and an incompatible element-rich component;
(3) Biotite- and two-mica-bearing, peraluminous and high-K granites derived from melting of pre-existing crustal lithologies, i.e. older TTGs and metasediments;
(4) hybrid granitoids with a wide range of petrographic and geochemical characteristics, resulting from interaction between magmas or source rocks from the first three groups.

The emplacement of these different granitoid groups follows a very typical, two-stage sequence in all Archean cratons worldwide: (i) a long period (0.2 to 0.5 Ga) of exclusively TTG magmatism, followed by (ii) a shorter stage (0.02–0.15 Ga) during which all the other granitoid groups were emplaced. This peculiar evolution, coupled to available Nd–Hf isotope data on late-Archean granitoids, shows that juvenile crust generation through TTG magmatism gave way to crustal recycling at two distinct levels, i.e. by classic intracrustal differentiation, and introduction of crustal-derived material into the mantle as a source component for sanukitoids s.l.

Both the nature of the granitoids related to the two stages and duration of these stages are consistent with a subduction–collision evolution. In particular, granitoids emplaced in modern collisional settings closely resemble those of the second stage, being characterized by coeval involvement of metasomatized mantle sources, and intracrustal melting. This type of evolution is scarce in the >3.0 Ga-old Archean record, and takes place only locally, indicating that the global extent of late-Archean geodynamic changes likely heralds the initiation of subduction–collision (Wilson) cycles on a planetary scale and thus of "modern-style" plate tectonic processes.

This late-Archean change in global geodynamics likely resulted from the evolution of several parameters, such as the thickness, temperature and rheology of oceanic and continental crusts, as well as an increase in the global volume of continents. In summary, the onset of "modern-style" plate tectonics resulted from the stabilization, by the end of the Archean, of lithospheric plates that were large, cold and stiff enough to undergo subduction and collision. This complex interplay of several factors induced local differences from one craton to another, but the overall evolution depended on a single, unifying mechanism: the progressive cooling of the Earth. As a result of this global control, the late-Archean geodynamic changes took place within a relatively short period (~0.5 Ga) and affected the whole planetary system.

## Acknowledgements

This work was principally funded by two scientific co-operations between France and South Africa, the PICS n°4828 as well as the !Khure programme, and was also supported by the European Research Council (ERC StG 279828). This paper was originally requested on the basis of an abstract presented at the EGU General Assembly 2012, and O.L.'s participation to this conference was possible thanks to funding by Région Auvergne. We are grateful to N. Eby and T. Horscroft for their invitation, their kind editorial assistance and their patience throughout the preparation of the manuscript. We also appreciated the detailed and constructive reviews by R. Dall'Agnol and an anonymous referee that contributed to significantly improve the original manuscript. We

would like to thank many colleagues for fruitful discussion regarding the ideas presented in this paper, in particular J.H. Bédard, S. Block, B. Bonin, L.S. Doucet, J. Halla, E. Heilimo, G. Stevens, A. Villaros and A. Zeh. We also thank F. van Wyk de Vries for her corrections of the English language. This research was financed by the French Government Laboratory of Excellence initiative n°ANR-10-LABX-0006 and the European Regional Development Fund. This is Laboratory of Excellence ClerVolc contribution number 108.

## Appendix A. Supplementary data

Supplementary data to this article can be found online at http://dx.doi.org/10.1016/j.lithos.2014.06.012.

## References

Abbott, D., Drury, R., Smith, H.F.S., 1994. Flat to steep transition in subduction style. Geology 22, 937–940.
Agranier, A., 2001. Un exemple de magmatisme ultrapotassique syn-orogénique: les lamprophyres du Massif Central Français. Approche géochimique et géochronologique. Unpublished M.Sc. thesis, Université Blaise Pascal, Clermont-Ferrand II, 51 pp.
Aikman, A.B., Harrison, T.M., Hermann, J., 2012. The origin of Eo- and Neo-himalayan granitoids, Eastern Tibet. Journal of Asian Earth Sciences 58, 143–157.
Aït-Malek, H., 1997. Pétrologie, géochimie et géochronologie U/Pb d'associations acide-basiques: exemples du SE du Velay (Massif central français) et de l'anti-Atlas occidental (Maroc). Unpublished Ph.D. thesis, Université de Nancy, 297 pp.
Almeida, J.A.C., Dall'Agnol, R., Dias, S.B., Althoff, F.J., 2010. Origin of the Archean leucogranodiorite–granite suites: evidence from the Rio Maria terrane and implications for granite magmatism in the Archean. Lithos 120, 235–257.
Almeida, J.A.C., Dall'Agnol, R., Leite, A.A.S., 2013. Geochemistry and zircon geochronology of the Archean granite suites of the Rio Maria granite–greenstone terrane, Carajás Province, Brazil. Journal of South American Earth Sciences 42, 103–126.
Almeida, J.A.C., Dall'Agnol, R., Oliveira, M.A., Macambira, M.J.B., Pimentel, M.M., Rämö, O.T. , Guimarães, F.V., Leite, A.A.S., 2011. Zircon geochronology, geochemistry and origin of the TTG suites of the Rio Maria granite–greenstone terrane: implications for the growth of the Archean crust of the Carajás Province, Brazil. Precambrian Research 187, 201–221.
Althoff, F.J., 1996. Étude pétrologique et structurale des granitoïdes de Marajoara (Pará, Brésil): leur rôle dans l'évolution archéenne du craton Amazonien (2.7–3.2 Ga). Unpublished Ph.D thesis. Université Henri Poincaré, Nancy I, France, 296 pp.
Althoff, F.J., Barbey, P., Boullier, A.M., 2000. 2.8–3.0 Ga plutonism and deformation in the SE Amazonian craton: the Archean granitoids of Marajoara (Carajás Mineral province, Brazil). Precambrian Research 104, 187–206.
Armstrong, R.L., 1981. Radiogenic isotopes: the case for crustal recycling on a near-steady-state no-continental-growth Earth. Philosophical Transactions of the Royal Society of London A 301, 443–472.
Atherton, M.P., Petford, N., 1993. Generation of sodium-rich magmas from newly underplated basaltic crust. Nature 362, 144–146.
Bagai, Z., Armstrong, R., Kampunzu, A.B., 2002. U– Pb single zircon geochronology of granitoids in the Vumba granite – greenstone terrain (NE Botswana): implication for the Archaean Zimbabwe craton. Precambrian Research 118, 149–168.
Barbey, P., Martin, H., 1987. The role of komatiites in plate tectonics: evidence from the Archaean and early Proterozoic crust in the eastern Baltic shield. Precambrian Research 35, 1–14.
Barbey, P., Marignac, C., Montel, J.M., Macaudière, J., Gasquet, D., Jabbori, J., 1999. Cordierite growth textures and the conditions of genesis and emplacement of crustal granitic magmas: the Velay granite complex (Massif Central, France). Journal of Petrology 40 (9), 1425–1441.
Barley, M.E., Pickard, A.L., 1999. An extensive, crustally-derived, 3325 to 3310 Ma silicic volcanoplutonic suite in the eastern Pilbara Craton: evidence from the Kelly Belt, McPhee Dome and Corunna Downs Batholith. Precambrian Research 96, 41–62.
Barker, F., Arth, J.G., 1976. Generation of trondhjemitic–tonalitic liquids and Archaean bimodal trondhjémite-basalt suites. Geology 4 (10), 596–600.
Barton Jr., J.M., Klemd, R., Zeh, A., 2006. The Limpopo Belt: a result of Archean to Proterozoic, Turkic-type orogenesis? Geological Society of America, Special Paper 405, 315–332.
Beard, J.S., Lofgren, G.E., 1991. Dehydration melting and water-saturated melting of basaltic and andesitic greenstones and amphibolites at 1, 3 and 6.9 kbar. Journal of Petrology 32 (2), 365–401.
Bédard, L.P., 1996. Archaean high-Mg monzodiorite plutonic suite: a reevaluation of the parental magma and differentiation. The Journal of Geology 104, 713–728.
Bédard, J.H., 2006. A catalytic delamination-driven model for coupled genesis of Archaean crust and sub-continental lithospheric mantle. Geochimica Cosmochimica Acta 70, 1188–1214.
Bédard, J.H., 2013. How many arcs can dance on the head of a plume? A 'Comment' on: a critical assessment of Neoarchaean 'plume only' geodynamics: evidence from the Superior Province, by Derek Wyman, Precambrian Research, 2012. Precambrian Research 229, 189–197.
Bédard, J.H., Brouillette, P., Madore, L., Berclaz, A., 2003. Archaean cratonization and deformation in the northern Superior Province, Canada: an evaluation of plate tectonic versus vertical tectonic models. Precambrian Research 127, 61–87.
Bédard, J.H., Harris, L.B., Thurston, P., 2013. The hunting of the snArc. Precambrian Research 229, 20–48.
Belousova, E.A., Kostitsyn, Y.A., Griffin, W.L., Begg, G.C., O'Reilly, S.Y., Pearson, N.J., 2010. The growth of the continental crust: constraints from zircon Hf-isotope data. Lithos 119 (3–4), 457–466.
Bibikova, E.V., Petrova, A., Claesson, S., 2005. The temporal evolution of sanukitoids in the Karelian Craton, Baltic Shield: an ion microprobe U–Th–Pb isotopic study of zircons. Lithos 79, 129–145.
Bibikova, E.V., Lobach-Zhuchenko, S.B., Artemenko, G.B., Claesson, S., Kovalenko, A.V., Krylov, I.N., 2008. Late Archean magmatic complexes of the Azov Terrane, Ukrainian Shield: geological setting, isotopic age, and sources of material. Petrology 16 (3), 211–231.
Bickle, M.J., Bettenay, L.F., Chapman, H.J., Groves, D.I., McNaughton, N.J., Campbell, I.H., de Laeter, J.R., 1989. The age and origin of younger granitic plutons of the Shaw Batholith in the Archaean Pilbara Block, Western Australia. Contributions to Mineralogy and Petrology 101, 361–376.
Bleeker, W., 2003. The late Archean record: a puzzle in ca. 35 pieces. Lithos 71, 99–134.
Blichert-Toft, J., Puchtel, I.S., 2010. Depleted mantle sources through time: evidence from Lu–Hf and Sm–Nd isotope systematics of Archean komatiites. Earth and Planetary Science Letters 297, 598–606.
Block, S., Moyen, J.-F., Zeh, A., Poujol, M., Jaguin, J., Paquette, J.-L., 2013. The Murchison Greenstone Belt. South Africa: accreted slivers with contrasting metamorphic conditions. Precambrian Research 227, 77–98.
Bonin, B., 2004. Do coeval mafic and felsic magmas in post-collisional to within-plate regimes necessarily imply two contrasting, mantle and crustal, sources? A review. Lithos 78, 1–24.
Bouilhol, P., Jagoutz, O., Hachar, J.M., Dudas, F.O., 2013. Dating the India-Eurasia collision through arc magmatic records. Earth and Planetary Science Letters 366, 163–175.
Bowring, S.A., Williams, I.S., 1999. Priscoan (4.00–4.03 Ga) orthogneisses from northwestern Canada. Contributions to Mineralogy and Petrology 134, 3–16.
Brandl, G., Kröner, A., 1993. Preliminary results of single zircon studies from various Archaean rocks of the northeastern Transvaal. Ext. Abstr. 16th International Colloquium of African Geology, Mbabane, Swaziland, pp. 54–56.
Brandl, G., Jaeckel, P., Kröner, A., 1996. Single zircon age for the felsic Rubbervale Formation, Murchison greenstone belt, South Africa. South African Journal of Geology 99 (3), 229–234.
Breaks, F.W., Moore, J.M., 1992. The Ghost Lake batholith, Superior Province of Northwestern Ontario: a ferile, S-type, peraluminous granite — rare-element pegmatite system. Canadian Mineralogist 30, 835–875.
Brown, M., 2006. A duality of thermal regimes is the distinctive characteristic of plate tectonics since the Neoarchean. Geology 34, 961–964.
Cagnard, F., Barbey, P., Gapais, D., 2011. Transition between "Archaean-type" and "modern-type" tectonics: insights from the Finnish Lapland Granulite Belt. Precambrian Research 187, 127–142.
Cassidy, K.F., Barley, M.E., Groves, D.I., Perring, C.S., Hallberg, J.A., 1991. An overview of the nature, distribution and inferred tectonic setting of granitoids of the late-Archaean Norseman–Wiluna Belt. Precambrian Research 51, 51–83.
Cawood, P., Kröner, A., Collins, W.J., Kusky, T.M., Mooney, W.D., Windley, B.F., 2009. Accretionary orogens through Earth history. Geological Society of London Special Publications 318, 1–36.
Champion, D.C., Sheraton, J.W., 1997. Geochemistry and Nd isotope systematics of Archaean granites of the Eastern Goldfields, Yilgarn Craton, Australia: implications for crustal growth processes. Precambrian Research 83 (1–3), 109–132.
Champion, D.C., Smithies, R.H., 1999. Archaean granites of the Yilgarn and Pilbara cratons, Western Australia: secular changes. In: Barbarin, B. (Ed.), The Origin of Granites and Related Rocks—IVth Hutton Symposium Abstracts Doc. BRGM, 290, p. 137.
Champion, D.C., Smithies, R.H., 2003. Archaean granites. In: Blevin, P.L., Chappell, B.W., Jones, M. (Eds.), Magmas to Mineralisation: the Ishihara Symposium. AGSOGeoscience Australia, pp. 19–24 (Record 2003/14).
Champion, D.C., Smithies, R.H., 2007. Geochemistry of Paleoarchean granites of the East Pilbara Terrane, Pilbara Craton, Western Australia: implications for early Archean crustal growth. In: van Kranendonk, M.J., Smithies, R.H., Bennett, V.C. (Eds.), Earth's Oldest Rocks, Developments in Precambrian Geology, vol. 15. Elsevier, Amsterdam, pp. 369–410.
Chardon, D., Gapais, D., Cagnard, F., 2009. Flow of ultra-hot orogens: a view from Precambrian, clues for the Phanerozoic. Tectonophysics 477 (3–4), 105–118.
Chung, S.-L., Liu, D., Ji, J., Chu, M.-F., Lee, H.-Y., Wen, D.-J., Lo, C.-H., Lee, T.-Y., Qian, Q., Zhang, Q., 2003. Adakite from continental collision zones: melting of thickened lower crust beneath southern Tibet. Geology 31, 1021–1024.
Choukroune, P., Bouhallier, H., Arndt, N.T., 1995. Soft lithosphere during periods of Archean crustal growth or crustal reworking. In: Coward, M.P., Ries, A.C. (Eds.), Early Precambrian Processes. Geological Society Special Publications, 95, pp. 67–86.
Clemens, J.D., Belcher, R.W., Kisters, A.F.M., 2010. The Heerenveen batholith, Barberton Mountain Land, South Africa: Mesoarchaean, potassic, felsic magmas formed by melting of an ancient subduction complex. Journal of Petrology 51 (5), 1099–1120.
Clemens, J.D., Darbyshire, D.P.F., Flinders, J., 2009. Sources of post-orogenic calcalkaline magmas: the Arrochar and Garabal Hill–Glen Fyne complexes, Scotland. Lithos 112, 524–542.
Clift, P., Vannucchi, P., 2004. Controls on tectonic accretion versus erosion in subduction zones: implications for the origin and recycling of the continental crust. Reviews of Geophysics 42, 1–31.
Clift, P., Schouten, H., Vannucchi, P., 2009. Arc–continent collisions, sediment recycling and the maintenance of the continental crust. In: Cawood, P.A., Kröner, A. (Eds.), Accretionary Orogens in Space and Time. Geological Society of London, Special Publications, 318, pp. 75–103.

Condie, K.C., 1981. Archaean greenstone belts. In: Windley, B.F. (Ed.), Developments in Precambrian Geology, 3 (434 pp.).
Condie, K.C., 1989. Geochemical changes in basalts and andesites across the Archean–Proterozoic boundary: identification and significance. Lithos 23 (1–2), 1–18.
Condie, K.C., O'Neill, C., 2010. The Archean–Proterozoic boundary: 500 my of tectonic transition in Earth history. American Journal of Science 310, 775–790.
Condie, K.C., O'Neill, C., Aster, R.C., 2009. Evidence and implications for a widespread magmatic shutdown for 250 My on Earth. Earth and Planetary Science Letters 282 (1–4), 294–298.
Corfu, F., Krogh, T.E., Kwok, Y.Y., Marmont, S., Jensen, L.S., 1989. U–Pb zircon geochronology in the south-western Abitibi greenstone belt, Superior Province. Canadian Journal of Earth Sciences 26, 1747–1763.
Couturié, J.P., 1977. Le massif granitique de la Margeride (Massif Central Français). Annales Scientifiques de l'Université de Clermont-Ferrand 62, 319.
Couzinié, S., Moyen, J.F., Villaros, A., Paquette, J.L., Marignac, C., 2014. Temporal relationship between Mg–K magmatism and catastrophic melting of the crust during late-collisional period: LA-ICP-MS dating of zircons from granitoids and coeval mafic rocks in the southeastern Velay complex, French Massif Central. Journal of Geosciences 59 (1), 69–86.
Dall'Agnol, R., Oliveira, M.A., Almeida, J.A.C., Althoff, F.J., Leite, A.A.S., Oliveira, D.C., Barros, C.E.M., 2006. Archean and Paleoproterozoic granitoids of the Carajás metallogenetic province, eastern Amazonian craton. In: Dall'Agnol, R., Rosa-Costa, L.T., Klein, E.L. (Eds.), Symposium on Magmatism.: Crustal Evolution, and Metallogenesis of the Amazonian Craton. Abstracts Volume and Field Trips Guide. Belém, PRONEX-UFPA/SBGNO. PRONEX-UFPA/SBGNO, Belém, pp. 99–150.
Davis, W.J., Hegner, E., 1992. Neodymium isotopic evidence for the accretionary development of the Late Archean Slave Province. Contributions to Mineralogy and Petrology 111, 493–503.
Davis, W.J., Bleeker, W., 1999. Timing of plutonism, deformation and metamorphism in the Yellowknife domain, Slave Province, Canada. Canadian Journal of Earth Sciences 36, 1169–1187.
Debon, F., Lemmet, M., 1999. Evolution of Fe/Mg ratios in Late Variscan plutonic rocks from the External Crystalline Massif of the Alps (France, Italy, Switzerland). Journal of Petrology 40 (7), 1151–1185.
Defant, M.J., Drummond, M.S., 1990. A model for trondhjemite–tonalite–dacite genesis and crustal growth via slab melting: Archaean to modern comparisons. Journal of Geophysical Research 95 (B-13), 21503–21521.
de Wit, M.J., Hart, R.A., 1993. Earth's earliest continental lithosphere, hydrothermal flux and crustal recycling. Lithos 30 (3–4), 309–335.
de Wit, M.J., Armstrong, R.A., Kamo, S.L., Erlank, A.J., 1993. Gold-bearing sediments in the Pietersburg greenstone belt: age equivalents of the Witwatersrand Supergroup sediments, South Africa. Economic Geology 88, 1242–1252.
de Wit, M.J., Roering, C., Hart, R.J., Armstrong, R.A., de Ronde, R.E.J., Green, R.W., Tredoux, M., et al., 1992. Formation of an Archaean continent. Nature 357, 553–562.
Dey, S., 2013. Evolution of Archaean crust in the Dharwar craton: the Nd isotope record. Precambrian Research 227, 227–246.
Dey, S., Nandy, J., Choudhary, A.K., Liu, Y., Zong, K., 2014. Origin and evolution of granitoids associated with the Kadiri greenstone belt, eastern Dharwar craton: a history of orogenic to anorogenic magmatism. Precambrian Research 246, 64–90.
Dey, S., Pandey, U.K., Rai, A.K., Chaki, A., 2012. Geochemical and Nd isotope constraints on petrogenesis of granitoids from NW part of the eastern Dharwar craton: possible implications for late Archaean crustal accretion. Journal of Asian Earth Sciences 45, 40–56.
Dhuime, B., Hawkesworth, C.J., Cawood, P.A., Storey, C.D., 2011. A change in the geodynamics of continental growth 3 billion years ago. Science 335, 1334–1336.
Didier, J., Barbarin, B., Gagny, C., Leistel, J.M., Kerrien, Y., 1989. Notice explicative, Carte géologique de la France (1/50000$^e$), feuille Noiretable. Bureau de recherches géologiques et minières, Orléans.
Downes, H., Shaw, A., Williamson, B.J., Thirlwall, M.F., 1997. Sr, Nd and Pb isotope geochemistry of the Hercynian granodiorites and monzogranites, Massif Central, France. Chemical Geology 136, 99–122.
Duretz, T., Gerya, T.V., 2013. Slab detachment during continental collision: Influence of crustal rheology and interactions with lithospheric delamination. Tectonophysics 602, 124–140.
Eglington, B.M., Armstrong, R.A., 2004. The Kaapvaal Craton and adjacent orogens, southern Africa: a geochronological database and overview of the geological development of the craton. South African Journal of Geology 107, 13–32.
England, P., Bickle, M., 1984. Continental thermal and tectonic regimes during the Archaean. The Journal of Geology 92 (4), 353–367.
Ellam, R.M., Hawkesworth, C.J., 1988. Is average continental crust generated at subduction zones? Geology 16, 314–317.
Eriksson, P.G., Banerjee, S., Nelson, D.R., Rigby, M.J., Catuneanu, O., Sarkar, S., Roberts, R.J., et al., 2009. A Kaapvaal craton debate: nucleus of an early small supercontinent or affected by an enhanced accretion event? Gondwana Research 15 (3–4), 354–372.
Feio, G.R.L., Dall'Agnol, R., Dantas, E.L., Macambira, M.J.B., Gomes, A.C.B., Sardinha, A.S., Oliveira, D.C., Santos, R.D., Santos, P.A., 2012. Geochemistry, geochronology, and origin of the Neoarchean Planalto Granite suite, Carajás, Amazonian craton: A-type or hydrated charnockitic granites? Lithos 151, 57–73.
Feng, R., Kerrich, R., 1992. Geochemical evolution of granitoids from the Archean Abitibi Southern Volcanic Zone and the Pontiac subprovince, Superior Province, Canada: implications for tectonic history and source regions. Chemical Geology 98, 23–70.
Ferré, E.C., Caby, R., Peucat, J.J., Capdevila, R., Monié, P., 1998. Pan-African, post-collisional, ferro-potassic granite and quartz–monzonite plutons of Eastern Nigeria. Lithos 45, 255–279.
Flament, N., Coltice, N., Rey, P.F., 2008. A case for late-Archaean continental emergence from thermal evolution models and hypsometry. Earth and Planetary Science Letters 275, 326–336.
Foley, S.F., Tiepolo, M., Vannucci, R., 2002. Growth of early continental crust controlled by melting of amphibolite in subduction zones. Nature 417, 637–640.
Friend, C.R.L., Nutman, A.P., 2005. Complex 3670–3500 Ma orogenic episodes superimposed on juvenile crust accreted between 3850 and 3690 Ma, Itsaq Gneiss Complex, Southern West Greenland. The Journal of Geology 113 (4), 375–397.
Frost, B.R., Barnes, C.G., Collins, W.J., Arculus, R.J., Ellis, D.J., Frost, C.D., 2001. A geochemical classification for granitic rocks. Journal of Petrology 42, 2033–2048.
Frost, C.D., Frost, B.R., Chamberlain, K.R., Huselbosch, T.P., 1998. The Late Archaean history of the Wyoming province as recorded by granitic magmatism in the Wind River Range, Wyoming. Precambrian Research 98, 145–173.
Frost, C.D., Frost, B.R., Kirkwood, R., Chamberlain, K.R., 2006. The tonalite–trondhjemite–granodiorite (TTG) to granodiorite–granite (GG) transition in the late Archean plutonic rocks of the central Wyoming Province. Canadian Journal of Earth Sciences 43, 1419–1444.
Galán, G., Corretgé, L.G., Laurent, O., 1997. Low-potassium vaugnerites from Guéret (Massif Central, France). Mafic magma evolution influenced by contemporaneous granitoids. Mineralogy and Petrology 59, 165–187.
Gao, Y., Yang, Z., Hou, Z., Wei, R., Meng, X., Tian, S., 2010. Eocene potassic and ultrapotassic volcanism in south Tibet: new constraints on mantle source characteristics and geodynamic processes. Lithos 117 (1–4), 20–32.
Garde, A.A., 1997. Accretion and evolution of an Archaean high-grade grey gneiss-amphibolite complex: the Fiskefjord area, southern West Greenland. Geology Greenland Survey Bulletin (114 pp.)..
Gardien, V., Vanderaeghe, O., Arnaud, N., Cocherie, A., Grange, M., Lécuyer, C., 2011. Thermal maturation and exhumation of a middle orogenic crust in the Livradois area (French Massif Central). Bulletin de la Societe Geologique de France 182 (1), 5–24.
Guitreau, M., 2012. Les isotopes de l'hafnium dans les TTG et leurs zircons: témoins de la croissance des premiers continents. Unpublished Ph.D. thesis, École Normale Supérieure de Lyon, 275 pp.
Guitreau, M., Blichert-Toft, J., Martin, H., Mojzsis, S., Albarède, F., 2012. Hafnium isotope evidence from Archean granitic rocks for deep-mantle origin of continental crust. Earth and Planetary Science Letters 337–338, 211–223.
Guo, Z., Wilson, M., 2012. The Himalayan leucogranites: constraints on the nature of their crustal source region and geodynamic setting. Gondwana Research 22 (2), 360–376.
Halla, J., 2005. Late Archean high-Mg granitoids (sanukitoids) in the southern Karelian domain, eastern Finland: Pb and Nd isotopic constraints on crust–mantle interactions. Lithos 79 (1–2), 161–178.
Halla, J., van Hunen, J., Heilimo, E., Hölttä, P., 2009. Geochemical and numerical constraints on Neoarchaean plate tectonics. Precambrian Research 174, 155–162.
Hargraves, R.B., 1986. Faster spreading or greater ridge length in the Archean? Geology 14 (9), 750–752.
Harris, N.B.W., Pearce, J.A., Tindle, A.G., 1986. Geochemical characteristics of collision-zone magmatism. Geological Society of London Special Publications 19, 67–81.
Harrison, T.M., Grove, M., McKeegan, K.D., Coath, C.D., Lovera, O.M., Le Fort, P., 1999. Origin and episodic emplacement of the Manaslu intrusive complex, central Himalaya. Journal of Petrology 40, 3–19.
Harrison, T.M., Lovera, O.M., Grove, M., 1997. New insights into the origin of two contrasting Himalayan granite belts. Geology 25, 899–902.
Hawkesworth, C.J., Dhuime, B., Pietranik, A.B., Cawood, P.A., Kemp, A.I.S., Storey, C.D., 2010. The generation and evolution of the continental crust. Journal of the Geological Society of London 167, 229–248.
Heilimo, E., Halla, J., Hölttä, P., 2010. Discrimination and origin of the sanukitoid series: geochemical constraints from the Neoarchean western Karelian Province (Finland). Lithos 115, 27–39.
Heilimo, E., Halla, J., Huhma, H., 2011. Single-grain zircon U–Pb age constraints of the western and eastern sanukitoid zones in the Finnish part of the Karelian Province. Lithos 121, 87–99.
Henderson, D.R., Long, L.E., Barton Jr., J.M., 2000. Isotopic ages and chemical and isotopic composition of the Archaean Turfloop Batholith, Pietersburg granite–greenstone terrane, Kaapvaal Craton, South Africa. South African Journal of Geology 103 (1), 38–46.
Hill, R.I., Chappell, B.W., Campbell, I.H., 1992. Late Archean granites of the southeastern Yilgarn Block, Western Australia: age, geochemistry, and origin. Transactions of the Royal Society of Edinburgh: Earth Sciences 83 (1–2), 211–226.
Iizuka, T., Horie, K., Komiya, T., Maruyama, S., Hirata, T., Hidaka, H., Windley, B.F., 2006. 4.2 Ga zircon xenocryst in an Acasta gneiss from northwestern Canada: evidence for early continental crust. Geology 34 (4), 245–248.
Jaguin, J., Gapais, D., Poujol, M., Boulvais, P., Moyen, J.-F., 2012. the Murchison Greenstone Belt (South Africa): a General Tectonic Framework. South African Journal of Geology 115 (1), 65–76.
Jahn, B.M., Glikson, A.Y., Peucat, J.-J., Hickman, A.H., 1981. REE geochemistry and isotopic data of Archaean silicic volcanics and granitoids from the Pilbara Block, western Australia: implications for the early crustal evolution. Geochimica et Cosmochimica Acta 45, 1633–1652.
Jahn, B.M., Auvray, B., Shen, Q.H., Liu, D.Y., Zhang, Z.Q., Dong, Y.J., Ye, X.J., Zhang, Q.Z., Cornichet, J., Macé, J., 1988. Archaean crustal evolution in China: the Taishan complex, and evidence for juvenile crustal addition from long-term depleted mantle. Precambrian Research 38, 381–403.
Jayananda, M., Moyen, J.-F., Martin, H., Peucat, J.-J., Auvray, B., Mahabaleswar, B., 2000. Late Archaean (2550–2520 Ma) juvenile magmatism in the Eastern Dharwar craton, southern India: constraints from geochronology, Nd–Sr isotopes and whole rock geochemistry. Precambrian Research 99, 225–254.
Jayananda, M., Chardon, D., Peucat, J.-J., Capdevila, R., 2006. 2.61 Ga potassic granites and crustal reworking in the western Dharwar craton, southern India: Tectonic, geochronologic and geochemical constraints. Precambrian Research 150 (1–2), 1–26.

Jayananda, M., Martin, H., Peucat, J.-J., Mahabaleswar, B., 1995. Late Archaean crust–mantle interactions: geochemistry of LREE-enriched mantle derived magmas. Example of the Closepet batholith, Southern India. Contributions to Mineralogy and Petrology 199, 314–329.

Jelsma, H.A., Vinyu, M.L., Valbracht, P.J., Davies, G.R., Wijbrans, J.R., Verdurmen, E.A.T., 1996. Constraints on Archaean crustal evolution of the Zimbabwe craton: a U–Pb zircon, Sm–Nd and Pb–Pb whole-rock isotope study. Contributions to Mineralogy and Petrology 124, 55–70.

Johnson, T., Brown, M., Kaus, B.J.P., van Tongeren, J.A., 2013. Delamination and recycling of Archaean crust caused by gravitational instabilities. Nature Geoscience 7, 47–52.

Kamber, B.S., Ewart, A., Collerson, K.D., Bruce, M.C., McDonald, G.D., 2002. Fluid-mobile trace element constraints on the role of slab melting and implications for Archaean crustal growth models. Contributions to Mineralogy and Petrology 144, 38–56.

Kamo, S.L., Davis, D.W., 1994. Reassessment of Archean crustal development in the Barberton Mountain Land, South Africa, based on U–Pb dating. Tectonics 13 (1), 167–192.

Kampunzu, A.B., Tombale, A.R., Zhai, M., Bagai, Z., Majaule, T., Modisi, M.P., 2003. Major and trace element geochemistry of plutonic rocks from Francistown, NE Botswana: evidence for a Neoarchaean continental active margin in the Zimbabwe craton. Lithos 71, 431–460.

Käpyaho, A., Mänttäri, I., Huhma, H., 2006. Growth of Archaean crust in the Kuhmo district, Eastern Finland: U–Pb and Sm–Nd isotope constraints on plutonic rocks. Precambrian Research 146, 95–119.

Keller, C.B., Schoene, B., 2012. Statistical geochemistry reveals disruption in secular lithospheric evolution about 2.5 Gyr ago. Nature 485, 490–495.

Kemp, A.I.S., Hawkesworth, C.J., 2003. Granitic perspectives on the generation and secular evolution of the continental crust. In: Rudnick, R.L. (Ed.), The Crust. Treatise on Geochemistry. Elsevier-Pergamon, Oxford, pp. 349–410.

Kemp, A.I.S., Hawkesworth, C.J., Collins, W.J., Gray, C.M., Blevin, P.L., Edinburgh Ion Microprobe Facility, 2009. Nd, Hf and O isotope evidence for rapid continental growth during accretionary orogenesis in the Tasmanides, eastern Australia. Earth and Planetary Science Letters 284, 455–466.

Kinny, P.D., 2000. U–Pb dating of rare metal (Sn–Ta–Li) mineralized pegmatites in Western Australia by SIMS analysis of Tin and Tantalum-bearing ore minerals. Abstracts and Proceedings, Beyond 2000. New Frontiers in Isotope Geoscience, Lorne, Victoria, pp. 113–116.

King, E.M., Valley, J.M., Davis, D.W., Edwards, G.R., 1998. Oxygen isotope ratios of Archean plutonic rocks from granite-greenstone belts of the Superior Province: indicator of magmatic source. Precambrian Research 92, 365–387.

Kleinhanns, I.C., Kramers, J.D., Kamber, B.S., 2003. Importance of water for Archaean granitoid petrology: a comparative study of TTG and potassic granitoids from Barberton Mountain Land, South Africa. Contributions to Mineralogy and Petrology 145, 377–389.

Kovalenko, A., Clemens, J.D., Savantenkov, V., 2005. Petrogenetic constraints for the genesis of Archaean sanukitoid suites: geochemistry and isotopic evidence from Karelia, Batlic Shield. Lithos 79, 147–160.

Kramers, J.D., Houri, H., 2011. The geochronology of the Limpopo Complex: a controversy solved. In: van Reenen, D.D., Kramers, J.D., McCourt, S., Perchuk, L.L. (Eds.), Origin and Evolution of Precambrian High-Grade Gneiss Terranes, with Special Emphasis on the Limpopo Complex of Southern Africa. Geological Society of America, Memoir, 207, pp. 85–106.

Kramers, J.D., Tolstikhin, I.N., 1997. Two major terrestrial Pb isotope paradoxes, forward transport modeling, core formation and the history of the continental crust. Chemical Geology 139, 75–110.

Kramers, J.D., McCourt, S., van Reenen, D.D., 2006. The Limpopo Belt. In: Johnson, M.R., Anhaeusser, C.R., Thomas, R.J. (Eds.), The Geology of South Africa. Geological Society of South Africa, Johannesburg, South Africa, pp. 209–236.

Kreissig, K., Nagler, T.F., Kramers, J.D., van Reenen, D.D., Smit, C.A., 2000. An isotopic and geochemical study of the Kaapvaal Craton and the Southern Marginal Zone of the Limpopo Belt: are they juxtaposed terranes? Lithos 50, 1–25.

Krogstad, E.J., Hanson, G.N., Rajamani, V., 1995. Sources of continental magmatism adjacent to the late Archean Kolar Suture Zone, South India: distinct isotopic and elemental signatures of two late Archean magmatic series. Contributions to Mineralogy and Petrology 122, 159–173.

Kröner, A., Jaeckel, P., Brandl, G., 2000. Single zircon ages for felsic to intermediate rocks from the Pietersburg and Giyani greenstone belts and bordering granitoid orthogneisses, northern Kaapvaal Craton, South Africa. Journal of African Earth Sciences 30 (4), 773–793.

Lagabrielle, Y., Goslin, J., Martin, H., Thirot, J.L., Auzende, J.M., 1997. Multiple active spreading centres in the hot North Fidji Basin (Southwest Pacific): a possible model for Archaean seefloor dynamics? Earth and Planetary Science Letters 149 (1–4), 1–13.

Laurent, O., 2012. Les changements géodynamiques à la transition Archéen-Protérozoïque: étude des granitoïdes de la marge Nord du craton du Kaapvaal (Afrique du Sud). Unpublished Ph.D. thesis, University Blaise Pascal, Clermont-Ferrand II, 512 pp (in French).

Laurent, O., Doucelance, R., Martin, H., Moyen, J.F., 2013a. Differentiation of the late-Archaean sanukitoid series and some implications for crustal growth: insights from geochemical modelling on the Bulai pluton, Central Limpopo Belt, South Africa. Precambrian Research 227, 186–203.

Laurent, O., Martin, H., Doucelance, R., Moyen, J.-F., Paquette, J.-L., 2011. Geochemistry and petrogenesis of high-K "sanukitoids" from the Bulai pluton, Central Limpopo Belt, South Africa: implications for geodynamic changes at the Archaean–Proterozoic boundary. Lithos 123, 73–91.

Laurent, O., Paquette, J.L., Martin, H., Doucelance, R., Moyen, J.F., 2013b. LA-ICP-MS dating of zircons from Meso- and Neoarchean granitoids of the Pietersburg block (South Africa): Crustal evolution at the northern margin of the Kaapvaal craton. Precambrian Research 230, 209–226.

Laurent, O., Rapopo, M., Stevens, G., Moyen, J.F., Martin, H., Doucelance, R., Bosq, C., 2014. Contrasting petrogenesis of Mg–K and Fe–K granitoids and implications for post-collisional magmatism: a case study from the late-Archean Matok pluton (Pietersburg block, South Africa). Lithos 196–197, 131–149.

Ledru, P., Courrioux, G., Dallain, C., Lardeaux, J.M., Montel, J.M., Vanderhaeaghe, O., Vitel, G., 2001. The Velay dome (French Massif Central): melt generation and granite emplacement during orogenic evolution. Tectonophysics 342 (3–4), 207–237.

Le Fort, P., Cuney, M., Deniel, C., France-Lanord, C., Sheppard, S.M.F., Upreti, B.N., Vidal, P., 1987. Crustal generation of the Himalayan leucogranites. Tectonophysics 134, 39–57.

Leite, A.A.S., Dall'Agnol, R., Macambira, M.J.B., Althoff, F.J., 2004. Geologia e geocronologia dos granitóides arqueanos da região de Xinguara e suas implicações na evolução do Terreno Granito–Greenstone de Rio Maria, Cráton Amazônico. Revista Brasileira de Geociencias 34, 447–458.

Liégeois, J.P., Navez, J., Hertogen, J., Black, R., 1998. Contrasting origin of post-collisional high-K calc-alkaline and shoshonitic versus alkaline and peralkaline granitoids. The use of sliding normalization. Lithos 45, 1–28.

Liu, S.W., Pan, Y.M., Xie, Q.L., Zhang, J., Li, Q., 2004. Archean geodynamics in the Central Zone, North China Craton: constraints from geochemistry of two constrasting series of granitoids in the Fuping and Wutai complexes. Precambrian Research 130, 229–249.

Lobach-Zhuchenko, S.B., Rollinson, H.R., Chekulaev, V.P., Arestova, N.A., Kovalenko, A.V., Ivanikov, V.V., Guseva, N.S., Sergeev, S.A., Matukov, D.I., Jarvis, K.E., 2005. The Archaean sanukitoid series of the Baltic Shield: geological setting, geochemical characteristics and implications for their origin. Lithos 79, 107–128.

Lobach-Zhuchenko, S.B., Rollinson, H., Chekulaev, V.P., Savatenkov, V.M., Kovalenko, A.V., Martin, H., Guseva, N.S., Arestova, N.A., 2008. Petrology of a Late Archaean, Highly Potassic, Sanukitoid Pluton from the Baltic Shield: insights into Late Archaean Mantle Metasomatism. Journal of Petrology 49 (3), 393–420.

McDonough, W.F., Sun, S.S., 1995. The composition of the Earth. Chemical Geology 120 (3–4), 223–253.

Mahéo, G., Blichert-Toft, J., Pin, C., Guillot, S., Pêcher, A., 2009. Partial melting of mantle and crustal sources beneath South Karakorum, Pakistan: implications for the Miocene geodynamic evolution of the India–Asia Convergence Zone. Journal of Petrology 20 (3), 427–449.

Martin, H., 1986. Effect of steeper Archaean geothermal gradient on geochemistry of subduction-zone magmas. Geology 14, 753–756.

Martin, H., 1987. Petrogenesis of Archaean trondhjemites, tonalites and granodiorites from Eastern Finland: major and trace element geochemistry. Journal of Petrology 28, 921–953.

Martin, H., 1993. The mechanisms of petrogenesis of the Archaean continental crust, comparison with modern processes. Lithos 30, 373–388.

Martin, H., 1994. The Archaean grey gneisses and the genesis of continental crust. In: Condie, K.C. (Ed.), Archaean Crustal Evolution. Developments in Precambrian Geology, 11, pp. 205–260.

Martin, H., 1999. Adakite magmas: modern analogs of Archaean granitoids. Lithos 46, 411–429.

Martin, H., Querré, G., 1984. A 2.5 G.a. reworked sialic crust: Rb–Sr ages and isotopic geochemistry of late archaean volcanic and plutonic rocks from E. Finland. Contributions to Mineralogy and Petrology 85, 292–299.

Martin, H., Moyen, J.F., 2002. Secular changes in TTG composition as markers of the progressive cooling of the Earth. Geology 30 (4), 319–322.

Martin, H., Moyen, J.F., Rapp, R.P., 2009. The sanukitoid series: magmatism at the Archaean–Proterozoic transition. Earth and Environmental Science Transactions of the Royal Society of Edinburgh 100 (1–2), 15–33.

Martin, H., Moyen, J.-F., Guitreau, M., Blichert-Toft, J., Le Pennec, J.-L., 2014. Why Archaean TTG cannot be generated by MORB melting in subduction zones. Lithos 198–199, 1–13.

Martin, H., Smithies, R., Rapp, R.P., Moyen, J.F., Champion, D., 2005. An overview of adakite, TTG, and sanukitoid: relationships and some implications for crustal evolution. Lithos 79 (1–2), 1–24.

Medeiros, H., Dall'Agnol, R., 1988. Petrologia da porção leste do Batólito Granodiorítico Rio Maria, sudeste do Pará. Congresso Brasileiro de Geologia, 35. Anais de Congresso Brasileiro de Geologia. SBG, Belém, pp. 1488–1499 (v 3).

Meyer, F.M., Robb, L.J., Reimold, W.U., de Bruiyn, H., 1994. Contrasting low- and high-Ca granites in the Archean Barberton Mountain Land, Southern Africa. Lithos 32 (1–2), 63–76.

Michon, G., 1987. Les vaugnérites de l'Est du Massif Central Français: apport de l'analyse multivariée à l'étude géochimique des éléments majeurs. Bulletin de la Societe Geologique de France 3 (3), 591–600.

Mikkola, P., Salminen, P., Torppa, A., Huhma, H., 2011a. The 2.74 Ga Likamännikkö complex in Suomussalmi, East Finland: lost between sanukitoids and truly alkaline rocks? Lithos 125, 716–728.

Mikkola, P., Huhma, H., Heilimo, E., Whitehouse, M., 2011b. Archean crustal evolution of the Suomussalmi district as part of the Kianta Complex, Karelia: constraints from geochemistry and isotopes of granitoids. Lithos 125, 287–307.

Miller, C., Schuster, R., Klotzli, U., Frank, W., Grasemann, B., 1999. Post-collisional potassic and ultrapotassic magmatism in SW Tibet: geochemical and Sr–Nd–Pb–O isotopic constraints for mantle source characteristics and petrogenesis. Journal of Petrology 40, 1399–1424.

Montel, J.-M., Weisbrod, A., 1986. Characteristics and evolution of "vaugneritic magmas": an analytical and experimental approach, on the example of the Cévennes Médianes (French Massif Central). Bulletin of Mineralogy 109, 575–587.

Moyen, J.F., 2011. The composite Archaean grey gneisses: petrological significance, and evidence for a non-unique tectonic setting for Archaean crustal growth. Lithos 123 (1–4), 21–36.
Moyen, J.F., Martin, H., 2012. Forty years of TTG research. Lithos 148, 312–336.
Moyen, J.F., Stevens, G., 2006. Experimental constraints on TTG petrogenesis: implications for Archean geodynamics. In: Benn, K., Mareschal, J.-C., Condie, K.C. (Eds.), Archean Geodynamics and Environments. AGU, pp. 149–178.
Moyen, J.F., van Hunen, J., 2012. Short-term episodicity of Archaean plate tectonics. Geology 40 (5), 451–454.
Moyen, J.F., Martin, H., Jayananda, M., 2001. Multi-element geochemical modelling of crust–mantle interactions during late-Archaean crustal growth: the Closepet granite (South India). Precambrian Research 112, 87–105.
Moyen, J.F., Martin, H., Jayananda, M., Auvray, B., 2003. Late Archaean granites: a typology based on the Dharwar Craton (India). Precambrian Research 127, 103–123.
Moyen, J.F., Stevens, G., Kisters, A., 2006. Record of mid-Archaean subduction from metamorphism in the Barberton terrain, South Africa. Nature 442 (3), 559–562.
Mshiu, E.E., Maboko, M.A.H., 2012. Geochemistry and petrogenesis of the late Archaean high-K granites in the southern Musoma-Mara Greenstone Belt: their influence in evolution of Archaean Tanzania Craton. Journal of Africa Earth Sciences 66–67, 1–12.
Nutman, A.P., Bennett, V.C., Friend, C.R.L., Horie, K., Hidaka, H., 2007. Ca. 3, 850 Ma tonalites in the Nuuk region, Greenland: geochemistry and their reworking within an Eoarchaean gneiss complex. Contributions to Mineralogy and Petrology 154 (4), 385–408.
Oliveira, M.A., Dall'Agnol, R., Almeida, J.A.C., 2011. Petrology of the Mesoarchean Rio Maria suite and the discrimination of sanukitoid series. Lithos 127, 192–209.
Nutman, A.P., Bennett, V.C., Friend, C.R.L., Hidaka, H., Yi, K., Lee, S.R., Kamiichi, T., 2013. The Itsaq Gneiss Complex of Greenland: episodic 3900 to 3660 Ma juvenile crust formation and recycling in the 3660 to 3600 Ma Isukasian orogeny. American Journal of Science 313 (9), 877–911.
Oliveira, M.A., Dall'Agnol, R., Althoff, F.J., Leite, A.A.S., 2009. Mesoarchean sanukitoid rocks of the Rio Maria Granite–Greenstone Terrane, Amazonian craton, Brazil. Journal of South American Earth Sciences 27, 146–160.
Oliveira, M.A., Dall'Agnol, R., Scaillet, B., Journal of Petrology, 2010. Petrological constraints on crystallization conditions of MesoArchean Sanukitoid Rocks, southeastern Amazonian craton, Brazil. Journal of Petrology 51, 2121–2148.
O'Neill, C., Jellinek, A.M., Lenardic, A., 2007a. Conditions for the onset of plate tectonics on terrestrial planets and moons. Earth and Planetary Science Letters 261, 20–32.
O'Neill, C., Lenardic, A., Moresi, L., Torsvik, T.H., Lee, C.A., 2007b. Episodic Precambrian subduction. Earth and Planetary Science Letters 262, 552–562.
Patiño-Douce, A.E., Johnston, D., 1991. Phase equilibria and melt productivity in the pelitic system: implications for the origin of peraluminous granitoids and aluminous granulites. Contributions to Mineralogy and Petrology 107, 202–218.
Patiño-Douce, A.E., Beard, J.S., 1995. Dehydration-melting of biotite gneiss and quartz amphibolite from 3 to 15 kbar. Journal of Petrology 36, 707–738.
Patiño-Douce, A.E., Beard, J.S., 1996. Effects on P, $f(O_2)$ and Mg/Fe ratio on dehydration melting of model metagreywackes. Journal of Petrology 37 (5), 999–1024.
Percival, J.A., 1994. Archaean high-grade metamorphism. In: Condie, K.C. (Ed.), Archaean Crustal Evolution. Elsevier, Amsterdam, pp. 357–410.
Percival, J.A., Sanborn-Barrie, M., Skulski, T., Stott, G.M., Helmstaedt, H., White, D.J., 2006. Tectonic evolution of the western Superior Province from NATMAP and lithoprobe studies. Canadian Journal of Earth Sciences 43, 1085–1117.
Poujol, M., 1997. Étude U–Pb et Pb–Pb de la Murchison greenstone belt et du bassin aurifère d'Evander, Afrique du Sud: implications pour l'évolution du Kaapvaal Craton. Unpublished Ph.D. thesis, Université de Montpellier, 247 pp.
Poujol, M., 2001. U–Pb isotopic evidence for episodic granitoid emplacement in the Murchison greenstone belt, South Africa. Journal of African Earth Sciences 33 (1), 155–163.
Poujol, M., Robb, L.J., 1999. New U–Pb zircon ages on gneisses and pegmatite from south of the Murchison greenstone belt, South Africa. South African Journal of Geology 102 (2), 93–97.
Poujol, M., Robb, L.J., Anhaeusser, C.R., Gericke, B., 2003. A review of the geochronological constraints on the evolution of the Kaapvaal Craton, South Africa. Precambrian Research 127 (1–3), 181–213.
Poujol, M., Robb, L.J., Respaut, J.-P., Anhaeusser, C.R., 1996. 3.07–2.97 Ga greenstone belt formation in the northeastern Kaapvaal Craton: implications for the origin of the Witwatersrand Basin. Economic Geology 91, 1455–1461.
Prabhakar, B.C., Jayananda, M., Shareef, M., Kano, T., 2009. Petrology and geochemistry of Late Archean granitoids in the northern part of Eastern Dharwar, southern India: implications for transitional geodynamic setting. Journal of the Geological Society of India 74, 299–317.
Rapp, R.P., Watson, E.B., 1995. Dehydration melting of metabasalt at 8–32 kbar: implications for continental growth and crust–mantle recycling. Journal of Petrology 36 (4), 891–931.
Rapp, R.P., Norman, M.D., Laporte, D., Yaxley, G.M., Martin, H., Foley, S.F., 2010. Continent formation in the Archean and chemical evolution of the cratonic lithosphere: melt–rock reaction experiments at 3–4 GPa and petrogenesis of Archean Mg-diorites (sanukitoids). Journal of Petrology 51 (6), 1237–1266.
Rapp, R.P., Shimizu, N., Norman, M.D., 2003. Growth of early continental crust by partial melting of eclogite. Nature 425, 605–609.
Rapp, R.P., Shimizu, N., Norman, M.D., Applegate, G.S., 1999. Reaction between slab-derived melts and peridotite in the mantle wedge: experimental constraints at 3.8 GPa. Chemical Geology 160, 335–356.
Rapp, R.P., Watson, E.B., Miller, C.F., 1991. Partial melting of amphibolite/eclogite and the origin of Archaean trondhjemites and tonalites. Precambrian Research 51, 1–25.
Reichardt, H., Weinberg, R.F., Andersson, U.B., Fanning, C.M., 2010. Hybridization of granitic magmas in the source: The origin of the Karakoram Batholith, Ladakh, NW India. Lithos 116 (3–4), 249–272.
Rey, P.F., Coltice, N., 2008. Neoarchean strengthening of the lithosphere and the coupling of the Earth's geochemical reservoirs. Geology 36, 635–638.
Reymer, A., Schubert, G., 1984. Phanerozoic addition rates to the continental crust and crustal growth. Tectonics 3, 63–77.
Robb, L.J., Brandl, G., Anhaeusser, C.R., Poujol, M., 2006. Archean granitoid intrusions. In: Johnson, M.R., Anhaeusser, C.R., Thomas, R.J. (Eds.), The Geology of South Africa. Geological Society of South Africa: Johannesburg/Council of Geosciences, pp. 57–94.
Roering, C., van Reenen, D.D., Smit, C.A., Barton, J.M., de Beer, J.H., de Wit, M.J., Stettler, E.H., van Schalkwyk, J.F., Stevens, G., Pretorius, S., 1992. Tectonic model for the evolution of the Limpopo Belt. Precambrian Research 55, 539–552.
Rudnick, R.L., Gao, S., 2003. Composition of the continental crust. In: Rudnick, R.L. (Ed.), The Crust. Treatise on Geochemistry. Elsevier-Pergamon, Oxford, pp. 1–64 (Chap. 3).
Sage, R.P., Lightfoot, P.C., Doherty, W., 1996. Geochemical characteristics of granitoid rocks from within the Archean Michipicoten Greenstone Belt, Wawa Subprovince, Superior Province, Canada: implications for source regions and tectonic evolution. Precambrian Research 76, 155–190.
Samsonov, A.V., Bogina, M.M., Bibikova, E.V., Petrova, A.Y., Shchipansky, A.A., 2005. The relationship between adakitic, calc-alkaline volcanic rocks and TTGs: Implications for tectonic setting of the Karelian greenstone belts, Baltic Shield. Lithos 79, 83–106.
Sanchez-Garrido, C.J.M.G., Stevens, G., Armstrong, R.A., Moyen, J.-F., Martin, H., Doucelance, R., 2011. Diversity in Earth's early felsic crust: Paleoarchean peraluminous granites of the Barberton Greenstone Belt. Geology 39 (10), 963–966.
Sarvothaman, H., 2001. Archaean high-Mg granitoids of mantle origin in the Eastern Dharwar Craton of Andhra Pradesh. Journal of the Geological Society of India 58, 261–268.
Schofield, D.I., Thomas, R.J., Goodenough, K.M., de Waele, B., Pitfield, P.E.J., Key, R.M., Bauer, W., Walsg, G.J., Lidke, D.J., Ralison, A.V., Rabarimanana, M., Rafahatelo, J.M., Randriamananjara, T., 2010. Geological evolution of the Antogil Craton, NE Madagascar. Precambrian Research 182, 187–203.
Scholl, D.W., von Huene, R., 2009. Implications of estimated magmatic additions and recycling losses at the subduction zones of accretionary (noncollisional) and collisional (suturing) orogens. In: Cawood, P.A., Kröner, A. (Eds.), Earth Accretionary Systems in Space and Time. Geological Society of London Special Publications, 318, pp. 105–125.
Shirey, S.B., Hanson, G.N., 1984. Mantle-derived Archaean monzodiorites and trachyandesites. Nature 310, 222–224.
Shirey, S.B., Richardson, S.H., 2011. Start of the Wilson cycle at 3 Ga shown by diamonds from subcontinental mantle. Science 333, 434–436.
Singh, J., Johannes, W., 1996. Dehydration melting of tonalites. 2. Compositions of melts and solids. Contributions to Mineralogy and Petrology 125, 26–44.
Sisson, T., Ratajeski, K., Hankins, W., Glazner, A., 2005. Voluminous granitic magmas from common basaltic sources. Contributions to Mineralogy and Petrology 148, 635–661.
Sizova, E., Gerya, T., Brown, M., Perchuk, L.L., 2010. Subduction styles in the Precambrian: insight from numerical experiments. Lithos 116, 209–229.
Skjerlie, K.P., Johnston, A.D., 1996. Vapour-absent melting from 10 to 20 kbar of crustal rocks that contain multiple hydrous phases: implications for anatexis in the deep to very deep continental crust and active continental margins. Journal of Petrology 37, 661–691.
Smithies, R.H., 2000. The Archaean tonalite–trondhjemite–granodiorite (TTG) series is not an analogue of Cenozoic adakite. Earth and Planetary Science Letters 182, 115–125.
Smithies, R.H., Champion, D.C., 1999a. High-Mg diorite from the Archaean Pilbara Craton; anorogenic magmas derived from a subduction-modified mantle. Geological Survey of Western Australia, Annual Review 45–59.
Smithies, R.H., Champion, D.C., 1999b. Late Archean felsic alkaline igneous rocks in the Eastern Goldfields, Yilgarn Craton, Western Australia: a result of lower crustal delamination? Journal of the Geological Society 156, 561–576.
Smithies, R.H., Champion, D.C., 2000. The Archaean high-Mg diorite suite: links to tonalite–trondhjemite–granodiorite magmatism and implications for early Archaean crustal growth. Journal of Petrology 41 (12), 1653–1671.
Smithies, R.H., Champion, D.C., Sun, S.S., 2004. Evidence for Early LREE-enriched mantle source regions: diverse magmas from the c. 3.0 Ga Mallina Basin, Pilbara Craton, NW Australia. Journal of Petrology 45 (8), 1515–1537.
Smithies, R.H., van Kranendonk, M.J., Champion, D.C., 2007. The Mesoarchean emergence of modern-style subduction. Gondwana Research 11 (1–2), 50–68.
Solgadi, F., Moyen, J.-F., Vanderhaeghe, O., Sawyer, E.W., Reisberg, L., 2007. The relative roles of crustal anatexis and mantle-derived magmas: generation of synorogenic, Hercynian granites in the Livradois area, French Massif Central. Canadian Mineralogist 45, 581–606.
Steenfelt, A., Garde, A.A., Moyen, J.F., 2005. Mantle wedge involvement in the petrogenesis of Archaean grey gneisses in West Greenland. Lithos 79, 207–228.
Stern, R.A., Hanson, G.N., 1991. Archaean High-Mg granodiorites: a derivative of light rare earth enriched monzodiorites of mantle origin. Journal of Petrology 32, 201–238.
Stern, R.A., Hanson, G.N., Shirey, S.B., 1989. Petrogenenesis of mantle-derived, LILE-enriched Archean monzodiorites and trachyandesites (sanukitoids) in southwestern Superior Province. Canadian Journal of Earth Sciences 26, 1688–1712.
Stevenson, R., Henry, P., Gariépy, C., 1999. Assimilation-fractional crystallization origin of Archaean sanukitoid suites: Western Superior Province, Canada. Precambrian Research 96, 83–99.
Sutcliffe, R.H., Smith, A.R., Doherty, W., Barnett, R.L., 1990. Mantle derivation of Archean amphibole-bearing granitoid and associated mafic rocks: evidence from the southern Superior Province, Canada. Contributions to Mineralogy and Petrology 105, 255–274.

Sylvester, P.J., 1994. Archaean granite plutons. In: Condie, K.C. (Ed.), Archaean Crustal Evolution. Developments in Precambrian Geology, vol. 11. Elsevier, Amsterdam, pp. 261–314.
Taylor, J., Nicoli, G., Stevens, G., Frei, D., Moyen, J.-F., 2014. The processes that control leucosome compositions in metasedimentary granulites: perspectives from the Southern Marginal Zone migmatites, Limpopo Belt, South Africa. Journal of Metamorphic Geology. http://dx.doi.org/10.1111/jmg.12087.
Taylor, S.R., 1987. Geochemical and petrological significance of the Archaean–Proterozoic boundary. In: Pharaoh, T.C., Beckinsale, R.D., Rickard, D. (Eds.), Geochemistry and Mineralization of Proterozoic Volcanic Suites. Geological Society Special Publication, 33, pp. 3–8.
Taylor, S.R., McLennan, S.M., 1985. The Continental Crust: Its Composition and Evolution. Blackwell Scientific, Boston, Mass (312 pp.).
Taylor, S.R., McLennan, S.M., 1995. The geochemical evolution of the continental crust. Reviews of Geophysics 33 (2), 241–265.
Thébaud, N., Rey, P.F., 2013. Archean gravity-driven tectonics on hot and flooded continents: controls on long-lived mineralised hydrothermal systems away from continental margins. Precambrian Research 229, 83–104.
Turner, S., Sandiford, M., Foden, J., 1992. Some geodynamic and compositional constraints on 'postorogenic' magmatism. Geology 20, 931–934.
Turpin, L., Cuney, M., Friedrich, M., Bouchez, J.L., Aubertin, M., 1990. Meta-igneous origin of Hercynian peraluminous granites in N.W. French Massif Central: implications for crustal history reconstructions. Contributions to Mineralogy and Petrology 104 (2), 163–172.
Valley, J.W., Lackey, J.S., Cavosie, A.J., Clechenko, C.C., Spicuzza, M.J., Basei, M.A.S., Bindeman, I.N., Ferreira, V.P., Sial, A.N., King, E.M., Peck, W.H., Sinha, A.K., Wei, C.S., 2005. 4.4 billion years of crustal maturation: oxygen isotope ratios of magmatic zircon. Contributions to Mineralogy and Petrology 150, 561–580.
Vanderhaeghe, O., 2010. The thermo–mechanical evolution of crustal orogenic belts at convergent plate boundaries: a reappraisal of the orogenic cycle. Journal of Geodynamics 56–57, 124–145.
van Hunen, J., Allen, M.B., 2011. Continental collision and slab break-off: a comparison of 3-D numerical models with observations. Earth and Planetary Science Letters 302 (1–2), 27–37.
van Hunen, J., van den Berg, A.P., 2008. Plate tectonics on the early Earth: Limitations imposed by strength and buoyancy of subducted lithosphere. Lithos 103, 217–235.
van Kranendonk, M.J., Smithies, H.R., Hickman, A.H., Champion, D.C., 2007. Review: secular tectonic evolution of Archean continental crust: interplay between horizontal and vertical processes in the formation of the Pilbara Craton, Australia. Terra Nova 19 (1), 1–38.
van Reenen, D.D., Barton Jr., J.M., Roering, C., Smit, C.A., van Schalkwyk, J.F., 1987. Deep crustal response to continental collision: the Limpopo belt of southern Africa. Geology 15, 11–14.
van Thienen, P., Vlaar, N.J., van den Berg, A.P., 2004. Plate tectonics on the terrestrial planets. Physics of the Earth and Planetary Interiors 142, 61–74.
Veizer, J., McKenzie, F.T., 2003. Evolution of sedimentary rocks. Treatise on Geochemistry, vol. 7. Elsevier-Pergamon, Oxford, pp. 369–407.
Vielzeuf, D., Holloway, J.R., 1988. Experimental determination of fluid absent melting relations in the pelitic system. Contributions to Mineralogy and Petrology 98, 257–276.
Vijaya Kumar, K., Ernst, W.G., Leelanandam, C., Wooden, J.L., Grove, M.J., 2011. Origin of ~2.5 Ga potassic granite from the Nellore Schist Belt, SE India: textural, cathodoluminescence, and SHRIMP U–Pb data. Contributions to Mineralogy and Petrology 162, 867–888.
von Raumer, J.F., Finger, F., Veselá, P., Stampfli, G.M., 2013. Durbachites–Vaugnerites — a geodynamic marker in the central European Variscan orogen. Terra Nova. http://dx.doi.org/10.1111/ter.12071.
Wang, Y., Zhang, Y., Zhao, G., Fan, W., Xia, X., Zhang, F., Zhang, A., 2009. Zircon U–Pb geochronological and geochemical constraints on the petrogenesis of Taishan sanukitoids (Shandong): implications for Neoarchean subduction in the Eastern Block, North China Craton. Precambrian Research 174, 273–286.
Watkins, J.M., Clemens, J.D., Treloar, P.J., 2007. Archaean TTGs as sources of younger granitic magmas: melting of sodic metatonalites at 0.6–1.2 GPa. Contributions to Mineralogy and Petrology 154, 91–110.
halen, J.B., Percival, J.A., McNicoll, V.J., Longstaffe, F.J., 2002. A mainly crustal origin for tonalitic granitoid rocks, Superior Province, Canada: implications for late Archean tectonomagmatic processes. Journal of Petrology 43 (8), 1551–1570.
halen, J.B., Percival, J.A., McNicoll, V.J., Longstaffe, F.J., 2004. Geochemical and isotopic (Nd–O) evidence bearing on the origin of late- to post-orogenic high-K granitoid rocks in the western Superior Province: implications for late-Archaean tectonomagmatic processes. Precambrian Research 132, 303–326.
ilde, S.A., Valley, J.W., Peck, W.H., Graham, C.M., 2001. Evidence from detrital zircons for the existence of continental crust and oceans on the Earth 4.4 Gyr ago. Nature 409, 175–178.
illbold, M., Hegner, E., Stracke, A., Rocholl, A., 2009. Continental geochemical signatures in dacites from Iceland and implications for models of early Archaean crust formation. Earth and Planetary Science Letters 279, 44–52.
illiams, H.M., Turner, S.P., Pearce, J.A., Kelley, S.P., Harris, N.B.W., 2004. Nature of the source regions for post-collisional, potassic magmatism in southern and northern Tibet from geochemical variations and inverse trace element modelling. Journal of Petrology 45, 555–607.
illiamson, B., Downes, H., Thirlwall, M., Beard, A., 1997. Geochemical constraints on restite composition and unmixing in the Velay anatectic granite, French Massif Central. Lithos 40 (2–4), 295–319.
illiamson, B.J., Downes, H., Thirlwall, M.F., 1992. The relationship between crustal magmatic underplating and granite genesis—an example from the Velay granite complex, Massif-Central, France. Transactions of the Royal Society of Edinburgh-Earth Sciences 83, 235–245.
indley, B.F., 1984. The Archaean–Proterozoic boundary. Tectonophysics 105 (1–4), 43–53.
olf, M.B., Wyllie, P.J., 1994. Dehydration-melting of amphibolite at 10 kbar: the effects of temperature and time. Contributions to Mineralogy and Petrology 115, 369–383.
, Y.G., Menzies, M.A., Thirlwall, M.F., Xie, G.H., 2001. Exotic lithosphere mantle beneath the western Yangtze craton: petrogenetic links to Tibet using highly magnesian ultrapostassic rocks. Geology 29, 863–866.
ng, J.H., Wu, F.Y., Wilde, S.A., Zhao, G., 2008. Petrogenesis and geodynamics of Late-Archaean magmatism in eastern Hebei, eastern North China Craton: geochronological, geochemical and Nd–Hf isotopic evidence. Precambrian Research 167, 125–149.
arron, L.M., 2003. Archaean granite petrogenesis and implications for the evolution of the Barberton Mountain Land, South Africa. Unpublished Ph.D thesis, Kingston University, London, 315 pp.
gers, T.E., van Keken, P.E., 2001. Middle Archean continent formation by crustal delamination. Geology 29 (12), 1083–1086.
h, A., Gerdes, A., 2012. U–Pb and Lu–Hf isotope record of detrital zircons from gold-bearing sediments of the Pietersburg Greenstone Belt (South Africa)—is there a common provenance with the Witwatersrand Basin? Precambrian Research 204–205, 46–56.
h, A., Gerdes, A., Barton Jr., J.M., 2009. Archean accretion and crustal evolution of the Kalahari Craton—the Zircon Age and Hf isotope record of granitic rocks from Barberton/Swaziland to the Francistown Arc. Journal of Petrology 50, 933–966.
h, A., Jaguin, J., Poujol, M., Boulvais, P., Block, S., Paquette, J.-L., 2013. Juvenile crust formation in the northeastern Kaapvaal Craton at 2.97 Ga—implications for Archean terrane accretion, and the source of the Pietersburg gold. Precambrian Research 233, 20–43.
ng, L., Gao, L.E., Xie, K., Liu-Zeng, J., 2011. Mid-Eocene high Sr/Y granites in the Northern Himalayan Gneiss Domes: melting thickened lower continental crust. Earth and Planetary Science Letters 303 (3–4), 251–266.
ai, M., Kampunzu, A.B., Modisi, M.P., Bagai, Z., 2006. Sr and Nd isotope systematics of the Francistown plutonic rocks, Botswana: implications for Neoarchean crustal evolution of the Zimbabwe craton. Geologische Rundschau 95, 355–369.
ao, Z., Mo, X., Dilek, Y., Niu, Y., dePaolo, D.J., Robinson, P., Zhu, D., Sun, C., Dong, G., Zhou, S., Luo, Z., Hou, Z., 2009. Geochemical and Sr–Nd–Pb–O isotopic compositions of the post-collisional ultrapotassic magmatism in SW Tibet: petrogenesis and implications for India intra-continental subduction beneath southern Tibet. Lithos 113, 190–212.

Available online at www.sciencedirect.com

ScienceDirect

Geochimica et Cosmochimica Acta 168 (2015) 261–279

Geochimica et Cosmochimica Acta

www.elsevier.com/locate/gca

# Ce isotope systematics of island arc lavas from the Lesser Antilles

Nina Bellot [a,*], Maud Boyet [a], Régis Doucelance [a], Christian Pin [b], Catherine Chauvel [c,d], Delphine Auclair [a]

[a] Laboratoire Magmas et Volcans, Université Blaise Pascal-CNRS-IRD-OPGC, 5 rue Kessler, 63038 Clermont-Ferrand, France
[b] CNRS, UMR 6524, LMV, F63038 Clermont-Ferrand, France
[c] Université Grenoble Alpes, ISTerre, F-38041 Grenoble, France
[d] CNRS, ISTerre, F-38041 Grenoble, France

Received 3 April 2015; accepted in revised form 1 July 2015; available online 9 July 2015

**Abstract**

The La-Ce systematics has one of the longest half-lifes ($T_{1/2} = 292.5$ Ga) of radioactive decay systems used in isotope geochemistry. Variations of the $^{138}Ce/^{142}Ce$ ratio are expected to be small and the use of Ce as isotopic tracer requires a very precise measurement. Compared to Sm–Nd studies, the La–Ce decay system can provide additional information about the nature of sediments recycled in subduction zones, because unusually large Ce anomalies relative to the neighboring rare earth elements exist in marine sediments such as fish teeth or hydrothermal deposits. Here, we present a chemical purification technique for Ce, and mass spectrometric technique to perform accurate and reproducible analyses of Ce isotopes of natural samples. We report a large set of Ce isotope data including analysis of 2 Ce reference material solutions (AMES and JMC-304), 2 rock standards (BCR-2 and BHVO-2), 2 chondrites (the carbonaceous chondrite Allende and the enstatite chondrite Sahara 97072), 4 mid-ocean ridge basalts, 30 arc lavas from the Martinique Island and 5 oceanic sediments from DSDP-site 144 drilled on the Demerara rise. The long-term, external precision obtained on the AMES reference material is 80 ppm (2 s.d., $^{138}Ce/^{142}Ce = 0.0225732 \pm 18$, $n = 89$). However, we note an evolution of isotopic ratios measured in static mode over the duration of this study (33 months). When the reproducibility is calculated from the AMES reference material measured during the same analytical session, it averages 40 ppm. All the $^{138}Ce/^{142}Ce$ ratios have been normalized to the AMES value of 0.0225746 (measured in session 7, 2 s.d. = 14 ppm, $n = 8$), a session during which the chondritic value has been defined and the peak tailing was negligible. The $^{138}Ce/^{142}Ce$ ratio measured for the JMC-304 Ce reference reagent is $0.0225706 \pm 9$ (2 s.d. = 38 ppm, $n = 10$). The analytical precision on natural samples is improved by a factor of about 4 in relation to previous studies on island arcs (Tanaka et al., 1987; Shimizu et al., 1992). The $^{138}Ce/^{142}Ce$ ratios of the two chondrites are identical within uncertainty and similar to previous determinations done on other meteorites; the average value is $0.0225654 \pm 7$ (2 s.d. = 32 ppm). Martinique samples show a limited but significant range of variations for $^{138}Ce/^{142}Ce$ ratios (~2 $\varepsilon$-units). The latter ratios correlate well with the Nd isotopes and define a binary mixing between a depleted mantle and subducted sediments that could be similar to those drilled at DSDP-site 144 (Leg 14). The Martinique lavas do not define a single curve in the $\varepsilon$Ce vs. $\varepsilon$Nd diagram, but a band. The apparent scattering can be explained by the involvement of sediments with different Ce isotope compositions and/or variations in the melting process itself such as the effect of melting on the light rare earth element ratios. The Ce isotopic signature of Martinique samples is dominated by the contribution of old terrigeneous sediments. However, according to our mixing models a low contribution of a few percent of marine sediment material in the source of the lavas is undetectable and therefore cannot be definitely excluded. Although the participation of marine sediments in this arc system is not demonstrated, our calculations show that the La–Ce system has a potential as geochemical tracer despite its very long half-life.


* Corresponding author.

http://dx.doi.org/10.1016/j.gca.2015.07.002
0016-7037/

## 1. INTRODUCTION

Long-lived isotopes are used in isotope geochemistry to date objects and processes and to trace the source of material involved in magmatism. Ce isotope ratios were first reported in the 80's (Tanaka and Masuda, 1982; Dickin, 1987) but very few studies were published when compared to studies based on the Sm–Nd, Lu–Hf, U–Th/Pb and Rb–Sr isotopic systems. The $^{138}$La–$^{138}$Ce has one of the longest half-lifes, about 3 times that of the $^{147}$Sm–$^{143}$Nd system. $^{138}$La exhibits branched decay to $^{138}$Ce by β-disintegration ($\lambda^{138}$La to $^{138}$Ce $= (2.37 \pm 0.10) \times 10^{-12}$ year$^{-1}$ or $T_{1/2} = 292.5$ Ga; branching ratio $\beta = 0.348$) and to $^{138}$Ba by electron capture ($\lambda^{138}$La to $^{138}$Ba $= 4.44 \times 10^{-12}$ year$^{-1}$ or $T_{1/2} = 156.1$ Ga; branching ratio EC $= 0.652$) (Sato and Hirose, 1981; Tanimizu, 2000). The use of the$^{138}$La–$^{138}$Ce systematics as isotopic tracer is challenging because variations in the abundance of $^{138}$Ce are small owing to the low abundance of $^{138}$La (0.09%), its long half-life and the small fractionation between parent and daughter elements during geological processes. Lanthanum and cerium are both refractory and lithophile rare earth elements (REE) that have very similar atomic radii. La is slightly more incompatible than Ce during magmatic processes but the La/Ce fractionation is small in igneous rocks. Moreover, $^{138}$Ce is a minor isotope (0.25%) relative to $^{140}$Ce (88.45%), which further complicates the $^{138}$Ce/$^{142}$Ce measurement by mass spectrometry.

The measurement of the La–Ce systematics is interesting for two reasons: (1) coupled to the Sm–Nd system, Ce isotopes can provide additional information about the shape of the Light REE pattern of the source material (Fig. 1A); (2) relative to Sm/Nd, larger La/Ce fractionation may occur in specific environments. In particular, at current oceanic conditions, Ce is partially oxidized into insoluble $Ce^{4+}$ and it is subtracted from seawater (Elderfield, 1988), resulting in large La/Ce fractionation in marine sediments formed in equilibrium with seawater (e.g. authigenic sediments, hydrothermal sediments, carbonates: see also Doucelance et al., 2014). In these materials, significant deviations of the $^{138}$Ce/$^{142}$Ce ratio from the chondritic reference can be generated in less than 100 Ma (Fig. 1B). Seawater and most marine sediments thus develop positive εCe through time (εCe are parts per ten thousand deviations from chondrites), whereas pure Fe–Mn crusts and nodules evolve toward negative εCe because $Ce^{4+}$ is strongly absorbed on their surfaces as they grow (Fig. 1B). Terrigeneous sediments that are not affected by such oxidative fractionation have intermediate values. Hence, the La–Ce system can offer new constraints on magma genesis in subduction zones because recycled marine sediments can be characterized by significant Ce isotope anomalies ($Ce_N/Ce^*$, where $Ce^* = [La_N + Pr_N]/2$) and their involvement should then produce Ce–Nd signatures that fall off of the mantle array correlation. Few Ce isotope studies of volcanic rocks from island arcs have been performed so far (Tanaka et al., 1987; Shimizu et al., 1992). Most analyzed samples display positive εNd and εCe and the involvement of marine sediments in their source was not detected. However, these studies were carried out more than 20 years ago and at that time the external precision on the $^{138}$Ce/$^{142}$Ce ratio was about 90 ppm (defined from the repeated measurements of the Ce reference material, Shimizu et al., 1992). Willbold (2007) has shown that using the new generation of thermo-ionization mass spectrometers allows the external precision to be improved by a factor of 4. Accordingly, it appears interesting to re-investigate the application of radiogenic Ce isotopes to the problematic of arc magma genesis.

In this paper we present an improved analytical technique that includes chemical purification of Ce, and mass spectrometry measurements based on the technique reported by Willbold (2007). Our Ce isotope dataset includes two basaltic rock standards (BCR-2 and BHVO-2) and two Ce reference material solutions (AMES and JMC-304) documented in previous publications (Tanaka and Masuda, 1982; Shimizu et al., 1984, 1988, 1990, 1992, 1994; Masuda et al., 1988; Amakawa et al., 1991; Makishima and Nakamura, 1991; Lee et al., 2001; Tanimizu and Tanaka, 2002; Hayashi et al., 2004; Tanimizu et al., 2004; Tazoe et al., 2007; Willbold, 2007). In a second part, we focus on the Lesser Antilles arc formed by the subduction of the Atlantic ocean lithosphere beneath the Caribbean plate for which a comprehensive set of geochemical data has already been published on both the arc lavas and the sediments present in front of the subduction zone (Carpentier et al., 2008, 2009; Labanieh et al., 2010, 2012). We report data obtained on 30 lavas from Martinique Island that erupted over the last 25 Ma and exhibit highly variable Sr–Nd–Pb isotopic compositions (Labanieh et al., 2010). In addition, we also report data for 5 sediments drilled at DSDP-site 144 that are representative of the potentially subducted sediments (Carpentier et al., 2008, 2009) and data for 4 mid-ocean ridge basalts (MORB) from the Atlantic and Pacific oceans. Finally we present an estimate of the present-day chondritic $^{138}$Ce/$^{142}$Ce ratio.

## 2. ANALYTICAL PROCEDURES

### 2.1. Chemical procedure

Terrestrial rocks analyzed in this study are basalts, dacites, andesites and sediments. Depending on their Ce concentration, the quantity of dissolved material ranges from 100 mg to 250 mg. Samples were acid-digested during 48 h at 75 °C in Savillex-PFA vessels using a 3:1 mixture of 48% HF and 65% $HNO_3$. Some perchloric acid ($HClO_4$) was added before the evaporation step to keep the precipitation of fluorides to a minimum. We checked the complete dissolution of the samples insuring that no precipitate or residual minerals were present in a 6 M HCl solution. For the sediments, prior to the digestion procedure, we destroyed the carbonated component with a 2 M-HCl:7 M-$HNO_3$ mixture.

For the chondrites, the dissolution was made with the same acids but the samples were placed in Teflon vessels in high-pressure steel-jacketed PTFE bombs (Parr) for one week (150 °C). The Teflon vessels were then opened and their content evaporated to dryness with $HClO_4$. After drying, a second dissolution under pressure was made

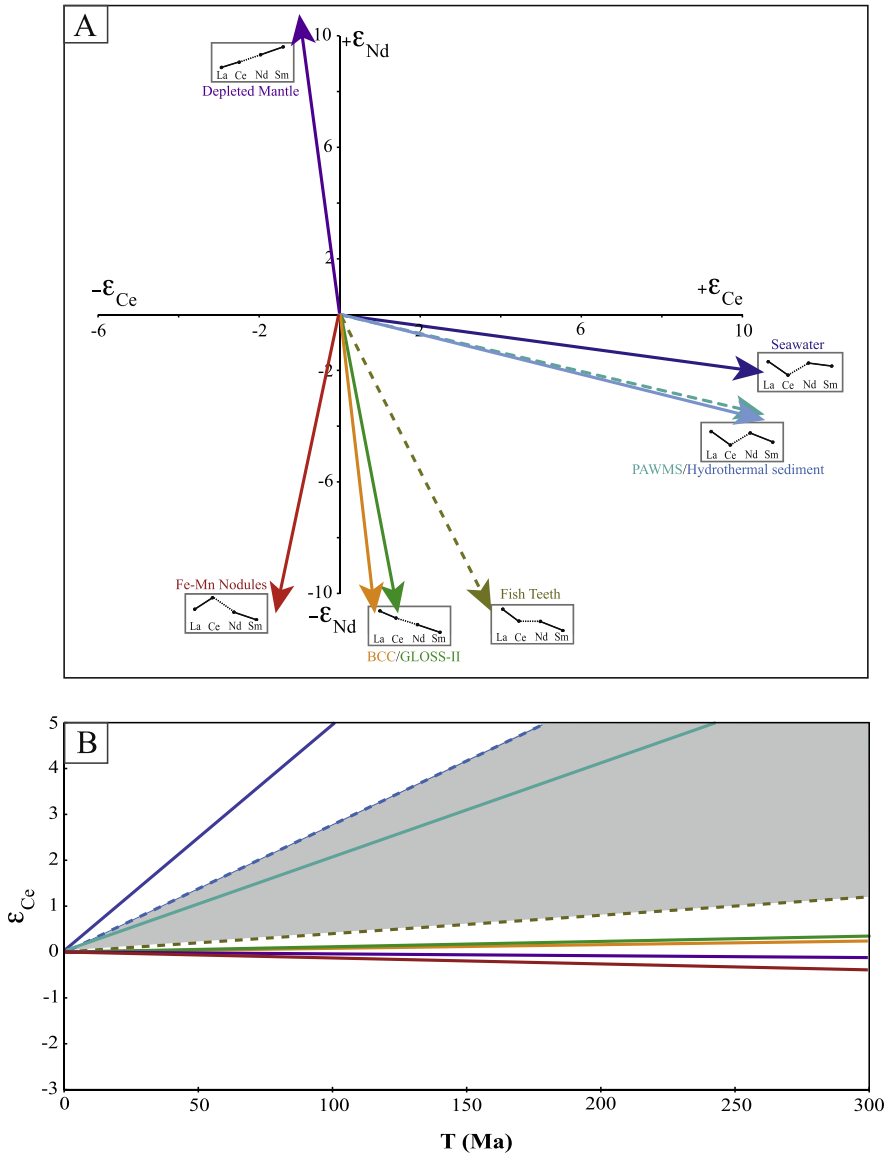


Fig. 1. (A) Schematic diagram of the Light REE pattern of the different reservoirs in a εNd *vs.* εCe space through time. εCe are parts per ten thousand deviations from chondrites ($\varepsilon Ce = [(^{138}Ce/^{142}Ce)_{reservoir}/(^{138}Ce/^{142}Ce)_{CHUR} - 1] \times 10^4$) and are calculated using $(^{138}Ce/^{142}Ce)_{CHUR} = 0.0225654$ (Shimizu et al., 1984; Makishima and Masuda, 1993; this study) and $(^{138}La/^{142}Ce)_{CHUR} = 0.00306$ (Makishima and Masuda, 1993). εNd are calculated using the CHUR values published in Bouvier et al. (2008): $^{143}Nd/^{144}Nd_{CHUR} = 0.512630$ and $^{147}Sm/^{144}Nd_{CHUR} = 0.1960$. (B) εCe values of Earth reservoirs and supergene environments as a function of time. The slope of each evolution line is given by the enrichment factor $f$(La/Ce) ($[La/Ce]_{reservoir}/[La/Ce]_{CHUR} - 1$, with $[La/Ce]_{CHUR} = 0.375$, Anders and Grevesse, 1989). Reservoirs and their $f$(La/Ce) and $f$(Sm/Nd) values are respectively as follows for both diagrams: Depleted MORB Mantle (DMM, Salters and Stracke, 2004): −0.22; 0.16; ferromanganese nodules collected at sites CHAIN-75-5 and AT-II-78-15 (Amakawa et al., 1991): −0.41; −0.34; GLObal Subducting Sediment GLOSS-II (Plank, 2014): 0.30; −0.33; Bulk Continental Crust (BCC, Rudnick and Gao, 2014): 0.20; −0.40; seawater (Alibo and Nozaki, 1999): 14.25; −0.37; fish teeth (Picard et al., 2002): 0.86; −0.44; Pacific Authigenic Weighted mean Sediment (PAWS, Hole et al., 1984): 5.91; −0.30; and hydrothermal Tonga sediments from site 596A (Plank and Langmuir, 1998): 8.02; −0.39. Sediments drilled at the South Antilles trench show the same La/Ce ratio as BCC, whereas those of the North Antilles trench resemble GLOSS-II (Plank, 2014). The gray field, in diagram (B), represents the cerium isotope evolution of various types of high La/Ce marine sediments. Their $^{138}Ce/^{142}Ce$ ratios will develop radiogenic values in few tens of million years. Although small, such variations from the CHUR evolution are larger than the analytical precision of about 0.4 ε-ppm obtained for Ce isotopes.

in 6 M HCl for another week (150 °C). If a residue was observed after centrifugation, the complete procedure was repeated. Due to the very low Ce contents of chondrites, large-size samples were used, specifically, 1.5 g for the carbonaceous chondrite Allende (CV3), and 2 g for the enstatite chondrite Sahara 97072 (EH3).

The isolation of REE from most other elements was performed by cation-exchange chromatography (15 mL of

AGW50-X8, 200–400 mesh) using 2.5 M HCl for introduction and 4 M HCl for REE elution. For the two chondrites, samples were split into 5–6 aliquots and loaded onto separate cation-exchange columns. The subsequent isolation of Ce was achieved by using two columns allowing the separation of the lanthanides in reverse order (see Fig. 2). A first Ce fraction was separated by using a long silica glass column ($L = 24$ cm, $D = 0.2$ cm, pressurized with $N_2$) filled with cationic resin (0.76 mL of AGW50-X8, 200–400 mesh) and 2-methylactic acid (2MLA equivalent to Hiba: α-hydroxyisobutyric acid) as eluent. We use a 0.27 M 2MLA solution adjusted to a pH of 4.6 by adding ammonia. The Ce fraction obtained from this column separation proved to be entirely free of La, but still contained small amounts of Nd and Pr, as an effect of column tailing. The Ce fraction was therefore further purified on a third column filled with Ln-Spec (Eichrom) extraction chromatography material, based on the HDEHP extractant loaded on a polymeric adsorbent Amberchrom CG71 ms (1.5 mL in 0.2 M HCl medium; Pin and Santos Zalduegui, 1997). In this separation scheme, Ce is eluted before both Pr and Nd and a pure Ce fraction is collected. The efficiency of the column was optimized by using resin with 20–50 μm particles instead of the more common, coarser grain-size (see Le Fèvre and Pin, 2005). Since Ce isotopes are measured as oxides, a very efficient separation of Pr and Ce is required. All PrO masses interfere on CeO masses and then the Pr signal cannot be monitored on a free mass during isotope measurement. The purity of the Ce fraction was evaluated by ICPMS (Agilent 7500) prior to Ce isotope measurements by thermo-ionization mass spectrometry (TIMS). The Ce/Pr ratio was always found to be higher

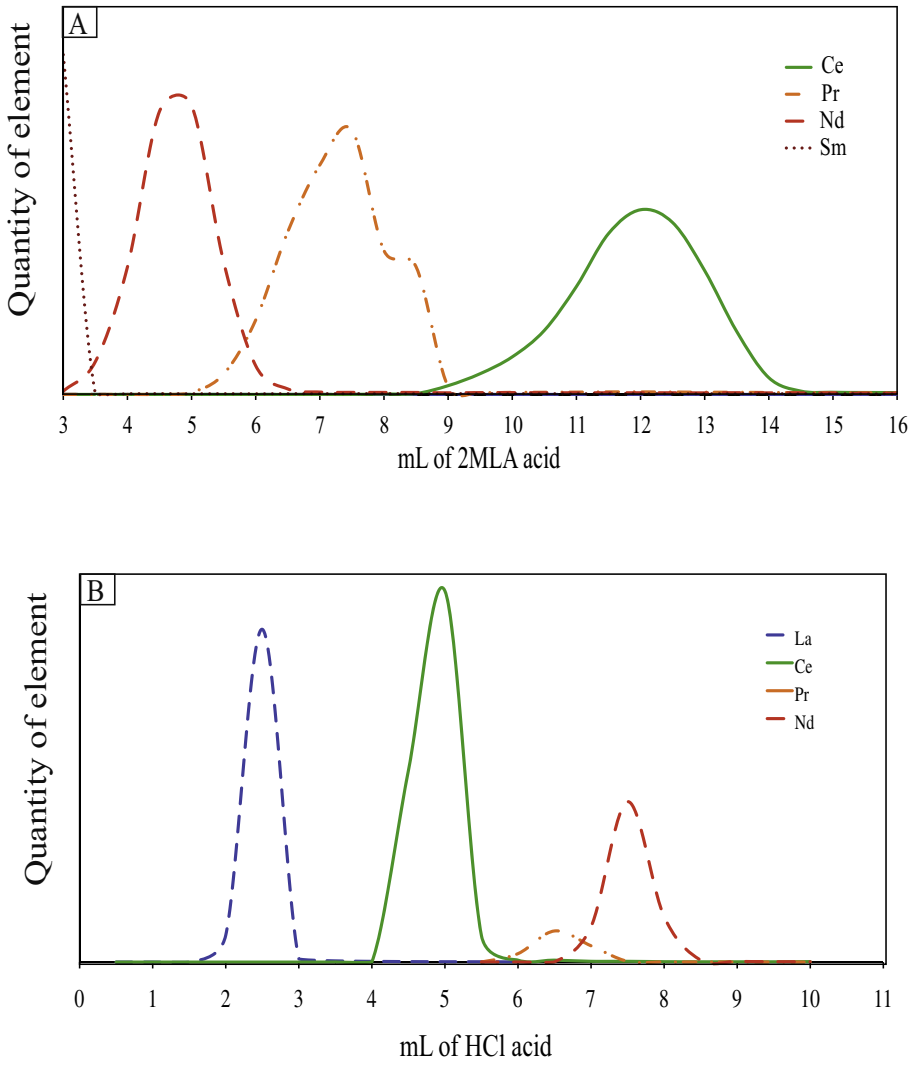


Fig. 2. Elution profile of the Rare Earth Elements (REE) during the two-combined separation. (A) Elution from heavy to light REE with 0.27 M 2MLA acid (pH = 4.6) under $N_2$ pressure. Approximately 15 mL are needed to collect Ce, but the elution profile may slightly change between different batches of prepared 2MLA solution. The REE standard loaded for the calibration here does not take into account the true proportion of the different REE. (B) Elution from Light REE to Heavy REE during LnSpec separation using 0.2 M HCl acid. The Ce is collected from 3.75 mL to 5.5 mL. Because it is difficult to measure precisely the Pr interference during TIMS analysis, the Ce peak is cut before the entire Ce elution to avoid any Pr in our sample. The yield is ~90%. Here the REE are in natural abundances.

than 1500 for terrestrial samples, and 200 for the meteorites. The Ba contribution is measured during the isotope measurement and the mean signal measured was never higher than the baseline for both reference materials and samples. During the course of this study, the total Ce chemistry blanks ranged from 260 pg to 960 pg and always remained negligible relative to the large quantity of Ce (>1 μg) present in the samples.

### 2.2. Mass spectrometry

#### 2.2.1. Isotope analysis

All previous Ce isotope ratio measurements of natural samples used TIMS (Dickin et al., 1987; Dickin, 1987; Makishima et al., 1987; Makishima and Nakamura, 1991; Tazoe et al., 2007). The study of Willbold (2007) compares results obtained on the Ames Ce reference material using both thermal- and plasma-ionization mass spectrometers. It is shown that accurate and reproducible measurements of the $^{138}Ce/^{136}Ce$ ratio can only be obtained using a TIMS and running Ce as the molecular oxide ion. All alternative approaches suffer from interferences that cannot be properly corrected. Based on these results, we used a Thermo-Finnigan Triton thermal ionization mass spectrometer at the Laboratoire Magmas et Volcans in Clermont-Ferrand (France) and measured the isotopic ratios on $CeO^+$ ion beams. A few preliminary tests on $Ce^+$ as the emitting species proved to be disappointing, mainly because relatively weak and unstable ion beams were obtained, confirming results obtained by Willbold (2007).

About 1 μg of Ce was loaded in 2.5 M HCl on pre-degassed Re filaments (99.99%; H. Cross Company) with double filament geometry. Since oxide molecular ions were measured, the type of oxygen supplement used besides residual gas in the source chamber is an important aspect of the method. Two kinds of added oxygen were investigated: (i) 1 μL of $3MH_3PO_4$ loaded on the evaporation filament together with the sample; and (ii) direct introduction of $O_2$ gas in the source through a gas bleed device. The O isotope fractionation during analysis is reduced with the introduction of $O_2$ (0.02–0.1% on the $^{18}O/^{16}O$ ratio) compared to the $H_3PO_4$ method (0.3–0.6%). However the source vacuum was impaired significantly to ca. $1 \times 10^{-7}$ mbar instead of $4–5 \times 10^{-8}$ mbar under normal conditions. A poorer source vacuum is likely to increase the pressure in the flight tube and may lead to a significant deterioration of the abundance sensitivity. Thus we decided to use phosphoric acid as the major oxygen source.

The Faraday cup configuration is given in Table 1. Ce has four naturally occurring isotopes ($^{136}Ce = 0.19\%$, $^{138}Ce = 0.25\%$, $^{140}Ce = 88.45\%$, and $^{142}Ce = 11.11\%$). The $^{140}Ce^{16}O^+$ ion, which might saturate the corresponding amplifier, was not included in the measurements so that we could increase significantly the ion beam size and measure the minor Ce isotopes more precisely. Each measurement corresponds to 24 blocks of 15 cycles (8 s integration) in static, multicollection mode, using amplifier rotation to circumvent differences in amplifier gains. The baseline is measured before each block (30 s) by deflecting the ion beam. Isotopic ratios are corrected for mass fractionation using an exponential law and $^{136}Ce/^{142}Ce = 0.01688$ (Makishima et al., 1987). One μg Ce loads allow stable intensities over the two hours of measurement. Samples that are poorer in Ce are measured at lower intensity or aborted before the end of the acquisition.

Table 1 shows that all CeO masses are affected by isobaric interferences of Ba, La, Pr and Nd oxide species. Correction for interferences from REE oxides cannot be done properly during measurements. Their absence in the Ce fraction was checked systematically by ICP-QMS measurement prior to isotope ratio analyses. For Ba interferences, measuring Ce as the oxide species is a major advantage since it offers further discrimination against Ba, a fairly ubiquitous element. Indeed Ba emits as metal species under the conditions used to produce large $CeO^+$ ion beams (the ionization potential is 5.2 eV for Ba, against 6.9 eV for BaO; see Lide David, 1994). The signal measured on L4 at mass 150 ($^{134}Ba^{16}O$) for both reference material and samples was similar to the baseline value. We conclude that once separated, Ba does not cause isobaric interferences during isotope ratio measurements on $CeO^+$ using TIMS, as discussed by Willbold (2007). The second cup configuration shown in the last line of Table 1 is used to estimate the tailing effect (see further details in Section 2.2.3).

#### 2.2.2. Oxygen correction

Since Ce isotopes are measured as $CeO^+$ ions, the $^{138}Ce/^{142}Ce$ ratio needs to be corrected for the contribution of molecular ions built with the minor isotopes of oxygen. Different correction methods have been proposed in previous studies: (i) using a constant atmospheric oxygen isotope composition based on literature values of $^{18}O/^{16}O$ and $^{17}O/^{16}O$ (e.g. Tanaka and Masuda, 1982); (ii) determining $^{18}O/^{16}O$ and $^{17}O/^{16}O$ isotopic ratios by using the nearby, mono-isotopic Pr (Makishima et al., 1987). In this case, the average values obtained on $PrO^+$ is used for the correction on Ce isotope ratios; and (iii) determining $^{18}O/^{16}O$ *in situ* by using an iterative calculation scheme that combines an exponential mass discrimination factor and measurements of $^{142}Ce^{18}O$ and $^{136}Ce^{16}O$ ion beams to calculate $^{18}O/^{16}O$ (Makishima and Masuda, 1994; Willbold, 2007). We compared the three methods during one sequence of measurements and the best external reproducibility was obtained with method 3. Accordingly, this method was used to calculate all the results presented in this study.

#### 2.2.3. Tailing correction

During isotope ratio measurements, the presence of a major isotope may interfere with the determination of adjacent minor isotopes, especially on the low mass side, because a small fraction of ions of the major isotope can lose some of their kinetic energy by colliding with molecules of residual gases in the flight tube of the mass spectrometer. These lower energy ions are more deflected by the magnetic field than their nominal mass would imply, and they are detected at a lower mass position, raising the background on the lower mass peaks. This "peak tailing" effect is of special concern in the case of Ce because the small peak of the

Table 1
Presentation of the Faraday cup configuration and corresponding emitted oxides and interference masses for Ce isotope analysis.

| Faraday cup | L4 | L3 | L2 | L1 | Ax | H1 | H2 | H3 | H4 |
|---|---|---|---|---|---|---|---|---|---|
| Line 1: Main masses | 150 | 152 | 153 | 154 | 155 | 158 | 159 | 160 | 161 |
| Oxides | $^{134}Ba^{16}O$ | $^{136}Ce^{16}O$ | $^{136}Ce^{17}O$ | $^{138}Ce^{16}O$ | $^{139}La^{16}O$ | $^{142}Ce^{16}O$ | $^{142}Ce^{17}O$ | $^{142}Ce^{18}O$ | $^{143}Nd^{18}O$ |
| Interference on main masses | $^{132}Ba^{18}O$ | $^{135}Ba^{17}O$ | $^{137}Ba^{16}O$ | $^{136}Ce^{18}O$ | $^{138}La^{17}O$ | $^{140}Ce^{18}O$ | $^{141}Pr^{18}O$ | $^{144}Nd^{16}O$ | $^{144}Nd^{17}O$ |
| | | $^{134}Ba^{18}O$ | $^{136}Ba^{17}O$ | $^{138}La^{16}O$ | $^{138}Ce^{17}O$ | $^{142}Nd^{16}O$ | | $^{143}Nd^{17}O$ | $^{145}Nd^{16}O$ |
| | | | $^{135}Ba^{18}O$ | $^{138}Ba^{16}O$ | $^{138}Ba^{17}O$ | $^{141}Pr^{17}O$ | | $^{148}Nd^{18}O$ | |
| | | | | $^{137}Ba^{17}O$ | $^{137}Ba^{18}O$ | | | | |
| | | | | $^{136}Ba^{18}O$ | | | | | |
| Line 2: Intermediate masses | 149.5 | 151.5 | 152.5 | 153.5 | 154.5 | 157.5 | 158.5 | 159.5 | 160.5 |

radiogenic isotope $^{138}Ce$ is measured close to the $^{140}Ce$ peak that is about 350 times more intense.

Here, we determined the impact of the $^{140}Ce^{16}O$ peak tailing on the measurement on its lower mass side using a two magnetic field steps acquisition procedure, with a first measurement at the center of the peaks (called line 1 in Table 1), followed by a second integration at half-mass position ($-0.5\ \Delta M$ called line 2 in Table 1). The signal was integrated during 8 s in the line 1 and during 4 s in the line 2 (with an idle time of 3 s following the magnetic field change). Data acquisition consists in 24 blocks of 15 cycles and the baseline is measured for 30 s before each block. The peak tailing is calculated using an exponential curve that fits the intensities measured at intermediate masses. A linear interpolation would not reproduce the curvature of the background and therefore overestimate both the $^{136}Ce$ and $^{138}Ce$ background intensities (Deschamps et al., 2003). The calculated $^{140}Ce^{16}O$ peak tail is then subtracted from the raw $^{136}Ce^{16}O$ and $^{138}Ce^{16}O$ signals measured in line 1 (see Table 1). The average intensities subtracted at masses 152 and 154 are $1 \times 10^{-5}$ V and $2 \times 10^{-5}$ V respectively for a signal of 10 V at mass 158. Fifteen Ames reference materials were measured over a period of one week using different source vacuum conditions ranging from $1.6 \times 10^{-7}$ to $4.2 \times 10^{-8}$ mbar (Table 2). The measurements done at high-pressure values reflect the introduction of pure oxygen in the source. There is no correlation between the tailing correction ($\Delta\varepsilon Ce$) and source vacuum (Fig. 3). Correction on the $^{138}Ce/^{142}Ce$ ratio, expressed in terms of epsilon values, range from 0.2 to 0.7 unit in this session. Fig. 4 shows that the $^{138}Ce/^{142}Ce$ ratios obtained after correction are identical within errors, whether they are corrected on-line using the 2-step acquisition procedure (Table 1), or offline by subtracting the peak-tail defined by averaging the correction calculated from reference material measurements. Hence, for the poorest samples we minimize the total running time by using the one line acquisition procedure. Then the off-line peak-tail correction, calculated from repeated reference material measurements with the 2-step acquisition procedure and analyzed over the same session, is applied to these samples. Session means that the mass spectrometer was used only for Ce measurement during this period. One session typically lasted between one week and one month. In conclusion the tailing correction is reproducible within a single session and independent of the source vacuum conditions. The tailing has to be redefined in each analysis session. During this study the correction on the $^{138}Ce/^{142}Ce$ ratio can be negligible (0.09 $\varepsilon$-unit in session 6) or as high as 1.1 $\varepsilon$-unit. On average the correction is equal to 0.7 $\varepsilon$-unit. The non-reproducibility of the tailing effect through time can be noticed also looking at the dataset published by Willbold (2007). We have no explanation since no correlation has been found between the amplitude of the tailing and the measurement conditions.

Our configuration is different from that presented in Willbold (2007) since we use 8 Faraday cups instead of 4. All the half masses are therefore measured simultaneously while Willbold (2007) used a 6-line procedure in which the half masses were measured in sequence during 1 s only, a non-optimal procedure for signals close to the noise level. The two different cup configurations have been compared during the same analytical session and results obtained on the Ames reference material are presented in Fig. 5. The integration time at half-masses in Willbold's configuration has been increased from 1 s to 4 s in order to compare signals integrated on similar time intervals. The peak tail correction on the $^{138}Ce/^{142}Ce$ ratio is more important using Willbold's configuration: 1.5 $\varepsilon$-unit compared to 0.7 with our configuration. The two configurations do not consider the same mass in axial cup (154 and 155, respectively) causing length difference between Faraday cups. Once measured data are corrected for the tailing effect, we obtain similar $^{138}Ce/^{142}Ce$ ratios (Fig. 5).

### 2.3. Results and reproducibility

#### *2.3.1. Ames and JMC-304 reference materials*

Our measurements were performed during 8 sessions over a period of 33 months. The Ames, $^{138}Ce/^{142}Ce$ average values determined in each session are reported in Table 3 and plotted in Fig. 6. The long-term, mean $^{138}Ce/^{142}Ce$ value calculated for the 89 Ames measurements is $0.0225732 \pm 18$ ($2\sigma = 80$ ppm). We note that the long-term reproducibility is slightly higher than the reproducibility obtained on AMES reference materials measured during a single analytical session (on average we have 40 ppm considering results obtained on the 8 sessions presented in Table 3). We also observe that the $^{138}Ce/^{142}Ce$ ratios measured during the two sessions #6 and #7 are significantly higher that those measured before and after. These sessions correspond to the two last analytical sessions performed before the replacement of the Faraday cups. When they are removed from the calculation, the external

Table 2
Ames reference materials measured over a week with variable source vacuum. $^{138}Ce/^{142}Ce$ non-corrected for the tailing effect and $^{138}Ce/^{142}Ce$ corrected for the tailing effect using online measurements at half-masses (see cup configuration in Table 1). Epsilon cerium expressed as $\varepsilon Ce = [(^{138}Ce/^{142}Ce)_{sample}/(^{138}Ce/^{142}Ce)_{CHUR} - 1 \times 10^4]$ with $(^{138}Ce/^{142}Ce)_{CHUR} = 0.0225654$ (this study). 2 s.e. errors are internal errors. The external reproducibility (2 s.d.) corresponds to twice the standard deviation.

| Run | Source vacuum | $^{138}Ce/^{142}Ce$ | 2 s.e. | $\varepsilon$ Ce | 2 s.e. | $^{138}Ce/^{142}Ce$ | 2 s.e. | $\varepsilon$ Ce | 2 s.e. | $\Delta\varepsilon Ce$ |
|---|---|---|---|---|---|---|---|---|---|---|
| | mbar | Non corrected of the tailing effect | | | | Corrected of the tailing effect | | | | |
| 1 | $1.48 \times 10^{-7}$ | 0.0225747 | 0.0000004 | 4.12 | 0.19 | 0.0225738 | 0.0000004 | 3.73 | 0.19 | 0.39 |
| 2 | $1.38 \times 10^{-7}$ | 0.0225756 | 0.0000003 | 4.53 | 0.13 | 0.0225746 | 0.0000003 | 4.06 | 0.13 | 0.47 |
| 3 | $1.19 \times 10^{-7}$ | 0.0225753 | 0.0000003 | 4.38 | 0.11 | 0.0225745 | 0.0000003 | 4.02 | 0.11 | 0.36 |
| 4 | $1.57 \times 10^{-7}$ | 0.0225753 | 0.0000003 | 4.39 | 0.13 | 0.0225739 | 0.0000003 | 3.78 | 0.13 | 0.61 |
| 5 | $1.48 \times 10^{-7}$ | 0.0225752 | 0.0000003 | 4.35 | 0.14 | 0.0225742 | 0.0000003 | 3.90 | 0.14 | 0.46 |
| 6 | $4.32 \times 10^{-8}$ | 0.0225756 | 0.0000003 | 4.51 | 0.12 | 0.0225747 | 0.0000003 | 4.12 | 0.12 | 0.39 |
| 7 | $4.70 \times 10^{-8}$ | 0.0225757 | 0.0000003 | 4.55 | 0.15 | 0.0225744 | 0.0000003 | 3.99 | 0.15 | 0.56 |
| 8 | $4.27 \times 10^{-8}$ | 0.0225761 | 0.0000002 | 4.76 | 0.11 | 0.0225748 | 0.0000002 | 4.19 | 0.11 | 0.58 |
| 9 | $4.10 \times 10^{-8}$ | 0.0225753 | 0.0000004 | 4.40 | 0.17 | 0.0225743 | 0.0000004 | 3.96 | 0.17 | 0.44 |
| 10 | $6.79 \times 10^{-8}$ | 0.0225754 | 0.0000004 | 4.42 | 0.16 | 0.0225744 | 0.0000004 | 3.98 | 0.16 | 0.44 |
| 11 | $5.67 \times 10^{-8}$ | 0.0225760 | 0.0000004 | 4.69 | 0.18 | 0.0225749 | 0.0000004 | 4.23 | 0.18 | 0.46 |
| 12 | $4.65 \times 10^{-8}$ | 0.0225763 | 0.0000003 | 4.83 | 0.14 | 0.0225750 | 0.0000003 | 4.25 | 0.14 | 0.58 |
| 13 | $4.46 \times 10^{-8}$ | 0.0225764 | 0.0000006 | 4.89 | 0.28 | 0.0225760 | 0.0000006 | 4.69 | 0.28 | 0.20 |
| 14 | $4.45 \times 10^{-8}$ | 0.0225763 | 0.0000005 | 4.83 | 0.24 | 0.0225754 | 0.0000005 | 4.41 | 0.24 | 0.42 |
| 15 | $4.24 \times 10^{-8}$ | 0.0225757 | 0.0000002 | 4.58 | 0.11 | 0.0225741 | 0.0000002 | 3.85 | 0.11 | 0.73 |
| Mean ± 2 s.d. | | 0.0225757 | 0.0000010 | 4.55 | 0.43 | 0.0225746 | 0.0000011 | 4.08 | 0.50 | 0.47 |

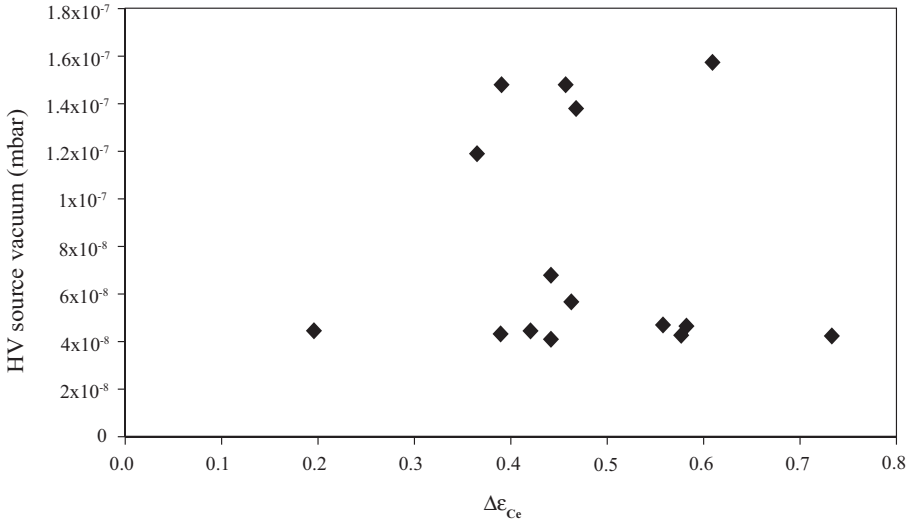


Fig. 3. Variation of the tailing correction ($\Delta\varepsilon Ce = (^{138}Ce/^{142}Ce)_{measured} - (^{138}Ce/^{142}Ce)_{tail\text{-}corrected}$) expressed in 10,000 deviation in function of the source vacuum.

reproducibility on the $^{138}Ce/^{142}Ce$ ratio improves significantly and reaches 22 ppm ($0.0225727 \pm 5$; 2 s.d; $n = 66$). Nevertheless, there is no reason to exclude the data obtained during those two sessions from the overall dataset.

The two mean values calculated including or not sessions #6 and #7 (mean values 1 and 2 in Table 3) are identical within uncertainty and similar to the value of $0.0225749 \pm 5$ (conversion of the $^{138}Ce/^{136}Ce$ ratio with a $^{136}Ce/^{142}Ce$ constant of 0.01688) reported in Willbold (2007) and determined on 34 AMES measurements. The two chondrites have been measured during the session #7, a session for which the peak tail was negligible. This is the reason why we have chosen to normalize all the $^{136}Ce/^{142}Ce$ ratios measured in our study to the mean AMES value measured in session #7 that is equal to $0.0225746 \pm 3$.

We have also measured the isotopic composition of the Johnson Matthey reference material, JMC-304, frequently used as the Ce isotope reference material in previous studies (Tanaka and Masuda, 1982; Shimizu et al., 1984, 1988, 1990, 1992, 1996; Masuda et al., 1988; Amakawa et al., 1991; Makishima and Nakamura, 1991; Lee et al., 2001; Tanimizu and Tanaka, 2002; Hayashi et al., 2004; Tanimizu et al., 2004; Tazoe et al., 2007). The values published for this reference material display a large scatter. One of the reasons is the different normalization values

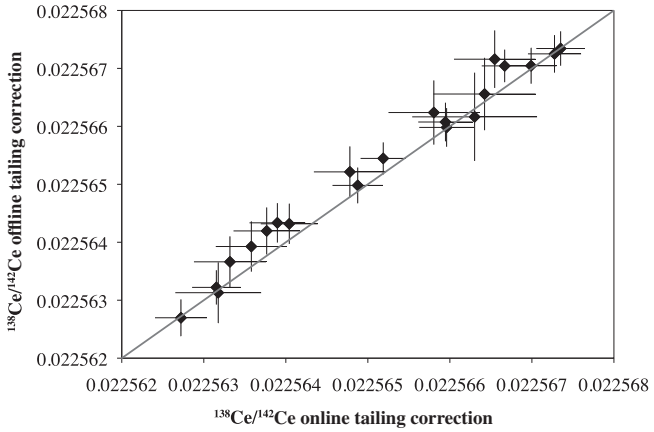


Fig. 4. On-line vs. off-line $^{140}Ce$ peak-tail corrections of $^{138}Ce/^{142}Ce$ ratios. All these samples have been measured during the same analytical session (session 8). For the off-line correction a constant value of $1.74 \times 10^{-6}$ (equivalent to $\Delta\varepsilon Ce = 0.77$) was determined from AMES reference material measurements and has been subtracted from the measured $^{138}Ce/^{142}Ce$ ratios of samples. All these samples plot on a 1:1 line.

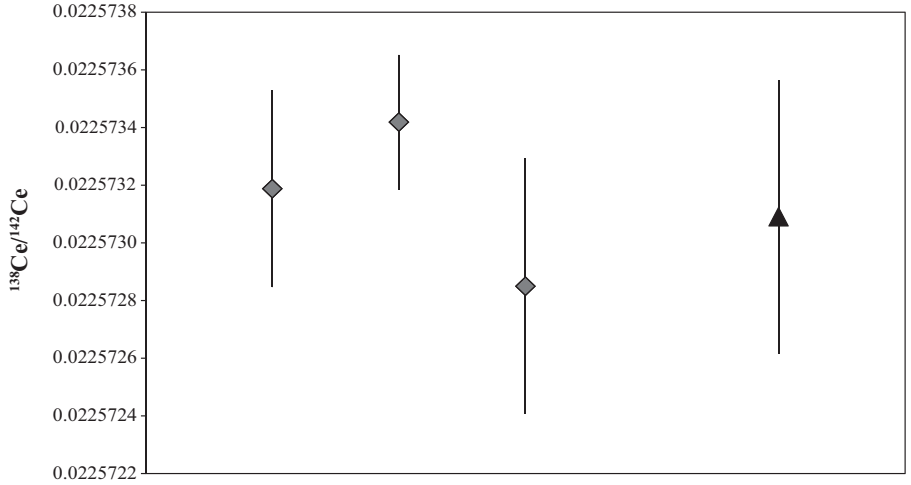


Fig. 5. Comparison of the $^{138}Ce/^{142}Ce$ ratios measured for the Ce Ames reference material on the LMV Triton using two different cup configurations. Diamonds correspond to measurements achieved with the two-line cup configuration used in this study (see also Table 1). The mean $\varepsilon Ce$ calculated from the 3 analyses is $3.44 \pm 0.25$ with the applied correction $\Delta\varepsilon = 0.7$. The triangle is the Ames $^{138}Ce/^{142}Ce$ ratio measured with the cup configuration proposed by Willbold (2007), i.e., using four Faraday cups and a six-line procedure to determine the peak-tail correction. Half-masses are all measured on the central Faraday cup with an integration time of 4 s (instead of 1 s as in the Willbold's study). The $\varepsilon Ce = 3.41 \pm 0.21$ with a $\Delta\varepsilon$ of 1.5. Final $^{138}Ce/^{142}Ce$ ratios are similar whatever the measurement and peak-tail-correction procedures operated. The peak-tail correction, however, is more important when half-masses are measured in the central Faraday cup.

used to correct for mass fractionation ($^{136}Ce/^{142}Ce = 0.01688$ or 0.0172). When all the data are calculated using $^{136}Ce/^{142}Ce = 0.01688$, $^{138}Ce/^{142}Ce$ values range from $0.0225684 \pm 19$ (Makishima and Nakamura, 1991) to $0.0225891 \pm 26$ (Tanimizu and Tanaka, 2002), which corresponds to ~9 $\varepsilon$-unit difference. Different batches of the JMC reference material (not reported in the publications) might have been used. We cannot exclude that the reference material is isotopically heterogeneous and also inter-laboratory biases. It must be also noted that studies reporting values of JMC-304 do not mention any peak-tail correction. However, the measurements were performed on mass spectrometers in which baselines were measured at half-masses, instead of deflecting the ion beam as within the Triton instrument. This procedure integrates directly the peak-tail correction into the baseline measurements, but considers a linear interpolation instead of an exponential one. Here, we report a $^{138}Ce/^{142}Ce$ value of $0.0225706 \pm 9$ (2 s.d. = 40 ppm, $n = 10$) for the JMC-304 (Table 3).

### 2.3.2. BHVO-2 and BCR-2 rock standards

$^{138}Ce/^{142}Ce$ measured on the two basaltic rock standards BHVO-2 and BCR-2 are given in Table 3. Repeated measurements on different dissolutions gave the following results: $^{138}Ce/^{142}Ce = 0.0225646 \pm 17$ (2 s.d. = 76 ppm; $n = 10$) for BHVO-2 and $^{138}Ce/^{142}Ce = 0.0225663 \pm 7$ (2 s.d. = 31 ppm; $n = 8$) for BCR-2. Makishima and

Table 3
$^{138}Ce/^{142}Ce$ ratios corrected for the tailing effect determined for solution standards, rock standards and meteorites. Ames standards have been measured over the 8 TIMS sessions. The $^{138}Ce/^{142}Ce$ ratios determined during the sessions 6 and 7 are significantly higher than those measured in other sessions and correspond to the reference materials measured just before the replacement of the Faraday cups of our Triton instrument. Ce isotopic ratios of JMC-304, rock standards BHVO-2, BCR-2 and meteorites are normalized to the average AMES ratio measured during session 7 ($^{138}Ce/^{142}Ce = 0.0225746$). Reported errors correspond to internal errors (2 s.e.) for single measurements and external errors (2 s.d.) for repeated measurements. $^{138}Ce/^{142}Ce$ ratios are expressed in $\varepsilon$-unit using $(^{138}Ce/^{142}Ce)_{CHUR} = 0.0225654$ (this study). Dup. means different duplicates of the same sample (different dissolutions) whereas re-run corresponds to several measurements of the same dissolution (+chemistry procedure).

| | Session | $^{138}Ce/^{142}Ce$ | 2 s.d. | $\varepsilon$ Ce | 2 s.d. |
|---|---|---|---|---|---|
| Ames | 1 ($n = 6$) | 0.0225725 | 0.0000015 | 3.15 | 0.68 |
| Ames | 2 ($n = 6$) | 0.0225728 | 0.0000011 | 3.27 | 0.51 |
| Ames | 3 ($n = 7$) | 0.0225729 | 0.0000008 | 3.31 | 0.31 |
| Ames | 4 ($n = 24$) | 0.0225729 | 0.0000010 | 3.31 | 0.45 |
| Ames | 5 ($n = 4$) | 0.0225723 | 0.0000006 | 3.06 | 0.24 |
| Ames | 6 ($n = 15$) | 0.0225746 | 0.0000011 | 4.08 | 0.50 |
| Ames | 7 ($n = 8$) | 0.0225746 | 0.0000003 | 4.09 | 0.14 |
| Ames | 8 ($n = 19$) | 0.0225730 | 0.0000009 | 3.35 | 0.40 |
| Mean $\pm$ 2 s.d. | ($n = 89$) | 0.0225732 $\pm$ 18 | | 3.45 $\pm$ 0.80 | |
| Mean $\pm$ 2 s.d. | ($n = 66$) | 0.0225727 $\pm$ 5 | | 3.24 $\pm$ 0.23 | |
| JMC-304 | | | | | |
| Mean $\pm$ 2 s.d. | ($n = 10$) | 0.0225706 $\pm$ 9 | | 2.32 $\pm$ 0.38 | |
| | Session | $^{138}Ce/^{142}Ce$ | 2 s.e. | $\varepsilon$ Ce | 2 s.e. |
| BHVO-2 $_{Dup}$ | 2 | 0.0225649 | 0.0000004 | −0.23 | 0.18 |
| BHVO-2 $_{rerun}$ | 2 | 0.0225640 | 0.0000005 | −0.62 | 0.22 |
| BHVO-2 $_{rerun}$ | 2 | 0.0225637 | 0.0000006 | −0.74 | 0.27 |
| BHVO-2 $_{Dup.}$ | 2 | 0.0225648 | 0.0000004 | −0.27 | 0.19 |
| BHVO-2 $_{rerun}$ | 2 | 0.0225654 | 0.0000005 | −0.02 | 0.22 |
| BHVO-2 $_{Dup.}$ | 3 | 0.0225653 | 0.0000004 | −0.05 | 0.17 |
| BHVO-2 $_{Dup.}$ | 3 | 0.0225662 | 0.0000005 | 0.37 | 0.21 |
| BHVO-2 $_{Dup.}$ | 3 | 0.0225637 | 0.0000005 | −0.77 | 0.24 |
| BHVO-2 $_{Dup.}$ | 4 | 0.0225644 | 0.0000003 | −0.42 | 0.14 |
| BHVO-2 $_{rerun}$ | 8 | 0.0225638 | 0.0000003 | −0.72 | 0.13 |
| Mean BHVO-2 $\pm$ 2 s.d. | ($n = 10$) | 0.0225646 $\pm$ 17 | | 0.35 $\pm$ 0.76 | |
| | Session | $^{138}Ce/^{142}Ce$ | 2 s.e. | $\varepsilon$ Ce | 2 s.e. |
| BCR-2 $_{Dup.}$ | 4 | 0.0225663 | 0.0000003 | 0.39 | 0.14 |
| BCR-2 $_{Dup.}$ | 4 | 0.0225664 | 0.0000003 | 0.43 | 0.12 |
| BCR-2 $_{rerun}$ | 6 | 0.0225663 | 0.0000004 | 0.40 | 0.16 |
| BCR-2 $_{Dup.}$ | 7 | 0.0225656 | 0.0000004 | 0.08 | 0.18 |
| BCR-2 $_{Dup.}$ | 7 | 0.0225663 | 0.0000003 | 0.39 | 0.14 |
| BCR-2 $_{rerun}$ | 8 | 0.0225662 | 0.0000003 | 0.34 | 0.12 |
| BCR-2 $_{rerun}$ | 8 | 0.0225664 | 0.0000003 | 0.43 | 0.12 |
| BCR-2 $_{rerun}$ | 8 | 0.0225669 | 0.0000005 | 0.65 | 0.23 |
| Mean BCR-2 $\pm$ 2 s.d. | ($n = 8$) | 0.0225663 $\pm$ 7 | | 0.39 $\pm$ 0.31 | |
| Allende | Session 7 | 0.0225657 | 0.0000004 | 0.12 | 0.17 |
| Sahara 97072 | Session 7 | 0.0225652 | 0.0000003 | −0.11 | 0.15 |
| Mean CHUR $\pm$ 2 s.d. | ($n = 2$) | 0.0225654 $\pm$ 7 | | 0.01 $\pm$ 0.32 | |

Nakamura (1991) measured the BCR-1 rock standard and we note a difference of 0.5 $\varepsilon$-unit between our BCR-2 result and their BCR-1 measurement. According to the study of Raczek et al. (2003), the two standards BCR-1 and BCR-2 have the same Nd isotope composition. Then it seems reasonable to assume that their Ce isotopic compositions are also identical and that the difference represents an analytical biais.

### 2.3.3. Chondrites

Two pioneer studies provided Ce isotopic values for meteoritic materials including chondrites and achondrites from the eucrite group (Shimizu et al., 1984; Makishima and Masuda, 1993). The average chondritic value for $^{138}Ce/^{142}Ce$ was defined at 0.0225652 $\pm$ 24 and is equal to 0.0225664 when the data are normalized to our BCR-2 value (see part 2.3.2). Here, we report values for the carbonaceous chondrite Allende and the enstatite chondrite Sahara 97072. The measured ratios are not only indistinguishable (0.0225654 $\pm$ 7, 2 s.d. = 32 ppm, $n = 2$) but also similar to the previously recommended value for chondrites considering the uncertainty (Table 3, Fig. 7). During the analysis of the chondrites, no significant tailing effect was observed ($\Delta\varepsilon Ce = 0.09$), so no peak-tail correction was applied to the chondritic $^{138}Ce/^{142}Ce$ ratio. This value is used here as CHUR reference to calculate all $\varepsilon$Ce values.

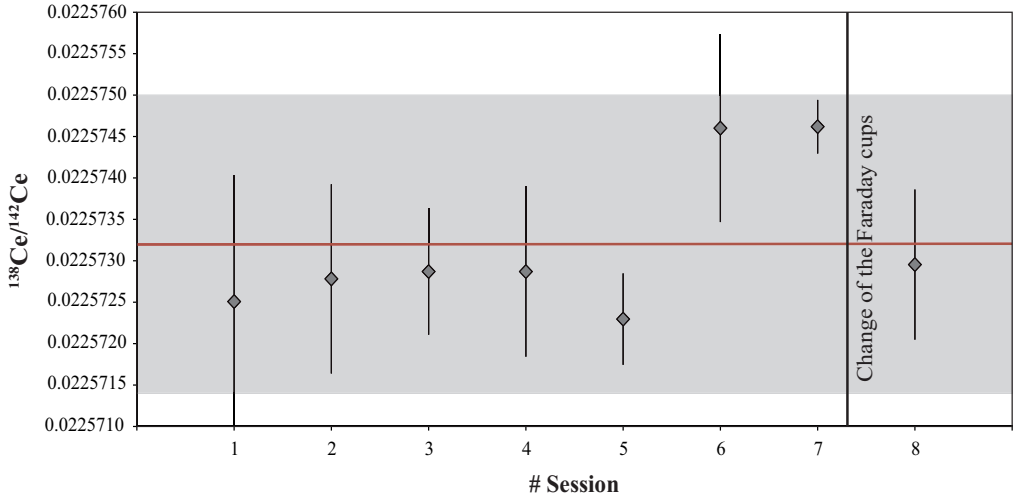


Fig. 6. Evolution of the mean $^{138}Ce/^{142}Ce$ ratios of the Ames reference material calculated for every analytical session. The thick line represents the average $^{138}Ce/^{142}Ce$ value of the Ames reference material; it is equal to 0.0225732. The gray field corresponds to the external reproducibility ($2\sigma = 80$ ppm).

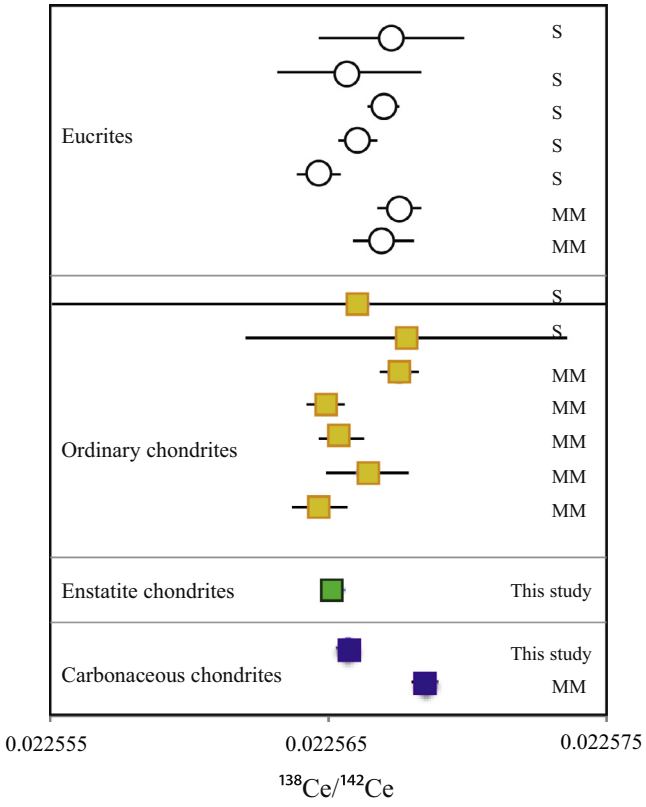


Fig. 7. $^{138}Ce/^{142}Ce$ ratios measured in chondrites (carbonaceous, ordinary and enstatite chondrites), and eucrites (here basaltic with a chondritic La/Ce ratio). Measurements in this study are compared to those published by Makishima and Masuda, 1993 (labeled MM) and Shimizu et al., 1984 (labeled S). Note here that we have improved the analytical precision and the two chondrites measured in this study have the same $^{138}Ce/^{142}Ce$ ratio. Literature data have been normalized to the BCR value (see text for more detail).

## 3. LESSER ANTILLES ARC: MARTINIQUE ISLANDS LAVAS

### 3.1. Framework and sample description

The Lesser Antilles arc results from the west-northwest subduction of the Atlantic lithosphere beneath the Caribbean Plate. Martinique is located in the central part of the Lesser Antilles arc and has recorded the most complete history of the arc with three main phases of volcanic activity (old volcanism: 24.8–20.8 Ma, intermediate volcanism: 16.1–7.1 Ma, and recent volcanism: 5.1 Ma-present-day; Germa et al., 2010, 2011a,b). Martinique lavas exhibit a large range of Sr–Nd–Pb–Hf isotopic compositions covering the entire range known for worldwide island arc lavas (White and Dupré, 1986; Davidson, 1987; Carpentier et al., 2008; Labanieh et al., 2010). The origin of these isotopic variations is linked to the involvement of sediments, but whether it is through crustal assimilation or by recycling of subducted sediments in the mantle wedge remains highly debated (Davidson, 1986, 1987; White and Dupré, 1986; Davidson and Harmon, 1989; Thirlwall et al., 1996; Smith et al., 1997; Labanieh et al., 2010, 2012; Bezard et al., 2014; Tang et al., 2014). The sediments deposited on the Atlantic plate that enters the Lesser Antilles subduction zone form a pile that gets thicker towards the South when approaching the South American continent. They have been intensively studied by Carpentier et al. (2008, 2009) who demonstrated the overwhelming influence of the terrigeneous material coming from the erosion of the Guyana and Brazilian shields (White and Dupré, 1986). They all have isotopic characteristics typical of old crustal material with radiogenic Sr and Pb isotope compositions and unradiogenic Nd and Hf (Carpentier et al., 2008, 2009).

We measured the Ce isotopic composition of 30 Martinique samples (11 basalts, 16 andesites and 3 dacites) representative of all the eruptive phases documented on the island and previously analyzed for major-, trace elements and Sr, Nd, Hf and Pb isotopes by Labanieh et al. (2010, 2012). We also analyzed 5 sediments drilled on the Demerara rise (Site DSDP 144: Leg 14) previously studied by Carpentier et al. (2008, 2009). The sediments include two samples from unit 5 (144-7-1W-125-130 and 144-6-1W-46-48-DD collected at 2799 and 2795 meters below sea level, respectively) that consist mainly of terrigeneous claystones, sillstones and sandstones with ages of 106 and 104 Ma, respectively. Sample 144A-6-1W-125-130 was collected 2663 m below the sea level (unit 3) and is a 90 Ma-old black shale. The two shallowest samples are from the unit 2 that corresponds to gray marl and chalk ooze (144-3-1W-120-121 and 144A-3-3W-125-126 with ages of 70 and 59 Ma, respectively). They were collected at 2644 and 2190 meters below the sea level, respectively. Site-144 sediments display large variation in Ce anomalies, $Ce/Ce^*$ between 0.6 and 1 (Carpentier et al., 2008). The five analyzed sediments cover this range of chemical composition: sample 144A-6-1W-125-130 has the highest negative Ce anomaly (0.61), whereas samples from unit 2 have intermediate values (0.86–0.92) and samples from unit 5 show no Ce anomalies (0.97–1.03). Rare earth element data are reported in the Supplementary material. Site 144 is located on the edge of the South American rise, 700 km southeast of the volcanic arc. DSP 78A Site-543 is located closer to the Antilles arc in front to Dominica Island however several isotope studies have shown that sediments from this drilling site do not correspond to the subducted material involved in the magma genesis, contrary to Site-144 sediments (Carpentier et al., 2008; Labanieh et al., 2010). To complete this study we analyzed 4 MORB samples coming from the northern Mid-Atlantic Ridge (Ridelente DR10 and Mapco CH98 DR11) and from the Pacific Ridges (Guayamas Basin: Searise 2 DR07, and East-Pacific Rise: Naudur DR21-4). Complementary geochemical data on these samples are published in Schiano et al. (1997), David et al. (2000), Chauvel and Blichert-Toft (2001), Debaille et al. (2006), Cottrell and Kelley (2013) and Gale et al. (2013).

### 3.2. Ce isotopic compositions

Results are presented in Table 4. Most samples have been measured several times including re-runs of the same filaments and duplicates (different dissolutions). On average the external reproducibility is equal to 38 ppm, equivalent to that determined on the repeated measurements of the BCR-2 standard. We note that 2 samples show larger uncertainties (06MT34 and 06MT23 with uncertainty of 1.3 epsilon). These two samples come from the submarine Jacob phase. We cannot exclude heterogeneities in the powder that could be due to seawater-derived phases. Martinique Island lavas define a range of εCe values from $-0.18 \pm 0.46$ (06MT71) to $1.69 \pm 0.94$ (06MT37). All these samples are relatively young in comparison to the $^{138}La$ half-life so the age correction is negligible (see Table 4). The maximum correction is applied to ancient lavas and is still lower than 0.16 ε-unit, so lower than the internal uncertainty. On average, old and intermediate lavas have the lowest Ce isotope ratios ($\varepsilon Ce < 0.4$) except the two intermediate lavas 06MT60 and 06MT72 that have higher Ce isotopic compositions ($\varepsilon Ce = 1.4$ and 1.6, respectively). Recent lavas have epsilon Ce values in the range −0.1 to 1.7.

MORB samples from both Atlantic and Pacific Ocean have the lowest Ce isotope ratios and define a εCe range between $-1.07 \pm 0.11$ (for Naudur) and $-0.38 \pm 0.37$ (for Ridelente DR10). The average MORB εCe is $-0.77 \div 0.58$. Makishima and Masuda (1994) analyzed 16 Atlantic and Pacific MORB and determined an average value of $\varepsilon Ce = -1.34$. Although this latter value and ours are in agreement within uncertainty, we suspect an analytical bias (see part 2.3.2). When the $^{138}Ce/^{142}Ce$ data of Makishima and Masuda (1994) are normalized with the BCR, their MORB average value is −0.98 εCe. This value is similar to our εCe mean MORB value ($-0.77 \pm 0.58$, 2 s.d.).

Sediments have high Ce isotopic ratios with εCe ranging from $1.38 \pm 0.14$ (144-6-1W-46-48-DD) to $2.44 \pm 0.12$ (144A-3-3W-125-126). $^{138}Ce/^{142}Ce$ ratios do not correlate with $La_N/Ce_N$ showing that sediments had different initial Ce isotopic compositions (see Supplementary data). Initial

Table 4
Measured Ce isotope ratios for Martinique lavas, sediments from the DSDP-site 144, and fresh MORB samples (Ridelente and Mapco are from Atlantic ocean, Naudur and Searise 2 from Pacific ocean). The $^{138}Ce/^{142}Ce$ are corrected for the tailing effect. $^{138}Ce/^{142}Ce$ expressed in $\varepsilon$-unit uses $(^{138}Ce/^{142}Ce)_{CHUR} = 0.0225654$ (this study). Reported errors correspond to internal errors (2 s.e.) for single measurements and external errors (2 s.d.) for average measurements.

| Sample name | Rock type | Age (Ma) | $^{138}Ce/^{142}Ce$ | 2 s.e. | $\varepsilon Ce$ | 2 s.e. | $^{138}Ce/^{142}Ce$ initial |
|---|---|---|---|---|---|---|---|
| Martinique lavas | | | | | | | |
| *Old arc lavas* | | | | | | | |
| 06MT53 | Andesite | 23.4 | 0.0225645 | 0.0000005 | −0.38 | 0.22 | 0.0225644 |
| 06MT53 Rerun | | | 0.0225646 | 0.0000008 | −0.37 | 0.33 | 0.0225644 |
| 06MT53 Dup | | | 0.0225660 | 0.0000009 | 0.25 | 0.39 | 0.0225658 |
| 06MT53 Dup | | | 0.0225651 | 0.0000005 | −0.11 | 0.20 | 0.0225650 |
| 06MT53 Rerun | | | 0.0225652 | 0.0000004 | −0.07 | 0.19 | 0.0225651 |
| **06MT53 mean (±2 s.d.)** | | | **0.0225651** | **0.0000012** | **−0.14** | **0.52** | |
| 06MT54 | Basaltic andesite | 20.8 | 0.0225647 | 0.0000005 | −0.30 | 0.21 | 0.0225646 |
| 06MT54 Dup | | | 0.0225653 | 0.0000003 | −0.06 | 0.15 | 0.0225651 |
| **06MT54 mean (±2 s.d.)** | | | **0.0225650** | **0.0000007** | **−0.18** | **0.33** | |
| 06MT68 | Basalt | 24.8 | 0.0225658 | 0.0000010 | 0.19 | 0.42 | 0.0225656 |
| 06MT68 Dup | | | 0.0225646 | 0.0000005 | −0.34 | 0.22 | 0.0225645 |
| **06MT68 mean (±2 s.d.)** | | | **0.0225652** | **0.0000017** | **−0.07** | **0.75** | |
| *Intermediate arc lavas* | | | | | | | |
| 06MT73 | Dacite | 16.1 | 0.0225652 | 0.0000006 | −0.09 | 0.27 | 0.0225651 |
| 06MT73 Dup | | | 0.0225664 | 0.0000003 | 0.46 | 0.14 | 0.0225663 |
| 06MT73 Dup | | | 0.0225648 | 0.0000003 | −0.26 | 0.13 | 0.0225647 |
| 06MT73 Rerun | | | 0.0225644 | 0.0000003 | −0.45 | 0.14 | 0.0225643 |
| **06MT73 mean (±2 s.d.)** | | | **0.0225652** | **0.0000018** | **−0.08** | **0.79** | |
| 06MT71 | Basalt | 10.3 | **0.0225650** | **0.0000010** | **−0.18** | **0.46** | **0.0225649** |
| 06MT69 | Basalt | 10.9 | 0.0225663 | 0.0000010 | 0.40 | 0.45 | 0.0225662 |
| 06MT69 Rerun | | | 0.0225665 | 0.0000005 | 0.48 | 0.20 | 0.0225664 |
| 06MT69 Dup | | | 0.0225661 | 0.0000003 | 0.30 | 0.13 | 0.0225660 |
| **06MT69 mean (±2 s.d.)** | | | **0.0225663** | **0.0000004** | **0.40** | **0.18** | |
| 06MT72 | Dacite | 7.1 | 0.0225687 | 0.0000005 | 1.45 | 0.22 | 0.0225686 |
| 06MT72 Dup | | | 0.0225693 | 0.0000003 | 1.72 | 0.13 | 0.0225692 |
| 06MT72 Rerun | | | 0.0225690 | 0.0000008 | 1.60 | 0.34 | 0.0225690 |
| 06MT72 Dup | | | 0.0225690 | 0.0000003 | 1.60 | 0.13 | 0.0225690 |
| 06MT72 Rerun 1 | | | 0.0225689 | 0.0000003 | 1.57 | 0.14 | 0.0225689 |
| 06MT72 Rerun 2 | | | 0.0225687 | 0.0000003 | 1.44 | 0.14 | 0.0225687 |
| **06MT72 mean (±2 s.d.)** | | | **0.0225689** | **0.0000005** | **1.56** | **0.21** | |
| 06MT60 | Andesite | 8.8 | 0.0225691 | 0.0000003 | 1.65 | 0.14 | 0.0225690 |
| 06MT60 Rerun | | | 0.0225686 | 0.0000004 | 1.40 | 0.16 | 0.0225685 |
| 06MT60 Dup | | | 0.0225685 | 0.0000003 | 1.36 | 0.12 | 0.0225684 |
| 06MT60 Dup | | | 0.0225676 | 0.0000003 | 0.98 | 0.15 | 0.0225675 |
| **06MT60 mean (±2 s.d.)** | | | **0.0225684** | **0.0000012** | **1.35** | **0.55** | |
| *Recent arc lavas* | | | | | | | |
| 06MT14 | Andesite | 1.53 | 0.0225674 | 0.0000004 | 0.91 | 0.18 | 0.0225674 |
| 06MT14 Rerun | | | 0.0225665 | 0.0000005 | 0.50 | 0.21 | 0.0225665 |
| 06MT14 Dup | | | 0.0225681 | 0.0000004 | 1.21 | 0.16 | 0.0225681 |
| **06MT14 mean (±2 s.d.)** | | | **0.0225674** | **0.0000016** | **0.87** | **0.71** | |
| 06MT30 | Basaltic andesite | 3.01 | 0.0225681 | 0.0000004 | 1.21 | 0.19 | 0.0225681 |
| 06MT30 Rerun | | | 0.0225668 | 0.0000005 | 0.64 | 0.23 | 0.0225668 |
| 06MT30 Dup | | | 0.0225664 | 0.0000004 | 0.46 | 0.19 | 0.0225664 |
| 06MT30 Rerun | | | 0.0225669 | 0.0000003 | 0.64 | 0.12 | 0.0225668 |
| **06MT30 mean (±2 s.d.)** | | | 0.0225671 | 0.0000015 | 0.74 | 0.65 | 0.0225670 |
| 06MT04 | Andesite | 1.87 | **0.0225664** | **0.0000004** | **0.46** | **0.20** | **0.0225664** |
| 06MT10 | Andesite | 2.11 | **0.0225677** | **0.0000004** | **1.03** | **0.19** | **0.0225677** |
| 06MT13 | Andesite | 2.55 | **0.0225677** | **0.0000004** | **1.03** | **0.19** | **0.0225677** |
| 06MT19 | Andesite | 1.75 | 0.0225668 | 0.0000005 | 0.63 | 0.21 | 0.0225668 |
| 06MT19 Dup | | | 0.0225672 | 0.0000003 | 0.79 | 0.12 | 0.0225672 |
| **06MT19 mean (±2 s.d.)** | | | **0.0225670** | **0.0000005** | **0.71** | **0.21** | |

Table 4 (*continued*)

| Sample name | Rock type | Age (Ma) | $^{138}Ce/^{142}Ce$ | 2 s.e. | εCe | 2 s.e. | $^{138}Ce/^{142}Ce$ initial |
|---|---|---|---|---|---|---|---|
| 06MT32 | Basalt | 5.13 | 0.0225659 | 0.0000004 | 0.20 | 0.20 | 0.0225658 |
| 06MT32 Rerun | | | 0.0225652 | 0.0000004 | −0.08 | 0.16 | 0.0225652 |
| 06MT32 Leached | | | 0.0225667 | 0.0000009 | 0.57 | 0.40 | 0.0225666 |
| 06MT32 Dup | | | 0.0225652 | 0.0000009 | −0.07 | 0.39 | 0.0225652 |
| 06MT32 Dup | | | 0.0225657 | 0.0000003 | 0.14 | 0.15 | 0.0225657 |
| **06MT32 mean (±2 s.d.)** | | | **0.0225657** | **0.0000012** | **0.15** | **0.53** | |
| 06MT23 | Basaltic andesite | 4.86 | 0.0225675 | 0.0000006 | 0.93 | 0.26 | 0.0225675 |
| 06MT23 Dup | | | 0.0225663 | 0.0000010 | 0.38 | 0.46 | 0.0225662 |
| 06MT23 Rerun | | | 0.0225642 | 0.0000004 | −0.52 | 0.17 | 0.0225642 |
| 06MT23 Dup | | | 0.0225650 | 0.0000004 | −0.18 | 0.19 | 0.0225649 |
| **06MT23 mean (±2 s.d.)** | | | **0.0225657** | **0.0000029** | **0.15** | **1.27** | |
| 06MT34 | Basaltic andesite | 4.10 | 0.0225654 | 0.0000004 | 0.00 | 0.19 | 0.0225654 |
| 06MT34 Dup | | | 0.0225646 | 0.0000008 | −0.37 | 0.35 | 0.0225645 |
| 06MT34 Dup | | | 0.0225675 | 0.0000006 | 0.92 | 0.25 | 0.0225674 |
| **06MT34 mean (±2 s.d.)** | | | **0.0225658** | **0.0000030** | **0.18** | **1.33** | |
| 06MT61 | Basaltic andesite | 1.12 | **0.0225652** | **0.0000005** | **−0.10** | **0.21** | **0.0225652** |
| 06MT55 | Andesite | 1.33 | **0.0225667** | **0.0000005** | **0.59** | **0.20** | **0.0225667** |
| IAR | Basalt | 0.64 | 0.0225671 | 0.0000004 | 0.77 | 0.20 | 0.0225671 |
| IAR Dup | | | 0.0225646 | 0.0000006 | −0.36 | 0.29 | 0.0225646 |
| IAR Dup | | | 0.0225665 | 0.0000003 | 0.51 | 0.14 | 0.0225665 |
| **IAR mean (±2 s.d.)** | | | **0.0225661** | **0.0000027** | **0.30** | **1.19** | |
| 06MT40 | Andesite | 0.19 | 0.0225666 | 0.0000004 | 0.51 | 0.18 | 0.0225665 |
| 06MT40 Rerun | | | 0.0225655 | 0.0000005 | 0.04 | 0.24 | 0.0225655 |
| 06MT40 Rerun | | | 0.0225656 | 0.0000003 | 0.07 | 0.15 | 0.0225656 |
| 06MT40 Dup | | | 0.0225654 | 0.0000004 | 0.01 | 0.18 | 0.0225654 |
| **06MT40 mean (±2 s.d.)** | | | **0.0225658** | **0.0000011** | **0.16** | **0.47** | |
| 06MT18 | Andesite | 0.35 | **0.0225665** | **0.0000004** | **0.50** | **0.19** | **0.0225665** |
| 06MT28 | Andesite | 0.54 | **0.0225663** | **0.0000002** | **0.42** | **0.10** | **0.0225663** |
| 04MT07 | Andesite | 0.34 | 0.0225680 | 0.0000009 | 1.17 | 0.38 | 0.0225680 |
| 04MT07 Dup | | | 0.0225681 | 0.0000003 | 1.20 | 0.14 | 0.0225681 |
| 04MT07 Rerun | | | 0.0225681 | 0.0000006 | 1.19 | 0.28 | 0.0225681 |
| 04MT07 Rerun | | | 0.0225692 | 0.0000004 | 1.68 | 0.16 | 0.0225692 |
| **04MT07 mean (±2 s.d.)** | | | **0.0225684** | **0.0000011** | **1.31** | **0.50** | |
| 06MT21 Rerun | Andesite | 0.89 | 0.0225682 | 0.0000004 | 1.24 | 0.17 | 0.0225682 |
| 06MT21 Dup | | | 0.0225679 | 0.0000003 | 1.12 | 0.14 | 0.0225679 |
| 06MT21 Rerun | | | 0.0225679 | 0.0000003 | 1.11 | 0.13 | 0.0225679 |
| 06MT21 Rerun | | | 0.0225680 | 0.0000008 | 1.14 | 0.34 | 0.0225680 |
| 06MT21 Dup | | | 0.0225676 | 0.0000003 | 0.99 | 0.15 | 0.0225676 |
| **06MT21 mean (±2 s.d.)** | | | **0.0225679** | **0.0000004** | **1.12** | **0.18** | |
| 06MT36 | Dacite | 1.00 | 0.0225685 | 0.0000006 | 1.39 | 0.28 | 0.0225685 |
| 06MT36 Rerun | | | 0.0225680 | 0.0000005 | 1.17 | 0.20 | 0.0225680 |
| 06MT36 Dup | | | 0.0225683 | 0.0000003 | 1.30 | 0.12 | 0.0225683 |
| 06MT36 Rerun | | | 0.0225682 | 0.0000005 | 1.25 | 0.22 | 0.0225682 |
| **06MT36 mean (±2 s.d.)** | | | **0.0225683** | **0.0000004** | **1.28** | **0.19** | |
| 06MT37 | Basaltic andesite | 0.32 | 0.0225685 | 0.0000005 | 1.36 | 0.21 | 0.0225685 |
| 06MT37 Rerun | | | 0.0225700 | 0.0000005 | 2.03 | 0.22 | 0.0225700 |
| **06MT37 mean (±2 s.d.)** | | | **0.0225692** | **0.0000021** | **1.69** | **0.94** | |
| 06MT06 | Andesite | 0.77 | **0.0225687** | **0.0000004** | **1.45** | **0.19** | **0.0225687** |
| 06MT50 | Andesite | 0.0019 | 0.0225668 | 0.0000006 | 0.62 | 0.28 | 0.0225671 |
| 06MT50 Dup | | | 0.0225663 | 0.0000003 | 0.41 | 0.12 | 0.0225659 |
| **06MT50 mean (±2 s.d.)** | | | **0.0225666** | **0.0000007** | **0.51** | **0.30** | |
| 06MT51 | Andesite | 0.0019 | **0.0225663** | **0.0000004** | **0.41** | **0.19** | **0.0225663** |

Sediments site-144

| | Lithological unit | Age (Ma) | $^{138}Ce/^{142}Ce$ | 2 s.e. | εCe | 2 s.e. | $^{138}Ce/^{142}Ce$ at 24.8 Ma |
|---|---|---|---|---|---|---|---|
| 144-7-1W-125-130 | U5: Quartzose Marlstone | 106 | 0.0225691 | 0.0000003 | 1.62 | 0.15 | 0.0225688 |
| 144-7-1W-125-130 Rerun | | | 0.0225688 | 0.0000008 | 1.50 | 0.34 | 0.0225686 |
| **144-7-1W-125-130 mean (±2 s.d.)** | and carbonaceous clay | | **0.0225689** | **0.0000004** | **1.56** | **0.16** | |

(*continued on next page*)

Table 4 (*continued*)

| Sediments site-144 | | | | | | | |
|---|---|---|---|---|---|---|---|
| | Lithological unit | Age (Ma) | $^{138}Ce/^{142}Ce$ | 2 s.e. | εCe | 2 s.e. | $^{138}Ce/^{142}Ce$ at 24.8 Ma |
| 144-6-1W-46-48-DD | U5: Quartzose Marlstone and carbonaceous clay | 104 | **0.0225685** | **0.0000003** | **1.38** | **0.14** | **0.0225683** |
| 144-A6-1W-125-130 | U3: black shales | 90 | **0.0225698** | **0.0000004** | **1.93** | **0.18** | **0.0225693** |
| 144-3-1W-120-121 | U2: zeolitic greenish gray marl | 70 | **0.0225705** | **0.0000003** | **2.27** | **0.12** | **0.0225703** |
| 144-A3-3W-125-126 | U2: zeolitic greenish gray marl | 59 | **0.0225709** | **0.0000003** | **2.44** | **0.12** | **0.0225706** |

| MORB | | | | | | |
|---|---|---|---|---|---|---|
| | Latitude | Longitude | $^{138}Ce/^{142}Ce$ | 2 s.e. | εCe | 2 s.e. |
| Ridelente DR10 | 16°09′N | 46°40′W | 0.0225642 | 0.0000003 | −0.51 | 0.12 |
| Ridelente DR10 Rerun | | | 0.0225648 | 0.0000005 | −0.25 | 0.23 |
| **Ridelente DR10 mean (±2s.d.)** | | | **0.0225645** | **0.0000008** | **−0.38** | **0.37** |
| Mapco CH98 DR11 | 30°41′N | 1°50′W | 0.0225635 | 0.0000003 | −0.83 | 0.12 |
| Searise 2 DR07 | 20°07′N | 113°43′W | 0.0225636 | 0.0000002 | −0.81 | 0.10 |
| Naudur DR21-4 | 18°45′S | 113°26′W | 0.0225630 | 0.0000003 | −1.07 | 0.11 |

The bold values corresponds to the mean values of repeated measurements of a same sample, and they are the one used in the figures for those samples.

εCe values range from 1.27 (144-6-1W-46-48-DD) to 2.34 (144A-3-3W-125-126): they have slightly higher εCe than the Martinique lavas.

### 3.3. Discussion

Ce isotope ratios measured for Martinique lavas are intermediate between the values measured for MORB and for the local sediments drilled at DSP-site 144. This is also the case for Nd isotopes, as testified by the Ce *vs.* Nd isotope variation diagram in which Martinique lavas all plot between the two end-members (Fig. 7). In detail, old and intermediate lavas are closer to the depleted end-member than younger ones, except samples 06MT60 and 06MT72 that present negative εNd and radiogenic Ce signature similar to those measured in sediments. The two samples have high $La_N/Sm_N$ ratios (3 and 3.6, respectively) whereas other lavas have lower ratios comprised between 1 and 1.5. Samples 06MT60 and 06MT72 are garnet-bearing dacites from Gros Ilet, which suggests that their elevated $La_N/Sm_N$ value could be explained by fractionation of garnet (Labanieh et al., 2012). They also show high Sr and Pb isotope compositions together with low Nd and Hf signatures compared to other samples (Labanieh et al., 2010). Thus a large proportion of sediments up to 20% has also been proposed to account for their extreme isotopic compositions (cf. Davidson and Harmon, 1989; Labanieh et al., 2010). In Fig. 8 sample 06MT72 plots in the field formed by DSP-site 144 sediments. The sedimentary component involved in its genesis could be similar to sediments sampled in Unit 2 that have the highest Ce isotope ratios.

Labanieh et al. (2010) have proposed a binary mixing model between depleted and enriched end-members to explain the Sr–Nd–Pb–Hf isotope compositions of Martinique lavas. The curvature and the asymptotes of mixing hyperbolas allowed them to precisely determine the isotope compositions of the different end-members. They suggested the involvement of two enriched end-members with distinct Sr and Pb isotopic compositions but similar $^{143}Nd/^{144}Nd$ ratios. The Ce–Nd isotope compositions of Martinique lavas, Atlantic MORB and sediment samples from DSP-site 144 support their binary mixing model. The apparent scattering of our data furthermore offers additional information involving the participation of sediments with different Ce isotope compositions and/or variations in the melting process itself such as the effect of melting on the Light REE ratios.

#### 3.3.1. Mixing of two components and effect of partial melting

In Fig. 8A we illustrate the two-end-members mixing model discussed by Labanieh et al. (2010) and consider the effect of partial melting of sediments on the curvature of the mixing trends. The depleted end-member corresponds to the average of the MORB samples. εCe and εNd are −0.77 and 10.3, respectively (mean value of measured compositions after BCR-2 standard normalization of Ce isotope data), whereas Ce and Nd concentrations are taken as similar to the Depleted MORB Mantle (Ce = 0.772 ppm and Nd = 0.713 ppm (Ce/Nd = 1;08), see Salters and Stracke, 2004). The enriched end-member corresponds to the mean value of the 5 sediments from DSDP-site 144, i.e., εCe = 1.92 and εNd = −14 (all isotopic compositions and concentrations are summarized in Table 5). Its Ce/Nd ratio controls the curvature of the mixing curve. Labanieh et al. (2010) did not use the trace element concentrations measured in the sediments to constrain mixing hyperbolas, but they considered instead the concentrations of the carbonate-free local sediments as calculated by Carpentier et al. (2009). The reason was that sediments drilled at DSDP-site 144 were deposited at shallow water-level on the Demerara rise whereas subducted sediments have reached a depths greater than the

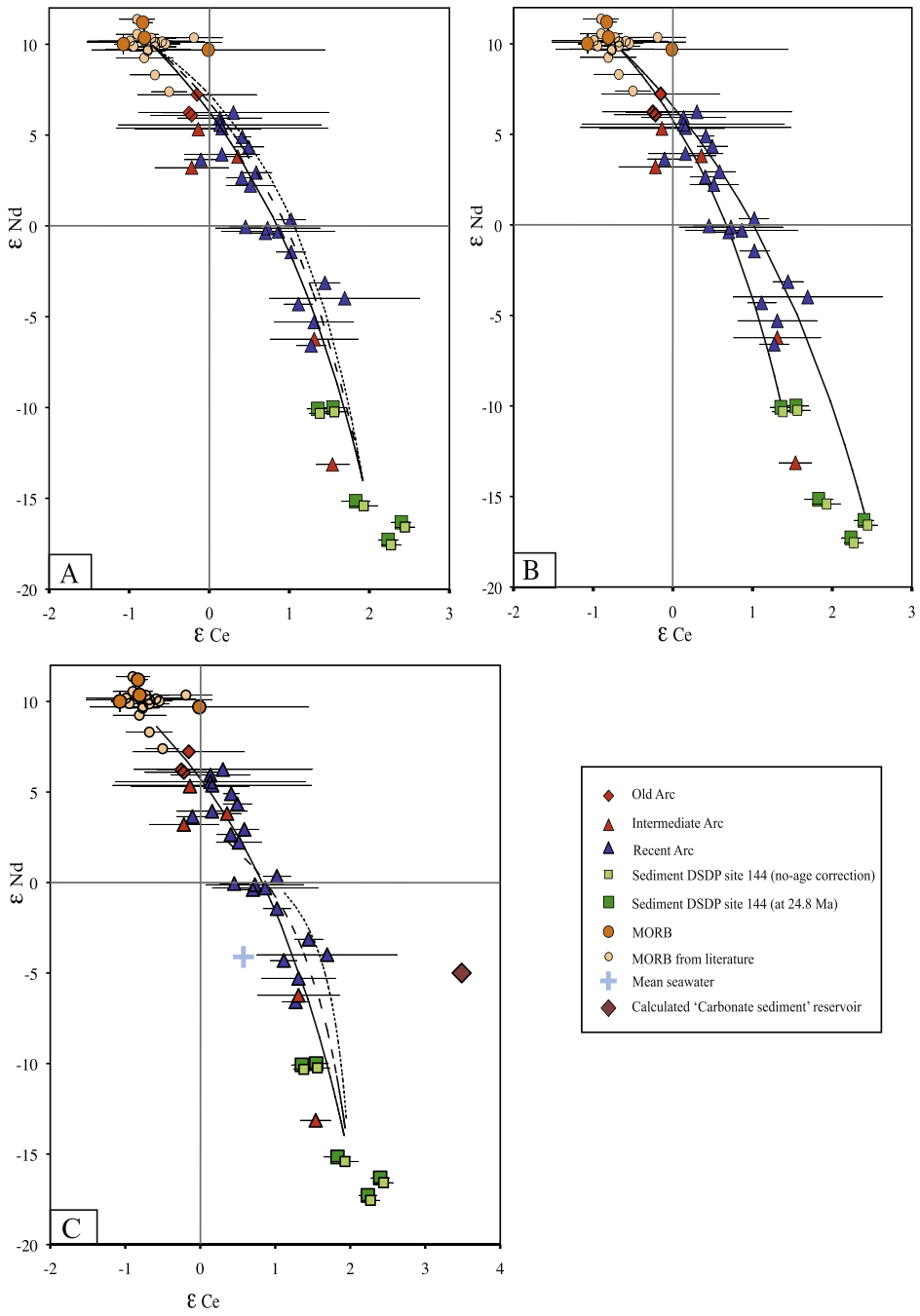


Fig. 8. $\varepsilon$Nd *vs.* $\varepsilon$Ce isotope diagram showing the position of Martinique lavas relative to MORB samples and sediments from DSDP-site 144. Ce and Nd isotope ratios were not corrected for radioactive decay between emplacement ages and present, except for sediments, we used the age of the oldest lava (24.8 Ma), in order to quantify their composition at the age of arc construction. Nd data are from literature (Martinique samples: Labanieh et al., 2010; sediments: Carpentier et al., 2008; MORB: Chauvel and Blichert-Toft, 2001; Debaille et al., 2006). Previously published MORB samples are from Makishima and Masuda (1994). $(^{138}Ce/^{142}Ce)_{CHUR} = 0.0225654$ (this study); $(^{143}Nd/^{144}Nd)_{CHUR} = 0.512630$ (Bouvier et al., 2008). Error bars are either 2 s.e. when a single analyses has been made on the sample or 2 s.d. when the sample has rerun and/or duplicate analysis (see Table 4). The external reproducibility on Ames reference material is 80 ppm. In each diagram hyperbolas are calculated considering the end-members defined in Table 5. (A) Mixing between 2 end-members but considering different Ce and Nd concentrations of the enriched end-member that reflect the effect of partial melting on the Ce/Nd ratio. An increase of 44% of the Ce/Nd ratio is a maximum (see text for more explanation, dotted curve). (B) Solid–solid mixing with two enriched end-members corresponding to the two extreme values measured in sediments from DSDP-site 144. (C) Mixing models with three end-members. The third end-member has been calculated from the seawater composition (Shimizu et al., 1994; Tazoe et al., 2011) and considering an evolution during 100 Ma of a carbonate reservoir similar to the Mean Carbonate Sediments from DSDP site 495 (Patino et al., 2000) for the Ce and Nd concentrations. The contribution of this carbonate reservoir in the mixing is 1% (plain curve), 10% (dashed curve), and 20% (dotted curve).

Table 5
Trace element concentrations and isotopic ratios of the various end-members used to model the mixing arrays shown in Fig. 8. The depleted end-member isotope composition corresponds to the average of MORB samples ($^{138}Ce/^{142}Ce = 0.0225633$ and $^{143}Nd/^{144}Nd = 0.51314$; this study; Makishima and Masuda, 1994; Chauvel and Blichert-Toft, 2001; Debaille et al., 2006). The concentrations are those calculated for the Depleted MORB Mantle by Salters and Stracke (2004). The enriched end-member in Fig. 8A is the mean value of the 5 sediments from DSDP-site 144. *The three different Ce and Nd concentrations correspond to the plain, dashed and dotted mixing curves (see text). In Fig. 8B the two different enriched end-members correspond to the two extreme sediments from DSDP-site 144, 144A-3-3W-125-126 and 144-6-1W-46-48-DD. In Fig. 8C three end-members are defined. The two first ones are those defined in 8A and the last one is a calculated "carbonate sediment reservoir". We have considered the Ce–Nd isotopic composition of seawater (Shimizu et al., 1994; Tazoe et al., 2011) and an evolution during 100 Ma using the Ce and Nd concentrations of the Mean Carbonate Sediments calculated by Patino et al. (2000) from the samples drilled at DSDP-site 495 (Patino et al., 2000).

| | 8A | | 8B | | 8C | | |
|---|---|---|---|---|---|---|---|
| | Depleted end-member | Enriched end-member | Depleted end-member | Enriched end-member | Depleted end-member | Enriched end-member | Calculated "carbonate sediment" reservoir |
| $^{138}Ce/^{142}Ce$ | 0.0225633 | 0.0225697 | 0.0225633 | 0.0225685/ 0.0225709 | 0.0225633 | 0.0225697 | 0.0225733 |
| $^{143}Nd/^{144}Nd$ | 0.51314 | 0.51191 | 0.51314 | 0.51210/ 0.51178 | 0.51314 | 0.51191 | 0.51237 |
| [Nd] ppm | 0.713 | 22.6/22.6/10* | 0.713 | 15.4/8.2 | 0.713 | 14 | 6.79 |
| [Ce] ppm | 0.772 | 50.5/60/32* | 0.772 | 33.7/17.9 | 0.772 | 29.9 | 2.4 |
| Ce/Nd | 1.08 | 2.2/2.7/3.2 | 1.08 | 2.2/2.2 | 1.08 | 2.14 | 0.35 |

Carbonate Compensation Depth (CCD). This choice corresponds to a Ce/Nd ratio of 2.2 and the associated mixing trend is represented in Fig. 8A by the plain curve. We note that about half of our samples can be explained by this mixing-trend. All others fall to the right of the plain curve.

As an alternative, the Ce/Nd ratio of the enriched end-member can be determined from the Ce/Nd *vs.* $^{143}Nd/^{144}Nd$ anti-correlation by the Martinique lavas (see Supplementary material D). Considering that the enriched component has a $^{143}Nd/^{144}Nd$ ratio of 0.51181 (Labanieh et al., 2010) gives a value of 2.7 for the Ce/Nd ratio, slightly higher than the one determined by Carpentier et al. (2009). The associated mixing curve is plotted with a dashed line in Fig. 8A. The increase of the curvature allows to explain some of the datapoints falling to the right of the plain curve, but not those with the most radiogenic Ce compositions at a given εNd.

Lastly, Johnson and Plank (1999) have shown that partial melting increases the Ce/Nd ratio by 10–44% depending on the *P–T* conditions (800 °C/900 °C at 2 GPa) whereas dehydration has a limited effect on REE fractionation. Another way to increase the Ce/Nd ratio of the enriched-member, and thus to explain the data to the right of the plain and dashed curves in Fig. 8A, may be to integrate the effect of partial melting during sediment recycling by subduction. Doing this, we obtain a Ce/Nd ratio of 3.2 for the enriched end-member when the maximum increase of 44% is considered. This new value corresponds to the dotted mixing curve in Fig. 8A and allows reproducing datapoints that were not explained by previous mixing curves. Thus, the incorporation of sediments similar to those drilled at DSDP-site 144 through variable degrees of partial melting can explain the isotope signature of Martinique lavas.

### 3.3.2. Heterogeneity in the enriched end-member

The apparent scattering of our data in the εCe vs. εNd diagram may also reflect the contribution of sediments with different Ce isotopic compositions, as suggested by the range of variations observed for sediments from DSDP-Site 144. Hence, the two curves reported in Fig. 8B consider the depleted end-member defined in subsection 3.3.1 and two enriched end-members having distinct Ce contents and isotope compositions corresponding to those of the two sediment samples with extreme $^{138}Ce/^{142}Ce$ ratios (144-6-1W-46-48-DD and 144A-3-3W-125-126). This coincidentally corresponds to the same Ce/Nd ratio of 2.2 for both enriched end-members as sample 144-6-1W-46-48-DD has Ce and Nd contents about twice those of sample 144A-3-3W-125-126 (Carpentier et al., 2008). Most of our Martinique samples fall between the two modeled mixing curves in the εCe vs. εNd diagram, thus suggesting that the width of the mixing array may be due to the intrinsic, isotopic and chemical heterogeneity of subducted sediments. This is furthermore reinforced by the fact that we have no evidence that the 5 documented samples define the whole range of variations of Ce compositions.

### 3.3.3. Incorporation of pelagic sediments

Finally a third scenario considers the involvement of sediments, with negative Ce anomalies (i.e., $Ce/Ce^* < 1$). Most of the Martinique lavas present small negative Ce anomalies between 0.87 and 1.00, except sample 06MT34 that shows a $Ce/Ce^*$ ratio of 0.68 (see Supplementary data). Such Ce signatures are difficult to explain with the two scenarios previously discussed (subsections 3.3.1 and 3.3.2). Sediments sampled at DSDP-site 144 indeed show Ce anomalies of the same order than lavas (except sample 144A-6-1W-125-130 with a $Ce/Ce^*$ of 0.65) and mixing with depleted MORB mantle material in the mantle wedge should have reduced if not cancel the cerium anomalies. Hence, the involvement of a third end-member with large negative Ce anomalies such as hydrothermal and/or authigenic materials (e.g. fish debris) in the mixing could explain the REE patterns of the lavas.

Fig. 1B shows that within 100 Ma, hydrothermal and average authigenic sediments increase their Ce isotope composition by about 2 εCe-units. Based on this observation, we modeled the Ce and Nd isotopic compositions of a

"theoretical" carbonate sediment reservoir that would have formed from seawater 100 Ma ago (which corresponds to the age of the subducted plate). Its initial isotope composition corresponds to the average seawater calculated from literature data, i.e., $\varepsilon Ce = 0.58$ and $\varepsilon Nd = -4.11$ (Shimizu et al., 1994; Tazoe et al., 2011) which is in agreement with the seawater Nd isotope signature estimated for Atlantic ocean from the measurements of late Cretaceous biogenic apatite (fish teeth and bones) and foraminifera (see the compilation in Moiroud, 2014). Its present-day isotope composition results from 100-Ma radioactive decay with a La/Ce ratio of 3.7. This last value corresponds to the mean carbonate sediment determined by Patino et al. (2000) from samples drilled at DSDP-site 495; it is consistent with the determination of Plank and Langmuir (1998) based on samples from the same site (see also Doucelance et al., 2014). Three-end-member mixing models including depleted mantle, terrigeneous sediments (both as defined in Fig. 8A) and the modeled carbonate sediment reservoir are presented in Fig. 8C. They consider the involvement of carbonate sediments in mass proportions of 1% (plain curve), of 10% (dashed curve) and of 20% (dotted curve), respectively. A contribution as low as 1% does not modify the mixing curves; the plain curves in Fig. 8A and C are identical. Higher contributions move the mixing curves to the right of the εCe vs. εNd diagram, as expected. However, maximum εNd thus calculated are ~0 so that our intermediate and old samples from Martinique are not reproduced anymore. Lastly, contributions higher than 10% would produce samples that will be mainly located in the lower-right quadrant of the diagram (positive εCe, negative εNd signature). Alternatively, a two-component mixing between a depleted end-member and the carbonate sediment reservoir would increase εNd values. However, it would plot as a convex curve in the εCe vs. εNd diagram because the Ce/Nd ratio of the carbonate sediment reservoir is lower than that in the depleted end-member (0.35 and 1.08, respectively). Hence, such a mixing would not reproduce samples plotting in the upper-right quadrant of the εCe vs. εNd diagram (positive εCe and εNd), as it is the case for some of our samples and also for samples from other arc lavas. Notably samples from Solomon and Bonin Islands are mainly characterized by positive values for both εCe and εNd (up to +2.6 εCe for a εNf of +7.1) (Shimizu et al., 1992).

## 4. SUMMARY

We present a study on the Ce isotope systematics using the most recent generation of TIMS. Ce isotopes are measured as oxide species on a Finnigan Triton instrument in static mode with relay matrix rotation on double Re filaments. A correction of the $^{140}Ce$ peak-tail is performed using a two magnetic field step measurement procedure. The Ce reference material used here is an AMES standard with an average $^{138}Ce/^{142}Ce$ of $0.0225732 \pm 18$ (2 s.d.; 80 ppm; $n = 89$). This value is in agreement with previous measurements by Willbold (2007); however the uncertainty is higher owing to drift of isotopic ratios measured in static mode over the duration of this study (33 months). When the reproducibility is calculated from standards measured during the same analytical session, it is on average equal to 40 ppm. All the $^{138}Ce/^{142}Ce$ ratios have been normalized to the AMES value of 0.0225746 (measured in session 7, 2 s.d. = 14 ppm, $n = 8$), a session during which the chondritic value has been defined and the peak tailing was negligible. Repeated dissolutions and measurements of the two rock-standards BHVO-2 and BCR-2 provide external reproducibilities of 76 ppm ($n = 10$) and 31 ppm ($n = 8$), respectively. All duplicate and rerun analyses of Martinique Island lavas fall within these external reproducibility estimates. Finally, the analyses of two chondrites provide a value of $0.0225654 \pm 7$ in good agreement with previous studies.

$^{138}Ce/^{142}Ce$ ratios measured for Martinique lavas show a limited range (~2 ε-units) that generally follows binary mixtures between depleted and enriched end-members when coupled to Sm–Nd isotopic systems. As for Sr, Nd and Pb isotopes, the Ce isotope composition of the enriched end-member is consistent with that of subducted sediments similar to those sampled at DSDP-site 144. The Martinique lavas in the εCe vs. εNd diagram define a broad mixing array. The apparent scattering can be explained by the participation of sediments with different Ce isotope compositions and/or variation in the melting process itself as the effect of melting on the LREE ratios. The Ce isotope compositions of the lavas, however, do not require the presence of authigenic and/or hydrothermal sediments in the mixing.

More Ce studies on various subduction zones, MORB, OIB and continental material will help to further understand the Ce history on Earth reservoirs. The full potential of Ce isotopes as a petrogenetic tracer should be best expressed in ancient settings, where Rb–Sr and U–Th–Pb systematics are often blurred by severe disturbances inherent to the great elemental mobility of both parent and daughter isotopes and where La and Ce are not affected by alteration and metamorphism.

## ACKNOWLEDGMENTS

We would like to thank Matthias Willbold for providing us the Ames Ce reference material and Masaharu Tanimizu for the JMC-304 reference material. We also acknowledge Pierre Schiano for furnishing the MORB samples and the Smithsonian Institution National Museum of Natural History and the Muséum National d'Histoire Naturelle de Paris for the meteorites. We are grateful to Chantal Bosq who helped us in the clean lab. The paper was improved by critical reviews by Associate Editor Andreas Stracke, two anonymous reviewers and William White. Frances van Wyk de Vries helped us with the quality of the manuscript. This research was financed by the French Government Laboratory of Excellence initiative n°ANR-10-LABX-0006, the Région Auvergne and the European Regional Development Fund. This is Laboratory of Excellence ClerVolc contribution number 125.

## APPENDIX A. SUPPLEMENTARY DATA

Supplementary data associated with this article can be found, in the online version, at http://dx.doi.org/10.1016/j.gca.2015.07.002.

## REFERENCES


Alibo D. S. and Nozaki Y. (1999) Rare earth elements in seawater: particle association, shale-normalization, and Ce oxidation. *Geochim. Cosmochim. Acta* **63**(3/4), 363–372.

Amakawa H., Ingri J., Masuda A. and Shimizu H. (1991) Isotopic composition of Ce, Nd and Sr in ferromanganese nodules from the Pacific and Atlantic Oceans, the Baltic and Barents seas, and the Gulf of Bothnia. *Earth Planet. Sci. Lett.* **105**, 554–565.

Anders E. and Grevesse N. (1989) Abundances of the elements: meteoritic and solar. *Geochim. Cosmochim. Acta* **53**, 197–214.

Bezard R., Davidson J. P., Turner S., Macpherson C. G., Lindsay J. M. and Boyce A. J. (2014) Assimilation of sediments embedded in the oceanic arc crust: myth or reality?. *Earth Planet. Sci. Lett.* **395** 51–60.

Bouvier A., Vervoort J. D. and Patchett P. J. (2008) The Lu–Hf and Sm–Nd isotopic composition of CHUR: constraints from unequilibrated chondrites and implications for the bulk composition of terrestrial planets. *Earth Planet. Sci. Lett.* **273**, 48–57.

Carpentier M., Chauvel C. and Mattielli N. (2008) Pb–Nd isotopic constraints on sedimentary input into the Lesser Antilles arc system. *Earth Planet. Sci. Lett.* **272**, 199–211.

Carpentier M., Chauvel C., Maury R. C. and Mattielli N. (2009) The "zircon effect" as recorded by the chemical and Hf isotopic composition of Lesser Antilles forearc sediments. *Earth Planet. Sci. Lett.* **287**, 86–99.

Chauvel C. and Blichert-Toft J. (2001) A hafnium isotope and trace element perspective on melting of the depleted mantle. *Earth Planet. Sci. Lett.* **190**, 137–151.

Cottrell E. and Kelley K. A. (2013) Redox heterogeneity in Mid-Ocean Ridge Basalts as a function of mantle source. *Science* **340**, 1314–1317.

David K., Schiano P. and Allègre C. J. (2000) Assessment of the Zr/Hf fractionation in oceanic basalts and continental materials during petrogenetic processes. *Earth Planet. Sci. Lett.* **178**, 285–301.

Davidson J. P. (1986) Isotopic and trace element constraints on the petrogenesis of subduction-related lavas from Martinique, Lesser Antilles. *J. Geophys. Res.* **91**, 5943–5962.

Davidson J. P. (1987) Crustal contamination versus subduction zone enrichment: examples from Lesser Antilles and implications for mantle source compositions of island arc volcanic rocks. *Geochim. Cosmochim. Acta* **51**, 2185–2198.

Davidson J. P. and Harmon R. S. (1989) Oxygen isotope constraints on the petrogenesis of volcanic arc magmas from Martinique, Lesser Antilles. *Earth Planet. Sci. Lett.* **95**, 255–270.

Debaille V., Blichert-Toft J., Agranier A., Doucelance R., Schiano P. and Albarede F. (2006) Geochemical component relationships in MORB from the Mid-Atlantic Ridge, 22–35°N. *Earth Planet. Sci. Lett.* **241**, 844–862.

Deschamps P., Doucelance R., Ghaleb B. and Michelot J. L. (2003) Further investigations on optimized tail correction and high-precision measurement of uranium isotopic ratios using multi-collector ICP-MS. *Chem. Geol.* **201**, 141–160.

Dickin A. P. (1987) La–Ce dating of Lewisian granulites to constrain the $^{138}$La β-decay half-life. *Nature* **325**, 337–338.

Dickin A. P., Jones N. W., Thirlwall M. F. and Thompson R. N. (1987) A Ce/Nd isotope study of crustal contamination processes affecting Palaeocene magmas in Skye, Northwest Scotland. *Contrib. Mineral. Petrol.* **96**, 455–464.

Doucelance R., Bellot N., Boyet M., Hammouda T. and Bosq C. (2014) What coupled cerium and neodymium isotopes tell us about the deep source of oceanic carbonatites. *Earth Planet. Sci. Lett.* **407**, 175–186.

Elderfield H. (1988) The oceanic chemistry of rare-earth elements. *Philos. Trans. R. Soc. A* **325**, 105–126.

Gale A., Dalton C. A., Langmuir C. H., Su Y. and Schilling J. G. (2013) The mean composition of ocean ridge basalts. *Geochem. Geophys. Geosyst.* **14**, 489–518.

Germa A., Quidelleur X., Labanieh S., Lahitte P. and Chauvel C. (2010) The eruptive history of Morne Jacob volcano (Martinique Island, French West Indies): geochronology, geomorphology and geochemistry of the earliest volcanism in the recent Lesser Antilles arc. *J. Volcanol. Geotherm. Res.* **198**(3–4), 297–310.

Germa A., Quidelleur X., Labanieh S., Chauvel C. and Lahitte P. (2011a) The volcanic evolution of Martinique Island: insights from K–Ar dating into the Lesser Antilles arc migration since the Oligocene. *J. Volcanol. Geotherm. Res.* **208**(3–4), 122–135.

Germa A., Quidelleur X., Lahitte P., Labanieh S. and Chauvel C. (2011b) The K–Ar Cassignol–Gillot technique applied to western Martinique lavas: a record of Lesser Antilles arc activity from 2 Ma to Mount Pelee volcanism. *Quat. Geochronol.* **6**(3–4), 341–355.

Hayashi T., Tanimizu M. and Tanaka T. (2004) Origin of negative Ce anomalies in Barberton sedimentary rocks, deduced from La–Ce and Sm–Nd isotope systematics. *Precambrian Res.* **135**, 345–357.

Hole M. J., Saunders A. D., Marriner G. F. and Tarney J. (1984) Subduction of pelagic sediments: implications for the origin of Ce-anomalous basalts from the Marianna Islands. *J. Geol. Soc. London* **141**, 453–472.

Johnson M. C. and Plank T. (1999) Dehydration and melting experiments constrain the fate of subducted sediments. *Geochem. Geophys. Geosyst.* **1** (Art. no. 1999GC000014).

Labanieh S., Chauvel C., Germa A., Quidelleur X. and Lewin E. (2010) Isotopic hyperbolas constrain sources and processes under the Lesser Antilles arc. *Earth Planet. Sci. Lett.* **298**, 35–46.

Labanieh S., Chauvel C., Germa A. and Quidelleur X. (2012) Martinique: a clear case for sediment melting and slab dehydration as function of distance to the trench. *J. Petrol.* **53**, 2441–2464.

Le Fèvre B. and Pin C. (2005) A straightforward separation scheme for concomitant Lu–Hf and Sm–Nd isotope ratio and isotope dilution analysis. *Anal. Chim. Acta* **543**, 209–221.

Lee S.-G., Masuda A., Shimizu H. and Song Y.-S. (2001) Crustal evolution history of Korean Peninsula in East Asia: the significance of Nd, Ce isotopic and REE data from the Korean Precambrian Gneisses. *Geochem. J.* **35**, 175–187.

Lide David R. (1994) *CRC Handbook of Chemistry and Physics*, 75th ed. CRC Press.

Makishima A. and Masuda A. (1993) Primordial Ce isotopic composition of the solar system. *Chem. Geol.* **106**, 197–205.

Makishima A. and Masuda A. (1994) Ce isotope ratios of N-type MORB. *Chem. Geol.* **118**, 1–8.

Makishima A. and Nakamura E. (1991) Precise measurement of cerium isotope composition in rock samples. *Chem. Geol.* **94**, 1–11.

Makishima A., Shimizu H. and Masuda A. (1987) Precise measurement of Cerium and Lanthanum isotope ratios. *Mass Spectrosc.* **35**, 64–72.

Masuda A., Shimizu H., Nakai S., Makishima A. and Lahti S. (1988) $^{138}$La β-decay constant estimated from geochronological studies. *Earth Planet. Sci. Lett.* **89**, 316–322.

Moiroud M. (2014) Evolution de la circulation océanique profonde Durant le Crétacé – apport des isotopes du néodyme, Thèse Université de Bourgogne. 257 p.

Patino L. C., Carr M. J. and Feigenson M. D. (2000) Local and regional variations in Central American arc lavas controlled by

variations in subducted sediment input. *Contrib. Mineral. Petrol.* **138**, 265–283.

Picard S., Lécuyer C., Barrat J. A., Garcia J. P., Dromart G. and Sheppard S. M. F. (2002) Rare earth contents of Jurassic fish and reptile teeth and their potential relation to seawater composition (Anglo-Paris Basin, France and England). *Chem. Geol.* **186**, 1–16.

Pin C. and Santos Zalduegui J. F. (1997) Sequential separation of light rare-earth elements, thorium and uranium by miniaturized extraction chromatography: application to isotopic analyses of silicate rocks. *Anal. Chim. Acta* **339**, 79–89.

Plank T. (2014) The chemical composition of subducting sediments. In *Treatise on Geochemistry* (second edition). vol. 4, pp. 607–629.

Plank T. and Langmuir C. H. (1998) The chemical composition of subducting sédiment and its conséquences for the crust and mantle. *Chem. Geol.* **145**, 325–394.

Raczek I., Jochum P. and Hofmann A. W. (2003) Neodymium and strontium isotope data for USGS reference materials BCR-1, BCR-2, BHVO-2, AVG-1, AVG-2, GSP-1, GSP-2 and eight MPI-DING reference glasses. *Geostand. Newsl.* **27**, 173–179.

Rudnick R.L. and Gao S. (2014) Composition of the continental crust. In *Treatise on Geochemistry* (second edition), vol. 4, pp. 1–51.

Salters V. J. M. and Stracke A. (2004) Composition of the depleted mantle. *Geochem. Geophys. Geosyst.* **5**(5).

Sato J. and Hirose T. (1981) Half-life of lanthanum-138. *Radiochem. Radioanal. Lett.* **46**, 145–152.

Schiano P., Birck J. L. and Allègre C. J. (1997) Osmium–strontium–neodymium–lead isotopic covariations in mid-ocean ridge basalt glasses and the heterogeneity of the upper mantle. *Earth Planet. Sci. Lett.* **150**, 363–379.

Shimizu H., Tanaka T. and Masuda A. (1984) Meteoritic $^{138}Ce/^{142}Ce$ ratio and its evolution. *Nature* **307**, 251–252.

Shimizu H., Nakai S., Tasaki S., Masuda A., Bridgwater D., Nutman A. P. and Baadsgaard H. (1988) Geochemistry of Ce an Nd isotopes and REE abundances in the Amîtsoq gneisses, West Greenland. *Earth Planet. Sci. Lett.* **91**, 159–169.

Shimizu H., Umemoto N., Masuda A. and Appel P. W. U. (1990) Sources of iron-formations in the Archean Isua and Malene supracrustals, West Greenland: evidence from La–Ce and Sm–Nd isotopic data and REE abundances. *Geochim. Cosmochim. Acta* **54**, 1147–1154.

Shimizu H., Sawatari H., Kawata Y., Dunkley P. N. and Masuda A. (1992) Ce and Nd isotope geochemistry on island arc volcanic rocks with negative Ce anomaly: existence of sources with concave REE patterns in the mantle beneath the Solomon and Bonin island arcs. *Contrib. Mineral. Petrol.* **110**, 242–252.

Shimizu H., Tachikawa K., Masuda A. and Nozaki Y. (1994) Cerium and neodymium isotope ratios and REE patterns in seawater from the North Pacific Ocean. *Geochim. Cosmochim. Acta* **58**, 323–333.

Shimizu H., Lee S. G., Masuda A. and Adachi M. (1996) Geochemistry of Nd and Ce isotopes and REE abundances in Precambrian orthogneiss clasts from the Kamiaso conglomerate, central Japan. *Geochem. J.* **30**, 57–69.

Smith H. J., Leeman W. P., Davidson J. and Spivack A. J. (1997) The B isotopic composition of arc lavas from Martinique, Lesser Antilles. *Earth Planet. Sci. Lett.* **146**, 303–314.

Tanaka T. and Masuda A. (1982) The La–Ce geochronometer: a new dating method. *Nature* **300**, 515–518.

Tanaka T., Shimizu H., Kawata Y. and Masuda A. (1987) Combined La–Ce and Sm–Nd isotope systematics in petrogenetic studies. *Nature* **327**, 113–117.

Tang M., Rudnick R. L. and Chauvel C. (2014) Sedimentary input to the source of Lesser Antilles lavas: a Li perspective. *Geochim. Cosmochim. Acta* (In press).

Tanimizu M. (2000) Geophysical determination of the $^{138}La$ β-decay constant. *Phys. Rev. C* **62**(1), 017601-1–017601-4.

Tanimizu M. and Tanaka T. (2002) Coupled Ce–Nd isotope systematics and rare earth elements différenciation of the moon. *Geochim. Cosmochim. Acta* **66**, 4007–4014.

Tanimizu M., Hayashi T. and Tanaka T. (2004) Development of the Ce isotope analysis for cosmochemistry using the dynamic multicollector technique. *J. Mass Spectrom. Soc. Jpn.* **52**, 177–181.

Tazoe H., Obata H. and Gamo T. (2007) Determination of cerium isotope ratios in geochemical samples using oxidative extraction technique with chelating resin. *J. Anal. At. Spectrom.* **22**, 616–622.

Tazoe H., Obata H. and Gamo T. (2011) Coupled isotopic systematics of surface cerium and neodymium in the Pacific Ocean. *Geochem. Geophys. Geosyst.* **12**, 1–14.

Thirlwall M. F., Graham A. M., Arculus R. J., Harmon R. S. and Macpherson C. G. (1996) Résolution of the effects of crustal assimilation, sédiments subduction, and fluid transport in island arc magmas: Pb–Sr–Nd–O isotope geochemistry of Grenada, Lesser Antilles. *Geochim. Cosmochim. Acta* **60**, 4785–4810.

White W. M. and Dupré B. (1986) Sediment subduction and magma genesis in the Lesser Antilles: isotopic and trace element constraints. *J. Geophys. Res.* **91**, 5927–5941.

Willbold M. (2007) Determination of Ce isotopes by TIMS and MC-ICPMS and initiation of a new, homogeneous Ce isotopic reference material. *J. Anal. At. Spectrom.* **22**(22), 1364–1372.

*Associate editor:* Andreas Stracke

Journal of African Earth Sciences 56 (2010) 59–74

Contents lists available at ScienceDirect

Journal of African Earth Sciences

journal homepage: www.elsevier.com/locate/jafrearsci

# Quaternary extrusive calciocarbonatite volcanism on Brava Island (Cape Verde): A nephelinite-carbonatite immiscibility product

Cyntia Mourão [a,b,*], João Mata [a,b], Régis Doucelance [c], José Madeira [a,d,e], António Brum da Silveira [a,d,e], Luís C. Silva [b,f], Manuel Moreira [g]

[a] Faculdade de Ciências da Universidade de Lisboa, Departamento de Geologia (GeoFCUL), Campo Grande, C6, 1749-016 Lisboa, Portugal
[b] Centro de Geologia da Universidade de Lisboa (CeGUL), Campo Grande, C6, 1749-016 Lisboa, Portugal
[c] Laboratoire Magmas et Volcans (UMR 6524 CNRS), Observatoire de Physique du Globe de Clermont-Ferrand, Université Blaise Pascal, 5 rue Kessler, 63038 Clermont-Ferrand Cedex, France
[d] LATTEX – Laboratório de Tectonofísica e Tectónica Experimental, 1749-016 Lisboa, Portugal
[e] IDL – Instituto D. Luís, 1250-102 Lisboa, Portugal
[f] Instituto de Investigação Científica e Tropical, 1300-344 Lisboa, Portugal
[g] Laboratoire de Géochimie et Cosmochimie (UMR 7579 CNRS), Institut de Physique du Globe de Paris, Université Paris 7, 4 Place Jussieu, 75252 Paris Cedex, France

ARTICLE INFO

*Article history:*
Received 3 October 2008
Received in revised form 29 May 2009
Accepted 9 June 2009
Available online 14 June 2009

*Keywords:*
Extrusive carbonatite
Brava Island
Cape Verde
Sr–Nd isotopes
Immiscibility

ABSTRACT

The Cape Verde volcanic archipelago, located in the oceanic portion of the African plate some 500 km west of the Senegal coast, is renowned for the occurrence of carbonatites on at least 5 of its 10 islands. In this study we report the occurrence of about twenty new small outcrops of extrusive carbonatites on Brava Island (64 km$^2$), the south-westernmost island of the archipelago. These new occurrences are studied from geological, petrographic, mineral chemistry and whole rock (elemental and isotopic) geochemical points of view, allowing for a discussion of their petrogenesis and emphasising their geological and geochemical peculiarities in the context of the Cape Verde carbonatites.

Most of the extrusive carbonatitic formations correspond to pyroclastic rocks, comprising magmatic and/or phreatomagmatic ash and lapilli fall deposits and one probable pyroclastic flow. Lava flows occur at one locality. The predominance of pyroclastic facies demonstrates the significant explosivity of these magmas characterised by very low viscosity. Independent of the modes of emplacement, all samples are calciocarbonatites and exhibit a remarkable compositional uniformity, considering that they represent several different eruptions and present a wide geographical dispersion.

Brava extrusive carbonatites belong to the younger (probable Holocene – Pleistocene) volcanic sequence of the island. This feature is unique in the context of Cape Verde geology, because in the other islands (including Brava) of the archipelago carbonatites are commonly assigned to the basal complexes, having formed during a fairly early stage of the emerged evolution of volcanic construction.

Compared with the older intrusive sövitic rocks occurring at Middle Unit of Brava Island, extrusive facies are more iron and manganese rich and yield higher contents of trace elements like Ba, Th, U, Nb, Pb and REE, but somewhat lower Sr abundances. New initial Sr and Nd isotope data (0.703557–0.703595 and 0.512792–0.512816, respectively) determined in extrusive calciocarbonatitic rocks are clearly different from those obtained in intrusive rocks (0.703340–0.703356 and 0.512910–0.512912, respectively), which demonstrates that the studied rocks were ultimately the product of a source distinct from those that produced the older intrusive carbonatites. Brava extrusive carbonatites yield isotope signatures that are clearly distinct from all other Cape Verde carbonatites, but akin to the Southern Cape Verde silicate rocks. We propose that the extrusive carbonatites resulted from an immiscibility process that also produced conjugate melts of nephelinitic composition.



## 1. Introduction

Carbonatites are igneous rocks containing more than 50% by volume of carbonate minerals. Intrusive facies clearly dominate over extrusive ones, which represent only ≈10% of the known occurrences worldwide (Woolley and Church, 2005).

Despite the fact that carbonatite–oceanic mantle interactions have been shown to occur in some areas (e.g., Polynesia: Hauri

* Corresponding author. Address: Faculdade de Ciências da Universidade de Lisboa, Departamento de Geologia (GeoFCUL), Campo Grande, C6, 1749-016 Lisboa, Portugal.
*E-mail address:* ccmourao@fc.ul.pt (C. Mourão).

1464-343X/$ - see front matter © 2009 Elsevier Ltd. All rights reserved.
doi:10.1016/j.jafrearsci.2009.06.003

et al., 1993; Chauvel et al., 1997; Grande Comore: Coltorti et al., 1999; Madeira: Mata et al., 1999; Kerguelen: Mattielli et al., 2002; Cape Verde: Martins et al., 2007), exposures of oceanic carbonatites are extremely rare and have been identified so far only in the Cape Verde archipelago (e.g., Assunção et al., 1965; Alves et al., 1979; Silva et al., 1981; Kogarko, 1993) and the Canary Islands (e.g., Fúster et al., 1968; Allègre et al., 1971), both located on the African plate (see also Hoernle et al., 2002). In the Canary archipelago, carbonatites are represented only by intrusive calciocarbonatites within the basal complex of Fuerteventura (e.g., Muñoz et al., 2005; De Ignacio et al., 2006). In the Cape Verde islands carbonatites occur on at least 5 of the 10 islands and on the islets near Brava (Aires-Barros, 1968; Machado et al., 1968; Fig. 1). They range in composition from calcio- to magnesiocarbonatites. In this archipelago, intrusive carbonatites are clearly dominant, despite an important volcanic occurrence described by Silva et al. (1981) on Santiago Island and those reported hereafter on Brava Island.

Assunção et al. (1965) were the first authors to coin the term "carbonatites" to describe carbonate rocks considered of igneous origin on Brava. Subsequently, Machado et al. (1968) mapped several outcrops of intrusive carbonatites within the basal complex (see also Madeira et al., 2006). The first mention of Brava extrusive carbonatites was made in an abstract (Peterson et al., 1989). More recently, Hoernle et al. (2002) briefly mentioned an occurrence of carbonatite lava flows on Brava Island related to a small cone at Cachaço, on the central part of the island, to which they assigned a very recent age (<1000 years) based on its non-eroded morphology. They also offered a petrographic description with the element and isotopic compositions of one sample. During two field campaigns in 2006 and 2007, we discovered several (≈20) new outcrops of volcanic carbonatites corresponding to at least five distinct eruptions (Fig. 1).

Compared with their intrusive counterparts, extrusive carbonatites are usually considered more probably representative of the pristine compositions of carbonatite magmas (e.g., Bailey, 1993; Woolley and Church, 2005). Given the recognised importance of extrusive carbonatites to the understanding of the petrogenesis of these non-silicate magmas, we describe in this paper the newly discovered occurrences on Brava from geological, petrographic and whole rock (elemental and isotopic) geochemical points of view. This allows us to (1) discuss the petrogenesis of the extrusive carbonatites; (2) determine whether they are ultimately derived from the source that previously delivered the intrusive carbonatites from the Middle Unit; (3) compare their geochemical characteristics with those reported for the other Cape Verde carbonatites; and (4) emphasise the uniqueness of the Brava extrusive carbonatitic rocks in the context of Cape Verde volcano-stratigraphy.

## 2. Geology

The Cape Verde Archipelago consists of 10 major islands and several islets (Fig. 1), arranged in a westward open "horseshoe" emplaced on a 2.2 km-high and 1200 km-wide topographic "swell" (Cape Verde Rise). This swell correlates with geoid and gravimetric anomalies (Monnereau and Cazenave, 1990), and is considered the result of the impingement of lithosphere by a deeply anchored mantle plume (e.g., Montelli et al., 2006), with resulting plate thinning and heating.

Brava is a small island (64 $km^2$) located on the south-western tip of the approximately NE–SW alignment formed by the Southern Cape Verde islands (Fig. 1). Three major volcano-stratigraphic units are identified (Fig. 1B; Madeira et al., 2006). The older Lower Unit is composed of an uplifted nephelinite/ankaratrite submarine volcanic sequence that includes pillow lavas, pillow breccias and hyaloclastites. This represents the upper part of the submarine seamount precursor of the island. A subvolcanic plutonic complex intrudes the Lower Unit and includes syenites, pyroxenites, ijolites and carbonatites. This Middle Unit corresponds to magma chambers related to a volcanic phase that is no longer preserved in the geologic record.

The younger volcanic sequence, forming the Upper Unit, rests on an important erosional discontinuity truncating the older basement (Lower and Middle units). This sequence is dominated by products of phonolite volcanism characterised by phreatomagmatic and phreatoplinian eruptions and by the extrusion of domes and lava flows. Rare mafic products, predominantly of nephelinitic composition, are also present and include a phreatomagmatic crater, a strombolian cone and a few scattered small-volume lava flows. Although no eruptions have occurred since settlement in the mid-XVth century, the fresh morphology of craters and domes indicates that volcanism must be considered active. This fact, together with the occurrence of fault scarps, frequent seismicity, and strong relief, indicates a significant risk to the population of Brava related to volcanic, seismo-tectonic, mass movement and tsunami hazards. On Brava major mass movements occur in relation to steep slopes of erosive (sea cliffs and fluvial valleys) or structural nature (Madeira et al., 2009).

Extrusive carbonatites (Fig. 1B) exposed within the Upper Unit constitute the main aim of this contribution. During field works in 2006 and 2007, at least 20 small outcrops of dark-brown to blackish extrusive carbonatites were found, none of which corresponds to the location described by Hoernle et al. (2002). These occur in three areas: NE of the island, around Nova Sintra (Fig. 1B and C), SW near Campo Baixo (Fig. 1B and D), and S around Cachaço and Morro das Pedras (Fig. 1B and E). All extrusive carbonatites were deposited on or near the top of the younger volcanic sequence.

Unlike the description of Hoernle et al. (2002), most outcrops are made up of pyroclastic formations, comprising magmatic and/or phreatomagmatic ash and lapilli fall deposits and one probable pyroclastic flow, and most contain abundant lithic fragments of phonolite and occasionally other lithologies. Lava (alvikite) flows may also be present in the Santa Bárbara outcrop.

Near Nova Sintra village, extrusive carbonatites crop out in two locations (Fig. 1B and C). One is located 300 m to the north of Santa Bárbara where carbonatite ash (Fig. 4a) partially fills a wide and shallow crater carved into the NE slope of the island, forming a small step in the morphology. Just outside the volcanic depression, carbonatite deposits display a massive texture and may correspond to the remains of lavas that flowed towards the eastern shore (Fig. 4b). Stratigraphically, these deposits are the youngest in the area, covering all other formations and cropping out on the topographic surface.

On the road to Mato Grande, 750 m SW of the centre of Nova Sintra village (Fig. 1B and C), the road-cut exposes a carbonatite pyroclastic fall deposit intercalated between phonolitic phreatomagmatic pyroclasts and a phonolitic pumice fall deposit (Fig. 2A). The deposit is composed of fine stratified ash containing mica crystals and small phonolite lithic fragments. It was displaced by N–S-trending normal faults and is truncated by an erosional surface. To the NW, carbonatite tuffites, containing terrestrial gastropods, represent sedimentary removal of the volcanic carbonatite ashes. Grain-size analysis of the deposit shows that it is mostly composed of fine to very fine-ash and dust ($\sim$95 wt.% < $-1$ $\Phi$). The coarser fraction contains lithic fragments of phonolite from the Upper Unit, and pyroxenite and sövite from the Middle Unit. This is the oldest of the observed extrusive carbonatite deposits.

The outcrops SW of Campo Baixo (Figs. 1B and D, 2B) include pyroclastic fall deposits, a feeder dike (Fig. 3a) and the remains of a small hornito or spatter rampart (Fig. 3b). In cross section, the deposit is composed of layers of vesicular lapilli (5–10 mm in

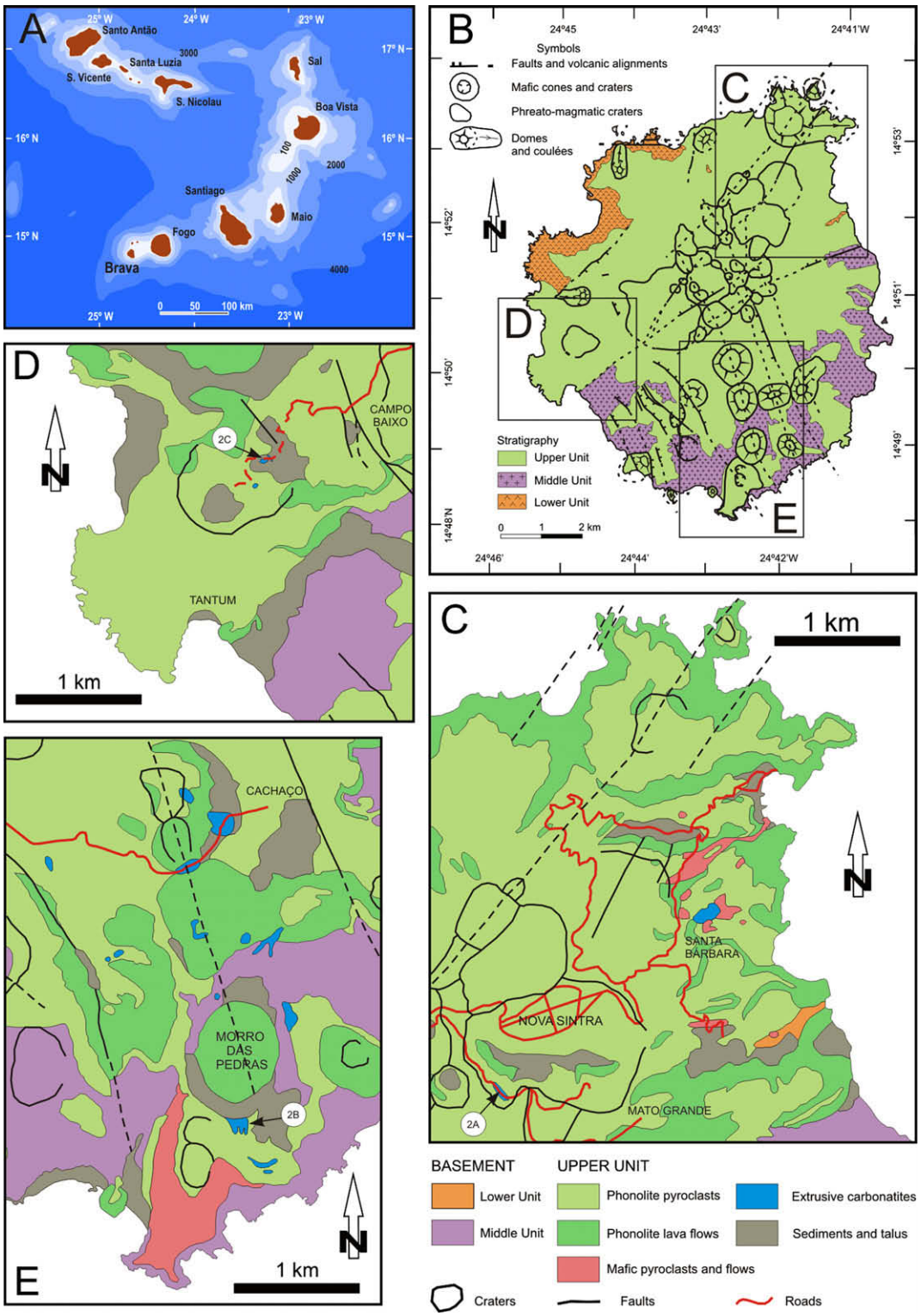


**Fig. 1.** Geology of Brava Island. (A) Location of Brava in the Cape Verde archipelago, (B) simplified geological map of Brava representing the main stratigraphic units and structures. Rectangles (C), (D), and (E) correspond to areas shown below in more detailed geologic maps. Orange and lilac colours represent the older basement (Lower and Middle Units). In the Upper Unit, blue areas correspond to the mapped extrusive carbonatite outcrops. The locations of geological sections from Fig. 2 are marked with labels 2A, 2B and 2C. Localities cited in the text are indicated.

diameter; Fig. 3c) and a crystal-rich tuff (Fig. 3d). The pyroclasts are preserved in two small outcrops blanketing a few tens of square metres of the present topography, one of which can be linked to the feeder dike, whereas the second lies 250 m from the eruptive centre. The NW–SE-trending 1 m-thick conduit displays a fragmented (pyroclastic) texture in the centre and massive chilled margins (Fig. 4c and d). It contains abundant lithic fragments of variable size (Fig. 3a). A small hornito or spatter rampart is constructed above the dike, forming a small mound on the topography (Fig. 3b). These deposits represent the youngest

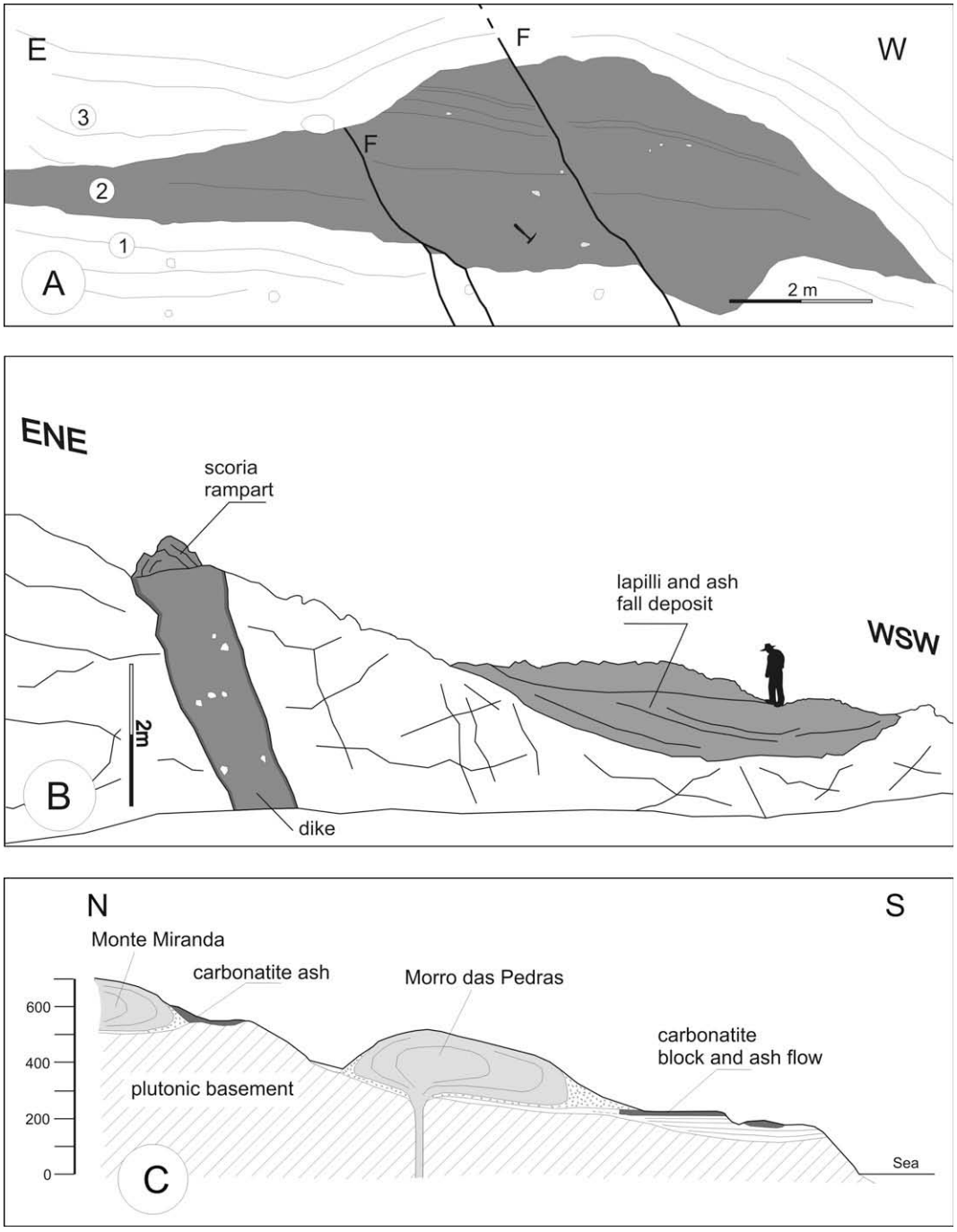


**Fig. 2.** Field sketches of recent extrusive carbonatites (in dark-grey); locations indicated in Fig. 1 C–E. (A) Section on the road to Mato Grande: carbonatitic fine-ash deposit overlies a phonolitic phreatomagmatic tuff and is covered by a coarse phonolitic pumice fall deposit. Erosion truncated the carbonatite deposit prior to the pumice fall event. The deposits are displaced by two surface ruptures along N-S-trending faults, (B) exposure along the road to Tantum exposing a carbonatitic dike, the remains of a spatter rampart, and a lapilli and ash-fall deposit. Note the presence of chilled margins (darker) and lithic fragments in the dike. The view is oblique and the scale (given by the vertical bar and figure in the background) is variable. Details of this outcrop are displayed in the photos in Fig. 3a–c and d, and (C) stratigraphic relations and location of the carbonatite deposits surrounding the Morro das Pedras phonolite dome. Carbonatitic block and ash-flow deposit is located south of the dome and partially covered by it. To the north, in higher topographic positions, there are several outcrops of a carbonatite ash-fall deposit, probably belonging to the same eruptive event. The vent of the carbonatitic eruption must be concealed by the younger dome. Photos of the block and ash-flow are presented in Fig. 3e and f.

volcanic event in the area, because they are stratigraphically above all others.

The outcrops south of Morro das Pedras (Figs. 1B and E, 2C) correspond to a flow deposit, probably a block and ash-flow. The deposit flowed down a wide, shallow valley and presents variable thickness (7 m-thick in the centre, thinning laterally) and a flat top (Fig. 3e). It is composed of a slightly consolidated carbonatite ash matrix supporting abundant lithic fragments, exclusively of phonolite composition. Bigger clasts, ranging in size from 40 cm up to 3 m in diameter, are rounded (but not polished) and covered by a thin, dark-grey film of massive carbonatite, probably formed by agglutinated and partially welded ash (Figs. 3f, 4e). In contrast, smaller fragments are angular, suggesting that bigger lithic fragments suffered abrasion during transport, whereas smaller clasts were immersed in ashes and preserved from abrasion. This was the penultimate event in the region, predating the formation of


**Fig. 3.** Field photographs of three outcrops of the recent extrusive carbonatites of Brava Island. (a) Carbonatite dike, 1 m-wide, exposed along the road to Tantum. The dike crosscuts a highly fractured landslide deposit of phonolitic nature. The walking stick to the left of dike is 1.10 m-long, (b) remains of carbonatite spatter rampart standing on the topographic surface above the feeder dike. Hammer for scale, (c) and (d) details of carbonatite lapilli fall deposits at outcrop along the road to Tantum. Pen point is 1 mm wide: vesicular carbonatite lapilli-fall layer (c); crystal-tuff layer formed by accumulation of 1 mm-thick, 2–3 mm-long tabular calcite crystals (d), (e) general view of the carbonatitic block and ash-flow of the Morro das Pedras area, looking north. The carbonatite is the darker deposit on which the human figure (circled) stands. The carbonatites rest on phonolitic phreatomagmatic tuffs. The very young phonolite dome and related breccia overlie the carbonatite, (f) detail of a phonolite block rounded by abrasion within the carbonatitic block and ash-flow from the same locality and (g) small outcrop of spatter accumulation in the Cachaço area, indicating proximity to the eruptive centre. Hammer for scale.

the impressive phonolite dome of Morro das Pedras (250 m in height), which presents an almost untouched volcanic morphology (Fig. 3e). To the north and west of the dome, several small outcrops of carbonatite ash may correspond to pyroclastic fall deposits related to the same eruption. The position of the carbonatitic fall and flow deposits suggests that the eruptive centre for this event may have been covered by the Morro das Pedras dome. Fall deposits were blown to the N and NW of the eruptive centre, whereas ash flows followed the fluvial valley downwards to the south.

A few more outcrops of carbonatite are located to the NW, W and SW of the village of Cachaço (Fig. 1B and E). Most appear to represent consolidated lapilli and ash deposits (Fig. 4f), yielding some solution (corrosion) morphologies. The eruptive centre for these deposits must be placed on the SE slope of the Cachaço phonolite dome, where the carbonatite outcrops display a granular texture that may represent accumulations of agglutinated coarse lapilli and spatter, suggesting proximity to the volcanic source (Fig. 3g). All other deposits lie to the west of this location, indicating easterly winds during this event. Carbonatitic pyroclasts overlie all other volcanic deposits in the area, indicating a very recent age for the event.

The described stratigraphic and structural relations, as well as the geographic distribution of the extrusive carbonatites, points to at least five distinct, very recent carbonatitic eruptions. The

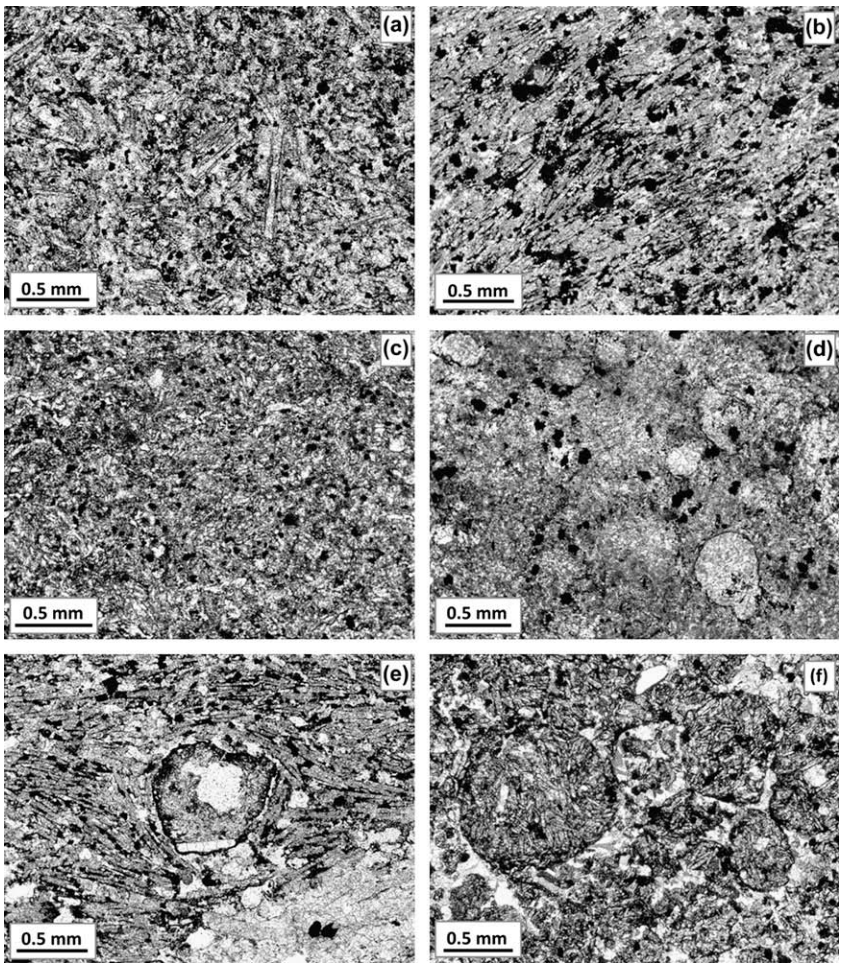


**Fig. 4.** Photomicrographs of representative extrusive carbonatites of Brava Island. (a) Tabular calcite phenocrysts with random orientations supported by very fine-grained ash matrix (sample CY-219) in the Santa Bárbara carbonatite outcrop, (b) well-developed trachytic-like texture of a lava flow, produced by oriented tabular calcite crystals in the same locality (sample CY-222), (c) and (d) aspects of the chilled margin of the carbonatite dike exposed on the road to Tantum; (c) is a very fine-grained carbonatite, whereas thin section (d) of the inner edge of the chilled margin shows a few spherical droplets of carbonatite in a fine-grained matrix (Sample CY-261), (e) tabular calcite crystals showing a well-developed flow orientation, from the film enveloping the phonolite blocks from the block and ash-flow deposit to the south of Morro das Pedras (sample CY-94) and (f) tear-drop ash-tuff cropping out to the SW of the village of Cachaço (sample CY-246). The deposit is composed of spherical ash particles with secondary spathic calcite filling interstitial voids.

older eruption must be the one that deposited the Mato Grande ash deposit, another is related to the Morro das Pedras event, the Cachaço deposits represent a third eruption, and the Santa Bárbara and Tantum outcrops probably represent the youngest (fourth and fifth) carbonatitic volcanic events.

## 3. Petrography

### 3.1. Extrusive carbonatites from the Upper Unit

According to the systematics of Woolley and Kempe (1989), all sampled outcrops of extrusive carbonatites are made up of calciocarbonatites.

Most pyroclastic deposits are ash-tuffs, with grains mostly smaller than 0.20 mm. Some consist of juvenile, tear-drop and spherical particles containing small tabular carbonate crystals without any preferential orientation, with the spaces between particles filled with secondary spathic calcite (Fig. 4f). Usually, pyroclastic particles are fine-grained and have ill-defined grain boundaries, which in some cases can result from a late re-crystallisation process. In a few samples, secondary spathic calcite cement is almost absent, and the rock is formed essentially by agglutinated, very fine carbonatite ash, with large tabular phenocrysts of calcite (Fig. 4a). These rocks are essentially composed of calcite, with apatite and biotite found in minor quantities. Alkali feldspar is very rare. Frequent accidental material, namely pyroxenite and phonolite, and coarse-grained calcite (from sövite) are present in the pyroclastic deposits, reflecting the lithological nature of the formations crossed by carbonatitic magma during its ascent.

Samples representing carbonatite lava flows (Fig. 4b) and agglutinated ash (Fig. 4e) show a marked flow orientation marked by the same kind of tabular carbonate crystals as in tuffs, creating a trachytic-like texture. The crystals are sub-angular laths with rounded edges, indicating the development of rhombohedral and pyramidal crystal faces. They often produce folded flow lines. The matrix, consisting of fine-grained calcite and oxide dust (magnetite?), is interpreted as resulting from quenching of the remaining carbonatite melt during eruption. Calcite is largely predominant, and apatite and biotite occur rarely.

### 3.2. Intrusive carbonatites from the Middle Unit

Intrusive calciocarbonatites occur only within the alkaline–carbonatite intrusive complex of the Middle Unit. They are here described for comparison with extrusive carbonatites.

Intrusive carbonatites tend to be equigranular, although some samples display a seriate texture. They are hypidiomorphic to allotriomorphic and are fine- to coarse-grained (0.02 mm–1.5 cm).

Two samples, however, show very large (>2 cm) carbonate crystals. Calcite, which is present in variable amounts, makes up the principal carbonate minerals in these rocks. Other constituents include apatite, alkaline feldspar and oxide minerals. Mica is lacking in many samples but, when present, can be fairly abundant (this mineral phase occurs in 5 of 14 samples). Sodic pyroxene, titanite, analcime and cancrinite are found as accessories.

## 4. Mineral chemistry

Selected EMP analyses of the main mineral phases of the pyroclastic deposits and lava flows are reported in Table 1, whereas Table 2 gives representative analyses of the most abundant minerals in the intrusive carbonatites from the Middle Unit for comparison.

### 4.1. Analytical procedures

The mineral compositions were determined at CeGUL/CREMINER (Faculdade de Ciências da Universidade de Lisboa) on a JEOL JXA 8200 microprobe, using a range of natural minerals as standards. An accelerating voltage of 15 kV was combined with a beam current of 10 nA and a beam diameter of 5 μm. Due to the low stability of some minerals under an electron beam and strong loss of Na, a defocused beam diameter (up to 20 μm) was sometimes used.

### 4.2. Results

The analysed apatites have very high F contents (>3.3 wt.%; > 0.88 atoms p.f.u.), even compared with those described in carbonatites worldwide (e.g., Seifert et al., 2000; Brassinnes et al., 2005; D'Orazio et al., 2007). They are, thus, fluorapatites. However, it should be emphasised that fluorapatite analyses from the studied extrusive carbonatites yielded F contents significantly above the stoichiometric value of 3.77 wt.% (up to 4.2 wt.% and 1.095 atoms p.f.u.). This is not very common but has been reported for some carbonatites (e.g., Bünh et al., 2001) and can be considered the result of coupled substitution involving the replacement of phosphorus by tetravalent carbon and of $O^{2-}$ by $F^{-}$ in order to maintain the charge balance: $[PO4]^{3-} \leftrightarrow [CO_3.F]^{3-}$;

**Table 1**
Representative EMP analyses (wt.%) of the major mineral phases of extrusive carbonatites.

| Phase sample | Apatite | | | Calcite | | | | Biotite | | | |
|---|---|---|---|---|---|---|---|---|---|---|---|
| | CY-95 | CY-95 | CY-95 | CY-95 | CY-95 | CY-221 | CY-221 | CY-95 | CY-95 | CY-221 | CY-221 |
| | ap2 | ap4 | ap5 | cb21 | cb43 | cb12 | cb24 | mc5 | mc11 | mc1 | mc4 |
| *Major elements (wt.%)* | | | | | | | | | | | |
| $SiO_2$ | – | – | – | – | – | – | – | 36.88 | 36.78 | 36.19 | 38.38 |
| $TiO_2$ | – | – | – | bdl | bdl | bdl | bdl | 3.85 | 2.01 | 3.41 | 2.79 |
| $Cr_2O_3$ | – | – | – | – | – | – | – | 0.01 | bdl | bdl | bdl |
| $Al_2O_3$ | – | – | – | – | – | – | – | 10.12 | 13.26 | 10.00 | 6.75 |
| $FeO^T$ | 0.07 | 0.08 | 0.05 | 0.01 | 0.06 | 0.76 | 0.31 | 24.98 | 20.18 | 24.10 | 23.95 |
| MnO | bdl | 0.06 | 0.02 | – | – | – | – | 0.89 | 0.87 | 0.81 | 0.64 |
| MgO | – | – | – | 0.97 | 0.52 | 0.63 | 0.75 | 9.45 | 12.30 | 10.99 | 12.18 |
| CaO | 54.97 | 55.09 | 54.77 | 53.15 | 54.67 | 49.82 | 51.94 | 0.08 | 0.05 | bdl | 0.02 |
| SrO | 0.61 | 0.63 | 0.62 | 0.31 | 0.14 | 0.68 | 0.64 | – | – | – | – |
| BaO | – | – | – | bdl | 0.05 | 0.74 | 0.60 | 0.70 | 0.16 | 0.23 | 0.08 |
| $Na_2O$ | 0.19 | 0.17 | 0.14 | 0.03 | 0.02 | 0.16 | 0.14 | 0.49 | 0.20 | 0.51 | 0.43 |
| $K_2O$ | – | – | – | – | – | – | – | 8.61 | 9.57 | 9.17 | 9.55 |
| $P_2O_5$ | 41.50 | 41.66 | 41.98 | – | – | – | – | – | – | – | – |
| $La_2O_3$ | 0.06 | 0.09 | 0.23 | 0.02 | bdl | 0.09 | 0.04 | – | – | – | – |
| $Ce_2O_3$ | 0.23 | 0.23 | 0.32 | 0.03 | 0.04 | 0.46 | 0.38 | – | – | – | – |
| $Nd_2O_3$ | 0.18 | 0.03 | 0.15 | 0.01 | bdl | 0.01 | 0.02 | – | – | – | – |
| F | 4.04 | 4.15 | 4.12 | – | – | – | – | – | – | – | – |
| Cl | 0.02 | 0.02 | bdl | – | – | – | – | – | – | – | – |
| O≡F | 1.70 | 1.75 | 1.74 | – | – | – | – | – | – | – | – |
| O≡Cl | 0.00 | 0.00 | 0.00 | – | – | – | – | – | – | – | – |
| Total | 100.17[a] | 100.46[a] | 100.67[a] | 54.53 | 55.48 | 53.36 | 54.81 | 96.08 | 95.38 | 95.42 | 94.76 |
| No oxygens | 24 | 24 | 24 | 6 | 6 | 6 | 6 | 22 | 22 | 22 | 22 |
| Si | | | | | | | | 5.904 | 5.730 | 5.773 | 6.165 |
| Ti | | | | | | | | 0.464 | 0.236 | 0.409 | 0.337 |
| Cr | | | | | | | | 0.001 | 0.000 | 0.000 | 0.000 |
| Al | | | | | | | | 1.910 | 2.435 | 1.880 | 1.277 |
| $Fe^{2+}$ | 0.010 | 0.011 | 0.007 | 0.000 | 0.002 | 0.023 | 0.009 | 3.343 | 2.629 | 3.215 | 3.217 |
| Mn | 0.000 | 0.009 | 0.003 | | | | | 0.121 | 0.114 | 0.109 | 0.087 |
| Mg | | | | 0.049 | 0.026 | 0.034 | 0.039 | 2.256 | 2.856 | 2.614 | 2.917 |
| Ca | 9.841 | 9.844 | 9.841 | 1.943 | 1.968 | 1.909 | 1.924 | 0.014 | 0.009 | 0.000 | 0.004 |
| Sr | 0.059 | 0.061 | 0.060 | 0.006 | 0.003 | 0.014 | 0.013 | | | | |
| Ba | | | | 0.000 | 0.001 | 0.010 | 0.008 | 0.044 | 0.009 | 0.015 | 0.005 |
| Na | 0.061 | 0.054 | 0.046 | 0.002 | 0.001 | 0.011 | 0.009 | 0.153 | 0.062 | 0.159 | 0.134 |
| K | | | | | | | | 1.758 | 1.901 | 1.866 | 1.957 |
| P | 5.871 | 5.882 | 5.960 | | | | | | | | |
| La | 0.004 | 0.005 | 0.014 | 0.000 | 0.000 | 0.001 | 0.001 | | | | |
| Ce | 0.014 | 0.014 | 0.019 | 0.000 | 0.000 | 0.006 | 0.005 | | | | |
| Nd | 0.011 | 0.002 | 0.009 | 0.000 | 0.000 | 0.000 | 0.000 | | | | |
| Sum cation | 15.871 | 15.882 | 15.960 | 2.001 | 2.000 | 2.009 | 2.007 | 15.969 | 15.981 | 16.039 | 16.099 |
| F | 1.067 | 1.095 | 1.094 | | | | | | | | |
| Cl | 0.002 | 0.003 | 0.000 | | | | | | | | |
| OH calc | 0.931 | 0.902 | 0.906 | | | | | | | | |

[a] Total minus oxygen for F and Cl; bdl, below detection limit; –, not determined. Mineral abbreviations: ap, apatite; cb, carbonate; mc, mica. OH is calculated assuming (F + Cl + OH) = 2. FeOT, all Fe as FeO.

**Table 2**
Representative EMP analyses (wt.%) of the major mineral phases of Intrusive carbonatites.

| Phase sample | Apatite | | | | | | Calcite | | | | Biotite | |
|---|---|---|---|---|---|---|---|---|---|---|---|---|
| | CY-116 | CY-116 | CY-116 | CY-145 | CY-145 | CY-145 | CY-116 | CY-116 | CY-145 | CY-1145 | CY-116 | CY-116 |
| | ap1 | ap2 | ap8 | ap2 | ap4 | ap7 | cb1 | cb7 | cb2 | cb7 | mc4 | mc8 |
| *Major elements (wt.%)* | | | | | | | | | | | | |
| $SiO_2$ | – | – | – | – | – | – | – | – | – | – | 36.12 | 37.06 |
| $TiO_2$ | – | – | – | – | – | – | 0.04 | bdl | bdl | bdl | 4.41 | 3.71 |
| $Cr_2O_3$ | – | – | – | – | – | – | – | – | – | – | bdl | 0.02 |
| $Al_2O_3$ | – | – | – | – | – | – | – | – | – | – | 13.13 | 12.56 |
| FeOT | 0.03 | 0.07 | 0.05 | 0.01 | 0.02 | bdl | 0.36 | 0.30 | 0.79 | 0.57 | 20.16 | 19.28 |
| MnO | 0.04 | 0.03 | 0.02 | 0.02 | 0.02 | 0.01 | – | – | – | – | 0.48 | 0.45 |
| MgO | – | – | – | – | – | – | 0.27 | 0.27 | 0.19 | 0.12 | 11.54 | 12.56 |
| CaO | 54.69 | 54.45 | 55.01 | 54.41 | 54.46 | 54.33 | 53.64 | 51.72 | 52.70 | 52.37 | bdl | 0.09 |
| SrO | 0.47 | 0.53 | 0.55 | 0.91 | 0.97 | 0.88 | 0.68 | 0.59 | 0.15 | 0.41 | - | - |
| BaO | – | – | – | – | – | – | 0.04 | 0.07 | 0.02 | 0.04 | 0.39 | 0.30 |
| $Na_2O$ | 0.23 | 0.28 | 0.24 | 0.13 | 0.16 | 0.16 | 0.01 | 0.02 | bdl | 0.02 | 0.33 | 0.33 |
| $K_2O$ | – | – | – | – | – | – | – | – | – | – | 9.43 | 9.50 |
| $P_2O_5$ | 42.33 | 42.20 | 41.07 | 42.11 | 41.91 | 42.05 | – | – | – | – | – | – |
| $La_2O_3$ | 0.03 | 0.07 | 0.16 | 0.15 | 0.08 | 0.15 | 0.01 | bdl | 0.00 | bdl | – | – |
| $Ce_2O_3$ | 0.28 | 0.39 | 0.15 | 0.20 | 0.26 | 0.24 | 0.01 | 0.07 | 0.08 | 0.04 | – | – |
| $Nd_2O_3$ | 0.10 | 0.20 | 0.07 | 0.03 | 0.10 | 0.05 | bdl | bdl | 0.018 | 0.01 | – | – |
| $H_2O$ calc | – | – | – | – | – | – | – | – | – | – | 4.01 | 4.12 |
| F | 3.31 | 3.45 | 3.64 | 3.63 | 3.60 | 3.51 | – | – | – | – | – | – |
| Cl | 0.01 | 0.01 | 0.01 | bdl | bdl | 0.00 | – | – | – | – | – | – |
| O≡F | 1.39 | 1.45 | 1.53 | 1.53 | 1.51 | 1.48 | – | – | – | – | – | – |
| O≡Cl | 0.00 | 0.00 | 0.00 | – | – | 0.00 | – | – | – | – | – | – |
| Total | 100.13[a] | 100.22[a] | 99.42[a] | 100.09[a] | 100.06[a] | 99.90[a] | 55.06 | 53.05 | 53.95 | 53.58 | 95.99 | 95.88 |
| No oxygens | 24 | 24 | 24 | 24 | 24 | 24 | 6 | 6 | 6 | 6 | 22 | 22 |
| Si | | | | | | | | | | | 5.658 | 5.769 |
| Ti | | | | | | | 0.001 | 0.000 | 0.000 | 0.000 | 0.520 | 0.434 |
| Cr | | | | | | | | | | | 0.000 | 0.003 |
| Al | | | | | | | | | | | 2.423 | 2.304 |
| $Fe^{2+}$ | 0.004 | 0.010 | 0.007 | 0.001 | 0.003 | 0.000 | 0.010 | 0.009 | 0.023 | 0.017 | 2.641 | 2.510 |
| Mn | 0.006 | 0.004 | 0.002 | 0.003 | 0.003 | 0.002 | | | | | 0.064 | 0.059 |
| Mg | | | | | | | 0.014 | 0.014 | 0.010 | 0.006 | 2.694 | 2.921 |
| Ca | 9.844 | 9.802 | 9.838 | 9.839 | 9.821 | 9.835 | 1.960 | 1.962 | 1.963 | 1.967 | 0.000 | 0.015 |
| Sr | 0.046 | 0.051 | 0.054 | 0.089 | 0.095 | 0.086 | 0.013 | 0.012 | 0.003 | 0.008 | | |
| Ba | | | | | | | 0.000 | 0.001 | 0.000 | 0.001 | 0.024 | 0.018 |
| Na | 0.075 | 0.092 | 0.076 | 0.044 | 0.051 | 0.051 | 0.001 | 0.001 | 0.000 | 0.001 | 0.100 | 0.101 |
| K | | | | | | | | | | | 1.884 | 1.887 |
| P | 6.021 | 6.003 | 5.804 | 6.017 | 5.973 | 6.015 | | | | | | |
| La | 0.002 | 0.005 | 0.010 | 0.009 | 0.005 | 0.009 | 0.000 | 0.000 | 0.000 | 0.000 | | |
| Ce | 0.017 | 0.024 | 0.009 | 0.012 | 0.016 | 0.015 | 0.000 | 0.001 | 0.001 | 0.001 | | |
| Nd | 0.006 | 0.012 | 0.004 | 0.002 | 0.006 | 0.003 | 0.000 | 0.000 | 0.000 | 0.000 | | |
| Sum cation | 16.021 | 16.003 | 15.804 | 16.017 | 15.973 | 16.015 | 2.001 | 2.001 | 2.000 | 2.001 | 16.008 | 16.022 |
| F | 0.880 | 0.917 | 0.960 | 0.969 | 0.957 | 0.938 | | | | | | |
| Cl | 0.001 | 0.002 | 0.001 | 0.000 | 0.000 | 0.000 | | | | | | |
| OH calc | 1.119 | 1.081 | 1.039 | 1.031 | 1.043 | 1.061 | | | | | | |

[a] Total minus oxygen for F and Cl; bdl, below detection limit; –, not determined. Mineral abbreviations: ap, apatite; cb, carbonate; mc, mica. OH is calculated assuming (F + Cl + OH) = 2. $FeO^T$, all Fe as FeO.

Binder and Troll (1989). As is typical of carbonatite apatites, they are relatively rich in SrO (up to 0.91 wt.%) and poor in MnO (⩽0.06 wt.%). Their light rare earth element contents are clearly higher than those determined for calcite in the same samples, in agreement with the *D* values compiled by Bünh et al. (2001). The rare earth element incorporation was probably accompanied by the incorporation of $Na^+$ in order to balance charges ($Ca^{2+} + Ca^{2+} \leftrightarrow REE^{3+} + Na^+$; Rønsbo, 1989; Seifert et al., 2000), which would explain the relatively high $Na_2O$ contents (0.13–0.28 wt.%).

In Tables 1 and 2, the calcitic character of carbonates is evident from the low MgO (<0.90 wt.%) and FeO (<0.78 wt.%) contents. Calcites from extrusive carbonatites are clearly more Mg-rich and Fe-poor than their intrusive counterparts, which translates into distinct MgO/(MgO + FeO) contents (extrusives: 0.45–0.99; intrusives: 0.17–0.48). SrO can be as high as 0.69 wt.%.

All present mica is characterised by low $X_{phl}$ (<0.55) and is thus referred to as biotite. K is partially substituted by Na, Ba, and Ca, which occupy up to 11% of the interlayer site. The $TiO_2$ concentrations are very high (up to 4.41 wt.%), which is remarkable given the very low $TiO_2$ contents of the host carbonatitic rocks.

## 5. Whole rock geochemistry

### 5.1. Analytical procedures

Nineteen samples of extrusive carbonatites considered representative of different outcrops were studied petrographically; of these, nine samples were selected for major and trace element whole rock analyses. The studied samples are representative of two of three areas where extrusive carbonatites were identified (samples CY-219, CY-221, CY-222 and CY-225 come from the north-eastern part of the island, and samples CY-95, CY-231, CY-238, CY-241 and CY-246 were collected in the south). For comparison, data on 12 of 19 collected samples of older intrusive calciocarbonatite were also selected for chemical analysis.

Samples of 1–2 kg were prepared at the Departamento de Geologia da Universidade de Lisboa. After reducing the sample to centimeter-sized chips in a hydraulic press, the freshest pieces were selected and coarsely pound using a jaw crusher and then powdered in an agate swing mill.

Both major- and trace-element analyses were performed at the Activation Laboratories Ltd., Ancaster, Ontario, Canada. For whole rock analysis, major oxide contents were obtained using Inductively Coupled Plasma-Optical Emission Spectrometry (ICP-OES). Trace element contents were obtained using Inductively Coupled Plasma-Mass Spectrometry (ICP-MS), with the exception of Ba and Sr, which were obtained by ICP-OES. Samples were prepared and analysed in a batch system. Each batch contained a method reagent blank, certified reference material and 17% replicates. Samples were mixed with a flux of lithium metaborate and lithium tetraborate and fused in an induction furnace. The molten melt was immediately poured into a solution of 5% nitric acid containing an internal standard and mixed continuously until completely dissolved (~30 min). The samples were run for major oxides and selected trace elements on a combination simultaneous/sequential Thermo Jarrell-Ash ENVIRO II ICP or a Spectro Cirros ICP. Calibration was performed using seven prepared USGS and CANMET certified reference materials. One of the seven standards was used during the analysis for every group of ten samples. The prepared sample solution was spiked with internal standards to cover the entire mass range and was further diluted and introduced into a Perkin Elmer SCIEX ELAN 6000 or 6100 ICP-MS using a proprietary sample introduction methodology. Fluorine was analysed by the Ion Selective Electrode technique (ISE) and $CO_2$ by Coulometry.

All elements were analysed under the control of certified international standards. In general, there is good agreement between results obtained by different methods on the same samples. Duplicate measurements give an estimate of the total reproducibility of our analyses. For whole rock carbonatite samples, the reproducibility is better than: (i) 1 relative-% for major element contents ($SiO_2$, $Fe_2O_3$, MnO, MgO and CaO); (ii) 3 relative-% for Rare Earth Elements; and (iii) 2 relative-% for elements generally highly incompatible in an oceanic context (Rb, Ba, U, Th). The accuracy of the analyses, evaluated by analysing international standards, is generally better than 12 relative-%, with results for many elements within ± 6% of the recommended values. More information on the procedure, precision and accuracy of the Actlabs analyses can be found at http://www.actlabs.com.

Sr and Nd isotope analyses were performed on three representative extrusive calciocarbonatite samples (Upper Unit). Isotopic analyses of two intrusive samples (Middle Unit) were taken from Mata et al. (2006). Whole-rock samples (100 mg) were first treated with distilled water and left at 75 °C for a period of 3 h. After the supernatant were removed, drying of samples at 75 °C on hot plates, dissolution of the residue was performed in Savillex beakers with a mixture of 2 ml HF (45 M) + 0.5 ml $HNO_3$ (14 M), at 75 °C for 24 h (Savillex closed). Then, 0.2 ml $HClO_4$ (12 M) + 3 ml $HNO_3$ (7 M) was added to dissolve any residual fluorides. This mixture was evaporated first on a hot plate (at 50 °C for 3 days and 95 °C for 6 h) and then under the *epiradiator* (for 2 h). This was followed by the addition of 5 ml of distilled HCl (6 N) at 75 °C for 24 h and additional drying of the samples at 65 °C on hot plates. The residue was recovered in 10 ml HCl (1.25 M) and centrifuged for 10 min. Sr and Nd separations were performed with the "cascade" column procedure (Sr Spec, True Spec and Ln Spec columns) described by Pin and Bassin (1992) and Pin et al. (1994), after most of the iron was removed through an AG50X4 column. A mixture of $HNO_3$ (5 M) + HF (0.1 M) was used to collect Sr and REE. Sr and Nd blanks for the complete procedure were <0.5 ng and <0.2 ng, respectively.

Nd and Sr isotope measurements were obtained by thermal ionisation mass spectrometry (TIMS) at the *Laboratoire Magmas et Volcans* (France), using a Finnigan Triton mass spectrometer operating in the static multicollection mode with relay matrix rotation (also called the virtual amplifier) equipped with nine Faraday detectors. Sr samples were loaded on double W filaments with 1 μl $H_3PO_4$ (3 M) and Nd samples were loaded on the same type of filaments with 1 μl $H_3PO_4$ (1 M). Measurements of $^{87}Sr/^{86}Sr$ were corrected for $^{87}Rb$ interference. Sr measurements were mass-fractionation-corrected to $^{86}Sr/^{88}Sr = 0.1194$ and normalised to $^{87}Sr/^{86}Sr = 0.71025$ for the NIST SRM987 standard. Nd isotopic ratios were mass-fractionation-corrected to $^{146}Nd/^{144}Nd = 0.7219$ and normalised to $^{143}Nd/^{144}Nd = 0.51196$ for the Rennes-AMES standard. Repeated analyses of the two standards gave $^{87}Sr/^{86}Sr = 0.710246 \pm 0.000005$ ($2\sigma$, $n = 16$) and $^{143}Nd/^{144}Nd = 0.511961 \pm 0.000007$ ($2\sigma$, $n = 12$). A typical run consists of at least nine blocks of 10 cycles in order to allow a full rotation of the virtual amplifier system.

### 5.2. Results

#### 5.2.1. Major and trace elements

Representative major and trace elements compositions of Brava extrusive carbonatites are listed in Table 3. Data on older intrusive calciocarbonatites are also shown for comparison (Table 4).

Independently of the mode of emplacement (pyroclastic deposits vs. lava flows), Brava extrusive carbonatites exhibit a remarkable compositional uniformity, considering that they represent several (at least five) different eruptions and present a wide geographic dispersion. All selected samples of this group yield high CaO contents (>44 wt.%), which classifies them as calciocarbonatite (Fig. 5; Woolley and Kempe, 1989). Despite the fact that their compositional range in terms of $CaO-MgO-Fe_2O_3^t + MnO$ is completely overlapped by the intrusive counterpart, extrusive facies are more iron ($\overline{x}\ Fe_2O_3^t = 6.06$; from 3.31 to 9.76 wt.%) and manganese ($\overline{x}\ MnO = 1.24$; 0.83 to 1.93 wt.%) rich than sövitic rocks ($Fe_2O_3^t:\ \overline{x} = 2.97$; from 0.26 to 13.50 wt.%; $MnO:\ \overline{x} = 0.40$; from 0.23 to 0.87 wt.%).

Extrusive carbonatites are significantly richer in trace elements like Ba, Th, U, Nb, Pb and REE, but somewhat less enriched in Sr than the majority of intrusive calciocarbonatites (Figs. 6 and 7). The latter are compositionally more variable and yield more fractionated REE patterns, with $(La/Yb)_n$ up to 102 vs. up to 35. Both extrusive and intrusive calciocarbonatites are commonly depleted in MREE relative to LREE and HREE, resulting into slightly concave upwards patterns.

Primitive mantle-normalised trace element variations (Fig. 7) show that intrusive calciocarbonatite samples are highly variable, with concentration ranges in some elements of two to three orders of magnitude (e.g., Rb, Th, U, Nb, P and Ti). Significant depletions are observed in K, Th, P, Ti, Zr and Hf, with a few samples yielding abundances below primitive mantle values, which are not uncommon in carbonatites elsewhere (Nelson et al., 1988; Woolley and Kempe, 1989). Fig. 8 further illustrates the chemical differences between intrusive and extrusive carbonatites, as well as the larger variability of the Middle Unit intrusive carbonatites.

#### 5.2.2. Sr–Nd isotopic data

The whole rock Nd and Sr isotopic compositions of Brava calciocarbonatites are listed in Table 6 and plotted in Fig. 9. The element differences reported above are confirmed by isotopic data, which produce two distinct clusters on the $^{143}Nd/^{144}Nd$ vs. $^{87}Sr/^{86}Sr$ diagram. Both groups are characterised by Sr and Nd isotopic signatures indicating their ultimate origin from sources with time-integrated depletion in the more incompatible elements. Intrusive calciocarbonatites of the Middle Unit have higher initial $^{143}Nd/^{144}Nd$ ratios and lower initial $^{87}Sr/^{86}Sr$ ratios than the extrusive calciocarbonatites of the Upper Unit (see Table 6).

**Table 3**
Major (wt.%) and trace element (ppm) analyses of Extrusive Carbonatites from the Upper Unity of Brava Island.

| Sample | Extrusive calciocarbonatites | | | | | | | | |
|---|---|---|---|---|---|---|---|---|---|
| | CY-95 | CY-219 | CY-221 | CY-222 | CY-225 | CY-231 | CY-238 | CY-241 | CY-246 |
| *Major elements (wt.%)* | | | | | | | | | |
| $SiO_2$ | 2.03 | 0.78 | 1.11 | 0.56 | 1.20 | 3.23 | 0.85 | 1.21 | 1.39 |
| $TiO_2$ | 0.183 | 0.174 | 0.316 | 0.198 | 0.236 | 0.279 | 0.166 | 0.159 | 0.156 |
| $Al_2O_3$ | 0.82 | 0.23 | 0.40 | 0.25 | 0.40 | 1.31 | 0.40 | 0.38 | 0.64 |
| $Fe_2O_3^T$ | 5.06 | 5.73 | 9.76 | 6.38 | 7.24 | 7.51 | 5.04 | 4.51 | 3.31 |
| MnO | 0.964 | 1.217 | 1.929 | 1.337 | 1.466 | 1.464 | 1.015 | 0.949 | 0.832 |
| MgO | 1.00 | 1.12 | 1.52 | 1.06 | 1.16 | 0.84 | 0.54 | 0.72 | 0.84 |
| CaO | 50.04 | 48.06 | 48.22 | 50.96 | 46.98 | 44.88 | 50.04 | 51.79 | 49.55 |
| $Na_2O$ | 0.20 | 0.43 | 0.40 | 0.21 | 0.45 | 0.26 | 0.13 | 0.16 | 0.07 |
| $K_2O$ | 0.13 | 0.03 | 0.12 | 0.08 | 0.09 | 0.18 | 0.07 | 0.13 | 0.09 |
| $P_2O_5$ | 0.90 | 1.08 | 2.21 | 0.98 | 1.19 | 1.86 | 1.09 | 1.02 | 0.39 |
| LOI | 37.21 | 37.24 | 34.08 | 37.97 | 36.65 | 38.12 | 37.14 | 37.78 | 42.44 |
| F | 1.10 | 0.70 | 0.45 | 0.46 | 0.82 | 1.14 | 0.77 | 0.84 | 0.13 |
| Total | 99.64 | 96.79 | 100.52 | 100.45 | 97.88 | 101.07 | 97.25 | 99.65 | 99.84 |
| *Trace elements (ppm)* | | | | | | | | | |
| Rb | 5.0 | 4.0 | 8.0 | 2.0 | 7.0 | 20.0 | 8.0 | 12.0 | 12.0 |
| Sr | 6596 | 7961 | 6811 | 4799 | 8434 | 7999 | 6671 | 5600 | 3008 |
| Y | 157 | 199 | 294 | 193 | 222 | 197 | 159 | 175 | 132 |
| Zr | 99 | 108 | 143 | 74 | 113 | 121 | 66 | 68 | 53 |
| Nb | 140 | 113 | 186 | 147 | 108 | 102 | 143 | 145 | 75 |
| Cs | 0.3 | 0.1 | 0.3 | <0.1 | 0.2 | 2.6 | 0.2 | 0.5 | 0.3 |
| Ba | 10330 | 6019 | 9200 | 5634 | 3834 | 12140 | 11460 | 16130 | 431 |
| Hf | 1.4 | 2.4 | 2.5 | 1.5 | 2.2 | 1.8 | 1.2 | 1.1 | 1.0 |
| Ta | 0.62 | <0.01 | <0.01 | <0.01 | <0.01 | <0.01 | <0.01 | 0.51 | 0.16 |
| Pb | 32 | 38 | 51 | 37 | 44 | 45 | 39 | 34 | 36 |
| Th | 25.3 | 35.0 | 56.0 | 34.4 | 36.6 | 35.9 | 26.7 | 24.7 | 20.2 |
| U | 4.07 | 5.24 | 8.09 | 2.50 | 5.67 | 3.13 | 3.65 | 2.47 | 2.41 |
| La | 531 | 363 | 722 | 511 | 416 | 421 | 327 | 417 | 506 |
| Ce | 507 | 636 | 1370 | 920 | 725 | 734 | 586 | 759 | 746 |
| Pr | 95 | 119 | 170 | 122 | 138 | 136 | 103 | 95 | 89 |
| Nd | 311 | 391 | 571 | 405 | 458 | 439 | 341 | 310 | 264 |
| Sm | 46.4 | 58.8 | 87.0 | 61.5 | 68.2 | 66.1 | 50.5 | 45.4 | 34.5 |
| Eu | 15.0 | 18.6 | 27.8 | 19.9 | 22.5 | 21.3 | 16.2 | 15.1 | 10.9 |
| Gd | 38.0 | 50.0 | 76.0 | 54.7 | 57.0 | 54.0 | 41.1 | 40.3 | 28.2 |
| Tb | 5.11 | 6.88 | 10.20 | 7.15 | 7.88 | 7.32 | 5.50 | 5.18 | 3.85 |
| Dy | 28.1 | 36.3 | 51.5 | 36.2 | 41.3 | 37.8 | 29.2 | 28.2 | 21.2 |
| Ho | 5.01 | 6.62 | 9.11 | 6.50 | 7.26 | 6.50 | 5.04 | 5.48 | 4.00 |
| Er | 13.6 | 17.9 | 26.1 | 17.6 | 19.5 | 17.2 | 13.6 | 15.9 | 11.5 |
| Tm | 1.81 | 2.44 | 3.88 | 2.44 | 2.58 | 2.21 | 1.75 | 2.24 | 1.57 |
| Yb | 11.0 | 15.0 | 24.2 | 14.5 | 15.2 | 13.0 | 10.5 | 13.3 | 9.7 |
| Lu | 1.53 | 2.10 | 3.27 | 1.97 | 2.06 | 1.73 | 1.44 | 1.79 | 1.37 |
| ∑REE | 1609 | 1724 | 3152 | 2180 | 1980 | 1957 | 1532 | 1754 | 1732 |

## 6. Discussion

### 6.1. Occurrence and volcano-stratigraphy

On a global scale, extrusive carbonatites are very rare, compared with intrusive ones (Woolley and Church, 2005). Brava extrusive carbonatites are dominated by pyroclastic deposits, which demonstrate that these magmas can be characterised by significant explosivity, despite their extremely low viscosity (see Keller, 1989, for additional examples). Interestingly, one of the Brava occurrences must correspond to a carbonatitic pyroclastic flow deposit, strengthening the conviction that this kind of volcanic events also occurs in carbonatitic volcanism, despite the reservations expressed by Keller (1989).

In Cape Verde, carbonatites are usually assigned to the basal complexes of the islands, being formed during a relatively early stage of the emerged evolution of the volcanic construction (e.g., Serralheiro, 1976; Alves et al., 1979; Silva et al., 1981; Jørgensen and Holm, 2002; Madeira et al., 2005). In Fuerteventura (Canary archipelago), carbonatites are restricted to the basal complex (Muñoz et al., 2005; De Ignacio et al., 2006). Carbonatites on Brava occur in two distinct volcano-stratigraphic positions. Intrusive carbonatites are intimately associated with intrusive plutonic silicate rocks (mainly nepheline syenites, syenites and pyroxenites) belonging to the basal complex, while the extrusive ones correspond to the youngest volcanism of the island. Brava extrusive carbonatites are, therefore, exceptional among the oceanic carbonatites and unique in the context of the Cape Verde geology, as they are associated with the latest magmatic events in the island.

The only age determinations in Brava are those from Obradovich (reported by Lancelot and Allègre (1974)) and Knill (reported by Hoernle et al. (2002)), who measured K–Ar ages of 3.7 and 2.1 Ma, respectively, in biotites of intrusive carbonatites (Middle Unit). Hoernle et al. (2002) suggested for the extrusive carbonatite that they studied an age of <1000 years, based on geomorphological arguments. So far, the ≈2 Ma time lag between the formation of intrusive and extrusive carbonatites cannot be better constrained. However, such a time gap seems reasonable, given that the two episodes of carbonatite formation were separated by a major erosional phase and important uplift of up to 350 m of the submarine formations and intrusive rocks of the basal complex.

### 6.2. Geochemical comparison with the other Cape Verde carbonatites

In agreement with the time lag mentioned above, the ultimate sources of both groups of Brava carbonatites are clearly distinct, as shown by Sr and Nd isotope differences (Fig. 9). Despite similar

**Table 4**
Major (wt.%) and trace element (ppm) analyses of Intrusive Carbonatites from the Middle Unit of Brava Island.

| Sample | Intrusive calciocarbonatites | | | | | | | | | | | |
|---|---|---|---|---|---|---|---|---|---|---|---|---|
| | CY-23 | CY-56 | CY-116 | CY-139 | CY-142 | CY-144 | CY-145 | CY-156 | CY-157 | CY-161 | BR-15 | BR-23 |
| *Major elements (wt.%)* | | | | | | | | | | | | |
| $SiO_2$ | 0.42 | 0.09 | 11.92 | 0.29 | 2.03 | 1.49 | 0.92 | 5.80 | 0.36 | 16.90 | 3.04 | 0.27 |
| $TiO_2$ | 0.027 | <0.001 | 0.913 | <0.001 | <0.001 | 0.621 | <0.001 | 0.049 | 0.005 | 0.223 | 0.216 | 0.007 |
| $Al_2O_3$ | 0.12 | 0.03 | 4.37 | 0.09 | 0.52 | 0.33 | 0.27 | 0.32 | 0.19 | 4.85 | 0.52 | 0.10 |
| $Fe_2O_3^T$ | 0.71 | 0.26 | 4.93 | 1.88 | 1.38 | 13.50 | 0.86 | 2.79 | 2.10 | 4.48 | 3.93 | 2.16 |
| MnO | 0.500 | 0.269 | 0.251 | 0.528 | 0.461 | 0.310 | 0.352 | 0.236 | 0.874 | 0.233 | 0.270 | 0.368 |
| MgO | 0.30 | 0.10 | 2.31 | 2.07 | 0.27 | 0.13 | 0.18 | 0.51 | 3.80 | 0.70 | 0.45 | 0.12 |
| CaO | 53.09 | 54.64 | 38.84 | 51.01 | 52.11 | 45.15 | 52.91 | 48.48 | 46.08 | 37.81 | 49.75 | 53.87 |
| $Na_2O$ | 0.06 | 0.04 | 1.36 | 0.07 | 0.32 | 0.15 | 0.09 | 0.89 | 0.09 | 2.00 | 0.31 | 0.08 |
| $K_2O$ | 0.08 | <0.01 | 1.82 | <0.01 | <0.01 | 0.12 | 0.12 | 0.06 | 0.05 | 1.19 | 0.26 | 0.05 |
| $P_2O_5$ | 0.46 | <0.01 | 4.33 | 0.37 | 0.05 | 1.18 | 0.12 | 0.38 | 0.08 | 1.67 | 5.63 | 0.21 |
| LOI | 42.13 | 43.14 | 27.23 | 42.68 | 41.70 | 34.93 | 42.63 | 38.09 | 42.31 | 28.09 | 34.2 | 42.33 |
| F | 0.08 | <0.01 | 0.55 | 0.14 | 0.04 | 0.12 | 0.04 | 0.08 | 0.23 | 0.18 | - | - |
| Total | 97.98 | 98.57 | 98.82 | 99.13 | 98.88 | 98.03 | 98.49 | 97.69 | 96.17 | 98.33 | 98.58 | 99.57 |
| *Trace elements (ppm)* | | | | | | | | | | | | |
| Rb | 7.0 | <1.0 | 94.0 | <1.0 | <1.0 | 8.0 | 4.0 | 9.0 | <1.0 | 38.0 | 27.0 | 26.0 |
| Sr | >10000 | >10000 | 5955 | 3174 | 7835 | 8869 | 8563 | >10000 | >10000 | 9152 | 8466 | 8622 |
| Y | 115 | 121 | 117 | 112 | 89 | 93 | 100 | 63 | 145 | 68 | 115 | 99 |
| Zr | <4 | <4 | 160 | 55 | <4 | 40 | <4 | 316 | 61 | 553 | 103 | 247 |
| Nb | 1.8 | 0.4 | 46.6 | 6.3 | 2.5 | 6.0 | 6.0 | 4.5 | 6.5 | 41.7 | 10.8 | 4.6 |
| Cs | <0.1 | <0.1 | 0.9 | <0.1 | <0.1 | <0.1 | <0.1 | <0.1 | <0.1 | 0.4 | - | - |
| Ba | 1016 | 531 | 1062 | 1427 | 763 | 454 | 459 | 568 | 5803 | 1274 | 314 | 1041 |
| Hf | 0.2 | 0.2 | 2.3 | 0.6 | 0.2 | 0.6 | 0.2 | 4.2 | 0.9 | 8.7 | 1.5 | 0.2 |
| Ta | <0.01 | <0.01 | 1.05 | <0.01 | <0.01 | <0.01 | 0.08 | <0.01 | <0.01 | 0.49 | - | - |
| Pb | <5 | <5 | 14 | <5 | 8 | 6 | 9 | <5 | 16 | 6 | - | - |
| Th | 0.2 | 0.1 | 5.1 | 28.1 | 1.9 | 1.6 | 10.8 | 1.0 | 8.5 | 6.2 | 7.1 | 1.9 |
| U | 0.13 | 0.02 | 0.71 | 1.93 | 1.15 | 0.49 | 3.25 | 0.35 | 3.60 | 1.08 | 1.06 | 3.11 |
| La | 386 | 354 | 324 | 675 | 285 | 281 | 259 | 196 | 1380 | 203 | 307 | 280 |
| Ce | 671 | 615 | 640 | 1340 | 496 | 483 | 458 | 314 | 2560 | 342 | 608 | 502 |
| Pr | 66 | 60 | 72 | 133 | 49 | 48 | 45 | 30 | 263 | 34 | 65 | 48 |
| Nd | 227 | 209 | 282 | 452 | 163 | 163 | 155 | 98 | 935 | 117 | 241 | 166 |
| Sm | 32.2 | 30.6 | 45.8 | 61.1 | 24.4 | 25.6 | 24.2 | 14.7 | 135.0 | 18.7 | 39.1 | 26.8 |
| Eu | 10.2 | 9.5 | 14.2 | 16.5 | 7.3 | 7.9 | 7.6 | 4.5 | 38.8 | 5.8 | 11.1 | 7.9 |
| Gd | 25.8 | 24.8 | 36.1 | 38.1 | 18.5 | 20.5 | 19.6 | 12.2 | 92.3 | 15.3 | 32.8 | 22.8 |
| Tb | 3.94 | 3.83 | 5.21 | 4.47 | 2.78 | 3.13 | 3.23 | 1.93 | 9.82 | 2.33 | 4.35 | 3.33 |
| Dy | 21.2 | 21.0 | 25.5 | 21.2 | 15.2 | 16.7 | 17.7 | 10.4 | 38.9 | 12.5 | 21.5 | 17.1 |
| Ho | 3.96 | 3.98 | 4.56 | 3.87 | 2.94 | 3.10 | 3.36 | 2.01 | 6.04 | 2.32 | 3.87 | 3.20 |
| Er | 11.5 | 11.5 | 11.8 | 12.5 | 9.1 | 8.9 | 10.2 | 6.0 | 14.6 | 6.7 | 10.7 | 9.2 |
| Tm | 1.63 | 1.60 | 1.49 | 2.12 | 1.39 | 1.26 | 1.56 | 0.87 | 1.69 | 0.96 | 1.48 | 1.36 |
| Yb | 10.2 | 9.7 | 8.4 | 16.8 | 8.9 | 7.6 | 10.0 | 5.1 | 9.1 | 5.7 | 8.4 | 9.0 |
| Lu | 1.47 | 1.38 | 1.14 | 2.77 | 1.27 | 1.03 | 1.39 | 0.70 | 1.06 | 0.80 | 1.12 | 1.28 |
| ∑REE | 1472 | 1356 | 1472 | 2779 | 1084 | 1071 | 1016 | 697 | 5485 | 767 | 1356 | 1098 |

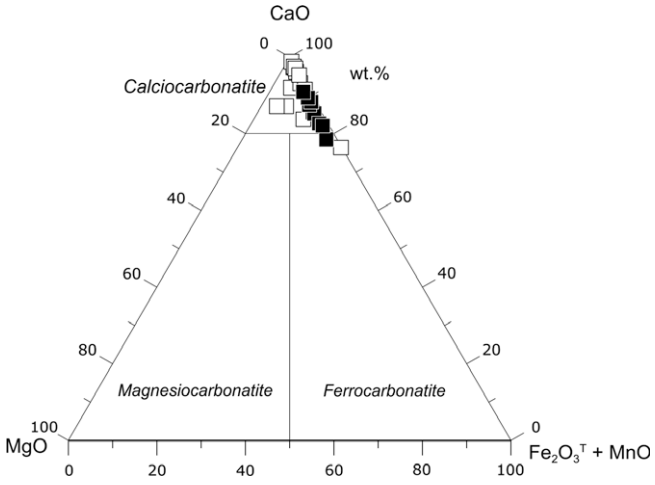


**Fig. 5.** Extrusive and intrusive carbonatite samples of Brava Island in the classification diagram of Woolley and Kempe (1989) using wt.% oxides. Open squares: intrusive calciocarbonatite, closed squares: extrusive calciocarbonatites.

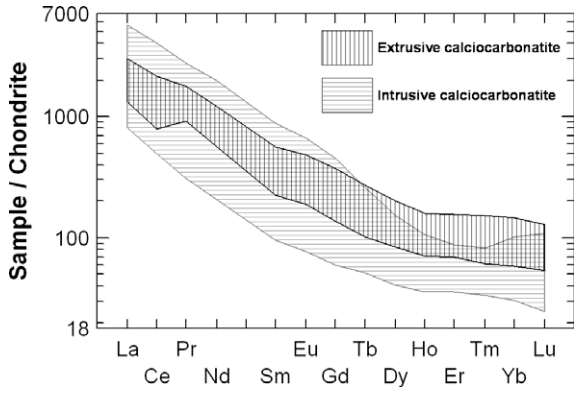


**Fig. 6.** REE patterns of extrusive calciocarbonatite samples, Upper Unit. Intrusive calciocarbonatites, Middle Unit, are shown for comparison. Normalising values are from Palme and O'Neill (2003).

ranges in isotopic variability, the extrusive carbonatites are clearly more homogeneous than the intrusive ones in terms of their elemental characteristics (Fig. 8), suggesting that they underwent less complex magmatic evolution, like crystal fractionation and/or cumulative processes. This suggests that the extrusive carbonatites were subject to relatively shorter residence times in magma chambers, which, different from occurred for the intrusive magmas, prevented significant magma evolution (see also Woolley and Church,

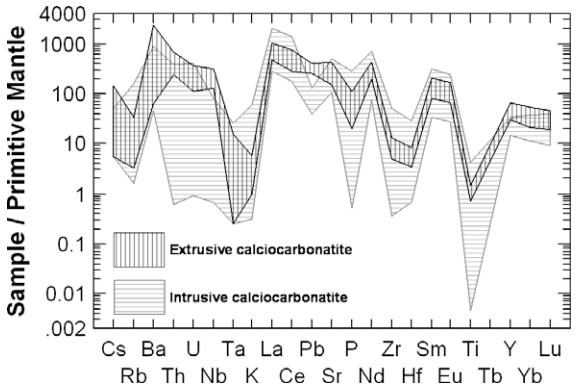


**Fig. 7.** Trace-element abundances of extrusive calciocarbonatite, Upper Unit, compared with intrusive calciocarbonatite, Middle Unit. Normalising values are from Palme and O'Neill (2003).

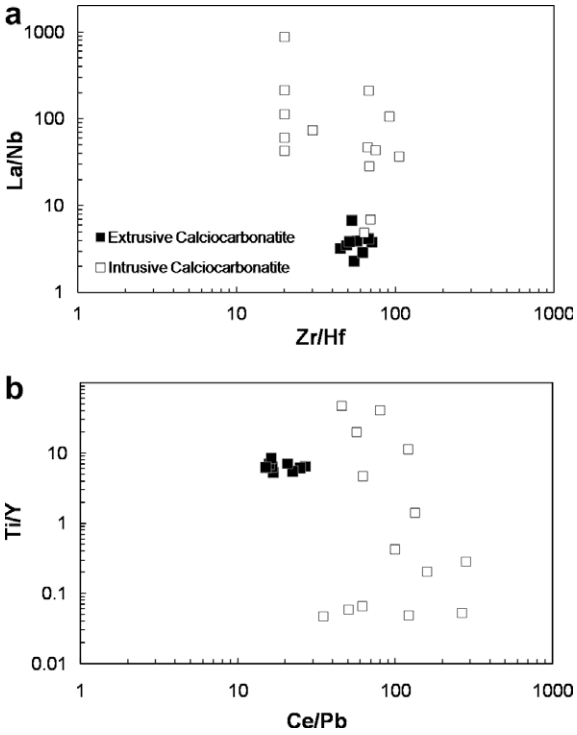


**Fig. 8.** Zr/Hf vs. La/Nb (a) and Ce/Pb vs. Ti/Y, (b) diagrams comparing extrusive and intrusive calciocarbonatites from Brava Island.

2005). From this perspective, the very pronounced Ti and P negative anomalies of the intrusive carbonatites from the Middle Unit, compared with the extrusive ones, can be explained by the effect of apatite and Ti-rich phase fractionation.

The Cape Verde magmatic rocks are highly heterogeneous in terms of their isotopic signatures. Gerlach et al. (1988) considered that, from an isotopic point of view, the Cape Verde islands can be subdivided into two groups. The northern islands are representative of sources with comparatively higher time-integrated depletion of Rb and Nd relative to Sr and Sm, being simultaneously more radiogenic than the southern islands in terms of $^{206}Pb/^{204}Pb$ ratios (see also Doucelance et al., 2003). The intrusive carbonatites, independent of their occurrence in the northern or southern islands, yield Sr and Nd isotopic compositions that cluster in a zone of the Sr–Nd diagram where the northern and southern silicate rock fields overlap (see Hoernle et al., 2002; Fig. 5). The same conclusion can be drawn from the existing data for Brava intrusive cal-

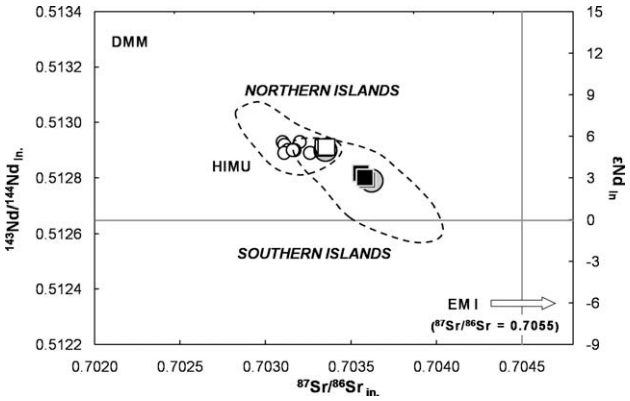


**Fig. 9.** Initial Nd vs. initial Sr isotope plot. Data are compared with those of other Cape Verde carbonatites: small open circles – Santiago, Fogo and São Vicente calciocarbonatites (Hoernle et al., 2002); large grey-filled circles – Brava calciocarbonatites (intrusive and extrusive occurrences; Hoernle et al., 2002); open squares – Brava intrusive calciocarbonatite (this study); closed squares – Brava extrusive calciocarbonatites (this study). *in*, initial.

ciocarbonatites. However, the extrusive carbonatites described in this paper plot clearly within the field defined by the Southern Cape Verde islands. This demonstrates that the extrusive carbonatites of Brava were ultimately the products of a source clearly distinct from those producing the other Cape Verde carbonatites, either in the northern islands (S. Vicente) or in the southern islands (Maio, Santiago, Fogo and Brava intrusives).

### 6.3. Petrogenesis

The genesis of carbonatitic magmas is usually addressed in terms of three distinct processes: (1) a very low degree of partial melting of a carbonated peridotite; (2) extreme fractional crystallisation of a carbonated silicate magma; and (3) immiscibility from carbonated nephelinitic or phonolitic magmas (see below for references).

The isotopic similitude between Brava extrusive calciocarbonatites and the silicate rocks from the Upper Unit makes the two last genetic models feasible, whereas in the context of the first hypothesis, it would be possible to hypothesise that the carbonatitic and nephelinitic magmas were ultimately derived from a homogeneous mantle source, with different degrees of partial melting.

Experimental studies on model and natural systems at high pressures (>2.0 GPa) have shown that melting of carbonate-bearing peridotites yields magnesiocarbonatite liquids (e.g., Dalton and Wood, 1993; Wyllie and Lee, 1998; Lee et al., 2000; Foley et al., 2009, and references therein). However, experimental work at lower pressures has shown that magnesiocarbonatite liquids rising through the lithospheric mantle may react with peridotites, forming wehrlites and becoming progressively more calcium-rich as a consequence of the reaction with orthopyroxene to produce olivine and clinopyroxene. If magmas experimentally produced by partial melting process are characterised by Ca/(Ca + Mg) up to 0.88, it is theoretically likely that carbonatitic melts in equilibrium with wehrlite could have Ca/(Ca + Mg) as high as 0.96 (Dalton and Wood, 1993). This is not significantly different from the characteristics of Brava extrusive carbonatites. However, the studied rocks are characterised by very low concentrations in transition elements (Ni < detection limit (20 ppm); Cr < detection limit (5 ppm); Sc < 0.3 ppm) and $Mg/(Mg + Fe^t) < 0.18$, which impede the consideration that the Brava extrusive calciocarbonatites were generated in equilibrium with mantle residual olivine and/or pyroxene (see Eggler, 1989).

**Table 5**
Major (wt.%) and trace element (ppm) analyses of representative samples of alkaline silicate rocks from the Upper Unit of Brava Island.

| Sample | Mafic rocks | | | | | | Phonolites | | | | | |
|---|---|---|---|---|---|---|---|---|---|---|---|---|
| | CY-32 | CY-98 | CY-124 | CY-199 | CY-200 | CY-247 | CY-80 | CY-123 | CY-168 | CY-188 | CY-215 | CY-265 |
| *Major elements (wt.%)* | | | | | | | | | | | | |
| $SiO_2$ | 42.31 | 39.32 | 43.88 | 44.71 | 44.66 | 38.81 | 54.41 | 51.38 | 50.80 | 53.46 | 46.02 | 51.91 |
| $TiO_2$ | 3.765 | 3.945 | 2.839 | 2.551 | 2.625 | 3.836 | 0.339 | 0.379 | 0.353 | 0.408 | 2.166 | 0.394 |
| $Al_2O_3$ | 14.39 | 11.81 | 15.19 | 14.97 | 15.06 | 11.08 | 22.20 | 20.90 | 21.90 | 21.79 | 17.96 | 21.87 |
| $Fe_2O_3^T$ | 11.87 | 12.74 | 10.33 | 9.69 | 9.87 | 12.70 | 2.77 | 3.25 | 3.39 | 3.43 | 8.09 | 3.41 |
| MnO | 0.204 | 0.205 | 0.198 | 0.187 | 0.188 | 0.182 | 0.210 | 0.136 | 0.194 | 0.201 | 0.201 | 0.201 |
| MgO | 5.76 | 9.59 | 6.43 | 7.47 | 7.47 | 12.89 | 0.13 | 0.25 | 0.45 | 0.23 | 2.69 | 0.27 |
| CaO | 11.66 | 13.07 | 9.74 | 8.83 | 8.99 | 13.09 | 0.98 | 1.99 | 1.68 | 1.98 | 7.50 | 1.76 |
| $Na_2O$ | 5.80 | 3.79 | 5.53 | 5.97 | 5.97 | 4.47 | 11.42 | 11.66 | 11.26 | 10.65 | 9.14 | 10.03 |
| $K_2O$ | 0.92 | 1.33 | 2.46 | 2.88 | 2.98 | 2.01 | 6.33 | 6.33 | 6.37 | 6.34 | 4.03 | 7.14 |
| $P_2O_5$ | 0.64 | 0.64 | 0.56 | 0.49 | 0.49 | 0.55 | 0.06 | 0.07 | 0.04 | 0.06 | 0.54 | 0.05 |
| LOI | 1.79 | 2.65 | 2.52 | 1.28 | 1.02 | 0.64 | 1.25 | 3.73 | 3.15 | 2.07 | 1.41 | 2.54 |
| Total | 99.11 | 99.08 | 99.67 | 99.02 | 99.33 | 100.30 | 100.10 | 100.10 | 99.57 | 100.60 | 99.75 | 99.56 |
| *Trace elements (ppm)* | | | | | | | | | | | | |
| Rb | 25.0 | 16.0 | 36.0 | 51.0 | 52.0 | 42.0 | 224.0 | 180.0 | 210.0 | 198.0 | 66.0 | 224.0 |
| Sr | 973 | 793 | 998 | 841 | 873 | 726 | 482 | 573 | 747 | 876 | 1313 | 1292 |
| Y | 33 | 31 | 26 | 24 | 26 | 23 | 21 | 13 | 20 | 22 | 31 | 21 |
| Zr | 347 | 302 | 342 | 354 | 342 | 214 | 885 | 878 | 733 | 787 | 440 | 725 |
| Nb | 87.7 | 73.7 | 75.7 | 74.9 | 74.5 | 66.5 | 128.0 | 148.0 | 101.0 | 111.0 | 105.0 | 102.0 |
| Cs | 0.9 | 0.6 | 1.1 | 1.1 | 0.9 | 0.3 | 2.6 | 2.5 | 2.3 | 2.6 | 1.3 | 2.0 |
| Ba | 650 | 602 | 1102 | 877 | 972 | 593 | 254 | 927 | 655 | 1132 | 1636 | 1806 |
| Hf | 7.8 | 7.5 | 7.0 | 7.4 | 7.2 | 5.4 | 14.6 | 13.0 | 10.9 | 12.2 | 7.9 | 10.9 |
| Ta | 5.37 | 5.70 | 4.34 | 3.70 | 3.85 | 4.09 | 3.03 | 4.11 | 1.77 | 2.44 | 4.90 | 2.30 |
| Pb | 8 | 5 | 16 | 7 | 8 | 5 | 22 | 12 | 22 | 22 | 11 | 15 |
| Th | 6.4 | 4.7 | 6.7 | 7.1 | 7.0 | 3.2 | 17.9 | 14.4 | 18.8 | 18.0 | 8.9 | 11.0 |
| U | 1.41 | 1.23 | 1.63 | 1.74 | 1.51 | 0.84 | 6.17 | 4.11 | 5.86 | 6.15 | 1.81 | 3.27 |
| La | 64 | 55 | 56 | 48 | 50 | 44 | 49 | 31 | 42 | 64 | 80 | 65 |
| Ce | 132 | 119 | 114 | 98 | 102 | 93 | 84 | 54 | 72 | 101 | 153 | 110 |
| Pr | 14.70 | 14.00 | 12.50 | 10.80 | 11.20 | 10.80 | 7.42 | 5.30 | 6.64 | 9.03 | 16.20 | 9.58 |
| Nd | 58 | 57 | 48 | 42 | 44 | 42 | 22 | 18 | 21 | 27 | 56 | 28 |
| Sm | 10.6 | 10.5 | 8.7 | 7.6 | 7.9 | 8.3 | 3.3 | 2.8 | 3.3 | 3.9 | 9.3 | 4.1 |
| Eu | 3.5 | 3.5 | 2.9 | 2.5 | 2.7 | 2.7 | 1.1 | 0.9 | 1.1 | 1.3 | 3.1 | 1.3 |
| Gd | 9.9 | 10.1 | 7.8 | 7.0 | 7.3 | 7.1 | 2.6 | 2.2 | 2.4 | 2.8 | 7.3 | 3.2 |
| Tb | 1.38 | 1.32 | 1.11 | 1.00 | 1.03 | 1.00 | 0.50 | 0.37 | 0.48 | 0.53 | 1.11 | 0.57 |
| Dy | 6.84 | 6.39 | 5.69 | 5.00 | 5.25 | 5.05 | 3.12 | 2.18 | 3.08 | 3.36 | 5.72 | 3.41 |
| Ho | 1.18 | 1.13 | 0.99 | 0.89 | 0.94 | 0.83 | 0.66 | 0.43 | 0.64 | 0.71 | 1.03 | 0.68 |
| Er | 3.06 | 2.91 | 2.59 | 2.37 | 2.44 | 2.10 | 2.23 | 1.31 | 2.09 | 2.32 | 2.80 | 2.12 |
| Tm | 0.421 | 0.384 | 0.353 | 0.330 | 0.344 | 0.255 | 0.385 | 0.211 | 0.349 | 0.387 | 0.391 | 0.341 |
| Yb | 2.43 | 2.21 | 2.09 | 2.04 | 2.08 | 1.44 | 2.64 | 1.45 | 2.51 | 2.70 | 2.41 | 2.36 |
| Lu | 0.333 | 0.297 | 0.298 | 0.286 | 0.290 | 0.189 | 0.413 | 0.217 | 0.385 | 0.421 | 0.339 | 0.348 |
| ∑REE | 309 | 284 | 263 | 227 | 237 | 219 | 180 | 120 | 158 | 220 | 338 | 231 |

**Table 6**
Strontium and neodymium isotopic compositions of Brava carbonatites.

| Sample | Occurrence | Type | Age (Ma) | [Rb] (ppm) | [Sr] (ppm) | $^{87}Rb/^{86}Sr$ | $^{87}Sr/^{86}Sr$ | | [Sm] (ppm) | [Nd] (ppm) | $^{147}Sm/^{144}Nd$ | $^{143}Nd/^{144}Nd$ | |
|---|---|---|---|---|---|---|---|---|---|---|---|---|---|
| | | | | | | | Measured | Initial | | | | Measured | Initial |
| BR-15[a] | Intrusive | Ca-carb. | 2 | 27 | 8466 | 0.0092 | 0.703340 (12) | 0.703340 | 39.1 | 241 | 0.0981 | 0.512910 (07) | 0.512908 |
| BR-23[a] | Intrusive | Ca-carb. | 2 | 1 | 8622 | 0.0003 | 0.703356 (08) | 0.703356 | 26.8 | 166 | 0.0976 | 0.512912 (09) | 0.512911 |
| CY-95 | Extrusive | Ca-carb. | 0 | 5 | 6596 | 0.0022 | 0.703595 (06) | 0.703595 | 46.4 | 311 | 0.0902 | 0.512792 (05) | 0.512792 |
| CY-222 | Extrusive | Ca-carb. | 0 | 2 | 4799 | 0.0012 | 0.703557 (07) | 0.703557 | 61.5 | 405 | 0.0918 | 0.512816 (08) | 0.512816 |
| CY-238 | Extrusive | Ca-carb. | 0 | 8 | 6671 | 0.0035 | 0.703580 (06) | 0.703580 | 50.5 | 341 | 0.0895 | 0.512801 (06) | 0.512801 |

[a] Isotopic analysis were taken from Mata et al. (2006).

Petrological evidence for the formation of carbonatite magma through extreme fractionation of a carbonated silicate parent has been presented by some authors (e.g., Watkinson and Wyllie, 1971; Otto and Wyllie, 1993; Lee and Wyllie, 1994; Church and Jones, 1995). This implies that variation diagrams are characterised by discernible liquid-line-of-descent that can explain the evolution, by fractional crystallisation, from silicate to carbonatitic magmas. Clearly, this is not observed for volcanics of the Upper Unit (Table 5, Fig. 10). Indeed, the Zr depletion of carbonatites cannot be explained by fractionation of zircon or amphibole, because this would also deplete carbonatitic magmas in Lu and Th, in the case of zircon, and in Y in the case of amphibole, which is not observed. Moreover, none of these mineral phases are reported in the phonolitic rocks. In addition, the significant $K_2O$ depletion of carbonatites cannot be explained by alkali feldspar fractionation, given the carbonatite enrichment in Sr and Ba relative to phonolites (Fig. 10).

The frequent intimate association of carbonatites with highly silica-undersaturated, alkaline, silicate rocks, coupled with field and melt inclusion evidence, gave rise to the hypothesis that carbonatitic magmas could be generated through liquid immiscibility, an idea repeatedly confirmed by experimental data (e.g., Koster van Groos and Wyllie, 1963; Kjarsgaard and Hamilton, 1988, 1989; Kjarsgaard and Peterson, 1991; Kjarsgaard et al., 1995; Lee and Wyllie, 1997, 1998a, 1998b; Ray and Shukla, 2004; Panina and Motorina, 2008). It has been suggested that pure calciocarbonatites (>80% $CaCO_3$) cannot form by immiscibility and must be

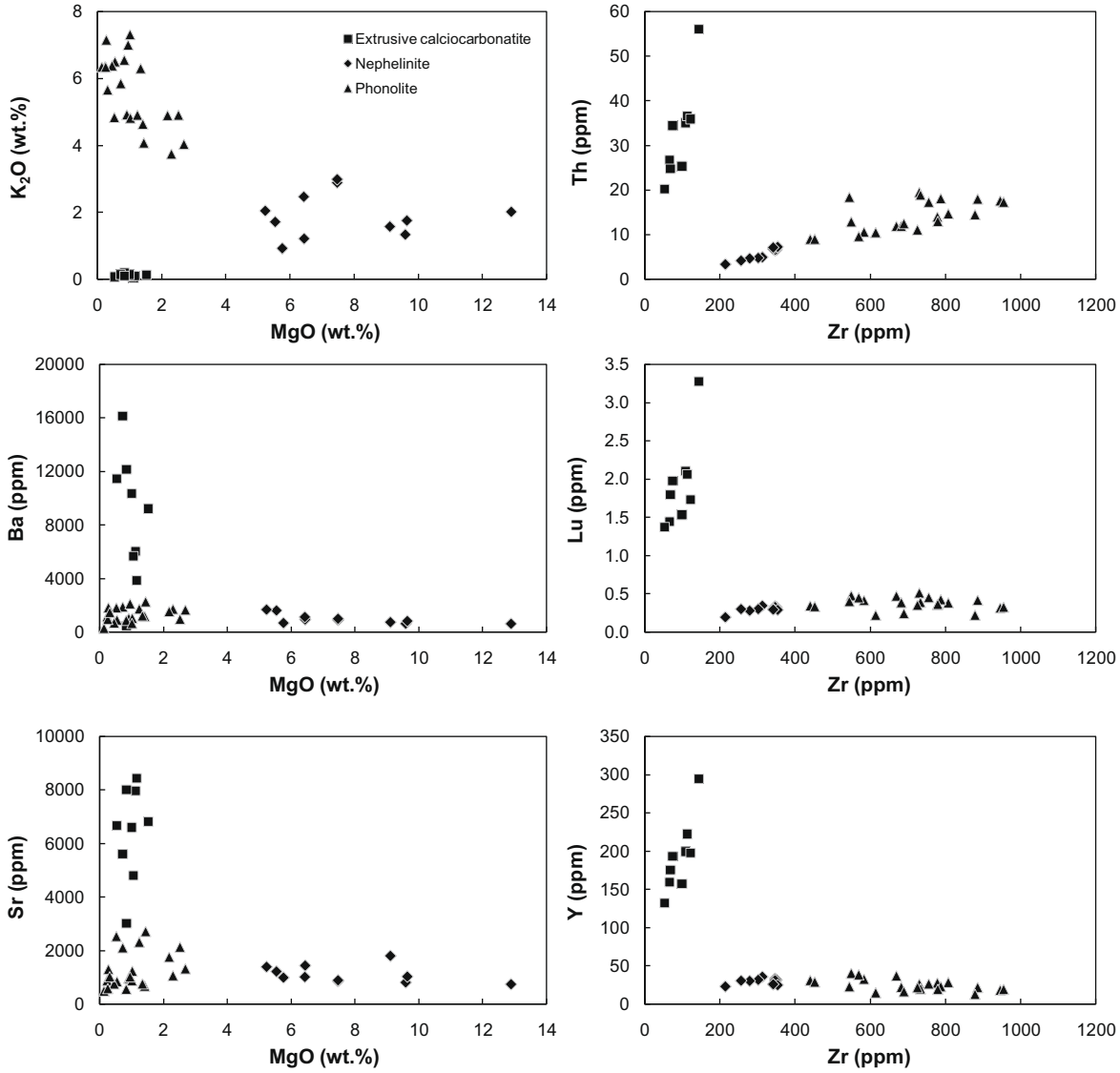


**Fig. 10.** Plot of $K_2O$, Ba and Sr vs. MgO, and Th, Lu and Y vs. Zr for alkaline silicate rocks and extrusive calciocarbonatites from Brava.

considered cumulates, given that they plot in the so-called "forbidden volume" in $[CaO + MgO - FeO^t]$–$[Na_2O + K_2O]$–$[SiO_2 + Al_2O_3 + TiO_2]$-space (Lee and Wyllie, 1996). From this perspective, Brava extrusive carbonatites and most of the naturally occurring calciocarbonatites cannot represent the carbonate fraction that was separated by immiscibility from a silicate parent. However, Kjarsgaard (1998) obtained calciocarbonatite liquids with very high Ca/(Ca + Mg) ratios (down to 0.91) and moderate alkali contents through low-pressure (0.2–0.5 GPa) liquid immiscibility experiments, providing support for the possibility of a genesis of calciocarbonatites by immiscibility. In order to test the applicability of the immiscibility model for the Brava extrusive calciocarbonatites, their compositions and those from their potential silicate conjugates (Table 5) were plotted on the pseudo-ternary triangle $(SiO_2 + Al_2O_3)$–$(Na_2O + K_2O)$–Cafemics presented by Freestone and Hamilton (1980) (Fig. 11). From the positioning in this diagram, carbonatites can be viewed as the result of an immiscibility process, from which also resulted a silicate conjugate of nephelinitic composition, given that they plot at the opposite ends of one of the experimental conjugation lines. If this model applies to the studied rocks, the trace-element enrichment/depletion of the extrusive calciocarbonatites with respect to their potential silicate conjugates should be consistent with the available experimental data on the trace-element partitioning between immiscible silicate–carbonate liquids. Fig. 12 shows the concentrations of selected elements of three extrusive carbonatites, normalised to the composition of the nephelinitic rock from the Upper Unit (Table 5) plotting closest to the solvus and to the end of the conjugation line.

With respect to the nephelinitic rock, the calciocarbonatites are highly depleted in the alkaline elements K, Na, Rb and Cs, and also in Zr, Hf, Ta and Ti. However, they are enriched in P, Sr, Ba, Nb and REE. These results are in agreement with the experimental data obtained by Veksler et al. (1998) for the partitioning of trace elements between carbonatitic and silicate melts: $D_{Ba}^{carb/sil} = 5.2$; $D_{Sr}^{carb/sil} = 4.1$; $D_{Ti}^{carb/sil} = 0.41$; $D_{Zr}^{carb/sil} = 0.016$; $D_{Nb}^{carb/sil} = 0.503$; $D_{Ta}^{carb/sil} = 0.099$. Note that this process also offers a plausible explanation for the decoupling between pairs of elements considered geochemically coherent. Indeed, the Nb/Ta and Zr/Hf ratios of carbonatitic and nephelinitic rocks are clearly distinct (carbonatites: Nb/Ta $\geqslant$ 226, Zr/Hf $\geqslant$ 45; nephelinites: Nb/Ta $\leqslant$ 16.3, Zr/Hf $\leqslant$ 42.3), reflecting significant differences in the partition coefficients of these elements during immiscibility $K_{D\,Nb/Ta}^{carb/sil} = 5.1$; $K_{D\,Zr/Hf}^{carb/sil} = 1.7$; Veksler et al., 1998). In conclusion, the isotopic similarity between carbonatites and contemporaneous nephelinitic rocks, their positioning in the $(SiO_2 + Al_2O_3)$–$(Na_2O + K_2O)$–Cafemics diagram, and the

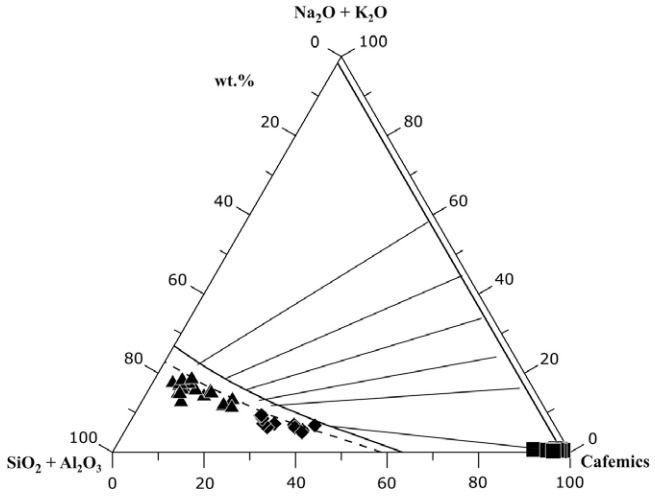


**Fig. 11.** Carbonate–silicate liquid immiscibility in the experimental system ($SiO_2 + Al_2O_3$)–($Na_2O + K_2O$)–Cafemics (CaO + FeO + MgO + MnO) (Kjarsgaard and Hamilton, 1988). The silicate limb of immiscibility at 0.5 GPa (bold continuous line) and 0.8 GPa (dashed line) and experimentally determined tie-lines to different carbonatite compositions are indicated. Symbols are the same as those used in Fig. 10. Our alkaline silicate rocks present an evolution along the limb of the solvus for 0.8 GPa. The compositions of some nephelinites found in association with the carbonatites can be seen to have conjugate liquids carbonates plotting very close to the Cafemic corner, i.e., very poor in K + Na, but rich in Ca, Mg, Fe, Mn.

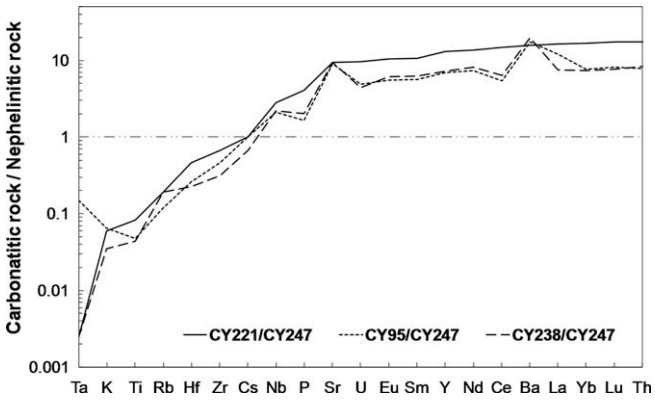


**Fig. 12.** Enrichment factor for selected elements of three extrusive calciocarbonatites with respect to the composition of a nephelinitic rock from the Upper Unit (sample CY-247) plotting closest to the solvus and to the end of the conjugation line drawn in Fig. 11.

elemental characteristics of these two types of rocks support a carbonatite genesis by carbonate/silicate liquid unmixing. This genetic model is also supported by the close temporal and spatial association of carbonatites and nephelinites.

Hamilton et al. (1989) demonstrated a significant pressure dependence of the $D^{sil/carb}$ for the rare earth elements. The $D^{sil/carb}$ values for REE decrease as P increases, becoming slightly less than 1 at about 0.6 GPa. This means that the REE enrichment of Brava carbonatites relative to nephelinites points to the occurrence of the immiscibility process at pressures of at least around 0.6 GPa.

The occurrence of immiscibility processes in the Upper Unit of Brava was already suggested by Kogarko (1993), who described the occurrence of carbonatite globules in phonolitic rocks. However, from our data we conclude that phonolite–carbonatite melt unmixing was not responsible for the generation of the outcropping carbonatites. Indeed, these are too alkali-poor to have been in equilibrium with melts of phonolitic composition (Fig. 11).

## 7. Conclusions

On the Island of Brava (Cape Verde), carbonatites occur in two distinct volcano-stratigraphic positions. Intrusive carbonatites are intimately associated with intrusive plutonic silicate rocks (mainly nepheline syenites, syenites and pyroxenites) belonging to the basal complex, whereas extrusive ones, the central aim of this paper, are part of the youngest volcanism of the island.

At least 20 small outcrops of dark-brown to blackish extrusive carbonatites were found on this island, most of which were made up of pyroclastic products, comprising magmatic and/or phreatomagmatic ash and lapilli fall deposits and one probable pyroclastic flow. Lava (alvikite) flows may also be present in one locality (Santa Bárbara). These extrusive carbonatites, corresponding to at least five distinct eruptions, are unique in the context of the Cape Verde geology, given that they are the only ones formed during a late stage of the development of island building. They are also unique in terms of geochemistry. Indeed, extrusive carbonatites have lower $^{143}Nd/^{144}Nd$ and higher $^{87}Sr/^{86}Sr$ compared with all other Cape Verde carbonatites, either in the northern (S. Vicente) or in the southern islands (Maio, Santiago, Fogo and Brava intrusives), plotting clearly within the field defined by the silicate rocks of the Southern group of Cape Verde.

Based on the results obtained in this study for carbonatites and silicate rocks from Brava, we propose a genetic model invoking carbonatite–nephelinite immiscibility. This is supported by the intimate association of carbonatites with nephelinitic rocks, the similarities in their radiogenic isotope signatures, the comparison of their major element compositions with the results of experimental data, and carbonatite/nephelinite trace element enrichment/depletion factors compatible with experimental data on the partitioning of trace elements between nephelinite/carbonate liquid pairs.

## Acknowledgements

This work was supported by FCT/FEDER through project PLINT (POCTI/CTA/45802/2002), GEODYN (LATTEX, POCTI-ISFL-5-32) and by a PhD scholarship from FCT (SFRH/BD/39493/2007) co-financed by FEDER for C. Mourão. We also acknowledge the supports of the Calouste Gulbenkian Fundation, which provided access to the analytical facilities of the Institute de Physique du Globe de Paris and the Laboratoire Magmas et Volcans (France). The authors are grateful to C. Bosq and P. Rodrigues for skilled assistance during the chemical separation of Sr and Nd and electron microprobe analyses, respectively. We acknowledge the suggestions of the reviewers Bernard Bonin and Christian Koeberl, which helped to improve this paper.

## References

Aires-Barros, L., 1968. Petrografia do ilhéu Grande (ilha Brava, Cabo Verde). Garcia de Orta 16, 249–258.
Allègre, C.J., Pineau, F., Bernat, M., Javoy, M., 1971. Evidence for the occurrence of carbonatites on Cape Verde and Canary Islands. Nature Physical Science 233, 103–104.
Alves, M.C.A., Macedo, J.R., Silva, L.C., Serralheiro, A., Peixoto Faria, A.F., 1979. Estudo geológico, petrológico e vulcanológico da ilha de Santiago (Cabo Verde). Garcia de Orta 3 (1–2), 47–74.
Assunção, C.F.T., Machado, F., Gomes, R.A.D., 1965. On the occurrence of carbonatites in the Cape Verde Islands. Boletim da Sociedade Geológica de Portugal 16, 179–188.
Bailey, D.K., 1993. Carbonate magmas. Journal of the Geological Society 150, 637–651.
Binder, G., Troll, G., 1989. Coupled anion substitution in natural carbon-bearing apatites. Contributions to Mineralogy and Petrology 101, 394–401.
Brassinnes, S., Balaganskaya, E., Demaiffe, D., 2005. Magmatic evolution of the differentiated ultramafic, alkaline and carbonatite intrusion of Vuoriyarvi (Kola Peninsula, Russia).A LA-ICP-MS study of apatite. Lithos 85, 76–92.
Bünh, B., Wall, F., Le Bas, M.J., 2001. Rare-earth element systematics of carbonatitic fluorapatites, and their significance for carbonatite magma evolution. Contributions to Mineralogy and Petrology 141, 572–591.

Chauvel, C., McDonough, W., Guille, G., Maury, R., Duncan, R., 1997. Contrasting old and young volcanism in Rurutu Island, Austral chain. Chemical Geology 139, 125–143.

Church, A.A., Jones, A.P., 1995. Silicate–carbonate immiscibility at Oldoinyo Lengai. Journal of Petrology 36, 869–889.

Coltorti, M., Bonadiman, C., Hinton, R.W., Siena, F., Upton, B.G.J., 1999. Carbonatite metasomatism of the oceanic upper mantle: evidence from clinopyroxenes and glasses in ultramafic xenoliths of Grande Comore, Indian Ocean. Journal of Petrology 40, 133–165.

Dalton, J.A., Wood, B.J., 1993. The compositions of primary carbonate melts and their evolution through wallrock reaction in the mantle. Earth and Planetary Science Letters 119, 511–525.

De Ignacio, C., Muñoz, M., Sagredo, J., Fernández-Santín, S., Johansson, A., 2006. Isotope geochemistry and FOZO mantle component of the alkaline–carbonatitic association of Fuerteventura, Canary Islands, Spain. Chemical Geology 232, 99–113.

D'Orazio, M., Innocenti, F., Tonarini, S., Doglioni, C., 2007. Carbonatites in a subduction system: The Pleistocene alvikites from Mt. Vulture (southern Italy). Lithos 98, 313–334.

Doucelance, R., Escrig, S., Moreira, M., Gariépy, C., Kurz, M.D., 2003. Pb–Sr–He isotope and trace element geochemistry of the Cape Verde Archipelago. Geochimica et Cosmochimica Acta 67, 3717–3733.

Eggler, D.H., 1989. Carbonatites, primary melts and mantle dynamics. In: Bell, K. (Ed.), Carbonatites – Genesis and Evolution. Unwin Hyman, London, pp. 561–579.

Foley, S.F., Yaxley, G.M., Rosenthal, A., Buhre, S., Kiseeva, E.S., Rapp, R.P., Jacob, D.E., 2009. The composition of near-solidus melts of peridotite in the presence of $CO_2$ and $H_2O$ between 40 and 60 kbar. Lithos, doi:10.1016/j.lithos.2009.03.020.

Freestone, I.C., Hamilton, D.L., 1980. The role of liquid immiscibility in the genesis of carbonatites – an experimental study. Contributions to Mineralogy and Petrology 73, 105–117.

Fúster, J.M., Cendrero, A., Gastesi, P., Ibarrola, E., López-Ruiz, J., 1968. Geología y Volcanología de las Islas Canarias, Fuerteventura. Instituto Lucas Mallada, CSIC, Madrid. 239 p.

Gerlach, D.C., Cliff, R.A., Davies, G.R., Norry, M., Hodgeson, N., 1988. Magma sources of the Cape Verdes Archipelago: isotopic and trace element constraints. Geochimica et Cosmochimica Acta 52, 2979–2992.

Hamilton, D.L., Bedson, P., Esson, J., 1989. The behavior of trace elements in the evolution of carbonatites. In: Bell, K. (Ed.), Carbonatites: Genesis and Evolution. Unwin Hyman, London, pp. 405–427.

Hauri, E.H., Shimizu, N., Dieu, J.J., Hart, S.R., 1993. Evidence for hotspot-related carbonatite metasomatism in the oceanic upper mantle. Nature 364, 221–227.

Hoernle, K.A., Tilton, G., LeBas, M.J., Duggen, S., Garbe-Schönberg, D., 2002. Geochemistry of oceanic carbonatites compared with continental carbonatites: mantle recycling of oceanic crustal carbonate. Contributions to Mineralogy and Petrology 142, 520–542.

Jørgensen, J.Ø., Holm, P.M., 2002. Temporal variation and carbonatite contamination in primitive ocean island volcanics from Sao Vicente, Cape Verde Islands. Chemical Geology 192, 249–267.

Keller, J., 1989. Extrusive carbonatites and their significance. In: Bell, K. (Ed.), Carbonatites: Genesis and Evolution. Unwin Hyman, London, pp. 70–88.

Kjarsgaard, B.A., 1998. Phase relations of a carbonated high-CaO nephelinite at 0.2 and 0.5 GPa. Journal of Petrology 39, 2061–2075.

Kjarsgaard, B.A., Hamilton, D.L., 1988. Liquid immiscibility and the origin of alkali-poor carbonatites. Mineralogical Magazine 52, 43–55.

Kjarsgaard, B.A., Hamilton, D.L., 1989. The genesis of carbonatites by immiscibility. In: Bell, K. (Ed.), Carbonatites: Genesis and Evolution. Unwin Hyman, London, pp. 388–404.

Kjarsgaard, B.A., Peterson, T.D., 1991. Nephelinite–carbonatite immiscibility at Shombole volcano, East Africa: petrographic and experimental evidence. Mineralogy and Petrology 43, 293–314.

Kjarsgaard, B.A., Hamilton, D.L., Peterson, T.D., 1995. Peralkaline nephelinite/carbonatite liquid immiscibility: comparison of phase compositions in experiments and natural lavas from Oldoinyo Lengai. In: Bell, K., Keller, J. (Eds.), Carbonatite Volcanism: Oldoinyo Lengai and the Petrogenesis of Natrocarbonatites. Springer-Verlag, Berlin, pp. 4–22.

Kogarko, L.N., 1993. Geochemical characteristics of oceanic carbonatites from the Cape Verde Islands. South African Journal of Geology 96, 119–125.

Koster van Groos, A.F., Wyllie, P.J., 1963. Experimental data bearing on the role of liquid immiscibility in the genesis of carbonatites. Nature 199, 801–802.

Lancelot, J.R., Allègre, C.J., 1974. Origin of carbonatite magma in the light of the Pb–U–Th isotope system. Earth and Planetary Science Letters 22, 233–238.

Lee, W.-J., Wyllie, P.J., 1994. Experimental data bearing on liquid immiscibility, crystal fractionation, and the origin of calciocarbonatites. International Geology Review 36, 797–819.

Lee, W.J., Wyllie, P.J., 1996. Liquid immiscibility in the join $NaAlSi_3O_8$-$CaCO_3$ to 2.5 GPa and the origin of calciocarbonatite magmas. Journal of Petrology 37, 1125–1152.

Lee, W.-J., Wyllie, P.J., 1997. Liquid immiscibility in the join $NaAlSiO_4$–$NaAlSi_3O_8$ $CaCO_3$ at 1 GPa: Implications for crustal carbonatites. Journal of Petrology 38, 1113–1135.

Lee, W.-J., Wyllie, P.J., 1998a. Petrogenesis of Carbonatite Magmas from Mantle to Crust, Constrained by the System CaO–(MgO + FeO )–($Na_2O$ + $K_2O$)–($SiO_2$ + $Al_2O_3$ + $TiO_2$)–$CO_2$. Journal of Petrology 37, 495–517.

Lee, W.-J., Wyllie, P.J., 1998b. Processes of crustal carbonatite formation by liquid immiscibility and differentiation, elucidated by model systems. Journal of Petrology 39, 2005–2013.

Lee, W.-J., Fanelli, M.F., Cava, N., Wyllie, P.J., 2000. Calciocarbonatite and magnesiocarbonatite rocks and magmas represented in the system CaO–MgO–CO2–H2O at 0.2 GPa. Mineralogy and Petrology 68, 225–256.

Machado, F., Azeredo Leme, J., Monjardino, J., Seita, M.F., 1968. Carta geológica de Cabo Verde, notícia explicativa da Ilha Brava e dos Ilhéus Secos. Garcia de Orta 16, 123–130.

Madeira, J., Munhá, J., Tassinari, C.C.G., Mata, J., Brum da Silveira, A., Martins, S., 2005. K/Ar Ages of Carbonatites from the Island of Fogo (Cape Verde). XIV Semana de Geoquímica/VIII Congresso de Geoquímica dos Países de Língua Portuguesa. Aveiro, Portugal. pp. 475–478.

Madeira, J., Mata, J., Mourão, C., 2006. Volcano-tectonic structure of Brava Island (Cape Verde). VII Congresso Nacional de Geologia. Évora, Portugal. pp. 279–282.

Madeira, J., Brum da Silveira, A., Mata, J., Mourão, C., Martins, S., 2009. The role of mass movements on the geomorphologic evolution of island volcanoes: examples from Fogo and Brava in the Cape Verde archipelago. Comunicações Geológicas 95, 99–112.

Martins, S., Mata, J., Munhá, J., Mattielli, N., 2007. Plume–lithosphere interaction at Santiago Island (Cape Verde) (abstract). Geochimica et Cosmochimica Acta 75 (15S), A630.

Mata, J., Munhá, J., Kerrich, R., 1999. Evidências para a ocorrência de metassomatismo carbonatítico na fonte mantélica da Ilha da Madeira (abstract). In: Anais do V Congresso Geoquímico dos Países de Língua Portuguesa Porto Seguro, Brasil. pp. 550–551.

Mata, J., Moreira, M., Doucelance, R., Silva, L.C., Martins, S., Mourão, C., Raquin, A., Martins, L., Madureira, P., 2006. Sr, Nd and noble gases isotopic constraints on the origin of the Cape Verde carbonatites (abstract). VII Congresso Nacional de Geologia. Évora, Portugal. pp. 201–203.

Mattielli, N., Weis, D., Blichert-toft, J., Albarede, F., 2002. Hf isotope evidence for a Miocene change in the Kerguelen Mantle plume composition. Journal of Petrology 43, 1327–1339.

Monnereau, M., Cazenave, A., 1990. Depth and geoid anomalies over oceanic hotspot swells: a global survey. Journal of Geophysical Research 95, 429–438.

Montelli, R., Nolet, G., Dahlen, F.A., Masters, G., 2006. A catalogue of deep mantle plumes: new results from finite-frequency tomography. Geochemistry, Geophysics, Geosystems 7, Q11007. doi:10.1029/2006GC001248.

Muñoz, M., Sagredo, J., de Ignacio, C., Fernández-Suárez, J., Jeffries, T.E., 2005. New data (U–Pb, K–Ar) on the geochronology of the alkaline–carbonatitic association of Fuerteventura, Canary Islands, Spain. Lithos 85, 140–153.

Nelson, D.R., Chivas, A.R., Chappell, B.W., McCulloch, M.T., 1988. Geochemical and isotopic systematics in carbonatites and implications for the evolution of ocean island sources. Geochimica et Cosmochimica Acta 52, 1–17.

Otto, J.W., Wyllie, P.J., 1993. Relationships between silicate melts and carbonate-precipitating melts in CaO–MgO–SiO2–CO2–H2O at 2 kbar. Mineralogy and Petrology 48, 343–365.

Palme, H., O'Neill, H., 2003. Cosmochemical estimates of mantle compositions. In: Carlson, R. (Ed.), Treatise on Geochemistry. The Mantle and Core, vol. 2. Elsevier, Washington, pp. 1–38.

Panina, L.I., Motorina, I.V., 2008. Liquid immiscibility in deep-seated magmas and the generation of carbonatite melts. Geochemistry International 46, 448–464.

Peterson, A.L., Wolff, J.A., Turbeville, B.N., 1989. Eruption mechanisms of extrusive carbonatites on an ocean island: Brava, Cape Verde islands. EOS Transactions of the American Geophysical Union 70, 1421 (abstract).

Pin, C., Bassin, C., 1992. Evaluation of a strontium-specific extraction chromatographic method for isotopic analysis in geological materials. Analytica Chimica Acta 269, 249–255.

Pin, C., Briot, D., Bassin, C., Poitrasson, F., 1994. Concomitant separation of strontium and samarium–neodymium for isotopic analysis in silicate samples, based on specific extraction chromatography. Analytica Chimica Acta 268, 209–217.

Ray, J., Shukla, P.N., 2004. Trace element geochemistry of Amba Dongar carbonatite complex, India: Evidence for fractional crystallization and silicate–carbonate melt immiscibility. Proceedings – Indian Academy of Science 113, 519–531.

Rønsbo, J.G., 1989. Coupled substitutions involving REEs and Na and Si in apatites in alkaline rocks from the Ilimaussaq intrusion, South Greenland. American Mineralogist 74, 896–901.

Seifert, W., Kämpf, H., Wasternack, J., 2000. Compositional variation in apatite, phlogopite and other accessory minerals of the ultramafic Delitzsch complex, Germany: implication for cooling history of carbonatites. Lithos 53, 81–100.

Serralheiro A., 1976. A geologia da ilha de Santiago. Boletim do Museu e Laboratório Mineralógico e Geológico da Faculdade de Ciências de Lisboa, vol. 14, 218 p.

Silva, L., Le Bas, M.J., Robertson, A.H.F., 1981. An oceanic carbonatite volcano on Santiago, Cape Verde Islands. Nature 294, 644–645.

Veksler, I.V., Petibon, C., Jenner, G.A., Dorfman, A.M., Dingwell, D.B., 1998. Trace element partitioning in immiscible silicate–carbonate liquid systems: an initial experimental study using a centrifuge autoclave. Journal of Petrology 39, 2095–2104.

Watkinson, D.H., Wyllie, P.J., 1971. Experimental study of the join NaAlSi3O8-CaCO3–H2O and the genesis of alkalic rock carbonatite complexes. Journal of Petrology 12, 357–378.

Woolley, A.R., Church, A.A., 2005. Extrusive carbonatites: a brief review. Lithos 85, 1–14.

Woolley, A.R., Kempe, D.R.C., 1989. Carbonatites: nomenclature, average chemical compositions, and element distribution. In: Bell, K. (Ed.), Carbonatites: Genesis and Evolution. Unwin Hyman, London, pp. 1–14.

Wyllie, P.J., Lee, W.-J., 1998. Model system controls on conditions for formation of magnesiocarbonatite and calciocarbonatite magmas from the mantle. Journal of Petrology 39, 1885–1893.

Earth and Planetary Science Letters 291 (2010) 70–83

Contents lists available at ScienceDirect

Earth and Planetary Science Letters

journal homepage: www.elsevier.com/locate/epsl

# Noble gas and carbon isotopic signatures of Cape Verde oceanic carbonatites: Implications for carbon provenance

João Mata [a,b,*], Manuel Moreira [c], Régis Doucelance [d,e,f], Magali Ader [g], Luís C. Silva [b,h]

[a] Faculdade de Ciências da Universidade de Lisboa, Departamento de Geologia (GeoFCUL), Campo Grande, C6, 1749-016 Lisboa, Portugal
[b] Centro de Geologia da Universidade de Lisboa (CeGUL), Portugal
[c] Laboratoire de Géochimie et Cosmochimie (UMR 7154 CNRS), Institut de Physique du Globe de Paris, Université Paris 7, 4 place Jussieu, 75252 Paris cedex 05, France
[d] Clermont Université, Université Blaise Pascal, Laboratoire Magmas et Volcans, BP 10448, F-63000 Clermont-Ferrand, France
[e] CNRS, UMR 6524, LMV, F-63038 Clermont-Ferrand, France
[f] IRD, R 163, LMV, F-63038 Clermont-Ferrand, France
[g] Laboratoire de Géochimie des Isotopes Stables (UMR 7154 CNRS), Institut de Physique du Globe de Paris, Université Paris 7, 4 place Jussieu, 75252 Paris cedex 05, France
[h] Instituto de Investigação Científica e Tropical, Portugal

ARTICLE INFO

*Article history:*
Received 19 August 2009
Received in revised form 15 December 2009
Accepted 23 December 2009

Edited by: R.W. Carlson

*Keywords:*
noble gases
carbon isotopes
carbonatites
deep Earth carbon cycle
mantle plume
Cape Verde

ABSTRACT

We discuss noble gas (He, Ne, Ar, Kr, and Xe) and C isotope signatures of carbonatites from the Cape Verde Archipelago. These are the first noble gas compositions ever reported for oceanic carbonatites. The noble gas analyses were performed by crushing the calcite and apatite separates. Some of the analyzed calcites present low $^4He/^3He$ ratios (down to 46,700; R/Ra up to 15.5) that cannot be explained by the addition of cosmogenic $^3He$, demonstrating that carbonatite magmas came from a reservoir characterised by low time-integrated $(U+Th)/^3He$. Such a reservoir is thought to be localised in the deep lower mantle, constraining the depth of origin of the Cape Verde plume. In contrast, apatite samples return highly radiogenic $^4He/^3He$ signatures due to their high Th and U contents. An in situ source for $^4He$ in these apatites is further supported by air-like or lower $^{20}Ne/^{22}Ne$ ratios and relatively high $^{21}Ne/^{22}Ne$ ratios (up to 0.0485), which result from $^{21}Ne$ (and $^{22}Ne$) formation by nucleogenic reactions. Some apatites plot to the left of the MORB line in the neon three-isotope diagram. This is explained by mass-fractionation processes since these apatites are also characterised by $^{38}Ar/^{36}Ar$ ratios lower than the air value or even than the range of values usually used to characterise the MORB-OIB field. Considering that carbonate recycling, which could be characterised by high levels of Te and Ba, would simultaneously increase with time the $^{129}Xe$ and $^{130}Xe$, the observed $^{129}Xe$ anomalies ($^{129}Xe/^{130}Xe$ up to 6.84) cannot be explained by models calling upon crustal carbonate recycling. We attribute these anomalies to an ancient mantle origin by decay of the now extinct $^{129}I$. Moreover, experimental work has suggested that crustal carbonates are unlikely to be transported to deep lower mantle depths as a consequence of their removal by melting reactions at subduction. Thus, our noble gas data are indicative of a non-recycled origin for carbon, endorsing the role of primordial carbon in the genesis of Cape Verde carbonatites. This conclusion is supported by typical mantle $\delta^{13}C$ values ($-8.0$ to $-4.2$‰) that are lighter than those characterising crustal inorganic carbonates. The fact that He is the noble gas element characterised by the highest solubility in magmas, the faster diffusion and the lower mineral/melt partition coefficients is taken as an explanation for its decoupling from the other noble gases, with He being the one better retaining a deep lower mantle signal.



## 1. Introduction

Carbonatites are magmatic rocks containing more than 50% modal carbonate minerals (Le Maitre et al., 2002). The role of the mantle in carbonatite genesis is well established; it serves either as a direct source for carbonate rich magmas generated by a low degree of melting, or as the source of primary carbonated silicate magmas that, by immiscibility, produce carbonatites in addition to silica-undersaturated magmas (e.g., Mitchell, 2005). However, the ultimate origin of the carbon present in carbonatites has been disputed, and models invoking the role of crustal carbonate recycling are becoming increasingly popular (e.g., Ray et al., 1999; 2009; van Achterbergh et al., 2002; Hoernle et al., 2002; Walter et al., 2008). A crustal origin for carbon in diamonds has also been defended (e.g., Menzies et al., 2003; Tappert et al., 2005; Mohapatra and Honda, 2006).

Noble gases are characterised by chemical inertness, high volatility, and a large range of masses, which induces distinct

* Corresponding author. Faculdade de Ciências da Universidade de Lisboa, Departamento de Geologia (GeoFCUL), Campo Grande, C6, 1749-016 Lisboa, Portugal. Tel.: +351 217500357; fax: +351 217500119.
*E-mail address:* jmata@fc.ul.pt (J. Mata).

0012-821X/$ – see front matter © 2010 Elsevier B.V. All rights reserved.
doi:10.1016/j.epsl.2009.12.052

behaviours during physical processes. These characteristics have conferred an important role to the elemental and isotopic composition of noble gases in deciphering the mantle structure. Indeed, their ability to distinguish mantle domains with different degassing histories make noble gases an important tool for unravelling chemical geodynamics (e.g., Zindler and Hart, 1986; Allègre, 1987; Porcelli and Wasserburg, 1995). It has been also demonstrated that carbon and helium correlate in ultramafic xenoliths from some oceanic hotspots, suggesting a coherent behaviour of these elements during fluid migration in the mantle (Trull et al., 1993). Later, Sasada et al. (1997) extended this idea to noble gases as a whole and considered them good tracers of carbon in the mantle.

Considering that noble gases are, like $CO_2$, volatile elements and that their isotopic compositions in the atmosphere are clearly distinct from mantle ratios (e.g., Moreira et al., 1998), the study of noble gases can be considered of utmost importance for deciphering carbonatite genesis, which in turn plays a major role in understanding the deep Earth carbon cycle. Notwithstanding their potential significance, published studies on the rare gas signatures of carbonatitic rocks are still rare and confined to continental occurrences. These studies revealed that no unique mantle domain can be considered as the ultimate source for carbonatitic magmas. Indeed, although a deep mantle source was invoked to explain noble gas isotopic signatures for occurrences in Kola, Brazil and Canada (Sasada et al., 1997; Marty et al., 1998; Tolstikhin et al., 2002), the role of recycled crustal noble gases introduced into the lithospheric mantle was emphasised for Indian carbonatites (Basu and Murty, 2006; Murty et al., 2007). For the natrocarbonatites expelled by the only active carbonatite volcano (Oldoinyo Lengai, Tanzania), Javoy et al. (1989) identified a $^4He/^3He$ ratio of 95,000 (or $^3He/^4He = 7.6$ Ra, where Ra corresponds to the atmospheric value of $1.384 \times 10^{-6}$), similar to the MORB value (e.g. Allègre et al., 1995). For the Oldoinyo Lengai fumaroles, Teague et al. (2008) obtained R/Ra values between 4 and 7. More recently Fischer et al. (2009) presented He isotope ratios ranging from 6.70 to 6.86 Ra, for gases emitted by the Oldoinyo Lengai eruption of July 2005. These results, as well those obtained for $CO_2/^3He$, $\delta^{15}N$ and $\delta^{13}C$, were used by the authors to consider such gases indistinguishable from those emitted along mid-ocean ridges.

Reported ages for worldwide carbonatites range from the Archean to the present (e.g., Veizer et al., 1992) and their occurrences are essentially restricted to continental areas (Wooley, 1989). The most notable oceanic exception is the Cape Verde Archipelago, where the presence of "calcareous dykes" and "calcareous mass of volcanic origin" were first described by Bebiano (1932). However, the formal occurrence of carbonatites was only recognised some thirty years later (e.g., Assunção et al., 1965; Allègre et al., 1971). Cape Verde is exceptional in that carbonatites are present in at least 6 of the 10 islands, and because the carbonatite volume is significantly larger than that reported for the Canary Islands (e.g., Hoernle et al., 2002; Muñoz et al., 2005). Despite the extreme rarity of oceanic carbonatites, somewhat contrasting models have been proposed to these occurrences. Hoernle et al. (2002) considered Cape Verde and Canary calcio-carbonatites as resulting from recycling and ageing ($\approx$1.6 Ga) of carbonated eclogite, while the model of de Ignacio et al. (2006), for Fuerteventura carbonatites (Canary), implicitly favours a primordial origin for carbon. For the Cape Verde magnesio-carbonatites Hoernle et al. (2002) proposed a source incorporating recycled subcontinental lithospheric mantle.

In this paper, we will focus on the noble gas and carbon isotopic signatures of mineral separates obtained from Cape Verde carbonatites outcropping on 3 of the Southern Islands (Brava, Fogo and Santiago) and one of the Northern Islands (São Vicente), which span an age range of approximately 9 Ma (see below and the Supplementary Material). These are the first noble gas results ever obtained for oceanic carbonatites and aim to contribute to a better understanding of the genesis of the Cape Verde carbonatites and of the deep Earth carbon cycle.

## 2. Regional geology and geochemistry

The volcanic Cape Verde Archipelago is located in the East Central Atlantic, 600 to 900 km from the western African coast (Fig. 1). It occurs at the southwestern part of the largest oceanic swell (Cape Verde Rise) which is approximately 1200 km wide and characterised by a depth anomaly of $1900 \pm 200$ m. It is also coincident with important geoid ($7.6 \pm 0.3$ m), heat flow ($16 \pm 4$ mW m$^{-2}$) and gravimetric anomalies (Courtney and White, 1986; Monnereau and Cazenave, 1990; Pim et al. 2008). The lithosphere is 120 to 140 Ma (Williams et al., 1990) and approximately 83 km thick (Cazenave et al., 1988). Crustal thickness is anomalously high (up to 22 km) beneath the islands, which is attributed to magmatic transfer from the plume to crustal levels (Lodge and Helffrich, 2006). However, between the islands the crust has $\approx$7km thickness, which is normal for oceanic settings (Pim et al., 2008). Crough (1978) first considered the Cape Verde Rise to represent a hotspot swell, associated with an underlying mantle plume, by dynamic uplift (e.g. Courtney and White, 1986; Pim et al., 2008). The plume is, arguably, deep-rooted as imaged by finite-frequency tomography data that show a reasonably resolved P-wave velocity anomaly beneath the archipelago extending down to the core–mantle boundary (cf. Montelli et al., 2006; Zhao, 2007; Helffrich et al., 2010).

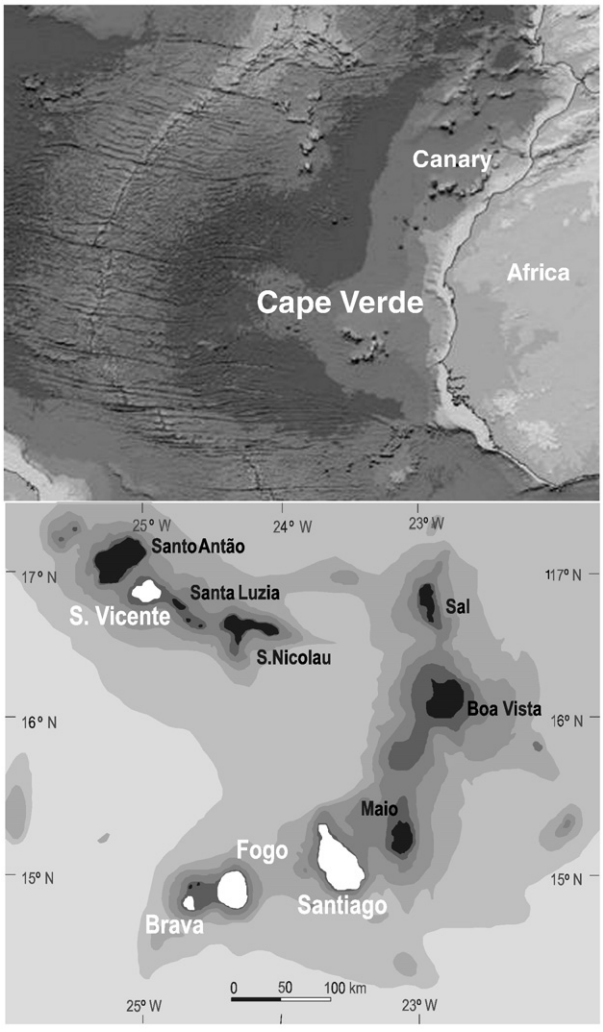


**Fig. 1.** Map of the Cape Verde Archipelago, where the occurrence of carbonatites was first recognised by Assunção et al. (1965). Carbonatites are now described in the islands of Maio, Santiago, Fogo, Brava, S. Vicente and S. Nicolau and also in the islets neighbouring Brava (see the main text for references). The islands from which the carbonatites studied in this article were collected are shown in white. Location map slightly adapted from Google Earth.

Cape Verde is characterised by low magma production rates with some 0.026 $km^3\ a^{-1}$ of magma added to the crust, corresponding to a volume flux of ≈28 $m^3\ s^{-1}$, which is only ≈9% of the one calculated for Hawaii (Holm et al., 2008). The swell is located close to the rotation pole of the slowing drifting African plate (Pollitz, 1991). Such quasi-stationary position explains how a so prominent swell was produced by a weak plume.

The archipelago (Fig. 1) is subdivided into two groups of islands (windward vs. leeward or Northern vs. Southern) that also reflect geochemical characteristics. In fact, the groups are markedly different in terms of radiogenic isotope signatures. Southern Islands are less Nd- and Pb-radiogenic and more Sr-radiogenic than the Northern Islands, which are also characterised by more unradiogenic He signatures. Such distinction is also possible using a $^{206}Pb/^{204}Pb$ vs. $^{208}Pb/^{204}Pb$ diagram. While the Northern Islands tend to plot along the North Hemisphere Reference Line (NHRL; Hart, 1984) the Southern Islands are positioned above the NHRL. Even thought the role of shallow-level interactions had been recently emphasised as an important constrainer of the Cape Verde geochemistry (e.g. Millet et al., 2008), the above mentioned dichotomy between Northern and Southern islands has been mainly ascribed to the distinct role of HIMU- and EM1- type end-members on magma genesis processes of these two groups of islands. On Southern islands a EM1-type end-member dominates while on the Northern islands the isotopic signatures are dominated by a HIMU-type end-member, flavoured with a contribution of the lower mantle in order to account for the unradiogenic He isotopic signatures (Gerlach et al., 1988; Davies et al., 1989; Christensen et al., 2001; Jørgensen and Holm, 2002; Doucelance et al., 2003; Escrig et al., 2005; Holm et al., 2006; Millet et al., 2008; Barker et al., 2009; Martins et al., 2009). For submarine lavas of the Flamengos formation (Santiago Island) it was also proposed the contribution of a FOZO-like component (Barker et al., 2009).

Cape Verde carbonatites are isotopically distinct from their silicate counterparts. This is, for example, evident from lead and osmium signatures. Indeed, for both systems, carbonatites tend to be more radiogenic (i.e. higher $^{206}Pb/^{204}Pb$ and $^{187}Os/^{188}Os$) than associated silicate rocks (Hoernle et al., 2002; Jørgensen and Holm, 2002; Escrig et al., 2005). Moreover, in opposition to silicate rocks (see above), Cape Verde intrusive carbonatites, independently of their occurrence at the Northern or Southern islands, yield Sr and Nd isotopic compositions that cluster in a zone of the Sr–Nd diagram where the Northern and Southern silicate rock fields overlap (see Hoernle et al., 2002). This justifies that in this paper the noble gas and carbon isotopic signatures of carbonatites from Northern and Southern islands are treated in conjunction.

As compared with their continental counterparts, Cape Verde- and Canary carbonatites present a much more restricted compositional range and depict the most radiogenic Nd isotopic signatures of all carbonatites (Hoernle et al., 2002). Cape Verde carbonatites are relatively enriched in Ti, REE, Zr, Li, Co, V and Sc, and impoverished in Nb, Sr, Ba and Pb when compared with continental carbonatites (Kogarko, 1993).

Despite the Cape Verde carbonatites having been formally first described in the sixties (Assunção et al., 1965), the petrogenesis of these rocks is still poorly understood, given that most of the published papers concentrate on the description of field geology and of petrographic and geochemical characteristics of these rocks. The most notable exceptions are the papers from Kogarko (1993), Hoernle et al. (2002) and Mourão et al. (2010). The role of silicate–carbonate immiscibility processes on the genesis of these rocks were emphasised by Kogarko (1993) and Mourão et al. (2010), while Hoernle et al. (2002) considered Cape Verde calcio-carbonatites as the product of low degree of partial melting of an ascending plume containing ancient recycled carbonated oceanic crust. While the role of immiscibility processes seems to be indisputable in the case of the Brava extrusive carbonatites described by Mourão et al. (2010), the usual significant isotopic differences between carbonatites and silicate rocks (see above) precludes the generalized application of the model to the Cape Verde carbonatites. On the other hand, considering carbonatites mainly as partial melting products, such isotopic differences imply the heterogeneous character of the Cape Verde mantle plume (see also Jørgensen and Holm, 2002; Doucelance et al., 2003).

The carbonatites studied here are mainly intrusive and crop out either at Northern islands (São Vicente) or at Southern islands (Santiago, Fogo and Brava) (Fig. 1). Field and petrographic details of the studied occurrences are given as supplementary material. Considering the outcrops from which the studied samples were collected and the published ages (Bernard-Griffiths et al., 1975; Hoernle et al., 2002; Madeira et al., 2005), the following values are reasonable for our samples: Brava, 2 Ma; Fogo, 4 Ma; São Vicente, 5.7 Ma; Santiago, 9 Ma. In Cape Verde, carbonatites were also described on Maio (e.g., Assunção and Canilho, 1969; Stillman et al., 1982) and São Nicolau (Kogarko, 1993) islands as well on the Secos islets located in the vicinity of Brava Island (Machado et al., 1968). The occurrence of volcanic carbonatites is well documented in Santiago (Silva et al., 1981) and Brava (Mourão et al., 2010).

## 3. Analytical procedures

Noble gas analyses were performed on calcite and apatite separates. Based on Sr and Nd isotopic analyses of mineral/rock pairs (Doucelance et al., unpublished data), those minerals are considered in isotopic equilibrium with the whole rock.

Calcite is clearly the most abundant mineral in these rocks and its noble gas isotopic signatures are thought to be a proxy for magma composition at the moment of its crystallization. On the other hand, apatite is known for its resistance to alteration and, based on textural analysis of thin sections, can be considered as a liquidus phase in some of the studied carbonatites. Despite some inconvenience arising from its high U and Th content, apatite's usefulness for studies of noble gases in carbonatites has been proven (e.g., Sasada et al., 1997; Basu and Murty, 2006; Murty et al., 2007). We believe that the combined data obtained from both minerals has the potential to deliver the magmatic noble gas isotopic signatures characterising Cape Verde carbonatites.

Apatite concentrates were obtained by dissolving carbonates with HCl and then electromagnetically separating the residue using a Frantz isodynamic separator. Sporadically, heavy liquids were used prior to electromagnetic separation. Carbonates were concentrated using the electromagnetic separator. Finally, both types of separated preparations were handpicked using a binocular microscope with flexible fibre-optic lights in order to ensure the purity of the concentrates. X-ray diffraction (XRD) was used to confirm mineral identification. From these studies, we learned that the apatite group was represented by fluoro-apatite and that the great majority of carbonate concentrates were composed of calcite. Dolomite was the carbonate phase separated from 2 of the samples from Santiago Island (S-316 and S-339). The carbonate type was chemically confirmed by ICP-MS. Calcites are characterised by a Ca content ranging from 29.7% to 34.2%, a Mg content of up to 0.07%, and an Fe content of up to 0.41%. Dolomites have a Mg content ranging from 7.65% to 8.31%, a Ca content of up to 18.5%, and an Fe content of up to 2.09%.

Noble gas isotopic analyses were performed at the Institut de Physique du Globe de Paris (IPGP) using the glass mass spectrometer ARESIBO I coupled to a Pyrex® glass extraction and purification line. Prior to their introduction into the extraction line, mineral separates were rinsed with double-distilled water, ethanol and acetone. Once introduced into the extraction line, separates to be analyzed were subjected, before extraction and under vacuum conditions, to an overnight heating at 130 °C, in order to remove any atmospheric gases adsorbed on grain surfaces. Gases were extracted by step-crushing. The step-crushing method was selected, as opposed to the step-heating method, because step-crushing allows the

preferential extraction of noble gases retained in fluid inclusions and thus better avoids the products of radiogenic, nucleogenic and fissiogenic processes that occurred in the mineral matrix. The gas extraction was made with a new crusher where a piston rotates constrained by a thread and exerts pressure (2 or 10 times) over the samples. We used this new crusher in order to get low xenon blanks (the piston stays cold during crushing, contrary to the ball system previously used at the IPGP). The gas, released under high vacuum by pressing the samples 2 to 10 times, was purified successively by two hot titanium getters (800 °C) and by two cold SAES getters. After purification, noble gases were adsorbed onto charcoal at 13 K and then, by progressive trap heating, were sequentially released (helium: 30 K; neon: 70 K; argon: 130 K; krypton: 160 K; xenon: 320 K) and introduced into the mass spectrometer. For Ar, Kr and Xe, the gas transfer from the cold head was done using another charcoal trap at liquid nitrogen temperature. All isotopes, excluding $^{4}$He and $^{40}$Ar, were measured on an electron multiplier (in ion pulse counting mode). $^{4}$He and $^{40}$Ar were measured using a Faraday cup. $H_2$ was measured during helium analysis in order to correct mass 3 from $HD^+$. The $H_2$ signal was always lower than 20,000 cps, resulting in a HD signal below 3–5 cps. $CO_2$ and $^{40}$Ar were measured during neon analysis in order to correct for $CO_2^{++}$ and $^{40}Ar^{++}$ interferences on masses 22 and 20, respectively. The $CO_2^+$ signal was lower than 1000 cps and $^{40}Ar^+$ lower than 100 cps, leading to a minor correction on masses 22 and 20. The $^{4}$He blank was $2.3 \pm 0.2 \times 10^{-8}$ ccSTP, and the $^{22}$Ne blank was $1.3 \pm 0.3 \times 10^{-13}$ ccSTP. Mean $^{20}Ne/^{22}Ne$ and $^{21}Ne/^{22}Ne$ ratios of the blanks were respectively $10.05 \pm 0.08$ and $0.0293 \pm 0.0007$, respectively (air = 9.8 and 0.0290, respectively). Uncertainties are 1 standard deviation. The mean $^{36}$Ar blank was $8.0 \pm 2.5 \times 10^{-12}$ ccSTP. The mean $^{38}Ar/^{36}Ar$ and $^{40}Ar/^{36}Ar$ ratios of the blanks were $0.190 \pm 0.007$ and $295 \pm 13$, respectively (air = 0.188 and 295.5 respectively). The $^{84}$Kr blank was $2 \pm 1 \times 10^{-13}$ ccSTP. The $^{130}$Xe blank, before and after an intervention on the purification line, was $5 \pm 2 \times 10^{-16}$ and $3 \pm 2 \times 10^{-15}$ ccSTP, respectively. Isotopic ratios of the Kr and Xe blanks were similar to air.

Variable but low apatite helium closure temperatures have been determined (e.g., Farley, 2000; Shuster et al., 2006). However, considering that we preferentially analyzed helium from inclusions, the fact that the baking temperature was higher than the closure temperature is not considered a problem for this study.

Carbon isotopes were analyzed at the IPGP. Approximately 2 to 5 mg of powdered sample was reacted in a He-flushed Exetainer® vial with anhydrous phosphoric acid, initially at 25 °C for 4 h to extract $CO_2$ from calcite, and then at 80 °C for 2 h to extract $CO_2$ from dolomite. The carbon isotopic compositions were measured using a helium continuous-flow isotope ratio mass spectrometer (AP-2003). The results are expressed, after normalisation to the PDB standard, using the conventional $\delta$-notation. Reproducibility of $\delta^{13}$C measurements using this technique is typically of 0.1‰.

## 4. Results

Carbon isotope results are shown in Table 1. Rare gas concentrations and isotopic ratios are given in Tables 2–4, where the determined ratios are compared with those from the air (e.g., Ozima and Podosek, 2002). In the sample references, S stands for Santiago Island, F for Fogo Island, Br for Brava Island and SV for São Vicente Island.

$\delta^{13}$C values determined for calcites range from −8.0 to −4.2‰ (Table 1) and are similar to the typical values for the mantle (e.g., Deines, 2002). In contrast, the $\delta^{13}$C obtained for dolomite separates (−0.6‰ to −0.2‰) are clearly not mantle-derived. The determined values for both types of carbonates are identical to those reported by Hoernle et al. (2002) for Cape Verde carbonatites. Thus, our data endorse the conclusion of these authors that magnesium-rich type lithotypes in this archipelago represent carbonatites that are severely affected by secondary processes. Considering the significant secondary alteration of magnesio-carbonatites, we will concentrate our discussion on the noble gas signatures of calcio-carbonatites. Indeed, for an apatite separate obtained from a magnesio-carbonatite (S-316), all the rare gas isotopic ratios are, within uncertainties, identical to the atmospheric values, with one exception: the $^{4}He/^{3}He$ ratio shows a MORB-like value of 95,000 for the first step but has an extremely high uncertainty (±40 000); this ratio is radiogenic for the second step.

**Table 1**
Carbon isotope compositions of carbonates from Cape Verde carbonatites.

| Sample | Carbonate type | $\delta^{13}$C ±0.1‰ |
|---|---|---|
| S-309 | Calcite | −6.8 |
| S-309 | Calcite | −6.8 |
| S-311 I | Calcite | −7.1 |
| S-311 I | Calcite | −7.1 |
| S-311 II | Calcite | −7.2 |
| S-311 II | Calcite | −7.0 |
| S-339 | Dolomite | −0.4 |
| S-339 | Dolomite | −0.2 |
| S-339 | Dolomite | −0.5 |
| S-339 | Dolomite | −0.6 |
| S-352 | Calcite | −6.7 |
| S-352 | Calcite | −6.6 |
| S-569 | Calcite | −6.9 |
| S-569 | Calcite | −6.9 |
| F-211C | Calcite | −7.7 |
| F-211C | Calcite | −7.6 |
| F-230A | Calcite | −7.4 |
| F-230B | Calcite | −7.4 |
| F-230B | Calcite | −7.4 |
| F-230C | Calcite | −7.4 |
| Br-15 I | Calcite | −8.0 |
| Br-15 II | Calcite | −7.9 |
| Br-23 I | Calcite | −7.8 |
| Br-23 I | Calcite | −7.7 |
| Br-23 II | Calcite | −7.7 |
| Br-23 II | Calcite | −7.6 |
| SV-170 I | Calcite | −5.4 |
| SV-170 I | Calcite | −5.5 |
| SV-170 II | Calcite | −6.2 |
| SV-170 II | Calcite | −6.3 |
| SV-178 | Calcite | −4.2 |
| SV-178 | Calcite | −4.4 |
| SV-186 I | Calcite | −7.0 |
| SV-186 I | Calcite | −7.0 |
| SV-186 II | Calcite | −6.7 |
| SV-186 II | Calcite | −6.6 |
| SV-187 | Calcite | −6.2 |
| SV-187 | Calcite | −5.8 |
| SV-188 | Calcite | −4.7 |
| SV-188 | Calcite | −4.8 |

In the sample references, S stands for Santiago Island, F for Fogo Island, Br for Brava Island and SV for São Vicente Island. I and II stands for analyses performed on different size fractions of carbonate separates. Duplicate analyses were done for the majority of samples, which is indicated by the repetitions of sample references.

Gases extracted from the Cape Verde carbonatite apatites are characterised by $^{4}$He concentrations in the range of $1.7 \times 10^{-8}$ to $1.6 \times 10^{-6}$ ccSTP/g. Concentrations ranging from $1.1 \times 10^{-7}$ to $8.3 \times 10^{-7}$ ccSTP/g were observed in calcites. Apatites present very high $^{4}He/^{3}He$ ratios ($7.4 \times 10^{4}$ to $2.8 \times 10^{7}$) that, when normalised to the $^{3}He/^{4}He$ air value of $1.384 \times 10^{-6}$ translate to R/Ra usually lower than 2 (Table 2; Fig. 2). These values are significantly lower than R/Ra = 8, the reported value for MORB or the oceanic lithosphere (e.g., Allègre et al., 1995). Brava apatites are exceptional given that a R/Ra ratio of 9.8 was determined. Despite the fact that the analyzed calcites present $^{4}$He concentrations in the range of those determined for apatites, their R/Ra values (6.7 to 15.5) are clearly greater and indicate a $^{3}$He content of up to 3 orders of magnitude higher than that reported for apatites. R/Ra values usually decrease from the first to the second step crushing (2 vs. 10 crushing proceedings) as more radiogenic $^{4}$He comes from the matrix.

$^{22}$Ne concentrations in apatites range from $1.5 \times 10^{-12}$ to $4.9 \times 10^{-11}$ ccSTP/g and are generally lower than those reported for calcites ($1.5 \times 10^{-11}$ to $1.6 \times 10^{-10}$ ccSTP/g). $^{20}Ne/^{22}Ne$ ratios from calcites are remarkably constant and similar to the air ratio, while values up to 10.36 are reported for apatites (Table 2). The apatite

**Table 2**
He and Ne concentrations (ccSTP/g) and isotopic ratios.

| | $^{4}He$ ($10^{-8}$) | $^{3}He$ ($10^{-14}$) | $^{4}He/^{3}He$ ($10^{4}$) | R/Ra | 1σ | $^{22}Ne$ ($10^{-12}$) | $^{20}Ne/^{22}Ne$ | 1σ | $^{21}Ne/^{22}Ne$ | 1σ |
|---|---|---|---|---|---|---|---|---|---|---|
| ***Apatite*** | | | | | | | | | | |
| S-309 step1 | 14.9 | 34.0 | 43.9 | 1.65 | 0.17 | 1.91 | 9.73 | 0.11 | 0.0298 | 0.0015 |
| S-309 step2 | 47.3 | 52.4 | 90.3 | 0.80 | 0.05 | 3.37 | 9.66 | 0.06 | 0.0324 | 0.0010 |
| S-309 duplicate | 9.61 | 22.5 | 42.8 | 1.69 | 0.28 | 2.43 | 9.94 | 0.13 | 0.0295 | 0.0024 |
| S-311 step1 | 8.52 | 10.7 | 79.8 | 0.91 | 0.31 | 9.91 | 9.88 | 0.03 | 0.0291 | 0.0007 |
| S-311 step2 | 7.67 | 6.32 | 121 | 0.60 | 0.28 | 9.59 | 9.90 | 0.04 | 0.0290 | 0.0008 |
| S-316 step1 | 1.68 | 17.6 | 9.51 | 7.60 | 3.20 | 6.11 | 9.98 | 0.09 | 0.0296 | 0.0014 |
| S-316 step2 | 5.52 | 5.19 | 106 | 0.68 | 0.75 | 12.8 | 9.84 | 0.06 | 0.0286 | 0.0009 |
| S-352 step1 | 68.0 | 133 | 51.2 | 1.41 | 0.11 | 39.8 | 9.88 | 0.04 | 0.0296 | 0.0007 |
| S-352 step2 | 160 | 150 | 107 | 0.68 | 0.05 | 49.4 | 9.90 | 0.03 | 0.0301 | 0.0006 |
| F-211C step1 | 27.2 | n.d. | – | – | 0.11 | 1.53 | 10.05 | 0.22 | 0.0485 | 0.0057 |
| F-211C step2 | 87.0 | 3.16 | 2754 | 0.03 | 0.04 | 2.77 | 9.83 | 0.14 | 0.0374 | 0.0030 |
| F-230B step1 | 10.7 | 10.1 | 107 | 0.68 | 0.14 | 21.3 | 9.88 | 0.03 | 0.0293 | 0.0005 |
| F-230B step2 | 34.2 | 15.2 | 226 | 0.32 | 0.04 | 26.5 | 9.85 | 0.03 | 0.0290 | 0.0005 |
| F-230B duplicate step1 | 15.6 | 10.6 | 147 | 0.49 | 0.16 | 21.1 | 9.83 | 0.04 | 0.0309 | 0.0009 |
| F-230B duplicate step2 | 40.7 | 9.02 | 452 | 0.16 | 0.07 | 28.7 | 9.82 | 0.03 | 0.0289 | 0.0005 |
| F-230C step1 | 12.3 | 19.1 | 64.2 | 1.13 | 0.38 | 11.6 | 10.21 | 0.07 | 0.0280 | 0.0012 |
| F-230C step2 | 38.1 | 21.4 | 178 | 0.41 | 0.15 | 17.8 | 10.22 | 0.04 | 0.0301 | 0.0011 |
| Br-15 step1 | 6.90 | 93.3 | 7.40 | 9.76 | 0.51 | 6.67 | 10.34 | 0.04 | 0.0314 | 0.0008 |
| Br-15 step2 | 9.67 | 107 | 9.02 | 8.01 | 0.36 | 7.53 | 10.36 | 0.04 | 0.0298 | 0.0010 |
| ***Calcite*** | | | | | | | | | | |
| SV-186 step1 | 51.0 | 1091 | 4.68 | 15.5 | 0.22 | 61.0 | 9.83 | 0.02 | 0.0289 | 0.0005 |
| SV-186 step2 | 32.0 | 686 | 4.67 | 15.5 | 0.27 | 35.0 | 9.85 | 0.02 | 0.0290 | 0.0004 |
| SV-188 | 83.0 | 1445 | 5.74 | 12.6 | 0.20 | 155 | 9.83 | 0.02 | 0.0294 | 0.0004 |
| F-230B | 11.0 | 102 | 10.8 | 6.71 | 0.43 | 15.1 | 9.86 | 0.05 | 0.0318 | 0.0011 |
| Br-23 | 16.0 | 200 | 8.01 | 9.02 | 0.71 | 94.1 | 9.89 | 0.02 | 0.0301 | 0.0005 |
| **Air** | | | **72.3** | **1.00** | | | **9.80** | | **0.0290** | |

In the sample references, S stands for Santiago Island, F for Fogo Island, Br for Brava Island and SV for São Vicente Island.

ratios, which are distinct from air ratios, were obtained from samples from Brava and Fogo islands. These samples plot clearly to the left of the MORB line (Fig. 3), which represents the line proposed by Sarda et al. (1988) as describing the mixing between the air and the hypothetical pristine MORB value. Some other apatite samples simultaneously present a $^{20}Ne/^{22}Ne$ ratio similar to the air ratio and a $^{21}Ne/^{22}Ne$ ratio as high as 0.0485, which generates a sub-horizontal trend on the neon three-isotope diagram and probably reflects the presence of nucleogenic neon from the matrix.

Total $^{36}Ar$ concentrations vary from 3 to $149\times10^{-11}$ ccSTP/g in apatites and from 4.3 to $135\times10^{-10}$ ccSTP/g in calcites. $^{40}Ar/^{36}Ar$ ratios are higher than the air value of 296, reaching 4164 in apatites and 414 in calcites (Table 3). Considering the low K content of apatites, these differences indicate less significant atmospheric contamination of apatite and thus support our decision to use apatites

**Table 3**
Ar and Kr concentrations (ccSTP/g) and isotopic ratios.

| | $^{36}Ar$ ($10^{-11}$) | $^{38}Ar/^{36}Ar$ | 1σ | $^{40}Ar/^{36}Ar$ | 1σ | $^{84}Kr$ ($10^{-13}$) | $^{78}Kr/^{84}Kr$ | 1σ |
|---|---|---|---|---|---|---|---|---|
| ***Apatite*** | | | | | | | | |
| S-309 step1 | 4.29 | 0.1880 | 0.0006 | 736 | 9 | 8.28 | 0.017 | 0.001 |
| S-309 step2 | 6.77 | 0.1872 | 0.0006 | 725 | 6 | 14.7 | 0.017 | 0.001 |
| S-309 duplicate | 4.03 | 0.1853 | 0.0008 | 613 | 7 | 7.84 | 0.020 | 0.004 |
| S-311 step1 | 15.9 | 0.1881 | 0.0005 | 445 | 2 | 31.8 | 0.012 | 0.002 |
| S-311 step2 | 17.2 | 0.1886 | 0.0005 | 428 | 2 | 31.2 | 0.015 | 0.005 |
| S-316 step1 | 16.8 | 0.1881 | 0.0005 | 312 | 1 | 45.7 | 0.017 | 0.003 |
| S-316 step2 | 37.5 | 0.1878 | 0.0004 | 313 | 1 | 114 | 0.009 | 0.001 |
| S-352 step1 | 117 | 0.1883 | 0.0005 | 2472 | 10 | 258 | 0.011 | 0.001 |
| S-352 step2 | 149 | 0.1883 | 0.0005 | 2515 | 9 | 318 | 0.009 | 0.001 |
| F-211C step1 | 3.04 | 0.1889 | 0.0008 | 3889 | 91 | 7.01 | 0.043 | 0.011 |
| F-211C step2 | 6.65 | 0.1889 | 0.0006 | 4164 | 47 | 23.6 | 0.015 | 0.002 |
| F-230B step1 | 17.1 | 0.1884 | 0.0004 | 531 | 2 | 31.8 | 0.011 | 0.001 |
| F-230B step2 | 19.5 | 0.1883 | 0.0004 | 566 | 2 | 31.8 | 0.011 | 0.002 |
| F-230B duplicate step1 | 22.4 | 0.1890 | 0.0006 | 472 | 2 | 44.2 | 0.012 | 0.002 |
| F-230B duplicate step2 | 28.4 | 0.1879 | 0.0004 | 487 | 2 | 61.5 | 0.008 | 0.001 |
| F-230C step1 | 23.1 | 0.1829 | 0.0005 | 325 | 1 | 29.7 | 0.017 | 0.008 |
| F-230C step2 | 34.8 | 0.1843 | 0.0006 | 334 | 1 | 49.1 | 0.011 | 0.001 |
| Br-15 step1 | 12.5 | 0.1851 | 0.0004 | 624 | 2 | 19.5 | 0.012 | 0.003 |
| Br-15 step2 | 13.0 | 0.1863 | 0.0006 | 657 | 3 | 19.7 | 0.015 | 0.002 |
| ***Calcite*** | | | | | | | | |
| SV-186 step1 | 130 | 0.1882 | 0.0005 | 354 | 18 | 437 | | |
| SV-186 step2 | 77.0 | 0.1885 | 0.0006 | 357 | 18 | 273 | 0.0074 | 0.0002 |
| SV-188 | 330 | 0.1879 | 0.0004 | 363 | 19 | 1180 | 0.0062 | 0.0001 |
| F-230B | 43.3 | 0.1871 | 0.0004 | 414 | 21 | 125 | 0.0150 | 0.0020 |
| Br-23 | 1350 | 0.1879 | 0.0004 | 363 | 19 | | | |
| **Air** | | **0.1880** | | **296** | | | **0.0061** | |

In the sample references, S stands for Santiago Island, F for Fogo Island, Br for Brava Island and SV for São Vicente Island.

**Table 4**
Xe concentrations (ccSTP/g) and isotopic ratios.

| | $^{130}$Xe ($10^{-14}$) | $^{124}$Xe/$^{130}$Xe | 1σ | $^{126}$Xe/$^{130}$Xe | 1σ | $^{128}$Xe/$^{130}$Xe | 1σ | $^{129}$Xe/$^{130}$Xe | 1σ | $^{131}$Xe/$^{130}$Xe | 1σ | $^{132}$Xe/$^{130}$Xe | 1σ | $^{134}$Xe/$^{130}$Xe | 1σ | $^{136}$Xe/$^{130}$Xe | 1σ |
|---|---|---|---|---|---|---|---|---|---|---|---|---|---|---|---|---|---|
| ***Apatite*** | | | | | | | | | | | | | | | | | |
| S-309 step1 | 1.36 | 0.030 | 0.005 | 0.018 | 0.006 | 0.521 | 0.022 | 6.84 | 0.21 | 5.36 | 0.16 | 6.78 | 0.22 | 2.68 | 0.08 | 2.35 | 0.08 |
| S-309 step2 | 1.61 | 0.019 | 0.004 | 0.025 | 0.005 | 0.495 | 0.022 | 6.57 | 0.19 | 5.15 | 0.18 | 6.70 | 0.19 | 2.61 | 0.09 | 2.22 | 0.10 |
| S-309 duplicate | 2.83 | 0.028 | 0.003 | 0.018 | 0.005 | 0.485 | 0.040 | 6.53 | 0.13 | 5.23 | 0.11 | 6.64 | 0.14 | 2.61 | 0.06 | 2.24 | 0.06 |
| S-311 step1 | 4.36 | 0.020 | 0.002 | 0.025 | 0.004 | 0.463 | 0.040 | 6.40 | 0.11 | 5.20 | 0.09 | 6.69 | 0.12 | 2.58 | 0.04 | 2.20 | 0.05 |
| S-311 step2 | 3.04 | 0.021 | 0.002 | 0.021 | 0.006 | 0.465 | 0.060 | 6.30 | 0.11 | 5.12 | 0.11 | 6.47 | 0.14 | 2.53 | 0.05 | 2.18 | 0.06 |
| S-316 step1 | 19.3 | 0.023 | 0.001 | 0.021 | 0.003 | 0.474 | 0.027 | 6.52 | 0.07 | 5.24 | 0.07 | 6.65 | 0.09 | 2.61 | 0.03 | 2.19 | 0.03 |
| S-316 step2 | 35.4 | 0.023 | 0.001 | 0.023 | 0.002 | 0.466 | 0.015 | 6.44 | 0.06 | 5.18 | 0.05 | 6.57 | 0.07 | 2.56 | 0.03 | 2.16 | 0.02 |
| S-352 step1 | 25.7 | 0.024 | 0.001 | 0.023 | 0.004 | 0.478 | 0.035 | 6.75 | 0.07 | 5.24 | 0.07 | 6.74 | 0.09 | 2.63 | 0.03 | 2.31 | 0.04 |
| S-352 step2 | 28.1 | 0.024 | 0.001 | 0.024 | 0.004 | 0.463 | 0.032 | 6.77 | 0.08 | 5.27 | 0.06 | 6.65 | 0.09 | 2.64 | 0.03 | 2.27 | 0.04 |
| F-211C step1 | 2.57 | 0.029 | 0.006 | 0.035 | 0.007 | 0.477 | 0.037 | 6.53 | 0.27 | 5.30 | 0.23 | 6.74 | 0.28 | 2.52 | 0.10 | 2.21 | 0.12 |
| F-211C step2 | 5.96 | 0.026 | 0.004 | 0.021 | 0.004 | 0.464 | 0.015 | 6.52 | 0.12 | 5.17 | 0.11 | 6.65 | 0.16 | 2.65 | 0.09 | 2.21 | 0.04 |
| F-230B step1 | 2.09 | 0.025 | 0.004 | 0.022 | 0.005 | 0.468 | 0.018 | 6.34 | 0.13 | 4.99 | 0.10 | 6.36 | 0.14 | 2.53 | 0.06 | 2.08 | 0.04 |
| F-230B step2 | 2.91 | 0.020 | 0.002 | 0.027 | 0.003 | 0.469 | 0.015 | 6.54 | 0.14 | 5.14 | 0.11 | 6.64 | 0.16 | 2.55 | 0.05 | 2.21 | 0.04 |
| F-230B dup. step1 | 4.76 | 0.026 | 0.003 | 0.023 | 0.005 | 0.481 | 0.039 | 6.79 | 0.14 | 5.45 | 0.13 | 6.84 | 0.17 | 2.70 | 0.06 | 2.32 | 0.06 |
| F-230B dup. step2 | 6.85 | 0.026 | 0.002 | 0.026 | 0.003 | 0.463 | 0.027 | 6.55 | 0.11 | 5.27 | 0.09 | 6.67 | 0.12 | 2.59 | 0.05 | 2.20 | 0.04 |
| F-230C step1 | 4.79 | 0.025 | 0.006 | 0.021 | 0.006 | 0.476 | 0.048 | 6.74 | 0.14 | 5.33 | 0.14 | 6.82 | 0.17 | 2.62 | 0.06 | 2.26 | 0.07 |
| F-230C step2 | 6.98 | 0.022 | 0.003 | 0.020 | 0.004 | 0.453 | 0.032 | 6.61 | 0.12 | 5.27 | 0.09 | 6.87 | 0.15 | 2.61 | 0.05 | 2.25 | 0.05 |
| Br-15 step1 | 1.58 | 0.016 | 0.005 | 0.017 | 0.007 | 0.501 | 0.036 | 6.71 | 0.21 | 5.26 | 0.17 | 6.66 | 0.20 | 2.64 | 0.11 | 2.12 | 0.07 |
| Br-15 step2 | 1.74 | 0.029 | 0.006 | 0.015 | 0.004 | 0.482 | 0.036 | 6.59 | 0.25 | 5.24 | 0.21 | 6.66 | 0.26 | 2.66 | 0.12 | 2.19 | 0.08 |
| ***Calcite*** | | | | | | | | | | | | | | | | | |
| SV-186 step1 | 19.3 | 0.023 | 0.001 | 0.022 | 0.001 | 0.470 | 0.007 | 6.48 | 0.05 | 5.16 | 0.04 | 6.55 | 0.06 | 2.55 | 0.02 | 2.14 | 0.02 |
| SV-186 step2 | 12.2 | 0.023 | 0.001 | 0.022 | 0.001 | 0.472 | 0.008 | 6.44 | 0.06 | 5.24 | 0.05 | 6.64 | 0.08 | 2.57 | 0.03 | 2.18 | 0.02 |
| SV-188 | 48.0 | 0.023 | 0.001 | 0.023 | 0.001 | 0.465 | 0.005 | 6.43 | 0.05 | 5.14 | 0.04 | 6.53 | 0.05 | 2.54 | 0.02 | 2.17 | 0.01 |
| F-230B Br-23 | 7.94 | 0.025 | 0.002 | 0.023 | 0.003 | 0.465 | 0.016 | 6.44 | 0.11 | 5.19 | 0.12 | 6.67 | 0.15 | 2.66 | 0.09 | 2.19 | 0.05 |
| **AIR** | | **0.023** | | **0.022** | | **0.472** | | **6.50** | | **5.21** | | **6.61** | | **2.56** | | **2.18** | |

In the sample references, S stands for Santiago Island, F for Fogo Island, Br for Brava Island and SV for São Vicente Island.

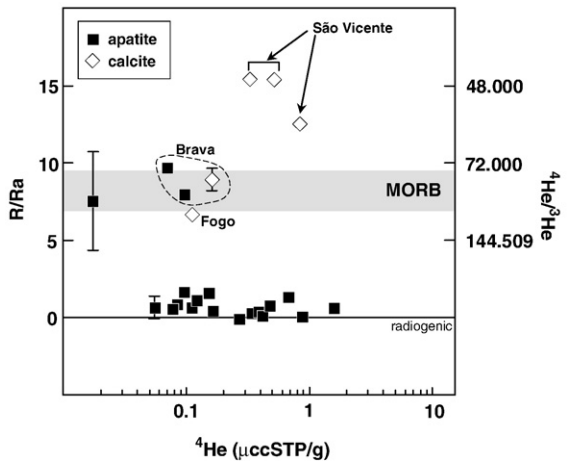


**Fig. 2.** $^4$He/$^3$He and R/Ra ratios vs. the $^4$He concentration (μccSTP/g) obtained by crushing apatite and calcite samples from Cape Verde carbonatites. R is the $^3$He/$^4$He ratio and Ra is the atmospheric ratio. Apatite samples show an almost purely radiogenic signature.

in this study. Most of the $^{38}$Ar/$^{36}$Ar values are, within uncertainties, indistinguishable from air. The most exception is a sample from Fogo (F-230C) for which a $^{38}$Ar/$^{36}$Ar ratio as low as $0.1829 \pm 0.0005$ was measured.

$^{84}$Kr concentrations are higher in calcites (1.3 to $12 \times 10^{-11}$ ccSTP/g) than in apatites, in which concentrations vary from $7.0 \times 10^{-13}$ to $3.2 \times 10^{-11}$ ccSTP/g. With the exception of $^{78}$Kr/$^{84}$Kr ratios, all krypton isotopic ratios are similar to the air (Table 3).

$^{130}$Xe concentrations are similar in apatites and calcites, ranging from 1.4 to $48 \times 10^{-14}$ ccSTP/g (Table 4). However, while calcites present $^{129}$Xe/$^{130}$Xe similar to air, some of the apatites are characterised by $^{129}$Xe anomalies ($^{129}$Xe/$^{130}$Xe up to 6.84) compared with an atmospheric ratio of 6.50 (Fig. 4). Some of the Cape Verde apatites are also characterised by excesses of fissiogenic Xe ($^{131}$Xe/$^{130}$Xe up to 5.45; $^{132}$Xe/$^{130}$Xe up to 6.87; $^{134}$Xe/$^{130}$Xe up to 2.70; $^{136}$Xe/$^{130}$Xe up to 2.35). These isotopic ratios are positively correlated as well as radiogenic ($^{129}$Xe) and fissiogenic Xe. The trend of these data on a $^{136}$Xe/$^{130}$Xe vs. $^{129}$Xe/$^{130}$Xe diagram has a slope similar to that reported for MORB or plume magmas. However, the observed excesses are lower than the maximum reported for MORB, as it has been described for some mantle plumes (e.g., Staudacher and Allègre, 1982; Poreda and Farley, 1992; Trieloff et al., 2000; 2002).

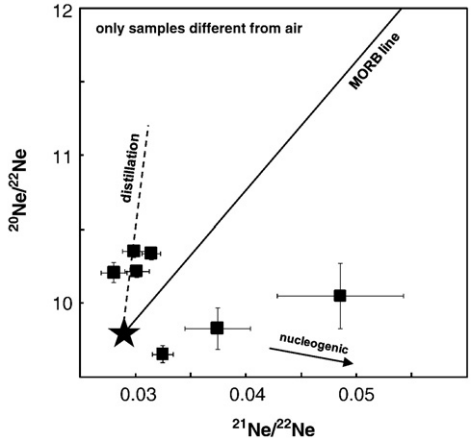


**Fig. 3.** Three-neon isotope diagram showing the apatite samples from Cape Verde carbonatites. Note that only samples with ratios different from air are reported. Two populations of samples can be observed: one represents nucleogenic neon whereas the other presents a "plume"-like neon signature. However, as shown in the main text, this signature rather stems from a mass-fractionation process.

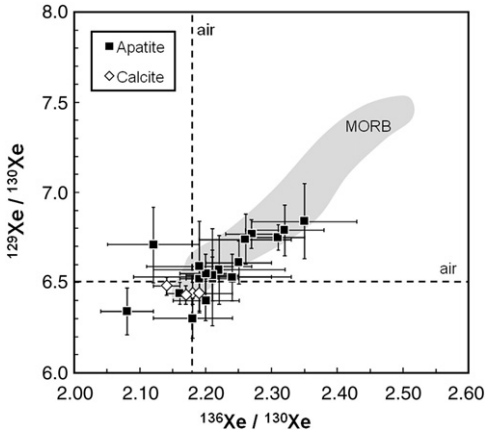


**Fig. 4.** $^{129}$Xe/$^{130}$Xe vs. $^{136}$Xe/$^{130}$Xe ratios. Carbonatite samples show $^{129}$Xe and $^{136}$Xe excesses when compared to air. These excesses reflect the presence of a mantle component that could be MORB- or OIB-derived. Only samples with blanks lower than 15% of the measured xenon are reported.

## 5. Discussion

The following discussion will focus on three primary subjects, including: the origin of the radiogenic/nucleogenic component observed in the samples; the contribution of deep lower mantle-derived material in the carbonatites from the Cape Verde Islands; and the carbon origin.

### 5.1. Radiogenic, nucleogenic and cosmogenic noble gases

The abundance of primordial noble gases in mantle-derived samples is sufficiently low that addition of radiogenic and nucleogenic noble gases can significantly alter mantle isotope ratios. The modal abundance of apatite, its resistance to alteration and its liquidus character in some of the Cape Verde carbonatites justified the use of this mineral in a study aiming to unravel the noble gas isotopic signatures of their precursor magmas. However, apatite is known to be relatively rich in the two $^4$He producing elements, Th and U (Dawson and Hinton, 2003), and $^4$He extraction from the matrix, during crushing, was described for clinopyroxene (Scarsi, 2000). In order to better evaluate the significance of $^4$He production to the noble gas inventory of the Cape Verde samples, mineral separates were also analyzed for trace elements. U and Th concentrations (up to 133 ppm

**Table 5**
Th and U concentrations and the calculated $^4$He* production.

| | Th (ppm) | U (ppm) | Approximate age (Ma) | $^4$He* (μccSTP/g) |
|---|---|---|---|---|
| S-309-AP | 55.8 | 7.6 | 9 | 22.4 |
| S-311-AP | 30.2 | 1.0 | 9 | 8.7 |
| S-316-AP | 18.6 | 0.2 | 9 | 4.9 |
| S-316-C | 1.1 | 0.5 | 9 | 0.9 |
| S-339-C | 9.8 | 1.5 | 9 | 4.1 |
| S-352-AP | 44.6 | 15.2 | 9 | 27.9 |
| F-211C-AP | 133 | 13.9 | 4 | 21.7 |
| F-211C-C | 2.5 | 0.6 | 4 | 0.6 |
| F-230B-AP | 44.2 | 11.0 | 4 | 10.3 |
| F-230B-C | 0.4 | 0.3 | 4 | 0.2 |
| F-230C-AP | 77.1 | 10.2 | 4 | 13.6 |
| Br-15-AP | 39.5 | 3.4 | 2 | 3.0 |
| Br-15-C | 1.7 | 0.1 | 2 | 0.1 |
| Br-23-C | 0.9 | 0.2 | 2 | 0.1 |
| SV-186-C | 3.8 | 1.4 | 5.7 | 1.6 |
| SV-188-C | 20.4 | 2.7 | 5.7 | 5.1 |

$^4He^* \sim 2.8 \times 10^{-8}(4.35 + \frac{Th}{U})[U] \cdot t$ was used for the calculation of the radiogenic helium $^4$He*. [Th] and [U] in ppm, $t$ in Ma. AP and C stand for apatite and carbonate, respectively. In the sample references, S stands for Santiago Island, F for Fogo Island, Br for Brava Island and SV for São Vicente Island. Th and U were analyzed at Actlabs (Canada) by ICP-MS.

for Th and 15 ppm for U) as well as calculated radiogenic $^4$He in situ-produced are shown in Table 5. Based on these results, the He isotopic signatures of apatites samples (see Table 2; Fig. 2) are, with the exception of the samples from Brava, mainly controlled by the extraction of matrix-produced radiogenic $^4$He during crushing. For example, in a sample with 56 ppm Th and 8 ppm U, in 9 Ma, the radiogenic $^4$He produced in the matrix is approximately $2.3\times10^{-5}$ ccSTP/g, compared with a measured $^4$He content of few $10^{-7}$ ccSTP/g. Therefore, even the usually low percentage of this radiogenic helium extracted from matrix during crushing will dominate the mantle-derived helium (see Scarsi, 2000).

Cosmogenic helium also can be extracted by crushing processes. Depending on the quality of the crushing, up to some 10% of the cosmogenic $^3$He and the $^{21}$Ne located in the olivine matrix can be released (cf., Scarsi, 2000; Yokochi et al., 2005; Moreira and Madureira, 2005). As we did not find evidence for significant cosmogenic $^3$He production (see below), the high amount of $^4$He in situ-produced would also explain the occurrence of samples characterised by low $^{20}$Ne/$^{22}$Ne ratios (air-like or lower) but relatively high $^{21}$Ne/$^{22}$Ne ratios (up to 0.0485) as the result of $^{21}$Ne (and $^{22}$Ne) growth by in situ nucleogenic reactions (e.g., $^{18}$O(α, n)$^{21}$Ne). The $^{21}$Ne/$^4$He production ratio is approximately $5\times10^{-8}$ in apatite (Gautheron et al., 2006). Therefore, for a sample with 133 ppm Th and 13.9 ppm U, the nucleogenic $^{21}$Ne can be estimated to be $1.1\times10^{-12}$ ccSTP/g, about the same order of magnitude as the measured $^{21}$Ne. An extraction of 3% of that nucleogenic $^{21}$Ne from the matrix would increase the $^{21}$Ne/$^{22}$Ne ratio from the air value (0.029) to ≈0.049 (using F-211C sample age and concentrations, as an example, and a nucleogenic $^{21}$Ne/$^{22}$Ne ratio of 0.9).

In conclusion, it is clear that both $^4$He and $^{21}$Ne are extracted from the matrix during crushing of the samples. They dominate the mantle signal that is trapped in the apatite fluid/melt inclusions.

Calcites, which contain significantly lower Th (up to 20.4 ppm) and U (up to 2.7 ppm), are not neatly affected by in situ $^4$He and $^{21}$Ne radiogenic/nucleogenic production. These should therefore better preserve the isotopic signatures of the magmas from which they crystallised. This seems to be the case for five of the carbonate samples we analyzed. Moreover, calcites contain more $^3$He (up to $1.4\times10^{-11}$ ccSTP/g) than apatite (up to $1.5\times10^{-12}$ ccSTP/g), reflecting the higher fluid inclusion volume, indicated by petrographic observations. A $^4$He/$^3$He ratio as low as 46,700 (R/Ra = 15.5) was measured in one sample from São Vicente Island. Based on the similarity of values obtained on the same sample for two steps of crushing and the high $^3$He concentration, we believe that such relatively unradiogenic helium isotopic ratios cannot be explained by cosmogenic $^3$He production. To get such a high $^3$He content only from extraction of the cosmogenic $^3$He located in the matrix, the sample would need to have an age of 50 Ma (assuming no erosion, a production of 100 at/g/an and extraction of 10% of the matrix-sited helium). This is not realistic as São Vicente carbonatites have ages close to 5.7 Ma (Hoernle et al., 2002). We therefore consider the helium isotopic ratio from the carbonate samples to be reflective of mantle-derived helium.

### 5.2. Evidence for a deep lower mantle signal

Gases released by some of the studied apatites are characterised by $^{129}$Xe excesses when compared with air (Fig. 4). The samples fall on the MORB/OIB-line, which clearly reflect a mantle-derived component in the Cape Verde carbonatites (see Staudacher and Allègre, 1982; Kunz et al., 1998; Trieloff et al., 2000; 2002). This is endorsed by the determined $\delta^{13}$C (Table I; see also Kogarko, 1993; Hoernle et al., 2002) which are similar to typical mantle values (e.g. Deines, 2002).

As previously mentioned Cape Verde carbonatites are chemically distinct from their silicate counterparts in what concerns, for example, the lithophile isotope tracers (see Section 2 and also Hoernle et al., 2002; Jørgensen and Holm, 2002; Doucelance et al., 2003; Escrig et al., 2005). This clearly shows that these two types of magmatic rocks cannot be related by immiscibility or fractionation processes. Carbonatites can also be envisaged as the product of very low degree melting events (e.g., Wallace and Green, 1988; Wyllie and Lee, 1998). Experimental work has demonstrated that incipient melting of a peridotite source of appropriate composition would produce magnesio-carbonatite magmas at pressures in excess of 2.0 GPa (Wyllie and Lee, 1998; Foley et al., 2009; Ghosh et al., 2009), which is at odds with the calcium-rich nature of the studied carbonatites. However, experimental work at lower pressures has shown that a wall–rock reaction of carbonatite melts with peridotites can produce calcio-carbonatites magmas and wehrlites (Dalton and Wood, 1993; Lee and Wyllie, 2000) and thus offers an explanation for the calcium-rich composition of the studied Cape Verde carbonatites (see also Hoernle et al., 2002). Moreover, experimental data show that calcium-rich carbonatites can be produced directly by partial melting if, instead carbonated peridotite, carbonated eclogite is considered as the carbonatite source (e.g. Hammouda, 2003; Yaxley and Brey, 2004; Dasgupta et al., 2005).

Considering the almost exclusive occurrence of carbonatites in continental settings, and the presumable occurrence of a delaminated sub-continental lithosphere mantle (SCLM) domain beneath the Southern Cape Verde islands (e.g., Gerlach et al. 1988; Doucelance et al. 2003; Bonadiman et al., 2005; Martins et al., 2009), Cape Verde carbonatites could be considered to have derived from incipient melting of the SCLM domain, eventually induced by heat transfer from the plume. However, we emphasise that such a SCLM domain, which is inferred from the EM1-like isotope signatures for silicate rocks, could not produce the studied carbonatites, which can present $^4$He/$^3$He ratios as low as 46,700 (R/Ra up to 15.5). Indeed the carbonatites in this study present isotopic signatures that imply derivation from a source characterised by significantly higher time-integrated U/Pb and Sm/Nd ratios and lower (U + Th)/$^3$He ratios than those presumably produced by melting of SCLM (e.g., R/Ra ≈ 6.5, Gautheron and Moreira, 2002; Gautheron et al., 2005; Day et al., 2005; R/Ra = 8 to 10, Czuppon et al., 2009). Moreover, EM1-type signatures are restricted to the Southern Cape Verde islands (e.g., Gerlach et al., 1988; Doucelance et al., 2003; Millet et al., 2008), while carbonatites occur in both the Northern and Southern islands. All these arguments exclude SCLM as an origin for the Cape Verde carbonatites.

On the other hand it should be emphasised that Cape Verde is located on old (120–140 Ma; Williams et al., 1990) and thick oceanic lithosphere in a situation similar to that of Canary Archipelago, the other oceanic locality characterised by the occurrence of carbonatites. In this region of the Eastern Atlantic the only existing noble gases measured in mantle materials derived from the Canary sub-oceanic lithosphere (Vance et al. 1989). Considering the age of the lithosphere (150–175 Ma; e.g. Schmincke et al., 1998) and that the analyses were mainly performed in clinopyroxenes, an U-"rich" mineral, the results (R/Ra ≈ 6) are not very useful for this discussion. However, Yamamoto et al. (2009) determined $^4$He/$^3$He ratios indistinguishable from those of the MORB, for Pacific sub-oceanic 135 Ma lithosphere xenoliths. These data strongly suggest that the old oceanic lithosphere cannot be considered the source for the Cape Verde carbonatites which, as mentioned before, can be clearly more unradiogenic than MORB.

From the above discussion an origin of the Cape Verde carbonatites by melting of lithosphere domains (oceanic or continental) can be discarded. Notwithstanding that an important lithospheric contribution to the genesis of some carbonatites has been recently defended (e.g. Basu and Murty, 2006), a conclusion similar to ours has emerged from the study of carbonatites elsewhere, based on the usual involvement of the HIMU and FOZO mantle components on their genesis (e.g. Tilton and Bell, 1994; Bell and Simonetti, 2009) and on the spatial and temporal links between Large Igneous Provinces (LIP) and carbonatites (Ernst and Bell, 2009). While the first argument point to a sub-lithospheric source for carbonatitic melts, the second one strongly suggests a relation between carbonatitic magmas and

deep rooted mantle plumes. As it has been proposed for continental carbonatites elsewhere (Bell and Tilton, 2001; Bell and Simonetti, 2009) we suggest that the role played by thick oceanic lithosphere on the origin of carbonatites may be restricted to the favouring of the concentration of volatiles at the upper levels of the ascending Cape Verde mantle plume.

Some models invoke a shallow mantle origin for low $^4He/^3He$ signatures (e.g. Meibom et al., 2003; Meibom and Anderson, 2003). However, as shown by Putirka (2008), mantle temperatures are negatively correlated with $^4He/^3He$ ratios. This is inconsistent with those models which assume that MORB and OIB derive from the same heterogeneous upper mantle, but instead shows low $^4He/^3He$ as tied to a lower thermal boundary layer (see also Pik et al., 2006).

The well known dichotomy between MORB, characterised by relatively uniform He isotopic ratios ($^4He/^3He \approx 90{,}000 \pm 10{,}000$; $R/Ra = 8 \pm 1$), and ocean island basalts (OIB), characterised by significantly more variable and less radiogenic signatures ($^4He/^3He$ down to around 15,000; $R/Ra \approx 50$; Stuart et al., 2003), has been regarded as supporting the existence of a chemically layered mantle. A layered mantle would be composed of reservoirs with different degassing histories, including a lower mantle representing a relatively undegassed, primordial reservoir (e.g., Kurz et al., 1982; Allègre et al., 1983; Allègre and Lewin, 1989). This model is supported by the fact that hotspot basalts are characterised by air-corrected $^{21}Ne/^{22}Ne$ ratios that are clearly distinct from MORB (e.g., Honda et al., 1991; Moreira and Allègre, 1998; Moreira et al., 2001).

However, because tomographic studies clearly show the existence of subducting mass flux across the 670 km discontinuity (Castle and Creager, 1999; Kárason and Van der Hilst, 2000; Hall and Spakman, 2002) it is difficult to accept that the whole lower mantle is a relatively primitive and undegassed reservoir. In addition, recent experiments (e.g., Brooker et al., 2003; Parman et al., 2005; Heber et al., 2007) have confirmed earlier theoretical studies (Wood and Blundy, 2001) that concluded that during mantle melting, noble gases are probably less incompatible than their radioactive parents. This leads to the preferential extraction of U, Th and K relatively to the noble gases in situations where the residue is dominated by olivine. The confluence of these lines of evidence led to the proposition that low $^4He/^3He$ and $^{21}Ne/^{22}Ne$ domains could be developed from previous melt extraction events (e.g., Graham et al., 1990; Coltice and Ricard, 2002; Heber et al., 2007). Recently, low $^4He/^3He$ ratios in plumes were thought to reflect incomplete degassing of mantle domains by melting and posterior isolation from convecting mantle for around 1–2 Ga (Class and Goldstein, 2005).

However, as shown by Porcelli and Elliott (2008), a problem arise from the difficulty that such depleted residue could maintain He concentrations high enough to impart their low $^4He/^3He$ ratios to OIB, on which other components are usually present. These authors modelled the secular evolution of the convecting mantle and concluded that $^4He/^3He$, as low as those reported for the Iceland magmas erupted some 60 Ma ago, were only possible prior to 3 Ga, implying that since then the low $^4He/^3He$ domains were preserved from entraining and convective mixing.

Samuel and Farnetani (2003) demonstrated that a density contrast of around 2.5% would be enough to isolate a reservoir, in the mantle bottom, from the convecting mantle for more than 2.3Ga, which can offer a simultaneous explanation for the location of such reservoir and for the D″ layer. Indeed, it was proposed that the origin of this layer was either an early (around 3.9 Ga) accumulation of basaltic protocrust together with a chondrite-like regolith containing solar-wind-implanted gases (Tolstikhin and Hofmann, 2005; Tolstikhin et al., 2006) or a layer of melt formed at the base of the Earth's mantle early in its history (Labrosse et al., 2007). In both cases, the D″ would be a reservoir enriched in rare-gases and incompatible elements and, following Hirschmann and Dasgupta (2009), also eventually C enriched. The Earth's core has also been proposed as a plausible

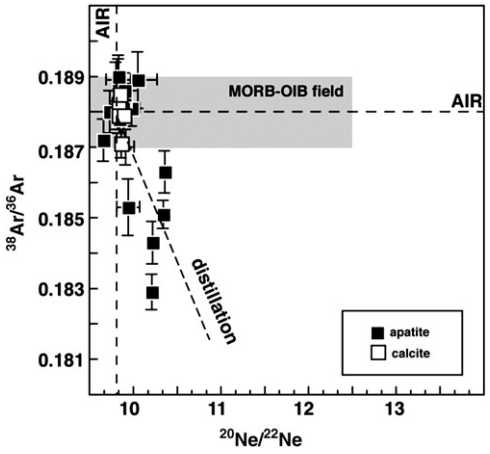


**Fig. 5.** $^{38}Ar/^{36}Ar$ ratios vs. the $^{20}Ne/^{22}Ne$ ratios for Cape Verde carbonatite samples. Samples presenting plume-like neon signatures (i.e., those that fall on a line between air and solar neon) present $^{38}Ar/^{36}Ar$ ratios lower than air. In mantle-derived material, the $^{38}Ar/^{36}Ar$ ratio is similar to the atmospheric value (MORB-OIB field from Kunz, 1999; Trieloff et al., 2000, 2002; Raquin and Moreira, 2009). A line called "distillation" has been reported. This line reflects a Rayleigh-like distillation ($R = R_0 f^{\alpha - 1}$, where $\alpha = (m_2/m_1)^{1/2}$, $m$ is the atomic mass and $f$ is the remaining fraction, assumed here to be the same for neon and argon). Samples fall on this distillation curve, implying that the "primitive" neon observed in some samples reflects the addition of neon and argon with atmospheric isotopic compositions but with mass fractionation.

reservoir for helium enriched in $^3He$ (Porcelli and Halliday, 2001; Jephcoat et al., 2008) and carbon (Wood, 1993; Nakajima et al., 2009), which could contribute to the mantle He and C budget through exchange mechanisms at the core–mantle boundary (e.g. Tingle, 1998).

From the above models one can conclude that it is still valid to invoke the existence of reservoir(s) that have been isolated from mantle convection in the long term to explain the low $^4He/^3He$ characterising some of the OIB. These reservoirs are most probably located at the bottom of the mantle or in the core.

Considering all these arguments we believe that the low $^4He/^3He$ ratios determined for the São Vicente carbonatites (down to 46,700; R/Ra up to 15.5) are indicative of a deep lower mantle contribution. The involvement of such a reservoir in the genesis of Cape Verde magmatism is also endorsed by the relatively unradiogenic He ratios obtained by Christensen et al. (2001) and Doucelance et al. (2003) for olivines separated from silicate rocks from Santo Antão ($R/Ra = 13.8$), São Vicente ($R/Ra = 12.3$), and São Nicolau ($R/Ra = 15.7$) islands.

These noble gas signatures of the Cape Verde hotspot endorse the finite-frequency tomography, which shows the existence of a reasonably resolved P-wave velocity anomaly beneath the archipelago that extends down to the core–mantle boundary (Montelli et al., 2006; Zhao, 2007). It is interesting to note that Montelli et al. (2006) consider the Cape Verde plume as an isolated anomaly down to about 1000 km, after which it merges with the Azores and Canary plumes toward the deepest levels of the mantle. The island of La Palma in Canary is characterised by R/Ra values of up to 9.6, which are attributed to the mixing between low $^4He/^3He$ plume material and depleted MORB mantle characterised by $^4He/^3He$ ratios around 90,000 (Hilton et al., 2000). For the Azores, a lower mantle contribution is revealed from both R/Ra values greater than 9 and an air-corrected $^{21}Ne/^{22}Ne$ ratio of 0.052 characterising Terceira Island magmas (Moreira et al., 1999; Madureira et al., 2005).

The determined low $^4He/^3He$ ratios could lead to the interpretation that the apatite samples plotting to the left of MORB line in the neon three-isotope diagram (samples Br-15 and F-230C) reflect mixing processes between an atmospheric component and a plume-like component with solar-like neon signatures (Honda et al., 1991; Moreira et al., 1995; 2001; Honda and McDougall, 1998; Moreira and Allègre, 1998). However, these samples are also characterised by $^{38}Ar/$

$^{36}$Ar ratios lower than the air value of 0.188 or even than the range of values usually used to characterise the MORB-OIB field (Kunz, 1999; Trieloff et al., 2002; Raquin and Moreira, 2009). This strongly suggests that the higher-than-air $^{20}$Ne/$^{22}$Ne ratios are caused by mass-fractionation processes rather than reflect a plume source. Indeed, in a $^{20}$Ne/$^{22}$Ne-$^{38}$Ar/$^{36}$Ar space, these samples fall on a Rayleigh distillation curve (Fig. 5). Therefore, none of the neon isotopic ratios measured in the samples can be considered as evidence for a lower mantle contribution. Instead, they suggest significant atmospheric contamination which, considering the intrusive character of these carbonatites, probably occurred during magma crustal transport/emplacement by reaction with the volcanic island basement.

From the above discussion, it is evident that only He isotopes are retaining relatively unradiogenic signatures, a fact deserving an explanation. Experimental work has demonstrated that the solubility of noble gases in silicate magmas increases with decreasing atomic number, while partition coefficients for mineral/melt pairs increase towards the heaviest noble gases (Jambon et al., 1986; Broadhurst et al., 1992; Shibata et al., 1998; Heber et al., 2007). If these trends apply to carbonatitic magmas, He will be the noble gas least affected by vesiculation during melt ascent and the more partitioned into liquid during melting. This would make He less prone to atmospheric contamination by interaction with seawater-altered volcanic pile, which is in agreement with the idea that heavy noble gases may develop an atmospheric isotopic signature due to their higher susceptibility to contamination by seawater (e.g., Moreira et al., 2003).

In addition, decompression during magma ascent induces gas exsolution in an attempt to re-establish chemical and thermodynamic equilibrium (e.g. Mangan and Sisson, 2000). Bubble growth, at expenses of gas molecules randomly dispersed in the melt, is controlled by diffusion. Given the swiftness of bubble growing (e.g. Proussevitch and Sahagian, 2005; Ruzié and Moreira, in press) disequilibrium such as those here testified by $^{38}$Ar/$^{36}$Ar and Ne isotopes (Fig. 5) is expectable during degassing. Furthermore, Paonita and Martelli (2006) demonstrated that the degree of kinematic fractionation heavily depends on the rate of magma ascent. Considering the very low viscosity and density, as well as the high wetting capacity of carbonatitic magmas (e.g. Wolff, 1994; Minarik and Watson, 1995; Dobson et al, 1996) it is theoretically expectable that the ascent rate of this type of magmas is, as a rule, very high, thus favouring kinematic fractionation. On the other hand considering that diffusion coefficients for He can be two orders of magnitude higher than for heavier noble gases (e.g. Aubaud et al., 2004) we admit that helium isotope ratios were not affected by fractionation during degassing, a conclusion obtained by Paonita and Martelli (2007) in modelling systems characterised by $CO_2$ supersaturation.

The fact that He is the noble gas element characterised by the highest solubility in magmas, the faster diffusion and the lower mineral/melt partition coefficients is taken as an explanation for its decoupling from the other noble gases, with He being the one better retaining a deep lower mantle signal.

### 5.3. The carbon origin

The origin of carbon can be considered one of the most intriguing aspects of carbonatite genesis (e.g., Ray et al., 2009). Even if a consensus is reached regarding a mantle origin for carbonatites, it is more difficult to decide if the carbon forming such unusual type of magmas is primordial or, alternatively, if it results from crustal carbon recycled to the mantle via subduction. Despite the extreme rarity of oceanic carbonatites, these two hypotheses have been proposed to explain Canary and Cape Verde carbonatite (c.f., de Ignacio et al., 2006; Hoernle et al., 2002).

The mantle is thought to be the biggest carbon reservoir on Earth (see Hirschmann and Dasgupta, 2009 and references therein). However, taking into account that only up to around 40% (e.g., Coltice et al., 2004) of total amount of subducted $CO_2$ ($1.53\times10^{14}$ g/a; Jarrard, 2003) is returned to the surface by arc magmatism, we are forced to admit that significant amounts of recycled carbon exist in the mantle (see also Kerrick and Connolly, 2001). Some of the Cape Verde calcio-carbonatites exhibit HIMU-like Pb, Nd and Sr isotopic signatures which led Hoernle et al. (2002) to consider them derived from the melting of ancient (around 1.6 Ga) recycled carbonated oceanic crust after a period of incubation at the base of the mantle. Considering the long time lag envisaged in such models between carbon recycling and carbonatite genesis, this hypothesis cannot be immediately rejected based on our noble gas data. Indeed, it could be admitted, as a working hypothesis, that the crustal carbonatite precursor acquired, by He diffusion, the above reported lower mantle signal during mantle cycling.

The fate of carbonates carried to the mantle by a subducting slab was experimentally investigated by Hammouda (2003) and Yaxley and Brey (2004). Their results strongly suggest that carbonates are unlikely to be transported to depth levels below approximately 300 km as a consequence of carbonate removal from the slab by melting reactions, while Dasgupta et al. (2004) showed that solidus of carbonated eclogite appears not to intersect typical subduction geotherms at least until the transition zone. In all, if these data does not completely preclude the recycling of some carbon to the lower mantle (see Dasgupta et al., 2004) it strongly suggests that carbon recycling shall not go beyond the highest levels of the lower mantle. Therefore, considering that the low $^{4}$He/$^{3}$He ratios presented by some of the Cape Verde carbonatites seems to imply their provenance from a reservoir at the bottom of the mantle, the recycled model does seems not apply to Cape Verde carbonatites.

This conclusion is endorsed by Xe and C isotopic signatures. As previously discussed, we found some apatites characterised by $^{129}$Xe in excess of reported air values ($^{129}$Xe/$^{130}$Xe ratios up to 6.84). As shown by Moreira (2007), such signatures cannot be explained by recycling of Te- and/or Ba-enriched carbonates. Indeed, the successive decay from $^{128}$Te to $^{129}$Te (by neutron capture), $^{129}$I and $^{129}$Xe would be accompanied by double beta decay of $^{130}$Te to $^{130}$Xe and would result in a decrease of the $^{129}$Xe/$^{130}$Xe ratio rather than an increase. In addition, the elevated Ba content of carbonates altering the oceanic crust (see Kelley et al., 2003) would increase the $^{130}$Xe content, by double beta decay of $^{130}$Ba. Thus, the $^{129}$Xe anomalies observed in our samples can only be interpreted in terms of a very ancient mantle origin resulting from the decay of the now extinct $^{129}$I.

In addition, compilations of carbon isotopic signatures of diamonds, mantle xenoliths and magmatic rocks (e.g. Cartigny, 2005; Deines, 2002) point to the existence of a dominant mantle reservoir having a $\delta^{13}$C close to −5‰, which may reflect a major contribution from primitive meteorites (Hashizume et al., 2004). Thus, a mantle origin for carbon in the Cape Verde carbonatites is strongly suggested by the $\delta^{13}$C values determined for calcites in this study (−8.0 to −4.2‰), which are clearly distinct from the heavier crustal carbon signatures (Deines, 2002) and are also lower than the reported values (e.g., −3.2‰: Ray et al., 1999; −2.1‰: van Achterbergh et al., 2002) for carbonatites that are considered to incorporate some recycled inorganic carbon.

Considering all of the above reasoning and the unradiogenic character of He observed in some carbonatites (R/Ra up to 15.5), we consider the studied Cape Verde intrusive carbonatites to be ultimately derived from an ascending heterogeneous mantle plume carrying, to the surface, entrained material from a low (U + Th)/$^{3}$He reservoir located in the deep lower mantle and that contained non-recycled, i.e., primordial, carbon. The existence of such a reservoir containing primordial carbon is considered one of the possible explanations for the constancy of the mantle $\delta^{13}$C through the Earth's history (Coltice et al., 2004). The storage mechanism for carbon in the deep mantle is beyond the scope of this paper. However, considering the experimental data of Shcheka et al. (2006) it is expectable that carbon in such a deep-seated reservoir must be stored in a separate

carbon-rich phase (see also Isshiki et al., 2004; Oganov et al., 2006) rather than in the volumetrically dominant nominally volatile-free minerals.

A problem arises from the difficulty in conciliating the described noble gases signatures (including $^4He/^3He$ down to 46 700; R/Ra up to 15.5) with the lithophile radiogenic isotopes which can be considered akin of HIMU-type magmas (e.g. $^{206}Pb/^{204}Pb$ up to 20.4; Hoernle et al. 2002). Indeed HIMU-type magmas are usually characterised by radiogenic He isotopic signatures ($^4He/^3He$ up to 137,000; R/Ra down to 5.3; Hanyu and Kaneoka, 1997; Moreira and Kurz, 2001; Parai et al., 2009) as compared with the canonical MORB values ($^4He/^3He = \approx 90{,}000 \pm 10{,}000$; $R/Ra = 8 \pm 1$) which is at odds with the He isotopic ratios here reported for the Cape Verde carbonatites.

Several lines of evidence have recently put forward that the low $^4He/^3He$ signatures pointing to the contribution of a deep reservoir are not consistent with the expected signatures for the lithophile or siderophile radiogenic tracers in the same reservoir (e.g. Brandon et al., 2007; Jackson et al., 2009). This inconsistency, also evidenced by the Cape Verde carbonatites, can be explained assuming that the recycling of crustal materials, down to the pre-existing low $^4He/^3He$ reservoir constrain, the isotopic characteristics of the mantle plume Sr, Nd and Pb but that the He isotopic evolution is affected on a significantly lesser degree. Indeed the deep mantle reservoir would be characterised by $(U+Th)/^3He$ low enough to be "unaffected" by the addition of materials depleted in He by degassing at mid-ocean ridges and, lately, during subduction processing (Jackson et al., 2009). Such a model is endorsed by the globally elevated titanium, tantalum and niobium in low $^4He/^3He$ basalts (Jackson et al., 2008), by the correlation of $^4He/^3He$ and $^{187}Os/^{186}Os$, but not with $^{186}Os/^{188}Os$, in Icelandic picrites (Brandon et al., 2007), and by the He–Nd and He–Sr isotope relations in the Yellowstone–Snake River Plain province (Graham et al., 2009).

Despite that we defend a non-recycled origin for the carbon in the Cape Verde carbonatites, we do not believe that carbonatites worldwide can be considered the result of a single process or carbon source. Experimental work demonstrates that carbonatitic melts can be released from carbonated peridotites or eclogites at depths close to or equivalent to the transition zone (Hammouda, 2003; Yaxley and Brey, 2004; Dasgupta et al., 2004; Dalou et al., 2009).These data, in conjunction with heavy carbon isotope signatures (e.g. van Achterbergh et al., 2002; Ray et al., 2009 ), lend support to the hypothesis that some of the carbonatites result from ancient recycled crustal carbonated materials.

## 6. Conclusions

We presented and discussed the first noble gas isotopic results obtained for oceanic carbonatites. Some of the studied carbonatites preserve low $^4He/^3He$ ratios (down to 46 700; R/Ra up to 15.5) that were considered as evidence for a deep lower mantle contribution to the Cape Verde carbonatites. Such relatively unradiogenic He signatures are similar to those described by Christensen et al. (2001) and Doucelance et al. (2003) for some of the silicate rocks on Northern Cape Verde islands, and thus endorse the results of tomographic studies pointing to the presence of a deep-rooted mantle plume in the region (see Montelli et al., 2006; Zhao, 2007).

The conjunction of those relatively unradiogenic He isotopic signatures with high $^{129}Xe/^{130}Xe$ ratios (up to 6.84) and mantle-like $\delta^{13}C$ (−8 to −4.2‰) favours a non-recycled origin for the carbon in the Cape Verde carbonatites.

## Acknowledgments

Noble gas and carbon isotopes were analyzed at the Institut de Physique du Globe de Paris, during a sabbatical license of the first author. J.M. acknowledges FCT for a Bolsa de Licença Sabática. We are indebted to C. Mourão, S. Martins, and L. Martins for their help with mineral separations and XRD determinations. The skillful assistance of A. Raquin during noble gases isotope determinations is appreciated. Funding for this study was provided by the FEDER/FCT project PLINT (POCTI/CTA/45802/2002) and by the IPGP. Two anonymous reviewers and the editor (R. Carlson) are thanked for their constructive and helpful comments and suggestions.

## Appendix A. Supplementary data

Supplementary data associated with this article can be found, in the online version, at doi:10.1016/j.epsl.2009.12.052.

## References

Allègre, C.J., 1987. Isotope geodynamics. Earth Planet. Sci. Lett. 86, 175–203.
Allègre, C.J., Lewin, E., 1989. Chemical structure and history of the Earth, evidence from global non-linear inversion of isotopic data in a three-box model. Earth Planet. Sci. Lett. 96, 61–88.
Allègre, C.J., Staudacher, T., Sarda, P., Kurz, M., 1983. Constraints on evolution of Earth's mantle from rare gas systematics. Nature 303, 762–766.
Allègre, C.J., Pineau, F., Bernat, M., Javoy, M., 1971. Evidence for the occurrence of carbonatites on the Cape Verde and Canary Islands. Nat. Phys. Sci. 233, 103–104.
Allègre, C.J., Moreira, M., Staudacher, T., 1995. $^4He/^3He$ dispersion and mantle convection. Geophys. Res. Lett. 22, 2,325–2,328.
Assunção, C.F.T., Canilho, M.H., 1969. A petrografia da ilha de Maio e suas relações com a petrografia do arquipélago de Cabo Verde. Bol. Mus. Lab. Min. Geol. F.C.U.Lisboa 11, 161–191.
Assunção, C.F.T., Machado, F., Gomes, R.A., 1965. On the occurrence of carbonatites in the Cape Verde Islands. Bol. Soc. Geol. Port. 16, 179–188.
Aubaud, C., Pineau, F., Jambon, A., Javoy, M., 2004. Kinetic disequilibrium of C, He, Ar and carbon isotopes during degassing of mid-ocean ridge basalt. Earth Planet. Sci. Lett. 222, 391–406.
Barker, A.K., Holm, P.M., Peate, D.W., Baker, J.A., 2009. Geochemical stratigraphy of submarine lavas (3–5 Ma) from the Flamengos Valley, Santiago, Southern Cape Verde Islands. J. Petrol. 50, 169–193.
Basu, S., Murty, S.V.S., 2006. Noble gases in carbonatites of Sung Valley and Ambadongar: implications for trapped components. Chem. Geol. 234, 236–250.
Bebiano, J.B., 1932. A geologia do arquipélago de Cabo Verde. Comun. Serv. Geol. Portugal 18, 276p.
Bell, K., Simonetti, A., 2009. Source of parental melts to carbonatites — critical isotopic constraints. Mineral. Petrol. doi:10.1007/s00710-009-0059-0.
Bell, K., Tilton, G.R., 2001. Nd, Pb and Sr isotopic compositions of East African carbonatites: evidence for mantle mixing and plume inhomogeneity. J. Petrol. 42, 1927–1945.
Bernard-Griffiths, J., Cantagrel, J.-M., Alves, C.A.M., Mendes, F., Serralheiro, A., Macedo, J.R., 1975. Données radiometriques potassium-argon sur quelques formations magmatiques des îles de l'archipel du Cap Vert. C. R. Acad. Sc. Paris (Série D) 280, 2429–2432.
Bonadiman, C., Beccaluva, L., Coltorti, M., Siena, F., 2005. Kimberlite-like metasomatism and "garnet signature" in spinel-peridotite xenoliths from Sal, Cape Verde archipelago: relics of a subcontinental mantle domain within the Atlantic Ocean lithosphere? J. Petrol. 46, 2465–2493.
Brandon, A.D., Graham, D.W., Waight, T., Gautason, B., 2007. $^{186}Os$ and $^{187}Os$ enrichments and high $^3He/^4He$ sources in the Earth's mantle: evidence from Icelandic picrites. Geochim. Cosmochim. Acta 71, 4570–4591.
Broadhurst, C.L., Drake, M.J., Hagee, B.E., Bernatowicz, T.J., 1992. Solubility and partitioning of Ne, Ar, Kr, and Xe in minerals and synthetic basaltic melts. Geochim. Cosmochim. Acta 56, 709–723.
Brooker, R.A., Du, Z., Blundy, J.D., Kelley, S.P., Allan, N.L., Wood, B.J., Chamorro, E.M., Wartho, J.-A., Purton, J.A., 2003. The "zero charge" partitioning behaviour of noble gases during melting. Nature 423, 738–741.
Cartigny, P., 2005. Stable isotopes and the origin of diamond. Elements 1, 79–84.
Castle, J.C., Creager, K.C., 1999. A steeply dipping discontinuity in the lower mantle beneath IZU-Bonin. J. Geophys. Res. 104 (B4), 7279–7292.
Cazenave, A., Dominh, K., Rabinowicz, M., Ceuleneer, G., 1988. Geoid and depth anomalies over ocean swells and troughs: evidence of an increasing trend of the geoid to depth ratio with age of plate. J. Geophys. Res. 93, 8064–8077.
Christensen, B.P., Holm, P.M., Jambon, A., Wilson, J.R., 2001. Helium, argon and lead isotopic composition of volcanics from Santo Antão and Fogo, Cape Verde Islands. Chem. Geol. 178, 127–142.
Class, C., Goldstein, S.L., 2005. Evolution of helium isotopes in the Earth's mantle. Nature 436, 1107–1112.
Coltice, N., Ricard, Y., 2002. On the origin of noble gases in mantle plumes. Philos. Trans.-R. Soc. Lond., Ser. A 360, 2633–2648.
Coltice, N., Simon, L., Lécuyer, C., 2004. Carbon isotope cycle and mantle structure. Geophys. Res. Lett. 31, 1–5.
Courtney, R., White, R., 1986. Anomalous heat flow and geoid across the Cape Verde Rise: evidence for dynamic support from a thermal plume in the mantle. Geophys. J. R. Astron. Soc. 87, 815–868.
Crough, S.T., 1978. Thermal origin of mid-plate hot-spot swells. Geophys. J. R. Astronm. Soc. 55, 451–469.

Czuppon, G., Matsumoto, T., Handler, M.R., Matsuda, J., 2009. Noble gases in spinel peridotite xenoliths from Mt Quincan, North Queensland, Australia: undisturbed MORB-type noble gases in the subcontinental lithospheric mantle. Chem. Geol. 266, 19–28.
Dalou, C., Koga, K.T., Hammouda, T., Poitrasson, F., 2009. Trace element partitioning between carbonatitic melts and mantle transition zone minerals: Implications for the source of carbonatites. Geochim. Cosmochim. Acta 73, 239–255.
Dalton, J.A., Wood, B.J., 1993. The compositions of primary carbonate melts and their evolution through wallrock reaction in the mantle. Earth Planet. Sci. Lett. 119, 511–525.
Dasgupta, R., Hirschmann, M., Withers, A.C., 2004. Deep cycling of carbon constrained by the solidus of anhydrous, carbonated eclogite under upper mantle conditions. Earth Planet. Sci. Lett. 227, 73–85.
Dasgupta, R., Hirschmann, M.M., Dellas, N., 2005. The effect of bulk composition on the solidus of carbonated eclogite from partial melting experiments at 3 GPa. Contrib. Mineral. Petrol. 149, 288–305.
Davies, G.R., Norry, D.C., Gerlach, D.C., Cliff, R.A., 1989. A combined chemical and Pb–Sr–Nd isotope study of the Azores and Cape Verde hot-spots: the geodynamic implications. In: Saunders, A.D., Norry, M.J. (Eds.), Magmatism in the Ocean Basins: Geological Society Special Publication, vol. 42, pp. 231–255.
Dawson, J.B., Hinton, R.W., 2003. Trace-element content and partitioning in calcite, dolomite and apatite in carbonatite, Phalaborwa, South Africa. Min. Mag. 67, 921–930.
Day, J.M.D., Hilton, D.R., Pearson, D.G., Macpherson, C.G., Kjarsgaars, B.A., Janney, P.E., 2005. Absence of a high time-integrated $^{3}He/(U+Th)$ in the mantle beneath continents. Geology 33, 733–736.
de Ignacio, C., Muñoz, M., Sagredo, J., Fernandez-Santin, S., Johansson, A., 2006. Isotope geochemistry and FOZO mantle component of the alkaline–carbonatitic association of Fuerteventura, Canary Islands, Spain. Chem. Geol. 232, 99–113.
Deines, P., 2002. The carbon isotope geochemistry of mantle xenoliths. Earth Sci. Rev. 58, 247–278.
Dobson, D., Jones, A.P., Rabe, R., Sekine, T., Kurita, K., Taniguchi, T., Kondo, T., Kato, T., Shimomura, O., Urakawa, S., 1996. In-situ measurement of viscosity and density of carbonate melts at high pressure. Earth Planet. Sci. Lett. 143, 207–215.
Doucelance, R., Escrig, S., Moreira, M., Gariépy, C., Kurz, M.D., 2003. Pb–Sr–He isotope and trace element geochemistry of the Cape Verde Archipelago. Geochim. Cosmochim. Acta 67 (717–3), 733.
Ernst, R.E., Bell, K., 2009. Large igneous provinces (LIPs) and carbonatites. Mineral. Petrol. doi:10.1007/s00710-009-0074-1.
Escrig, S., Doucelance. R., Moreira, M., Allègre, C.J., 2005. Os isotope systematics in Fogo Island: evidence for lower continental crust fragments under the Cape Verde Southern islands. Chem. Geol. 219, 93–113219:93–113.
Farley, K.A., 2000. Helium diffusion from apatite: general behavior as illustrated by Durango fluorapatite. J. Geophys. Res. 105, 2903–2914.
Fischer, T.P., Burnard, P., Marty, B., Hilton, D.R., Füri, E., Palhol, F., Sharp, Z.D., Mangasini, F., 2009. Upper-mantle volatile chemistry at Oldoinyo Lengai volcano and the origin of carbonatites. Nature 459, 77–80.
Foley, S.F., Yaxley, G.M., Rosenthal, A., Buhre, S., Kiseeva, E.S., Rapp, R.P., Jacob, D.E., 2009. The composition of near-solidus melts of peridotite in the presence of $CO_2$ and $H_2O$ between 40 and 60 kbar. Lithos. doi:10.1016/j.lithos.2009.03.020.
Gautheron, C., Moreira, M., 2002. Helium signature of the subcontinental lithospheric mantle. Earth Planet. Sci. Lett. 199, 39–47.
Gautheron, C., Moreira, M., Allègre, C., 2005. He, Ne and Ar composition of the European lithospheric mantle. Chem. Geol. 217, 97–112.
Gautheron, C., Tassan-Got, L., Farley, K.A., 2006. (U–Th)/Ne chronometry. Earth Planet. Sci. Lett. 243, 520–535.
Gerlach, D.C., Cliff, R.A., Davies, G.R., Norry, M., Hodgeson, N., 1988. Magma sources of the Cape Verdes Archipelago: isotopic and trace element constraints. Geochim. Cosmochim. Acta 52, 2979–2992.
Ghosh, S., Ohtani, E., Litasov, K.D., Terasaki, H., 2009. Solidus of carbonated peridotite from 10 to 20 GPa and origin of magnesiocarbonatite melt in the Earth's deep mantle. Chem. Geol. 262, 17–28.
Graham, D.W., Lupton, F., Albarède, F., Condomines, M., 1990. Extreme temporal homogeneity of helium isotopes at Piton de la Fournaise, Réunion Island. Nature 347, 545–548.
Graham, D.W., Reid, M.R., Jordan, B.T., Grunder, A.I., Leeman, W.P., Lupton, J.E., 2009. Mantle source provinces beneath the Northwestern USA delimited by helium isotopes in young basalts. J. Volcanol. Geotherm. Res. 188, 128–140.
Hall, R., Spakman, W., 2002. Subducted slabs beneath the eastern Indonesia–Tonga region: insights from tomography. Earth Planet. Sci. Lett. 201, 321–336.
Hammouda, T., 2003. High-pressure melting of carbonated eclogite and experimental constraints on carbon recycling and storage in the mantle. Earth Planet. Sci. Lett. 214, 357–368.
Hanyu, T., Kaneoka, I., 1997. The uniform and low $^{3}He/^{4}He$ ratios of HIMU basalts as evidence for their origin as recycled materials. Nature 390, 273–276.
Hart, S.R., 1984. Large-scale isotope anomaly in the Southern Hemisphere mantle. Nature 309, 753–757.
Hashizume, K., Chaussidon, M., Marty, B., Terada, K., 2004. Protosolar carbon isotopic composition: implications for the origin of meteoritic organics. Astrophys. J. 600, 480–484.
Heber, V.S., Brooker, R.A., Kelley, S.P., Wood, B.J., 2007. Crystal-melt partitioning of noble gases (helium, neon, argon, krypton, and xenon) for olivine and clinopyroxene. Geochim. Cosmochim. Acta 71, 1041–1061.
Helffrich, G., Faria, B., Fonseca, J.F.B.D., Lodge, A., Kaneshima, S., 2010. Transition zone structure under a stationary hot spot: CapeVerde. Earth Planet. Sci. Lett. 289, 156–1614.
Hilton, D.R., Macpherson, C.G., Elliott, T.R., 2000. Helium isotope ratios in mafic phenocrysts and geothermal fluid from La Palma, the Canay Islands (Spain): implications for HIMU mantle sources. Geochim. Cosmochim. Acta 64 (119–2), 132.
Hirschmann, M.M., Dasgupta, R., 2009. The H/C ratios of the Earth's near-surface and deep reservoirs, and consequences for deep Earth volatile cycles. Earth Planet. Sci. Lett. 262, 4–16.
Hoernle, K., Tilton, G., LeBas, M.J., Duggen, S., Garbe-Schönberg, D., 2002. Geochemistry of oceanic carbonatites compared with continental carbonatites: mantle recycling of oceanic crustal carbonate. Contrib. Mineral. Petrol. 142, 520–542.
Holm, P.M., Wilson, J.R., Christensen, B.P., Hansen, L., Hansen, S.L., Hein, K.M., Mortensen, R., Pederson, R., Plesner, S., Runge, M.K., 2006. Sampling the Cape Verde mantle plume: evolution of melt compositions on Santo Antão, Cape Verde Islands. J. Pertol. 47, 145–189.
Holm, P.M., Grandvuinet, T., Friis, J., Wilson, J.R., Barker, A.B., Plesner, S., 2008. An $^{40}Ar–^{39}Ar$ study of the Cape Verde hot spot: temporal evolution in a semistationary plate environment. J. Geophys. Res. 113, B08201. doi:10.1029/2007JB005339.
Honda, M., McDougall, I., 1998. Primordial helium and neon in the Earth — a speculation on early degassing. Geophys. Res. Lett. 25, 1951–1954.
Honda, M., McDougall, I., Patterson, D.B., Doulgeris, A., Clague, D., 1991. Possible solar noble-gas component in Hawaiian basalts. Nature 349, 149–151.
Isshiki, M., Irifune, T., Hirose, K., Ono, S., Ohishi, Y., Watanuki, T., Nishiborl, E., Takata, M., Sakata, M., 2004. Stability of magnesite and its high-pressure from the lowermost mantle. Nature 427, 60–63.
Jackson, M.G., Hart, S.R., Saal, A.E., Shimizu, N., Kurz, M.D., Blusztajn, J.S., Skovgaard, A., 2008. Globally elevated titanium, tantalum, and niobium (TITAN) in ocean island basalts with high $^{3}He/^{4}He$. Geochem. Geophys. Geosyst. 9. doi:10.1029/2007GC001876.
Jackson, M.G., Kurz, M.D., Hart, S.R., 2009. Helium and neon isotopes in phenocrysts from Samoan lavas: evidence for heterogeneity in the terrestrial high $^{3}He/^{4}He$ mantle. Earth Planet. Sci. Lett. 287, 519–528.
Jambon, A., Weber, H., Braun, O., 1986. Solubility of He, Ne, Ar, Kr and Xe in a basalt melting in the range 1250–1600 °C. Geochemical implications. Geochim. Cosmochim. Acta 50, 401–408.
Jarrard, R.D., 2003. Subduction fluxes of water, carbon dioxide, chlorine, and potassium. Geochem. Geophys. Geosyst. 4. doi:10.1029/2002GC000392.
Javoy, M., Pineau, F., Staudacher, T., Cheminee, J.L., Krafft, M., 1989. Mantle volatiles sampled from a continental rift: the 1988 eruption of Oldoinyo Lengai (Tanzania). Terra abstracts 1, 324.
Jephcoat, A.P., Bouhifd, M.A., Porcelli, D., 2008. Partitioning experiments in the laser-heated diamond anvil cell: volatile content in the Earth's core. Philos. Trans. R. Soc. London, Ser. A 366, 4295–4314.
Jørgensen, J., Holm, P.M., 2002. Temporal variation and carbonatite contamination in primitive ocean island volcanics from São Vicente, Cape Verde Islands. Chem. Geol. 192, 249–267.
Kárason, H., Van der Hilst, R.D., 2000. Constraints on mantle convection from seismic tomography. In: Richards, M.R., Gordon, R., Van der Hilst, R.D. (Eds.), The History and Dynamics of Global Plate Motion. Geophysical Monograph, vol. 121. American Geophysical Union, Washington, D.C, pp. 277–288.
Kelley, K.A., Plank, T., Ludden, J., Staudigel, H., 2003. Composition of altered oceanic crust at ODP Sites 801 and 1149. Geochem. Geophys. Geosyst. 4. doi:10.1029/2002GC000435.
Kerrick, D.M., Connolly, J.A.D., 2001. Metamorphic devolatilization of subducted oceanic metabasalts: implications for seismicity, arc magmatism and volatile recycling. Earth Planet. Sci. Lett. 189, 19–29.
Kogarko, L.N., 1993. Geochemical characteristics of oceanic carbonatites from the Cape Verde Islands. S. Afr. J. Geol. 96, 119–125.
Kunz, J., 1999. Is there solar argon in the Earth's mantle? Nature 399, 649–650.
Kunz, J., Staudacher, T., Allègre, C.J., 1998. Plutonium-fission xenon found in Earth's Mantle. Science 280, 877–880.
Kurz, M.D., Jenkins, W.J., Hart, S.R., 1982. Helium isotopic systematics of oceanic islands and mantle heterogeneity. Nature 297, 43–47.
Labrosse, S., Hernlund, J.W., Coltice, N., 2007. A crystallizing dense magma ocean at the base of the Earth's mantle. Nature 450, 866–869.
Lee, W.J., Wyllie, P.J., 2000. The system $CaO–MgO–SiO_2–CO_2$ at 1 GPa, metasomatic wehrlites, and primary carbonatite magmas. Contrib. Mineral. Petrol. 138, 214–228.
Le Maitre, R.W., Streckeisen, A., Zanettin, B., Le Bas, M.J., Bonin, B., Bateman, P., Bellieni, G., Dudek, A., Efremova, S., Keller, J., Lameyre, J., Sabine, P.A., Schmid, R., Sørenson, H., Woolley, A.R., 2002. Igneous rocks, a classification and glossary of terms: recommendations of the International Union of Geological Sciences, subcommission on the systematics of igneous rocks, 2nd ed. Cambridge University Press.
Lodge, A., Helffrich, G., 2006. A depleted swell root beneath the Cape Verde Islands. Geology 34, 449–452.
Machado, F., Azeredo Leme, J., Monjardino, J., Seita, M.F., 1968. Carta geológica de Cabo Verde, notícia explicativa da folha da Ilha Brava e dos ilhéus Secos (na escala 1/50000). Garcia de Orta 16 (S. Geol.), 123–130.
Madeira, J., Munhá, J., Tassinari, C., Mata, J., Brum da Silveira, A., Martins, S., 2005. K/Ar ages of carbonatites from the island of Fogo (Cape Verde). Actas do VIII Congresso de Geoquímica dos Países de Língua Portuguesa, pp. 475–478.
Madureira, P., Moreira, M., Mata, J., Allègre, C.J., 2005. Primitive helium and neon isotopes in Terceira island: constraints on the origin of the Azores archipelago. Earth Planet. Sci. Lett. 233, 429–440.
Mangan, M., Sisson, T., 2000. Delayed, disequilibrium degassing in rhyolite magma: decompression experiments and implications for explosive volcanism. Earth Planet. Sci. Lett. 183, 441–455.
Martins, S., Mata, J., Munhá, J., Mendes, M.H., Maerschalk, C., Caldeira, R., Mattielli, N., 2009. Chemical and mineralogical evidence of the occurrence of mantle metasomatism by carbonate-rich melts in an oceanic environment (Santiago Island, Cape Verde). Miner. Petrol. doi:10.1007/s00710-009-0078-x.
Marty, B., Tolstikhin, I., Kamensky, I.L., Nivin, V.A., Balaganskaya, E.G., Zimmermann, J.-L., 1998. Plume-derived rare gases in 380 Ma carbonatites from the kola region (Russia)

and the argon isotopic composition in the deep mantle. Earth Planet. Sci. Lett. 164, 179–192.
Meibom, A., Anderson, D.L., 2003. The statistical upper mantle assemblage. Erath Planet. Sci. Lett. 217, 123–139.
Meibom, A., Anderson, D.L., Sleep, N.H., Frei, R., Chamberlain, C.P., Hren, M.T., Wooden, J.L., 2003. Are high $^{3}He/^{4}He$ ratios in oceanic basalts an indicator of deep-mantle plume components? Earth Planet. Sci. Lett. 208, 197–204.
Menzies, A.H., Carlson, R.W., Shirey, S.B., Gurney, J.J., 2003. Re–Os systematics of diamond-bearing eclogites from the Newlands kimberlite. Lithos 71, 323–336.
Millet, M.A., Doucelance, R., Schiano, P., David, K., Bosq, C., 2008. Mantle plume heterogeneity versus shallow-level interactions: a case study, the São Nicolau Island, Cape Verde archipelago. J. Volcanol. Geotherm. Res. 176, 265–276.
Minarik, W.G., Watson, E.B., 1995. Interconnectivity of carbonate melt at low melt fraction. Earth Planet. Sci. Lett. 133, 423–437.
Mitchell, R.H., 2005. Carbonatites and carbonatites and carbonatites. Can. Mineral. 43, 2,049–2,068.
Mohapatra, R.K., Honda, M., 2006. "Recycled" volatiles in mantle-derived diamonds — evidence from nitogen and noble gas isotopic data. Earth Planet. Sci. Lett. 252, 215–219.
Monnereau, M., Cazenave, A., 1990. Depth and geoid anomalies over oceanic hotspot swells: a global survey. J. Geophys. Res. 95, 429–438.
Montelli, R., Nolet, G., Dahlen, F.A., Masters, G., 2006. A catalogue of deep mantle plumes: new results from finite-frequency tomography. Geochem. Geophys. Geosyst. 7. doi:10.1029/2006GC001248.
Moreira, M., 2007. Constraints on the origin of the $^{129}Xe$ on Earth using the tellurium double beta decay. Earth Planet. Sci. Lett. 264, 114–122.
Moreira, M., Allègre, C.J., 1998. Helium–neon systematics and the structure of the mantle. Chem. Geol. 147, 53–59.
Moreira, M., Kurz, M., 2001. Subducted oceanic lithosphere and the origin of the "high" basalt helium isotopic signature. Earth Planet. Sci. Lett. 189, 49–57.
Moreira, M., Madureira, P., 2005. Cosmogenic helium and neon in 11My old ultramafic xenoliths: consequences for mantle signatures in old samples. Geochem. Geophys. Geosyst. 6. doi:10.1029/2005GC000939.
Moreira, M., Staudacher, T., Sarda, P., Schilling, J.-G., Allègre, C.J., 1995. A primitive plume neon component in MORB: the Shona ridge-anomaly, South Atlantic (51–52 S). Earth Planet. Sci. Lett. 133, 367–377.
Moreira, M., Kunz, J., Allègre, C.J., 1998. Rare gas systematics on popping rock: estimates of isotopic and elemental compositions in the upper mantle. Science 279, 1178–1181.
Moreira, M., Doucelance, R., Kurz, M.D., Dupré, B., Allègre, C.J., 1999. Helium and lead isotope geochemistry of the Azores Archipelago. Earth Planet. Sci. Lett. 169, 189–205.
Moreira, M., Breddam, K., Curtice, J., Kurz, M.D., 2001. Solar neon in the Icelandic mantle: evidence for an undegassed lower mantle. Earth Planet. Sci. Lett. 185, 15–23.
Moreira, M., Blusztajn, J., Curtice, J., Hart, S.R., Dick, H., Kurz, M.D., 2003. He and Ne isotopes in oceanic crust: implications for noble gas recycling in the mantle. Earth Planet. Sci. Lett. 216, 635–643.
Mourão, C., Mata, J., Doucelance, R., Madeira, J., Brum da Silveira, A., Silva, L.C., Moreira, M., 2009. Quaternary extrusive calciocarbonatite volcanism on Brava Island (Cape Verde): a nephelinite–carbonatite immiscibility product. J. Afr. Earth Sci 56, 59–74.
Muñoz, M., Sagredo, J., de Ignacio, C., Fernández-Suárez, J., Jeffries, T.E., 2005. New data (U–Pb, K–Ar) on the geochronology of the alkaline–carbonatitic association of Fuerteventura, Canary Islands, Spain. Lithos 85, 140–153.
Murty, S.V.S., Basu, S., Kumar, A., 2007. Noble gases in South Indian carbonatites: trapped and in situ components. J. Asian Earth Sci. 30, 154–169.
Nakajima, Y., Takahashi, E., Suzuki, T., Funakoshi, K., 2009. "Carbon in the core" revisited. Phys. Earth Planet. Int. 174, 202–211.
Oganov, A.R., Glass, C.W., Ono, S., 2006. High-pressure phases of $CaCO_3$: crystal structure prediction and experiment. Earth Planet. Sci. Lett. 241, 95–103.
Ozima, M., Podosek, F.A., 2002. Noble Gas Geochemistry, 2nd edition. Cambridge University Press, 286 pp.
Paonita, A., Martelli, M., 2006. Magma dynamics at mid-ocean ridges by noble gas kinetic fractionation: assessment of magmatic ascent rates. Earth Planet. Sci. Lett. 241, 138–158.
Paonita, A., Martelli, M., 2007. A new view of the He–Ar–$CO_2$ degassing at mid-ocean ridges: homogeneous composition of magmas from the upper mantle. Geochim. Cosmochim. Acta 71, 1747–1763.
Parai, R., Mukhopadhyay, S., Lassiter, J.C., 2009. New constraints on the HIMU mantle from neon and helium isotopic compositions of basalts from the Cook-Austral Islands. Earth Planet. Sci. Lett. 277, 253–261.
Parman, S.W., Kurz, M.D., Hart, S.R., Grove, T.L., 2005. Helium solubility in olivine and implications for high $^{3}He/^{4}He$ in ocean island basalts. Nature 437, 1140–1143.
Pik, R., Marty, B., Hilton, D.R., 2006. How many mantle plumes in Africa? The geochemical point of view. Chem. Geol. 226, 100–114.
Pim, J., Peirce, C., Watts, A.B., Grevemeyer, I., Krabbenhoeft, A., 2008. Crustal structure and origin of the Cape Verde Rise. Earth. Planet. Sci. Lett. 272, 422–428.
Pollitz, F.F., 1991. Two-stage model of African absolute motion during the last 30 millions years. Tectonophysics 194, 91–106.
Porcelli, D., Elliott, T., 2008. The evolution of He isotopes in the convecting mantle and the preservation of high $^{3}He/^{4}He$ ratios. Earth Planet. Sci. Lett. 269, 175–185.
Porcelli, D., Halliday, A.N., 2001. The core as a possible source of mantle helium. Earth Planet. Sci. Lett. 192, 45–56.
Porcelli, D., Wasserburg, G.J., 1995. Mass transfer of helium, neon, argon and xenon through a steady-state upper mantle. Geochim. Cosmochim. Acta 59, 4,921–4,937.
Poreda, R.J., Farley, K.A., 1992. Rare gases in Samoan xenoliths. Earth Planet. Sci. Lett. 113, 129–144.
Proussevitch, A., Sahagian, D., 2005. Bubbledrive-1: a numerical model of volcanic eruption mechanisms driven by disequilibrium magma degassing. J. Volcanol. Geotherm. Res. 143, 89–111.
Putirka, K., 2008. Excess temperatures at oceanic islands: implications for mantle layering and convection. Geology 36, 283–286.
Raquin, A., Moreira, M., 2009. Air $^{38}Ar/^{36}Ar$ in the mantle: implication for the nature of the parent bodies of the Earth. Earth Planet. Sci. Lett. 287, 551–558.
Ray, J.S., Ramesh, R., Pande, K., 1999. Carbon isotopes in Kerguelen plume-derived carbonatites: evidence for recycled inorganic carbon. Earth Planet. Sci. Lett. 170, 205–214.
Ray, J.S., Shukla, A.D., Dewangan, L.K., 2009. Carbon and oxygen isotopic composition of Newania dolomite carbonatites, Rajasthan, India: implications for source of carbonatites. Miner. Petrol. doi:10.1007/s00710-009-0073-2.
Ruzié, L., Moreira, M., in press. Magma degassing processes during plinian eruptions. J. Volcanol. Geotherm. Res.
Samuel, H., Farnetani, D.M., 2003. Thermochemical convection and helium concentrations in mantle plumes. Earth Planet. Sci. Lett. 207, 39–56.
Sarda, P., Staudacher, T., Allègre, C.J., 1988. Neon isotopes in submarine basalts. Earth Planet. Sci. Lett. 91, 73–88.
Sasada, T., Hiyagon, H., Bell, K., Ebihara, M., 1997. Mantle-derived noble gases in carbonatites. Geochim. Cosmochim. Acta 61, 4219–4228.
Scarsi, P., 2000. Fractional extraction of helium by crushing of olivine and clinopyroxene phenocrysts: effects on the $^{3}He/^{4}He$ measured ratio. Geochim. Cosmochim. Acta 64, 3751–3762.
Schmincke, H.U., Klügel, A., Hansteen, T., Hoernle, K., Boogard, P., 1998. Samples from the Jurassic ocean crust beneath Gran Canaria, La Palma and Lanzarote (Canary Islands). Earth Planet. Sci. Lett. 163, 343–360.
Shcheka, S.S., Wiedenbeck, M., Frost, D.J., Keppler, H., 2006. Carbon solubility in mantle minerals. Earth Planet. Sci. Lett. 245, 730–742.
Shibata, T., Takahashi, E., Matsuda, J., 1998. Solubility of neon, argon, and xenon in binary and ternary silicate systems: a new view of noble gases solubility. Geochim. Cosmochim. Acta 62, 1241–1253.
Shuster, D.L., Flowers, R., Farley, K.A., 2006. The influence of natural radiation damage on helium diffusion kinetics in apatite. Earth Planet. Sci. Lett. 249, 148–161.
Silva, L.C., Le Bas, M.J., Robertson, A.H.F., 1981. An oceanic carbonatite volcano on São Tiago, Cape Verde Islands. Nature 294, 644–645.
Staudacher, T., Allègre, C.J., 1982. Terrestrial xenology. Earth Planet. Sci. Lett. 60, 389–406.
Stillman, C.J., Furnes, H., Le Bas, M.J., Robertson, A.H.F., Zielonka, J., 1982. The geological history of Maio, Cape Verde Islands. J. Geol. Soc. London 139, 347–361.
Stuart, F.M., Lass-Evans, S., Fitton, J.G., Ellam, R.M., 2003. High $^{3}He/^{4}He$ ratios in picritic basalts from Baffin Island and the role of a mixed reservoir in mantle plumes. Nature 424, 57–59.
Tappert, R., Stachel, T., Harris, J.W., Muehlenbachs, K., Ludwing, T., Brey, G.P., 2005. Subducting oceanic crust: the source of deep diamonds. Geology 33, 565–568.
Teague, A.J., Seward, T.M., Harrisson, D., 2008. Mantle sources for Oldoinyo Lengai carbonatites: evidence from helium isotopes in fumarole gases. J. Volcanol. Geotherm. Res. 175, 386–390.
Tilton, G.R., Bell, K., 1994. Sr–Nd–Pb isotope relationships in late Archean carbonatites and alkaline complexes: Aplications to the geochemical evolution of Archean mantle. Geochim. Cosmochim. Acta 58, 3145–3154.
Tingle, T.N., 1998. Accretion and differentiation of carbon in the early Earth. Chem. Geol. 147, 3–10.
Tolstikhin, I.N., Hofmann, A.W., 2005. Early crust on top of the Earth's core. Phys. Earth Planet. Int. 148, 109–130.
Tolstikhin, I.N., Kamensky, I.L., Marty, B., Nivin, V.A., Vetrin, V.R., Balaganskaya, E.G., Ikorsky, S.V., Gannibal, M.A., Weiss, D., Verhulst, A., 2002. Rare gas isotopes and parent trace elements in ultrabasic–alkaline–carbonatite complexes, Kola Peninsula: identification of lower mantle plume component. Geochim. Cosmochim. Acta 66, 881–901.
Tolstikhin, I.N., Kramers, J.D., Hofmann, A.W., 2006. A chemical Earth model with whole mantle convection: the importance of a core–mantle boundary layer (D″) and its early formation. Chem. Geol. 226, 79–99.
Trieloff, M., Kunz, J., Clague, D.A., Harrison, D., Allègre, C.J., 2000. The nature of pristine noble gases in mantle plumes. Science 288, 1036–1038.
Trieloff, M., Kunz, J., Allègre, C.J., 2002. Noble gas systematics of the reunion mantle plume source and the origin of primordial noble gases in Earth's mantle. Earth Planet. Sci. Lett. 200, 297–313.
Trull, T., Nadeau, S., Pineau, F., Polvé, M., Javoy, M., 1993. C–He systematics in hotspot xenoliths: implications for mantle carbon contents and carbon recycling. Earth Planet. Sci. Lett. 118, 43–64.
van Achterbergh, E., Griffin, W.L., Ryan, C.G., O'Reilly, S.Y., Pearson, N.J., Kivi, K., Doyle, B.J., 2002. Subduction signature for quenched carbonatites from the deep lithosphere. Geology 30, 743–746.
Vance, D., Stone, J.O.H., O'Nions, R.K., 1989. He, Sr and Nd isotopes in xenoliths from Hawaii and other oceanic islands. Earth Planet. Sci. Lett. 96, 147–160.
Veizer, J., Bell, K., Jansen, S.L., 1992. Temporal distribution of carbonatites. Geology 20, 1147–1149.
Wallace, M.E., Green, D.H., 1988. An experimental determination of primary carbonatite magma composition. Nature 335, 343–346.
Walter, M.J., Bulanova, G.P., Armstrong, L.S., Keshav, S., Blundy, J.D., Gudfinnsson, G., Lord, O.T., Lennie, A.R., Clark, S.M., Smith, C.B., Gobbo, L., 2008. Primary carbonatite melt from deeply subducted oceanic crust. Nature 454, 622–626.
Williams, C.A., Hill, I.A., Young, R., White, R.S., 1990. Fracture zones across the Cape Verde Rise, N.E. Atlantic. J. Geol. Soc. 147, 851–857.
Wolff, J., 1994. Physical properties of carbonatite magmas inferred from molten salt data, and application to extraction patterns from carbonatite–silicate magma chambers. Geol. Mag. 131, 145–153.
Wood, B.J., 1993. Carbon in the core. Earth Planet. Sci. Lett. 117, 593–607.

Wood, B.J., Blundy, J.D., 2001. The effect of cation charge on crystal-melt partitioning of trace elements. Earth Planet. Sci. Lett. 188, 59–71.
Wooley, A.R., 1989. The spatial and temporal distribution of carbonatites. In: Bell, K. (Ed.), Carbonatites: Genesis and Evolution. Unwin Hyman Ltd., London, UK, pp. 15–37.
Wyllie, P.J., Lee, W.-J., 1998. Model system controls on conditions for formation of magnesiocarbonatite and calciocarbonatite magmas from the mantle. J. Petrol. 39, 1885–1893.
Yamamoto, J., Hirano, N., Abe, N., Hanyu, T., 2009. Noble gas isotopic compositions of mantle xenoliths from northwestern Pacific lithosphere. Chem. Geol. 269, 313–323.
Yaxley, G.M., Brey, G.P., 2004. Phase relations of carbonate-bearing eclogite assemblages from 2.5 to 5.5 GPa: implications for petrogenesis of carbonatites. Contrib. Mineral. Petrol. 146, 606–619.
Yokochi, R., Marty, B., Pik, R., Burnard, P., 2005. High $^{3}He/^{4}He$ ratios in peridotite xenoliths from SW Japan-Revisited: evidence for cosmogenic $^{3}He$ released by vacuum crushing. Geochem. Geophys. Geosyst. 6, Q01004. doi:10.1029/2004GC000836.
Zhao, D., 2007. Seismic images under 60 hotspots: search for mantle plumes. Gondwana Res. 12, 335–355.
Zindler, A., Hart, S.R., 1986. Chemical geodynamics. Annu. Rev. Earth Planet. Sci. 14, 493–571.

Available online at www.sciencedirect.com
ScienceDirect
Geochimica et Cosmochimica Acta 74 (2010) 7261–7282
Geochimica et Cosmochimica Acta
www.elsevier.com/locate/gca

# Geochemical constraints on depth of origin of oceanic carbonatites: The Cape Verde case

Régis Doucelance [a,b,c,*], Tahar Hammouda [a,b,c], Manuel Moreira [d], João C. Martins [e]

[a] Clermont Université, Université Blaise Pascal, Laboratoire Magmas et Volcans, BP 10448, F-63000 Clermont-Ferrand, France
[b] CNRS, UMR 6524, LMV, F-63038 Clermont-Ferrand, France
[c] IRD, R 163, LMV, F-63038 Clermont-Ferrand, France
[d] Laboratoire de Géochimie et Cosmochimie (UMR 7579 CNRS), Institut de Physique du Globe de Paris, Université Paris 7, 4 Place Jussieu, 75252 Paris Cedex 05, France
[e] Centro de Geologia da Universidade de Lisboa, Portugal

Received 24 March 2010; accepted in revised form 17 September 2010; available online 19 October 2010

**Abstract**

We present new Sr–Nd isotope compositions together with major- and trace element concentrations measured for whole rocks and mineral separate phases (apatite, biotite and calcite) from fifteen Cape Verde oceanic carbonatites (Atlantic Ocean). Trace element patterns of calcio- and magnesio-carbonatites present a strong depletion in K, Hf, Zr and Ti and an overall enrichment in Sr and REE relative to Cape Verde basalts, arguing for distinct source components between carbonatites and basalts. Sr and Nd isotopic ratios show small, but significant variations defining a binary mixing between a depleted end-member with unradiogenic Sr and radiogenic Nd values and a "enriched" end-member compatible with old marine carbonates. We interpret the depleted end-member as the Cape Verde oceanic lithosphere by comparison with previous studies on Cape Verde basalts. We thus propose that oceanic carbonatites are resulting from the interaction of a deep rooted mantle plume carrying a lower $^4He/^3He$ signature from the lower mantle and a carbonated metasomatized lithosphere, which by low degree melting produced carbonatite magmas. Sr–Nd compositions and trace element patterns of carbonatites argue in favor of a metasomatic agent originating from partial melting of recycled, carbonated oceanic crust. We have successfully reproduced the main geochemical features of this model using a Monte-Carlo-type simulation.


## 1. INTRODUCTION

Carbonatite rocks are found on every continent, except Antarctica (see Fig. 2 in the compilation-study by Chakhmouradian (2006) for the geographical distribution of carbonatites). Their occurrence in an oceanic setting, however, is very rare and oceanic carbonatites have been reported only at the Cape Verde and Canary archipelagos, North and Central Atlantic Ocean. More precisely, they have been found on six out of 10 islands (Brava, Fogo, Santiago, Maio and São Vicente; a carbonatite dyke from São Nicolau was also reported by Kogarko, 1993) of the Cape Verde archipelago, and on only one (Fuerteventura) amongst seven islands of the Canaries.

Geochemical studies based on stable, radiogenic and noble gas isotopes have led to the general consensus that parental magmas to continental carbonatites originate in the mantle (Bell et al., 1982; Nelson et al., 1988; Deines, 1989; Sasada et al., 1997). For oceanic carbonatites, their mantle origin is not debated either. They have been associated to the mantle plumes that originated the Cape Verde and Canary archipelagos (Hoernle et al., 2002; De Ignacio et al., 2006; Mata et al., 2010).

The way carbonatites are generated, however, is more controversial. Three petrogenetic models related to experi-

* Corresponding author at: Laboratoire Magmas et Volcans, Observatoire de Physique du Globe de Clermont-Ferrand, 5, rue Kessler, 63038 Clermont-Ferrand Cedex, France. Tel.: +33 4 73 34 67 65; fax: +33 4 73 34 67 44.
*E-mail address:* R.Doucelance@opgc.univ-bpclermont.fr (R. Doucelance).

0016-7037/$ - see front matter © 2010 Elsevier Ltd. All rights reserved.
doi:10.1016/j.gca.2010.09.024

mental results are generally invoked. These are: (1) direct partial melting of a carbonated mantle source (peridotite + $CO_2$, cf. Wyllie and Huang, 1975, 1976; Eggler, 1978; Wallace and Green, 1988; Wyllie and Lee, 1998); (2) immiscible separation from a carbonated silicate melt (Koster van Groos and Wyllie, 1963; Kjarsgaard and Hamilton, 1989; Brooker, 1998); and (3) fractional crystallization of a carbonated alkaline silicate liquid (King and Sutherland, 1960; Lee and Wyllie, 1994; Veksler et al., 1998).

Furthermore, there is a strong paradox between experimental petrology predicting that carbonated melts formed in the mantle should be magnesio-carbonatites (dolomitic) and the calcitic nature of most sampled carbonatites (Woolley, 1989). In order to resolve this paradox, it has been suggested that magnesio-carbonatites are enriched in calcium during their ascent by reaction with their surrounding environment (Dalton and Wood, 1993). However, calcium enrichment predicted by such model does not reach values observed in nature. In addition melt/rock interaction model requires that carbonatitic melts have time to interact with their environment, which is in contradiction with their high mobility (Hunter and McKenzie, 1989; Treiman, 1989; Hammouda and Laporte, 2000).

An alternative solution considers the source of carbonatites to be located into the mantle and to be constituted of recycled oceanic crust + carbonated sediments. Melting experiments with such a source as starting composition have indeed led to the generation of calcitic, carbonatitic melts in P–T conditions of subduction (Hammouda, 2003).

The aim of this study is threefold. Firstly, we report new Sr–Nd isotope data, as well as major- and trace element contents measured on 15 Cape Verde carbonatites (whole-rock samples and separate phases) collected on the islands of Brava, Fogo, Santiago and São Vicente. Secondly, we discuss the relationship that exists between Sr–Nd data and the geographical location of carbonatites in the Cape Verde archipelago and focus on the comparison between distributions of (i) carbonatite chemical compositions and (ii) those of silicate rocks of the Cape Verde (Gerlach et al., 1988; Jørgensen and Holm, 2002; Doucelance et al., 2003; Escrig et al., 2005; Holm et al., 2006; Millet et al., 2008; Barker et al., 2009, 2010; Martins et al., 2010). Finally, we discuss the different sources that were previously proposed for the origin of carbonatites and propose an alternative model: plume-induced melt generation within heterogeneous, carbonatite-metasomatized oceanic lithosphere with small assimilation of plume melt.

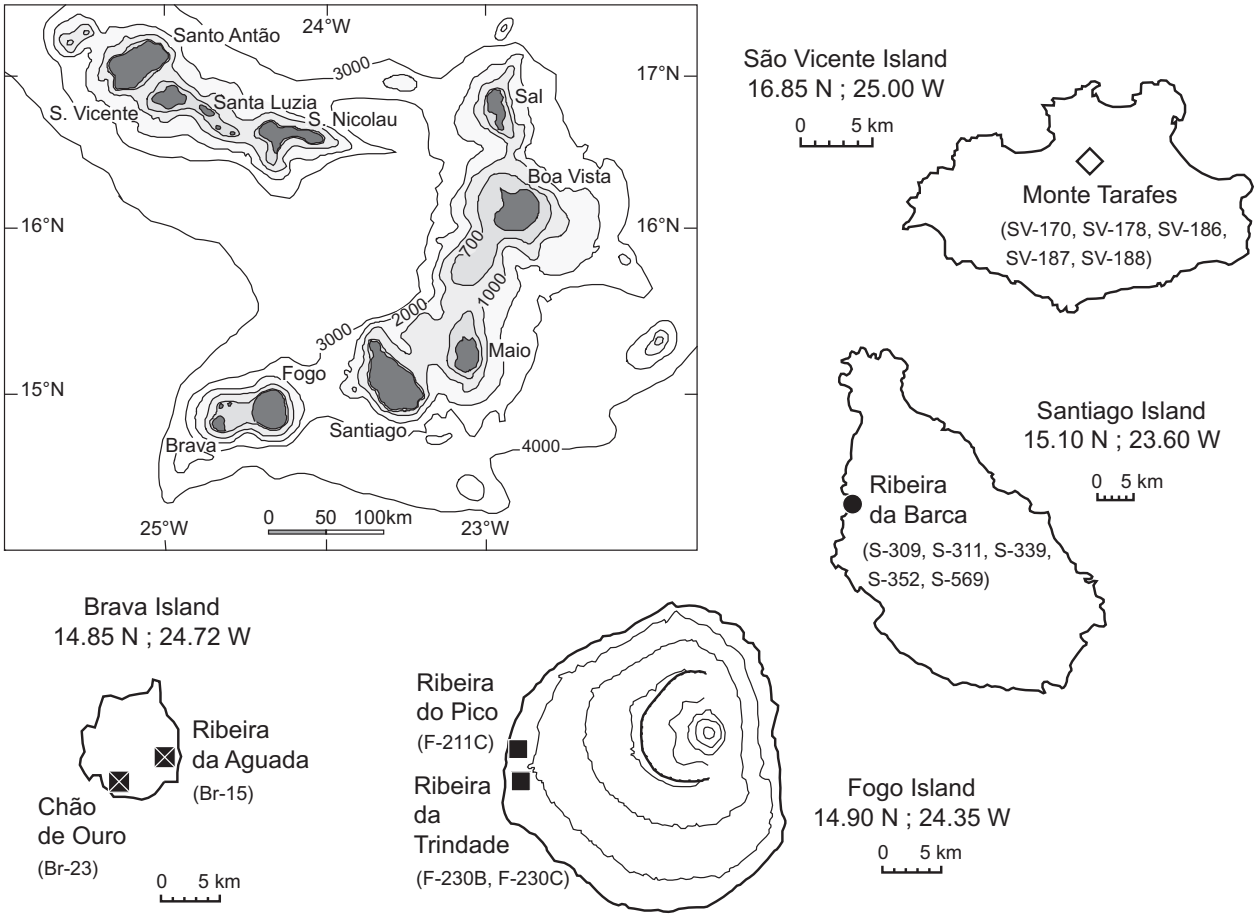


Fig. 1. Geographical map of the Cape Verde archipelago with sampling location of carbonatites.

## 2. GEOGRAPHIC LOCATION AND TECTONIC SETTING

The Cape Verde archipelago is composed of 10 islands and some islets located 450 km away from the Senegal coast, in western Africa (Fig. 1). Its volcanic character is well evidenced by the Fogo Island where the last eruption occurred in 1995 and some 11 eruptions happened since Portuguese settlement in the 15th century. The islands form two quasi-linear groups converging eastward, which have been considered distinct in what concerns to the geochemical (elemental and isotopic) characteristics of magmatic rocks (e.g. Gerlach et al., 1988; Doucelance et al., 2003). They occur on top of the Cape Verde Rise, an oceanic mega-swell characterized by a thickened crust (≈22 km) and a geoid to topography ratio of about 4.4 consistent with lithospheric reheating (Grevemeyer, 1999; Lodge and Helffrich, 2006). The swell is considered as the result of a mantle plume (e.g. Montelli et al., 2006; Zhao, 2007). As a consequence of its age (120–140 Ma) the lithosphere is significantly thick (≈83 km) in the oceanic context (Cazenave et al., 1988).

Cape Verde basalts have been intensively studied by geochemists during the last 30 years (Gerlach et al., 1988; Davies et al., 1989; Christensen et al., 2001; Jørgensen and Holm, 2002; Doucelance et al., 2003; Escrig et al., 2005; Holm et al., 2006; Millet et al., 2008; Barker et al., 2009, 2010; Martins et al., 2010). Notably they show Sr–Nd–Pb isotope compositions in relation to their geographical location (see archipelago-scale studies: Gerlach et al., 1988; Doucelance et al., 2003) that are best explained by variable mixing between three end-members: (1) a radiogenic Pb end-member with relatively primitive He and intermediate Sr and Nd, seen in all islands, thought to represent the deep-seated source of the Cape Verde plume; (2) an enriched end-member with a EM1-like isotope signature prevalent in the Southern Islands; and (3) a depleted end-member, mainly influencing Northern Island compositions. The depleted end-member resembles Atlantic MORB dredged at the latitude of the Cape Verde archipelago (around 15°N) for radiogenic isotopes and corresponds to the local oceanic lithosphere, assimilated by ascending plume melts (Millet et al., 2008). In the same way, Escrig et al. (2005) have invoked a shallow-level process to explain the EM1-like signature of samples from the Southern Islands. Observed trends result of assimilation, via AFC processes, of sub-continental lithosphere and lower continental crust, delaminated during the Atlantic opening and left behind into the oceanic lithosphere under the Cape Verde archipelago. Both models (shallow-level assimilation of oceanic lithosphere and delaminated sub-continental material) are supported by global co-variations between major-, trace element contents and isotope ratios (Millet et al., 2008).

The Cape Verde Islands are also renowned as one of the two only occurrences of oceanic carbonatites. The latter are recognized since the sixties (e.g. Assunção et al., 1965). They were described in one of the Northern Islands (São Vicente) and in 4 Southern Islands (Maio, Santiago, Fogo and Brava). In the present paper we report new Sr–Nd isotope data, as well as major- and trace element contents measured on 15 Cape Verde carbonatites (whole-rock samples and mineral separate phases) collected on the islands of Brava, Fogo, Santiago and São Vicente (Fig. 1). These new data were obtained for the same samples, in which carbon and rare gas isotope signatures of calcite separates were measured by Mata et al. (2010). Details about field observation and petrography can be found in their paper.

## 3. ANALYTICAL PROCEDURE

### 3.1. Major- and trace elements

Carbonatite samples were spilt into different aliquots for whole-rock analysis and, in some cases, for mineral separations. Apatite and biotite concentrates were obtained by dissolving carbonates with HCl and subsequent electromagnetic separation of the residue using a Frantz isodynamic separator. Sporadically, heavy liquids were used prior to electromagnetic separation. Carbonates were concentrated using the electromagnetic separator. Both type of separates were finally handpicked under binocular microscope. Pyroxenes (aegirine-augite and diopside; F-211C, Br-15 and S-309), sphene (F-211C and F-230C), zirconolite (S-309), amphibole (S-309), and opaque minerals, mostly Ti-magnetites (F-211C, F-230C and Br-15), were also observed. However, their amount was not sufficient to perform elemental and isotopic analyzes. The identification of carbonate type was achieved by X-ray Diffraction (XRD) and further confirmed by ICP-MS analysis. Prior to chemical analysis whole-rock samples were gently crushed in an agate mortar. On the contrary, separate minerals were not crushed before chemical analyzes.

Both major- and trace element contents of samples were determined at the Actlabs laboratory, Canada. For whole-rock carbonatites, contents were obtained using Inductively Coupled Plasma-Optical Emission Spectrometry (ICP-OES) and Inductively Coupled Plasma-Mass Spectrometry (ICP-MS), after alkaline melting with lithium metaborate/tetraborate and nitric acid dissolution (except for Cd, Cu, Ni and Zn measurements that were performed after acid digestion). For mineral and carbonate fractions, measurements were performed by ICP-MS after Aqua Regia extraction (AR-MS). Duplicate measurements of the lowest-concentration sample for each type of techniques give an estimate of the total reproducibility of analyzes. For whole-rock carbonatite samples, the reproducibility (range/mean of the two analyses of sample S-339) is: (i) in the order of 1% for major-element contents ($SiO_2$, $Fe_2O_3$, MnO, MgO and CaO); (ii) better than 3% for Rare Earth Elements (REE, except for Gd which gives 6.5%); (iii) around 5% for High Field Strength Elements (HFSE, except for Ti which is determined with major elements by ICP-OES and then displays a bad reproducibility of ~45%); and (iv) better than 2% for highly incompatible elements (Rb, Ba, U, Th). For minerals and carbonate matrix, the reproducibility (range/mean of the two analyzes of sample Br-15 Cb) is: (i) better than 10% for major elements (Al, Fe, Mg, Ca, K and P); and (ii) better than 8% for REE (other trace element analyses display a variable reproducibility ranging between 1% for Ba and 30% for Th). As an

Table 1
Major- (%) and trace-element (ppm) concentrations of Cape Verde whole-rock carbonatites.

| | Brava | | Fogo | | | Santiago | | | | | São Vicente | | | | | BIR-1 | | NIST694 | | SY-3 | | Mica–Fe | |
|---|---|---|---|---|---|---|---|---|---|---|---|---|---|---|---|---|---|---|---|---|---|---|---|
| | Br-15 | Br-23 | F-211C | F-230B | F-230C | S-309 | S-311 | S-339 | S-352 | S-569 | SV-170 | SV-178 | SV-186 | SV-187 | SV-188 | Meas. | Cert. | Meas. | Cert. | Meas. | Cert. | Meas. | Cert. |
| $SiO_2$ | 3.04 | 0.27 | 4.62 | 5.81 | 1.79 | 4.12 | 0.84 | 3.55 | 0.57 | 1.24 | 0.32 | 1.34 | 0.80 | 0.67 | 0.56 | 47.36 | 47.77 | 11.17 | 11.2 | 60.49 | 59.62 | | |
| $TiO_2$ | 0.216 | 0.007 | 0.294 | 0.094 | 0.074 | 0.471 | 0.080 | 0.013 | 0.106 | 0.012 | 0.031 | 0.016 | 0.035 | 0.011 | 0.031 | 0.954 | 0.96 | 0.116 | 0.11 | 0.148 | 0.15 | | |
| $Al_2O_3$ | 0.52 | 0.10 | 1.02 | 1.44 | 0.34 | 0.35 | 0.11 | 0.06 | 0.06 | 0.09 | 0.05 | 0.36 | 0.18 | 0.20 | 0.08 | 15.39 | 15.35 | 1.87 | 1.8 | 11.73 | 11.76 | | |
| $Fe_2O_3$ | 3.93 | 2.16 | 3.54 | 1.87 | 0.80 | 4.67 | 2.64 | 2.32 | 1.62 | 0.63 | 1.05 | 1.46 | 1.20 | 1.31 | 1.10 | 11.14 | 11.26 | 0.73 | 0.79 | 6.55 | 6.49 | | |
| MnO | 0.270 | 0.368 | 0.180 | 0.227 | 0.151 | 0.265 | 0.311 | 0.610 | 0.208 | 0.250 | 0.346 | 0.462 | 0.102 | 0.439 | 0.226 | 0.169 | 0.171 | 0.011 | 0.012 | 0.328 | 0.32 | | |
| MgO | 0.45 | 0.12 | 1.05 | 0.57 | 0.26 | 1.89 | 0.38 | 15.7 | 0.58 | 0.55 | 0.51 | 2.66 | 0.58 | 0.91 | 0.67 | 9.51 | 9.68 | 0.32 | 0.33 | 2.58 | 2.67 | | |
| CaO | 49.75 | 53.87 | 49.51 | 49.35 | 53.40 | 48.82 | 53.92 | 33.34 | 52.25 | 54.52 | 54.35 | 51.06 | 54.76 | 54.15 | 54.59 | 13.22 | 13.24 | 42.73 | 43.6 | 8.36 | 8.25 | | |
| $Na_2O$ | 0.31 | 0.08 | 0.21 | 0.61 | 0.18 | 0.31 | 0.16 | 0.09 | 0.09 | 0.16 | 0.09 | 0.14 | 0.11 | 0.12 | 0.11 | 1.82 | 1.75 | 0.89 | 0.86 | 4.13 | 4.12 | | |
| $K_2O$ | 0.26 | 0.05 | 0.42 | 0.28 | 0.18 | 0.13 | 0.08 | 0.05 | 0.07 | <0.01 | 0.04 | 0.26 | 0.18 | 0.03 | 0.09 | 0.04 | 0.03 | 0.6 | 0.51 | 4.35 | 4.23 | | |
| $P_2O_5$ | 5.63 | 0.21 | 3.30 | 2.11 | 0.94 | 8.94 | 2.39 | 0.05 | 1.20 | 0.62 | 1.17 | 2.93 | 3.27 | 1.58 | 0.56 | 0.02 | 0.05 | 30.11 | 30.2 | 0.58 | 0.54 | | |
| LOI | 34.20 | 42.33 | 35.93 | 36.78 | 41.11 | 29.26 | 39.56 | 42.96 | 41.43 | 41.91 | 41.8 | 39.35 | 39.39 | 41.07 | 42.00 | | | <0.01 | | <0.01 | | | |
| Rb | 27 | <1 | 26 | 8 | 8 | 8 | 5 | <1 | <1 | <1 | <1 | 5 | 3 | 2 | 1 | <1 | 0.3 | | | 217 | 206 | >1000 | 2200 |
| Ba | 314 | 1041 | 535 | 450 | 471 | 337 | 878 | 4073 | 342 | 1284 | 1609 | 3819 | 1582 | 3796 | 7201 | 6 | 7 | | | 426 | 450 | 189 | 150 |
| Th | 7.05 | 1.95 | 32.1 | 6.65 | 2.14 | 38.9 | 10.6 | 14.1 | 9.03 | 4.20 | 11.0 | 26.5 | 11.9 | 22.2 | 25.2 | <0.05 | 0.03 | | | 982 | 1000 | 158 | 150 |
| U | 1.06 | 3.11 | 6.75 | 2.11 | 1.94 | 30.6 | 115 | 2.36 | 6.28 | 1.30 | 2.29 | 12.70 | 4.48 | 5.42 | 3.04 | 0.02 | 0.01 | | | 593 | 650 | 80.5 | 80 |
| Nb | 10.8 | 4.6 | 14.9 | 51.1 | 64.9 | 69.1 | 255 | 130 | 47.2 | 7.5 | 7.6 | 15.8 | 7.5 | 9.1 | 15.2 | 0.4 | 0.6 | | | 186 | 148 | 291 | 270 |
| La | 307 | 280 | 335 | 231 | 244 | 517 | 445 | 1160 | 364 | 461 | 59.7 | 196 | 85.9 | 90.9 | 159 | 0.68 | 0.62 | | | 1340 | 1340 | 201 | 200 |
| Ce | 608 | 502 | 689 | 394 | 403 | 1170 | 789 | 1970 | 768 | 842 | 70.8 | 244 | 95.8 | 141 | 204 | 1.98 | 1.95 | | | 2310 | 2230 | 429 | 420 |
| Pr | 65.1 | 48.3 | 76.8 | 44.5 | 44.6 | 142 | 79.9 | 200 | 87.5 | 90.0 | 6.67 | 23.3 | 8.62 | 16.2 | 18.4 | 0.37 | 0.38 | | | 222 | 223 | 51.2 | 49 |
| Nd | 241 | 166 | 299 | 166 | 164 | 583 | 284 | 725 | 337 | 338 | 25.3 | 83.3 | 29.5 | 67.4 | 57.6 | 2.4 | 2.5 | | | 732 | 670 | 185 | 180 |
| Sr | 8466 | 8622 | 7301 | 9222 | 8411 | 8568 | >10000 | 875 | >10000 | >10000 | 4456 | 2961 | 5146 | 3615 | 6423 | 106 | 108 | | | 311 | 302 | 24 | 5 |
| Sm | 39.1 | 26.8 | 48.9 | 28.5 | 28.0 | 101 | 44.4 | 103 | 55.5 | 52.8 | 6.89 | 17.0 | 5.47 | 19.0 | 8.39 | 1.11 | 1.1 | | | 128 | 109 | 35.7 | 33 |
| Hf | 1.5 | 0.2 | 1.3 | 1.6 | 1.0 | 0.6 | 0.5 | 0.9 | 0.8 | 0.5 | 0.2 | 0.6 | 0.2 | 0.5 | 0.3 | 0.6 | 0.6 | | | 10.8 | 9.7 | 26.5 | 26 |
| Zr | 103 | <4 | 247 | 223 | 91 | 539 | 33 | 94 | 111 | 22 | 9 | 53 | 11 | 29 | 7 | 10 | 16 | | | 362 | 320 | <4 | 800 |
| Eu | 11.1 | 7.95 | 14.5 | 8.60 | 8.48 | 28.2 | 13.1 | 27.1 | 15.9 | 15.9 | 2.73 | 6.07 | 1.92 | 6.92 | 3.21 | 0.555 | 0.54 | | | 19 | 17 | 0.645 | 0.7 |
| Gd | 32.8 | 22.8 | 41.2 | 25.9 | 25.7 | 79.7 | 36.1 | 64.0 | 43.9 | 43.8 | 8.89 | 17.7 | 5.85 | 21.3 | 9.58 | 1.87 | 1.85 | | | 120 | 105 | 23.6 | 21 |
| Tb | 4.35 | 3.33 | 5.14 | 3.36 | 3.35 | 9.00 | 4.60 | 5.21 | 5.32 | 5.30 | 1.61 | 2.91 | 0.94 | 3.21 | 1.72 | 0.39 | 0.36 | | | 22 | 18 | 2.73 | 2.7 |
| Dy | 21.5 | 17.1 | 24.7 | 16.6 | 16.3 | 39.4 | 22.2 | 16.5 | 24.7 | 25.1 | 10.0 | 17.6 | 5.59 | 16.3 | 10.4 | 2.6 | 2.5 | | | 134 | 118 | 10.9 | 11 |
| Ho | 3.87 | 3.20 | 4.14 | 2.90 | 2.94 | 6.07 | 3.97 | 2.53 | 4.05 | 4.18 | 2.08 | 4.08 | 1.30 | 3.01 | 2.14 | 0.56 | 0.57 | | | 28.2 | 29.5 | 1.44 | 1.6 |
| Y | 115 | 98.8 | 120 | 94.4 | 96.1 | 169 | 119 | 63.3 | 127 | 129 | 75.7 | 135 | 50.3 | 109 | 74.9 | 15.7 | 16 | | | 736 | 718 | 47.6 | 48 |
| Er | 10.7 | 9.22 | 10.9 | 7.85 | 7.97 | 14.9 | 10.7 | 6.66 | 10.8 | 11.1 | 6.19 | 13.6 | 4.47 | 8.25 | 6.68 | 1.68 | 1.7 | | | 85.5 | 68 | 3.84 | 3.8 |
| Tm | 1.48 | 1.36 | 1.40 | 1.08 | 1.09 | 1.85 | 1.47 | 1.03 | 1.41 | 1.48 | 0.975 | 2.39 | 0.799 | 1.19 | 1.14 | 0.271 | 0.26 | | | 13 | 11.6 | 0.545 | 0.48 |
| Yb | 8.41 | 9.00 | 7.80 | 6.09 | 6.11 | 9.92 | 8.76 | 6.42 | 8.01 | 8.83 | 6.05 | 15.7 | 5.54 | 7.86 | 7.83 | 1.69 | 1.65 | | | 70 | 62 | 3.46 | 3.5 |
| Lu | 1.12 | 1.28 | 1.01 | 0.783 | 0.808 | 1.18 | 1.14 | 0.868 | 1.06 | 1.20 | 0.833 | 2.21 | 0.887 | 1.06 | 1.18 | 0.246 | 0.26 | | | 8.54 | 7.9 | 0.474 | 0.5 |

independent way to assess accuracy and precision of analyzes, major- and trace element contents of the BIR-1, NIST694, SY-3 and Mica–Fe standards were determined in the same session of analyzes as our samples (see Table 1). BIR-1 is Icelandic basalt; phosphate rock NIST694 displays similar major element concentrations except for $P_2O_5$ as our carbonatite samples; syenite SY-3 is an analog for LREE contents and iron-rich biotite Mica–Fe has similar HREE.

### 3.2. Sr–Nd isotopic ratios

Isotope results were obtained at Laboratoire Magmas et Volcans. Whole-rock samples (~100 mg) were first acid-digested using 2 N HCl for 3 h (savillex closed). Then, after removing of the supernatant, residues of centrifugation were mixed with 500 µl of 22 N HF and 200 µl of 14 N $HNO_3$ during 12 h ($T$ ~75 °C) before being evaporated with an additional mixture of 2 ml 7 N $HNO_3$ + 200 µl 12 N $HClO_4$ (2 days in closed vessels at 50 °C, 5 h at 95 °C and 3 h under the epiradiator). Lastly 5 ml of 6 N HCl were added together with the supernatant of the diluted HCl solution (12 h at 75 °C in a closed savillex) before final evaporation. Carbonate fractions (~100 mg) were treated using the same procedure than whole rocks, whereas separated biotites and apatites (~50 mg) were directly dissolved with the HF-$HNO_3$ mixture. Sr and Nd separations were performed with the "cascade" column procedure (Sr Spec, True Spec and Ln Spec columns) described in Pin and Bassin (1992) and Pin et al. (1994), after removing of most iron through an AG50x4 column. Sr and Nd blanks for the complete procedure were <5 ng and <200 pg, respectively. All measurements were performed on a Finnigan Triton thermo-ionization mass spectrometer in static mode with relay matrix rotation (also called the virtual amplifier) on double W filaments (Re filaments are prohibited because the LMV TIMS instrument is also used for Re-Os analyzes). Isotopic measurements were mass-fractionation-corrected using an exponential law with (1) $^{86}Sr/^{88}Sr = 0.1194$ and normalized to $^{87}Sr/^{86}Sr = 0.71025$ for the NIST SRM987 standard; and (2) $^{146}Nd/^{144}Nd = 0.7219$ and normalized to $^{143}Nd/^{144}Nd = 0.51296$ for the in-house Rennes-AMES standard. A typical run consists of at least 9 blocks of 10 cycles in order to allow a full rotation of the virtual amplifier system. Duplicate analyzes of the two standards during the course of the study gave $^{87}Sr/^{86}Sr = 0.710240 \pm 6$ (2SD, $n = 6$) and $^{143}Nd/^{144}Nd = 0.512962 \pm 5$ (2SD, $n = 9$) in agreement with long-term reproducibility: $^{87}Sr/^{86}Sr = 0.710254 \pm 23$ (2SD, $n = 76$) and $^{143}Nd/^{144}Nd = 0.512959 \pm 9$ (2SD, $n = 120$).

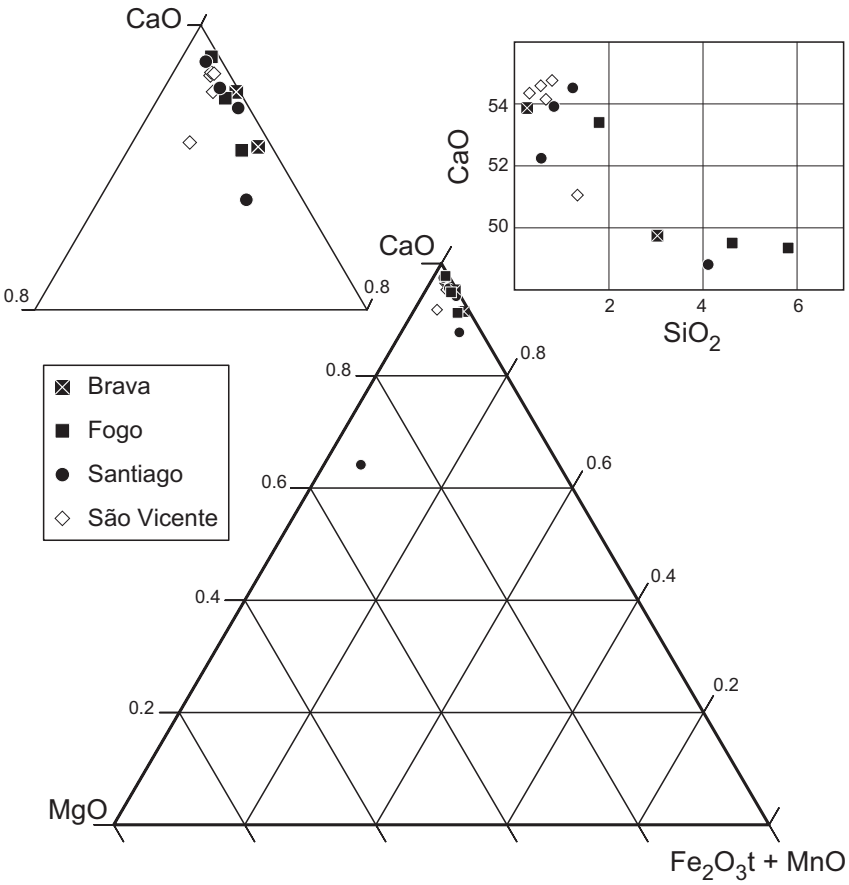


Fig. 2. Plot of Cape Verde carbonatites in terms of CaO–MgO–($Fe_2O_3t$ + MnO) together with CaO vs. $SiO_2$. All samples but one are calcio-carbonatites. The broad negative trend between CaO and $SiO_2$ suggests either mechanical mixing between a pure carbonate end-member with CaO = 56 wt.% and silicates entrained during ascent, or traces of silicates dissolved in carbonate during partial melting.

## 4. RESULTS

### 4.1. Major- and trace element variations of whole-rock samples

Whole-rock carbonatites display CaO and MgO contents ranging from 33.34 to 54.76 wt.% and from 0.12 to 15.70 wt.%, respectively (Fig. 2, Table 1). This mainly reflects the two types of carbonatites (calcio- and magnesio-carbonatites) that outcrop on the Cape Verde Islands. Excluding the only magnesio-carbonatite (S-339 from Santiago), major element contents present significant variations with CaO = 48.82–54.76 wt.%, $SiO_2$ = 0.27–5.81 wt.%, $Fe_2O_3t$ = 0.63–4.67 wt.%, $P_2O_5$ = 0.21–8.94 wt.% and LOI = 29.26–42.96 wt.%. These variations are comparable with previous Cape Verde values (Gerlach et al., 1988; Hoernle et al., 2002). They do not present any clear relationship with the geographical location of samples. For example, São Vicente samples display $SiO_2$ values amongst the least and most elevated, whereas highest $Fe_2O_3$ contents are measured for Brava, Fogo and Santiago (Table 1). Broad negative co-variations can be observed between $SiO_2$ and CaO (Fig. 2), and $Fe_2O_3t$ and CaO (not shown), suggesting either mechanical mixing between a pure carbonate end-member with CaO = 56 wt.% and silicates entrained during ascent, or traces of silicates dissolved in carbonate during partial melting (Dalton and Presnall, 1998).

Trace element data measured for carbonatites are reported in primitive mantle-normalized patterns (Hofmann, 1988) and are compared with (i) previous carbonatite data (from the same outcrops and from different locations for a given island) and (ii) mean Cape Verde basaltic rocks (Fig. 3). Most elements present large variations that cover several orders of magnitude. Our Santiago samples, for example, display U, Nb and Zr contents in the range 1.3–115 ppm, 7.5–255 ppm, and 22–539 ppm, respectively, uncorrelated with the type (magnesio vs. calcio) of carbonatites (Table 1). These variations are even larger when considering previous data, suggesting either a high heterogeneity into the source of carbonatites, or a high degree of elemental fractionation by partial melting and/or magmatic evolution processes. Whatever, the importance of variations, overall enrichment in REE, Ba, Th, U and Sr and depletion in HFSE, Rb and K relative to basaltic rocks are observed as it is generally the case for carbonatites (Hoernle et al., 2002). HFSE ratios also show greater variations in calcio-carbonatites than in basaltic rocks. Notably, Zr/Hf and Nb/Ta ratios measured in carbonatites yield variations in the ranges 23.3–898.3 (mean = 143.6) and 13.7–6500 (mean = 778.8), respectively, compared to 39.4–50.1 (mean = 44.5) and 2.8–275.1 (mean = 63.9) for Cape Verde basalts (data from Doucelance et al., 2003). These ranges are in agreement with worldwide calcio-carbonatite data (Chakhmouradian, 2006).

### 4.2. Separate phases

Fig. 4 illustrates the relationship between whole-rock trace element data and mineral separates (see also Table 2). Trace element primitive mantle-normalized patterns

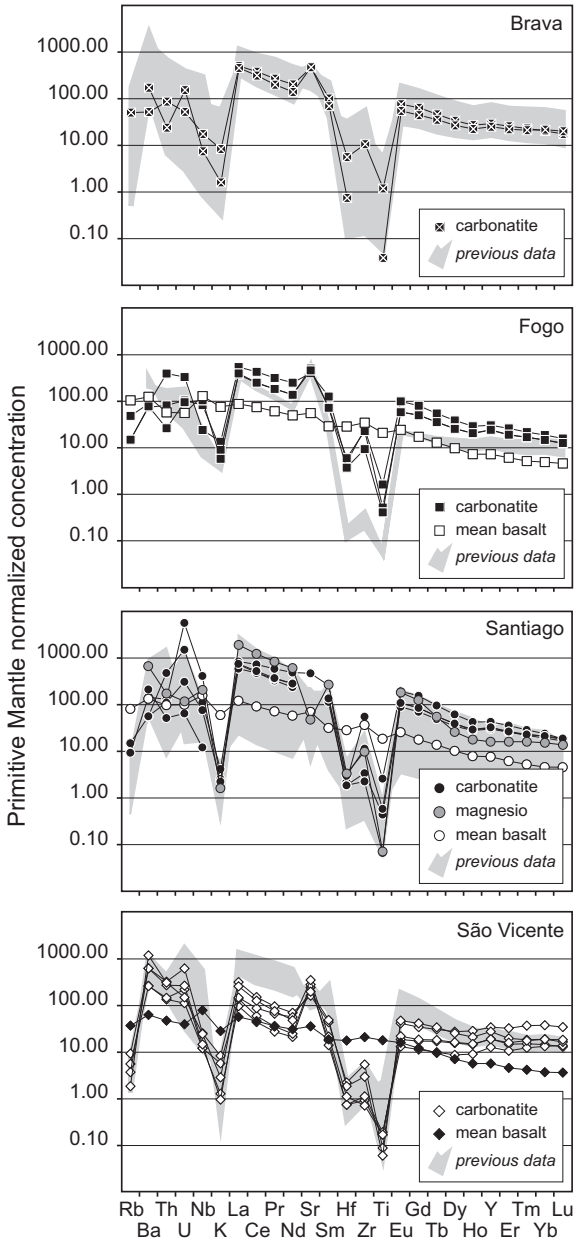


Fig. 3. Abundances of trace elements in carbonatite samples from Brava, Fogo, Santiago, and São Vicente Islands normalized to the primitive mantle values (Hofmann, 1988). Also given for comparison are fields defined by previous carbonatite data (Hoernle et al., 2002; Mourão et al., 2010) and mean basalt compositions for each Cape Verde Island (Gerlach et al., 1988; Jørgensen and Holm, 2002; Doucelance et al., 2003).

are sub-parallel with most elements (Th, La, Ce, Nd, Eu, Y) presenting the following features: (1) apatites show higher contents than carbonatites, (2) conversely, biotites have lower contents than whole-rock samples, and (3) concentrations measured for carbonates are similar to those determined for carbonatites. This suggests that trace element variations are mostly controlled by crystallization of apatites and biotites. Some elements such as Zr also display systematic depletion (except in São Vicente samples) in

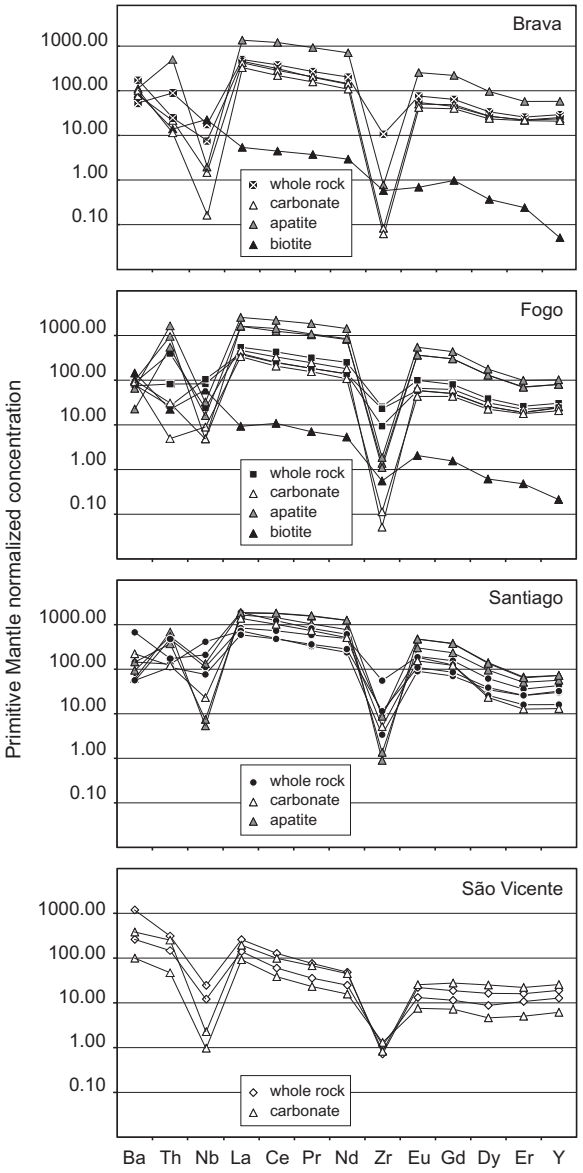


Fig. 4. Abundances of trace elements in separate phases and whole-rock carbonatites from Brava, Fogo, Santiago and São Vicente Islands normalized to the primitive mantle values (Hofmann, 1988).

separate phases relative to carbonatite samples requiring at least one another enriched phase to equilibrate their budget. This is also the case for Nb, although unbalance of Nb is less significant. Additional minerals (pyroxenes, sphenes, zirconolites and opaque minerals: mostly Ti-magnetite; no evidence for the presence of zircons) were observed in our samples, but were not analyzed due to their too small amount. Pyroxenes separated from alkaline rocks sometimes display high contents of Zr (~7% wt. $ZrO_2$ in aegirine, cf. Jones and Peckett, 1981), which can balance the Zr depletion of apatites, biotites and carbonate fractions. Partition coefficients that have been determined between CPX (augite) and carbonatite melts shows large variations: 0.29 (Green et al., 1992; Sweeney et al., 1995); 0.14–0.81

Table 2
Trace-element (ppm) concentrations in separate phases of Cape Verde carbonatites.

| | Apatite | | | | | | Carbonate | | | | Biotite | |
|---|---|---|---|---|---|---|---|---|---|---|---|---|
| | BR-15 | F-211C | F-230B | F-230C | S-309 | S-311 | S-352 | BR-15 | BR-23 | F-211C | F-230B | S-339 | SV-186 | SV-188 | BR-15 | F-211C |
| Rb | 1.7 | 0.5 | 8.5 | 0.8 | 0.5 | 1.2 | 0.5 | 1.0 | 0.8 | 0.8 | 1.1 | 1.2 | 0.9 | 1.0 | >500 | >500 |
| Ba | 671 | 397 | 137 | 599 | 376 | 881 | 573 | 467 | 613 | 596 | 554 | 1340 | 603 | 2310 | 517 | 874 |
| Th | 39.5 | 133.0 | 44.2 | 77.1 | 55.8 | 30.2 | 44.6 | 1.7 | 0.9 | 2.5 | 0.4 | 9.8 | 3.8 | 20.4 | 1.1 | 1.8 |
| U | 3.4 | 13.9 | 11.0 | 10.2 | 7.6 | 1.0 | 15.2 | 0.1 | 0.2 | 0.6 | 0.3 | 1.5 | 1.4 | 2.7 | <0.1 | 0.7 |
| Nb | 1.2 | 20.0 | 9.9 | 3.0 | 3.3 | 4.6 | 82.4 | 0.9 | 0.1 | 3.0 | 5.5 | 14.2 | 0.6 | 1.4 | 13.8 | 37.2 |
| La | 834 | 1560 | 983 | 995 | 1120 | 1010 | 1150 | 260 | 201 | 285 | 206 | 850 | 56.4 | 119 | 3.3 | 5.7 |
| Ce | 1930 | 3500 | 2000 | 2300 | 2850 | 2310 | 2910 | 456 | 349 | 530 | 330 | 1630 | 61.4 | 158 | 7.11 | 17.3 |
| Nd | 842 | 1700 | 967 | 1010 | 1480 | 919 | 1500 | 172 | 129 | 214 | 128 | 608 | 18.7 | 53.4 | 3.48 | 6.36 |
| Sr | >1000 | >1000 | >1000 | >1000 | >1000 | >1000 | >1000 | >1000 | >1000 | >1000 | >1000 | 720.0 | >1000 | >1000 | 138.0 | 50.9 |
| Sm | >100 | >100 | >100 | >100 | >100 | >100 | >100 | 25.2 | 19.2 | 32.8 | 20.1 | 81.8 | 3.1 | 8.4 | 0.5 | 1.0 |
| Hf | 0.3 | 0.3 | 0.2 | 0.2 | 0.2 | 0.1 | 0.4 | <0.1 | <0.1 | <0.1 | <0.1 | 0.2 | <0.1 | <0.1 | <0.1 | <0.1 |
| Zr | 7.5 | 18.1 | 13.4 | 10.7 | 8.7 | 13.2 | 85.0 | 0.8 | 0.6 | 0.5 | 1.1 | 49.9 | 12.7 | 8.0 | 5.6 | 5.4 |
| Eu | 37.1 | 79.6 | 52.8 | 53.1 | 69.5 | 43.9 | 68.9 | 7.3 | 6.1 | 9.6 | 6.3 | 22.4 | 1.1 | 3.7 | 0.1 | 0.3 |
| Tb | 12.5 | 25.4 | 16.8 | 17.2 | 20.0 | 13.4 | 19.9 | 3.1 | 2.6 | 3.7 | 2.6 | 4.5 | 0.5 | 2.5 | <0.1 | <0.1 |
| Y | 228 | 402 | 317 | 316 | 285 | 223 | 285 | 92.5 | 83.7 | 99.0 | 81.5 | 51.5 | 24.2 | 101 | 0.20 | 0.84 |
| Yb | 13.4 | 20.9 | 15.5 | 14.9 | 14.0 | 11.3 | 14.8 | 8.2 | 8.7 | 7.4 | 5.9 | 5.9 | 2.6 | 9.5 | <0.1 | <0.1 |
| Lu | 1.5 | 2.2 | 1.6 | 1.7 | 1.7 | 1.2 | 1.6 | 1.1 | 1.2 | 1.0 | 0.8 | 0.8 | 0.4 | 1.3 | <0.1 | <0.1 |

(Klemme et al., 1995); 0.15–1.4 (Blundy and Dalton, 2000); and 0.34 (Adam and Green, 2001), arguing in favor of a moderately incompatible to compatible behavior of Zr. Thus, CPX could control the Zr budget, providing that $D$ values determined for augite can be extrapolated to aegirine. Sphene and zirconolite are also capable of harboring significant amounts of Zr and Nb, as reported in carbonatites from other localities (Chakhmouradian, 2006). Lastly, the occurrence of Nb-rich ilmenite lamellae within titanomagnetites has also been described in carbonatites (Gaspar and Wyllie, 1983). Thus these minerals could also explain the Zr and Nb budgets of the carbonatites.

REE partition coefficients calculated between apatites and carbonatitic melts have been plotted in the Onuma diagram (Fig. 5). Carbonatitic melts have been recalculated from whole-rock carbonatites by removing apatites, using the simplifying assumption that the $P_2O_5$ content of whole rocks was related to apatites only. Three main features can be observed: (1) each sample shows a near-parabolic variation of $D^{REE}$ vs. ionic radius; (2) "parabolic" curves are parallel; and (3) heights of curves are related to the geographical location of samples (Fogo apatites display higher $D^{REE}$ values than Brava than Santiago). We used the lattice strain model of Blundy and Wood (1994) to quantify chemical and physical parameters of apatites. The model describes partitioning of elements $i$ with valence $n+$ entering lattice site $\alpha$ as a function of $r_i$, the radius of $i^{n+}$, $r^{n+}_{0(\alpha)}$, the ideal site radius, $E^{n+}_{\alpha}$, the effective Young's modulus of the site, and $D^{n+}_{0(\alpha)}$, the strain-free partition coefficient for a cation of radius $r^{n+}_{0(\alpha)}$:

$$D_{i^{n+}} = D^{n+}_{o(\alpha)} \cdot \exp\left( \frac{-4\pi E^{n+}_{\alpha} N_A \left[ \frac{r^{n+}_{o(\alpha)}}{2} (r_i - r^{n+}_{o(\alpha)})^2 + \frac{1}{3}(r_i - r^{n+}_{0(\alpha)})^3 \right]}{RT} \right) \quad (1)$$

with $R$, the gas constant, $N_A$, Avogadro's number and $T$, the temperature in Kelvin. $D^{n+}_{0(\alpha)}$, $r^{n+}_{0(\alpha)}$ and $E^{n+}_{\alpha}$ values range from (9.746, 0.975 Å, 306 GPa) to (4.134, 0.968 Å, 354 GPa) for the highest and lowest parabola ($T$ = 1000 °C), respectively. The fact that the observed $D^{REE}$ can be satisfactorily described by the lattice strain model strongly suggests that apatite and melt reached chemical equilibrium. $D^{REE}$ values all greater than unity are in agreement with experimental data of Ryabchikov et al. (1993) who determined partition coefficients of 1.3 and 1.13 for Ce and Yb (Exp. 3), respectively. This is in disagreement, however, with experimental results of Klemme and Dalpé (2003), who measured $D^{REE} < 1$ for apatite, although values determined for ideal site radius (0.94 Å) and Young's modulus (223–405 GPa) are comparable with ours.

### 4.3. Sr–Nd isotopic results

Measured $^{87}Sr/^{86}Sr$ and $^{143}Nd/^{144}Nd$ ratios for whole-rock calcio-carbonatites have a very narrow range (respectively, 0.703098–0.703356 and 0.512890–0.512944, respectively, see Table 3), compared to Cape Verde basaltic rocks ($^{87}Sr/^{86}Sr = \sim 0.7029$–$0.7039$ and $^{143}Nd/^{144}Nd = \sim 0.51260$–$0.51305$, see Escrig et al., 2005). These restricted isotope compositions are in agreement with previously published data for Cape Verde carbonatites (Gerlach et al., 1988; Hoernle et al., 2002; Escrig et al., 2005). Radioactive decay corrections do not affect Sr ratios and modify Nd values insignificantly, yielding $(^{143}Nd/^{144}Nd)_i = 0.512884$–$0.512941$.

Separate phases display uncorrected Sr–Nd isotope compositions in agreement with associated whole-rock carbonatites except for biotites from sample F-211C (Fogo) that show more radiogenic values for Sr. Once corrected for radioactive decay, all separates and related carbonatites display coherent initial Sr–Nd isotopic ratios (Table 3),

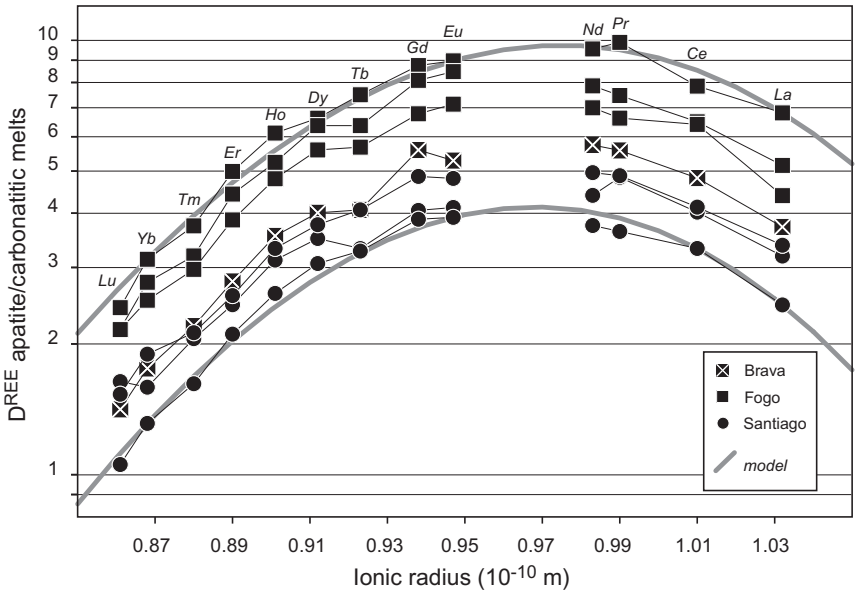


Fig. 5. Onuma diagrams of partition coefficients plotted vs. ionic radius in sixfold coordination for the REE (Shannon, 1976) showing compatible behavior of REE between apatites and carbonatite melts. Grey curves are best fit using the lattice strain model (Blundy and Wood, 1994).

Table 3
Strontium and neodymium isotopic compositions of Cape Verde carbonatites.

| Sample | Type[a] | Location | Age[b] Ma | [Rb] ppm | [Sr] ppm | $^{87}Rb/^{86}Sr$ | $^{87}Sr/^{86}Sr$ | $^{87}Sr/^{86}Sr_{INI}$ | [Sm] ppm | [Nd] ppm | $^{147}Sm/^{144}Nd$ | $^{143}Nd/^{144}Nd$ | $^{143}Nd/^{144}Nd_{INI}$ |
|---|---|---|---|---|---|---|---|---|---|---|---|---|---|
| Br-15 | WR | Brava | 2.0 | 27 | 8466 | 0.0092 | 0.703340 (12) | 0.703340 | 39.1 | 241 | 0.0981 | 0.512910 (07) | 0.512908 |
| Br-15 | Ap | Brava | 2.0 | 1.7 | >1000 | <0.0049 | 0.703322 (10) | 0.703322 | >100 | 842 | >0.0718 | 0.512912 (06) | 0.512911 |
| Br-15 | Cb | Brava | 2.0 | 1 | >1000 | <0.0029 | 0.703336 (08) | 0.703336 | 25.2 | 172 | 0.0886 | 0.512912 (04) | 0.512911 |
| Br-23 | WR | Brava | 2.0 | <1 | 8622 | <0.0003 | 0.703356 (08) | 0.703356 | 26.8 | 166 | 0.0976 | 0.512912 (09) | 0.512911 |
| F-211C | WR | Fogo | 4.0 | 26 | 7301 | 0.0103 | 0.703105 (11) | 0.703105 | 48.9 | 299 | 0.0989 | 0.512944 (05) | 0.512941 |
| F-211C | Ap | Fogo | 4.0 | 0.5 | >1000 | <0.0014 | 0.703116 (08) | 0.703116 | >100 | 1700 | >0.0356 | 0.512945 (06) | 0.512944 |
| F-211C | Bt | Fogo | 4.0 | >500 | 50.9 | >28.4282 | 0.704723 (10) | 0.703108 | 1 | 6.36 | 0.0950 | 0.512943 (08) | 0.512941 |
| F-211C | Cb | Fogo | 4.0 | 0.8 | >1000 | <0.0023 | 0.703117 (11) | 0.703117 | 32.8 | 214 | 0.0927 | 0.512944 (04) | 0.512941 |
| F-230B | WR | Fogo | 4.0 | 8 | 9222 | 0.0025 | 0.703108 (10) | 0.703108 | 28.5 | 166 | 0.1038 | 0.512942 (04) | 0.512939 |
| F-230C | WR | Fogo | 4.0 | 8 | 8411 | 0.0028 | 0.703098 (12) | 0.703098 | 28 | 164 | 0.1032 | 0.512944 (07) | 0.512941 |
| S-309 | WR | Santiago | 9.0 | 8 | 8568 | 0.0027 | 0.703184 (09) | 0.703183 | 101 | 583 | 0.1047 | 0.512902 (08) | 0.512896 |
| S-311 | WR | Santiago | 9.0 | 5 | >10000 | <0.0014 | 0.703210 (09) | 0.703209 | 44.4 | 284 | 0.0945 | 0.512890 (06) | 0.512885 |
| S-339 | WR | Santiago | 9.0 | <1 | 875 | <0.0033 | 0.703599 (12) | 0.703599 | 103 | 725 | 0.0859 | 0.512895 (06) | 0.512889 |
| S-352 | WR | Santiago | 9.0 | <1 | >10000 | <0.0003 | 0.703196 (07) | 0.703196 | 55.5 | 337 | 0.0996 | 0.512905 (14) | 0.512899 |
| S-569 | WR | Santiago | 9.0 | <1 | >10000 | <0.0003 | 0.703191 (10) | 0.703191 | 52.8 | 338 | 0.0944 | 0.512896 (06) | 0.512890 |
| SV-170 | WR | S. Vicente | 5.7 | <1 | 4456 | <0.0006 | 0.703136 (11) | 0.703136 | 6.89 | 25.3 | 0.1646 | 0.512896 (07) | 0.512890 |
| SV-178 | WR | S. Vicente | 5.7 | 5 | 2961 | 0.0049 | 0.703121 (08) | 0.703121 | 17 | 83.3 | 0.1234 | 0.512902 (05) | 0.512898 |
| SV-186 | WR | S. Vicente | 5.7 | 3 | 5146 | 0.0017 | 0.703124 (09) | 0.703124 | 5.47 | 29.5 | 0.1121 | 0.512901 (07) | 0.512897 |
| SV-187 | WR | S. Vicente | 5.7 | 2 | 3615 | 0.0016 | 0.703132 (12) | 0.703132 | 19 | 67.4 | 0.1704 | 0.512890 (10) | 0.512884 |
| SV-188 | WR | S. Vicente | 5.7 | 1 | 6423 | 0.0005 | 0.703120 (08) | 0.703120 | 8.39 | 57.6 | 0.0881 | 0.512907 (13) | 0.512904 |

Initial Sr ratio of sample F-211C-Bt was calculated using $^{87}Rb/^{86}Sr = 28.4282$; initial Nd compositions of samples Br-15-Ap and F-211C-Ap were determined using $^{147}Sm/^{144}Nd$ values of 0.0718 and 0.0356, respectively. Numbers in parentheses are 2σ errors referring to the last significant digits.

[a] WR: whole rock; Ap: apatite; Bt: biotite; Cb: carbonate fraction.

[b] Ages are taken from Mata et al. (2010).

which confirm their cogenetic link, with apatites and biotites resulting from batch crystallization.

In a $^{143}Nd/^{144}Nd_{ini}$ vs. $^{87}Sr/^{86}Sr_{ini}$ plot of calcio-carbonatites, samples of each island define a narrow field that does not overlap with those of other islands (Fig. 6). This may partly result from a sampling bias as all carbonatites from Santiago and São Vicente Islands come from the same outcrop in each case (Fig. 1). When considering previous data for calcio-carbonatites (Gerlach et al., 1988; Hoernle et al., 2002; Escrig et al. 2005; Mourão et al., 2010) ranges of variations are extended to higher values without overlapping of carbonatite/island fields. Within each island, most of the variation of isotope compositions is related to Sr, whereas Nd is almost constant. Adding São Vicente carbonatites analyzed by Gerlach et al. (1988) and Hoernle et al. (2002) increases the $^{87}Sr/^{86}Sr$ variability by a factor >30 while $^{143}Nd/^{144}Nd$ is not modified. In the same way, additional data for Fogo and Santiago (Gerlach et al., 1988; Hoernle et al., 2002; Escrig et al., 2005) mostly affect the Sr range of variations. This suggests that part of the Sr composition of calcio-carbonatites could reflect low temperature/supergenic alteration, as it was already stated by Hoernle et al. (2002) for some Santiago magnesio-carbonatite samples, based on $\delta^{13}C$ and $\delta^{18}O$ results. Calcio-carbonatites from Brava also show larger variations for both Sr and Nd isotopic ratios than samples from other islands. This has to be related to the peculiar characteristics of Brava Island, where calcio-carbonatites were emplaced both before and after the shield phase (Turbeville and Wolff, 1989; Hoernle et al., 2002; Mourão et al., 2010; Madeira et al., 2010). Taken separately, samples from the basement (pre-shield activity, 2 Ma, with $^{87}Sr/^{86}Sr = 0.703340–0.703356$ and $^{143}Nd/^{144}Nd = 0.512900–0.512911$), on the one hand, and samples from the late stage of the development of the island (post-shield activity, <1000a, with $^{87}Sr/^{86}Sr = 0.703557–0.703630$ and $^{143}Nd/^{144}Nd = 0.512790–0.512816$), on the other hand, show restricted ranges of isotopic variations and form two distinct groups.

Magnesio-carbonatites (represented here by sample S-339 from Santiago Island) were previously interpreted as reflecting secondary process for their major- and trace element characteristics because of the presence of secondary dolomite replacing calcite and high $\partial^{13}C$ and $\partial^{18}O$ values (Hoernle et al., 2002). Initial Nd and Pb isotope compositions measured for these samples, however, were shown to be inconsistent with secondary processes, and were interpreted as source-derived. Note that Sr isotopic ratio of magnesio-carbonatite S-339 is more radiogenic than Santiago calcio-carbonatites (0.703599 compared to 0.703184–0.703210), although both types have similar Nd compositions (0.512895 compared to 0.512890–0.512905, see Table 3), in agreement with observations made by Hoernle et al. (2002).

Calcio-carbonatites that have been sampled in Fuerteventura, Canary (the only other oceanic locality for carbonatites) also show restricted ranges of initial Sr and Nd isotopic ratios with $^{87}Sr/^{86}Sr = 0.70319–0.70331$ and $^{143}Nd/^{144}Nd = 0.51284–0.51288$ (data from Hoernle et al., 2002; De Ignacio et al., 2006). Sr compositions measured in Fuerteventura carbonatite samples are on average more radiogenic than those of Fogo, Santiago and São Vicente, but less than Brava. Conversely, Nd isotopic ratios are higher for Cape Verde calcio-carbonatites (except "young" Brava) than for Fuerteventura. Nevertheless, Cape Verde and Canary calcio-carbonatites display close isotope compositions compared to the isotopic variability of continental carbonatites (Hoernle et al., 2002; De Ignacio et al., 2006).

Cape Verde basaltic rocks show a strong dichotomy of their geochemical signature between the Northern and the

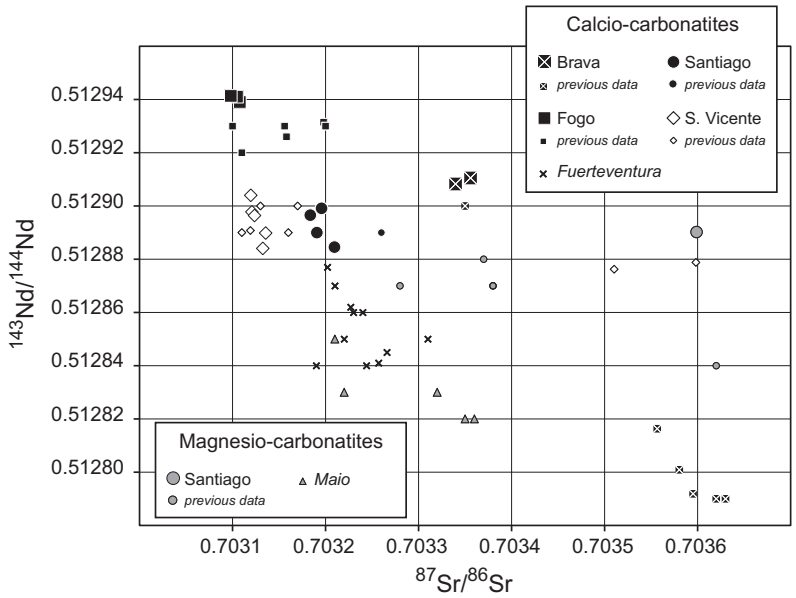


Fig. 6. Sr–Nd initial isotope compositions of Cape Verde carbonatites and comparison with literature data (Gerlach et al., 1988; Hoernle et al., 2002; Escrig et al., 2005; Mourão et al., 2010; Fuerteventura: Hoernle et al., 2002; De Ignacio et al., 2006). Note that data from Escrig and co-authors are not age-corrected, but radioactive decay corrections do not modify Sr–Nd values significantly.

Southern Islands. From an isotopic point of view, samples collected on Fogo, Santiago and Maio plot above the North Hemisphere Reference Line (NHRL, cf. Hart, 1984) in a $^{208}Pb/^{204}Pb$ vs. $^{206}Pb/^{204}Pb$ isotope variation diagram, whereas basalts from Santo Antão, São Vicente, São Nicolau and Sal all display Pb compositions below the NHRL (see whole-archipelago studies for a complete overview of the dichotomy: Gerlach et al., 1988; Doucelance et al., 2003). In the same way, samples from the Southern Islands display more radiogenic Sr values than samples from the Northern Islands. Conversely, Nd isotope compositions are less radiogenic for samples from the Southern Islands than for those collected on the Northern Islands (Fig. 7). Such a relationship between the isotopic signature of samples and geography is not observed at first sight for carbonatites. Except 0.0 Ma-old samples from Brava, all calcio-carbonatites fall in the field of the Northern Islands for Sr and Nd isotopes (Fig. 7). However, carbonatites from the Southern Islands tend to plot on the right part of the mantle array, whereas samples from the Northern Islands plot to the left. Considering Pb isotopes confirms that calcio-carbonatites do not share the same compositional divide as silicate rocks (Fig. 8). Carbonatites either fall in the field of basalts from the Northern Islands or show more radiogenic $^{206}Pb/^{204}Pb$ ratios, whereas basalts from the Southern Islands present less radiogenic values.

## 5. DEPTH OF ORIGIN OF CAPE VERDE CARBONATITES

### 5.1. Previous models for the origin of oceanic carbonatites

Geochemical studies of Cape Verde and Canary carbonatites (Hoernle et al., 2002; De Ignacio et al., 2006; Mourão et al., 2010; Mata et al., 2010) have proposed that carbonatites are plume-derived. From a chemical point of view, carbonatites and silicate melts can derive from a common, plume-related parent by low, but distinct, degrees of melting (e.g. Gudfinnsson and Presnall, 2005; Dasgupta et al., 2006). However, the association of both types of magmas can also be generated, either by immiscible separation from a carbonated silicate melt (Koster van Groos and Wyllie, 1963; Kjarsgaard and Hamilton, 1989; Brooker, 1998) or by crystal fractionation of a carbonated silicate liquid (King and Sutherland, 1960; Lee and Wyllie, 1994; Veksler et al., 1998).

#### *5.1.1. Model 1: Melting of recycled crustal material carried by the plume*

Hoernle et al. (2002) have interpreted the long-lived isotope signature measured in Cape Verde calcio-carbonatite samples as deriving from Early to Middle Proterozoic carbonated oceanic crust (recycling age of ~1.6 Ga), whereas magnesio-carbonatites are related to the plume recycling

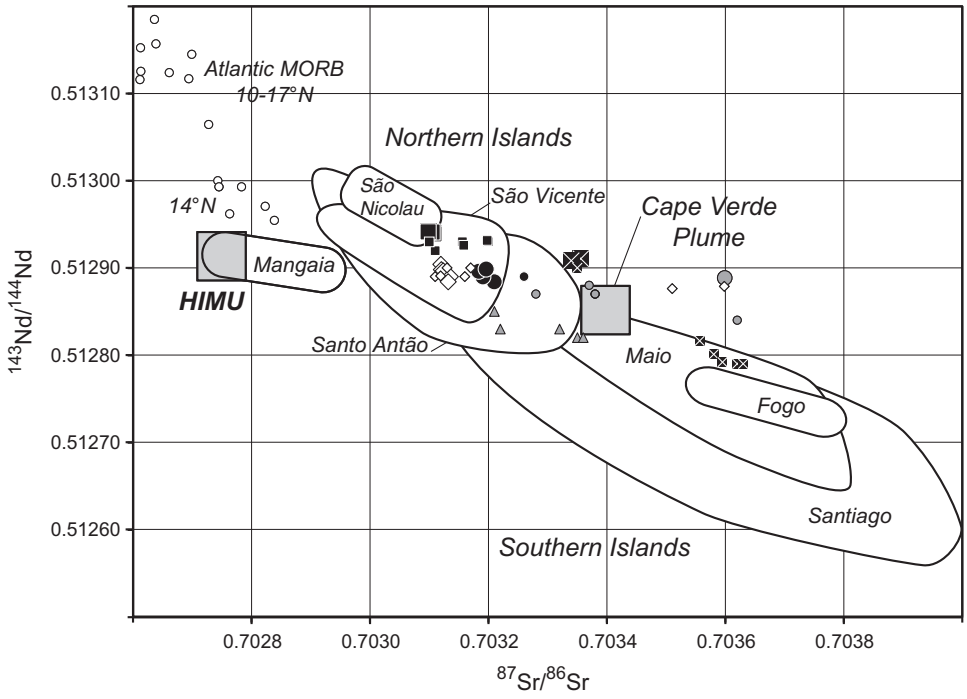


Fig. 7. Comparison between carbonatites and silicate rocks from the Cape Verde archipelago in the $^{143}Nd/^{144}Nd$ vs. $^{87}Sr/^{86}Sr$ diagram. Fields for basalts from the Northern and the Southern Islands of the Cape Verde archipelago are drawn using literature data (Gerlach et al., 1988; Jørgensen and Holm, 2002; Doucelance et al., 2003; Escrig et al., 2005; Holm et al., 2006; Millet et al., 2008; Barker et al., 2009, 2010; Martins et al., 2010). The isotopic composition of the Cape Verde plume is from Millet et al. (2008). Small open circles correspond to Atlantic MORB sampled between latitudes 10 and 17°N (Dosso et al., 1993). Mangaia Island (data from Woodhead, 1996) represents the extreme HIMU signature. Other symbols are as in Fig. 6.

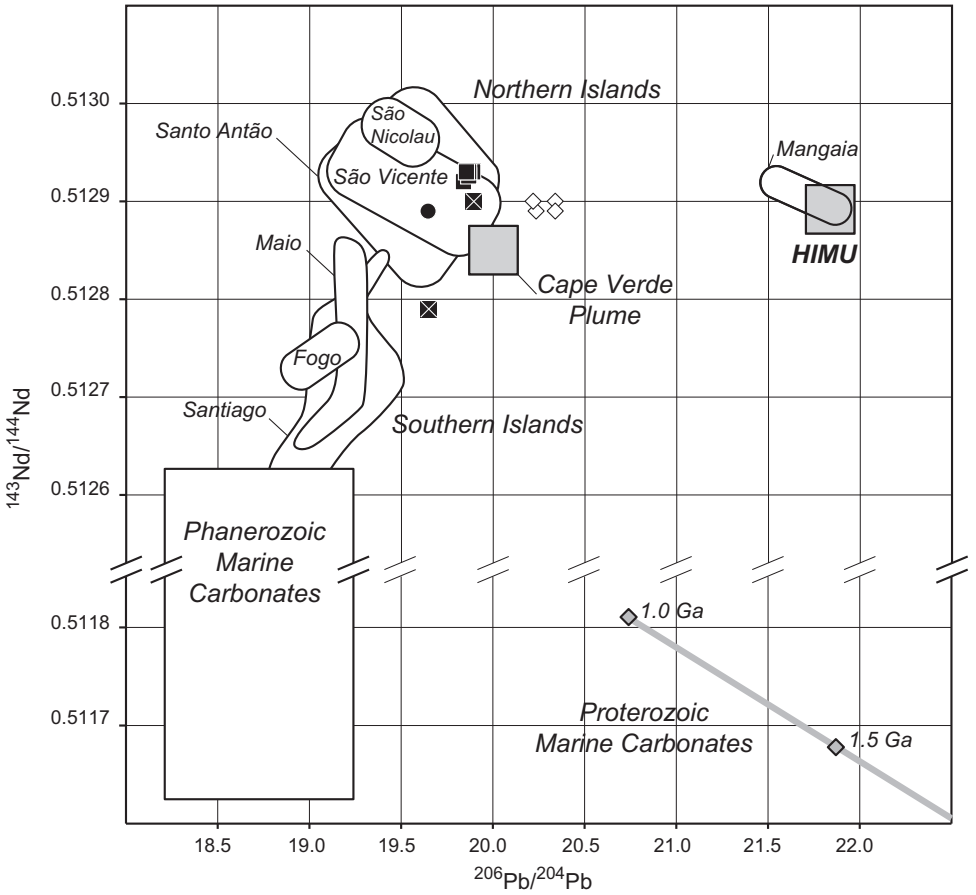


Fig. 8. Comparison between calcio-carbonatites and silicate rocks from the Cape Verde archipelago in the $^{143}Nd/^{144}Nd$ vs. $^{206}Pb/^{204}Pb$ diagram. Calcio-carbonatite data are from Hoernle et al. (2002) and Escrig et al. (2005). Symbols are as in Fig. 6. Fields for basalts from the Northern and Southern Islands are drawn using literature data (Gerlach et al., 1988; Jørgensen and Holm, 2002; Escrig et al., 2005; Holm et al., 2006; Millet et al., 2008; Barker et al., 2009, 2010). Fields for Phanerozoic and Proterozoic marine carbonates come from Hoernle et al. (2002). The isotopic composition of the Cape Verde plume is from Millet et al. (2008). Mangaia Island (data from Woodhead, 1996) represents the extreme HIMU signature.

of sub-continental lithosphere because, among other arguments, of unusual isotopic ratios (less radiogenic Nd and Pb isotopic ratios, together with negative Δ7/4 values relative to calcio-carbonatites) that were only measured in the Smoky Butte lamproites, Montana (Fraser et al., 1985/86). Some of the magnesio-carbonatites are also thought to reflect secondary process for their major- and trace element characteristics because of the presence of secondary dolomite replacing calcite and of high $\partial^{13}C$ and $\partial^{18}O$ values. This last point was already outlined by Javoy et al. (1985) who interpreted the highest $\partial^{18}O$ and $\partial^{13}C$ values of carbonatites as magmatic evolution combined with alteration and contamination by seawater and/or interaction with surrounding pillow lavas because of the positive correlation between stable isotopes and REE contents. The model of Hoernle et al. (2002) is compatible with available Os isotope data measured by Escrig et al. (2005) who found initial $^{187}Os/^{188}Os$ values of 0.1698 and 0.1718 for two calcio-carbonatites from Fogo. These are expected values for recycling of old, carbonated oceanic crust. However, these Os values do not provide a unique solution, as we will discuss in the following sections.

Melting of recycled oceanic crust (eclogite) was originally proposed by Nelson et al. (1988) to explain some continental carbonatites. It relies on the fact that (1) carbon must be recycled into the mantle to balance continuous $CO_2$ emission by volcanism (Zhang and Zindler, 1993) and (2) contrary to water, carbon remains trapped in the subducted plate as carbonates during early stages of subduction, allowing to consider deep recycling into the mantle (Molina and Poli, 2000). However, experimental studies have also shown that subducted slabs will decarbonate at maximum 10–11 GPa, excluding recycling of carbonated oceanic crust to depths greater than 300 km (Hammouda, 2003). This last result raises the question of how carbonates can be recycled deeply in the mantle (670 or 2900 km) in order to be incorporated in the source of mantle plumes.

*5.1.2. Model2: Melting of non-recycled origin, i.e. primitive material in the plume*

Mata et al. (2010) measured relatively unradiogenic $^{4}He/^{3}He$ ratios in calcite separates from São Vicente calcio-carbonatites, as well as mantle-like $\partial^{13}C$ values, favoring a deep mantle, non-recycled origin for the source of

Cape Verde carbonatites. Since the Cape Verde plume is deeply rooted in the lower mantle (Montelli et al., 2006; Zhao, 2007) they proposed that the source of calcio-carbonatites is located at the base of the mantle. It could be constituted either of basaltic protocrust with a chondrite-like regolith containing solar-wind-implanted gases (Tolstikhin and Hofmann, 2005; Tolstikhin et al., 2006) or of melt produced at the mantle bottom early in the Earth history (Labrosse et al., 2007). This last model is partly in agreement with results by Dasgupta et al. (2009) who have shown that trace-element contents obtained by small-degree partial melts generated from a primitive composition have values similar to natural oceanic carbonatites. This is also partly in agreement with conclusion from De Ignacio et al. (2006) who have proposed that Canary calcio-carbonatites are derived from a heterogeneous mantle plume with a FOZO-HIMU mixing-like component.

### 5.2. Testing the models against Sr–Nd data

Fig. 9 compares initial Sr–Nd ratios determined for carbonatites from the Cape Verde and Canary Islands (data from Gerlach et al., 1988; Hoernle et al., 2002; Escrig et al., 2005; De Ignacio et al., 2006; Mourão et al., 2010; this study) with measurements of Atlantic MORB samples collected at latitudes 10–17°N (Dosso et al., 1993), Smoky Butte lamproites (Fraser et al., 1985/86), Proterozoic and Phanerozoic marine carbonates (see figure caption for references), and Lower Mantle (LM, Doucelance et al., 2003), HIMU (interpreted as recycled, 1.5–2 Ga oceanic crust, cf. Weaver, 1991; Chauvel et al., 1992), D″ (Tolstikhin et al., 2006), and FOZO (Hauri et al., 1994; Stracke et al., 2005; Jackson et al., 2007) compositions. Several comments in relation with previous studies can be made:

- The involvement of a FOZO component is difficult to evaluate. Most Sr–Nd ratios of calcio-carbonatites lie in the FOZO box (Hauri et al., 1994) of Fig. 9a. Hence it is impossible to state about a HIMU–FOZO mixing as proposed by De Ignacio et al. (2006). This is not better when considering recent definitions of the FOZO component (Stracke et al., 2005; FOZO B – Northern Hemisphere: Jackson et al., 2007) with most carbonatites plotting outside of the FOZO–HIMU mixing field (Fig. 9a). Furthermore, it has to be noted that a FOZO component is not necessarily required to explain Canary basalts (Hoernle et al., 1991; Widom et al., 1999; Gurenko et al., 2006).
- Calcio-carbonatites do not plot between recycled oceanic crust (HIMU) and ~1.6 Ga (or older) marine carbonates (Fig. 9b). This is particularly true for Brava 2 Ma samples. Thus their compositions cannot be explained as resulting from the binary mixing between these two components as proposed by Hoernle et al. (2002). The same conclusion is reached on the basis of Pb isotopes (Fig. 8): $^{206}Pb/^{204}Pb$ isotopic ratios measured for Cape Verde calcio-carbonatites range between 19.646 and 20.338 (data from Hoernle et al., 2002; Escrig et al., 2005), whereas ~1.6 Ga marine carbonates and recycled oceanic crust are expected to show values >21.5 (Fig. 8; Chauvel et al., 1992).
- Smoky Butte lamproites resemble 0.75–1.75 Ga marine carbonates (similar Sr and lower Nd) so influence of sub-continental lithosphere is difficult to qualify based on Sr–Nd isotope systematic only.
- Comparison with modeled Lower Mantle (LM) and D″ compositions (Doucelance et al., 2003; Tolstikhin et al., 2006) also shows that Cape Verde carbonatites cannot be explained by melting of such components only, but require, at least, one additional component.

Looking in more details at calcio-cabonatites in the $^{143}Nd/^{144}Nd_{ini}$ vs. $^{87}Sr/^{86}Sr_{ini}$ plot (Fig. 9a) reveals that variations registered by our São Vicente samples, on the one hand, and our Brava carbonatites (including the 3 datapoints by Mourão et al. (2010) that were also determined in Clermont-Ferrand with the same chemical protocol and the same TIMS instrument), on the other hand, define two alignments enclosing all calcio-carbonatites and intercepting at low Sr and high Nd isotopic values ($^{87}Sr/^{86}Sr$ ~0.7028 and $^{143}Nd/^{144}Nd$ ~0.5131) close to the field of Atlantic MORB collected between 10 and 17°N (Dosso et al., 1993). This last observation argues in favor of a mixing between an end-member with a MORB-like Sr–Nd isotopic composition and two other end-member with more enriched compositions (more radiogenic Sr and unradiogenic Nd) to explain calcio-carbonatites, rather than the involvement of recycled oceanic crust. This could also reveal a pseudo-binary mixing between the MORB-like end-member and a second one resulting from earlier mixing, as it will be developed in the following sections.

### 5.3. Shallow vs. deep origin for oceanic carbonatites

Radiogenic isotope ratios of Cape Verde basalts show relationship with geographical location. They are best explained by variable mixing between three end-members: (1) a radiogenic Pb end-member with intermediate Sr and Nd, common to all islands; (2) an enriched end-member with a EM1-like isotope signature prevalent in the Southern Islands; and (3) a depleted end-member, mainly influencing Northern Island compositions. The high $^{3}He/^{4}He$ ratios associated with the radiogenic Pb end-member (Christensen et al., 2001; Doucelance et al., 2003) implies a deep origin, leading to the conclusion this end-member represents the deep-seated source of the Cape Verde plume. The elevated Nb/U signature found in Northern Island basalts uncorrelated with isotopic tracers, however, suggests melting of an amphibole/phlogopite-bearing source that is unstable in a mantle plume (Class and Goldstein, 1997). Together with correlation of $Na_2O$ contents and Sr isotopes at the archipelago scale, this rather indicates mixing of plume melts with lithospheric melts (Millet et al., 2008). Consequently, the depleted end-member has been identified as being the Cape Verde lithosphere (Millet et al., 2008). In the same way, the relationship between time, isotope ratios and differentiation markers in Southern Island basalts suggests assimilation of the Southern Island enriched end-member (Hoernle et al., 1991; Escrig et al., 2005). Os isotopic composition have been thus explained by the melting of subcontinental lithosphere material together with lower

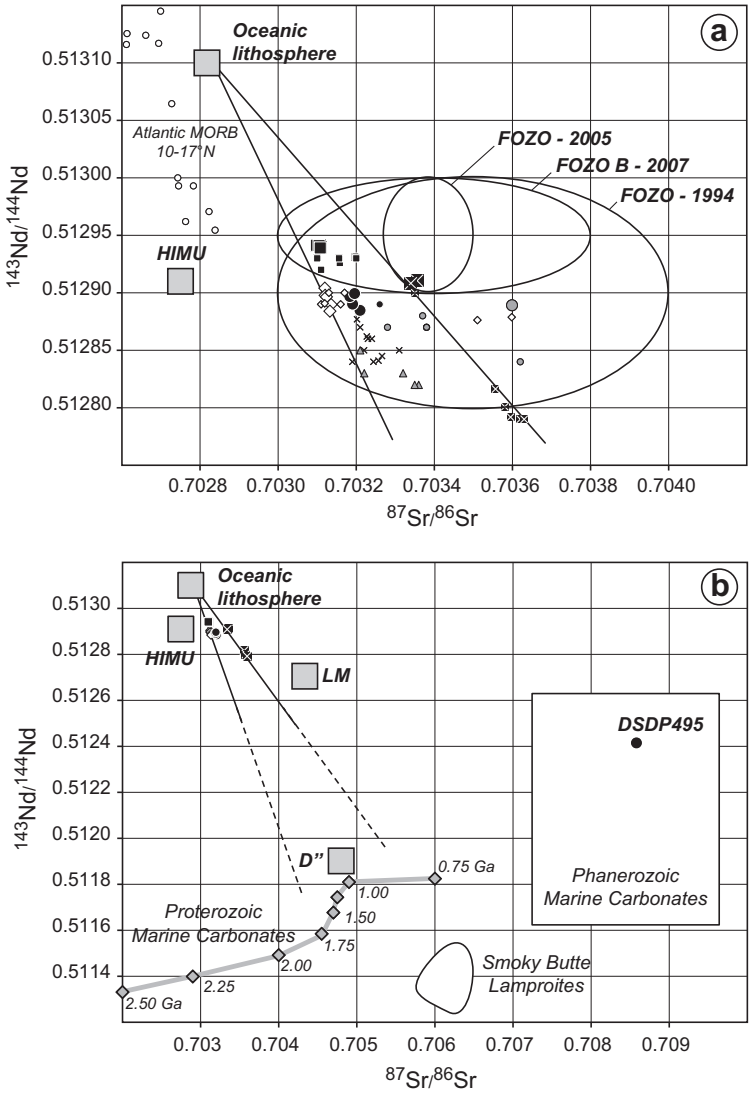


Fig. 9. (a) Cape Verde calcio-carbonatites show Sr–Nd isotopic variations enclosed in a triangular shape, defined by São Vicente and Brava samples. They are interpreted as the mixing between a depleted end-member (unradiogenic Sr and radiogenic Nd), similar in composition to MORB samples (10–17°N, data from Dosso et al., 1993) and identified to the local oceanic lithosphere, and two other enriched end-members (radiogenic Sr and unradiogenic Nd). *FOZO-1994*, *FOZO-2005* and *FOZO B-2007* (Northern Hemisphere) are from Hauri et al. (1994), Stracke et al. (2005) and Jackson et al. (2007), respectively. (b) Comparison with Phanerozoic and Proterozoic marine carbonates. The curve for Proterozoic marine carbonates corresponds to average seawater (Derry and Jacobsen, 1988; Shields and Veizer, 2002). The field for Phanerozoic marine carbonates corresponds to measurements of shells (Whittaker and Kyser, 1993), foraminiferes (Janz and Vennemann, 2005), fish teeth (Staudigel et al., 1985/86; Martin and Haley, 2000), barites (Martin et al., 1995), biogenic apatites (Bertram et al., 1992; Holmden et al., 1996) and marine carbonates (Blair, 2006). DSDP495 is from Plank and Langmuir (1998). The field for Smoky Butte lamproites was drawn after data from Fraser et al. (1985/86). LM corresponds to the Lower Mantle (Doucelance et al., 2003). D″ is from Tolstikhin et al. (2006). Other symbols are as in Fig. 6. Note that straight lines do not correspond to calculated mixing lines: they indicate that calcio-carbonatites correspond to a three-component mixing system.

continental crust fragments incorporated within the Cape Verde oceanic lithosphere during the opening of the Atlantic Ocean (Escrig et al., 2005).

Therefore, it can be inferred from the comparison with Cape Verde silicate rocks that the depleted end-member involved in the genesis of calcio-carbonatites also corresponds to the local oceanic lithosphere. The identification of enriched end-members, however, is more difficult. They can be associated neither with the EM1-like sub-continental lithosphere identified in Cape Verde basalts (the sub-continental lithosphere is rather related to magnesio-carbonatites, see Section 5.1) nor with Cape Verde plume pristine melts that present too low Sr isotopic ratios to explain Brava calcio-carbonatites (Fig. 7). This is also the case when considering Pb isotopes. The estimated composition of the Cape Verde plume (Millet et al., 2008) does plot as an end-member of calcio-carbonatites in the $^{143}Nd/^{144}Nd$ vs. $^{206}Pb/^{204}Pb$ plot (Fig. 8). On the contrary, the Cape Verde plume presents intermediate $^{206}Pb/^{204}Pb$ ratios relative to calcio-carbonatites. The isotopic composition of the

enriched end-members is rather in agreement with old, marine carbonates (Fig. 9b), as proposed by Hoernle et al. (2002), or any component with a similar composition. For example, Tolstikhin et al. (2006) have argued for the existence of an ancient, isolated reservoir located at the core–mantle boundary and presenting enriched compositions (Sr–Nd isotopic ratios close to 0.7048 and 0.5119, respectively). This reservoir (D″ layer) could be the source of high $^{3}He/^{4}He$ ratios determined for Cape Verde basalts from the Northern Islands (Doucelance et al., 2003) as it has been proposed that the Cape Verde plume is deeply rooted in the mantle down to the core-mantle boundary (Montelli et al., 2006; Zhao, 2007).

Therefore, different models can be proposed for the source of Cape Verde calcio-carbonatites. The latter could not to be supplied by the Cape Verde mantle plume, but would reside at shallow level in the oceanic lithosphere. In this case, their source would be composed of either lithospheric material metasomatized by carbonatitic melts, or veins of marine carbonates deeply located in the oceanic lithosphere. In such a model, the contribution from the Cape Verde plume for the genesis of calcio-carbonatites is then limited to be thermal, as previously proposed for the origin of Cape Verde basalts showing a HIMU-like isotope signature (Kokfelt et al., 1998), causing partial melting of the heterogeneous Cape Verde lithosphere. This would be also in agreement with Allègre et al. (1971) who concluded that oceanic carbonatites could be related to pre-Mid-Atlantic rifting.

Mixing of veins of marine carbonates and lherzolite could explain the Sr–Nd isotope compositions of carbonatites. However, higher $\partial^{13}C$ ratios than measured mantle values (Kogarko, 1993; Hoernle et al., 2002; Mata et al., 2010) are expected with such an origin. Considering that there is no simple mechanism to incorporate marine carbonates deeply into the oceanic lithosphere, this model will be no longer discussed.

Direct partial melting of a metasomatized mantle source was already advanced to explain the genesis of continental carbonatites (Wyllie and Huang, 1975; Wallace and Green, 1988; Wyllie and Lee, 1998). Notably, Bell et al. (1982) and Kalt et al. (1997) have proposed that melting of sub-continental lithospheric material generated Canadian and East African Rift carbonatites. A lithospheric origin for carbonatites can explain three important, no-isotopic features of oceanic carbonatites. (1) At the archipelago scale (Cape Verde or Canary), heterogeneous metasomatism of the oceanic lithosphere can explain why carbonatites do not occur on every island of these two archipelagos, compared to plume-related basalts that build all islands. (2) At a more global scale (mantle scale), such a model can also explain why carbonatites are so rare in an oceanic setting. Their occurrence is indeed restricted to the presence of a mantle plume underneath an oceanic lithosphere with a pre-existing, complex history (which is not always the case). (3) Lastly, this model does not require deep recycling into the mantle (at depth greater than 300 km, see Hammouda, 2003) of marine carbonates being sampled in a second stage by a mantle plume. It should be noted, however, that other oceanic localities present the same characteristics than Cape Verde and Canary archipelagos, i.e. an old, metasomatized lithosphere together with a mantle plume, for which these are no outcropping carbonatites, although carbonatitic melts have been evidenced at depth (Samoa: Hauri et al., 1993; Comores: Coltorti et al., 1999; Fernando de Noronha: Kogarko et al., 2001; Kerguelen: Moine et al., 2004).

The existence of a metasomatized lithosphere underneath the Cape Verde archipelago was recently discussed (Bonadiman et al., 2005). Spinel-peridotite xenoliths collected on Sal Island present secondary parageneses that are characterized by pyroxene minerals associated with the destabilization of clino- and ortho-pyroxenes after reaction with metasomatic, kimberlite-like fluids. In the same way, Martins et al. (2010) described Santiago xenoliths where orthopyroxene reacted to clinopyroxene. These xenoliths are also characterized by the presence of hydrated minerals and calcite, compatible with the occurrence of metasomatic events involving a low silica activity metasomatic agent. Some aspects of the lavas geochemistry (very low Ti/Eu, high Sr/Sm) were interpreted as reflecting a carbonatitic nature of the metasomatic agent. It has to be noted, however, that textural observations made on Sal xenoliths were also interpreted as reaction during transport of the xenoliths to the surface (Shaw et al., 2006).

As an alternative, the source of calcio-carbonatites could be mostly related to the Cape Verde mantle plume, being composed of material from the D″ layer assimilating the oceanic lithosphere as it was proposed for silicate rocks (Millet et al., 2008). This would explain the relatively primitive $^{4}He/^{3}He$ signature measured in calcite separates from São Vicente carbonatites (Mata et al., 2010). This would be also in agreement with the modeling of trace element patterns of carbonatites presented by Dasgupta et al. (2009). We have modeled assimilation using Sr and Nd contents of 82.775 and 5.406 ppm, respectively, for D″ (D″ is estimated to contain 17.5% of the terrestrial amount of incompatible trace elements, cf. Tolstikhin et al., 2006) together with $^{87}Sr/^{86}Sr$ and $^{143}Nd/^{144}Nd$ isotopic ratios of 0.7048 and 0.5119 (Tolstikhin et al., 2006), as well as reasonable Sr and Nd contents of 10 and 1 ppm with $^{87}Sr/^{86}Sr = 0.7028$ and $^{143}Nd/^{144}Nd = 0.5131$ for the Cape Verde oceanic lithosphere (Fig. 9a). Unreasonably large amounts of lithosphere assimilation (>95%) are required to obtain isotopic ratios compatible with the depleted Sr–Nd isotope compositions of carbonatites. The end-result would be no longer a carbonatite.

Turning to magnesio-carbonatites, our set of data is limited to one sample. Nevertheless, assuming that sub-continental lithosphere indeed explains Nd and Pb isotope compositions measured in magnesio-carbonatites (Hoernle et al., 2002), we propose their source to be also related to fragments of sub-continental lithosphere incorporated into the oceanic lithosphere during the opening of the Atlantic ocean (Escrig et al., 2005).

## 6. MODELING OF CAPE VERDE CALCIO-CARBONATITE SOURCE

We have tested a model that takes into account all observations discussed earlier, except carbon isotopes. Mantle products (OIB and MORB, see Cartigny et al.,

1998) as well as Cape Verde carbonatites have a $\partial^{13}C$ average values of ~-5.5‰, interpreted as representative of the mantle. However, they also show some variability (from −8.0‰ to +1.9‰ in the case of Cape Verde calcio-carbonatites, cf. Kogarko, 1993; Hoernle et al., 2002; Mata et al., 2010; from −8.0‰ to −3.0‰ when ignoring one sample from Santiago). This suggests the existence of fractionation processes that are presently not well constrained. Our model considers that the source of calcio-carbonatites is located in the oceanic lithosphere (see Section 5.4.) and consists of lherzolite metasomatized by carbonatitic melts. Two distinct origins have been considered for the carbonatitic metasomatic agent: (1) melts originating from partial melting of recycled, carbonated oceanic crust, or (2) melts resulting from partial melting of Cape Verde plume material. In this second model, the HIMU-like Cape Verde plume contains recycled, carbonated oceanic crust from which carbonatitic melts are released before metasomatizing the oceanic lithosphere. This model is similar to the one proposed by Baker et al. (1998) for metasomatism of the Yemen lithosphere by the Afar plume. Trace element patterns as well as radiogenic isotope ratios (Sr, Nd) of carbonatites can only be satisfactorily reproduced by the model that involves a metasomatic agent derived from recycling, while He compositions are explained by interaction with melts originating from the Cape Verde plume.

It has to be noted that the Cape Verde mantle plume could also carry out part of the depleted component involved in calcio-carbonatites. This would result in a hybrid model with a lower proportion of Cape Verde lithosphere compared to what will be discussed in the following sections.

### 6.1. Description of trace element, and Sr and Nd isotope modeling

The model consists of three successive stages: (1) Genesis of the metasomatic agent; (2) Metasomatism of the oceanic lithosphere consisting of lherzolite by infiltrating carbonatitic melts; and (3) Partial melting of metasomatized lherzolite and final emplacement of calcio-carbonatites. For step (1), we consider the two alternative scenarios discussed above. Trace element budget for melting of plume material was determined using partition coefficients of Dasgupta et al. (2009) assuming mineralogy of a peridotite (0.55/0.25/0.11/0.09 for ol/opx/cpx/gt). Initial trace element composition of plume material is taken identical to either D″ component, assuming that D″ contains 17.5% of the terrestrial amount of incompatible trace elements (Tolstikhin et al., 2006), or a mixing of 42% of 2 Ga-old recycled oceanic crust (taken identical to MORB) and 58% of lower mantle material (Doucelance et al., 2003). On the other hand, trace element budget for melting of carbonated eclogite was determined using partition coefficients of Hammouda et al. (2009) combined with Dasgupta et al. (2009) for Rb, Ba, Nb, Zr and Hf. Here, we assumed that garnet and clinopyroxene were the main phase controlling trace element budget, using the mineralogy experimentally determined by Hammouda et al. (2009), i.e. cpx = 44.5% and garnet = 23.8%. For step (2) and (3), we used partition coefficient of Adam and Green (2001) at 2.5 GPa (the Cape Verde lithosphere is estimated to ~80–90 km, Cazenave et al., 1988) for all trace elements, assuming control by clinopyroxene. The mineralogy of lherzolite is taken similar to that of Cape Verde lherzolite xenoliths with cpx = 13% (Bonadiman et al., 2005). Its initial trace element composition is assumed to be similar to that of the depleted MORB mantle (DMM, Workman and Hart, 2005). Initial trace element compositions of recycled oceanic crust and marine carbonates are from Hofmann (1988) and Plank and Langmuir (1998, DSDP495), respectively. Batch partial melting at step (1) was 5%, assuming that melting degree is controlled by the amount of carbonates in the mixing of marine carbonates and oceanic crust (5%). For step (2), we considered a simple addition of melt to the lherzolite followed by equilibration with clinopyroxene in mass proportions 1.5/98.5. Because of the low melt fraction, we did not consider a chromatographic model. For step (3), we considered 1.5% degree of batch melting, assuming that the mass proportion of carbonatitic melts controls the melting degree. Trace element contents of end-members are given in Table 4.

The "first" model (metasomatic agent originating from the plume) does not reproduce trace-element patterns of calcio-carbonatites (Fig. 10a). Notably the model fails to reproduce the positive (Ba, Sr) and negative (Rb, Nb) anomalies of samples. Conversely, the "second" model (partial melting of recycled, carbonated oceanic crust forming the metasomatic agent) permits to retrieve most trace element characteristics of calcio-carbonatites (Fig. 10b) keeping in mind that carbonatite samples do not correspond to quenched melts. Notably the model reproduces the positive (Ba, Sr) and negative (Rb, Nb, Zr, Hf) anomalies of calcio-carbonatites, as well as the higher fractionation of light REE relative to heavy REE, together with the small positive Y anomaly. A more robust approach, in the form of a Monte-Carlo-type numerical simulation where the source composition, the partition coefficients and the melting fraction are randomly chosen within a ±30% range of variations of their nominal values confirms the good match between the "second" model and measured Cape Verde carbonatite trace-element patterns.

In the following step, strontium and neodymium isotopic ratios were modeled considering the second scenario only. For this purpose, we used average Sr and Nd contents of 1500 and 10 ppm (Plank and Langmuir, 1998) and isotopic ratios of 0.707 and 0.5122 (Fig. 9b and Burke et al., 1982) for recycled, Phanerozoic carbonates, reasonable values of 150 and 10 ppm for Sr and Nd contents together with $^{87}Sr/^{86}Sr$ and $^{143}Nd/^{144}Nd$ ratios of 0.7025 and 0.5127 for recycled, 400 Ma-old MORB (using evolution curves of the depleted mantle by Workman et al. (2005) and Vervoort and Blichert-Toft (1999), respectively), as well as Sr and Nd contents of 10 and 1 ppm and isotopic compositions of 0.7028 and 0.5131 (Fig. 9a) for lherzolite. Note that 400 Ma-old carbonates and crust are chosen to illustrate the model because they are in agreement with geodynamic models of closure of the Rheic Ocean and opening of the Central Atlantic (Scotese, 2002). Our data do not allow constraining tightly the timing of recycling, and a bit older or younger carbonates are also possible candidates. At first

Table 4
Trace element concentrations (ppm) of end-members used in models.

| | PM[a] | DMM[b] | LM[c] | D″[d] | MORB[e] | Carbonate[f] | Carb. eclogite[g] | CV plume[h] |
|---|---|---|---|---|---|---|---|---|
| Rb | 0.5353 | 0.05 | 0.454 | 2.433 | 1.262 | 7.7 | 1.58 | 0.79 |
| Ba | 6.049 | 0.563 | 5.127 | 27.496 | 13.87 | 2145 | 120.43 | 8.80 |
| Nb | 0.6175 | 0.1485 | 0.539 | 2.807 | 3.507 | 0.79 | 3.37 | 1.79 |
| La | 0.6139 | 0.192 | 0.543 | 2.791 | 3.895 | 14.22 | 4.41 | 1.95 |
| Ce | 1.6011 | 0.55 | 1.425 | 7.278 | 12.001 | 5.13 | 11.66 | 5.87 |
| Pr | 0.2419 | 0.107 | 0.219 | 1.100 | 2.074 | 1.42 | 2.04 | 1.00 |
| Nd | 1.1892 | 0.581 | 1.087 | 5.406 | 11.179 | 10.13 | 11.13 | 5.33 |
| Sr | 18.21 | 7.664 | 16.438 | 82.775 | 113.2 | 1504 | 182.74 | 57.08 |
| Sm | 0.3865 | 0.239 | 0.362 | 1.757 | 3.752 | 2.48 | 3.69 | 1.79 |
| Hf | 0.2676 | 0.157 | 0.249 | 1.216 | 2.974 | 0.17 | 2.83 | 1.39 |
| Zr | 9.714 | 5.082 | 8.936 | 44.156 | 104.24 | 5.9 | 99.32 | 48.96 |
| Eu | 0.1456 | 0.096 | 0.137 | 0.662 | 1.335 | 0.49 | 1.29 | 0.64 |
| Gd | 0.5128 | 0.358 | 0.487 | 2.331 | 5.077 | 2.63 | 4.95 | 2.41 |
| Tb | 0.094 | 0.07 | 0.090 | 0.427 | 0.885 | 0.47 | 0.86 | 0.42 |
| Dy | 0.6378 | 0.505 | 0.615 | 2.899 | 6.304 | 3.05 | 6.14 | 3.00 |
| Ho | 0.1423 | 0.115 | 0.138 | 0.647 | 1.342 | 0.65 | 1.31 | 0.64 |
| Y | 3.94 | 3.328 | 3.837 | 17.910 | 35.82 | 31.9 | 35.62 | 17.27 |
| Er | 0.4167 | 0.348 | 0.405 | 1.894 | 4.143 | 1.8 | 4.03 | 1.98 |
| Tm | 0.0643 | 0.055 | 0.063 | 0.292 | 0.621 | 0.26 | 0.60 | 0.30 |
| Yb | 0.4144 | 0.365 | 0.406 | 1.884 | 3.9 | 1.57 | 3.78 | 1.87 |
| Lu | 0.0637 | 0.058 | 0.063 | 0.290 | 0.589 | 0.24 | 0.57 | 0.28 |

[a] Primitive Mantle: Hofmann (1988).
[b] Depleted MORB Mantle: Workman and Hart (2005).
[c] Lower Mantle = binary mixing between primitive mantle and depleted mantle in proportions 16.8:83.2 (Doucelance et al., 2003).
[d] D″ corresponds to 17.5% of the terrestrial amount of incompatible trace elements (Tolstikhin et al., 2006).
[e] Hofmann (1988).
[f] DSDP495: Plank and Langmuir (1998).
[g] Carbonated eclogite = binary mixing between MORB and carbonates in mass proportions 95:5.
[h] Cape Verde plume = binary mixing between MORB and lower mantle in mass proportions 42:58.

sight, calculations do not allow us reproducing Sr–Nd isotope compositions of calcio-carbonatites. Instead, we obtain $^{87}Sr/^{86}Sr$ and $^{143}Nd/^{144}Nd$ isotopic ratios of 0.70386 and 0.51279 that plot out of the field of carbonatites for 95:5 basalt to carbonate sediment ratio at stage1 and 98.5:1.5 mixing ratio at stage2. However, acceptable modification of input parameters (notably mixing proportions between recycled carbonates and MORB set to 3:97 and between carbonatitic melts and lithosphere to 1:99) helps improving results with $^{87}Sr/^{86}Sr$ and $^{143}Nd/^{144}Nd$ isotopic ratios of 0.70343 and 0.51280. This result is confirmed with a Monte-Carlo-type numerical simulation in which isotope compositions of end-members, mixing and melting proportions (first and second mixing) and partition coefficients are randomly chosen within ±150 ppm, ±20%, ±60% and ±25% ranges of variations relative to their nominal values, respectively. Modeled Sr–Nd isotope compositions define a field that encompasses that of natural carbonatite samples (Fig. 11). The Monte-Carlo-type simulation, more especially the ±150 ppm relative variation on isotopic ratios, also allows integrating the radioactive decay of $^{87}Rb$ and $^{147}Sm$ in the different components, which was not taken into account in the direct calculation.

The model, however, does not explain relatively primitive $^4He/^3He$ ratios that were measured in calcite separates from São Vicente (Mata et al., 2010) because recycled carbonates, MORB and oceanic lithosphere are expected to present MORB-like to radiogenic He signatures.

### 6.2. Helium modeling

The low $^4He/^3He$ signature in both basalts and carbonatites from the Northern Cape Verde Islands has been associated with the Cape Verde plume (Christensen et al., 2001; Doucelance et al., 2003; Mata et al., 2010). A way to reconcile radiogenic isotope ratios and rare gas signatures would be then the assimilation of plume melts by carbonatites. Such an idea is reinforced by the similar, regional distribution of $^4He/^3He$ ratios in both silicate rocks and carbonatites from the Cape Verde archipelago, with samples from the Northern Islands displaying relatively primitive He signatures whereas samples from the Southern Islands have MORB-like values (Doucelance et al., 2003; Mata et al., 2010). Assimilation may be strongly limited due to the very low miscibility of silicate and carbonatitic melts. Our data show that calcio-carbonatites have maximum $SiO_2$ contents of around 5 wt.% (~3 wt.% in samples from Hoernle et al., 2002). These contents are partly related to the presence of biotites. Thus only a maximum mass proportion of 2–3% can be considered for contamination of the carbonatite source by plume melts.

The $^4He/^3He$ ratio of plume melts can be estimated with a two-stage model assuming that the source of Cape Verde basalts corresponds to the mixing of recycled, old oceanic crust and lower mantle material in the mass proportions of ~40:60 (Doucelance et al., 2003; Millet et al., 2008). In detail, we first calculate the Pb isotopic composition of

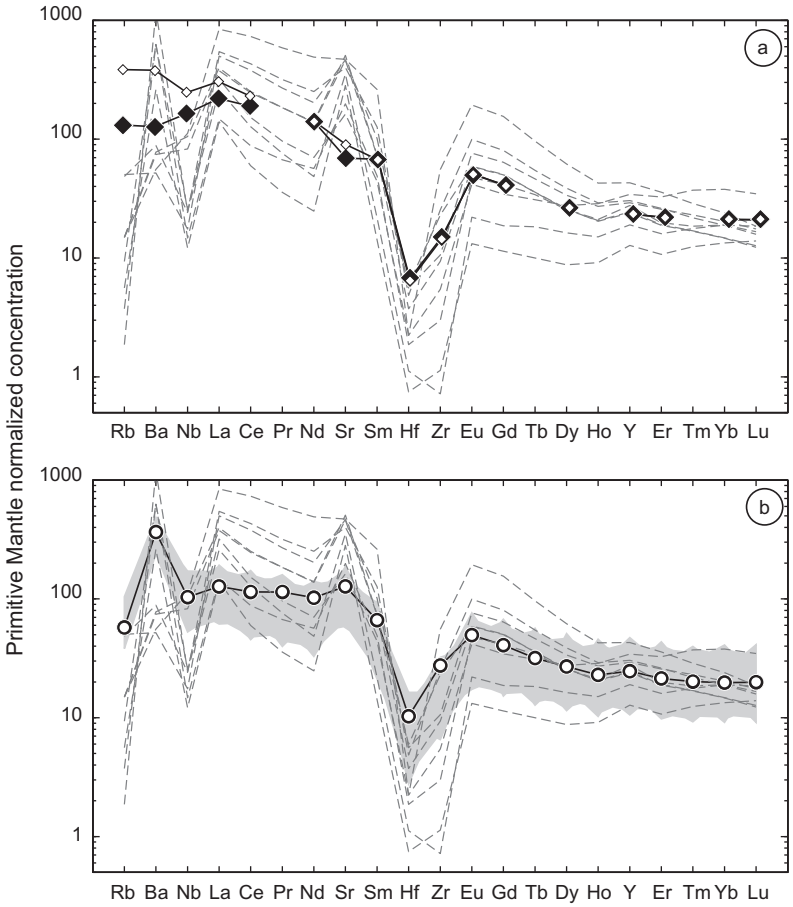


Fig. 10. Trace element contents of calcio-carbonatites modeled by partial melting of metasomatized oceanic lithosphere by carbonatitic melts. (a) Carbonatitic melts result from partial melting of Cape Verde plume material, assuming either a D″ composition (open diamonds) or a ROC–LM mixing composition (filled diamonds). Dashed grey lines are carbonatite samples from Cape Verde (this study). Comparison shows that model fails at reproducing trace element characteristics of natural samples. (b) Filled circles correspond to carbonatitic melts originating from partial melting of recycled, carbonated oceanic crust. Open circles include small assimilation of plume melts (Average São Nicolau basalts, Millet et al., 2008). Dashed grey lines are as in Fig. 10a. The grey area correspond to a Monte-Carlo-type numerical simulation in which trace element contents and partition coefficients are randomly chosen within a ±30% interval. Modeling allows retrieving general characteristics of natural samples, notably the positive (Ba, Sr) and negative (Rb, Nb, Zr, Hf) anomalies, as well as the higher fractionation of light REE relative to heavy REE, together with the small positive Y anomaly. See text for details of calculations.

the Cape Verde plume source that results from the mixing between 2-Ga recycled oceanic crust (ROC, 2 stage-model with $\mu_1 = 8$, $\mu_2 = 21$, $\kappa_1 = 3.8$ and $\kappa_2 = 3.05$) and lower mantle material (LM, see Doucelance et al., 2003 for details of calculations) using Pb contents of 0.3 and 0.2 ppm for ROC and LM, respectively. We then determine the $^4$He content of ROC using Th and U concentrations determined with μ and κ data. ROC R/Ra value, however, is set to zero due to degassing at ridge. Lastly, assuming a $^4$He content of $1 \times 10^{-4}$ ccSTP/g for LM (Allègre et al., 1987) and a $R/Ra$ value corresponding to the most unradiogenic value measured for OIB in Baffin Island samples (Stuart et al., 2003), we obtain a $R/Ra$ value of ~43.7 for plume melts. In a second step, we consider the assimilation of plume melts by the degassed, carbonatized lithosphere. For this purpose, the $^4$He content is assumed to be minimum $2 \times 10^{-8}$ ccSTP/g for plume melts (Doucelance et al., 2003) and $1 \times 10^{-9}$ ccSTP/g for the lithosphere. The $R/Ra$ value of the latter is taken identical to that of MORB, i.e. $R/Ra = 8$ (Allègre et al., 1995). Assimilation in mass proportions between 3:97 and 2:98 gives $^4$He/$^3$He ratios ranging from 43,985 to 51,439 in agreement with published data (46,700–57,400, cf. Mata et al., 2010).

Taking into account a late assimilation of plume melts (in mass proportions of 2:98) does not modify modeled $^{87}$Sr/$^{86}$Sr and $^{143}$Nd/$^{144}$Nd isotopic ratios of carbonatites. We calculate identical values of 0.70343 and 0.51281 when assuming Sr and Nd contents of respectively 730 and 40 ppm (average basalts contents, cf. Millet et al., 2008) and Sr and Nd isotopic ratios of 0.7034 and 0.51285 (Fig. 7) for plume melts. These values are in agreement with the range of variations observed in our carbonatite samples (0.7031–0.7036 and 0.51279–0.51294, see Table 3). In conclusion, late assimilation of small proportion of plume melts to calcio-carbonatite source allows satisfactory modeling of He composition, without modifying Sr–Nd isotopic ratio nor trace element patterns of modeled carbonatites (Figs. 10b and 11).

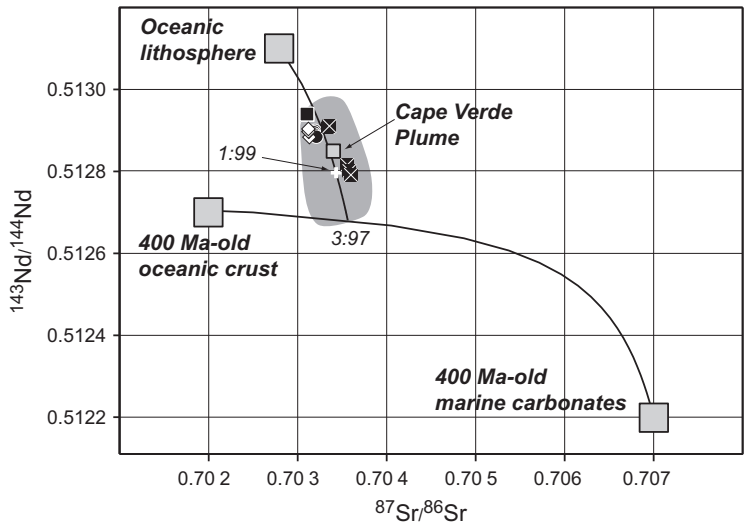


Fig. 11. Sr–Nd isotope ratios of calcio-carbonatites modeled by partial melting of oceanic lithosphere metasomatized by carbonatitic melts originating from partial melting of 400 Ma-old recycled, carbonated oceanic crust. All symbols are as in Fig. 6. Mixing curves illustrates the two step model at the origin of carbonatites: (1) partial melting of recycled oceanic crust and marine carbonates in proportions 97:3; (2) mixing of carbonatitic melts thus generated and oceanic lithosphere in proportions 1:99 (materialized by the white cross). They grey area correspond to a Monte-Carlo-type numerical simulation in which end-member isotope compositions, mixing and melting proportions (first and second mixing) and partition coefficients are randomly chosen within ±150 ppm, ±20%, ±60% and ±25% ranges of variations. Overlapping of model and natural sample fields demonstrates the good match between modeling and data. See text for details of calculations.

## 7. SUMMARY

Cape Verde calcio-carbonatites show small, but significant Sr–Nd isotope variations defining mixing trends between a depleted end-member (unradiogenic Sr and radiogenic Nd) and either marine carbonates or any other component with similar Sr–Nd to explain their compositions. Comparison with silicate rocks from the Cape Verde archipelago leads to the interpretation that the depleted end-member corresponds to the local oceanic lithosphere. As a consequence, we propose that Cape Verde calcio-carbonatites result from plume-induced melt generation of the carbonatite-metasomatized oceanic lithosphere with small assimilation of Cape Verde plume melts. The metasomatic agent would result from the subduction and recycling into the mantle of ~400 Ma-old marine and secondary carbonates and MORB during closure of the Rheic Ocean. The Cape Verde oceanic lithosphere would then result from the incorporation of carbonatitic-metasomatized mantle during opening of the Central Atlantic. Trace element patterns as well as Sr–Nd–He isotopic compositions of natural samples are reproduced using partition coefficients that were experimentally determined as well as trace element contents and isotope signatures previously published. Thus, this makes the shallow origin a reasonable and valid alternative to the plume origin model.

A shallow origin for oceanic carbonatites could furthermore explain the rarity of oceanic carbonatites because it requires very specific conditions: (1) the oceanic lithosphere must be thick in order to favor plume-induced partial melting at its base; (2) the oceanic lithosphere must have had a complex history (metasomatism by carbonatitic melts and, for Cape Verde, incorporation of fragments of sub-continental lithosphere); and (3) there must be a mantle plume.

## ACKNOWLEDGMENTS

The authors thank J. Mata for fruitful discussions on the manuscript, as well as providing carbonatite samples together with L.C. Silva. They also greatly thank C. Nicollet for his help with geodynamical models. R.D. is grateful to C. Bosq for skilled assistance during chemical separation of Sr and Nd. This paper was improved by critical comments by D.W. Peate, C. Bonadiman and an anonymous reviewer. Funding for this study was provided by the FEDER/FCT project PLINT (POCTI/CTA/45802/2002) and the INSU project SEDIT 2007&2009.

## REFERENCES

Adam J. and Green T. (2001) Experimentally determined partition coefficients for minor and trace elements in peridotite minerals and carbonatitic melt, and their relevance to natural carbonatites. *Eur. J. Mineral.* **13**, 815–827.

Allègre C. J., Pineau F., Bernat M. and Javoy M. (1971) Evidence for the occurrence of carbonatites on the Cape Verde and Canary Islands. *Nat. Phys. Sci.* **233**, 103–104.

Allègre C. J., Staudacher T. and Sarda P. (1987) Rare gas systematics: formation of the atmosphere, evolution and structure of the Earth's mantle. *Earth Planet. Sci. Lett.* **81**, 121–150.

Allègre C. J., Moreira M. and Staudacher T. (1995) $^{4}He/^{3}He$ dispersion and mantle convection. *Geophys. Res. Lett.* **22**, 2325–2328.

Assunção C. F. T., Machado F. and Gomes R. A. (1965) On the occurrence of carbonatites in the Cape Verde Islands. *Bol. Soc. Geol. Port.* **16**, 179–188.

Baker J., Chazot G., Menzies M. and Thirlwall M. (1998) Metasomatism of the shallow mantle beneath Yemen by the Afar plume – implications for mantle plumes, flood volcanism, and intraplate volcanism. *Geology* **26**, 431–434.

Barker A. K., Holm P. M., Peate D. W. and Baker J. A. (2009) Geochemical stratigraphy of submarine lavas (3–5 Ma) from

the Flamengos Valley, Santiago, southern Cape Verde islands. *J. Petrol.* **50**, 169–193.

Barker A. K., Holm P. M., Peate D. W. and Baker J. A. (2010) A 5 million year record of compositional variations in mantle sources to magmatism on Santiago, southern Cape Verde archipelago. *Contrib. Mineral. Petrol.* **160**, 133–154.

Bell K., Blenkinsop J., Cole T. J. S. and Menagh D. P. (1982) Evidence from Sr isotopes for long-lived heterogeneities in the upper mantle. *Nature* **298**, 251–253.

Bertram C. J., Elderfield H., Aldridge R. J. and Conway Morris S. (1992) $^{87}Sr/^{86}Sr$, $^{143}Nd/^{144}Nd$ and REEs in Silurian phosphatic Fossils. *Earth Planet. Sci. Lett.* **113**, 239–249.

Blair S. W. (2006) Nd isotopes: investigation of Cretaceous ocean anoxic event 2 and a systematic study of Fe–Mn oxide coatings. *Master thesis*, Univ. Florida.

Blundy J. D. and Wood B. J. (1994) Prediction of crystal-melt partition coefficients from elastic moduli. *Nature* **372**, 452–454.

Blundy J. and Dalton J. (2000) Experimental comparison of trace element partitioning between clinopyroxene and melt in carbonate and silicate systems, and implications for mantle metasomatism. *Contrib. Mineral. Petrol.* **139**, 356–371.

Bonadiman C., Beccaluva L., Coltorti M. and Siena F. (2005) Kimberlite-like metasomatism and 'garnet signature' in spinel-peridotite xenoliths from Sal, Cape Verde archipelago: relics of a sub-continental mantle domain within the Atlantic oceanic lithosphere. *J. Petrol.* **46**, 2465–2493.

Brooker R. A. (1998) The effect of $CO_2$ saturation on immiscibility between silicate and carbonate liquids: an experimental study. *J. Petrol.* **39**, 1905–1915.

Burke W. H., Denison R. E., Hetherington E. A., Koepnick R. B., Nelson H. F. and Otto J. B. (1982) Variation of seawater $^{87}Sr/^{86}Sr$ throughout Phanerozoic time. *Geology* **10**, 516–519.

Cartigny P., Harris J. W., Phillips D., Girard M. and Javoy M. (1998) Subducted-related diamonds? The evidence for a mantle-derived origin from coupled $\partial^{13}C$–$\partial^{15}N$ determinations. *Chem. Geol.* **147**, 147–159.

Cazenave A., Dominh K., Rabinowicz M. and Ceuleneer G. (1988) Geoid and depth anomalies over ocean swells and troughs: evidence of an increasing trend of the geoid to depth ratio with age of plate. *J. Geophys. Res.* **93**, 8064–8077.

Chakhmouradian A. R. (2006) High-field-strength elements in carbonatitic rocks: Geochemistry, crystal chemistry and significance for constraining the sources of carbonatites. *Chem. Geol.* **235**, 138–160.

Chauvel C., Hofmann A. W. and Vidal P. (1992) HIMU–EM" The French Polynesian connection. *Earth Planet. Sci. Lett.* **110**, 99–119.

Christensen B. P., Holm P. M., Jambon A. and Wilson J. R. (2001) Helium, argon and lead isotopic compositions of volcanics from Santo Antão and Fogo, Cape Verde Islands. *Chem. Geol.* **178**, 127–142.

Class C. and Goldstein S. L. (1997) Plume–lithosphere interactions in the ocean basins: constraints from the source mineralogy. *Earth Planet. Sci. Lett.* **150**, 245–260.

Coltorti M., Bonadiman C., Hinton R. W., Siena F. and Upton B. G. J. (1999) Carbonatite Metasomatism of the oceanic upper mantle: evidence from clinopyroxenes and glasses in ultramafic xenoliths of grande comore, Indian Ocean. *J. Petrol.* **40**, 133–165.

Dalton J. A. and Presnall D. C. (1998) The continuum of primary carbonatitic–kimberlitic melt compositions in equilibrium with lherzolite: data from the system $CaO–MgO–Al_2O_3–SiO_2–CO_2$ at 6 GPa. *J. Petrol.* **39**, 1953–1964.

Dalton J. A. and Wood B. J. (1993) The compositions of primary carbonate melts and their evolution through wallrock reaction in the mantle. *Earth Planet. Sci. Lett.* **119**, 511–525.

Dasgupta R., Hirschmann M. M. and Stalker K. (2006) Immiscible transition from carbonate-rich to silicate-rich melts in the 3 GPa melting interval of eclogite + $CO_2$ and genesis of silica-undersaturated ocean island lavas. *J. Petrol.* **47**, 647–671.

Dasgupta R., Hirschmann M. M., McDonough W. F., Spiegelman M. and Withers A. C. (2009) Trace element partitioning between garnet lherzolite and carbonatite at 6.6 and 8.6 GPa with applications to the geochemistry of the mantle and of mantle-derived melts. *Chem. Geol.* **262**, 57–77.

Davies G. R., Norry M. J., Gerlach D. C. and Cliff R. A. (1989) A combined chemical and Sr–Nd–Pb isotope study of the Azores and Cape Verde hot-spots: the geodynamic implications. In *Magmatism in the Ocean Basins*, vol. 42 (eds. A. D. Saunders and M. J. Norry). Geol. Soc. Spec. Publ., pp. 231–255.

De Ignacio C., Muñoz M., Sagredo J., Fernandez-Santin S. and Johansson A. (2006) Isotope geochemistry and FOZO mantle component of the alkaline–carbonatitic association of Fuerteventura, Canary Islands, Spain. *Chem. Geol.* **232**, 99–113.

Deines P. (1989) Stable isotope variations in carbonatites. In *Carbonatites: Genesis and Evolution* (ed. K. Bell). Unwin Hyman Ltd., London, UK, pp. 301–359.

Dosso L., Bougault H. and Joron J.-L. (1993) Geochemical morphology of the North Mid-Atlantic Ridge, 10–24 N: trace element-isotope complementarity. *Earth Planet. Sci. Lett.* **120**, 443–462.

Doucelance R., Escrig S., Moreira M., Gariépy C. and Kurz M. D. (2003) Pb–Sr–He isotope and trace element geochemistry of the Cape Verde Archipelago. *Geochim. Cosmochim. Acta* **67**, 3717–3733.

Eggler D. H. (1978) The effect of carbon dioxide upon partial melting of peridotite in the system sodium oxide-calcium oxide-aluminum oxide-magnesium oxide-silicon dioxide-carbon dioxide to 35 kb, with an analysis of melting in a peridotite-water-carbon dioxide system. *Am. J. Sci.* **278**, 305–343.

Escrig S., Doucelance R., Moreira M. and Allègre C. J. (2005) Os isotope systematics in Fogo basalts: evidence for lower continental crust residing in the oceanic lithosphere beneath the Cape Verde Islands. *Chem. Geol.* **219**, 93–113.

Fraser K. J., Hawkesworth C. J., Erlank A. J., Mitchell R. H. and Scott-Smith B. H. (1985/1986) Sr, Nd and Pb isotope and minor element geochemistry of lamproites and kimberlites. *Earth Planet. Sci. Lett.* **76,** 57–70.

Gaspar J. and Wyllie P. J. (1983) Ilmenite in the carbonatites from the Jacupiranga Complex, Brazil. *Am. Mineral.* **68**, 960–971.

Gerlach D. C., Cliff R. A., Davies G. R., Norry M. and Hodgson N. (1988) Magma sources of the Cape Verdes archipelago: isotopic and trace element constraints. *Geochim. Cosmochim. Acta* **52**, 2979–2992.

Green T. H., Adam J. and Hie S. H. (1992) Trace element partitioning between silicate minerals and carbonatite at 25 kbar and application to mantle metasomatism. *Mineral. Petrol.* **46**, 179–184.

Grevemeyer I. (1999) Isostatic geoid anomalies over mid-plate swells in the Central North Atlantic. In Hotspots and oceanic crust in interaction (eds. P. Charvis, J.J. Danobeitia). *J. Geodyn.* **28**, pp. 41–50.

Gudfinnsson G. H. and Presnall D. C. (2005) Continuous gradations among primary carbonatitic, kimberlitic, melilititic, basaltic, picritic and komatiitic melts in equilibrium with garnet lherzolite at 3–8 GPa. *J. Petrol.* **46**, 1645–1659.

Gurenko A. A., Hoernle K. A., Hauff F., Schmincke H.-U., Han D., Miura Y. N. and Kaneoka I. (2006) Major, trace element and Nd–Sr–Pb–O–He–Ar isotope signatures of shield stage lavas from the central and western Canary Islands: insights into mantle and crustal processes. *Chem. Geol.* **233**, 75–112.

Hammouda T. (2003) High-pressure melting of carbonated eclogite and experimental constraints on carbon recycling and storage in the mantle. *Earth Planet. Sci. Lett.* **214**, 357–368.

Hammouda T. and Laporte D. (2000) Ultrafast mantle impregnation by carbonatite melts. *Geology* **28**, 283–285.

Hammouda T., Moine B. N., Devidal J. L. and Vincent C. (2009) Trace element partitioning during partial melting of carbonated eclogites. *Phys. Earth Planet. Int.* **174**, 60–69.

Hart S. R. (1984) A large-scale isotope anomaly in the Southern Hemisphere mantle. *Nature* **309**, 753–757.

Hauri E. H., Shimizu N., Dieu J. J. and Hart S. R. (1993) Evidence for hotspot-related carbonatite metasomatism in the oceanic upper mantle. *Nature* **365**, 221–227.

Hauri E. H., Whitehead J. A. and Hart S. R. (1994) Fluid dynamic and geophysical aspects of entrainment in mantle plumes. *J. Geophys. Res.* **99**, 24275–24300.

Hoernle K., Tilton G. and Schmincke H.-U. (1991) Sr–Nd–Pb isotopic evolution of Gran Canaria: evidence for shallow enriched mantle beneath the Canary Islands. *Earth Planet. Sci. Lett.* **106**, 44–63.

Hoernle K., Tilton G., LeBas M. J., Duggen S. and Garbe-Schönberg D. (2002) Geochemistry of oceanic carbonatites compared with continental carbonatites: mantle recycling of oceanic crustal carbonate. *Contrib. Mineral. Petrol.* **142**, 520–542.

Hofmann A. W. (1988) Chemical differentiation of the Earth: the relationship between mantle, continental crust and oceanic crust. *Earth Planet. Sci. Lett.* **90**, 297–314.

Holm P. M., Wilson J. R., Christensen B. P., Hansen L., Hansen S. L., Hein K. M., Mortensen A. K., Pedersen R., Plesner S. and Runge M. K. (2006) Sampling the Cape Verde mantle plume: evolution of melt composition on Santo Antão, Cape Verde Islands. *J. Petrol.* **47**, 145–189.

Holmden C., Creaser R. A., Muehlenbachs K., Bergstrom S. M. and Leslie S. A. (1996) Isotopic and elemental systematics of Sr and Nd in 454 Ma biogenic apatites: implications for paleo-seawater studies. *Earth Planet. Sci. Lett.* **142**, 425–437.

Hunter R. S. and McKenzie D. (1989) The equilibrium geometry of carbonate melts in rocks of mantle composition. *Earth Planet. Sci. Lett.* **92**, 347–356.

Jackson M. G., Kurz M. D., Hart S. R. and Workman R. K. (2007) New Samoan lavas from Ofu Island reveal a hemispherically heterogeneous high $^{3}He/^{4}He$ mantle. *Earth Planet. Sci. Lett.* **264**, 360–374.

Janz H. and Vennemann T. W. (2005) Isotopic composition (O, C, Sr, and Nd) and trace element ratios (Sr/Ca, Mg/Ca) of Miocene marine and brackish ostracods from North Alpine Foreland deposits (Germany and Austria) as indicators for palaeoclimate. *Palaeogeog. Palaeoclim. Palaeoecol.* **225**, 216–247.

Javoy M., Weis D., Hodgson N. and Agrinier P. (1985) Stable and radiogenic isotope systematics in Cape Verde carbonatites and basaltic lavas. *EOS* **66**, 1137.

Jones A. P. and Peckett A. (1981) Zirconium-bearing aegirines from Motzfeldt, South Greenland. *Contrib. Mineral. Petrol.* **75**, 251–255.

Jørgensen J. ø. and Holm P. M. (2002) Temporal variation and carbonatite contamination in primitive ocean island volcanics from São Vicente, Cape Verde Islands. *Chem. Geol.* **192**, 249–267.

Kalt A., Hegner E. and Satir M. (1997) Nd, Sr and Pb isotopic evidence for diverse lithospheric mantle sources of East African Rift carbonatites. *Tectonophysics* **278**, 31–45.

King B. C. and Sutherland D. L. (1960) Alkaline rocks of eastern and southern Africa. *Sci. Prog.* **47**, 298–321, 504–524, 709–720.

Kjarsgaard B. A. and Hamilton D. L. (1989) The genesis of carbonatites by immiscibility. In *Carbonatites: Genesis and Evolution* (ed. K. Bell). Unwin Hyman Ltd., London, UK, pp. 388–404.

Klemme S. and Dalpé C. (2003) Trace-element partitioning between apatite and carbonatite melt. *Am. Mineral.* **88**, 639–646.

Klemme S., van der Laan S. R., Foley S. F. and Günther D. (1995) Experimentally determined trace and minor element partitioning between clinopyroxene and carbonatite melt under upper mantle conditions. *Earth Planet. Sci. Lett.* **133**, 439–448.

Kogarko L. N. (1993) Geochemical characteristics of oceanic carbonatites from the Cape Verde Islands. *S. Afr. J. Geol.* **96**, 119–125.

Kogarko L. N., Kurat G. and Ntaflos T. (2001) Carbonate metasomatism of the oceanic mantle beneath Fernando de Noronha Island, Brazil. *Contrib. Mineral. Petrol.* **140**, 577–587.

Kokfelt T. F., Holm P. M., Hawkesworth C. J. and Peate D. W. (1998) A lithospheric mantle source for the Cape Verde Island magmatism: trace element and isotopic evidence from the island of Fogo. *Min. Mag.* **62A**, 801–802.

Koster van Groos A. F. and Wyllie P. J. (1963) Experimental data bearing on the role of liquid immiscibility in the genesis of carbonatites. *Nature* **199**, 801–802.

Labrosse S., Hernlund J. W. and Coltice N. (2007) A crystallizing dense magma ocean at the base of the Earth's mantle. *Nature* **450**, 866–869.

Lee W. J. and Wyllie P. J. (1994) Experimental data bearing on liquid immiscibility, crystal fractionation, and the origin of calciocarbonatites and natrocarbonatites. *Int. Geol. Rev.* **36**, 797–819.

Lodge A. and Helffrich G. (2006) Depleted swell root beneath the Cape Verde Islands. *Geology* **34**, 449–452.

Madeira J., Mata J., Mourão C., Brum da Silveira A., Martins S., Ramalho R. and Hoffmann D. L. (2010) Volcano-stratigraphic and structural evolution of Brava Island (Cape Verde) based on $^{40}Ar/^{39}Ar$, U-Th and field constraints. *J. Volcanol. Geotherm. Res* **196**, 219–235.

Martin E. E. and Haley B. A. (2000) Fossil fish teeth as proxies for seawater Sr and Nd isotopes. *Geochim. Cosmochim. Acta* **64**, 835–847.

Martin E. E., Macdougall J. D., Herbert T. D., Paytan A. and Kastner M. (1995) Strontium and neodymium isotopic analyses of marine barite separates. *Geochim. Cosmochim. Acta* **59**, 1353–1361.

Martins S., Mata J., Munha J., Mendes M. H., Maerschalk C., Caldeira R. and Mattielli N. (2010) Chemical and mineralogical evidence of the occurrence of mantle metasomatism by carbonate-rich melts in an oceanic environment (Santiago Island, Cape Verde). *Mineral. Petrol.* **99**, 43–65.

Mata J., Moreira M., Doucelance R., Ader M. and Silva L. C. (2010) Noble gas and carbon isotopic signatures of Cape Verde oceanic carbonatites. Implications for carbon provenance. *Earth Planet. Sci. Lett.* **291**, 70–83.

Millet M.-A., Doucelance R., Schiano P., David K. and Bosq C. (2008) Mantle plume heterogeneity versus shallow-level interactions: a case study, the São Nicolau Island, Cape Verde archipelago. *J. Volcanol. Geotherm. Res.* **176**, 265–276.

Moine B. N., Grégoire M., O'Reilly S. Y., Delpech G., Sheppard S. M. F., Lorand J. P., Renac C., Giret A. and Cottin J. Y. (2004) Carbonatite melt in oceanic upper mantle beneath the Kerguelen Archipelago. *Lithos* **75**, 239–252.

Molina J. F. and Poli S. (2000) Carbonate stability and fluid composition in subducted oceanic crust: an experimental study on $H_2O$–$CO_2$-bearing basalts. *Earth Planet. Sci. Lett.* **176**, 295–310.

Montelli R., Nolet G., Dahlen F. A. and Masters G. (2006) A catalogue of deep mantle plumes: new results from finite-frequency tomography. *Geochem. Geophys. Geosyst.* **7**, doi: 10.1029/2006GC001248.

Mourão C., Mata J., Doucelance R., Madeira J., Brum da Silveira A., Silva L. C. and Moreira M. (2010) Quaternary extrusive calcio-carbonatite volcanism in Brava Island (Cape Verde). *J. Afr. Earth Sci.* **56**, 59–74.

Nelson D. R., Chivas A. R., Chappell B. W. and McCulloch M. T. (1988) Geochemical and isotopic systematics in carbonatites and implications for the evolution of ocean-island sources. *Geochim. Cosmochim. Acta* **52**, 1–17.

Pin C. and Bassin C. (1992) Evaluation of a strontium-specific extraction chromatographic method for isotopic analysis in geological materials. *Anal. Chim. Acta* **269**, 249–255.

Pin C., Briot D., Bassin C. and Poitrasson F. (1994) Concomitant separation of strontium and samarium–neodymium for isotopic analysis in silicate samples, based on specific extraction chromatography. *Anal. Chim. Acta* **298**, 209–217.

Plank T. and Langmuir C. H. (1998) The chemical composition of subducting sediment and its consequences for the crust and mantle. *Chem. Geol.* **145**, 325–394.

Ryabchikov I. D., Orlova G. P., Senin V. G. and Trubkin N. V. (1993) Partitioning of rare earth elements between phosphate-rich carbonatite melts and mantle peridotites. *Mineral. Petrol.* **49**, 1–12.

Sasada T., Hiyagon H., Bell K. and Ebihara M. (1997) Mantle-derived noble gases in carbonatites. *Geochim. Cosmochim. Acta* **61**, 4219–4228.

Scotese C. R. (2002) Available from: <http://www.scotese.com>, (PALEOMAP website).

Shannon R. D. (1976) Revised effective ionic radii and systematic studies of interatomic distances in halides and chalcogenides. *Acta Crystallogr.* **32**, 751–767.

Shaw C. J., Heidelbach F. and Dingwell D. B. (2006) The origin of reaction textures in mantle peridotite xenoliths from Sal Island, Cape Verde: the case for "metasomatism" by the host lava. *Contrib. Mineral. Petrol.* **151**, 681–697.

Stracke A., Hofmann A. W. and Hart S. R. (2005) FOZO, HIMU, and the rest of the mantle zoo. *Geochem. Geophys. Geosyst.* **6**, doi: 10.1029/2004GC000824.

Staudigel H., Doyle P. and Zindler A. (1985/86) Sr and Nd isotope systematics in fish teeth. *Earth Planet. Sci. Lett.* **76**, 45–56.

Stuart F. M., Lass-Evans S., Fitton J. G. and Ellam R. M. (2003) High $^{3}He/^{4}He$ ratios in picritic basalts from Baffin Island and the role of a mixed reservoir in mantle plumes. *Nature* **424**, 57–59.

Sweeney R. J., Prozesky V. and PrzybylowIicz W. (1995) Selected trace and minor element partitioning between peridotite minerals and carbonatite melts at 18–46 kb pressure. *Geochim. Cosmochim. Acta* **59**, 3671–3683.

Tolstikhin I. N. and Hofmann A. W. (2005) Early crust on top of the Earth's core. *Phys. Earth Planet. Int.* **148**, 109–130.

Tolstikhin I. N., Kramers J. D. and Hofmann A. W. (2006) A chemical Earth model with whole mantle convection: the importance of a core–mantle boundary layer (D″) and its early formation. *Chem. Geol.* **226**, 79–99.

Treiman A. H. (1989) Carbonatite magma: properties and processes. In *Carbonatites Genesis and Evolution* (ed. K. Bell). Unwin Hyman, London, pp. 89–104.

Turbeville B. N. and Wolff J. A. (1989) Hydroclastic volcanism and phonolitic tuff ring development, Brava, Cape Verde Islands. *EOS* **67**, 125.

Veksler I. V., Nielsen T. F. D. and Sokolov S. V. (1998) Mineralogy of crystallized melt inclusions from Gardiner and Kovdor ultramafic alkaline complexes: implications for carbonatite genesis. *J. Petrol.* **39**, 2015–2031.

Vervoort J. D. and Blichert-Toft J. (1999) Evolution of the depleted mantle: Hf isotope evidence from juvenile rocks through time. *Geochim. Cosmochim. Acta* **63**, 533–556.

Wallace M. E. and Green D. H. (1988) An experimental determination of primary carbonatite magma composition. *Nature* **335**, 343–346.

Weaver B. L. (1991) The origin of ocean island basalt end-member compositions: trace element and isotopic constraints. *Earth Planet. Sci. Lett.* **104**, 381–397.

Whittaker S. G. and Kyser T. K. (1993) Variations in the neodymium and strontium isotopic composition and REE content of molluscan shells from the Cretaceous Western Interior seaway. *Geochim. Cosmochim. Acta* **57**, 4003–4014.

Widom E., Hoernle K. A., Shirey S. B. and Schmincke H.-U. (1999) Os isotope systematics in the Canary Islands and Madeira: lithospheric contamination and mantle plume signatures. *J. Petrol.* **40**, 279–296.

Woodhead J. D. (1996) Extreme HIMU in an oceanic setting: the geochemistry of Mangaia Island (Polynesia), and temporal evolution of the Cook-Austral hotspot. *J. Volcanol. Geotherm. Res.* **72**, 1–19.

Woolley A. R. (1989) The spatial and temporal distribution of carbonatites. In *Carbonatites* (ed. K. Bell). Genesis and Evolution, Unwin Hyman, London, pp. 15–37.

Workman R. K. and Hart S. R. (2005) Major and trace element composition of the depleted MORB mantle (DMM). *Earth Planet. Sci. Lett.* **231**, 53–72.

Wyllie P. J. and Huang W. L. (1975) Peridotite, kimberlite and carbonatite explained in the $CaO–MgO–SiO_2–CO_2$. *Geology* **3**, 621–624.

Wyllie P. J. and Huang W. L. (1976) Carbonation and melting reactions in the system $CaO–MgO–SiO_2–CO_2$ at mantle pressures with geophysical and petrological applications. *Contrib. Mineral. Petrol.* **54**, 79–107.

Wyllie P. J. and Lee W. J. (1998) Model system controls on conditions for formation of magnesiocarbonatite and calcio-carbonatite magmas from the mantle. *J. Petrol.* **39**, 1885–1893.

Zhang Y. and Zindler A. (1993) Distribution and evolution of carbon and nitrogen in Earth. *Earth Planet. Sci. Lett.* **117**, 331–345.

Zhao D. (2007) Seismic images under 60 hotspots: search for mantle plumes. *Gondwana Res.* **12**, 335–355.

*Associate editor:* Martin A. Menzies

Earth and Planetary Science Letters 407 (2014) 175–186

Contents lists available at ScienceDirect

Earth and Planetary Science Letters

www.elsevier.com/locate/epsl

# What coupled cerium and neodymium isotopes tell us about the deep source of oceanic carbonatites

Régis Doucelance [a,b,c,*], Nina Bellot [a,b,c], Maud Boyet [a,b,c], Tahar Hammouda [a,b,c], Chantal Bosq [a,b,c]

[a] Clermont Université, Université Blaise Pascal, Laboratoire Magmas et Volcans, BP 10448, F-63000 Clermont-Ferrand, France
[b] CNRS, UMR 6524, LMV, F-63038 Clermont-Ferrand, France
[c] IRD, R 163, LMV, F-63038 Clermont-Ferrand, France

ARTICLE INFO

*Article history:*
Received 26 March 2014
Received in revised form 17 September 2014
Accepted 23 September 2014
Available online xxxx
Editor: B. Marty

*Keywords:*
oceanic carbonatites
Cape Verde/Canary archipelagos
Ce isotopes
geochemistry

ABSTRACT

We present the first Ce isotope compositions together with Nd and Pb isotope ratios measured for whole rocks and mineral separates (apatite, titanite) from oceanic carbonatites and associated silicate samples from the Cape Verde and Canary archipelagos (Atlantic Ocean). We compare them with measurements performed on carbonatites from Tamazert (Morocco) for which a common source has been suggested. We couple the La/Ce and Sm/Nd systems in order to model the rare-earth-element concentrations and the Ce–Nd isotope compositions of marine carbonates and mantle and/or mantle-derived reservoirs, notably the D″ boundary layer. We discuss the two contrasting models that have been previously presented for the origin of the carbon of the oceanic carbonatite source: recycled marine carbonates via subduction vs. primordial carbon. Our measurements favour the recycling of marine carbonates in the source of oceanic carbonatites. We use Pb isotope ratios together with experimental petrology constraints to discuss the age and depth of carbonate recycling in the mantle.



## 1. Introduction

Carbonatites are rare, magmatic rocks consisting mainly of calcium- (calcite), calcium and magnesium- (dolomite) or iron- and magnesium carbonates (sidero-magnesite), accompanied by accessory minerals (silicates and/or phosphates, oxides, sulphides, sulphates, etc.). They have been found on every continent (Woolley and Kjarsgaard, 2008). Geochemical studies based on stable, radiogenic and noble gas isotopes have led to the general consensus that their parental magmas originate in the mantle (Bell and Blenkinsop, 1987; Bell and Tilton, 2001; Cartigny et al., 1998; Deines, 1989; Marty et al., 1998; Nelson et al., 1988; Sasada et al., 1997). Such an origin is in agreement with petrographical observations, since xenocrysts from the mantle, generally chromite spinels, are found in some extrusive carbonatites (Bailey, 1989; Mourtada et al., 1997). This is also in agreement with results of experimental petrology: carbonated melts can be generated by melting of a mixture of peridotite and $CO_2$ (Eggler, 1978; Wallace and Green, 1988; Wyllie and Huang, 1976; Wyllie et al., 1983).

Experimental petrology predicts that carbonated melts formed in the mantle should be magnesio-carbonatites (dolomitic), but most sampled carbonatites are calcic (Woolley and Kempe, 1989; Woolley and Kjarsgaard, 2008). Thus it has been suggested that magnesio-carbonatites are enriched in calcium during their ascent by reaction with their surrounding mantle environment (Dalton and Wood, 1993; Hammouda et al., 2014). An alternative solution considers that the source of carbonatites consists instead of recycled oceanic crust + carbonated sediments. Melting experiments using such materials as their starting composition have led to the generation of calcitic, carbonatitic melts in subduction P-T conditions (Hammouda, 2003; Kiseeva et al., 2012). In this scenario all carbonatite sources should contain recycled oceanic crust.

Oceanic carbonatites are less frequent than their continental counterpart. They have been reported only at the Cape Verde and Canary archipelagos, Atlantic Ocean (Woolley and Kjarsgaard, 2008). The mantle origin of their parental magmas is attested (Lancelot and Allègre, 1974). However, contrasting models have been proposed for the origin of the carbon of their source. They involve either primordial carbon or marine carbonates that have been recycled via subduction. The genetic models also cover a wide spectrum, from a deep mantle origin, which might contain recycled carbon (see De Ignacio et al., 2006, 2012; Hoernle et al., 2002; Mata et al., 2010; Mourão et al., 2010, 2012), to a more superficial

* Corresponding author at: Clermont Université, Université Blaise Pascal, Laboratoire Magmas et Volcans, BP 10448, F-63000 Clermont-Ferrand, France.
*E-mail address:* R.Doucelance@opgc.univ-bpclermont.fr (R. Doucelance).

http://dx.doi.org/10.1016/j.epsl.2014.09.042
0012-821X/

one (lithosphere previously metasomatized by carbonatite liquids related to recycling of Devonian carbonates, see Doucelance et al., 2010). Moreover, the role of the plume in the genesis of carbonatites is debated. The melting of the plume gives rise to the carbonatite melt in the case of a deep origin. Its role is mostly limited to its thermal expression in the case of a lithospheric origin. Finally, it was also proposed that carbonatites from the Cape Verde and Canary Islands share a common source with those of Tamazert in Morocco (Bouabdellah et al., 2010).

In this study we present the first cerium isotope ratios, together with Nd and Pb measurements, of calcio-carbonatites from the Cape Verde and Canary archipelagos and from the Tamazert massif in Morocco. $^{138}$La decays to stable $^{138}$Ce (138 Lanthanum; β-decay with a half-life of 292.5 Ga; Tanimizu, 2000) and $^{138}$Ba (138 Barium; electron capture with a half-life of 156.1 Ga; Sato and Hirose, 1981). Coupling the La/Ce and Sm/Nd systems may help to distinguish between the two proposed origins for the carbon of oceanic carbonatites: recycled carbon vs. primordial carbon. Marine carbonates show rare-earth-element (REE) patterns distinct from those assumed or measured for mantle and mantle-derived reservoirs so that old recycled carbonates and mantle-related materials are likely to display very contrasted $\varepsilon$Ce and $\varepsilon$Nd values with time. We will show that the Ce–Nd isotope compositions of oceanic calcio-carbonatites are in agreement with the recycling of marine carbonates in the source of their parental magmas.

## 2. Previous studies of oceanic calcio-carbonatites

Hoernle et al. (2002) have presented the first, radiogenic and stable, multi-isotope study of oceanic carbonatites from both the Cape Verde and Canary archipelagos. For Cape Verde, they proposed that calcio-carbonatites derive from the melting of recycled, 1.6 Ga-old oceanic crust containing secondary calcitic carbonates. The model was developed to explain the Sr–Nd–Pb isotopic compositions measured in samples, but fails to reproduce the low $^4$He/$^3$He isotopic ratios (down to 46,700; $R/R_a$ up to 15.5) recently documented by Mata et al. (2010) for samples from the same outcrops. Neither does the model explain the mantle-like $\partial^{13}$C values (−8.0‰ to −4.2‰) measured in the samples. This last observation, however, must be balanced as eclogites have $\partial^{13}$C ranging from −34‰ to +4‰ (Pearson et al., 1994) with an average value close to that observed in the calcio-carbonatites.

As an alternative, Mata et al. (2010) proposed that the source of Cape Verde carbonatites is deeply seated in the mantle, being located at the D″ boundary layer. Such a source is supposed to be enriched in primordial rare gases and carbon, thus explaining the measured He and C isotopic compositions. Unradiogenic Sr–Nd isotopic ratios and intermediate Pb are not, however, reproduced by such a scenario, as is also the case for trace element patterns (Doucelance et al., 2010).

Mourão et al. (2012) then proposed an intermediate model for calcio-carbonatites from Brava (the western island of the Cape Verde southern group) in which the carbonatites result from liquid immiscibility, being thus genetically related to silicate magmas from the same island. The model relies notably on the similarity of isotope signatures between the calcio-carbonatites and the silicate formations of Brava. The Sr–Nd–Pb–He isotopic compositions of silicate samples from the Cape Verde archipelago are usually interpreted as the contribution of a high-μ (HIMU)-type end-member, which represents an ancient recycled oceanic crust, with lower mantle material (Doucelance et al., 2003; Holm et al., 2006; Millet et al., 2008; Mourão et al., 2012). Again, such a source can explain the Sr–Nd–Pb–He isotope compositions of carbonatites, but maybe not their $\partial^{13}$C. Furthermore, the model cannot be extended to other islands of the archipelago such as Fogo or Santiago, since silicate samples show Sr–Nd–Pb isotope compositions significantly distinct from those of carbonatites. In the same way, De Ignacio et al. (2012) proposed that the calcio-carbonatites from São Vicente (Northern Islands) represent fractionation products of the parental magma of nephelinites, whose outcrops are spatially related to those of carbonatites. Although close, the nephenelites and calcio-carbonatites still present significantly distinct Sr–Nd–Pb values, which undermines the model.

Lastly, it has also been proposed that oceanic calcio-carbonatites are related to the recycling of marine carbonates at shallow mantle depth. The latter are the origin of metasomatized oceanic lithosphere, Cape Verde plume-induced partial melting giving rise to carbonatite parental magmas. A small contamination of carbonatitic melts by Cape Verde plume material explains both Sr–Nd–Pb and He isotopic compositions of carbonatites. The model would suggest heavier $\partial^{13}$C ratios than are actually measured, but is in agreement with the $^{187}$Os/$^{188}$Os isotopic ratios of carbonatites that present more radiogenic values than mantle end-members (Escrig et al., 2005), as is also the case for the model by Hoernle et al. (2002). Although radiogenic Os ratios could also result from minor seawater contamination during their emplacement, Re/Os whole-rock isochrones give a consistent age of 3.2 ± 1.2 Ma for carbonatites.

Data measured in carbonatite samples from the Canaries are less numerous. Hoernle et al. (2002) have proposed that the calcio-carbonatites from the basal complex of Fuerteventura Island also result from melting of secondary calcitic carbonate in recycled oceanic crust, similar to the Cape Verde calcio-carbonatites. The model relies on the similar geochemical characteristics of calcio-carbonatites from both archipelagos. On the other hand, De Ignacio et al. (2006) have proposed that the calcio-carbonatites derive from a heterogeneous mantle plume with a FOZO-HIMU mixing-like component. Both models would explain HIMU-like initial radiogenic isotopic compositions measured in Fuerteventura samples, with uniform $^{87}$Sr/$^{86}$Sr and $^{143}$Nd/$^{144}$Nd and relatively large range in Pb isotopic compositions. Turning to the Tamazert massif in Morocco, calcio-carbonatite samples with low $^{87}$Sr/$^{86}$Sr ratios have mantle-type O and C isotopic compositions (Bouabdellah et al., 2010). Their source was interpreted to contain HIMU- and EMI-type components, as for the Cape Verde and Canary Island case (De Ignacio et al., 2012; Hoernle et al., 2002; Mourão et al., 2012). Thus, given the close similarity in carbonatite isotopic composition between the three localities, Bouabdellah et al. (2010) concluded that there was a common source for these rocks.

Two distinct types of models can thus be distinguished from the previous studies: 1) models involving primordial carbon in the oceanic carbonatite source vs. 2) models invoking marine carbonates recycled via subduction. Within the carbonate recycling models, two possible depths of recycling have been considered: the base of the oceanic lithosphere and the lower mantle.

## 3. Analytical procedures

100–200 g of each sample were reduced into chips in a jaw crusher before being powdered in an agate swing mill. Fine crushing was carried out in three rounds: 1) the first crushing run was conducted to pre-contaminate the agate mill; 2) the second run was kept for potential major element determinations; and 3) the third one for trace elements and Ce–Nd–Pb isotope analyses.

Trace-element ratios and cerium, neodymium and lead isotope separations and measurements were carried out at the Laboratoire Magmas et Volcans. 100 mg of sample powders were first acid-digested using HCl. Then, after removing of the supernatant, residues of centrifugation were dissolved with an HF–$HNO_3$ mixture. Sample solutions were then separated in three aliquots for Ce–Nd, Pb and trace element analyses, respectively.

Ce and Nd separation and purification were achieved using three successive columns. The first two columns involved cationic exchange resin AG50W-X8 (REE extraction in an HCl medium followed by Nd–Ce separation using HIBA acid under pressure), whereas the third one used Ln-Spec resin and HCl, and allows isolation of Ce and Nd (Bellot et al., 2013). Pb separation and purification was conducted using clean pipette tip columns filled with ~0.2 ml of AG1-X8 resin (100–200 mesh) following the procedure of Manhès et al. (1978). Ce, Nd and Pb procedural blanks were negligible with respect to sample concentrations.

Trace-element abundances were determined by quadrupole ICPMS (Agilent 7500). External calibration of the signal was done every three samples using two dilutions of the traceable-to-NIST CMS reference material standard (Inorganics Ventures).

Cerium isotopes were measured as $CeO^+$ on a Finnigan Triton TIMS in static mode with relay matrix rotation on double Re filaments. Cerium ratios were corrected online for oxygen and mass fractionation following the procedure described in Willbold (2007) that uses an exponential law with $^{136}Ce/^{142}Ce = 0.01688$. On the contrary, correction for $^{140}Ce^{16}O$ tailing was operated offline. For this purpose, the average tail effect determined from measurements of AMES standard (Willbold, 2007) at the beginning of a session of analysis was applied to unknown samples from the same session. More specifically, we fitted an exponential law to 151.5 and 154.5 half-mass measurements of AMES in order to establish the tailing curve and thus determine the intensity to be removed at CeO masses. The procedure was checked with the two Fogo carbonatite samples (NF43 and F1C) that gave consistent results between internally tail-corrected values and external ones (Supplementary file A1). A typical run consisted of 24 blocks of 15 cycles (8 s integration) with 60 s baseline measurement every block (deflected ion beams). 1 µg of Ce was loaded per analysis, allowing the $^{142}Ce^{16}O$ beam to be maintained to 10–12 V. Long-term reproducibility of the Ce AMES standard is 44 ppm, i.e., $^{138}Ce/^{142}Ce = 0.0225747 \pm 0.0000010$ (2sd, $n = 53$). Such a result is in agreement with previous determinations using a similar protocol ($0.0225750 \pm 0.0000005$, cf. Willbold, 2007). Same-order reproducibilities were also obtained for duplicate analyses of carbonatites and rock standards BHVO-2 and BCR-2 (Supplementary files A1 to A3).

Nd measurements were also made in static mode on the Finnigan Triton TIMS with relay matrix rotation and double Re filaments. A typical run consisted of at least nine blocks of ten cycles to allow a full rotation of the virtual amplifier system. Isotope ratios were mass-fractionation corrected with $^{146}Nd/^{144}Nd = 0.7219$. Repeated analyses of the Nd JNDi-1 standard during the course of the study gave $^{143}Nd/^{144}Nd = 0.512111 \pm 0.000009$ (2sd, $n = 7$).

Pb isotopic measurements were performed on a Finnigan Neptune MC-ICP-MS in static mode. Mass discrimination was monitored using the Tl-doping technique and an exponential law. The $^{205}Tl/^{203}Tl$ ratio was adjusted at each session so that the mean of measured NIST SRM981 standards gave values of Doucelance and Manhès (2001) recalculated at $^{208}Pb/^{206}Pb = 2.1677$ ($^{207}Pb/^{206}Pb = 0.91488$ and $^{204}Pb/^{206}Pb = 0.059027$, cf. Baker et al., 2004). $2\sigma_{mean}$ errors were maximum 100 ppm for each $^{20X}Pb/^{204}Pb$ ratio. NIST SRM981 standards were reproducible at the 50-ppm level for each $^{20X}Pb/^{204}Pb$ ratio ($2\sigma$, $n = 9$). Aliquots of a single sample solution showed same-order reproducibilities (30 ppm) for all Pb isotopic ratios except for sample Ta1692 (400 ppm).

## 4. Ce–Nd–Pb isotopic results

Ten carbonatite samples were analyzed for Ce, Nd and Pb isotopes: four from the Cape Verde archipelago, two from Fuerteventura (Canary), and four from the Tamazert Massif (Morocco). F1C and NF43 are calcio-carbonatites from Fogo Island, whereas CY-250 and CY-114 are from Brava (CY-250 is a calcio-carbonatite; CY-114 is a magnesio-carbonatite). Carbonatites from these two Cape Verde islands were chosen because Fogo and Brava occupy extreme positions in Sr–Nd–Pb isotope diagrams (Doucelance et al., 2010). Samples 26257 and 53658 are titanite and apatite separates, respectively, from Fuerteventura calcio-carbonatites collected in the Branco de Agua Salada area. Mineral separates were preferred to whole rocks because our samples present evidence for supergene alteration. Ta2a92, Ta1692, Ta1792 and Is1093 are low-$^{87}Sr/^{86}Sr$, Moroccan calcio-carbonatites. Ta2a92, Ta1692 and Ta1792 are samples from Tamazzart, whereas Is1093 is from Issali Igban. For comparison purpose, 10 silicate samples from the Cape Verde archipelago were also analyzed, together with MORB samples from Cape Verde Jurassic basement. The former are four basalts from Fogo, two basalts and two syenites from Brava, and two basalts from São Vicente. These 10 samples present a wide range of Sr–Nd–Pb isotopic ratios nearly spanning the whole range of silicate field from the Cape Verde archipelago (Doucelance et al., 2003).

Initial Ce, Nd and Pb isotope ratios of carbonatites were calculated assuming emplacement ages of ~2, 4, 25 & 39 Ma for Brava, Fogo, Fuerteventura and Tamazert, respectively (Tables 1 and 2). $(^{138}Ce)_t = (^{138}Ce)_o + (^{138}La)_t \times \lambda_\beta/(\lambda_\beta + \lambda_{ec}) \times (\exp((\lambda_\beta + \lambda_{ec}) \times t) - 1)$ where suffixes $o$ and $t$ correspond to the emplacement (initial) and the present ages, and $\lambda_\beta$ and $\lambda_{ec}$ to $\beta$ and electron capture decay constants, respectively. Natural variations of the Ce isotopic composition ($^{138}Ce/^{142}Ce$) are small so they are usually normalized to the chondritic value (CHUR) using the $\varepsilon$ notation, as is the case for Nd isotopes: $\varepsilon Ce = [(^{138}Ce/^{142}Ce)_{Sample}/(^{138}Ce/^{142}Ce)_{CHUR} - 1] \times 10{,}000$, with $(^{138}Ce/^{142}Ce)_{CHUR} = 0.0225654$ (mean value of carbonaceous and ordinary chondrites: Makishima and Masuda, 1993; Bellot et al., 2013). Cerium isotope ratios show small variations ranging from $\varepsilon Ce = -0.6$ to $\varepsilon Ce = -0.1$. Nd and Pb ratios show more contrasted values ranging between $\varepsilon Nd = +3.5$ and $\varepsilon Nd = +6.2$, and $^{206}Pb/^{204}Pb = 19.146$ and $^{206}Pb/^{204}Pb = 19.996$ (Fig. 1). Nd results are in agreement with previous studies that have shown that Nd compositions measured in Fuerteventura carbonatite samples are on average less radiogenic than those of Cape Verde calcio-carbonatites (Hoernle et al., 2002; Doucelance et al., 2010) but more radiogenic than those of Tamazert (Bouabdellah et al., 2010). In the same way, Pb isotopic ratios show close but distinct values for Cape Verde, Canary and Tamazert. This suggests that calcio-carbonatites derived from a similar but distinct source, as previously proposed by Hoernle et al. (2002) for Cape Verde and Canary carbonatites. This is in disagreement, however, with conclusions by Bouabdellah et al. (2010) who suggested a common source.

Turning to the comparison with silicate samples, Ce, Nd and Pb isotopic compositions measured in the Brava carbonatite plot at the end of the trend defined by Brava basalts and syenites, similar to what was already observed by Mourão et al. (2012) for Sr isotopes. Fogo carbonatites show also Ce values comparable to extreme ones measured in basalts, however Nd and Pb ratios are significantly distinct. Thus, although some of the Cape Verde carbonatites may be related to basaltic rocks by immiscibility, such a relationship cannot be generalized to the whole archipelago.

## 5. Discussion

In this section we discuss the origin of parental magmas of oceanic carbonatites in the light of cerium, neodymium and lead isotopic ratios. For this purpose, we first consider the REE concentrations of the different components inferred to enter the carbonatites' source in order to model their isotopic compositions and to compare them with our results. Secondly, we use Pb isotopes to

**Table 1**
Ce and Nd isotopic compositions of carbonatites and basalts. Ages for carbonatite samples are from Lancelot and Allègre (1974) for Fogo, Madeira et al. (2010) for Brava, Cantagrel et al. (1993) for Fuerteventura, and Bouabdellah et al. (2010) for Tamazert. Ages for basalts are from Escrig et al. (2005) for Fogo, Madeira et al. (2010) for Brava, and Bosse et al. (2007) for São Vicente.

| Sample | Type | Age (Ma) | $^{138}Ce/^{142}Ce$ | $2\sigma_{mean}$ | La/Ce | $^{138}La/^{142}Ce$ | $\varepsilon Ce(T)$[a] | $^{143}Nd/^{144}Nd$ | $2\sigma_{mean}$ | Sm/Nd | $^{147}Sm/^{144}Nd$ | $\varepsilon Nd(T)$[a] |
|---|---|---|---|---|---|---|---|---|---|---|---|---|
| *Cape Verde – Fogo* | | | | | | | | | | | | |
| F1C | Ca-carbonatite | 3.4 | 0.02256430 | 0.00000019 | 0.522 | 0.004264 | −0.5 | 0.512943 | 0.000003 | 0.156 | 0.0943 | +6.1 |
| NF43 | Ca-carbonatite | 3.4 | 0.02256413 | 0.00000025 | 0.518 | 0.004232 | −0.6 | 0.512944 | 0.000004 | 0.151 | 0.0913 | +6.2 |
| CV-98-F-07 | Basalt | (a.d. 1951) | 0.02256500 | 0.00000029 | *0.452* | 0.003689 | −0.2 | 0.512747 | 0.000003 | *0.189* | 0.1143 | +2.3 |
| CV-98-F-10 | Basalt | (a.d. 1785) | 0.02256424 | 0.00000031 | *0.477* | 0.003899 | −0.5 | 0.512777 | 0.000004 | *0.191* | 0.1154 | +2.9 |
| CV-98-F-16 | Basalt | (a.d. 1995) | 0.02256506 | 0.00000030 | *0.468* | 0.003823 | −0.2 | *0.512737* | *0.000004* | *0.190* | 0.1147 | +2.1 |
| CV-98-F-18 | Basalt | – | 0.02256462 | 0.00000038 | *0.492* | 0.004020 | −0.3 | *0.512764* | *0.000003* | *0.185* | 0.1119 | +2.6 |
| *Cape Verde – Brava* | | | | | | | | | | | | |
| CY-250 | Ca-carbonatite | 1.55 | 0.02256480 | 0.00000044 | 0.521 | 0.004260 | −0.3 | 0.512910 | 0.000004 | 0.149 | 0.0903 | +5,5 |
| CY-114 | Mg-carbonatite | 1.55 | 0.02256464 | 0.00000029 | 0.376 | 0.003073 | −0.3 | 0.512905 | 0.000005 | 0.185 | 0.1117 | +5,4 |
| CY-39 | Syenite | 1.5 | 0.02256453 | 0.00000045 | *0.461* | 0.003764 | −0.4 | *0.512905* | *0.000006* | *0.176* | 0.1063 | +5.4 |
| CY-179 | Syenite | 1.5 | 0.02256374 | 0.00000029 | *0.427* | 0.003490 | −0.7 | 0.512918 | 0.000003 | *0.185* | 0.1118 | +5.6 |
| CY-11 | Basalt | 2 | 0.02256358 | 0.00000032 | *0.444* | 0.003629 | −0.8 | 0.512913 | 0.000004 | *0.217* | 0.1315 | +5.5 |
| CY-165 | Basalt | 2.28 | 0.02256327 | 0.00000030 | *0.459* | 0.003749 | −1.0 | 0.512913 | 0.000003 | *0.190* | 0.1149 | +5.5 |
| *Cape Verde – São Vicente* | | | | | | | | | | | | |
| CV-98-SV-01 | Basalt | 6.17 | 0.02256428 | 0.00000031 | *0.474* | 0.003869 | −0.5 | 0.512900 | 0.000003 | *0.211* | 0.1276 | +5.3 |
| CV-98-SV-12 | Basalt | 5.99 | 0.02256461 | 0.00000029 | *0.458* | 0.003744 | −0.4 | 0.512902 | 0.000003 | *0.205* | 0.1239 | +5.4 |
| *Cape Verde – MORB samples from Jurassic basement*[b] | | | | | | | | | | | | |
| S16 | Basalt | – | 0.02256331 | 0.00000027 | *0.292* | 0.002386 | −0.9 | 0.513107 | 0.000008 | *0.450* | 0.2720 | +9.3 |
| S17 | Basalt | – | 0.02256238 | 0.00000030 | *0.290* | 0.002370 | −1.3 | 0.513136 | 0.000002 | *0.421* | 0.2545 | +9.8 |
| S56 | Basalt | – | 0.02256197 | 0.00000045 | *0.296* | 0.002415 | −1.5 | 0.513119 | 0.000003 | *0.420* | 0.2536 | +9.5 |
| *Canary – Fuerteventura* | | | | | | | | | | | | |
| 53658 | Apatite (Ca-Carb.) | 25 | 0.02256473 | 0.00000074 | 0.487 | 0.003977 | −0.3 | 0.512863 | 0.000004 | 0.146 | 0.0885 | +4.9 |
| 26257 | Titanite (Ca-Carb.) | 25 | 0.02256480 | 0.00000023 | 0.407 | 0.003325 | −0.3 | 0.512847 | 0.000003 | 0.196 | 0.1185 | +4.5 |
| *Morocco – Tamazert* | | | | | | | | | | | | |
| Ta2a92 | Ca-carbonatite | 39 | 0.02256466 | 0.00000028 | 0.635 | 0.005183 | −0.4 | 0.512786 | 0.000004 | 0.135 | 0.0816 | +3.6 |
| Ta1692 | Ca-carbonatite | 39 | 0.02256489 | 0.00000029 | 0.652 | 0.005328 | −0.3 | 0.512787 | 0.000003 | 0.132 | 0.0795 | +3.6 |
| Ta1792 | Ca-carbonatite | 39 | 0.02256482 | 0.00000028 | 0.573 | 0.004677 | −0.3 | 0.512781 | 0.000003 | 0.136 | 0.0824 | +3.5 |
| Is1093 | Ca-carbonatite | 39 | 0.02256555 | 0.00000029 | 0.767 | 0.006264 | −0.1 | 0.512792 | 0.000003 | 0.128 | 0.0773 | +3.8 |

[a] $\varepsilon$-values are initial, parts per ten thousand deviations from chondrites. $(^{138}Ce/^{142}Ce)_{CHUR} = 0.0225654$ and $(^{138}La/^{142}Ce)_{CHUR} = 0.00306$ (Makishima and Masuda, 1993; Bellot et al., 2013); $(^{143}Nd/^{144}Nd)_{CHUR} = 0.51263$ and $(^{147}Sm/^{144}Nd)_{CHUR} = 0.196$ (Bouvier et al., 2008).

[b] MORB samples from the Cape Verde Jurassic basement are corrected for 3.4-Ma radioactive decay (similarly to Fogo). Values in italics are literature data (Doucelance et al., 2003; Millet et al., 2008; Mourão et al., 2012).

**Table 2**
Pb isotopic compositions of carbonatites.

| Sample | Age (Ma) | $^{206}Pb/^{204}Pb$ | $^{207}Pb/^{204}Pb$ | $^{208}Pb/^{204}Pb$ | U/Pb | $^{238}U/^{204}Pb$ | Th/Pb | $^{232}Th/^{204}Pb$ | $^{206}Pb/^{204}Pb_{Ini}$ | $^{207}Pb/^{204}Pb_{Ini}$ | $^{208}Pb/^{204}Pb_{Ini}$ |
|---|---|---|---|---|---|---|---|---|---|---|---|
| *Cape Verde – Fogo* | | | | | | | | | | | |
| F1C | 3.4 | 19.9129 | 15.6226 | 39.2603 | 0.263 | 17.26 | 1.761 | 119.21 | 19.904 | 15.622 | 39.240 |
| NF43 | 3.4 | 19.9827 | 15.6337 | 39.2557 | 0.031 | 2.01 | 1.686 | 114.26 | 19.982 | 15.634 | 39.236 |
| *Cape Verde – Brava* | | | | | | | | | | | |
| CY-250 | 1.55 | 19.8753 | 15.6201 | 39.2644 | 0.059 | 3.84 | 0.318 | 21.54 | 19.874 | 15.620 | 39.263 |
| CY-114 | 1.55 | 20.0021 | 15.6521 | 39.3357 | 0.417 | 27.41 | 3.093 | 209.84 | 19.996 | 15.652 | 39.320 |
| *Canary – Fuerteventura* | | | | | | | | | | | |
| 53658 | 25 | 20.0415 | 15.6297 | 41.7031 | 1.052 | 71.26 | 18.443 | 1290.82 | 19.765 | 15.617 | 40.106 |
| 26257 | 25 | 22.7031 | 15.7777 | 43.3416 | 9.848 | 704.84 | 37.476 | 2771.46 | 19.964 | 15.650 | 39.912 |
| *Morocco – Tamazert* | | | | | | | | | | | |
| Ta2a92 | 39 | 19.1831 | 15.5781 | 39.0634 | 0.007 | 0.48 | 0.240 | 16.01 | 19.180 | 15.578 | 39.032 |
| Ta1692 | 39 | 19.1516 | 15.5856 | 39.0542 | 0.015 | 1.00 | 0.103 | 6.91 | 19.146 | 15.585 | 39.041 |
| Ta1792 | 39 | 19.6763 | 15.6106 | 39.1156 | 0.900 | 58.67 | 0.360 | 24.25 | 19.320 | 15.594 | 39.069 |
| Is1093 | 39 | 19.9316 | 15.6389 | 39.7571 | 0.096 | 6.31 | 0.311 | 21.18 | 19.893 | 15.637 | 39.716 |

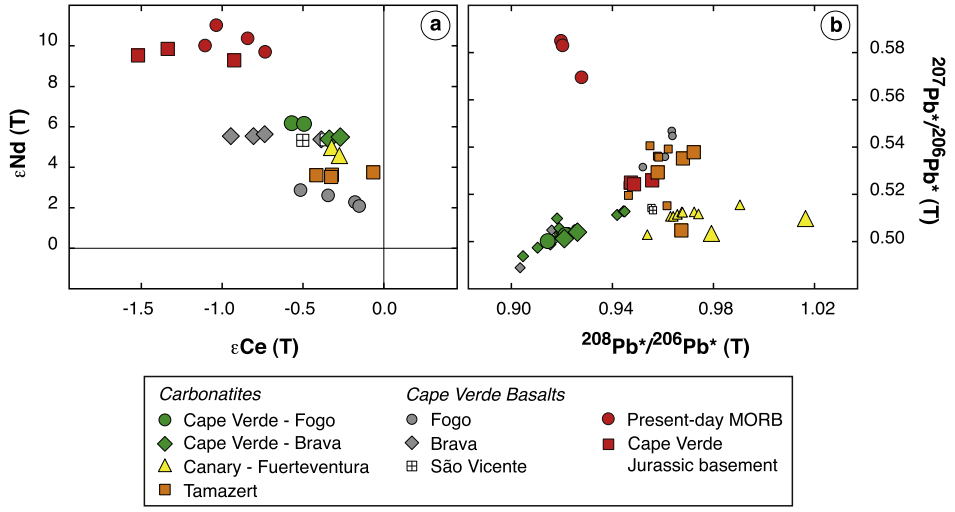


**Fig. 1.** (a) $\varepsilon$Nd vs. $\varepsilon$Ce and (b) $^{207}Pb^*/^{206}Pb^*$ vs. $^{208}Pb^*/^{206}Pb^*$ initial isotope ratios of Cape Verde, Canary and Tamazert carbonatites, and comparison with silicate samples from the Cape Verde Islands and MORB samples from the Cape Verde Jurassic basement (corrected for 3.4-Ma radioactive decay similar to Fogo). Present-day MORB Ce–Nd are from Bellot et al. (2013). Pb literature data (Bouabdellah et al., 2010; De Ignacio et al., 2006; Hoernle et al., 2002; Mourão et al., 2012) are marked with small symbols. Error-bars (30 ppm for Ce, 20 ppm for Nd and 100 ppm for Pb) have been omitted to make the figure easier to read.

constrain the age and depth of potential carbonate recycling into the mantle.

### 5.1. Modelling of $^{138}Ce/^{142}Ce$ and $^{143}Nd/^{144}Nd$ isotopic ratios at the D″ boundary layer

The REE distribution of mantle reservoirs such as the Depleted MORB Mantle (DMM) or the D″ reservoir cannot be directly obtained from surface samples. This is also the case for the Ce and Nd isotopic compositions of D″ but not of DMM whose isotopic signature is recorded in MORB samples. Here, we consider two distinct models in order to determine the Ce and Nd isotopic compositions of D″ as well as concentrations of both DMM and D″. The first model assumes that the Continental Crust (CC) formed by the continuous depletion of the primitive Earth mantle throughout geological time (called single evolution). Ce and Nd isotope ratios measured in CC and DMM thus show complementary values with respect to the chondritic Bulk Silicate Earth (BSE), and the deeper part of the Earth mantle possesses a primitive (or nearly primitive) composition for both Nd and Ce. By contrast, the second model considers that the whole Earth mantle has followed a two-stage evolution: (1) the mantle started to evolve with a chondritic composition 4.568 Ga ago; (2) then, at 4.518 Ga (~ 50 Ma after Solar System formation), it experienced a global differentiation event that led to the creation of complementary incompatible element-enriched (Early Enriched Reservoir – EER) and – depleted (Early Depleted Reservoir – EDR) mantle reservoirs as suggested by the superchondritic $^{142}Nd/^{144}Nd$ ratio measured in all terrestrial rocks (Boyet and Carlson, 2005, 2006), and from 4.518 Ga to the present, the continuous extraction of Continental Crust increased the depletion of EDR, while EER remained at the bottom of the mantle and now corresponds to the D″ layer. A schematic illustration of both models is given in Fig. 2.

Using Model 1 we could calculate sialic indexes $W^{Ce}$ and $W^{Nd}$ (Allègre and Lewin, 1989) using previously published $^{138}Ce/^{142}Ce$ and $^{143}Nd/^{144}Nd$ ratios for CC, DMM and BSE (Table 3). Given Ce and Nd contents for CC and BSE, we obtained inconsistent mass fraction values of CC depending on the chosen elements: ~0.018 using Ce and ~0.026 using Nd. Although such results are obviously dependent on the values of trace-element contents and isotopic ratios used in the calculations, notably the Ce isotope composition of CC, variations within reasonable range of input data did not totally erase the difference between the two estimates. Hence, this may suggest that the single-evolution model is not valid, and for this reason we only considered Model 2. Thus, we first determined the Nd isotope composition and the REE content of DMM assuming a Lu content of 0.063 ppm, identical Lu/Hf, Sm/Hf, Ce/Nd and La/Ce ratios between DMM and MORBs (Salters and Stracke, 2004),

**Table 3**
Composition of major terrestrial reservoirs (CC, continental crust; BSE, bulk silicate Earth; DMM, depleted MORB mantle; EDR, early depleted reservoir; EER, early enriched reservoir). All contents are in ppm.

| | CC | DMM | | BSE | EDR | EER = D″ |
|---|---|---|---|---|---|---|
| | T&M/R&G[a] | W&H[b] | This study | M&S[c] | This study | This study |
| La | 18 | 0.192 | 0.264 | 0.648 | 0.36 | 9.89 |
| Ce | 38 | 0.550 | 0.874 | 1.675 | 1.08 | 20.97 |
| Nd | 18 | 0.581 | 0.807 | 1.250 | 0.90 | 12.52 |
| Sm | 3.7 | 0.239 | 0.294 | 0.406 | 0.31 | 3.43 |
| $^{138}Ce/^{142}Ce$ ($\varepsilon$Ce) | 0.0225683 (+1.3) | 0.0225633 (−0.9) | 0.0225633 (−0.9) | 0.0225654 | 0.0225633 (−0.9) | 0.0225688 (+1.5) |
| $^{143}Nd/^{144}Nd$ ($\varepsilon$Nd) | 0.51177 (−16.7) | 0.51313 (+9.8) | 0.513156 (+10.3) | 0.51263 | 0.513023 (+7.7) | 0.511714 (−17.9) |

[a] Mean of Taylor and McLennan (1995) and Rudnick and Gao (2003) except $^{138}Ce/^{142}Ce$ (Amakawa et al., 1996; Tanaka et al., 1987) and $^{143}Nd/^{144}Nd$ (Goldstein and Jacobsen, 1988).
[b] Workman and Hart (2005) except $^{138}Ce/^{142}Ce$ (mean $\varepsilon$Ce value of MORB samples = −0.93: Bellot et al., 2013).
[c] McDonough and Sun (1995) except $^{138}Ce/^{142}Ce$ (mean value of carbonaceous and ordinary chondrites: Makishima and Masuda, 1993; Bellot et al., 2013) and $^{143}Nd/^{144}Nd$ (Bouvier et al., 2008).

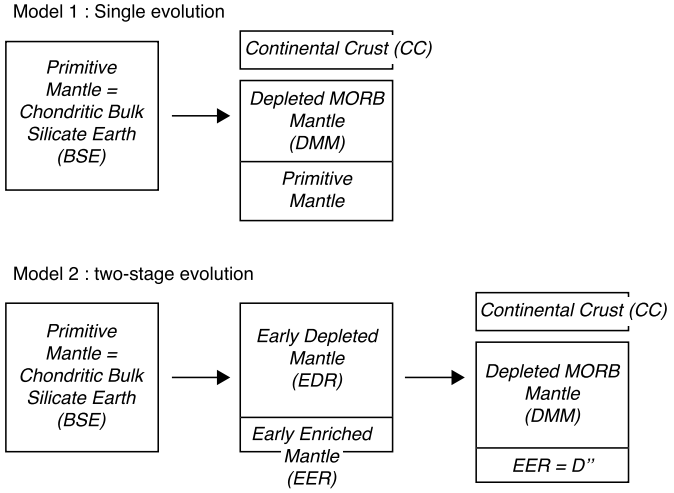


**Fig. 2.** Schematic illustration of the two box-models used to determine the Ce and Nd isotopic compositions of the deeper part of the mantle (D″ boundary layer).

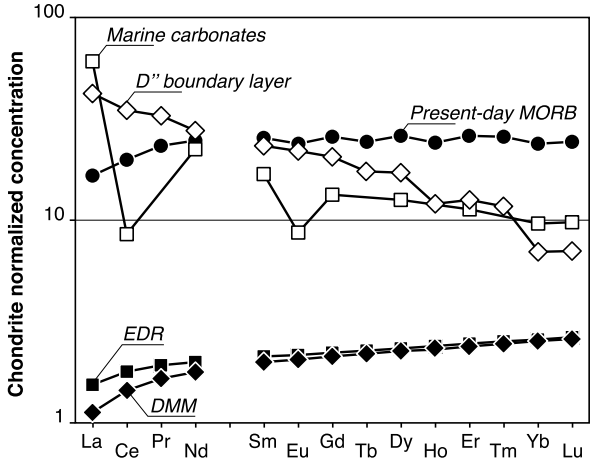


**Fig. 3.** Rare-earth-element chondrite-normalized patterns (chondrite data from Anders and Grevesse, 1989). Marine carbonates (data from Plank and Langmuir, 1998) and modelled D″ boundary layer (Table 3) have La/Ce ratios higher than unity and Sm/Nd lower than unity. Conversely, the Depleted MORB Mantle (DMM, Table 3), the Early Depleted Mantle (EDR, Table 3) and MORB samples (data from Hofmann, 1988) show La/Ce < 1 and Sm/Nd > 1. Consequently recycled carbonates and D″ material are likely to display $\varepsilon$Ce > 0 and $\varepsilon$Nd < 0 with time, whereas mantle-related materials will show $\varepsilon$Ce < 0 and $\varepsilon$Nd > 0.

as well as $^{147}Sm/^{144}Nd$ ratios of 0.1960, 0.2085 and 0.2200 for the three-step evolution of DMM (the DMM, two-stage model discussed above is calculated using three steps) that reproduces the Nd isotope composition of MORBs (4.568–4.518 Ga, 4.518–2.0 Ga, 2.0 Ga-actual, see Carlson and Boyet, 2008). Given the REE content of CC, we then calculated the $W^{Nd}$ sialic index and the mass fraction of CC involved in the EDR budget, and then EDR. Assuming $4.18 \times 10^{24}$ kg is the total mass of the mantle (sum of the masses of the upper mantle, transition zone, lower mantle and D″ layer) gives an EDR/Mantle mass ratio of at least 97%, or EER = 3%, in agreement with the mass fraction of D″. This proportion is thus entered into the BSE budget equation (BSE = EER + EDR), allowing calculation of REE contents of EER together with $\varepsilon$Ce and $\varepsilon$Nd values of about +1.5 and −18, respectively (Fig. 3; Table 3). It must be repeated that the values are dependent on input data for CC. The Nd isotope composition we propose for D″, however, is consistent with that of Tolstikhin et al. (2006) who give an $\varepsilon$Nd value of −15.

### 5.2. Modelling of $^{138}Ce/^{142}Ce$ and $^{143}Nd/^{144}Nd$ isotopic ratios in recycled oceanic crust and marine carbonates

Present-day marine carbonates (Plank and Langmuir, 1998) show REE patterns similar to that of seawater. Notably, they show chondrite-normalized ratios $(La/Ce)_N > 1$ and $(Sm/Nd)_N < 1$ (Fig. 3). Hence, old recycled carbonates are likely to display $\varepsilon$Ce > 0 and $\varepsilon$Nd < 0. Conversely, partial melting of Recycled Oceanic Crust (ROC) produces $\varepsilon$Ce < 0 and $\varepsilon$Nd > 0 if approximated to MORBs, as the latter present $(La/Ce)_N$ and $(Sm/Nd)_N$ ratios with inverse fractionation values (Hofmann, 1988; Fig. 3).

#### 5.2.1. Recycled carbonates

We model the Nd isotope composition of recycled carbonates assuming an initial isotopic composition similar to that determined for the seawater through time (Bertram et al., 1992; Derry and Jacobsen, 1988) and calculating present-day values using Sm/Nd ratios measured in marine carbonates (mean Carbonate Sediments in Patino et al., 2000). This corresponds to $\varepsilon Nd = -3.4$ for 400 Ma-old carbonates, and to $\varepsilon Nd = -15.3$ for 1.6 Ga-old ones. At present there is no published Ce isotope data for old seawater (and/or marine carbonates). To determine the initial Ce isotopic composition of recycled carbonates we consider that the Nd and Ce isotopic compositions of seawater result from the contribution of continental inputs and from the weathering of volcanic rocks from the ocean floor (Shimizu et al., 1994). We use the DMM, two-stage model discussed in Section 5.1 to calculate the Ce and Nd isotopic composition of the volcanic seafloor 400 Ma and 1.6 Ga ago. For the continental crust, we use the present-day value for 400 Ma-old rocks and the Ce–Nd data of Tanaka et al. (1987) for 1.6 Ga-old ones (Broderic Falls granodiorite S-83002B and Bushveld gabbro KS-70030821). We calculate mass proportions needed to explain $\varepsilon$Nd values of 400 Ma-old and 1.6 Ga-old seawater and apply them to $\varepsilon$Ce (Supplementary file A4). We then determine the

**Table 4**
Composition of recycled marine and secondary carbonates and oceanic crust. All contents are in ppm.

| | Recycled oceanic crust[a] | Marine carbonates[b] | Mantle wedge[c] | Carbonatite metasomatized mantle[d] | Carbonatite source | 1.6 Ga-old recycled oceanic crust[e] | 1.6 Ga-old secondary carbonates[b] |
|---|---|---|---|---|---|---|---|
| | 400 Ma ago | 400 Ma ago | 400 Ma ago | 400 Ma ago | Today | Today | Today |
| [La] | 2.03 | 8.78 | 0.26 | 1.69 | 1.69 | 3.90 | 8.78 |
| [Ce] | 5.38 | 2.40 | 0.87 | 4.15 | 4.15 | 12.00 | 2.40 |
| $^{138}Ce/^{142}Ce$ | 0.02256096 | 0.02256799 | 0.02256096 | 0.02256103 | 0.02256420 | 0.02256399 | 0.02266810 |
| $\varepsilon Ce(T)$ | −0.7 | +2.4 | −0.7 | −0.7 | −0.5 | −0.6 | +45.5 |
| [Sm] | 2.60 | 1.45 | 0.29 | 1.13 | 1.13 | 3.75 | 1.45 |
| [Nd] | 7.25 | 6.79 | 0.81 | 4.51 | 4.51 | 11.18 | 6.79 |
| $^{143}Nd/^{144}Nd$ | 0.512580 | 0.511700 | 0.512580 | 0.512560 | 0.512955 | 0.512975 | 0.511844 |
| $\varepsilon Nd(T)$ | +9.1 | −8.1 | +9.1 | +8.7 | +6.4 | +6.7 | −15.3 |
| [U] | 0.06 | 0.15 | 0.003 | 0.05 | 0.05 | 0.07 | 0.15 |
| [Pb] | 0.17 | 3.70/0.46* | 0.02 | 0.20/0.14* | 0.20/0.14* | 0.21 | 3.70/0.46* |
| $^{206}Pb/^{204}Pb$ | 17.141 | 18.150 | 17.141 | 17.508/17.208 | 18.482/18.632 | 21.575 | 16.674/22.158 |

[a] La, Ce, Sm, Nd and U concentrations are from Patino et al. (2000); Pb is adjusted in order to have $^{238}U/^{204}Pb = 22$ (Chauvel et al., 1992).
[b] La, Ce, Sm, Nd, U and Pb concentrations are from Patino et al. (2000); *Pb is adjusted in order to have $^{238}U/^{204}Pb = 22$ (Hoernle et al., 2002).
[c] Pb and U concentrations are from Workman and Hart (2005).
[d] Calculations are done using mass proportions of 3:97 between 400 Ma-old marine carbonates and recycled oceanic crust, and of 2:98 between carbonatitic liquids and mantle wedge. La, Ce, Sm, Nd, U and Pb concentrations assume that garnet and clinopyroxene are controlling trace element budget. The mineralogy and associated partition coefficients are from the experimental studies of Hammouda et al. (2009) and Jones et al. (1995).
[e] La, Ce, Sm, Nd, and U concentrations are from Hofmann (1988); Pb is adjusted in order to have $^{238}U/^{204}Pb = 22$ (Chauvel et al., 1992).

present-day $^{138}Ce/^{142}Ce$ ratios of marine carbonates using their La and Ce contents, in the same way as for the Sm/Nd system. This gives $\varepsilon Ce = +13.7$ and $\varepsilon Ce = +45.5$ for 400 Ma-old and 1.6 Ga-old carbonates, respectively (Table 4).

Modelled $\varepsilon Ce$ values are far higher than what has been measured in surface and deep seawater (max $= +1.8$, see Shimizu et al., 1994; Tazoe et al., 2011). However, cerium is oxidized into insoluble $Ce^{4+}$ at ambient oceanic conditions, and it is scavenged rapidly from the seawater (Elderfield, 1988). Hence, large La/Ce fractionations characterize marine sediments, resulting in radiogenic Ce isotopic ratios with passage of time.

#### 5.2.2. Recycled oceanic crust

We use the DMM, two-stage model together with appropriate REE contents to determine the present-day isotopic ratios of recycled oceanic crust. We consider REE contents of altered oceanic crust (mixing of upper altered oceanic crust (UAOC) and lower altered oceanic crust (LAOC) in the proportions of 0.25:0.75, as reported in Patino et al., 2000) for the recycling of 400 Ma-old material (shallow recycling model), assuming that only the altered part of the oceanic crust contributes to partial melting. This gives present-day $\varepsilon Ce$ and $\varepsilon Nd$ values of around −0.7 and +10, respectively. In the case of the deeply recycled, 1.6 Ga-old oceanic crust we consider MORB-like REE contents, assuming that the whole recycled oceanic crust will interact with recycled carbonates. This leads to present-day $\varepsilon Ce$ and $\varepsilon Nd$ values of around −0.6 and +6.7, respectively (Table 4).

### 5.3. Ce–Nd evidence for recycled marine carbonates in the source of carbonatite parental magmas

Fig. 4 compares Ce–Nd ratios measured in carbonatites with those of mantle reservoirs (DMM, EDR or EER, discussed in Section 5.1) and of recycled material (oceanic crust and carbonates). Cape Verde, Canary and Morocco carbonatites have Ce and Nd isotopic signatures that do not match any of the mantle or recycled components. Thus, measured compositions indicate the involvement of at least two components.

Also shown in Fig. 4 are mixing curves: (a) between depleted MORB mantle (DMM) and D″ boundary material, (b) between 1.6 Ga-old, recycled oceanic crust (ROC) and D″ boundary material, (c) between 1.6 Ga-old, recycled oceanic crust (ROC) and recycled carbonates, and (d) between the mantle wedge (DMM-like) and a second end-member resulting from earlier mixing between 400 Ma-old recycled marine carbonates and oceanic crust. Carbonatites plot on (or are close to) each of the four curves. Although at first sight carbonate-recycling models and a deep source as origin of the carbon are in agreement with the data, a detailed examination of the models gives us relevant information about the origin of oceanic carbonatites.

#### 5.3.1. Deep source – primordial carbon

Mata et al. (2010) measured maximum helium $R/R_a$ values of 15.5 for Cape Verde carbonatites, which implicitly requires that the deep mantle signature of parental magmas is diluted by low $R/R_a$ materials. Both the asthenospheric mantle and the oceanic lithosphere have a DMM-like isotopic composition and a low-$R/R_a$ ratio. Thus, the curve related to the mixing of DMM and D″ (Fig. 4a) could illustrate the model proposed by Mata et al. (2010). The question as to whether the asthenosphere or the oceanic lithosphere participates in the magmatism of Cape Verde Islands was previously discussed for silicate rocks (Escrig et al., 2005; Millet et al., 2008). Combining major- and trace-elements with Sr–Nd–Pb–Os isotopes provides evidence for shallow-level assimilation, and argues in favour of a lithospheric origin for the DMM-like component involved in the Cape Verde magmatism. Mixing curves reported in Fig. 4a were produced assuming solid–solid mixing. In this case, DMM mass proportions that best explain our data for the DMM-D″ mixing range between 97.5 and 99%. In our understanding of the model by Mata et al. (2010), the D″ material carried by the Cape Verde plume melted before assimilating the oceanic lithosphere. This does not significantly change the shape of the DMM-D″ mixing curve, as Ce and Nd may have relatively similar behaviour during partial melting. However, because the carbonatitic melts would have been richer in Ce and Nd, an even larger assimilation of lithospheric material has to be considered, and the end-result of such assimilation can hardly be a carbonatite. Thus, although isotopic ratios measured in carbonatite samples can be reproduced with a binary mixing involving DMM- and D″-like materials, mixing proportions obtained from Ce–Nd isotope systems, combined with petrological evidence, argue against such a model.

Old recycled oceanic crust has a low $R/R_a$ ratio, resulting from He depletion through degassing at mid-ocean ridges (Hanyu and Kaneoka, 1997; Moreira and Kurz, 2001; Parai et al., 2009). Hence, mixing of D″-like materiel with recycled oceanic crust could also explain the helium $R/R_a$ values measured for Cape

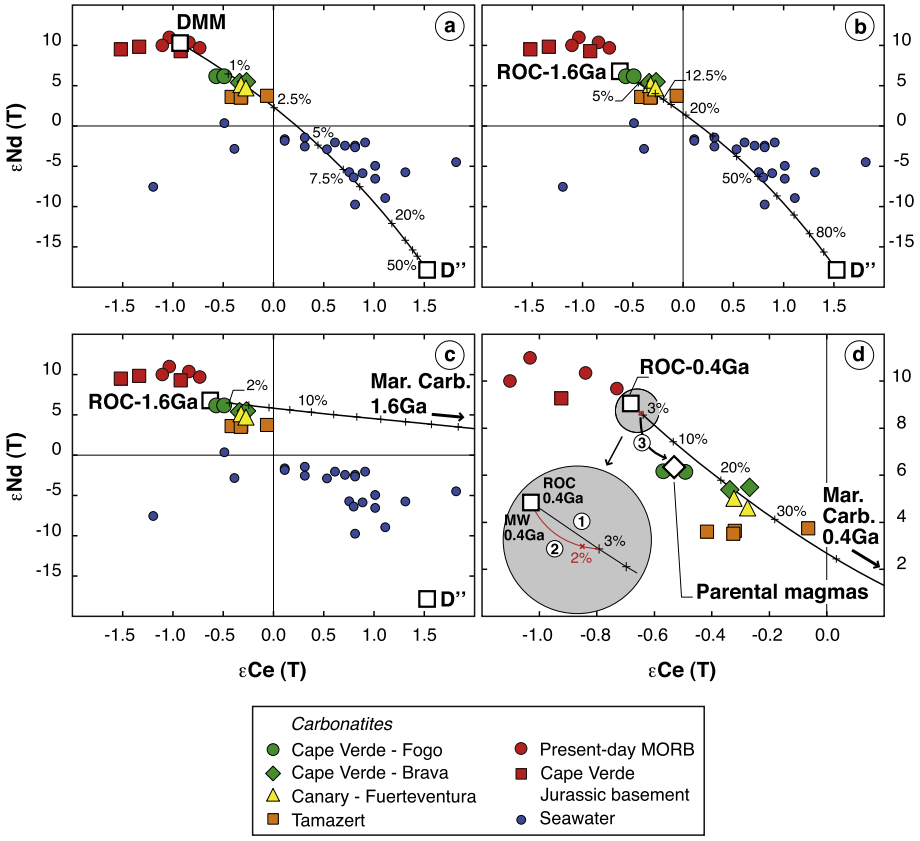


**Fig. 4.** Comparison between carbonatites, marine carbonates, recycled oceanic crust (ROC) and modelled Depleted Mantle (DMM) and D″ Boundary layer (D″) in the $\varepsilon$Nd(T) vs. $\varepsilon$Ce(T) diagram. (a) and (b) illustrate the binary mixing between D″-like material and either DMM-like oceanic lithosphere or 1.6 Ga-old recycled oceanic crust (Mata et al., 2010). (c) illustrates the binary mixing between 1.6 Ga-old recycled oceanic crust and secondary calcitic carbonates (Hoernle et al., 2002). (d) corresponds to the three-stage model by Doucelance et al. (2010): (1) partial melting of 400 Ma-old recycled oceanic crust and marine carbonates in mass proportions of 97:3; (2) mixing of carbonatitic melts generated at step 1 with mantle wedge (MW) in mass proportions of 2:98; and (3) radioactive decay and partial melting. For step 1, garnet and clinopyroxene are assumed to control trace element budget. Mineralogy and partition coefficients from the experimental study of Hammouda et al. (2009) are used for Ce and Nd content calculations. The melting degree is taken as being equal to the amount of carbonates in the mixing of marine carbonates and oceanic crust. The open diamond represents one specific model that allows reproducing Fogo carbonatites. Values for each mixing component are present-day values except for (d), for which it corresponds to 400 Ma-old ones. Ticks correspond to mass proportions of D″-like material (a&b) or recycled carbonates (c&d). Seawater data are from Shimizu et al. (1994) and Tazoe et al. (2011).

Verde carbonatites. Here, Ce–Nd ratios of Cape Verde samples imply mixing proportions of around 5:95 for D″-like material and recycled oceanic crust, respectively (Fig. 4b), in agreement with Mourão et al. (2012) who involved 1.3 Ga-old recycled oceanic crust with lower mantle material in mass proportions of 90:10 for the source of Brava carbonatites. This corresponds to $R/R_a \sim 8.3$ ($^4$He/$^3$He $\sim$ 87,500) for calcio-carbonatites, assuming $R/R_a = 0$ for ROC, and $R/Ra = 50$ ($^4$He/$^3$He $\sim$ 14,450) for lower mantle (Stuart et al., 2003), together with respective $^4$He contents of $3 \times 10^{-5}$ ccSTP/g (radioactive decay with U and Th MORB-like values during 1.6 Ga) and $1 \times 10^{-4}$ ccSTP/g (Allègre et al., 1986). Such a value is consistent with the $R/R_a$ values of 6.7 and 9 that Mata et al. (2010) measured for Fogo and Brava carbonatites. This does not explain, however, the high values ($R/R_a$ – 12.6–15.5) of São Vicente samples.

Mixing proportions obtained from Ce–Nd isotope systems can also be integrated into discussions on the carbon content of parental magmas of carbonatites. The bulk silicate Earth contains 765 ± 300 ppm of carbon (Marty, 2012), and some lower mantle domains may deliver up to 840 ppm C (3100 ppm $CO_2$, see Dasgupta, 2013). Thus, the mixing between oceanic lithosphere (20 ppm C, Marty, 2012) or recycled oceanic crust (containing no carbon) with D″-like material in mass proportions of 1 to 5% leads to maximum $CO_2$ contents of between 70 and 150 ppm for the source of carbonatite parental magmas, which limits the partial melting rate to 0.015% in the best case. Such a low value questions the possibility of connecting small drops of carbonatitic melts and for the carbonatite melts to subsequently reach the surface. Thus, although isotopic ratios measured in carbonatite samples can be reproduced with a binary mixing involving ROC- and D″-like materials, combining mixing proportions inferred from Ce–Nd and He and C data does not support such a model.

### 5.3.2. Recycled carbon

Turning to carbonate-recycling models (melting of recycled oceanic crust and carbonate mixtures), calculated Ce–Nd values reproduce measured isotopic compositions of carbonatites (Fig. 4c, d). Corresponding carbonate proportions are in the order of a few %. This corresponds to reasonable amounts of C to produce carbonatitic melts able to reach the surface, as well as a reasonable amount of carbonate sediments compared to that of the oceanic crust. This is also in agreement with He ratios measured in calcio-carbonatites. Doucelance et al. (2010) showed that a late assimilation of a small proportion (~2%) of plume melts by ocean-lithosphere carbonatitic melts allows satisfactory modelling of He composition, without modifying Nd isotope ratios. In the same way, in the case of deep recycling, secondary calcitic carbonates and subducted ocean crust can pick up high $^3$He/$^4$He during storage in D″ (or simply within the lower mantle). Our calculations show that a 5% contribution of the high-$^3$He reservoir is enough to explain the carbonatite $^3$He/$^4$He data. Both models of carbonate recycling involve altered oceanic crust and marine and/or secondary

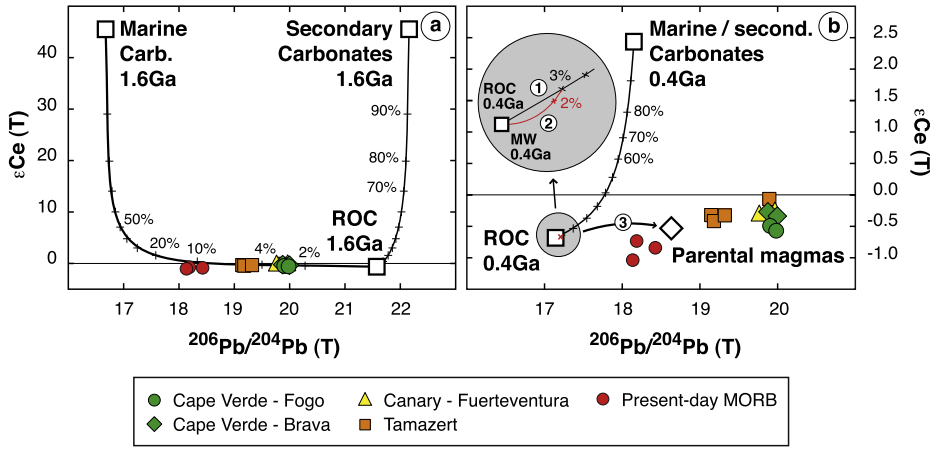


**Fig. 5.** Comparison between carbonatites, recycled oceanic crust (ROC), marine and secondary carbonates in the $\varepsilon$Ce(T) vs. $^{206}Pb/^{204}Pb$(T) diagram. (a) illustrates the binary mixing between 1.6 Ga-old recycled oceanic crust and marine and secondary calcitic carbonates (Hoernle et al., 2002). Ce and Pb isotope compositions are present-day values. (b) corresponds to the three-stage model by Doucelance et al. (2010): (1) partial melting of 400 Ma-old recycled oceanic crust and marine carbonates in mass proportions of 97:3; (2) mixing of carbonatitic melts generated at step 1 with mantle wedge (MW) in mass proportions of 2:98; and (3) radioactive decay and partial melting. For step 1, garnet and clinopyroxene are assumed to control trace element budget. Mineralogy and partition coefficients from the experimental studies of Hammouda et al. (2009) and Jones et al. (1995) are used for Ce and Pb content calculations. The melting degree is taken as being equal to the amount of carbonates in the mixing of marine carbonates and oceanic crust. Values for each mixing component are 400 Ma-old values. The open diamond represents the specific model that allows reproducing Ce–Nd isotope compositions of Fogo carbonatites (see Fig. 4). Ticks correspond to mass proportions of recycled carbonates. Pb data for present-day MORB are from Schiano et al. (1997) and Debaille et al. (2006).

calcitic carbonates. Although they present major differences concerning the age and depth of recycling, they end up with similar Ce–Nd isotopic compositions for carbonatites.

### 5.4. Pb isotope constraints on the age and depth of carbonate recycling

The carbonate recycling models discussed above involve altered oceanic crust combined with marine and/or secondary calcitic carbonates. Ce and Nd isotopes are barely (if not) sensitive to the nature of the carbonates (marine or secondary) compared to U–Pb, because La–Ce and Sm–Nd pairs behave similarly. Marine carbonates have a low U/Pb ratio of 0.04 (Patino et al., 2000) whereas secondary calcitic carbonates show a wide range of values from 0.0005 to 10 (mean value = 1.4, see supplementary data in Kelley et al., 2005). Thus secondary carbonates are expected to develop more radiogenic Pb isotope ratios than carbonate sediments with time.

The depth of carbonate recycling is also related to their nature. Hammouda (2003) and Yaxley and Brey (2004) have shown that carbonates recycled into the mantle are unlikely to be transported to depths greater than ~300 km due to melting reactions occurring along the subduction geotherm, whereas Dasgupta et al. (2004) proposed that the solidus of carbonated eclogite will not intersect the subduction geotherm before the transition zone. Furthermore, subducted sediments (including carbonates) are supposed to detach from the downgoing slab to form buoyant diapirs that may reduce the transport of trace elements and volatiles such as $CO_2$ into the deep mantle (Behn et al., 2011). Thus, if carbonates can be recycled, experimental studies strongly suggests they cannot survive transportation to the base of the lower mantle. As a consequence, only secondary carbonates trapped in deep fractures of the oceanic crust may escape melting and be recycled down to the deepest part of the lower mantle (Hammouda, 2003).

Hoernle et al. (2002) linked the genesis of Cape Verde and Canary calcio-carbonatites to the melting of secondary calcitic carbonates in 1.6 Ga-old, deeply recycled (down to the lower mantle), oceanic crust (the age of 1.6 Ga was determined from the Canary and Cape Verde carbonatite Pb data that form a linear trend in the uranogenic Pb isotope diagram). They considered that U is preferentially partitioned into carbonates and that carbonate precipitation mostly controls the U budget in altered oceanic crust (Staudigel et al., 1996). Hence, they estimated the Pb isotope composition of altered oceanic crust using a two-stage model. Stage 1 is from the Stacey and Kramers (1975) evolution curve and stage 2 uses a high $^{238}U/^{204}Pb$ ratio of 22 (or U/Pb ~ 0.33) corresponding to the value compiled for carbonate rocks by Faure (1986). The model was in agreement with the HIMU-like compositions of silicate samples from the Cape Verde archipelago that were explained by the recycling of an ancient, altered oceanic crust (Gerlach et al., 1988) thus suggesting that silicate and carbonatite samples from both archipelagos were related to the same, plume-related components. Fig. 5a compares the $^{206}Pb/^{204}Pb$ isotopic ratio that is calculated for altered oceanic crust (or secondary carbonates) following Hoernle et al. (2002) with that of calcio-carbonatites. Natural samples have significantly less radiogenic Pb ratios. Considering mixing with recycled oceanic crust does not lower $^{206}Pb/^{204}Pb$ values, as 1.6 Ga-old, recycled oceanic crust also presents $^{206}Pb/^{204}Pb$ ratios higher than those of carbonatites. On the contrary, radioactive ingrowth with a lower μ-value of ~2.5 (U/Pb = 0.04), as measured in carbonate sediments, gives $^{206}Pb/^{204}Pb$ ratios of ~16.67 that are able to balance the radiogenic Pb signature of recycled Proterozoic oceanic crust (see also Table 4). However, deep recycling of marine carbonates remains uncertain, thus suggesting that secondary carbonates have a lower $^{238}U/^{204}Pb$ ratio than that proposed by Hoernle et al. (2002).

On the other hand, Doucelance et al. (2010) proposed that oceanic carbonatites resulted from plume-induced partial melting of oceanic lithosphere containing portions of mantle wedge metasomatized by carbonatitic melts associated with the recycling of ~400 Ma-old marine carbonates and oceanic crust, together with minor assimilation of plume melts. The age of 400 Ma was selected to illustrate the model only because it was in agreement with geodynamic models of closure of the Rheic Ocean and opening of the Central Atlantic. Partial melting of 400 Ma-old oceanic crust and marine carbonates in mass proportions of 97:3 and subsequent metasomatism of the mantle wedge gives 400 Ma-old, carbonatite-metasomatized mantle with $^{206}Pb/^{204}Pb$ ratios of between 17.3 and 17.5, whose present-day value strongly depends on the U/Pb ratio of recycled carbonates. Considering marine carbonates with U/Pb = 0.04 gives $^{206}Pb/^{204}Pb$ ratios of around 18.5 (Fig. 5b). Such values are less radiogenic than those measured for Cape Verde and Canary calcio-carbonatites. Alternatively,

secondary calcitic carbonates with a higher U/Pb ratio may develop more radiogenic Pb compositions. However, considering U/Pb = 0.33 ($^{238}U/^{204}Pb \sim 22$) due to preferential partitioning of U gives $^{206}Pb/^{204}Pb$ ratios of ~18.6 for carbonatites, again less radiogenic than measured values (Fig. 5b and Table 4). This last result is related to our modelling of U and Pb concentrations of secondary carbonates. In order to increase the U/Pb ratio from 0.04 to 0.33, we have considered that secondary carbonates have the same U content as marine carbonates, but lower Pb. The higher U/Pb ratio of secondary carbonates is then balanced by their lower Pb concentration. This illustrates how dependent the model is on U and Pb concentrations (and thus U/Pb ratios) in secondary carbonates, as is the case for Hoernle et al. (2002). For example, using average U and Pb concentrations of 3 and 12 ppm (U/Pb = 0.25) measured in secondary carbonates by Kelley et al. (2005) gives a $^{206}Pb/^{204}Pb$ ratio of ~19. Finally, another solution is to age recycling in order to allow higher $^{206}Pb/^{204}Pb$ in-growth by radioactive decay. For example, using the same model with 600–700 Ma-old marine carbonates and oceanic crust gives $^{206}Pb/^{204}Pb$ isotopic ratios of between 19.5 and 19.8, in agreement with values measured in carbonatites from the Cape Verde and Canary archipelago.

Pb isotope compositions measured in oceanic calcio-carbonatites are more variable than Ce and Nd ones. They are associated with $^{238}U/^{204}Pb$ ratios ranging from 0.2 to 362 (Hoernle et al., 2002; De Ignacio et al., 2006, 2012; this study), also more variable than their $^{138}La/^{142}Ce$ and $^{147}Sm/^{144}Nd$ counterparts. Most of them, however, show values <20 (26 out of 32 samples with measured U and Pb contents). Values calculated in the source of carbonatite parental magmas define a small range of 20–25 when considering deep and shallow, marine and secondary carbonate recycling models. Decrease of the U/Pb ratio during carbonatite source partial melting is in agreement with augite/carbonate liquid partition coefficients determined for these two elements by Jones et al. (1995). However, the experimental results of Dasgupta et al. (2009) show that U is more incompatible than Pb during peridotite-derived carbonatite genesis under upper mantle conditions, thus suggesting that $^{238}U/^{204}Pb$ measured in natural carbonatites should be greater than 25. The disagreement between the experimental partitioning data, together with the great variability of U/Pb ratios in secondary carbonates, makes the modelling of U/Pb fractionation and evolution during carbonatite genesis difficult.

## 6. Conclusions

Oceanic calcio-carbonatites from the Cape Verde and Canary archipelagos (Atlantic Ocean) and Moroccan samples from Tamazert massif show Ce–Nd isotope compositions that plot on a mixing trend between a depleted end-member (unradiogenic Ce and radiogenic Nd) and either marine carbonates or an enriched component with similar Ce–Nd to that inferred for the D″ boundary layer. Mixing proportions obtained from Ce–Nd isotopes coupled to petrological considerations favour the recycling of marine carbonates as the source of carbon rather than primordial one. In any case, the D″-like component inferred from high $^{3}He/^{4}He$ ratios occurs in minor proportions in the source of parental magmas of carbonatites.

Pb isotope compositions lead to investigation into the age and depth of carbonate recycling. However, both remain difficult to constrain due to large uncertainties in U/Pb fractionation in recycled carbonates and also in Pb behaviour during carbonatite source partial melting.

It may seem that the ‘shallow’ recycling scenario requires very specific conditions compared to the ‘deep’ one: the oceanic lithosphere must contain carbonatite-melt metasomatized portions and it has to be thick enough in order to favour plume-induced partial melting at its base. However, this may explain why oceanic carbonatites are so rare and are not observed in all HIMU-like archipelagos.

Finally, whatever the recycling model, we would like to emphasize that our results suggest that organic carbon has to be recycled together with marine and/or secondary carbonates in order to balance their zero $\partial^{13}C$ value. Indeed, carbon from carbonatites usually possesses isotopic composition with $\partial^{13}C$ around −5.5‰, which is interpreted as representing “mantle carbon”, although the ultimate origin of the carbon has never been properly debated. As an alternative, our results may also suggest that melting after recycling of MORB and carbonates as well as migration into the mantle is able to shift carbon isotopes towards mantle values. These last points underline the necessity of improving our understanding of the $\partial^{13}C$ values of mantle reservoirs.

## Acknowledgements

The authors wish to thank João Mata who kindly provided Brava samples and Saïd Mourtada for Tamazert ones. The authors are also grateful to Delphine Auclair and Jean-Luc Piro for support during Ce–Nd isotope and trace element analyses and Christian Pin for his contribution to the development of the La–Ce systematics. Frances van Wyk de Vries helped us with the quality of the manuscript. The paper was also improved by critical comments from two anonymous reviewers. This research was financed by the French Government Laboratory of Excellence initiative n° ANR-10-LABX-0006, the Région Auvergne, the European Regional Development Fund, and INSU projects SYSTER 2013 & 2014. This is Laboratory of Excellence ClerVolc contribution number 122.

## Appendix A. Supplementary material

Supplementary material related to this article can be found online at http://dx.doi.org/10.1016/j.epsl.2014.09.042.

## References

Allègre, C.-J., Lewin, E., 1989. Chemical structure and history of the Earth: evidence from global non-linear inversion of isotopic data in a three-box model. Earth Planet. Sci. Lett. 96, 61–88.

Allègre, J.-C., Staudacher, T., Sarda, P., 1986. Rare gas systematics: formation of the atmosphere, evolution and structure of the Earth’s mantle. Earth Planet. Sci. Lett. 81, 127–150.

Amakawa, H., Nozaki, Y., Masuda, A., 1996. Precise determination of variations in the $^{138}Ce/^{142}Ce$ ratios of marine ferromanganese nodules. Chem. Geol. 131, 183–195.

Anders, E., Grevesse, N., 1989. Abundances of the elements: meteoritic and solar. Geochim. Cosmochim. Acta 53, 197–214.

Bailey, D.K., 1989. Carbonate-rich melts from the mantle in the volcanoes of south–east Zambia. Nature 338, 415–418.

Baker, J., Peate, D., Waight, T., Meyzen, C., 2004. Pb isotopic analysis of standards and samples using a Pb–Pb double spike and thallium to correct for mass bias with a double-focusing MC-ICP-MS. Chem. Geol. 211, 275–303.

Behn, M.D., Kelemen, P.B., Hirth, G., Hacker, B.R., Massonne, H.-J., 2011. Diapirs as the source of the sediment signature in arc lavas. Nat. Geosci. 4, 641–646.

Bell, K., Blenkinsop, J., 1987. Nd and Sr isotopic compositions of East African carbonatites: implications for mantle heterogeneity. Geology 15, 99–102.

Bell, K., Tilton, G.R., 2001. Nd, Pb and Sr isotopic compositions of East African carbonatites: evidence for mantle mixing and plume inhomogeneity. J. Petrol. 42, 1927–1945.

Bellot, N., Boyet, M., Pin, C., Chauvel, C., Doucelance, R., Auclair, D., 2013. Development of the La–Ce Systematics: application to Arc Magmas. Mineral. Mag. 77, 682.

Bertram, C.J., Elderfield, H., Aldridge, R.J., Conway Morris, S., 1992. $^{87}Sr/^{86}Sr$, $^{143}Nd/^{144}Nd$ and REEs in Silurian phosphatic fossils. Earth Planet. Sci. Lett. 113, 239–249.

Bosse, V., Doucelance, R., Fornari, M., Mata, J., 2007. Temporal evolution of the Cabo Verde archipelago: new constraints from $^{40}Ar–^{39}Ar$ data. Geochim. Cosmochim. Acta 71, Suppl. 1, A110.

Bouabdellah, M., Hoernle, K., Kchit, A., Duggen, S., Hauff, F., Klügel, A., Lowry, D., Beaudoin, G., 2010. Petrogenesis of the Eocene Tamazert Continental Carbonatites (Central High Atlas, Morocco): implications for a common source for

the Tamazert and Canary and Cape Verde Island carbonatites. J. Petrol. 51, 1655–1686.
Bouvier, A., Vervoort, J.D., Patchett, P.J., 2008. The Lu–Hf and Sm–Nd isotopic composition of CHUR: constraints from unequilibrated chondrites and implications for the bulk composition of terrestrial planets. Earth Planet. Sci. Lett. 273, 48–57.
Boyet, M., Carlson, R.W., 2005. $^{142}$Nd evidence for early (>4.53 Ga) global differentiation of the silicate Earth. Science 309, 576–581.
Boyet, M., Carlson, R.W., 2006. A new geochemical model for the Earth's mantle inferred from $^{146}$Sm–$^{142}$Nd systematics. Earth Planet. Sci. Lett. 250, 254–268.
Cantagrel, J.-M., Fuster, J.-M., Pin, C., Renaud, U., Ibarrola, E., 1993. Lower Miocene carbonatites from Fuerteventura (23 Ma: U–Pb, Zircon) and the early magmatism of an oceanic island (Canary Islands). C. R. Acad. Sci. Paris 316, 1147–1153.
Carlson, R.W., Boyet, M., 2008. Composition of the Earth's interior: the importance of early events. Philos. Trans. R. Soc. A 366, 4077–4103.
Cartigny, P., Harris, J.W., Phillips, D., Girard, M., Javoy, M., 1998. Subducted-related diamonds? The evidence for a mantle-derived origin from coupled $\partial^{13}C$–$\partial^{15}N$ determinations. Chem. Geol. 147, 147–159.
Chauvel, C., Hofmann, A.W., Vidal, P., 1992. HIMU-EM: the French Polynesian connection. Earth Planet. Sci. Lett. 110, 99–119.
Dalton, J.A., Wood, B.J., 1993. The compositions of primary carbonate melts and their evolution through wallrock reaction in the mantle. Earth Planet. Sci. Lett. 119, 511–525.
Dasgupta, R., 2013. Ingassing, storage, and outgassing of terrestrial carbon through geologic time. Rev. Mineral. Geochem. 75, 183–229.
Dasgupta, R., Hirschmann, M., Withers, A.C., 2004. Deep cycling of carbon constrained by the solidus of anhydrous, carbonated eclogite under upper mantle conditions. Earth Planet. Sci. Lett. 227, 73–85.
Dasgupta, R., Hirschmann, M.M., McDonough, W.F., Spiegelman, M., Withers, A.C., 2009. Trace element partitioning between garnet lherzolite and carbonatite at 6.6 and 8.6 GPa with applications to the geochemistry of the mantle and of mantle-derived melts. Chem. Geol. 262, 57–77.
Debaille, V., Blichert-Toft, J., Agranier, A., Doucelance, R., Schiano, P., Albarede, F., 2006. Geochemical component relationships in MORB from the Mid-Atlantic Ridge, 22–35° N. Earth Planet. Sci. Lett. 241, 844–862.
De Ignacio, C., Muñoz, M., Sagredo, J., Fernandez-Santin, S., Johansson, A., 2006. Isotope geochemistry and FOZO mantle component of the alkaline–carbonatitic association of Fuerteventura, Canary Islands, Spain. Chem. Geol. 232, 99–113.
De Ignacio, C., Muñoz, M., Sagredo, J., 2012. Carbonatites and associated nephelinites from São Vicente, Cape Verde Islands. Mineral. Mag. 76, 311–355.
Deines, P., 1989. Stable isotope variations in carbonatites. In: Bell, K. (Ed.), Carbonatites: Genesis and Evolution. Unwin Hyman Ltd., London, UK, pp. 301–359.
Derry, L.A., Jacobsen, S.B., 1988. The Nd and Sr isotopic evolution of Proterozoic seawater. Geophys. Res. Lett. 15, 397–400.
Doucelance, R., Manhès, G., 2001. Reevaluation of precise lead isotope measurements by thermal ionization mass spectrometry: comparison with determinations by plasma source mass spectrometry. Chem. Geol. 176, 361–377.
Doucelance, R., Escrig, S., Moreira, M., Gariépy, C., Kurz, M.D., 2003. Pb–Sr–He isotope and trace element geochemistry of the Cape Verde Archipelago. Geochim. Cosmochim. Acta 67, 3717–3733.
Doucelance, R., Hammouda, T., Moreira, M., Martins, J.C., 2010. Geochemical constraints on depth of origin of oceanic carbonatites: the Cape Verde case. Geochim. Cosmochim. Acta 74, 7261–7282.
Eggler, D.H., 1978. The effect of carbon dioxide upon partial melting of peridotite in the system sodium oxide–calcium oxide–aluminum oxide–magnesium oxide–silicon dioxide–carbon dioxide to 35 kb, with an analysis of melting in a peridotite–water–carbon dioxide system. Am. J. Sci. 278, 305–343.
Elderfield, H., 1988. The oceanic chemistry of the rare-earth elements. Philos. Trans. R. Soc. Lond. A 325, 105–126.
Escrig, S., Doucelance, R., Moreira, M., Allègre, C.J., 2005. Os isotope systematics in Fogo basalts: evidence for lower continental crust residing in the oceanic lithosphere beneath the Cape Verde Islands. Chem. Geol. 219, 93–113.
Faure, G., 1986. Principles of Isotope Geology. Wiley, Chichester.
Gerlach, D.C., Cliff, R.A., Davies, G.R., Norry, M., Hodgeson, N., 1988. Magma sources of the Cape Verdes Archipelago: isotopic and trace element constraints. Geochim. Cosmochim. Acta 52, 2979–2992.
Goldstein, S.J., Jacobsen, S.B., 1988. Nd and Sr isotopic systematics of river water suspended material: implications for crustal evolution. Earth Planet. Sci. Lett. 87, 249–265.
Hammouda, T., 2003. High-pressure melting of carbonated eclogite and experimental constraints on carbon recycling and storage in the mantle. Earth Planet. Sci. Lett. 214, 357–368.
Hammouda, T., Moine, B.N., Devidal, J.L., Vincent, C., 2009. Trace element partitioning during partial melting of carbonated eclogites. Phys. Earth Planet. Inter. 174, 60–69.
Hammouda, T., Chantel, J., Manthilake, G., Guignard, J., Crichton, W., 2014. Hot mantle geotherms stabilize calcic carbonatite magmas up to the surface. Geology 42, 911–914.
Hanyu, T., Kaneoka, I., 1997. The uniform and low He/He ratios of HIMU basalts as evidence for their origin as recycled materials. Nature 390, 273–276.
Hoernle, K., Tilton, G., LeBas, M.J., Duggen, S., Garbe-Schönberg, D., 2002. Geochemistry of oceanic carbonatites compared with continental carbonatites: mantle recycling of oceanic crustal carbonate. Contrib. Mineral. Petrol. 142, 520–542.
Hofmann, A.W., 1988. Chemical differentiation of the Earth: the relationship between mantle, continental crust, and oceanic crust. Earth Planet. Sci. Lett. 90, 297–314.
Holm, P.M., Wilson, J.R., Christensen, B.P., Hansen, L., Hansen, S.L., Hein, K.M., Mortensen, A.K., Pedersen, R., Plesner, S., Runge, M.K., 2006. Sampling the Cape Verde mantle plume: evolution of melt composition on Santo Antão, Cape Verde Islands. J. Petrol. 47, 145–189.
Jones, J.H., Walker, D., Pickett, D.A., Murrell, M.T., Beattie, P., 1995. Experimental investigations of the partitioning of Nb, Mo, Ba, Ce, Pb, Ra, Th, Pa, and U between immiscible carbonate and silicate liquids. Geochim. Cosmochim. Acta 59, 1307–1320.
Kelley, K.A., Plank, T., Farr, L., Ludden, J., Staudigel, H., 2005. Subduction cycling of U, Th, and Pb. Earth Planet. Sci. Lett. 234, 369–383.
Kiseeva, E.S., Yaxley, G.M., Hermann, J., Litasov, K.D., Rosenthal, A., Kamenetsky, V.S., 2012. An experimental study of carbonated eclogite at 3.5–5.5 GPa – implications for silicate and carbonate metasomatism in the cratonic mantle. J. Petrol. 53, 727–759.
Lancelot, J., Allègre, C.J., 1974. Origin of carbonatitic magma in the light of the Pb–U–Th isotope system. Earth Planet. Sci. Lett. 22, 233–238.
Madeira, J., Mata, J., Mourão, C., Brum da Silveira, A., Martins, S., Ramalho, R., Hoffmann, D.L., 2010. Volcano-stratigraphic and structural evolution of Brava Island (Cape Verde) based on $^{40}$Ar/$^{39}$Ar, U–Th and field constraints. J. Volcanol. Geotherm. Res. 196, 219–235.
Makishima, A., Masuda, A., 1993. Primordial Ce isotopic composition of the Solar System. Chem. Geol. 106, 197–205.
Manhès, G., Minster, J.-F., Allègre, C.J., 1978. Comparative U–Th–Pb and Rb–Sr study of the St-Séverin amphoterites: consequence for early solar system chronology. Earth Planet. Sci. Lett. 39, 14–24.
Marty, B., 2012. The origins and concentrations of water, carbon, nitrogen and noble gases on Earth. Earth Planet. Sci. Lett. 313–314, 56–66.
Marty, B., Tolstikhin, I., Kamensky, I.L., Nivin, V., Balaganskaya, E., Zimmermann, J.-L., 1998. Plume-derived rare gases in 380 Ma carbonatites from the Kola region (Russia) and the argon isotopic composition in the deep mantle. Earth Planet. Sci. Lett. 164, 179–192.
Mata, J., Moreira, M., Doucelance, R., Ader, M., Silva, L.C., 2010. Noble gas and carbon isotopic signatures of Cape Verde oceanic carbonatites: implications for carbon provenance. Earth Planet. Sci. Lett. 291, 70–83.
McDonough, W.F., Sun, S.-S., 1995. The composition of the Earth. Chem. Geol. 120, 223–253.
Millet, M.-A., Doucelance, R., Schiano, P., David, K., Bosq, C., 2008. Mantle plume heterogeneity versus shallow-level interactions: a case study, the São Nicolau Island, Cape Verde archipelago. J. Volcanol. Geotherm. Res. 176, 265–276.
Moreira, M., Kurz, M., 2001. Subducted oceanic lithosphere and the origin of the "high" basalt helium isotopic signature. Earth Planet. Sci. Lett. 189, 49–57.
Mourão, C., Mata, J., Doucelance, R., Madeira, J., Brum da Silveira, A., Silva, L.C., Moreira, M., 2010. Quaternary extrusive calcio-carbonatite volcanism in Brava Island (Cape Verde). J. Afr. Earth Sci. 56, 59–74.
Mourão, C., Mata, J., Doucelance, R., Madeira, J., Millet, M.-A., Moreira, M., 2012. Geochemical temporal evolution of Brava Island magmatism: constraints on the variability of Cape Verde mantle sources and on carbonatite–silicate magma link. Chem. Geol. 334, 44–61.
Mourtada, S., LeBas, M.J., Pin, C., 1997. Petrogenesis of Mg-carbonatites from Tamazert in the Moroccan High Atlas. C. R. Acad. Sci. Paris 325, 559–564.
Nelson, D.R., Chivas, A.R., Chappell, B.W., McCulloch, M.T., 1988. Geochemical and isotopic systematics in carbonatites and implications for the evolution of ocean-island sources. Geochim. Cosmochim. Acta 52, 1–17.
Parai, R., Mukhopadhyay, S., Lassiter, J.C., 2009. New constraints on the HIMU mantle from neon and helium isotopic compositions of basalts from the Cook-Austral Islands. Earth Planet. Sci. Lett. 277, 253–261.
Patino, L.C., Carr, M.J., Feigenson, M.D., 2000. Local and regional variations in Central American arc lavas controlled by variations in subducted sediment input. Contrib. Mineral. Petrol. 138, 265–283.
Pearson, D.G., Boyd, F.R., Haggerty, S.E., Pasteris, J.D., Field, S.W., Nixon, P.H., Pokhilenko, N.P., 1994. The characterization and origin of graphite in cratonic lithospheric mantle: a petrological carbon isotope and Raman spectroscopic study. Contrib. Mineral. Petrol. 115, 449–466.
Plank, T., Langmuir, C.H., 1998. The chemical composition of subducting sediment and its consequences for the crust and mantle. Chem. Geol. 145, 325–394.
Rudnick, R.L., Gao, S., 2003. Composition of the continental crust. In: Rudnick, R.L., Holland, H.D., Turekian, K.K. (Eds.), The Crust. In: Treatise on Geochemistry, vol. 3. Elsevier–Pergamon, Oxford, pp. 1–64.
Salters, V.J.M., Stracke, A., 2004. Composition of the depleted mantle. Geochem. Geophys. Geosyst. 5. http://dx.doi.org/10.1029/2003GC000597.
Sasada, T., Hiyagon, H., Bell, K., Ebihara, M., 1997. Mantle-derived noble gases in carbonatites. Geochim. Cosmochim. Acta 61, 4219–4228.
Sato, J., Hirose, T., 1981. Half-life of $^{138}$La. Radiochem. Radioanal. Lett. 46, 145–152.

Schiano, P., Birck, J.-L., Allègre, C.J., 1997. Osmium–strontium–neodymium–lead isotopic covariations in mid-ocean ridge basalt glasses and the heterogeneity of the upper mantle. Earth Planet. Sci. Lett. 150, 363–379.

Shimizu, H., Tachikawa, K., Masuda, A., Nozaki, Y., 1994. Cerium and neodymium isotope ratios and REE patterns in seawater from the North Pacific Ocean. Geochim. Cosmochim. Acta 58, 323–333.

Stacey, J.S., Kramers, J.D., 1975. Approximation of terrestrial lead isotope evolution by a two-stage model. Earth Planet. Sci. Lett. 26, 207–221.

Staudigel, H., Plank, T., White, B., Schminke, H.-U., 1996. Geochemical fluxes during seafloor alteration of the basaltic upper oceanic crust: DSDP Sites 417 and 418. In: Subduction: Top to Bottom. In: Geophysical Monograph, vol. 96. American Geophysical Union, Washington, DC, pp. 19–38.

Stuart, F.M., Lass-Evans, S., Fitton, J.G., Ellam, R.M., 2003. High $^{3}He/^{4}He$ ratios in picritic basalts from Baffin Island and the role of a mixed reservoir in mantle plumes. Nature 424, 57–59.

Tanaka, T., Shimizu, H., Kawata, Y., Masuda, A., 1987. Combined La–Ce and Sm–Nd isotope systematics in petrogenetic studies. Nature 327, 113–117.

Tanimizu, M., 2000. Geophysical determination of the $^{138}La$ $\beta^{-}$ decay constant. Phys. Rev. C 62, 017601.

Taylor, S.R., McLennan, S.M., 1995. The geochemical evolution of the continental crust. Rev. Geophys. 33, 241–265.

Tazoe, H., Obata, H., Gamo, T., 2011. Coupled isotopic systematics of surface cerium and neodymium in the Pacific Ocean. Geochem. Geophys. Geosyst. 12. http://dx.doi.org/10.1029/2010GC003342.

Tolstikhin, I.N., Kramers, J.D., Hofmann, A.W., 2006. A chemical Earth model with whole mantle convection: the importance of a core–mantle boundary layer (D″) and its early formation. Chem. Geol. 226, 79–99.

Wallace, M.E., Green, D.H., 1988. An experimental determination of primary carbonatite magma composition. Nature 335, 343–346.

Willbold, M., 2007. Determination of Ce isotopes by TIMS and MC-ICPMS and initiation of a new, homogeneous Ce isotopic reference material. J. Anal. At. Spectrom. 22, 1364–1372.

Woolley, A.R., Kempe, D.R.C., 1989. Carbonatites: nomenclature, average chemical compositions, and element distribution. In: Bell, K. (Ed.), Carbonatites, Genesis and Evolution. Unwin Hyman, London, pp. 1–14.

Woolley, A.R., Kjarsgaard, B.A., 2008. Carbonatite Occurrences of the World: Map and Database. Geological Survey of Canada, Open File. 1 CD-ROM + 1 map.

Workman, R.K., Hart, S.R., 2005. Major and trace element composition of the depleted MORB mantle (DMM). Earth Planet. Sci. Lett. 231, 53–72.

Wyllie, P.J., Huang, W.L., 1976. Carbonation and melting reactions in the system $CaO–MgO–SiO_2–CO_2$ at mantle pressures with geophysical and petrological applications. Contrib. Mineral. Petrol. 54, 79–107.

Wyllie, P.J., Huang, W.-L., Otto, J., Byrnes, A.P., 1983. Carbonation of peridotites and decarbonation of siliceous dolomites represented in the system $CaO–MgO–SiO_2–CO_2$ to 30 kbar. Tectonophysics 100, 359–388.

Yaxley, G.M., Brey, G.P., 2004. Phase relations of carbonate-bearing eclogite assemblages from 2.5 to 5.5 GPa: implications for petrogenesis of carbonatites. Contrib. Mineral. Petrol. 146, 606–619.

AGU PUBLICATIONS

Geochemistry, Geophysics, Geosystems

RESEARCH ARTICLE
10.1002/2014GC005235

**Key Points:**
- We characterize the geochemical heterogeneity of the Socompa avalanche deposit
- We present Sr-Nd isotope ratios for matrices and rock fragments from the deposit
- The isotopic heterogeneity of the deposits increases from source to front

**Supporting Information:**
- Data table
- Additional figures
- Readme

**Correspondence to:**
R. Doucelance,
r.doucelance@opgc.univ-bpclermont.fr

**Citation:**
Doucelance, R., K. Kelfoun, P. Labazuy, and C. Bosq (2014), Geochemical insights into the internal dynamics of debris avalanches. A case study: The Socompa avalanche, Chile, *Geochem. Geophys. Geosyst.*, *15*, doi:10.1002/2014GC005235.

Received 8 JAN 2014
Accepted 18 APR 2014
Accepted article online 23 APR 2014

# Geochemical insights into the internal dynamics of debris avalanches. A case study: The Socompa avalanche, Chile

**Régis Doucelance[1,2,3], Karim Kelfoun[1,2,3], Philippe Labazuy[1,2,3], and Chantal Bosq[1,2,3]**

[1]Laboratoire Magmas et Volcans, Université Blaise Pascal, Clermont-Ferrand, France, [2]CNRS, UMR 6524, LMV, Clermont-Ferrand, France, [3]IRD, R 163, LMV, Clermont-Ferrand, France

**Abstract** One way to infer the internal dynamics of debris avalanches is to characterize the heterogeneity of their deposits. Here we present high-precision Sr-Nd isotope compositions, plus major and trace element concentrations, of matrix samples and rock fragments from the Socompa debris-avalanche deposit (Chile). The Socompa blocks are easily identifiable in the field, but distinguishing substrate debris from disaggregated material formed at the volcano is difficult to do with only field criteria. Combining isotope data with field observations can help with this. Measured Sr and Nd isotope ratios show significant variations, defining a binary mixing array where matrix and rock deposits overlap. This testifies to the mixing of crushed rocks during collapse and/or movement. Assimilation of Socompa basement appears to be variable; overall, it is far lower than was previously proposed. Comparison between matrix and block samples in contact, over the whole surface area of the deposit, shows that the isotopic heterogeneity increases from source to front. Close to the Socompa, matrices are resulting from simple crushing of adjacent rocks. At the front, rock samples with distinct compositions are found in a close relationship with matrices that result either from mixing of these (or some of these) rocks or from crushing of basement material. Between the source and the front, the efficient mixing of Socompa rocks (and basement rocks) generates matrices with isotopic compositions distinct from those of the blocks they are in contact with. We interpret these results as being due to more efficient vertical mixing during the avalanche emplacement.

## 1. Introduction

Volcanic debris avalanches are hazardous phenomena resulting from the gravitational collapse of volcanic edifice flanks [*Voight et al.*, 1981; *Ui*, 1983; *Crandell et al.*, 1984; *Siebert*, 1984]. They comprise large volumes of crushed rock (millions of $m^3$ to tens of $km^3$).

A major characteristic of large debris avalanches is their very long runout: they often reach some tens of kilometres for a thickness of tens to hundreds of meters, with inferred velocities of up to 100 m $s^{-1}$. The ability of avalanches to travel large distances in a fluid-like manner is not well understood, and a number of possible friction reduction mechanisms have been proposed [e.g., *Davies and McSaveney*, 1999; *Legros*, 2002; *Collins and Melosh*, 2003, and references therein].

To better understand the emplacement of large debris avalanches and to determine what mechanisms are involved in their long runouts, we must answer the following key questions. Do the avalanches behave as a solid that slides on its base, or do they behave globally as a fluid? In the latter case, where are the fluid parts located? Does the fluidity change in time and space? How, where, and when do the rocks of the long runout avalanches break and mix? This last point can provide insight into the movements that affect the broken rocks during emplacement. It also allows the energy needed for, and released by, rock breaking to be estimated. Understanding these different aspects is of particular interest for natural hazard management [*Stoopes and Sheridan*, 1992; *Capra et al.*, 2002].

Numerical modeling and laboratory experiments can be used to answer the above questions. Some models simulate the set of particles as a continuous flow [e.g., *Mangeney et al.*, 2000; *Iverson and Denlinger*, 2001; *Kelfoun and Druitt*, 2005]. Thus, they allow the global mechanical behavior of the natural flows to be determined, and their emplacement history reconstructed. They cannot, however, simulate the complexity of particle interactions. Discrete element models simulate each particle of the destabilization and of the flow [e.g., *Campbell*, 1989; *Morgan and McGovern*, 2005; *Mollon et al.*, 2012]. They show that the initial distribution of rocks is globally conserved along the avalanche and that particles mix over distances of a few particle

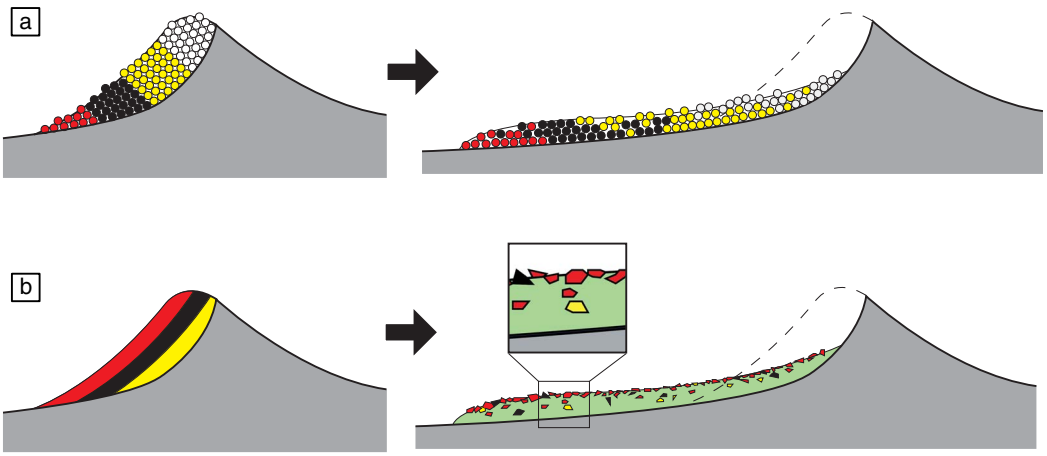


**Figure 1.** Schematic cartoons showing the different mechanisms of debris-avalanche internal dynamics, as seen by (a) laboratory experiments and discrete element modeling and (b) field observations. Models in Figure 1a simulate the distribution of particles (here represented by colored circles) after collapse. Field works in Figure 1b show that initially coherent rocks are crushed and then form the matrix of the avalanche (in green). None of these approaches are able to explain where, when, and how the formation of the matrix occurs.

diameters (Figure 1). Laboratory experiments based on granular mass spreading [*Shea and van Wyk de Vries*, 2008] lead to similar lithology distributions than discrete element simulations. They also produce morphologies and structures that resemble those observed in the field. The maximum number of particles that can be modeled limits both approaches, and the finest particle is equivalent to blocks larger than several meters in the field.

Field observations suggest that the very high fluidity of natural flows and the long runouts of debris avalanches are related to the presence of abundant, fine particles. The latter ones are resulting from the crushing of transported rocks from the volcanic edifice, and their whole set define the matrix of the avalanche (Figure 1) that can represent a large proportion of the deposits ($\geq$50%) [cf., *Crandell*, 1989; *van Wyk de Vries et al*., 2001]. Understanding the matrix formation and studying its behavior are thus of great importance. However, up to date neither numerical nor laboratory models are simulating rock breaking, matrix formation, and mixing within the matrix. Furthermore, constraints brought to the matrix formation by field observations are limited due to difficulties in deciphering the origin of crushed rocks. Hence, we need a new tool to study how the rock breaks and mixes in debris avalanches in order to better understand their dynamics.

In this study, we focus on the Socompa debris-avalanche deposits in Chile. Their location in the Atacama desert, which has one of the most arid climates on the Earth's surface, has led to very good preservation of their morphology, structure, and lithology [*Ramirez*, 1988] and also guarantees that their chemical composition has barely been modified (if at all) by low-temperature/supergene alteration. The Socompa avalanche shares the same morphological and structural characteristics as other debris avalanches worldwide (notably Aucanquilcha, Lastarria, and Llullaillaco debris avalanches) [cf., *Richards and Villeneuve*, 2001; *Shea and van Wyk de Vries*, 2008]. Thus, it constitutes one of the best places to study debris-avalanche deposits.

We present geochemical analyses (major and trace element concentrations, as well as isotope ratios) of the main constituents of the deposits: (1) rock fragments (or blocks) transported on the deposit surface, which are inferred to be derived directly from the volcanic edifice affected by gravitational collapse and (2) matrix samples, resulting from the crushing of transported rocks from the volcanic edifice, possibly incorporating rocks on which the avalanche flowed. We combine high-precision $^{87}Sr/^{86}Sr$ and $^{143}Nd/^{144}Nd$ source tracers with differentiation markers (major and trace elements). Using these, we are able to infer the degree of heterogeneity of the Socompa deposits and thus the internal dynamics and the spatial scale of mixing in the deposits. We are also interested in whether the matrix results solely from the crushing and mixing of the volcanic rocks that collapsed, or whether rocks covered by the avalanche also participate, and if so, to what extent.

We will show that relationships between blocks and matrices in contact are related to the sector of the avalanche where they have been collected, and to the history of their emplacement. Thus, at large scale, the level of heterogeneity of deposits is increasing with the distance from the Socompa edifice summit. Mixing

involving rocks on which the avalanche emplaced, however, seems to be limited. In any case, such a contribution is variable.

## 2. Geological Setting and Sampling Details

The Socompa debris-avalanche deposits (Figure 2) were initially interpreted as resulting from a large eruption and pyroclastic flow [*Deruelle*, 1978] because of their high percentage of pumice clasts. Subsequently, *Francis et al*. [1985] recognized them as the collapse of a 70° sector of the northwestern flank of Socompa volcano.

The Socompa debris avalanche took place about 7200 yr BP ($^{14}$C estimate) [see *Wadge et al*., 1995]. The deposit covers an area of 490 km$^2$ (35 km length) and has a volume of at least 15 km$^3$. Four main zones can be distinguished based on the morphology of deposits: (1) the proximal zone; (2) the distal zone that corresponds to large extensional areas in the backward movement sector where matrix crops out; (3) the median escarpment that delimits the front of the backward movement; and (4) the frontal zones and levees (Figure 2).

*Wadge et al*. [1995] and *van Wyk de Vries et al*. [2001] inferred that the Socompa volcano basement rocks have played a role in the avalanche. Here the term basement does not refer to crystalline rocks, but to surface rocks covered by the avalanche. The latter ones include gravels, pyroclastic flow deposits, and lava flows, making up the Quebrada Salin Beds formation, intercalated toward the top with sheets of the Arenosa and Tucucaro ignimbrites [*Wadge et al*., 1995; *van Wyk de Vries et al*., 2001]. The uppermost part of the basement crops out around and within the debris-avalanche deposits and is well preserved at the locality of La Flexura (Figure 2). *Wadge et al*. [1995] calculated a volumetric contribution of basement material to the deposits of ~60%. Using new field measurements, facilitated by roads accessing water-drilling platforms, *van Wyk de Vries et al*. [2001] revised these proportions and proposed that about 80% of the Socompa avalanche deposits is La Flexura-like basement material.

Numerical modeling of the Socompa avalanche has successfully reproduced both the morphology and measured thickness of deposits [*Kelfoun and Druitt*, 2005]. The conclusions drawn from the model have been confirmed by detailed analysis of the avalanche deposit morphology and structures and by the reconstruction of surface displacements [*Kelfoun et al*., 2008]. This allows us to place important constraints on the mass movement and timing of the avalanche emplacement, which we used to select sample locations and to provide a framework for interpreting our results. The deposit morphologies and structures are explained by complex movements of the avalanche due to the shape of the Monturaqui basin, the topographic depression into which it was emplaced. Initially, the avalanche resulting from the collapse of Socompa travelled northwestward, across the basin. It then slowed down on reaching the north side of the basin, where the frontal part of the deposits stopped and formed a marginal levee. The rest of the avalanche thickened before moving about 15 km back toward the center of the depression, with the front of the backward movement forming the median escarpment, one of the main features of the Socompa debris-avalanche deposit [*Francis et al*., 1985]. According to the numerical simulation of *Kelfoun and Druitt* [2005], the whole debris-avalanche deposit was emplaced in about 12 min.

In order to understand the relationship between the matrix and the rocks from the Socompa debris-avalanche deposits and the associated dynamical aspects, we focused on key zones that have already been studied [*Francis et al*., 1985; *Wadge et al*., 1995; *van Wyk de Vries et al*., 2001; *Kelfoun et al*., 2008]. We collected deposit samples as well as rocks representative of the basement (La Flexura inlier and tertiary volcanism) and local magnesium-rich and calcium-rich unconsolidated sediments. Avalanche deposit samples were of two distinct types: either rocks or matrix (crushed) samples. We also collected samples from Torevas (located at the beginning of the proximal zone; cf., Figure 2), which are large, coherent blocks that collapsed but were not dismantled [*Wadge et al*., 1995]. The absence of deposits on their tops suggests that they slid into place during or after the main debris avalanche passed downslope.

Matrices were generally fine grained, but sometimes contained larger inclusions (cm to few cm, or even greater) with no size continuity through to the smaller particles. Hence, we did not consider the elements greater than a few millimetres in size as being part of the matrix samples. Instead, they were categorized as clasts and considered as distinct samples. We chose the value of 1–2 mm as the matrix/clast division in

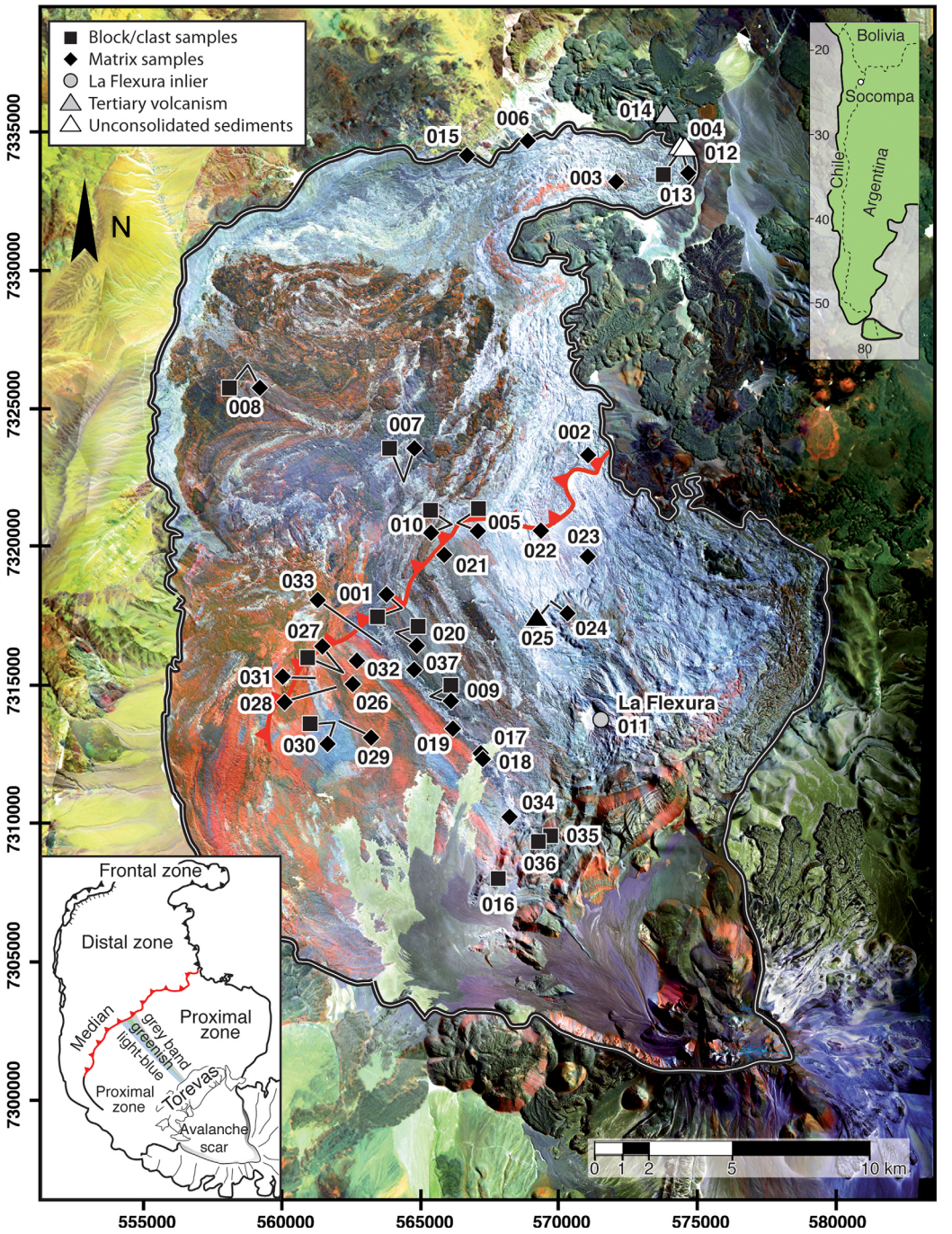


**Figure 2.** Geographical map of the Socompa debris-avalanche deposits with sample locations and outcrop numbers (modified from *Kelfoun et al.* [2008]). Colors are obtained by combining bands 7, 4, and 1 of Landsat image. The thick, red line corresponds to the median escarpment; inset at the bottom left shows the four main zones that can be distinguished based on the morphology of deposits: (1) the proximal zone; (2) the distal zone that corresponds to the large extensional areas in the backward movement sector; (3) the median escarpment that delimits the front of the backward movement; and (4) the frontal zones and levees. UTM coordinates: WGS84, zone 19S.

order to make it possible to distinguish visually between clasts and matrices in the field and thus facilitate sampling of the avalanche deposits. Where possible, we collected matrix and representative rock samples that were in contact.

Samples are labelled as follows: Outcrop number—R or M for Rock or Matrix—sample number. For instance, 5-M2 is the second matrix sample at outcrop 5. Their locations are shown in Figure 2, where only the outcrop

numbers have been marked so as to make it easier to read (see also supporting information Figure S1). Rocks refer to either blocks or clasts. Their distinction is not related to their composition or their size, but it notifies where they were sampled: at the surface of the deposits for blocks, or within matrices for clasts.

## 3. Analytical Procedures and Methodology

### 3.1. Major and Trace Elements and Sr-Nd Isotopic Ratios

Hundred to two hundred grams of each sample were reduced into chips in a jaw crusher before being powdered in an agate swing mill. Fine crushing was performed in three steps: (1) the first crushing run was conducted to precontaminate the agate mill; (2) the second run was used for major and trace element determinations; and (3) the third one for Sr-Nd isotope analyses.

Both major and trace element (Ba and Sr) contents were determined at the Magmas and Volcans Laboratory (LMV) using Inductively Coupled Plasma-Atomic Emission Spectrometry (ICP-AES, Ultima-C instrument) after alkaline melting with lithium metaborate/tetraborate and nitric acid dissolution (100 mg of sample). BHVO-1 standard measurements along with Socompa samples, as well as duplicate measurements of the lowest-$SiO_2$ sample from La Flexura (11-B3), give an estimate of the total reproducibility of analyses. For BHVO-1, the reproducibility (here expressed as the 2 standard deviation/mean ratio of the 16 analyses performed during the course of the study) is better than 5% for major element contents, except for $N_2O$ (13%), $K_2O$ (18%), and $P_2O_5$ (8%), and around 3 and 24% for Sr and Ba, respectively. For 11-B3 sample, this is of the same order, with a maximum of 2.5% for major element contents, except for MnO (5%), $K_2O$, and $P_2O_5$ (10%), around 3% for Sr and around 15% for Ba (supporting information Table S1).

Sr and Nd isotope separations and measurements were also carried out at the LMV. Hundred milligrams of sample powders were acid-digested with a HF-$HNO_3$ mixture and passed through the "cascade" column protocol (Sr Spec, True Spec, and Ln Spec columns) described in *Pin and Bassin* [1992] and *Pin et al*. [1994] after most of the iron had been removed through an AG50X4 column. Total procedure blanks were $<1$ ng and $<0.2$ ng for Sr and Nd, respectively. A few samples were also spiked with a $^{150}Nd$ tracer solution in order to determine their Nd content by isotope dilution. All measurements were made in static mode on a Finnigan Triton thermo-ionization mass spectrometer (TIMS) with relay matrix rotation (also called the virtual amplifier) and double W filaments. A typical run consisted of at least nine blocks of 10 cycles to allow a full rotation of the virtual amplifier system. Isotope ratios were mass-fractionation corrected with $^{86}Sr/^{88}Sr = 0.1194$ and normalized to $^{87}Sr/^{86}Sr = 0.71025$ for the NIST-SRM987 standard; with $^{146}Nd/^{144}Nd = 0.7219$ and normalized to $^{143}Nd/^{144}Nd = 0.511960$ for the Rennes-AMES standard [*Chauvel and Blichert-Toft*, 2001]. Repeated analyses of the two standards during the course of the study gave $^{87}Sr/^{86}Sr = 0.710244 \pm 0.000007$ (2sd, n = 56) and $^{143}Nd/^{144}Nd = 0.511960 \pm 0.000007$ (2sd, n = 44).

### 3.2. Grain-Size Dependence of Matrix Samples

To assess the influence of particle-size distribution of matrix on measured chemical and isotopic compositions, we passed a large sample (33-M1) through a manual sieve shaker with meshes of 1 and 0.1 mm. The three fractions ($\leq$0.1 mm; 0.1–1 mm; and $>$1 mm, denoted as 33-M1a, 33-M1b, and 33-M1c, respectively) show isotopic compositions in agreement with that of the whole-rock sample when considering error bars of $7 \times 10^{-6}$ (see above) for Sr-Nd ratios (Figure 3a). Major and trace element content results, however, contrast. Although the large and intermediate size fractions show maximal differences of $\pm$5% compared with the whole-rock matrix sample for major and trace elements analyzed with a similar precision ($SiO_2$, $Al_2O_3$, $Fe_2O_3$, MgO, and Sr), smaller particles ($\leq$0.1 mm) have significantly distinct contents (between 5 and 15% for $SiO_2$, $Al_2O_3$, $Fe_2O_3$, and MgO, and up to 50% for Sr; cf., Figure 3b). Differences are correlated on Harker diagrams (Figures 3c–3f): small, intermediate, and large particle subsamples plot on the general trends defined by the whole set of Socompa deposits. Given the constant Sr-Nd isotopic composition measured in all fractions, variations recorded by major elements thus seem simply to reflect variations in mineral proportions. The fine particle subsample presents a higher proportion of a component with a $SiO_2$-rich composition (mesostasis?) relative to the intermediate and large grain distributions. Conversely, the latter are consistent with higher amounts of plagioclase and/or augite and/or amphibole. Comparison of all particle sizes thus suggests that major element results, as well as Sr and Ba, depend on sampling. Coupled to reproducibility of major and trace element contents, this implies that very small differences ($\leq$10%) between two

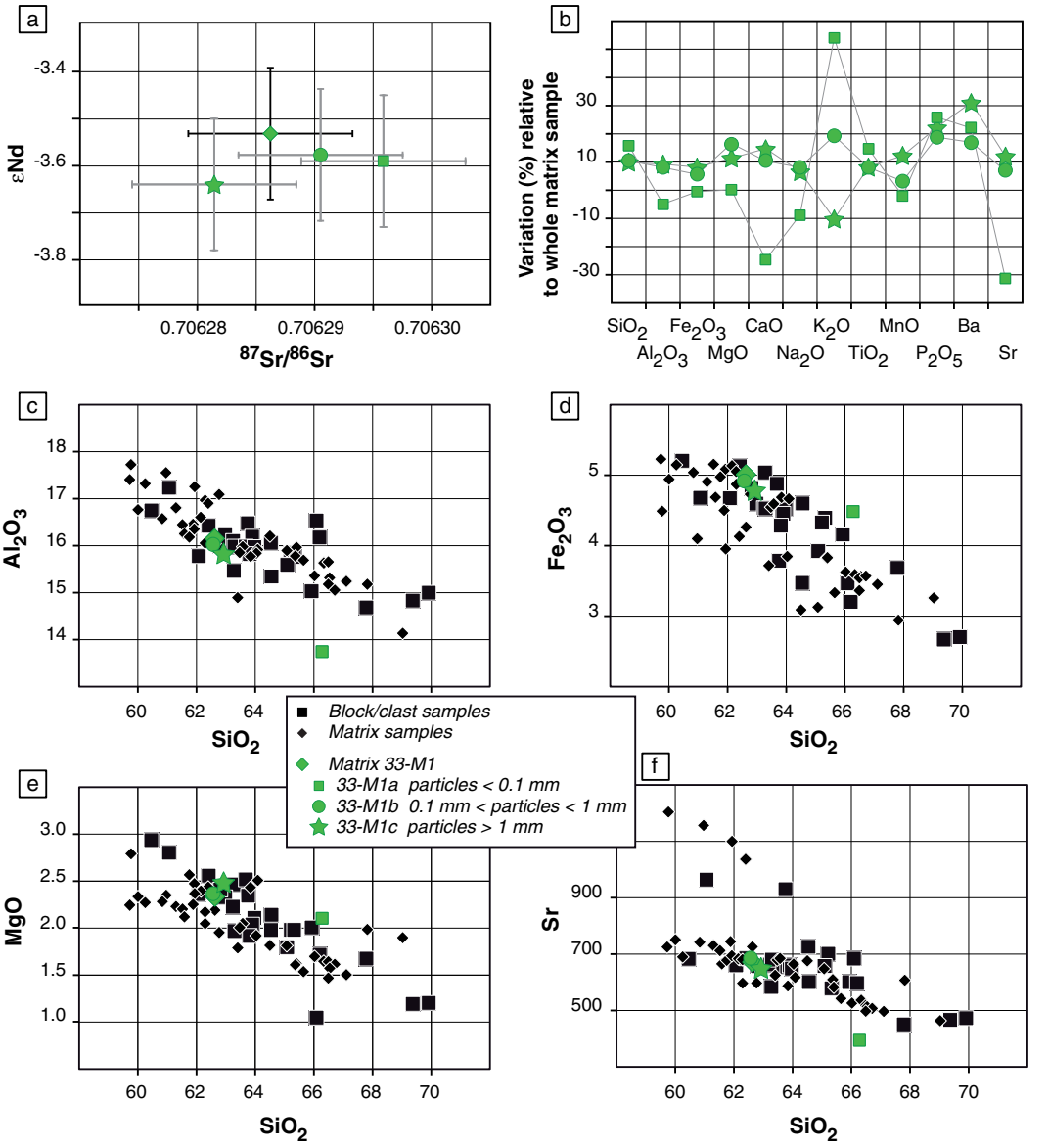


**Figure 3.** Influence of particle-size distribution of matrix sample 33-M1 on major and trace element, and isotope signatures. (a) εNd versus $^{87}Sr/^{86}Sr$, (b) variations (%) relative to whole-matrix sample for major and trace elements, and (c–f) comparison with all matrix and block samples from the Socompa avalanche deposits in Harker diagrams (wt %). All fractions show reproducible Sr-Nd isotopic compositions but distinct major element contents interpreted as reflecting variable mineral proportions.

samples cannot be considered as significant. Furthermore, beyond the sampling bias, using major element may induce wrong conclusions if granulometric sorting occurs during the avalanche emplacement. Consequently, discussion will be based primarily on Sr-Nd isotopes.

### 3.3. How Representative Are Matrix Signatures of Individual Outcrops?

We have also checked how representative matrix sampling is of a given outcrop. For this purpose, we have collected several visually identical matrix samples, separated by a few 10s of cm at given locations. An example is illustrated in Figure 4 (outcrop 7). The four matrix samples collected at intervals of 30 cm present Sr-Nd isotope compositions of 0.706291–0.706306 and 0.512451–0.512458, as well as $SiO_2$ contents ranging from 60.01 to 61.59 wt %. This corresponds to relative variations of 21 ppm, 13 ppm, and 2.6%, respectively. Such values are similar to reproducibilities based on standard measurements (see section 3.1), making differences between them insignificant. Furthermore, the four matrix data points plot within the

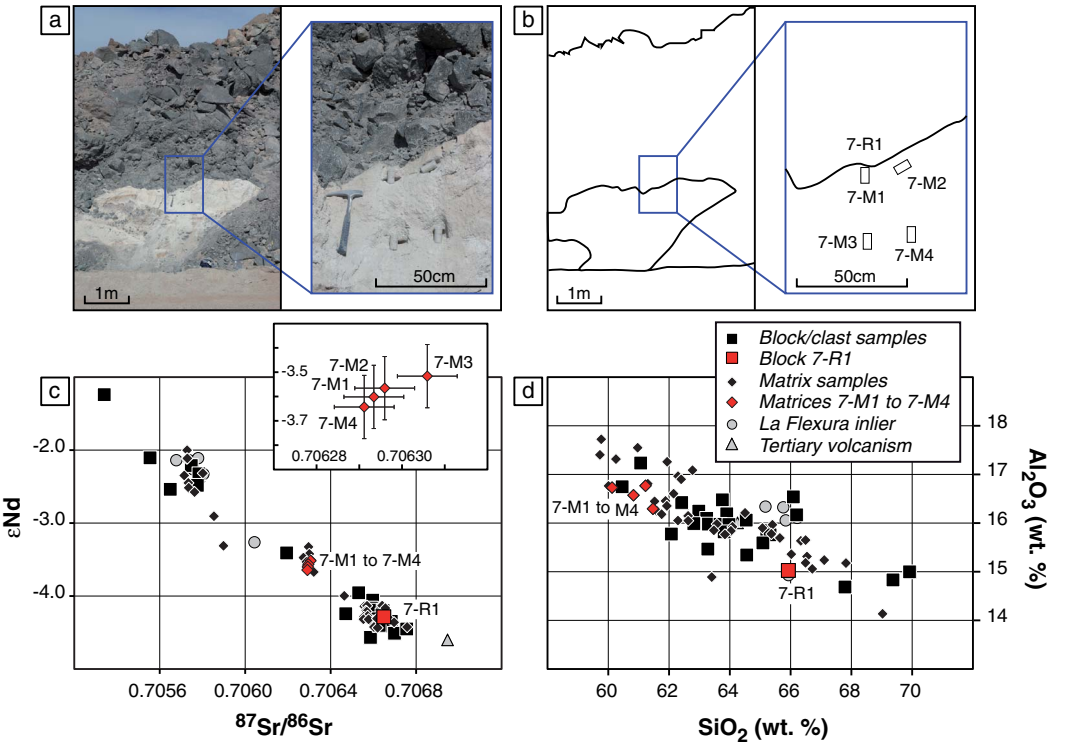


**Figure 4.** (a) Photograph, (b) schematic field relationship, (c) εNd versus $^{87}Sr/^{86}Sr$, and (d) $Al_2O_3$ versus $SiO_2$ diagrams for samples from outcrop 7 (distal zone of the avalanche, see Figure 2 for exact location). The four matrix samples, 7-M1 to 7-M4, show only minor isotope and major element variations that can be considered as insignificant with respect to analytical uncertainties and reproducibilities. Block sample at contact (7-R1), however, presents significantly distinct isotopic and chemical signatures. Note the ingestion of the lava into the matrix (left of the caption).

trend defined by the entire set of Socompa deposits in the $Al_2O_3$ versus $SiO_2$ diagram, suggesting that part of the major element variability could be related to varying proportions of small, intermediate, and/or large grain size particles in the four matrix samples. However, massive blocks of dacite at the contact show differences far higher than analytical uncertainties for both isotopes and major elements. Thus, the outcrop 7 test, duplicated at locations 8 and 9 with the same results (supporting information Table S1), shows that matrix samples are representative of one to several meter-sized matrix outcrops with respect to analytical uncertainties for both isotopes and major elements.

## 4. Geochemical Compositions of Socompa Debris-Avalanche Deposits and Basement

Sample deposits show similar major element variations, whatever their type. Massive blocks and clasts have $SiO_2$ contents ranging from 61.40 to 70.10 wt %, recalculated on an anhydrous basis. All but two samples fall within the andesite to trachy-andesite and dacite to trachydacite fields when plotted in the total alkali-silica diagram (Figure 5). The two exceptions are rhyolitic clasts coming from the same location (outcrop 10). Matrix samples have similar $SiO_2$ (61.19–69.79 wt %). Their alkali contents ($Na_2O+K_2O$), however, are lower overall than those of rock samples; they all plot in the andesite and dacite fields, except four samples which are categorized as trachydacites. La Flexura samples have narrower, dacitic compositional ranges for seven of the eight samples; only 11-B3 is an andesite. Rock and matrix samples divide into medium-K and high-K types, the former being predominant, whereas La Flexura samples are all medium-K (supporting information Figure S2). Rock samples and clasts show low loss on ignition (LOI) values ranging from 0.05 to 2.10 wt % (mean = 0.76 wt %). Conversely, matrix and La Flexura samples have higher LOI values of 0.20–5.55 wt % (mean = 1.91 wt %) and 1.23–7.85 wt % (mean = 3.35 wt %), respectively. These differences may either reflect the higher alterability, even in an arid climate, of crushed material compared to rock blocks or

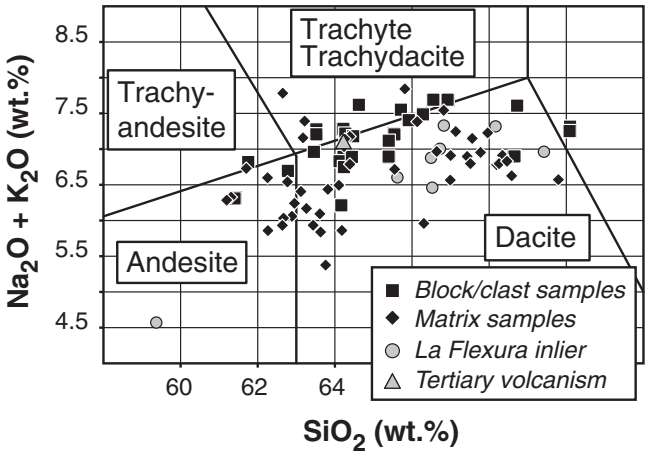


**Figure 5.** Total alkali-silica diagram [*Le Maître*, 2002] for Socompa debris-avalanche deposits, La Flexura inlier, and tertiary volcanism.

suggest water input into matrix samples. The Chemical Index of Alteration (CIA) quantifies the extent of weathering (based on conversion of feldspar minerals) of a given rock [*Nesbitt and Young*, 1982]: fresh samples show CIA $\leq$ 50, whereas altered ones have higher values of up to 100. Socompa rock and matrix samples have quite similar ranges of CIA, from 45.8 to 49.3 and from 45.4 to 53.4, respectively (supporting information Figure S3a). The upper limit for the matrix samples is set by a single sample; excluding it results in a range of 45.4–50.4. This suggests that all samples are unaltered, or only weakly altered. This is confirmed by the calculation of the Weathering index (W) [*Otha and Arai*, 2007]. Our samples do not deviate from the unweathered igneous rock trend in the MFW ternary diagram (where M, F, and W represent the mafic source, felsic source, and weathered material; see supporting information Figure S3b).

The Tertiary sample (14-R1), collected from the Negrillar lavas to the north of the studied deposits (Figure 2), has no relationship with the debris avalanche (there is no evidence for a genetic link with Socompa volcano either). It has a dacitic composition similar to that of average rock samples. Unconsolidated sediment samples show contrasted results: 25-S1 is Mg-rich, whereas 4-S1 and 12-S1 are Ca-rich.

Measured $^{87}Sr/^{86}Sr$ and $^{143}Nd/^{144}Nd$ isotope ratios for Socompa avalanche deposits range from 0.705340 to 0.706758 and from 0.512404 ($\varepsilon Nd = -4.57$) to 0.512574 ($\varepsilon Nd = -1.24$) ($\varepsilon Nd$ is the deviation from the Chondritic Uniform Reservoir (CHUR) evolution line in parts per 10,000), respectively. No radioactive decay correction is applied to values as deposits all come from Socompa volcano, whose activity is Quaternary [*Mamani et al*., 2010]. Sample values of $^{143}Nd/^{144}Nd$ ($\varepsilon Nd$) decrease with increasing $^{87}Sr/^{86}Sr$. Matrix and rock deposit values overlap, while the three Toreva samples (16-R1, 35-R1, and 36-R1) have among the most radiogenic Sr ratio values (Figure 6). La Flexura samples also plot along the Sr-Nd anticorrelation, but their variation ranges are less than those of Socompa deposits, being confined to rather low $^{87}Sr/^{86}Sr$ (0.705677–0.706043) and high $^{143}Nd/^{144}Nd$ ratios (0.512471–0.512530). The Tertiary sample from the Negrillar lavas and the unconsolidated sediment samples (12-S1 and 25-S1) show the highest $^{87}Sr/^{86}Sr$ ratios. The Tertiary lava occupies an end-member position with respect to Socompa deposits, while the magnesium-rich and calcium-rich unconsolidated sediments lie off the trend.

## 5. Discussion

### 5.1. Outcrop-Scale Relationships Between Matrix and Block Samples and Implications for Dynamics

Strontium-87/$^{86}Sr$ and $^{143}Nd/^{144}Nd$ isotope ratios define a negative trend for block/clast samples (Figure 6). Similarly, $SiO_2$ correlates negatively with all other major elements (Figures 3c–3f) except $K_2O$ (positive correlation). Matrix samples define very similar correlations to the blocks in both $^{143}Nd/^{144}Nd$ versus $^{87}Sr/^{86}Sr$ and Harker diagrams. Hence, variations in the chemical and isotopic compositions of matrix samples seem to result from a simple, mechanical mixing of Socompa rocks after crushing. However, major elements and isotope ratios do not vary together. Such a decoupling suggests that matrix samples result from numerous mixing events with variable end-members. In the following sections, we discuss relationships between matrix and block samples in the key sectors of the avalanche in order to better understand its dynamics.

#### 5.1.1. The Proximal Zone

Field observations and satellite images suggest that the proximal zone corresponds to strong stretching of the avalanche. Deposits form well-defined, parallel colored bands in the central part of the sector (Figure 2)

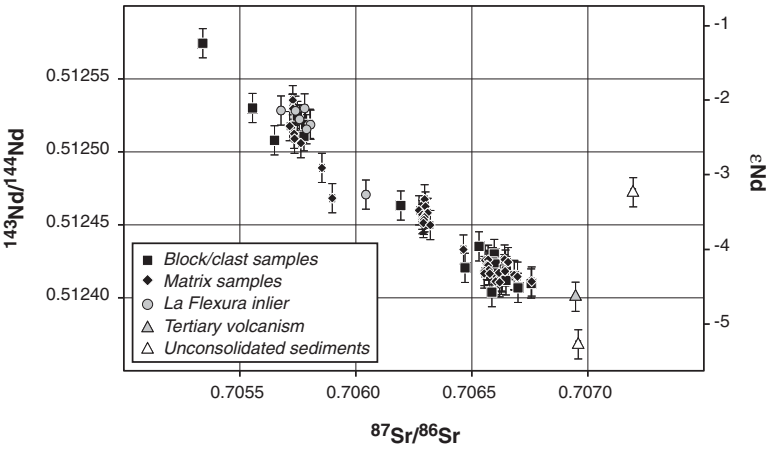


**Figure 6.** Comparison of matrices with blocks/clasts from the Socompa avalanche deposits on a $^{143}Nd/^{144}Nd$ ($\varepsilon$Nd) versus $^{87}Sr/^{86}Sr$ diagram. $\varepsilon$Nd is the deviation from the Chondritic Uniform Reservoir (CHUR; with $^{143}Nd/^{144}Nd_{Today} = 0.512638$) [cf., *Jacobsen and Wasserburg*, 1984] evolution line in parts per 10,000. La Flexura-like basement samples, as well as sample 14-R1, representative of regional tertiary volcanism, and local unconsolidated sediments are also shown. All samples except unconsolidated sediments plot on the same, well-defined, negative correlation.

indicating a unique direction toward the north-west. Rocks at the surface of each band seem to be homogeneous (in terms of nature and mineralogy) [*Francis et al*., 1985; *Wadge et al*., 1995; *van Wyk de Vries et al*., 2001; *Kelfoun et al*., 2008].

Our analyses show that matrix samples collected from this area have homogeneous compositions within a given colored band, similar to the blocks. For example, matrix samples 17-M1, 18-M1, 19-M1, and 33-M1 that were collected in a light blue, elongated area (Figure 2) show similar isotope ratios (supporting information Table S1). This is also true for 9-M1–9-M4 and 37-M1, which belong to the greenish band located immediately to the east. Their isotope signatures are similar, although different from those of the former samples. Hence, samples from distinct color areas present different isotopic compositions, even if they are located near one another.

Our analyses also show that matrices and blocks sampled in contact with each other have identical isotope ratios, although matrices present a globally white color, contrary to neighboring blocks that give the color of the bands on the satellite image. This is observed at outcrops 9 (supporting information Table S1) and 20 (gray band located to the east of the greenish one (Figure 2)). This result indicates that matrices are derived from surface blocks by simple crushing. All avalanche outcrops show that the matrix dominates below the zero to few meter-thick surface crust of deposits, which suggests that crushing operated over most of the deposit thickness (probably more than 90% of the thickness).

Differences in Sr-Nd isotope compositions observed in matrices from the parallel bands (light blue, greenish, and gray; Figure 2) show that lateral mixing is limited in the proximal zone. The similarity of ratios between blocks and matrices in a given colored band also suggests that there is no mixing with rocks crushed at greater depth, regardless of their origin (rocks from the Socompa volcano or from the basement) unless they have the same composition.

Outcrop 20 is of particular interest as it also illustrates how difficult it is to distinguish between compositions on the field. Here the three visually distinct matrices in contact have the same isotope composition (Figure 7). The visual distinction between them could be related to different degrees of alteration. The uppermost matrix (sample 20-M3) is red-brown, compared to gray and light gray matrices sampled directly below (20-M1 and 20-M2), which could represent alteration of iron minerals. Their distinct appearances could be also related to the proportion of blocks disseminated through the matrices, or they simply reflect original matrix materials that were initially in contact (before the avalanche) but were not mixed by crushing.

The southwest edge of the proximal zone is a more complex sector, whose structures are not easy to interpret [*Kelfoun et al*., 2008]. The initial direction of stretching is perpendicular to the local slope; thus, movement was probably not unidirectional. An example of the relationship between blocks and matrices in contact is given

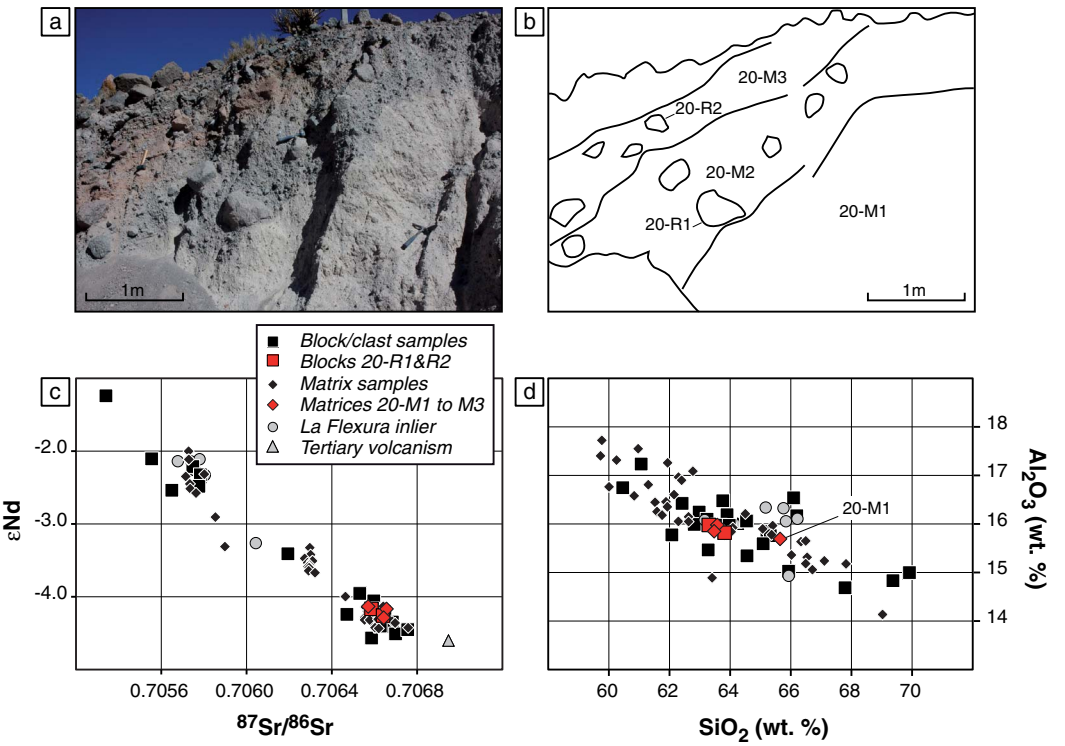


**Figure 7.** (a) Photograph, (b) schematic field relationship, (c) $\varepsilon$Nd versus $^{87}Sr/^{86}Sr$, and (d) $Al_2O_3$ versus $SiO_2$ diagrams for samples from outcrop 20 (proximal zone of the avalanche, see Figure 2 for location). The three matrix layers, 20-M1 to 20-M3, show distinct field characteristics (presence/absence of clasts, color), but very similar isotopic compositions, as do the two block samples (20-R1 and 20-R2).

by outcrop 27 (Figure 8). Here a visually homogenous rock cover caps two distinct matrices. In the field, the pink matrix (27-M1) seems to result from the incorporation of red blocks (represented by sample 27-R1) into a white matrix (27-M2). However, Sr and Nd isotope compositions measured for 27-M1 are not intermediate between those of samples 27-M2 and 27-R1. In fact the white matrix (27-M2) and the rock cover (27-R1) have very similar isotope signatures, whereas the pink matrix (27-M1) has significantly distinct Sr-Nd ratios. Thus, if 27-M1 is related to 27-M2 and 27-R1 through a mixing process, an unidentified, unsampled component is needed to explain its chemical composition. Alternatively, we can interpret the 27-M1 matrix as a very localized event, resulting from the crushing of rocks with a distinct isotope signature to that of the 27-R1 sample. This possibility highlights the difficulty of limited sampling of representative rock fragments/blocks. This also illustrates that field observations should be made with caution in relation to chemical compositions.

### 5.1.2. The Distal Zone

In the distal region, the avalanche deposits were laid down and then subjected to a back surge, which created large shear zones and stretching. These large structures allow the matrices to be observed in areas where blocks cap the whole surface. For example, outcrop 7 shows the contact between a white matrix and a dismantled lava block unit (Figure 4). There, the disaggregation of the lava unit and its ingestion into the matrix are visible. However, the four matrix samples collected at intervals of 30 cm (7-M1–7-M4) show exactly the same isotopic composition regardless of their distance from, and direction in relation to, the block chosen as representative of the lava unit (7-R1), and the block and matrices have contrasting major and trace element and isotope signatures. Such differences preclude the matrices being derived from the adjacent blocks by a simple crushing process, but suggest a binary mixing between block 7-R1 and an unidentified, unsampled component. The geochemical homogeneity of the matrix indicates large-scale mixing to incorporate the lava so efficiently into the matrix.

The same kind of relationship is observed at outcrop 8 (Figure 9), where a thin, ~50 cm, layer of fragmented rocks, here represented by sample 8-R1, caps a thick layer of matrix (more than a few meters thick). Again, Sr-Nd isotope compositions of matrix samples 8-M1 and 8-M2 are similar, but distinct from those of block 8-R1, collected at, or close to, the contact. Such features probably indicate the complete mixing of the lower

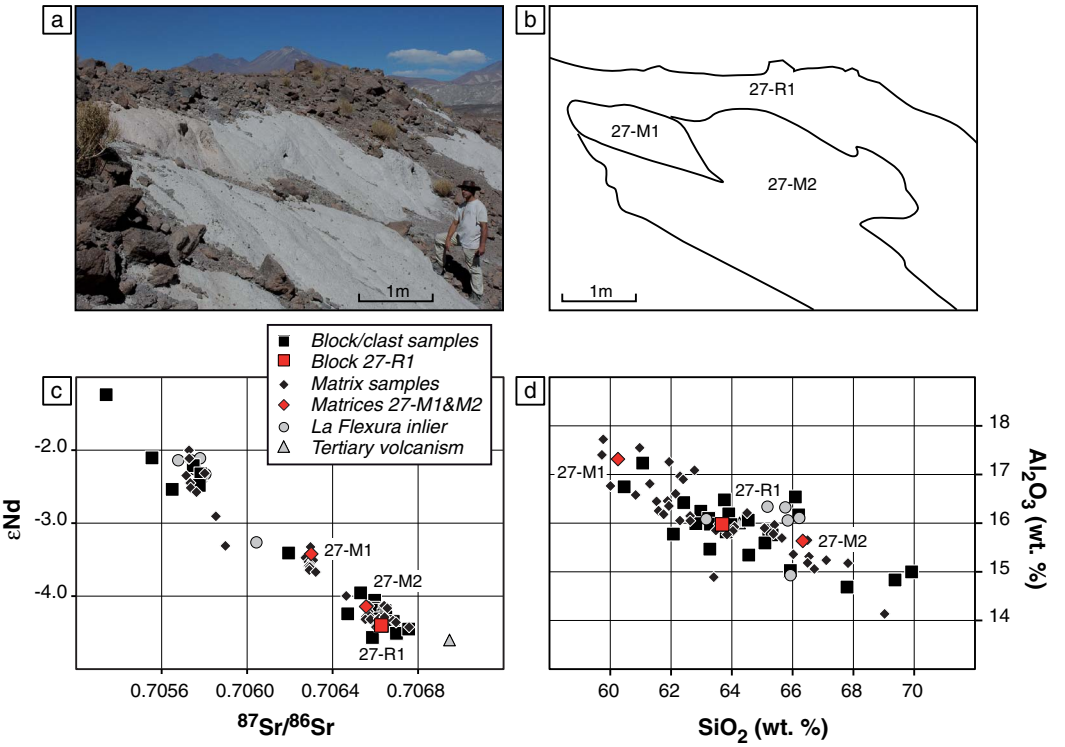


**Figure 8.** (a) Photograph, (b) schematic field relationship, (c) εNd versus $^{87}Sr/^{86}Sr$, and (d) $Al_2O_3$ versus $SiO_2$ diagrams for samples from outcrop 27 (see Figure 2 for location). The southwest edge of the proximal zone of the avalanche shows complex relationships between matrices and blocks in contact compared to the central part where both types of samples have identical isotope ratios.

part of the rock cap into the underlying matrix. Hence, more than 90% of the deposit thickness seems to have been affected by mixing in the distal area. It should also be noted that the matrix samples collected at outcrops 7 and 8 have distinct Sr-Nd ratios, arguing for a heterogeneous distal zone and thus a heterogeneous matrix at the scale of a few km.

### 5.1.3. The Frontal Zone

The frontal lobe of the avalanche is a specific zone whose surface contains a high proportion of matrix material, as is also the case for frontal levees from the north-northwest region. Structures are not clearly defined, and outcropping rocks seem to be heterogeneous. We focused on outcrop 13, located at the front of the avalanche deposits and representative of this area. There, a great variety of rock fragments disseminated into the matrix can be observed (Figure 10). Samples 13-R1–13-R11 show Sr-Nd isotope ratios spanning the whole range of measured compositions for Socompa avalanche deposits, whereas matrix sample 13-M1 has an isotopic signature close to that of La Flexura samples. Major element contents determined for these samples show similar ranges, so the matrix could result from the incomplete mixing of rocks with isotopic compositions similar to 13-R1/R11. Alternatively, 13-M1 could result either from the mixing of at least two unsampled components or from the crushing of La Flexura-like material. In either case, the distribution of blocks in the matrix indicates that the frontal lobe was affected by strong mingling reaching down to the underlying deposits.

### 5.1.4. The Median Escarpment

The median escarpment delimits the backward movement of the avalanche toward the south-east. There, the matrix samples we collected at the contact are not easy to ascribe an origin to. For example, outcrop 10 is composed of two color-contrasted matrices (a pink matrix: samples 10-M1 and 10-M2, and a blue matrix: samples 10-M3 and 10-M4) containing three main types of small clasts (a few cm in size): pink clasts (sample 10-R1) are dispersed in pink matrix 10-M1, and dark (10-R2) and light (10-R3) fragments in blue matrices 10-M3 and 10-M4 (Figure 11). Our analyses show that the matrices of distinct colors are homogeneous: Sr-Nd ratios, and major and trace element contents, show similar values for samples 10-M1 and 10-M2, and for

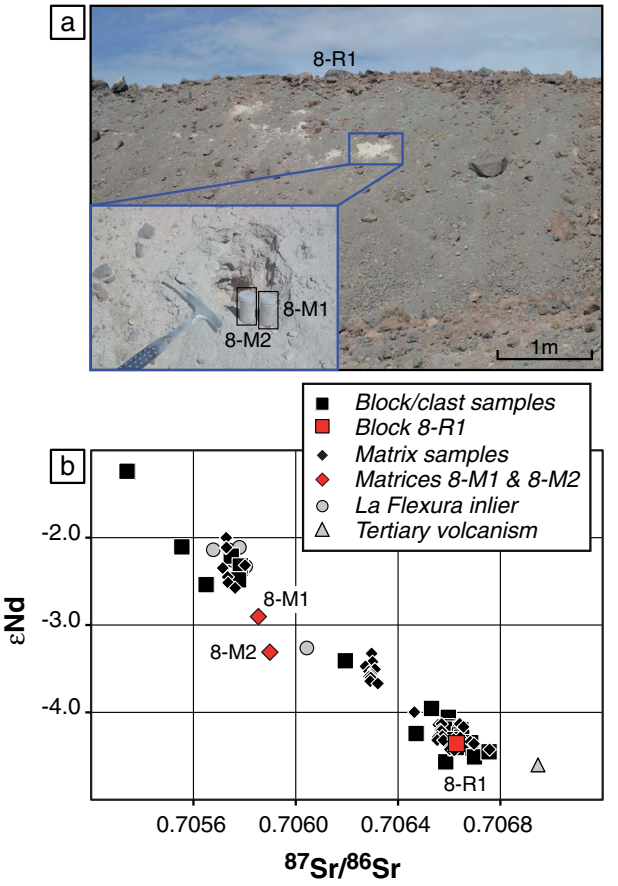


**Figure 9.** (a) Photograph and (b) $\varepsilon$Nd versus $^{87}Sr/^{86}Sr$ diagram for samples from outcrop 8 (distal zone of the avalanche, see Figure 2 for exact location). Note there is only a thin, ~50 cm, layer of fragmented rocks, here represented by sample 8-R1, over a thick—more than a few meters—layer of matrix (samples 8-M1 and 8-M2). As for outcrop 7, matrices and block in contact present significantly distinct isotopic signatures.

samples 10-M3 and 10-M4. The two types of matrices, however, present significantly distinct isotopic and chemical compositions from each other. Thus, there is no interaction between the two matrices, which is in agreement with their very sharp contact. The three color-based types of clasts also have distinct signatures, not only from each other but also when compared with matrix samples. Thus, neither of the two matrices can be explained by the simple crushing of material resembling one of the three types of clasts (pink, dark, or light color). For example, the pink matrix cannot result from crushing of pink clasts. Again, this illustrates that field observations should be made with caution.

In the $\varepsilon$Nd versus $^{87}Sr/^{86}Sr$ plot (Figure 11c), the five samples collected at outcrop 10 define a negative correlation. The relative location of matrix and block/fragment samples on this diagram suggests that matrices 10-M1 and 10-M2 result from the binary mixing between rocks with either 10-R1 and 10-R2 or 10-R1 and 10-R3 compositions, whereas matrices 10-M3 and 10-M4 could result from mixing between either 10-R1 and 10-R2 or 10-R2 and 10-R3. In this scenario, whatever the two end-members involved, the mixing must have been mechanical and incomplete as fragments still exist to be sampled. However, equivalent relationships to those observed for isotopes are not found on an $Al_2O_3$ versus $SiO_2$ diagram; for example, the three rock fragments show higher $SiO_2$ contents than matrix samples (Figure 11d). Thus, if mixing were to be the process which resulted in the two matrices (pink and blue) at outcrop 10, at least one of the components of the mixing remains unidentified and consequently unsampled at this location. Alternatively, the two matrices might have no relationship to each other, or to the blocks or clasts. Whatever the explanation, this shows that the homogeneous matrix contains, or was formed by, rocks of various origins. Thus, the avalanche was fluid or shaken enough to allow mechanical mixing, as also inferred for the outcrops in the distal zone. Our study also indicates that strong mixing affected the deposits up to their surface. Homogeneous matrices were formed by the grinding of various rocks, as testified by remaining clasts that are also homogeneously distributed throughout the matrices. The sharp contact between the two matrices (pink and blue) indicates that the strong mixing phase was followed by a phase during which mixing was no longer possible. The matrices were then put in contact by granular faults in a material that henceforth behaved in a brittle manner.

### 5.2. Basement Involvement in Debris-Avalanche Deposits

#### 5.2.1. La Flexura-Like Basement Involvement

Some of the outcrops described in previous sections suggest the involvement of an unidentified component in matrix samples. Here we look into the possibility that the debris avalanche eroded basement rocks

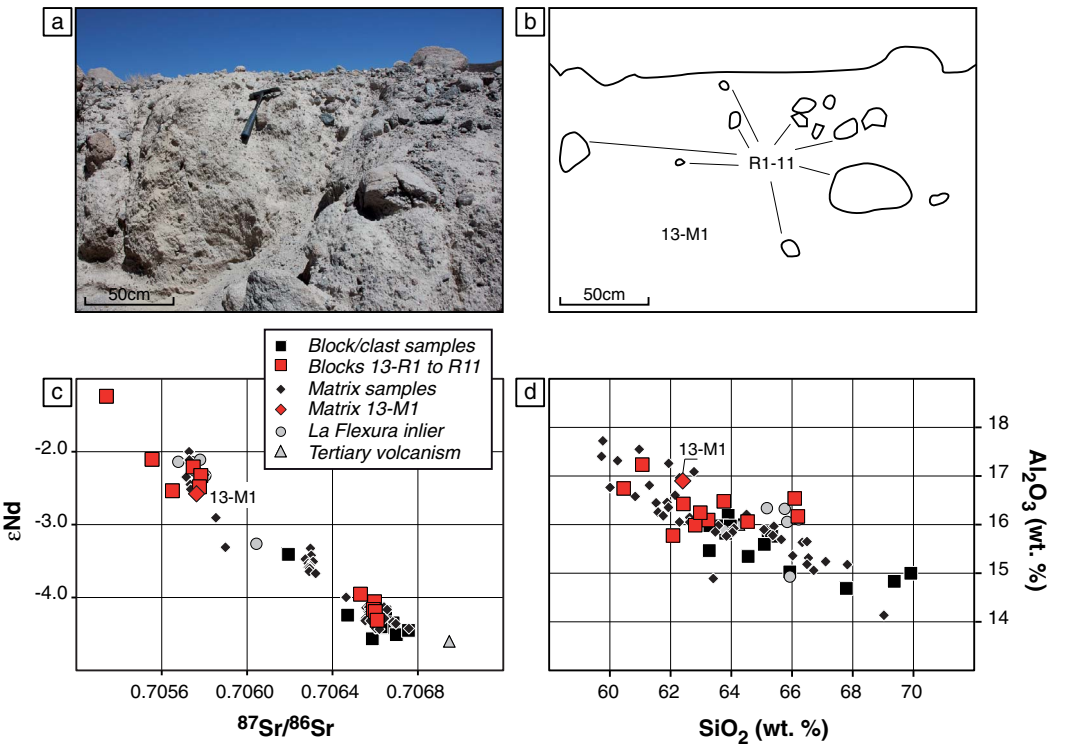


**Figure 10.** (a) Photograph, (b) schematic field relationship, (c) $\varepsilon$Nd versus $^{87}Sr/^{86}Sr$, and (d) $Al_2O_3$ versus $SiO_2$ diagrams for samples from outcrop 13 (front part of the avalanche, see Figure 2 for exact location). Eleven visually distinct rock samples, namely 13-R1 to 13-R11, have been collected into matrix 13-M1; their compositions span the whole range of variations of Socompa avalanche deposits. Matrix 13-M1 has an isotopic signature close to that of La Flexura samples.

of the Socompa volcano and incorporated 60–80% within it [*Wadge et al.*, 1995; *van Wyk de Vries et al.*, 2001]. For this purpose, we assume that each matrix sample results from mixing between crushed Socompa rocks from the same outcrop and La Flexura-like material, and we determine mixing proportions to fit our data. We consider both major element and isotope calculations, which must both give similar mixing proportions. Results show that mixing with La Flexura-like material in proportions ranging from 15 to ~95% can explain the chemical and isotopic compositions of several matrix samples, provided that all La Flexura-like compositions are considered (from andesite to dacite; see Figure 12). Others, however, cannot be modeled by such mixing. For example, matrix sample 27-M2 does not fall on a trend joining La-Flexura and block 27-R1 from outcrop 27 (located in the proximal zone; see section 5.1.1). Moreover, a few outcrops have adjacent matrix and rock samples with similar geochemical characteristics, thus making mixing with La Flexura-like basement material unnecessary (outcrops 9 and 20 also located in the proximal zone). Thus, our data do not exclude La Flexura-like basement assimilation by the Socompa avalanche, but it appears to be not nearly as significant as previous studies suggest. This conclusion is based on the hypothesis that La Flexura samples are representative of the whole Socompa basement, but it should be noted that the La Flexura inlier was also used as a reference by previous studies to estimate the degree of involvement of Socompa basement in deposits.

### 5.2.2. Monturaqui Unconsolidated Sediment Incorporation

Ca-rich and Mg-rich unconsolidated sediments have been also sampled to the north and east of the Socompa avalanche deposits. Measured isotopic compositions show high Sr ratios and low Nd ratios ($^{87}Sr/^{86}Sr = 0.706959–0.707195$ and $^{143}Nd/^{144}Nd = 0.512368–0.512474$), so average sediments can be plotted as an end-member for Socompa matrix and block samples in the $^{143}Nd/^{144}Nd$ versus $^{87}Sr/^{86}Sr$ diagram (Figure 6). Thus, it could be proposed that matrix samples result from binary mixing between Sr unradiogenic material from Socompa volcano and unconsolidated sediments (instead of basement rocks). In this case, the mass proportions required to explain intermediate matrix compositions (i.e., $^{87}Sr/^{86}Sr \sim 0.706300$) are around 30% when considering $^{87}Sr/^{86}Sr$ isotopic ratios of 0.706959 (Ca-rich sample) and

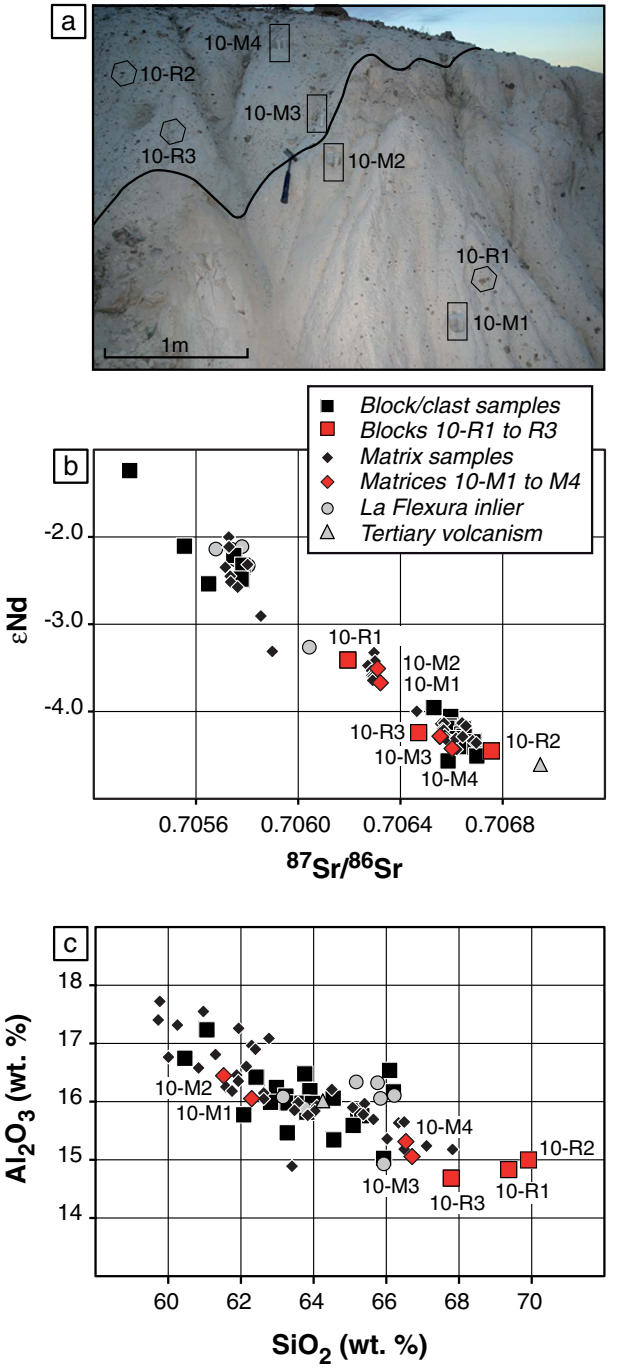


**Figure 11.** (a) Photograph, (b) εNd versus $^{87}Sr/^{86}Sr$, and (c) $Al_2O_3$ versus $SiO_2$ diagrams for samples from outcrop 10 (median escarpment, see Figure 2 for exact location). Matrix samples divide into pink (10-M1 and 10-M2) and blue (10-M3 and 10-M4) matrices. Pink clast 10-R1 is collected in matrix 10-M1, whereas 10-R2 and 10-R3 are samples of disseminated, dark, and light rock fragments from 10-M3 and 10-M4 blue matrices. Matrices of distinct colors are homogeneous. Both types, however, present significantly distinct isotopic and chemical compositions. In the same way, the three types of clasts show distinct signatures, not only between the groups but also when compared with matrix samples.

0.705340 (which corresponds to the least Sr radiogenic sample 13-R3), together with Sr contents of 2345 and 685 ppm for the sediments and the Socompa Sr unradiogenic end-member, respectively. Such mass proportions result in maximum $SiO_2$ contents of ~58 wt % for a rhyolite-like starting composition (calculations are carried out with $SiO_2$ = 29.5 wt % for Ca-rich unconsolidated sediments; supporting information Table S1) and thus do not explain the andesitic and dacitic compositions of most matrix samples. The same conclusions are reached using Mg-rich samples, where mixing proportions of ~68% can reproduce the isotopic ratios of matrices with an intermediate composition, but this gives maximum $SiO_2$ contents of 25.5 wt %, far below that of the observed dacitic and andesitic compositions. Thus, if the avalanche eroded unconsolidated sediments from the Monturaqui basin, there is no evidence of them at the deposit surface. Alternatively, this could suggest that erosion was very low, despite the fact that the avalanche was emplaced onto a low-strength substratum.

### 5.3. Internal Dynamics of the Avalanche

We quantify the level of heterogeneity of a given outcrop using the Sr-Nd isotopic difference ($D_{Sr\text{-}Nd}$) between matrices and blocks/clasts that were sampled at a given location. This involves calculating the geochemical distance between two samples (one matrix and one block) on the $^{143}Nd/^{144}Nd$ versus $^{87}Sr/^{86}Sr$ plot using a least squares-type formula

$$D^2_{Sr-Nd} = \left[\left(^{87}Sr/^{86}Sr\right)_{C/B} - \left(^{87}Sr/^{86}Sr\right)_M\right]^2 / \sigma^2_{Sr} + \left[\left(^{143}Nd/^{144}Nd\right)_{C/B} - \left(^{143}Nd/^{144}Nd\right)_M\right]^2 / \sigma^2_{Nd} \quad (1)$$

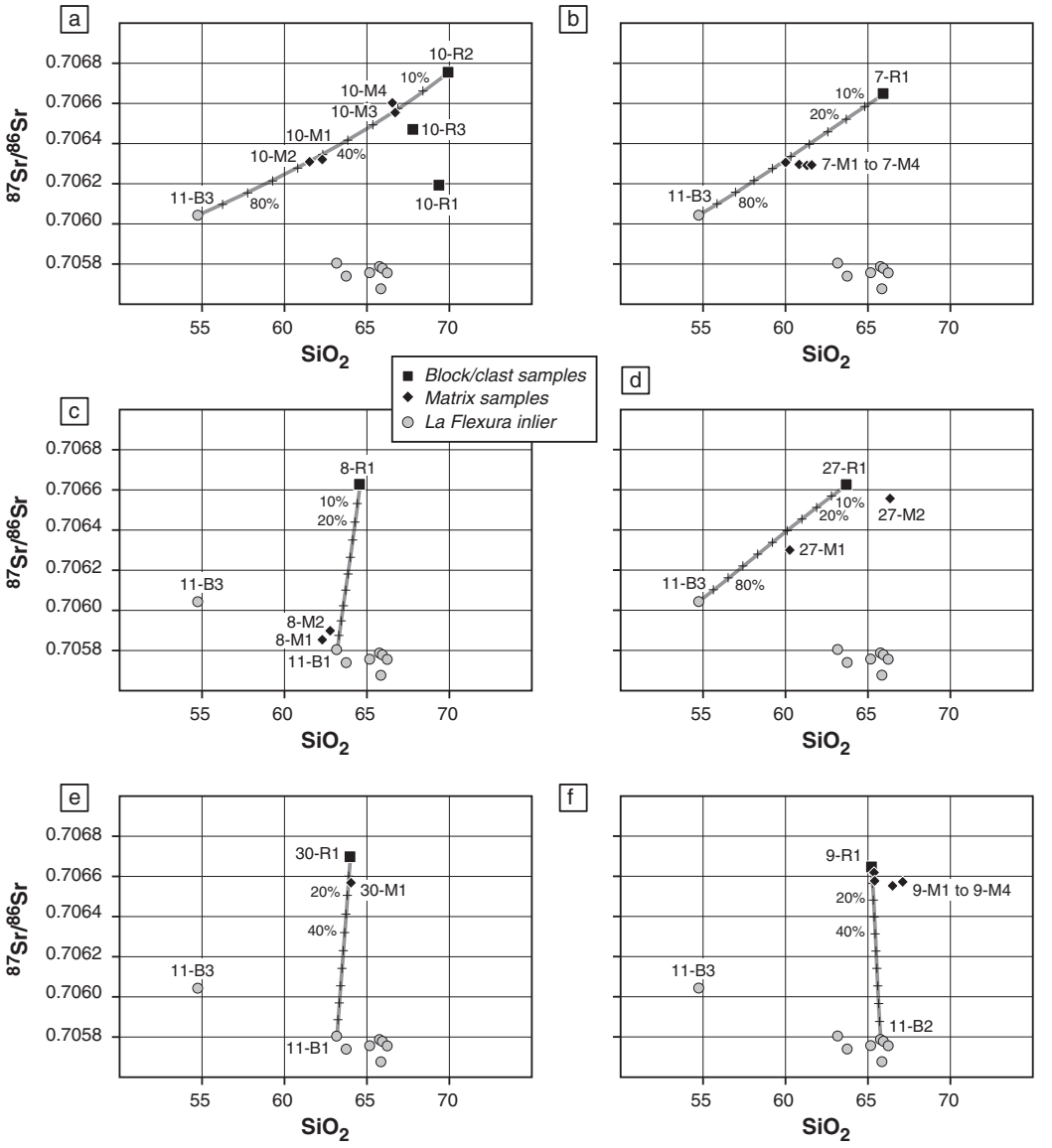


**Figure 12.** Strontium-87/$^{86}$Sr versus $SiO_2$ contents for La Flexura samples together with blocks and matrices from (a) outcrop 10, (b) outcrop 7, (c) outcrop 8, (d) outcrop 27, (e) outcrop 30, and (f) outcrop 9. Chemical and isotopic compositions of some matrix samples in contact with blocks displaying distinct contents and isotopic ratios can be explained by a binary mixing of materials resulting from the crushing of blocks and La Flexura-like samples. In this case, mixing proportions range from 15 to 95% of La Flexura-like material. Such a mixing, however, does not explain all matrix samples (for example, 27-M2, 9-M3, and 9-M4). For outcrops 7, 10, and 27, the only suitable sample for the basement end member is andesitic sample 11-B3 that has clearly different major element and isotope compositions relative to other La Flexura samples.

*C/B* refers to clast/block samples and *M* to matrices, and $\sigma_{Sr}$ and $\sigma_{Nd}$ are the standard deviations of our $^{87}Sr/^{86}Sr$ and $^{143}Nd/^{144}Nd$ measurements determined for blocks and matrices. Analogue distances are usually determined to assess the quality of a model by comparing modeled values and measured ones [e.g., *Debaille et al*., 2006]. Where there is more than one possibility for the calculation (i.e., there is more than one combination of matrix and block samples for a given outcrop), distances for all combinations are determined.

Results show marked variations, from 0.04 to 3.04 (normalized Sr-Nd isotopic scale), illustrating the various relationships observed between blocks/clasts and matrices: both types of sample can indeed show identical (or very similar) isotopic compositions as well as distinct ones (see section 5.1). Figure 13a illustrates the level of heterogeneity for each outcrop, or $D_{Sr\text{-}Nd}$ value, as a function of the linear distance from Socompa's

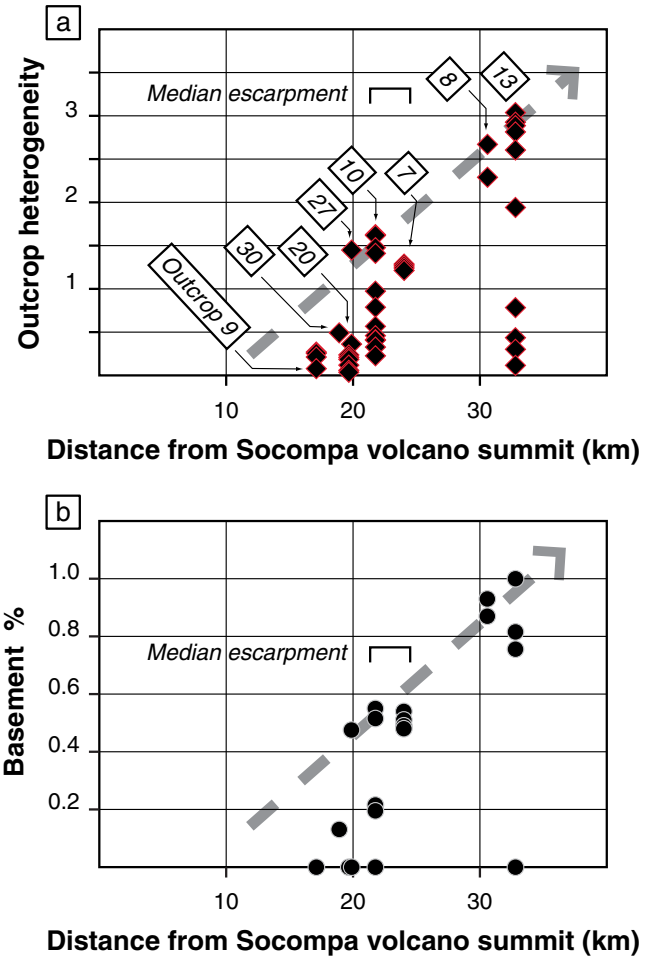


**Figure 13.** (a) Outcrop heterogeneity (here defined as the Sr-Nd isotopic distance between matrices and associated blocks/clasts in the $^{143}Nd/^{144}Nd$ versus $^{87}Sr/^{86}Sr$ plot) and (b) La Flexura-like basement proportions in matrix samples, as a function of the distance from Socompa's summit (UTM coordinates: WGS84; zone 19S; easting = 576500; and northing = 7301634). Numbers in italics refer to outcrops.

summit. No correlation between the two variables is observed when all the data are considered. However, maximum values of $D_{Sr\text{-}Nd}$ increase with distance from Socompa's summit. Assuming that the latter distance is a good proxy for the distance of movement, this allows several constraints relative to the internal dynamics of the Socompa debris avalanche during motion to be identified (schematized in Figure 14).

1. In the proximal zone of the avalanche, vertical and horizontal mixing is either limited to the deeper part of deposits, or is nonexistent. Sampled matrices and surface blocks show similar chemical and isotopic compositions, which results in a low $D_{Sr\text{-}Nd}$ value (as observed, e.g., at outcrop 9). This feature seems to be valid for most of the deposits located south of the median escarpment (Figure 2) as demonstrated by the chemical and isotopic homogeneity of matrices along colored bands of the Landsat image (e.g., samples 17-M1, 18-M1, 19-M1, and 33-M1, which were collected in the light blue band; see section 5.1.1).

2. North of the median escarpment, matrices record mixing of at least two components. Such mixing is more efficient than that affecting deposits in the proximal zone: we now observe a decoupling between matrices and blocks/clasts in terms of chemistry (see e.g., outcrops 7 and 8; Figures 4 and 9).

3. At the debris-avalanche front, the level of deposit heterogeneity continues to increase and outcrops show matrices involving the greatest variety of blocks/clasts in terms of chemical and isotopic composition (outcrop 13; Figure 10). These matrices could result from the mixing of one (or any) of the sampled rocks. In this case, mixing is incomplete as rocks are incorporated whole into the matrix rather than being totally assimilated. Alternatively, matrices could correspond to La Flexura-like basement material. Thus, there would be mingling relationships between rocks and matrices rather than mixing. A hybrid version might also exist between these two alternatives.

Figure 13b shows the proportions of assimilated, La Flexura-like basement material that can be calculated for matrix samples (see section 5.2.1) as a function of the distance from Socompa's summit. As was found for the level of outcrop heterogeneity, there is no real relationship between these two parameters. However, maximum proportions again increase with distance from the summit. This suggests either a higher proportion of La Flexura-like material at the front of the deposit, or a more efficient mixing related to a higher distance of motion permitting La-Flexura-like material to reach the deposit surface.

Finally, superimposed onto these large-scale dynamics are the effects of granular faults mobilised during avalanche emplacement. These put matrices with distinct histories into contact on a local scale. It must also

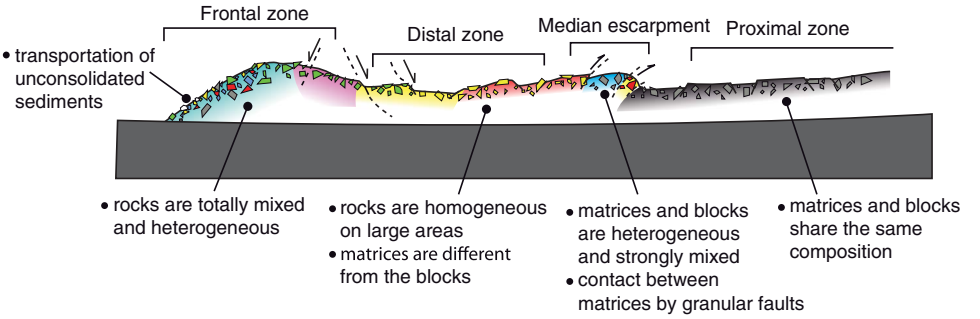


**Figure 14.** Schematic cartoon showing the key sectors of the avalanche together with conclusions drawn from our geochemical study.

be noted that evidence for mingling (Figures 10 and 11) at the surface shows that the material constituting the avalanche must have been fairly fluid in the top level of the deposits, at least during part of the emplacement period. It also suggests that, for the uppermost part of the avalanche, there was not enough collisional energy and/or stress anisotropy to crush and totally assimilate fragments of blocks (or clasts).

## 6. Conclusions

Chemical and isotopic analyses of the main constituents of the Socompa debris-avalanche deposits reveal a great variety of compositions, regardless of the type of material studied, i.e., matrices or blocks. Such compositions define unique and clear correlations on isotope and major element variation diagrams, but they do not show a straightforward relationship with the geographical location of samples. This results from their double origin: compositions reflect mixing of crushed material after (and/or during) the collapse of Socompa, as well as differences inherited from Socompa magmas.

Our main conclusions concern the relationships between blocks and matrices in contact. There is no simple relationship between compositions of both types of sample. They can show very similar compositions as well as very distinct ones, which is sometimes inconsistent with field observations. For example, matrices and blocks with distinct, macroscopic aspects (colors and granulometries) can be very similar in terms of both Sr-Nd ratios and major and trace element contents. On a bigger scale, our results confirm the working hypothesis of *Wadge et al.* [1995] and *Kelfoun et al.* [2008] that Landsat images are a powerful tool for identifying rocks of a similar nature (where the climate favors deposit preservation). This last observation must be balanced for matrices. The latter formations indeed present a globally white color and hence are difficult to distinguish from each other. Conversely, isotope geochemistry appears to be a powerful tool for matrix determination.

Matrix samples do not show compositions consistent with that of the La Flexura-like Socompa basement, except for matrices located at the deposit front. If mixing involved basement rocks, then their contribution is variable and it possibly increases from source to front in the surface deposits of the avalanche.

At large scale, the level of heterogeneity of deposits is increasing with the distance from the Socompa edifice summit. This is a completely new result that was never shown by previous numerical and laboratory models. This was not put into evidence by field observations either.

Matrix samples show constant compositions over long distances, from the source to the median escarpment (∼15–20 km). This suggests that there was either no mixing over this distance or no evolution of mixing conditions during motion. At the front, however, we observe a much greater diversity of block/clast samples (with distinct compositions) in a close relationship with matrices that result either from mixing of these (or some of these) blocks or from crushing of La Flexura-like basement material. For outcrops located between the proximal zone and the front, several processes are superimposed. The efficient mixing of Socompa rocks (or Socompa and basement rocks) generates matrices with chemical and isotopic compositions distinct from those of the blocks they are in contact with. The overall result of our study shows a very dynamic matrix, in which mixing is efficient right up to the top level of the avalanche. Whatever the mechanisms involved, this strong mixing was probably related to a very fluid state throughout nearly all of the avalanche, at least during certain stages of emplacement, and before the formation of granular faults. This questions the classical vision of debris

avalanches; they must be viewed as a complex flow (subject to rheological changes) rather than a granular mass spreading only along its base. The fact that the matrix of the avalanche most certainly behaved as a fluid is in agreement with long-distance transportation over a low slope observed for debris avalanches worldwide.

Our study demonstrates that only isotope geochemistry is able to quantify the matrix formation. Thus, our approach deserves other case studies in order to test conclusions drawn on the Socompa debris avalanche deposits. In order to optimize the number of isotope measurements, we believe it makes sense to focus sampling on a longitudinal profile, and possibly a transverse one where preferential stretching is observed. There, sampling of blocks and matrices at contact must be favored. Moreover, it is also appropriate to consider deposits that can be sampled over their whole thickness, from base to top, in order to better determine vertical lengths of mixing and the influence of basement rocks.

**Acknowledgments**

The authors wish to thank Jean-François Marini (head of IRD-Chile) and the whole IRD Santiago team (a special thanks to Nelda Leiva) for their welcome as well as logistical support during the three sampling campaigns of Socompa deposits. The help of Jean-Luc Froger, Thomas Shea, and Eder Gonzales was also greatly appreciated. The authors are grateful to Delphine Auclair for TIMS maintenance and support during Sr-Nd isotope analyses and to Mhammed Benbakkar for ICP-AES analyses. Frances van Wyk de Vries helped us with the quality of the manuscript, and Jim Vallance made helpful comments on a previous version of the manuscript. The paper was improved by critical reviews by Jeremy Richards, Allen Glazner, and Editor Cin-Ty Lee. Funding for this study was initially provided by the INSU project Reliefs de la Terre 2007/2008. This is Laboratory of Excellence ClerVolc contribution n°93.

## References

Campbell, C. S. (1989), Self-lubrication for long runout landslides, *J. Geol.*, *97*, 653–665.

Capra, L., J. L. Macías, K. M. Scott, M. Abrams, and V. H. Garduño-Monroy (2002), Debris avalanches and debris flows transformed from collapses in the Trans-Mexican Volcanic Belt, Mexico—Behavior, and implications for hazard assessment, *J. Volcanol. Geotherm. Res.*, *113*, 81–110.

Chauvel, C., and J. Blichert-Toft (2001), A hafnium and trace element perspective on melting of the depleted mantle, *Earth Planet. Sci. Lett.*, *190*, 137–151.

Collins, G. S., and H. J. Melosh (2003), Acoustic fluidization and the extraordinary mobility of sturzstroms, *J. Geophys. Res.*, *108*(B10), 2473, doi:10.1029/2003JB002465.

Crandell, D. R. (1989), Gigantic debris avalanche of Pleistocene age from ancestral Mount Shasta Volcano, California, and debris-avalanche hazard zonation, *U.S. Geol. Surv. Bull. 1861*, 32 p.

Crandell, D. R., C. D. Miller, H. X. Glicken, R. L. Christiansen, and C. G. Newhall (1984), Catastrophic debris avalanche from ancestral Mount Shasta volcano, California, *Geology*, *12*, 143–146.

Davies, T. R., and M. J. McSaveney (1999), Runout of dry granular avalanches, *Can. Geotech. J.*, *3*, 313–320.

Debaille, V., R. Doucelance, P. Schiano, and D. Weis (2006), Multi-stage mixing in subduction zones: Application to Merapi volcano (Java Island, Sunda Arc), *Geochim. Cosmochim. Acta*, *70*, 723–741.

Deruelle, B. (1978), The Negros de Aras nuee ardente deposits: A cataclysmic eruption of Socompa volcano (Andes of Atacama, north Chile), *Bull. Volcanol.*, *413*, 175–186.

Francis, P. W., M. Gardeweg, C. F. Ramirez, and D. A. Rothery (1985), Catastrophic debris avalanche deposit of Socompa volcano, northern Chile, *Geology*, *13*, 600–603.

Iverson, R. M., and R. P. Denlinger (2001), Flow of variably fluidized granular masses across three-dimensional terrain: 1. Coulomb mixture theory, *J. Geophys. Res.*, *106*, 537–552.

Jacobsen, S. B., and G. J. Wasserburg (1984), Sm-Nd isotopic evolution of chondrites and achondrites, II, *Earth Planet. Sci. Lett.*, *67*, 137–150.

Kelfoun, K., and T. H. Druitt (2005), Numerical modeling of the emplacement of Socompa rock avalanche, *Chile, J. Geophys. Res.*, *110*, B12202, doi:10.1029/2005JB003758.

Kelfoun, K., T. Druitt, B. van Wyk de Vries, and M.-N. Guilbaud (2008), Topographic reflection of the Socompa debris avalanche, *Chile, Bull. Volcanol.*, *70*, 1169–1187.

Legros, F. (2002), The mobility of long-runout landslides, *Eng. Geol.*, *63*, 301–331.

Le Maître, R. W. (2002), *Igneous Rocks. A Classification and Glossary of Terms, Recommendations of the International Union of Geological Sciences Subcommission on the Systematics of Igneous Rocks*, 236 pp., Cambridge Univ. Press, Cambridge, U. K.

Mamani, M., G. Wörner, and T. Sempere (2010), Geochemical variations in igneous rocks of the Central Andean orocline (13°S to 18°S): Tracing crustal thickening and magma generation through time and space, *GSA Bull.*, *122*, 162–182.

Mangeney, A., P. Heinrich, and R. Roche (2000), Analytical solution for testing debris avalanche numerical models, *Pure Appl. Geophys.*, *157*, 1081–1096.

Mollon, G., V. Richefeu, P. Villard, and D. Daudon (2012), Numerical simulation of rock avalanches: Influence of a local dissipative contact model on the collective behavior of granular flows, *J. Geophys. Res.*, *117*, F02036, doi:10.1029/2011JF002202.

Morgan, J. K., and P. J. McGovern (2005), Discrete element simulations of gravitational volcanic deformation: 1. Deformation structures and geometries, *J. Geophys. Res.*, *110*, B05402, doi:10.1029/2004JB003252.

Nesbitt, H. W., and G. M. Young (1982), Early Proterozoic climates and plate motions inferred from major element chemistry of lutites, *Nature*, *299*, 715–717.

Otha, T., and H. Arai (2007), Statistical empirical index of chemical weathering in igneous rocks: A new tool for evaluating the degree of weathering, *Chem. Geol.*, *240*, 280–297.

Pin, C., and C. Bassin (1992), Evaluation of a strontium-specific extraction chromatographic method for isotopic analysis in geological materials, *Anal. Chim. Acta*, *269*, 249–255.

Pin, C., D. Briot, C. Bassin, and F. Poitrasson (1994), Concomitant separation of strontium and samarium-neodymium for isotopic analysis in silicate samples, based on specific extraction chromatography, *Anal. Chim. Acta*, *298*, 209–217.

Ramirez, C. F. (1988), The geology of Socompa volcano and its debris avalanche deposit, northern Chile, MSc dissertation, Open Univ., Milton Keynes, U. K.

Richards, J. P., and M. Villeneuve (2001), The Llullaillaco volcano, northwest Argentina: Construction by Pleistocene volcanism and destruction by sector collapse, *J. Volcanol. Geotherm. Res.*, *105*, 77–105.

Shea, T., and B. van Wyk de Vries (2008), Structural analysis and analogue modeling of the kinematics and dynamics of rockslide avalanches, *Geosphere*, *4*, 657–686.

Siebert, L. (1984), Large volcanic debris avalanches: Characteristics of source areas, deposits, and associated eruptions, *J. Volcanol. Geotherm. Res.*, *22*, 163–197.

Stoopes, G. R., and M. F. Sheridan (1992), Giant debris avalanches from the Colima Volcanic Complex, Mexico: Implications for long-runout landslides (>100 km) and hazard assessment, *Geology*, *20*, 299–302.

Ui, T. (1983), Volcanic dry avalanche deposits—Identification and comparison with nonvolcanic debris stream deposits, *J. Volcanol. Geotherm. Res.*, *18*, 135–150.

van Wyk de Vries, B., S. Self, P. W. Francis, and L. Keszthelyi (2001), A gravitational spreading origin for the Socompa debris avalanche, *J. Volcanol. Geotherm. Res.*, *105*, 225–247.

Voight, B., H. Glicken, R. J. Janda, and M. Douglass (1981), Catastrophic rockslide avalanche of may 18, in *The 1980 Eruptions of Mount St. Helens, Washington*, edited by P. Lipman and D. R. Mullineaux, U.S. Geol. Surv. Prof. Pap., 1250, 347–377.

Wadge, G., P. W. Francis, and C. F. Ramirez (1995), The Socompa collapse and avalanche event, *J. Volcanol. Geotherm. Res.*, *66*, 309–336.

ELSEVIER

Chemical Geology 176 (2001) 361–377

CHEMICAL GEOLOGY
INCLUDING
ISOTOPE GEOSCIENCE

www.elsevier.com/locate/chemgeo

# Reevaluation of precise lead isotope measurements by thermal ionization mass spectrometry: comparison with determinations by plasma source mass spectrometry

R. Doucelance *, G. Manhès

*Laboratoire de Géochimie et Cosmochimie, Institut de Physique du Globe de Paris, 4 place Jussieu, 75252 Paris cedex 05, France*

Accepted 2 October 2000

**Abstract**

In this study we focus on precise lead isotope analysis by thermal ionization mass spectrometry (TIMS) with silica gel technique. We present extensive measurements of SRM981 and SRM982 standards, of chemically pure Pb and of an equal-atom mixture of the four stable Pb isotopes. Measurements at temperatures lower than 1175°C display reproducible values and are coherent with the usual mass discrimination laws at the level of precision achievable with multicollector mass spectrometers. In contrast, the evolution of mass fractionation at higher temperatures does not follow classical laws of mass discrimination. We observe systematic shifts, the most pronounced of which concerns $^{207}$Pb with a total deviation that can reach values up to 400 ppm. This confirms the recent observation by Thirlwall [Chem. Geol. 163 (2000) 299]. Similarly, we do not have at present a physical explanation for this abnormal behaviour.

We propose new precise isotopic compositions for the SRM981 and SRM982 standards. Assuming a $^{208}$Pb/$^{206}$Pb ratio equal to the nominal value ($^{208}$Pb/$^{206}$Pb = 2.1681 and 1.00016, respectively, cf. J. Res. Natl. Bur. Stand. 72A (1968) 261), the values for $^{207}$Pb/$^{206}$Pb and $^{204}$Pb/$^{206}$Pb ratios are $0.914970 \pm 17$ and $0.059019 \pm 5$ ($2\sigma$) for SRM981, and $0.467080 \pm 10$ and $0.027212 \pm 2$ ($2\sigma$) for SRM982. These compositions are in agreement with the recent measurements achieved with multicollection mass spectrometers with an inductively coupled plasma-source (MC-ICP-MS). 

*Keywords:* Lead; Isotope; Mass discrimination; TIMS; MC-ICP-MS

## 1. Introduction

For natural samples with a Pb content of a few parts per million or less, the precision of Pb isotope determination is still essentially related to the rigorous control of analytical contamination. This has been recently highlighted by Thirlwall (2000). The precision of Pb isotope measurements by thermal ionization mass spectrometry (TIMS) is related to the determination of instrumental mass discrimination. Since all the lead isotopes except $^{204}$Pb result from radioactive decay of uranium and thorium, no naturally constant ratio can be used for internal normalization of the mass discrimination.

* Corresponding author. Fax: +33-1-44-27-37-52.
*E-mail address:* doucelan@ipgp.jussieu.fr (R. Doucelance).

0009-2541/01/$ - see front matter 
PII: S0009-2541(00)00409-5

The mass discrimination factor is currently evaluated with an external calibration by routine measurements of certified standards (most frequently SRM981). The thermal ionization of Pb with silica gel technique (Akishin et al., 1957; Cameron et al., 1969) induces a mass discrimination on the order of $0.10 \pm 0.03\%$ per amu. The precision of Pb isotope measurements is thus limited to few $10^{-4}$ per amu with this external calibration procedure.

Most geological studies using lead isotopes show natural variations greater than this relative precision of about a few $10^{-4}$ per amu. However, improvements of the precision would be useful in some cases such as the fine characterization of mixing end-members and mantle sources of oceanic and continental basalts or the precise chronology for ages younger than 1 Ga. Such an improvement is essential when considering ratios involving $^{207}$Pb, which do not show large variations in natural samples due to the present-day near-extinction of $^{235}$U.

A rigorous correction of the analytical mass discrimination can be achieved by using "multi-spike" methods (Dodson, 1963). Most of the groups, which have developed such a technique (Compston and Oversby, 1969; Hamelin et al., 1985; Woodhead et al., 1995; Todt et al., 1996; Galer and Abouchami, 1998; Thirlwall, 2000), have specified the isotopic composition of the NIST lead standards SRM981 and SRM982. The recent determinations are achieved with multicollector instruments. The analytical precision (around 50 ppm for the $^{207}$Pb/$^{206}$Pb and $^{208}$Pb/$^{206}$Pb ratios, around 150 ppm for the $^{204}$Pb/$^{206}$Pb) is significantly smaller than the overall limit of error defined at the time of standard certification (around 360 ppm for the $^{207}$Pb/$^{206}$Pb and $^{208}$Pb/$^{206}$Pb ratios, around 630 ppm for the $^{204}$Pb/$^{206}$Pb, cf. Catanzaro et al., 1968). So all the new determinations are coherent with the certified values, but they show some discrepancy between them.

This study is focussed on the mass discrimination effect that is induced by the silica gel technique.

The experimental part of this work is comparable and complementary to Thirlwall's (2000); more variable run conditions (i.e. larger temperature range and larger mass discrimination evolution) have been investigated. We present measurements with multicollector mass spectrometers of SRM981 and SRM982 standards, of chemically pure lead and of an equal-atom mixture of the four Pb stable isotopes. This systematics allows us to define new precise evaluations of the certified standards.

## 2. Mass discrimination law and graphic representation of data

### 2.1. Choice of a reference mass discrimination law

During ion production by thermal ionization an isotopic evolution due to the progressive mass dependant depletion of Pb on the filament is observed. Isotopic ratios measured in the beginning of the run thus display an apparent enrichment in light isotopes.

Ozard and Russel (1970) have shown that the mass discrimination law can be reproduced to a first order by a linear function when assuming that mass discrimination only depends on the mass of the measured isotopes. More complex fractionation laws, such as exponential or power laws, have also been developed in order to take into account mass discrimination effects for elements lighter than Pb, mostly Ca (Russel et al., 1978; Hart and Zindler, 1989). For the masses of Pb isotopes, the use of various laws displays differences smaller than 5–10 ppm per amu relative to the linear law, for the range of mass discrimination factors currently observed with the silica gel technique ($\sim 1 \times 10^{-3}$ per amu). Such differences are not distinguishable with the current precision of multicollector mass spectrometers. Thus, we will use here, as a reference, a linear mass discrimination law.

### 2.2. $\Delta^{207}Pb/^{206}Pb$ *vs.* $^{208}Pb/^{206}Pb$ *and* $\Delta^{204}Pb/^{206}Pb$ *vs.* $^{208}Pb/^{206}Pb$ *diagrams*

Each Pb isotopic diagram potentially brings the same information if raw data are correctly treated with propagation of error correlations (Hamelin et al., 1985). Nevertheless, decoupling of $^{204}$Pb, the least abundant isotope, is useful for plotting the data. We have chosen to work with isotopic ratios normalized to $^{206}$Pb. Moreover, we use new plots; these are $\Delta^{204}$Pb/$^{206}$Pb vs. $^{208}$Pb/$^{206}$Pb and $\Delta^{207}$Pb/$^{206}$Pb

vs. $^{208}Pb/^{206}Pb$ representations, where $\Delta^{204}Pb/^{206}Pb$ and $\Delta^{207}Pb/^{206}Pb$ correspond to the differences between measured and calculated ratios according to the reference linear mass discrimination law, for a given $^{208}Pb/^{206}Pb$ ratio. Compared with classical Pb–Pb diagrams, they allow us to highlight small variations at the level of 100 ppm per amu along a mass discrimination evolution on the order of $1 \times 10^{-3}$ per amu (Fig. 1). These diagrams are similar to those used by Hart and Zindler (1989) for Ca isotope measurements.

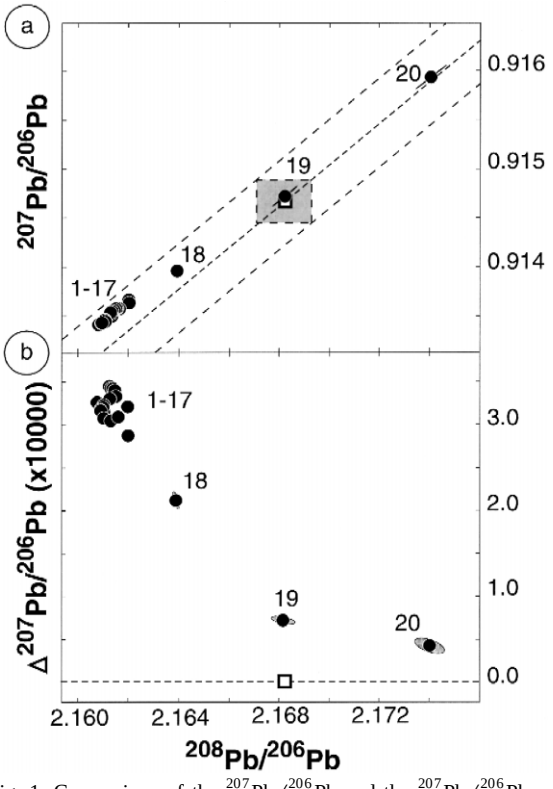


Fig. 1. Comparison of the $^{207}Pb/^{206}Pb$ and the $^{207}Pb/^{206}Pb$ vs. $^{208}Pb/^{206}Pb$ diagrams. A typical experiment with the SRM981 standard (Table 1) is shown. Each full dot plots a data block with its corresponding number. The uncertainty associated to each block is smaller than the symbol size, blocks 18 to 20 excepted. Open-square plots the nominal value of the SRM981 with its overall limit of error (Catanzaro et al., 1968). Dashed lines plot the mass discrimination lines through the certified value. The $^{207}Pb/^{206}Pb$ representation points out more clearly than the Pb–Pb diagram the small but significant scatter of the data set and the deviation of the mass discrimination from a linear evolution.

## 3. Pb measurements

### 3.1. Experimental procedure

All experiments have been carried out on multi-collector mass spectrometers in static mode. The majority of samples have been measured on a Finnigan-MAT262. Some complementary runs were also made on the Vacuum Generator VG354 at IPGP and on another Finnigan-MAT262 at the Laboratoire des Sciences du Climat et de l'Environnement (LSCE, CNRS-CEA) in Gif/Yvette. Gain calibrations were made once a day by injecting $9 \times 10^{-11}$ A currents into the different Faraday amplifiers. Reproducibility of the electrical gains is better than 20 ppm/day. Each data block corresponds to 20 simultaneous measurements of isotopes integrated for 64 s. Baselines are measured before and after each data block wherein the high voltage is off for 64 s; the average of these two measurements is subtracted to the raw peak data. Dark noise for 64-s measurement ranges between $1 \times 10^{-16}$ and $2 \times 10^{-16}$ A ($2\sigma$). One data block takes about 25 min.

Samples (SRM981 and SRM982 standards, pure common lead (99.9999% Pb) and equal-atom mixture) were loaded on tungsten, platinum or rhenium filaments using the silica gel technique (Akishin et al., 1957; Cameron et al., 1969). Tungsten filaments were used on our Finnigan-MAT262, because Re–Os isotopes are also measured on this instrument. Most of the measurements were effected with $1 \times 10^{-6}$ g of lead and $25 \times 10^{-6}$ g of silica gel having a $H_3PO_4/SiO_2$ molar ratio of 7.25. Loads were spreaded on the filament (about 7 mm width). We used such large amounts of Pb ($1 \times 10^{-6}$ g) in order to maintain a minimum signal of $2 \times 10^{-12}$ A for mass 204. Under these conditions, the dark noise to $^{204}Pb$ beam is not greater than 100 ppm. In order to enhance mass discrimination effects, the temperature was systematically increased from about 1050°C to 1500°C (temperature of the visible filament side). The evolution of mass fractionation was around 0.2% per amu. This variation is one order of magnitude larger than that observed during a routine sample analysis.

We also considered various amounts of Pb, between 0.25 and $3 \times 10^{-6}$ g, and various quantities of

silica gel ($10–50 \times 10^{-6}$ g), in order to test different Si/Pb ratios. Some loads were centered on the filament for comparison (about 2.5 mm width).

### 3.2. Blank experiment

Repeated opening of the mass spectrometer source and exposure of the sample magazine to the atmosphere is the cause of contamination of the ion source by organic molecules. Degassing of the source metal surfaces during runs can continuously release these molecules which are then ionized on the filament. In order to minimize these effects, we systematically bake the mass spectrometer source for 8 h at a temperature of 90°C after each source venting and introduction of a new sample magazine. Each magazine position is also simultaneously heated with its own side filament for 45 min. Lastly, we use a liquid nitrogen trap during Pb measurements.

Blanks were measured with a run protocol similar to the samples (loading conditions, pre-heating procedure and data acquisition). Beam intensity was maintained at a constant level by increasing filament temperature in order to simulate data acquisition of samples. The use of $2 \times 10^{-12}$ g of $^{205}$Pb spike allowed us to measure the Pb content of the silica gel bead on the order of $10^{-11}$ g. Mean isotopic composition, once corrected from the $^{205}$Pb spike contribution, is 18.50, 15.50 and 36.75 for the $^{206}$Pb/$^{204}$Pb, $^{207}$Pb/$^{204}$Pb and $^{208}$Pb/$^{204}$Pb ratios, respectively. This typical common Pb composition shows that organic contribution must be negligible for measurements over a temperature range of 1000–1500°C. For $10^{-6}$ g of SRM981, it is less than 1 ppm for the $^{206}$Pb/$^{204}$Pb ratio, less than 0.1 ppm for the $^{207}$Pb/$^{204}$Pb and less than 0.1 ppm for $^{208}$Pb/$^{204}$Pb, respectively.

## 4. Results

### 4.1. Experiment with the SRM981 standard

A typical experiment ($10^{-6}$ g Pb, spread load) is reported in Table 1 and illustrated in Fig. 2a. All SRM981 sample runs display five features (listed below).

(i) First measurement at "low" temperatures, between 1050°C and 1175°C, display coherent values (see details below).

(ii) With time and temperature increase, measurements systematically show a nonlinear isotopic evolution in diagrams involving mass 207. The relative deviation from a linear law ranges between 300 and 400 ppm for the $^{207}$Pb/$^{206}$Pb ratio relative to the $^{208}$Pb/$^{206}$Pb ratio. This nonlinear evolution is most apparent for the last data blocks at high temperatures, but it is continuous during the whole experiment. It is also observed for the runs with different amounts of Pb and silica gel.

(iii) The isotopic evolution of the $^{207}$Pb/$^{206}$Pb ratio relative to the $^{208}$Pb/$^{206}$Pb ratio differs from run to run. Recorded evolutions are dependent on the filament heating sequence used to maintain a $^{204}$Pb beam intensity around $2 \times 10^{-12}$ A (Fig. 2b).

(iv) The isotopic evolution is not obvious when considering the $^{204}$Pb–$^{206}$Pb–$^{208}$Pb triplet. Some runs show a linear evolution of the $^{204}$Pb/$^{206}$Pb ratio relative to the $^{208}$Pb/$^{206}$Pb within an uncertainty of 100 ppm (Fig. 3a). Other runs display a nonlinear evolution of the mass discrimination (Fig. 3b): the total deviation reaches 400 ppm.

(v) The observed deviations are in the overall limit of error defined by the certification of the SRM981 standard (Catanzaro et al., 1968).

We tested and excluded the possibility this effect could result from instrumental artefact, from organic interferences or from the presence of an inorganic impurity in the standard solution. Measurements have been operated on different mass spectrometers (Finnigan-MAT262 and VG354) with different Faraday cup configurations, using loads on tungsten, platinum and rhenium filaments. They systematically show nonlinear isotopic evolution. We thus rule out instrumentation artefact. Progressive decrease with filament heating of organic interferences affecting preferentially mass 207 could also explain such nonlinear evolution of the $^{207}$Pb/$^{206}$Pb ratio relative to the $^{208}$Pb/$^{206}$Pb. However, a contribution of $1 \times 10^{-12}$ A on mass 207 in order to induce a relative deviation of 300 or 400 ppm for about $3 \times 10^{-11}$ A of signal is never observed on loading blanks for temperatures between 1000°C and 1500°C.

Lastly, measurements of chemically pure common lead (99.9999% of purity) and SRM981 standard

Table 1
Raw data for a typical experiment with the SRM981 standard presented on Fig. 1

| # | $T$ (°C) | $^{207}Pb/^{206}Pb$ | $^{208}Pb/^{206}Pb$ | $^{206}Pb/^{204}Pb$ | $^{207}Pb/^{204}Pb$ | $^{208}Pb/^{204}Pb$ | $\rho 7/6–8/6$ | $\rho 4/6–8/6$ | $\Delta^{207}Pb/^{206}Pb$ ($\times 10000$) | $\Delta^{204}Pb/^{206}Pb$ ($\times 100000$) |
|---|---|---|---|---|---|---|---|---|---|---|
| 1 | 1062 | 0.913538 (25) | 2.161241 (83) | 16.8877 (11) | 15.4275 (10) | 36.4983 (24) | 0.8495 | 0.2840 | 3.45 | −1.4 |
| 2 | 1081 | 0.913549 (17) | 2.161305 (76) | 16.8903 (10) | 15.4301 (10) | 36.5051 (30) | 0.8422 | −0.3408 | 3.42 | −2.1 |
| 3 | 1098 | 0.913566 (13) | 2.161383 (41) | 16.8916 (7) | 15.4316 (7) | 36.5093 (18) | 0.2038 | −0.2015 | 3.43 | −2.4 |
| 4 | 1116 | 0.913579 (13) | 2.161456 (30) | 16.8921 (7) | 15.4322 (7) | 36.5115 (17) | 0.7436 | −0.1631 | 3.40 | −2.4 |
| 5 | 1132 | 0.913580 (13) | 2.161498 (27) | 16.8923 (9) | 15.4325 (9) | 36.5128 (19) | 0.5646 | 0.2900 | 3.33 | −2.3 |
| 6 | 1147 | 0.913529 (17) | 2.161263 (51) | 16.8902 (7) | 15.4297 (8) | 36.5043 (22) | 0.7634 | −0.4989 | 3.31 | −2.2 |
| 7 | 1159 | 0.913436 (19) | 2.160885 (54) | 16.8867 (7) | 15.4249 (8) | 36.4903 (21) | 0.8907 | −0.5576 | 3.18 | −2.0 |
| 8 | 1172 | 0.913469 (12) | 2.161017 (32) | 16.8882 (9) | 15.4268 (8) | 36.4956 (20) | 0.6089 | −0.1762 | 3.23 | −2.2 |
| 9 | 1185 | 0.913420 (11) | 2.160768 (30) | 16.8854 (7) | 15.4235 (6) | 36.4855 (18) | 0.4560 | −0.5124 | 3.27 | −1.9 |
| 10 | 1199 | 0.913461 (21) | 2.160994 (91) | 16.8878 (7) | 15.4264 (9) | 36.4945 (26) | 0.9359 | −0.4490 | 3.20 | −2.1 |
| 11 | 1220 | 0.913438 (17) | 2.160902 (75) | 16.8876 (9) | 15.4258 (10) | 36.4925 (29) | 0.7515 | −0.5980 | 3.16 | −2.3 |
| 12 | 1243 | 0.913577 (57) | 2.161595 (253) | 16.8934 (22) | 15.4334 (28) | 36.5167 (86) | 0.9714 | −0.8153 | 3.09 | −2.4 |
| 13 | 1252 | 0.913667 (17) | 2.161968 (51) | 16.8966 (9) | 15.4379 (9) | 36.5299 (23) | 0.8532 | −0.2722 | 3.20 | −2.5 |
| 14 | 1272 | 0.913462 (09) | 2.161024 (26) | 16.8885 (7) | 15.4270 (7) | 36.4964 (17) | 0.3781 | −0.2967 | 3.15 | −2.3 |
| 15 | 1292 | 0.913456 (15) | 2.161030 (76) | 16.8890 (9) | 15.4274 (9) | 36.4977 (29) | 0.8614 | −0.5388 | 3.07 | −2.4 |
| 16 | 1318 | 0.913508 (30) | 2.161293 (139) | 16.8907 (12) | 15.4298 (15) | 36.5057 (47) | 0.9139 | −0.8017 | 3.04 | −2.3 |
| 17 | 1353 | 0.913636 (77) | 2.161981 (372) | 16.8957 (24) | 15.4365 (35) | 36.5282 (115) | 0.9864 | −0.9533 | 2.87 | −2.2 |
| 18 | 1399 | 0.913962 (34) | 2.163886 (235) | 16.9109 (22) | 15.4559 (23) | 36.5933 (80) | 0.8958 | −0.6823 | 2.11 | −2.3 |
| 19 | 1451 | 0.914727 (228) | 2.168170 (1111) | 16.9449 (90) | 15.5000 (121) | 36.7394 (384) | 0.9992 | −0.9954 | 0.72 | −2.5 |
| 20 | 1483 | 0.915933 (277) | 2.174031 (1370) | 16.9920 (108) | 15.5636 (146) | 36.9412 (467) | 0.9980 | −0.9913 | 0.42 | −2.9 |

Numbers in parentheses correspond to 1sd and refer to the least significant digits. $\rho 7/6–8/6$ and $\rho 4/6–8/6$ are the correlation coefficients between $^{207}Pb/^{206}Pb$ and $^{208}Pb/^{206}Pb$ and between $^{204}Pb/^{206}Pb$ and $^{208}Pb/^{206}Pb$, respectively.

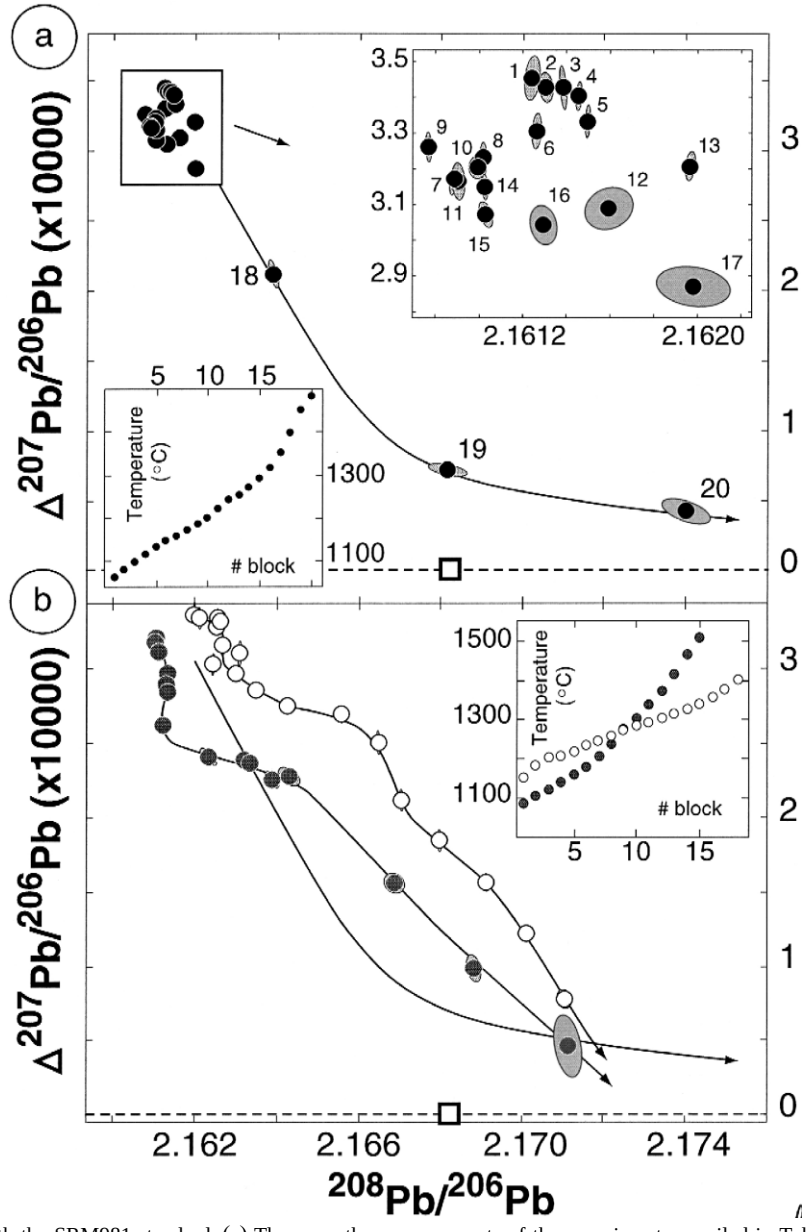


Fig. 2. Experiments with the SRM981 standard. (a) These are the measurements of the experiment compiled in Table 1. Numbers refer to data blocks, ellipses show the uncertainties. The inset on the right highlights the isotopic evolution from block 1 to 17. The inset on the left shows the step heating (Table 1) to maintain the $^{204}$Pb beam at around $2 \times 10^{-12}$ A. The dashed line plots the linear mass discrimination passing through the nominal value of the SRM981 standard (open square). The last data blocks (18 to 20) display the most important shifts, but a deviation from the linear evolution appears from block 5 after about 2 h of heating. (b) This shows distinct evolutions observed for three similar experiments ($1 \times 10^{-6}$ g Pb, spread loads). The dashed line without any symbol corresponds to the experiment plotted in (a). The isotopic evolution mostly depends on the heating conditions (inset).

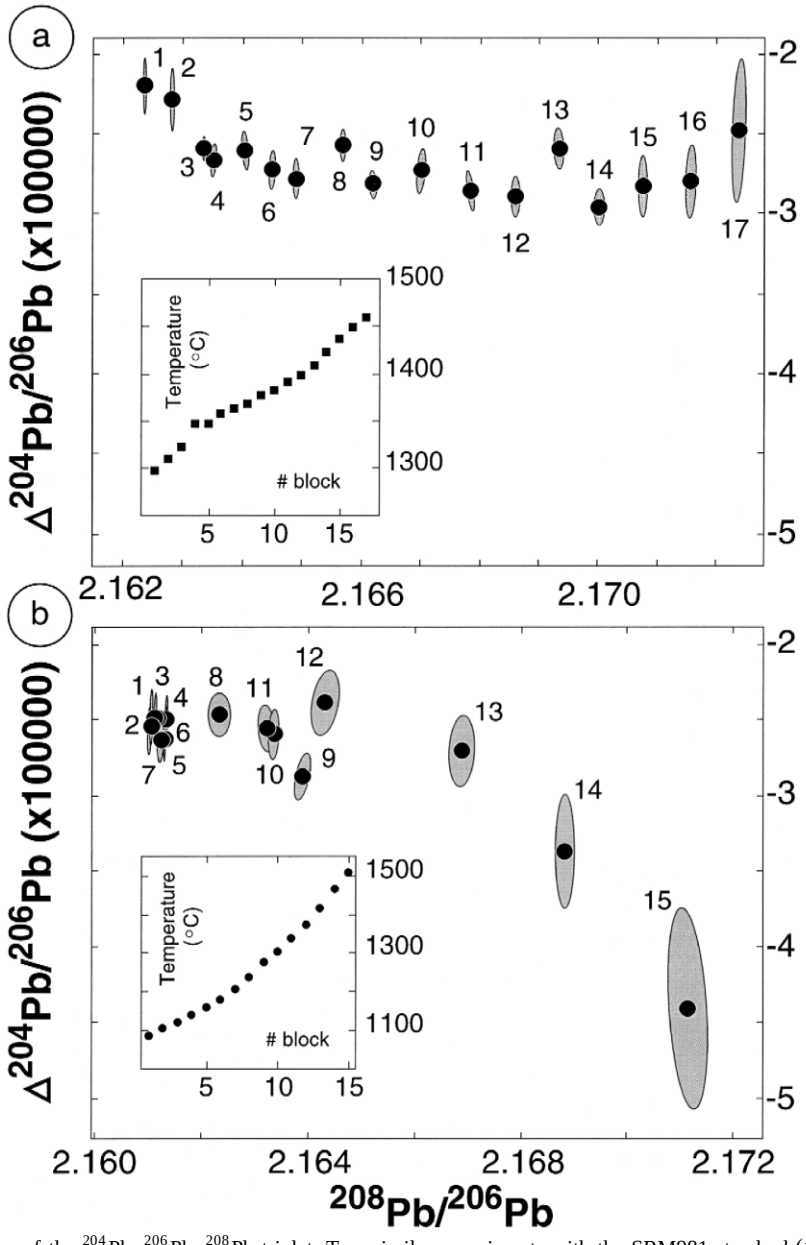


Fig. 3. Isotopic evolution of the $^{204}$Pb–$^{206}$Pb–$^{208}$Pb triplet. Two similar experiments with the SRM981 standard ($1 \times 10^{-6}$ g Pb, spread loads) are shown in the $\Delta^{204}Pb/^{206}Pb$ vs. $^{208}Pb/^{206}Pb$ diagram. Numbers refer to the data blocks. Insets show the step heating to maintain the $^{204}$Pb beam at about $2 \times 10^{-2}$ A. Experiment in (a) follows a linear isotopic evolution whereas experiment in (b) shows a progressive deviation from a linear mass discrimination, up to about 400 ppm.

purified by ion exchange chromatography also display nonlinear evolution for isotope 207 relative to other Pb isotope.

We consider these “abnormal” isotopic evolutions as the superposition of a classical mass discrimination evolution with a nonlinear fractionation whose

physical origin is not identified yet. We attribute the occurrence of this effect to the use of silica gel.

The consistency of the first measurement at "low" temperatures has been noted above We evaluate here the reproducibility of the data sets which include the first five blocks of each experiment. The time interval to achieve such a data set is about 2.5 h, including 6400 s of Pb beam measurement and 380 s of background measurement. This is a maximum time interval for a sample routine analysis. We define the reproducibility of $^{207}Pb/^{206}Pb$ and $^{204}Pb/^{206}Pb$ ratios by the dispersion of data around a linear mass

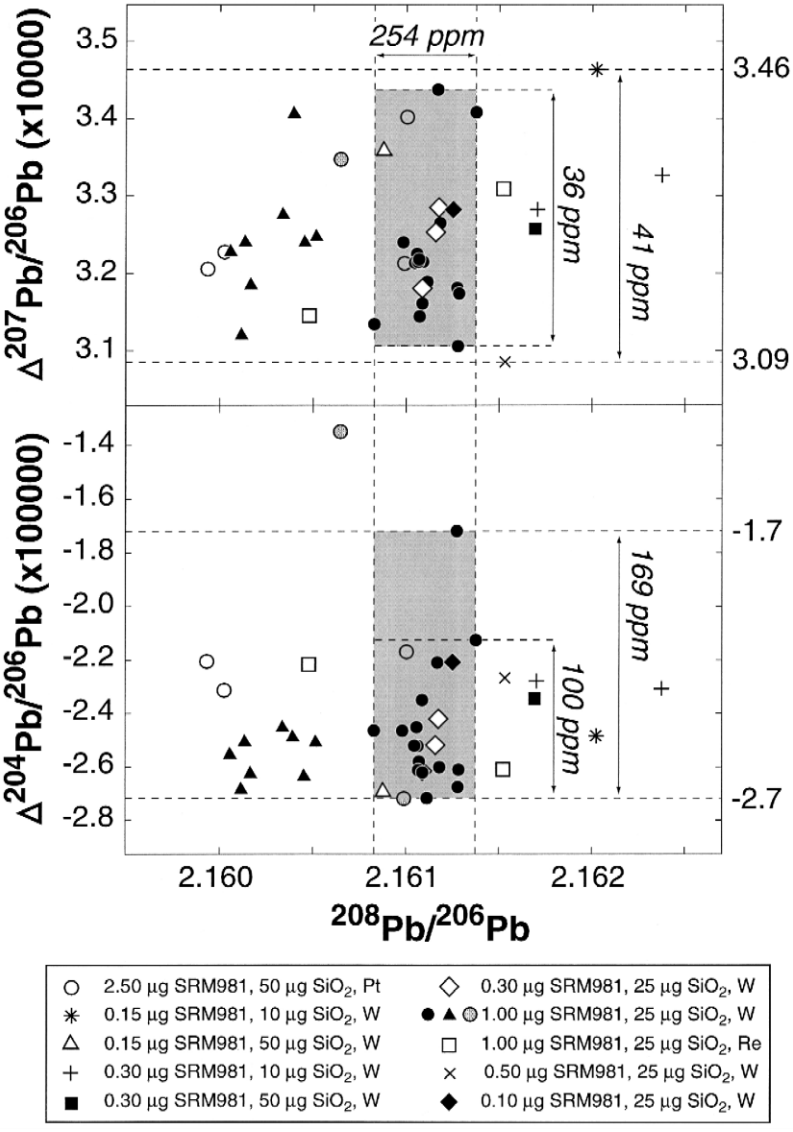


Fig. 4. External reproducibilities of $^{207}Pb/^{206}Pb$ and $^{204}Pb/^{206}Pb$ ratios. Black and grey circles are for $1 \times 10^{-6}$ g Pb spread loads; running temperature ranges between 1050°C and 1175°C for the first, and between 990 and 1010 for the second, respectively. Black triangles correspond to $1 \times 10^{-6}$ g Pb centered loads. For given amounts of lead and silica-gel, spread and centered loads show small distinct mass discrimination (around $1.8 \times 10^{-4}$ per amu) but similar reproducibilities.

discrimination law relative to the $^{208}Pb/^{206}Pb$ ratio. This is the reproducibility of the $\Delta^{207}Pb/^{206}Pb$ and $\Delta^{204}Pb/^{206}Pb$ parameters. For 16 runs between June 1996 and January 1999 ($1 \times 10^{-6}$ g Pb, spread load) they are 36 ppm ($\Delta^{207}Pb/^{206}Pb = 3.27 \times 10^{-4} \pm 0.17 \times 10^{-4}$, $2\sigma$) and 169 ppm ($\Delta^{204}Pb/^{206}Pb = 2.2 \times 10^{-5} \pm 0.5 \times 10^{-5}$, $2\sigma$), respectively (Fig. 4). The $^{204}Pb/^{206}Pb$ reproducibility is limited by one high value ($\Delta^{204}Pb/^{206}Pb = -1.7 \times 10^{-5}$) and it is 100 ppm without this latter value. This is similar to the uncertainty associated to a dark noise around $2 \times 10^{-16}$ A. Lastly, the $^{208}Pb/^{206}Pb$ reproducibil-

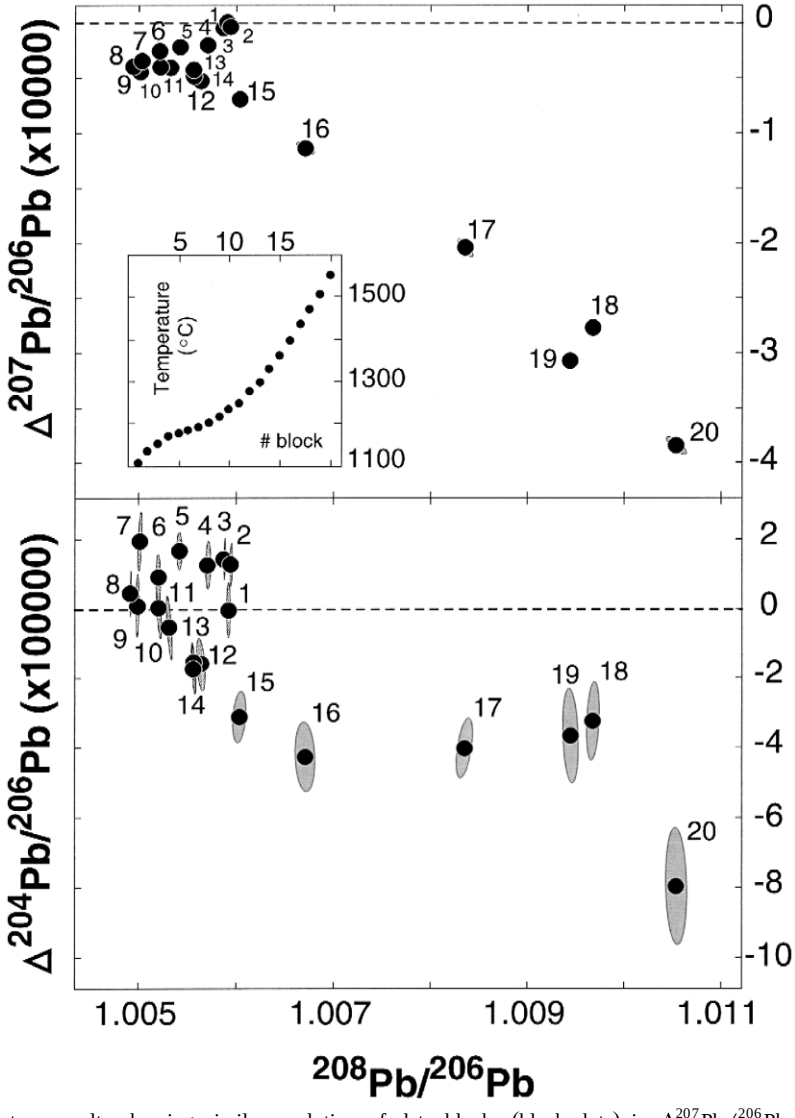


Fig. 5. Equal-atom mixture results showing similar evolution of data blocks (black dots) in $\Delta^{207}Pb/^{206}Pb$ and $\Delta^{204}Pb/^{206}Pb$ vs. $^{208}Pb/^{206}Pb$ diagrams. The deviation from the linear mass discrimination reaches 100 and 400 ppm for the $^{204}Pb/^{206}Pb$ and $^{207}Pb/^{206}Pb$ isotopic ratios, respectively. The inset shows the step heating to maintain a signal of $7.5 \times 10^{-11}$ A for each peak. Theoretical values of $^{204}Pb/^{206}Pb$ and $^{207}Pb/^{206}Pb$, for a given $^{208}Pb/^{206}Pb$ ratio, are calculated relative to the first data block. The dashed line corresponds to the expected linear evolution of data blocks.

ity, 254 ppm ($2\sigma$), measures the reproducibility of mass discrimination, about $\pm 0.065‰$ ($2\sigma$) per amu.

When considering various amounts of lead and silica gel, as also centered loads, the reproducibilities of $^{207}Pb/^{206}Pb$ and $^{204}Pb/^{206}Pb$ are nearly identical with 41 ppm and 169 ppm, respectively. The reproducibility of the $^{208}Pb/^{206}Pb$ ratio, however, is largely higher with 1130 ppm.

For measurements operated at around 1000°C, the $^{208}Pb$ beam intensity was $1 \times 10^{-11}$ A. $\Delta^{207}Pb/^{206}Pb$ values for $10^{-6}$ g Pb runs are coherent with the first data blocks obtained between 1050°C and 1175°C. Isotopic ratios involving $^{204}Pb$ show larger uncertainties due to the baseline influence, but $\Delta^{204}Pb/^{206}Pb$ are consistent with first measurements between 1050°C and 1175°C (Fig. 4).

### 4.2. Experiment with an equal-atom mixture

In order to clarify the isotopic evolution for the $^{204}Pb$–$^{206}Pb$–$^{208}Pb$ triplet observed on SRM981 standard, we analysed a mixture of equal proportions of the four lead isotopes. This allowed us to measure the $^{204}Pb$ beam with the same precision as other Pb isotopes. All the measurements were operated with a minimum beam intensity of $6 \times 10^{-11}$ A for each isotope. The evolution of the $^{207}Pb/^{206}Pb$ ratio relative to the $^{208}Pb/^{206}Pb$ ratio shows a systematic deviation from the linear evolution of mass discrimination, up to 400 ppm (Fig. 5). This evolution is similar to that observed during the SRM981 runs. Simultaneously, we clearly observe a nonlinear evolution of the $^{204}Pb/^{206}Pb$ ratio relative to the $^{208}Pb/^{206}Pb$ ratio. The deviation from a linear evolution of mass discrimination is up to about 100 ppm. It is four times smaller than the deviation observed in the $\Delta^{207}Pb/^{206}Pb$ vs. $^{208}Pb/^{206}Pb$ diagram. Such a deviation is not clearly distinguishable in the case of the SRM981 experiment because of the 100 ppm dark noise ratio.

The external reproducibilities for $\Delta^{207}Pb/^{206}Pb$ and $\Delta^{204}Pb/^{206}Pb$ parameters for the first five data blocks obtained with four runs are similar ($\sim 20$

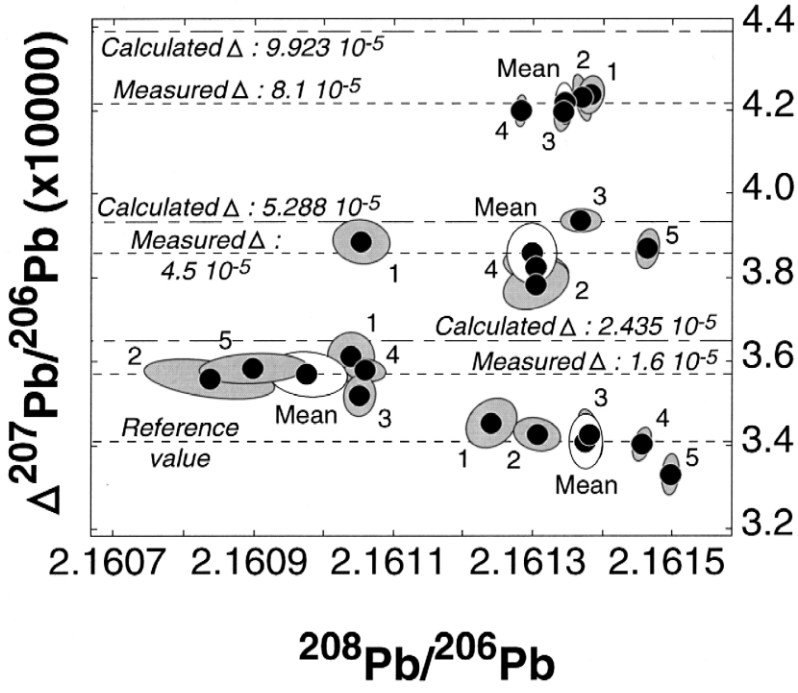


Fig. 6. Experiments with enriched standards.

Table 2
Recent determinations of the SRM981 standard with TIMS and MC-ICP-MS

| | $^{208}Pb/^{206}Pb$ | $^{207}Pb/^{206}Pb$ | $^{204}Pb/^{206}Pb$ | N | Graph Ref |
|---|---|---|---|---|---|
| Catanzaro et al. (1968) | | | | | |
| Mean ± 2sd | 2.168 ± 8 | 0.91464 ± 33 | 0.059042 ± 37 | | 1 |
| *TIMS* | | | | | |
| This study, $^{207}Pb/^{206}Pb$ and $^{204}Pb/^{206}Pb$ isotopic ratios being recalculated for a $^{208}Pb/^{206}Pb$ value of 2.1681 (Catanzaro et al., 1968) with a linear mass discrimination law. | | | | | |
| median ± range/2 | 2.1681 | 0.914970 ± 17 | 0.059019 ± 5 | 16 | 2 |
| mean ± 2sd | 2.1681 | 0.914965 ± 18 | 0.059016 ± 5 | 16 | |
| Thirlwall (2000), normalized using a $^{207}Pb-^{204}Pb$ double spike, calibrated against SRM982, with an assuming $^{208}Pb/^{206}Pb$ value of 1.00016 (Catanzaro et al., 1968). | | | | | |
| Mean ± 2sd | 2.16770 ± 21 | 0.91469 ± 7 | 0.059029 ± 8 | 31 | 3 |
| Galer and Abouchami (1998), normalized using a $^{207}Pb-^{206}Pb-^{204}Pb$ triple spike, calibrated against SRM982 values of Todt et al. (1996). | | | | | |
| Mean ± 2sd | 2.16771 ± 10 | 0.91475 ± 4 | 0.059030 ± 5 | 60 | 4 |
| Todt et al. (1996), using a mixture between SRM981 and a $^{205}Pb-^{202}Pb$ double spike, calibrated against SRM982, with an assuming $^{208}Pb/^{206}Pb$ value of 1.00016 (Catanzaro et al., 1968). | | | | | |
| Mean ± 2sd | 2.16701 ± 43 | 0.91459 ± 13 | 0.059047 ± 8 | 11 | 5 |
| Woodhead et al. (1995), fractionation corrected using independant mixtures with a $^{207}Pb-^{204}Pb$ double spike. Calibration method unclear. | | | | | |
| Mean ± 2sd | 2.16723 | 0.91468 | 0.059042 ± 14 | 109 | 6 |
| Hamelin et al. (1985), fractionation corrected using two mixtures of SRM981 and $^{207}Pb-^{204}Pb$ double spike. | | | | | |
| Mean ± 2sd | 2.16747 | 0.91472 | 0.059031 ± 19 | 10 | 7 |
| *MC-ICP-MS* | | | | | |
| Rehkämper and Halliday (1998), normalized using the certificate value of $^{203}Tl/^{205}Tl$ SRM997. | | | | | |
| Mean ± 2sd[a] | 2.16522 ± 10 | 0.91438 ± 5 | 0.059078 ± 18 | 32 | 8 |
| Mean ± 2sd[b] | 2.16589 ± 10 | 0.91450 ± 5 | 0.059068 ± 18 | 32 | 9 |
| Rehkämper and Halliday (1998), normalized using a $^{203}Tl/^{205}Tl$ value adjusted to give lead results consistent with those of Todt et al. (1996). | | | | | |
| Mean ± 2sd[a] | 2.16652 ± 10 | 0.91466 ± 5 | 0.059039 ± 18 | 32 | 10 |
| Mean ± 2sd[b] | 2.16677 ± 14 | 0.91469 ± 5 | 0.059044 ± 19 | 32 | 11 |
| Mean ± 2sd[c] | 2.16599 ± 65 | 0.91460 ± 12 | 0.059028 ± 16 | 32 | 12 |
| Belshaw et al. (1998), normalized using the certificate value of $^{203}Tl/^{205}Tl$ SRM997. | | | | | |
| Mean ± 2sd[b] | 2.1661 ± 2 | 0.91455 ± 6 | 0.059070 ± 24 | 80 | 13 |
| Belshaw et al. (1998), normalized using a $^{203}Tl/^{205}Tl$ value adjusted to give lead results consistent with those of Todt et al. (1996). | | | | | |
| Mean ± 2sd[b] | 2.1665 ± 2 | 0.91463 ± 6 | 0.059060 ± 24 | 80 | 14 |
| Hirata (1996), normalized using the certificate value of $^{203}Tl/^{205}Tl$ SRM997. | | | | | |
| Mean ± 2sd[a] | 2.16469 ± 86 | 0.91433 ± 3 | 0.059077 ± 31 | 8 | 15 |
| Hirata (1996), normalized using the certificate value of $^{203}Tl/^{205}Tl$ SRM997 and mass-corrected with thallium external method. | | | | | |
| Mean ± 2sd[a] | 2.16636 ± 82 | 0.91462 ± 4 | 0.059063 ± 31 | 8 | 16 |

This compilation is modified after Thirlwall (2000). ±2sd refers to the least significant digits. *N* is the number of determinations. Graph ref number is used in Fig. 8 for data identification.
[a]Power law.
[b]Exponential law.
[c]Linear law.

Table 3
Recent determinations of the SRM982 standard with TIMS and MC-ICP-MS. ±2sd refers to the least significant digits

| | $^{208}Pb/^{206}Pb$ | $^{207}Pb/^{206}Pb$ | $^{204}Pb/^{206}Pb$ | *N* |
|---|---|---|---|---|
| Catanzaro et al. (1968) | | | | |
| Mean ± 2sd | 1.00016 ± 36 | 0.46707 ± 20 | 0.027219 ± 27 | |
| *TIMS* | | | | |
| This study, $^{207}Pb/^{206}Pb$ and $^{204}Pb/^{206}Pb$ isotopic ratios being recalculated for a $^{208}Pb/^{206}Pb$ value of 1.00016 (Catanzaro et al., 1968) with a linear mass discrimination law. | | | | |
| Median ± range/2 | 1.00016 | 0.467080 ± 10 | 0.027212 ± 2 | 5 |
| Mean ± 2sd | 1.00016 | 0.467079 ± 10 | 0.027213 ± 2 | 5 |
| Thirlwall (2000), normalized to $^{208}Pb/^{206}Pb = 1.00016$ (Catanzaro et al., 1968). | | | | |
| Mean ± 2sd | 1.00016 | 0.466990 ± 39 | 0.027216 ± 5 | 11 |
| Todt et al. (1996), normalized to $^{208}Pb/^{206}Pb = 1.00016$ (Catanzaro et al., 1968). | | | | |
| Mean ± 2sd | 1.00016 | 0.467006 ± 22 | 0.027211 ± 1 | 10 |
| *MC-ICP-MS* | | | | |
| Hirata (1996), normalized using the certificate value of $^{203}Tl/^{205}Tl$ SRM997 and mass-corrected with thallium external method. | | | | |
| Mean ± 2sd | 0.99986 ± 8 | 0.46703 ± 5 | 0.027239 ± 20 | 8 |

ppm); they are comparable to the external reproducibilities of the $\Delta^{207}Pb/^{206}Pb$ parameter in the case of SRM981 runs.

### 4.3. Experiments with enriched standards

In order to validate the reproducibility of about 40 ppm for the measurement of the $^{207}Pb/^{206}Pb$ isotopic ratio (relative to the $^{208}Pb/^{206}Pb$ ratio, cf. Section 4.1), we prepared three enriched standards by mixing SRM981 with a small quantity of lead highly enriched in $^{207}Pb$. We obtained absolute enrichments of $2.5\times10^{-5}$, $5\times10^{-5}$ and $1\times10^{-4}$ respectively for the $^{207}Pb/^{206}Pb$ isotopic ratio relative to the intrinsic value of the SRM981 standard.

Fig. 6 shows the measurements for all the enriched standards in the $\Delta^{207}Pb/^{206}Pb$ vs. $^{208}Pb/^{206}Pb$ diagram, as well as a SRM981 run on the same magazine. For each enriched standard, the first data blocks are consistent with a linear isotopic evolution. We observed good agreement between the geometric means defined for these sets of data ($1.6\times10^{-5}$, $4.5\times10^{-5}$ and $8.1\times10^{-5}$) and the calculated isotopic enrichments ($2.44\times10^{-5}$, $5.29\times10^{-5}$ and $9.92\times10^{-5}$). Differences between mean values and calculated values never exceed 20 ppm.

### 4.4. New determination of the SRM981 and SRM982 standards

We consider that the measurements at low temperatures (1050–1175°C) of loads with $1\times10^{-6}$ g of Pb and $25\times10^{-6}$ g of silica gel are less affected or are not affected at all by the abnormal fractionation effect, within the analytical precision defined above. We thus define a new precise composition for the SRM981 standard, based on the data obtained at low temperatures (1050–1175°C). Mass fractionation is corrected using the certified $^{208}Pb/^{206}Pb$ value of the SRM981 standard ($^{208}Pb/^{206}Pb = 2.1681$) as a reference. The values of the $^{207}Pb/^{206}Pb$ and $^{204}Pb/^{206}Pb$ ratios are $0.914970 \pm 17$ and $0.059019 \pm 5$ ($2\sigma$, see Table 2), respectively.

Similarly, we define a new isotopic composition for the SRM982 standard. The certified $^{208}Pb/^{206}Pb$ value of the SRM982 standard ($^{208}Pb/^{206}Pb = 1.00016$) is used as a reference. The values of the $^{207}Pb/^{206}Pb$ and $^{204}Pb/^{206}Pb$ ratios are $0.467080 \pm 10$ and $0.027212 \pm 2$ ($2\sigma$, see Table 3), respectively.

## 5. Comparison with previous studies

### 5.1. Comparison with TIMS measurements

This comparison concerns the precise and recent measurements of the SRM981 standard, which are consecutive to the development of "multi-spike" techniques (Woodhead et al., 1995; Todt et al., 1996; Thirlwall, 2000). Published data are illustrated in Fig. 7.

Thirlwall (2000) investigated errors in lead isotopic analyses by using a $^{204}Pb + ^{207}Pb$ double spike. He has clearly shown that the $^{207}Pb/^{206}Pb$ ratio displays systematic decrease with increasing $^{208}Pb/^{206}Pb$ for temperatures higher than 1250°C. He concludes that $^{207}Pb$ does not obey theoretical mass discrimination laws. He does not provide a physical reason for this apparent "abnormal behaviour of $^{207}Pb$". Our results confirm his conclusion. Nevertheless, we measure greater deviations by a factor two for the $\Delta^{207}Pb/^{206}Pb$. This difference certainly results from different run conditions between the two studies. Thirlwall (2000) uses $50\times10^{-9}$ g Pb for his runs; temperatures range from 1150°C to 1450°C, and the time of measurement is about 30 min. We use larger amounts of lead, between $250\times10^{-9}$ and $3\times10^{-6}$ g; a larger range of temperatures is explored, between 1000°C and 1500°C, especially for the first measurements. Our runs are significantly longer, from 2 to 12 h. These conditions generate large mass discrimination variations, about 0.2% per amu, which are twice as big as those observed by Thirlwall (2000). We noted the variability of isotopic evolutions between runs. This feature is also visible in Thirlwall's work. We disagree with his conclusion that fractionation of lead isotopes 204, 206 and 208 follows classical laws. Our experiments show deviations of the $\Delta^{204}Pb/^{206}Pb$ parameters relative to the $^{208}Pb/^{206}Pb$ ratio at the level of $2\times10^{-5}$ for the SRM981 standard and $1\times10^{-4}$ for the equal-atom mixture. These deviations appear only after few hours of measurement

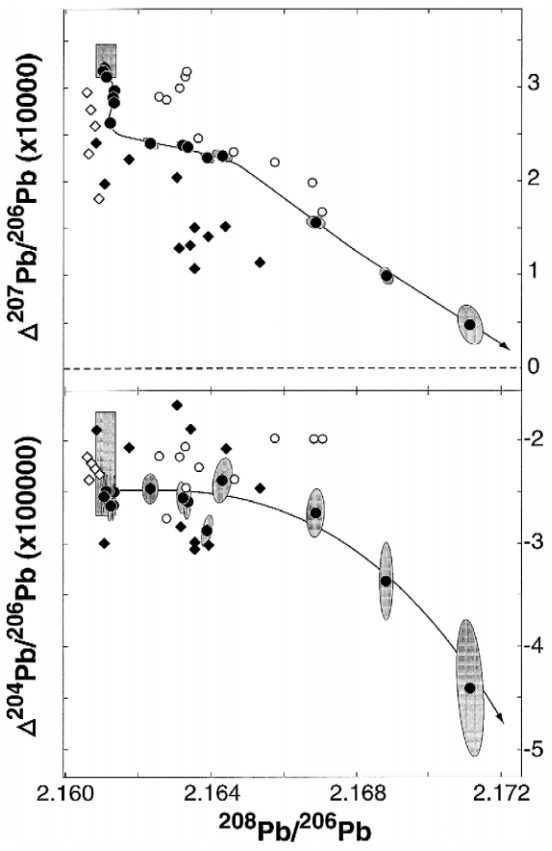


Fig. 7. Recent TIMS measurements with SRM981. Raw isotopic compositions (i.e. not corrected for mass discrimination) are plotted. Full circles along the dashed line show a typical isotopic evolution of this study. Rectangles show the domain of reproductibility of our first low temperature measurements. Open circles are for Thirlwall (2000), open diamonds for Woodhead et al. (1995) and black diamonds for Todt et al. (1996). The data of Woodhead et al. (1995) and Todt et al. (1996) are average run measurements. Each data set shows a nonlinear evolution in the $\Delta^{207}Pb/^{206}Pb$ vs. $^{208}Pb/^{206}Pb$ plot. Previous data are coherent with our first data blocks in the $\Delta^{204}Pb/^{206}Pb$ vs. $^{208}Pb/^{206}Pb$ diagram.

and/or a significant isotopic fractionation. Such run conditions are not explored by Thirlwall.

Raw data published by Woodhead et al. (1995) and Todt et al. (1996) (i.e. not corrected for mass discrimination) fall close to the isotopic paths observed by Thirlwall (2000) and this study. Measurements of Woodhead et al. (1995) are obtained at temperatures between 1100°C and 1200°C. They display a mass discrimination factor similar to what we observed at low temperatures (1050–1175°C). Absolute deviations of the $^{204}Pb/^{206}Pb$ ratio relative to the $^{208}Pb/^{206}Pb$ are around $2.3 \times 10^{-5}$; they are in agreement within the range of variations we observe at low temperatures. Deviations of the $^{207}Pb/^{206}Pb$ ratio relative to the $^{208}Pb/^{206}Pb$ ratio, which range between 1.8 and $3 \times 10^{-4}$, are slightly lower and more variable than our measurements at low temperatures.

Data of Todt et al. (1996) are collected at temperatures higher than 1400°C. They show a mass discrimination range similar to what we observe between 1050 and 1375°C (cf. Table 1 and Fig. 2). Deviations of the $^{204}Pb/^{206}Pb$ ratio for a given $^{208}Pb/^{206}Pb$ range from $-1.7 \times 10^{-5}$ to $-3 \times 10^{-5}$. They are not correlated with the evolution of the $^{208}Pb/^{206}Pb$ ratio and are comparable with those observed in our experiments. Deviations of the $^{207}Pb/^{206}Pb$ ratio relative to the $^{208}Pb/^{206}Pb$ vary between $1.0 \times 10^{-4}$ and $2.5 \times 10^{-4}$.

From this comparison, we emphasize three major points:

(i) All the published raw SRM981 data show deviations with respect to theoretical laws of mass discrimination and variable isotopic evolutions.

(ii) These deviations are within the range of variations that we observe, using deliberately more variable conditions for our experiments (temperature and time).

(iii) Our low temperature measurements show the greatest deviation of the $^{207}Pb/^{206}Pb$ ratio relative to the $^{208}Pb/^{206}Pb$ ratio ($\Delta^{207}Pb/^{206}Pb = 3.3 \pm 0.2 \times 10^{-4}$) with respect to a linear mass discrimination evolution associated to the nominal value of the SRM981 standard. They also show the lowest dispersion. We consider that the published results are more affected by the abnormal fractionation of $^{207}Pb$ than our measurements at low temperatures.

### 5.2. Comparison with recent determinations of SRM981 and SRM982 standards

Recent determinations of the SRM981 standard (Hamelin et al., 1985; Woodhead et al., 1995; Todt et al., 1996; Galer and Abouchami, 1998; Thirlwall, 2000) are compiled in Table 2 and illustrated in Fig.

8. Values defined by Galer and Abouchami (1998) and Thirlwall (2000) are similar with respect to the estimated uncertainties, whereas the isotopic compositions defined by Hamelin et al. (1985), Woodhead et al. (1995) and Todt et al. (1996) display a difference in the mass discrimination factor of about $1.1 \times 10^{-4}$, $0.5 \times 10^{-4}$ and $1.6 \times 10^{-4}$ per amu, respectively.

For the $^{206}Pb$–$^{207}Pb$–$^{208}Pb$ triplet, our composition differs from previous studies. Deviation of the $^{207}Pb/^{206}Pb$ ratio relative to the $^{208}Pb/^{206}Pb$ is about $1.7 \times 10^{-4}$. This study and Thirlwall (2000) show that deviations are depending on run conditions. The SRM981 composition of Thirlwall is extrapolated with an experimental law that does not integrate the variability of the isotopic paths. We think that our composition better specifies the SRM981 standard because it is derived from measured values, which are unaffected by this abnormal fractionation within the analytical uncertainty defined above.

For the $^{204}Pb$–$^{206}Pb$–$^{208}Pb$ triplet, our determination is coherent with published values (Fig. 8).

For the SRM982 standard, we observe similar features between our determination and published values (Todt et al., 1996; Thirlwall, 2000; cf. Table 3). For the $^{206}Pb$–$^{207}Pb$–$^{208}Pb$ triplet, deviation of the $^{207}Pb/^{206}Pb$ ratio relative to the $^{208}Pb/^{206}Pb$ is about $1.7 \times 10^{-4}$. For the $^{204}Pb$–$^{206}Pb$–$^{208}Pb$ triplet, all determinations are coherent.

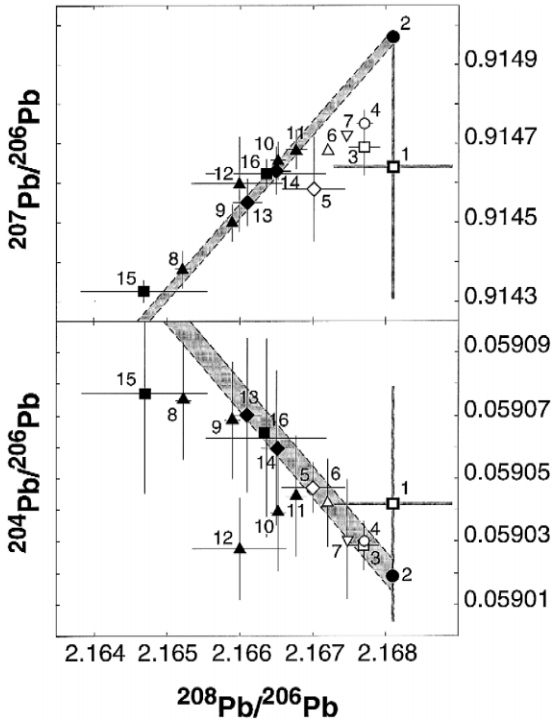


Fig. 8. Comparison of recent SRM981 determinations by TIMS and MC-ICP-MS. Numbers refer to the reference column in Table 2. They grey domains are defined by the mass discrimination lines passing through the interval of uncertainty of our determination. In the $^{207}Pb/^{206}Pb$ vs. $^{208}Pb/^{206}Pb$ diagrams, MC-ICP-MS data and our TIMS determination are coherent. This is not the case for the other TIMS data. In the $^{204}Pb/^{206}Pb$ vs. $^{208}Pb/^{206}Pb$ diagram, all TIMS data are coherent. MC-ICP-MS determinations show larger uncertainties; some are not in agreement with TIMS data.

### 5.3. Comparison with MC-ICP-MS measurements

Because the lack of Pb isotope standard certified with an accuracy of 100 ppm, the comparison between recent TIMS determinations and measurements achieved with an instrumentation involving a different ionization process like multicollector mass spectrometers with an inductively coupled plasma-source (MC-ICP-MS) is an opportunity to validate the high precision measurements by both techniques. It is important to note two features of the instrumental isotopic fractionation associated to MC-ICP-MS. For the heavy element Pb, isotopic fractionation is around 1% per amu: this is an order of magnitude larger than the fractionation observed for TIMS measurements. This fractionation can be kept constant during data acquisition since the analytical solution used for atomization and ionization processes is continuously renewed.

Recent MC-ICP-MS determinations of the SRM981 standard (Hirata, 1996; Belshaw et al., 1998; Rehkämper and Halliday, 1998) are compiled in Table 2 and plotted with TIMS results in Fig. 8. For $^{206}Pb$, $^{207}Pb$ and $^{208}Pb$ isotopes, MC-ICP-MS data, once corrected for instrumental fractionation using a thallium standard, fall on the same theoretical mass discrimination line. Our value for the SRM981 standard is consistent with MC-ICP-MS results in the sense that it plots on the same fractionation line. This is not the case for previous published TIMS determinations.

For $^{204}Pb$, $^{206}Pb$ and $^{208}Pb$ isotopes, TIMS data are coherent and more precise than MC-ICP-MS. This comparison appears useful today to validate the MC-ICP-MS Pb measurements, particularly to evaluate the best mass fractionation law.

For the SRM982 standard, our determination is coherent with the unique published value of Hirata (1996) (Table 3).

## 6. Conclusions

Our measurements at low temperatures (1050–1175°C) display external $2\sigma$ reproducibilities of 250, 40 and 100 ppm for the $^{208}Pb/^{206}Pb$, $^{207}Pb/^{206}Pb$ and $^{204}Pb/^{206}Pb$ ratios, respectively. These results show that the reproducibility of mass discrimination is accessible with careful loading conditions at the level of $\pm 0.065$‰ per amu.

Our experiments at higher temperatures show evolutions of Pb isotopic ratios which do not follow classical mass discrimination laws at the level of precision achieved with multicollector mass spectrometers in static mode (20 ppm). The most important deviation with respect to theoretical laws, around 400 ppm, is observed for $^{207}Pb$ relative to other isotopes. Nevertheless, all three isotope systems show nonlinear isotopic evolution at the 50 ppm level.

We attribute these isotopic evolutions to the superposition of the classical mass discrimination evolution with a nonlinear effect whose physical origin has not been identified yet. We exclude the contribution of "organic" interferences and of polyatomic ions resulting from the presence of inorganic impurity introduced in the beads. In such cases, the physical phenomenon responsible for the observed deviations would induce a fractionation of lead isotopes which is not related to their mass differences.

We consider that our first measurements at low temperature (1050–1175°C) are less affected than previous studies or are unaffected at all within the precision of the measurements by the abnormal fractionation effect. We define new isotopic compositions for the SRM981 and SRM982 standards. Once corrected for mass fractionation using the certified $^{208}Pb/^{206}Pb$ values ($^{208}Pb/^{206}Pb = 2.1681$ and 1.00016 respectively, cf. Catanzaro et al., 1968) as a reference, the $^{207}Pb/^{206}Pb$ and $^{204}Pb/^{206}Pb$ ratios are $0.914970 \pm 17$ and $0.059019 \pm 5$ for SRM981, and $0.467080 \pm 10$ and $0.027212 \pm 2$ for SRM982 ($2\sigma$ uncertainty). These compositions are distinct from previous determinations for the $^{206}Pb$–$^{207}Pb$–$^{208}Pb$ triplet. They are consistent with recent MC-ICP-MS measurements.

## Acknowledgements

We thank Laurent Turpin, who permitted us to work with the TIMS at the Laboratoire des Sciences du Climat et de l'Environnement in Gif sur Yvette. We also thank Matthew Thirlwall for sending to us the revised version of his manuscript as well as his raw data. Jean-Louis Birck, Bernard Bourdon and Christa Göpel made critical comments and suggestions during the course of measurements and the redaction. Youngsook Huh helped us for the quality of the manuscript. This paper was improved by constructive review by R. Mundil. This study is dedicated to Mitsunobu Tatsumoto. This is IPG contribution 1718.

## References

Akishin, P.A., Nikitin, O.T., Panchenkov, G.M., 1957. A new effective ionic emitter for the isotopic analysis of lead. Geokhimiya 5, 425.

Belshaw, N.S., Freedman, P.A., O'Nions, R.K., Frank, M., Guo, Y., 1998. A new variable dispersion double-focusing plasma mass spectrometer with performance illustrated for Pb-isotopes. Int. J. Mass Spectrom. Ion Processes 181, 51–58.

Cameron, A.E., Smith, D.H., Walker, R.L., 1969. Mass spectrometry of nanogram-size samples of lead. Anal. Chem. 41, 525–526.

Catanzaro, E.J., Murphy, T.J., Shields, W.R., Garner, E.L., 1968. Absolute isotopic abundance ratios of common, equal-atom and radiogenic lead isotopic standards. J. Res. Natl. Bur. Stand. 72A, 261–267.

Compston, W., Oversby, V.M., 1969. Lead isotopic analysis using a double spike. J. Geophys. Res. 74, 4338–4348.

Dodson, M.H., 1963. A theoretical study of the use of internal standards for precise isotopic analysis by surface ionization technique: Part I. General first-order algebraic solutions. J. Sci. Instrum. 40, 289–295.

Galer, S.J.G., Abouchami, W., 1998. Practical application of lead triple spiking for correction of instrumental mass discrimination. Min. Mag. 62A, 491–492.

Hamelin, B., Manhès, G., Albarède, F., Allègre, C.J., 1985. Precise lead isotope measurements by the double spike technique: a reconsideration. Geochim. Cosmochim. Acta 49, 173–182.

Hart, S.R., Zindler, A., 1989. Isotope fractionation laws: a test using calcium. Int. J. Mass Spectrom. Ion Process. 89, 287–301.

Hirata, T., 1996. Lead isotopic analyses of NIST standard reference material using multiple collector inductively coupled plasma mass spectrometry with a modified external correction method for mass discrimination effect. Analyst 121, 1407–1411.

Ozard, J.M., Russel, R.D., 1970. Discrimination in solid source lead isotope abundance measurement. Earth Planet. Sci. Lett. 8, 331–336.

Rehkämper, M., Halliday, A., 1998. Accuracy and long-term reproducibility of lead isotopic measurements by MC-ICPMS using an external method for correction of mass discrimination. Int. J. Mass Spectrom. Ion Processes 181, 123–133.

Russel, W.A., Papanastassiou, D., Tombrello, T.A., 1978. Ca isotope fractionation on the Earth and other solar system materials. Geochim. Cosmochim. Acta 42, 1075–1090.

Thirlwall, M.F., 2000. Inter-laboratory and other errors in Pb isotope analyses investigated using a $^{207}Pb$–$^{204}Pb$ double spike. Chem. Geol. 163, 299–322.

Todt, W., Cliff, R.A., Hanser, A., Hofmann, A.W., 1996. Evaluation of a $^{202}Pb$–$^{205}Pb$ double spike for high-precision lead isotope analysis. In: Basu, A., Hart, S. (Eds.), Earth Processes: Reading the Isotopic Code. Geophys. Monogr. 95. American Geophys. Union, Washington, pp. 429–437.

Woodhead, J.D., Volker, F., McCulloch, M.T., 1995. Routine lead isotope determinations using a lead-207 lead-204 double spike: a long-term assessment of analytical precision and accuracy. Analyst 120, 35–39.

ELSEVIER

Chemical Geology 201 (2003) 141–160

CHEMICAL GEOLOGY
INCLUDING
ISOTOPE GEOSCIENCE

www.elsevier.com/locate/chemgeo

# Further investigations on optimized tail correction and high-precision measurement of uranium isotopic ratios using multi-collector ICP-MS

Pierre Deschamps[a,b,*], Régis Doucelance[a,1], Bassam Ghaleb[a], Jean-Luc Michelot[b]

[a] *GEOTOP-UQAM-McGILL, P.O. Box 8888, Succ. Centre-Ville, Montréal, QC, Canada H3C 3P8*
[b] *FRE CNRS-UPS OrsayTerre, Université Paris-Sud, Bâtiment 504, 91 405 Orsay, France*

Accepted 25 June 2003

**Abstract**

In the present paper, we further examine the optimum conditions for rapid, precise and accurate determination of $^{234}U/^{238}U$ ratios in geological materials by multiple collector (magnetic-sector) inductively coupled plasma mass spectrometry (MC-ICP-MS). In our experiments, isotopic measurements were performed on a Micromass IsoProbe™ instrument, using Faraday collectors in static mode only. Unlike the ion counting system coupled with an energy filter, this technique eliminates the difficulty of proper calibration of the Daly/Faraday gain ratio. On the other hand, since our Micromass instrument has a poor abundance sensitivity (the proportion of the $^{238}U$ ion beam measured at mass 237 is $\sim 25$ ppm), the major issue to be addressed is the tail correction. For this purpose, we have developed a tail correction method slightly modified from Thirlwall [J. Anal. At. Spectrom. 16 (2001) 1121]. This method is based on correction of the actual tail contribution under each peak, as assessed by the tail shape measurements on mono-isotopic ion beams, instead of the usual half-mass zeroes baseline estimation. Our approach enabled us to correct for the large offset that can be observed on isotopic data when tail correction is done by means of linear interpolation between half-mass zeroes, and showed that this latter tail correction method results in nearly 3% underestimation of $^{234}U/^{238}U$ ratios on the GEOTOP IsoProbe™ for material at secular equilibrium.

A $^{236}U-^{233}U$ double spike was employed to correct for mass discrimination bias. Using an Aridus™ micro-concentric, desolvating nebulizer sample introducing system, a minimum of 200 ng of sample-U was consumed to carry out a precise $^{234}U/^{238}U$ analysis, thereby allowing a $^{234}U$ signal of $\sim 4-5$ mV to be monitored for 50 measurement cycles of 5 s each. This time-consuming, 10-min procedure allowed us to obtain an external reproducibility of 0.8‰ ($2\sigma$) for isotopic measurements of the NBL-112a standard solution. Replicate measurements of this reference material yielded a mean $\delta^{234}U$ value of $-36.42 \pm 0.80$‰ ($2\sigma$, $n=19$), which is highly consistent with values reported by other laboratories. The total

* Corresponding author. GEOTOP-UQAM-McGILL, P.O. Box 8888, Succ. Centre-Ville, Montréal, QC, Canada H3C 3P8. Tel.: +1-514-987-3000x1581; fax: +1-514-987-3635.

*E-mail address:* m106050@er.uqam.ca (P. Deschamps).

[1] Now at Laboratoire 'Magmas et Volcans', Université Blaise Pascal, CNRS (UMR 6524), Observatoire de Physique du Globe de Clermont-Ferrand, 5 Rue Kessler, 63 038 Clermont-Ferrand Cedex, France.

0009-2541/$ - see front matter 
doi:10.1016/S0009-2541(03)00226-2

reproducibility, including both chemical separation and spectrometric measurement, was assessed using geological samples (a coral and a carbonate rock); the long-term reproducibility obtained was about 1.3 ‰ (2$\sigma$).


*Keywords:* Uranium isotopes; Multiple collector ICP-MS; Tail correction; Standard; Accuracy; Precision

## 1. Introduction

Multiple collector inductively coupled plasma mass spectrometry (MC-ICP-MS) has proved to be a powerful tool for high-precision measurement of isotopic compositions, leading to a wide array of new applications in Earth and planetary sciences and cosmochemistry (Halliday et al., 1998).

This technique has been successfully used for precise measurements of U and Th isotopic compositions (Luo et al., 1997; Stirling et al., 2000, 2001; Henderson, 2002; Robinson et al., 2002; Shen et al., 2002). MC-ICP-MS, and more generally, ICP sources, have several advantages over conventional thermal ionization mass spectrometry (TIMS), which many other studies have already reported (e.g. Halliday et al., 1998; Stirling et al., 2000):

(a) The plasma source yields a very high ionization efficiency (>90%) of nearly all elements having a low first ionization potential (Jarvis et al., 1992; Taylor, 2001);
(b) Ionization efficiency is not a function of load size;
(c) To a first approximation, the mass discrimination is time-independent during data acquisition, since fresh aerosol sample is continuously introduced into the ICP;
(d) Fewer chemical steps are needed during sample preparation.

Nevertheless, MC-ICP-MS has two major drawbacks not encountered in TIMS with respect to U(−Th) isotopic analysis: (i) high plasma-generated ion source instability (Shen et al., 2002); and (ii) poor abundance sensitivity of some instruments (Thirlwall, 2001). The abundance sensitivity is a parameter that allows the estimation of the magnitude of the tail contribution, and is usually defined as the proportion of $^{238}$U ion beam measured at mass 237 (Chen et al., 1992; Thirlwall, 2001). Because of the large atom ratios encountered in the U(−Th) systematics (for example, the $^{238}$U/$^{234}$U atom ratio is close to 18,200 for a sample in secular equilibrium), the tail effect may limit the analytical accuracy (see discussion in Chen et al., 1992). With TIMS analyses, this problem is generally circumvented by using a Daly detector coupled with an energy filter: electrostatic (ESA), Retarding Potential Quadripole (RPQ) or Wide Aperture Retarding Potential (WARP) filter (Edwards, 1988; Chen et al., 1992; Cheng et al., 2000; Rubin, 2001). With such a system, abundance sensitivity is greatly improved to $\ll$1 ppm, and the remaining tail contribution is corrected by using a linear interpolation between half-mass zeroes. The stable thermal-generated ion source allows an analysis in magnet-controlled peak jumping mode on a single detector placed behind the energy filter.

In MC-ICP-MS, the high instability of the ion beam produced by the plasma source makes this approach impractical. Depending on the instrument, different protocols were adopted to overcome this problem.

In this paper, we outline and discuss the advantages and limitations of the technique we developed for precise measurement of uranium concentration and isotopic composition using a Micromass IsoProbe™ MC-ICP-MS instrument. In contrast to what other MC-ICP-MS users have done (Luo et al., 1997; Robinson et al., 2002; Shen et al., 2002), we used Faraday detectors in static mode only. This strategy obviates many of the problems related to gain calibration of the Daly/Faraday detectors. However, since we did not use a Daly detector and the energy filter normally coupled with it, the tail contribution induced by the high abundance sensitivity of the instrument ( $\sim$ 25 ppm) proved to be a critical bias. We addressed this issue following an approach slightly modified from Thirlwall (2001).

In the forthcoming sections, we outline the general protocol used to optimize correction for significant tailing effects. We also describe the entire mass

spectrometric procedure that can be used with an IsoProbe™ MC-ICP-MS instrument for precise measurement of $^{234}U/^{238}U$ ratios. Finally, based on measurements of standard reference materials and geological samples (corals and limestones), we address the issue of the overall analytical precision and accuracy that can be achieved using this technique.

## 2. Overview of current procedures for U isotopic analysis by ICP-MS

Using a VG Elemental Plasma 54™ MC-ICP-MS instrument, Luo et al. (1997) proposed to perform U(−Th) analyses by combining Faraday cups and a Daly detector coupled with an energy filter, either in static or in multi-static mode. Since Faraday and Daly detectors are used simultaneously, their relative gain must be carefully determined in order to achieve maximum precision and accuracy. Two data acquisition protocols were developed. They differ in the way variations in the relative Faraday/Daly gain are monitored. With the static procedure, it is determined externally by a standard bracketing method. With the multi-static procedure, the relative Faraday/Daly gain is monitored and calibrated during the sample analysis by comparing the results of two sequential $^{235}U/^{238}U$ measurements with two different collector configurations (Daly/Faraday and Faraday/Faraday). Luo et al. (1997) and Stirling et al. (2000) argued that the latter approach is superior even though it requires slightly larger sample sizes and is more time-consuming. Because a Daly detector coupled with an energy filter is used to measure the minor mass ($^{234}U$), the contribution of the tail effect underneath this peak may be considered negligible or, at least, well corrected for by the linear interpolation between half-mass zeroes.

Using a Nu™ MC-ICP-MS, Robinson et al. (2002) proposed to perform measurements in static mode on Faraday collectors for major peaks and on an ion counting channel for the minor peak ($^{234}U$). In contrast to observations made on the Daly detector of the Plasma 54™ instrument (Luo et al., 1997) and our IsoProbe™ instrument, the relative gain between the ion counting channel and the Faraday cups remains constant throughout an analysis with the Nu™ collector system, so that no internal drift correction is required. However, because the ion counting channel is not coupled with an energy filter, abundance sensitivity is in the order of 5 ppm at 1 amu. With this instrument, this causes an offset of $<0.5$ ‰ to the measured $^{235}U/^{234}U$ ratio (Robinson et al., 2002). Robinson et al. (2002) argued that the standard bracketing measurement procedure they followed corrects not only for the relative gain between Faraday cups and the ion counting channel, but for this tail offset as well. This means that all sample measurements are taken with reference to a given standard, in this case, CRM-145, and that one makes the assumption that the system behaves linearly. They assessed the validity of their approach by comparing analyses of the CRM-145 standard (also called NBL-112a, NIST-4321, and formerly U-960 or NBS SRM-960) with analyses of the Harwell uraninite (HU-1), which Cheng et al. (2000) have shown to be in secular equilibrium for the $^{238}U-^{234}U$ sequence.

Using a sector-field ICP-MS equipped with a single electron multiplier, Shen et al. (2002) also performed a precise, accurate U−Th isotopic analysis. Their approach obviates many of the problems associated with the intercalibration of ion-counting and Faraday detectors, but requires (i) that the error introduced by source instabilities be minimized; and (ii) more particularly, that the tail correction problem be addressed. The first problem is overcome by installing a guard electrode (GE) sheath around the torch and by employing a rapid peak switching method. The second problem requires precise determination of the tail shape between each mass. Furthermore, the intensity bias inherent in the electron multiplier (see also Cheng et al., 2000) must be corrected for. The correction value is determined once a day by comparing the CRM-145 measured $\delta^{234}U$ with its accepted value. In much the same way as the experiments conducted by Robinson et al. (2002), this protocol requires that all sample analyses be done with reference to a standard sample.

## 3. Experimental procedure used for U-isotope measurements

### 3.1. Instrumentation and data acquisition

All the results presented here were obtained using a Micromass IsoProbe™ MC-ICP-MS at the GEOTOP-

UQAM-McGILL Research Center from July 2001 to May 2002. The instrument is similar to that used by Thirlwall (2001, 2002). It is equipped with an array of nine Faraday cups with $10^{11}$ Ω positive feedback resistors, two ion counting detectors (Channeltron) and a Daly ion counting system inserted immediately behind a retarding filter (WARP).

The U isotopic data are acquired in static multi-collection mode by means of Faraday collectors with cup efficiencies set at unity. The Faraday amplifier gain is calibrated daily before the analytical session. Ignition of the plasma and application of the accelerating high voltage is followed by a warm-up period of about 90 min. Collectors are aligned H1: mass 233 to H6: mass 238, using the configuration shown in Table 1. For uranium isotopic determinations, since the $^{234}U$ ion beam has to be measured on a Faraday cup with a minimum intensity of ~4–5 mV, the $^{238}U$ beam would exceed 80 V for a sample assumed to be in secular equilibrium for the $^{238}U$–$^{234}U$ sequence. This greatly exceeds the capacity of Faraday cups equipped with a $10^{11}$ Ω resistor. In such cases, the H6 detector is moved away from the $^{238}U$ beam in order to avoid any beam collection. However, this collector is occasionally used to determine U concentration in low U-content samples as well as to conduct specific tests (for instance, spike calibration). Abundance sensitivity, usually defined as the proportion of the $^{238}U$ ion beam tail measured at mass 237, is monitored online during each analysis from H5 output, with H5 set for mass 237. The $^{238}U$ intensity is calculated from the $^{235}U$ ion beam (H3) using the natural $^{238}U/^{235}U$ ratio of 137.88 (see Section 4.2). A double spike ($^{236}U$–$^{233}U$) with a ratio of ≈ 0.7 is used to correct for mass discrimination. The measured isotope ratios are then normalized using a linear law (see Section 5.2). In general, samples are spiked so that the resulting $^{235}U/^{233}U$ and $^{233}U/^{234}U$ ratios are close to 11, thereby optimizing dynamic range and precision.

All measurements are performed using a high-efficiency desolvating microconcentric nebulizer system, the ARIDUS MCN 6000™. The sweep gas (Ar and $N_2$) settings are optimized to maximize the sensitivity and minimize oxide levels. The uptake rate of the nebulizer is kept constant at ~ 50 μl/min. Under such conditions, a 6–7 ppb $^{238}U$ solution generates a signal over 1 V. The total sensitivity, combining ionization with MS transmission efficiencies, is about 5‰. Argon flows are set at ~ 15.0 l/min for the cool gas, at ~ 1.03 l/min for the intermediate gas and at ~ 0.90–0.99 l/min for the nebulizer gas.

Table 1
Collector configuration for U isotopic analysis on the GEOTOP IsoProbe™ MC-ICP-MS

| Collector | Axial | High 1 | High 2 | High 3 | High 4 | High 5 | High 6 |
|---|---|---|---|---|---|---|---|
| Uranium | – | $^{233}U$ | $^{234}U$ | $^{235}U$ | $^{236}U$ | (237) | $^{238}U$ |

The sample is introduced into the mass spectrometer in a 2% $HNO_3$ solution. The inlet system is cleaned with 4% $HNO_3$ followed by 2% $HNO_3$ between sample runs until a negligible U background is achieved (see Section 3.2). Depending on the cleanliness of the nebulizer, the washout procedure requires from 10 to 20 min. The first step of the data acquisition procedure consists of a 1-min measurement of the electronic backgrounds of each Faraday cup, subsequently defined as the Mass Spectrometer Background (MSB), with no ion beam (valve off) in the analyzer, in order to determine the amplifier drifts. After the valve (LOS) is opened, the "on-peak zero" baseline (OPZ) is measured for 1 min with the same 2% $HNO_3$ batch solution that was used to dilute samples. Finally, samples are analyzed for one block of 50 scan cycles with a 5 s integration time per cycle. A routine analytical procedure time is around 10 min. With this protocol, the amount of U consumed per analysis is at least 200 ng. This produces a signal of ~ 1 V for $^{235}U$ and >0.005 V for $^{234}U$ (for samples close to $^{238}U$–$^{234}U$ secular equilibrium).

Raw signal intensities are corrected for resistor gains only. They are then transferred to an Excel spreadsheet for further offline cycle-by-cycle manipulations (correction for OPZs, tailing and mass discrimination).

### 3.2. Accuracy and background

In the Excel spreadsheet, the on-peak zeroes (OPZs), determined before sample acquisition, are subtracted from sample peak intensities to correct for: (i) amplifier drifts; (ii) U in the blank solution; (iii) U memory effect in the inlet system; and (iv) potential isobaric interferences that may be associated with the 2% $HNO_3$ solution. The OPZ correction significantly controls the precise determination of

the small $^{234}U$ signal and thus the accuracy of U isotopic measurements. The effect of MS backgrounds and absolute on-peak zero ($OPZ_{abs}$) intensities (estimated by subtracting the MSB from OPZ) on accuracy and precision are discussed separately in the next sections.

### 3.2.1. MS background

Daily variations in the electronic background (MSB) were monitored during 64 s on each Faraday cup throughout the first step of the sample analytical procedure. These were around 20–30 μV ($2\sigma$; $n \approx 20$ analysis per day) depending on the day of analysis. However, a general drift was observed on all the Faraday cup baselines in the course of a day, demonstrating that, to a first approximation, the electronic backgrounds monitored on each cup co-varied with time. This phenomenon might be associated with temperature fluctuations of the system (MC-ICP-MS, room temperature).

We define dark noise here as the fluctuation around this first-order drift. This noise is below 10 μV ($2\sigma$) for the MSB measurements of each Faraday cup, based on a 64-s integration time. Included in this value is the intrinsic error associated with the amplifier noise (see discussion in Ludwig, 1997), and also the error related to the drift in the amplifier background, during the integration. This value represents the actual irreproducibility associated with the background correction. It also provides an estimate of the limits, in terms of precision and accuracy, which can be achieved on the GEOTOP IsoProbe™. Thus, in order to obtain an external reproducibility and an internal precision of 1‰ to 2‰ on each measured ratio, the signal/dark noise ratio must be equal to or greater than 500 for each ion beam. For the minor isotope ($^{234}U$), this requires monitoring a signal intensity of at least 5 mV. Under such conditions, baseline variations occurring during data collection will not affect signals measured within the desired level of precision. However, large fluctuations we observed within a day made it necessary to monitor the MS background during each analysis.

### 3.2.2. Absolute OPZ values

The $OPZ_{abs}$ values give direct indications about the U content in the blank solution, U-memory effects in the inlet system and potential isobaric contributions. The 2% $HNO_3$ blank solution is prepared with ultrapure reagents and is identical to the blank solution used to dilute samples and standards. Theoretically, this should make it possible to thoroughly correct for any U contamination present and to avoid any change in the acid molarity that could remove additional U from the inlet system (Thirlwall, 2002). During our U isotopic measurements, constant contamination associated with the 2% $HNO_3$ remained undetectable on $^{235}U$ and thus, a fortiori, on $^{234}U$.

Concerning sample cross-contamination, a longer washout time (up to 20 min) is sometimes required between two successive analyses in order to make $OPZ_{abs}$ values negligible in comparison with signal intensities (i.e. signal/$OPZ_{abs}$ $\gg$500). Memory effects do not appear to be directly related to the most recent sample intensity. In practice, for uranium isotopic determinations, data acquisition is initiated when measured OPZs do not differ from MS background values for masses 233, 234 and 236 within the range of dark noise irreproducibility (i.e. $-20\ \mu V < OPZ_{abs} < 20\ \mu V$, where $OPZ_{abs} = OPZ - MSB$). With respect to $^{235}U$ measurement, the analysis criterion is that the $OPZ_{abs}$ value on H3 remains $<50$ μV. However, while memory effects are well constrained using the suggested cleaning procedure for routine $^{234}U/^{238}U$ isotopic measurements, they remain a serious problem for standards such as U-500 or NBL-117, as well as for tests and spike analyses that require monitoring $^{238}U$ ion beams. In fact, such standard or spike solutions have $^{238}U/^{235}U$ ratios (e.g. $^{238}U/^{235}U \approx 1$, for NBL-117 and U-500) that are very different from natural uranium ($^{238}U/^{235}U = 137.88$). During such analyses, any variations in the uranium baseline from the OPZ measurement will cause significant inaccuracies in the final results.

No isobaric interferences were observed on the monitored masses of uranium. If there were any, they remained within the dark noise range. However, we identified a substantial constant interference on mass 237, with an $OPZ_{abs}$ significantly higher than the MS background ($OPZ_{abs}$(mass 237) ≈ 60 to 100 μV). This suggests a mono-isobaric interference, which might be associated with the presence of Au (gold coating of the hexapole ion guide, cf. Rehkämper and Mezger, 2000) and Ar in the inlet system.

## 4. The tailing contribution

### 4.1. The half-mass zero estimation of the baseline

Correction for tail from adjacent peaks onto a given mass is commonly done by subtracting values interpolated from signals measured at half-mass positions ( ± 0.5 amu) from the peak to be corrected (Chen et al., 1986; Edwards et al., 1987). This approach has the advantage of an online correction of the tailing contribution, but also has two major drawbacks. First, each peak is corrected for its own tailing. Second, because the tail profile has a negative curvature, linear interpolation between half-mass backgrounds overestimates the actual tail contribution under the peak. This problem was first reported by Chen et al. (1986) and Bard et al. (1990) for U–Th analyses. Bard et al. (1990) have shown that the linear tailing correction is no longer appropriate for U–Th TIMS analyses when abundance sensitivity increases due to vacuum deterioration. They proposed a parabolic interpolation to correct for the total tail contribution under the $^{234}$U and $^{235}$U peaks. Nevertheless, they acknowledged that this parabolic fit was not able to correct properly for tailing biases under the $^{236}$U peak. Shen et al. (2002) also used the log-mean of the signals measured at half-masses to subtract tail contribution from $^{233}$U, $^{234}$U and $^{235}$U intensity beams. However, they showed that this calculation was no longer appropriate for mass 236 because of the significant contribution of the $^{235}$U peak, superimposed on the major $^{238}$U tailing, over the mass interval 235.5–236.5. They therefore established an empirical formula, which was a function of the signal measured at mass 236.5, to estimate the total tail contribution at mass 236.

When applied to our IsoProbe™ MC-ICP-MS data, the linear and exponential interpolation result in a systematic offset, which is illustrated by $\delta^{234}$U values of − 26 ‰ and − 15 ‰, respectively, for the Harwell uraninite standard (see Fig. 1 and Section 6.1 for more details) instead of the expected value for secular equilibrium, $\delta^{234}$U = 0 ‰ (Ludwig et al., 1992; Cheng et al., 2000). This large offset is due to the poor abundance sensitivity ( ~ 25 ppm) of the GEOTOP IsoProbe MC-ICP-MS. Below, we will show that with this instrument, even exponential corrections (i.e. the log-mean of the signals measured at half-mass positions) overestimate the real tail contribution.

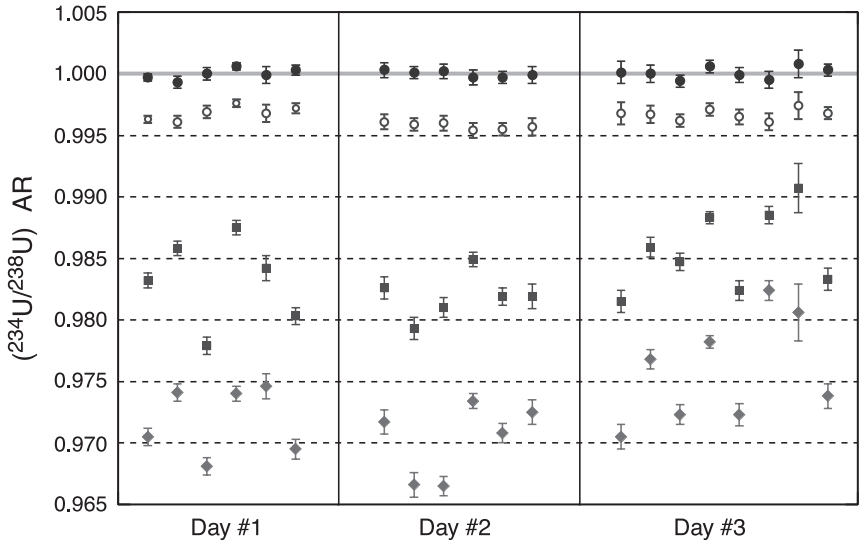


Fig. 1. Repeated analyses of the ($^{234}$U/$^{238}$U) activity ratio of the HU-1 uraninite conducted on the Micromass IsoProbe™ MC-ICP-MS instrument over a 3-day analytical run. Results obtained using a tail correction based either on linear (filled diamonds) or exponential (filled squares) interpolation of half-mass zeroes are compared with results obtained using the tail correction method we developed (circles). The latter approach is based on the actual, precise quantification of tail contributions underneath each peak due to adjacent ion beams, as assessed by tail shape measurements on mono-isotopic ion beams. Blank circles refer to the correction which is done when the measured tail shape only is used; filled circles refer to results obtained by this same model using the tail shape corrected according to the $\theta$ coefficient (see full explications in the text).

### 4.2. The tail correction method

The method that we finally retained for tail correction is based on the actual, precise quantification of tail contributions underneath each peak due to adjacent ion beams. Thirlwall (2001, 2002) used the same method for optimizing tail corrections on MC-ICP-MS instruments with poor abundance sensitivity, such as the IsoProbe™. He showed, for example, that for high-precision Pb isotope measurements, his method corrects for discrepancies of up to ~ 700 ppm relative to the standard half-mass zero correction for the $^{208}Pb/^{206}Pb$ ratio on the NIST SRM-982 reference standard (Thirlwall, 2001).

Our approach requires precise determination of the tail profile on both sides of a mono-isotopic peak in an array of several atomic mass units (amu). This is accomplished by measuring mono-isotopic solutions within the mass range of the element of interest (see Section 4.3). The total tail under a given peak then becomes the sum of contributions from all adjacent peaks. This can be mathematically formalized by:

$$I^{m}_{\text{Tailcor}} = I^{m}_{\text{Measured}} - \sum_{\substack{i=-5 \\ i\neq 0}}^{+3} Z_i \times I^{m-i}_{\text{Tailcor}} \qquad \text{(S)}$$

where $I^{m}_{\text{Tailcor}}$ is the tail-corrected beam intensity on mass $m$, $I^{m}_{\text{Measured}}$ is the measured beam intensity, and $Z_i$ is the proportional tail, expressed in ppm, at $i$ amu away from a mono-isotopic peak. This expression is similar to that proposed by Thirlwall (2001), but it dispels one ambiguity. From a theoretical point of view, one must consider the tail-corrected beam intensity in the right part of the expression (S). In the equation proposed by Thirlwall (2001), it is unclear whether the tail-corrected intensities or the measured ones are considered. However, for uranium analysis, the artefact induced by using the measured intensities is small: 0.2 ‰ for the $^{234}U/^{238}U$ ratio and 0.5 ‰ for the concentration.

Since we do not monitor the $^{238}U$ ion beam, its intensity is calculated using $^{235}U$ intensity, corrected for mass discrimination according to:

$$I^{238}_{\text{Estimate}} = 137.88 \times I^{235}_{\text{Tailcor}}(1 + \Delta_m \varepsilon)^{-1}.$$

where $\varepsilon$ is the linear discrimination bias (see Section 5) calculated by using the $^{236}U/^{233}U$ double-spike ratio and $\Delta_m$ is the mass difference between $^{238}U$ and $^{235}U$.

Thus, for the determination of the $^{234}U/^{238}U$ ratios, this approach leads to a linear system of four equations for four unknowns ($I^{233}_{\text{Tailcor}}$, $I^{234}_{\text{Tailcor}}$, $I^{235}_{\text{Tailcor}}$, $I^{236}_{\text{Tailcor}}$), which is solved offline by inverting the associated matrix in the Excel spreadsheet. This calculation is done cycle by cycle.

### 4.3. Determination of the tail profile

The tail profile was determined using separate isotope solutions. $^{233}U$ solutions were used for the range from −5 to −1 amu. Both $^{238}U$ and $^{232}Th$ solutions were analyzed for the range from +1 to +3 amu. Before dilution and analysis, the parent solutions of $^{233}U$ and $^{232}Th$ were purified by means of anion exchange resin to avoid any presence of uranium in $^{232}Th$ solutions and of thorium in $^{233}U$ solutions.

We took great care in precise quantification of the tail profile over the range from −5 to −1 amu because this is the tail contribution of the major $^{238}U$ ion beam that mainly controls the accuracy of uranium isotopic analysis. Four $^{233}U$ mono-isotopic solutions were prepared in order to yield $^{233}U$ ion beam intensity over the range from 25 to 140 V. That way, the experiments were carried out in the same intensity conditions as for uranium analyses. The alignment of the Faraday cups, optimized for uranium isotope analysis (H1: mass 233 to H5: mass 237; see Table 1), was conserved. The ion beams monitored at masses 228 (H1) to 232 (H5) were measured with an intensity of at least 0.05 mV. Since the $^{233}U$ intensity beam was not monitored for these solutions, the "abundance sensitivity", defined here as $Z_{-1}$, could not be determined online. However, we were able to determine the $(Z_{-i}/Z_{-1})$ ratios precisely.

Two dilute solutions of a shelf of thorium and two HU-1 uraninite solutions were prepared to yield ion beam intensities on the main peak ($^{238}U$ or $^{232}Th$) over the 4–8.5 V range. The major isotope was monitored on the H2 Faraday cup. This permitted online calculation of abundance sensitivity $Z_{-1}$, using the H1/H2 ratio, as well as the other $Z_{\geq +1}$ parameters.

Tests were performed on 2 days in July and November 2001. In July, three $^{233}U$ solutions yielding a $^{233}U$ beam intensity over the 25–100 V range and the two $^{232}Th$ solutions were analyzed. In November, we performed three analyses of a $^{233}U$ solution with a 140 V signal intensity together with the two $^{238}U$ solutions. Each analysis consisted of three blocks of

12-scan cycles with a 5-s integration time per cycle. Prior to each block, half-mass zeroes (+0.5 and −0.5 amu) were measured for 1 min. Using this protocol, we determined the tail contribution at half-masses (that is to say the $Z_{\pm i.5}$ values) with the same precision as at unit masses.

The results are presented in Tables 2a and 2b and illustrated in Fig. 2. For the $^{233}$U tests, we determined all the results ($Z_{-5.5}$ to $Z_{-0.5}$), fixing the abundance sensitivity ($Z_{-1}$) arbitrarily at 27 ppm. That way, the GEOTOP tail profile could be directly compared with the one determined by Thirlwall in 2001, who measured a mean abundance sensitivity of 27 ppm on the Royal Holloway IsoProbe™ (Thirlwall, 2001). Since then, following repairs to two major leaks in the analyzer, the abundance sensitivity of the Royal Holloway Isoprobe™ has been improved to 8 ppm (Thirlwall, 2002).

For the $^{238}$U and $^{232}$Th tests, the data were also normalized to the reference value of 27 ppm. In correcting for tail effect on standard and sample data, we used the average results obtained in July and November, except for $Z_{+2}$ and $Z_{+3}$, for which the half-mass log-mean estimation appears to be better. In fact, for these two parameters, we observed interferences and/or contamination during measurements at unit mass. For the $^{232}$Th tests, this can be easily attributed to the presence of $^{235}$U traces on H5. For the $^{238}$U tests, however, interferences observed on masses 240 and 241 are not explained.

In Tables 2a and 2b, we calculate (1) the theoretical tail correction, expressed in ppm, as generated by linear and exponential interpolations of half-mass zeroes for a mono-isotopic peak, and (2) the differences ($\Delta$) between these corrections and the actual tail contribution. Our results confirm the previous work done by Thirlwall (2001), in that the total contribution for a given peak is significantly lower than the average of half-mass zeroes. However, the tail shape as a whole is not identical to Thirlwall's, especially at −5 and −4 amu. This may be due to the specific methods in which Thirlwall and we determined our profiles.

Table 2a
Tail profile for a mono isotopic uranium peak in the range of −5.5 to −0.5 amu from the central peak, as estimated in this study on the GEOTOP IsoProbe™ instrument

| Test/analysis period | Intensity (V) | Tail contribution (ppm) from central peak | | | | | | | | | | |
|---|---|---|---|---|---|---|---|---|---|---|---|---|
| | | $Z_{-5.5}$ | $Z_{-5}$ | $Z_{-4.5}$ | $Z_{-4}$ | $Z_{-3.5}$ | $Z_{-3}$ | $Z_{-2.5}$ | $Z_{-2}$ | $Z_{-1.5}$ | $Z_{-1}$ | $Z_{-0.5}$ |
| *Royal Holloway IsoProbe* (Thirlwall, 2001) | | | | | | | | | | | | |
| $^{238}$U solution | ~ 8 | – | – | 1.2 | 2.3 | 3.5 | 4.7 | 6.8 | 8.5 | 13.5 | 27 | 370 |
| ± 2S.E. | | | | 0.3 | 0.7 | 1.0 | 0.7 | 0.9 | 0.6 | 0.6 | 1.4 | 35.8 |
| *GEOTOP IsoProbe (this study)* | | | | | | | | | | | | |
| Test $^{233}$U July 2001 | | | | | | | | | | | | |
| Solution 1 | ~ 25 | 1.70 | 1.77 | 1.65 | 2.41 | 2.36 | 4.07 | 4.65 | 8.41 | 11.20 | 27 | 173 |
| Solution 2 | ~ 85 | 1.27 | 1.48 | 1.98 | 2.52 | 3.06 | 4.13 | 5.84 | 8.46 | 13.41 | 27 | 226 |
| Solution 3 | ~ 100 | 1.27 | 1.59 | 1.89 | 2.41 | 3.02 | 4.35 | 5.67 | 8.70 | 13.07 | 27 | 211 |
| Mean July | | 1.27 | 1.53 | 1.93 | 2.47 | 3.04 | 4.24 | 5.75 | 8.58 | 13.24 | 27 | 218 |
| Test $^{233}$U November 2001 | | | | | | | | | | | | |
| Solution 4 Run #1 | ~ 140 | 1.39 | 1.69 | 1.98 | 2.46 | 3.01 | 4.34 | 5.24 | 8.51 | 12.86 | 27 | 326 |
| Solution 4 Run #2 | ~ 140 | 1.39 | 1.71 | 1.95 | 2.49 | 3.08 | 4.14 | 5.47 | 8.40 | 13.18 | 27 | 287 |
| Solution 4 Run #3 | ~ 140 | 1.48 | 1.73 | 2.04 | 2.57 | 3.17 | 4.15 | 5.54 | 8.37 | 13.35 | 27 | 271 |
| Mean November | | 1.42 | 1.71 | 1.99 | 2.50 | 3.09 | 4.21 | 5.41 | 8.43 | 13.13 | 27 | 295 |
| Mean study | | 1.36 | 1.64 | 1.97 | 2.49 | 3.07 | 4.22 | 5.55 | 8.49 | 13.17 | 27 | 264 |
| ± 2$\sigma$ | | 0.09 | 0.11 | 0.06 | 0.06 | 0.06 | 0.11 | 0.22 | 0.13 | 0.22 | | 47 |
| Half-mass zero mean | | | 1.66 | | 2.52 | | 4.31 | | 9.36 | | 139 | |
| $\Delta_{mean}$ | | | 0.02 | | 0.03 | | 0.09 | | 0.88 | | 112 | |
| Half-mass zero log-mean | | | 1.64 | | 2.46 | | 4.13 | | 8.55 | | 59 | |
| $\Delta_{log\text{-}mean}$ | | | 0.00 | | −0.03 | | −0.09 | | 0.06 | | 32 | |

The tail profile as determined by Thirlwall (2001) on the Royal Holloway IsoProbe™ for $^{238}$U, is also given.
The theoretical tail correction (in ppm) for a mono-isotopic peak (estimated by the linear or the exponential interpolation of half-mass zeroes), and the differences ($\Delta$) between these corrections and the effective tail contribution, are calculated.

Table 2b
Tail profile for a mono isotopic uranium peak in the range of +0.5 to +3.5 amu from the central peak, as estimated in this study on the GEOTOP IsoProbe™ instrument

| Test/analysis period | Intensity (V) | Tail contribution (ppm) from central peak | | | | | | | | |
|---|---|---|---|---|---|---|---|---|---|---|
| | | $Z_{-1}$ | $Z_{-0.5}$ | $Z_{+0.5}$ | $Z_{+1}$ | $Z_{+1.5}$ | $Z_{+2}$ | $Z_{+2.5}$ | $Z_{+3}$ | $Z_{+3.5}$ |
| *Royal Holloway IsoProbe* (Thirlwall, 2001) | | | | | | | | | | |
| $^{238}$U solution | ~ 8 | 27 | | 30.2 | 12.6 | 6.6 | 3.8 | 2.5 | 1.3 | 0.3 |
| ± 2S.E. | | 1.4 | | 3.5 | 0.8 | 1.0 | 0.4 | 0.6 | 0.5 | 0.5 |
| *GEOTOP IsoProbe (this study)* | | | | | | | | | | |
| Test $^{232}$Th July 2001 | | | | | | | | | | |
| Solution 1 | ~ 4.1 | 27 | 261 | 35.2 | 16.9 | 8.0 | 5.3 | 3.1 | 3.2 | 0.9 |
| Solution 2 | ~ 6.7 | 27 | 248 | 33.9 | 15.0 | 7.8 | 5.2 | 2.6 | 3.7 | 0.6 |
| Mean July | | 27 | 255 | 34.6 | 15.9 | 7.9 | 5.2 | 2.9 | 3.4 | 0.7 |
| Test $^{238}$U November 2001 | | | | | | | | | | |
| Solution 1 | ~ 7.4 | 27 | 260 | 32.4 | 14.2 | 6.0 | 6.6 | 2.7 | 4.5 | 2.1 |
| Solution 2 | ~ 8.4 | 27 | 294 | 35.6 | 16.4 | 7.6 | 7.1 | 3.3 | 5.3 | 2.0 |
| Mean November | | 27 | 277 | 34.0 | 15.3 | 6.8 | 6.9 | 3.0 | 4.9 | 2.1 |
| Mean study | | 27 | 266 | 34.3 | 15.6 | 7.3 | 6.0 | 2.9 | 4.2 | 1.4 |
| ± 2$\sigma$ | | | | 1.4 | 1.3 | 0.9 | 1.0 | 0.3 | 0.9 | 0.8 |
| Final values for this study | | 27 | | 34.3 | 15.6 | 7.3 | *4.6* | 2.9 | *2.0* | 1.4 |

The tail profile, as determined by Thirlwall (2001) on the Royal Holloway IsoProbe™ for $^{238}$U, is also given.
Values in italic correspond to log-mean estimations. The measured $Z_i$ values for these masses are certainly affected by interferences or contamination.

For exponential tail correction, the difference between the log-mean calculations and the effective contributions is negligible, at −5, −4, −3 and +3 amu. However, this exponential interpolation significantly overestimates the real tail contribution near the peak between −2 and +2 amu (see Tables 2a and 2b). Thus, for uranium isotopic analysis, the exponential estimation cannot optimize the tail correction

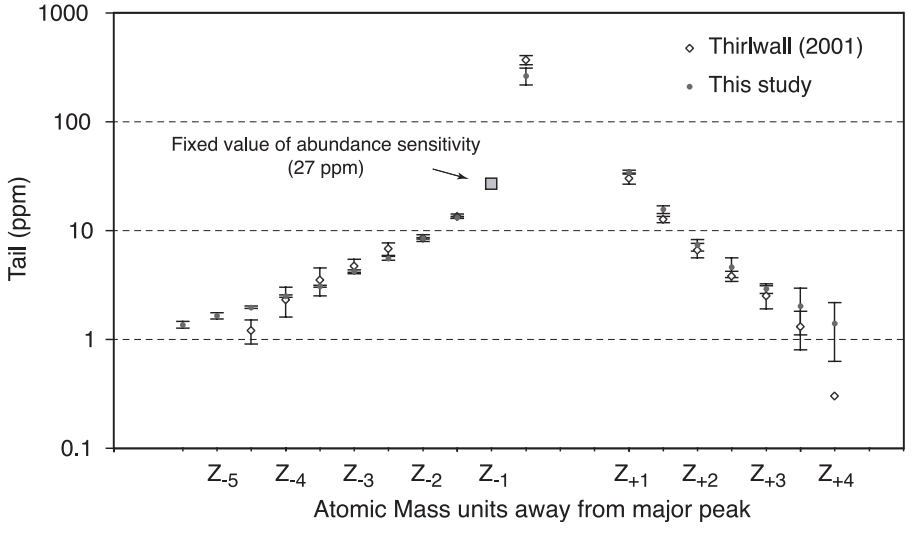


Fig. 2. Tail shape between −5.5 and +3 amu, as determined for uranium on the GEOTOP IsoProbe™ instrument (filled circles; data from Tables 2a and 2b). Also reported are the results obtained by Thirlwall (2001) on the Royal Holloway IsoProbe™ instrument (open diamonds). For comparison purposes, the tail profile observed on the GEOTOP instrument was normalized to the average abundance sensitivity value observed on the Royal Holloway IsoProbe™ (27 ppm).

around the major $^{235}U$ peak. In this mass range, the juxtaposed $^{235}U$ and $^{238}U$ tails do not display an exponential shape. This implies that, for our IsoProbe™ instrument, exponential tail correction onto the $^{236}U$ beam and onto the $^{234}U$ beam is inappropriate (see Tables 2a and 2b and Fig. 2).

### 4.4. Time fluctuation of the abundance sensitivity

During a U isotope analysis, abundance sensitivity can be estimated online by means of intensity monitoring on mass 237 (H5). In fact, considering the dynamic of such an analysis, the tail contribution of the minor peaks integrated onto mass 237 is negligible compared with that of the $^{238}U$ peak. Since the intensity measured on H5 is essentially associated with the tail contribution of the $^{238}U$ peak, the proportion of the $^{235}U$ peak contribution is only of the order of 0.1%, for example (see Table 2b). Therefore, $I_{237}$ provides an online approximation of the abundance sensitivity, via:

$$Z_{-1} = I^{237}/I^{238}_{\text{Estimate}}$$

where $I^{238}_{\text{Estimate}}$ is determined in the same way as in Section 4.2., by means of an average linear discrimination bias, $\varepsilon$.

While estimating abundance sensitivity in this way, we observed variations from 23 to 32 ppm (mean ~ 25 ppm) in the course of this study. These variations might be due to the irreproducibility of the cup alignment or pressure fluctuation within the analyzer from one day to the next. However, we also observed significant variations in abundance sensitivity in the course of a single day (usually a decrease of a few ppm). This phenomenon cannot be caused by the irreproducibility of the Faraday cup alignment. Fluctuations in the vacuum within the analyzer in the course of the day could account for it. Nevertheless, we are not able to clearly explain such variations at this time.

These abundance sensitivity variations were taken into account for the tail correction. In each analysis, we used the $Z_{-1}$ value determined online, and the $Z_i$ parameters were normalized to this value (see Section 4.3). This way, the daily reproducibility obtained on the HU-1 standard is significantly improved (see Section 6.1) in comparison with the consideration of a daily mean value for the abundance sensitivity. This demonstrates that (i) the interference measured on mass 237 during the OPZ monitoring is constant at the time scale of an analysis (see Section 3.2) and (ii) that its measurement is sufficiently accurate to properly determine the abundance sensitivity and its fluctuations.

### 4.5. Linearity of the system

An inherent condition for using the tail profile correction method described above is that the system must behave linearly. This means that:

(i) Tail shape is independent of the peak considered. First, we could consider this assumption to be true at a first order over the mass range of the element analyzed (here, 233 to 238). It must be observed that this is not the case over a broader mass spectrum (see for example, the tail shape difference for $^{238}U$ and $^{209}Bi$, as shown by Thirlwall, 2001).
(ii) The tail shape remains independent of the peak height over the range of beam intensities monitored during analysis: a few mV for $^{234}U$ to 200 V for $^{238}U$. It is clear that for uranium isotopic analysis this assumption has to be essentially verified over the entire range of beam intensities of the two largest peaks ($^{238}U$ and $^{235}U$) monitored during an analysis, since the tail contributions of the minor peaks ($^{233}U$, $^{234}U$ and $^{236}U$) are negligible.

The $^{233}U$ tests carried out to determine the tail shape provide the first clue that the second assumption is true, since the results we obtained over a wide range of $^{233}U$ signals are reproducible (Tables 2a and 2b).

To obtain further confirmation of this assumption, we analyzed, over a 1-day period, seven unspiked HU-1 solutions over a wide range of intensities. By monitoring the total tail contribution at each half-mass and at U-free unit mass, we were able to test the constancy of tail shape over the mass spectrum of uranium over a period of time (1 day) at different intensities. The results, which are illustrated in Fig. 3, are expressed in the form of ($I_{233}/I_{237}$), ($I_{233.5}/I_{237}$), ($I_{234.5}/I_{237}$), ($I_{235.5}/I_{237}$), ($I_{236}/I_{237}$) ratios as a function of the $I_{238}$ intensity, as estimated according to $I_{235}$ intensity. These values represent the total tail contribution of $^{238}U$, $^{235}U$ and $^{234}U$ peaks at mass ($237 - i$), normalized to the tail contribution monitored at mass 237. This normaliza-

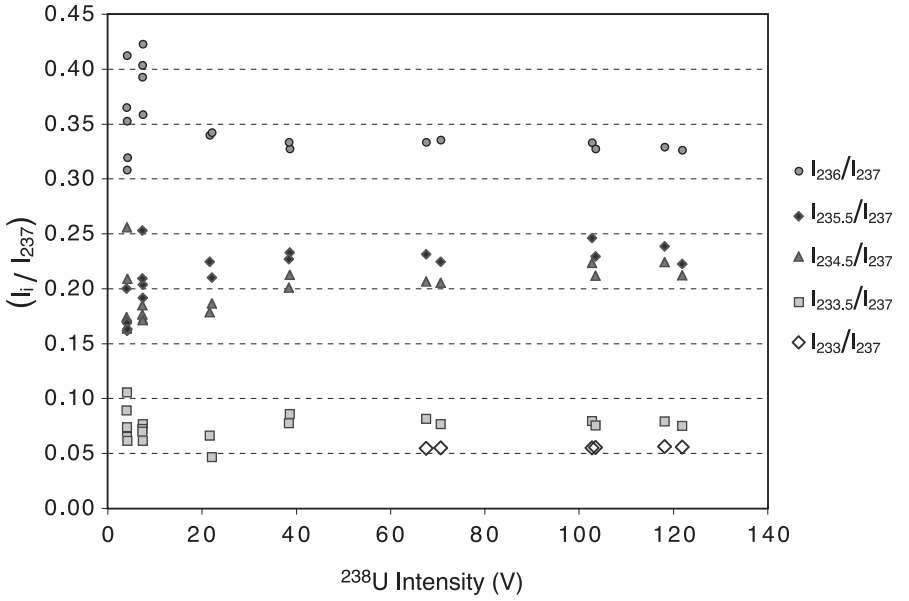


Fig. 3. Linearity of the tailing effect. Total tail contributions at half-mass and at U-free unit mass were monitored during successive analyses of seven unspiked HU-1 solutions covering a wide range of intensities. Results are expressed in the form of ($I_{233}/I_{237}$), ($I_{233.5}/I_{237}$), ($I_{234.5}/I_{237}$), ($I_{235.5}/I_{237}$), ($I_{236}/I_{237}$) ratios as a function of $I_{238}$ intensity. The good reproducibility that can be observed for each ratio demonstrates the constancy of the tail shape, in the course of a day, over (1) the mass spectrum of uranium; and (2) different intensity scales.

tion makes it possible to take into account variations in abundance sensitivity observed in the course of the day (see above). The ($I_{237\ -i}/I_{237}$) ratios remained constant (see Fig. 3); the greater irreproducibility is observed in analyses carried out at low $^{238}$U intensities and is due to the very low intensities monitored at half-masses and at U-free unit masses for these analyses.

These experiments confirm that the integrated tail contribution of $^{238}$U, $^{235}$U and $^{234}$U peaks onto a given mass is constant over a wide range of intensities in the course of a single day. Therefore, if one assumes that tail shape is independent of the peak considered, these tests demonstrate that tail shape, characterized by the ($Z_{-i}/Z_{-1}$) ratios, is independent of peak height.

## 5. Correction for mass discrimination

### 5.1. Spike calibration

The $^{236}$U–$^{233}$U double spike used to monitor and correct for mass discrimination was prepared from pure $^{236}$U and $^{233}$U solutions. To calibrate it, we developed a method similar to that proposed for Pb double/triple-spike calibration against the NIST SRM-982 reference standard (Hamelin et al., 1985; Galer, 1999). The spike composition is calibrated in reference to natural uranium with the accepted nominal value of 137.88 for the $^{238}$U/$^{235}$U ratio (see Cowan and Adler, 1976; Cheng et al., 2000). In practice, we used a solution of the natural uraninite HU-1 in much the same way as NIST SRM-982 is used for Pb double/triple-spike calibration. The true isotopic composition of the spike is determined by considering the mathematical system built by: (i) analysis of the spike alone, and (ii) analysis of a mixed solution of spike and natural uranium (HU-1) (see Hofmann, 1971).

To our knowledge, this approach is new for the U–Th community. In the past, $^{236}$U–$^{233}$U double spikes have been calibrated by using a certified reference material, the CRM U-500 (Chen and Wasserburg, 1981; Chen et al., 1986; Edwards et al., 1987; Cheng et al., 2000). In this case, the isotopic composition of the spike is determined by analyzing a mixed solution of the spike and this standard. This provides the absolute $^{236}$U/$^{233}$U ratio of the spike, normalized for mass discrimination to the reference $^{238}$U/$^{235}$U value of U-500 (Cheng et al., 2000). The abundance of trace

isotopes in the spike ($^{234}U$, $^{235}U$, $^{238}U$) is then determined by another analysis (Cheng et al., 2000).

The double-spike calibration method we propose here has certain advantages. First, the precise determination of the $^{236}U/^{233}U$ ratio is done relative to a natural uranium solution (HU-1), which avoids having to take into account the trace impurities contained in standard reference materials such as U-500 (essentially $^{236}U$ for this standard) and their associated errors. Second, this spike calibration protocol takes into account only the widely accepted and used reference value of natural uranium ($^{238}U/^{235}U = 137.88$). For instance, for mono spike techniques, correction for mass discrimination is performed by normalizing the measured $^{238}U/^{235}U$ ratio against the nominal value of 137.88 (e.g. Bard et al., 1990; Luo et al., 1997; Delanghe et al., 2002; Robinson et al., 2002). For double-spike techniques, the $^{234}U/^{238}U$ ratio is calculated by dividing the calculated $^{234}U/^{235}U$ ratio by the natural $^{238}U/^{235}U$ value of 137.88 when the $^{238}U$ is not monitored (e.g. Chen et al., 1986; Ludwig et al., 1992; Cheng et al., 2000; Shen et al., 2002 or this study). Since this is the only reference value we take into account throughout our protocol (including spike calibration and analysis procedures), we avoid accumulating systematic errors associated with both the $^{238}U/^{235}U$ of the U-500 standard and the nominal value of natural uranium in determining the total error propagation in a $^{234}U/^{238}U$ analysis. Moreover, we can disregard the error associated with the nominal value of natural uranium as is often done, in practice, with $^{234}U/^{238}U$ isotopic analysis on geological samples.

### 5.2. Mass discrimination correction models

Unlike in TIMS, the mass discrimination effect in a plasma source can be considered independent of time during the analysis and is characterized by the preferential transport of heavier isotopes of a given element into the mass analyzer. Various mass fractionation laws, namely linear, power and exponential laws, are commonly used to correct for this mass bias. It should be observed that, for the "exponential" law, different mathematical forms are described in the literature. Taylor et al. (1995) have evaluated these three mass discrimination correction models and have shown that, for their Plasma-54 MC-ICP-MS, the power and exponential functions result in the best correction for uranium analysis.

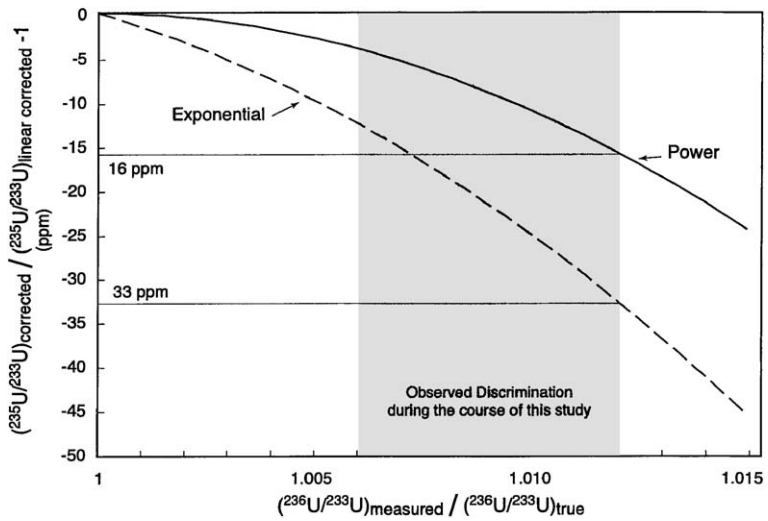


Fig. 4. Simulation of the difference between the "exponential" or the "power" law mass discrimination corrections and the linear law correction for the $^{235}U/^{233}U$ ratio as a function of the measured spike reference ratio ($^{236}U/^{233}U$). The mass discrimination, expressed by the ratio $(^{236}U/^{233}U)_{measured}/(^{236}U/^{233}U)_{true}$, varied from 1.006 to 1.012 in the course of this study. Within this range of variation, the error induced on corrected $^{235}U/^{233}U$ ratios does not exceed 33 ppm, irrespective of the mass discrimination law used. This error is insignificant relative to the total error of a $^{234}U/^{238}U$ analysis ( ~ 1‰).

In our opinion, the linear law corrects with sufficient accuracy at the level of precision we need for our experiments. In fact, in the course of this study, the GEOTOP IsoProbe™ displayed a bias factor of 0.2–0.4% per amu in the mass range of U isotopes. Since this bias is low, unlike the bias observed on the Plasma 54 ( ~ 1%) by Taylor et al. (1995) (see also Luo et al., 1997), the difference between the linear mass bias correction and the power or exponential corrections is negligible in comparison to the total analytical precision. This is illustrated in Fig. 4, which shows the simulated difference between the exponential and power corrections of the $^{235}U/^{233}U$ ratio relative to the linear correction as a function of the measured reference ratio ($^{236}U/^{233}U$), varying over the mass bias range observed in the course of this study. This difference does not exceed 33 ppm for the $^{235}U/^{233}U$ ratio (Fig. 4) and is of the same order for the $^{234}U/^{233}U$ ratio (not shown).

There are two main advantages in using the linear law. The error-correlation calculations and error propagations in mass discrimination correction are made easier. In the same way, resolution of the double-spike system (Hofmann, 1971; Hamelin et al., 1985; Galer, 1999), as described above for uranium, becomes simpler with the linear mass discrimination model than with any other one.

## 6. Precision and accuracy

### 6.1. HU-1 uraninite

The HU-1 uraninite is commonly assumed and used as a secular equilibrium standard (Ludwig et al., 1992). This was recently proved by Cheng et al. (2000) for the $^{238}U–^{234}U$ series. In fact, these authors have shown that this uraninite solution exhibits a $^{234}U/^{238}U$ atomic ratio that is highly consistent with geological materials that were likely to have behaved as closed systems and to have reached the secular equilibrium state. These results enabled Cheng et al. (2000) to precisely re-determine the half-life of $^{234}U$. For the remainder of the text, all the results are presented in the form of activity ratios using the $^{234}U$ half-life value calculated by these authors ($T_{1/2}$ = 245,250 ± 490 years). However, the error associated with this value is not propagated.

The HU-1 uraninite was analyzed according to the method described in Section 3.1. Fig. 1 compares the results of 20 analyses measured over a 3-day period with the results obtained for the same analysis using linear and exponential tail correction (see Section 4.1). Several conclusions can be drawn from this figure.

First, besides having greater analytical precision, our ''tail form correction'' model dramatically improves external reproducibility over the other two tail correction models ( ~ 1%, 2$\sigma$). This significant irreproducibility is due to imprecise measurement of the signal monitored at half-masses. In fact, since the half-mass correction of tail represents up to ~ 4% of the signal measured at mass 234 (for a sample at secular equilibrium), a precise estimate of the baseline is required. This entails a sufficient integration time for these signals. For the analyses presented in Fig. 1, the time acquisition of a half-mass signal consists of 12 scan cycles with a 5-s integration time per cycle. This 1-min integration time is certainly insufficient to measure this signal accurately. Moreover, because the half-mass sequence is monitored before the main analytical sequence, the signal measured at half-mass position is not necessarily representative of the true signal monitored during the main sequence. More particularly, it does not take into account any signal fluctuations that can occur during the analysis. Since the tail correction model we propose obviates the need to measure the half-mass baselines, the external reproducibility obtained by this method is improved to around 0.1% (2$\sigma$) for each analysis day (see Fig. 1).

Second, although our procedure improves analytical precision significantly, it systematically induces an offset of ~ 0.3% (see Fig. 1). Although the reasons for this gap are not fully understood, this bias might result from the way we determine the tail shape (see Section 4.3). For this determination, we conserved the Faraday cup alignment, even though they were optimized for uranium isotope analysis (H1: mass 233 to H5: mass 237), and assumed that the tail shape produced by a $^{233}U$ beam (i.e. $Z_i$ parameters) was equivalent to the tail shape produced by the $^{238}U$ peak. This assumption may not be completely valid, and may result in a distortion in our tail estimates with respect to the actual tail shape of the $^{238}U$ peak. Since this model leads to a result lower than the expected value, the estimated tail

Table 3
Comparison between $^{234}U/^{238}U$ measurements for the NBL-112a standard (formerly NIST NBS-960) on the GEOTOP MicroMass IsoProbe™ MC-ICP-MS and TIMS or ICP-MS compiled values given by other laboratories

| Method | Analysis | $^{234}U/^{238}U$ Atomic ratio | $\delta^{234}U(‰)$[a] |
|---|---|---|---|
| *MC-ICP-MS* | | | |
| This study | | | |
| Day #1 | #1 | 0.00005287 ± 3 | − 36.7 ± 0.6 |
| Day #1 | #2 | 0.00005291 ± 3 | − 35.9 ± 0.6 |
| Day #1 | #3 | 0.00005288 ± 3 | − 36.5 ± 0.5 |
| Day #1 | #4 | 0.00005287 ± 2 | − 36.7 ± 0.4 |
| Day #1 | #5 | 0.00005284 ± 3 | − 37.3 ± 0.5 |
| Day #2 | #6 | 0.00005288 ± 3 | − 36.5 ± 0.5 |
| Day #2 | #7 | 0.00005291 ± 2 | − 35.9 ± 0.4 |
| Day #2 | #8 | 0.00005291 ± 2 | − 36.0 ± 0.4 |
| Day #2 | #9 | 0.00005286 ± 2 | − 37.0 ± 0.3 |
| Day #2 | #10 | 0.00005290 ± 2 | − 36.1 ± 0.3 |
| Day #2 | #11 | 0.00005289 ± 2 | − 36.4 ± 0.4 |
| Day #2 | #12 | 0.00005285 ± 3 | − 37.1 ± 0.5 |
| Day #2 | #13 | 0.00005289 ± 3 | − 36.3 ± 0.5 |
| Day #2 | #14 | 0.00005290 ± 2 | − 36.2 ± 0.3 |
| Day #2 | #15 | 0.00005290 ± 3 | − 36.2 ± 0.6 |
| Day #3 | #16 | 0.00005292 ± 2 | − 35.8 ± 0.5 |
| Day #3 | #17 | 0.00005289 ± 2 | − 36.5 ± 0.4 |
| Day #4 | #18 | 0.00005289 ± 2 | − 36.4 ± 0.4 |
| Day #4 | #19 | 0.00005289 ± 2 | − 36.4 ± 0.4 |
| | Mean ($\pm 2\sigma$, $n=19$) | 0.00005289 ± 4 | − 36.42 ± 0.80 $n=19$ |
| | $2\sigma$ (%) | 0.08% | |
| Luo et al. (1997) | (1) | 0.00005286 ± 6 | − 36.9 ± 1.1 $n=8$ |
| Shen et al. (2002) | (2) | 0.00005285 ± 7 | − 37.1 ± 1.2 $n=10$ |
| Robinson et al. (2002) | (3) | 0.00005287 ± 9 | − 36.7 ± 1.7 $n=8$ |
| *TIMS* | | | |
| Chen et al. (1986) I | (4) | 0.00005267 ± 11 | − 40.4 ± 2.0 $n=6$ |
| Chen et al. (1986) II | (5) | 0.00005266 ± 16 | − 40.6 ± 2.9 $n=4$ |
| Banner et al. (1990) | (6) | 0.00005277 ± 10 | − 38.6 ± 1.8 $n=4$ |
| Stein et al. (1991) | (7) | 0.00005267 ± 15 | − 40.4 ± 2.7 $n=9$ |
| Edwards et al. (1993) | (8) | 0.00005285 ± 7 | − 37.0 ± 1.2 $n=8$ |
| Gariépy et al. (1994) | (9) | 0.00005277 ± 13 | − 38.6 ± 2.4 $n=12$ |
| Stirling et al. (1995) | (10) | 0.00005288 ± 9 | − 36.6 ± 1.6 $n=6$ |
| Bard et al. (1996a,b) | (11) | 0.00005288 ± 19 | − 36.6 ± 3.5 $n=6$ |
| Luo et al. (1997) | (12) | 0.00005284 ± 16 | − 37.3 ± 2.9 $n=15$ |
| Israelson and Wohlfarth (1999) | (13) | 0.00005290 ± 31 | − 36.2 ± 5.6 $n=7$ |
| McCulloch and Esat (2000) | (14) | 0.00005277 | − 38.6 $n=5$ |
| Cheng et al. (2000) | (15) | 0.00005286 ± 10 | − 36.9 ± 1.7 $n=21$ |
| Delanghe et al. (2002) | (16) | 0.00005283 ± 10 | − 37.6 ± 1.9 $n=33$ |
| *NBS Certification* | | | |
| Delanghe et al. (2002) | | 0.00005290 ± 20 | − 36.2 ± 3.6 |

[a] $\delta^{234}U=[(^{234}U/^{238}U)-1]\times 1000$, where $(^{234}U/^{238}U)$ is the activity ratio. All the $\delta^{234}U$ values are calculated using the half-life values given by Cheng et al. (2000).

shape and, more specifically, the most sensitive parameter $Z_{-4}$ are overestimated. Moreover, small variations in the daily mean of HU-1 analyses are observed from day to day (from 0.996 to 0.999). We think that this variation is caused by the irreproducibility of the Faraday cup alignment, especially the H5 cup that monitors mass 237.

To deal with these two problems, we applied a correction coefficient, $\theta$, to the $Z_{-4}$ parameter for each day of analysis. This coefficient, calculated from more than 10 days of analyses, spread over a 6-month period, varies from 0.91 to 0.98, which represents a decrease of 2% to 9% below the expected value of $Z_{-4}$. This pragmatic approach translates the results so that the daily mean of HU-1 analyses is set to 1 (see Fig. 1).

In practice, we analyzed at least six spiked HU-1 samples per day. This enabled us to determine the $\theta$ correction coefficient, which was then applied to the other analyses carried out during the day. This implies that, in much the same way as Robinson et al. (2002) and Shen et al. (2002), the analyses are done with reference to the accepted value of a standard material (here HU-1).

### 6.2. NBL-112a standard

The New Brunswick Laboratory Certified Reference Material 112a (NBL-112a standard, also called

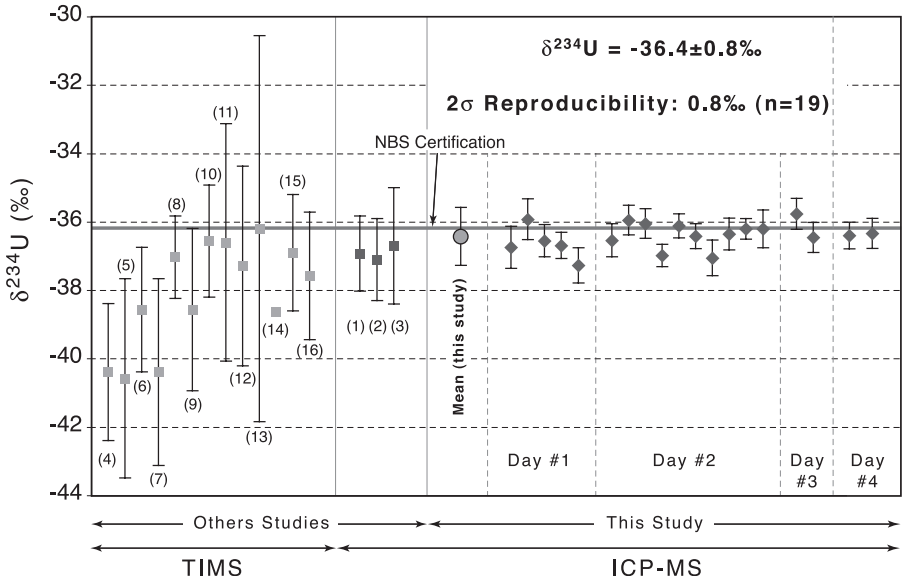


Fig. 5. Assessment of the $^{234}U/^{238}U$ external reproducibility (expressed as $\delta^{234}U$ values) with the NBL-112a standard solution (formerly NIST NBS-960). For comparison purposes, previously published results (squares) are also reported. Numbers in brackets refer to the reference column in Table 3. All $\delta^{234}U$ values were re-calculated using half-life values from Cheng et al. (2000). Mean $\delta^{234}U$ value (present study): $-36.42 \pm 0.80$ ‰ ($2\sigma$, $n=19$). All error bars refer to $2\sigma$ analytical precision. Within-run $2\sigma$ analytical precision typically ranges from 0.3 ‰ to 0.6 ‰.

CRM-145—formerly NBS SRM-960) was analyzed to assess the validity of our approach. Corrected $^{234}U/^{238}U$ isotope ratios are listed in Table 3 and shown in Fig. 5. Between 200 and 800 ng of uranium were consumed per analysis. Analyses were performed on 4 different days, with at least 1-week intervals between each day of analysis. The results yield a mean $\delta^{234}U$ value of $-36.42 \pm 0.80$ ‰ ($2\sigma$, $n=19$). This is consistent with values previously reported by other laboratories and determined on MC-ICP-MS, as well as on TIMS (see compiled values in Table 3). Two major conclusions can be drawn from these results. First, the pragmatic approach that consists in applying a correction coefficient $\theta$ (estimated from HU-1 analyses) to the $Z_{-4}$ parameter for each day of analysis is validated. Second, these results confirm that the HU-1 and the NBL-112a admitted values are consistent within error, and therefore, that the HU-1 uraninite is indeed in secular equilibrium for the $^{238}U-^{234}U$ series.

The use of this second standard allows us to assess our external analytical reproducibility, which was 0.8 ‰ ($2\sigma$, $n=19$) when measured on 4 different days. This is consistent with the error anticipated according to Faraday cup irreproducibility.

### 6.3. Experiments with natural samples

In order to assess our total long-term reproducibility (chemical and analytical combined) on natural samples, replicated measurements of carbonate samples were performed during the study. Two types of carbonates were analyzed: one coral from the Rendez-Vous Hill, Barbados (5a isotope stage), and a sedimentary carbonate rock core sample taken from a borehole at a depth of 470 m in the Mesozoic sedimentary rocks of the eastern Paris basin. These two kinds of material were chosen because they are representative of two major applications of the U–Th systematics in the Earth sciences, which have a growing need for high precision and accuracy:

(1) Absolute dating of marine carbonates such as corals, used for paleo-sea level studies (Stirling et al., 2001; Gallup et al., 2002) and paleo-reconstitution of ($^{234}U/^{238}U$) seawater (Henderson, 2002), for instance.
(2) Studies of radionuclide migration in deep geological formations conducted to assess the safety of radioactive waste disposal in such environ-

ments (see, for example, Schwarcz et al., 1982; Smellie and Stuckless, 1985; Gascoyne and Schwarcz, 1986; Smellie et al., 1986; Gascoyne and Cramer, 1987; Ivanovich et al., 1992; Griffault et al., 1993).

The second application is primarily concerned with determining whether a geological system is at secular equilibrium or not. Most of the studies in this field were conducted by means of α-counting techniques. The results obtained by this analytical method generally do not have a precision better than 4–5% (2σ), based on counting statistics. Excluding highly altered and/or fractured zones, this is not accurate enough for host-rock studies, in which disequilibria should not be significant. The application of advanced analytical techniques, such as MC-ICP-MS, should open up new perspectives in this field.

Table 4
Replicate $\delta^{234}$U and [U] measurements of two in-house standards on the GEOTOP VG Sector TIMS and MicroMass IsoProbe™ MC-ICP-MS

| Method | Sub-sample | $^{238}$U (ppb) | $\delta^{234}$U (‰)[a] |
|---|---|---|---|
| *Rendez-Vous Hill Coral (Barbados)* | | | |
| TIMS | | | |
| GEOTOP | #1 | 3163.2 ± 15.3 | 116.2 ± 10.2 |
| | #2 | 3130.1 ± 18.6 | 111.1 ± 9.4 |
| | #3 | 3152.9 ± 15.6 | 109.7 ± 8.0 |
| | #4 | 3146.5 ± 18.2 | 116.7 ± 9.9 |
| | #5 | 3179.8 ± 17.3 | 115.3 ± 9.6 |
| | #6 | 3184.7 ± 13.0 | 114.3 ± 3.4 |
| | #7 | 3181.0 ± 14.0 | 120.6 ± 5.7 |
| | #8 | 3204.4 ± 14.7 | 109.9 ± 7.0 |
| | #9 | 3210.8 ± 16.4 | 111.8 ± 12.3 |
| | #10 | 3208.7 ± 8.4 | 109.5 ± 12.9 |
| | Mean (± 2σ, n = 10) | 3194.9 ± 29.1 | 113.5 ± 7.4 |
| | 2σ (%) | 0.91% | 0.67% |
| MC-ICP-MS | | | |
| GEOTOP | #1 | 3209.2 ± 2.9 | 116.8 ± 0.5 |
| | #2 | 3205.9 ± 2.4 | 118.5 ± 0.8 |
| | #3 | 3204.8 ± 2.4 | 118.3 ± 0.5 |
| | #4 | 3207.4 ± 2.4 | 117.6 ± 0.4 |
| | #5 | 3201.6 ± 2.4 | 117.1 ± 0.6 |
| | #6 | 3211.0 ± 3.3 | 118.0 ± 0.5 |
| | #7 | 3200.9 ± 4.6 | 117.9 ± 0.5 |
| | #8 | 3203.3 ± 2.4 | 118.6 ± 0.4 |
| | #9 | 3220.6 ± 3.1 | 119.1 ± 0.4 |
| | #10 | 3216.8 ± 4.9 | 117.1 ± 0.5 |
| | #11 | 3202.5 ± 2.4 | 118.2 ± 0.4 |
| | Mean (± 2σ, n = 11) | 3208.1 ± 12.9 | 117.9 ± 1.4 |
| | 2σ (%) | 0.40% | 0.13% |
| Oxford University (Henderson and Robinson, pers. com) | | | 116.9 ± 0.8 |
| *Carbonate Rock Sample (HTM-02924 A #1, ANDRA)* | | | |
| MC-ICP-MS | | | |
| | #1 | 526.7 ± 0.4 | 9.6 ± 0.8 |
| | #1 bis# | 527.0 ± 0.4 | 10.6 ± 1.0 |
| | #2 | 524.0 ± 0.5 | 10.3 ± 0.9 |
| | #2 bis | 524.3 ± 0.5 | 11.2 ± 0.7 |
| | #3 | 527.9 ± 0.4 | 9.5 ± 1.0 |
| | #3 bis | 528.2 ± 0.4 | 11.3 ± 0.4 |
| | #4 | 526.4 ± 0.4 | 11.5 ± 1.0 |
| | #5 | 528.4 ± 0.5 | 9.8 ± 1.3 |
| | #5 bis | 528.1 ± 0.5 | 11.1 ± 0.8 |
| | #6 | 528.4 ± 0.5 | 11.0 ± 1.1 |
| | #7 | 528.0 ± 0.5 | 9.9 ± 1.2 |
| | #7 bis | 527.6 ± 0.5 | 11.1 ± 1.3 |
| | #8 | 526.4 ± 0.5 | 10.6 ± 0.6 |
| | #9 | 527.7 ± 0.5 | 10.2 ± 0.7 |
| | Mean (± 2σ, n = 14) | 527.1 ± 2.9 | 10.5 ± 1.4 |
| | 2σ (%) | 0.54% | 0.13% |
| | Mean (± 2σ, n = 9) | 527.1 ± 2.8 | 10.3 ± 1.3 |
| | 2σ (%) | 0.54% | 0.13% |

#: The suffix "bis" indicates a duplicated measurement of the sample solution.

[a] $\delta^{234}U=[(^{234}U/^{238}U)-1]\times 1000$, where $(^{234}U/^{238}U)$ is the activity ratio. The $\delta^{234}$U values are calculated using the half-life values given by Cheng et al. (2000).

### 6.3.1. Rendez-Vous Hill coral sample (Barbados)

About 100 g of the coral were finely ground to ensure homogeneity of the sample. The coral sub-samples weighed from 100 to 400 mg. After addition of the $^{236}U-^{233}U$ spike, the sub-samples were dissolved in $HNO_3$. U and Th were then co-precipitated with Fe carrier. Finally, the samples were processed through anion exchange columns in order to separate and purify the uranium fraction, using a procedure similar to that reported by Edwards et al. (1987).

We prepared 11 samples over three distinct series. The MC-ICP-MS analyses were performed in the course of 5 days of analysis spread over a 5-month period. The results are listed in Table 4 and presented in Fig. 6. The external reproducibility on this in-house

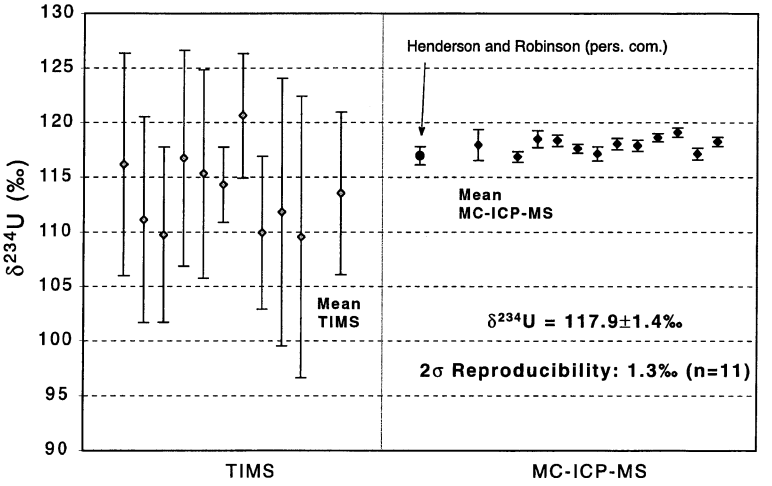


Fig. 6. External reproducibility of the $^{234}U/^{238}U$ ratio (expressed as $\delta^{234}U$ values) determined by replicate analyses of a coral sample (Barbados). Data are listed in Table 4. MC-ICP-MS results are compared with TIMS measurements also obtained at GEOTOP on a VG Sector™ mass spectrometer equipped with a 10-cm electrostatic analyzer and a pulse-counting Daly detector. Also reported is the analysis performed by Henderson and Robinson (pers. com.) on a Nu™ MC-ICP-MS at Oxford University (filled circle). All $\delta^{234}U$ values are calculated using the half-life values determined by Cheng et al. (2000). Error bars represent $2\sigma$ analytical precision. The MC-ICP-MS total external reproducibility is estimated to be $\pm$ 1.3 ‰ ($2\sigma$, $n = 11$).

standard is 1.3 ‰ ($2\sigma$, $n = 11$) and the results are consistent within error with (i) our TIMS measurements and (ii) an external analysis of this sample carried out by Henderson and Robinson (pers. com.) at Oxford University on a NU™ MC-ICP-MS (see Table 4 and Fig. 6). Moreover, the measurements were taken over a range of $^{234}U$ intensities from 5 to 22 mV, indicating that the tail contribution can be modelled as a linear system.

### 6.3.2. Carbonate rock sample

The sedimentary carbonate sample we used here as another in-house standard is part of a study in relation to investigations conducted by ANDRA (Agence nationale pour la gestion des déchets radioactifs—the French agency for nuclear waste management) into the feasibility of high-level-waste repository in a deep clayey environment. ANDRA is building a scientific Underground Research Laboratory at a depth of 450 m in a deep Jurassic clay layer of the Paris basin (Callovo-Oxfordian argilites). Borehole core samples from the target formation and its bounding limestone formations were analyzed for their uranium content and isotopic composition in order (i) to document the mobility of this element in such deposits, and (ii) to constrain the time scale of the geological phenomena responsible for an eventual remobilization.

The sample (HTM 02924 A #1) we chose as an internal standard belongs to a transect performed perpendicular to a major sub-horizontal stylolitic joint located in the Bathonian limestone, near the interface with the Callovo-Oxfordian formation (Deschamps et al., 2002). The chemical procedure developed for these types of carbonates is quite different from the usual chemical procedure, as described above, because of the large amount of clay and organic impurities in the matrix. This chemical protocol will be described more precisely elsewhere.

The sample was finely powdered. Nine sub-samples, weighed from 0.8 to 1.9 g, were then chemically prepared over six distinct series. The MC-ICP-MS analyses were performed in the course of 7 days of analysis spread over an 8-month period. The results are listed in Table 4 and illustrated in Fig. 7. The results of some sub-sample solutions that were analyzed twice on 2 different days of analysis are also given. These duplicate measurements are consistent, within error, with previous analyses. Con-

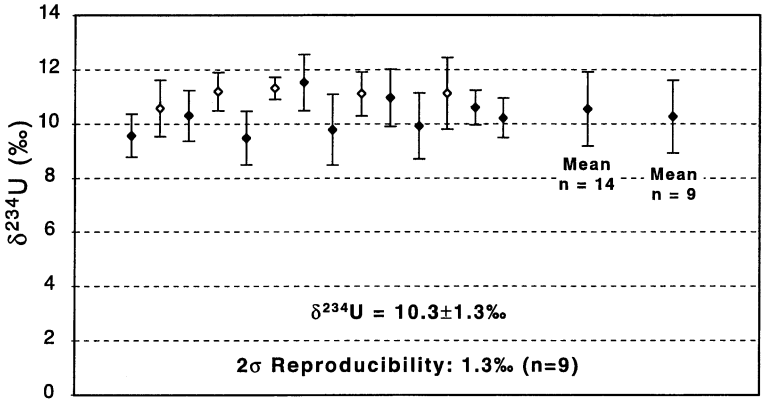


Fig. 7. $\delta^{234}$U (‰) replicate analyses of the HTM 02924 A #1 carbonate rock sample using the GEOTOP IsoProbe™ instrument. Data are from Table 4. Filled diamonds: single measurements; open diamonds: duplicate measurement of the previous sub-sample solution. $\delta^{234}$U values are calculated using the half-life values determined by Cheng et al. (2000). Error bars indicate 2$\sigma$ analytical precision. The total external reproducibility is estimated to be ± 1.3 ‰ (2$\sigma$, $n$ = 9).

sidering only the first MC-ICP-MS analysis of each sub-sample, the total reproducibility on this internal standard is about 1.3 ‰ (2$\sigma$, $n$ = 9). This is of the same order as the reproducibility obtained from the coral standard, indicating that the heavy chemical protocol does not induce significant drift in the results.

This sample displays a significant disequilibrium ($\delta^{234}$U = + 10.3 ± 1.3 ‰), as do all the transect samples (see Deschamps et al., 2002), indicating that U remobilization has occurred in the system within a period of 1 Ma. These results highlight the importance of using highly precise and accurate techniques, such as MC-ICP-MS, as opposed to α-counting spectrometry, in studies on natural radionuclide migration over recent geologic time in host-rock formations.

## 7. Conclusion

In this paper, we have shown that precise, accurate $^{234}$U/$^{238}$U measurements can be achieved using Faraday collectors only. However, the problem caused by the poor abundance sensitivity of the GEOTOP IsoProbe™ instrumentation needed to be fully addressed. The tail correction method we developed enabled us to correct for the large offset observed in the results obtained with the usual linear or exponential interpolation of baseline measurement monitored at ± 0.5 amu of each peak. This model can be of great relevance to the precise, accurate analysis of isotopic ratios with a wide dynamic range, such as those in the U–Th series, on instruments with relatively poor abundance sensitivity.

Our external analytical precision and reproducibility, as determined on replicate analyses of the NBL-112a standard solution, is 0.8 ‰ at the 95% confidence level. On natural carbonate samples, the external reproducibility (combined chemical separations plus spectrometric measurements) is about 1.3 ‰. The technique we developed on the GEOTOP IsoProbe™ is therefore a robust tool for U isotopic studies, especially when very high precision data are required and large amounts of uranium (at least 200 ng) are available, such as in radionuclide migration studies on radioactive waste repository safety.

## Acknowledgements

The authors thank Pr. C. Hillaire-Marcel, Dr. H. Isnard, A. Poirier and Dr. Dan Sinclair for their constructive help and comments. We are also very grateful to G. Henderson and L. Robinson for agreeing to perform an external analysis of our in-house coral standard on the Oxford University NU™ MC-ICP-MS. Dr. A. Simonetti's assistance with MC-ICP-MS measurement was also appreciated. The

paper benefited from careful and helpful reviews from S. Galer and an anonymous reviewer. ANDRA provided drill-core samples and financial support for PD's PhD. RD was supported by a Lavoisier post-doctoral fellowship. **[PD]**

## References

Banner, J.L., Wasserburg, G.J., Chen, J.H., Moore, C.H., 1990. $^{234}U-^{238}U-^{230}Th-^{232}Th$ systematics in saline groundwaters from central Missouri. Earth Planet. Sci. Lett. 101 (2–4), 296–312.

Bard, E., Hamelin, B., Fairbanks, R.G., Zindler, A., Mathieu, G., Arnold, M., 1990. U/Th and $^{14}C$ ages of corals from Barbados and their use for calibrating the $^{14}C$ time scale beyond 9000 years BP. Nucl. Instrum. Methods Phys. Res., B 52, 461–468.

Bard, E., Hamelin, B., Arnold, M., Montaggioni, L., Cabioch, G., Faure, G., Rougerie, F., 1996a. Deglacial sea-level record from Tahiti corals and the timing of global meltwater discharge. Nature 382, 241–244.

Bard, E., Hamelin, B., Arnold, M., Montaggioni, L., Cabioch, G., Faure, G., Rougerie, F., 1996b. Pleistocene sea levels and tectonic uplift based on dating of corals from Sumba Island, Indonesia. Geophys. Res. Lett. 23 (12), 1473–1476.

Chen, J.H., Wasserburg, G.J., 1981. Isotopic determination of uranium in picomole and subpicomole quantities. Anal. Chem. 53, 2060–2067.

Chen, J.H., Edwards, R.L., Wasserburg, G.J., 1986. $^{238}U$, $^{234}U$ and $^{232}Th$ in seawater. Earth Planet. Sci. Lett. 80 (3–4), 241–251.

Chen, J.H., Edwards, R.L., Wasserburg, G.J., 1992. Mass spectrometry and applications to uranium-series disequilibrium. In: Ivanovich, M., Harmon, R.S. (Eds.), Uranium-Series Disequilibrium; Applications to Earth, Marine, and Environmental Sciences. Clarendon Press, Oxford, UK, pp. 174–206.

Cheng, H., Edwards, R.L., Hoff, J., Gallup, C.D., Richards, D.A., Asmerom, Y., 2000. The half-lives of Uranium-234 and Thorium-230. Chem. Geol. 169 (1–2), 17–33.

Cowan, G.A., Adler, H.H., 1976. The variability of the natural abundance of $^{235}U$. Geochim. Cosmochim. Acta 40, 1487–1490.

Delanghe, D., Bard, E., Hamelin, B., 2002. New TIMS constraints on the uranium-238 and uranium-234 in seawaters from the main ocean basins and the Mediterranean Sea. Mar. Chem. 80 (1), 79–93.

Deschamps, P., Doucelance, R., Ghaleb, B., Hillaire-Marcel, C., Michelot, J.L., 2002. Evidence for micro-scale U-mobility along sedimentary discontinuities in a deep limestone formation as inferred by $^{234}U/^{238}U$ disequilibria. Abstracts of the 12th Annual V.M. Goldschmidt Conference, Geochimica et Cosmochimica Acta, Special Supplement, 66, p. 179.

Edwards, R.L., 1988. High precision thorium-230 ages of corals and the timing of sea level fluctuations in the late Quaternary. PhD Thesis, California Institute of Technology, Pasadena, United States.

Edwards, R.L., Chen, J.H., Wasserburg, G.J., 1987. $^{238}U-^{234}U-^{230}Th-^{32}Th$ systematics and the precise measurement of time over the past 500,000 years. Earth Planet. Sci. Lett. 81 (2–3), 175–192.

Edwards, R.L., Beck, J.R., Burr, G.S., Donahue, D.J., Chappell, J.M.A., Bloom, A.L., Druffel, E.R.M., Taylor, F.W., 1993. A large drop in atmospheric $_{14}C/_{14}C$ and reduced melting in the Younger Dryas, documented with $_{230}Th$ ages of corals. Science 260, 962–968.

Galer, S.J.G., 1999. Optimal double and triple spiking for high precision lead isotopic measurement. Chem. Geol. 157, 255–274.

Gallup, C.D., Cheng, H., Taylor, F.W., Edwards, R.L., 2002. Direct determination of the timing of sea level change during termination II. Science 295, 310–313.

Gariépy, C., Ghaleb, B., Hillaire, M.C., Mucci, A., Vallières, S., 1994. Early diagenetic processes in Labrador Sea sediments; uranium-isotope geochemistry. Can. J. Earth Sci. 31 (1), 28–37.

Gascoyne, M., Cramer, J.J., 1987. History of actinide and minor element mobility in an Archean granitic batholith in Manitoba, Canada. Appl. Geochem. 2 (1), 37–53.

Gascoyne, M., Schwarcz, H.P., 1986. Radionuclide migration over recent geologic time in a granitic pluton. Chem. Geol., Isot. Geosci. Sect. 59 (1), 75–85.

Griffault, L.Y., Gascoyne, M., Kamineni, C., Kerrich, R., Vandergraaf, T.T., 1993. Actinide and Rare Earth Element characteristics of deep fracture zones in the Lac du Bonnet granitic batholith, Manitoba, Canada. Geochim. Cosmochim. Acta 57 (6), 1181–1202.

Halliday, A.N., Lee, D.C., Christensen, J.N., Rehkämper, M., Yi, W., Luo, X., Hall, C.M., Ballentine, C.J., Pettke, T., Stirling, C., 1998. Applications of multiple collector-ICPMS to cosmochemistry, geochemistry and paleoceanography. Geochim. Cosmochim. Acta 62 (6), 919–940.

Hamelin, B., Manhès, G., Albarède, F., Allègre, C.J., 1985. Precise lead isotope measurements by the double spike technique: a reconsideration. Geochim. Cosmochim. Acta 49, 173–182.

Henderson, G.M., 2002. Seawater ($^{234}U/^{238}U$) during the last 800 thousand years. Earth Planet. Sci. Lett. 199 (1–2), 97–110.

Hofmann, A.W., 1971. Fractionation corrections for mixed-isotope spikes of Sr, K and Pb. Earth Planet. Sci. Lett. 10, 397–402.

Israelson, C., Wohlfarth, B., 1999. Timing of the last-interglacial high sea level on the Seychelles Islands, Indian Ocean. Quat. Res. 51, 306–316.

Ivanovich, M., Latham, A.G., Longworth, G., Gascoyne, M., 1992. Applications to radioactive waste disposal studies. In: Ivanovich, M., Harmon, R.S. (Eds.), Uranium-Series Disequilibrium; Applications to Earth, Marine, and Environmental Sciences. Clarendon Press, Oxford, UK, pp. 583–630.

Jarvis, K.E., Gray, A.L., Houk, R.S., 1992. Handbook of Inductively Coupled Plasma Spectrometry. Blackie, Glasgow.

Ludwig, K.R., 1997. Optimization of multicollector isotope-ratio measurement of strontium and neodymium. Chem. Geol. 135 (3–4), 325–334.

Ludwig, K.R., Simmons, K.R., Szabo, B.J., Winograd, I.J., Landwehr, J.M., Riggs, A.C., Hoffman, R.J., 1992. Mass-spectrometric $^{230}Th-^{234}U-^{238}U$ dating of the Devils Hole calcite vein. Science 258 (5080), 284–287.

Luo, X., Rehkämper, M., Lee, D.C., Halliday, A.N., 1997. High

precision $^{230}Th/^{232}Th$ and $^{234}U/^{238}U$ measurements using energy-filtered ICP magnetic sector multi-collector mass spectrometry. Int. J. Mass Spectrom. Ion Process. 171, 105–117.

McCulloch, M.T., Esat, T., 2000. The coral record of last interglacial sea levels and sea surface temperatures. Chem. Geol. 169, 107–129.

Rehkämper, M., Mezger, K., 2000. Investigation of matrix effects for Pb isotope ratio measurements by multiple collector ICP-MS: verification and application of optimized analytical protocols. J. Anal. At. Spectrom. 15, 1451–1460.

Robinson, L.F., Henderson, G.M., Slowey, N.C., 2002. U–Th dating of marine isotope stage 7 in Bahamas slope sediments. Earth Planet. Sci. Lett. 196 (3–4), 175–187.

Rubin, K.H., 2001. Analysis of $^{232}Th/^{230}Th$ in volcanic rocks: a comparison of thermal ionization mass spectrometry and other methodologies. Chem. Geol. 175 (3–4), 723–750.

Schwarcz, H.P., Gascoyne, M., Ford, D.C., 1982. Uranium-series disequilibrium studies of granitic rocks. Chem. Geol. 36 (1–2), 87–102.

Shen, C.-C., Edwards, L.R., Cheng, H., Dorale, J.A., Thomas, R.B., Bradley, M.S., Weinstein, S.E., Edmonds, H.N., 2002. Uranium and thorium isotopic and concentration measurements by magnetic sector inductively coupled plasma mass spectrometry. Chem. Geol. 185 (3–4), 165–178.

Smellie, J.A.T., Stuckless, J.S., 1985. Element mobility studies of two drill-cores from the Goetemar Granite (Kraakemaala test site), Southeast Sweden. Chem. Geol. 51 (1–2), 55–78.

Smellie, J.A.T., Mackenzie, A.B., Scott, R.D., 1986. An analogue validation study of natural radionuclide migration in crystalline rocks using uranium-series disequilibrium studies. Chem. Geol. 55 (4), 233–254.

Stein, M., Wasserburg, G.J., Lajoie, K.R., Chen, J.H., 1991. U-series ages of solitary corals from the California coast by mass spectrometry. Geochim. Cosmochim. Acta 55, 3709–3722.

Stirling, C.H., Esat, T.M., McCulloch, M.T., Lambeck, K., 1995. High-precision U-series dating of coral from Western Australia and implication for the timing and duration of the Last Interglacial. Earth Planet. Sci. Lett. 135, 115–130.

Stirling, C.H., Lee, D.C., Christensen, J.N., Halliday, A.N., 2000. High-precision in situ $^{238}U–^{234}U–^{230}Th$ isotopic analysis using laser ablation multiple-collector ICP-MS. Geochim. Cosmochim. Acta 64 (21), 3737–3750.

Stirling, C.H., Esat, T.M., Lambeck, K., McCulloch, M.T., Blake, S.G., Lee, D.C., Halliday, A.N., 2001. Orbital forcing of the marine isotope stage 9 interglacial. Science 291, 290–293.

Taylor, H.E., 2001. Inductively Coupled Plasma Mass Spectrometry. Practice and Techniques. Academic Press, San Diego, CA. 294 pp.

Taylor, P., De Bievre, P., Walder, A., Entwistle, A., 1995. Validation of the analytical linearity and mass discrimination correction model exhibited by a multiple collector inductively coupled plasma mass spectrometer by means of a set of synthetic uranium isotope mixtures. J. Anal. At. Spectrom. 10, 395–398.

Thirlwall, 2001. Inapropriate tail corrections can cause large inaccuracy in isotope ratio determination by MC-ICP-MS. J. Anal. At. Spectrom. 16, 1121–1125.

Thirlwall, M.F., 2002. Multicollector ICP-MS analysis of Pb isotopes using a $^{207}Pb–^{204}Pb$ double spike demonstrates up to 400 ppm/amu systematic errors in Tl-normalization. Chem. Geol. 184 (3–4), 255–279.

Vol. 33 — N° 2 06 09 p. 195–204

GEOSTANDARDS and GEOANALYTICAL RESEARCH

# Effective Correction of Mass Bias for Rhenium Measurements by MC-ICP-MS

André **Poirier** (1, 2)* and Régis **Doucelance** (1, 2)

(1) GEOTOP-UQAM-McGill Research Center, C.P. 8888, Succ. Centre-Ville, Montréal, QC, Canada, H3C 3P8
(2) Laboratoire Magmas et Volcans, Université Blaise Pascal - CNRS, 5, rue Kessler, 63038 Clermont-Ferrand Cedex, France
* Corresponding author. e-mail: poirier.andre@courrier.uqam.ca

**The geochemistry of Re-Os and the recent use of Re as a non-traditional stable isotope both need accurate and precise quantification of $^{187}Re/^{185}Re$ ratios. This paper reports rhenium isotopic data obtained from the analysis of a standard solution and geological samples by MC-ICP-MS. We show that measured isotopic ratios are modified by matrix effects that cannot be accounted for by the standard solution bracketing technique. The bias resulting from measurements on a spiked ($^{185}Re$-enriched) sample is shown to alter the apparent Re concentration by several percent. When spiking samples and calibrators with tungsten, simultaneous measurement of tungsten and rhenium isotopes compensates for the matrix-induced modification of mass bias. Rhenium and tungsten are shown to have different fractionation factors. This may be due to the fact that the two elements fractionate in a different but systematic way, or that the reference isotopic ratios used for elemental Re and W are incoherent with one another. The consistency of fractionation through time can be used to obtain an empirical relationship between W and Re measured ratios from a standard solution to obtain a sample's fractionation-corrected $^{187}Re/^{185}Re$ spiked ratio on samples containing pg $g^{-1}$ levels of Re, even if some matrix capable of affecting mass bias remains in the final solution.**

Keywords: matrix effect, mass bias, standard solution bracketing, rhenium isotopes, tungsten isotopes, MC-ICP-MS.

***La géochimie du Re-Os, de même que l'utilisation récente du Re comme isotope stable, nécessite une mesure à la fois juste et précise du rapport isotopique $^{187}Re/^{185}Re$. Cette article présente les résultats de mesures isotopiques de rhénium obtenues par MC-ICP-MS, sur solutions étalons et sur échantillons naturels. Nous comparons les méthodes de correction du fractionnement de masse instrumental par encadrement de mesure d'étalons, d'une part, et par correction pseudointerne par addition de tungstène, d'autre part. Nous démontrons que la matrice résiduelle d'un échantillon naturel, en sortie de chimie, modifie significativement la concentration apparente en Re mesurée par spectrométrie de masse. Cette modification du fractionnement de masse est impossible à éliminer par encadrement, mais est corrigée par addition de tungstène. Cet effet matrice peut fausser de plusieurs pourcents les concentrations calculées par dilution isotopique (échantillon additionné d'un traceur enrichi en $^{185}Re$); la méthode par encadrement d'étalons est donc limitée par rapport à l'addition de W. Le tungstène et le rhénium ont des facteurs de biais de masse différents sur notre instrument, mais leur différence est constante et quantifiable. Ceci résulte, soit de comportements différents des deux éléments en termes de fractionnement, soit de valeurs de normalisations incohérentes entre les deux éléments. Une relation empirique liant le fractionnement des deux éléments obtenue sur solutions étalons permet de corriger du fractionnement le rapport $^{187}Re/^{185}Re$ spiké d'un échantillon (contenant du Re au niveau de quelques pg $g^{-1}$) dopé au tungstène, et permet ainsi de compenser un éventuel effet de la matrice.***

*Mots-clés : effet matrice, fractionnement de masse instrumental, encadrement de mesures d'étalon, isotopes du rhénium, isotopes du tungstène, MC-ICP-MS.*

**Received 01 Oct 08 – Accepted 12 Jan 09**

The Re-Os system has now made its way into the geochemical toolbox as a robust and reliable method. One of the interests in this system lies in the fact that it conveys complementary information from the other long-lived isotopic systems, because of the different geochemical behaviour of Re and Os (both are chalcosiderophile elements). Osmium isotopic composition and concentration (by isotope dilution, ID, involving the addition of an enriched tracer to the sample, $^{190}Os$ in this case) are typically determined by single mass spectrometic analysis, followed by deconvolution of the spike/sample mixture. Rhenium has a constant isotopic composition at a given time, and the correct quantification of its abundance in a given sample can be achieved by techniques such as quadrupole ICP-MS. However, for applications that need a high precision quantification of Re content, the isotope dilution technique is as yet unsurpassed. In order to achieve the desired high precision, a precisely and accurately measured $^{187}Re/^{185}Re$ spiked ratio is needed; such a requirement identifies the magnetic sector mass spectrometer, with its flat topped peaks, as the favoured instrument to be used. Thermal ionisation mass spectrometry in the negative-ion mode (N-TIMS) has been shown to be a sensitive and precise analytical method for Re measurements (Creaser *et al.* 1991). Laboratories that routinely determine Re-Os possess such instruments, but many of these laboratories use the same TIMS instrument to determine other elements as well. Neodymium, Sr and Pb are generally determined using filaments made up of pure rhenium metal, with all the potential contamination for subsequent Re determinations when the same instrument is used. Even in a Re-Os dedicated mass spectrometer, in which no Re filaments are used, Re background is not zero. Rhenium seems to be mobilised from the entire source housing, contaminating low-Re sample measurements. Furthermore, it is known that the spiked Re composition measured by a TIMS can change with time towards the natural Re composition, reflecting a gradual increase through time of contamination from filament and/or source housing (e.g., Birck *et al.* 1997). The technological breakthrough of merging an inductively coupled plasma source (ICP) with a multi-collector magnetic sector mass spectrometer eliminates the thermal-source related problems outlined above, while keeping the flat-topped isotope peaks needed to achieve high-precision isotopic ratios.

Isotopes determined by MC-ICP-MS experience a rather large instrumental mass bias (~ 1% at rhenium masses) that needs to be monitored and corrected. For elements that have at least three isotopes with one isotope ratio that is fixed in nature, it is possible to evaluate fractionation internally through the measurement of a naturally constant isotopic ratio. However, for an element that comprises isotopic ratios all of which are variable, such as Pb or for spiked two-isotope elements, akin to rhenium ID analysis, it is not possible to monitor fractionation in this way.

The standard solution bracketing technique (SSBT) is a method that applies a fractionation factor to a sample interpolated from the analyses of a known standard solution before and after the sample. This method will yield good results as long as the fractionation effect is stable, or at least evolving at a regular rate through time. Residual matrix can have a strong effect on the observed fractionation that limits the effectiveness of SSBT (for examples, see Galy *et al.* 2001, Albarède *et al.* 2004, Pietruszka *et al.* 2006). Concomitant elements within the matrix can modify the fractionation of the sample compared to that which effects the bracketing standard solution (see Reuer *et al.* 2003 and Rehkämper and Mezger 2000 for conflicting views on the effect of low mass concomitant elements on the isotopic fractionation of Pb).

An alternative to standard solution bracketing is the "pseudo-internal" correction technique, which is now widely employed for Pb isotope measurements by MC-ICP-MS. This technique involves the spiking of the analyte with another non-isobaric element of the same mass range, thallium in the case of lead, and applying the fractionation of Tl to Pb either directly, of after some mathematical treatment to account for the slight differences in fractionation between the two elements (Longerich *et al.* 1987, Rehkämper and Halliday 1998, Thirlwall 2002, Reuer *et al.* 2003).

In Montréal, Re filaments were used in the available negative polarity TIMS, and the $ReO_4^-$ background levels were not negligible (Re and Os are measured as oxides in N-TIMS), even though a Re-Os dedicated focusing assembly was used. This fact led us to measure the rhenium ID on the MC-ICP-MS Micromass IsoProbe. Before an instrument upgrade in 2004, fractionation of rhenium was evolving irregularly with time on this MC-ICP-MS, so the SSBT was inappropriate at that time. To overcome this mass bias instability, we added W to a Re standard solution (Poirier 2001, 2006, Poirier *et al.* 2004).

This paper reports Re and W isotopic measurements acquired simultaneously for a standard solution

as well as for real samples (processed through the chemical procedure). We compare the use of both standard solution bracketing and W-spiking techniques, demonstrating the inadequacy of SSBT when a matrix component remains in the final solution following chemical purification. We also compare the mathematical treatment that link up rhenium and tungsten mass biases in our instrument.

## Experimental

The Re-W results presented here were acquired on a Micromass IsoProbe instrument, using an Aridus desolvating membrane. Standard operating parameters are described elsewhere (Poirier *et al.* 2004). Briefly, the Faraday cup configuration was as follows: $^{184}W$, $^{185}Re$, $^{186}W$, $^{187}Re$ and $^{188}Os$ in the Axial to High-4 positions respectively; later experiments used an Axial to High-6 configuration to include low-masses $^{182}W$ and $^{183}W$ (i.e., Faraday cup high-1 being the first cup on the high-mass side of the Axial cup, the latter being in the optical axis of the mass spectrometer). It was necessary to monitor $^{188}Os$ because of potential Os interferences on masses 184, 186 and 187. Tungsten and Re are neighbours in the periodic table and do not contribute any isobars. The Os signal was always negligible during this study and no polyatomic interferences were seen in the mass range of interest. A single batch of nitric acid (2% v/v) was used for both the standard solution and sample dilution, and was also used to measure the 60 s "on-peak-zeros", which monitored for any remaining memory effects of the whole system prior to analysis.

Prior to an instrument upgrade in the summer of 2004, abundance sensitivity on our instrument was measured at 27-30 ppm $^{238}U$ at mass 237 (Deschamps *et al.* 2003). A leak in the hexapole collision cell assembly was diagnosed and repaired during the upgrade. This leak caused fractionation instability for about the first hour every morning, which was thought to be the time needed to purge the air from the collision cell with the injected Ar gas. Following the upgrade, abundance sensitivity was repeatedly measured at 12-18 ppm, depending on the vacuum status in the analyser section (1.8 to 2.6 x $10^{-6}$ Pa, 1.8 to 2.6 x $10^{-8}$ mbar). The stability of fractionation also improved much after the upgrade. In any case, the abundance sensitivity effect was found to be negligible on the measured rhenium concentrations (less than 0.01%).

The analysed Re standard solution was prepared by dissolving a degassed rhenium filament (zone refined grade, Rhenium Alloys, Inc.) in hot concentrated nitric acid, and further diluting this solution afterwards, similar to the procedure of Birck *et al.* (1997). The tungsten solution used for spiking was an off-the-shelf ICP-MS standard solution (Alfa-Aesar, SpecPure grade). Sensitivities of both elements were similar: 110 and 100 volts/$\mu$g ml$^{-1}$ for Re and W respectively. These values indicated that a good isotope dilution measurement could be obtained on picogram size test portions of Re (e.g., ~ 60 pg in 0.5 ml of 2% v/v $HNO_3$, translating into *ca.* 15 mV of the total Re spiked signal). In order to analyse a complex matrix solution, one basalt from Cape Verde (SN-13 of Millet *et al.* 2008) and one black shale sample from the eastern Québec Appalachian Mountains were processed through a regular chemical procedure (Birck *et al.* 1997).

### Fractionation laws

Power and exponential laws (Russell *et al.* 1978, Hart and Zindler 1989) are the two mass fractionation laws generally used to account for mass discrimination during MC-ICP-MS runs (Walder *et al.* 1993, Hirata 1996, Belshaw *et al.* 1998, Rehkämper and Halliday 1998, White *et al.* 2000). The mathematical expression of the power fractionation law is given by:

$$R_{True} = R_{Meas.} \times (1 + \alpha)^{\Delta m} \quad (1)$$

where $R_{True}$ and $R_{Meas.}$ refer to the true and fractionated values of the isotopic ratio *R*, respectively, $\alpha$ corresponds to the mass bias per atomic unit, and $\Delta$m is the mass difference between the two isotopes involved in the isotopic ratio R.

The equivalent expression for the exponential fractionation law is :

$$R_{True} = R_{Meas.} \times (m_1/m_2)^{\beta} \quad (2)$$

where $m_1$ and $m_2$ are the respective masses of isotopes 1 and 2 involved in the isotopic ratio R, and $\beta$ denotes the mass fractionation coefficient. It is noted that these two fractionation laws are special cases of a more general mass discrimination law (see Maréchal *et al.* 1999 and Albarède *et al.* 2004 for the mathematical formalism).

The fractionation coefficient of the power law $\alpha$ (or $\beta$ in the case of exponential law) can be derived from a stable isotope ratio having an "accepted" value (which may be an absolute value in the best of cases

or a commonly used normalising value). Then, this alpha (or beta) derived from an invariant ratio is applied to a second, variable ratio to correct it from mass bias. The consistency, for a given element, of $\alpha$ or $\beta$ values (e.g., $\alpha^{207}Pb/^{206}Pb = \alpha^{208}Pb/^{207}Pb$, $\beta^{207}Pb/^{206}Pb = \beta^{208}Pb/^{207}Pb$), implies that raw values that are measured for two distinct isotopic ratios $R^1_{meas.}$ and $R^2_{meas.}$ of the same element will plot on a straight line in a $\ln(R^2_{meas.})$ vs. $\ln(R^1_{meas.})$ diagram. If fractionation evolves according to the power law, the slope of this line will be specified by:

$$S_{power} = \Delta m_2/\Delta m_1 \quad (3)$$

where $\Delta m_1$ and $\Delta m_2$ are the mass differences between the two isotopes involved in isotopic ratios $R^1_{meas.}$ and $R^2_{meas.}$, respectively.

Alternatively, exponential fractionated ratios $R^1_{meas.}$ and $R^2_{meas.}$ define a line which slope is given by:

$$S_{exponential} = \ln(m_2/m_1)/\ln(m_3/m_1) \quad (4)$$

where $m_1$ and $m_2$ correspond to the masses of the two isotopes involved in $R^2_{meas.}$, and $m_1$ and $m_3$ in $R^1_{meas.}$, respectively.

We will demonstrate later that our dataset could not discriminate between the power and exponential fractionation models. For the remainder of the discussion, we will thus focus our attention on the exponential law. It has to be noted that it was previously proposed that there could be a mass dependence of the $\beta$ values for different isotopic ratios of the same elements (Thirlwall 2002).

## Results and discussion

In this section, we report long-term analyses (from year 2001 to 2008) of a Re standard solution along with unspiked natural samples, all doped with W. Using admitted IUPAC mass values, one can calculate the theoretical slope to determine which fractionation model better suits the mass bias of its dataset. For instance, if we consider tungsten ratios $^{186}W/^{184}W$ and $^{186}W/^{183}W$ in a ln-ln diagram, the slope according to the power and exponential laws would be 1.4995 and 1.5036, respectively. We empirically determined a slope of 1.541 ± 0.073 (95% confidence level, regression performed using Isoplot, Ludwig 2003) which, because of the level of uncertainty, does not allow us to discriminate between the two models. Thus, for simplicity's sake, we will only present the exponential law data for the remaining of the discussion.

Following the major hardware upgrade in 2004, the stability of fractionation evolution much improved. We thus carried out tests to see how the SSBT performed compared to W-spiking. We noticed that the transmission of Re (and added W) was strongly inhibited on the MC-ICP-MS when a 2% v/v $HNO_3$ solution had a blue tint following the chemical procedure. The colour originated from significant residual reduced Cr accompanying the purified Re (Cr is a reagent used in the chemical procedure; Birck *et al.* 1997). Other chemical protocols, such as the Carius Tube digestion (Shirey and Walker 1995) would not be affected by this problem, as no $CrO_3$ reagent is used. This inhibition effect can potentially occur within the Aridus or within the plasma. Nevertheless, when an additional purification step was undertaken to remove the excess Cr, a normal signal was then obtained. Figure 1 shows the effect of adding a pure Cr solution to the Re-W standard solution. To our surprise, we found that the addition of a little chromium enhanced the transmission of both Re and W by about 40% (up to ~ 2 $\mu g\ g^{-1}$ Cr). However, more Cr then inhibited the transmission (lower by 70% at 80 $\mu g\ g^{-1}$ Cr). At first, we suspected this enhancement was due to rhenium and tungsten blanks in the Cr solution. Measurement of pure $^{185}Re$-spike doped with 2 $\mu g\ g^{-1}$ Cr yielded an uncontaminated spike ratio, implying a "clean" chromium and a real signal enhancement. We note that the measured Re isotopic ratio diverged slightly from the correct value at very high Cr content (20 $\mu g\ g^{-1}$), indicative of a modification of the physics of the mass bias induced by the matrix. This observation demonstrates that excellent chemical purification of the analyte is paramount to obtain accurate results.

### Standard solution bracketing technique

In order to show a matrix effect from real samples, we processed unspiked basalt and black shale through the Re chemistry procedure (Birck *et al.* 1997, HF-HBr digestion) and analysed them spiked with tungsten, in exactly the same way as the standard solution. Black shales contain a significant amount of Re (a few ng of Re per gram of powdered sample), and thus allows the measurement to be replicated several times on the same aliquot. The basaltic sample was measured at *ca.* 500 pg $g^{-1}$ Re.

Mass scans of the final solution of the basaltic sample (dissolved in 2% v/v nitric acid matrix) showed many elements to be still present following the chemical procedure. The most notable ones seen at volt

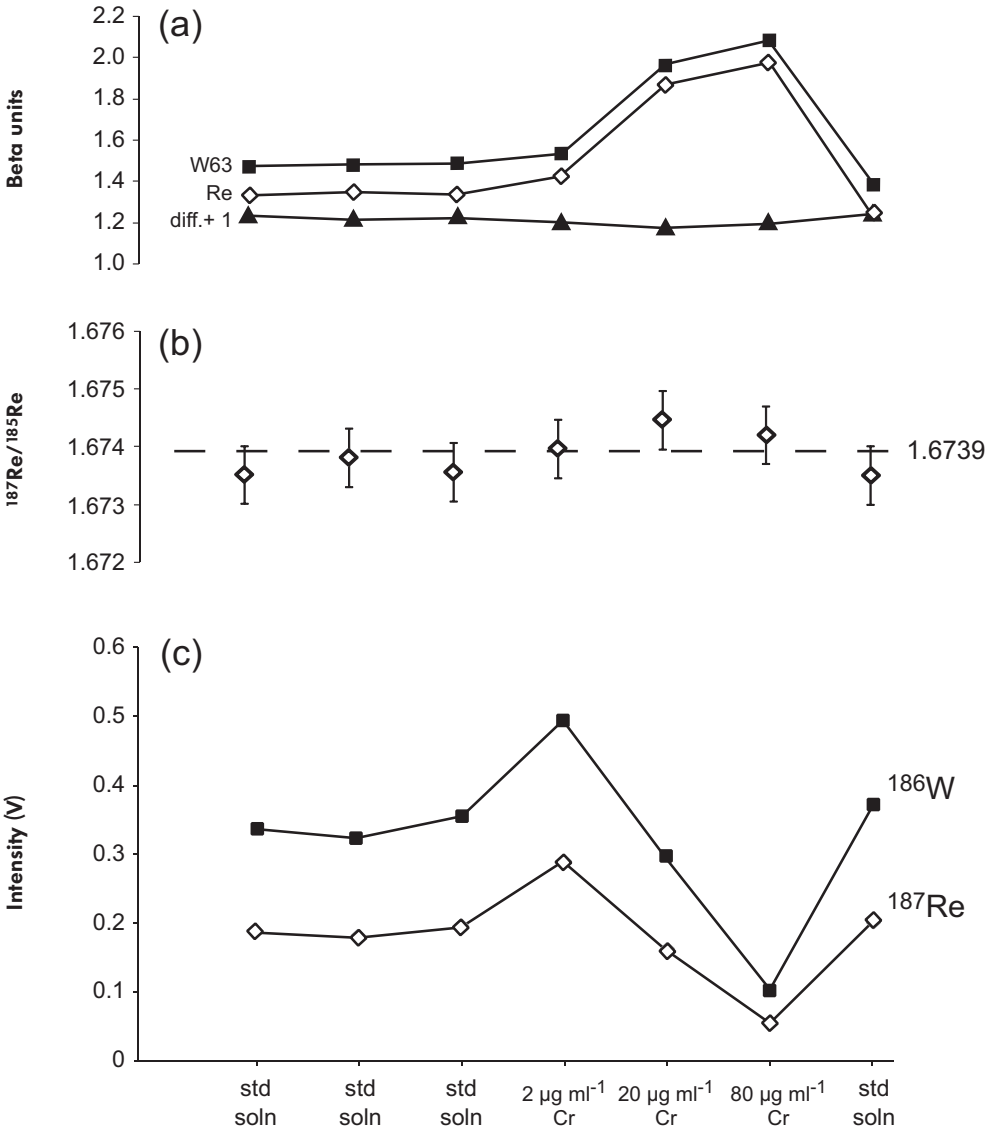


**Figure 1. Effect of the addition of chromium as a concomitant element on a mixed rhenium and tungsten standard solution. (a) Fractionation of tungsten and rhenium calculated with the exponential law. The difference in beta values plus one unit ($\Delta\beta$+1) is also shown. W63 is the fractionation factor for the $^{186}W/^{183}W$ ratio. (b) Corrected Re ratio using W to asses fractionation (see text for details). (c) Intensity of ion beams of $^{187}Re$ and $^{186}W$ as a function of the Cr content of the solution. std soln = standard solution.**

levels were Zn, Br, Nb, Mo, Ta, with minor amounts (mV levels) of Ag, Cu, Ba, Sb, Tl, Pb and U. Gold was present at 2 V, part of this signal coming most probably from the gold-plated hexapole rods of the IsoProbe's collision cell. Major cations such as Na, Mg, Al were quantitatively removed by the iso-amylic alcohol chemical procedure of Birck *et al.* (1997), since no signal was observed in the low mass range, except for a few mV of $^{39}K$ (and a few hundred mV of m = 30 ($NO^+$), most probably originating from the 2% v/v nitric acid matrix and Aridus $N_2$ gas). Black shale residual matrix consisted of volt levels of Mo, Fe, Ni, Tl and mV levels of Pb and U. The chemical procedure used here was designed by Birck *et al.* (1997) to accomplish separation of Os from Re for TIMS analysis, and it achieves its goal, as no Os remains in the Re fraction. For comparison, Woodhead's (2002) deliberate incomplete Pb chemical purification on glassy basalt produced a solution with matrix impurities of Zn, Sr and Ba, which also caused a large change in the observed mass bias.

Figure 2 shows $\beta$ values (fractionation factor of the exponential law) of repeated analysis of the Re standard solution and the black shale Re during one analytical

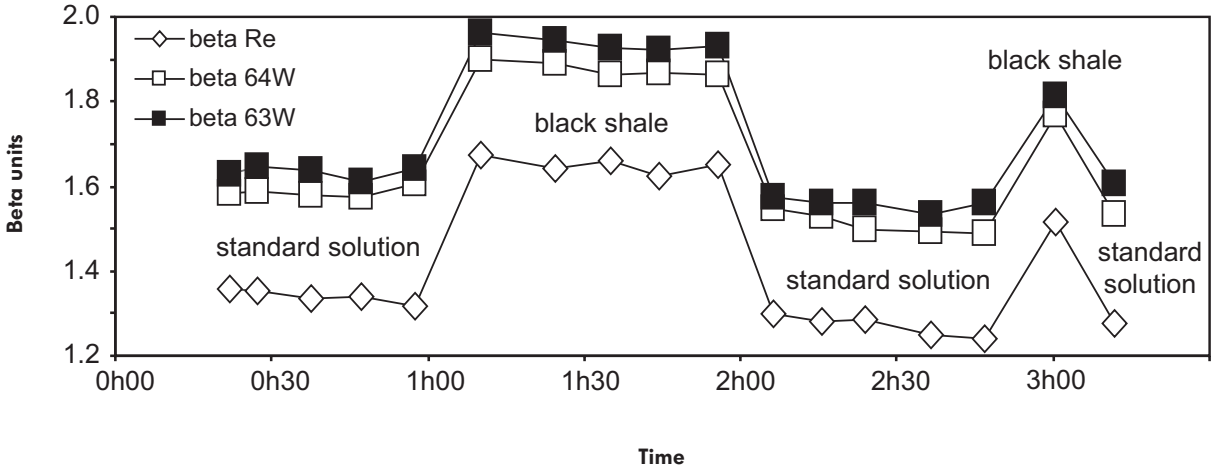


**Figure 2. Measured beta values (exponential fractionation law) for a Re standard solution and for Re chemically isolated from an unspiked black shale sample. Both Re solutions were doped with the same W solution, with similar Re/W ratios of ~ 3.**

session. Although the evolution of the fractionation - drift - was smoothly evolving, one can observe that the real samples behaved quite differently than their bracketing standard solutions. We compared different matrices, and found that the basalt from Cape Verde behaved differently from the black shale: the measured isotopic ratio was shifted by 3‰ for the black shale when compared to the standard solution, while the basalt was modified by *ca.* 2‰. In contrast to the observation made by Reuer *et al.* (2003), our matrix-rich sample had a preferential transmission of the heavy isotopes, shown as higher β values in Figure 2 (for $^{187}Re/^{185}Re$, $^{186}W/^{184}W$ and $^{186}W/^{183}W$ ratios, with heavy/light isotope ratios). None of the concomitant elements involved seemed to have accumulated either on the cones or within the Aridus, since the effect disappeared when reverting to a pure standard solution following regular wash-out.

The offset in isotopic ratios created by the matrix effect of the samples would generate a significant bias in the calculated concentration of a spiked sample. If, similarly to Figure 2, a larger value of β was obtained on a optimally-spiked black shale sample, the standard solution bracketing technique would give a misleading concentration that would be several percent off target of the true Re concentration. Mass bias resulting from the matrix effect can be variable, depending on the nature and abundance of the concomitant elements, so that the standard solution bracketing technique cannot remedy such a variable effect.

## Re-W relative fractionation

In Figure 2, one can see that the $^{186}W/^{184}W$ and $^{186}W/^{183}W$ ratios behaved similarly and had close β values; for this reason, only the $^{186}W/^{184}W$ ratio will be further discussed in the comparison with the $^{187}Re/^{185}Re$ ratio. When plotted on a ln-ln diagram, the isotopic compositions of Re vs. W of the standard solution define a straight line with a slope of 1.013 ± 0.062, and an intercept of 0.5887 ± 0.0035 (95% confidence limit, Figure 3). When compared to theoretical values, the ln-ln space of isotopic ratios $^{187}Re/^{185}Re$ and $^{186}W/^{184}W$ should have a slope of 0.9943 to comply with the exponential law of fractionation, which is within the uncertainty of the empirical value, and allows us to use this law for the discussion.

Fractionation of both W and Re are modified according to the matrix in which they are carried to the plasma (Figure 2). Fractionation of both elements evolved through time on a smooth trend most probably related to the overall stabilisation of the instrument (collision cell thermal and gaseous conditions, electronics, etc). Matrix-rich black shale data seemed to have evolved on a slope that parallels the standard solution's evolution line. Consequently, the beta ratio $\beta_W/\beta_{Re}$ evolved through time in the dataset from this analytical session, with the difference $\Delta\beta = \beta_W - \beta_{Re}$ being stable. In the long term, $\beta_W/\beta_{Re}$ = 1.15 ± 0.10 (2*s*), while $\Delta\beta$ was 0.21 ± 0.10 (2*s*).

When the natural logarithm of the measured ratio for Re and for W are plotted against each other, the

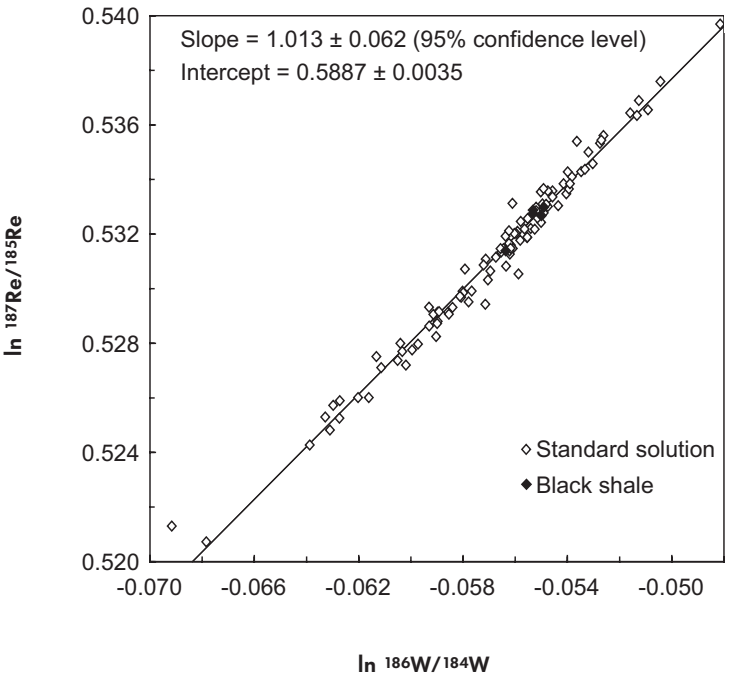


**Figure 3. Relationship between the isotopic composition of unspiked Re and W standard solutions measured on the IsoProbe plotted in ln-ln geometric space. Regression values were obtained with Isoplot Ex v3.0 (Ludwig 2003).**

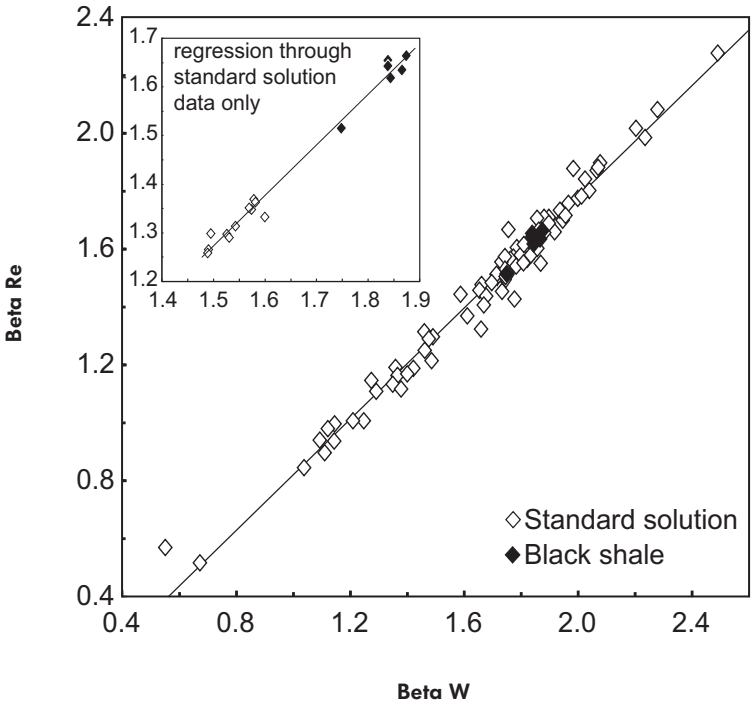


**Figure 4. Beta values for the unspiked black shale Re and added W isotopic compositions plotted for the long term standard solution database. Inset shows beta Re vs. beta W for a single analytical session (regression on standard solutions only), slope = 1.03 ± 0.36 and intercept = 0.18 ± 0.48, (95% confidence limit), which is within uncertainty of the full standard solution dataset, which has a slope = 0.96 ± 0.03 and intercept = -0.14 ± 0.05.**

black shale data fall on the same long term trend as the standard solution dataset (Figure 3). This remains true in the β space (Figure 4), which incorporates "true ratios" for the calculation of the beta values. From a pragmatic point of view, the absolute values of the calculated beta factors are unimportant (they depend on assumptions about the "true" ratio), what matters is the consistency of the behaviour of these beta values for a matrix-rich sample and the standard solution to allow empirical correction of the Re mass bias. The standard solution data acquired during a single 3 hour period produced a regression that was within error equal to the long term value (several years; inset in Figure 4). The Re-W results for the black shale fell on the standard solution regression lines (Figures 3 and 4); this strongly suggests that fractionation of Re and W from

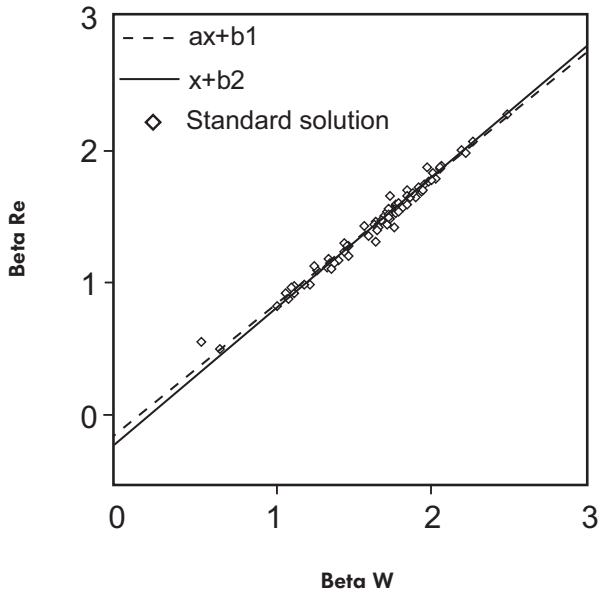


**Figure 5. Comparison between two empirical models of the relationship between beta W and beta Re. See text section Re-W relative fractionation for explanation.**

the analysis of matrix-rich samples behaved similarly to fractionation from standard solutions. These results are compatible with the observation of matrix-rich Pb (+Tl) analyses by Woodhead (2002), which show that induced mass bias can be generated by measuring samples which have been, to different extents, deliberately imperfectly purified to provoke an increasing matrix effect.

The long-term regression results in Figure 4 yielded a linear function that can be defined as $\beta_{Re} = a\beta_W + b$ (with a = 0.96 ± 0.03 and b = - 0.14 ± 0.05, 2*s*). One can observe that the slope is near unity, but the intercept is significantly different from zero. When compared to the range of beta values obtained throughout all analytical sessions (*ca.* 0.4 to 2.6), this intercept value amounts to between 5 and 25% of the Re beta value. As the measured fractionation factors for $\beta_{Re}$ and $\beta_W$ are different, this empirical law is needed to retrieve the Re ratio corrected for mass bias when real samples are analysed using the tungsten-spiking technique.

Because of the near unity of the slope (a ~ 1), we may also consider the special case where both beta values are only separated by a constant value (b ~ 0.21, with the slope forced to one). This case corresponds to similar behaviour of Re and W in terms of fractionation, but to incoherent accepted ratios for the two examined isotopic ratios. Figure 5 presents the comparison between the calculated regression and the approximation (assuming a = 1). The difference in calculated $^{187}Re/^{185}Re$ ratio for a given $^{186}W/^{184}W$ ratio for both empirical calculations is less than 0.04 beta units, which has an insignificant effect on the final calculated Re concentration.

**Rhenium natural isotopic composition:** The mass bias calculated for a given element depends on assumptions about the *true* isotopic ratio. The $^{187}Re/^{185}Re$ isotopic ratio has an accepted value of 1.6739 ( 0.0011 (Gramlich *et al.* 1973), which is the isotopic reference value for Re employed throughout the Re-Os research community. This value, even though it has a large uncertainty, is not achieved if we assume that Re and W fractionate similarly (i.e., the case where a = 1) using the accepted W values of Lee and Halliday (1995) or Völkening *et al.* (1991).

One could then wonder if the problem arises from the value used to evaluate tungsten fractionation from the $^{186}W/^{184}W$ ratio. If so, other W ratios should give different fractionation values. Figure 2 shows the good coherence between mass bias from two W isotopic ratios using reference values from Lee and Halliday (1995). Regression of tungsten data for $\beta_{186/184}$ vs. $\beta_{186/183}$ yielded a slope of 1.025 ± 0.048 and an intercept of 0.008 ± 0.080, which corresponds to y = x within uncertainty limits. As a working hypothesis, we will assume that the W composition of Lee and Halliday (1995) is true, in order to observe the effect of a direct fractionation correction of Re with W. This is a plausible case since the two elements have similar volatility and atomic mass numbers. The outcome of such an assumption implies that for the Re isotopic composition to be coherent with W isotopes, $^{187}Re/^{185}Re$ needs to be 1.6701 ± 0.0002 (2*s*) (note that we calculated a value -0.004% lower, which is within error, using the tungsten isotopic ratio of Völkening *et al.* 1991) which is significantly lower than the value of Gramlich *et al.* (1973, 1.67398 ± 0.00110). It must be noted that this new value would depend on $\beta_{Re} = \beta_W$, and the assumption that both beta values could reach zero fractionation simultaneously, a purely hypothetical result on a MC-ICP-MS (see Maréchal *et al.* 1999). Modification of the $^{187}Re/^{185}Re$ natural ratio has consequences for the decay constant of radioactive $^{187}Re$ (i.e., a faster decay rate). The new value would translate to a ~ 80 Ma reduction in the half-life value of isotope 187 of rhenium (~ 42 Ga), which is still within the uncertainty of the current value, but would cause a shift in all data using Re-Os as a geochronometer.

As the evaluation of the isotopic composition of tungsten is relative (i.e., not calibrated against a gravimetrical reference material; Lee and Halliday 1995), its ratio cannot be used as an absolute reference. The internal coherence of the W isotopic composition (i.e., the fractionation is uniform for all isotope pairs as reported by Lee and Halliday (1995) and supported by our dataset) suggests that the true composition must lie on a fractionation line encompassing these observed ratios. As rhenium has only two isotopes, it is not possible to verify internal coherence for the isotopic composition for this element on a MC-ICP-MS, but its isotopic composition was calibrated against a gravimetric reference material (Gramlich *et al.* 1973), so its absolute composition can be considered to be robust within reported uncertainty.

## Conclusions

We have presented the W-spiking technique to correct the Re isotopic ratio for instrumental mass bias occurring in a MC-ICP-MS. The key advantage of this technique resides in its ability to correct accurately real samples, including matrix-rich ones that fractionate differently from pure standard solutions, and that cannot be corrected accurately with classical standard solution bracketing. On the instrument used in this study, this technique allowed measurement of the Re concentration accurately at the pg $g^{-1}$ level, for geological samples for which a gram of material was available.

## Acknowledgements

Both authors wish to express their gratitude to Prof. Clément Gariépy (1953-2004), who provided support for this study. Le Fonds Québécois de Recherche sur la Nature et les Technologies (FQRNT) is acknowledged for having granted a postdoctoral fellowship to AP. This is contribution GEOTOP-2009-0001.

## References

**Albarède F., Télouk P., Blichert-Toft J., Boyet M., Agranier A. and Nelson B. (2004)**
Precise and accurate isotopic measurements using multiple-collector ICP-MS. Geochimica et Cosmochimica Acta, 68, 2725-2744.

**Belshaw N.S., Freedman P.A., O'Nions R.K., Frank M. and Guo Y. (1998)**
A new variable dispersion double-focusing plasma mass spectrometer with performance illustrated for Pb isotopes. International Journal Mass Spectrometry, 181, 51-58.

**Birck J.-L., Roy-Barman M. and Capmas F. (1997)**
Re-Os isotopic measurements at the femtomole level in natural samples. Geostandards Newsletter: The Journal of Geostandards and Geoanalysis, 21, 19-27.

**Creaser R.A., Papanastassiou D.A. and Wasserburg G.J. (1991)**
Negative thermal ion mass spectrometry of osmium, rhenium and iridium. Geochimica et Cosmochimica Acta, 55, 397-401.

**Deschamps P., Doucelance R., Ghaleb B. and Michelot J.-L. (2003)**
Further investigations on optimized tall correction and high-precision measurement of uranium isotopic ratios using multi-collector ICP-MS. Chemical Geology, 201, 141-160.

**Galy A., Belshaw N.S., Halicz L. and O'Nions R.K. (2001)**
High-precision measurement of magnesium isotopes by multiple collector inductively coupled plasma-mass spectrometry. International Journal Mass Spectrometry, 208, 89-98.

**Gramlich J.W., Murphy T.J., Garner E.L. and Shields W.R. (1973)**
Absolute isotopic abundance ratio and atomic weight of a reference sample of rhenium. Journal of Research of the National Bureau of Standards, 77A, 691-698.

**Hart S.R. and Zindler A. (1989)**
Isotope fractionation laws: A test using calcium. International Journal of Mass Spectrometry and Ion Processes, 89, 287-301.

**Hirata T. (1996)**
Lead isotopic analyses of NIST Standard Reference Materials using multiple collector inductively coupled plasma-mass spectrometry coupled with a modified external correction method for mass discrimination effect. The Analyst, 12, 1407-1411.

**Lee D.C. and Halliday A.N. (1995)**
Precise determination of the isotopic compositions and atomic weights of molybdenum, tellurium, tin and tungsten using ICP magnetic sector multiple collector mass spectrometry. International Journal Mass Spectrometry and Ion Processes, 146/147, 35-46.

**Longerich H.P., Fryer B.J. and Strong D.F. (1987)**
Determination of lead isotope ratios by inductively coupled plasma-mass spectrometry (ICP-MS). Spectrochimica Acta, 42B, 39-48.

**Ludwig K. (2003)**
IsoPlot/Ex: A geochronological toolkit for Microsoft Excel. Berkeley Geochronology Center, Special Publication No. 4.

**Maréchal C.N., Télouk P. and Albarède F. (1999)**
Precise analysis of copper and zinc isotopic compositions by plasma source-mass spectrometry. Chemical Geology, 156, 251-273.

## references


**Millet M.-A., Doucelance R., Schiano P., David K. and Bosq C. (2008)**
Mantle plume heterogeneity versus shallow-level interactions: A case study, the São Nicolau Island, Cape Verde archipelago. Journal of Volcanology and Geothermal Research, 176, 265-276.

**Pietruszka A., Walker R.J. and Candela P. (2006)**
Determination of mass-dependent molybdenum isotopic variations by MC-ICP-MS: An evaluation of matrix effects. Chemical Geology, 225, 131-136.

**Poirier A. (2001)**
Online rhenium fractionation correction using tungsten-doping technique on a magnetic sector ICP-MS. American Geophysical Union, Fall Meeting 2001, abstract #V22A-1007.

**Poirier A., Doucelance R. and Gariépy C. (2004)**
Radiogenic isotope investigation of the St-Robert H5 fall. Meteoritics and Planetary Science, 39, 1983-1993.

**Poirier A. (2006)**
Re-Os and Pb isotope systematics in reduced fjord sediments from Saanich Inlet (Western Canada). Earth and Planetary Science Letters, 249, 119-131.

**Rehkämper M. and Halliday A.N. (1998)**
Accuracy and long-term reproducibility of lead isotopic measurements by multiple-collector inductively coupled plasma mass spectrometry using an external method for correction of mass discrimination. International Journal Mass Spectrometry, 181, 123-133.

**Rehkämper M. and Mezger K. (2000)**
Investigation of matrix effects for Pb isotope ratio measurements by multiple collector ICP-MS: Verification and application of optimized analytical protocols. Journal of Analytical Atomic Spectrometry, 15, 1451-1460.

**Reuer M.K., Boyle E.A. and Grant B.C. (2003)**
Lead isotope analysis of marine carbonates and seawater by multiple collector ICP-MS. Chemical Geology, 200, 137-153.

**Russell A.D., Papanastassiou D.A. and Tomborello T.A. (1978)**
Ca isotope fractionation on the earth and other solar system materials. Geochimica et Cosmochimica Acta, 42, 1075-1090.

**Shirey S.B. and Walker R.J. (1995)**
Carius tube digestion for low-blank rhenium-osmium analysis. Analytical Chemistry, 67, 2136-2141.

**Thirlwall M.F. (2002)**
Multicollector ICP-MS analysis of Pb isotopes using a $^{207}Pb$-$^{204}Pb$ double spike demonstrates up to 400 ppm/amu systematic errors in Tl-normalization. Chemical Geology, 184, 255-279.

**Völkening J., Köppe M. and Heumann K.G. (1991)**
Tungsten isotope ratio determinations by negative thermal ionization mass spectrometry. International Journal Mass Spectrometry and Ion Processes, 107, 361-368.

**Walder A.J., Platzner I. and Freedman P.A. (1993)**
Isotope ratio measurement of lead, neodymium and neodymium-samarium mixtures, hafnium and hafnium-lutetium mixtures with a double focusing multiple collector inductively coupled plasma-mass spectrometer. Journal of Analytical Atomic Spectrometry, 8, 19-23.

**White W., Albarède F. and Télouk P. (2000)**
High-precision analysis of Pb isotope ratios by multi-collector ICP-MS. Chemical Geology, 167, 257-270.

**Woodhead J. (2002)**
A simple method for obtaining highly accurate Pb isotope data by MC-ICP-MS. Journal of Analytical Atomic Spectrometry, 17, 1381-1385.